



JENGRAIMUKH COLLEGE

জেংবাইমুখ মহাবিদ্যালয়

Affiliated to Dibrugarh University

Estd: 1973

**Supporting Documents for
NAAC Self Study Report (SSR)
(3rd Cycle)**

Period: 2018-2023

Criterion 3

Research, Innovations and Extensions

**Key Indicator
3.3**

Research Publication and Awards

**Metric No.
3.3.1**

Total Number of Research Papers in the Journals Notified on the UGC website during last five years.

***Prepared and Submitted by
Jengraimukh College***

JENGRAIMUKH COLLEGE

জেংবাইমুখ মহাবিদ্যালয়

Affiliated to Dibrugarh University



**Policy Document on Research
Papers**

Research Papers

LIST FOR SUPPORTING DOCUMENTS

1. **Das, Binod.**, Mising Community of Majuli: At a Glance, Published in Assam College Teachers Association Journal Vol: XLrsI, 2029, ISSN: 2229-69
2. **Das, Binod.**, Prospects and Problems of Ecotourism in Majuli with special reference to Mising Tribes , Economics, Aruhu Kuruhu, 2023, ISSN: 2347-5048
3. **Changsan, L.**, Status and Position of Women – A brief study of the Kuki Women in Assam, Journal of Emerging Technologies and Institutional Research, 6(6), Page No. 529-532. Department of Pol. Science, 2029, ISSN: 2349-5162
4. **Saikia, P.**, Binsha Shatikar Nabboir Dashakar Asomiya Chutigalpat Samakalin Santrash : Eti Bishleshan, Pierian Spring, 156-163. 2019, ISSN no. 2349-3410.
5. **Saikia, P.**, Asom Andolana : 'Asomiya'r Atmapratishthar Sangram, Srotaswini, Women's cell, Kamrup College, 2019, Page 190-195 , ISSN no. 2454-8146
6. **Saikia, P.**, P. Asom Andonal aru Asomar Sanskritik Jagaran, Satsari, published by Jayanta Baruah, Guwahati-21 in August, 2019, ISSN no. 2319-8893. 30-35
7. **Saikia, P.**, Asom Andolanar Prekshapatat Janajatiya Astitya aru Parichayar Punaruthan, Satsari, published by Jayanta Baruah, Guwahati-21, February, 2019, Page 46-53, ISSN no. 2319-8893.
8. **Boruah, M. J.**, Gogoi, A., & Ahmed, G. A. Physics, Scattering by interstellar graphite and fayalite composite dust analogues: computer simulation and laser-based laboratory measurements, Journal of Astrophysics and Astronomy, Springer, 2021, ISSN: 0973-7758, doi:10.1007/s12036-021-09713-7
9. **Das, Binod.**, Socio economic condition of Mayamara Sect in Majuli, Economics, Nagfani, 2023, ISSN: 2321-1504
10. **Tamuly, B.** and Saikia, L.R., "Physico-chemical Analysis of Crude Oil Contaminated Soil in and around Dikom Oil Well of Assam", Botany, Ecology Environment and Conservation, 2022, ISSN: 0971-765X, doi: 10.53550/EEC.2022.v28i04.059
11. **Gogoi, C.R.**, Rahman, A., Saikia, B. and Baruah, A. Protein Dihedral Angle Prediction: The State of the Art Chemistry, Chemistry Select, 2023, ISSN: 2365-6549, doi.org/10.1002/slct.202203427
12. Rahman, A., Saikia, B., **Gogoi, C.R.**, Baruah, A., "Advances in the understanding of protein misfolding and aggregation through molecular dynamics simulation", Chemistry, Progress in Biophysics and Molecular Biology, 2022, ISSN: 0079-6107, doi.org/10.1016/j.pbiomolbio.2022.08.007
13. Dutta, B., **Hazarika, R.**, Kalita, B.R., Bhuyan, K., Bhuyan, P.K., Ionospheric variations during geomagnetic storms of 7–8 September, 2017 "", Physics, IEEE Xplore, 2022, ISSN: 2473-2001, DOI: 10.23919/URSI-RCRS56822.2022.10118457
14. **Deka, Nandita.**, Challenges faced by Transwomen and hijras In Assam with special reference to NRC and CAA Debate, Political Science "Research Journal of Humanities and Social Science", 2022 ISSN: 2454-3837

15. **Saikia, P.**, Mishing Janagoshtheer Janma. Mrityu Aru Bibah Shamparkeeya Loka-bishwas Assamese, Pierian Spring, 2021, ISSN: 2349-3410
16. Dutta, R., Dhar, S., Baruah, K., Dutta, N., **Doley, S.**, Sedai, P., Dolui, S.K., Ray, B.C. and Karmakar, B., Removal of organic solvents and oils from waste water by absorption with cross linked poly (ethylene-co-vinyl acetate) modified by acetyl alcohol, Chemistry, Journal of Water Process Engineering, 2022, ISSN: 2214-7144, doi: 10.1016/j.jwpe.2022.103073
17. Dutta R., Baruah B., Dhar S., Ahmed A, Dutta N., **Doley S.** et al., Removal of oils and organic solvents from wastewater through swelling of porous crosslinked poly(ethylene-co-vinyl acetate): Preparation of adsorbent and their oil removal efficiency, Marine Pollution Bulletin, **186**, Elsevier, 2022, ISSN: 0025-326X, <https://doi.org/10.1016/j.marpolbul.2022.114488>
18. Ahmed, S., Lahkar, S., **Doley, S.**, Mohanta, D. and Dolui, S.K., A hierarchically porous MOF confined CsPbBr₃ quantum dots: Fluorescence switching probe for detecting Cu (II) and melamine in food samples, Journal of Photochemistry and Photobiology A: Chemistry, 2023, ISSN:2454-3837, doi.org/10.1016/j.jphotochem.2023.114821
19. Baruah, K., Dutta, R., **Doley, S.**, and Dolui, S. K., Grafted polymeric organogel using low molecular weight gelator as an effective medium for expulsion and purification of cationic dyes and organic pollutants from contaminated surface water, European Polymer Journal, 2023, ISSN: 0014-3057, doi.org/10.1016/j.eurpolymj.2023.112213
20. **Boruah, K.**, Hazarika, B., Bashirov, A. E., Solvability of differential equations by numerical methods, Bol. Soc. Paran. Mat., 2021, ISSN: 0037-8712, doi:10.5269/bspm.39444
21. **Boruah, K.**, Hazarika, B., Some basic properties of bigeometric calculus and its applications in numerical analysis, Afr. Mat., 2021, Springer, ISSN: 1012-9405, doi:10.1007/s13370-020-00821-1
22. Garain, S., Kuila, S., Garain, B.C., Kataria, M., **Borah, A.**, Pati, S.K. and George, S.J., Arylene diimide phosphors: aggregation modulated twin room temperature phosphorescence from pyromellitic diimides, Chemistry, Angewandte Chemie International Edition, 2021, ISSN: 1521-3773, doi:10.1007/s10965-021-02485-2
23. Petersen, J B., Ding You-Song., Gupta S., **Borah, A.**, Electron Paramagnetic Resonance Spectra of Pentagonal Bipyramidal Gadolinium Complexes, *Inorg. Chem.* 2023, 62, 8435–8441, ACS Publications <https://doi.org/10.1021/acs.inorgchem.3c01227>
24. **Borah, A.** and Murugavel, R., Magnetic relaxation in single-ion magnets formed by less-studied lanthanide ions Ce (III), Nd (III), Gd (III), Ho (III), Tm (II/III) and Yb (III)", Chemistry Coordination Chemistry Reviews, 2022, 0010-8545, doi: 10.1016/j.ccr.2021.214288
25. **Borah, A.**, Saha, J., Sharma, S., Chaudhary, S., Gupta, S. K., Rajaraman, G., ... & Murugavel, R., Ligand-Field Directed Electronic Effects in Heterogenized Bifunctional Co (II) Molecular Clusters Accomplish Efficient Overall Water Splitting. Chemistry, ACS Catalysis 2023, 2155-5435, doi.org/10.1021/acscatal.2c05942
26. **Borah, A.**, Dey, S., Gupta, S. K., Rajaraman, G., & Murugavel, R., Field-Induced SIM Behaviour in Early Lanthanide (III) Organophosphates Incorporating 18-crown-6, Chemistry, Dalton Transactions, 2023, 1477-9234, doi.org/10.1039/D3DT01206A

ISSN : 2229-693X

অসম কলেজ শিক্ষক সংস্থা আলোচনী
Assam College Teachers' Association

JOURNAL

Peer Reviewed
Volume : XLI, 2019



EDITORS
Ananta Rajbongshi
Sanjib Phukan

MISING COMMUNITY OF MAJULI : AT A GLANCE

Binod Das

Asst. Professor, Jengraimukh college, Majuli

Abstract :

Every society has been facing some social, economic and political problems which stand on the way of need. Systematic studies to sort out the causes and their remedies are relatively essential. Needless to say that without finding out the real cause, its remedy is not predictable. It is quite sincerely anticipated that the findings and conclusions drawn from the study will contribute a lot to the store houses of knowledge of the readers engaged in higher study about the origin, social, religion, cultural, political and economic life of the Mising community.

Introduction :

Assam is diversified by its various castes and sub-castes. The Mising community is originally known as 'Miri, the second largest tribes of Assam scattering mostly in eight districts of upper Assam, viz. Golaghat, Jorhat, Sivasagar, Dibrugarh and Tinsukia in the southern bank Sonitpur, Lakhimpur Dhemaji on the northern bank of the mighty river Brahmaputra.

The Mising tribe is one of the most dominant tribes of Majuli Distric. As per 2011 census of India, the total population of Majuli was 1,71,662. Out of it 76,317 belongs to scheduled tribes (ST) i.e. 44 per cent of the total population. The overall decadal growth rate of tribal population of Majuli since 2001 to 2011 was 10.64 per cent. The total number of cadastral villages of Majuli is 243, where 96 villages belongs to Mising community, 3 villages belong to Deories and 1 village belongs to Sonowal Kachari.

The tribes mean very backward section of the society. Those people who were backward mainly on social and economic fronts they are regarded as Scheduled Tribes(ST). According to the social status they are labelled as untouchables. On the basis of the criteria of untouchability they are specified and considered as ST by constitutional order of Assam, under the provision of Articles 342 part (i) and 34part (ii). The article 17 provides for abolition of untouchability. The national objective of identifying them as ST is to uplift their socio-economic status as per with the General people.

In our study area untouchability is not so acute because of the influence of Neo-Vaishnavism and Christianity. Yet, untouchability in various disguised forms is prevalent in social gathering or in private meet or in eating in the same place or sitting in the same line with higher castes and inter-caste marriage is not held formally. As a result, they have been separated from the rest of the society. This aloofness results in their socio-economic stagnation.

The Mising were formerly referred to as 'Miri' during the Ahom reign. The non-tribes people of Assam call Mising as 'Miri'. But they like to call themselves as 'Mising'. During the 15th century, this word was first used by the Vaishnava Guru Sankardeva. Therefore, these words also appear in the articles written by the English administrators, tourists and Baptist Missionaries who came to Assam in the 19th century. The word Mising was divided into the syllabi i.e. 'Mi' as man and 'Sing' as white i.e. the holy man. According to E.A.Gait, Mising means middle man. Again, ex-president of

Asom Sahitya Sabha, Dr. Lila Gogoi said that very simple men are the Mising. This word was broadly used during the period of 1960s and 1970s after independence.

Regarding arrival of the Mising people in Assam, there is no any definite data in history. Someone deduced that they were contemporary of Ahom. Many of them believed that originally they lived in the North Mountains of Assam i.e. the Siyang and the Subansiri district of modern Arunachal Pradesh. In search of fertile agricultural land, they came down from hills to plains group wise. Someone opined that due to regular fights or clashes among the clans viz. Paddam Minyong, Galong, Damro etc. had to migrate. They have come from different places at different times in Assam. Their movement to the plains started in the last part of the reign of the Chutia kings as per historical records

There are nine sub-clans of Mising viz. Pagro, Oyan, Sayang, Moying, Delu, Dambuk, Tamar, Chamaguria and Somuang. The people of the Mising community live in the separate group from the rest of the communities. They like to settle themselves in the river banks for fresh air, using of fertile land and easy transportation. They were made of wood and bamboos. The front side of the houses are generally faced the river. The houses were on piles of about 4 ft. to 5 ft. above the ground. The houses are about 40 ft. to 100 ft. in length and 10 ft. to 15 ft. in width. The dimension of the houses were looked north-south in origin. A few sections of Misings now speak Assamese, but they use their own dialect amongst them. Various types of utensils are used by the Mising, which is similar to the Non-Misings.

The food habits of Mising tribes of Assam are bearing special characteristics. Rice is the staple food. Chicken and pork with rice are their favourite dishes. All the villagers go together for fishing in the tanks, rivers, and ponds. The Mising women prepare liquor with boiled rice called *Apong*. The people drink in the evening to get relief from extreme fatigueness of hard day's work. The whole family drinks *apong* and guest are also offered *apong* before meal. On festive occasions Mising people take *Puarng Apin* with pork.

The Mising women of Assam are playing an important role in the economic life of the family viz. rearing hens, pigs, goats, ducks etc. They have also

some additional activities at home like wearing, cooking, fishing, washing, gathering firewood, childcare etc. The creation of *Miri Jim* made by the women is most popular blankets which is famous not only in Assam but all over in India also. The women weave the traditional garments like *Ribi Gasang*, *Yambo*, *Gapa Gare*, *Gapa*, *Gonro Ugan* etc. The major portions of the Mising women are self-dependent.

The institution of marriage of Mising tribes of Assam is different from others. The marriage within the same clan i.e. Pegu with Pegu or Doley with Doley will never be permitted. Similarly marriage is restricted within the sub-clans. Cross-cousin marriage is common among them. After the marriage, the bridegroom and her children accept surname of the father. Monogamy is the general practice, polygamy is also seen in the community but is considered as dishonour and polyandry is restricted. Similarly widow or widower marriage is possible but child marriage is strictly prohibited. The dowry, which is known as *Ga-Dhan* is prevalent in the marriage in the Mising society.

The Mising people have preserved many of their ancient beliefs, customs and traditions. At vedic age, the worship of gods and goddesses to get rid of danger, was a regular practice of the Mising community. They regarded sun, moon, fire, rain, water, tree etc. are the gods and the goddesses. The gods and the goddesses are the creators, the masters or the owners of different things and forms of land-water as they believed. They are still worshippers of *Uyu* or spirit. The Mising regard the sun (*Do:ny*) and the moon (*Po:lo*) as their ancestors. They regard the moon as their father and the sun as their mother. On the eve of any ritual and festival they recite mantras offering their worship to *Do:ny* and *Po:lo*. Some of the main festivals of Misings are *Po:rag*, *Ali-ai-ligang*, *Dobur*, *Asi uyu*, *Yumrang Uyu* and *Dod gang*.

As a part of the study, information regarding socio-economic condition of 110 nos. of Mising tribal households are randomly selected from 10 Gaon Panchayats of Majuli. To know the socio-economic condition of Majuli, we purposively selected 10 sample villages from 10 Gaon Panchayats. The sample villages are selected in such a way that they reflect all the dimensions of the Mising community of Majuli.

The aims and objectives of my study is to split out the socio-economic conditions of Mising community of Majuli district in various dimensions. To know about their socio-economic conditions we confined two consecutive years i.e. 2018 and 2019.

Education :

Education is the major criteria for the upliftment of a society. Except basic need, vocational, technical and professional educations are essential for job placement and acquiring a higher status. To obtain the real scenario of the literacy level of the households we confined following heads.

Table 1 : Distribution of respondent couples by the level of education

Sl. No.	Level of Education	No. Of Husbands	%	No. of Wives	%
1	Illiterate	32	29.91	45	40.91
2	Up to primary (i-v)	26	24.29	25	22.73
3	Middle School completed (vi-ix)	21	19.63	19	17.27
4	High School completed	17	15.89	13	11.82
5	Beyond High School	11	10.28	8	7.27
	Total	107	100	110	100

The table reveals that out of 107 husbands 29.91 per cent are illiterate and 70.09 per cent are literate. Similarly out of 110 no. of wives 40.91 per cent are illiterate and 59.09 are literate. The total literacy is 64.59 per cent and the gap between the male and female is 11 per cent. The literacy level of female is found to be less than male. According to 2011 census of India, the literacy rate is 74.04 per cent, where 82.14 per cent is male and 65.46 per cent is female. By comparison of all data we can conclude that the Mising people are lagging behind in case of literacy. After independence, union and state government adopted various policies for STs to improve the educational status as

constitutional privileges. Despite these special facilities, they are still poor in education. In case of female education they are still lagging behind the male in my study area.

Income Distributors :

Income is the most important key factor to know about the economic condition. In order to have an idea regarding the intensity of poverty among the ST people, in the words of IRDP, booklet published by DRDA, Kamrup, Assam, we have graded the sample households into five categories on the basis of their income viz. The monetary values of the respondent's came from agriculture and allied activities.

Table 2 : Distribution of households by family income.

Sample households	Income categories	No. Of Households	%
Extremely poor	0 ----- 4000	4	3.64
Very much poor	4000-----6000	18	16.36
Very poor	6000 -----8500	35	31..82
Poor	8500 -----1 1000	28	25.45
Rich	1 1000 +	25	22.73
	Total	110	100.00

From the table it is clear out of 110 households only 22.73% cross the boundary line of poverty and other 77.27% is belong to poverty line. The intensity of their poverty is due to socio-economic backwardness arising out of both economic factors like lack of economic and natural resources, inequalities of income and wealth, low productivity, unfavourable market and

non-economic factors like conservation, eastism, religious and joint family system.

Occupational Pattern :

To obtain the real picture of the occupational pattern of the surveyed respondents we have divided their occupation in to six classes. The maximum income earned by the respondents is from agriculture and allied activities.

Table 3 : Distribution of couples by occupational status.

Sl. No.	Name of occupation	No. of husbands	%	No. of wives	%
1	Cultivator	54	50.47	62	56.36
2	Service	11	10.28	6	5.45
3	Business	9	8.41	2	1.82
4	Agricultural labours	25	23.36	28	25.45
5	Marginal workers	3	2.81	2	1.82
6	Non-workers	5	4.67	10	11.00
	Total	107	100	110	100

The Table reveals the distribution of couples by occupational status of sample households. From the table it is clear that the major portion of male and female i.e. 50.47 per cent and 56.36 per cent are directly engaged in agriculture and allied activities. Therefore, only 1.82 per cent wives are engaged in business. It is

also observed that wives participation in agriculture and allied activities are more than husbands.

Family Structure :

Both joint and nuclear families are found among the Mising community. As time passes the nuclear families have transferred due to economic hardship and depending on ideology of individualism and materialism.

Table4 : Distribution of household by family type.

Family type	No. of Households	%
Nuclear	93	84.55
Joint	17	15.45
Total	110	100.00

The Table shows that out of 110 households, 84.55 per cent are nuclear and 15.45 per cent are joint type families. But the portion of nuclear type of family is higher than the joint family.

Housing Condition :

The Mising community have some speciality in case of living, which identifies themselves as tribes at first sight.

Table 5 : Distribution of Households by Housing condition.

Type of House	No. of Households	%
Pakka	12	10.91
Semi-pakka	36	32.73
Kutchha	62	56.36
Total	110	100.00

The Table reveals that 10.91 per cent have Pakka houses, 32.73 per cent have Semi-pakka and 56.36 per cent are found Kutchha houses. A large number of downtrodden people are lived in kutchha houses.

Living Room :

Table 6 : Distribution of sample households by living rooms.

No. of living rooms	No. of households	%
Up to 3	54	49.00
4 ---- 6	45	41.00
7 +	11	10.00
Total	110	100.00

From the table it is also observed that major portion of families i.e. 49 per cent are living up to 3 nos. of rooms, 41 per cent have 4 to 6 nos. of rooms and only 10 per cent have 7 nos. and above rooms.

Family Size :

Table 7 : Distribution of sample households by family size.

No. of family Members	No. of households	%
Up to 4	41	37.27
5 ---- 8	58	52.73
9 +	11	10.00
Total	110	100

The Table shows that the family size of the study area is mostly big having 5 to 8 members i.e. 52.73 per cent. The average family size is worked out to be 5.41 per cent.

Age Effective Marriage :

Table 8 : Distribution of Respondents by age at Effective Marriage.

Respondents at Effective Marriage (Years)	No. of Respondents	%
Up to 18	50	45.45
19 ---- 24	38	34.55
25 +	22	20.00
Total	110	100

The custom of early marriage is found to be very much prevalent among the women of the study area, as 45.45 per cent got married within the age of 18 years, the legal minimum age of 19 to 24 have 34.55 per cent and 25 years and above have only 20 per cent.

Sex Ratio :

There is no 1 : 1 correspondence in the male and female in case of birth, the number of male babies are always slightly high.

Table 9 : Age specific sex-ratio of the sample population.

Age (Years)	No. of Females	No. of Males	Total	Sex-ratio
0 ---- 4	46	43	89	1069.77
5 ---- 9	44	56	90	956.52
10 ---- 14	25	30	55	833.33
15 ---- 19	23	29	52	793.13
20 ---- 24	20	22	42	909.10
25 ---- 29	21	20	41	1050.00
30 ---- 34	24	21	45	1142.85
35 ---- 39	22	23	45	956.52
40 ---- 44	19	25	44	760.00
45 ---- 49	20	22	42	909.10
50 ---- 54	12	15	27	800.00
55 ---- 59	8	6	14	1333.33
60 +	5	4	9	1250.00
Total	289	306	595	944.44

The table shows that out of 595 total sample populations, 289 are found females and 306 are males. The sex-ratio among the Mising community is found to be 944 females per 1000 males as against the sex-ratio of 940 in India (2011 census).

Conclusion :

In our concluding remarks we may say that the proper implementation of various govt. schemes, Non-Government Organisations like TMPK, MMK, Village Unnyan Samities, Gaon Panchayats, Mahila Samities are required for changing socio-economic condition in desired directions.

Reference :

1. Borah, Rupjyoti: Demographic Profile of Adis. Dibrugarh, Department of Economics, Dibrugarh University.
2. Shyam, Suprity : Fertility Behaviour of the Konyak Nagas of Assam.
3. Taid, T. R. Glimpses: Dhemaji, General Secretary Mising Agom Kebang.
4. Bazbaruah, D. K.: Socio-Economic Change and Dimension of Social Mobility among the Kaibartas of Assam.
5. Padun, N. :Mising Thought Mising Eyes, Jorhat: I CARD, P. B. 125. :Mising Lokageet. Dhemaji: Prabhat Mili on behalf of Mising Agom Kebang.
6. Kagyung, B:Mising Sanskritise Alekhya.
7. Vidyarti, L. P. :The Tribal Culture in India. New Delhi: Concept Publishing Company.
8. Mahanta, P. K.: Majuli. Jorhat. Urukhapaja, Bimbari: Bhigumuni.
9. Kothari, C. R. :The Tribal Culture in India. New Delhi: Naurang Rai, Concept Publishing Company.
10. Gunamoni, N. Aspects of Tribal Village Economy- A Sociological study of the Mising Village Kalitapara , Jorhat

ISSN - 2747 - 5048



ಅರುಣ ಕುರುಣ

ಸಾಹಿತ್ಯ ಮತ್ತು ಸಂಸ್ಕೃತಿಯ ಶೋಧದಲ್ಲ...

Arundha Kuruhu

In Pursuit of Literature and Culture...

ಕಂ. ೩, ಸಂ.೩, ಜನವರಿ ೨೦೨೩ Vol. 13 Issue 51 January, 2023

ಯುಜಿಸಿ ಕೆಆರ್-ವಜ್ಜಯಲ್ಲರವ ಮತ್ತು ತಜ್ಞ-ಪರಿಶೀಲಿತ ದ್ವಿ-ಭಾಷಾ ಪತ್ರಿಕೆ
UGC CARE - LISTED AND PEER - REVIEWED BI-LINGUAL JOURNAL



ISSN: 2347 - 5048

ಅರುಹು ಕುರುಹು

ಸಾಹಿತ್ಯ ಸಂಸ್ಕೃತಿಯ ಶೋಧದಲ್ಲಿ

Aruhu Kuruhu

In pursuit of Literature and Culture

ಯುಜಿಸಿ ಕೇರ್ ಪಟ್ಟಿಯಲ್ಲಿರುವ ಮತ್ತು ತಜ್ಞ-ಪರಿಶೀಲಿತ ದ್ವಿ-ಭಾಷಾ ಮಾಸ ಪತ್ರಿಕೆ
UGC CARE-LISTED AND PEER-REVIEWED BI-LINGUAL MONTHLY JOURNAL

ಸಂಪುಟ : ೧೩ ಸಂಖ್ಯೆ : ೫೧, ಜನವರಿ-೨೦೨೩

Volume :13, Issue : 51, January-2023

PEER REVIEW COMMITTEE

Prof. Niranjan Vanalli

Vice-Chancellor, Bengaluru North University, Kolar

Prof. Vijayakumari S Karikal

Director, KKIS, Mysuru University, Mysuru

Prof. Muzafer Assadi

Professor, Mysore University, Mysuru

Dr. Anamika

Asst. Professor, Jawahar Nehru University, Delhi

Dr. N. Amareswaran Reddy

Asst. Professor, NEHU, Shillong, Meghalaya

Dr. H. N. Narasingappa

Professor, Hasanamba B.Ed College, Hassan

Dr. Meti Mallikarjuna

Professor, Kuvempu University, Shivamogga

Dr. Shanthappa N Dambala

Professor, Kannada VV Extension Center, Deodurga

Dr. Paramashivamurthy

Professor, Tumkur University, Tumkur

Dr. Vijayakumar H. Vishwamanava

Professor, Karnataka Central University, Kalaburgi

ಸಂಪಾದಕರು

ಪ್ರೊ. ಎಚ್ ಎಸ್ ಉಮೇಶ

Editor

Prof. H.S Umesh

ವ್ಯವಸ್ಥಾಪಕ ಸಂಪಾದಕರು

ಹಾ ತಿ ರತ್ನ

Managing Editor

H T Rathna

ಮುಖಪುಟ ವಿನ್ಯಾಸ

ಗಂಗೋತ್ರಿ ಮಹೇಶ್

ಶಾಂತಿಕ ಸಹಕಾರ

ವಿಫುಲ್ ಹಾಲತಿ

ಅರುಹು ಕುರುಹು ದ್ವಿ-ಭಾಷಾ ಮಾಸಿಕ ಪತ್ರಿಕೆ
#೧೦, 'ಬೆಳಕು', ಕುವೆಂಪು ರಸ್ತೆ, ಪೃಥ್ವಿ ಬಡಾವಣೆ, ದಟ್ಟಿಗಲ್ಯ ೩ನೆಯ ಹಂತ
ಮೈಸೂರು-೫೭೦೦೩೩, ಫೋನ್: ೯೮೮೬೬೨೨೨೨೨

ARUHU KURUHU Bi-lingual Monthly Journal

10, Belaku, Kuvempu Road, Pruthvi Layout, Dattagalli 3rd Stage

Mysuru-570033, mob: 9886622833,

Email: aruhukuruhu@gmail.com

Prospects and Problems of Ecotourism in Majuli with special reference to Mising Tribes

Binod Das

Assistant Professor, Department of Economics
Jengraimukh College, Majuli, Assam. binodd463@gmail.com

Abstract: In this paper, we have studied about prospects and problems of ecotourism in Majuli with special reference to Mising Tribes. There are great prospects of ecotourism in Mising tribes like Festival: Ali-A:ye-Ligang, Handloom and textile, Food habits, Traditional House and dance and songs. We have also studied the major problems of ecotourism in Mising tribes.

Introduction: Ecotourism is a form of tourism involving responsible travel to natural areas, conserving the environment, and improving the well-being of local people. Majuli has plenty of natural beauty and resources like rich culture, bio-diversity, archeological remains etc, and enough scope for tourism promotion. The various tourist-attracted themes are Satras of Majuli, the colorful culture of Mising tribes, Pottery making, Mask making, Raas Leela, Pal Nam, migratory birds, Flora and Fauna etc. In this paper, we are trying to focus on tribal tourism only. The Mising were formerly referred to as 'Miri' during the Ahom reign. The non-tribes people of Assam call Mising as 'Miri'. But they would like to call themselves as 'Mising'. During the 15th century, this word was first used by the Vaishnava Guru Sankardeva. Therefore, this word also appears in the article written by the English administrators, tourists and Baptist Missionaries who came to Assam in the 19th century. The word Mising was divided into syllabi i.e. 'Mi' as man and 'Sing' as white i.e. the Holy man. According to E.A. Gait, Mising means middle man. Again, the ex-president of Asom Sahitya Sabha, Dr. Lila Gogoi said that very simple men are the Mising. This word was broadly used during the period of 1960s and 1970s after the independence. As per 2011 census of India, the total population of Majuli was 1,71,662. Out of it 76,317 belongs to scheduled tribes (ST) i.e. 44 per cent of the total population. The overall decadal growth rate of tribal population of Majuli from 2001 to 2011 was 10.64 percent. The total number of cadastral villages of Majuli is 243, where 96 villages belong to Mising

community, 3 villages belong to Deories and 1 village belong to SonowalKachari.

Regarding the arrival of the Mising people in Assam, there is no definite data in history. Someone deduced that they were contemporary of the Ahom. Many of them believed that originally they lived in the North Mountains of Assam i.e. the Siyang and the Subansiri district of modern Arunachal Pradesh. In search of fertile agricultural land, they came down from hills to plains group wise. Someone opined that due to regular fights or clashes among the clans viz. Paddam, Minyong, Galong, Damro etc. they had to migrate from hill to plain areas of Assam. They had come from different places at different times in Assam. Their movement to the plains started in the last part of the reign of the Chutia kings as per historical records.

Methodology: Data is collected through both primary and secondary sources with the help of observation and interviews with local people. Here, the descriptive research method is used.

Objectives: The main objectives of this work are as follows:

1. To highlight the potentialities of ecotourism in Mising tribes.
2. To highlight the problems associated with tribal tourism.
3. To find out the relationship between tribal life style and ecotourism.

The Prospect of ecotourism in Mising tribes: There are great prospects of ecotourism in Mising tribes by using proper utilization of resources in a planned manner. Some of the prospects are given below-

(a) Festival: Ali-A:ye-Ligang is one of the most popular festivals of Mising tribes, celebrates on the first Wednesday of the month of Phagun. The term Ali-A:ye- Ligang means the festival of sowing seeds; Ali means seeds i.e. Alu, A:ye means Fruits and Ligang means starting day of sowing seeds. This festival is equivalent to Bahag Bihu of others community. It is a colorful festival of Misings associated with agriculture. The festival is marked by organizing a grand community feast with various traditional dishes, especially made with Pork, Purang Apin (Boiled rice c beer). Nowadays govt. of Assam celebrated Ali-A:ye-Ligang centrally in every year for the greater interest of the state. Po:rag is another agricul-

tural festival observed by the Mising community. It is celebrated at the post-harvesting periods i.e. August-September after harvesting the ahu crops, or during the season of November-December after harvesting the Sali crops. Po:rag is popularly known as Nara ChigaBihu by others. Both the festival attracted tourists for their traditional culture.

b) Handloom and textile: Mising women can weave golden dreams in cloths, and pour their hearts out on them. The handloom products woven by womenfolk of Misings are renowned. The creation of *Miri Jim* made by women is the most popular blanket which is famous not only in Assam but all over India also. Gadoo (A form of Blanket), Ege (Mising Mekhela), Ribi Gaseng (Mising Shawl), Mibu Galuk (Half sleeved Mising Jacket), Gonro Ugon (Mising Dhuti), Tongani Dumer (Mising Gamusa) are some of the master products woven by women folk.

c) Food habits: The Mising tribes generally take non-vegetarian food items on their choice and taste. Boiled foods, pork, chicken, naming (powder of dry fish) and fish is popular among the Mising tribes. Rice is the staple food. The Mising women prepare liquor with boiled rice called *Apong* (two types: *black beer and white beer*). People drink it to get relief from the extreme fatigue of a hard day's work. The whole family drinks *Apong* and guest are also offered *Apong* before a meal. On festive occasions, Mising people take *Puarng Apin* with pork.

d) Traditional House: The Mising people live in Chang Ghar. Chang Ghar is made from bamboo, wood and thatch. It is sustainable, eco-friendly and hygiene in nature. They believed that Chang Ghar is more secure from some natural challenges than other houses. The house is built facing to the river. For which, their house is North-South in direction. Now a days most of the Mising people like to have modern houses instead of traditional houses. But tourists are always preferred traditional houses. Therefore, the line of unique traditional houses always attracted tourists.

e) Dances and Songs: In the Ali-A:ye-Ligang festival, all boys, girls, men and women are dressed colorful clothes, and performed a dance named Gumrag. Maksong Soman is also a common dance to festive celebrations. It is a group dance performed by boys and girls at their house. Ruktab So:man is another typical ridiculous dance performed by adult people. There are various types of folk songs called Ni:tom performed

on different occasions. The types of Ni:tom are A:bang, Bi:rik, Midang, Oi-Nitom and Ko-Ninam.

In addition, there is enough scope for ecotourism in Mising community viz. mud house, buffalo riding, boat riding, traditional agriculture methods, wildlife, flora fauna, etc. could attract the new generation of tourists.

The major problems of ecotourism in Mising tribes: The major problems of ecotourism in Majuli are mentioned below-

- a) The major portion of the population of Majuli living in remote areas are educationally backward and their attitude towards tourism is not conceptually clear. They are not fully aware of the various segments of tourism and their participatory role is important for growth and development.
- b) There is a lack of dedicated office and tourist guides to assist the tourist.
- c) There is a lack of good accommodation and resort facilities for tourists in every part of Majuli.
- d) The present communication particularly ferry service is not secure. Illegal collection of money and frequent rises in fares hampers the economy to a great extent.
- e) Absence of proper ecotourism policy adopted by state govt. and central govt.
- f) Due to flood and erosion every year, Majuli can give opportunities to tourists only for three to four months.

REFERENCE:

1. Nath, D. The Majuli Island society: economy and culture, *Anshah Publishing*, 2009.
2. Padun, N. Mising through Mising eyes, *I-CARD, P.B. 125, Jorhat*.
3. Taid, T. Glimpses, *General Secretary Missing Agom Kebang, Dhemaji, Assam*, 2007.
4. Kagyung. B, *Missing Sanskrities Alekhya (Assamese edition), Bhigumuni, Urukhapaja, Birubari*, 1989.
5. Kuli, J.J. *The Mising: Their history and culture, Ayir, Guwahati*, 1998.

Status and Social Position of Women- A Brief Study of the Kuki Women in Assam

Lienkhomang Changsan

Assistant Professor

Department of Political Science

Jengraimukh College, Majuli Dist. Assam, India.

Abstract: The status of a woman can be judged mainly by the roles they play in society. Their roles are determined to a large extent through the system of descent. With the exception of Khasi, Jaintia and Garo in Meghalaya, the tribals of North East India mostly follow patriarchal form of society in which women have little or no role to play in the male dominated society. The study is an attempt to analyse the extent to which women are sanctioned in the domain of the power structure of the male dominated Kuki society of Assam. It also deals with the degree in which modern developments like education and their conversion into Christianity has ushered egalitarian ideas and principles in the relationship of men and women in the society.

Keywords-Women, Kuki, Status, Assam

Objective of the study:

The main objectives of the study are-

1. To identify the gender based inequality.
2. To analyse the various dimensions and consequence of injustice faced by women.
3. To put forward some suggestions based on the findings of the study.

Methodology:

In order to make a vivid study on the role and position of the Kuki women, descriptive and analytical methods of study are undertaken. Moreover valuable information has been extracted through interviews with the leaders of Kuki Women Society of Assam, male dominated institutions and intellectual groups of the society. Secondary sources like articles in magazines, books, journals, newspapers and books of literature provided the much needed help in course of study.

Area of the study:

The Kuki community is found in most of the North Eastern states of India. In Manipur, they constitute one of the major tribe besides the Meiteis. Likewise Nagaland, Mizoram, Meghalaya and Tripura have a considerable number of Kuki people. Assam is no exception to that. In Assam, the Kukis are found mostly in Karbi Anglong and Dima Hasao. The present study would be confined to the Dima Hasao which is a home of 15171 (Census 2011) Kuki tribes. It is in this area that the study is undertaken.

The Kukis- A Brief Introduction

The word *Kuki* is a generic term which includes a number of tribes and clans. This generic term covers a large number of people who migrated to different parts of North East India from contiguous areas lying further east at different points of time. The origin of the word *Kuki* is not known. It first appeared in Bengal, Rawling's writing of Cucis or mountaineers of Tiperah. There are many conjectures and theories about the origin of the word *Kuki*. The word *Kuki* is said to be coined by other people rather than the Kukis themselves.¹⁸ They are known by their neighbours by different names. The British knew them by *Kookies*, *Lushais*, *Pois*, *Sindus* and *Chins*. The plain people called these tribes *Kukis* or *Kuki-Chin*, whereas the Dimasa Kacharis called them *Thanggunsa* and in Manipur the Meitei name for the *Kuki* is *Khonjai* or *Khongsai*.

The Kukis are one of the indigenous tribe of Assam. Since time immemorial they have been living in the twin hill district namely, Karbi Anglong and Dima Hasao (formerly called North Cachar Hills). It is pertinent to note that like many tribes of North East India, the Kukis embraced a patriarchal form in which the male takes all the important decision in matters ranging from family issues to societal affairs.

Introduction:

The status of *Kuki* women is equivocal. They have important responsibilities at home and are accorded respect. At the same time the customary law is largely gender insensitive and restricts women's change in status in some fundamental change such as deprivation of inheritance of landed property. Although society does not exist in a vacuum and constantly transforms and invents itself, much of the earlier structure and customs continue to dominate.

In order to understand the position and role of women in a *Kuki* society, it is necessary to discuss the socio-cultural, economic, religious and political status.

Socio-cultural Status: In a *Kuki* society if a man dies without male issue, his property will devolve to his eldest/younger brother of his line or if he has no eldest/ younger brother or son, the property goes to the nearest male line. Therefore, a male child is always preferred to a female child to continue and preserve the lineage. Unfortunately the daughter has no share in landed property. The only items they are entitled to be those given at the time of marriage, which include *Tupheng* (Hoe), *Lel* (Basket with a cover in it) and *Thilbu* (implement for weaving). However of late, there has been a change and some thoughtful parents divide their property among both sons and daughters.

The institution of marriage is universal among the Kukis. Celibacy in any form was not encouraged by their cultural traditions. Celibacy was generally regarded as a social deviant, which was looked with disgrace. However, customs and culture does not always reduce women to a mere shadow. They were also honoured and were given importance in the society. Some of the customs which the Kukis follow till today are preferential marriage of mother's brother's daughter called *Nei* with the mother's own son. *Neinu* marriage (marrying a cousin

from the mother's side) was preferred as a means of cementing bonds between the concerned families. However with the passage of time *Neinu* marriage has become more and more insignificant.

Political Status: In the political sphere, women is regarded as unfit to participate in the decision making process as reflected in the folksong, "*Numei Thusei le jana vacha ham*" which means the chattering of a woman are like birds chirping at night. This signifies that woman has no say in the running of the village administration. There is no place reserved for them in the village council. However there are instances where woman have been able to influence the decision of the court and indirectly influence village affairs. It is when they stand in for a minor son or ailing husband. Political status of Kuki women is extricably linked to and determined by the prevalent patriarchal socio-cultural values and ethos of society. It is pertinent to note that no Kuki woman have so far been elected as members of the North Cachar Hills Autonomous Council.

Religious Status: In the religious affairs too, the position of Kuki women is not so encouraging. They have little or no place in the religious activity. The advent of Christianity saw the dawn of some space for the women since they began to enjoy some status. The church gives ample room for women to be leaders and to take part in the decision making process but here too it appertains only to the women organisation or society. So far, there is no such religious body in the study area in which a woman is allowed to plays the lead role except in women's wing. Similarly, the Kuki Women Society of Dima Hasao, established in 20-06-2014 have very limited role to play in the society although its President and the Secretary are entitled to cast their vote in the election of the executive members of Kuki Inpi Assam, the apex body of the Kukis in Assam.

The limited encouragement in religious affairs has no relevance in the social and political aspect of the society. It relates purely to religious matters.

Economic Status: Women have played a very vital role in the economic life of the Kuki society. All the household chores are considered as the responsibility of the women. The domestic work of Kuki women is well documented by J Shakespeare "A woman has to rise early, fill her basket with empty bamboo tubes and trudge off before daylight dawn the hills, and the supply of water is frequently so scanty that it takes her sometimes to fill her bamboos. Having conveyed her basket to the house, she has to set work cleaning the rice for the day on the shelf over the hearth and this she now precedes to pound in a mortar in front veranda, and winnow on an oval bamboo tray till it is clean enough for use. The breakfast of rice has then to be cooked, and it should be ready by the time her husband is awake. After the meal, the real work of the day begins."

This illustrates the sacrifice made by the Kuki women and at the same time shows the position and status she holds in the family. In fact there is no slack season for women. In this aspect there is another saying, "*Numei kholjin, suktum to jin*" which means a travelling woman carries with her a wooden pestle. So even while travelling women are expected to assist the host family. The Kuki women who are able to wake up early and do all the domestic works and know the pros and cons, the ins and outs of this art are highly valued in the marriage market.

The death of a divorced woman is treated as unnatural and therefore the body was taken out for burial not through the door but through the hole made in the wall. Rites and ritual were not performed. The practice is however not relevant in the contemporary days. A married woman does not have the right to claim her children after she is divorced by her husband.

Change and continuity in the status of women: The Kuki society of Assam has witness a substantial changes in the form of up-gradation of the status of women. Before the advent of the British and the Christian missionaries, the condition of women in the society was definitely not encouraging. In the traditional Kuki society, women have very little role to play. It is mainly because like many societies in north east India, the Kuki society is a male dominated in which customary law is still very strong.

However, this does not mean that women were completely disempowered. They are also honoured although in a different manner. According to T.S. Gangte, great importance is given to the relationship of the mother's brother and the sister's son in the Kuki society. This has significance in view of the practice of preferential marriage of mother brother's daughter. The *tucha-sunggao* relationship⁷ of the Kukis is also reckoned from a female line *luongman* or corpse price is another peculiar system of the Kukis. This is the price for a woman when she dies. Her father or elder/younger sons have to claim the price in their father's absence as a token of love and affection between the relatives. This also reveals the important position held by a woman in a family life.

In the traditional Kuki society, the women may not be given due recognition of her role but the existence of *Lom-Upanu* (female leader of a labour corps) itself is her important character as priestess. Among the many ceremonies and festivals that they celebrate, *Chang-ai* (rice festival) is the only one where the Kuki women play the leading role. While the role of men in human capital formation has been stresses and studied, women's role has been ignored though their roles were substantial. The economic role played by women in the traditional rural society particularly in the field of agriculture and the cottage industry is significant. Even in the past, the role of women, especially in the economic sphere was necessary. Her primary duty is to be a helpmate to her husband and to provide a warm and safe haven for her family.

In the contemporary Kuki society the condition and status of women have often seem to have improved. In one way domestic appliances like washing machine, rice cookers, water heaters, rice mill etc reduce the work time of the women but in reality it would be more pertinent to say that although the nature of work is different the workload of women still continues. To be more precise it is only a shift from old wine in a new bottle. As in the past, all domestic works are regarded as unproductive and do not form part of the family income. The traditional notion of clear cut division of labour still persists and it is taboo for man to do a woman's work. What is considered to be the job of a woman would not be touch by man, probably fearing of being dubbed as 'henpecked'. The workload of working women is greater as they bear a double burden, working at home and outside as they are expected to. This is perhaps the reason why women are not prominent in

the public domain. Also the laws, norms and mores customs of society are framed in such a way that to have a control over the women and to prove authority over them.

However it may be noted that with the coming of Christian missionaries and the spread of western education the position of women in the Kuki society witness some transformation. The Christian missionaries who brought education among the hills tribes has greatly benefitted in the empowerment of the life of the people of north east in general and the women in particular. However mention can be made that the untiring effort of the missionaries took time to create awareness on the necessity of educating both boys and girls. Therefore in many Kuki villages in the Dima Hasao district of Assam educating a girl child was considered by many parents as a waste of time and money.

Impact of Christianity and Modern Education: There were no fundamental or radical changes either in the status of women or the functioning of society, economy and politics until the advent of Christian missionaries who introduced not only a new faith to the Kukis but introduced them to modern education. The missionaries often exalted the Bible as the ultimate source of authority and made it as a condition that if an individual had to worship God he must be able to read and write. In other words, conversion into Christianity necessitates the Kukis into mass literacy campaign which benefits both men and women.

Today, changes have been witness in the sense that more and more women have been inducted in schools and in most cases it is found that the girls have perform better than the boys in boards and competitive examinations. In this connection mention may be made to the academic achievement of the next generation women of a Kuki village called Songpijang which is situated in the vicinity of Haflong town and their largest village in terms of the number with 349 house hold. This includes- Indian Administrative Service (1), Indian Engineering Service (1), Assam Civil Service (5), Bachelor of Medicine, Bachelor of Surgery (8), Bachelor of Engineering (1).

It is to be noted here that when the foreign missionaries came to the Northeast India, they not only brought the gospel but also brought education and enlightenment. They taught the importance of education and opened schools wherever they established their mission. When the missionaries opened School at Haflong, the district headquarter of N. C. Hills, many of the first generation Kuki Christian studied in the Mission Schools.

The British government did not give so much of importance to education or development works in this region. Even the works of education was handed down to the missionaries which was why the missionaries shouldered this responsibility. Therefore the impact and influence of the missionaries was great, especially on the Kukis who attended the mission schools. Literature too played an important role in creating a new tribal culture. This led to translation of not only the Christian scriptures but along with education, the Kukis of Dima Hasao seemed to have benefitted tremendously from the languages which produced in a written form.

Major Findings: From the above discussion, it has been observed that on the surface it would appear that Kuki women are empowered. But when one delves deeper, it is opponent that there is a bias in the customs and more which degrade the status of women. The study shows that (a) Kuki women hold a high position in the family but not in the society (b) Kuki women are subordinate to their husband in all aspects of life (c) they are subjected to unequal division of labour (d) with the introduction of modern education and the coming Christianity, the position of the Kuki women has undergone substantial changes.

However Kuki society is still bound by inherited laws of customs and the Kuki women continue to be affected by the absence of codified law. Kuki women are not entitled to inherit their father's or husband's property. It is true that Christianity has ushered in egalitarian ideas and principles particularly in the relationship of men and women in the society but the basic societal laws have not undergone any change.

Suggestions: Following are the few suggestions for the upliftment and protection of the Kuki women.

1. The age old custom and tradition should be revisited so as to empower women.
2. Women should be motivated to participate in political representation.
3. Both electronic and print media can play a very significant role in restructuring the tribal society in general and the Kukis in particular, acts as agents of political socialization for inculcating the values of gender equality.
4. There is need for more research and study on the status of women which can help in establishing society based on gender equality.

Conclusion: Education has also brought significant changes in the Kuki society by uplifting the status of women. In all the head hunting societies tribal women has no position in the society. This was mainly because while men led risky lives in hunting, women were left to do the household chores. Today, there is no discrimination between male and female child because importance is given to the education of both male and female. Kuki women today hold high post in the government offices. The old adage of women's place being the kitchen, seems to be no longer holds true in the Kuki society of Dima Hasao.

However, it is pertinent to note that women empowerment in the Kuki society is still a distant dream. The real empowerment of Kuki women could be achieved if their economic and social status is improved and when women take part in the decision making process. In a nutshell, if women can run their family successfully, one cannot doubt their capacity to lead the community nation. As Swami Vivekananda had said "that country and that nation which doesn't respect women will never become great now and nor will ever in future.

REFERENCES:

1. Ahuja Ram, 2002 : *Research Methods*, Rawat Publications, Jaipur.
2. Baruah K. Apurba., 2003 : *Tribal traditions and crises governance in North East India with special reference to Meghalaya*. Crisis State Programme Working Papers no. 22.

3. Bordoloi B.N & Thakur G.C. Sarmah, 1988 : *Tribes of Assam*, part 11, Tribal Research Institute, Assam, Guwahati.
4. Doungel Ncy, 2007 : *Puchon Pachon; Customary Practices of Thadou Kuki Part-I*, Manipur Tribal Development.
5. Gangte S. T., 1993. : *The Kukis of Manipur; A historical Analysis*, Gyan Publishing, New Delhi.
6. Gohain B.K., 2006. : *Continuity and Change in the Hills of Assam* : Karbi Anglong, Assam, Omsons Publication, New Delhi.
7. Goswami Tarun, 1985. : *Kuki Life and Lore*, N.C. Hills District Council, Haflong.
8. Gurung B.S., 1995. : *Glimpses of Haflong in 100 years of Haflong Centenary commemorative Souvenir (1895-1995)* Published by Central Centenary Celebration Committee, Haflong
9. Haokip Paokhohao, 2013. : *Reinculcating Traditional Values of the Kukis with Special Reference to lom and som*, in Haokip Thongkholal (ed) *The Kukis of Northeast India*, Bookwell Publishing, Delhi.
10. Haokip Seilen, 2010 : *Rhetorics of Kuki Nationalism- A Treaty*, published in Haokip N. & Lunminthang Michael (ed): *Kuki Society- Past, Present, Future*, Maxford Books, New Delhi.
11. Haokip Thangkholal, 2009; *The Kuki Tribes of Meghalaya*- Kuki International Forum.
12. Haokip Afrina, 2012 : *Position of Women in the Kuki Society of Manipur-A Historical Study*, Manipur University
13. Haolai Thangkim, 2006 : *Kuki Culture in North Cachar Hills, Before and after the advent of Christianity*; Guwahati Bohniman Printers.
14. Shakespear J, 1912 : *Lushai-Kuki Clans*, Cultural Publishing House, Delhi.
15. Census of India 2011
16. Field Study in the month of December 2018.



Summer 2019, Vol. 11

ISSN 2349-3410

PIERIAN SPRING

Fountain of Learning

A Bi-Annual Peer-Reviewed Multi-Disciplinary International Journal



CREATIVE WRITERS' CIRCLE
PUBLICATIONS



www.qr.net/QRPU

Editor-in-Chief

Dr. Jai Ram Jha

Associate Editors

Dr. Rajiv Kumar

Kumar Sambalam

- ❖ নিৰ্মলপ্ৰভা বৰদলৈৰ 'জলপদ্ম' উপন্যাসত অসম সম্পৰ্কীয় অধ্যয়নৰ সমল Page 71 – 79
 ❧ মিনাক্ষী হাজৰিকা
- ❖ দেউৰী জনগোষ্ঠীৰ খাদ্যাভ্যাস Page 80 – 88
 ❧ মনোৰঞ্জন বৰদলৈ
- ❖ গবেষণা পত্ৰ "আধুনিক সমালোচনা সাহিত্যৰ বিকাশত ফাৰ্ডিনাৰড দ্য চচ্যুৰ প্ৰভাৱ" Page 89 – 94
 ❧ পল্লৱী দত্ত
- ❖ সাহিত্যৰ চলচ্চিত্ৰকৰণত অসমীয়া মহিলা চলচ্চিত্ৰ পৰিচালকৰ অৱদান : এক বিশ্লেষণাত্মক অধ্যয়ন Page 95 – 107
 ❧ প্ৰদীপ বড়া
- ❖ বিবাহৰ লগত জড়িত স্ত্ৰী-লোকাচাৰ Page 108 – 113
 ❧ বৰ্ণালী শইকীয়া
- ❖ জ্যোতিপ্ৰসাদৰ শিল্পীৰ পৃথিৱী অভিভাষণত প্ৰকাশিত সংস্কৃতি চেতনা Page 114 – 119
 ❧ স্বপ্নালী গগৈ
- ❖ তাই খাময়াং জনগোষ্ঠীৰ সমাজত মহিলাৰ স্থান : এক ক্ষেত্ৰভিত্তিক অধ্যয়ন Page 120 – 123
 ❧ কুকিলা শ্যাম
- ❖ মিচিং জনগোষ্ঠীৰ লোকবিশ্বাস Page 124 – 129
 ❧ দেৱজিৎ খাউণ্ড
- ❖ চেমা নগাসকলৰ ভৌতিক সংস্কৃতি : এক বিশ্লেষণাত্মক অধ্যয়ন Page 130 – 136
 ❧ নীহাৰিকা ফুকন
- ❖ পালা নাটকৰ পৰিবেশন শৈলী Page 137 – 143
 ❧ নৱকপা চুতীয়া
- ❖ সোনোৱাল কছাৰীসকলৰ বিহৃত বিশ্বায়নৰ প্ৰভাৱ Page 144 – 148
 ❧ স্মিতা দাস
- ❖ অসমৰ লোক পৰিবেশ্য কলা : সতীশ ডট্টাচাৰ্যৰ 'মহাৰাজা' নাটকৰ আধাৰত এক বিশ্লেষণাত্মক অধ্যয়ন। Page 149 – 155
 ❧ বাহুল কলিতা
- ❖ বিংশ শতিকাৰ নব্বৈৰ দশকৰ অসমীয়া চুটিগল্পত সমকালীন সম্ভাৱন : এটি বিশ্লেষণ Page 156 – 163
 ❧ ড° পংকজ শইকীয়া
- ❖ মিচিং ভাষা আৰু সাহিত্য Page 164 – 175
 ❧ ড° দীপক কুমাৰ দলে

বিংশ শতিকাৰ নব্বৈৰ দশকৰ অসমীয়া চুটিগল্পত সমকালীন সন্ত্ৰাস : এটি বিশ্লেষণ

ড° পংকজ শইকীয়া
সহকাৰী অধ্যাপক, অসমীয়া বিভাগ
জেংৰাইমুখ মহাবিদ্যালয়

সংক্ষিপ্ত-সাৰ

(বিংশ শতিকাৰ নব্বৈৰ দশকটো অসমীয়া জাতীয় জীৱন আৰু সংস্কৃতিৰ বাবে ভয়াৱহ দুৰ্যোগৰ সময় আছিল। জাতীয় জীৱনক গভীৰভাৱে প্ৰভাৱিত কৰা আশীৰ দশকৰ অসম আন্দোলন, তদুপৰতী কালত এদল অসমীয়া যুৱকৰ উগ্ৰ জাতীয়তাবাদী কাৰ্যকলাপ, অগপ চৰকাৰৰ প্ৰতাৰণা, আশীৰ দশকৰ শেহৰ বছৰটোত অসমত জাপি দিয়া ৰাষ্ট্ৰপতি শাসন আৰু সশস্ত্ৰ বাহিনীৰ বিশেষ ক্ষমতা আইন আদিয়ে পৰৱৰ্তী দশকৰ আৰ্থ-সামাজিক, ৰাজনৈতিক, সাংস্কৃতিক আদি বিভিন্ন ক্ষেত্ৰত আৰু মানসিক জগতখনত সৰ্বগ্ৰাসী প্ৰভাৱ পেলায়। এই দশকত উগ্ৰপন্থী সংগঠন আলফাৰ হিংসাত্মক কাৰ্যকলাপে চূড়ান্ত স্তৰ পায়। আনফালে সমান্তৰালভাৱে উগ্ৰপন্থী দমনৰ নামত চলে সামৰিক-অৰ্ধসামৰিক বাহিনীৰ নিৰীহৰ ওপৰত অত্যাচাৰ। এনেদৰে এফালে উগ্ৰপন্থীৰ সন্ত্ৰাস আৰু আনফালে ৰাষ্ট্ৰ বা সামৰিক সন্ত্ৰাসত জনজীৱন বিপৰ্যস্ত হৈ পৰিল।

নব্বৈৰ দশকৰ সন্ত্ৰাসে আৱৰা অসমৰ সমাজ আৰু ৰাষ্ট্ৰ-ব্যৱস্থা, উত্তেজিত, ক্ষোভিত, ত্ৰাসিত, অত্যাচাৰিত, দমিত আৰু বিধ্বস্ত অসমীয়া মানুহৰ জীৱনচৰ্যা তথা মানসিকতা সমকালৰ গল্পকাৰসকলে উপেক্ষা কৰিব পৰা নাছিল। এই দশকটোৰ শক্তিশালী গল্পকাৰ হিচাপে যিকেইজন স্বীকৃত হৈছে, তেওঁলোকৰ প্ৰায় প্ৰত্যেকেই সমকালীন সন্ত্ৰাসৰ ছবি বলিষ্ঠ ৰূপত ৰূপায়ণ কৰিছে। সমকালীন সমাজখনৰ প্ৰেক্ষাপটত গল্পটো কিদৰে গঢ়ি তোলা হৈছে, সন্ত্ৰাস আৰু ইয়াৰ লগত জড়িত আনুষংগিক সমস্যাৰ কিদৰে ৰূপায়ণ ঘটিছে, সন্ত্ৰাসজৰ্জৰ ব্যক্তিজীৱনৰ প্ৰতিক্ৰিয়া কেনে, সন্ত্ৰাসৰ বিৰুদ্ধে প্ৰতিবাদ আৰু তাৰ বিৰুদ্ধে মানুহে সাব্যস্ত কৰা বিজয়— এই দিশবোৰেই গৱেষণা-পত্ৰখনত আলোচনা কৰা হ'ব।)

0.0 প্ৰস্তাৱনা :

বিংশ শতিকাৰ একেবাৰে শেহৰ অৰ্থাৎ নব্বৈৰ দশকৰপৰা অসমীয়া সাহিত্যত সন্ত্ৰাসৰ প্ৰসংগৰ আলোচনা বা উপস্থাপন অৱধাৰিতভাৱে হ'বলৈ ধৰে। কাৰণ এই দশকটোত অসমৰ সামাজিক, সাংস্কৃতিক আৰু ৰাজনৈতিক প্ৰেক্ষাপটত গভীৰভাৱে প্ৰভাৱ পেলালে উগ্ৰ জাতীয়তাবাদ কিম্বা সন্ত্ৰাসবাদী কাৰ্যকলাপে। সমকাল-চেতনাবে পৰিপুষ্ট লেখকে উক্ত প্ৰভাৱশালী কাৰকটোক উপেক্ষা নকৰিলে আৰু সেয়ে সাহিত্যত সন্ত্ৰাসৰ স্বৰূপ-চৰিত্ৰ চিত্ৰণত গুৰুত্ব দিলে। নব্বৈৰ দশকৰ সন্ত্ৰাসে আৱৰা অসমৰ সমাজ আৰু ৰাজনীতি; উত্তেজিত, ক্ষোভিত, ত্ৰাসিত, অত্যাচাৰিত, দমিত আৰু বিধ্বস্ত অসমীয়া মানুহৰ জীৱনচৰ্যা তথা মানসিকতা সমকালৰ গল্পকাৰসকলৰ গল্পত কলাসূলভভাৱে প্ৰকাশ পাইছে। সন্ত্ৰাস আৰু ইয়াৰ লগত জড়িত আনুষংগিক সমস্যা, সন্ত্ৰাসজৰ্জৰ ব্যক্তিজীৱন, সন্ত্ৰাসৰ সাফল্য আৰু বিফলতা, সন্ত্ৰাসৰ বিৰুদ্ধে প্ৰতিবাদ — এই দিশবোৰ লক্ষ্যণীয়। এই অধ্যয়নৰ জৰিয়তে সমকালীন সমাজৰ সন্ত্ৰাসৰ স্বৰূপ উদ্ঘাটন কৰিবলৈ চেষ্টা কৰা হ'ব।

0.2 গৱেষণা-পত্ৰৰ লক্ষ্য আৰু উদ্দেশ্য :

- ক) বিংশ শতিকাৰ নব্বৈৰ দশকৰ সমকালীন সমাজৰ সন্ত্ৰাসৰ স্বৰূপ বিচাৰ কৰা
- খ) সন্ত্ৰাসৰ সাফল্য আৰু বিফলতা নিৰ্ণয় কৰা
- গ) সন্ত্ৰাস আৰু ইয়াৰ লগত জড়িত আনুষংগিক সমস্যাবোৰ বিচাৰ কৰা
- ঘ) সন্ত্ৰাসজৰ্জৰ ব্যক্তিজীৱন সম্পৰ্কে বিশ্লেষণ কৰা

০.৩ গবেষণা-পত্ৰৰ পদ্ধতি আৰু পৰিসৰ :

গবেষণা-পত্ৰখনত বিশ্লেষণাত্মক পদ্ধতি ব্যৱহাৰ কৰা হ'ব। সন্ত্ৰাসবাদৰ সংজ্ঞা আৰু ধাৰণাৰ আধাৰত গল্পসমূহত ফুটি উঠা বিষয়বস্তু বিচাৰ-বিশ্লেষণ কৰা হ'ব।

বিংশ শতিকাৰ নব্বৈৰ দশকৰ কেইজনমান উল্লেখযোগ্য গল্পকাৰ হ'ল কুল শইকীয়া, মনোজ কুমাৰ গোস্বামী, অপূৰ্ব শৰ্মা, হৰেকৃষ্ণ ডেকা, শিবানন্দ কাকতি, ইমবান ছেইন, জ্যোতিষ শিকদাৰ, দেৱব্ৰত দাস, অপূৰ্ব শইকীয়া আদি। গবেষণা-পত্ৰখন প্ৰস্তুত কৰা হ'ব এইকেইটা গল্পক ভিত্তি কৰি : কুল শইকীয়াৰ 'তীৰ্থ ডেকাৰ নিৰুদ্দেশৰ পিছৰছোৱা', মনোজ কুমাৰ গোস্বামীৰ 'মোক জুইশলা বাহটো দিয়ক' আৰু 'সমীৰণ বৰুৱা আহি আছে', শিবানন্দ কাকতিৰ 'আমৃত্যু অমৃত', ইমবান ছেইনৰ 'জিঘাংসা', অপূৰ্ব শৰ্মাৰ 'মজিয়াত তেজ', হৰেকৃষ্ণ ডেকাৰ 'বন্দীয়াৰ', অপূৰ্ব শইকীয়াৰ 'বন্দুকৰ ভাষাৰে'। ইয়াৰ উপৰি প্ৰসংগক্ৰমে দেৱব্ৰত দাস, প্ৰশান্ত কুমাৰ দাস, জ্যোতিষ শিকদাৰ, মনোবমা দাস মেধি, জয়ন্ত কুমাৰ চক্ৰৱৰ্তী, জয়ন্ত মাধৱ বৰা আদিৰ গল্পৰ জেৰ টানি অনা হ'ব।

১.০ সন্ত্ৰাসবাদৰ ধাৰণা :

সন্ত্ৰাসবাদ(terrorism) এটা বহুচৰ্চিত বিষয়। কেৱল অসম, উত্তৰ-পূৰ্বাঞ্চল অথবা ভাৰতবৰ্ষতে নহয়; আন্তৰ্জাতিক স্তৰতো এতিয়া সন্ত্ৰাসবাদ সম্বন্ধে উচ্চাৰিত এটা শব্দ। উন্নত আৰু উন্নয়নশীল— উভয় শ্ৰেণীৰ ৰাষ্ট্ৰকে সন্ত্ৰাসবাদে প্ৰভাৱিত কৰিছে।

Ram Ahuja-ই তেওঁৰ Social Problems in India শীৰ্ষক গ্ৰন্থত সন্ত্ৰাসবাদৰ সংজ্ঞা দিবলৈ গৈ Encyclopedia of Social Sciences-ৰ উদ্ধৃতি ব্যৱহাৰ কৰিছে এনেদৰে— It also defined as 'a method whereby an organized group or party seeks to achieve its a vowed aims chiefly through the systematic use of violence'.

N. Jose Chander-এ সন্ত্ৰাসবাদৰ সংজ্ঞা দিছে এনেদৰে— Terrorism is an organized effort, involving a series of violent acts that produce terror in the minds of the affected as well as of the likly-to-be-affected. It aims at inspiring terror, which is a psychological experience.^২

সন্ত্ৰাসবাদৰ ব্যাখ্যা ড^o দেৱপ্ৰসাদ বৰুৱাই এনেদৰে দিছে— 'সন্ত্ৰাস(বাদ) মানে এনে এটা মত যিটোৱে ক্ষমতা লাভৰ কাৰণে, মূনাফাৰ পাহাৰ গঢ়াৰ কাৰণে, ৰাজনৈতিক ক্ষমতা লাভৰ কাৰণে অত্যাচাৰ, ভীতি প্ৰদৰ্শন, হত্যা প্ৰভৃতি নানা ত্ৰাসজনক কাৰ্য চলোৱাটো উচিত বুলি গণ্য কৰে।'^৩

সন্ত্ৰাস মানে অতিশয় ভয় বা আতংক। সন্ত্ৰাসবাদ হৈছে এটা মত বা পদ্ধতি, যিটোৱে উদ্দেশ্যপ্ৰণোদিতভাৱে সন্ত্ৰাস সৃষ্টি কৰে বা বিয়পায়। এই সন্ত্ৰাসবাদ শব্দটো হিংসা (violence) বা বিদ্ৰোহাৱস্থা (insurgency)ৰ নামান্তৰ নহয়। সন্ত্ৰাসবাদতহে এই হিংসা পূৰ্বনিৰ্দিষ্ট লক্ষ্যত উপনীত হ'বৰ বাবে কোনো সংগঠিত দল বা সংগঠনে (সন্ত্ৰাসবাদী) পদ্ধতিগতভাৱে প্ৰয়োগ কৰে।

সন্ত্ৰাসবাদীসকলৰ চাৰিত্ৰিক বৈশিষ্ট্য প্ৰায় একেধৰণৰ হয়। তেওঁলোকে এনেধৰণৰ কাৰিকৰী কৌশল ব্যৱহাৰ কৰে— ৰাজহুৱাভাৱে মৃত্যুদণ্ড কাৰ্যত পৰিণত কৰা, বলেৰে ব্যক্তি অপহৰণ কৰা, বোমা বিস্ফোৰণ কৰা, যান-বাহন অপহৰণ কৰা, গৃহদাহ, গুপ্তহত্যা, সশস্ত্ৰ আক্ৰমণ, শত্ৰু বুলি গণ্য কৰাসকলৰ প্ৰতি বন্দীয়াৰ অৱৰোধৰ পৰিস্থিতিৰ (hostage-barricade situation) সৃষ্টি কৰা, প্ৰতিহিংসাৰে পোটক তোলা, মৃত্যুদণ্ডৰে শাস্তি দিব খোজাসকলৰ তালিকা প্ৰস্তুত কৰি কাৰ্যকৰী কৰা, নাক-কাণ কাটি দিয়া, আঁঠুৰ ঘিলা কঢ়া (knee capping) ধৰণৰ শাস্তি দিয়া ইত্যাদি।^৪

সন্ত্ৰাসবাদ বুলিলে প্ৰধানতঃ দুটা প্ৰকাৰ মনলৈ আহে : ৰাষ্ট্ৰসন্ত্ৰাস আৰু ব্যক্তিসন্ত্ৰাস। ইয়াৰ উপৰি বৰ্তমান ৰাজনৈতিক সন্ত্ৰাস, ৰাজনৈতিক সন্ত্ৰাসবাদ, আন্তৰ্জাতিক সন্ত্ৰাসবাদ আদি অৱধাৰণাৰো চৰ্চা হৈছে।

২.০ বিংশ শতিকাৰ নব্বৈৰ দশক আৰু তাৰ প্ৰাক্কালৰ হিংসা আৰু সন্ত্ৰাসজৰ্জৰ অসম :

বিংশ শতিকাৰ নব্বৈৰ দশকটো অসমীয়া জাতীয় জীৱন আৰু সংস্কৃতিৰ বাবে ভয়াৱহ দুৰ্যোগৰ সময় আছিল। হত্যা-হিংসা-সন্ত্ৰাসে অসমীয়া মানুহৰ মনত সঞ্চাৰ কৰিছিল ভীতি, ত্ৰাস আৰু উৎকণ্ঠা। অসমৰপৰা অবৈধ বিদেশী প্ৰব্ৰজনকাৰী বহিষ্কাৰ কৰাৰ দাবীত ১৯৭৯-৮৫ চনলৈ যি 'অসম আন্দোলন' (প্ৰথমে বহিৰাগত খেদা আন্দোলন আছিল) সংঘটিত হৈছিল, সেই আন্দোলনৰ

সম্ভ্রাসজৰ্জৰ অসম এখন গঢ়াত কিছু পৰিমাণে পৰোক্ষ ভূমিকা আছে। এই আন্দোলনৰ পটভূমিতে সৃষ্টি হৈছিল সংযুক্ত মুক্তি বাহিনী— অসম বা আলফা আৰু অসম গণ পৰিষদ বা অগপৰ। অসমৰ সমাজ-জীৱন, ৰাজনীতি, অৰ্থনীতি আদি ক্ষেত্ৰত এই দুটা সংগঠন বা দলে যে গভীৰ প্ৰভাৱ পেলাই আহিছে সি অনস্বীকাৰ্য। 1979 চনৰ 7 এপ্ৰিলত জন্ম লাভ কৰা আলফা অসম আন্দোলনত জড়িত হৈছিল যদিও তেওঁলোকৰ দাবী, মতাদৰ্শ আৰু পন্থা আছিল বেলেগ। অসমক বিদেশীমুক্ত কৰিবলৈ তেওঁলোকে স্বাধীন অসমৰ পোষকতা কৰে আৰু ভাৰত-ৰাষ্ট্ৰৰ বিৰুদ্ধে বিক্ষিপ্ত হিংসাত্মক কাৰ্য চলাই যায়। 1983 চনৰ অসমৰ মধ্যৰাতীকালীন নিৰ্বাচনৰ সময়ৰপৰা আলফাৰ সাংগঠনিক তৎপৰতা আৰম্ভ হয় আৰু হত্যা, অপহৰণ, বোমা বিস্ফোৰণ, ধন দাবী, বেংক ডকাইতি, পণবন্দীৰ মুক্তিৰ বিনিময়ত ধন দাবী, ভাবুকি আদিৰে সম্ভ্রাস সৃষ্টি কৰে। প্ৰণিধানযোগ্য যে অসমক সম্ভ্রাসবিধ্বস্ত ৰাজ্যত পৰিণত কৰাত আটাইতকৈ বেছি ভূমিকা থকা সংগঠন বুলিলে এতিয়া আলফালৈয়ে আঙুলি টোওঁৱা হয়। তদুপৰি 'তাৰে প্ৰেৰণা লৈ বড়ো, কাৰ্বি, ডিমাছা, মাল্টা আদি ক্ষেত্ৰীয় উগ্ৰপন্থী গোট কিছুমানৰো সৃষ্টি হ'ল যি বিলাকে চুবুৰীয়া মাইনমাৰ, বাংলাদেশ, ভূটান আদিত শিবিৰ পাতি বিদেশী শক্তিবোৰে ত্ৰিগুণক হৈ ৰাজ্যখনত হত্যা, লুণ্ঠন, অপহৰণৰ বেহা চলাবলৈ ধৰিলে।'⁵ আলফাৰ সশস্ত্ৰ কাৰ্যকলাপৰ সমান্তৰালকৈ 1987 চনৰপৰা সদৌ বড়ো ছাত্ৰ সন্থা (আবছু)-ই divide Assam fifty fifty শ্লোগানেৰে বড়োলেণ্ডৰ দাবীত হিংসাত্মক আন্দোলনৰ সূত্ৰপাত ঘটায়। আবছুৰ সৈতে তদানীন্তন নেতৃত্বৰ 1993 চনত হোৱা চুক্তিমৰ্মে কিছুকাল শান্তি বৰ্তি আছিল যদিও নব্বৈৰ দশকৰ শেষৰফালে বি এল টি এফে (বড়ো লিবাৰেশ্যন টাইগাৰ্ছ ফৰ্ছ) সম্ভ্রাস আৰম্ভ কৰি দিয়ে।

1985 চনত অসম চুক্তি স্বাক্ষৰিত হোৱাৰ পাছত অসম আন্দোলনত জড়িত প্ৰভাৱশালী পক্ষটোৱে অসম গণ পৰিষদ দল গঠন কৰে আৰু নিৰ্বাচনৰ মাধ্যমেৰে শাসনাধিষ্ঠিত হয়। অসমত পৰোক্ষভাৱে হ'লেও এক সম্ভ্রাসৰ পৰিৱেশ ৰচনাত এই দলটোৰ ভূমিকা আছে। প্ৰথমটো কাৰ্যকালত এই দলে গ্ৰহণ কৰা জনজাতিবিৰোধী তথা দমনমূলক কাৰ্যকলাপৰ বাবেই বিশেষতঃ বড়ো জনজাতিৰ মনত বিচ্ছিন্নতাকামী মনোভাৱ পুনৰ্জাগ্ৰত হৈ উঠে। আনহাতে অগপৰ দ্বিতীয়টো আমোলত, নব্বৈৰ দশকৰ শেষৰ্ধত চৰকাৰী পৃষ্ঠপোষকতাত বিয়পি পৰে গুপ্তহত্যাৰ সম্ভ্রাস। এই গুপ্তহত্যাৰ ৰাজনৈতিক সম্ভ্রাসৰ অন্তৰ্গত এক কৌশলী ৰণনীতি আখ্যা দিব পাৰি।

1990 চনৰ 28 নবেম্বৰ তাৰিখে অসমত ৰাষ্ট্ৰপতি শাসন প্ৰবৰ্তন হয় আৰু সশস্ত্ৰ বাহিনীৰ বিশেষ ক্ষমতা আইনৰ অধীনত ৰাজ্যখনক অশান্ত অঞ্চল হিচাপে ঘোষণা কৰে। ফলস্বৰূপে উগ্ৰপন্থী দমনৰ নামত চলে সামৰিক বাহিনীৰ নিৰীহৰ ওপৰত অত্যাচাৰ। দৰাচলতে ইয়েই সম্ভ্রাসবাদৰ অন্য এক চৰিত্ৰ সামৰিক বা ৰাষ্ট্ৰসম্ভ্রাস। উগ্ৰপন্থীৰ পৰিয়াল সৈন্যবাহিনীৰদ্বাৰা নজৰবন্দী হৈ ৰোৱা, উগ্ৰপন্থী বিচাৰৰ নামত সৰ্বসাধাৰণক হাৰাশাস্তি, সেনা-উগ্ৰপন্থীৰ গুলীয়াগুলী, ভুৱা সংঘৰ্ষ ৰচনা কৰি নিৰীহ যুৱকক হত্যা, আত্মসমৰ্পণকাৰীক সতীৰ্থৰ জৰিয়তে হত্যা, ধৰ্ষণ, বলাৎকাৰ, ভাবুকি প্ৰদান— এইবোৰৰ জৰিয়তেই অসমত ৰাষ্ট্ৰসম্ভ্রাস বিয়পি পৰে।

মুঠতে, বিংশ শতিকাৰ নব্বৈৰ দশক আৰু তাৰ প্ৰাক্কালৰ অসমত সম্ভ্রাসে চৰম সীমা পাইছিলগৈ।

3. 0 নব্বৈৰ দশকৰ সমকাল চেতনা-প্ৰকাশক অসমীয়া চুটিগল্প আৰু স্তম্ভ : চমু আভাস :

অসমীয়া গল্প-সাহিত্যৰ ক্ষেত্ৰখনত বিংশ শতিকাৰ শেষৰ দশকটোৰ চুটিগল্পৰ ঐতিহাসিক গুৰুত্ব আছে। নব্বৈৰ দশকৰ অসমীয়া সমাজখন ঘোৰ অনিশ্চয়তা, নিৰাপত্তাহীনতা, সংকটৰ সন্মুখীন হৈছিল আৰু মানুহৰ মানসিক জগতলৈয়ো ইবোৰৰ সংক্ৰমণ ঘটি ঘনীভূত ৰূপ লৈছিল। এই দশকতে যেন মানৱীয় প্ৰমূল্যবোধৰ অপমৃত্যু ঘটিছিল। এই সমাজ-মানসিকতাৰ পৰিৱৰ্তনৰ অন্তৰালত ক্ৰিয়া কৰা প্ৰধান কাৰকটো আছিল নিশ্চিতভাৱে সম্ভ্রাস। আনহাতে, এই দশকতে মুক্ত অৰ্থনীতিৰ সন্মুখীন হৈ অসমীয়া পৰম্পৰাগত সমাজখন দ্বিধা-দ্বন্দ্বত জৰ্জৰিত হৈ পৰিছিল। নব্বৈৰ দশকৰ গল্পকাৰে সেয়ে তেওঁলোকৰ ৰচনাত সম্ভ্রাসবাদ, ভোগবাদ, অস্তিত্ব আৰু মূল্যবোধৰ সংকট, প্ৰকৃত জীৱনবোধৰ অন্বেষণ, শোষণ আৰু বঞ্চনা, শাসকৰ লেতেৰা দুৰনীতি, শিপাৰিচ্ছিন্ন হোৱাৰ যত্না আদি বিষয়ক কেন্দ্ৰীয় বিষয় হিচাপে বাছি লৈছে। গভীৰ সমকাল চেতনা আৰু সমাজ-বাস্তৱতা, সামাজিক দায়বদ্ধতা এই দশকৰ গল্পৰ বিশিষ্ট লক্ষণ।

যুগচেতনাৰ সংবেদনাত্মক উপলব্ধিৰে সমাজ আৰু মানসিকতাৰ পৰিৱৰ্তনক চুটিগল্পৰ মাজেৰে ধৰি ৰখাৰ প্ৰচেষ্টা কৰা নব্বৈৰ দশকৰ কেইজনমান প্ৰতিভাশালী গল্পকাৰ হৈছে— মনোজ কুমাৰ গোস্বামী, হৰেকৃষ্ণ ডেকা, অপূৰ্ব শৰ্মা, অপূৰ্ব কুমাৰ শইকীয়া,

ইমৰান ছছেইন, ববীন শৰ্মা, শিৱানন্দ কাকতি, মনোবমা দাস মেধি, অৰুণা পটংগীয়া কলিতা, জয়ন্ত কুমাৰ চক্ৰৱৰ্তী, নৱনীতা গগৈ, মৌচুমী কন্দলী, প্ৰশান্ত কুমাৰ দাস, জ্যোতিষ শিকদাৰ, দেৱব্ৰত দাস, ভূপেন্দ্ৰ নাৰায়ণ ভট্টাচাৰ্য, বিপুল খাটনিয়াৰ আদি।

৪.০ নব্বৈৰ দশকৰ অসমীয়া চুটিগল্পত সন্ত্ৰাস-প্ৰসংগ :

এই দশকটোৰ শক্তিশালী গল্পকাৰ হিচাপে যিকেইজন স্বীকৃত হৈছে, তেওঁলোকৰ প্ৰায় প্ৰত্যেকেই সমকালীন সন্ত্ৰাসৰ ছবি বলিষ্ঠ ৰূপত ৰূপায়ণ কৰিছে।

৪.১ সন্ত্ৰাসবাদ আৰু তাৰ লগত জড়িত আনুষংগিক সমস্যাৰ বিপৰ্যস্ত, সংকটচ্ছন্ন জনজীৱন :

সন্ত্ৰাসবাদীসকলে প্ৰয়োগ কৰা বিভিন্ন কৌশলে সৰ্বসাধাৰণৰ জীৱনযাত্ৰা কিদৰে বিপৰ্যস্ত কৰিছিল তাৰ নিদৰ্শন সন্ত্ৰাসকেন্দ্ৰিক গল্পসমূহত পোৱা যায়। নব্বৈৰ দশকত হত্যাকাণ্ড আছিল অতি সহজ ঘটনা। উগ্ৰপন্থী সংগঠন আলফাই বোমা বিস্ফোৰণ অথবা বিভলভাৰ-বন্দুকৰে এটাৰ পিছত এটাকৈ হত্যাকাণ্ড সংঘটিত কৰি গৈছিল। তদুপৰি মুক্তিপণ নাপালে অপহৃত ব্যক্তিকো অতি নিষ্ঠুৰভাৱে হত্যা কৰিছিল। বিতোপন বৰবৰাৰ 'মৃগয়া', ইমৰান ছছেইনৰ 'জিঘাংসা', জেহিৰুল ছছেইনৰ 'মৃগয়া', জ্যোতিষ শিকদাৰৰ 'হত্যা' আদি গল্পত উগ্ৰপন্থীৰদ্বাৰা ব্যক্তিহত্যাৰ ঘটনা বৰ্ণিত হৈছে। হত্যাকাণ্ডৰ ঘটনা সঘন হোৱা বাবেই সি কিমান তুচ্ছ গুৰুত্ব লাভ কৰিছিল তাৰ সম্যক উপলব্ধিৰ বাবে এই বৰ্ণনাই যথেষ্ট— "...পিছদিনাখন পুৱাই ঘাঁহনিৰ ওপৰত বাগৰি থকা খৰ্গেশ্বৰৰ মৃতদেহটো পোৱা গ'ল— দুদিন পিছতে বাতৰিকাকতৰ পিছফালে এচুকত প্ৰকাশ হ'ল— বহুসাময়ভাৱে অজ্ঞাত এক আততায়ীৰ হাতত ওলীবিদ্ধ হোৱা খৰ্গেশ্বৰৰ মৃত্যুৰ এটা সৰু খবৰ..."^৬

কিন্তু মৃত্যুক বাতৰিকাকতে গুৰুত্বহীন গণ্য কৰিলেও ভুক্তভোগীৰ বাবে ই আছিল শংকা আৰু আতংকৰ কাৰণ। উগ্ৰপন্থী, সৈন্যবাহিনী অথবা মধ্যম স্থানত থকা নিৰীহ লোকৰ পৰিয়ালে যেন সদায় আসন্ন মৃত্যুৰ ক্ষণ গণি চেপা উত্তেজনাৰে কাল অতিবাহিত কৰিছিল। উগ্ৰপন্থী-সেনাৰ সংঘৰ্ষত যিটো পক্ষৰে মৃত্যু নহওক, তেওঁলোক আছিল একো একোটা পৰিয়ালৰ অবিচ্ছিন্ন সদস্য। তদুপৰি সেনাই সন্দেহবশতঃ ধৰি নি কিম্বা ভুৱা সংঘৰ্ষৰে নিৰ্দোষী ডেকা ল'ৰাক হত্যা কৰাটো আছিল তেনেই সাধাৰণ ঘটনা। ফলস্বৰূপে ব্যক্তিসন্ত্ৰাস আৰু ৰাষ্ট্ৰসন্ত্ৰাসৰ কবলত অসমৰ সৰ্বস্তৰৰ জনসাধাৰণেই মৃত্যুশংকাত আচ্ছন্ন আৰু সন্ত্ৰস্ত হৈ পৰিছিল। এই সন্ত্ৰাস আছিল ব্যক্তিমানসত ভিৰ কৰা সৰ্বগ্ৰাসী সন্ত্ৰাস আৰু সন্ত্ৰাসজৰ্জৰ আবহাৱাই সৰ্বমানৱৰ হৃদয়ৰ গভীৰত সঞ্চাৰ কৰিছিল গভীৰ বেদনাবোধৰ। ইয়াৰ মৰ্মোপলব্ধিৰ বাবে মনোজ কুমাৰ গোস্বামীৰ 'সূৰ্যৰ পোহৰত এজন আততায়ী' আৰু কুল শইকীয়াৰ 'তীৰ্থ ডেকাৰ নিৰুদ্দেশৰ পিছৰছোৱা' গল্পকেইটালৈ মন কৰিব পাৰি। প্ৰথমটো গল্পত মৃতদেহ উদ্ধাৰৰ খবৰ পালেই এজন ৰুগীয়া বৃদ্ধ বিল্লৱৰ নামত ওলাই যোৱা পুত্ৰক চিৰকাললৈ হেৰুওৱাৰ আশংকাত কঁপি উঠে। এই বৃদ্ধজন দৰাচলতে গাঁও-চহৰৰপৰা অৰণ্যলৈ টাপলি মেলা শ শ অসমীয়া ডেকা ল'ৰাৰ দুৰ্ভগীয়া, অসহায়, আতংকগ্ৰস্ত, বেদনাবোধত পীড়িত বৃদ্ধ পিতৃৰ প্ৰতিনিধি। 'তীৰ্থ ডেকাৰ নিৰুদ্দেশৰ পিছৰছোৱা' গল্পটো হঠাৎ ঘৰৰপৰা নিখোজ হোৱা ডেকা ল'ৰা এটাৰ পিতৃ-মাতৃৰ মানসিক ক্ৰিয়া-প্ৰতিক্ৰিয়া আৰু হৃদয়-যন্ত্ৰণাৰ চিত্ৰণ। ডেকা ল'ৰাটোৰ তীৰ্থ নামটোৰ অন্তৰালত প্ৰচ্ছন্ন হৈ আছে প্ৰতীকী তাৎপৰ্য। এই তাৎপৰ্য অনুধাৱন কৰি সমালোচক অৰিন্দম বৰকটকীয়ে সুন্দৰ ব্যাখ্যা আগবঢ়াইছে—

"...প্ৰত্যেক পিতৃৰ বাবে নিজৰ সন্তান তেনে এক তীৰ্থযাত্ৰাৰেই নামান্তৰ।...তেনে এক প্ৰাৰ্থনা জীৱনৰপৰা হেৰাই হৈছে বুলি নিজকে প্ৰত্যয় নিয়াবলৈ বাধ্য হোৱাটো এজন অভিভাৱকৰ বাবে কিমান বেছি নিৰ্মম আৰু যন্ত্ৰণাদায়ক হ'ব পাৰে, এই গল্পটোত সেই অনুভূতি মৰ্মভেদী ৰূপত প্ৰকাশ পাইছে—'...যেতিয়াই কাৰোবাৰ মৃতদেহ পুলিচে উদ্ধাৰ কৰে, নকুল ডেকা আৰু উদগ্ৰীৰ হৈ পৰে এই কথা জানিবলৈ— কপালত তীৰ্থৰ থকাৰ দৰে মৃতদেহটোৰো তুলসীৰ দাগ আছে নেকি? পাছ মুহূৰ্ততে নিজকে প্ৰত্যয় নিয়ায় এইবুলি— কপালত তুলসীৰ পাত থকা ল'ৰা অকল তীৰ্থই আছনে? কত মানুহৰ তেনে দাগ থাকিব পাৰে।..."^৭

গল্পটোত নকুল ডেকাই সন্মুখীন হোৱা সংকটক বৰকটকীয়ে মানৱীয়তালৈ অহা সংকট বুলি অভিহিত কৰিছে।^৮

অপূৰ্ব শৰ্মাৰ 'মজিয়াত তেজ' গল্পতো সন্ত্ৰাস-কবলিত সময়ৰ বুকুত মানৱীয় সংকটৰ প্ৰতিচ্ছবি ভাস্বৰ হৈ উঠিছে। গল্পটোত মাতৃ বিল্লৱী হোৱাৰ সূত্ৰেই এজন অধ্যাপকে ৰাষ্ট্ৰৰ ওচৰত পণবন্দিত্ব স্বীকাৰ কৰি ল'বলগীয়া হৈছে। লগতে স্বীকাৰ কৰি ল'বলগা হৈছে সেনাৰ সঘন আতিশয্যকো। মজিয়াত তেজ পৰাৰ যিটো সন্ত্ৰাস এই গল্পত ব্যঞ্জিত হৈছে সিয়েই নিৰ্ণয় কৰে সমকালৰ সন্ত্ৰাসৰ ভয়াবহতা আৰু ৰাষ্ট্ৰযন্ত্ৰৰ নিৰ্দয় ৰূপ।

4.2 সন্ত্ৰাসসৃষ্টি বাতাবৰণত মানসিকতা আৰু মানবীয় মূল্যবোধৰ পৰিৱৰ্তিত ৰূপ :

সন্ত্ৰাসজৰ্জৰ নব্বৈ দশকৰ স্থিৰতাহীন আৰু জটিল সময়ছোৱাত মানুহৰ পূৰ্বাপৰ প্ৰচলিত ধ্যান-ধাৰণা আৰু মূল্যবোধ চকুত লগাকৈ বিভ্ৰান্তি আৰু খহনীয়াৰ গ্ৰাসত পৰিছিল। চতুৰ্দিশৰ হিংসা-দ্বেষ্টৰ লগত সহায়স্থান কৰি থাকোঁতে এদিন তাৰ আকৰ্ষণতে পৰি দলে দলে ডেকা ল'ৰাই জিঘাংসাৰ হাতবাউলিৰ প্ৰতি সঁহাৰি দিছিল। নতুন প্ৰজন্মৰ মাজত এই নেতিৰ আগ্ৰাসী ৰূপ দেখি এচামে দুঃচিত্তত কাল নিয়াইছিল। ইমবান হুছেইনৰ 'জিঘাংসা' গল্পত এই ভাবৰ কলাত্মক প্ৰকাশ লক্ষ্য কৰা যায়।

'জিঘাংসা'ত বৈপৰীত্যৰ প্ৰয়োগেৰে কথাবস্তু চমৎকাৰভাৱে উপস্থাপন কৰা হৈছে: চহৰত উগ্ৰপছীয়ে সংঘটিত কৰা হত্যাকাণ্ডৰ পিছত সেনাৰ অত্যাচাৰ চলাৰ বিপৰীতে গাঁৱত এজন পিতৃয়ে হোষ্টেলৰপৰা ঘৰলৈ অহা পুত্ৰক খুৱাবলৈ পাৰ মৰা মানুহ বিচাৰি ফুৰিছে। কিন্তু পুত্ৰই অপ্ৰত্যাশিতভাৱে পাৰকেইটা মুচৰি মুচৰি বধ কৰিছে। এই চাক্ষুস অভিজ্ঞতা লভা পিতৃৰ ভাবজগতৰ বৰ্ণনা এনেকুৱা— "মহীচন্দ্ৰৰ চকুৰ আগতে পাৰকেইটা খপখপকৈ মাটিত পবিল। তেওঁ দেখিলে হাৰিকেনৰ ক্ষীণ পোহৰতো সোণটিৰ চকুদুটা অদ্ভুতভাৱে झलিছে। তেওঁৰ মূৰটো আচন্দ্ৰাই কৰি উঠিল, ভৰিৰ তলৰ মাটি কঁপিবলৈ ধৰিলে। জঠৰ হৈ তেওঁ পুতেকৰ ৰঙা, অচিনাকি চকুহাললৈ চাই ব'ল।" ⁹

সন্ধিয়া সময়ত ঘটা এই ঘটনাত সন্ধ্যাৰ আলো-ছাঁৰ দ্বৈধ ৰূপটোৰ দৰেই সেই বৃদ্ধ পিতৃজনক বিস্মিত, সন্দিহান আৰু আতংকিত কৰিব পৰা কাৰক উপস্থিত আছিল। সমকালৰ জটিল, ভয়াৱহ পৰিস্থিতিত মানসিকতাৰ পৰিৱৰ্তন আৰু মূল্যবোধৰ পতন ঘটা যুৱচামৰ ওচৰত মহীচন্দ্ৰৰ দৰে অনেক পিতৃ অসহায়, নিৰ্বাক, সন্ত্ৰস্ত।

4.3 সন্ত্ৰাসবাদ আৰু সন্ত্ৰাসজৰ্জৰ পৰিস্থিতিত সৰ্বসাধাৰণৰ প্ৰতিক্ৰিয়াৰ চিত্ৰায়ন :

এচাম মুষ্টিমেয় লোকৰ বাহিৰে সন্ত্ৰাসবাদৰ প্ৰতি অসমৰ সৰ্বসাধাৰণ লোকৰ মনোভংগী আছিল নেতিবাচক। কাৰণ নব্বৈ দশকৰ সন্ত্ৰাসবাদত দোষী-নিৰ্দোষী বাছ-বিচাৰ নকৰাকৈ কঠোৰতম শাস্তি প্ৰদান কৰাৰ প্ৰথা আছিল; সাধাৰণ নিৰীহ লোক ক্ষতিগ্ৰস্ত হৈছিল অধিক। মাজে মাজে সন্ত্ৰাসবাদৰ বিৰুদ্ধে স্কেভো প্ৰকাশ পাইছিল।

'জিঘাংসা' গল্পত বৃদ্ধ মহীচন্দ্ৰ সন্ত্ৰাসবাদীৰ কাৰ্যকলাপৰ প্ৰতি বিৰক্ত হৈ উঠিছে। এই বিৰক্তি কেবল মহীচন্দ্ৰে নহয়, ই সেই সময়ৰ অধিকাংশ লোকৰে সামূহিক প্ৰতিক্ৰিয়া আছিল।

মনোজ কুমাৰ গোস্বামীৰ 'সমীৰণ বৰুৱা আহি আছে' গল্পত দুৰ্ধৰ্ষ সন্ত্ৰাসবাদীজনৰ সন্ত্ৰাস আগমনৰ বাৰ্তা পায়ো সৰ্বসাধাৰণে যি চূড়ান্ত নিস্পৃহতা প্ৰদৰ্শন কৰিছে, তাত প্ৰচ্ছন্ন হৈ আছে সন্ত্ৰাসবাদৰ প্ৰতি অৱহেলাৰ মনোভাৱ। আনহাতে, সমীৰণ বৰুৱা অহাৰ খবৰে আনৰ সৈতে বিয়া হৈ যোৱা তেওঁৰ প্ৰেমিকাক আলোড়িত কৰাৰ সলনি ভীত আৰু ত্ৰস্তমানহে কৰিছে। অৰ্থাৎ সন্ত্ৰাসবাদৰ প্ৰতি স্বয়ং উগ্ৰপছীৰ একালৰ প্ৰণয়পাত্ৰীৰে আস্থাৰূচক প্ৰতিক্ৰিয়া প্ৰকাশ পোৱা নাই: "আজি সি ঘূৰি আহিছে, প্ৰেম-কলুষিত সেই সম্বন্ধই আজি যিকোনো মুহূৰ্ততে ভাঙি চূৰমাৰ কৰি দিব পাৰে তাইৰ এই সজোৱা ঘৰ। যিৰিকীৰ ৰডত গাল থৈ নীলা খৰ লাগি ৰৈ থাকে।" ¹⁰

সন্ত্ৰাসবাদৰ গৰ্ভতে জন্ম লভা আৰু ৰাষ্ট্ৰব্যৱস্থায়ো সঁহাৰি দিয়া এক পথ হৈছে আত্মসমৰ্পণ বা মূল সুঁতিলৈ ঘূৰি অহা ব্যৱস্থা। কিন্তু আত্মসমৰ্পণকাৰী উগ্ৰবাদীয়ে বহু সময়ত সৰ্বসাধাৰণৰপৰা অকুণ্ঠ সঁহাৰি লাভ নকৰে। শিৱানন্দ কাকতিৰ 'আমৃত্যু অমৃত' গল্পত মূল সুঁতিলৈ ঘূৰি অহা অমৃতক গাঁওবাসীয়ে সহজভাৱে লোৱা নাই। তাৰ ওচৰত তেওঁলোক আছিল অস্বস্তিকৰভাৱে সংযমী; ব্যৱহাৰ-পাতিৰ ক্ষেত্ৰতো আছিল কৃত্ৰিমতা। ইয়াৰপৰা প্ৰতীয়মান হয় যে সন্ত্ৰাসবাদৰ সৈতে তেওঁলোকৰ যি এক অদৃশ্য সম্পৰ্ক বৰ্তি আছিল তাৰ ভিত্তিভূমি আছিল ভয়— আস্থা বা আনুগত্য নহয়। ¹¹

হিংসা-সন্ত্ৰাসেৰে ভৰি থকা দুঃস্থ বাতাবৰণত কোনো লোকে কেতিয়াবা অপ্ৰত্যাশিত প্ৰতিক্ৰিয়া প্ৰদৰ্শন কৰিছিল। 'সূৰ্যৰ পোহৰত এজন আততায়ী' গল্পত উগ্ৰপছী ভাতৃৰ মৃতদেহৰ উদ্ধাৰৰ পিছত ককায়েকে তাক স্বচক্ষে দেখিও ৰে'লৰ চকাত পিষ্ট হ'বলৈ এৰি দিছে। কাৰণ ঘৰ চলোৱা, আবিয়ে ভনীয়েকক বিয়া দিয়া, ভাতৃৰ শ্ৰাদ্ধ কৰা— এনে অথালি-পথালি ভাৱভ্ৰোতৰ মাজত সেই নিৰ্মম সিদ্ধান্তকে ল'বলৈ বাধ্য হ'ল।

4.4 সন্ত্ৰাসবাদৰ ব্যৰ্থতা তথা নিষ্ফলতাৰ কলাত্মক প্ৰকাশ :

আশীৰ দশকতে অসমত সূচনা হোৱা সন্ত্ৰাসবাদৰ সুদীৰ্ঘ ত্ৰিছ বছৰ অতিক্ৰম কৰাৰ পাছতো যে কোনো সুফল বা সমাধান পোৱা

নগল তাৰ প্ৰমাণ বিগত সময়ছোৱাৰ ইতিহাসেই দিয়ে। বৰঞ্চ অসমৰ জাতীয় জীৱনৰ বিভিন্ন দিশৰ উন্নতিত সন্ত্ৰাসবাদে বাধাহে জন্মালে। আলফাৰ দৰে উগ্ৰপন্থী সংগঠনৰ ব্যৰ্থতা আৰু নিষ্ফল ভূমিকা বহু বুদ্ধিজীৱী-সাহিত্যিকৰ জৰিয়তে সমালোচিত হৈছে। এই ব্যৰ্থতাৰ চিত্ৰখনৰ অংকন কেইবাটাও অসমীয়া গল্পত অতি সজীৱ আৰু সমকালক তুলি ধৰিব পৰা।

সন্ত্ৰাসবাদৰ সম্ভাৱ্য ব্যৰ্থতাক কলাত্মকভাৱে তুলি ধৰিব পৰা চুটিগল্পৰ ভিতৰত আগৰ শাৰীত থাকিব মনোজ কুমাৰ গোস্বামীৰ 'সমীৰণ বৰুৱা আহি আছে' গল্পটো। সমীৰণ নামৰ দুৰ্ঘৰ্ষ সন্ত্ৰাসবাদীজনৰ আগমন-বাৰ্তা পাই সাংবাদিকে চাঞ্চল্যকৰ বাতৰি পৰিবেশন কৰিছে, ৰাজনৈতিক নেতাই সুযোগ বিচাৰি ফুৰিছে, পূৰ্বপ্ৰণয়ী শংকিত হৈছে, মহানগৰীও ব্যস্ত আৰু প্ৰাণচঞ্চল। এনে দৃশ্যপটে স্বপ্নাতুৰ সন্ত্ৰাসবাদীজনৰ মোহভংগ ঘটাইছে : "সিটো ভাবিছিল, ট্ৰেন দুফটনাতে বিপৰ্যন্ত কোনো ডবাৰ ভিতৰত যেনেকৈ যন্ত্ৰণাত চটফট কৰি মুহূৰ্ত গণে সকলোৱে, তেনে এক অস্থিৰতাৰ মাজত সকলো বৈ আছে। কিন্তু ক'তা, কোনোতো সাজু হৈ থকা নাই। কি সহজ-সাৱলীল গতিৰে সকলো গৈ আছে। চাৰিওপিনে কি প্ৰাচুৰ্য, বৈভৱ আৰু উল্লাস। এইবোৰৰ মাজত তাৰ প্ৰয়োজন আছিলে?"^{১১} গল্পটোৰ প্ৰসংগত হৰেকৃষ্ণ ডেকাই কৈছে, "আহি থকাৰ উৎকণ্ঠা আৰু অহাৰ নিষ্ফলতাৰ মাজত গল্পৰ সময়ছোৱা। দৃশ্যৰ টুকুৰাৰ মাজেৰে কলাজ সৃষ্টি কৰি ভিন ভিন চৰিত্ৰৰ চপল, উদাসীন, ৰোমাণ্টিক প্ৰতিক্ৰিয়াৰ মাজেদি যি তাৎপৰ্যৰ সৃষ্টি কৰা হৈছে, তাৰ ইংগিত এনেধৰণৰ ৰোমাণ্টিক বিদ্ৰোহৰ ব্যৰ্থতাৰ প্ৰতি।"^{১২}

হৰেকৃষ্ণ ডেকাৰ 'বন্দীয়াৰ' গল্পত নাটকীয়ভাৱে সন্ত্ৰাসবাদীজনে বন্দুকৰ গুলীৰে আত্মহননৰ পথ বাছি লৈছে। কিন্তু পঢ়ুৱৈয়ে তাৰ আগমুহূৰ্ত ভাবিবলৈ বাধ্য হয় যে সন্ত্ৰাসবাদীজনে টোৱাই থকা বন্দুকৰ গুলীয়ে পণবন্দীজনৰহে বুকু থকা-সৰকা কৰিব। এই ওলোটো দৃশ্যপটে সন্ত্ৰাসবাদৰ নিষ্ফলতাকে প্ৰকট কৰে।

স্বপন নামৰ এজন হতাশাগ্ৰস্ত লোক পিষ্টলৰ প্ৰতি আকৰ্ষিত হৈয়ো পাছত সুস্থ জীৱনশৈলী গ্ৰহণ কৰিছে প্ৰশান্ত কুমাৰ দাসৰ 'মহানিৰ্বাণ' শীৰ্ষক গল্পত। চৰম হতাশাৰ অন্ততো যে সন্ত্ৰাসবাদৰ আশ্ৰয় লোৱাটো উচিত নহয় তাৰেই ব্যঞ্জনা গল্পটোত অনুৰণিত হৈছে।

৪.৫ সন্ত্ৰাসৰ প্ৰতি বিৰোধমূলক দৃষ্টিভংগী :

সন্ত্ৰাসে আৱৰি থকা নব্বৈৰ দশকৰ সময়ছোৱাত মানুহ অস্তিত্বৰ সংকটত ভুগিছিল। যুৱ প্ৰজন্মৰ মানসিক পৰিৱৰ্তন আৰু তাৰ ফলস্বৰূপে জাতীয় জীৱনত আহি পৰা চৰম অনিশ্চয়তা আৰু আতংকময় পৰিবেশত সৰ্বসাধাৰণে শান্তিৰ বাবে হাহাকাৰ কৰিছিল। প্ৰকাশ্যে নহ'লেও মানুহে মানসিক স্তৰত সন্ত্ৰাসৰ প্ৰতি বিৰোধ-ভাৱ পোষণ কৰিছিল। আনহাতে, সন্ত্ৰাসবাদৰ প্ৰতি বহু সাহিত্যিক-বুদ্ধিজীৱীয়ে মুকলি বিৰোধ প্ৰদৰ্শন কৰিছিল। অৱশ্যে সন্ত্ৰাসকেন্দ্ৰিক গল্পত সন্ত্ৰাস-বিৰোধিতাৰ যি নিদৰ্শন ৰক্ষিত হৈছে, সেয়া নিতান্তই কলাসুলভ।

'সমীৰণ বৰুৱা আহি আছে' গল্পত সন্ত্ৰাসবাদৰ প্ৰতি ফুটি উঠা চৰম ভ্ৰুকুটিয়ে আমাক ভাবিবলৈ বাধ্য কৰে যে গল্পটোৰ অন্তঃস্ৰোত হিচাপে আছে তীব্ৰ বিৰোধ। মনোজ কুমাৰ গোস্বামীৰ আন এটা গল্প 'মোক জুইশলা বাহটো দিয়ক'তো 'এই সন্ত্ৰাস, দুৰ্ভাবনা আৰু ত্ৰাসৰ মাজত এটা শিশুৰ হাঁহি হয়তো খুবুই প্ৰয়োজনীয়' বুলি কৰা অনুভৱ সন্ত্ৰাসবিৰোধী মনোভাবৰ পৰিচায়ক।

জেহিৰুল হুছেইনৰ 'সৰুধেমালি বৰধেমালি' শীৰ্ষক গল্পত সন্ত্ৰাসবিৰোধী মনোভংগী বিদ্যমান। অধিবাস্তৱবাদী দৰ্শনৰ প্ৰভাৱ থকা এই গল্পত নদীয়েদি উটি অহা ডেকা ল'ৰা এটাৰ শ এজাক ল'ৰা-ছোৱালীৰ আৱাহনী মন্ত্ৰত যেন প্ৰাণ পাই উঠিছে। গল্পটোৰো উত্তৰণ ঘটিছে প্ৰাত্যহিকতাৰপৰা এক অপাৰ্থিৰ মৃত্যুবিজয়ী চেতনালৈ।^{১৩} সন্ত্ৰাসৰ বিৰুদ্ধে মানুহৰ এই কাল্পনিক বিজয় সন্ত্ৰাসবিৰোধিতাৰে নামাস্তৰ।

৪.৬ সন্ত্ৰাসবাদৰ স্বৰূপ নিৰ্ণয়ৰ প্ৰচেষ্টা :

সন্ত্ৰাসবাদৰ স্বৰূপ নিৰ্ণয়ৰ প্ৰচেষ্টা নব্বৈৰ দশকৰ দুটামান চুটিগল্পৰ কেন্দ্ৰীয় বিষয়। অপূৰ্ব কুমাৰ শহীকীয়াৰ 'বন্দুকৰ ভাৰাৰে' শীৰ্ষক গল্পত নব্বৈৰ দশকৰ অসমভূমিৰ সন্ত্ৰাসবাদক সমাজতাত্ত্বিক দৃষ্টিৰে সূক্ষ্মভাৱে পৰ্যবেক্ষণ কৰিছে। সন্ত্ৰাসবাদৰ উৎস বা কাৰণ নিৰ্ণয়ৰ প্ৰচেষ্টা আৰু তীক্ষ্ণ সমালোচনা গল্পটোৰ মূল সুৰ।

হৰেকৃষ্ণ ডেকাৰ 'বন্দীয়াৰ' গল্পত বন্দী অথবা পণবন্দী কোন : সন্ত্ৰাসবাদী নে সন্ত্ৰাসবাদীয়ে অপহৰণ কৰি অনা নাগৰিক— এই প্ৰশ্ন গল্পটোৰ অন্তৰালত বিদ্যমান। মানসিক স্তৰত এজন সন্ত্ৰাসবাদীও বন্দী হ'ব পাৰে। এই বন্দিত্বৰ অৱসান ঘটাবলৈকে

গল্পটোত বৰ্ণিত সন্ত্ৰাসবাদীজনে আত্মহননৰ পথ বাছি লৈছে।

ব্যক্তিসন্ত্ৰাসৰ স্বৰূপ উন্মোচনৰ প্ৰচেষ্টা নিহিত থকা আন এটা উল্লেখনীয় গল্প জেহিৰুল হুছেইনৰ মৃগয়া।

5.0 উপসংহাৰ :

বিংশ শতিকাৰ নব্বৈৰ দশকৰ সন্ত্ৰাসজৰ্জৰ অসমীয়া সমাজখনৰ প্ৰতিচ্ছবি ধৰি ৰাখিবলৈ সমকালৰ প্ৰায়বোৰ শক্তিশালী গল্পকাৰেই চেষ্টা কৰিছিল আৰু তাৰ ফলত কেইবাটাও কালচেতনা-প্ৰকাশক, সাৰ্থক চুটিগল্পৰ সৃষ্টি হৈছিল। এনেধৰণৰ দুটামান সৃষ্টিকৰ্ম : 'সমীৰণ বৰুৱা আহি আছে', 'জিঘাংসা', 'বন্দীয়াৰ', 'মজিয়াত তেজ', 'আমৃত্যু অমৃত', 'বন্দুকৰ ভাষাৰে' আদি।

ব্যক্তিসন্ত্ৰাস আৰু ৰাষ্ট্ৰসন্ত্ৰাসৰ কবলত আতংকৰ মাজেৰে দিন নিওৱা ব্যক্তিমানসৰ অসহায়তা, বিস্ময়-বিমূঢ় অৱস্থা গল্পকাৰসকলে আন্তৰিকতাৰে তুলি ধৰিছে। দুৰ্যোগৰ বিভিন্ন চিত্ৰৰ অংকন গল্পবোৰত অতি সজীৱ : ৰোমাণ্টিক বিদ্ৰোহ এটাৰ আহান গ্ৰহণ কৰি অসমৰ শ শ যুৱকে হাতত অস্ত্ৰ তুলি লৈছে, হিংসাত্মক কাৰ্যকলাপ চলাই গৈছে, কিন্তু তাৰ মাজতে বহুতৰে এদিন মোহভংগ ঘটিল। ফলত কিছুমানে স্বাভাৱিক জীৱনৰ মাজলৈ ঘূৰি আহিছে আৰু কেতবোৰে আত্মহত্যাও কৰিছে। যুৱ প্ৰজন্মৰ এই পৰিৱৰ্তিত মানসিকতাক অসমৰ অধিকাংশ লোকেই অস্বীকাৰ কৰিছে। তেওঁলোকে সন্ত্ৰাসত পৰ্যুদস্ত হৈ নতুন সময় আৰু ৰাষ্ট্ৰব্যৱস্থাৰ প্ৰতি বিৰাগহে প্ৰদৰ্শন কৰিলে। সন্ত্ৰাসক তেওঁলোকে ধিকাৰ দিলে, আনকি মূল সূতিলৈ ঘূৰি অহা যুৱককো সহজভাৱে গ্ৰহণ কৰিব নোৱাৰিলে।

নব্বৈৰ দশকৰ গল্পকাৰসকলৰ দৃষ্টিভংগী আছিল সন্ত্ৰাসবিৰোধী। শ্ৰেয়, বাঞ্ছনা আদিৰ মাধ্যমেৰে তেওঁলোকে সন্ত্ৰাসবাদৰ অসাবতা আৰু ব্যৰ্থতাৰ ছবিখন পৰিষ্কাৰ ৰূপত দাঙি ধৰিছে।

নব্বৈৰ দশকৰ চুটিগল্প অসমৰ ইতিহাসৰ এছোৱা দুৰ্যোগপূৰ্ণ সময়ৰ দলিল। মানবীয় মূল্যবোধ আৰু অস্তিত্বৰ সংকটকালত ব্যক্তি যি গভীৰ বেদনাবোধেৰে পীড়িত হৈছিল, তাক সহৃদয় গল্পকাৰে উপলব্ধি কৰিব পাৰিছিল। সেইবাবেই ব্যক্তিসন্ত্ৰাসৰ দুৰ্ভাবনা আৰু পীড়াক সাৰ্থকভাৱে তুলি ধৰিব পাৰিলে। গল্পসমূহত স্পষ্টতঃ কোনো পথ-নিৰ্দেশনা নাই। কাৰণ চুটিগল্পত সমস্যা সমাধানৰ উপায় বিচাৰি ফুৰিলে তাৰ কলাসুলভ গুণৰ হানি হয়। কিন্তু আওপকীয়াকৈ এই গল্পত কোৱা হৈছে যে অসমীয়া ঐতিহ্য আৰু পৰম্পৰাত সন্ত্ৰাসবাদৰ কোনো স্থান নাই।

মুঠতে, আলোচ্য প্ৰতিটো গল্পই সন্ত্ৰাসজৰ্জৰ সময়ৰ অসমীয়া মানুহৰ ভাবজগতৰ ধ্বনি-প্ৰতিধ্বনি; জীৱনধাৰাৰ একো একোটা খণ্ডচিত্ৰ।

প্ৰসংগ-সূত্ৰ :

1. Ram Ahuja, Social Problems in India, 2007, p.422
2. N. Jose Chander, 'International Terrorism : Theoretical Question', G. Gopa Kumar (ed.), *International Terrorism and Global Order in the 21st Century*, 2003, p.
3. দেৱপ্ৰসাদ বৰুৱা, 'সন্ত্ৰাসবাদৰ দেহ-বিচাৰ : অসমৰ পৰা সন্ত্ৰাস নিৰ্মূলৰ ৰাজনৈতিক-সামাজিক পথৰ সন্ধানত', প্ৰমোদ শৰ্মা (সম্পা.), অশান্ত উত্তৰ-পূৰ্বাঞ্চল, 2010, পৃ. 33
4. উল্লিখিত, পৃ. 35
5. গোলাপ বৰুৱা, 'বিদেশী বিতাৰণ আন্দোলন ব্যৰ্থ হৈছিল কিয়? এতিয়াও বাস্তৱ সমাধানৰ উপায় কি?', হীৰেন গোহাঁই আৰু দিলীপ বৰা (সম্পা.), অসম আন্দোলন : প্ৰতিশ্ৰুতি আৰু ফলশ্ৰুতি, 2007, পৃ. 116
6. অৰিন্দম বৰকটকী (সংক. আৰু সম্পা.), নিৰ্বাচিত অসমীয়া গল্প, 2006, পৃ.469
7. অৰিন্দম বৰকটকী, 'সাম্প্ৰতিক অসমীয়া গল্পৰ স্বৰূপ বৈশিষ্ট্য', অৰিন্দম ৰাজখোৱা (সম্পা.), অসমীয়া চুটিগল্পৰ গতি-প্ৰকৃতি, 2009, পৃ.101
8. উল্লিখিত
9. অৰিন্দম বৰকটকী, পূৰ্বোল্লিখিত, পৃ.575

১০. উল্লিখিত, পৃ.৫৩১

১১. উল্লিখিত, পৃ.৫৩৭

১২. হৰেকৃষ্ণ ডেকা, 'বামধেনু যুগৰ পৰৱৰ্তী সময়ৰ অসমীয়া চুটিগল্পৰ গতি-প্ৰকৃতি', অপূৰ্ব বৰা (সম্পা.), অসমীয়া চুটিগল্প : ঐতিহ্য আৰু বিৱৰ্তন, ২০১২, পৃ.৪০০

১৩. অৰিন্দম বৰকটকী, পূৰ্বোল্লিখিত, পৃ.৫২৫

১৪. দেৱব্ৰত শৰ্মা, 'জৈহিকল ডেইনৰ গল্প : অসমীয়া গল্পৰ প্ৰগতিশীল ধাৰাৰ প্ৰতি সবল অৱদান', অপূৰ্ব বৰা (সম্পা.), পূৰ্বোল্লিখিত, পৃ.৪৫২

সহায়ক-গ্ৰন্থ :

(ক) অসমীয়া :

গোহাঁই, হীৰেন (সম্পা.), বৰা, দিলীপ বৰকটকী, অৰিন্দম (সংক. আৰু সম্পা.)	:	অসম আন্দোলন : প্ৰতিশ্ৰুতি আৰু ফলশ্ৰুতি বনলতা, ডিব্ৰুগড়-১, দ্বিতীয় সংস্কৰণ, ২০০৭ নিৰ্বাচিত অসমীয়া গল্প ক্ৰান্তিকাল প্ৰকাশন, নগাঁও-১, দ্বিতীয় প্ৰকাশ, ২০০৬
বৰা, অপূৰ্ব (সম্পা.)	:	অসমীয়া চুটিগল্প : ঐতিহ্য আৰু বিৱৰ্তন যোৰহাট কেন্দ্ৰীয় মহাবিদ্যালয় প্ৰকাশন কোষ, যোৰহাট-১, প্ৰথম প্ৰকাশ, ২০১২
ৰাজখোৱা, অৰিন্দম (সম্পা.)	:	অসমীয়া চুটিগল্পৰ গতি-প্ৰকৃতি দত্ত পাব্লিকেশ্যনছ, লক্ষীমপুৰ, প্ৰথম প্ৰকাশ, ২০০৯
শৰ্মা, প্ৰমোদ (সম্পা.)	:	অশান্ত উত্তৰ-পূৰ্বাঞ্চল অসম পাবলিচিং কোম্পানী, গুৱাহাটী-১, দ্বিতীয় প্ৰকাশ, ২০১০

(খ) ইংৰাজী :

Ahuja, Ram	:	<i>Social Problems in India</i> Rawat Publications, New Delhi-110002, 2007
Kumar, G Gopa (ed.)	:	<i>International Terrorism and Global Order in the 21st Century</i> Kaniska Publishers, New Delhi-110002, 1st published, 2003

□□□

ISSN-2454-8146

শ্রোতস্বিনী **SROTASWINEE**

A PEER REVIEWED BILINGUAL MULTIDISCIPLINARY ANNUAL RESEARCH JOURNAL
IMPACT FACTOR (PIF) FOR THE YEAR 2019 : 3.560
VOLUME V-2019

Editors

Dr. Saiki Talukdar
Runu Saloi

Women's Cell
Kamrup College, Chamata, Nalbari

অসমীয়া শিতান :

ধৰ্মনিৰপেক্ষতাৰ বিতৰ্ক আৰু ভাবত	ড° ভবেন কাকতি	182
অসম আন্দোলন : 'অসমীয়া'ৰ আত্ম-প্ৰতিষ্ঠাৰ সংগ্ৰাম	ড° পংকজ শইকীয়া	190
ভোলানাথ দাসৰ জীৱন আৰু সাহিত্যকৰ্ম	ড° ধ্ৰুৱজ্যোতি নাথ	196
পদ্মনাথ গোহাঞিবৰুৱাৰ 'টেটোন-তামুলি' প্ৰহসনত		
লোকসাংস্কৃতিক উপাদান	ড° দীপামণি বৰুৱা দাস	200
অসমীয়া উপন্যাস সাহিত্যত নদীকেন্দ্ৰীক উপন্যাসৰ স্থান :		
এক অধ্যয়ন	ডেইজী তালুকদাৰ	207
অসমীয়া সাহিত্যত দেশীবাদ	ড° কমী কাকতি	211
বড়ো সমাজৰ ভোগালী বিহু : মাগু'/Magu	মধুকৰগিৰি বসুমতাৰী	217
সামাজিক প্ৰগতিত নাৰী শিক্ষাৰ অৱদান :		
অনুবাধা শৰ্মা পূজাৰীৰ 'মেৰেং'ৰ ওপৰত এক আলোকপাত	দুলুমণি তালুকদাৰ	220
দেৱী-তত্ত্বজ্ঞান লাভত গুৰুৰ প্ৰয়োজনীয়তা	ড° সুবোধ কুমাৰ মিশ্ৰ ভাগৱতী	225
উত্তৰাকাণ্ড ৰামায়ণ'ৰ সীতা চৰিত্ৰৰ পুনৰ নিৰ্মাণ		
(শংকৰদেৱ আৰু তুলসীদাসৰ বিশেষ উল্লিখনসহ)	নীতামণি ডেকা	229
নলবাৰী জিলাৰ কৈৱৰ্ত্ত জাতিৰ মাজত প্ৰচলিত		
একচেতীয়া উৎসৱ-পাৰ্বণ : এটি অধ্যয়ন	শ্ৰী নন্দিতা তালুকদাৰ	234

অসম আন্দোলন : 'অসমীয়া'ৰ আত্ম-প্ৰতিষ্ঠাৰ সংগ্ৰাম

ড° পংকজ শইকীয়া

বিংশ শতিকাৰ প্ৰথমভাগৰপৰাই অসমীয়া সচেতন মধ্যবিত্ত শ্ৰেণীৰ মনত সংশয় উপজিছিল যে বহিৰাগত আৰু বিদেশী লোকৰ অবাধ প্ৰব্ৰজনৰ ফলত গৃহভূমিতে অসমৰ খিলঞ্জীয়া লোকসকল সংখ্যালঘুত পৰিণত হ'ব। উনৈশ শতিকাৰ শেহৰ দশকৰপৰাই পূৰ্ববংগ (ময়মনসিংহ, বংপুৰ, পাবনা আদি জিলা) ৰপৰা বহু বাঙালী মুছলমান লোক মাটিৰ সন্ধানত অসমলৈ আহিছিল আৰু থলুৱা লোকৰ সহায় লাভ কৰি অসমৰ নামনি ভাগত বসবাস কৰিবলৈ লৈছিল। ব্যাপকভাৱে হোৱা প্ৰব্ৰজন লক্ষ্য কৰি চি এছ মুলানে ১৯৩১ চনত যি ভাৰ-ভাষা লোকপিয়লৰ প্ৰতিবেদনত ব্যৱহাৰ কৰিছিল সি অসমৰ ৰাইজক গভীৰভাৱে ভবাই তুলিছিল। ইয়াৰ পাছত দেশ বিভাজনৰ ফলস্বৰূপে অসমলৈ অহা সাত লাখৰো অধিক পাকিস্তানী ভগনীয়াক অসমত সংস্থাপন দিয়া হৈছিল। আকৌ ১৯৭১ চনত বাংলাদেশৰ মুক্তি সংগ্ৰামৰ সময়ত শৰণাৰ্থী হিচাপে অহা কেইবালাখ বাংলাদেশী অসমত থাকি গৈছিল। এইদৰে বিভিন্ন সময়ত হোৱা বৈধ-অবৈধ অনুপ্ৰৱেশ অসমৰ বাবে উদ্বেগজনক হৈ পৰে। থলুৱা অসমীয়াৰ দখলত থকা মাটিও প্ৰব্ৰজনকাৰীসকলৰ দখললৈ গৈছিল। পমুৱা ভূমি সংস্থাপন আঁচনি, ছাদুল্লা চৰকাৰৰ ভূমি উন্নয়ন আঁচনি বা খাদ্য শস্যৰ অধিক উৎপাদন আঁচনি (গ্ৰ' ম'ৰ ফুড) আদিৰ যোগেদি অসমৰ মাটি প্ৰব্ৰজিত লোকসকলে

লাভ কৰিছিল। ভূ-সম্পদৰ লগতে চাকৰিৰ ক্ষেত্ৰতো অধিকাংশ পশ্চিমবংগ আৰু পূৰ্ববংগৰপৰা অহা লোকসকলে হস্তগত কৰিছিল। ইয়াৰ প্ৰতিক্ৰিয়াস্বৰূপে অসমীয়া জাতীয়তাবাদী মধ্যবিত্ত লোকসকলে সন্দেহ আৰু আশংকা প্ৰকাশ কৰিছিল যে এনে প্ৰব্ৰজন বোধ কৰিব নোৱাৰিলে অসমৰ থলুৱা লোক সংখ্যালঘুত পৰিণত হ'ব, ভাষা-সংস্কৃতি বিপদাপন্ন হ'ব, ৰাজনৈতিক-অৰ্থনৈতিক নিয়ন্ত্ৰণ এদিন বিদেশীৰ হাতলৈ যাব। অসম আন্দোলনৰ এগৰাকী কঠোৰ সমালোচক অমলেন্দু গুহয়ো আনকি আন্দোলন আৰম্ভ হোৱাৰ পূৰ্বে প্ৰব্ৰজনপ্ৰসূত পৰিস্থিতিৰ বাস্তৱ বিৱৰণ দিছিল— “জনপ্ৰব্ৰজন অবিৰতভাৱে চলি থাকিলে অসমীয়াসকল তেওঁলোকৰ বাসভূমি ব্ৰহ্মপুত্ৰ উপত্যকাত ভাষিক সংখ্যালঘুত পৰিণত নহ'বনে? কেৱল নগৰীয়া মধ্যবিত্ত শ্ৰেণীটোৰেই নহয়, কৃষকসমাজৰ মনকো এই প্ৰশ্নটোৱে ভাৰাক্ৰান্ত কৰিলে।” এনে দীৰ্ঘদিনীয়া ভীতিৰ ফলস্বৰূপেই অসমৰ জাতীয়তাবাদী সংগঠন আছু, জাতীয়তাবাদী সভা অসম সাহিত্য সভা আৰু জাতীয়তাবাদী দল পি এল পি, অসম জাতীয়তাবাদী দল আৰু এইবোৰৰ যৌথ মঞ্চ সদৌ অসম গণ সংগ্ৰাম পৰিষদৰ উদ্যোগত অসম আন্দোলন গঢ় লৈ উঠিছিল। আন্দোলনৰ মূল দাবী বিদেশী বহিষ্কৰণ আছিল যদিও ইয়াৰ অন্তৰালত আছিল ভাষিক-সাংস্কৃতিক আত্মৰক্ষা, ৰাজনৈতিক

আৰু অৰ্থনৈতিক আত্ম-নিয়ন্ত্ৰণ তথা আত্ম-প্ৰতিষ্ঠাৰ প্ৰয়াস।

বামপন্থী দলসমূহে ১৯৭৯-১৯৮৫ চনলৈ চলা অসম আন্দোলনক অগণতান্ত্ৰিক, ফেচীবাদী, দাম্প্ৰদায়িক, আৰেগিক, বিচ্ছিন্নতাবাদী বুলি আখ্যা দিলেও মূল দাবী বিদেশী বহিষ্কৰণক সমৰ্থন জনাইছিল। ঐতিহাসিকভাৱে দেখা যায় যে বাস্তৱ আৰু যুক্তিসংগত কাৰণতেই অসম আন্দোলন সংঘটিত হৈছিল। বিদেশী বিতাড়নৰ লগতে আন্দোলনকাৰীসকলে স্বকীয় ভাষা-সংস্কৃতিৰ অস্তিত্ব ৰক্ষাৰ বাবে কেন্দ্ৰীয় চৰকাৰৰ ওচৰত দাবী উত্থাপন কৰিছিল। এনেধৰণৰ দাবীবো বাস্তৱ আৰু ঐতিহাসিক ভিত্তি আছিল বুলি সংবাদ-পত্ৰ, আলোচনীত আলোচিত হৈছিল।

অসম আন্দোলনত অসমৰ জাতি-ধৰ্ম-বৰ্ণ নিৰ্বিশেষে সকলোৱে যোগ দি ইয়াক এক বৃহৎ জনজাগৰণৰ ৰূপ দিছিল। অসমৰপৰা বিদেশীক বহিষ্কাৰ কৰিলেহে ভূ-সম্পদ, অৰ্থনীতি, ৰাজনীতি, স্বকীয় ভাষা-সংস্কৃতিৰ সুৰক্ষা আৰু নিৰাপত্তা নিশ্চিত হ'ব বুলি তেওঁলোকে অনুভৱ কৰিছিল। অৱশ্যে অসম বহুভাষিক আৰু বহুসাংস্কৃতিক ৰাজ্য হোৱাৰ বাবে অসম আন্দোলনৰ প্ৰেক্ষাপটতে সমস্যাই গা কৰি উঠে। ক্ষুদ্ৰ ক্ষুদ্ৰ জনগোষ্ঠীয় সত্তা বিশেষকৈ জনজাতিসকলৰ একাংশ স্বকীয় জাতিসত্তা, স্বকীয় অস্তিত্বৰ বাবে সচেতন হৈ উঠিছিল। তথাপি আন্দোলনটো আৰু ইয়াক কেন্দ্ৰ কৰি হোৱা বৃহৎ জনজাগৰণে বিশ্বৰ দৃষ্টি আকৰ্ষণ কৰিছিল। অসমৰ শৈক্ষিক সংস্থা, শ্ৰমিক সংস্থা, সামাজিক অনুষ্ঠান-প্ৰতিষ্ঠান, সাহিত্যিক-সাংস্কৃতিক অনুষ্ঠান, জনগোষ্ঠীয় অনুষ্ঠান তথা সংস্থাসমূহে আন্দোলনৰ প্ৰতি সমৰ্থন আগবঢ়াইছিল। ছাত্ৰই নেতৃত্ব বহন কৰা আন্দোলন হিচাপে অসম আন্দোলন সমগ্ৰ বিশ্বৰ ভিতৰতে সৰ্ববৃহৎ আছিল। আন্দোলনত শ্ৰমিক, কৰ্মচাৰী আৰু সাধাৰণ জনতাৰ অংশগ্ৰহণ আছিল

সবাতোকৈ গুৰুত্বপূৰ্ণ। সদৌ অসম ৰাজ্যিক চৰকাৰী প্ৰতিষ্ঠানৰ কৰ্মীসকলৰ ফেডাৰেশ্বনৰ অন্তৰ্ভুক্ত অসম ক্ষুদ্ৰ উদ্যোগ উন্নয়ন নিগম, অসম এগ্ৰো ইণ্ডাষ্ট্ৰীজ শ্ৰমিক সংঘ, অসম উদ্যোগ উন্নয়ন নিগম, অসম গভৰ্ণমেণ্ট কনষ্ট্ৰাক্‌শ্বন নিগম, অসম কণ্ট্ৰাক্‌টৰছ এণ্ড টিউবছ লিমিটেড, অসম বীজ নিগম, ফাৰ্টিকেম ৱাৰ্কাৰ্ছ যুনিয়ন, অসম গেছ কোং, প্ৰকাশন ব'ৰ্ড, অসম ৰাজ্যিক এপ্ৰিকালচাৰেল মাৰ্কেটিং নিগম, অসম হিলছ স্মল ইণ্ডাষ্ট্ৰীজ কৰ্পৰেশ্বন, অসম ষ্টেট ৱায়াৰ হাউছিং নিগম, অসম প্ৰেণ্টেশ্বন এণ্ড কৰ্পৰেশ্বন উন্নয়ন নিগম, অসম ৰাজ্যিক পাঠ্যপুথি প্ৰকাশন নিগম, অ'-বি-চি উন্নয়ন নিগম, অনুসূচিত জাতি উন্নয়ন নিগম, অসম অনুসূচিত জনজাতি উন্নয়ন নিগম, ষ্টেটফেড কৰ্মী যুনিয়ন আদি অসংখ্য চৰকাৰী কৰ্মচাৰী সংঘ বা সংস্থাই আন্দোলনৰ নেতৃত্ববহনৰ বাবে যোৰিত কাৰ্যসূচীৰ প্ৰতি সঁহাৰি জনাইছিল। মন কৰিবলগীয়া কথাটো হ'ল এই যে বামপন্থী দল আৰু বুদ্ধিজীৱীসকলেও শ্ৰমিক-কৃষকৰ উৎসাহ-উদ্দীপনালৈ লক্ষ্য কৰি আন্দোলনৰ ব্যাপকতা স্বীকাৰ কৰি লৈছিল। আনকি অসমৰ খিলঞ্জীয়া মুছলমান, নেপালী সম্প্ৰদায়ৰ একাংশ, চাহ বনুৱাসকল— এওঁলোকেও আন্দোলনৰ প্ৰতি সমৰ্থন জনাইছিল। জনজাতীয় দাবী, স্বাৰ্থবোৰ কিছু তল পেলাই জনজাতিসকলেও প্ৰথম অৱস্থাত আন্দোলনটো সমৰ্থন কৰিছিল। মাথোঁ বাঙালী অধ্যুষিত বৰাক উপত্যকাৰ বিশেষকৈ কাছাৰ জিলাত আন্দোলনৰ প্ৰভাৱ সীমিত আছিল। গতিকে জাতীয়-জনগোষ্ঠীয় ব্যৱধান থাকিলেও ব্যাপক গণভিত্তিৰ ফালৰপৰা অসম আন্দোলন অসমীয়া জাতিসত্তা ৰক্ষাৰ আন্দোলন হৈ পৰিছিল।

জাতীয়তাবাদী পক্ষটোৱে আন্দোলনটো যে 'অসমীয়াৰ অস্তিত্ব ৰক্ষাৰ শেষ সংগ্ৰাম' সেই কথা ব্যাখ্যা-বিবৃতিৰ যোগেদি জনসাধাৰণৰ মাজত প্ৰচাৰ

কৰাত সফল হৈছিল। অসম জাতীয়তাবাদী দল (গিবীন বৰুৱা)ৰপৰা দিয়া এটা বিবৃতিত কোৱা হৈছিল— “এই আন্দোলনেই অসমৰ ভাগ্য নিৰ্ণয় কৰিব। এই আন্দোলনত কৃতকাৰ্যতা অৰ্জন কৰিব নোৱাৰিলে হয়তো অসমৰ নাম চিৰদিনৰ বাবে বুৰঞ্জীৰ পাতৰ পৰা বিলুপ্ত হৈ যাব।”^২ আন্দোলনৰ উদ্দেশ্য সম্পৰ্কে আছৰে এক বিবৃতিত কৈছিল—

সদৌ অসম ছাত্ৰ সন্থাই কেইবামাহো জুৰি অসমবাসীৰ আস্থা, বিশ্বাস, দৃঢ়তা আৰু ঐক্যক মূলধন কৰি লৈ অসমক বিদেশীৰ কবলৰ পৰা মুক্ত কৰি অসমৰ ভৱিষ্যত সম্পৰ্কে থলুৱা ৰাইজৰ অধিকাৰ সাব্যস্ত কৰিবলৈ বৰ্তমানৰ আন্দোলন চলাই আহিছে।... বৰ্তমানৰ আন্দোলনৰ মূল উদ্দেশ্য হ'ল অসমৰ পৰা সকলো বিদেশী নাগৰিকক চিনাক্তকৰণৰ পাছত বহিষ্কাৰ কৰা আৰু ভৱিষ্যতলৈ অসমৰ জাতীয় অস্তিত্ব ৰক্ষা হোৱাৰ বিষয়ে নিশ্চিত হোৱা।^৩

জাতীয়তাবাদী চিন্তা-চেতনাৰে পৰিচালিত অনুষ্ঠান অসম সাহিত্য সভাৰ মঞ্চৰপৰাও অসম আন্দোলনক অসমীয়াৰ আত্ম-প্ৰতিষ্ঠাৰ সুবৰ্ণ সুযোগ হিচাপে আখ্যা দিয়া হৈছিল। অসম সাহিত্য সভাৰ ৰহা অধিবেশনৰ সভাপতি যতীন্দ্ৰনাথ গোস্বামীয়ে সভাপতিৰ অভিভাষণত কৈছিল— “আপোনালোকক নকলেও হ'ব যে অসমীয়া জাতিয়ে বিভিন্ন ক্ষেত্ৰত কেইবাখনো শৰাইঘাট অতিক্ৰম কৰিবলগীয়া হৈছে। অসমীয়া ভাষা পুনৰ প্ৰচলন, অসমত শোষণাগাৰ স্থাপন, অসমীয়া ভাষাক ৰাজ্যভাষা কৰা, অসমীয়া ভাষাক উচ্চ শিক্ষাৰ মাধ্যম কৰা আদি আমাৰ সংগ্ৰামৰ একো একোটা স্তম্ভ। এতিয়া লোক-গণনাৰ প্ৰাক্কালত অসমীয়াৰ অস্তিত্ব ৰক্ষাৰ সংগ্ৰাম আৰম্ভ হৈছে। অসমীয়াই আত্মপ্ৰতিষ্ঠা কৰাৰ এয়ে সুবৰ্ণ সুযোগ।”^৪ এজন মুছলমান সম্প্ৰদায়ৰ ব্যক্তিয়ে দৈনিক অসমৰ পাতত লিখিছিল— “অসমীয়াৰ জাতীয়

অস্তিত্ব ৰক্ষাৰ শেষ সংগ্ৰামত আজি অসমীয়া জাতিব তনু-মন-প্ৰাণ উদ্বেলিত হৈ উঠিছে। অসমীয়াই আজি বুজিবলৈ বাকী নাই যে ইমানদিনে আওকাণ কৰি থাকোঁতে থাকোঁতে নিজ পিতৃভূমিতেই অসমীয়াৰ জাতীয় স্থিতি লুপ্ত হবলৈ ওলাইছে।”^৫

অসম আন্দোলনৰ নেতৃত্বই অসমীয়া জাতিসত্তাৰ অস্তিত্ব সুৰক্ষিত কৰাৰ উদ্দেশ্যে অৰ্থনৈতিক, ৰাজনৈতিক, সাংস্কৃতিক দিশ সামৰি এক জাতীয় কৰ্মসূচী গ্ৰহণৰ বাবে প্ৰচেষ্টা আৰম্ভ কৰিছিল। ইয়াৰ উপৰি অসমীয়াৰ স্বাৰ্থৰ হকে সমসাময়িক অৰ্থনৈতিক দিশতো মাত মাতিলিছিল। মূল্যবৃদ্ধি, কেবাচিন, ডিজেল আদি অত্যাৱশ্যকীয় সামগ্ৰীৰ সমবিতৰণ আৰু কৃত্ৰিম নাটনি— এনে বিষয়ত প্ৰতিবাদ সাব্যস্ত কৰিছিল আৰু চৰকাৰৰ ওপৰত চাপ বৃদ্ধি কৰিবলৈ সমৰ্থ হৈছিল। অসম আন্দোলনৰ এটা গুৰুত্বপূৰ্ণ কাৰ্যসূচী আছিল অৰ্থনৈতিক অৱৰোধ। অসমৰ তেল শোষণাগাৰবোৰৰপৰা আন্তঃৰাজ্যিক তেলৰ সৰবৰাহ আন্দোলনৰ সমৰ্থনকাৰীসকলে বন্ধ কৰি কেন্দ্ৰ আৰু ৰাজ্য চৰকাৰৰ ওপৰত অসমৰ সমস্যা সমাধানৰ হকে হেঁচা প্ৰয়োগ কৰিছিল। কেৱল খাৰুৱা তেলৰ ক্ষেত্ৰতে নহয়— বাঁহ, কাঠ, প্লাইউড আদি সামগ্ৰীৰ সৰবৰাহো সাময়িকভাৱে বন্ধ কৰা হৈছিল। আন্দোলন চলি থকা কালতে সচেতন জাতীয়তাবাদীসকলে উপলব্ধি কৰিছিল যে বিদেশী বহিষ্কাৰণৰ লগতে অৰ্থনৈতিক স্বাৱলম্বী লাভ কৰিলেহে অসমীয়া জাতীয় সত্তাৰ ভৱিষ্যৎ সুৰক্ষিত হ'ব। সেয়েহে জাতীয় কৰ্মসূচী গ্ৰহণৰ লগতে স্বাৱলম্বী হোৱাৰ প্ৰচেষ্টা চলাইছিল। এক দীৰ্ঘম্যাদী অৰ্থনৈতিক সূচীৰ প্ৰয়োজনীয়তা অনুভৱ কৰি আছৰ এক বিবৃতিত সাধাৰণ সম্পাদক ভৃগু কুমাৰ ফুকনে কৈছিল— “অৰ্থনৈতিক আৰু ৰাজনৈতিক শক্তি অসমৰ থলুৱা ৰাইজৰ হাতলৈ আনিব লাগিব। ইয়াৰ অৰ্থ এইটো নহয়

যে অসমত বাস কৰা অখিলঞ্জীয়া ভাৰতীয় সকলৰ প্ৰতি অবিচাৰ কৰিব খোজা হৈছে। অসমৰ খিলঞ্জীয়া বহুইজ্জ বাজনৈতিক অৰ্থনৈতিক শক্তিৰ চালক হ'ব লোৱাৰিলে সামাজিক, সাংস্কৃতিক ঐতিহ্য, পৰম্পৰা ৰক্ষা নপৰে, বিকশিত নহয়।”^{১৬} মন কৰিবলগীয়া যে অসম আন্দোলন সৃষ্টিৰ এটা কাৰক আছিল কেন্দ্ৰই অসমৰ ওপৰত চলোৱা ঔপনিৱেশিক শাসন আৰু শোষণৰ অনুভৱ। নিবাৰণ বৰাৰ 'ইছলামাবাদ বনাম ঢাকা : দিল্লী বনাম দিছপুৰ' শীৰ্ষক প্ৰবন্ধলানিত উক্ত ঔপনিৱেশিক শাসন আৰু শোষণৰ স্বৰূপ তথ্যসহকাৰে দাঙি ধৰা হৈছিল। অৰ্থনৈতিক ক্ষেত্ৰত এনেধৰণৰ সচেতনতা আৰু আকাংক্ষাই অসমীয়া জাতিসত্তাৰ আত্মপ্ৰতিষ্ঠাৰ মানসিকতাকে প্ৰতিফলিত কৰে।

আছোৱে ১৯৮৪ চনৰ ১১-১২ জানুৱাৰীত আয়োজন কৰা যোৰহাট জাতীয় অভিবৰ্তনত জাতীয় কৰ্মসূচী প্ৰণয়নৰ বিষয়টো অতি গুৰুত্বসহকাৰে আলোচনা হৈছিল। অসমীয়া সমাজখনৰ পুনৰ্নিৰ্মাণৰ কাৰণে বাজনৈতিক, আৰ্থ-সামাজিক তথা সাংস্কৃতিক দিশ সামৰি সকলো জনগোষ্ঠীৰ আশা-আকাংক্ষাক প্ৰতিফলিত কৰিব পৰাকৈ এখন সামগ্ৰিক কৰ্মসূচী প্ৰণয়ন কৰাটো তেওঁলোকে অতি জৰুৰী বুলি বিবেচনা কৰিছিল। এই কৰ্মসূচী এক জাতীয় দলিল, অসমৰ আয়ুস-ৰেখা, অসমবাসীৰ এক সুনিয়ন্ত্ৰিত জীৱন দৰ্শন হ'ব বুলি তেওঁলোকে উপলব্ধি কৰিছিল। ইয়াৰ বাস্তৱ ৰূপায়ণৰ বাবে একে বছৰে ৯-১২ এপ্ৰিললৈ গুৱাহাটী বিশ্ববিদ্যালয় চৌহদত জাতীয় কৰ্মসূচী প্ৰণয়ন কৰ্মশালা অনুষ্ঠিত কৰা হয়। কৰ্মশালাখনক চাৰিটা ভাগত ভাগ কৰি লোৱা হয়। প্ৰতিটো ভাগৰে সঞ্চালনাৰ দায়িত্বত অসমৰ জাতীয় জীৱনৰ প্ৰভাৱশালী ব্যক্তিক নিয়োজিত কৰা হৈছিল। উদাহৰণস্বৰূপে, ভাষা-সাহিত্য আৰু সমাজ-সম্পৰ্কীয় শাখা : বীৰেন্দ্ৰ কুমাৰ ভট্টাচাৰ্য; সাংস্কৃতিক শাখা :

অশোক গোস্বামী; বাজনৈতিক, সাংবিধানিক আৰু আইন শাখা : দেৱ প্ৰসাদ বৰুৱা; অৰ্থনৈতিক শাখা : অনিল শৰ্মা। ২১-২৩ নৱেম্বৰলৈ যোৰহাটৰ কৃষি বিশ্ববিদ্যালয় চৌহদত অনুষ্ঠিত অভিবৰ্তনত কিছু সংশোধন কৰি চূড়ান্ত জাতীয় কৰ্মসূচীখন গ্ৰহণ কৰা হয়। এই জাতীয় কৰ্মসূচীখন অসমৰ জাতীয় জীৱনৰ অস্তিত্ব আৰু সুৰক্ষাৰ দিশত এক দীৰ্ঘদিনীয়া আকাংক্ষাৰ ফলপ্ৰসূ বহিঃপ্ৰকাশ আছিল।

নৱেম্বৰত অনুষ্ঠিত অভিবৰ্তনৰ এক বিশেষ উদ্দেশ্য আছিল অসমৰ জনসাধাৰণক বাজনৈতিকভাৱে সজাগ কৰিবলৈ কাৰ্যকৰী পন্থা উদ্ভাৱন কৰা আৰু ৰাজ্যৰ আঞ্চলিক দলসমূহৰ একত্ৰীকৰণৰ জৰিয়তে এখন উমৈহতীয়া বাজনৈতিক মঞ্চ তৈয়াৰ কৰাৰ পৰিৱেশ গঢ় দিয়া। অৰ্থনৈতিক আঁচনিৰ সফল ৰূপায়ণৰ বাবে যে অসমীয়াৰ স্বাৰ্থৰ অনুকূলে এক বাজনৈতিক মঞ্চৰ প্ৰয়োজনীয়তা আছে সেই কথা অভিবৰ্তনত উপস্থিত অধিকাংশই অনুভৱ কৰিছিল। সেয়েহে বিভিন্ন জনগোষ্ঠীৰ প্ৰতিনিধিৰে এক বাজনৈতিক মঞ্চ গঠন কৰিবলৈ এই অভিবৰ্তনতে এখন এঘাৰজনীয়া সমিতি গঠন কৰা হয়। এইদৰে এক বিকল্প বাজনৈতিক দল গঠনৰ প্ৰক্ৰিয়াটোৱে পূৰ্ণতা পাইছিল অগপ দল গঠনৰ যোগেদি। ১৯৮৫ চনৰ ১২ অক্টোবৰৰপৰা অনুষ্ঠিত হোৱা গোলাঘাট বাজনৈতিক অভিবৰ্তনত গ্ৰহণ কৰা এই সম্পৰ্কীয় প্ৰস্তাৱটো আছিল এনেধৰণৰ—

বৈচিত্ৰ্যৰ মাজত ঐক্যৰ প্ৰতীক বিভিন্ন জনগোষ্ঠীৰ মিলনভূমি আৰু নানা জাতিৰ বাবেৰহণীয়া সাংস্কৃতিৰ সমন্বয়ৰ তীৰ্থ অসমৰ নিজস্ব জাতীয় সত্তাৰ সুৰক্ষাৰ বাবে ধৰ্ম-নিৰপেক্ষতা, গণতন্ত্ৰ আৰু সমাজবাদৰ আদৰ্শৰে, জ্ঞান-বিজ্ঞান, প্ৰযুক্তিবিদ্যা আৰু কলা-সাংস্কৃতিৰ পূৰ্ণ বিকাশেৰে সুসমৃদ্ধ কৃষি আৰু উদ্যোগৰ ভিত্তিত বাজনৈতিক, অৰ্থনৈতিক, সামাজিক আৰু সাংস্কৃতিক বিকাশৰ যোগেদি পুৰুষ আৰু মহিলাৰ সমমৰ্যাদা

প্ৰতিষ্ঠাৰে ভাৰতৰ জাতীয় জীৱন গঢ়ি তুলিবলৈ এখন সমৃদ্ধ অসম গঢ়ি তোলাৰ প্ৰত্যয় আৰু প্ৰতিশ্ৰুতিৰে এটা ৰাজনৈতিক (ৰাজ্যিক) দল গঠন কৰা হওক।^১

এনেদৰেই অসমীয়াৰ আত্মপ্ৰতিষ্ঠাৰ ক্ষেত্ৰত এক দৃঢ়, সুদূৰপ্ৰসাৰী ৰাজনৈতিক পদক্ষেপ অসম আন্দোলনৰ প্ৰেক্ষাপটত সম্ভৱ হৈ উঠিছিল।

যোৰহাট দ্বিতীয় জাতীয় অভিবৰ্তনত শাসনাধিষ্ঠিত হিতেশ্বৰ শইকীয়া নেতৃত্বাধীন চৰকাৰখনক দুৰ্নীতিপৰায়ণ আৰু অবৈধ বুলি অভিহিত কৰি বিধান পৰিষদ ভংগৰ বাবে এক প্ৰস্তাৱ গ্ৰহণ কৰা হৈছিল। এই দৃষ্টিকোণৰপৰা ক'ব পাৰি যে আছো এটা অৰাজনৈতিক সংগঠন হ'লেও অসমৰ ৰাজনৈতিক ক্ষেত্ৰখনত ছাত্ৰ সংগঠনটোৰ ভূমিকা অতি প্ৰভাৱশালী হৈ পৰিছিল। অশুদ্ধ ভোটাৰ তালিকা শুদ্ধ কৰাৰ দাবী, তিৰাশীৰ অবৈধ নিৰ্বাচন প্ৰতিৰোধ আদি পদক্ষেপৰ যোগেদিও আছোৱে অসমৰ ৰাজনীতিত বলিষ্ঠ ভূমিকাৰে অৱতীৰ্ণ হৈছিল। লক্ষ্যণীয় যে প্ৰাক্তন আছো আৰু অন্যান্য জাতীয়তাবাদী সংগঠনৰ সদস্যসকলেই অসম চুক্তিৰ পাছত অগপ গঠন কৰিছিল। ১৯৮৫ চনৰ সাধাৰণ নিৰ্বাচনত এই দলৰ চৰকাৰ গঠন হৈছিল আৰু ইয়াৰ জৰিয়তে অসমীয়া জাতিসত্তাৰ ৰাজনৈতিক আত্ম-প্ৰতিষ্ঠাৰ আকাংক্ষা পূৰ্ণ হৈছিল। 'অসমীয়া জাতি'ৰ স্ব-নিয়ন্ত্ৰণৰ অধিকাৰ সাব্যস্ত কৰিবলৈ ৰাজনৈতিক ক্ষমতা যে হস্তগত কৰিব লাগিব সেই উপলব্ধি অসম আন্দোলনৰ প্ৰেক্ষাপটে গভীৰ হৈছিল আৰু এই আন্দোলনেই অসমীয়া জাতীয়তাবাদক ৰাজনৈতিক ক্ষমতাৰ অধিকাৰী কৰাত সহায় কৰিলে।

অৰ্থনৈতিক আৰু ৰাজনৈতিক দিশৰ লগতে সামাজিক আৰু সাংস্কৃতিক দিশৰ অস্তিত্ব সুৰক্ষিত কৰিবলৈ আন্দোলনকাৰী জাতীয়তাবাদীয়ে কৰ্ম-আঁচনি প্ৰস্তুত কৰিছিল। অসম আন্দোলনৰ অন্যতম প্ৰধান অংশীদাৰ দল অসম জাতীয়তাবাদী দলে ১৯৮২ চনৰ মাৰ্চত অনুষ্ঠিত যোৰহাট অধিবেশনত

ৰাজনৈতিক, অৰ্থনৈতিক আৰু সাংস্কৃতিক ক্ষেত্ৰত নতুন কাৰ্যসূচী ঘোষণা কৰে। জাতীয় স্ব-নিয়ন্ত্ৰণৰ বাবে আঞ্চলিক ৰাজনৈতিক দলটোৱে অসমত পূৰ্ণ স্বায়ত্ত শাসনৰ দাবী তুলিছিল। তেনেদৰে অসমত দিন-নাগৰিকত্ব প্ৰবৰ্তনৰ যোগেদি কেৱল অসমীয়া লোকসকলকহে ৰাজনৈতিক, অৰ্থনৈতিক আৰু অন্যান্য সা-সুবিধাসমূহ প্ৰদান কৰাৰ পোষকতা কৰিছিল। অসমৰ নিষ্পেষিত জনসাধাৰণৰ আশা-আকাংক্ষাৰ বাস্তৱ ৰূপায়ণৰ বাবে এই দলে এখন শোষণহীন, বৈষম্যহীন সমাজৰ কথা কৈছিল। লগতে অসমৰ সামাজিক দিশৰ সমৃদ্ধি, উত্তৰণৰ বাবে দৰিদ্ৰতা দূৰীকৰণ, দুৰ্নীতি নিৰ্মূলকৰণ, পিছপৰা লোক বিশেষকৈ অনুসূচিত জাতি-জনজাতি, চাহ-শ্ৰমিকসকলৰ বাবে বিশেষ ব্যৱস্থা গ্ৰহণ, নিৰক্ষৰতা দূৰীকৰণ, সামাজিক সচেতনতাৰ জাগৰণ, যাতায়াত-যোগাযোগ ব্যৱস্থাৰ সম্প্ৰসাৰণ, শিশুৰ বাবে বিনামূলীয়া পুষ্টিকৰ আহাৰ যোগান, চিকিৎসা সেৱাৰ সম্প্ৰসাৰণ আৰু সু-ব্যৱস্থা আদি সামাজিক কাৰ্যসূচী গ্ৰহণৰ কথা ঘোষণা কৰিছিল। শৈক্ষিক আৰু সাংস্কৃতিক ক্ষেত্ৰত কৰা প্ৰধান ঘোষণাবোৰ আছিল— খিলঞ্জীয়া জনগোষ্ঠীৰ ভাষাসমূহৰ পূৰ্ণ বিকাশ, থলুৱা ভাষা (যেনে— বড়ো, মিচিং, কাৰ্বি, টাই আদি)ৰ মাধ্যমৰ শিক্ষানুষ্ঠানবোৰক বাদ দি আন সকলোবোৰ শিক্ষানুষ্ঠান পৰ্যায়ক্ৰমে ৰাজ্যিক ভাষাৰ মাধ্যমলৈ ৰূপান্তৰ কৰা, অনুসূচিত জাতি-জনজাতিৰ লগতে কৃতী ছাত্ৰ-ছাত্ৰীৰ বাবে জলপানীৰ ব্যৱস্থা কৰা, বিজ্ঞান, কাৰিকৰী আৰু নিয়োগমুখী শিক্ষা-ব্যৱস্থাৰ প্ৰবৰ্তন, প্ৰশিক্ষণৰ ব্যৱস্থা গ্ৰহণ, অধিক পঢ়াশালি স্থাপন, গ্ৰন্থাগাৰ আৰু গৱেষণাগাৰ স্থাপন, খিলঞ্জীয়া জনগোষ্ঠীৰ কলা-সংস্কৃতিৰ সংৰক্ষণ আৰু বিকাশ আদি।^২

এইখিনিতে এটা মন কৰিবলগীয়া কথা হ'ল এই যে আন্দোলনৰ নেতৃত্বত থকা দল-সংগঠনবোৰে

অসমৰ বিভিন্ন জনগোষ্ঠীৰ মাজত সমন্বয় আৰু সংহতি স্থাপনৰ কথা বাবে বাবে দোহাৰিছিল। আছৰ নেতৃত্বত প্ৰথম হোৱা জাতীয় কৰ্মসূচী অথবা অসম জাতীয়তাবাদী দলে ঘোষণা কৰা কৰ্মসূচীত অনুসূচিত জাতি-জনজাতি আৰু অন্যান্য পিছপৰা শ্ৰেণীৰ কল্যাণৰ বাবেও আঁচনি আছিল। 'সুস্থ-সবল অসমীয়া জাতি' গঠনৰ বাবে অসমৰ সকলো খিলঞ্জীয়া জনগোষ্ঠীৰে কল্যাণ হ'ব লাগিব বুলি তেওঁলোকে প্ৰকাশ কৰিছিল। বিদেশী নাগৰিকৰ মমস্যাটোৰ ফলত অসমৰ জনগোষ্ঠীবোৰৰ স্বকীয় সাংস্কৃতিক সত্তা ধ্বংস হোৱাৰ উপক্ৰম হৈছে বুলি তেওঁলোকে সংবাদ-মাধ্যমৰ যোগেদি ব্যক্ত কৰিছিল। অসমৰ খিলঞ্জীয়া মুছলমান, চাহ-শ্ৰমিক, খিলঞ্জীয়া নেপালী, জনজাতীয় লোকসকলকো অসমীয়া জাতীয়ত্বৰ অন্তৰ্ভুক্ত কৰি এক সামগ্ৰিক অস্তিত্ব বক্ষাৰ কথা জাতীয়তাবাদী পক্ষটোৱে কৈছিল। সেইবাবে এক অশুভ শক্তিয়ে তেওঁলোকৰ মাজত বিভেদ সৃষ্টি কৰিবলৈ প্ৰয়াস কৰাৰ প্ৰসংগটো নেতৃত্বই বাবে বাবে উত্থাপন কৰিছিল। লক্ষ্যণীয় যে 'অসমীয়াৰ আত্ম-প্ৰতিষ্ঠাৰ সংগ্ৰাম'ত সকলো জনগোষ্ঠীৰে অংশগ্ৰহণ প্ৰয়োজনীয় বুলি জাতীয়তাবাদীসকলে কোৱাৰ বিপৰীতে জনজাতিসকলৰ একাংশই কেতবোৰ কাৰণত আন্দোলনটো 'উচ্চ বৰ্ণহিন্দুৰহে আত্ম-প্ৰতিষ্ঠাৰ আন্দোলন' বুলি আখ্যা দিছিল।

অসমীয়াৰ জাতীয় জীৱনৰ সুৰক্ষা আৰু আত্ম-প্ৰতিষ্ঠাৰ প্ৰশ্নত অসম আন্দোলনৰ পৰিণাম শুভ নে অশুভ সেয়া বিতৰ্কৰ বিষয় আৰু ই এক অন্য প্ৰসংগ। কিন্তু এই কথা ঠিক যে অসম আন্দোলনৰ প্ৰেক্ষাপটত জাতীয়তাবাদী চিন্তা-চেতনাৰ যি উত্থান ঘটিছিলিয়েই আন্দোলনটোক 'অসমীয়া'ৰ আত্ম-প্ৰতিষ্ঠাৰ আন্দোলন হিচাপে গঢ় দিছিল। ৰাজনৈতিক, অৰ্থনৈতিক, সামাজিক, সাংস্কৃতিক সকলো দিশতে

স্বকীয় অস্তিত্ব আৰু স্ব-নিয়ন্ত্ৰণৰ বাবে অসমীয়াৰ মাজলৈ এক ব্যাপক জাগৰণ আহিছিল। কেন্দ্ৰীয় চৰকাৰৰ ঔপনিবেশিক শোষণ, বিদেশীৰ ক্ৰমবৰ্ধমান আত্ৰাসনৰ বিৰুদ্ধে সংঘটিত অসম আন্দোলন এটা জাতিসত্তাৰ আত্ম-প্ৰতিষ্ঠাৰ সংগ্ৰাম আছিল।
প্ৰসংগ-সূচী :

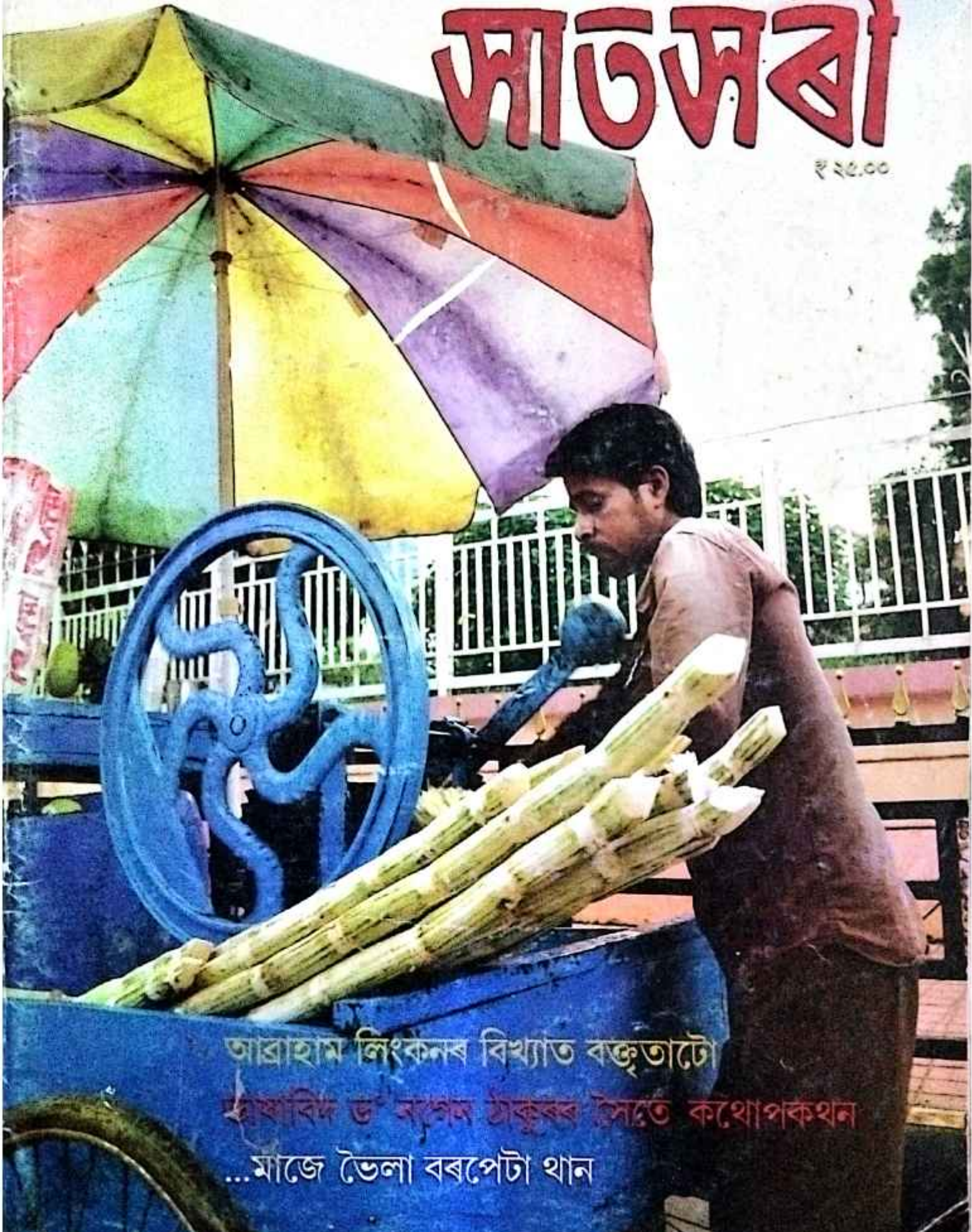
১. অমলেন্দু গুহ, প্লেণ্টাৰ ৰাজৰপৰা স্বৰাজলৈ, গোপাল বৰদলৈ (অনু.), ২০১৬, পৃ. ২২৬
২. '৫৮ ঘণ্টা জোৰা অসম বন্ধৰ জৰিয়তে অসমবাসীৰ বিদ্বেষৰ তীব্ৰতা প্ৰকাশ', কীৰ্তিনাথ হাজৰিকা (সম্পা.), দৈনিক অসম, ষোড়শ বছৰ, ১৪৯ সংখ্যা, ৪ জানুৱাৰী, ১৯৮০, পৃ. ৪
৩. 'ছাত্ৰ সন্থা দায়িত্ব সম্পৰ্কে সজাগ আৰু মূল লক্ষ্যত অবিচল', কীৰ্তিনাথ হাজৰিকা (সম্পা.), দৈনিক অসম, ষোড়শ বছৰ, ১৮১ সংখ্যা, ৯ ফেব্ৰুৱাৰী, ১৯৮০, পৃ. ১
৪. 'অসমীয়াই আত্মপ্ৰতিষ্ঠা কৰাৰ এয়ে সুবৰ্ণ সুযোগ', কীৰ্তিনাথ হাজৰিকা (সম্পা.), দৈনিক অসম, ষোড়শ বছৰ, ২২৩ সংখ্যা, ২৩ মাৰ্চ, ১৯৮০, পৃ. ১
৫. এম ইছলাম, 'অসমীয়াৰ জাতীয় জাগৰণ আৰু অস্বিকাগিৰি', কীৰ্তিনাথ হাজৰিকা (সম্পা.), দৈনিক অসম, ষোড়শ বছৰ, ১৪৭ সংখ্যা, ২ জানুৱাৰী, ১৯৮০, পৃ. ৩
৬. 'আন্দোলনৰ লগতে দীৰ্ঘম্যাদী অৰ্থনৈতিক আঁচনিৰো প্ৰয়োজন : ছাত্ৰ সন্থা', কীৰ্তিনাথ হাজৰিকা (সম্পা.), দৈনিক অসম, সপ্তদশ বছৰ, ২৬৯ সংখ্যা, ১৪ মে', ১৯৮১, পৃ. ১
৭. 'নতুন আঞ্চলিক দল 'অসম গণ পৰিষদ' গঠিত', কীৰ্তিনাথ হাজৰিকা (সম্পা.), দৈনিক অসম, একবিংশতিতম বছৰ, ৭১ সংখ্যা, ১৫ অক্টোবৰ, ১৯৮৫, পৃ. ১
৮. ব্ৰষ্টাৰ, 'জাতীয়তাবাদী দলৰ যোৰহাট অধিবেশনৰ সিদ্ধান্ত : ৰাজনৈতিক, অৰ্থনৈতিক, সাংস্কৃতিক দিশত নতুন কাৰ্যসূচী ঘোষণা', মুনীন্দ্ৰনাৰায়ণ দত্তবৰুৱা (সম্পা.), সাপ্তাহিক নীলাচল, ৬৭১ সংখ্যা, ১৭ মাৰ্চ, ১৯৮২, পৃ. ৩ আৰু ৮

ISSN: 2319-8893

পঞ্চদশ বছৰ, প্রথম সংখ্যা, আগষ্ট ২০১৯

সাতসৰী

₹ ২৬.০০



আব্রাহাম লিংকনৰ বিখ্যাত বক্তৃতাটো

দ্রষ্টব্যবিদ ড° অগম ঠাকুৰৰ সৈতে কথোপকথন

...মাজে ভৈলা বৰপেটা থান

বিশেষ
লেখা | ড° বিৰিঞ্চি কুমাৰ দাস • আব্রাহাম লিংকনৰ বিখ্যাত বক্তৃতাটো • ২৮
অপৰাজ • কৃষ্ণগহুৰৰ আলোকচিত্ৰ আৰু... • ৪০

প্ৰবন্ধ
নিবন্ধ | অনিল বায়চৌধুৰী • ...মাজে ভৈলা বৰপেটা থান • ২৪
ড° পংকজ শইকীয়া • অসম আন্দোলন আৰু অসমৰ সাংস্কৃতিক জাগৰণ • ৩০
ভাস্কৰজ্যোতি নাথ • বমন্যাসবাদ আৰু অসমীয়া কবিতা • ৩৬
ড° পৰমানন্দ মজুমদাৰ • 'চেতনা'ৰ আলোড়িত পৃষ্ঠা • ৪২
অনিল শইকীয়া • অসমত আধুনিক গীত চৰ্চাৰ পটভূমি • ৪৬
আব্দুল মালিক • ভ্ৰমণ-কাহিনীকাৰ চৈয়দ আব্দুল মালিক • ৫১

কবিতা

ৰুদ্ৰ সিংহ মটক, সৌৰভ শইকীয়া • ৫৪
নীলকান্ত শইকীয়া, বাজীৰ চন্দ্ৰ দেব গোস্বামী • ৫৫
কৰবী ডেকা হাজৰিকা, অমিতাভ ফুকন, ডাঃ বাজীৰ ভট্টাচাৰ্য • ৫৬
বিজয় ববিদাস, অজিৎ গগৈ, ড° নীলিমা গোস্বামী শৰ্মা • ৯১
দেবপ্ৰসাদ তালুকদাৰ, স্বীমান বৰ্মন • ৯২

নিয়মীয়া লেখা

দেবব্ৰত দাসৰ
হিয়াৰ পখিলাবোৰ • ৮৯

গল্প | নিৰ্মালি সন্দিকৈৰ চাৰিটা গল্প • যশোদা, প্ৰাইড্ এণ্ড প্ৰেজুডিচ, জেওৰা, তৃতীয় • ৮২

অনুবাদ
গল্প

মূল : গুলজাৰ, অনুবাদ : সুপৰ্ণা লাহিড়ী বৰুৱা • বাভিব পাঁবত • ৮৫
মূল : ইছমাইল গৌহৰ, অনুবাদ : ময়ূৰী শৰ্মা বৰুৱা • দেউতা • ৮৭
মূল : মাচাদো ডি আছিছ, অনুবাদ : বশিৰেখা গগৈ • মিডনাইট মাছ • ১১২

বাৰ্তালাপ



ভাষা-গবেষক ড° নগেন ঠাকুৰৰ সৈতে
অতনু ভট্টাচাৰ্য আৰু ড° প্ৰাপ্তি ঠাকুৰৰ
কথোপকথন

৭২

অনুবাদ
কবিতা | মোছে দবজে ঠংচি • ১১০
ইন্দ্ৰনীল গায়ন • ১১১

বাৰ্তা
বাস্তৱ

নিশা জুঞা • ৬৬



অসম আন্দোলন আৰু . অসমৰ সাংস্কৃতিক জাগৰণ

ড° পংকজ শইকীয়া

১৯৭৯-১৯৮৫ সময়ছোৱাত চলা প্ৰায় ছবছৰীয়া অসম আন্দোলনৰ প্ৰভাৱত অসমৰ সাংস্কৃতিক ক্ষেত্ৰখনলৈ এক ধৰণৰ জাগৰণ আহিছিল। অসম আন্দোলন প্ৰধানতঃ ৰাজনৈতিক আন্দোলন হ'লেও এই আন্দোলনে বিদেশী বহিষ্কৰণৰ জৰিয়তে অসমীয়াৰ স্বকীয় ৰাজনৈতিক, আৰ্থ-সামাজিক আৰু সাংস্কৃতিক অস্তিত্ব সুৰক্ষিত কৰাৰ আকাংক্ষা বহন কৰিছিল। সেয়েহে আন্দোলনটোক 'অসমীয়াৰ আত্মপ্ৰতিষ্ঠাৰ সংগ্ৰাম' আখ্যা দিয়া হৈছিল। 'অসমীয়াৰ অস্তিত্ব ৰক্ষাৰ শেষ সংগ্ৰাম' হিচাপে গণ্য কৰা এই আন্দোলনৰ সমান্তৰালভাৱে অসমীয়া জাতীয়তাবাদৰ প্ৰতিনিধিসকলে 'সাংস্কৃতিক ৰণ'খন আগবঢ়াই নিয়াৰ কথা ভাবিছিল।

অসমীয়াৰ স্বকীয়ত্ব প্ৰতিষ্ঠাৰ বাবে তথাকথিত 'মূলসুঁতিৰ অসমীয়াসকল' আন্দোলনৰ প্ৰেক্ষাপটত অতি সচেতন হৈ পৰিছিল। ইয়াৰ বিপৰীতে জনজাতীয় গোষ্ঠীবোৰে নিজৰ নিজৰ সাংস্কৃতিক ঐতিহ্য আৰু উপাদানবোৰৰ স্বীকৃতি আৰু চৰ্চাৰ বাবে সচেতন হৈ উঠিছিল।

ঐতিহ্য আৰু সংস্কৃতিৰ প্ৰতীকসমূহৰ নৱ-মূল্যায়ন :

ভাৰতৰ স্বাধীনতা আন্দোলনৰ পটভূমিত জাতীয়তাবোধৰ মনোভাব জাগ্ৰত কৰিবলৈ অসমীয়া লেখক-সাহিত্যিকে অসমৰ ইতিহাসৰ বীৰ-বীৰাংগনাসকলৰ অতীতৰ শৌৰ্য-বীৰ্যৰ কাহিনী, মাতৃভূমিৰ গুণানুকীৰ্তন আৰু গৌৰৱগাথা সাহিত্যৰ মাধ্যমেৰে দাঙি ধৰিছিল। একেদৰে অসম আন্দোলনৰ সময়তো সংবাদপত্ৰ-আলোচনীৰ যোগেদি এনে বীৰ-বীৰাংগনা, শিল্পীসকলক প্ৰক্ষেপ কৰা হৈছিল।

অসম আন্দোলনৰ নেতৃত্বৰ আহ্বানক্ৰমে জ্যোতিপ্ৰসাদ আগৰৱালা আৰু বিষ্ণুপ্ৰসাদ ৰাভাৰ স্মৃতিত ক্ৰমে 'শিল্পী দিবস' আৰু 'বিষ্ণু ৰাভা দিবস' সমগ্ৰ অসমতে পালন কৰা

হৈছিল। জাতীয়তাবাদী শিবিৰে অসমীয়া সমাজ-সংস্কৃতিৰ ঐতিহ্য হিচাপে পৰিগণিত হোৱা এই শিল্পী দুগৰাকীক অসমীয়া সংস্কৃতি, সভ্যতা আৰু জাতীয়তাৰ প্ৰতীকৰ ৰূপত উপস্থাপন কৰিছিল। দৈনিক অসমত লিখিছিল— “সদৌ অসম ছাত্ৰ সন্থাৰ আহ্বানত আজি সমগ্ৰ অসমতে বিভিন্ন কাৰ্যসূচীৰে শিল্পী দিবস উদ্‌যাপন কৰা হয়। সদৌ অসম ছাত্ৰ সন্থাৰ সভাপতি শ্ৰীপ্ৰফুল্ল মহন্তই আজিৰ এই পবিত্ৰ দিনটোত অসমীয়া কৃষ্টি-সংস্কৃতি, সভ্যতা আৰু মুক্তিকামী জনতাৰ আকাংক্ষাক জীৱন্ত ভাষা দিবলৈ অসমৰ শিল্পী-সাহিত্যিক-সাংবাদিক আৰু বুদ্ধিজীৱীসকলক আহ্বান জনাইছে।”

শিল্পী দিবসক প্ৰতিবাদ সাব্যস্তকৰণৰ মাধ্যম হিচাপেও জাতীয়তাবাদী পক্ষই ব্যৱহাৰ কৰিছিল। ১৯৮০ চনৰ ১৭ জানুৱাৰীত ‘অসম শিল্পী দিবস সমিতি’য়ে অনুষ্ঠিত কৰা সভাত আৰম্ভণিতে ইতিমধ্যে ছহিদ হিচাপে ঘোষিত খৰ্গেশ্বৰ তালুকদাৰ আৰু দিলীপ হাজুৰিৰ স্মৃতিত মৌন শ্ৰদ্ধা নিবেদন কৰাৰ লগতে উত্তৰ কামৰূপত সামৰিক বাহিনীয়ে চলোৱা অত্যাচাৰৰ প্ৰতিবাদ কৰি প্ৰস্তাৱ গ্ৰহণ কৰিছিল। এই সভাত ‘জাতীয়তাবোধ আৰু সংহতিৰ ক্ষেত্ৰত জ্যোতিপ্ৰসাদৰ অৱদান’ শীৰ্ষক আলোচনাচক্ৰত ভূপেন হাজৰিকা, চন্দ্ৰপ্ৰসাদ শইকীয়া, জীৱেশ্বৰ গোস্বামী, নিৰ্মলপ্ৰভা বৰদলৈ আৰু কনকসেন ডেকাৰ দৰে বিশিষ্ট ব্যক্তিয়ে অংশগ্ৰহণ কৰিছিল। জাতীয়তাবাদী নেতৃত্বই জ্যোতিপ্ৰসাদৰ সাংস্কৃতিক চিন্তা আৰু জাতীয় চেতনাৰ আধাৰত ‘নতুন অসম’ গঢ়িবলৈ আকাংক্ষা কৰিছিল। জাতীয়তাবাদী কাকতে জ্যোতিপ্ৰসাদৰ কবিতাৰ পংক্তি প্ৰকাশ কৰি অসমৰ নতুন প্ৰজন্মৰ মন সংগ্ৰামী কৰিবলৈ চেষ্টা কৰিছিল। তেনে ধৰণৰ উদাহৰণ হ’ল— ‘আয়ে দিয়া বিহু-গামোচাৰে/গুলী বোৰা তেজ মচি,/বৰদেৱতাৰ বঙা খাপনাৰ জ্বলাওঁ/শলিতাগছি/পুনৰ সপ্তম—সাজু হৈছে/দিবলে জীৱন দান’ অথবা ‘মোৰ তেজৰ এটি টোপেই/আই তোকে/কৰিব সোণালী/মোৰ অগ্নিৰে ধেমালি।”

জ্যোতিপ্ৰসাদ আৰু বিষ্ণু বাভাৰ উপৰি অসমীয়া জাতীয়তাৰ সমৃদ্ধিত অৰিহণা যোগোৱা বাগীৰ নীলমণি ফুকন আৰু অস্থিকাগীৰী ৰায়চৌধুৰী অসম আন্দোলনৰ সময়ত বিশেষভাৱে চৰ্চিত হৈছিল। এওঁলোকৰ চিন্তা আৰু কৰ্মক জাতীয়তাবাদী দল-সংগঠন-ব্যক্তিয়ে বিশেষ স্বীকৃতি প্ৰদান কৰিছিল। সেই অনুসৰি অসম সাহিত্য সভাৰ আহ্বানক্ৰমে নীলমণি ফুকনৰ জন্ম শতবৰ্ষ পূৰ্তি উপলক্ষে ১৯৮০ চনৰ ২২ জুন তাৰিখটো ‘জাতীয় স্বাৰ্থৰক্ষা দিবস’ হিচাপে পালন কৰিবলৈ সিদ্ধান্ত লোৱা হয়।

লাচিত বৰফুকন, মূলাগাভৰু, মণিৰাম দেৱান, পিয়লি ফুকন— এইসকলে নিজৰ বীৰত্বব্যঞ্জক আৰু স্বদেশপ্ৰীতিপ্ৰাপক কৰ্মৰ জৰিয়তে অসমৰ অতীত ইতিহাসত বীৰ-বীৰাংগনাৰ মৰ্যাদা লাভ কৰিছিল। এওঁলোকৰ কীৰ্তি আৰু কাৰ্যকলাপৰ সৌবৰণৰ যোগেদি অসমীয়া জাতীয় জীৱন সদায় অনুপ্ৰাণিত হৈ আহিছে। সেয়েহে অসম আন্দোলনৰ প্ৰেক্ষাপটত এই চৰিত্ৰবোৰ অসমীয়া জাতীয় ঐতিহ্য, সংস্কৃতি আৰু স্বাভিমানৰ প্ৰতীকৰ ৰূপত প্ৰক্ষেপিত হৈছিল। ২৪ নৱেম্বৰৰ দিনটো ‘লাচিত দিবস’ হিচাপে পালন কৰাত জাতীয়তাবাদী ছাত্ৰ সংগঠন অসম জাতীয়তাবাদী যুৱ-ছাত্ৰ পৰিষদে বিশেষভাৱে আগভাগ লৈছিল। এই দিনটোত লাচিতৰ প্ৰতিমূৰ্তিৰ আগত

হেঁদাং অৰ্পণ, অসমৰ জাতীয় স্বাৰ্থৰ বিপক্ষে কাৰ্যকলাপ চলোৱা ‘ঘৰ-বিভীষণ আৰু কাপৰুৰ মোমাইহঁত’ৰ বিৰুদ্ধে জেহাদ ঘোষণা, দেশপ্ৰেমমূলক কবিতা আবৃত্তি, দেশমাতৃৰ অস্তিত্ব বন্ধাৰ্থে সংকল্প গ্ৰহণ— এনে ধৰণৰ কাৰ্যসূচী ৰূপায়ণ কৰা হৈছিল। অসমীয়াৰ অস্তিত্বৰ হকে যুঁজিবলৈ নাৰীসকলক অন্তৰ্ভুক্ত কৰি মূলাগাভৰুৰ নামত ‘মূলাগাভৰু সন্থা’ আৰু যুৱকসকলক অন্তৰ্ভুক্ত কৰি লাচিতৰ নামত ‘লাচিত সেনা’ গঠন কৰাৰ সংবাদ আন্দোলনটোৰ সমকালীন সংবাদপত্ৰই দাঙি ধৰে। আনহাতে মণিৰাম দেৱান আৰু পিয়লি ফুকনৰ নাম লোৱাৰ নৈতিক অধিকাৰ চৰকাৰী পক্ষৰ নাই বুলি ‘আছু’য়ে বিবৃতি প্ৰকাশ কৰি স্বাভিমান ব্যক্ত কৰিছিল। লগতে অতীতৰ ঘটনাক বৰ্তমানৰ প্ৰেক্ষাপটত বিচাৰ কৰি নৱমূল্যায়ন আগবঢ়াইছিল। আছুৰ ভাষ্য অনুসৰি, জাতীয় বীৰ দুজনে ঔপনিৱেশিক ব্ৰিটিছৰ বিৰুদ্ধে যুঁজি ফাঁচীকাঠত ওলমিছিল; সেইদৰে ঔপনিৱেশিক দিল্লীৰ চৰকাৰে অসমৰ সংগ্ৰামী ছাত্ৰ-যুৱক-পুৰুষক গুলীয়াই মাৰিছিল।

অসমৰ ঐতিহ্য আৰু সংস্কৃতিৰ প্ৰতীকস্বৰূপ বীৰ-নেতা-শিল্পীসকলৰ এনে ধৰণৰ নতুন মূল্যায়নক এচামে কিন্তু সহজভাৱে লোৱা নাছিল। বিষয়টো সন্দৰ্ভত নাগৰিক, জনক্ৰান্তিৰ দৰে অসম আন্দোলনৰ সমালোচনা আগবঢ়াই অহা কাকতত এইচাম লেখক-বুদ্ধিজীৱীয়ে যুক্তিসহকাৰে আপত্তি দৰ্শাইছিল। এওঁলোকে জ্যোতি-বিষ্ণুৰ সঠিক মূল্যায়ন হোৱা নাই বুলি কোৱাৰ লগতে আন্দোলনত জড়িত জাতীয়তাবাদী পক্ষই জ্যোতিপ্ৰসাদৰ ভাবাদৰ্শ, সৃষ্টিক বিকৃত কৰিছে বুলি অভিযোগ উত্থাপন কৰে। এওঁলোকৰ মতে সুন্দৰৰ পূজাৰী, সমাজকৰ্মী, বিপ্লৱী আৰু সংগ্ৰামী জ্যোতিপ্ৰসাদৰ দৰে শিল্পীক সীমাবদ্ধভাৱে ‘বেছি অসমীয়া’ কৰিবলৈ যোৱাৰ ফলতে অসমত সংস্কৃতিৰ নামত ভঙামি চলিছে আৰু তাৰ ফলস্বৰূপে সাংস্কৃতিক সংকটৰ সৃষ্টি হৈছে। মাৰ্ক্সবাদী লেখকসকলে বিশ্লেষণ কৰি কৈছিল যে জ্যোতিপ্ৰসাদ আৰু বিষ্ণু বাভাৰ জীৱনাদৰ্শ আৰু কৰ্মজীৱনত সাম্যবাদ আৰু জাতীয় চেতনাৰ মাজত যোগসূত্ৰ আছিল। কিন্তু জাতীয়তাবাদীসকলে এই দুটাক বিচ্ছিন্ন কৰি বিকৃত মূল্যাংকন কৰিছে। সাম্ৰাজ্যবাদ আৰু ধনতন্ত্ৰবাদৰ বিৰুদ্ধে সংগ্ৰামী স্থিতি লৈ পাহাৰ-ভৈয়ামৰ সম্প্ৰীতিৰ ভেটিত প্ৰগতিশীল সমাজ প্ৰতিষ্ঠাৰ সপোন দেখা জ্যোতিপ্ৰসাদৰ ‘আজি ৰাঙলী কৰি দে বগাসন’ শীৰ্ষক গীতেৰে আন্দোলনকাৰী ডেকা-গাভৰুক সংগ্ৰামৰ বাবে আহ্বান জনোৱা হৈছিল; অথচ সাম্ৰাজ্যবাদবিৰোধী পল ৰবচনৰ নামত চান্দমাৰীত প্ৰতিষ্ঠা হোৱা ‘ৰবচন সংঘ’ ভঙ্গীভূত কৰি তাৰ কাষতে ‘লাচিত সংঘ’ প্ৰতিষ্ঠা কৰা হৈছে।” হোমেন বৰগোহাঞিয়ে জ্যোতিপ্ৰসাদ অথবা বিষ্ণু বাভাৰ চিন্তা-আদৰ্শৰ এটা অংশক বিচ্ছিন্ন কৰি উলিয়াই সেইখিনিক পূজা কৰা আৰু বাকীখিনিক অৱজ্ঞা কৰাটোক মহৎ শিল্পী দুজনৰ প্ৰতি চৰম অসম্মান বুলি মন্তব্য দিছিল। এনে ধৰণৰ সমালোচনা আৰু ব্যাখ্যা-বিশ্লেষণৰ পৰা অনুমান কৰিব পাৰি যে আন্দোলনৰ সময়ত মতাদৰ্শগত কাৰণতে অসমৰ সাংস্কৃতিক ঐতিহ্যৰ মূল্যায়নে এক নতুন গতি লৈছিল। জাতীয়তাবাদী দৃষ্টিকোণৰ পৰা হোৱা ঐতিহ্যৰ পুনৰ্মূল্যায়নে অসমৰ সাংস্কৃতিক জীৱনধাৰা আৰু জাতীয়তাবাদী ধাৰাত নতুনত্বৰ সংযোগ ঘটাইছিল।

অসম আন্দোলনৰ প্ৰেক্ষাপটত অসমীয়া সংস্কৃতি আৰু ঐতিহ্যৰ দুটা অপৰিহাৰ্য উপাদান তথা প্ৰতীকৰ প্ৰায়োগিক দিশত কেনে নতুনত্ব বা পৰিৱৰ্তন পৰিলক্ষিত হৈছিল, সেই

সম্পর্কে তলত বিচাৰ কৰা হৈছে। সেই উপাদান দুটা হ'ল—
(ক) বিহু, (খ) সাজপাৰ।

অসম আন্দোলনৰ প্ৰেক্ষাপটত অসমৰ 'জাতীয় উৎসৱ'ৰূপত বিহুৰ মূল্যায়ন কৰাৰ প্ৰচেষ্টা চলিছিল। অসমীয়া জাতীয়তাৰ প্ৰতি সচেতন ব্যক্তিয়ে বিহু উৎসৱ উদ্‌যাপনৰ সময়ত অসমীয়াৰ অস্তিত্ব বক্ষাৰ বিষয়টো জড়িত কৰি অসমীয়াৰ আত্মধ্বংসী প্ৰবণতা চিনাক্ত কৰিছিল। আলোচনাবোৰৰ মূল বক্তব্য আছিল এই যে বিহুৰ লগত জড়িত খাদ্যাভ্যাস, পোছাক-পৰিচ্ছদৰ ক্ষেত্ৰত অসমীয়াই পূৰ্বণি কালত যি স্বাভাৱিকতা, কৰ্মকুশলতা, দৃঢ়তাৰ পৰিচয় দিছিল, সেয়া লাহে লাহে পৰিবৰ্তন হৈ পৰনিৰ্ভৰশীলতালৈ পৰ্যবসিত হৈছে। ফুলাম বিহুৱান, গৰুৰ ডিঙিত দিয়া ন-পখাডাল, বিহুৰ ঢোলটো, পিঠাপনা— বিহুৰ এই অত্যাৱশ্যকীয় সামগ্ৰীবোৰৰ ক্ষেত্ৰত অসমীয়াসকল অনা-অসমীয়া ব্যবসায়ীৰ ওপৰত নিৰ্ভৰশীল হৈ পৰিল। বিশেষকৈ দক্ষিণ ভাৰতৰ ব্যবসায়ীয়ে গানোচা আৰু পিঠাপনাৰ চাহিদালৈ লক্ষ্য কৰি সেই সুযোগ গ্ৰহণ কৰিলে। এই দৃষ্টিকোণৰ পৰা 'অসমীয়া জাতি' বিপৰ্যন্ত হৈছে বুলি কোৱাৰ লগতে অসমীয়াই অস্তিত্ব বক্ষাৰ সংগ্ৰামত বিজয়ী হ'বলৈ সামাজিক, সাংস্কৃতিক সকলো দিশতে অভিযান চলাব লাগিব বুলি উপলক্ষি কৰা হৈছিল।^{১২}

অসম আন্দোলনৰ নেতৃত্বই বিহুৰ উছাহ-উদ্দীপনাৰ লগত 'অসমীয়াৰ অস্তিত্ব বক্ষাৰ সংগ্ৰাম'ক একাকাৰ কৰি পেলাইছিল। আন্দোলনৰ বস্তুতাপূৰ্ণ কাৰ্যসূচী আৰু অনিশ্চয়তা তথা আশংকাৰ পৰিস্থিতিৰ মাজত বিহু অনাড়ম্বৰভাৱে উদ্‌যাপিত হৈছিল। ১৯৮০ চনৰ ১৪ এপ্ৰিলৰ দিনা বঙালী বিহু মাথোঁ এদিনীয়া কাৰ্যসূচীৰে পালন কৰাৰ সিদ্ধান্ত লোৱা হয়। তদুপৰি বিভিন্ন বিহুতলীত পুৱা 'শ্ৰীময়ী অসমীৰ...' শীৰ্ষক দেশপ্ৰেমমূলক সংগীত গোৱা, ছহিদ তপৰ্ণ কৰাৰ যোগেদি জাতীয় আবেগ সৃষ্টি কৰা হৈছিল। আন্দোলনঘটিত পৰিস্থিতিত বিহুৰ দৰে আনন্দোৎসৱ এটা কিদৰে মান পৰিছিল সেই কথা প্ৰকাশ কৰি দৈনিক অসম কাকতে সংবাদ পৰিবেশন কৰিছিল— 'এইবেলি বিহু মলঙি গ'ল'। ইয়াৰ বিপৰীতে এই এদিনীয়া বিহু 'সংকল্প গ্ৰহণৰ উৎসৱ' হিচাপে পালন কৰা হৈছিল। 'অসম মৰিলে আমিও মৰিম'— এই দৃঢ়তাৰেই সমগ্ৰ অসমবাসীয়ে ব'হাগৰ বতৰত প্ৰতিশ্ৰুতিবদ্ধ হৈছিল। ৰাজ্যখনৰ ইমূৰৰ পৰা সিমূৰলৈ বিহুতলীয়ে বিহুতলীয়ে এই জাগ্ৰত জনচেতনাৰ টো বিয়পি গৈছিল।^{১৩} এইদৰেই অসমীয়া সংস্কৃতিৰ প্ৰতীক বিহু আন্দোলনৰ প্ৰেক্ষাপটত জাতীয় আবেগ আৰু 'জাতিৰ প্ৰাণপ্ৰতিষ্ঠা'ৰ আধাৰ হৈ পৰিল। আনফালে বঙালী বিহুৰ মঞ্চত অসমৰ বিভিন্ন জনজাতীয় গোষ্ঠী যেনে— বড়ো, মিচিং, কাৰ্বি, ৰাভা, ডিমাছা, গাৰো, দেউৰী আদিৰ সংস্কৃতি পৰিবেশন কৰা হৈছিল। এনেদৰে জাতি-উপজাতিৰ মাজত সংহতি আৰু ঐক্য স্থাপনেৰে অসমীয়াৰ মনোবল বৃদ্ধি কৰিব খোজা হৈছিল। বিহুৰ মঞ্চক জনজাগৰণ সৃষ্টিৰ মাধ্যমৰূপ দি বীৰেন্দ্ৰ কুমাৰ ভট্টাচাৰ্যই আহ্বান জনাইছিল— "মাত মাতক, কথা কওক, লিখক, গাওক, নাচক। আমাৰ আচৰণত সত্য ফুটি উঠক। লুইতৰ পাৰ মৈদাম হ'বলৈ নিদিব। বিদেশীৰ সমস্যা অৰ্থাৎ প্ৰেমৰ শক্তিয়ে সমাধান কৰিব লাগিব।"^{১৪}

অসম আন্দোলনৰ সময়তে বিহু উৎসৱ ৰাজনৈতিক উৎসৱলৈ ৰূপান্তৰিত হোৱা বুলি অভিযোগ উত্থাপন হৈছিল। 'এটা বিশেষ ৰাজনৈতিক দলৰ অবাঞ্ছিত ৰূপৰে সজা বিহুমঞ্চবোৰত এচাম তথাকথিত সংস্কৃতিপ্ৰেমীক ৰাজনীতিৰ পুতলা শিল্পী সজাই এদল ৰাজনীতিকক কমতালিকাৰ হীন

ষড়যন্ত্ৰত লিপ্ত হৈ অসমৰ জাতীয় উৎসৱ বিহুৰ কলুষিত কৰা'ৰ চেষ্টা চলাইছে বুলি কোৱা হৈছিল। বিহুৰ ৰাজনীতিকৰণৰ বিপক্ষে থিয় দি আছুৰে ১৯৮২ চনতে ৰাইজক সতৰ্ক কৰি দিয়ে।

অসমীয়া সংস্কৃতিৰ প্ৰতীক বিহুৰ নতুন ধৰণে উপস্থাপন আৰু ইয়াৰ সংকীৰ্ণ স্বার্থত হোৱা ব্যৱহাৰৰ বিৰুদ্ধে সজাগতা সৃষ্টি কৰাৰ সমান্তৰালভাৱে এই উৎসৱৰ উপাদানবোৰৰ বিকৃতিকৰণ সম্পৰ্কতো চিন্তাচৰ্চা হৈছিল। নাগৰিকৰ পাতত বিহুদলবোৰৰ 'পূজি সংগ্ৰহ অভিযান', বিকৃত বিহুগীত'ৰ প্ৰসংগ উল্লেখ কৰি বিহুৰ বক্ষা কৰিবলৈ আহ্বান জনোৱা হৈছিল। নিৰ্মলপ্ৰভা বৰদলৈয়ে 'টুক-বাছ ৰখাই আলিবাটত বিহু নাচি পইচা খোজা' কাৰ্যক বিকৃত মানসিকতা বুলি কৈ ভিক্ষাবৃত্তিৰ লগত বিজাইছিল।^{১৫} আটাইতকৈ উদ্বেগজনক কথাটো হ'ল এই যে অসমৰ জনজাতীয় লোকৰ এটা অংশই বিভিন্ন জনগোষ্ঠীৰ আবেগিক ঐক্য আৰু সমন্বয়ৰ প্ৰতীকস্বৰূপ বিহু বৰ্জন কৰাৰ কথা ঘোষণা কৰিছিল।^{১৬}

অসমীয়া জাতীয়তাৰ স্বকীয় ঐতিহ্যৰ হীনভেটি অথবা ক্ৰম-অৱলুপ্তিৰ প্ৰসংগ অসম আন্দোলনৰ সময়ত চৰ্চিত হৈছিল। লগতে হেৰাই যাবলৈ ধৰা ঐতিহ্যৰ পুনৰুদ্ধাৰৰ জৰিয়তে জাতীয় জীৱন আৰু সাংস্কৃতিক সমৃদ্ধ কৰাৰ প্ৰচেষ্টাও পৰিলক্ষিত হয়। সংস্কৃতিৰ অন্যান্য অংগৰ দৰে সাজপাৰেও জাতীয় জীৱনৰ স্বকীয় বৈশিষ্ট্য প্ৰকাশ কৰে। কিন্তু আধুনিকতা, অনুকৰণপ্ৰিয়তা আৰু নতুনত্বৰ প্ৰতি ওপজা আকৰ্ষণৰ ফলস্বৰূপে অসমীয়াৰ ঐতিহ্যপূৰ্ণ সাজপাৰৰ ক্ষেত্ৰত পৰিবৰ্তন দেখা গৈছিল। হিন্দী চিনেমাৰ অনুকৰণত অসমীয়া নাৰীয়ে সেই সময়ত চুৰিদাৰ, চেলেৱাৰ, কুৰ্তা, পায়জামা পিন্ধিবলৈ লয়। অসমীয়া জাতীয় সাজ-পোছাকৰ পৰিবৰ্তে এনেদৰে আনৰ সাংস্কৃতিক পৰম্পৰা গ্ৰহণ কৰাৰ বাবে সচেতন লোকসকল চিন্তিত হৈছিল। ইয়াৰ জৰিয়তে দেশৰ বৃহৎ পুঞ্জিপতি আৰু শিল্পপতি অৰ্থাৎ অনা-অসমীয়া ব্যবসায়ীসকলৰ লাভ হৈছিল। ইয়াৰ লগে লগে স্বকীয় ঐতিহ্য-পৰম্পৰা বিসৰ্জন দিয়াৰ বাবে অসমীয়াৰ জাতীয় সংস্কৃতি আৰু জাতীয় পৰিচয় অৱক্ষয়ৰ গৰাহত পৰিছিল।^{১৭} অসম আন্দোলনৰ প্ৰেক্ষাপটত সাংস্কৃতিক অস্তিত্ব তথা সুৰক্ষাৰ প্ৰশ্নত এনে ধৰণৰ আলোচনা-সমালোচনা সাংস্কৃতিক পুনৰুদ্ধাৰৰ প্ৰয়াস হিচাপে বিবেচিত হ'বৰ যোগ্য।

অসমৰ কাকত-আলোচনীত অসমীয়া জীৱনী-বোৱাৰীৰ শাৰীপ্ৰীতিৰ বিষয়ে কটু সমালোচনা কৰা হৈছিল। অসম সাহিত্য সভাই অসমীয়া নাৰীক শাৰী পৰিত্যাগ কৰি জাতীয় সাজপাৰ মেখেলা-চাদৰ পৰিধান কৰিবলৈ সকায়াই দিছিল। পুৰুষৰ জাতীয় সাজপাৰৰ প্ৰসংগত চোলা-চুৰিয়া পৰিধানৰ কথা উত্থাপিত হোৱাৰ লগতে বিদেশী চাহাবৰ অনুকৰণত কোট-পেণ্ট-টাই পিন্ধিবলৈ লোৱা বিষয়টোৰো চৰ্চা হৈছিল। অসম আন্দোলনৰ প্ৰেক্ষাপটত হোৱা এনে ধৰণৰ সমালোচনাবোৰে জাতীয় সংস্কৃতি আৰু ঐতিহ্য বক্ষাৰ প্ৰতি এটা সচেতনতা আনে। ইয়াৰ ফলস্বৰূপে অসমীয়া সমাজৰ সাজপাৰৰ ক্ষেত্ৰলৈ এটা পৰিবৰ্তন অহা পৰিলক্ষিত হয়। বিশেষকৈ চাদৰ-মেখেলাৰ প্ৰতি অসমীয়া নাৰীৰ মৰম আৰু শ্ৰদ্ধা আন্দোলনৰ সময়ত বৃদ্ধি পাইছিল।^{১৮} সাজপাৰৰ ক্ষেত্ৰত জন্ম হোৱা এনে সচেতনতাবোধে খলুৱা বস্ত্ৰশিল্পৰ উন্নতিৰ সম্ভাৱনাও বৃদ্ধি কৰিছিল।

দৈনিক অসমৰ এটা সম্পাদকীয়ত কটন কলেজৰ দৰে অসমৰ এখন আগশাৰীৰ শৈক্ষিক অনুষ্ঠানৰ ছাত্ৰ-ছাত্ৰীসকলে শাৰী, চেলোৱাৰ-কামিজ, জীনছ পৰিহাৰ কৰি ঐতিহ্যনুসাৰে পোছাক পিন্ধিবলৈ লোৱা সিদ্ধান্তৰ কথা গুৰুত্বসহকাৰে প্ৰকাশ হৈছিল। এই সম্পাদকীয়তে গোটেই দেশৰ বাবে প্ৰযোজ্য হোৱাকৈ জাতীয় পোছাক নিৰ্ধাৰণৰ প্ৰয়োজনীয়তাৰ কথাও ব্যক্ত কৰা হৈছিল।^{১১}

কৰ্মসংস্কৃতি :

অসম আন্দোলনৰ সময়ত অসমত স্বাৱলম্বী হোৱাৰ এটা জাগৰণ দেখিবলৈ পোৱা গৈছিল। আন্দোলনৰ নেতৃত্বই দিয়া আহানক্ৰমে ১৯৮২ চনৰ ১১ ফেব্ৰুৱাৰীৰ পৰা ২০ ফেব্ৰুৱাৰীলৈ সমগ্ৰ অসমতে এলানি সমাজ কল্যাণৰ কাৰ্যসূচী কৰা হয়। এই কাৰ্যসূচীৰ অধীনত পথ নিৰ্মাণ, অনুষ্ঠান-প্ৰতিষ্ঠানৰ মেৰামতি তথা পৰিষ্কাৰকৰণ, চিকিৎসালয় পৰিষ্কাৰকৰণ, গছপুলি ৰোপণৰ লগতে স্বনিৰ্ভৰশীলতাৰ বাবে বিভিন্ন ব্যৱহাৰিক কাৰ্যপদ্ধতিৰ জ্ঞান দিবলৈ আহান জনাইছিল।

অসমীয়াসকলক স্বাৱলম্বী আৰু পৰিশ্ৰমী হিচাপে গঢ়ি তুলিবলৈ আন্দোলনৰ প্ৰাৰম্ভিক অৱস্থাতে পৰা এক সজাগতাৰ সৃষ্টি হৈছিল। অসমীয়া কাকত-পত্ৰই এইক্ষেত্ৰত গুৰুত্বপূৰ্ণ ভূমিকা গ্ৰহণ কৰিছিল। প্ৰফুল্ল কটকীয়ে *নীলাচল* পাতত লিখিছে— “আত্মচেতনা আত্মপ্ৰতিষ্ঠাৰ প্ৰধান ভিত্তি। আত্মনিৰ্ভৰশীলতা ইয়াৰ এক কাৰ্যকৰী উপাদান। আত্মনিৰ্ভৰশীলতা অবিহনে আত্মচেতনা হ'ব অৰ্থহীন; কাৰণ পৰমুখ্যাপেক্ষী জাতি এটাই কেতিয়াও তাৰ আৰ্থিক, সামাজিক, ৰাজনৈতিক কোনো প্ৰকাৰ স্বকীয়তাকে ৰক্ষা কৰিব নোৱাৰে।”^{১২} আন্দোলনটোৰ পৰিপ্ৰেক্ষিতত জাগ্ৰত হোৱা অসমীয়াৰ জাতীয় চেতনাক কাৰ্যত ৰূপায়ণ কৰি আত্মপ্ৰতিষ্ঠা লাভৰ অৰ্থে কটকীয়ে সমালোচনাৰ লগতে দিহা দিছিল এনেদৰে—

আজিকালি গাঁৱে-ভূঞা কলেজ আদি গঢ়ি উঠিছে। ই ভাল কথা। কিন্তু কলেজত পঢ়িবলৈ যোৱা ডেকা-গাভৰুৱোৰ মাজত আৰামপ্ৰিয়তা গা কৰি উঠা লক্ষ্যত পৰিছে আৰু সাধাৰণ অৱস্থাত কৰা দৈনন্দিন কামকাজবিনোদ নকৰি পৰিশ্ৰম ঘৃণা কৰি বিলাসক সাৰটি লোৱা দেখা গৈছে। এনেবোৰ লক্ষণ আত্মঘাতী লক্ষণ। কিন্তু মাৰোৱাৰীসকলৰ ভিতৰত দেখিব, কলেজত পঢ়া ল'ৰায়ো গাদীত বহিছে, মাল বেচিছে, আৰু পৰীক্ষাত ভাল কৃতকাৰ্যতাও লাভ কৰিছে।... গৃহস্থালি এখনৰ অৰ্থনৈতিক দিশটো পাৰ্থ্যমানে স্বাৱলম্বী কৰি তুলিব লাগিব। গৰু-ছাগলী, হাঁহ-কুকুৰা পোহা, কল, তামোল, শাক-পাচলি ৰুই তাৰ দ্বাৰাও দুপইচা উপাৰ্জন কৰা, তাঁতশালখন তৰি লৈ শৰীৰ আৰু মনক ব্যস্ত ৰখাৰ আমাৰ অসমীয়া সমাজৰ স্বাৱলম্বনৰ প্ৰাচীন আদৰ্শ ঘৰে ঘৰে পুনৰ উজ্জীৱিত হ'ব লাগিব।^{১৩}

আন্দোলনৰ নেতৃত্বৰ 'নতুন অসম গঢ়াৰ আঁচনি'ত এই স্বাৱলম্বিতাৰ আদৰ্শই বিশেষভাৱে গুৰুত্ব পাইছিল। 'নতুন অসম গঢ়াৰ আঁচনি : এটি প্ৰাসংগিক চিন্তা' শীৰ্ষক লেখাত কমলাকান্ত দাসে স্বাৱলম্বিতাৰ লক্ষ্যত উপনীত হ'বৰ বাবে

সকলো কামৰ প্ৰতি শ্ৰদ্ধা, কামৰ প্ৰতি কৰ্মচাৰীৰ আন্তৰিকতা, অৰ্থনীতিবিদৰ পৰামৰ্শ, উদ্যোগ বিভাগৰ সেৱা-পৰামৰ্শ, ৰাইজৰ আন্তৰিকতা, সামাজিক ঐক্য— এনেবোৰ বিষয় লাগতিয়াল বুলি বিবেচনা কৰিছিল।^{১৪} মন কৰিবলগীয়া যে জ্ঞাননাথ বৰাই *আসামত বিদেশী গ্ৰহুত বিদেশীৰ আগ্ৰাসনৰ পৰা অসমীয়াৰ*



ঐতিহাসিক অসম চুক্তিৰ এটি মুহূৰ্ত

সৰ্বদিশৰ অন্তিৱৰ সুৰক্ষাৰ বাবে আত্মনিৰ্ভৰশীলতাৰ আদৰ্শ স্বাধীনতাপূৰ্ব কালতে দাঙি ধৰিছিল।

স্বাৱলম্বিতাৰ আদৰ্শৰ প্ৰতি অসমীয়া সমাজে প্ৰথম অৱস্থাত আশানুকূপভাৱে সঁহাৰি জনাইছিল। আগতে অনা-অসমীয়া অথবা বহিৰাগতৰ দখলত থকা সৰুসুৰা ব্যৱসায়-বৃত্তি যেনে— বিস্মা চলোৱা, ঠেলা চলোৱা, ফেৰিৱালাৰ কাম, চকীদাৰী, পাণ-তামোলৰ দোকান দিয়া, জোতা চিলাই কৰা, চুলি-দাড়ি কটা, মালবস্ত্ৰ কঢ়িওৱা আদিবোৰ কৰিবলৈ অসমীয়া লোক ওলাই আহিছিল।^{১৫} মুঠতে এই আদৰ্শ স্বাৱলম্বিতাৰ আন্দোলন বা বিপ্লৱ হিচাপে পৰিচিত হৈছিল আৰু এক জাতীয় জাগৰণৰ সৃষ্টি কৰিছিল।

কিন্তু স্বাৱলম্বিতাৰ জৰিয়তে বিদেশী বা বহিৰাগতৰ আগ্ৰাসন ৰোধ কৰি জাতীয় অৰ্থনীতিৰ ভেটি শক্তিশালী কৰাৰ যি পৰিকল্পনা প্ৰস্তুত কৰা হৈছিল, তাৰ সফল ৰূপায়ণৰ ক্ষেত্ৰত আশংকাও জড়িত হৈ আছিল। এই বিষয়ে এনেদৰে সকাঁয়নি দিয়া হৈছিল— “অসমীয়া জাতিৰ বাবে এটা সুস্থ অৰ্থনৈতিক ভেঁটি আমি আন্দোলনৰ লগে লগে গঢ়ি তুলিব নোৱাৰিলে, দহ বছৰৰ পাছত পুনৰ বিদেশী বিতাড়নৰ বাবে ঋগেৰুৰহঁতৰ দৰে বহুতো যৌৱনে অকালতে প্ৰাণ দিব লাগিব।”^{১৬}

দেখা গ'ল যে অসমীয়া জনজীৱনত ঠন ধৰি উঠা কৰ্মসংস্কৃতিৰ প্ৰৱণতা পৰৱৰ্তী সময়ত দুদিনীয়া ভাৰোচ্ছাসত পৰিণত হ'ল। আন্দোলনৰ সময়ৰ আটাইতকৈ দৰকাৰী কাৰ্যসূচী আছিল 'স্বাৱলম্বিতা'। কিন্তু, বিশেষকৈ যুৱক-যুৱতীসকলে ইয়াক অতি ঠেক গুণীলৈ লৈ গ'ল। দুদিনমানৰ বাবে বে'ল ষ্টেচনত বোজা কঢ়িওৱা, ট্ৰেনপৰ্ট ষ্টেচনত জোতা চাফ কৰা অথবা কাগজ বিক্ৰী কৰাটো স্বাৱলম্বিতাৰ এক সীমাবদ্ধ ধাৰণাহে। জাতীয় আত্মপ্ৰতিষ্ঠাৰ বাবে দৰকাৰী এই আদৰ্শক প্ৰধানতঃ আন্তৰিকভাৱে গ্ৰহণ কৰিব নোৱাৰাৰ বাবেই ই এক ব্যৰ্থ প্ৰয়াসত পৰিণত হৈছিল।^{১৭}

সাংস্কৃতিক সমন্বয়ৰ প্ৰচেষ্টা :

অসম আন্দোলনৰ সফলতা অসমৰ সকলো খিলঞ্জীয়া

জনগোষ্ঠীৰ একাবন্ধ সংগ্ৰামৰ দ্বাৰাহে যে সম্ভৱ হ'ব সেই কথা আন্দোলনৰ নেতৃত্বই উপলব্ধি কৰিছিল। সেয়েহে বিভিন্ন ব্যাখ্যা-বিবৃতিৰ জৰিয়তে জনসাধাৰণক সমন্বয় আৰু সংহতি বন্ধ কৰিবলৈ আহ্বান জনাইছিল। তেওঁলোকৰ মতে এটা সমাজবিৰোধী তথা 'অসমবিৰোধী চক্ৰ'ই আন্দোলন ব্যৰ্থ কৰিবলৈ প্ৰচেষ্টা চলাই গৈছে। এনে ষড়যন্ত্ৰ প্ৰতিহত কৰিবলৈ অসমৰ জনসাধাৰণৰ মাজত সাম্প্ৰদায়িক সম্প্ৰীতি অটুট বন্ধাৰ প্ৰয়োজনীয়তা আছে। সাংস্কৃতিক সমন্বয়ৰ নিদৰ্শন দেখুৱাবলৈ আন্দোলনৰ নেতৃত্বই সাংস্কৃতিক শোভাযাত্ৰা, সৰ্বধৰ্মীয় প্ৰাৰ্থনা, জনজাতীয় সংস্কৃতিৰ পৰিবেশনৰ লগতে আন আন কাৰ্যসূচীও গ্ৰহণ কৰিছিল। ১৯৮০ চনৰ ২৭ এপ্ৰিলৰ দিনা আছু আৰু সদৌ অসম গণ সংগ্ৰাম পৰিষদৰ যৌথ আহ্বানত চলা 'ৰণধ্বনি' শীৰ্ষক কাৰ্যসূচীত বিভিন্ন জনগোষ্ঠীৰ সাংস্কৃতিক শোভাযাত্ৰা সম্পন্ন হৈছিল। এই কাৰ্যসূচীত নানা ধৰণৰ বাদ্যযন্ত্ৰৰ ধ্বনি আৰু উৰুলি, হাতচাপৰি, চাইকেল-বিক্ৰা-গাড়ীৰ হৰ্ন বজাই শাব্দিক প্ৰতীকী প্ৰতিবাদ সাব্যস্ত কৰা হৈছিল। বাদ্যযন্ত্ৰৰ ভিতৰত লোকবাদ্য, জনজাতীয় বাদ্য আৰু মাগীয় ধাৰাৰ বাদ্যৰ সমাৱেশ ঘটাই সাংস্কৃতিক সমন্বয়ৰ আদৰ্শ দাঙি ধৰিছিল। সেই বাদ্যযন্ত্ৰবোৰ আছিল এনে ধৰণৰ— 'দবা', শঙ্ক (শংখ?), মূদং, খোল, ঢোল, তাল, বৰকাঁহ, নাগাৰা, কালীয়া, বিগুন, ম'হৰ শিঙৰ পেঁপা, নাৰিকল আৰু কলপাতৰ পেঁপা, শিঙ, বেণ্ড ট্ৰাম্পেট আদি।

১৯৮৩ চনৰ সাধাৰণ নিৰ্বাচনৰ সময়ছোৱাত সংঘটিত হিংসাত্মক ঘটনাৰাজিৰ পাছত অসমৰ বিভিন্ন জনগোষ্ঠীৰ মাজত সম্প্ৰীতি, সংহতি বৰ্তাই ৰাখিবলৈ আন্দোলনৰ নেতৃত্বকে ধৰি বিভিন্ন জাতীয়-জনজাতীয় সংগঠনে চেষ্টা কৰা পৰিলক্ষিত হয়। অসমীয়া সংবাদ মাধ্যমে বিবৃতি, মন্তব্য প্ৰকাশ কৰি এইক্ষেত্ৰত যথেষ্ট সহযোগিতা আগবঢ়ায়। দৈনিক অসমত আছু আৰু নিখিল বড়ো ছাত্ৰ সন্থাই যুটীয়াভাৱে দিয়া এক বিবৃতিত শান্তিপূৰ্ণ সমাজ গঠনৰ বাবে যে সাংস্কৃতিক সমন্বয়ৰ প্ৰয়োজন সেই কথা প্ৰকাশ পাইছে— "...অসমৰ সংস্কৃতি, সভ্যতাৰ বিকাশৰ কাৰণে বৈচিত্ৰ্যপূৰ্ণ বিভিন্ন জনগোষ্ঠীৰ ভাষা-সংস্কৃতি অক্ষুণ্ণ ৰাখি ইয়াৰ আত্মবিকাশৰ কাৰণে প্ৰচেষ্টা চলাব লাগিব আৰু তেতিয়াহে সম-অধিকাৰৰ ভিত্তিত বিভিন্ন জনগোষ্ঠীৰ মাজৰ মহামিলন অধিক কটকটীয়া হৈ পৰিব আৰু শান্তিপূৰ্ণ সমাজ গঢ়ি উঠিব।" নিৰ্বাচনৰ পাছত অসমৰ বিভিন্ন জনগোষ্ঠীৰ মাজত পাৰস্পৰিক শংকা, সন্দেহ, অস্থিৰতাৰ ভাব বৃদ্ধি পাইছিল। অসমৰ ভাষিক-সাংস্কৃতিক সমস্যাসমূহে ৰাজনৈতিক চৰিত্ৰ গ্ৰহণেৰে সাংস্কৃতিক বিচ্ছিন্নতাবাদৰ ফালে অগ্ৰসৰ হৈছিল। কিয়নো 'সদৌ অসম জনজাতি ছাত্ৰ সন্থা'ৰ উদ্যোগত টাই, বড়ো, ৰাভা, কছাৰী, কাৰ্বি, তিৱা, মিচিং, গাৰো, খাচিসকলৰ বাবে নিজৰ ভাষাত শিক্ষাৰ মাধ্যম আৰু জিলা পৰিষদৰ দাবী উত্থাপন হৈছিল। এনে উদ্বেগজনক পৰিস্থিতিত অসমৰ বাৰেৰহগীয়া সাংস্কৃতিক ঐতিহ্য অক্ষুণ্ণ ৰাখিবলৈ নাগৰিক কাকততো প্ৰচেষ্টা চলে। এই কাকতত দিনেশ গোস্বামীয়ে 'সংস্কৃতি বন্ধ জলাশয় নহয়, বোৰতী সূঁতিহে' বুলি কৈ 'পুনৰবাৰ শঙ্কৰী ঐতিহ্যৰ সৈতে থলুৱা জনগোষ্ঠীসমূহৰ ঐতিহ্যৰ সংমিশ্ৰণ ঘটাই নতুন যুগৰ অসমীয়াৰ সাংস্কৃতিক গঢ় দিয়া'ৰ পোষকতা কৰিছিল।

১৯৮৩ চনৰ ফেব্ৰুৱাৰীৰ নিৰ্বাচনী প্ৰেক্ষাপটত ঘটা সংঘৰ্ষ আৰু নিৰ্বাচনোত্তৰ হিংসা-প্ৰতিহিংসাত অসমৰ সাতামপুৰুষীয়া ঐক্য আৰু সংহতি বিনষ্ট হৈছিল। সেয়েহে বিভিন্ন জনগোষ্ঠীৰ

মাজত সমন্বয়, সংহতি পুনৰ সুদৃঢ় কৰিবৰ উদ্দেশ্যে এটি 'সমন্বয় সাংস্কৃতিক বাহিনী'য়ে ভূপেন হাজৰিকা আৰু বীৰেন্দ্ৰ কুমাৰ ভট্টাচাৰ্যৰ নেতৃত্বত অসমৰ বিভিন্ন অঞ্চল ভ্ৰমণ কৰিছিল।

অসম সাহিত্য সভাই অসম আন্দোলনৰ ফলত গা কৰি উঠা বিভাজনমুখী প্ৰৱণতাৰ প্ৰতি উদ্বিগ্নতা প্ৰকাশ কৰিছিল। এই সময়ছোৱাত সভাপতি হিচাপে কাৰ্যনিৰ্বাহ কৰা বীৰেন্দ্ৰ কুমাৰ ভট্টাচাৰ্য আৰু সীতানাথ ব্ৰহ্মচৌধুৰীয়ে অসমীয়া সংস্কৃতিৰ সামন্বয়িক ৰূপটো স্বীকাৰ কৰি অসমৰ জাতি-গোষ্ঠীৰ মাজত সমন্বয়, সংহতি সুদৃঢ় হোৱাটো কামনা কৰিছিল। এইক্ষেত্ৰত এক ফলপ্ৰসূ কৰ্ম-আঁচনি যুগত কৰি সভাই তাৰ কাৰ্যকৰীকৰণৰ্থে প্ৰচেষ্টা চলায়। জাতীয় সংহতি বন্ধাৰ উদ্দেশ্যে সমগ্ৰ অসমতে প্ৰচাৰ চলাবৰ বাবে এই আঁচনিখন গ্ৰহণ কৰাৰ কথা নগাঁৱৰ 'আনন্দবাম ডেকিয়াল ফুকন মহাবিদ্যালয়'ত অনুষ্ঠিত এখন সভাত বীৰেন্দ্ৰ কুমাৰ ভট্টাচাৰ্যই ১৯৮৩ চনৰ ২৯ নৱেম্বৰত ব্যক্ত কৰিছিল। অসমৰ জনজাতীয় গোষ্ঠীবোৰৰ লগত সম্ভাৱ গঢ়ি তুলিবলৈ সভাই তেওঁলোকৰ সাহিত্য-সংস্কৃতিৰ উন্নতিৰ প্ৰতিও গুৰুত্ব দিছিল। বিভিন্ন সামাজিক গোটেৰ সাংস্কৃতিক চেতনা আৰু জাতীয় চেতনাৰ সমন্বয়ৰ পোষকতা কৰি ভট্টাচাৰ্যই কৈছিল— "অসমৰ জাতীয় বিকাশ অসমৰ সকলো সামাজিক গোটেৰে সাংস্কৃতিক বৈশিষ্ট্যৰ ভাল গুণখিনিৰ সমন্বয় সাধনৰ যোগেদিহে হ'ব।"

দেখা যায় যে ঐতিহ্য আৰু সাংস্কৃতিক প্ৰতীকসমূহৰ নবমূল্যায়ন আৰু সেইবোৰত গুৰুত্ব প্ৰদানৰ জৰিয়তে অসম আন্দোলনৰ সময়ত এক সাংস্কৃতিক জাগৰণৰ প্ৰেক্ষাপট তৈয়াৰ হৈছিল। বিহ উৎসৱ জাতীয় জীৱনৰ বাবে অনুপ্ৰেৰণাৰ মাধ্যম হৈ পৰিছিল; নাবীৰ সাজপাৰ মেখেলা-চাদৰে পুনৰ জনপ্ৰিয়তা লাভ কৰিছিল। অৰ্থাৎ স্বকীয় সংস্কৃতি আৰু ঐতিহ্য বন্ধাৰ বাবে জনসাধাৰণ সচেতন হৈ পৰিছিল। কিন্তু এই ধৰণৰ জাতীয়তাবাদী আবেগ যে সাময়িকহে আছিল সেই কথা প্ৰমাণিত হ'বলৈ বেছিপৰ নালাগিল। কাৰণ কৰ্মসংস্কৃতিৰ প্ৰবল জোৱাৰ দিন যোৱাৰ লগে লগে ভাটাত পৰিণত হ'ল। অসমীয়াসকল যে আৱেগপ্ৰৱণ সেই কথা অসম আন্দোলনৰ এই নিখল প্ৰয়াসবোৰেই উদঙাই দিয়ে।

প্ৰসংগসূচী আৰু পাদটীকা :

১. 'ছাত্ৰ সন্থাৰ আহ্বান', কীৰ্তিনাথ হাজৰিকা (সম্পা.), দৈনিক অসম, ষোড়শ বছৰ, ১৬১ সংখ্যা, ১৮ জানুৱাৰী, ১৯৮০, পৃ. ১
২. দ্ৰষ্টব্য, 'শিল্পী দিবস', উল্লিখিত
৩. কীৰ্তিনাথ হাজৰিকা (সম্পা.), দৈনিক অসম, অষ্টাদশ বছৰ, ১৪৭ সংখ্যা, ১৪ এপ্ৰিল, ১৯৮৩, পৃ. ৩
৪. দ্ৰষ্টব্য, 'কাইলৈ জাতীয় স্বাৰ্থ বন্ধা দিবস', কীৰ্তিনাথ হাজৰিকা (সম্পা.), দৈনিক অসম, ষোড়শ বছৰ, ৩১১ সংখ্যা, ২১ জুন, ১৯৮০, পৃ. ১
৫. দ্ৰষ্টব্য, (ক) 'লাচিত দিবসৰ কাৰ্যসূচী', কীৰ্তিনাথ হাজৰিকা (সম্পা.), দৈনিক অসম, সপ্তদশ বছৰ, ১০৭ সংখ্যা, ২৩ নৱেম্বৰ, ১৯৮০, পৃ. ১; (খ) 'লাচিত দিবস', কীৰ্তিনাথ হাজৰিকা (সম্পা.), দৈনিক অসম, সপ্তদশ বছৰ, ১০৯ সংখ্যা, ২৫ নৱেম্বৰ, ১৯৮০, পৃ. ১

৬. "বাহজানী-পকোৱা মৌজা সংগ্ৰাম পৰিষদ আৰু ছাত্ৰ সন্থাৰ উদ্যোগত পতা এখন সভাত শ্ৰীমতী অহলা ডেকাক সভানেত্ৰী হিচাপে মনোনীত কৰি এখন মূলা বাহিনী গঠন কৰা হয়।"

— 'মূলা-গাভৰু সন্থা গঠন', কীৰ্তিনাথ হাজৰিকা (সম্পা.), *দৈনিক অসম*, ষোড়শ বছৰ, ২৯২ সংখ্যা, ২ জুন, ১৯৮০, পৃ. ১

৭. দ্ৰষ্টব্য, 'লাচিতৰ মুৰ্তি ক'লৈ গ'ল?', হোমেন বৰগোহাঞি (সম্পা.), *সাদিনীয়া নাগৰিক*, তৃতীয় বছৰ, ১২১ সংখ্যা, ২৪ এপ্ৰিল, ১৯৮০, পৃ. ৯

৮. দ্ৰষ্টব্য, 'চৰকাৰৰ মণিৰাম, পিয়লিৰ নাম লোৱাৰ অধিকাৰ নাই : ছাত্ৰ সন্থা', কীৰ্তিনাথ হাজৰিকা (সম্পা.), *দৈনিক অসম*, অষ্টাদশ বছৰ, ১০ সংখ্যা, ১৩ আগষ্ট, ১৯৮২, পৃ. ১

৯. দ্ৰষ্টব্য, 'চৈয়দ আফতাব আৰু প্ৰবীণ দেৱশৰ্মা, 'জ্যোতিপ্ৰসাদ আৰু বিষ্ণুপ্ৰসাদৰ সপোনৰ অসম', হোমেন বৰগোহাঞি (সম্পা.), *সাদিনীয়া নাগৰিক*, তৃতীয় বছৰ, ১১২ সংখ্যা, ৩১ জানুৱাৰী, ১৯৮০, পৃ. ৪, ৯, ১১

১০. দ্ৰষ্টব্য, 'খনি দাস, 'জ্যোতিপ্ৰসাদ-বিষ্ণুপ্ৰসাদৰ উত্তৰসূৰী', হোমেন বৰগোহাঞি (সম্পা.), *সাদিনীয়া নাগৰিক*, তৃতীয় বছৰ, ১১৬ সংখ্যা, ২৮ ফেব্ৰুৱাৰী, ১৯৮০, পৃ. ৩, ৪, ১১, ১২

১১. দ্ৰষ্টব্য, 'হোমেন বৰগোহাঞি, 'ৰাভা দিবস : চৰকাৰী আৰু বে-চৰকাৰী', হোমেন বৰগোহাঞি (সম্পা.), *সাদিনীয়া নাগৰিক*, চতুৰ্থ বছৰ, ১৭৭ সংখ্যা, ২৫ জুন, ১৯৮১, পৃ. ১

১২. দ্ৰষ্টব্য, 'ফটিক হাজৰিকা, 'বিহু উৎসৱ আৰু অস্তিত্ব বন্ধাৰ চেতনা', তিলক হাজৰিকা (সম্পা.), *অসম বাণী*, ২৮শ বছৰ, ৩৮ সংখ্যা, ১৫ এপ্ৰিল, ১৯৮৩, পৃ. ১, ২৪

১৩. দ্ৰষ্টব্য, 'সংগ্ৰামৰ সংকল্প লৈ এইবেলি অসমে বিহু সামৰিলে', কীৰ্তিনাথ হাজৰিকা (সম্পা.), *দৈনিক অসম*, ষোড়শ বছৰ, ২৪৫ সংখ্যা, ১৪ এপ্ৰিল, ১৯৮০, পৃ. ১

১৪. 'বিহুতলীত জাগ্ৰত জাতিৰ প্ৰাণ-স্পন্দনৰ ধ্বনি', কীৰ্তিনাথ হাজৰিকা (সম্পা.), *দৈনিক অসম*, সপ্তদশ বছৰ, ২৪০ সংখ্যা, ১৪ এপ্ৰিল, ১৯৮১, পৃ. ১

১৫. 'জাতীয় উৎসৱ বিহু ৰাজনৈতিক উৎসৱলৈ ৰূপান্তৰিত', কীৰ্তিনাথ হাজৰিকা (সম্পা.), *দৈনিক অসম*, বিংশতিতম বছৰ, ২২৯ সংখ্যা, ৬ এপ্ৰিল, ১৯৮৫, পৃ. ১

১৬. 'বিহু নামৰ নমুনা এনেকুৱা আছিল— "এ চম্পা ছাত্ৰ সন্থা জিন্দাবাদ/এ চম্পা চি পি এম মুৰ্দাবাদ/এ চম্পা এছ এফ আই গৰুচোৰ/এ চম্পা চি পি এম তিৰীচোৰ"

— 'সময়ৰ চিন্তা : বিহুৰ ৰক্ষা কৰক', হোমেন বৰগোহাঞি (সম্পা.), *সাদিনীয়া নাগৰিক*, চতুৰ্থ বছৰ, ১৭১ সংখ্যা, ৭ মে', ১৯৮১, পৃ. ৫

১৭. দ্ৰষ্টব্য, 'নিৰ্মলপ্ৰভা বৰদলৈ, 'অসমীয়া সংস্কৃতি কোন পথে?', কীৰ্তিনাথ হাজৰিকা (সম্পা.), *দৈনিক অসম*, বিংশতিতম বছৰ, ২৬০ সংখ্যা, ৫ মে', ১৯৮৫, পৃ. ২

১৮. "যোৱা ডিচেম্বৰ মাহৰ মাজভাগত লক্ষীমপুৰ জিলাৰ গোগামুখত অনুষ্ঠিত সদৌ মিচিং ছাত্ৰ সন্থাৰ বিশেষ অধিবেশনত সৰ্বসন্মতিক্ৰমে অসমৰ 'তথাকথিত' জাতীয় উৎসৱ বিহু মিচিংসকলে বৰ্জন কৰিব লাগে বুলি প্ৰস্তাৱ গ্ৰহণ কৰা হয়। যোৱা মাঘ বিহু জোনাই, চিলাপথাৰ আদি মিচিং অধ্যুষিত অঞ্চলত হেনো আংশিকভাৱেহে উদ্‌যাপন কৰিছে। দুই, তিনি আৰু চাৰি জানুৱাৰীত অনুষ্ঠিত সদৌ মুৰ্কংচেলেক মিচিং ছাত্ৰ সন্থাৰ

অধিবেশনত অসমৰ আটাইবোৰ জনজাতীয় ছাত্ৰ সংগঠনৰ নেতাৰ যোগদানো বিশেষ তাৎপৰ্য্যপূৰ্ণ। অৰ্থাৎ অন্যান্য জনজাতিবোৰেও অচিন্তে বিহু বৰ্জন কৰিব পাৰে।"

— লক্ষীনাথ পাংগিং, 'জনজাতিবোৰ অসমীয়া হৈ নাথাকে', হোমেন বৰগোহাঞি (সম্পা.), *সাদিনীয়া নাগৰিক*, চতুৰ্থ বছৰ, ১৬৯ সংখ্যা, ২৩ এপ্ৰিল, ১৯৮১, পৃ. ৩

১৯. দ্ৰষ্টব্য, 'বলীন বৰগোহাঞি, 'আধুনিকতাব নামত অপসংস্কৃতি কিয়?', হোমেন বৰগোহাঞি (সম্পা.), *সাদিনীয়া নাগৰিক*, পঞ্চম বছৰ, ২৭৩ সংখ্যা, ৩০ জুন, ১৯৮৩, পৃ. ৬

২০. দ্ৰষ্টব্য, 'নিবেদিতা শৰ্মা, 'আমাৰ সাজপাৰত আন্দোলনৰ প্ৰভাৱ', তিলক হাজৰিকা (সম্পা.), *অসম বাণী*, ২৮শ বছৰ, ৩১ সংখ্যা, ২৫ ফেব্ৰুৱাৰী, ১৯৮৩, পৃ. ৭

২১. দ্ৰষ্টব্য, 'জাতীয় পোছাক', কীৰ্তিনাথ হাজৰিকা (সম্পা.), *দৈনিক অসম*, অষ্টাদশ বছৰ, ৩৮ সংখ্যা, ১২ ছেপ্টেম্বৰ, ১৯৮২, পৃ. ২

২২. 'প্ৰফুল্ল কটকী, 'স্বাৰলক্ষী হ'ম কেনেকৈ?', মুনীন্দ্ৰনাৰায়ণ দত্তবৰুৱা (সম্পা.), *সাপ্তাহিক নীলাচল*, ৫৯৩ সংখ্যা, ২০, আগষ্ট, ১৯৮০, পৃ. ৬

২৩. উল্লিখিত
২৪. দ্ৰষ্টব্য, 'কমলাকান্ত দাস, 'নতুন অসম গঢ়াৰ আঁচনি : এটি প্ৰাসংগিক চিন্তা', মুনীন্দ্ৰনাৰায়ণ দত্তবৰুৱা (সম্পা.), *সাপ্তাহিক নীলাচল*, ৫৯৩ সংখ্যা, ২০ আগষ্ট, ১৯৮০, পৃ. ৫

২৫. দ্ৰষ্টব্য, 'ক) 'অসমীয়া মানুহ বিবিধ শ্ৰমলৈ ওলাই আহিছে', সতীশ চন্দ্ৰ কাকতী (সম্পা.), *অসম বাণী*, ২৫শ বছৰ, ৩৫ সংখ্যা, ৭ মাৰ্চ, ১৯৮০, পৃ. ১; (খ) 'স্বাৰলক্ষী হোৱাৰ শিক্ষা', কীৰ্তিনাথ হাজৰিকা (সম্পা.), *দৈনিক অসম*, ষোড়শ বছৰ, ১১৬ সংখ্যা, ২৪ ফেব্ৰুৱাৰী, ১৯৮০, পৃ. ১

২৬. 'তোবেশ্বৰ তামুলী ফুকন, 'বাৰীৰ বাঁহডালত ধৰি থিয় দিয়ক', মুনীন্দ্ৰনাৰায়ণ দত্তবৰুৱা (সম্পা.), *সাপ্তাহিক নীলাচল*, ৫৯২ সংখ্যা, ১৩ আগষ্ট, ১৯৮০, পৃ. ৪

২৭. দ্ৰষ্টব্য, 'ক) বিশ্বজিৎ বৰুৱা, 'আন্দোলনৰ নেতৃত্ব অসমৰ ভৱিষ্যৎ আৰু মুৰ্বৰ স্বৰ্গ', কনকসেন ডেকা (সম্পা.), *অগ্ৰদূত*, পঞ্চদশ বছৰ, ৫০ সংখ্যা, ১৭ অক্টোবৰ, ১৯৮৪, পৃ. ৫; (খ) 'পুলকেশ বৰুৱা, 'দীৰ্ঘম্যাদী আন্দোলন আৰু গঠনমূলক কাৰ্যসূচীৰ চিন্তা', কনকসেন ডেকা (সম্পা.), *অগ্ৰদূত*, পঞ্চদশ বছৰ, ৪৫ সংখ্যা, ১৯ ছেপ্টেম্বৰ, ১৯৮৪, পৃ. ৪

২৮. 'ৰণধৰনি'ৰ কাৰ্যসূচীত গুৱাহাটীত ৫ লাখৰ অধিক লোকৰ যোগদান, কীৰ্তিনাথ হাজৰিকা (সম্পা.), *দৈনিক অসম*, ষোড়শ বছৰ, ২৫৮ সংখ্যা, ২৯ এপ্ৰিল, ১৯৮০, পৃ. ১

২৯. 'সাতামপুৰীয়া সম্প্ৰীতি ৰক্ষা কৰাত গুৰুত্ব', কীৰ্তিনাথ হাজৰিকা (সম্পা.), *দৈনিক অসম*, অষ্টাদশ বছৰ, ১৪১ সংখ্যা, ৮ এপ্ৰিল, ১৯৮৩, পৃ. ১

৩০. 'দিনেশ গোস্বামী, 'অসমৰ ঐক্য-সংহতিৰ বাবে সাংস্কৃতিক সমন্বয়ৰ প্ৰয়োজন', হোমেন বৰগোহাঞি (সম্পা.), *সাদিনীয়া নাগৰিক*, পঞ্চম বছৰ, ২৮১ সংখ্যা, ২৫ আগষ্ট, ১৯৮৩, পৃ. ৮

৩১. 'আবেগিক দৃষ্টিৰে নাচাই....', তিলক হাজৰিকা (সম্পা.), *অসম বাণী*, ২৯শ বছৰ, ৫ সংখ্যা, ১২ আগষ্ট, ১৯৮৩, পৃ. ১১

লেখকৰ ঠিকনা : সহকাৰী অধ্যাপক, অসমীয়া বিভাগ, জেংবাইমুখ মহাবিদ্যালয়, জেংবাইমুখ, জিলা : মাজুলী, ফোন : ৭০০২০-৬৮৯০৪

আগষ্ট, ২০১৯ সাতমৰী ৩৫

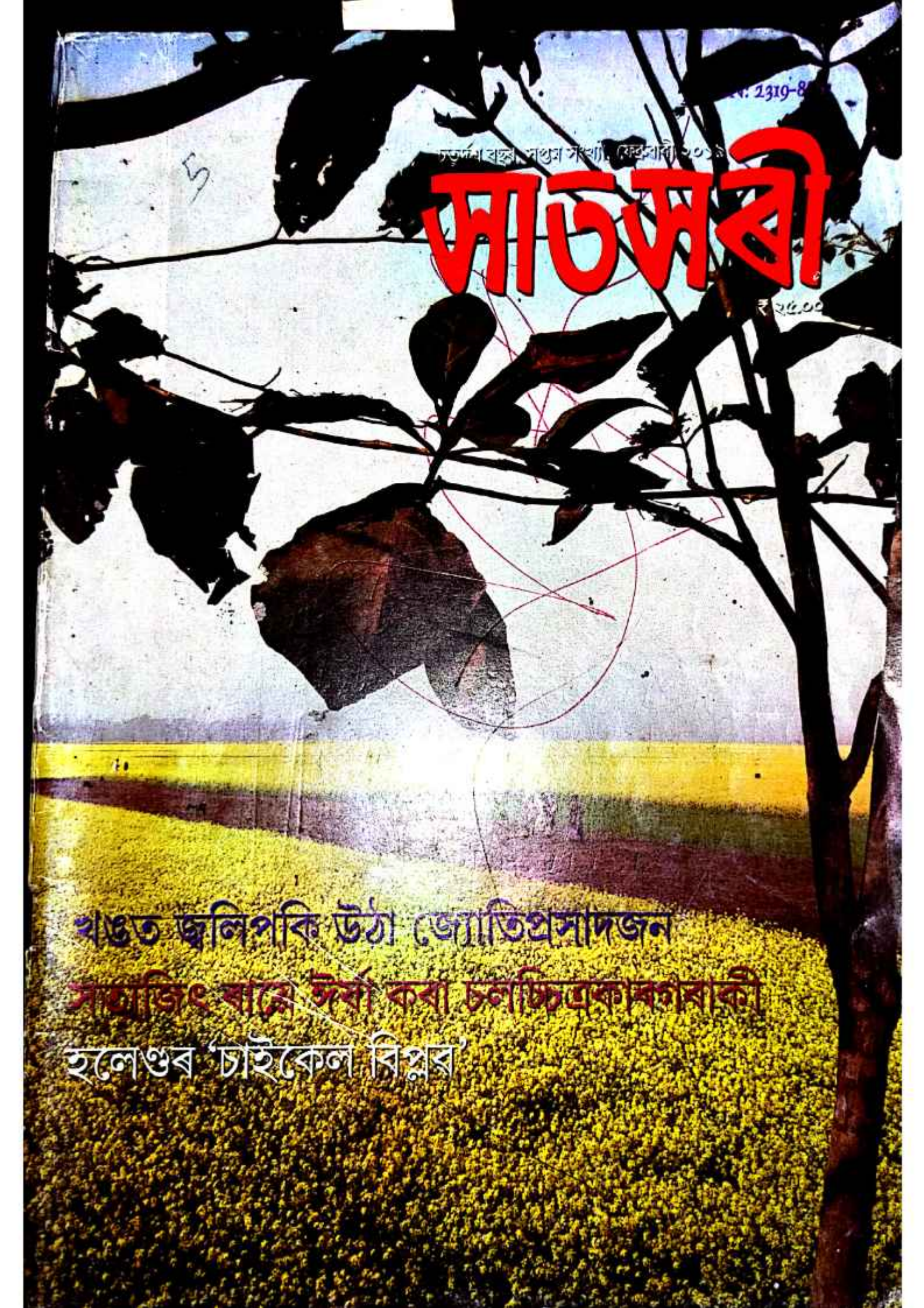
নং. 2319-8

চতুর্থ বর্ষ, পঞ্চম সংখ্যা, ফেব্রুৱাৰী ২০১৯

জাতসৰী

₹ ২৫.০০

খণ্ডত জ্বলি পকি উঠা জ্যোতিপ্ৰসাদজন
সমাজিক ষাণ্ডে সূৰ্য্য কৰা চলচ্চিত্ৰকাৰগৰাকী
হলেণ্ডৰ 'চাইকোল বিপ্লৱ'



অ ভি ম ত | হিমাংশু বৰুৱা • অসমীয়া চলচ্চিত্ৰ উদ্যোগৰ ভৱিষ্যৎ • ১৮

বি শে ষ
লে খা | পুলিন কলিতা • সত্যজিৎ ৰায়ে ঈৰ্ষা কৰা চলচ্চিত্ৰকাৰগৰাকী • ৫৭
বাণা গগৈ • হলেণ্ডৰ 'চাইকেল বিপ্লৱ' • ৬০

প্ৰ বন্ধ
নি বন্ধ | শৰৎ চন্দ্ৰ নেওগ • খঙত জ্বলিপকি উঠা জ্যোতিপ্ৰসাদজন • ৩১
বিঞ্জুমণি হাজৰিকা • নদীবান্ধৰ আন্দোলন আৰু সাহিত্য • ৩৬
ডুলুকান্ত মৰাণ • সমকামিতা : শিলা-সত্য নে স্বসৃষ্ট সমস্যা। • ৩৯
উদয় কুমাৰ শৰ্মা • কবিতাৰ ইংগিত আৰু কাব্যিক জীৱন • ৪৩
ড° পংকজ শইকীয়া • অসম আন্দোলনৰ প্ৰেক্ষাপটত জনজাতীয় অস্তিত্ব আৰু পৰিচয়ৰ পুনৰুত্থান • ৪৬
ড° পৰমানন্দ মজুমদাৰ • 'চেতনা'ৰ স্পন্দিত পৃষ্ঠা • ৫৪
ড° বাসু ৰাজখোৱা • মধ্যযুগীয় অসমৰ চিত্ৰকলা • ১০৭

ক বি তা | নিবেদন দাস পাটোৱাৰী, বিৰিঞ্চি কুমাৰ ৰাভা • ২৭
অমৰ শৰ্মা, প্ৰাঞ্জল তালুকদাৰ • ২৮
জ্ঞানমণি দাস, সমীৰ নয়ন কীৰ্তিকাৰ, গুণ মৰাণ • ২৯
দিগন্ত নিবিড়, অংকুৰ বৰুৱা ফুকন • ৩০

গল্প | বিপুল খাটনিয়াৰ • আকৌ জালিয়ানৱালাবাগ • ৭৪
সিদ্ধাৰ্থ গোস্বামী • এতিয়াও সি মোক খেদি ফুবে • ৭৭

অ নু বা দ
গল্প | মূল : ছমাৰছেট ম'ম, অনুবাদ : বাসন্তী বৰুৱা • আই • ৮০
মূল : হাঁসদা সৌভেন্দ্ৰ শেখৰ, অনুবাদ : অৰুনী বুঢ়াগোহাঁই • আদিবাসীৰোৰে আৰু নানাচে • ১০০



বৰ্ণনা
বৰ্ণনা | নিশা ভূঞা • ৬৬



অসম আন্দোলনৰ প্ৰেক্ষাপটত জনজাতীয় অস্তিত্ব আৰু পৰিচয়ৰ পুনৰুত্থান

ড° পংকজ শইকীয়া

১৯৭৯ চনৰ পৰা আৰম্ভ হোৱা অসম আন্দোলনৰ ইচ্ছা 'অবৈধ বিদেশী বহিষ্কৰণ'ৰ প্ৰতি অসমৰ প্ৰায় সকলো জনজাতিয়েই নৈতিক সমৰ্থন দিছিল। আন্দোলনটোত একাংশ জনজাতীয় লোকে সক্ৰিয় অংশগ্ৰহণো কৰিছিল। অৱশ্যে সেই সময়ত শক্তিশালী স্থিতিত থকা আবহু, বড়ো সাত্তা সভা, পি টি চি এ আদি জনজাতীয় সংগঠন আৰু অনুষ্ঠান আন্দোলনটোৰ নেতৃত্ব দায়িত্বত নাছিল। অসম আন্দোলনৰ নেতৃত্ব বহনকাৰী আছো অথবা সদৌ অসম গণ সংগ্ৰাম পৰিবদত লীন নোযোৱাকৈ এইবোৰে পৃথক অস্তিত্ব বৰ্তাই ৰাখিছিল। তথাপি জনজাতীয় স্বার্থ সুৰক্ষিত কৰাৰ খাতিৰতে উক্ত সংগঠন-অনুষ্ঠানবোৰে কেৱল বিদেশী বহিষ্কৰণৰ দাবীৰ প্ৰতি সমৰ্থন আগবঢ়াইছিল। অৰ্থাৎ প্ৰধান জনজাতীয় সংগঠন আৰু অনুষ্ঠানবোৰে আন্দোলনত সক্ৰিয় অংশগ্ৰহণ কৰা নাছিল অথবা সক্ৰিয় অংশগ্ৰহণৰ সুবিধা পোৱা নাছিল।

অৱশ্যে জনজাতীয় লেখকৰ বিশ্লেষণৰ পৰা এটা কথা স্পষ্ট হৈছে যে অসম আন্দোলনৰ প্ৰতি সমৰ্থনৰ অন্তৰালত ভিন্ন পক্ষৰ ভিন্ন উদ্দেশ্য নিহিত আছিল। লক্ষ্মীনাথ পাংগাঙে লিখিছে যে উক্ত জনজাতিসকলে ভাবে যে বহিৰাগত কিম্বা বিদেশীসকল অসমলৈ আহি অসমীয়াত্বত বিলীন হোৱাৰ ফলত অসমীয়াভাষীৰ সংখ্যা বৃদ্ধি হৈছে। কিন্তু তাৰ বিপৰীতে জনজাতি ভাষা-ভাষীৰ সংখ্যা কমি গৈছে। সেয়ে বহিৰাগত বা বিদেশীসকলক বহিষ্কাৰ কৰিলেহে অসমীয়াৰ বিৰুদ্ধে জনজাতিয়ে যুঁজ কৰিব পাৰিব। আনহাতে আন একাংশ জনজাতিৰ মতে, আন্দোলনটোৰ সহায়তে স্বায়ত্তশাসনৰ দাবীৰে নিজক প্ৰতিষ্ঠা কৰি জনজাতীয় অঞ্চলৰ পৰা বিদেশী আৰু ভাৰতীয়ক বহিষ্কাৰ কৰিব পাৰিব।

পৰৱৰ্তী সময়ত, আন্দোলন চলি থকা অৱস্থাতে জনজাতিসকলৰ অংশগ্ৰহণৰ ক্ষেত্ৰত স্পষ্টতঃ ভাঙোন পৰিলক্ষিত হৈছিল। লাহে লাহে আন্দোলনৰ নেতৃত্ব আৰু তেওঁলোকৰ আদৰ্শ, কাৰ্যপন্থা আৰু বক্তব্যৰ বিৰোধিতা কৰি জনজাতিসকলৰ এক বৃহৎ অংশ আন্দোলনৰ পৰা আঁতৰি গৈছিল।

আন্দোলনৰ এবছৰ পূৰ্ব নৌহওঁতেই ১৯৮০ চনৰ ৪ মে'ত 'সদৌ অসম জনজাতি সংৰক্ষণ সংগ্ৰাম সমিতি'ৰ জন্ম দিয়া হৈছিল। আন্দোলন পূৰ্ণোদ্যমে চলি থকা অবস্থাতে ইয়াৰ বিৰোধিতা কৰিবলৈ সকলো অৰাজনৈতিক জনজাতীয় সংগঠন লগ হৈ গঠন কৰা এই মঞ্চখন আন্দোলনটোৰ বাবে প্ৰতিবন্ধকস্বৰূপ হৈ পৰে। জনজাতিসকলৰ সূকীয়া অস্তিত্ব আৰু বৈশিষ্ট্যৰ কথা দোহাৰি এই সমিতিয়ে ইয়াৰ ক্ৰমবিলোপকৰণ সম্বন্ধে জনজাতিক সূকীয়াই দিছিল। ইয়াৰ কাৰণে তেওঁলোকে বিদেশী প্ৰব্ৰজনক জগৰীয়া কৰা নাই; বিদেশী প্ৰব্ৰজনৰ মূলতে থকা ক্ষমতালোভী অসমীয়া আৰু জনজাতিৰ ক্ষেত্ৰত তেওঁলোকৰ ৰাজনৈতিক আৰু অৰ্থনৈতিক দমননীতিকো জনজাতীয় অস্তিত্বৰ বাবে ভাবুকি বুলি ঠাৱৰ কৰিছিল। জনজাতি ৰাইজে আন্দোলনত যোগ দি জে'লত সোমোৱা বা পুলিচী নিৰ্যাতন ভোগ কৰাটো এই সংগঠনে আন্দোলনকাৰীৰ পৰিকল্পিত সুবিধাবাদ বুলিহে গণ্য কৰিছিল। 'এই আন্দোলন আমাৰ আন্দোলন নহয়', 'অসমীয়াৰ অস্তিত্ব ৰক্ষাৰ সংগ্ৰাম জনজাতিৰ অস্তিত্ব ৰক্ষাৰ সংগ্ৰাম হ'ব নোৱাৰে' বুলি মুকলিভাবে কৈ এই সমিতিয়ে আন্দোলন আৰু নেতৃত্বৰ স্বৰূপ জনজাতীয় ৰাইজৰ আগত উন্মোচন কৰিবলৈ চেষ্টা কৰিছিল। জনজাতি ৰাইজৰ মাজত তেওঁলোকে সংবাদপত্ৰ, আলোচনীৰ মাধ্যমেৰে প্ৰচাৰ চলালে— 'বৰ্তমান চলি থকা আন্দোলন ধনী, উচ্চ বৰ্ণ হিন্দু অসমীয়া উগ্ৰ জাতীয়তাবাদীসকলৰ দ্বাৰা পৰিচালিত। অসমবাসী ৰাইজক তেওঁলোকে বিপথে চলাবলৈ যত্ন কৰিছে।' এনে ধৰণৰ প্ৰচাৰৰ দ্বাৰা সহজ-সৰল জনজাতি ৰাইজ আশ্বস্ত হৈছিল বুলি অনুমন কৰিব পাৰি। লগতে আন্দোলনটো 'জাতিবিদ্বেষলৈ কপালবিত হোৱা'ৰ অভিযোগ তোলা হৈছিল। 'জনজাতিসকল আন্দোলনৰ পৰা আঁতৰি গ'ল'—এই কথাটোও কাকতৰ যোগেদি প্ৰচাৰ কৰা হৈছিল।

ইয়াৰ উপৰি আন্দোলনবিৰোধী জনজাতীয় পক্ষটোৱে সমকালীন সংবাদপত্ৰ আৰু আলোচনীসমূহৰ জৰিয়তে নেতৃত্বৰ বিপক্ষে কিছুমান গুৰুতৰ অভিযোগ উত্থাপন কৰিছিল। মূল অভিযোগটো আছিল— আছৰ 'মোহনদফীয়া দাবীচন্দ'ত তিনিটা জনজাতিবিৰোধী দাবী যেনে— ট্ৰাইবেল বেণ্ট আৰু ব্ৰুক উঠাই দিয়া, জনজাতিৰ বাবে চাকৰি-সংৰক্ষণ উঠাই দিয়া, জনজাতি ছাত্ৰ-ছাত্ৰীৰ বাবে জলপানি দিয়া' অন্তৰ্ভুক্ত হৈছে। ট্ৰাইবেল বেণ্ট আৰু ব্ৰুকৰ প্ৰবৰ্তনৰ জৰিয়তে জনজাতিৰ বাবে যি সাংবিধানিক ৰক্ষাকৰচৰ ব্যৱস্থা কৰা হৈছিল তাৰ বাতিলকৰণৰ প্ৰসংগ উত্থাপন হোৱাৰ ফলত জনজাতিসকলৰ মনত অস্তিত্বৰ সংকট ঘনীভূত হৈ পৰিছিল। লক্ষ্য কৰিবলগীয়া যে 'জনজাতীয় বেণ্ট আৰু ব্ৰুকসমূহৰ প্ৰয়োজন এই কাৰণেই উপলব্ধি কৰা গৈছিল যে উপযুক্ত ৰক্ষণাবেক্ষণৰ অভাৱত অশিক্ষিত জনজাতিসকলে প্ৰায়েই বহিৰাগতৰ হাতত মাটি হেৰুৱাব লগাত পৰিছিল। কিন্তু চৰকাৰৰ হেমাৰ্হিৰ নিমিত্তে আৰু বিভিন্ন ৰাজনৈতিক নেতাৰ স্বার্থৰ কবলত পৰি এই জনজাতীয় বেণ্ট আৰু ব্ৰুকসমূহ সংৰক্ষণ কৰিব পৰা নগ'ল।' অসম আন্দোলনৰ পটভূমিত এইদৰে জনজাতীয় বেণ্টনী আৰু অঞ্চলবোৰৰ ভূমি অবৈধ বিদেশী নাগৰিকে দখল কৰা বিষয়টো পুনৰ উত্থাপন হৈছিল। এয়াও উচ্চবৰ্ণ অসমীয়াৰ এক পৰিকল্পিত ষড়যন্ত্ৰ বুলি একাংশ জনজাতীয় নেতাই ব্যাখ্যা-বিশ্লেষণ কৰি দেখুৱায়। জনজাতীয় নেতা তথা সংগঠনে জনজাতীয় বেণ্ট আৰু ব্ৰুকসমূহৰ সংকোচনৰ আঁৰত থকা উচ্চবৰ্ণৰ অসমীয়াৰ ষড়যন্ত্ৰ

সম্পৰ্কত দিয়া ব্যাখ্যা এনে ধৰণৰ—

"...অসমৰ জনজাতি অঞ্চল আৰু বেণ্টনীবোৰত (Tribal belt and blocks) অসমীয়া আৰু অজনজাতীয় লোকসকলে মাটিৰ বন্দবস্তি পালে কেনেকৈ? তাৰ বাবে জগৰীয়া অসমীয়া মণ্ডল কাননগো আৰু ৰাজহ বিয়াবোৰেই নহয় জানো? তেওঁবিলাকে আইনৰ সুৰুঙাৰ মাজেদি তেতিয়াৰ পাকিস্তানৰ পৰা অহা শৰণাৰ্থীসকলক জনজাতি অঞ্চল আৰু বেণ্টনীবোৰত মাটিৰ বন্দবস্তি দিছিল। লক্ষ্য আছিল জনজাতিসকলৰ অস্তিত্ব বিপদাপন্ন কৰা আৰু অদূৰ ভৱিষ্যতে জনজাতিসকলক নিৰ্মূল কৰা। তেতিয়াৰ উচ্চবৰ্ণ হিন্দু অসমীয়া ৰাজনৈতিক নেতাসকলে সদায় লক্ষ্য বাৰিছিল যাতে জনজাতিসকল জনজাতি অধ্যুষিত অঞ্চলবোৰতে সংখ্যালঘুত পৰিণত হয় আৰু ফলত কোনো সমষ্টিৰ পৰা জনজাতীয় মানুহ বিধানসভালৈ প্ৰতিনিধি হিচাপে নিৰ্বাচিত হ'ব নোৱাৰে।"

এনেদৰে আন্দোলনৰ সময়তে চৰ্চা হৈছিল যে উচ্চবৰ্ণৰ অসমীয়াৰ প্ৰবোচনা আৰু যড়যন্ত্ৰৰ বাবেই জনজাতিসকল সংখ্যালঘু হৈছে আৰু অস্তিত্বৰ প্ৰতি সংকট আহিছে। জনজাতীয় নেতৃত্বৰ বিচাৰধাৰাত আছৰ আছিল উচ্চবৰ্ণ অসমীয়া মধ্যবিত্ত শ্ৰেণীৰ প্ৰতিনিধি। গতিকে প্ৰচাৰেই হওক বা অপপ্ৰচাৰেও হওক, ট্ৰাইবেল বেণ্ট আৰু ব্ৰুক বিলোপকৰণ প্ৰসংগই জনজাতীয় চেতনাক গভীৰভাৱে আলোড়িত কৰিছিল। এনে ধৰণৰ অভিযোগবোৰ ৰাজহুৱা হোৱাৰ লগে লগে অসমীয়া উচ্চবৰ্ণৰ শ্ৰেণীটোৰ প্ৰতি জনজাতীয় সৰ্বসাধাৰণ লোক ক্ষুব্ধ হৈ পৰিছিল আৰু ইয়াৰ সমান্তৰালভাৱে শংকাগ্ৰস্তও হৈছিল। ক্ষোভ আৰু শংকাৰ বহিঃপ্ৰকাশ আছিল এনেকুৱা : "...তেওঁলোকৰ দাবীচন্দত জনজাতীয়সকলৰ বিপক্ষে কেইটামান দাবী আছে— যিবোৰ দাবী কাৰ্যকৰী হ'লে জনজাতীয়সকলৰ অস্তিত্ব অসমৰ পৰা চিৰদিনৰ কাৰণে হেৰাই যাব। সেয়েহে জনজাতীয়সকলে বৰ্তমানৰ আন্দোলনত সক্ৰিয়ভাৱে অংশগ্ৰহণ কৰিব নোৱাৰে।"

অসম আন্দোলনৰ সময়ত 'অতীতৰ ভুলৰ পৰা শিক্ষা' ল'বলৈ আৰু ভৱিষ্যতে তেনে ভুলৰ পুনৰাবৃত্তি নহ'বলৈ জনজাতি ৰাইজ আৰু জনজাতীয় নেতৃত্বক সূকীয়াই দিয়া হৈছিল। এই অতীতৰ ভুলটো হ'ল বড়োসকলে ৰোমান লিপিৰ দাবীত কৰা আন্দোলনৰ সময়ত হোৱা ভুল। ১৯৭৪-৭৫ চনৰ ৰোমান লিপিৰ দাবীত অসমৰ বৃহৎ জনজাতি বড়োসকলে কৰা আন্দোলনৰ প্ৰতি অসমীয়া মধ্যবিত্ত শ্ৰেণীৰ প্ৰতিনিধি আছৰ অথবা অসম সাহিত্য সভাই সঁহাৰি দিয়া নাছিল। বৰঞ্চ এই আন্দোলন কঠোৰভাৱে দমন কৰাৰ ক্ষেত্ৰত ৰাজ্য আৰু কেন্দ্ৰীয় চৰকাৰক এওঁলোকে সহযোগে কৰিছিল। লিপি আন্দোলনত ১৮গৰাকী বড়ো যুৱক-যুৱতীয়ে অৰ্ধসামৰিক বাহিনীৰ গুলীত প্ৰাণ হেৰুৱাইছিল। কিন্তু অসমৰ বুদ্ধিজীৱী, শিক্ষান্বিত, ৰাজনীতিবিদ অথবা ছাত্ৰনেতাসকলৰ কোনোৱেই তেতিয়া পুলিচী নিৰ্যাতনৰ বিৰুদ্ধে বক্তব্য প্ৰদান কৰা নাছিল। আনকি বড়োভিন্ন অন্য জনজাতিয়েও চৰকাৰী অত্যাচাৰৰ বিৰুদ্ধে কোনো প্ৰতিবাদ সাব্যস্ত কৰা নাছিল। অসম আন্দোলনৰ সময়ছোৱাত অতীতৰ এই অভিজ্ঞতা অসমীয়া মধ্যবিত্ত শ্ৰেণীৰ বিশ্বাসঘাতকতাৰ নিদৰ্শন বুলি চৰ্চিত হয়। লগতে জনজাতীয় গোষ্ঠীসমূহৰ নীৰৱ ভূমিকা এক ডাঙৰ ভুল বুলি বিশেষভাৱে সমালোচিত হয়। শিক্ষিত, মধ্যবিত্ত অসমীয়াৰ এনে 'প্ৰত্যাগা'ৰ সৌৱৰণ কৰি তাৰ পৰা শিক্ষা ল'বলৈ আন্দোলনৰ সময়ত

৬
 অসম আন্দোলনৰ
 সময়ত গৌৰবোজ্জ্বল
 ইতিহাসৰ সৌৰৰণ
 জনজাতীয়
 পুনৰ্জাগৰণৰ
 প্ৰভাৱশালী কাৰক হৈ
 নুঠিলেও মাইবং,
 ডিমাপুৰ, খাছপুৰ,
 শোণিতপুৰ আদিত
 জনজাতীয় বজাৰ
 প্ৰতাপী ৰাজত্ব, সপ্তম
 শতিকাৰ উত্তৰ-পূব
 ভাৰতত বড়ো ভাষাৰ
 প্ৰাধান্য আদি বিষয়ৰ
 আলোচনাই জনজাতীয়
 মানসিকতাক কিছু
 হ'লেও প্ৰভাৱান্বিত
 কৰিছিল বুলি অনুমান
 কৰিব পাৰি।

জনজাতি ৰাইজক বাবে বাবে আহ্বান জনোৱা হৈছিল। গতিকে অতীত ইতিহাসৰ পৰা লাভ
 কৰা শিক্ষা আৰু জাতীয় গৌৰৱৰ সৌৰৰণ জনজাতীয় পৰিচয় আৰু অস্তিত্ব প্ৰতিষ্ঠাৰ পুনৰ্জাগৰণত
 বিশেষভাৱে সহায়ক হৈ উঠিছিল।

অসমৰ জনজাতিসকলৰ যে এক গৌৰৱময় ইতিহাস আছে, সেই প্ৰসংগ আন্দোলনৰ সময়ত
 চৰ্চালৈ আহিছিল। দেখা যায়, অতীতৰ গৌৰবোজ্জ্বল ইতিহাসৰ পটভূমিত পৃথিৱীৰ বহু অৱনত
 জাতিৰ চিন্তা-চেতনাৰ পুনৰ্জাগৰণ ঘটিছিল। অসম আন্দোলনৰ সময়ত গৌৰবোজ্জ্বল ইতিহাসৰ
 সৌৰৰণ জনজাতীয় পুনৰ্জাগৰণৰ প্ৰভাৱশালী কাৰক হৈ নুঠিলেও মাইবং, ডিমাপুৰ, খাছপুৰ,
 শোণিতপুৰ আদিত জনজাতীয় বজাৰ প্ৰতাপী ৰাজত্ব, সপ্তম শতিকাৰ উত্তৰ-পূব ভাৰতত বড়ো
 ভাষাৰ প্ৰাধান্য^{১০} আদি বিষয়ৰ আলোচনাই জনজাতীয় মানসিকতাক কিছু হ'লেও প্ৰভাৱান্বিত
 কৰিছিল বুলি অনুমান কৰিব পাৰি।

অসম আন্দোলনৰ মাজত জনজাতীয় নেতৃত্বই উগ্ৰ জাতীয়তাবাদী আৰু আধিপত্যবাদী
 দৃষ্টিভঙ্গী আৱিষ্কাৰ কৰিছিল। আন্দোলনৰ নেতৃত্ব বহন কৰা আছ, সদৌ অসম গণ সংগ্ৰাম
 পৰিষদ আৰু এওঁলোকৰ সহযোগী অসম জাতীয়তাবাদী দল, অসম সাহিত্য সভা, অসম উৰ্দ্ধল
 সংস্থা আদিবোৰ আছিল জাতীয়তাবাদী মতাদৰ্শৰে পৰিচালিত। এনে সংগঠনসমূহৰ চৰিত্ৰ আৰু
 আকাংক্ষাৰ প্ৰতি জনজাতীয় নেতৃত্ব ঐতিহাসিক কাৰণতে সচেতন আছিল। অসম আন্দোলনৰ
 নেতৃত্বৰ কেতবোৰ প্ৰতিক্ৰিয়াশীল কাৰ্যকলাপে আন্দোলনৰ মাজভাগতে জনজাতীয় ৰাইজৰ
 মনত অৱহেলা, অৱদমন, প্ৰতাৰণা আৰু সন্দেহৰ অনুভৱ বিয়পাই দিছিল। পূৰ্বৰ তিত্ত অভিজ্ঞতাৰ
 সৌৰৰণে এনে উপলব্ধি আৰু বেছি দৃঢ় কৰিছিল। 'অসম সাহিত্য সভাই বহা অধিবেশনত
 গ্ৰহণ কৰা এটা প্ৰস্তাবে জনজাতিৰ মনত তীব্ৰ প্ৰতিক্ৰিয়াৰ সৃষ্টি কৰে। সেই প্ৰস্তাৱটিত অনা-
 অসমীয়া মাধ্যমৰ স্কুলবোৰত অসমীয়া মাধ্যম প্ৰৱৰ্তন কৰিব লাগে আৰু তাকে নকৰালৈকে
 সেইবোৰ স্কুলত মজুৰি নিদিবলৈ চৰকাৰক কোৱা হৈছে।'^{১১} জনজাতীয় চেতনাত আঘাত কৰিব
 পৰা অসম জাতীয়তাবাদী দলৰ এটি মন্তব্যও সেই সময়ত চৰ্চিত হৈছিল— "...অসম
 জাতীয়তাবাদী দলৰ মতে অসমত অসমীয়াৰহে স্থান, তাত অনা-অসমীয়াৰ স্থান নাই।
 তেওঁলোকৰ মতে যিসকলে অসমীয়া ভাষা কয়, অসমীয়া ভাষাত লিখা-পঢ়া কৰে, তেওঁবিলাকহে
 অসমীয়া। এই সূত্ৰমতে আমি জনজাতীয় সকলো অনা-অসমীয়াৰ শাৰীত পৰিম। কাৰণ
 জনজাতীয়সকলৰ নিজ নিজ মাতৃভাষা আছে আৰু তেওঁবিলাকৰ মাতৃভাষা অসমীয়া নহয়।"^{১২}

আনহাতে ১৯৮০ চনৰ মাজভাগতে আছ আৰু সদৌ অসম গণ সংগ্ৰাম পৰিষদে 'ৰাষ্ট্ৰীয়
 নাগৰিকপঞ্জী' প্ৰণয়ন আৰু অসমৰ প্ৰত্যেক লোকৰ বাবে 'নাগৰিক পৰিচয়পত্ৰ' প্ৰদানৰ কথা
 ঘোষণা কৰাত বিষয়টোৱে 'ভূমিপত্ৰ' বুলি দাবী কৰি অহা জনজাতীয় লোকৰ আত্মসংগঠন
 আঘাত দিছিল। এই ঘোষণাই জনজাতীয় গোষ্ঠীবোৰৰ মানসিকতাত ভয় আৰু সন্দেহো বিয়পাই
 দিছিল। তদুপৰি জনজাতীয় স্বাভিমান পুনৰ্জাগৰণ হৈ উঠিছিল। তেওঁলোকৰ মতে, আছ অথবা
 গণ সংগ্ৰাম পৰিষদ বেচৰকাৰী সংগঠন আৰু সেইবাবেই নাগৰিকৰ পৰিচয়পত্ৰ প্ৰদানৰ অধিকাৰ
 সংগঠন দুটাৰ নাই। তদুপৰি জনজাতিসকল অহাৰ বহু পাছতহে উচ্চবৰ্গৰ অসমীয়াসকল অসমলৈ
 আহিছিল। এনে ধৰণৰ পৰিস্থিতি অথবা কাৰণৰ পৰিপ্ৰেক্ষিততে স্বকীয় অস্তিত্ব বৰ্তাই ৰাখিবৰ
 বাবে, স্বকীয় পৰিচয় প্ৰতিষ্ঠাৰ বাবে, সামাজিক-সাংস্কৃতিক-ৰাজনৈতিক অধিকাৰপ্ৰাপ্তি তথা
 স্বীকৃতি লাভৰ বাবে, ৰাজনৈতিক নিয়ন্ত্ৰণ লাভৰ বাবে জনজাতীয় চেতনা কেন্দ্ৰীভূত হ'ল।
 অৰ্থাৎ অতীত ইতিহাসৰ শিক্ষা-অনুপ্ৰেৰণা আৰু অসম আন্দোলনৰ নেতৃত্বৰ বিভিন্ন স্পৰ্শকাণ্ডৰ
 কাৰ্য-ঘটনা— এই দুয়োটা অসমত জনজাতীয় পৰিচয়-চেতনাৰ পুনৰ্জাগৰণৰ প্ৰধান কাৰক হৈ
 উঠিল। এই পুনৰ্জাগৰণৰ লক্ষণবোৰ আন্দোলনৰ সময়তে কিছু ফলিয়াবলৈ আৰম্ভ কৰিছিল।

'অসম অসমীয়া' বুলি যি দাবী এচাম আন্দোলনকাৰীয়ে তুলিছিল সেয়া জনজাতীয়
 দৃষ্টিকোণৰ পৰা উগ্ৰ জাতীয়তাবাদী শ্লোগান বুলিহে নিৰ্ণীত হৈছিল। অসম আন্দোলনত 'উগ্ৰ
 জাতীয়তাবাদী' উপাদানৰ প্ৰত্যক্ষীকৰণে জনজাতীয় জাতীয়তাবাদৰ পুনৰ্জাগৰণত ইন্ধন যোগালে।
 জাতিসত্তাবোৰৰ সম-অধিকাৰ আৰু স্বনিয়ন্ত্ৰণৰ দাবীক স্বীকৃতি তথা স্বাগতম জনোৱাৰ বিপৰীতে
 আন্দোলনৰ নেতৃত্বই 'বৃহৎ জাতিসুলভ দাস্তিকতাবে' এক দমনশীল কৰ্তৃত্বহে বহুৱাবলৈ চেষ্টা
 কৰি আহিছে। 'বিদেশী খেদা আন্দোলনে অসমীয়া জাতিক খানবান কৰিলে', 'বিভিন্ন জাতি-
 অনৈকাৰ বীজ ৰোপণ কৰিলে'^{১৩} বুলি স্পষ্টভাৱেই জনজাতীয় পক্ষটোৱে ক'বলৈ আৰম্ভ কৰিছিল।

অসম আন্দোলনৰ নেতৃত্ব আৰু এটা কাৰ্যই জনজাতীয় পক্ষটোৱে ক'বলৈ আৰম্ভ কৰিছিল।
 স্বাৰ্থৰ হকে মাত মাতি অহা আবহুকে ধৰি কোনো এটা জনজাতীয় সংগঠনৰ আন্দোলন

নেতৃত্ব অংশীদার কৰা হোৱা নাছিল। আনকি জনজাতি অধ্যয়িত অঞ্চলবোৰতো জনজাতীয় সংগঠনৰ সদস্যৰ জৰিয়তে আন্দোলনৰ প্ৰচাৰকাৰ্য চলোৱা হোৱা নাছিল।

অসম আন্দোলনৰ সময়ত জনজাতি-অসমীয়াৰ প্ৰসংগ উত্থাপন হোৱাটো জনজাতীয় পক্ষটোৱে সহজভাৱে ল'ব পৰা নাছিল। আছ, আন্দোলনৰ সমৰ্থক অথবা জনজাতীয় আছ নেতায়ে জনজাতি কিম্বা জনজাতীয় সমস্যাক অসমীয়াৰ সমস্যাৰ পৰা পৃথককৈ উপস্থাপন কৰিছিল। উদাহৰণস্বৰূপে, ১৯৭৯ চনৰ ৪ তাৰিখে 'দৈনিক অসম' কাকতত প্ৰকাশ পোৱা '৮ জুনৰ 'অসম বন্ধ' সফল কৰিবলৈ আহ্বান' শীৰ্ষক আছৰ বিবৃতিটোত জনজাতিৰ সমস্যাকে বিশেষভাৱে দেখুওৱা হৈছিল।^{১৪} 'নীলাচল কাকতত 'এই সংগ্ৰাম আমাৰ জনজাতিবো অস্তিত্ব বন্ধাৰ সংগ্ৰাম'^{১৫}, 'জনজাতি স্বাৱলম্বী নহ'লে জনজাতীয় অস্তিত্ব অসমত বিলুপ্ত হ'ব'^{১৬}, 'জনজাতীয় লোকহে বিদেশীৰ দ্বাৰা আক্ৰান্ত হৈছে'^{১৭}— এনে ধৰণৰ অনেক নিবন্ধ প্ৰকাশ পাইছিল। সমস্যাবোৰ সামূহিক ৰূপত উপস্থাপন কৰাৰ পৰিৱৰ্তে পৃথকভাৱে দেখুওৱাত জনজাতিৰ মানসিকতাত বিৰূপ প্ৰভাৱ পৰিছিল।

লাহে লাহে জনজাতিসকলৰ সচেতন অংশটোৱে উপলব্ধি কৰিলে যে অসম আন্দোলন দৰাচলতে অসমীয়া মধ্যবিত্ত শ্ৰেণীটোৰ দ্বাৰা পৰিচালিত। সেইবাবেই অসমীয়া মধ্যবিত্তৰ আধিপত্য থকা ব্ৰহ্মপুত্ৰ উপত্যকা অসম আন্দোলনৰ সমৰ্থনত তোলপাৰ লাগিছে। জনজাতীয় দৃষ্টিকোণ অনুসৰি জাতীয়তাবাদী মতাদৰ্শৰ ভিত্তিত সংঘবদ্ধ হোৱা অসমীয়া মধ্যবিত্ত শ্ৰেণীয়ে নিজৰ শ্ৰেণীস্বার্থ সুৰক্ষিত কৰাৰ উদ্দেশ্যতে এই অসম আন্দোলন সংঘটিত কৰিছে। তেওঁলোকৰ মুখ্য উদ্দেশ্য হ'ল ৰাজনীতি, অৰ্থনীতি, সামাজিক, সাংস্কৃতিক সকলো ক্ষেত্ৰতে নিজৰ নিয়ন্ত্ৰণ, আধিপত্য, কৰ্তৃত্বশীলতা স্থাপন কৰা। বড়ো, মিচিং, কাৰ্বি, ৰাভা, তিৱা আদি ক্ষুদ্ৰ ক্ষুদ্ৰ জাতিসত্তাবোৰৰ সমৰ্থন আৰু স্বনিয়ন্ত্ৰণৰ দাবীক উপেক্ষা কৰি অসমীয়া ধনী, বুৰ্জোৱা, মধ্যবিত্ত শ্ৰেণীটোৱে বৃহৎ জাতিসুলভ দান্তিকতাবে যি আধিপত্য প্ৰতিষ্ঠা কৰিবলৈ বিচাৰিছিল তাক জনজাতীয় সমালোচকে বাতৰিকাকতৰ পাতত আঙুলিয়াই দিছিল। 'ট্ৰিবিউন গোস্টী'ৰ সংবাদপত্ৰ (আসাম ট্ৰিবিউন, দৈনিক অসম), দৈনিক জনমভূমি, নীলাচল আদিৰ বুৰ্জোৱা মালিকগোষ্ঠীৰ বিৰুদ্ধে লিখিছিল— "অসমৰ জনগণৰ পিছপৰা অৰ্থনীতিৰ তুলনাত এই কাকতসমূহৰ মালিকগোষ্ঠী বৃহৎ ধনী অসমীয়া পৰিয়াল হোৱাত তেওঁলোকে নিজৰ শ্ৰেণীস্বার্থ বজাই ৰখাৰ বাবে গোকট মিছা কথা লিখি সত্যৰ অপলাপ কৰিছে। আন্দোলনৰ সামূহিক চৰিত্ৰয়ো সিহঁতৰ স্বার্থৰক্ষাৰ বাবে অনুকূল বাতৰবগকে সৃষ্টি কৰিছে।"^{১৮} একেটা নিবন্ধতে ক্ষোভসূচক উপলব্ধিৰ এনেদৰে উমান পোৱা যায়—

"উগ্র জাতীয়তাবাদৰ গাৰ্হবিঘুলিত নিমজ্জিত হৈ, জাতিপ্ৰেমৰ নামত জাতিৰ শত্ৰুৰ দালালি কৰি, জনগণক বিদেশী নাগৰিকৰ সমস্যাটোৰ বিকৃত ব্যাখ্যা দি, মানৱতা আৰু গণতান্ত্ৰিক প্ৰমূল্যবোৰৰ গৰাখহনীয়া সৃষ্টি কৰি, জাতি-ভাষা-ধৰ্ম-সম্প্ৰদায় ভিত্তিত থকা অবৈৰীমূলক দ্বন্দ্ববোৰক বৈৰীমূলক দ্বন্দ্বলৈ পৰ্যবসিত কৰি, ক্ষুদ্ৰ ক্ষুদ্ৰ জাতি-উপজাতিসমূহৰ স্বনিয়ন্ত্ৰণ আৰু সম-অধিকাৰৰ দাবীক স্বীকৃতি প্ৰদান নকৰি, অসমীয়াৰ মহাজাতি গঠনৰ প্ৰক্ৰিয়াক ব্যাহত কৰি, সৰ্বসাধাৰণ ৰাইজৰ অৰ্থনৈতিক অনগ্রসৰতাৰ পূৰ্ণ সুযোগ গ্ৰহণ কৰি, বৃহৎ মালিক-জমিদাৰ ধনিক গোস্টীৰ স্বার্থ বন্ধা কৰি, কৃষক-মজদুৰ-শ্ৰমিক— এই শোষিতসকলক দৰিদ্ৰতাৰ মাজলৈ আৰু এৰোজ আগবঢ়াই দি, বিশাল ভাৰতৰ অখণ্ডতাক অমান্য কৰি, বিচ্ছিন্নতাবাদৰ পৃষ্ঠপোষকতা কৰি, জনজাতি ৰাইজৰ আবেগ-অনুভূতিক লৈ হেতালি খেলি, জনগণৰ— বিশেষকৈ মধ্যবিত্তৰ আবেগ-অনুভূতিক শিখণীৰূপে লৈ যোৱা এবছৰে অসমত বিক্ষিপ্ত হিংসাত্মক আৰু অগণতান্ত্ৰিক কাৰ্যকলাপেৰে বুৰ্জোৱা নেতাসকলে যি জাতিবিদ্বেষী আন্দোলন চলালে...।"^{১৯}

বুৰ্জোৱা আৰু মধ্যবিত্ত শ্ৰেণীৰ বিৰুদ্ধে এক ধৰণৰ মাৰ্গী জীৱনবীক্ষাৰে কৰা এনে সমালোচনাই অৰ্থনৈতিক দিশত জনজাতীয় চিন্তাক এক নতুন গতি দিব পাৰিছিল।

আন্দোলনকালীন সময়তে জনজাতিবোৰে নিজৰ 'অসমীয়াত্ব' সম্পৰ্কে সন্দেহ প্ৰকাশ কৰিবলৈ ধৰে। লক্ষ্মীনাথ পাংগিঙৰ এটা প্ৰবন্ধত 'জনজাতিবোৰ অসমীয়া হৈ নাথাকে' বুলি কৈ অসমীয়াত্বকে অগ্ৰাহ্য কৰা হয়। অসমীয়াত্ব বৰ্জন কৰাৰ সমান্তৰালভাৱে অসমীয়া জাতীয় সংস্কৃতিৰ প্ৰতি অৱহেলা বা বিৰাগ প্ৰদৰ্শনো স্পষ্টকৈ প্ৰতিফলিত হৈছিল। 'অসমীয়াৰ বাপতিসাহেন'খ্যাত বিহু বৰ্জন কৰিবলৈ মিচিংসকলে ৰাজহুৱা সভাত প্ৰস্তাৱ গ্ৰহণ কৰা^{২০}ৰ কথাৰ পৰাই জনজাতিৰ মানসিকতাত 'অসমীয়াবিদ্বেষ' কিমান দলৈ শিপাইছিল তাক সহজে অনুমান কৰিব পাৰি। নিজৰ সাংস্কৃতিক ঐতিহ্যৰ চৰ্চা, পালন-পোষণ আৰু তাৰ আধাৰতে সংগঠিত হোৱাৰ এক আকাংক্ষা— জনজাতীয় দৃষ্টিভংগীৰ মাজত এনে এক ধাৰণাৰো ইংগিত পোৱা গৈছিল। আন্দোলনৰ মাজভাগতে বড়ো, মিচিং, কাৰ্বি, ডিমাছ, ৰাভা, দেউৰী, তিৱা আদি ভাষাৰ স্বীকৃতিৰ দাবী উত্থাপন হৈছিল।

6

জনজাতিসকলৰ সচেতন অংশটোৱে উপলব্ধি কৰিলে যে অসম আন্দোলন দৰাচলতে অসমীয়া মধ্যবিত্ত শ্ৰেণীটোৰ দ্বাৰা পৰিচালিত। সেইবাবেই অসমীয়া মধ্যবিত্তৰ আধিপত্য থকা ব্ৰহ্মপুত্ৰ উপত্যকা অসম আন্দোলনৰ সমৰ্থনত তোলপাৰ লাগিছে। জনজাতীয় দৃষ্টিকোণ অনুসৰি জাতীয়তাবাদী মতাদৰ্শৰ ভিত্তিত সংঘবদ্ধ হোৱা অসমীয়া মধ্যবিত্ত শ্ৰেণীয়ে নিজৰ শ্ৰেণীস্বার্থ সুৰক্ষিত কৰাৰ উদ্দেশ্যতে এই অসম আন্দোলন সংঘটিত কৰিছে।

9

বড়ো ভাষাক অসমত সহযোগী চৰকাৰী ভাষাৰ মৰ্যাদা দিব লাগে বুলি দাবী উঠিছিল। উল্লেখ্য যে ১৯৭৮ চনত মিচিংসকলৰ বৃহত্তম ভাষা-সাহিত্যৰ অনুষ্ঠান 'মিচিং আগম কাৰাণ্ড' (মিচিং সাহিত্য সভা)এ মিচিং ভাষাৰ বাবে বোমান লিপি গ্ৰহণৰ সিদ্ধান্ত গ্ৰহণ কৰিছিল। ইয়াৰ পাছত আন্দোলনকালীন সময়তে অসমীয়া লিপিতকৈ বোমান লিপিৰ অধিক ব্যৱহাৰযোগ্যতা প্ৰতিপন্ন কৰাৰ চেষ্টা চলে।^{১৩} ১৯৮৪ চনৰ ৫ মে'ত সদৌ মিচিং ছাত্ৰ সন্থাই অসম চৰকাৰক দিয়া ১৪ দফীয়া স্মাৰকপত্ৰত মিচিং ভাষাক শিক্ষাৰ মাধ্যম হিচাপে প্ৰবৰ্তন কৰাৰ দাবী জনোৱা হৈছিল। সাহিত্যিক দিশত দেখা যায়, জনজাতি— বিশেষকৈ মিচিংসকলক অসমীয়া সাহিত্যত কিদৰে ইতিকিং বা উপেক্ষা কৰা হৈছে তাৰ পদ-প্ৰমাণ উদ্ধৃত কৰি সেই সময়ত জনজাতীয় লেখকে ক্ষোভৰ বহিঃপ্ৰকাশ ঘটাইছিল।^{১৪} এয়া এফালে 'বৃহত্তৰ অসমীয়া জাতীয় জীৱন'ৰ বাবে অৱক্ষয়সূচক হোৱাৰ বিপৰীতে জনজাতীয় জীৱনত আছিল সাংস্কৃতিক চৈতন্যৰ পুনৰুত্থান। ভাষা-লিপি-সাহিত্য— এই ক্ষেত্ৰবোৰত তথাকথিত 'মূলসুঁতি'ৰ অসমীয়াৰ আধিপত্য ওফৰাই স্বকীয়ত্ব প্ৰতিষ্ঠা কৰাৰ প্ৰচেষ্টাৰ মাজতে 'জনজাতীয় জাতীয়তাবাদ'ৰ ভেটিটো শক্তিশালী হৈ পৰে।

আৰ্যমূলীয় ভাষাকে ধৰি অসমীয়া সংস্কৃতিৰ বিভিন্ন অংগ আৰু অসমীয়া জাতীয়তাক অস্বীকাৰ কৰাৰ পাছত অসম ৰাজ্যৰ নাম বদলিকৰণৰ বাবে জনমত গঠন কৰিবলৈকো জনজাতীয় বাইজক আহ্বান জনোৱা হৈছিল। 'অসম' আৰু 'অসমীয়া'— এই দুয়োটা পৰিচয়কে অগ্ৰাহ্য কৰি একাংশ জনজাতিয়ে আন্দোলনটোৰ সময়তে স্বকীয় অস্তিত্ব গজগজীয়া কৰিব খুজিছিল। অসম আন্দোলনে জনজাতিৰ মাজত 'খিলঞ্জীয়া', 'খলুৱা' অথবা 'ভূমিপুত্ৰ'ৰ গৌৰৱবোধ আৰু অভিমানো জাগ্ৰত কৰে। ফলত অসম ৰাজ্যত উচ্চ বৰ্ণহিন্দু অসমীয়া শ্ৰেণীটোৰ আধিপত্য নস্যাত্ কৰি তেওঁলোকে কৈছিল— "অসমীয়া শব্দৰ অৰ্থ মানে জনজাতিসকলে তেওঁলোকক বাদ দিয়া শব্দ বুলিহে ভাবে। ...সম্প্ৰতি তামিলনাডু, মহাৰাষ্ট্ৰ, কৰ্ণাটক আদিৰ নতুন নামকৰণ হৈছে। সেয়ে সাম্প্ৰতিক অসমৰ নাম 'কৈৰাতিকা' নাইবা 'পূৰ্বাঞ্চল' ৰাখিব লাগে।"^{১৫} উক্ত 'কৈৰাতিকা' শব্দৰ উত্থাপনে অসম ভূখণ্ডত মংগোলীয় প্ৰাধান্য প্ৰতিষ্ঠাৰ ইচ্ছাকে প্ৰতিফলিত কৰে।

বিপ্ৰেষণৰ জৰিয়তে লক্ষ্য কৰা যায়, আন্দোলনৰ প্ৰেক্ষাপটত অসমীয়া জাতীয়তাবাদৰ উত্থান তথা সফলতা মনোযোগেৰে লক্ষ্য কৰা এটা জনজাতীয় শিক্ষিত, সচেতন শ্ৰেণী আছিল। এই শ্ৰেণীটোৱে ইতিমধ্যে চাকৰি-ব্যৱসায়ৰ মাধ্যমেৰে নিজকে মধ্যবিত্ত শ্ৰেণীলৈ উন্নীত কৰিছিল। এওঁলোকৰো চৰিত্ৰ অসমীয়া মধ্যবিত্ত শ্ৰেণীৰ দৰেই সুবিধাবাদী আছিল। এই জনজাতীয় মধ্যবিত্ত শ্ৰেণীয়ে ৰাজনৈতিক স্বাৰ্থৰ খাতিৰতে নিজৰ নিজৰ জাতীয়তাবাদক শক্তিশালী কৰিবলৈ সচেষ্ট হৈ উঠিছিল। এওঁলোকৰ একাংশই ইচ্ছাকৃতভাৱেই অসম আন্দোলনৰ বিৰুদ্ধে সংবাদপত্ৰৰ যোগেদি জনমত গঠন কৰাত লাগিছিল। এনে বিৰোধৰ মাজেৰেই ক্ৰমে জনজাতীয় জাতীয়তাবাদ (উপ-জাতীয়তাবাদ)ৰ ভেটিটো শক্তিশালী হৈ উঠিছিল আৰু অসম আন্দোলনৰ সমাপ্তিৰ পাছত বিশেষতঃ ৰাজনৈতিক ক্ষমতা হস্তগত কৰিবলৈ আন্দোলন গঢ়ি তুলিছিল। অসমীয়া জাতীয়তাবাদ উগ্ৰ হৈ পৰা বুলি তেওঁলোকে অসম আন্দোলনৰ সময়ত অভিযোগ তুলিছিল। কিন্তু লক্ষ্যীয়ভাৱে জনজাতীয় আন্দোলনবোৰতো সেই উগ্ৰ জাতীয়তাবাদী উপাদানৰ প্ৰয়োগ ঘটি ভ্ৰাতৃঘাতী সংঘৰ্ষৰ ৰূপ পৰিগ্ৰহ কৰিছিল।

জনজাতীয় জাতীয়তাবাদৰ যিয়েই উদ্দেশ্য নাথাকক— অসম আন্দোলনৰ পটভূমিতে যে স্বকীয় পৰিচয় তথা অস্তিত্ব প্ৰতিষ্ঠাৰ ধাৰণাৰে জনজাতীয় চেতনা গভীৰভাৱে প্ৰভাৱান্বিত হৈছিল সেই কথা স্বীকাৰ্য্য। সমাজ-সংস্কৃতি, শিক্ষা-ৰাজনীতি সকলো ক্ষেত্ৰতে অসমীয়া মধ্যবিত্ত শ্ৰেণীৰ আধিপত্যই তেওঁলোকক ইতিপূৰ্বে ভীতিগ্ৰস্ত কৰি তুলিছিল। ১৯৬০ৰ ভাষা আন্দোলন, ১৯৭২-ৰ মাধ্যম আন্দোলন জনজাতীয় বিচাৰধাৰাত আছিল বৃহৎ অসমীয়া জাতিসত্তাৰ অস্তিত্ব সুৰক্ষাৰ অৰ্থে কৰা আছিল বৃহৎ অসমীয়া জাতিসত্তাৰ অস্তিত্ব সুৰক্ষাৰ অৰ্থে কৰা একো একোটা নমুনা। লগতে অনুভৱ কৰিছিল যে বড়ো, মিচিং আদিয়ে ক্ষুদ্ৰ ক্ষুদ্ৰ জাতিসত্তা হিচাপে উত্থান লাভ কৰাৰ প্ৰচেষ্টাত অসমীয়াসকলে সঁহাৰি জনোৱা নাই; বৰঞ্চ তেওঁলোকৰ মৰ্যাদা আৰু গুৰুত্বক অৱহেলা কৰা হৈছে আৰু তেওঁলোকক বিভিন্ন সময়ত ব্যৱহাৰহে কৰা হৈছে। এনে ধৰণৰ মনোভাবৰ প্ৰতিক্ৰিয়া আৰু পৰিণাম হৈছিল সুদূৰপ্ৰসাৰী। অসমত জনজাতিসকলৰ অস্তিত্ব বিপন্ন হৈছে অসমীয়াভাষীসকলৰ কাৰণেহে— এই আন্দোলনৰ প্ৰেক্ষাপটতে দৃঢ় হৈ উঠিছিল। বড়ো, ধাৰণা অসম আন্দোলনৰ প্ৰেক্ষাপটতে দৃঢ় হৈ উঠিছিল। বড়ো, মিচিং, ৰাভা, মেছ, লালুং, দেউৰীসকলে 'অসমীয়া নহয়'— এই মানসিকতাৰে স্বকীয় অস্তিত্ব আৰু বৈশিষ্ট্য ৰক্ষাৰ বাবে সংগঠিত হোৱাৰ যো-জা কৰিবলৈ ধৰিছিল। এনেদৰে জনজাতীয় গোষ্ঠীৰ আত্মপৰিচয় আৰু আত্মবিকাশ অসমীয়া জাতি-সংস্কৃতিৰ পৰা বিচ্ছিন্ন হৈ লাভ কৰাৰ আকাংক্ষা পূৰ্বৰ ভাষা অথবা মাধ্যম আন্দোলনকেদৰিক বিচ্ছিন্নতাবোধ আৰু পৰিচয়-আকাংক্ষাতকৈও তীব্ৰ আছিল।

অসম আন্দোলন, আন্দোলনৰ নেতৃত্ব আৰু অজনজাতিৰ প্ৰতি জনজাতিসকলৰ মোহভংগ ঘটাব ক্ষেত্ৰত ১৯৮৩ চনৰ নিৰ্বাচনকেদৰিক ৰাজনৈতিক পৰিস্থিতি বহু পৰিমাণে জগৰীয়া বুলি চিহ্নিত কৰিব পাৰি। এই সময়ৰ পৰাই অধিকাংশ জনজাতি আন্দোলনৰ পৰা আঁতৰি আহিছিল। ১৯৮৩ চনৰ ফেব্ৰুৱাৰীত অসমৰ লোকসভা আৰু বিধানসভাৰ সাধাৰণ নিৰ্বাচনৰ দিন ঘোষণা হোৱাৰ লগে লগে আন্দোলনকাৰীয়ে নিৰ্বাচন বৰ্জনৰ সিদ্ধান্ত লয়। নিৰ্বাচন প্ৰতিৰোধ কৰিবলৈ আছু-সদৌ অসম গণ সংগ্ৰাম পৰিষদে বন্ধ, সন্তোষা প্ৰাৰ্থী ঘেৰাও, সৰ্বাত্মক অসহযোগ আদি বিভিন্ন কাৰ্যসূচী গ্ৰহণ কৰিছিল। এই সময়তে আন্দোলনটো আৱেগিক মনোভাৱেৰে পৰিচালিত হৈছিল। নেতৃত্বৰ দ্বাৰা ঘোষিত অহিংস নীতিৰ পৰিৱৰ্তে 'নিৰ্বাচন প্ৰতিৰোধী সংগ্ৰাম' ক্ৰমে হিংসাত্মক হৈ পৰে। ফলত নেলী, গহপুৰ, খৈৰাবাৰী, চমৰীয়া, গোৰেশ্বৰ, চিলাপথাৰ, চামগুৰি, ধুলা, থেকেৰাবাৰী, চাউলখোৱা চাপৰি আদি বিভিন্ন ঠাইত সাম্প্ৰদায়িক আৰু গোষ্ঠীসংঘৰ্ষ ঘটিল; ব্যাপকভাৱে হত্যা-হিংসা, গৃহদাহ সংঘটিত হৈছিল। গহপুৰত ঘটা সংঘৰ্ষৰ চৰিত্ৰ কিছু বেলেগ আছিল। এই সংঘৰ্ষত অজনজাতি (অৰ্থাৎ অসমীয়াভাষী) আৰু জনজাতি— বিশেষকৈ বড়ো-কছাৰী গোষ্ঠী— উভয়পক্ষই আক্ৰান্ত হৈছিল। পাৰস্পৰিক আক্ৰমণত ৪৩খন অসমীয়া আৰু ৩০খন বড়ো গাঁও জ্বলি ছাৰখাৰ হৈছিল; ৩০ৰো অধিক 'লোকৰ প্ৰাণহানি হৈছিল। পি টি চি এই উদয়াচলৰ দাবীৰে নিৰ্বাচন খেলাৰ ঘোষণা কৰাটোৱেই আছিল গহপুৰত হোৱা সংঘৰ্ষৰ অন্যতম কাৰণ। এই কথাৰ বাবেই অসমীয়াভাষী আন্দোলনকাৰীৰ মনত বড়ো-কছাৰীসকল ঘোৰ শত্ৰু হৈ পৰিছিল। অৰ্থাৎ বিদেশীৰ নাম সন্নিবিষ্ট ভোটৰ তালিকাৰে অসমত যি নিৰ্বাচন চৰকাৰে অনুষ্ঠিত কৰিব খুজিছিল,

ভাত যোগ দিয়া বা দিব খোজাসকলেই আছিল আন্দোলনৰ সমৰ্থকসকলৰ বাবে 'অসম' আৰু 'অসমীয়া'ৰ ঘোৰ শত্ৰু, বিদেশী বহিষ্কৰণৰ বিৰোধী। কিন্তু এনে ধৰণৰ ভাতৃঘাতী সংঘৰ্ষ কেবল আন্দোলনটোৰ বাবেই ডাঙৰ ক্ষতি নাছিল, 'বৃহত্তৰ অসমীয়া জাতীয়ত্ব' গঠনৰ ক্ষেত্ৰতো ইয়াৰ নেতিবাচক প্ৰভাৱ পৰিছিল। মুঠতে নিৰ্বাচনটোৱে 'অসমখনক চিৰদিনৰ কাৰণে ভাগ ভাগ কৰি পেলালে। জনজাতীয় লোকসকল, বিশেষকৈ বড়োসকল অসমৰ মূলসুঁতিৰ পৰা আঁতৰি গ'ল।"

১৯৮৩ৰ নিৰ্বাচনকেন্দ্ৰিক সংঘৰ্ষই সৃষ্টি কৰা পৰিস্থিতিৰ বাবে অসমৰ অন্যতম জনজাতি তিৱা (লালুং) সকলো উচ্চবৰ্ণৰ অসমীয়াৰ প্ৰতি ক্ষোভিত হৈ পৰে। নেলীৰ গণহত্যাৰ বাণ্টীয় সংবাদ মাধ্যমত যথেষ্ট চৰ্চা লাভ কৰিছিল। জনজাতিসকল জমিৰ পৰা বিতাড়ন হোৱাটোৱেই এই সংঘৰ্ষৰ মূল কাৰণ বুলি ব্যাখ্যা আগবঢ়োৱা হৈছিল। এই ব্যাখ্যাৰ আলম লৈ আছু আৰু সদৌ অসম গণ সংগ্ৰাম পৰিষদে গণহত্যাৰ সকলো দোষ পমুৱা মুছলমানৰ গাঁৱৰ কাষৰীয়া তিৱা জনজাতিৰ ওপৰত জাপি দিয়ে। কিন্তু বাস্তৱ সত্যটো আছিল এই আক্ৰমণত তিৱা জনজাতিৰ লগতে আন্দোলনকাৰী অসমীয়া স্থানীয় নেতাসকলো জড়িত আছিল। তিৱাসকলৰ জাতীয়তাবাদী সংগঠন 'লালুং যুথ ফ্ৰন্ট'এ 'নেলীৰ ঘটনালীৰ বাবে লালুংসকল দায়ী নহয়' বুলি স্পষ্ট প্ৰতিক্ৰিয়া ব্যক্ত কৰিছিল এনেদৰে— "এই সংঘৰ্ষত লালুং জনজাতিৰ লোক লিপ্ত থকাটো নুই কৰিব নোৱাৰি যদিও এই ঘটনাক লালুং ৰাইজে পমুৱাৰ ওপৰত চলোৱা আক্ৰমণ বুলিলে সত্য নহ'ব...।" এই ঘটনাটোৰ পাছত তিৱাসকলে অনাস্থা প্ৰকাশ কৰি আন্দোলনৰ পৰা লাহে লাহে আঁতৰি আহে। অসম আন্দোলনত জনজাতিসকলক নেতৃত্বই ব্যৱহাৰ কৰা বুলিও অভিযোগ উঠিছিল। লগতে কোনো গুৰুতৰ দোষত দোষী সাব্যস্ত হোৱাৰ পাছত নিজে তাৰ দায়িত্ব নলৈ জনজাতিৰ ওপৰত সেই দোষ জাপি দিয়াৰ প্ৰৱণতাৰ বাবেই জনজাতিসকল অসন্তুষ্ট হৈছিল। মিছাকৈ অপযশ দিয়াৰ এনে অপচেষ্টাই তিৱাসকলৰ গোষ্ঠীগত চেতনাত গভীৰভাৱে প্ৰভাৱ পেলাইছিল। তাৎক্ষণিক প্ৰতিক্ৰিয়া হিচাপে তিৱাসকলে স্বায়ত্তশাসিত জিলা (সুকীয়া লালুং জিলা) গঠনৰ দাবী তোলে। গতিকে এই প্ৰেক্ষাপটতে তেওঁলোক স্বকীয় অস্তিত্ব তথা আত্মপৰিচয় প্ৰতিষ্ঠাৰ প্ৰতি সচেতন হৈ উঠিছিল।

আটাইতকৈ গুৰুত্বপূৰ্ণ কথাটো হ'ল— ১৯৮৩ৰ পৰিঘটনাই জনজাতি-অজনজাতিৰ সম্পৰ্কৰ অধিক অৱনতি ঘটাইছিল। নিৰ্বাচনকেন্দ্ৰিক সংঘৰ্ষই অসমৰ ঐতিহ্য, সম্প্ৰীতি, ভাতৃবোধৰ বাতাবৰণ বিনষ্ট কৰিছিল আৰু বড়োৰ দৰে বৃহৎ জনজাতীয় গোষ্ঠী 'মূলসুঁতিৰ অসমীয়া' সমাজখনৰ পৰা আঁতৰি আহিছিল।

অসম আন্দোলনৰ সমাপ্তি কালৰ দুটা কাৰকৰ বাবে জনজাতীয় অস্তিত্ব তথা পৰিচয় প্ৰতিষ্ঠাৰ জাগৰণে চূড়ান্ত পৰ্যায় পাইছিল। সেই কাৰক দুটা আছিল— অসম চুক্তি আৰু অগপ চৰকাৰৰ শাসন। জনজাতীয় সংগঠনৰ কোনো মতামত নোলোৱাকৈ খৰতকীয়াভাৱে অসম চুক্তি স্বাক্ষৰিত হোৱাটোৰ বিৰুদ্ধে আপত্তি উঠিছিল। চুক্তিৰ ৬ নং দফাৰ বিৰুদ্ধে আবছু, ইউ টি এন এল এফ আদি সংগঠনে প্ৰতিবাদ সাব্যস্ত কৰিছিল। এই দফাটোত 'অসমীয়া ৰাইজৰ সাংস্কৃতিক, সামাজিক আৰু ভাষিক পৰিচয় আৰু ঐতিহ্য ৰক্ষা, সংৰক্ষণ আৰু বিকাশৰ বাবে যথোপযুক্ত ধৰণৰ সাংবিধানিক, আইনগত আৰু প্ৰশাসনিক

বক্ষণাবেক্ষণৰ ব্যৱস্থা কৰা হ'ব' বুলি ঘোষিত হৈছিল। কিন্তু 'অসমীয়া' শব্দৰ উল্লিখনে জনজাতীয় নেতৃত্বক সন্তুষ্ট কৰিব পৰা নাছিল। 'অসমীয়া কোন?'— এই প্ৰশ্ন উত্থৰ সেই সময়ত অস্পষ্ট আছিল। জনজাতিসকলে ইতিপূৰ্বে অসমীয়া নহয় বুলিহে মুকলিকৈ কোৱামেলা কৰিবলৈ লৈছিল। বহুতে সেই সময়ত 'অসমীয়া' বুলিলে অসমীয়াভাষীসকলকে নিৰ্দেশ কৰিছিল।

আনহাতে ১৯৮৫ চনৰ বিধানসভা নিৰ্বাচনৰ মাধ্যমেৰে প্ৰফুল্ল কুমাৰ মহন্তৰ নেতৃত্বত গঠিত অগপ চৰকাৰক জনজাতীয় পক্ষটোৱে আস্থাত ল'ব পৰা নাছিল। এজন জনজাতীয় বিধায়কে স্পষ্টভাৱে আঙুলিয়াই দিছিল যে অগপ মন্ত্ৰীসভাত ৬জন ব্ৰাহ্মণ বিধায়কৰ ভিতৰত ৫জনে কেবিনেট পৰ্যায়ত মন্ত্ৰী, ২১জন অসমীয়া উচ্চবৰ্ণৰ বিধায়কৰ ভিতৰত মুঠ ১৮জনে মন্ত্ৰীপদ লাভ কৰিছিল। কিন্তু ইয়াৰ বিপৰীতে মুঠ ১৮জন অনুসূচিত জনজাতিৰ বিধায়কৰ ভিতৰত মাত্ৰ ৪জনকহে মন্ত্ৰিত্ব প্ৰদান কৰা হ'ল।" আন্দোলনৰ পাছত এনেকৈ অসমৰ ৰাজনৈতিক ক্ষেত্ৰখনত হিন্দুপ্ৰধান উচ্চবৰ্ণৰ অসমীয়া শাসকগোষ্ঠীৰ নিয়ন্ত্ৰণ প্ৰতিষ্ঠা হোৱাটো তেওঁলোকে সহ্য কৰিব পৰা নাছিল। আকৌ অনা-অসমীয়া ছাত্ৰ-ছাত্ৰীৰ ওপৰত অসমীয়াক বাধ্যতামূলক তৃতীয় ভাষা হিচাপে জাপি দিয়া, ট্ৰাইবেল বেণ্ট আৰু ব্লকৰ পৰা বেদখলকাৰীক উচ্ছেদ কৰাৰ সঠিক ব্যৱস্থা নোলোৱা— অগপ চৰকাৰৰ এনে জনজাতিবিৰোধী পদক্ষেপ অসমৰ প্ৰায় সকলো ভৈয়াম জনজাতিৰ গোষ্ঠীগত চেতনাৰ পুনৰ্স্থাপনৰ অন্যতম কাৰণ হৈ উঠিছিল।

মুঠতে অসম আন্দোলনৰ পটভূমিতে আত্মপৰিচয় আৰু আত্মপ্ৰতিষ্ঠা লাভৰ দিশত জনজাতীয় চেতনাৰ পুনৰ্স্থাপন পৰিপূৰ্ণতা লাভ কৰিছিল। আনহাতে অসমীয়া জাতিসত্তাৰ ক্ষুদ্ৰ ক্ষুদ্ৰ জাতিসত্তাবোৰক খৰতকীয়াকৈ অন্তৰ্ভুক্ত কৰি বৃহৎ আৰু সুৰক্ষিত জাতিসত্তা হোৱাৰ যি প্ৰচেষ্টা চলাই আহিছিল সেয়া জনজাতীয় পৰিচয়ৰ পুনৰ্স্থাপনত থানবান হৈ পৰাৰ উপক্ৰম হয়। গতিকে 'বৃহত্তৰ অসমীয়া জাতিগঠন প্ৰক্ৰিয়া'ত এই ক্ষতি-এক বৃহৎ ক্ষতি হিচাপে বিবেচিত হ'বৰ যোগ্য।

অৱশ্যে জনজাতিসকলৰ ৰাজনৈতিক দাবীবোৰ অসম আন্দোলনৰ পৰিৱেশত কিছু তল পৰি আছিল। তেওঁলোকে আন্দোলনৰ মূল ইচ্ছাটোৰ প্ৰতি সমৰ্থন জনাইছিল আৰু নেতৃত্বৰ দ্বাৰা ঘোষিত অহিংস নীতিৰ ওপৰতো আস্থা ৰাখিছিল। অৱশ্যে জনজাতিৰ প্ৰতি আন্দোলনকাৰীৰ যি স্থিতি তথা ভূমিকা তাত সন্দেহ ওপজাৰ বাবে লাহে লাহে সমৰ্থন কমি গৈছিল। ১৯৮৩ৰ নিৰ্বাচনৰ পাছতে সদৌ অসম জনজাতি ছাত্ৰ সন্থা (All Assam Tribal Student Union-AATSU), সংক্ষেপে 'আটছু'ৰে তিনিটা দাবীৰ ভিত্তিত ১৫ জুলাইৰ পৰা পোন্ধৰদিনীয়া আন্দোলনৰ কাৰ্যসূচী ঘোষণা কৰিছিল। এই দাবী তিনিটা আছিল— (১) বড়োভাষী অধ্যয়িত অঞ্চলত বড়ো ভাষাক সহযোগী চৰকাৰী ভাষা হিচাপে ঘোষণা, (২) মিচিং, দেউৰী, ৰাভা, তিৱা আৰু কাৰ্বি ভাষা প্ৰাথমিক শিক্ষাস্তৰত প্ৰচলন তথা অসমৰ ভৈয়াম অঞ্চলত বাস কৰা কাৰ্বি, গাৰো, খাচি, মাৰ, নগা, আইটনীয়া, দোৱনীয়া, খাময়াং আদি জনজাতীয় গোষ্ঠীক ডাৰতীয় সংবিধানৰ সপ্তম অনুসূচিত জনজাতি বুলি স্বীকাৰ আৰু (৩) অসমৰ ভৈয়াম অঞ্চলৰ এইবোৰ জনজাতি গোষ্ঠীৰ বাবে স্বায়ত্তশাসিত জিলা আৰু পৰিষদ গঠন।"

আন্দোলনোত্তৰ কালত, ১৯৮৬ চনৰ পৰা অসমৰ সৰ্বমুহূৰ্ত্ত জনজাতীয় শোণী বড়োসকলৰ মাজত এক নতুন ৰাজনৈতিক জাগৰণ ঘটিছিল। অসমৰ আন আন জনজাতিসমূহো এই জাগৰণৰ দ্বাৰা প্ৰভাৱিত হৈছিল। এই ৰাজনৈতিক পুনৰ্স্থানৰ অন্তৰালত পি টি চি এৰ দৰে জনজাতীয় সংগঠনৰ নমনীয় স্থিতি, অসম আন্দোলনৰ ত্ৰিভুজ অস্তিত্বতা, অসমীয়া জাতীয়তাবাদী সংগঠনৰ ওপৰত অনাধা তথা সেইবোৰ সংগঠনৰ দ্বাৰা প্ৰভাৱিত হোৱাৰ উপলক্ষি, অসমীয়া মধ্যবিত্ত শ্ৰেণীৰ কৰ্তৃত্ব ওফৰাই আত্মপৰিচয়, আত্মবিকাশ, আত্মমৰ্যাদা লাভ আৰু ৰাজনৈতিক স্বনিয়ন্ত্ৰণৰ ইচ্ছা— এনে অনেক কাৰণ নিহিত আছিল।

অসম আন্দোলনৰ আগে আগে পি টি চি এৰ নেতৃত্বয়ো পূৰ্বজ ট্ৰাইবেল লীগৰ দৰেই সংসদীয় ৰাজনীতিত যোগদান কৰিছিল। অসমীয়া মধ্যবিত্ত শ্ৰেণীৰ দ্বাৰা নিয়ন্ত্ৰিত কংগ্ৰেছ চৰকাৰৰ মন্ত্ৰীসভাত যোগদানৰ পাছত পৰিষদখনৰ পূৰ্বৰ সিদ্ধান্ত সলনি হ'ল। ১৯৭৭ চনৰ এপ্ৰিল মাহত পৰিষদে উদয়চলৰ দাবী বিসৰ্জন দি 'স্বায়ত্তশাসিত অঞ্চল'ৰ দাবীকে পুনৰ উত্থাপন কৰে। এনে শিথিল স্থিতিক প্ৰত্যাহ্বান জনাই উক্ত পৰিষদৰে একাংশ যুৱক, ছাত্ৰই ১৯৭৯ চনৰ ২২ মে' 'প্ৰগতিশীল অসম ভৈয়াম জনজাতি পৰিষদ' (Progressive Plain Tribal Council of Assam: PPTCA) গঠন কৰিছিল। এই সংগঠনে ১৯৮০ চনৰ ৮ জুলাইত প্ৰধান মন্ত্ৰী ইন্দিৰা গান্ধীৰ ওচৰত 'মিচিং বড়োলেণ্ড' নামৰ এক 'কেন্দ্ৰীয়শাসিত অঞ্চল'ৰ দাবী উত্থাপন কৰে। সংগঠনটো ১৯৮৫ চনত গঠিত 'সংযুক্ত জনজাতি ৰাষ্ট্ৰীয় মুক্তি বাহিনী' বা ইউ টি এন এল এফ (United Tribal National Liberation Front-UTNLF)ত জাহ যায়। এমাহৰ পাছতে ইউ টি এন এল এফে আকৌ এখন স্বায়ত্তশাসিত অঞ্চলৰ দাবী ইন্দিৰা গান্ধীৰ ওচৰত দাঙি ধৰে। উত্থাপিত অঞ্চলৰ নামকৰণ হ'ল— 'ট্ৰাইবেল লেণ্ড'। আনহাতে দেৱনাগৰী লিপিব আৰোপকৰণত ক্ষুণ্ণ হৈ থকা বড়োসকলৰ ছাত্ৰ সংগঠন আবছুৰে পি টি চি এৰ স্থিতিৰ তীব্ৰ বিৰোধিতা কৰি বড়ো লোকৰ জনসমৰ্থন আদায় কৰিবলৈ সক্ষম হৈছিল। এই সমৰ্থন আৰু বেছি ব্যাপক হৈছিল ১৯৮৫ৰ অসম চুক্তি আৰু অসমীয়া মধ্যবিত্ত শ্ৰেণী-প্ৰভাৱিত অগপ চৰকাৰ— এই দুই কাৰকৰ প্ৰভাৱত।

১৯৮৫ চনৰ ১৫ আগষ্টত ভাৰত চৰকাৰ, অসম চৰকাৰ আৰু আবছুৰ বিষয়ববীয়াৰ মাজৰ ত্ৰিপাক্ষিক বৈঠকত স্বাক্ষৰিত হোৱা 'অসম চুক্তি'ক জনজাতিসকলৰ অধিকাংশই প্ৰত্যাহ্বান কৰিছিল। অটছুৰ সাঃ সম্পাদক বণোজ কুমাৰ পেণ্ড, সদৌ ৰাভা ছাত্ৰ সন্থা সাঃ সম্পাদক সবাসাচী ৰাভা আৰু সদৌ মিচিং ছাত্ৰ সন্থা বা টি এম পি কে (টোকাম মিচিং পবিন কীবাং)ৰ সাঃ সম্পাদক পৰমানন্দ চায়েঙীয়াই বাতৰিকাকতলৈ পঠোৱা এটা বিবৃতিত কোৱা হৈছিল— "...জনজাতীয় আৰু অন্যান্য প্ৰশ্ন সম্পূৰ্ণৰূপে অগ্ৰাহ্য কৰি ৰাজীৱ গান্ধীয়ে অসমীয়া বণহিন্দুৰ প্ৰতিনিধি সদৌ অসম ছাত্ৰ সন্থাৰ সৈতে যি চুক্তিত উপনীত হৈছে, তাৰ পৰিণামত জনজাতীয় আৰু অন্যান্য নিৰ্মাণিত জাতি-গোষ্ঠীক বঞ্চিত, শোষিত আৰু দলিত কৰাৰ এক নতুন বাট মুকলি কৰি দিছে।" অসম চুক্তিৰ আধাৰতে অসমীয়া উগ্ৰ জাতীয়তাবাদৰ পুনৰ্স্থান হোৱা বুলি গণ্য কৰি জনজাতীয় ৰাইজ শংকিত হৈ পৰিছিল। চুক্তিৰ ৬ নং দফাই

বিশেষতঃ তেওঁলোকৰ মনত সন্দেহৰ জন্ম দিছিল। তেওঁলোকৰ ধাৰণা বহুমূল হৈ উঠিছিল যে অসম আন্দোলন আচলতে পূৰ্বৰ বিভিন্ন আন্দোলনবোৰৰ দৰেই অসমীয়া মধ্যবিত্ত শ্ৰেণীৰ আধিপত্য আৰু অস্তিত্ব সুৰক্ষিত কৰাৰ এক আলমহে মাৰ্গো। ইয়াৰ পাছতে জনজাতীয় ৰাইজৰ হৃদয়ত দীৰ্ঘদিনীয়া পুঞ্জীভূত অভিমান জাগ্ৰত হৈ উঠে। অবশ্যে অসম চুক্তিৰ এটা দফাই জনজাতিৰ মনতো কিছু আশাৰ সঞ্চাৰ কৰিছিল। ১০ নং দফা অনুসৰি জনজাতীয় বেটনী আৰু খণ্ডৰ পৰা বেদখলকাৰীক উচ্ছেদ কৰাৰ নিশ্চয়তা তেওঁলোকৰ বাবে এটা ডাঙৰ সমাধান আছিল। কিন্তু চুক্তিৰ পাছত গঠন হোৱা অগপ চৰকাৰৰ আমোলত বেদখলকাৰী বিতাড়নৰ নামত বহু জনজাতীয় লোককহে উচ্ছেদ কৰা হ'ল। সেইদৰে অগপ চৰকাৰে জনজাতীয় স্বার্থত ব্যাঘাত জন্মাই ভাষিক আধিপত্য প্ৰতিষ্ঠাৰ চেষ্টাহে চলালে। ১৯৮৬ চনৰ ২৮ ফেব্ৰুৱাৰীত ছেবা (Secondary Board of Education of Assam, SEBA)ৰ জৰিয়তে দিয়া এক নিৰ্দেশনা অনুসৰি অসমীয়া বাধ্যতামূলক তৃতীয় ভাষা হ'ব বুলি ঘোষণা কৰা হৈছিল। এই ঘোষণাৰ ফলত বড়োসকলৰ মাজত জাতীয় চেতনা জাগ্ৰত হৈ উঠে। ১৯৮৬ চনৰ ৩ অক্টোবৰত ৰঞ্জন দৈমাৰীৰ নেতৃত্বত বড়োসকলৰ উগ্ৰ জাতীয়তাবাদী সংগঠন 'বড়ো ছিকিউৰিটি ফ'ৰ্চ'ৰ জন্ম হয় (পাছত 'নেশ্যনেল ডেম'ক্ৰেটিক ফ্ৰন্ট অব বড়োলেণ্ড, এন ডি এফ বি)। অসমীয়া সংবাদপত্ৰ-আলোচনীয়ে এইক্ষেত্ৰত বণহিন্দু অসমীয়াৰ আধিপত্যবাদ আৰু উগ্ৰ জাতীয়তাবাদী ভাবধাৰাক জগৰীয়া কৰিব খোজে। আনহাতে 'আবছু'ৰে ১৯৮৭ চনৰ ২ মাৰ্চৰ পৰা (Divide Assam Fifty Fifty) (ডিভাইড আছাম ফিফটি ফিফটি) শ্লোগান লৈ সুকীয়া গৃহভূমি 'বড়োলেণ্ড'ৰ দাবীত আন্দোলন আৰম্ভ কৰি দিছিল। এই আন্দোলনৰ নেতৃত্ব বহন কৰিছিল উপেন্দ্ৰ নাথ ব্ৰহ্মই। 'আবছু'ৰ ৯২ দফীয়া দাবীচনদৰ প্ৰধান ৰাজনৈতিক দাবী তিনিটা আছিল—

১. বড়োসকলৰ কাৰণে ব্ৰহ্মপুত্ৰৰ উত্তৰপাৰে 'বড়োলেণ্ড' নামেৰে এক সুকীয়া ৰাজ্য গঠন

২. ব্ৰহ্মপুত্ৰৰ দক্ষিণপাৰে জনজাতি অধ্যুষিত অঞ্চলসমূহক সামৰি স্বায়ত্তশাসিত জিলা পৰিষদ গঠন

৩. কাৰ্বি আংলঙত বসবাস কৰা বড়ো-কছাৰীসকলক ভাৰতীয় সংবিধান ষষ্ঠ অনুসূচীত অন্তর্ভুক্তিকৰণ

গতিকে স্পষ্ট হয় যে জনজাতীয় গোষ্ঠীসমূহৰ ৰাজনৈতিক সচেতনতা তথা পুনৰ্জাগৰণৰ ক্ষেত্ৰত অসম আন্দোলনৰ প্ৰভাৱশালী ভূমিকা আছে। এইখিনিতে মন কৰিবলগীয়া যে অসম আন্দোলনৰ পটভূমিতে ৰাজনৈতিক আৰু সাংস্কৃতিক অধিকাৰ প্ৰতিষ্ঠাৰ বাবে পৃথক পৃথক জনজাতীয় গোষ্ঠীয় শাসকগোষ্ঠীৰ ওপৰত চাপ প্ৰয়োগ কৰি গৈছিল; বড়োসকলৰ সাংস্কৃতিক আত্মপ্ৰতিষ্ঠাৰ বাবে মাত মতা বড়ো সাহিত্য সভাই বড়ো ভাষাক সহযোগী চৰকাৰী ভাষা হিচাপে স্বীকৃতি দিবলৈ যি সংগ্ৰাম কৰি আহিছিল, তাৰ বাস্তৱ ৰূপায়ণ হৈছিল ১৯৮৪ চনত। চৰকাৰে 'অসম চৰকাৰী ভাষা অধিনিয়ম' (The Assam Official Language Act)ৰ সংশোধনৰ জৰিয়তে বড়ো অধ্যুষিত জিলা কোকৰাঝাৰ আৰু দৰং জিলাৰ ওদালগুৰি মহকুমাত বড়ো ভাষাক সহযোগী চৰকাৰী ভাষাৰ মৰ্যাদা প্ৰদান কৰিবলৈ বাধ্য হৈছিল। ইয়াৰ পৰৱৰ্তী পদক্ষেপ হিচাপে সাহিত্য সভাখনে সমগ্ৰ অসমতে বড়ো ভাষাক সহযোগী চৰকাৰী

ভাষাৰ স্বীকৃতি দিয়াৰ দাবী উত্থাপন কৰিছিল। আনহাতে ১৯৮৬ চনৰ পৰা মিচিং অধ্যুষিত অঞ্চলত প্ৰাথমিক পৰ্যায়ত মিচিং ভাষাৰ প্ৰয়োগ সাধনৰ ব্যৱস্থা কৰা হৈছিল।

প্ৰসংগসূচী আৰু পাদটীকা :

১. দ্ৰষ্টব্য, লক্ষ্মীনাথ পাংগিং, 'জনজাতিবোৰ অসমীয়া হৈ নাথাকে', হোমেন বৰগোহাঞি (সম্পা.), *সাদিনীয়া নাগৰিক*, চতুৰ্থ বছৰ, ১৬৯ সংখ্যা, ২৩ এপ্ৰিল, ১৯৮১, পৃ: ৪
২. প্ৰণয়কুমাৰ মুছাহাৰী, 'এই আন্দোলনৰ আমাৰ আন্দোলন নহয়', হোমেন বৰগোহাঞি (অবৈ. সম্পা.) *সাপ্তাহিক জনক্ৰান্তি*, ২য় বছৰ, ১৫ সংখ্যা, ২২ ডিচেম্বৰ, ১৯৮২, পৃ: ২
৩. 'সদৌ অসম জনজাতি সংৰক্ষণ সংগ্ৰাম সমিতি'ৰ সাধাৰণ সম্পাদক প্ৰণয়কুমাৰ মুছাহাৰীৰ ভাষ্যমতে "আনে নহ'লেও আমাৰ জনজাতি ভাইসকল আমাৰ কথাত পতিয়ন গৈছিল আৰু তেওঁলোক সকলোৰে এই আন্দোলনত সক্ৰিয় অংশগ্ৰহণ কৰাৰ পৰা বিৰত থাকিল।" — উল্লিখিত
৪. লক্ষ্মীনাথ পাংগিং, 'জনজাতিসকল আন্দোলনৰ পৰা আঁতৰি গ'ল', 'হোমেন বৰগোহাঞি (সম্পা.), *সাদিনীয়া নাগৰিক*, তৃতীয় বছৰ, ২৬ সংখ্যা, ২৯ মে', ১৯৮০, পৃ: ১
৫. দ্ৰষ্টব্য, থানেশ্বৰ পাংগিং, 'জনজাতি আৰু সাম্প্ৰতিক আন্দোলন', হোমেন বৰগোহাঞি (সম্পা.), *সাদিনীয়া নাগৰিক*, তৃতীয় বছৰ, ১২৭ সংখ্যা, ৫ জুন, ১৯৮০, পৃ: ১
৬. পৰাগ কুমাৰ দাস, 'অসমৰ জনজাতীয় বাইজৰ সমস্যা : উদঘাটল আৰু অন্যান্য', 'ভবেন্দ্ৰনাথ শইকীয়া (মু. সম্পা.), *প্ৰান্তিক*, ২য় বছৰ, ১৬শ সংখ্যা, ১৬-৩১ জুলাই, ১৯৮৩, পৃ: ১৮
৭. প্ৰণয়কুমাৰ মুছাহাৰী, পূৰ্বোল্লিখিত, পৃ: ২
৮. গণেশ বসুমতাৰী, 'আন্দোলনৰ পৰা জনজাতীয় বাইজ কিয় আঁতৰি আহিছে?', হোমেন বৰগোহাঞি (সম্পা.), *সাদিনীয়া নাগৰিক*, তৃতীয় বছৰ, ১২৮ সংখ্যা, ১২ জুন, ১৯৮০, পৃ: ৯
৯. দ্ৰষ্টব্য, লক্ষ্মীনাথ পাংগিং, 'জনজাতিবোৰ অসমীয়া হৈ নাথাকে,' পূৰ্বোল্লিখিত
১০. দ্ৰষ্টব্য, লক্ষ্মীনাথ পাংগিং, 'জনজাতীয় বাইজে আন্দোলনত নামিবনে?', হোমেন বৰগোহাঞি (অবৈ. সম্পা.), *সাপ্তাহিক জনক্ৰান্তি*, ২য় বছৰ, ৬ষ্ঠ সংখ্যা, ১৩ অক্টোবৰ, ১৯৮২, পৃ: ৩
১১. দ্ৰষ্টব্য, গণেশ বসুমতাৰী, পূৰ্বোল্লিখিত, পৃ: ৯
১২. উল্লিখিত
১৩. লক্ষ্মীনাথ পাংগিং, 'জনজাতিবোৰ অসমীয়া হৈ নাথাকে,' পূৰ্বোল্লিখিত, পৃ: ১
১৪. "বহিৰাগতৰ অবাধ প্ৰব্ৰজনৰে ৰাজ্যখনৰ অৰ্থনৈতিক, সামাজিক, সাংস্কৃতিক জীৱন বিষময় কৰি তুলিছে, অসমৰ জনজাতীয় বাইজ এই প্ৰব্ৰজনৰ ফলত বিশেষভাৱে ক্ষতিগ্ৰস্ত হৈছে। জনজাতীয় অঞ্চলত অজনজাতীয় লোকে মাটি পোৱাৰ বিধি আছে যদিও চৰকাৰৰ আগতীয়া অনুমতিপত্ৰ লোৱাৰ নিয়ম সম্পূৰ্ণৰূপে উলংঘা কৰি বিদেশী প্ৰব্ৰজনকাৰীয়ে মাটি দখল কৰিছে।"
- ৮ জুনৰ 'অসম বন্ধ' সফল কৰিবলৈ আহ্বান', 'কীৰ্তিনাথ হাজৰিকা (সম্পা.), *দৈনিক অসম*, পঞ্চদশ বছৰ, ২৯৫ সংখ্যা, ৪ জুন, ১৯৭৯, পৃ: ১
১৫. "...সম্প্ৰতি অসমত চলি থকা আন্দোলন কেবল অসমীয়াৰ অস্তিত্ব ৰক্ষাৰ সংগ্ৰাম নহয়। এই আন্দোলন আমাৰ জনজাতীয়সকলৰো অস্তিত্ব ৰক্ষাৰ সংগ্ৰাম।"
- বৰছিং ৰংফাৰ, 'এই সংগ্ৰাম আমাৰ জনজাতিৰো অস্তিত্ব ৰক্ষাৰ সংগ্ৰাম', 'মুনীন্দ্ৰনাৰায়ণ দত্তবৰুৱা (সম্পা.), *সাপ্তাহিক নীলাচল*, ৫৯২ সংখ্যা, ১৩ আগষ্ট, ১৯৮০, পৃ: ১২
১৬. বীৰেন্দ্ৰনাথ দাস বড়ো, 'জনজাতি স্বাৱলম্বী নহ'লে জনজাতীয়

- অস্তিত্ব অসমত বিলুপ্ত হ'ব,' মুনীন্দ্ৰনাৰায়ণ দত্তবৰুৱা (সম্পা.), *সাপ্তাহিক নীলাচল*, ৫৯২ সংখ্যা, ১৩ আগষ্ট, ১৯৮০, পৃ: ৭
১৭. ইন্দ্ৰজিৎ পেগু, 'জনজাতীয় লোকহে বিদেশীৰ দ্বাৰা আক্ৰান্ত হৈছে', 'মুনীন্দ্ৰনাৰায়ণ দত্তবৰুৱা (সম্পা.), *সাপ্তাহিক নীলাচল*, ৫৮৮ সংখ্যা, ১৬ জুলাই ১৯৮০, পৃ: ১
১৮. জয়কান্ত পাটৰ, 'আন্দোলন আৰু জনজাতীয় দৃষ্টিভঙ্গী', হোমেন বৰগোহাঞি (সম্পা.), *সাদিনীয়া নাগৰিক*, চতুৰ্থ বছৰ, ১৫২ সংখ্যা, ২৬ ফেব্ৰুৱাৰী, ১৯৮১, পৃ: ৮
১৯. উল্লিখিত, পৃ: ১০
২০. "যোৱা ডিচেম্বৰ মাহৰ মাজভাগত লক্ষীমপুৰ জিলাৰ গোগামুখত অনুষ্ঠিত সদৌ মিচিং ছাত্ৰ সন্থাৰ বিশেষ অধিবেশনত সৰ্বসন্মতিক্ৰমে অসমৰ 'তথাকথিত' জাতীয় উৎসৱ বিহু মিচিংসকলে বৰ্জন কৰিব লাগে বুলি প্ৰস্তাব গ্ৰহণ কৰা হয়। যোৱা মাঘ বিহু জোনাই, চিলাপথাৰ আদি মিচিং অধ্যুষিত অঞ্চলত হেনো আংশিকভাৱেহে উদ্‌যাপন কৰিছে। দুই, তিনি আৰু চাৰি জানুৱাৰীত অনুষ্ঠিত সদৌ মুৰ্কেচেলেক মিচিং ছাত্ৰ সন্থাৰ অধিবেশনত অসমৰ আটাইবোৰ জনজাতীয় ছাত্ৰ সংগঠনৰ নেতাৰ যোগদানো বিশেষ তাৎপৰ্যপূৰ্ণ। অৰ্থাৎ অন্যান্য জনজাতিবোৰেও অচিৰেই বিহু বৰ্জন কৰিব পাৰে।" — লক্ষ্মীনাথ পাংগিং, পূৰ্বোল্লিখিত
২১. দ্ৰষ্টব্য, টাবু টাইদ, 'মিচিং ভাষাৰ লিপি আৰু অসমৰ সাহিত্য', হোমেন বৰগোহাঞি (সম্পা.), *সাদিনীয়া নাগৰিক*, তৃতীয় বছৰ, ১০ এপ্ৰিল ১৯৮০, পৃ: ৩
২২. দ্ৰষ্টব্য, বসন্ত কুমাৰ দলে, 'অসমীয়া সাহিত্যত মিচিংসকল', হোমেন বৰগোহাঞি (সম্পা.), *সাদিনীয়া নাগৰিক*, তৃতীয় বছৰ, ১২৮ সংখ্যা, ১২ জুন, ১৯৮০, পৃ: ৬, ১০
২৩. লক্ষ্মীনাথ পাংগিং, 'জনজাতীয় জাগৰণৰ পটভূমিত', হোমেন বৰগোহাঞি (সম্পা.), *সাদিনীয়া নাগৰিক*, তৃতীয় বছৰ, ১১২ সংখ্যা, ৩১ জানুৱাৰী, ১৯৮০, পৃ: ১০
২৪. মৃগাল তালুকদাৰ আৰু কিশোৰ কুমাৰ কলিতা, *অসম (খণ্ড-৫)*, ২০১৪, পৃ: ২৭৮
২৫. ষ্টাৰ্ক বিপটৰ, 'নেলীৰ ঘটনাৱলীৰ বাবে লালুংসকল দায়ী নহয় : লালুং যুধ ফ্ৰন্ট', কনকসেন ডেকা (সম্পা.), *অগ্ৰদূত*, পঞ্চদশ বছৰ, ১৫ সংখ্যা, ৬ জুন, ১৯৮৪, পৃ: ১১
২৬. "An angry tribal MLA pointed out that the AGP had 5 cabinet ministers out of 6 Asamiya Brahmin MLAs, 18 out of 21 Asamiya high caste MLAs because ministers; whereas only 4 ministers were chosen from 18 scheduled tribe MLAs."
২৭. দ্ৰষ্টব্য, দীনেশ গোস্বামী, 'ট্ৰাইবেলবাদ'ৰ ৰাজনীতিয়ে অসমৰ জনজাতি বাইজৰ উপকাৰ সাধিবনে?', হোমেন বৰগোহাঞি (সম্পা.), *সাদিনীয়া নাগৰিক*, ৫ম বছৰ, ২৭৬ সংখ্যা, ২১ জুলাই, ১৯৮৩, পৃ: ২
২৮. বিশেষ প্ৰতিনিধি, 'জনজাতীয় ছাত্ৰ সন্থাই অসম চুক্তিক প্ৰত্যাহ্বান কৰিছে', হোমেন বৰগোহাঞি (অবৈ. সম্পা.), *সাপ্তাহিক জনক্ৰান্তি*, ৫ম বছৰ, ৪৪ সংখ্যা, ১ ছেপ্টেম্বৰ, ১৯৮৫, পৃ: ১
২৯. 1. Creation of a separate state called 'Bodoland' on the north bank of the river Brahmaputra
2. Creation of autonomous district councils in the tribal dominated areas on the south bank of Brahmaputra
3. Inclusion of 'Bodo-Kacharis' of Karbi Anglong in the Sixth Schedule of the constitution of India— Keshab Basumatary, *Political Economy of the Bodo Movement of Assam : A Human Development Perspective*, 2010, p. 25

লেখকৰ ঠিকনা : সহকাৰী অধ্যাপক, অসমীয়া বিভাগ, জেংৰাইমুখ মহাবিদ্যালয়, মাজুলী, ফোন : ৭০০২০-৬৮৯০৪



Scattering by interstellar graphite and fayalite composite dust analogues: computer simulation and laser-based laboratory measurements

MANASH J. BORUAH^{1,*}, ANKUR GOGOI^{2,*} and GAZI A. AHMED¹

¹Department of Physics, Tezpur University, Tezpur 784028, India.

²Department of Physics, Jagannath Barooah College, Jorhat 785001, India.

*Corresponding author. E-mail: boruahmanash5@gmail.com; ankurgogoi@jbcollge.org.in

MS received 3 September 2020; accepted 3 November 2020

Abstract. Scattering properties of irregularly shaped interstellar composite dust analogues consisting of graphite and fayalite (Fe_2SiO_4) were studied using discrete dipole approximation (DDA). Two dust models were developed to calculate the scattering and extinction efficiencies, single scattering albedo, asymmetry parameter, phase functions and degree of linear polarizations. Laboratory measurements were also performed at three incident wavelengths 543.5, 594.5 and 632.8 nm on chemically synthesized graphite and fayalite composite particles of sizes ranging from 0.3 to 5 μm . A comparative analysis of the theoretical and experimental results of shape- and size-averaged scattering parameters shows that changes in the percentage composition of a two-species mixture model has a pronounced effect on the light-scattering properties of dust particles. The developed computational models are successful in representing a two-species mixture of interstellar dust analogues considering diverse size, shapes and percentage composition. This technique can be applied to fit observed scattering and absorption peaks in the visible region produced by astrophysical dust, provided large number of particle species are included and the influence of more physical parameters (e.g., porosity, fluffiness, temperature, density, etc.) are considered. Further, this study is also applicable to remote sensing, atmospheric and planetary sciences. All the physical parameters employed as variables in the models influence the oscillations observed in theoretical curves and change the values of scattering parameters.

Keywords. Light scattering—interstellar dust—phase function—DDSCAT.

1. Introduction

The composition of interstellar dust depends on their physical environment and the interactions of high energy radiations (both stellar and secondary radiations) with the constituent gas clouds (Siebenmorgen *et al.* 2014). These interactions determine the absorption and scattering properties of dust particles, which in turn, influence the interstellar medium (Aguirre 1999; Mennella *et al.* 2001; Calura *et al.* 2008). Notably, light-scattering properties of interstellar dust particles depend on their size, shape, composition, porosity, fluffiness, aggregation states along with the density and refractive index (Hulst & van de Hulst 1981; Bohren & Huffman 2008; Steinacker *et al.* 2010). In other words, light-scattering

properties of such dust particles carry their signatures in terms of their physical and optical properties. And also, the polarization curves of interstellar dust grains and its dependence on alignment of dust particles provide better insights into their optical and radiative properties both in optical and IR wavelengths (Andersson *et al.* 2015). It is, therefore, very important to investigate the scattering properties of interstellar dust particles as such, results can be utilized in inverse calculations for their proper classification and identification. In addition, such information is crucial for interpreting the spectrum of light sources including stars and galaxies (Draine 2003; Piovan *et al.* 2006; Siebenmorgen *et al.* 2014).

Unfortunately, scattering properties of interstellar dust grains are far from being quite well understood,

since it is extremely difficult to conduct *in situ* scattering measurements on dust grains found in different cosmic environments. Nevertheless, a number of strategies, including *in situ* dust analysis on spacecraft, sample capture and return mission, remote sensing, etc., have been implemented in the recent past to study the astrophysical dust particles. For instance, real interstellar dust grains are characterized in the Ulysses, Cassini, Galileo and Helios spacecrafts in the UV to far infrared wavelengths (Krüger *et al.* 2007; Altobelli *et al.* 2016). *In situ* measurements of cometary dust grains were also carried out with the Rosetta probe (Riedler *et al.* 2007; Ishiguro 2008; Fulle *et al.* 2010). Notably, in the first, STARDUST mission successfully brought back real dust samples from space, which were later used to carry out extensive investigations of cometary dust properties (Tuzzolino *et al.* 2003; Westphal *et al.* 2005, 2014; McKeegan *et al.* 2006; Brownlee 2014). Furthermore, the observations of interstellar extinction and polarization as well as absorption line have been conducted by using the Hubble space telescope to determine the composition of the interstellar dust particles (Savage & Sembach 1996). All these direct and/or indirect observations revealed that the dust present in the interstellar medium is mainly composed of amorphous silicate, amorphous carbon, graphite, carbonates, metal oxide grains, amorphous ice particles and nanodiamonds (Hulst & van de Hulst 1981; Tielens 2001; Rotundi *et al.* 2002; Groves *et al.* 2004; Pagani *et al.* 2010).

From the theoretical point of view, various theoretical approaches, e.g., Mie theory, discrete dipole approximation (DDA), T-matrix method, etc., that involved computation techniques were also developed for the proper interpretation of the observed interstellar extinction and polarization. In such theoretical calculations, dust models comprising of graphite, silicates and polycyclic aromatic hydrocarbons (PAH) as the principal component are generally used. Despite the availability of such high-performance theoretical calculations and dust models, exact composition of interstellar dust is still not well-known (Draine 2003). Significant discrepancies are generally observed between observations and calculations since it is very difficult to model the real dust particles in nature and at the same time different combinations of variable physical and optical parameters need to be incorporated in the models, which ultimately lead to complicated results (Tielens 2001; Groves *et al.* 2004). Further, dust models include assumptions based on specific regions of interest and wavelength ranges

under investigation. In contrast, such problems present lesser difficulties, while working with laboratory-based simulations using analogue samples. Undoubtedly, visual evidences and access to real samples are the best possible ways to verify the applicability and accuracy of the proposed dust models. Notably, the lack of sufficient amount of real extraterrestrial dust samples restricts most experiments and computational works of dust to analogue samples (Rotundi *et al.* 2002).

In recent developments in this field, a considerable amount of observational, computational and experimental studies has been carried out by several research groups which not only contributed significantly towards a better understanding of the absorption and scattering properties of astrophysical dust around stars, regoliths and comets, but also provided the valuable information about some of the prominent features observed in the spectrum of silicate and carbonaceous dust particles. Most important contributions include the detailed study of absorption profiles of composite silicate grains in circumstellar dust around M-type and asymptotic giant branch stars (IRAS and Spitzer data) for a wide spectral range (Gupta *et al.* 2016). Another significant work includes the extensive study of Comet 67P/Churyumov-Gerasimenko from 2-m Himalayan Chandra Telescope in India. The observational data are interpreted in terms of dust properties and compared to *in situ* Rosetta observations (Sen *et al.* 2019). Advanced dust grain models are developed using the DDA, effective medium approximation (EMA) and T-Matrix methods to study the dust around protoplanetary disks around young stars. Possible detection of silicon carbide (SiC) in the outer disk of a young sample star is one significant achievement of these dust models (Saikia *et al.* 2019). Light-scattering properties have also been studied with a large number of regolith analogue samples (e.g., alumina and olivine), which revealed that porosity has a pronounced effect on the observed value of reflectance, polarization and photometric colour (Deb *et al.* 2015; Kar *et al.* 2016; Sen *et al.* 2017). These findings have important applicability in the observational analyses of astrophysical dust.

In this paper, the results of laboratory simulation and theoretical modelling based on DDA are presented for interstellar composite dust analogue made of graphite and fayalite (an iron end-member of olivine which is an important component of silicates in space). Notably, graphite and silicate dust species are found in abundance in cosmic dust clouds (Draine & Li 2007) including solar system objects (meteorites)

(Messenger *et al.* 2005). Apart from their individual presence, these dust species can also be present in composite form. Notably, the relative abundances of silicates are higher than graphite and PAHs in interstellar dust (Nieva & Przybilla 2012). The primary aim of this work is to predict the combined effect of physical variables used in dust modelling (e.g., percentage composition, size distribution and particle shapes) on the light-scattering properties, keeping in mind complex nature of astrophysical observations. The number of orientation directions and number of dipoles are also varied in the computation to enhance the accuracy of the calculation. The theoretically calculated phase function (F_{11}) and polarization ($-F_{12}/F_{11}$) are compared with experimentally acquired results in the visible wavelength region for validation of the proposed models. Such comparison between theory and controlled experiments are extremely important to ensure the accuracy of developed models and their efficiency in predicting the properties of astrophysical dust.

2. Light-scattering fundamentals

It is well-known that the intensity and state of polarization of a beam of light can be completely described by Stokes vector $I = \{I, Q, U, V\}$, where I is the total intensity, Q the difference between the polarization intensities at 0° and 90° to the scattering plane, U the difference between the polarization intensities at $+45^\circ$ and -45° to the scattering plane and V the difference between the left and right circular polarization intensities (Bohren & Huffman 2008; Boruah *et al.* 2017). In a scattering event, the intensity and polarization of incident light is generally changed, thereby altering the incident Stokes vectors, due to the interaction of light with the scatterer. The Stokes vector describing the incident and the scattered light are connected by a 4×4 scattering matrix, F_{ij} , where $i, j = 1-4$, as given below.

$$\begin{pmatrix} I_s \\ Q_s \\ U_s \\ V_s \end{pmatrix} = \frac{1}{k^2 r^2} \begin{pmatrix} F_{11} & F_{12} & F_{13} & F_{14} \\ F_{21} & F_{22} & F_{23} & F_{24} \\ F_{31} & F_{32} & F_{33} & F_{34} \\ F_{41} & F_{42} & F_{43} & F_{44} \end{pmatrix} \begin{pmatrix} I_i \\ Q_i \\ U_i \\ V_i \end{pmatrix} \quad (1)$$

The subscripts i and s refer to the incident and scattered beams, k the wave vector and r the distance from the sample to the detector (Hulst & van de Hulst 1981; Bohren & Huffman 2008). It is noteworthy to

mention that the matrix F_{ij} , also known as the Mueller matrix, contains information about the size distribution, shape and refractive index of the scatterers (Volten *et al.* 1998). All the 16 elements of Mueller matrix are functions of the scattering angles (θ). The element F_{11} is called the phase function or scattering function and $-F_{12}/F_{11}$ is termed as degree of linear polarization for unpolarized incident light. Notably, the phase function can be experimentally determined by measuring the scattered light intensity as a function of scattering angle for unpolarized incident light. On the other hand, the degree of linear polarization can be measured by using proper combination of analysers in front of the detector.

$$-\frac{F_{12}}{F_{11}} = \frac{I_{\perp} - I_{\parallel}}{I_{\perp} + I_{\parallel}}, \quad (2)$$

where I_{\perp} and I_{\parallel} are parallel and perpendicular components of polarized light with reference to the direction of observation in the scattering plane. It is critical to note that the study of these two elements of the scattering matrix is indeed the most important in astrophysical observations because incident radiations (e.g., solar or stellar) are unpolarized in nature (Baba & Naoshi 2003). Therefore, in this work, we restricted our study to the determination of phase function and polarization.

3. Modelling approach

In this work, computational models of the interstellar composite dust consisting of graphite and fayalite are developed and their scattering properties have been simulated at three incident wavelengths in the visible region using DDA. DDA basically approximates a target by a finite array of polarizable points or dipoles. The points acquire dipole moments in response to the incident electric field and produce secondary sets of radiation or the scattered fields. The dipoles within the scattering volume also interact mutually via their electric fields resulting in the total scattered radiation (Purcell & Pennypacker 1973; Draine 1988).

The whole modelling and simulation scheme can be summarized as follows.

- (i) Two computational models of interstellar composite dust analogue composed of graphite and fayalite with different percentage compositions are developed as given in Table 1.
- (ii) Each model includes six standard irregular shapes suggested by Zubko *et al.* (2007) and Nousiainen & Muinonen (2007).

- (iii) The scattering and extinction efficiencies, single scattering albedo, asymmetry parameters, phase function (F_{11}) and polarization ($-F_{12}/F_{11}$) of the modelled dust particles are theoretically calculated using DDA code (DDSCAT 7.3.0) (Draine & Flatau 1994, 2013).
- (iv) All the theoretically calculated parameters are averaged over lognormal-size distribution for all the shapes. Further, all the values are averaged over the six shapes or target geometries. Such size and shape distributions are considered to simulate the situation present in real samples.
- (v) An indigenously developed MATLAB post-processing tool is used to perform the averaging over shapes, percentage compositions and sizes for all the scattering parameters calculated.
- (vi) The values of F_{11} and $-F_{12}/F_{11}$ are measured experimentally for laboratory-synthesized dust composites of graphite and fayalite using an indigenously developed light-scattering set-up.
- (vii) The parameters, e.g., size distribution, shape, refractive index and wavelength,

percentage composition of graphite and fayalite in the mixture, are varied to reproduce the experimental results. Similarly, number of dipoles and numbers of orientation directions are optimized for accuracy enhancement of the calculation.

- (viii) A comparative analysis is performed for the computed and experimental results at the three characterizing wavelengths of 543.5, 594.5 and 632.8 nm, to establish the efficiency of the modelling approach.

3.1 Computational dust models

Based on the shapes suggested by Zubko *et al.* (2007) and Nousiainen & Muinonen (2007), six random irregular Gaussian geometries are designed. The aspect ratios for all the shapes are fixed between 2 and 3. These geometries are provided in Figures 1 and 2. The geometries (or targets) are created with Blender 3D (2.7b)—a volumetric geometry design software freely accessible at Blender.org. These generated 3D targets are then converted to dipole arrays in the DDSCAT Convert open source tool available in nanohub.org (Feser & Sobh 2013). After conversion of these shapes into dipole arrays, the 3D-rendered representation is realized by using open source software 'Paraview'. These 3D volumetric targets are then directly incorporated into the DDSCAT code for carrying out the computations. The distance between two adjacent dipoles are kept flexible so as to fit in the target geometries of different shapes and sizes, as generated in the models, with uniform distribution while populating the whole target in the form of arrays. The number of dipoles used for the two models

Table 1. Percentage composition of graphite and fayalite particles for Model 1 and Model 2.

	Graphite (%)	Fayalite (%)
Model 1	50	50
Model 2	10	90
	30	70
	60	40
	90	10

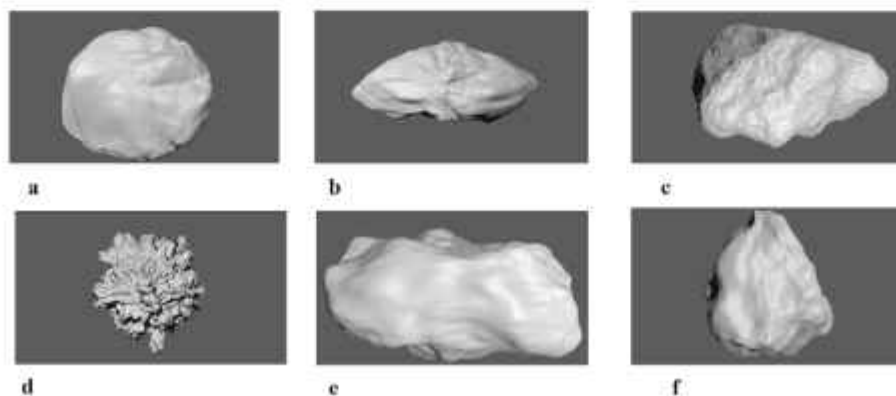


Figure 1. (a–f) Shows the blender representation of the target shapes: shape 1, shape 2, shape 3, shape 4, shape 5 and shape 6, respectively, used in DDA computations.

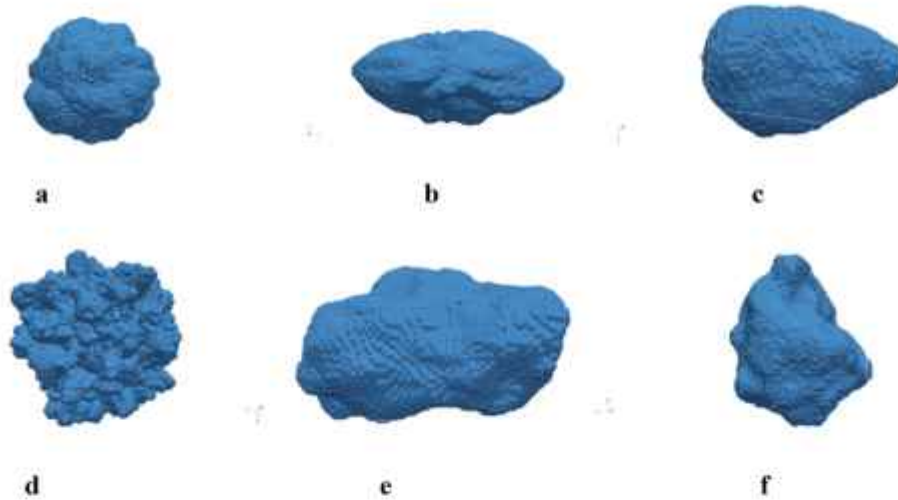


Figure 2. (a–f) 3d-rendered dipole representation of the modelled shapes using Paraview.

are fixed at 50 and 100 k, respectively. The detailed geometry design processes are described elsewhere (Boruah *et al.* 2016, 2017). However, the sequence of steps involved in these processes, including the modelling of shapes using Blender 3D, conversion of the modelled shapes to dipole arrays suitable for DDSCAT input file, use of Paraview to generate 3d-rendered dipole representation of the modelled shapes and DDSCAT calculation, have been explained in detail in ‘Appendix A’.

In this work, two models, Model 1 and Model 2 (Table 1) are employed to reproduce the experimental results acquired with interstellar dust analogue samples by using a number of parameters as variables in the DDA computations. In the later part of this study, it is proved that the employed modelling variables affect significantly the scattering properties of astrophysical dust particles, by using a comparative analysis between the two models at three visible laser wavelengths 543.5, 594.5 and 632.5 nm. The physical properties used in the models are percentage elemental composition of graphite and fayalite, irregular shapes, particle size distribution and refractive indices at the respective laser wavelengths. Among these parameters, the alignment of dust particles is most difficult to consider, while modelling. We have considered orientation averaging of the target to minimize the errors in the calculation of scattering matrix elements that may occur due to random errors. Orientational averaging of target samples is an important part of DDA computations. Several research groups have shown the minimum number of directions for random orientation averaging, ranging from 27 to 1000 to achieve

reasonable accuracies depending on the size parameter and wavelength employed for investigation (Gupta *et al.* 2016; Sen *et al.* 2017). Moreover, it is observed that for size parameter <40 and refractive index >1.3 , around 100 orientation directions provide reasonable computational accuracy (Kustova *et al.* 2020). In this work, all possible measures are taken to ensure higher accuracies in the calculations of orientation directions.

The measurements are performed in accordance with the random orientation conditions i.e., the measurements are performed over a long duration of time and the system is assumed to be ergodic. When these conditions are satisfied, the averaging over random orientations can be performed where time averaging can be replaced by ensemble averaging over orientation directions (Mishchenko *et al.* 2006; Mishchenko & Yurkin 2017).

On the other hand, the scattering system is defined by two coordinate systems: laboratory frame and target frame. Any one is dynamic with respect to the other with a common origin. This is another important condition for random orientation averaging (Mishchenko *et al.* 2006, 2014; Mishchenko & Yurkin 2017). In DDSCAT, the laboratory frame is defined in such a way that the incident beam propagates in the $+x$ direction. And the target is specified by two orthogonal unit vectors \hat{a}_1 and \hat{a}_2 assumed to be frozen in the target. The resultant target frame can be defined by using three-unit vectors \hat{a}_1 , \hat{a}_2 and \hat{a}_3 , where $\hat{a}_3 = \hat{a}_1 \times \hat{a}_2$. Further, three angles are used to represent the target orientations, which are θ , ϕ and β . θ and ϕ represent the direction of \hat{a}_1 relative to incident beam, while β represents the rotation of target around \hat{a}_1 axis.

For randomly oriented targets, the scattering matrix elements can be measured as (Draine & Flatau 2013):

$$\langle F \rangle = \frac{1}{8\pi^2} \int_0^{2\pi} d\beta \int_{-1}^1 d \cos \theta \int_0^{2\pi} d\phi F(\beta, \theta, \phi). \quad (3)$$

Now the random orientational averaging is achieved by running β and ϕ from 0° to 360° and θ from 0° to 180° (Feser & Sobh 2013). Notably, in order to achieve complete random orientation, a large number of orientation directions must be used in the DDA computations (Nousiainen *et al.* 2009; Zubko *et al.* 2013). However, due to the limited computational resources available, the number of orientations are restricted to lower values. Notably, the primary aim of this particular work is to study the combined effect of change in modelling variables on the scattering properties of dust particles.

The percentage elemental composition considered for Model 1 and Model 2 are provided in Table 1. In Model 1, the size distribution of the analogue mixture is considered to be ranging from 0.3 to 5 μm , whereas the six shapes, as provided in Figures 1 and 2, are used to represent shape dispersion. The parameters, e.g., complex refractive index, wavelength, size distribution and shapes, are kept fixed and the values assigned to the physical variables of Model 1 are percentage composition of the elements: 1:1 (50% graphite + 50% fayalite), number of dipoles: 50 K and orientation directions: 125. These values are same for all the three wavelengths 543.5, 594.5 and 632.8 nm employed in the simulation. After setting values to all the modelling variables, the computations are performed using DDSCAT 7.3.0.

In case of Model 2, the number of dipoles and number of orientation directions are increased. Moreover, the percentage compositions of graphite and fayalite are varied, while keeping the size distribution and shape dispersion same as that of Model 1. In Model 2, four elemental compositions ratios, 1:9, 3:7, 3:2, 9:1, of graphite and fayalite are used to compare with the experimental results. The number of dipoles and orientation directions are considered to be 100k and 180, respectively. The calculated scattering parameters are averaged over directions, shape, size distributions for the mixture. Finally, the values are averaged over the elemental percentage composition of graphite and fayalite. While the orientation averaging is done in the DDA code itself, the averaging over shapes, compositions and sizes are performed in an indigenously developed post-processing tool

developed in MATLAB platform. It uses DDA generated scattering parameter values to carry out automatic averaging over the user-defined ranges of shapes, compositions and sizes.

3.2 Restrictions in modelling

As is known, the efficiency and accuracy of calculating scattering efficiencies and parameters in DDA require the so called $|m|kd$ condition to be satisfied (Draine & Flatau 1994):

$$|m|kd \leq 1, \quad (4)$$

where m is the refractive index, k being the wave vector and d the number of dipoles. Typically, in computations involving interstellar dust analogues or atmospheric aerosols, the particle sizes ranging from 100 nm to about 100 μm are considered (Mathis *et al.* 1977; Pagani *et al.* 2010). In some cases, forsterite olivine particles of sizes <100 nm were also observed (Messenger *et al.* 2005). In our case, the maximum particle sizes are about 5 μm for both the samples. While the particle cut off size must be around 1 μm for the $|m|kd$ condition (in visible range), but it can be extended beyond that value (Vilaplana *et al.* 2006). It is possible to cut off the calculation at 1 μm accounting for major features of the size distribution, but in this case, the refractive index values especially the imaginary part is crucial provided the shape is fixed (Vilaplana *et al.* 2011). To consider the whole size range for the analogue samples, we have to calculate beyond this range, avoiding the condition at the cost of some computational accuracy. The considered size distribution of the particle corresponds to particles with large size parameters. Table 2 provides the particle sizes for each of the wavelengths up to which the $|m|kd$ criterion is fulfilled. Figure 3 shows the plot of $|m|kd$ values as a function of particle sizes to demonstrate the validity of computations (Vaidya & Gupta 1997; Gupta *et al.* 2016).

4. Experimental setup

An experimental setup was developed in the laboratory to measure light-scattering properties of particulate matter. It consists of a laser, a flexible particle sprayer system, photodetector and data acquisition system. The setup can measure $F_{11}(\theta)$ and $-F_{12}(\theta)/F_{11}(\theta)$, over the scattering angle range from 10° to 170° in steps of 5° . It uses three lasers of

wavelengths 543.5, 594.5 and 632.8 nm alternately according to the requirement of the experiment. A data acquisition system (National Instruments, model:

Table 2. Maximum particle sizes at which the $|m|kd \leq 1$ condition is satisfied.

Sample	Wavelength (nm)	Particle size at 50 K dipoles (μm)	Particle size at 100 K dipoles (μm)	$l mkd $ value	$l mkd $ value
Graphite	543.5	1	1.2	0.99	1.00
	594.5	1.1	1.3	0.99	0.99
	632.8	1.2	1.5	1.00	0.99
Fayalite	543.5	1.3	1.6	1.00	1.00
	594.5	1.4	1.6	0.99	0.99
	632.8	1.5	1.8	0.99	0.99

NI USB 6008) is used to collect and save the acquired results in a PC. A photodiode is used to detect the scattered visible light signals, which can be rotated through an angular range of 0–180° and vice versa using a stepper motor-based mechanism. The photodetector was capable of rotating in the scattering plane using a stepper motor-based rotor system. The light scattered from the samples was allowed to pass through a set of collection optics comprising of appropriate analysers and were detected by the photodetector. The amplified signals were fed to the data acquisition system (DAQ NI USB-6008) which was interfaced to the PC through the USB port for data storing and analysis.

A schematic diagram of the setup is shown in Figure 4. Further details of the setup are given in previous publications (Boruah *et al.* 2016, 2017). Due to technical difficulty in the setup, it is only possible to measure the scattered intensity from 10° angle in the forward scattering region. We have also excluded the

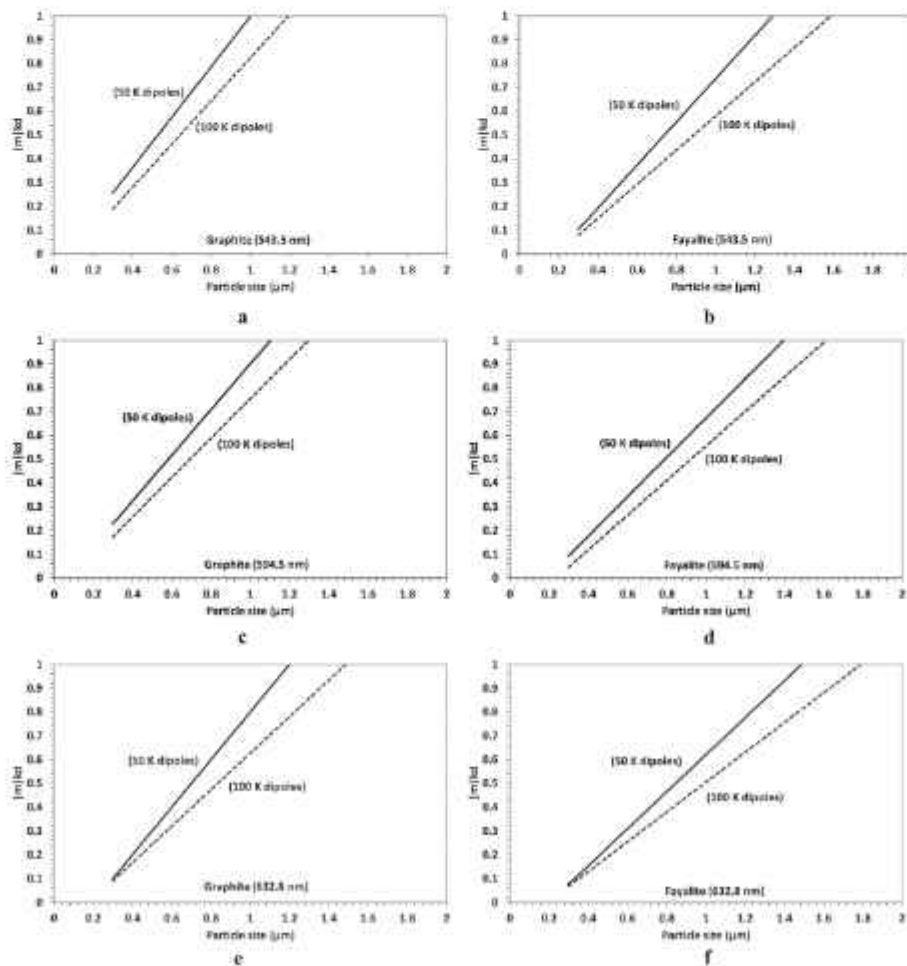


Figure 3. $l|mkd|$ as a function of particle size (a, c, e) for graphite and (b, d, f) for fayalite at 543.5, 594.5 and 632.8 nm, respectively.

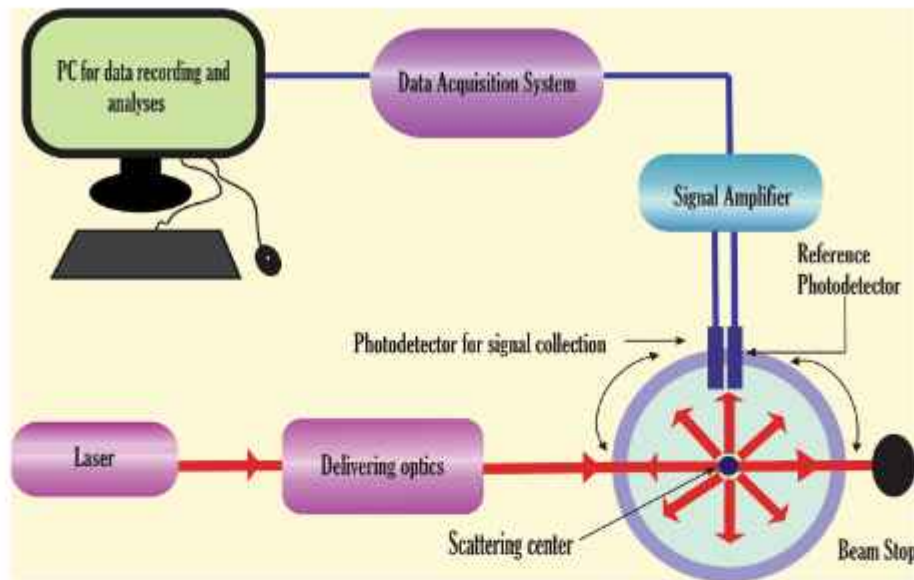


Figure 4. Light-scattering setup used in the experimental characterization.

extreme backward scattering angles beyond 170° due to similar reasons. The angular resolution or step of the motor is fixed at 5° such that each time we run the experiment, a set of 37 signals are collected by the data acquisition system.

The optical transducer system in the experimental setup consists of two highly sensitive UV–visible silicon photodiodes (S1227-16BR and BPW34) used for detecting the scattered light signals. Each of the silicon photodiodes are suitable for sensing faint light signals scattered from the target. This type of high efficiency detectors is also suitable for precision photometry with suppressed IR sensitivity. While simple OP07 (Op-amp IC with very low-input offset voltage)-based differential amplifier circuits are used for amplification of the photodiode outputs which are later fed to the DAQ. In case of the signal readout, the DAQ used in this case is NI USB-6008, which is a low-cost, multifunction DAQ I/O device. It consists of analog and digital I/O ports latched with a 32-bit counter. The advantage of the device is that it is easy to connect the terminals and make a compact construction. It is also fitted with advanced NI-DAQmx drivers and NI SignalExpress LE for direct data collection without any need for software triggers and synchronization. The final data is shown in the form of a visual graph on the screen and can be saved in the form of a file. The maximum sample rate or acquisition time of the NI USB-6008 is 10 KS/s (10 kilo samples per second), which is adjustable.

For calibration purpose, intensity of all the three lasers were measured at a distance of 250 mm

(scattering centre) from the source and a micro positioner was used for the adjustments.

The calibration process starts with alignment of the various active optical components in the setup namely lasers, photodiodes, polarizers, analysers, filters and collimators. These components of the setup are mounted on special flexible tables fitted with adjustable screws and lab jacks. By using highly directional test beams from the laser diodes, the alignments of the elements are individually checked and adjusted by levelling micrometer screws. The detector rotation axis and the laser beam direction are aligned by putting a temporarily black screen oriented in the axis position in the scattering plane.

For controlling the uncertainties in measurement and minimizing the experimental errors, following procedures have been adopted: it is well known that light-scattering measurements depend on the scattering volume, detector angles and laser beam width along with the scattering properties and scattering angles. It is practically very easy to understand that during a scattering event, as the detector rotates on the scattering plane, the scattering volume as viewed by the detector as well as the detectable signal intensity vary. These values are different for different positions of the detector on the scattering plane. Therefore, it is convenient to multiply the entire detected intensities at all scattering angles by a factor $\sin \theta$ to ensure a constant scattering volume for all detector viewing positions.

The next step is the correction for background noise and stray signals contributed by dust particles

contaminating the scattering volume. A high-power suction pump is used to force out dust particles that may be present in the scattering chamber. This significantly reduces the intensity of background or dark signals.

The background signals are first measured by allowing the laser beam to pass through the scattering volume without any scattering particle. These signals are then subtracted from the results acquired with the scatterer.

$$\text{Data}_{(\text{Corrected})} = \text{Data}_{(\text{Scatterer})} - \text{Data}_{(\text{Background})}. \quad (5)$$

A nebulizer or particle sprayer is used to spray the sample directly into the scattering volume in a controlled way. To ensure the accuracy of the experimental data, a number of repetitions (about 100) have been done for each of the data sets (Gogoi *et al.* 2009). The nebulizer used in the setup is capable of spraying dry particles. The aerosol sprayer as shown in Figure 5, for producing a flow of particulate matter sample consists of a simple electric roller (R), a mechanical piston (P), sample holder (T), flow tube (B), nozzle (N) and a high-tension spring coil (S). A metallic frame (H) provides mechanical support to the whole system. The powder sample is kept in the reservoir (a glass cuvette of 10 mm diameter) for an entire scattering experiment. When the sample holder is full, the piston is pushed backwards with a force and

is held by a high-tension spring coil fitted to a mechanical support. A small amount of sample is carried over by a specially designed electric roller into the socket. An electric dc motor (12 V) is used to rotate the roller at variable speeds. Once the roller takes away a reasonable amount of powder, the piston is pushed forward along with the sample. While in the downward motion, the roller socket feeds the sample into an air stream in the flow tube (B). The flow tube is a glass tube of 10 cm in length and 15 mm in diameter. Once the sample reaches the bottom end of the tube as aerosol particles, they are allowed to pass through a nozzle (N) such that a fine jet stream of particles can be formed. The particles are carried away under force by a vacuum suction pump to ensure minimum dust contamination. Finally, the aerosol jet comes within the scattering volume in the path of the laser beam. There is an arrangement (metallic tray) to collect the samples at the bottom of the sprayer system so that the sample can be reused.

To ensure minimal particle aggregation during the aerosol flow, the vacuum suction pump is always kept at the maximum possible force to provide minimum time to particles in the jet stream to form aggregates. Also, to ensure the quality of the particle to be intact during the nebulization process, we have adopted the approach suggested by Hovenier *et al.* (2003). A graphite tape was held at the jet stream for a very small time and scanning electron microscopy (SEM) images of the collected samples are taken. The photographic evidences show no aggregation of the particles (Figure 6).

Further, the instrumental errors are calculated by conducting 100 sets of experiments with water droplets of radius 0.5–5 μm. As measured from the data sets, it is found to be ±0.194 in arbitrary units. The instrumental errors are plotted as error bars in the experimental plots of all the comparative analyses.

Considering all the complexities involving the experimental procedure including the samples and their probability distribution in the scattering volume, instrumental errors and presence of dust, etc., a better match with computational model is impossible to acquire in our case. However, instead of all the limitations and drawbacks, proper techniques have been adopted to minimize the discrepancies occurring in both theoretical and experimental data.

The experimental setup is validated by performing measurements for spherical water droplets and comparing the results with standard Mie computations. The theoretical calculations are done using the software TUSCAT which is based on Mie theory and

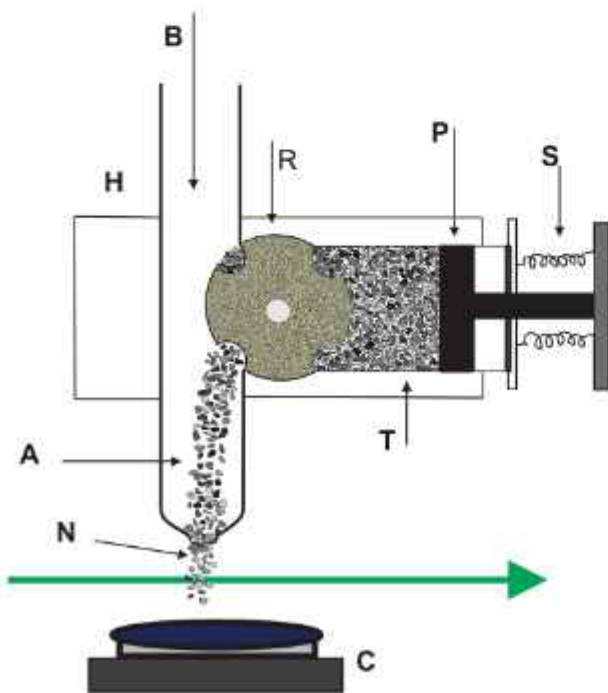


Figure 5. Schematic diagram of the aerosol sprayer system.

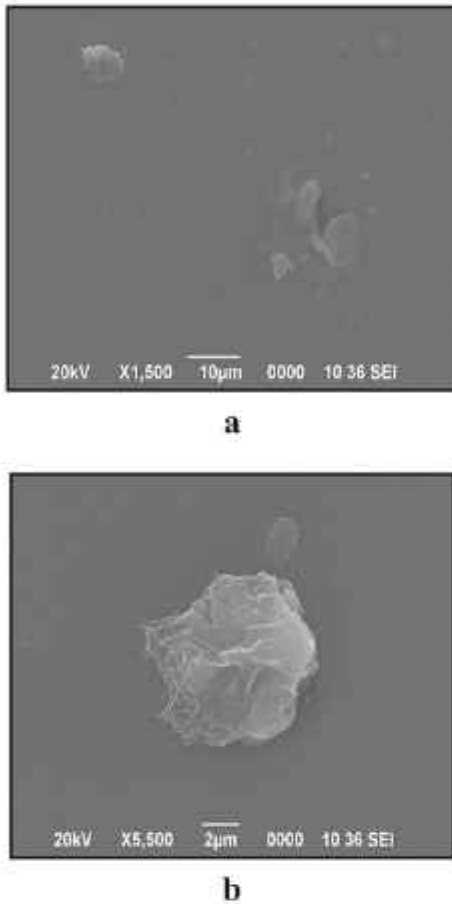


Figure 6. (a and b) SEM images of collected nebulized particles.

Table 3. Particle size distribution of water droplets.

Size distribution	lognormal
Minimum particle radius	0.5 μm
Maximum particle radius	5.0 μm
Modal radius (r_m)	2.0 μm
Standard deviation (σ_r)	1

T-Matrix approach (Gogoi *et al.* 2011). Table 3 provides the properties of water droplets used in the calculations.

The comparative plots of theoretical and experimental phase function and polarization for water droplets are provided in Figure 7.

It is observed from the comparative analyses that the experimental plots are almost identical in terms of overall shapes and major features with the computational results for both phase function and degree of linear polarization. As Mie theory provides exact solutions to spherical problems, the closeness of

theoretical and experimental plots is sufficient to validate the experimental measurements.

5. Graphite and fayalite samples

5.1 SEM and size distribution analyses

The graphite samples are collected from Sigma Aldrich, while the fayalite microparticles (Fe_2SiO_4) are synthesized in the laboratory using a chemical route as suggested by De Angelis *et al.* (2012). In the nebulizer (fitted in the setup), the fayalite and graphite microparticles are mixed in a 1:1 ratio. But after the samples are sprayed into the scattering volume, due to the probability distribution effects, this ratio will not remain same during a particular scattering event. The inefficiency of Model 1 in interpreting the experimental results may be a result of this effect. The SEM analyses reveal the highly irregular shapes of both graphite and fayalite samples. It also provides visual evidences of the particle size distribution and surface roughness. The SEM images are then used to model the shapes used in the computation. It is not possible to consider each and every shape, considering the high irregularity and dispersion in both shape and sizes. Therefore, it is reasonable to select a few shapes of interest which is supposed to resemble majority of the sample in both cases. The particle size distribution used in our computations is a lognormal function with modal radius $r_m = 1 \mu\text{m}$, size ranges $r = 0.3\text{--}5 \mu\text{m}$, and standard deviation $\sigma = 2.0$ (Heintzenberg 1994):

$$\frac{dn}{d \ln(r)} = \frac{N_d}{\sqrt{2\pi} \ln \sigma} \exp \left[-\frac{(\ln r - \ln r_m)^2}{2(\ln \sigma)^2} \right], \quad (6)$$

where N is the number of particles with modal radius r_m .

The SEM images of the highly irregular graphite and fayalite particles reveal that the samples are distributed over a wide size range (Figure 8a and b). It is possible to calculate an approximate size distribution range from the visual evidences or high-resolution images. A lognormal fit (Figure 8c) is used to represent the calculated size distribution which is relatively accurate enough considering the extremely complex mixture of both samples used in the laboratory simulation. It includes almost all the major size groups present in the distribution to provide an efficient representation for theoretical calculations.

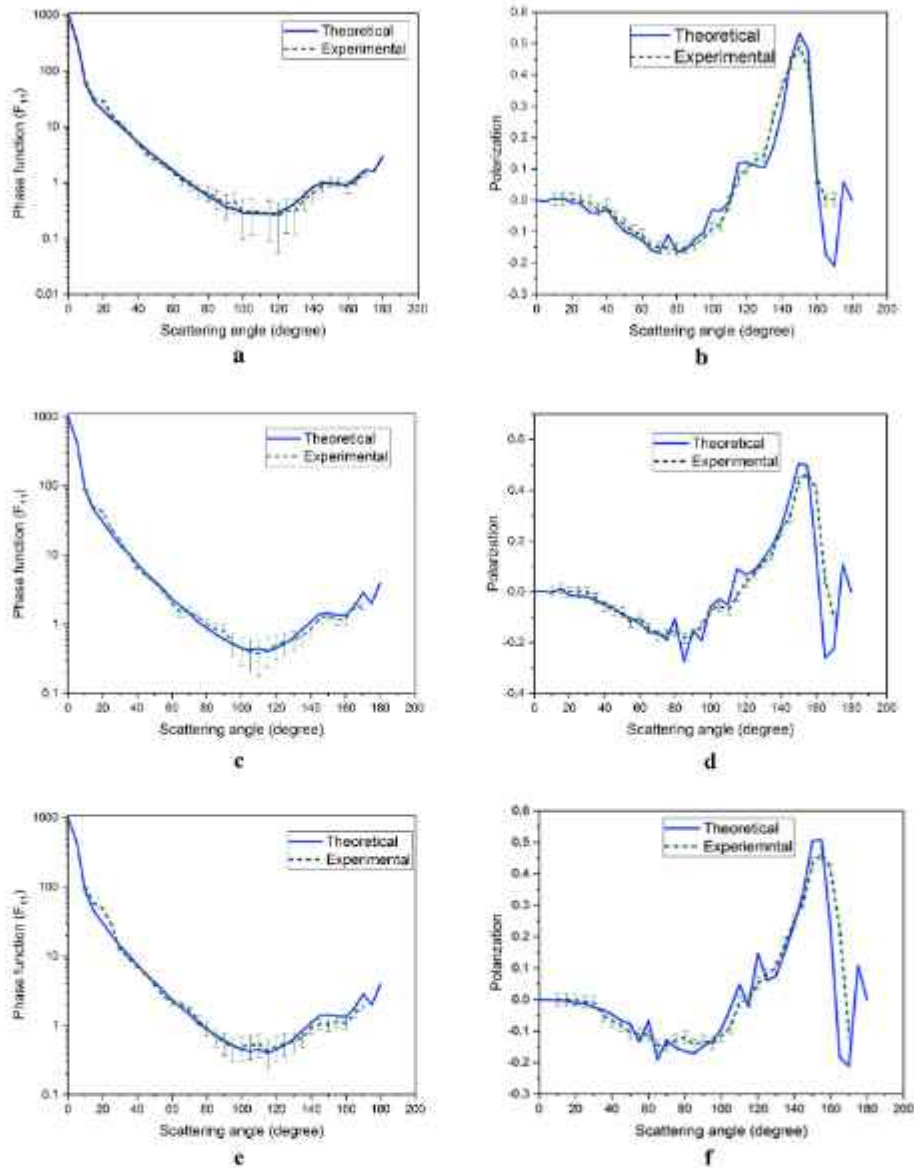


Figure 7. The comparative phase function and polarization for water droplets are shown in the left and right panels, respectively, for: (a and b) 543.5; (c and d) 594.5 and (e and f) 632.8 nm laser wavelengths, with symbols in the legends representing computational and experimental values (plotted with error bars).

The size distributions are calculated statistically from a large number of SEM images. For applicability in simulation, the overall size distribution of the mixture is considered to represent the models. It is evident that the individual size distributions of both the samples, graphite and fayalite, are slightly different. But the range of particle size distribution 0.3–5 μm , fit quite well with the real mixture considering the fact that an aerosol nebulizer is used to directly spray the particles into the laser beam. Also, the lognormal size distribution considered here is quite an accurate representative of the aerosol sprayer output. The main reason behind using a

single size distribution for both the samples is to reduce the computational complexities. We intended to use a fixed size distribution to measure the scattering properties of all the target shapes for both samples as the number of variables employed in the models are already large. Using different size distributions for both samples in the mixture will make the interpretation of computational results extremely difficult. It is evident that due to highly irregular shapes of the real dust analogues, the particle size distribution retrieval from the SEM image is a difficult process. However, an approximation must be introduced in order to simplify the

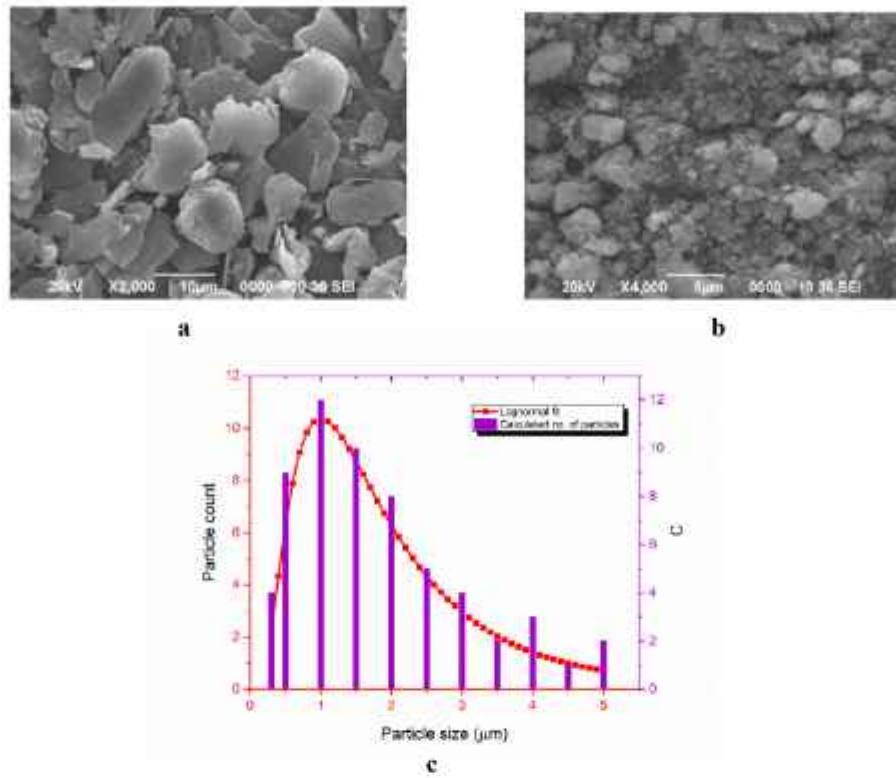


Figure 8. Scanning electron micrograph (SEM) images of (a) graphite, (b) fayalite and (c) particle size distribution (lognormal distribution function).

problem to some extent to fit in a particular size distribution employed in numerical simulation. Nonetheless, it is near impossible to consider each of the measured size from a distribution of non-spherical particles.

First, the particle surface area is measured using the maximum length of the irregular particle as reference with the surface equivalent radius. This radius is used as the effective size of the particulate sample to carry out the computations. As it is not possible to directly measure the surface of a highly irregular particle, it requires to assume the particle to be in the form of either a cuboid or a prolate ellipsoid. For this purpose, the surface equivalent radius is employed which can be defined as below.

Surface equivalent sphere radius (r_s): surface equivalent radius of a particle is the radius of a sphere with the same surface area as that of the particle.

Surface equivalent radius can be written as:

$$r_s = \left(\frac{3S_{\text{particle}}}{2\pi} \right)^{1/2}. \quad (7)$$

The refractive indices of graphite are used as provided by Draine & Lee (1984), while for fayalite, these values are obtained from Fabian *et al.* (2001)

Table 4. Refractive indices values of graphite and fayalite.

Sample	Wavelength (nm)	Real part of refractive index (n)	Imaginary part of refractive index (k)
Graphite	543.5	2.73	1.560
	594.5	2.77	1.593
	632.8	2.80	1.628
Fayalite	543.5	1.844	0.00087
	594.5	1.846	0.00108
	632.8	1.896	0.00144

and database of optical constants (<http://www.astro.uni-jena.de>). The values are tabulated in Table 4.

5.2 Size averaging of the scattering parameters

To compute the scattering parameters and perform the integration over sizes, the DDSCAT calculations are run for each of the sizes individually. Then, the computed values scattering matrix elements are averaged over sizes (in this case, a lognormal size distribution is considered). In order to simulate the properties of dust analogue samples, aided by laboratory experiments, a

post-processing MATLAB® code was developed which can compute the scattering parameters and efficiencies for a shape- and size-dispersed target. This code takes the files generated by DDSCAT for each size and performs the size averaging for the target sample. The same code can be used to carry out the averaging over the shapes with slight modification. The averaging for particle aggregates involves consideration of light scattering from a volume element with a number of particles, in order to model realistic particle systems since isolated single particle scattering parameters are not sufficient to explain the observed interstellar extinction as well as laboratory measurements. The MATLAB® post-processing tool that incorporates normal, lognormal and gamma size-distribution functions, are used to generate size and shape averaged plots of Mueller matrix elements. The sample MATLAB® code for calculating size averaged scattering parameters is provided in ‘Appendix B’.

6. DDA computations and comparative analyses for Model 1 and Model 2

The developed dust models Model 1 and Model 2 are used to calculate the light-scattering parameters phase function (F_{11}) and polarization ($-F_{12}/F_{11}$) along with the scattering efficiency (Q_{Sca}), extinction efficiency (Q_{Ext}), single scattering albedo (a) and asymmetry parameter (g). A comparative analysis with experimental F_{11} and $-F_{12}/F_{11}$ is performed to study the effects of physical variables in dust modelling and also to validate the models.

6.1 Analyses using Model 1

The modelling variables used for Model 1 are provided in Table 5.

6.1.1 Theoretically computed values of scattering efficiency, extinction efficiency, single scattering albedo and asymmetry parameter The computed values of scattering efficiency (Q_{Sca}), extinction efficiency (Q_{Ext}), single scattering albedo (a) and asymmetry parameter (g) are shown in Figure 9 along with findings and explanations. It is observed that the scattering and extinction efficiencies, single scattering albedo values are higher for fayalite, while the asymmetry parameter values are lower than that of graphite (Figure 9). The curves follow a similar pattern, with no observable differences in values for

Table 5. The modelling variables for computational Model 1.

Wavelength (nm)	No. of dipoles (k)	No. of scattering directions for $\langle \cos \theta \rangle$	No. of random orientations
543.5	50	144,148	125
594.5	50	124,985	125
632.8	50	113,121	125

the narrow range of wavelengths we have considered. Only a small discrepancy is observed in the extinction efficiency of fayalite between 543.5 and 594.5 nm wavelengths, which resulted in a peculiar curve for the single scattering albedo in the dust model calculations.

6.1.2 Experimental and theoretical comparison of F_{11} and $-F_{12}/F_{11}$ The comparative analyses are done to fit the theoretical and experimental values of the scattering parameters using the size- and shape-averaged computed results (Figure 10a–f). From the plots, it is observed that almost in all the cases, the normalized computational values are slightly higher than experimental ones at the three used wavelengths. As revealed later, it is because of the overestimation of scattering parameters in the theoretical model calculations. It may be due to the compositional imbalance between highly absorbing graphite particles as compared to fayalite samples with lower values of imaginary refractive index. The phase function (F_{11}) values are found to be closer in case of 632.8 nm wavelengths compared to other wavelengths. But polarization ($-F_{12}/F_{11}$) is found to be similar for all the wavelengths as revealed by the error analyses, with slightly lower values of rms errors for 543.5 nm wavelength. It indicates that polarization is a less sensitive function to small changes in wavelength but it is a relatively stronger function of particle sizes. A few negative values of polarization are also observed in the experimental results at higher scattering angles around 140–160° at all the wavelengths, not found in the theoretical calculations. However, such negative polarization values are observed in case of cometary dust in several occasions (Petrova *et al.* 2000; Kimura *et al.* 2006; Hadamcik *et al.* 2007).

Phase function values depend on the characterizing wavelengths and its closeness to the particle sizes along with averaging over shapes. As the incident radiation approaches particle sizes, the accuracy and efficiency of the modelling approach become more reasonable. The dominant parameter influencing the calculated values must be the particle size distribution

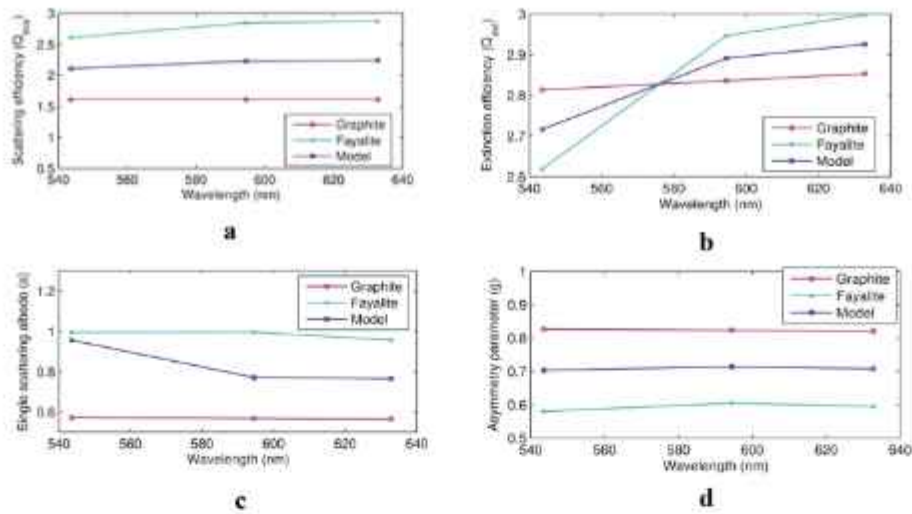


Figure 9. The computed values of (a) scattering efficiency, (b) extinction efficiency, (c) single scattering albedo and (d) asymmetry parameter vs. incident wavelengths for Model I.

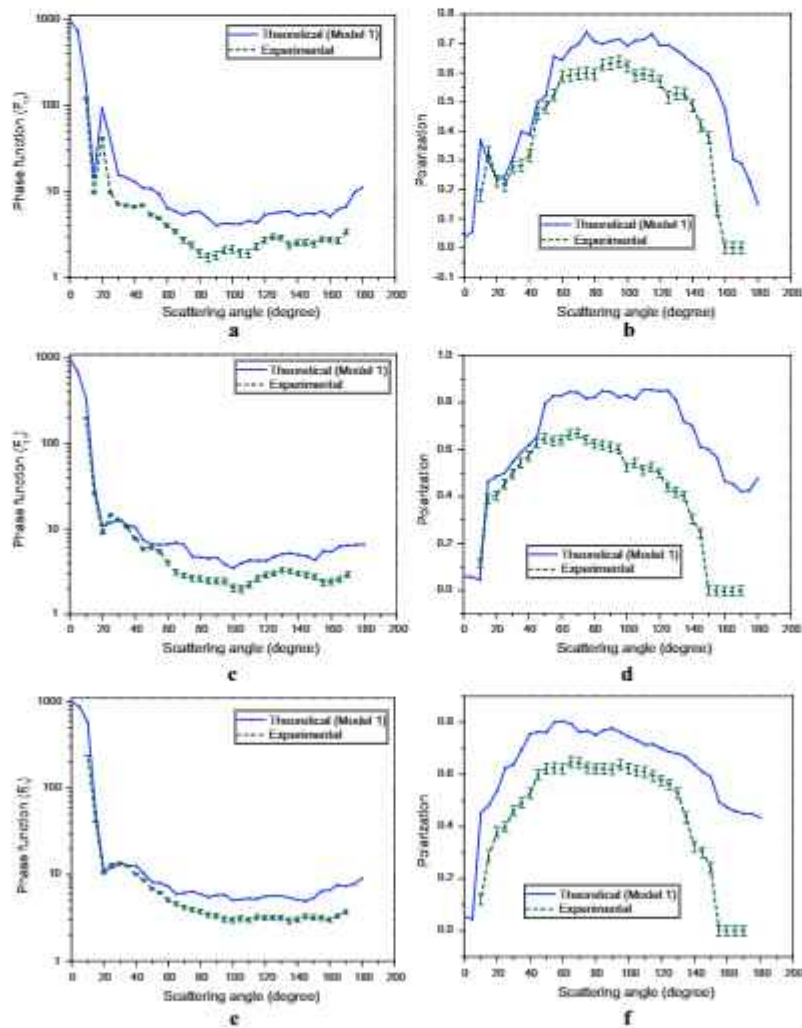


Figure 10. Theoretical (Model I) and experimental phase function and polarization values at incident wavelengths (a,b) 543.5 nm, (c,d) 594.5 nm and (e,f) 632.8 nm, respectively. Experimental curves are plotted with error bars

and its comparability to the incident wavelengths. The number of dipoles considered is another important factor in achieving accuracy and closeness to experimental results. The errors are a combined result of discrepancies in approximating number of directions considered for orientational averaging and compositional assumptions of graphite and silicates. And also, the errors are seen to be sensitive to slight changes in wavelength in case of phase function. The lesser number of peaks and dips contributing to oscillations in both the theoretical and experimental curves is a result of the extensive shape and size averaging performed to simulate realistic dust. The number of oscillations significantly reduces towards the higher wavelength side in the theoretical calculation for both the scattering parameter as seen in Figure 10a–f.

6.2 Analyses using Model 2

Modelling variables used in Model 2 are tabulated in Table 6.

Table 6. The modelling variables for computational Model 2.

Wavelength (nm)	No. of dipoles (K)	No. of scattering directions for $\langle \cos \theta \rangle$	No. of random orientations
543.5	100	144,148	180
594.5	100	124,985	180
632.8	100	113,121	180

In this model, we have changed the values of physical variables to achieve closeness to the experimental results as much as possible, considering the theoretical limitations in terms of high computational requirements.

The comparative analyses plots are shown in Figures 11–13 along with interpretations and important findings.

6.2.1 Theoretically computed values of scattering efficiency, extinction efficiency, single scattering albedo and asymmetry parameter The scattering and extinction efficiencies, single scattering albedos show similar pattern as Model 1, with slight changes in the values. But no observable differences between the curves are found other than the small variations in the single scattering albedo. The wavelength range considered is too narrow to differentiate between the computational results of these four parameters (Figure 11). But the asymmetry parameter (g) plays an important role in the calculation of the Henyey–Greenstein phase function, which can be used to validate modelling approach for spherical particles.

6.2.2 Theoretically calculated scattering efficiency (Q_{Sca}) vs. size parameter (X) values The computed values of scattering efficiency (Q_{Sca}) vs. size parameter (X) value are plotted for the final Model 2 at each wavelength for all the six shapes considering the refractive index to be fixed (Figure 12). The Q_{Sca} values are very important to determine the influence of size averaging on the calculated scattering matrix elements (Vilaplana *et al.* 2011). Particularly, the

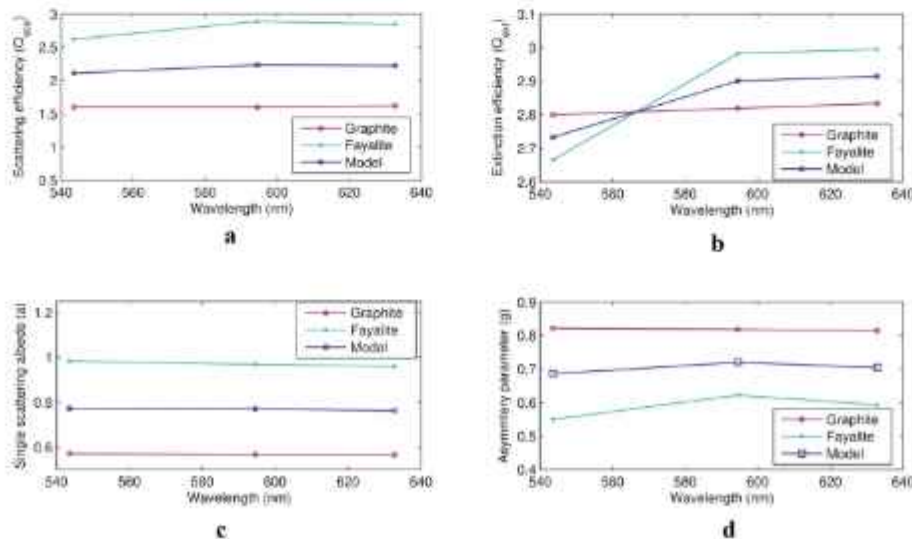


Figure 11. The computed values of (a) scattering efficiency, (b) extinction efficiency, (c) single scattering albedo and (d) asymmetry parameter vs. incident wavelength, for Model 2.

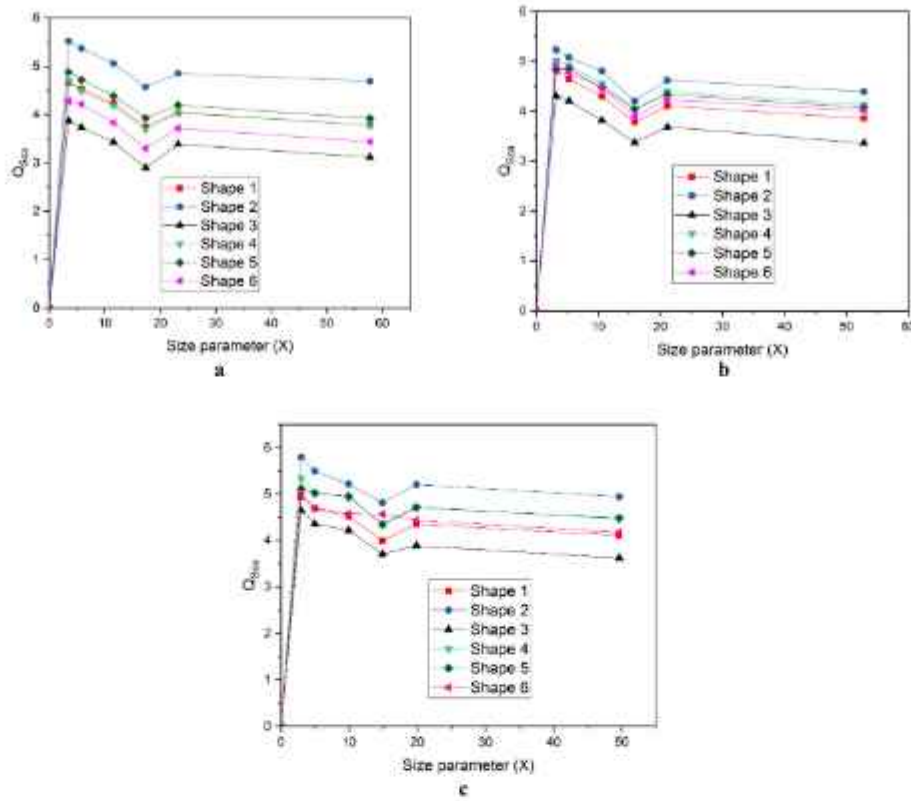


Figure 12. Theoretically calculated scattering efficiency (Q_{Sca}) vs. size parameter at (a) 543.5, (b) 594.5 and (c) 632.8 nm wavelengths, respectively.

shapes of these curves are crucial for proper interpretation of the computational results because it is necessary to cut off the calculations at some maximum particle size values to satisfy the $|m|kd$ condition and minimize errors. These plots (Figure 12a–c) show that the major oscillations including the 1st maxima of the curve are concentrated within a typical moderate size parameters range. While the curves are almost flat towards very large size parameters without any significant features extended up to 5 μm . It is evident that including sizes up to around 2 μm could still provide a quite accurate representation of the laboratory samples. This behaviour is almost comparable to a geometric optic regime where all small features of the size distribution are accounted for the computational curves (Vilaplana *et al.* 2011). Moreover, the strong shape dependence of the size-averaged Q_{Sca} curves is evident from the study where each shape produces a distinct pattern for easily distinguishable from the others. But as the wavelength increases, the curves move closer to each other with very narrow differences in their values. The aspect ratios also play a vital role in determining the Q_{Sca} values for fixed shapes with the maximum being

observed for shape 2 (maximum aspect ratio) and minimum for shape 3, while the near spherical irregular shapes attain closer intermediate values.

6.2.3 Experimental and theoretical comparison of F_{11} and $-F_{12}/F_{11}$ The size- and shape-averaged values of the theoretical scattering parameters are used to reproduce experimental results. The values for Model 1 are plotted alongside Model 2 to compare the changes after modification in the physical variables. It is found that the computational parameters are closer to the averaged values of experimentally measured F_{11} and $-F_{12}/F_{11}$ (Figure 13) in case of Model 2. We have calculated the rms error values averaged over the scattering angle θ for both the models which show significant reduction of discrepancies between theoretical and measured values in case of Model 2, provided in Table 7.

The root mean square error can be calculated using the simple formula:

$$\text{Error}_{\text{rms}} = \sqrt{\frac{\sum_{i=1}^N (T - E)^2}{N}}, \quad (8)$$

where T and E are theoretical and experimental values and N the total number of data points. At first, we have

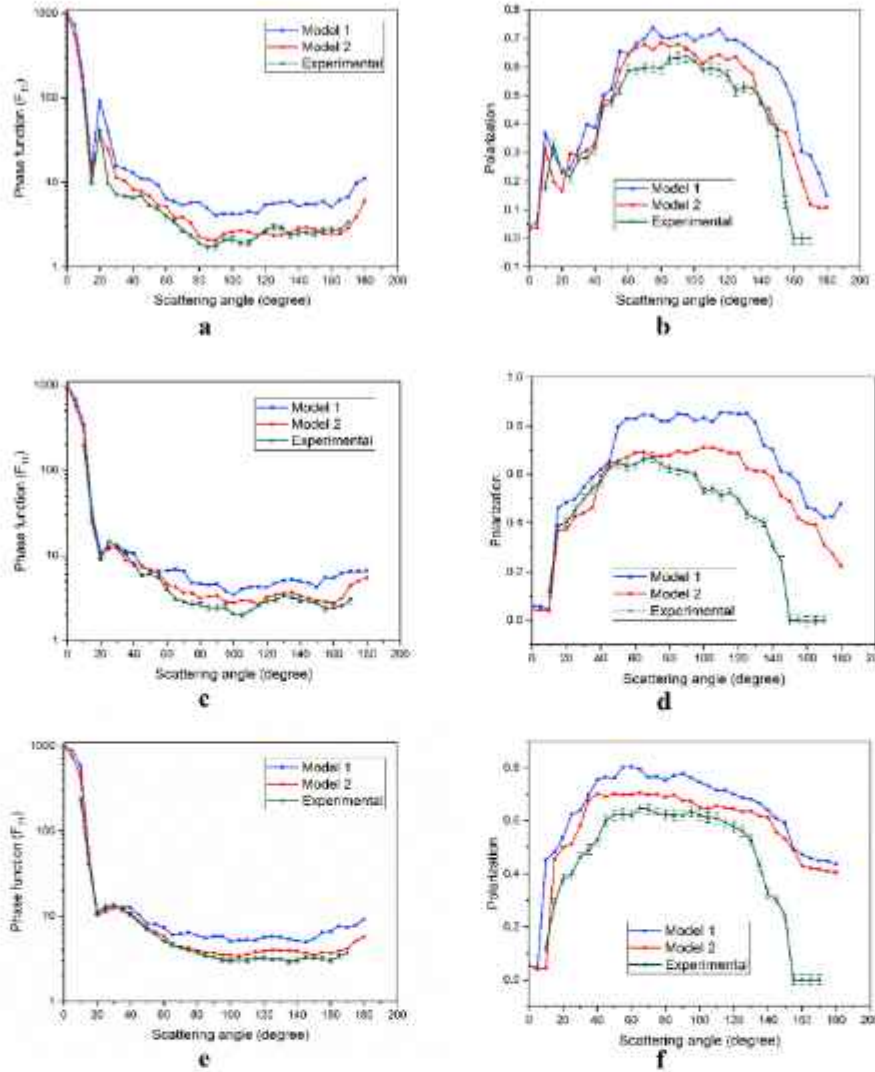


Figure 13. Theoretical and experimental phase function and polarization values at incident wavelengths (a and b) 543.5, (c and d) 594.5 and (e and f) 632.8 nm, respectively, for Model 2. Experimental curves are plotted with error bars.

Table 7. Calculated rms errors for experimental results as compared Model 1 with Model 2.

Wavelength (nm)	Phase function		Polarization	
	Model 1	Model 2	Model 1	Model 2
543.5	4.23e + 02	1.54e + 02	2.21e-01	1.47e-01
594.5	3.97e + 02	1.43e + 02	2.10e-01	1.23e-01
632.8	1.98e + 02	1.26e + 02	2.01e-01	1.19e-01

calculated the rms errors for all the scattering angles. Then, the errors are averaged over the whole scattering angle range to find out the average error per scattering angle. This has been done to simplify the comparative error analyses of the two models for all the wavelengths used.

Model 2 efficiently reproduces the experimentally acquired patterns of both the measured scattering

parameters F_{11} and $-F_{12}/F_{11}$ with higher accuracy as compared to Model 1. The F_{11} curves are found to be of typical shape. It is observed that there is a good agreement for the general curve shapes, while in the case of higher scattering angle, a few negative values of $-F_{12}/F_{11}$ appear in the experimental results, which are unaccounted for both our models. These values are mainly observed in the experimental results at higher

scattering angles around 140–160° or lower phase angles at all the wavelengths, not found in the theoretical calculations. Some parameters might be missing in the model right now which could explain the appearance of such negative features. These unaccounted peaks are previously reported a number of times in case of laboratory samples, which are common in case of cosmic and cometary dust (Petrova *et al.* 2000; Kimura *et al.* 2006; Hadamcik *et al.* 2007). It might be a result of the combined effects of complex refractive index, porosity, fluffiness and aggregation states. Some models could be found which provides reasonable explanations for occurrence of these negative branches of polarization (Zubko 2015).

We have plotted F_{11} and $-F_{12}/F_{11}$ for Model 1 and Model 2 alongside experimental measurements. In case of F_{11} , the values of Model 2 are closer to the experimental results with significant reduction in the calculated rms errors provided in Table 7. We have concluded from the comparative analyses that the first model leads to an overestimation of the scattering parameters mainly in the case of F_{11} . The values are lowered with a decrease in smaller features, peaks and dips. As a result, the curve becomes smooth as compared to Model 1, which is most obvious in the case of experimental curves of dust particles. The increase in the number of orientational averaging directions has an important effect in smoothing the computational curve making it near identical to the experimental values. The change in composition of the two constituent elements lowers the values of overestimated F_{11} as observed in the case of Model 1. This is because in the first case, the composition of the two elements are taken to be in the ratio of 1:1. As scattering efficiencies of fayalite are higher as compared to graphite, it raises the estimated values of scattering parameters. The elemental composition which produces the best results is found out to be the one in which the ratios of graphite and fayalite are 3:2 (or 60% graphite and 40% fayalite) (Table 1). The final plots provided for Model 2 are obtained with this composition of the elements. The increase in number of dipoles directly affects accuracy of the computation. It allows the $|m|kd$ condition to be satisfied up to larger values of particle size scattering parameters. The scattering parameters in our case, range from a minimum of 2.97724 to a maximum value of 57.77362. In the case of $-F_{12}/F_{11}$ for Model 2, the values still remain closer to those of Model 1, but lower values and weaker peaks ensure that it is more comparable to the relatively smoother experimental

curves with significant decrease in computational errors.

It is obvious that more the number of dipoles (100 K being the number of dipoles in the best model), the more is the accuracy in representing non-spherical shapes and surface features or structures. For more accurate and efficient simulations, larger number of dipoles should be used which requires more powerful computational resources. Our study has been performed with two sets of dipoles in order to demonstrate the enhancement of computational accuracy in the phase functions of non-spherical particles with a higher dipole number.

7. Summary

Shape modelling can be effective for polarization because of its dependence on surface irregularities and sharp edges in the scatterer. At lower scattering angles up to a value of about 25°, the values of theoretical and experimental F_{11} are found to match significantly at all the characterizing wavelengths. But deviations are observed at mid and higher scattering angles up to 170°. As in the first model, again small oscillations observed in the computational curves reduce with the increasing wavelength. A relatively smooth curve is observed for both the parameters in case of 632.8 nm wavelength as compared to 543.5 and 594.5 nm. These patterns are typical to irregularly shaped dust particles as observed for computational curves in previous studies (Yang *et al.* 2007; Mishchenko 2009). Similar patterns are also reported for experimental laboratory measurements (Volten *et al.* 2001; Dubovik *et al.* 2002; Muñoz & Hovenier 2011). This shows that as the characterizing wavelength approach the particle sizes, the random errors of computation tend to decrease significantly. One thing is clear from the comparative analyses that at higher wavelengths, the changes in modelling variables do not have a pronounced effect on the shapes of scattering parameter curves other than lowering the overestimated values. This is important in context of this paper, as it contributes in achieving closeness between the theoretical and experimental curves.

Similar works are performed by research groups to model light scattering by non-spherical aerosols using randomly oriented spheroid models (Dubovik *et al.* 2002). They employed inversion algorithms to retrieve desert dust properties from information obtained by

AERONET ground-based Sun/sky-radiometers, applicable in remote sensing studies. These studies are successful in showing the effects of non-sphericity on aerosol optical properties. Their techniques also show significant advantages over Mie-based retrieval techniques (Dubovik *et al.* 2002). Further, the retrieval of aerosol sources and their characterization have been facilitated by such modelling (Dubovik *et al.* 2002, 2008). Angular distribution of scattered light has been also employed to study the size distribution of aerosols and dusts for particle mixtures with different sizes and refractive index. Moreover, a technique to simultaneously measure the size distribution, complex refractive index and single scattering albedo has also been developed for non-spherical dust particles (Dubovik *et al.* 1995).

The shape-based variations of the calculated scattering parameters for both the models show that it affects the size-averaged values. This is critical in interpreting the results in case of experimental and astrophysical observations by differentiating between the contributions of size and shape dispersions.

As already mentioned, due to limitations in computational resources and the enormous amount of time required for calculating scattering parameters for each of the scattering directions, our computations are restricted to a lower number of orientation directions. But to avoid further errors, we have considered the whole angular range for all the three angles θ , φ and β , but with a small number of intervals in between. The inaccuracies in the $-F_{12}/F_{11}$ values at higher scattering angles near 180° (not equal to zero) could be overcome by increasing the number of orientation directions.

The averaging over shapes (considering surface roughness) tends to smooth out the theoretical curves decreasing the number of small features and oscillations as found in both the theoretical and experimental curves for F_{11} and $-F_{12}/F_{11}$. Such kinds of observations are reported in previous studies (Yang *et al.* 2007).

The principal aim of this paper is to demonstrate the combined effect of several physical properties or computational parameters on the scattering properties of dust particles and its influence on the modelling approach. Further, it is quite difficult to point out the effect of each of the variables separately in the theoretical results as several other factors (including computational and instrumental errors) may influence the comparative analysis. Nevertheless, there are some practical difficulties in the instrument itself being limited to the range of $10\text{--}170^\circ$. It is true that for particles larger than some microns, a large fraction of the light is scattered in a small region around 20° .

A study suggests that particles with size ranging from 1 to $4\ \mu\text{m}$ scatter about 18% of the total scattered light in that small region (Costello *et al.* 2007). This effect is more pronounced for single particle scattering. However, while dealing with the particle ensembling the cross-sectional area available for a light-scattering event is higher as compared to single particles (Costello *et al.* 2007). As large particles scatter more light, a significant amount of detectable signal can still be collected at relatively large scattering angles. Nonetheless, such collected light-scattering patterns are sufficient for quantitative comparative studies of phase functions and linear polarizations. Moreover, in our case, a very similar work has been successfully carried out by Volten *et al.* (2007) with similar-sized and relatively larger particles. The phase functions and polarizations are efficiently measured for an angular range of $5\text{--}174^\circ$. Hovenier *et al.* (2003) suggested a solution to overcome the limitations in measuring extremely large and small scattering angles. According to which, theoretical fits using Mie theory or geometric optics can be used to extrapolate the values of intensities for unmeasured angles. It is also observed that for randomly oriented particles, the forward scattered light is near independent of the particle shapes, while for non-spherical particles, the scattered light near 180° is flat for most of the cases. Thus, a simple extrapolation may not influence the results significantly. Nevertheless, the use of a point visibility meter in the light-scattering setup to measure angles $<5^\circ$ and near 180° is the most practical solution and is a part of our future plan (Hill *et al.* 1984; Moreno *et al.* 2002; Liu *et al.* 2003).

While comparing with the experimental results, the main conclusion that can be drawn about increasing the number dipoles is that it mainly increases the accuracy of the computed scattering matrix elements. While the increasing the number of orientation directions for averaging has a pronounced effect in smoothing out the small features (peaks and dips) in the curves. While the percentage composition of species plays the most significant role in the theoretical fits to the experimental data, while performing the computational analyses. Moreover, changes in composition mainly balance the overestimation of scattering efficiencies and subsequently, the phase function values as found out in this study with Model 2.

Although these models are not highly accurate, they could be considered reliable and efficient in reproducing the observed patterns for scattering parameters of dust mixtures with two or more constituent elements, mainly in the moderate size parameter range.

This modelling approach could explain light-scattering properties of single or mixtures of dust analogue samples with a higher degree of accuracy. However, small-scale errors are still present owing to the limitations in computational resources and also, the restriction applied by the computational technique involved. The complexity of such real dust systems makes it extremely difficult to be modelled. We have considered several parameters in the model which might affect the observed values of scattering parameters, and prove it efficient in simulating dust particles in the visible wavelength region and with moderate size parameters. Infrared wavelengths are, however, highly desirable in the experimental characterization due to the extremely large size dispersions of cosmic dust particles and could be an interesting topic for future research.

8. Conclusions and future works

An interstellar dust analogue model of graphite and fayalite is developed and studied at three incident wavelengths in the visible region. It provides a good approximation to the shape and size distribution of laboratory-synthesized realistic dust particles supposed to be present in the interstellar medium. Although the developed models are limited by the narrow size and shape ranges (owing to the computational restrictions of DDA), it is a very good demonstration of the systematic consideration and selection of particle size ranges, shapes, porosity, surface roughness and compositional ratios. The measures taken in order to achieve maximum accuracy for two dust species model distributed over both size and shape along with morphological irregularities over the particle surface are also provided. This study is also effective in separating out the effects of particle sizes and geometrical shapes on light-scattering patterns of unknown scatterers, which considerably simplifies the deconvolution process to identify the dust species from observed scattering patterns. It is also applicable to studies where the dust species are known, but the details of either size distributions or shape dispersions are required to be computed. This model can efficiently measure one of the properties provided, the other is well-predicted or known. We anticipate that this approach will be successful in interpretation of astrophysical data with the facility to incorporate all the physical parameters that can influence light-scattering patterns in a single scattering event. Importantly, the applicability of this computational approach can be extended to remote sensing of inaccessible scattering

particles, climate modelling and study of atmospheric aerosols along with extra-terrestrial dust.

At present, the experimental studies are limited to visible wavelengths, which do not allow the full utilization of the capabilities of DDA. With a view to characterize particles with large size parameters, longer or infrared wavelengths must be included (closely comparable to larger sizes) in the experimental characterization along with advanced opto-electronic transducer systems.

In addition, a number of dust species can be included, e.g., amorphous carbon, silicates (forsterite, enstatite) and PAHs, in a single dust model to make it more realistic as compared to the interstellar environments.

Appendices

Appendix A: Computational techniques

In this work, a computational technique has been developed based on the software packages mentioned below, to compute and calculate light-scattering properties of irregularly shaped aerosol and dust particles. The phase function $F_{11}(\theta)$ and degree of linear polarization $-F_{12}(\theta)/F_{11}(\theta)$ along with other scattering parameters were theoretically calculated using this technique.

The software packages are:

1. Blender 3D: Volumetric geometry design software for arbitrary shapes and materials used to model target geometries to replicate the particles employed in the experimental characterization.
2. DDSCATCONVERT: Software package to convert the volumetric random shapes (in the form of a 3D triangular mesh) to dipole arrays by assigning dipoles to each point and vertices.
3. ParaView: Software available in the public domain to realize 3D targets generated in any technique to an array of constituting points. This is used to ensure proper target generation during the conversion of developed models to dipole arrays.
4. DDSCAT: The original FORTRAN DDA code to calculate scattering efficiencies and cross-sections (scattering, absorption, polarization and extinction), asymmetry parameters, single scattering albedos and the sixteen elements of the Mueller matrix.
5. Post-processing tool: An indigenously developed code in MATLAB® platform to facilitate the automatic averaging over a wide range of shape and size distributions using the DDSCAT-generated computational calculations.



Figure A1. Graphical user interface of blender geometry generation software.

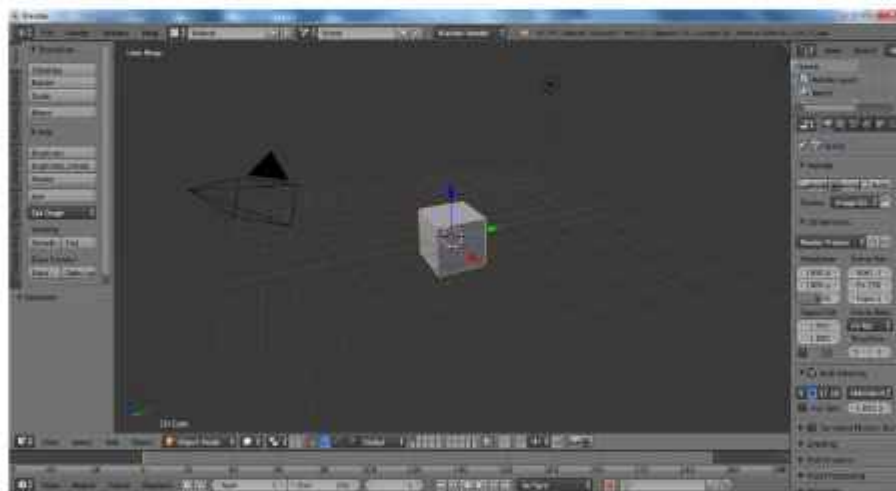


Figure A2. A primitive basis shape in blender.

Blender 3D The first step of the computational technique involves generation of targets for DDA simulation using different incident laser wavelengths. Blender is a software used to generate volumetric material targets for realistic investigation in modelling and simulation works (Figures A1 and A2). There are several advanced options provided in the software for the target generation. In one procedure, pre-defined algorithms can be used to develop random gaussian shapes. Another advantage is that targets can also be user-defined or user-modified in a manual mode. A primitive basis shape is modified using shape and

material modifiers. Smaller details of the particle shapes and surface can also be introduced by changing the positions of basis points. Also, each of the faces and vertices of the material target can be modified independently to add finer and specific details. The advantage of manual mode is that final target could be shaped into any non-spherical and highly irregular geometry. Along with the shape modifiers, other material properties like size and aspect ratio can be easily set to match the realistic particle in laboratory samples. As per the requirements of dipole conversion softwares, the generated object is arranged finally in a

triangular mesh (a specimen target is shown in Figure A3).

DDSCATConvert The second step involves conversion of the generated target geometries into dipole arrays. DDSCATConvert is a software available in the public domain nanohub.org which facilitates replacement of the volumetric target geometries by representative polarizable points or dipoles. At first, the shape generated in blender is input to the graphical

user interface (GUI) of DDSCATConvert in a wavefront.obj format. The requirement is that the input object must be in the form of a triangular mesh. Dipoles can be used to populate any arbitrary shape that is introduced in an object file format with locations of all the virtual points that formed the particular geometry. The algorithm of this software uses the point in a polyhedron method where a numerical algorithm first checks for a point within a volumetric box. Then, a dipole is assigned to that particular position or space coordinate. The produced target in the form of a dipole array can now be directly used by the DDA code for light-scattering calculations. The final output of this software is a shape file with 3D coordinates of all the point dipoles that populate the whole target volume. There are options available for setting the total number of dipoles for the conversion along with specifying the number of different materials that can be available in a particular target, along with facilities for specifying material dielectric properties for the different shapes present in the target sample.



Figure A3. Specimen shapes generated using blender 2.76b.



Figure A4. GUI of DDSCATConvert for shape file input.



Figure A5. Input parameters of DDSCATConvert.

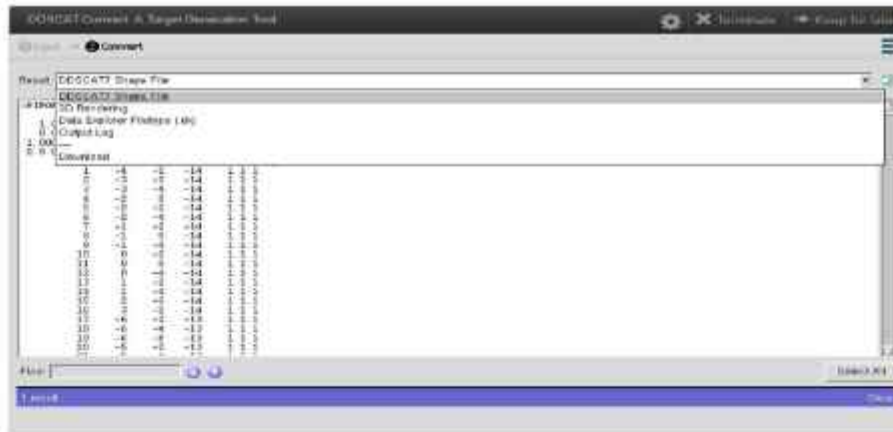


Figure A6. 3D coordinates of the dipoles in the converted target.

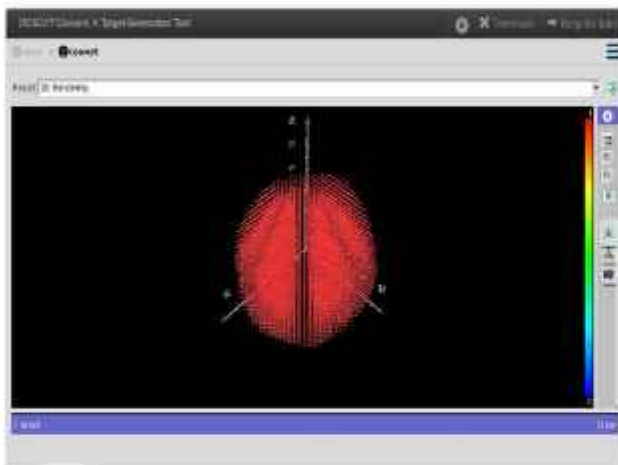


Figure A7. 3D representation of target in reference coordinate system.

Figure A4 shows the GUI of DDSCATConverter online html tool which provides the user an option to upload the target directly as an object file.

Figure A5 shows a screenshot of the input parameters for initiating the conversion of geometries into dipole arrays.

In the final stage of target conversion procedure, the software offers a option to save the generated files as shape and image files. Figure A6 shows a screen capture of the different files which can be directly downloaded from the remote server window of the website nanohub.org. Figure A7 shows the final generated target geometry. The whole process can be carried out online either in a html- or java-based window system. The conversion time is a function of the number of dipoles and also on the number of different shapes in the target volume.

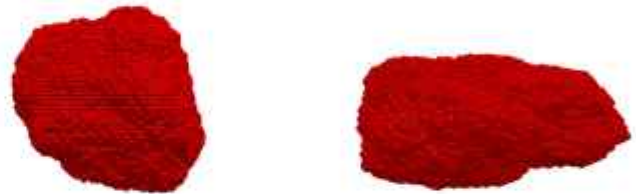


Figure A8. 3D-rendered representation of dipole arrays for specimen targets.

ParaView ParaView is a freely available software which facilitates visualization and processing of complex data sets. This software is incorporated in our computational technique to visualize the target geometries developed using Blender3D and converted to dipole arrays in DDSCATConvert. The produced shape file can be introduced into the ParaView interface and a 3D-rendered clear representation of the volumetric geometry of the shape is obtained as the final output. Its advantage is that the dipole arrays can be located in distinct and high resolution images in fine details. In advanced calculations, the positions and vacant spaces can also be obtained. A target in dipole representation is shown in Figure A8.

DDSCAT: advantages and limitations DDSCAT software package is available for download in the public domain scattport.org. DDSCAT is based on DDA and supports absorption and scattering calculations for a wide range of targets. Along with homogeneous and isotropic samples, it can also compute the light-scattering properties of inhomogeneous and anisotropic materials. But the most advantageous feature of this FORTRAN90 code is that it can identify any user introduced arbitrary


```

ddscat.par x
' ===== Parameter file for v7.3 ===== '
'**** Preliminaries ****'
'NOTORQ' = CMTORQ*6 (DOTORQ, NOTORQ) -- either do or skip torque calculations
'PBCGS2' = CMDSQL*6 (PBCGS2, PBCGST, GPBICG, QMRCCG, PETRKP) -- CCG method
'GPPAFT' = CMETHD*6 (GPPAFT, FFTMKL) -- FFT method
'GKOLDR' = CALPHA*6 (GKOLDR, LATTOR, FLTRCD) -- DDA method
'NOTBIN' = CBINFLAG (NOTBIN, ORIBIN, ALLBIN)
'**** Initial Memory Allocation ****'
500 500 500 = dimensioning allowance for target generation
'**** Target Geometry and Composition ****'
'FROM_FILE' = CSHAPE*9 shape directive
no SHPAR parameters needed
1 = NCOMP = number of dielectric materials
'./diel/fayalite' = file with refractive index 1
'**** Additional Nearfield calculation? ****'
0 = NRPLD (=0 to skip nearfield calc., =1 to calculate nearfield E)
0.0 0.0 0.0 0.0 0.0 0.0 (fract. extens. of calc. vol. in x,x,y,y,-z,+z)
'**** Error Tolerance ****'
1.00e-5 = TOL = MAX ALLOWED (NORM OF |G>=AC|E>-ACA|X>)/(NORM OF AC|E>)
'**** Maximum number of iterations ****'
500 = MXITER
'**** Integration cutoff parameter for PBC calculations ****'
1.00e-2 = GAMMA (1e-2 is normal, 3e-3 for greater accuracy)
'**** Angular resolution for calculation of <cos>, etc. ****'
0.1 = ETASCA (number of angles is proportional to [(3+x)/ETASCA]^2 )
'**** Vacuum wavelengths (micron) ****'
0.5435 0.5435 1 'INV' = wavelengths (first,last,how many,how=LIN,INV,LOG)
'**** Refractive index of ambient medium'
1.0000 = NAMBIENT
'**** Effective RadII (micron) ****'
2.0 2.0 1 'LIN' = eff. radII (first, last, how many, how=LIN,INV,LOG)
'**** Define Incident Polarizations ****'
(0,0) (1,0.) (0.,0.) = Polarization state #01 (k along x axis)
2 = IORTH (=1 to do only pol. state #01; =2 to also do orth. pol. state)
'**** Specify which output files to write ****'
1 = IWRKSC (=0 to suppress, =1 to write ".sca" file for each target orient.

```

Figure A9. DDSCAT input parameter file (Part A).

```

'**** Specify Target Rotations ****'
0. 0. 1 = BETAMI, BETAMX, NBETA (beta=rotation around a1)
0. 0. 1 = THETMI, THETMX, NTHETA (theta=angle between a1 and k)
0. 0. 1 = PHIMIN, PHIMAX, NPFI (phi=rotation angle of a1 around k)
'**** Specify first IIAV, IRAD, IORI (normally 0 0 0) ****'
0 0 0 = first IIAV, first IRAD, first IORI (0 0 0 to begin fresh)
'**** Select Elements of S_ij Matrix to Print ****'
6 = NSMELTS = number of elements of S_ij to print (not more than 9)
11 12 21 22 31 41 = indices ij of elements to print
'**** Specify Scattered Directions ****'
'LFRAME' = CMDFRM (LFRAME, TFRAME for Lab Frame or Target Frame)
1 = NPLANES = number of scattering planes
0. 0. 180. 5 = phi, theta_min, theta_max (deg) for plane A
90. 0. 180. 5 = phi, theta_min, theta_max (deg) for plane B

```

Figure A10. DDSCAT input parameter file (Part B).

random Gaussian and irregular shapes and calculate their optical and radiative properties.

The input parameters for DDA that require to be specified by the user are:

1. Incident wavelength.
2. Refractive index, particle size, user-defined shape file, particle-size distribution.
3. Number of iterations for the computations and number of different dielectric materials.

4. Number of scattering and polarization directions to be considered for calculation.
5. Number of orientations and the scattering parameters to be calculated.

Figures A9 and A10 show the input parameter files which need to be modified before carrying out the computation. All the input parameters must be keyed in manually in the parameter file which must be executed along with the main executable FORTRAN

file named 'ddscat'. After specifying the values of all the variables in the code, the shape file must be introduced in a DDSCAT compatible file format. Figure A11 shows the screen capture of the shape file with location of each and every dipole along with its dielectric properties.

After modifying the input parameters and loading the shape file with dipole locations, the main code of DDA is executed. The conversion time depends on particle size, number of dipoles and iterations required to perform the calculations of cross-sections and scattering parameters. The number of directions selected for orientational averaging further lengthens the time required for completion of the computational procedure. The computations in this entire thesis work are carried out in a workstation with 3.6 GHz core i7 processor equipped with 6 GB random access memory (RAM). The average timing for computations with different samples varies from a time range of 12–72 h, respectively, along with the time required for size and shape averaging. Once the computation completes, all the output files are automatically saved in folders specified by the user, which can be accessed later for data processing and graph plotting. Figures A12 and A13 show the output file containing the scattering, absorption and extinction efficiencies (Q_{sca} , Q_{abs} , Q_{ext} , respectively),

single scattering albedo (a), asymmetry parameter (g) and all the theoretical Mueller matrix elements (F_{ij}) including the polarization (P).

```

|PIP08J: point-in-polyhedron: NBX, NBY, NBZ= 57 107 50
102472 = NAT
1.0000 0.0000 0.0000 = A_1 vector
0.0000 1.0000 0.0000 = A_2 vector
1.000000 1.000000 1.000000 = lattice spacings (d_x,d_y,d_z)/d
0.0 0.0 0.0
JA IX IY IZ ICOMP(x,y,z)
1 -11 3 -24 1 1 1
2 -10 3 -24 1 1 1
3 -12 38 -24 1 1 1
4 -9 3 -24 1 1 1
5 -11 38 -24 1 1 1
6 -10 38 -24 1 1 1
7 -9 38 -24 1 1 1
8 -8 38 -24 1 1 1
9 -7 -4 -24 1 1 1
10 -7 38 -24 1 1 1
11 -6 38 -24 1 1 1
12 -5 38 -24 1 1 1
13 -4 38 -24 1 1 1
14 -3 38 -24 1 1 1
15 -2 38 -24 1 1 1
16 -1 38 -24 1 1 1
17 0 38 -24 1 1 1
18 -13 3 -23 1 1 1
19 -12 3 -23 1 1 1
20 -13 38 -23 1 1 1
21 -12 38 -23 1 1 1
22 -11 3 -23 1 1 1
23 -11 38 -23 1 1 1
24 -10 38 -23 1 1 1
25 -10 3 -23 1 1 1
26 -9 38 -23 1 1 1
27 -8 38 -23 1 1 1
28 -7 38 -23 1 1 1
29 -6 38 -23 1 1 1
    
```

Figure A11. Shape file after conversion with DDSCATConvert.

```

w000i000.avg *
DDSCAT --- DDSCAT 7.3.0 [13.05.03]
TARGET --->PIP08J: point-in-polyhedron: NBX, NBY, NBZ = 43 43 51
GKDLDR --- DDA method
PBCG52 --- CCG method
FROM_FILE --- shape
29675 = NAT0 = number of dipoles
0.05206740 = d/aeff for this target (d=dipole spacing)
0.052067 = d (physical units)
AEFF= 1.000000 = effective radius (physical units)
WAVE= 0.543500 = wavelength (in vacuo, physical units)
K*AEFF= 11.560590 = 2*pi*aeff/lambda
NAMBIENT= 1.000000 = refractive index of ambient medium
n= ( 2.7312 , 1.5600), eps.= ( 5.9233 , 0.5260) [m]kd= 1.8935 for subs. 1
TOL= 1.000E-05 = error tolerance for CCG method
( 1.00000 0.00000 0.00000 ) = target axis A1 in Target Frame
( 0.00000 1.00000 0.00000 ) = target axis A2 in Target Frame
NAVG= 5832 = (theta,phi) values used in comp. of Qsca,g
( 0.00193 0.00000 0.00000 ) = k vector (latt. units) in Lab Frame
( 0.00000, 0.00000 )( 1.00000, 0.00000 )( 0.00000, 0.00000 )=inc.pol.vec. 1 in LF
( 0.00000, 0.00000 )( 0.00000, 0.00000 )( 1.00000, 0.00000 )=inc.pol.vec. 2 in LF
0.000 0.000 = beta_min, beta_max ; NBETA= 1
0.000 0.000 = theta_min, theta_max; NTHETA= 1
0.000 0.000 = phi_min, phi_max ; NPHI= 1

0.5000 = ETASCA = param. controlling # of scatt. dirs used to calculate <cos> etc.
Results averaged over 1 target orientations
and 2 incident polarizations
      Qext      Qabs      Qsca      g(1)=<cos> <cos^2>      Qbk      Qpha
J0=1: 3.3327E+00 1.4826E+00 1.8502E+00 0.6824E-01 0.7209E-01 0.0515E-04 -1.4048E-01
J0=2: 3.3346E+00 1.4005E+00 1.9281E+00 0.5000E-01 0.6714E-01 1.2050E-02 -1.0304E-01
mean: 3.3337E+00 1.4445E+00 1.8892E+00 0.5893E-01 0.6714E-01 0.4275E-03 -1.5206E-01
Qpol= -1.9379E-03
      Qsca*g(1)  Qsca*g(2)  Qsca*g(3)  iter  nXiter  Nsca
J0=1: 1.6004E+00 -3.3261E-02 2.2168E-02 101 300 5832
J0=2: 1.6389E+00 2.7748E-02 -3.6203E-03 101 300 5832
mean: 1.6227E+00 -2.7566E-03 9.2741E-03
    
```

Figure A12. Main output file of DDSCAT (Part A).

Mueller matrix elements for selected scattering directions in Lab Frame

theta	phi	Pol.	S ₁₁	S ₁₂	S ₂₁	S ₂₂	S ₃₁	S ₄₁
0.00	0.00	0.01171	1.2511E+04	-2.3320E+01	-2.254E+01	1.251E+04	-1.440E+02	-5.266E+01
5.00	0.00	0.02581	7.5240E+03	-1.9444E+02	-1.930E+02	7.522E+03	-1.569E+01	-4.405E+01
10.00	0.00	0.12510	1.5845E+03	-1.9684E+02	-1.963E+02	1.583E+03	2.758E+01	-2.370E+01
15.00	0.00	0.01230	7.9568E+01	-4.7644E+01	-4.746E+01	7.764E+01	-1.102E+01	-4.143E+00
20.00	0.00	0.24694	2.8009E+02	-6.3409E+01	-6.323E+01	2.786E+02	-2.803E+01	-4.290E+00
25.00	0.00	0.36694	1.2129E+02	-6.7911E+01	-6.761E+01	1.206E+02	-1.255E+01	3.641E+00
30.00	0.00	0.36759	7.1707E+01	-2.6590E+01	-2.633E+01	7.147E+01	-1.753E+00	4.177E+00
35.00	0.00	0.38885	9.3332E+01	-3.6443E+01	-3.627E+01	9.310E+01	1.314E+00	4.494E+00
40.00	0.00	0.76955	4.1951E+01	-3.2337E+01	-3.220E+01	4.179E+01	2.345E+00	2.807E+00
45.00	0.00	0.59777	3.1469E+01	-1.8716E+01	-1.869E+01	3.126E+01	2.150E+00	1.732E+00
50.00	0.00	0.65632	3.1045E+01	-2.0730E+01	-2.070E+01	3.100E+01	2.129E+00	1.499E+00
55.00	0.00	0.92333	2.8349E+01	-1.8577E+01	-1.871E+01	2.804E+01	1.781E+00	8.213E-01
60.00	0.00	0.85776	2.1441E+01	-1.9066E+01	-1.921E+01	2.103E+01	1.254E+00	1.786E-01
65.00	0.00	0.95480	2.4768E+01	-2.3385E+01	-2.361E+01	2.440E+01	1.286E+00	2.264E-01
70.00	0.00	0.97417	2.4335E+01	-2.3519E+01	-2.364E+01	2.401E+01	1.778E+00	6.723E-01
75.00	0.00	0.94293	2.3003E+01	-2.1611E+01	-2.162E+01	2.269E+01	2.513E+00	9.656E-02
80.00	0.00	0.97467	1.9942E+01	-1.9292E+01	-1.933E+01	1.959E+01	1.878E+00	-1.408E+00
85.00	0.00	0.96051	1.9065E+01	-1.8562E+01	-1.869E+01	1.886E+01	-2.784E-01	-1.481E+00
90.00	0.00	0.96144	2.2934E+01	-2.2449E+01	-2.249E+01	2.277E+01	-1.270E+00	1.603E+00
95.00	0.00	0.90995	2.8610E+01	-2.8244E+01	-2.830E+01	2.828E+01	-2.901E-01	2.990E+00
100.00	0.00	0.90818	3.1351E+01	-2.9951E+01	-3.035E+01	3.074E+01	4.482E-01	2.270E+00
105.00	0.00	0.90768	2.6931E+01	-2.3803E+01	-2.444E+01	2.664E+01	-1.633E-01	-3.395E-01
110.00	0.00	0.73231	1.8262E+01	-1.2601E+01	-1.337E+01	1.749E+01	3.399E-01	-2.111E+00

Figure A13. Main output file of DDSCAT (Part B).

Appendix B: MATLAB® post-processing code

This code takes the files generated by DDSCAT for each size and performs the size averaging for the target sample. With slight modification, the same code can be used for shape averaging.

```
%DDA PostProcess: Program to calculate scattering Matrix for System
of particles using
%DDSCAT 7.3.0
%Developed by Manish Jyoti Boruah
sd = input('Select a size distribution: ', 's');
sd
if(sd == 1)
%Log Normal Size distribution
x = 5:0.5:5;
y = 1;
sigma = 1.5;
k = (log(x) - log(y)).^2;
kk = (log(sigma)).^2;
kkk = k./(2*kk);
u = exp(kkk);
l = (2*pi)^0.5*log(sigma);
nrm = 20*u./l;
z = numel(x);
elseif(sd == 2)
% Normal size distribution
x = 0.5:0.5:5;
y = 2;
sigma = 1.5;
k = 1./sigma;
nk = 1./(2*pi).^1/2;
kk = nk*k;
p = x*y;
pk = ((p).^2);
pn = 1./(2*(sigma).^2);
pp = exp(pk*pn);
nt = kk*pp;
nrm = 20*nt;
z = numel(x);
else
% Gamma size distribution
x = 0.5:0.5:5;
y = 2;
alpha = 0.3;
k = alpha./y;
kk = k.*(alpha+1);
l = 1./gamma(alpha+1);
g = x.^alpha;
s = (k*x);
p = exp(s);
nt = kk.*l.*g.*p;
nrm = 20*nt;
z = numel(x);
end
```

```
for n = 1:z
A = load(['w000r000.' num2str(z) '.avg']);
S = A(:,3:9);
B = A(:,1:2);
N = zeros(37,7,2);
S = nrm(n)*S;
N(:,n) = S;
end
for r = 1:z-1
SM = N(:,r) + N(:,r+1);
end
SD = SM(:,1);
SS = SM(:,2);
SP = SM(:,3:7);
M = max(SM);
SD = SD./M(1);
SS = SS./M(2);
SMR = [SS,SP];
SMC = [SD,SMR];
Lambda = input('Select a wavelength: ', 's');
Lambda
WAV = (Lambda).^2;
WAV1 = 4*((3.1412).^2);
WAVN = WAV./WAV1
SML = WAVN*SMC;
SMF = [B,SML];
format shortE;
SMF
semilogy(SMF(:,1),(-2:3))
save SMF.dat SMF -ascii
save SMF.avg SMF -ascii
save SMF.mat SMF -ascii
```

References

- Aguirre A. 1999, *Astrophys. J.* 525, 583
- Altobelli N., Postberg F., Fiege K. *et al.* 2016, *Science* 352, 312
- Andersson B. G., Lazarian A., Vaillancourt J. E. 2015, *Annu. Rev. Astron. Astrophys.* 53, 501
- Baba N., Naoshi M. 2003, *Publ. Astron. Soc. Pac.* 115, 1363
- Bohren C. F., Huffman D. R. 2008, *Absorption and Scattering of Light by Small Particles*. Wiley, Hoboken

- Boruah, M. J., Gogoi, A., Ahmed G. A. 2016, Planet. Space Sci. 125, 27
- Boruah M. J., Gogoi A., Nath B. C., Ahmed G. A. 2017, J. Quant. Spectrosc. Radiat. Transf. 196, 213
- Brownlee D. 2014, Annu. Rev. Earth Planet. Sci. 42, 179
- Calura F., Pipino A., Matteucci F. 2008, Astron. Astrophys. 479, 669
- Costello M. J., Johnsen S., Gilliland K. O., Freil C. D., Craig F. W. 2007, Investig. Ophthalmol. Vis. Sci. 48, 303
- DeAngelis M. T., Rondinone A. J., Pawel M. D., Labotka T. C., Anovitz L. M. 2012, Am. Mineral. 97, 653
- Deb S., Kar A., Sen A. K., Gupta R. 2015, Publ. Korean Astron. Soc. 30, 65
- Draine B. T. 1988, Astrophys. J. 333, 848
- Draine B. T. 2003, Annu. Rev. Astron. Astrophys. 41, 241
- Draine B. T., Flatau P. J. 1994, J. Opt. Soc. Am. A 11, 1491
- Draine B. T., Flatau P. J. 2013, arXiv preprint <https://arxiv.org/abs/1305.6497>
- Draine B. T., Lee H. M. 1984, Astrophys. J. 285, 89
- Draine B. T., Li A. 2007, Astrophys. J. 657, 810
- Dubovik O. V., Lapyonok T. V., Oshchepkov S. L. 1995, Appl. Opt. 34, 8422
- Dubovik O., Holben B. N., Lapyonok T. *et al.* 2002, Geophys. Res. Lett. 29, 54
- Dubovik O., Lapyonok T., Kaufman Y. J. *et al.* 2008, Atmos. Chem. Phys. 8, 209
- Fabian D., Henning Th., Jäger C., Mutschke H., Dorschner J., Wehrhan O. 2001, Astron. Astrophys. 378, 228
- Feser J., Sobh A. R. N. 2013, <https://nanohub.org/resources/ddaconvert>
- Fulle M., Colangeli L., Agarwal J. *et al.* 2010, Astron. Astrophys. 522, A63
- Gogoi A., Borthakur L. J., Choudhury A., Stanciu G. A., Ahmed G. A. 2009, Meas. Sci. Technol. 20, 095901
- Gogoi A., Rajkhowa P., Choudhury A., Ahmed G. A. 2011, J. Quant. Spectrosc. Radiat. Transf. 112, 2713
- Groves B. A., Dopita M. A., Sutherland R. S. 2004, Astrophys. J. Suppl. Ser. 153, 9
- Gupta R., Vaidya D. B., Dutta R. 2016, Mon. Not. R. Astron. Soc. 1, 867
- Hadamcik E., Renard J.-B., Rietmeijer F. J. M. *et al.* 2007, Icarus 190, 660
- Heintzenberg J. 1994, Aerosol. Sci. Technol. 21, 46
- Hill S. C., Clyde H. A., Barber P. W. 1984, Appl. Opt. 23, 1025
- Hovenier J. W., Volten H., Munoz O., Van der Zande W. J., Waters L. B. F. M. 2003, J. Quant. Spectrosc. Radiat. Transf. 79, 741
- Hulst H. C., van de Hulst H. C. 1981, Light Scattering by Small Particles. Courier Corporation, North Chelmsford
- Ishiguro M. 2008, Icarus 193, 96
- Kar A., Sen A. K., Gupta R. 2016, Icarus 277, 300
- Kimura H., Kolokolova L., Mann I. 2006, Astron. Astrophys. 449, 1243
- Krüger H., Landgraf M., Altobelli N., Grün E. 2007, Space Sci. Rev. 130, 401
- Kustova N., Konoshonkin A., Borovoi A. *et al.* 2020, in EPJ Web of Conferences, vol. 237, EDP Sciences
- Liu L., Mishchenko M. I., Hovenier J. W., Volten H., Muñoz O. 2003, J. Quant. Spectrosc. Radiat. Transf. 79, 911
- Mathis J. S., Rumpl W., Nordsieck K. H. 1977, Astrophys. J. 217, 425
- McKeegan K. D., Aléon J., Bradley J., Brownlee D., Busemann H., Butterworth A., Chaussidon M. *et al.* 2006, Science 314, 1724
- Mennella V., Brucato J. R., Colangeli L. 2001, Spectrochim. Acta A Mol. Biomol. Spectrosc. 57, 787
- Messenger S., Keller L. P., Lauretta D. S. 2005, Science 309, 737
- Mishchenko I. M. 2009, J. Quant. Spectrosc. Radiat. Transf. 110, 808
- Mishchenko M. I. 2014, Electromagnetic Scattering by Particles and Particle Groups: An Introduction. Cambridge University Press, Cambridge
- Mishchenko M. I., Yurkin M. A. 2017, Opt. Lett. 42, 494
- Mishchenko M. I., Travis L. D., Lacis A. A. 2006, Multiple Scattering of Light by Particles: Radiative Transfer and Coherent Backscattering. Cambridge University Press, Cambridge
- Moreno F., Munoz O., López-Moreno J. J., Molina A., Ortiz J. L. 2002, Icarus 156, 474
- Muñoz O., Hovenier J. W. 2011, J. Quant. Spectrosc. Radiat. Transf. 112, 1646
- Nieva M.-F., Przybilla N. 2012, Astron. Astrophys. 539, A143
- Nousiainen T., Zubko E., Niemi J. V. *et al.* 2007, Quant. Spectrosc. Radiat. Transf., 106, 389
- Nousiainen T., Zubko E., Niemi J. V. *et al.* 2009, J. Geophys. Res. Atmos. 114, D07207
- Pagani L., Steinacker J., Bacmann A., Stutz A., Henning T. 2010, Science 329, 1622
- Petrova E. V., Jockers K., Kiselev N. N. 2000, Icarus 148, 526
- Piovan L., Tantalò R., Chiosi C. 2006, Mon. Not. R. Astron. Soc. 366, 923
- Purcell E. M., Pennypacker C. R. 1973, Astrophys. J. 186, 705
- Riedler W., Torkar K., Jeszenszky H. *et al.* 2007, Space Sci. Rev. 128, 869
- Rotundi A., Brucato J. R., Colangeli L., Ferrini G., Mennella V., Palomba E., Palumbo P. 2002, Meteorit. Planet. Sci. 37, 1623
- Saikia G., Gogoi R., Gupta R., Vaidya D. B. 2019, Mon. Not. R. Astron. Soc. 484, 3582
- Savage B. D., Sembach K. R. 1996, Annu. Rev. Astron. Astrophys. 34, 279
- Sen A. K., Botet R., Vilaplana R., Choudhury N. R., Gupta R. 2017, J. Quant. Spectrosc. Radiat. Transf. 198, 164

- Sen A. K., Hadamcik E., Botet R., Lasue J., Roy C. S., Gupta R. 2019, *Mon. Not. R. Astron. Soc.* 487, 4809
- Siebenmorgen R., Voshchinnikov N. V., Bagnulo S. 2014, *Astron. Astrophys.* 561, A82
- Steinacker J., Pagani L., Bacmann A., Guieu S. 2010, *Astron. Astrophys.* 511, A9
- Tielens A. G. G. M. 2001, in *Tetons 4: Galactic Structure, Stars and the Interstellar Medium*, Vol. 231, p 92
- Tuzzolino A. J., Economou T. E., McKibben R. B. *et al.* 2003, *J. Geophys. Res. Planets* 108, 8115
- Vaidya D. B., Gupta R. 1997, *Astron Astrophys.* 328, 634
- Vilaplana R., Moreno F., Molina A. 2006, *J. Quant. Spectrosc. Radiat. Transf.* 100, 415
- Vilaplana R., Luna R., Guirado D. 2011, *J. Quant. Spectrosc. Radiat. Transf.* 112, 1838
- Volten H., De Haan J. F., Hovenier J. W. *et al.* 1998, *Limnol. Oceanogr.* 43, 1180
- Volten H., Muñoz O., Rol E. *et al.* 2001, *J. Geophys. Res. Atmos.* 106, 17375
- Volten H., Muñoz O., Hovenier J. W. *et al.* 2007, *Astron. Astrophys.* 470, 377
- Westphal A. J., Butterworth A. L., Snead C. *et al.* 2005, in *Lunar and Planetary Science Conference*, Vol. XXXVI, part 21
- Westphal A. J., Stroud R. M., Bechtel H. A. *et al.* 2014, *Science* 345, 786
- Yang P., Feng Q., Hong G. *et al.* 2007, *J. Aerosol. Sci.* 38, 995
- Zubko E. 2015, *Opt. Lett.* 40, 1204
- Zubko E., Muinonen K., Shkuratov Y., Videen G., Nousiainen T. 2007, *J. Quant. Spectrosc. Radiat. Transf.* 106, 604
- Zubko E., Muinonen K., Muñoz O. *et al.* 2013, *J. Quant. Spectrosc. Radiat. Transf.* 131, 175

UGC Care Listed

त्रैमासिक साहित्यिक पत्रिका

ISSN-2321-1504 Nagfani

RNI No. UTTHIN/2010/34408

वर्ष-12, अंक-43, अक्टूबर - दिसम्बर 2022

नागफनी

अरिमता, चेतना और स्वामिमान जगाने वाला साहित्य

भाग-3

मूल्य

₹ 150/-



भाग - 03

नागफनी

A Peer Reviewed Refereed Journal
(अस्मिता चेतना और स्वाभिमान जगाने वाला साहित्य)
त्रैमासिक साहित्यिक पत्रिका

ISSN-2321-1504 Nagfani RNI No. UTTHIN/2010/34408

वर्ष-12 अंक 43, अक्तूबर -दिसम्बर-2022 भाग-3

संपादक सपना सोनकर
सह संपादक रूपनारायण सोनकर
Co Editor(English) Prof.Rajesh karankal Dr.Santosh Kumar Sonkar
कार्यकारी संपादक डॉ.एन.पी.प्रजापति प्रोफेसर बलिराम धापसे

सलाहकार मण्डल (Peer Review Committee)

प्रोफेसर विष्णु सखदे, हैदराबाद (तेलंगाना)
प्रोफेसर आर. जयचंद्रन तिरुअर्नतपुरम (केरल)
प्रोफेसर दिनेश कुशवाह, सीवा (मध्य प्रदेश)
डॉ.एन. एस. परमार, बड़ोदा (गुजरात)
प्रो. दिलीप कुमार मेहरा, बी.बी.नगर (गुजरात)
डॉ. उमाकांत हनारिका, शिवसागर (असम)
डॉ. आर. कनागसेल्वम, इरोड (तमिलनाडु)

प्रोफेसर संजय एल. मादार, धारवाड़ (कर्नाटक)
प्रोफेसर गोविन्द बुरसे, औरंगाबाद (महाराष्ट्र)
डॉ. दादा साहेब सालुनके, महाराष्ट्र (औरंगाबाद)
प्रोफेसर अलका गडकरी, औरंगाबाद (महाराष्ट्र)
डॉ. साहिर बानो बी. बोरगल, हैदराबाद (तेलंगाना)
प्रोफेसर मोहनलाल 'आर्य' मुरादाबाद (उत्तर प्रदेश)
डॉ. जी. व्ही. रत्नाकर हैदराबाद (तेलंगाना)

प्रकाशन/मुद्रण

प्रकाशक रूपनारायण सोनकर की अनुमति से डॉ. एन. पी. प्रजापति एवं प्रोफेसर बलिराम धापसे द्वारा नमन प्रकाशन-423/A अंसारोड दरियागंज, नई दिल्ली 11002 में प्रकाशन एवं मुद्रण कार्य।

मुख्य पृष्ठ- उत्कर्ष प्रजापति, सिंगरीली - मध्य प्रदेश

संपादकीय/व्यवस्थापकीय कार्यालय

दून ब्यू कॉटेज रिपिंग रोड, मंसूरी -248179, उत्तराखण्ड, दूरभाष : 0135-6457809 मो.0941077111

शाखा कार्यालय

पी. डब्ल्यू. डी. आर. -62 ए ब्लॉक कॉलोनी बैडन, जिला-सिंगरीली म. प्र. पिन-486886 मो. 09752998467
सहयोग राशि -150/-रुपये, वार्षिक सदस्यता शुल्क (संस्था के लिए)-1500/-रुपये, पंच वार्षिक सदस्यता शुल्क (व्यक्ति के लिए)-3000/-रुपये
पंच वार्षिक संस्था और पुस्तकालयों के लिए -3500/-रुपये, विदेशों में \$50 आजीवन व्यक्ति-6000/-रुपये, संस्था-10,000/-रुपये।

सदस्यता शुल्क एवं सहयोग राशि-Dalit Utkarsh Samiti-A/C-31590110006504 .
IFSC Code-UCBA0003159 Branch-Waidhan ward no 40

नोट:-पत्रिका की किसी भी सामग्री का उपयोग करने से पहले संपादक की अनुमति आवश्यक है। संपादक-संचालक पूर्णतया अवैतनिक एवं अध्यक्षीय हैं। 'नागफनी' में प्रकाशित शोध-पत्र एवं लेख, लेखकों के विचार उनके स्वयं के हैं। जिनमें संपादक की सहमति अनिवार्य नहीं है। 'नागफनी' से संबंधित सभी विवादास्पद मामले केवल देहरादून न्यायालय के अधीन होंगे। अंक में प्रकाशित सामग्री के पुनर्प्रकाशन के लिए लिखित अनुमति अनिवार्य है। सारे भुगतान मनी ऑर्डर, बैंक/चेक/बैंक ट्रांसफर/ई-पेमेंट आदि से किए जा सकते हैं। देहरादून से बाहर के चेक में बैंक कमीशन 50/- अतिरिक्त जोड़ें।

लेख भेजने के लिए -Mail-ID- nagfani81@gmail.com
पत्रिका के बारे में विस्तार से जानने के लिए देखें Website:-http://naagfani.com

UGC Care Listed Journal

ISSN-1504Nagfani RNI N.-UTTHIN/2010/34408

Socio-Economic Condition of Mayamara Sct in Majuli

Binod Das

Assistant Professor
Department of Economics
Jengraimukh College, Majuli Pin: 785105

Abstract: In Indian society the caste system is said to be a peculiar one. A caste is not by birth but by occupation. A caste is generally defined according to their occupation. Accordingly, people who belong to occupation of fishing are known as fisherman i.e. Kaibartas. Since independence some efforts have been made at national and state level through the constitutional privileges, planning mechanism and participatory development for their steady and speedy development. Despite these efforts made at different levels of their betterment why the scheduled caste community lagging behind? In this regard, it is quite sincerely anticipated that the findings and conclusions drawn from the study contribute a lot for the planners and policy makers in presenting measures for solution of problems faced by the downcast class.

INTRODUCTION:

The Kaibartas are one of the aboriginal ethnic groups in Assam. They have been living in Brahmaputra valley from unknown past. After independence, the constitution of India ordered in 1950 the SC of Assam are composed of sixteen distinct groups which Kaibartas is one of the original groups. Out of sixteenth SC communities of India Kaibarta, Bonia, Namadra and Hira are found in Majuli district. Mayamara sect is also a sub-caste of Kaibarta community. According to historical evidence, Aniruddha Dev (1553-1626) the founder of the Mayamara sect of Vaishnavism of Assam the follower of him is called Mayamara. The word Mayamara is a combination of two Assamese words i.e. Maya (Illusion) and Mara (Shun, Renunciate) meaning that one should not be tempted or attracted towards worldly or mundane ostentation because illusion causes great misery in one's life. That is why the prophets of religion always keep themselves away from illusion as it breeds misery in life.

The study area "Senchowra" is a compound word meaning Sen- a kind of bird of Kite family and Chowra- to impart training to the birds for hunting another bird namely Konowra. As per tradition (generally from January to April) the hunting of Konowra bird by Sen bird show is organized for the Royal family itself for entertainment or amusement.

The caste system in India is said to be a peculiar feature in Indian society. With the growth of civilization the idea of self employment and self dependents grew up among the people to meet their increasing demand for their goods and services. As a result of division of labour came into existence in the society, it leads to creation of four varnas. The classification of varnas was made mainly on the basis of Gun- a (temperament) and Karma (action). So a caste is not by birth but by occupation. A caste is generally defined according to their occupation. Accordingly people who belong to occupation of fishing are known as fisherman i.e. Kaibartas. The Kaibartas are found in almost all places of Majuli living in their own exclusive villages. Some of their known villages are

Senchowra, Salmora, Kamalabari, Garamur, Kharjan, Nagargaon, Dhackajuli, Kakarikata, Chitakala, Dakhinpat, Dadhara etc. The present study is included only Senchowra cadastral village which is covered eight villages i.e. Deka Senchowra, Buha Senchowra, Balichhapori, Kathaniati, Bhusenchowra, Amguri Rongdoi, Thakurbari and Asokguri Dadhara. Here, one of the most remarkable facts is that all the inhabitants of said villages are Mayamara sect. The total geographical area of the island was 1250 sq.km prior to 1950s earthquake. Majuli was declared as a civil sub-division under Jorhat district of Assam on January 26, 1979. Recently Majuli is declared as district by BJP government in 8 September, 2016. Majuli is divided into two Development Blocks namely Majuli Development Block and Ujani Majuli Development Block. The Ujani Majuli Development Block was established in 1991. The revenue circle as well as the present district is divided into three Mouza namely Ahatguri, Salmora and Kamalabari. Moreover, the island was further divided into twenty Gaon Panchayats. As per 2011 census, the total size of population in Majuli is 1,67,304 and out of which 85,566 are males population while 81,738 are females. In 2011 there were 32,226 families residing in Majuli. The average sex-ratio of Majuli is 955. The density of population is 136.04 per sq. km. The average literacy rate of Majuli is 87.56% in which, male and female literacy were 86.16% and 70.62 % respectively. The total SC and ST population of Majuli are 23,878 (14.3%) and 63,761(46.4%) respectively. The district consists of 3 Mouzas, 20 Gaon Panchayats and 248 cadastral villages. The SC people of Majuli is scattered into 55 vilas.

2. OBJECTIVES: The main objectives of the study to highlight: (a) To trace out the origin of the Mayamara sect. (b) To explain the socio-economic conditions of the sample households. (c) To suggest measures to the policy makers, planners and governments for solution of their problems.

3. METHODOLOGY: The proposed study is confined to the entire Majuli district of Assam. 8 nos. of villages are purposively selected to collect required information of 120 couples, where Mayamara people are concentrating. In order to collect information relating to socio-economic conditions of Mayamara sect a interview schedule is composed among the respondents. The information are collected through door to door visit. The selected villages are Deka Senchowra, Kathaniati, Buha Senchowra, Bhuramara, Thakurbari, Senchpwa Balichhapori, Amguri Kangdoi and Ashokguri Dadhara.

4. PERIOD OF STUDY: To know about the socio-economic conditions of Mayamara sect of Majuli district we collected information through use of questionnaire in the year 2021.

5. SOCIO-ECONOMIC CONDITIONS OF KAIBARTTA-

As a part of the study, information regarding socio economic status of Mayamara sect of Majuli we purposively selected 120 no. of households from 8 villages. There are only 8 nos. of villages of Mayamara sect in Majuli district, which we selected to reflect all dimensions of the society.

Table No. 1: Population growth and sex ratio of SC commu

Sl.No.	Year	Male	Female	Sex ratio	Total
1	1971	6297	5338	847	11635
2	1991	10133	9145	902	19278
3	2001	11237	10242	911	21497
4	2011	12263	11615	948	23878

Source:-Statistical office, Majuli.

The Table show the overall picture of Schedule Caste population of Majuli District from 1971 to 2011. From the table it is clear that the sex- ratio is gradually increasing. According to 2011 census report, sex-ratio is 948, which is less than all India level (940). In 1981, they were not calculated due to Assam's agitation.

5. (a) SEX-RATIO: To get a clear picture of sex-ratio of sample households the following table is found.

Table No. 2: Distribution of village wise population in study area aity in Majuli

Sl. N o.	Name of the villages	Total House holds	Total Popu- lation	Male	Fe- male	Sex- ratio
1	Deka Sen- chowa	241	1206	658	548	832
2	Buha Sen- chowa	159	760	345	415	1202
3	Balichaponi	145	738	426	312	732
4	Thakurbari	168	838	440	398	904
5	Kathaniati	121	603	290	313	1079
6	Bhuramara	146	888	497	391	786
7	Amguri Rangdoi	68	295	104	91	875
8	Ashokguri Dadhara	82	368	204	164	803
	Total	1130	5696	2964	2632	887

Source: Field study.

From the Table No. 2, we find that sex-ratio is different in all villages. The total population of Mayamara sect is 5696, out of it 2964 is male and 2632 is female. The overall sex-ratio is 887, which is also low than all India level. It indicates that the SC people generally preferred male child rather than female child for additional labour force.

5. (b) FAMILY STRUCTURE:-Both joint and nuclear families are found among the Mayamara sect of my study area. As time passes the nuclear families have transferred due to economic hardship and depending on ideology of individualism and materialism.

TableNo.3: Distribution of households by family type

Family type	No. of households	Percentage
Nuclear	104	86.67
Joint	16	13.33
Total	120	100

From the Table No. 3 it is clear that out of 120 households, 86.67% belongs to nuclear family and 13.33% belongs to joint family. The gaps between nuclear and joint families are gradually increasing due to early marriage, Govt. poli- cies, self dependence, orthodoxy etc.

5. (c) HOUSING CONDITION:There is no any abnormal nature in case of housing structure of Mayamara sect. Nor- mally, we find three types of houses, i.e. pokka, semi- pok- ka and kecha. **Table No. 4** shows that 14.17% have pokka houses, 34.17% have semi-pokka houses and 51.66% are found in kecha houses. The maximum semi-pokka houses are built by the government scheme. A large number of downtrodden people are lived in kecha houses today.

Table No 4: Distribution of households by housing conditions

Type of house	No. of households	Percentage
Pokka	17	14.17
Semi-pokka	41	34.17
Kecha	62	51.66
Total	120	100

5. (d) TOILET FACILITIES:

TableNo.5: Distribution of households by toilets facilities.

Type	No. of households	Percentage
Pokka	34	28.33
Kecha	77	64.17
Open	9	7.50
Total	120	100

Latrine condition in the study area is very untidy. Out of 120 households, 28.33% have sanitary condition, 64.17% have kecha latrine which is made of bamboos & tree leaves and 7.50% have no any latrine and they used open field and riverbanks. The govt. offers low cost sanitary latrine for them, but they have not found.

5. (e) ELECTRICITY FACILITIES:

Table No. 6: Distribution of households by electricity facilities

Type	No. of households	Percentage
Commercial	5	4.17
Domestic	108	90.00
Untrust	7	5.83
Total	120	100

From **Table No. 6** it is clear that a major percent of house- holds i.e. 90% used power as domestic purposes, 4.33% used commercial purposes. Therefore, 5.83% households have no power supply due to economic hardship, orthodoxy aware of line up etc. Most of the families are benefited by the Kutir Jyoti Scheme offered by the Assam government.

5. (f) FAMILY PLANNING:-The family planning is a

constituent of population policy, which indicates the conscious limitation of the size of the family to a optimum level. The small size of family leads to improve standard of living, health condition of mother and children, economic condition, food shortage, per capita income, efficiency of people, unemployment problems etc. The family planning measures can be done by adopting some suitable methods like abstinence, contraceptives, sterilization, abortion, use of harmless effective device etc.

Table No. 7: Distribution of respondents by family planning technique

Family	No. of respondents	Percentage
Having knowledge	82	68.33
Not having knowledge	32	26.64
Total	120	100

From Table No.7, it is found that out of 120 households 68.33% have knowledge about family planning and 26.64% have not any knowledge of family planning. Here, remarkable point is that major portion of respondents used contraceptive, for which growth rate of SC population is not so high.

5. (g) EDUCATION: Education is the major criterion for the upliftment of a society. Except basic needs vocational, technical and professional education are essential for job placement and arriving at a higher status. To obtain the real scenario of the literacy level of the study area we confined following heads.

Table No. 8: Distribution of population by the level of education.

Sl. No.	Level of education	Male population	%	Female population	%
1	Illiterate	55	18.97	84	31.94
2	Up to primary(i-iv)	68	23.45	55	20.91
3	Middle school completed	60	20.69	51	19.39
4	High school completed	57	19.65	44	16.73
5	Beyond high school	50	17.24	29	11.03
	Total	290	100	263	100

It is clear that out of 290 male population 18.97% is illiterate and 81.97% literate. Similarly, out of 263 female population 31.94% is illiterate and 68.06% literate. The general literacy rate is 75.02%, which is simply highest than all India average (74.04%). Therefore, the table reveals that male literacy rate is higher than female literacy rate. Beyond the HSLC, female literacy is only 11.03%, because of early marriage. After independence union and state govt. Adopted various policies for SC to improve the educational status as constitutional privileges. Despite these special facilities, they are still poor in education. In case of female education they are still lagging behind the male in my study area.

5. (h) OCCUPATION:

To obtain the real scenario of the occupational pattern of the sample households we divided their occupations into four classes. For comparisons, two consecutive years were used i.e. 2011 and 2021.

TABLE 9: Distribution of households by occupation.

Sl. No.	Type of occupation	2011		2021	
		No. of households	%	No. of households	%
1	Agriculture and allied activities	97	80.83	82	68.33
2	Trade and commerce	15	12.5	22	18.33
3	Service	6	5.0	11	9.17
4	Manufacturing	1	1.66	5	4.17
	Total	120	100	120	100

From the table it is found that during the year 2011, 80.83% is directly engaged in agriculture and allied activities, 12.5% is belongs to trade and commerce, 5.0% is involved in service and 1.66% is involved in manufacturing activities. Similarly, in 2021, 68.33% is engaged in agriculture and allied activities, 9.17% is involved in service and 4.17% is involved in manufacturing activities. By comparing both the years, it is clear that the households are shifted from agriculture sector to the secondary and tertiary sector. Originally, the main occupation of SC community was fishing. But now-a-days, their occupations are gradually transferred into other activities say mason, carpenter, shopkeeper, driver etc. due to lack of fish at natural flows and government interference.

5. (i) INCOME DISTRIBUTION:

In order to have an idea regarding the intensity of poverty among the SC people, in the words of IRDP, booklet published by DRDA, Kamrup, Assam, we have graded the sample households into five categories on the basis of their income.

TABLE No. 10: Intensity of poverty among the sample households

Sl. No.	Sample households	Income categories	Total households	%
1	Extremely poor	0-----4000	4	3.33
2	Very much poor	4000-----6000	10	8.33
3	Very poor	6000-----8500	30	25.00
4	Poor	8500-----11000	44	36.67
5	Rich	11000 and above	32	26.67
	Total		120	100

Table No. 10 shows the intensity of poverty of sample households. Out of 120 households only 26.67% cross the boundary line of poverty and other 73.33% is belong to poverty line. The intensity of their poverty is due to their socio-economic backwardness arising out of both economic factors like lack of economic and natural resources, inequalities of income and wealth, low productivity, unfavourable market and non-economic factors like fatalism, conservatism, casteism, religious and joint family system.

6. CONCLUSION:-On the basis of the present study the following suggestions we have been put forwarded for the

upliftment of the socio-economic conditions of the

Mayamara sect. Fishing and fish trade is the traditional occupation of the study area. So, the rivers, beels and wetlands should be preserved by the Govt. for socio economic upliftment of the society. Most of the families rearing livestock i.e. cow, goat, duck, hen etc. But they are very few to maintain a family. So, they should provide Govt. loan for farming like dairy, poultry, fishery etc. Women education is very poor in higher level because of married below the legal minimum age. So, the Govt should take steps to control such type of marriages through child marriage restriction act. The social institutions like joint family system, religious beliefs, customs and the unproductive nature of the business should be refined for their upliftment. The Kaibartas should be given self-employment training courses free of cost by the Govt. to provide subsidiary engagement. To get responsible prices, provisions should be made for the cold storages facilities, improvement of transport facilities, removing the role of middlemen and brokers. In our concluding remarks, we may say that the proper implementation of these suggestions by the Govt, NGOs, Gaon Panchayats, Mahila Samitees and active involvement of the community are required for changing socio-economic conditions in desired directions.

7. REFERENCE:

1. Bezboruah, D.K.: Socio-economic changes and Dimension of social mobility among the Kaibartas of Assam.
2. Bezboruah, D.K.: Socio economic condition of scheduled caste people of Assam with special reference to Nalbari district.
3. Bordoloi, B.N.: Socio economic condition of the Kaibartas of Assam, AIRTSC Vol
4. Bezboruah, D.K.: Brahamaputra Upatyakar Kaibarta Jatir Ruprekha, Published by Bhagaban ch. Das.
5. Nath, D: The Majuli Island Society, Economy and Culture, Published by: ANSHAH PUBLISHING HOUSE, Delhi
6. Borah, . Rupjyoti: "Demographic Profile of Adis". Publish by department of Economics, Dibrugarh University.
7. 7. Shyam, Suprity : "Fertility Behaviour of the Konyak Nagas of Assam".
8. Mahanta, P. K. : "Majuli", Published by Manoj kr. Goswami and Anjali P. Goswami, A. T. Road, Tarajan, Jorhat.
9. Kothari, C. R.: "Research Methodology", 1985. Published by New Age International Pvt. Ltd. Ansari Road, New Delhi- 110002.

Changing Contours of Indian

Abstract- Morals are not uniform from person to person, societies to circumstances. Ethics are also governed by the coupled with Morality help behavior. Law is a body of rules are mandatorily obligated are the general principles define human conduct with. The liaison between Initially, both of them were time and liberalism, variations considered as diverse concepts -dependency between them the rule of law and moralities based upon social mo prepare is analytical in nature the role of Indian judiciary system through landmark contours of morals in law is

Key words: Law Morals
Introduction- Law and mo Societies. With the advent a spiritual foundation for were skeptical about relationship as according to them la different levels of practice school of jurisprudence a must be evolved to meet t velop new legal principles morality and are based up Legislators and judges do crafting laws and rendering influence their decisions. legal principles based on s Decision-making in the cou values because of its very law is morality, and this is from. According to *Del Vec* ethics and the moral subject

Physico-chemical Analysis of Crude Oil Contaminated Soil in and Around Dikom Oil Well of Assam

Borsha Tamuly^{1*} and L.R. Saikia²

¹Department of Botany, Jengraimukh College, Majuli 785 105, Assam, India

²Department of Life Sciences, Dibrugarh University, Dibrugarh 786 004, Assam, India

(Received 8 April, 2022; Accepted 22 June, 2022)

ABSTRACT

North eastern India holds a unique position in the oil map of India because it was the pioneer of Indian oil industry. Exploration, drilling, transportation and accidental spillage in oil field areas often lead to the tremendous effects on soil and water as well as vegetation. A study was conducted to determine the possible effects of crude oil drilling activities in the soil in and around oil well. Soil samples were collected using soil auger during summer and winter seasons at a depth of 0-15cm and a distance of 50m (point A), 100m (point B) and 150meters (point C) from oil spilled site. The soil parameters pH, electrical conductivity, moisture content, porosity, water holding capacity, available nitrogen, phosphorus and potassium were analyzed. The pH of the soil sample recorded from 4.36 to 5.29 in summer and 4.67 to 5.76 in winter season. Soil moisture content, WHC, porosity, EC, phosphorous content was lowest in point A compared to point B, point C and point D(control) in both the seasons. Soil organic carbon (OC), nitrogen, potassium content was recorded highest in point A, point B and point C compared to point D.

Key words: Crude oil, Vegetation, Accidental spillage, Tremendous.

Introduction

Soil is a life supporting system for plants, animals and microbes. Crude oil pollution has enormous detrimental influence on the environment and living organisms. The levels of N, P, K, organic and inorganic materials and conductivity are the main components of fertility status of soil Iram and Khan (2018). As a predominant energy resource crude oil is vital for human life and also serve as raw material for various petroleum products. Crude oil pollution in soil is a major environmental problem Dutta *et al.* (2017). Crude oil is known to diminish the availability of plant nutrient in soil Xu and Johnson (1997); Osuji *et al.* (2004); Tanne and Kinako (2008). However, during crude oil exploration a vast amount of drilling mud/fluid is generated which are deposited

on the land surface. These waste matters are often very unstable and become source of air, soil and water pollution. These may eventually lead to a loss of biodiversity, amenity and economic wealth Bradshaw (1993). Further, oil spillage, leakage and other release of petroleum occur frequently during its transportation and other activities that result in the contamination of cultivated soil and groundwater, especially when associated with accidental spills Prasad and Katiyar (2010). As crude oil is a mixture of hundreds of chemicals having different properties and toxicities, therefore it has significant impact on soil quality which also leads to the heavy disruption of ecological balance Holcomb (1970). Transportation of crude oil from point source to various components of the ecosystem is one of the major factors that jeopardize the well-being of the environment

*Corresponding author's email: borshatamuly@gmail.com

Sarma *et al.* (2016). The nature of oil spillage will depend on the local weather condition such as existence or non-existence of snow, drainage ability of soil and absorptive capacity of ground and local topography Greene *et al.* (1975); Sextone and Atlas (1977). Environmental pollution with crude oil is a common phenomenon associated with oil industries operating in Assam, India Baruah and Sarma (1993). Juxtaposition of oil field areas with agricultural field is predominant feature of the area.

Materials and Methods

The study was conducted in and around oil well at Dikom where accidental oil spillage has taken place. Dikom oil well was situated at midst of Dikom Tea Estate at 20 km from Dibrugarh, Assam. The area receives moderate to high rain fall, high relative humidity round the year. The sample taken at 50 metre, 100 metre and 150 metre distance from spilled point is demarcated as point A, point B and Point C respectively. Soil samples were collected at a depth of 0-15 cm by using soil augur. Three sub-samples were taken from each point and finally prepared a composite sample for the point by mixing the air-dried powder after sieving. The samples collected from the nearby point where the effect of oil spill remain nil is considered to be the control and demarcated as point D. Plant roots, pebbles and undesirable matters were removed from the soil samples and the samples were allowed to air dry in shade. The dried soil samples were crushed in mortar and pastel and sieved through 2 mm sieve following Devi and Dkhar (2014). The powdered samples were then stored in clean glass vials for further analysis. Soil moisture content, porosity and water holding capacity were determined using the method given by Pandey, Puri and Singh (1996). Soil pH was determined using a double electrode pH meter (digital pH meter 335, Systronic Co. Ltd.), EC on Elico conductivity bridge Jackson (1973), Organic carbon by colorimetric method Walkely and Black (1934). Available nitrogen (N) by the alkaline potassium permanganate ($KMnO_4$) method Subbiah and Asija (1956); available phosphorous by Bray and Kurtz (1945); available potassium by ammonium acetate method Hanway and Heidel, (1952).

Results and Discussion

Soil physico- chemical characteristics recorded un-

der crude oil contamination during summer and winter season are presented in Table 1 and Table 2 respectively. The soil moisture content was found to be less in point A (29.63%) than point B (31.32%), point C (40.56%) and point D (45.96%) of summer season. It indicates that soil was drier in highly polluted areas as compared to less polluted areas. Evidently oil penetration to the soil surface stops both upward and downward movements of water. Wein and Bliss (1973) reported that crude oil affected areas was drier than less affected areas. Porosity and WHC were less in point A (28.56%) (20.98%) respectively compared to point B (32.20%) (31.25%), point C (40.12%) (42.0%) and point D (46.20%) (43.69%) of summer season. Similarly, analysis of winter season soil sample resulted in less moisture content in point A (32.21%) compared to point B (42.10%), point C (56.31%) and point D (58.33%). The present investigation shows the reduction of porosity and water holding capacity in the order of point D (control) > point C (150 m distance from spilled point) > point B (100 m distance from spilled point) > Point A (50m distance from spilled point) in both summer and winter season.

The low soil moisture content in highly polluted site may be due to lower soil moisture recharge caused by hydrophobic nature of the polluted soil Rowell (1977) and De Jong (1980). The study revealed a decreasing trend with the increase of distance from spilled point, which may perhaps be attributed to seepage and leakage of formation water being rich in cations and anions.

pH value ranges from 5.29 to 4.36 in summer season and 5.76 to 4.67 in winter season (Fig. 1). Either very low or very high pH are not suitable for plant growth. The mobility of nutrients is affected by the value of soil pH. Soil nearby spilled point found to be more acidic compared to less polluted sites in

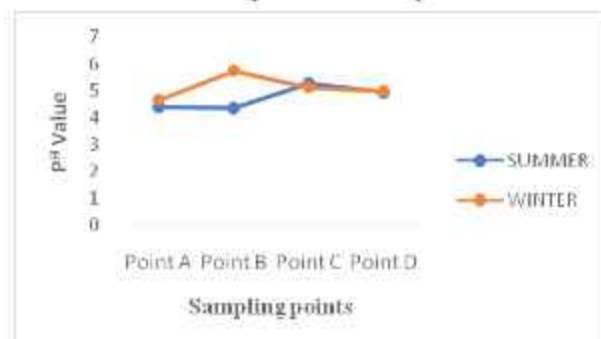


Fig. 1. pH of crude oil contaminated soil in both summer and winter season

Table 1. Physico-chemical characteristics of crude oil contaminated soil during summer

Sample points	Soil Moisture (%)	Porosity (%)	WHC (%)	pH	ECmS/cm	OC%	N (kg/ha)	P (kg/ha)	K (kg/ha)
Point A (50m)	29.63±.09	28.56±.11	20.98±.18	4.41±.25	.02±.01	1.92±.07	598.8±11.73	10.72±1.53	89.49±1.02
Point B (100m)	31.32±.12	32.20±.21	31.25±.19	4.36±.04	.04±.01	1.74±.21	552.4±10.3	20.55±2.45	78.20±1.45
Point C (150m)	40.56±.35	40.12±.14	42.0±.11	5.29±.08	.09±.01	1.72±.06	547.2±.96	21.03±2.26	75.29±1.09
Point D Control	45.96±.05	46.20±.09	43.69±.14	4.95±.05	.12±.10	1.67±.06	540.2±.79	29.3±.89	69.6±1.02

Mean ± SD of Mean

Table 2. Physico-chemical characteristics of crude oil contaminated soil during winter

Sample points	Soil Moisture	Porosity (%)	WHC (%)	pH	ECmS/cm	OC%	N (kg/ha)	P (kg/ha)	K (kg/ha)
Point A (50m)	32.21±.36	29.5±.27	18.20±1.25	4.67±.20	.10±.01	1.99±.07	613.5±1.12	10.72±.25	99.32±1.10
Point B (100m)	42.10±.78	34.2±.98	21.21±.24	5.76±.03	.01±.05	1.88±.21	585.5±1.15	19.66±.89	94.8±2.10
Point C (150m)	56.31±.34	40.12±.69	38.92±.69	5.14±.25	.01±.02	1.85±.24	569.8±.96	27.70±1.20	87.2±1.20
Point D Control	58.33±.68	48.29±.36	40.20±2.5	5.01±.36	.10±.02	1.81±.15	561.1±1.24	38.32±2.10	78.6±.63

Mean ± SD of Mean

both seasons. Alexander (1977) reported that hydrocarbons associated with crude oil are utilized by microbes which form organic acids. Thus, probably acid produced by hydrocarbon utilizing microbes reduce the pH level in polluted sites Nwachukwa and Ugoji (1995). EC content was recorded more in summer season compared to winter season (Fig. 2).

The present study reveals enhancement of soil parameters such as organic carbon, nitrogen, potassium in soil sample during winter season in comparison to summer season (Fig. 3, 4), which could be attributed by deposition of crude oil contaminated waste by monsoonal water to the associated soil system.

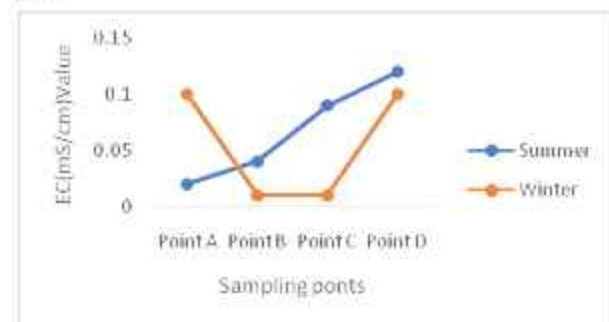


Fig. 2. EC of crude oil contaminated soil in both summer and winter season



Fig. 3. Organic carbon content of crude oil contaminated soil in both summer and winter season

Available nitrogen increases with increase of oil contamination in soil Udo and Fayemi (1975); Rao (1992). The increase amount of available nitrogen in oil degraded sites is due to fixation of more available nitrogen by microorganism which assimilated more hydrocarbons Schwendinger, (1968). Increase of crude oil level is directly proportional to increase in organic carbon Udo and Fayemi (1975).

Phosphorous level of the soil sample reduced in polluted sites compared to less polluted sites in both

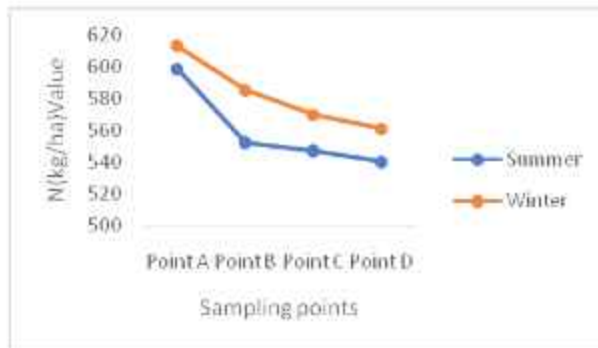


Fig. 4. Nitrogen content of crude oil contaminated soil in both summer and winter season

seasons (Fig. 5). Potassium was found to be high in point A (50m distance from spilled point) compared to Point B (100m distance from spilled point), Point C (150m distance from spilled point) respectively (Fig. 6). It may result due to leakage of saline effluent along with crude oil and therefore ionic concentration may build up more K^+ near spilled points.

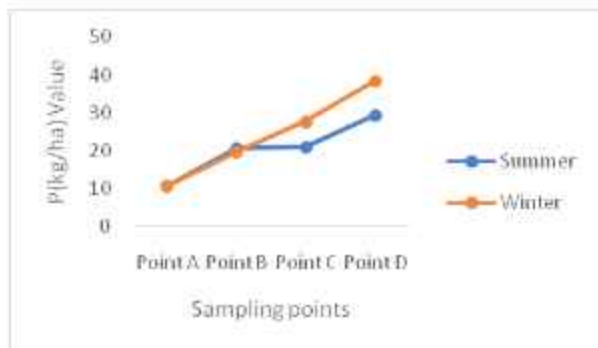


Fig. 5. Phosphorous content of crude oil contaminated soil in both summer and winter season

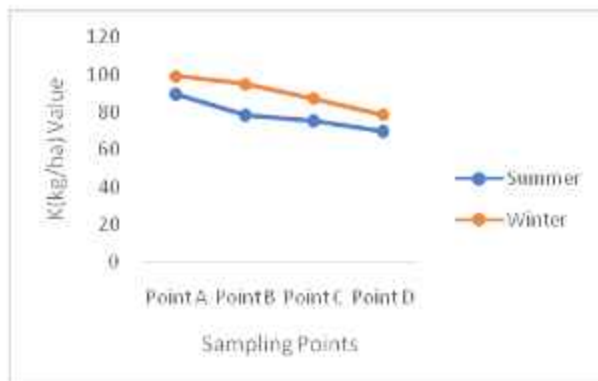


Fig. 6. Potassium content of crude oil contaminated soil in both summer and winter season

Conclusion

The analysis of physico-chemical characteristics of crude oil contaminated soil evidenced impact of oil drilling activities that lead to degradation of soil quality and destroys the equilibrium of plant growth promoting systems and producing long term consequences for sensitive plants like tea and paddy in and around oil spillage Sumithra *et al.* (2013). Thus, it has been observed that the unattended oil drilling activities in the area have contributed to the degradation of agricultural and grazing lands around the oil installations. As crude oil is a mixture of hundreds of chemicals (Polycyclic aromatic hydrocarbons and heavy metals), there is a possibility of bioaccumulation and their entry into the food chain. This is especially relevant in Assam since these oil field areas are mostly adjacent to tea gardens and rice field. This has given a strong foundation on environmental pollution caused by the developmental activities around the oil fields in Assam.

Acknowledgement

The authors are thankful to the Director, Central Muga Eri Research and Training Institute, Lahdoigarh, Jorhat, Assam, India for providing facility to carry out the work.

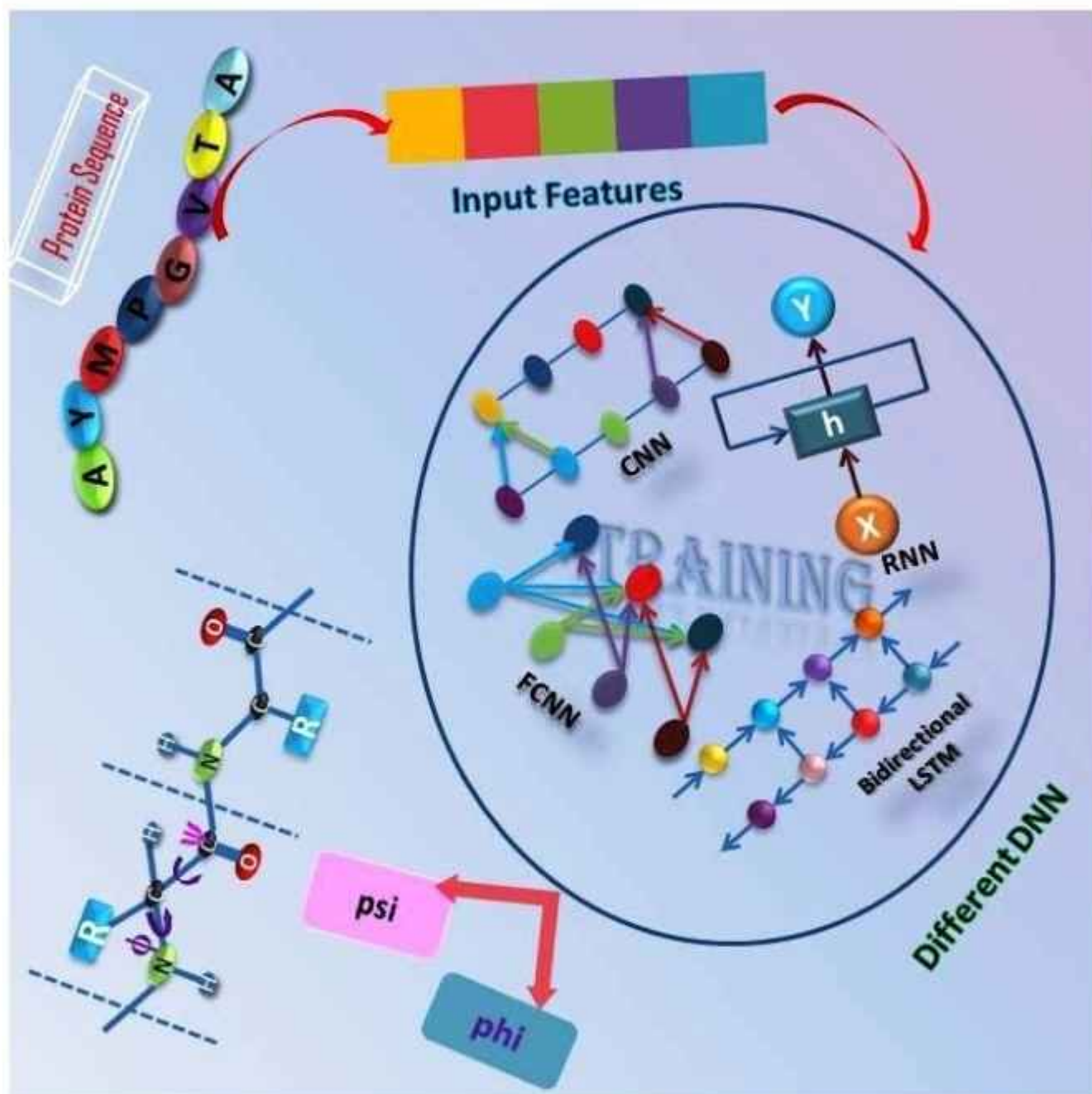
References

- Alexander, M.C. 1977. *Introduction to Soil Microbiology*. 2nd edition, John Wiley, New York. 25-40.
- Baruah, D. and Sarma, S. K. 1993. Distribution pattern of plant species as indicators of pollution stress conditions. *Journal of Ecotoxicology & Environmental Monitoring*. 3(2): 103-109.
- Bradshaw, A.D. 1993. Understanding the fundamentals of succession. In: *Primary Succession on Land*. (Miles, J. And Walton, D.H., Eds) Oxford, UK, Blackwell.
- Bray, R. H. and Kurtz, L. T. 1945. Determination of total, organic, and available forms of phosphorus in soils. *Soil Science*. 59(1): 39-46.
- De Jong, E. 1980. The effect of a crude oil spill on cereals. *Environmental Pollution Series A, Ecological and Biological*. 22(3): 187-196.
- Devi, H. R. and Dkhar, M. S. 2014. Comparative study on soil fungal diversity of Mawphlang sacred grove and disturbed forest North East India. *Ind. J. Sci. Res. Tech.* 2(5): 64-72.
- Dutta, M., Chanda, K. S., Bhuyan, M. and Kalita, S. 2017. Study on physico-chemical properties and heavy

- metal contents in crude oil contaminated soil of rudrasagar oil field, Assam, India. *J. Environ. Res. Develop.* 11(3): 2319-5983.
- Greene, G., Mackay, D. and Overall, J. 1975. Clean-Up after Territorial Oil Spills in the Arctic. *Arctic.* 28(2): 140-142.
- Hanway, J. J. and Heidel, H. 1952. Soil analysis methods as used in Iowa state college soil testing laboratory. *Iowa Agriculture.* 57: 1-31.
- Holcomb, R. W. 1970. Waste-water treatment: the tide is turning. *Science.* 169(3944): 457-459.
- Iram, A. and Khan, T. I. 2018. Analysis of Soil Quality Using Physico-Chemical Parameters with Special Emphasis on Fluoride from Selected Sites of Sawai Madhopur Tehsil, Rajasthan. *International Journal of Environmental Sciences & Natural Resources.* 12(5): 125-132.
- Jackson, M. L. 1973. Soil chemical analysis, pentice hall of India Pvt. Ltd., New Delhi, India, 498: 151-154.
- Nwachukwu, S. U. and Ugoji, E. O. 1995. Impacts of crude petroleum spills on microbial communities of tropical soils. *Int. J. Ecol. Environ. Sci.* 21: 169-176.
- Osuji, L. C., Adesiyun, S. O. and Obute, G. C. 2004. PostImpact Assessment of Oil Pollution in Agbada West Plain of Niger Delta, Nigeria: Field Reconnaissance and Total Extractable Hydrocarbon Content. *Chemistry & Biodiversity.* 1(10): 1569-1578.
- Pandey, S. C., Puri, G.S. and Shing, J.S. 1996. *Research Methods in Plant Ecology.* Asia publishing house, India.
- Prasad, M. N. V. and Katiyar, S. C. 2010. Drill cuttings and fluids of fossil fuel exploration in north-eastern India: environmental concern and mitigation options. *Current Science.* 98(12): 1566-1569.
- Rao, D. N. 1992. A report on preliminary survey of industrial pollution and its ecological impact in certain areas of Assam (Cyclostyled Report).
- Rowell, M.J. 1977. The effect of crude oil spill on soil- A review. In: *Reclamation of Agricultural Soils After Oil Spills*, part I: Eds. J.A. Toogood, 1-13. Edmotor, Deptt. of Soil Science, University of Alberta.
- Sarma, H., Islam, N. F., Borgohain, P., Sarma, A. and Prasad, M. N. V. 2016. Localization of polycyclic aromatic hydrocarbons and heavy metals in surface soil of Asia's oldest oil and gas drilling site in Assam, north-east India: implications for the bio-economy. *Emerging Contaminants.* 2(3): 119-127.
- Schwendinger, R. B. 1968. Reclamation of soil contaminated with oil. *J Inst Petrol.* 54: 182-197.
- Sexstone, A. J. and Atlas, R. M. 1977. Response of microbial populations in Arctic tundra soils to crude oil. *Canadian Journal of Microbiology.* 23(10): 1327-1333.
- Subbiah, B. V. and Asija, G. L. 1956. A rapid method for the estimation of nitrogen in soil. *Current Science.* 26: 259-260.
- Sumithra, S., Ankalaiah, C., Rao, D. and Yamuna, R. T. 2013. A case study on physico-chemical characteristics of soil around industrial and agricultural area of Yerraguntla, Kadapa district, AP, India. *Int. J. Geo. Earth and Environ. Sci.* 3(2): 28-34.
- Tanee, F. B. G. and Kinako, P. D. S. 2008. Comparative studies of biostimulation and phytoremediation in the mitigation of crude oil toxicity in tropical soil. *Journal of Applied Sciences and Environmental Management.* 12(2).
- Xu, J. G. and Johnson, R. L. 1997. Nitrogen dynamics in soils with different hydrocarbon contents planted to barley and field pea. *Canadian Journal of Soil Science.* 77(3): 453-458.
- Udo, E. J. and Fayemi, A. A. A. 1975. The effect of oil pollution of soil on germination, growth and nutrient uptake of corn (Vol. 4, No. 4, pp. 537-540). American Society of Agronomy, *Crop Science Society of America, and Soil Science Society of America.*
- Walkley, A. and Black, I. A. 1934. An examination of the Degtjareff method for determining soil organic matter, and a proposed modification of the chromic acid titration method. *Soil Science.* 37(1): 29-38.
- Wein, R. W. and Bliss, L. C. 1973. Experimental crude oil spills on arctic plant communities. *Journal of Applied Ecology.* 671-682.

Special
Issue

Protein Dihedral Angle Prediction: The State of the Art

Chimi Rekha Gogoi, Aziza Rahman, Bondeepa Saikia, and Anupaul Baruah^{*[a]}

The three dimensional native structure plays an important role in determining the function of a protein. However, structure determination is tedious and costly, so prediction of protein three dimensional structures is a very important as well as a challenging task in computational biophysics. Prediction of dihedral angle is particularly helpful for predicting tertiary structure of proteins as knowledge of backbone torsion angles significantly narrow down the conformational search space for tertiary structure prediction. Dihedral angles provide a detailed description of local conformation of a protein. With the

advancement of machine learning and other relevant techniques, dihedral angle prediction may establish itself as a fascinating supplement to secondary structure prediction. Over the last two decades, research in this direction has led to development of several dihedral angle prediction methods. In this article we critically review available methods for protein dihedral angle prediction with an emphasis on deep learning based real value angle prediction methods. We believe this review will provide important insights into the state of the art of protein dihedral angle prediction.

1. Introduction


Proteins are a class of biomacromolecules consisting of amino acids as building blocks. They are essential molecules inside every living organism and are in regulation of almost every process within cells. Proteins play vital roles in biological processes which include metabolic reactions, pathway regulation etc. and the biological functions of protein is closely related to its three dimensional native structure^[1-2] and The three dimensional structure of a protein is encoded in its amino acid sequence. Determination of three dimensional native structure of proteins is referred to as protein structure prediction (PSP) problem. X-ray crystallography, Electron microscope and Nuclear magnetic resonance are three currently available experimental techniques which can predict the three dimensional structure of proteins with accuracy.^[3] However rapid increase in the number of known protein sequences has by far outpaced the experimental determination of their structures and hence the gap between the known protein sequences and their predicted three dimensional structures is also becoming wide. Thus reliable and efficient computational techniques for protein structure prediction from its sequence to bridge the gap between sequence and structure are a need of the hour. In current scenario of the protein structure prediction, computational techniques are often used for prediction of the structure of proteins for which no experimental information is available. However direct prediction of protein three dimensional structure is a challenging task in computational field, henceforth the ultimate goal of tertiary structure prediction problem can be transformed into several sub-programs such as prediction of secondary structure states,^[4-7] solvent accessibility,^[8-9] backbone dihedral angle of proteins,^[10] super-secondary structures,^[11-13] etc. In the last three decades, with the development of machine learning algorithms as well as use of evolutionary information have resulted in a substantial improvement in accuracy of protein structure prediction. Recent advancement in Deep Learning

algorithms leads to tremendous advances in the field of protein structure prediction.

Very recently, Google's DeepMind team has developed AlphaFold2 which has made a gargantuan leap in the area of protein structure prediction.^[14] AlphaFold2 is the second iteration of AlphaFold that was developed in 2018 and it clearly shows the potential of deep learning in protein structure prediction. Deep learning methods become successful to overcome some limitations of traditional artificial neural network. Now a days, various deep learning based methods are employed for prediction of local and non local structural properties of proteins. Since, major goal of this article is to extensively review the deep learning based dihedral angle prediction, thus detailed discussion on deep learning based protein structure prediction is beyond the scope of this review. To gain better insights on advances in protein structure prediction readers may go through recently published review articles.^[15,16] Ongoing prodigious development in the field of deep neural network has also impacted the research area of protein angle prediction resulting in exciting improvement in the prediction accuracy of dihedral angle prediction of proteins.

In this review article, we are providing an exposition to the protein dihedral angle prediction giving emphasis on deep learning based methods. In the literature significant numbers of review articles on protein secondary structure prediction as well as protein structure prediction are found but to the best of our knowledge review article on protein dihedral angle prediction which covers most of the dihedral angle prediction methods based on deep learning is not available. In this article, first as a background, we provide a brief discussion on the evolution of the protein dihedral angle prediction methods. After that, the article elaborates upon the different training algorithms such as convolutional neural network, recurrent neural network, support vector machine and also defines the commonly used performance measures in protein dihedral angle prediction. Since selection of input features plays an important role in dihedral angle prediction, so this review also provides insights on commonly used input features in protein dihedral angle predictions. Next, a detailed discussion on the evolution of deep learning based protein dihedral angle prediction methods along with their comparative performance is provided. Finally the methods are critically analysed and probable future directions in this area of research in the light of present day advancement is discussed. Therefore, we believe

[a] C. R. Gogoi, A. Rahman, B. Saikia, Dr. A. Baruah
Department of Chemistry, Dibrugarh University, Dibrugarh, Assam, India
E-mail: anupaulbaruah@dibru.ac.in

 Part of a joint Special Collection between EurJOC, EurJIC and ChemistrySelect in celebration of "100 years of University of Delhi".

this article will be informative and provide important insights to the readers.

1.1. Backbone Dihedral Angle of Proteins

There is a high correlation between protein dihedral angle and secondary structure, especially helical and sheet structure of proteins.^[7] Also there exists a strong correlation between the dihedral states of a particular residue and its immediate neighbours in the sequence which serves to precisely define the local ordering/confirmation in proteins. But secondary structure is a coarse grain description of the local backbone structure and boundary between different secondary structure states are arbitrarily defined. This arbitrariness leads to the development of backbone dihedral angle prediction either in discontinuous and continuous real values. One drawback associated with secondary structure prediction of proteins is that it does not distinguish one loop conformation from another one. However backbone dihedral angles accurately provide the local structural information that ultimately aids to define highly variable loop regions in a primary sequence.

Amino acids are the building blocks of proteins and each amino acid contains N, C_α and C atoms along with others atoms. A protein may have any of the 20 amino acids in any

order and any number subject to stoichiometric constraints and in a protein chain C and N atoms of every two consecutive amino acids form the peptide bond which is the backbone of that protein. Dihedral angles are the rotation angles of specific bonds on the protein backbone and for each amino acid there are three types of dihedral angles. Omega (ω) is the angle of rotation around the peptide bond and since ω angles are restricted to 180° (major cases) or 0° due to rigid planar peptide bonds,^[8] other two dihedral angles phi (φ), the angle of rotation between N and the C_α atom and psi (ψ), the angle of rotation between the C=O and the C_α atom basically define the overall backbone structure. Contrary to ω which does not show flexibility, φ and ψ angles can take different values and these are therefore the internal liberty angles of a protein and in control of protein conformation. A schematic representation of angles phi (φ) and psi (ψ) given in Figure 1. In addition to its application as substitute for secondary structure prediction,^[9–20] dihedral angle prediction benefits protein structure prediction from several aspects which includes generation of multiple sequence alignment^[21] fragment-free tertiary structure prediction,^[22] identification of protein folds.^[23–25] Moreover, prediction of dihedral angle may narrow the gap between sequences and structure alignment by refine multiple sequence



Dr. Anupaul Baruah was born in Sivasagar, Assam, India. He received his B.Sc. from Hindu College, University of Delhi and his M.Sc. and Ph.D. from University of Delhi, India. He is currently serving as an Assistant Professor at Department of Chemistry, Dibrugarh University since 2016. His area of interest includes:

- *In silico protein design.*
- *Application of machine learning/deep learning approaches to biophysics and chemistry.*
- *Study of protein-ligand and protein-protein interaction.*
- *Protein folding, misfolding, disorder, fold switch and allostery.*
- *Sequence Analysis.*
- *Coarse-grained Modelling and Potential Development.*



Chimi Rekha Gogoi received her M.Sc in Chemistry from Dibrugarh University. At present she is pursuing her Ph.D. at Dibrugarh University, Assam, India. Her research interest lies in protein structure prediction and protein design.



Aziza Rahman was born in Dibrugarh, Assam, India. She received her M.Sc in Chemistry from Cotton University in 2018. At present she is pursuing her Ph.D. at Dibrugarh University, Assam, India. Her research interest lies in protein misfolding and related neurodegenerative diseases.



Bondeepa Saikia was born in Dibrugarh, Assam, India. She received her M.Sc in Chemistry from Dibrugarh University in 2018. At present she is pursuing her Ph.D. at Dibrugarh University, Assam, India. Her research interest lies in in silico protein design.

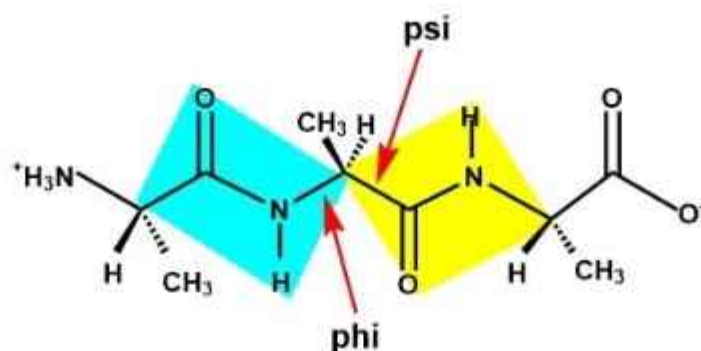


Figure 1. Schematic representation of Phi and Psi angles.

alignment, thereby helping de novo prediction of structural properties.

Backbone dihedral angles of a protein reduce the conformational search space for its tertiary structure prediction to a significant level. So dihedral angle prediction particularly helps in predicting tertiary structure of proteins.^[76] Also protein dihedral angle prediction informations are useful in fold recognition,^[77–28] improvement in protein secondary structure prediction,^[79] protein sequence modelling as well as in sequence alignment.

2. Background

Dihedral angles have acted as compact descriptions of a protein backbone's local topology for over 50 years.^[30] Therefore it may appear surprising that methods for predicting secondary structure of proteins predate those for dihedral angles by more than two decades and that dihedral angle prediction is still relatively less well known and implemented compared to secondary structure prediction. One reason for the comparatively late introduction of methods to predict dihedral angles may be that secondary structure prediction of protein is a classification task, whereas dihedral angle prediction is a regression task which is considered more difficult than classification in high dimensional spaces. The aim of the methods which were developed initially for protein dihedral angle predictions is to predict few discrete states based on their distribution in Ramachandran plot.^[31–35] Experimental procedures to determine protein dihedral angle prediction is manually intensive and very time consuming. Over the time, development of efficient algorithms accelerated the determination of protein dihedral angles. SHIFTOR is a program which can predict accurately a large number of protein torsion angles.^[36] This program uses ^1H , ^{13}C and ^{15}N chemical shift as input. Same lab developed another web server PREDITOR^[37] for torsional angle prediction of proteins. Combining the sequence information and chemical shift data this method predicts torsional angle of proteins.

In the course of time, a considerable number of methods have been developed for prediction of angles in continuous values and discrete states. A Hidden Markov Model HMMSTER reported in the year 2000 was used for prediction of backbone

angles of proteins in discrete classes.^[37] This method was successful to predict dihedral angles with a significant accuracy. Another method for prediction of backbone angles in discrete classes was reported in 2004.^[38] This method used a machine learning based approaches. In literature there are some methods for angle region predictions and these methods used different definition of basins.^[31,39] Specific region in a Ramachandran plot is referred to as a Ramachandran basin. Each angle pair (φ, ψ) of a residue is assigned a basin label. One important point is that if the number of basins increases, assigning basin label to a residue becomes harder. In a study by Gong et al. reported in 2005, they partitioned φ, ψ -space into 36 basins. Each basin is of size $60^\circ \times 60^\circ$, and from these mesostate (basin label) sequences alone, they are successful to reconstructed six proteins.^[40] Olav Zimmermann and Ulrich H. E. Hansmann in 2006 presented a multi-step support vector machine (SVM) procedure known as Dihedral Prediction (DHPRED) to predict the dihedral angle states of residues from sequences.^[31] Continuous, real value prediction of dihedral angles of proteins is more advantageous compared to prediction of a few states.

Continuous, real value prediction can provide high resolution description of protein backbone. Also it removes the arbitrariness of defining boundaries between discrete states. For real value prediction of dihedral angle ψ , Wood et al. first proposed a method based on machine learning in 2005, prediction results obtained are further used for prediction of the protein secondary structure with high accuracy.^[19] For real value prediction of phi and psi dihedral angle different methods such as Real-SPINE,^[41] ANGLOR^[42] and TANGLE^[43] were developed later. Real-SPINE was further developed to Real-SPINE2.0 as first method to predict both phi and psi angles using neural network.^[44] The prediction was further enhanced in the following methods: Real-SPINE 2.0,^[44] SPINE X and SPINE XI.^[45] Real-SPINE 3.0^[46] used a guided-learning mechanism to training a two-layer neural network. Wu et. al developed a method ANGLOR based on neural networks to predict phi angle and support vector machines to predict psi angle separately.^[47] TANGLE used a two-level SVM based regression approach to make prediction.^[43] In 2015, a new method was introduced SPIDER2.^[48] This method was improved from

SPIDER^[78] through iterative learning. State of the art methods of protein dihedral angle prediction mainly utilize deep neural networks and their complex variants.

3. Different Methods for Dihedral Angle Prediction of Protein

Although the dihedral angle prediction is comparatively a new idea, but with the growth in PDB database and computational and algorithmic advancement in machine learning it has picked up a notable progress to date. Most of the methods for prediction of protein dihedral angle available in literature are mainly based on supervised machine learning algorithm such as Support Vector Machines (SVM),^[31,43] Artificial Neural Networks (ANN),^[44,45] In recent years deep neural network based methods and its complex variants such as stacked sparse auto-encoder neural networks,^[46] long short-term memory (LSTM)^[50], bidirectional recurrent neural networks (BRNNs)^[51] and Residual Networks (ResNets)^[52] and their ensembles or layered iterations are mostly employed in state of the art methods of prediction of dihedral angles.

3.1. Commonly Used Training Algorithm

In this section a brief outline of the different commonly used machine learning/deep learning based algorithms used in protein dihedral angle prediction is presented. However, it is beyond the scope of this review to include detailed discussion of deep learning algorithms. Therefore we refer to some of the existing reviews for more information on different deep learning algorithms.^[53,54,55]

3.1.1. Artificial Neural Network

Artificial neural networks (ANNs) are computing networks inspired by the biological neural networks and they are analogous to biological neural systems in some basic characteristics. In the last two decades different types of ANN have been developed. Depending on their learning process two main types of ANN can be easily recognised, one is supervised learning and second is unsupervised learning. Supervised learning is a dependent process. Input is first presented to the network which generates the output. This output is then compared with the target/actual output. Based on their difference between the two outputs error signal is generated. Artificial neural network^[56] is comprised of input layer, one or more hidden layers and final output layers. The schematic representation of ANN is depicted in Figure 2. In ANN each neuron is connected to one another and each connection is associated with a weight ANN is connected to one another and a weight and threshold. Learning of an ANN takes place by alternating the weights. Simplest form of ANN is feed forward neural network where information are processed unidirectionally. In this simplest ANN, inputs are produced to the layer and then it is multiplied with the weights, followed by addition of each value to get a sum of the weighted input values. Node or a neuron of a layer is called activated if the output value of

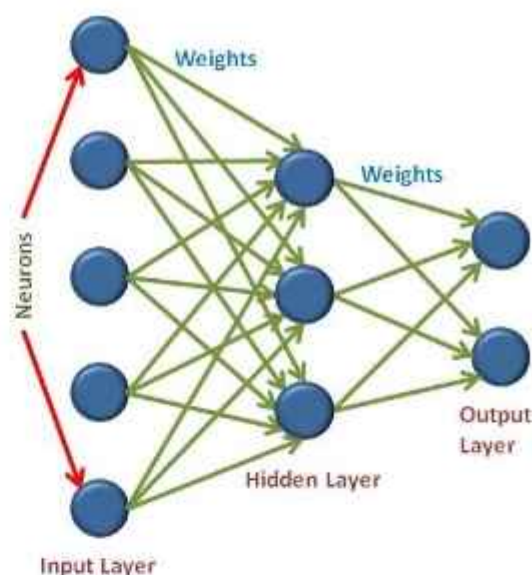


Figure 2. schematic representation of a artificial neural Network with one input layer, one hidden layer and one output layer.

that neuron is above a specific threshold value and then the data is passed to the next layer of the network. Although information in this particular ANN can move through multiple hidden nodes but it can never process the information in backward direction.

ANN have widely been employed in predicting different structural properties of proteins. Deep neural networks referring to artificial neural networks with more than two hidden layers, have widely been explored in prediction of local and nonlocal structural properties of proteins.

3.1.1.1. Convolutional Neural Network

Convolutional Neural Network^[57] is a type of artificial neural network, most commonly applied in image recognition and classification. This architecture mainly consists of two layers, one is convolution and second one is pooling. The schematic representation of CNN architecture is presented in Figure 3. Convolution operation of CNN extracts the complex features from inputs and generates the feature maps. Then pooling operation works on this feature maps. The input of a CNN is represented as a matrix and a kernel is used to scan the input matrix. The kernel which is a submatrix of the input is also known as filter or feature detector. The number of pixels that the kernel moves at each step is known as stride. Smaller stride value can retain more information to the next layer but if the stride value is large then it reduces the output size. Another important hyperparameter to be optimized in CNN architecture is type of padding. Padding in a CNN gives the idea on how the border of an image is handled. After generation of feature map by convolution operation, pooling operation then works on it. This operation then reduces the output size by aggregating the sub-matrix values from the feature map to

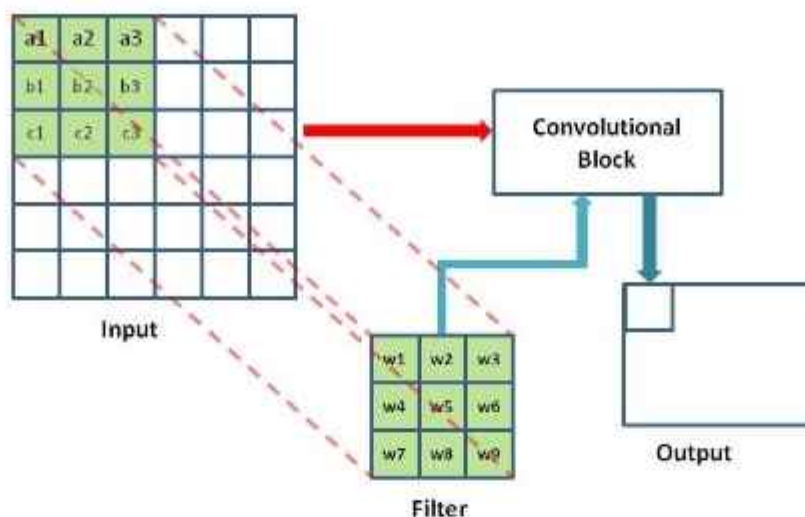


Figure 3. Block diagram of convolution process convolution layer.

single values. Pooling operation can speed up the CNN architecture as well as reduces its complexity. Another advantage of CNN is that it can handle input data of variable size. In recent times different types of CNN having huge networks containing architectural variants are in use. Resnet^[57] is one such kind of architecture that made great contribution to the development of protein bioinformatics. This CNN architecture is found to be used in protein dihedral angle prediction to achieve significant improvement in prediction accuracy.^[58]

3.1.1.2. Recurrent Neural Network

Recurrent Neural Network (RNN) is a class of deep neural network having wide applicability in processing sequential data. Standard RNNs consists of hidden layers where neurons

are recurrently connected.^[59] This neural network is a powerful one as it has internal memory unlike feed forward neural network. From input layer to output layer through hidden layers information moves in only one direction in feed forward neural network. But recurrent neural network considers current (present time step) input as well as information from output of the previous time step. This information cycles in a loop through the same hidden layer of neurons (represented by **h** in Figure 4) for a specific number of time steps. In case of feed forward neural network a weight matrix is assigned to the inputs whereas in RNN, weight is assigned not only to the current input (represented as **A** in both Figure 4 and 5) but also the previous output (represented as **B** in both Figure 4 and 5). In the last decade different variants of RNN such as Long short term memory (LSTM)^[50] Bidirectional Recurrent Neural Network (BRNN)^[51] etc. are used in different areas of bioinformatics^[60]

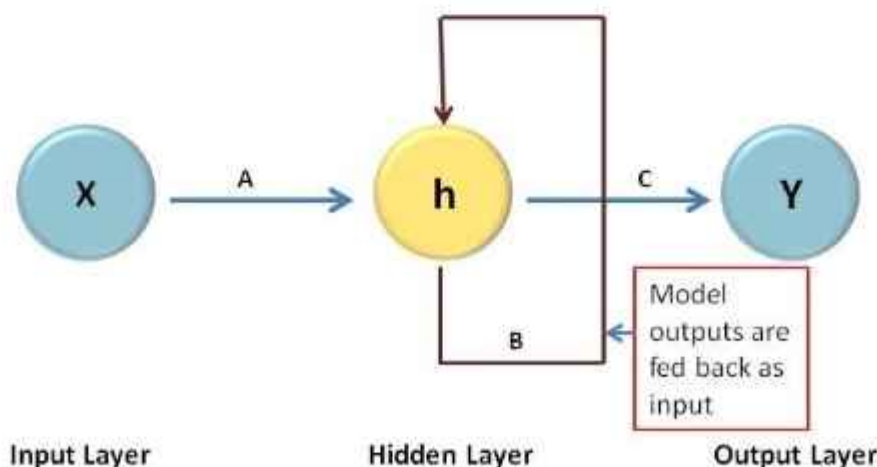


Figure 4. Diagram showing information flow in RNN. Here X = input layer, h = hidden layer, Y = output layer. A, B, and C are the network parameters (weights) used to improve the output of the model.

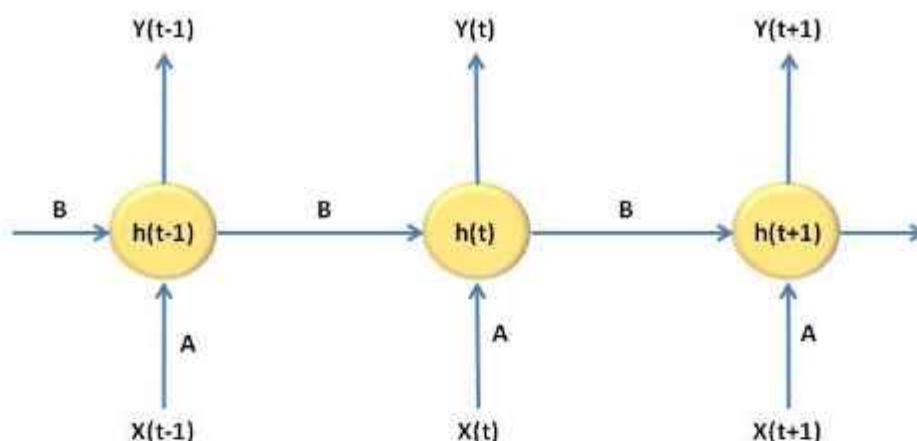


Figure 5. Unfolded view of RNN. Here $h(t)$ = New hidden state, $h(t-1)$ = old state, $x(t)$ = input vector at time t .

including protein structure prediction as well as protein angle prediction to achieve significantly improved performance. Recurrent neural network LSTM and BRNN can effectively capture the long range interactions. Vanishing gradient and exploding gradient are two major issues associated with RNN. The issue of vanishing gradient can be addressed by LSTM which is an extension of RNN.

Generally RNN has a short memory, but LSTM^[60] can remember the information for a longer period of time. BRNN which is another variant of RNN uses two recurrent neural nets to train the sequence in forward and backward directions. Both these recurrent nets are connected to the output layer and thus the output layer gets information from both past and future states. One advantage of BRNN is that it does not require input data to be fixed and it has the complete sequential information of all points before and after a particular point in a sequence. In recent years a novel architecture named Transformer^[61] is developed that contains encoder-decoder architecture. In case of Natural language processing(NLP), this new architecture exhibits better performance compared to BRNN. Introducing this approach some of the protein structure prediction methods have achieved improved results.^[62]

3.1.2. Support Vector Machines

Besides these deep learning based approaches, some studies related to protein structure prediction use machine learning technique such as Support Vector Machines (SVM). SVM is an algorithm based on statistical learning theory for classification as well as regression problems^[63] In SVM, input vectors are first mapped into feature space either linearly or non-linearly. Kernel function of SVM takes data as input and then transforms the input into required form of processing data. Selection of kernel function depends on input feature space. Proper selection of kernel function is crucial for obtaining good results. To find out the correct kernel function extensive search has to be conducted on the feature space and this often makes the process laborious and complex. In the second step a hyper-plane has to be constructed within the feature space to

separate the classes (either to two or many-classes) with minimal margin and least error. SVM can handle a large number of features as its training process always seeks global optimized solution and avoids overfitting. Sparseness of the solution and absence of local minima are significant characteristics of SVM.^[64]

3.2. Commonly Used Input Information

Most popular input feature used in almost all existing dihedral angle prediction approaches is Position Specific Scoring Matrix (PSSM).^[18,48,65] Other very commonly used input features in dihedral angle prediction of proteins are physico-chemical properties,^[18,66] predicted accessible surface area, hidden markov model(HMM) profiles^[67] etc. Surface area of a amino acid residue which is accessible by solvent is referred to as accessible surface area. Predicted or known Secondary structure of amino acid residues is also one of the important input features in angle prediction of proteins. Secondary structure of a protein is the local conformations of protein backbone which are stabilized by intramolecular or sometimes intermolecular hydrogen bonding. α -helix (H) and β -strand (E) are two main types of secondary structures. Amino acids of a protein which are not included in any of these two class of secondary structures are categorized as coil structure.^[68] But DSSP (Define Secondary Structure of Proteins), an algorithm developed by Kabsch and Sander^[69] classifies secondary structure of proteins into 8 states :H (α -helix), G (3-10-helix), I (n -helix), E (β -strand), B (isolated β -bridge), T (turn), S(bend), and C (others). In Real-SPINE three state secondary structures of residues of the protein sequence from DSSP are used for training, while for testing, the predicted secondary structures from SPINE are used.^[70]

3.2.1. Position-Specific Scoring Matrix (PSSM)

Position Specific Scoring Matrix is $N \times 20$ matrix which represents the probability of 20 amino acids in a specific position of a residue in the protein sequence. N corresponds to the

number of amino acid residues in the protein chain. This PSSM is obtained from PSI-BLAST using multiple sequence alignment^[69] and from PSSM we get important evolutionary information regarding the structure of the protein. PSSM obtained is transformed by applying the sigmoid function $\frac{1}{1+e^{-x}}$ where, x represents the PSSM entry.

3.2.2. Physicochemical Properties

Physicochemical properties of amino acids influence the structure of the proteins. So it can be used as important input information in protein dihedral angle prediction. Although the number of features that can be utilized for angle prediction is large, researchers generally use subset of these parameters. Steric parameter (graph shape index), volume, hydrophobicity, isoelectric point, polarisability, helix probability and sheet probability are the seven representative physico-chemical properties most frequently employed in protein angle prediction methods as input information.

3.2.3. HMM Profile

Like PSSM, HMM profiles also provide evolutionary information about the protein structure. Different methods developed for protein dihedral angle prediction use HMM profile as input features which is generated using HHBlits.^[77] HMM profiles establish a relationship of query sequence to statistical description of a family of sequences. In sequence based prediction of some evolutionarily conserved properties such as tertiary structure of protein, multiple sequence alignments (MSAs) are considered as an important intermediate step. HMM profiles can be called the condensed representation of MSAs. HMM profile of a protein sequence represents the probability of observing each of the 20 amino acids for each position of the sequence in evolutionary related proteins.

3.3. Commonly Used Performance Measures

In case of real value prediction of protein dihedral angle which is a regression problem generally Pearson Correlation coefficient (PCC) and Mean Absolute Error (MAE) are used to measure the prediction performance. PCC is calculated using Equation (1)

$$PCC = \frac{\sum_{i=1}^N (x_{obs} - \bar{x}_{obs})(x_{pred} - \bar{x}_{pred})}{\sqrt{\sum_{i=1}^N (x_{obs} - \bar{x}_{obs})^2} \times \sqrt{\sum_{i=1}^N (x_{pred} - \bar{x}_{pred})^2}} \quad (1)$$

Here, x_{obs} and x_{pred} are observed and predicted angle. Similarly \bar{x}_{pred} and \bar{x}_{obs} represent the mean of the predicted and observed angle respectively. Similarly, MAE can be calculated as shown in Equation (2)

$$MAE = \frac{1}{N} \sum_i \min(|x_{obs} - x_{pred}|, |360^\circ - (x_{obs} - x_{pred})|) \quad (2)$$

Although PCC is the performance measure for linear regression problems, considering the uneven distribution and cyclic nature of dihedral angle of proteins MAE is the robust and frequently used measure in dihedral angle prediction. N state performance accuracy Q_n is also used in some cases to represent prediction results of angle prediction.

4. Prediction of Real Value of Dihedral Angles

Protein dihedral prediction is performed in two ways: a) as a classification problem (binning) and b) as a regression problem (real value prediction). However, most state of the art methods focus on real value prediction of dihedral angles. Therefore, in this review we highlight the methods developed using different neural network and its complex variants for prediction of real value of dihedral angles.

The first work on real value prediction of a dihedral angle was reported in 2005 by Wood and Hirst^[79] which can be considered as the by-product of dihedral angle enhanced secondary structure prediction in their new approach DESTRUCT. In this method an iterative set of cascade-correlation neural networks is used to predict secondary structure of protein as well as dihedral angle. Cascade-Correlation is an architecture and supervised learning algorithm for artificial neural networks.^[79] This architecture begins with a minimal network, then automatically trains and adds new hidden units one at a time, resulting a multi-layer structure. Cascade-Correlation neural network attempts to resolve the slowness of existing learning algorithm such as back-propagation by addressing the two main cause of this slow learning speed: "step size" and "moving target". DESTRUCT method which is based on several generations on cascade-correlation networks were trained on a dataset of 513 proteins (CB513^[76]) to achieve three-state accuracy (Q_3) of 79.4% and Pearson Correlation Coefficient 0.47 for protein secondary structure prediction and protein backbone dihedral angle prediction respectively. For angle prediction this method used PSSMs of 513 proteins along with the output of a secondary structure prediction network as input and vice versa. In spite of the fact that the predictive accuracy is not so significant (a moderate PCC), but it contains adequate additional information to enhance the secondary structure prediction.

Zhou and his group^[81] in 2007 reported an integrated system of neural network called Real-SPINE. This method is the first method dedicated to real value ψ angle prediction and unlike DESTRUCT it predicts ψ only. This method uses a 10-fold cross validation on non redundant dataset of 2640 proteins with sequence identity less than 25% and X-ray resolution lower than 3Å available from protein data bank. The dataset used in this method is much larger compared to that used in the earlier method DESTRUCT. Also it yields a much better

correlation coefficient of 0.62 for dihedral angles as compared to the value obtained from DESTRUCT. The Neural network used in this work is back-propagation neural network with sigmoid activation function. In Real-SPINE prediction is made from two separate predictors, each comprising of one hidden layer with 200 hidden layer nodes. Using linear normalization, all input and output values were normalized for each network. For a given structural property, initially weights are generated by using random number generators and iteratively optimized to maximize Pearson's correlation coefficient (PCC) between predicted and actual values. Final prediction result is the average of the prediction results obtained from both the predictors. For dihedral angle prediction the model is trained independently and its inputs were PSI-BLAST generated PSSMs and SS predictions from SPINE. Real-SPINE inputted with predicted secondary structures attains a PCC value of 0.619 and MAE of 0.150 for normalized dihedral angles, while in the absence of secondary structures, the corresponding PCC and MAE values are 0.611 and 0.175, respectively. This result indicates that accuracy measured by PCC and MAE is improved noticeably with the information of secondary structures, thereby emphasizing the large effect of this additional input. Further, the prediction accuracy increased to 0.735 from 0.619 when known secondary structures from the DSSP program were used as input instead of predicted secondary structures. In this work the MAE for angle prediction is also analysed separately for different secondary structures and found that dihedral angle for residues in helix structure are more accurately predicted than those of coil and sheet structures. MAE values for angle of helix residues and sheet residues are found to be 0.092 (~33°) and 0.097 (~35°), but that of coil residues is much larger 0.23 (~83°). This method makes a relatively poor prediction for the angle around 0°. In fact, its accuracy between -36° and 36° is even lower than the accuracy by random prediction. The poor performance near 0° can be attributed to the angle periodicity because a prediction of 360° should be perfect for an actual angle of 0°, rather than an error of 360°. Angle transformation of Real-SPINE placed an ample amount of angles near the edges of neural network prediction range where it becomes very difficult for the neural network to predict at the edges (due to the shape of sigmoid function). This is another another reason for the low prediction accuracy near 0°.

In 2008, same group reported another method: Real-SPINE2.0^[44] with an objective to improve the prediction of ψ by reducing the impact of angle periodicity and to apply the new method to predict φ angle. Moreover, it is the first sequence-based method that predicts the real values of both φ and ψ angle. In the earlier method Real-SPINE the ψ dihedral angles in between 0° and -180° are changed to angle 0° to 360° by adding 360 to the angles in between 0° and -180°, keeping the ψ dihedral angles in the range 0° to 180° unchanged. This conversion of angles increases the population at 0° which leads to the poor accuracy of the prediction of the ψ angle prediction in Real-SPINE. Based on the distribution of ψ angles obtained from the protein set used in their earlier method, a simple angle shifting is performed to decrease angle periodicity

at 0° (or at 360°). In the ψ angle distribution plot, number of residues with $\psi \sim -100^\circ$ is seen to be lowest. So ψ angles are converted by adding 100 to the angles in the range -100° to 180° and and 460 to the angles in the range -100° to -180° respectively. This simple shift in ψ angle leads to a considerable improvement in ψ angle prediction. In case of φ angle lowest probability of angles occurs at $\sim 10^\circ$. Based on this distribution φ angles are converted to angles in between 0° and 360°. In this method, 10-fold cross-validated correlation coefficient between predicted and actual ψ angles obtained a marked improvement to 0.75 over 0.62 (given by Real-SPINE). Similarly, 10-fold cross-validated correlation coefficient between predicted and actual φ angle is found to be 0.71. Meanwhile MAE for ψ prediction reduced to 38° from 54° and MAE for φ prediction is reported as 25°. Using a consensus of 5 NN models in place of two predictor based consensus slight increase in angle prediction accuracy is observed. The accuracy of angle prediction increases slightly by expanding a two-predictor based consensus to a five-predictor-based consensus (1° in MAE and 0.005 in correlation coefficient).

After one year, in 2009^[45] the group reported a method to obtain better result of prediction by using a guiding technique for Neural Network weight and adding a second hidden layer. Application of most of the methods available at that time which are developed for improvement of backpropagation algorithm of neural network is limited only to small neural network. In backpropagation algorithm, errors are minimized by updating the model parameters while performing a backward pass. Although backpropagation algorithm has shown significant success in prediction accuracy, it often leads to local minima. However this guided technique for neural network has overcome this limitation and it can be applied to neural network of any size. The prediction results of this method have shown consistent improvement. Moreover a two layer neural network with bipolar activation function is found to be more effective in improving the prediction of ψ angle. But they have reported one interesting point that the correlation coefficient for φ angle prediction is less than that obtained from the earlier method Real-SPINE 2.0. This is due to the fact that correlation coefficient is calculated between shifted φ angles in Real-SPINE 2.0, whereas this new method used unshifted angle. Angle shifting is performed in the same way as the earlier method. On the basis of a 10 fold cross validation, prediction accuracy is reported.

ANGLOR^[47] is a composite prediction tool based on both Neural Network and SVM developed by Wu and Zhang aiming further improvement of φ and ψ prediction accuracy. Although SVM requires longer training time it has the advantage of identifying the global minimum and it can avoid the problem of local minima. Neural Network trains its parameters based on local minima. In order to find out the efficiency of the training technique both NN and SVM were tested for both φ and ψ angle prediction. Two softwares, Fast Artificial Neural Network software (FANN)^[75] and LIBSVM^[64] is used for NN and SVM respectively. MAE of φ angle prediction obtained by NN method is 10% less than that by SVM. But reverse is true for ψ angle prediction. In case of ψ prediction SVM shows better

results than NN. Average performance of the ANGLOR dihedral angle predictions has been tested on a large non-homologous set of proteins. The mean absolute errors, MAE, for all the residues are found to be 28.2° and 46.4° for phi and psi respectively. Comparing their method with SPINE, they reported that overall, ANGLOR has a clearly higher accuracy (with MAE=46.4°) than SPINE. The better performance of ANGLOR may be due to the optimized combination of both NN and SVM training techniques and the more training features. Same study has shown that different amino acids have different degrees of freedoms in the backbone torsion angles due to the various steric collision effects of side-chain with backbone atoms. This leads to much lower prediction accuracy of ANGLOR for some flexible amino acids than others. For example, MAE for both phi/psi of Glycine is 75°/67° and Proline has MAE of 60° whereas some other residues (ILE, LEU, PRO, VAL) have far more accurate value than the average. Since Glycine has no side chain except a proton, it has least steric restriction to the backbone dihedral angle motion and therefore it possesses higher angle entropy than the other 19 amino acids. This work also studied MAE of φ and ψ angle prediction for buried and exposed residues. Buried residues have relative solvent accessible area less than 25% and other residues are included in the category of exposed residues. MAE for buried residues is found to be 29% and 20% lower for φ and ψ angle respectively than the exposed residues. This lower value of MAE for buried residues can be attributed to low angle entropy of buried residues than that of the exposed ones. Like the earlier work in Real SPINE this method also reveals that the MAE value of angle prediction is larger for coil regions than for regular secondary structure regions. Another similar approach like ANGLOR is TANGLE (Torsional Angle)^[43] but it uses two level support vector regression in cascade with additional input features. In the first level of SVR in this method, all the sequence derived features are used as input to get the output which is initially predicted torsional angle. The second level of SVR accepts the initially predicted torsional angles to output the final refined torsional angles. Support Vector Regression is a supervised machine learning algorithm for real value prediction task which uses same principle as support vector machines. SVR with their generalization capacities behaves very well while dealing with high dimensional noisy data than other statistical and machine learning methods. The input features used by TANGLE include multiple sequence alignment profiles obtained from the position-specific scoring matrix (PSSM), predicted secondary structure, predicted solvent accessibility and predicted native disorder information along with other global sequence information such as amino acid contents, sequence length and sequence weight. Multiple sequence alignment profiles obtained from the position-specific scoring matrix (PSSM), predicted secondary structure, predicted solvent accessibility were used as input features in ANGLOR also. This new method is evaluated on large dataset of non-homologous proteins and found the mean absolute errors (MAEs) 27.8° for φ and 44.6° for ψ , which are respectively 1% and 3% lower than that obtained by using prediction tools ANGLOR. Similar to the earlier method ANGLOR, this method also reveals that the MAE

value for φ and ψ prediction is higher for residues in coil structure than the other two regular secondary structures helix and sheet. Also in the year 2006, multi-step support vector machine (SVM) procedure, dihedral prediction (DHPRED), was developed by Zimmermann and his group. But they have chosen to restrict themselves to the prediction of dihedral angle regions.^[31] SVM based method was developed by Kontouris and Hirst.^[18] The method DISSpred consists of two different sets of SVM that predict secondary structure and backbone dihedral angles, respectively. This method enhances the predictions of backbone dihedral angles and secondary structure by using various definitions of dihedral states. Two unsupervised machine learning algorithms are used to create different dihedral states. A set of 513 proteins having 25% sequence similarity was used in this method to train the SVMs. Two generations of such iterative training and clustering into seven dihedral angle region lead to obtain MAEs of 25.1° for φ and 38.5° for ψ . This reported technique predicts dihedral states; interestingly MAE of this method is comparable to MAE reported by real value prediction methods Real-SPINE 2.0 and Real-SPINE 3.0.

Another method based on neural network was reported by the authors of Real-SPINE is SPINEX. For prediction of dihedral angles this method uses a guided-learning artificial neural network and results in some improvement in prediction performance for ψ (MAE=35°). The neural network used in this method consists of two hidden layers with 101 nodes. After addition of Conditional Random Field to this method, increase in the prediction performance was noticed (MAE=33.4° for ψ) and this new method is known as SPINE XI. Comprehensive study shows that SPINE X outperforms earlier method ANGLOR and TANGLE in angle prediction especially in ψ angle prediction. The improvement in angle prediction is due to combined discrete and continuous real-value prediction of torsion angles and multistep training and prediction. But a substantial improvement was achieved by adding Conditional Random Field to further refine the predicted angles.^[45] Final predicted angles are significantly more accurate than multistate classifiers for predicting discrete states and their prediction accuracy is also nearly as accurate as the real-value angles derived from NMR chemical shifts. In machine learning combination of two different approaches generally yields improvement. Therefore CRF model was used along with NN in this approach. The conditional probability of the entire sequence, which is not used as input to the neural networks, is optimised in particular by the CRF model. Additionally CRF model considers the possible coupling between φ and ψ angles by using both angles together and finally predicted errors from the CRF model are used to refine the prediction of torsion angles.

Due to computational and algorithmic improvements, training of deep ANNs with several hidden layers has become feasible in the last few years and deep learning approaches have surged in popularity. ANNs with three or more hidden layers are known as deep neural network. Based on Deep NN, Lyons *et al.* reported a new method SPIDER.^[18] This method uses a deep auto-encoder network and it is reported to be the

first machine learning method to predict θ and τ angle. SPIDER predicts real values for the angle between $Ca_{i+1}-Ca_i-Ca_{i-1}$ (θ) and dihedral angle rotated about the Ca_i-Ca_{i+1} bond (τ). By stacked sparse auto-encoder, unsupervised weight initialization was done in this approach and this stacked sparse auto-encoder is comprised of three hidden layers each with 150 hidden nodes. Along with Position Specific Scoring Matrix (PSSM), seven representative amino-acid properties such as hydrophobicity, volume, a steric parameter (graph shape index), isoelectric point, polarizability helix probability, sheet probability as well as predicted secondary structures, predicted solvent accessibility from SPINE-X were used as input features. This method reports MAE values of 9° and 34° for θ and τ respectively. They compared this result with the prediction of these angles obtained by using the predicted φ and ψ angles from SPINE X and found an approximate improvement of 10%. Accuracy of local structures constructed based on these predicted θ/τ and φ/ψ can give insights on the relationship between predicted θ/τ and φ/ψ . When one layer ANN was used instead of 3 layered Deep Neural network, it is seen that deep neural methods used in this work yields small but statistically significant improvement (MAE 8.8° for θ angles and 34.1° for τ angle) in prediction. This method is further improved using three iterations of deep neural network to predict several structural properties at the same time.¹⁶⁷ Each iteration uses three hidden layers with 150 nodes in each layer. In the first iteration this method uses same input features as SPIDER to yield 12 output values of relative ASA, predicted probabilities for three secondary structure states, and sine and cosine of four angles θ , τ , φ , and ψ . In the second and third iterations along with 27 input features used in first iterations this 12 predicted output values are also utilized to predict secondary structure, ASA and angles separately. This method yields 5%–6% relative improvement in case of angle prediction. A novel approach RaptorX-Angle has recently been developed by Yujuan Gao and team¹⁶⁸ combining clustering and deep learning for real value prediction of protein backbone dihedral angle. This is a hybrid method to predict angles and confidence score simultaneously. In this approach, first a set of clusters of (φ and ψ) were generated from the training data, then deep learning method is used to predict discrete labels and finally real value angles were predicted by mixing empirical clusters with their predicted probabilities. The cluster level probabilities were predicted using a residual framework of convolutional neural network. The method was tested on the filtered PDB25¹⁶⁹ dataset and on the targets of Critical Assessment of protein Structure Prediction (CASP) and in terms of Mean Absolute Error (MAE) and Pearson Correlation Coefficient (PCC), this method shows better prediction performance than SPIDER2. When tested on the subset of PDB25, this method achieves an improvement of approximately 0.5° and 1.4° in MAE for φ and ψ respectively over SPIDER2. It also shows about 0.15 and 1% better performance in terms of MAE than SPIDER2 for φ and ψ on test set TS1267.¹⁶⁹ Although RaptorX-Angle shows better prediction performance than almost all other available methods at that time, still there was scope for improvement in prediction accuracy. RaptorX-Angle utilizes

one-dimensional features and adopts 1D Convolutional Neural Network (CNN) which is not able to extract information of long range interaction. To address this issue Heffernan *et al.* has developed more accurate method SPIDER3¹⁷⁰ employing Long Short-Term Memory (LSTM), Bidirectional Recurrent Neural Networks (BRNNs). Long Short-Term Memory (LSTM) based neural network was used to predict backbone torsional angle along with the secondary structure and the solvent accessible surface area. This Bidirectional Recurrent Neural Network (BRNN) utilizes two BRNN layers having 256 nodes in each direction which is followed by a two fully connected hidden layers comprised of 1024 and 512 nodes respectively. The BRNN layers use Long Short-Term Memory (LSTM) cells¹⁷⁰ due to their ability to learn both distant and close intra-sequence dependencies. The dihedral angle prediction results from this new method show significant improvement than that obtained from SPIDER2. SPIDER3 method is successful to reduce the mean absolute error for backbone φ , ψ , θ and τ angles obtained from SPIDER2 to 5%, 10%, 5%, and 10% respectively.

They reported another method SPIDER3-Single, a single sequence based prediction method which predicts protein secondary structure, solvent accessibility, backbone torsional angles. This method uses bidirectional long short term memory recurrent neural network which is trained on a dataset of 9993 proteins. In this method $20 \times L$ one hot vector is used to represent each single sequence of proteins. Here L is the length of each sequence. In this prediction method, two BRNN layers consisting of 256 nodes per directions followed by two fully-connected hidden layers are used. Mean Absolute Error for backbone φ , ψ , angles from this method is found to be 24.2° and 43.8° respectively.¹⁷⁰ In the year 2017, four different deep learning architectures including deep neural network (DNN) and deep restricted Boltzmann machine (DRBM), deep recurrent neural network (DRNN) and deep recurrent restricted Boltzmann machine (DReRBM) for prediction of protein torsion angles were developed by Haiou Li and group.¹⁷¹ In this method various combinations of different input features including two novel features (predicted contact number and error distribution of torsion angles of sequence fragments) are systematically examined and compared to improve the prediction accuracy. This method uses two novel features predicted contact number and error distribution of torsion angles of sequence fragments as input information. In this study various feature combinations such as memory length, window size and numbers of hidden nodes were tested in order to study their impact on the prediction accuracy. In the same study they compared their prediction performance results with SPIDER2. Comparative results in terms of MAE obtained in these methods on CASP12 free modeling targets are summarized in Table 1.

From the results DReRBM based method shows significant improvement in the result of ψ angle prediction. A new DeepRIN (deep residual inception network architecture) based architecture is reported in 2018 for prediction of φ and ψ angle.¹⁷² To eliminate angle periodicity this method predicts sine and cosine value of angles and then it is converted to angle values. In DeepRIN, local and global interactions between

Table 1. Comparison of prediction performance of torsion angles on CASP12 free modeling targets.

Torsional Angle	SPIDER2	DNN	DRBM	DRNN	DReRBN
ϕ	22.61	22.68	22.72	22.38	22.47
ψ	37.67	38.37	37.56	37.54	35.99

residues are captured using stacked inception module and residual shortcut. DReRBN and DRNN are unable to capture long range interactions between amino acid residues as they use sliding windows to create input to deep neural network. But in DeepRIN entire protein sequence is taken as input, and this makes DeepRIN different from DReRBN and DRNN. When prediction accuracy of this method is tested using CASP 10, CASP 11 and CASP 12 datasets of proteins this DeepRIN based method outperforms SPIDER2 and SPIDER3 resulting significant decrease in the MAE value for both ϕ and ψ angle prediction. Analysis of MAE for predicted angles across 8-state secondary structures for target in CASP12 protein clearly shows that for both angles prediction accuracy is higher for H(Helix structure) and lowest prediction accuracy is observed for S (bend structure). The method of DeepRIN is also available as software known as MUFoldAngle. Chao Fang *et al.*, presented a new web server known as MUFold-SSW^[81] that provides predictions of protein secondary structures, torsion angles, beta-turns and gamma-turns for a given protein sequence. The prediction performances by these methods were better than or comparable with other tools available during that time. NetSurf-2.0^[82] architecture is the extension of NetSurf-1.0^[83] developed in 2009 for prediction of secondary structure and solvent accessibility using a feed-forward neural network. But NetSurf-2.0 uses an architecture which is composed of a convolution and a long-short term memory neural network to predict backbone dihedral angle along with solvent accessibility, secondary structure as well as structural disorder for each residue of the input protein sequence. Similar to the other available methods for angle prediction this method also shows better performance for ϕ compared to ψ angle prediction and it yields low accuracy of prediction near disordered region like coil and loop regions. They have also studied the model using a conditional random field(CRF) layer downstream of the LSTM layer but it could not bring any advantage to the study. Also from the preliminary observation it is seen that CNN layer preceding the LSTM layer has little impact on improvement of prediction result. With the development of deep learning methods accuracy in the protein angle prediction is also increasing. But irrespective of the secondary structure class of residues most of the prediction methods generally utilize same deep learning model for prediction of angles of the residues.

However very recently developed method SAP4SS^[84] proposes to train separate deep learning models for each category of secondary structure. 3-state secondary structures of the residues were first predicted using SSpro8,^[85] followed by categorization of residues into three types. Then a separate DNN is trained on the residues belonging to each of the three types of secondary structure. This model uses a simple DNN

compared to other recently developed methods OPUS-TASS and SPOT-1D. OPUS-TASS^[67] employs an ensemble of deep neural network consisting of CNN, LSTM and Transformation layer. It predicts only ϕ and ψ angles while another recent method SPOT-1D^[66] predicts ϕ , ψ , θ and τ angles using 9 LSTM-BRNN and ResNets. SAP4SS method uses a Fully Connected Neural Network (FCNN) like SAP^[86] does to predict all the four ϕ , ψ , θ and τ angles. FCNN used in this approach consists of three hidden layers. Each layer of this neural network contains 150 neurons. This architecture is similar to the DNN architecture used in SPIDER and SPIDER 2. In addition to input features used in SAP, 20 residue substitution features from HMM profile generated by HHblits and 1 feature for ASA predicted by SPOT-1D is utilized as input features in SAP4SS. Both SAP and SAP4SS predict the direct value of angles. In some of the methods like SPIDER2, they predict sine and cosine values of angles to overcome the problem of angle periodicity. In Table 2 we will list different methods available for prediction of real value of dihedral angles. Different prediction methods use different algorithms and also there are many different ways to assess performance of dihedral angle prediction methods. Moreover, the methods are trained on different datasets. Hence direct comparison of results of the methods may be misleading in some cases. So this table is just for a rough comparison of prediction performance of different methods in terms of MAE.

From the Table 2 it is seen that most of the methods developed for dihedral angle prediction use PSSM generated by running PSI-BLAST as their sequence input. Since PSSM reflects the preferences of amino acids in a particular residue position and can give an idea of averaged local environment, it can provide indirect information on long range interactions. Since Phi, Psi angle of a residue in a protein sequence is strongly correlated with its neighbouring residues; most of the available methods for angle prediction include neighbouring residues in a window around the residue whose dihedral angles are to be calculated. As the size of window increases, local information for prediction also increases. Thereby a logical expectation is that with the increase of window size prediction performance would increase. On the other hand increase in window size also increases the inclusion of more noise. Hence beyond a certain size increasing the window size leads to decrease in the prediction performance. Table 2 shows that different methods use windows of different sizes to get the optimum prediction results.

5. Discussions and Future Directions

In the recent times AlphaFold/AlphaFold2 have revolutionized the field of protein structure prediction which demands

Table 2. List of some methods for prediction of real value Dihedral Angle.

Ref	Name of the Method	Methods	Window Size	Input Features	MAE (r ²)	ψ(r ²)	Availability
41	Real-SPINE	NN	21	PSSM, seven representative amino-acid properties (a steric parameter, hydrophobicity, volume, polarizability, isoelectric point, helix probability, and sheet probability), predicted secondary structures	–	54 ^a	http://sparis.informatics.lupui.edu .
	Real-SPINE 2.0	NN	21	Sequence profiles, seven representative amino-acid properties and predicted secondary structures by SPINE(predicted secondary structure is excluded in ψ prediction)	24.8	38.2	Website http://sparis.informatics.lupui.edu .
46	Real-SPINE 3.	NN	21	Sequence profiles, seven representative physical parameters, and the secondary structure	22.1	36.4	http://sparis.informatics.lupui.edu .
45	SPINE XI	NN, CRF	21	Seven representative amino acid properties (steric parameter, hydrophobicity, volume, polarizability, isoelectric point, helix probability, and sheet probability), PSSM, predicted solvent accessibility prediction and predicted three-state-secondary-structure probabilities	–	33.4	http://sparis.informatics.lupui.edu .
48	SPIDER 2	NN	17	Physicochemical properties of the amino acids (steric parameter, hydrophobicity, volume, polarizability, isoelectric point, helix probability, and sheet), PSSM, predicted SS, angles, and ASA	19.2	29.2	http://sparis-lab.org .
77	SPIDER 3	LSTM-BRNN	–	Multiple sequence alignment (PSSM) - 7 physicochemical features: steric parameter (graph shape index), hydrophobicity, volume, polarizability, isoelectric point, helix probability, and sheet probability	18.3	27.0	http://sparis-lab.org .
78	SPIDER3-Single	LSTM-BRNNs	–	Lx20 matrix of one-hot feature vectors, where L is the sequence length	24.2	43.8	http://sparis-lab.org .
42	ANGLOR	SVM, NN	21	PSSM, predicted secondary structure and solvent accessibility	28.2	46.4	http://zhang.bioinformatics.ku.edu/ANGLOR .
75	DISSorted	SVM	11	PSSM	25.1	38.5	http://sunflower.kuicr.kyoto-u.ac.jp/s/n/TANGLE/ .
43	TANGLE	SVM	9,11,13	PSSM, predicted secondary structure.	27.8	44.6	

Table 2. continued

Ref	Name of the Method	Methods	Window Size	Input features	MAE (p ^a)	RMSE (p ^b)	Availability
58	RaptorX-Angle	deep residual convolutional neural networks (ResNets) and k-means clustering	–	predicted solvent accessibility and predicted native disorder information, PSSM, position-specific frequency matrix (PSFM) of HHpred, primary sequence, solvent accessibility (ACC) and secondary structure(SS) probabilities	18.8	26.68	http://raptorx.uchicago.edu/
81	NetSurf P-2.0	convolutional and long short-term memory neural networks	–	one-hot (sparse) encoded sequences (20 features) plus the full HMM profiles from HH-suite (30 features)	17.90	26.63	http://www.cbs.dtu.dk/services/NetSurfP-2.0/
79	MUfold-Angle	Deep neural network	–	physicochemical properties of amino acids, PSI-BLAST profile, HHBlits profile, and predicted secondary structures	17.78	27.24	http://mufold.org/mufold-s8-angle
54	SPOT-ID	LSTM-BRNN and residual convolutional networks (ResNets)	–	PSSM/HMM, 7PCP, and contact maps	16.89	24.87	
62	OPUS-TASS	Ensembles of DNNs having CNN, LSTM, and Transformer FCNN	–	PSSM profile, HMM profile and 7 physicochemical properties	16.56	22.56	https://github.com/thuxugang/opus_tass
85	SAP	FCNN	5	8-stateSS predictions, PSSM and 7PCP	15.65	18.59	https://gitlab.com/mahneton/sap
83	SAP4SS	FCNN	5&9	8-stateSS predictions, PSSM, 7PCP and HMM profile	15.59 ^c	18.87	https://gitlab.com/mahnewton/sap4ss

reassessment of the importance and also success rates obtained in structure prediction subdomains like dihedral angle prediction. However it is important to point out that AlphaFold/AlphaFold2 predicts φ and ψ angles for each residue of a protein along with distance map and then the predicted values are used to create the initial predicted three dimensional structures.¹⁶⁴ This emphasizes the importance of protein dihedral angle prediction as they can be used as important input feature for protein structure prediction problem by more complex, more accurate and compute intense programs like AlphaFold/AlphaFold2 etc. On the other hand, computationally cheaper dihedral angle prediction methods can be utilized for some other important problems of protein biophysics in place of highly costly, albeit accurate three dimensional structure prediction methods. For example, dihedral angle prediction finds its application in generation of sequence/structure alignment.¹⁵⁸ It may also effectively be applied in fold recognition approaches¹⁷⁴ and structure quality assignment¹⁸⁷ as well as functional study such as ligand-binding site prediction.¹⁸⁸ It can aid the de novo prediction of structural properties. The improvement in protein dihedral angle prediction performance observed in the past years can be attributed to the growth of PDB database and advances in machine learning as well as deep learning algorithms. Also an exponential increase in the available computational power also contributed to the improvement in this research area. In the last couple of years we have witnessed development of some techniques which can successfully predict dihedral angle of proteins with high prediction accuracy. An analysis of the recent works clearly exhibits three trends in successful prediction of protein dihedral angles: first, recent methods such as OPUS-TASS, SPOT-1D etc. are increasingly utilizing a combination of two or more machine learning/deep learning algorithms instead of using only one particular type of deep learning algorithm; second, successful methods are utilizing more detailed structure related information as input features like predicted eight state secondary structures (SAP and SAP4SS), predicted contact maps (SPOT-1D) of residues etc; third, training more than one model for different groups of residues clustered according to probable structural context (SAP4SS trains three models for residues divided according to their probability to be in three different secondary structures). Although in the last two decades dihedral angle prediction has gained considerable importance and has achieved a great success to date, there is still scope for improvement and there are some areas which need further study. In the prediction of dihedral angles, periodicity of angles affects the prediction performance. Some methods tried to overcome this problem and various approaches have been tested to address it. Amongst those, one very effective way is to map the dihedral angles to their sine and cosine values. Some reported methods applied angle shifting to reduce the effect of periodicity of angles in their prediction performance. Also it is observed that phi angle prediction is always better than psi angle prediction. It is well known, prediction performance of machine learning based approaches have close relation with the distribution of angles in real structure. Generally phi angles are less diver-

gently distributed than psi angles and this can accounts for better prediction accuracy observed in of phi angle compared to psi angle. Accurate dihedral angle predictions in terms of fold recognition, sequence structure alignment also demands a large amount of advance study. Study on effect of cis omega angle and nearby disulphide bonds on dihedral preferences may expedite further improvement in protein structure prediction. Most of the methods for dihedral angle prediction use evolutionary information like PSSM, HMM etc. and structural information in terms of predicted secondary structure, surface accessibility, contact map etc. of the protein residues as input features. However, in principle all information required for dihedral angle prediction should be in the amino acid sequence of the protein. Hence as an academic/scientific interest attempts must be made to predict dihedral angles only from sequence information without using evolutionary information or any form of structural information. In this context there is scope of extensive study in the near future.

Acknowledgements

The authors gratefully acknowledge DST, India (Project No. ECR/2017/000494) and UGC, India (Project No. 30-406/2017 (BSR)) for financial assistance. C. R. Gogoi acknowledges financial assistance from DST, India (Project No. ECR/2017/000494). The financial assistance of the DST-FIST and UGC-SAP program to the Department of Chemistry, Dibrugarh University is also gratefully acknowledged.

Conflict of Interest

The authors declare no conflict of interest.

Data Availability Statement

Data sharing is not applicable to this article as no new data were created or analyzed in this study.

Keywords: Dihedral angle · deep learning · machine learning · mean absolute error · protein structure prediction

- [1] C. M. Dobson, *Semin. Cell Dev. Biol.* **2004**, *15*, 3–16.
- [2] R. Pearce, Y. Zhang, *Curr. Opin. Struct. Biol.* **2021**, *68*, 194–207.
- [3] E. Faraggi, A. K. Dunker, J. L. Sussman, A. Kloczkowski, *J. Biomol. Struct. Dyn.* **2018**, *36*, 2331–2341.
- [4] L. Kurgan, F. Miri Disfani, *Curr. Protein Pept. Sci.* **2011**, *12*, 470–89.
- [5] C. Cole, J. D. Barber, G. J. Barton, *Nucleic Acids Res.* **2008**, *36*, 197–201.
- [6] L. J. McGuffin, K. Bryson, D. T. Jones, *Bioinformatics.* **2000**, *16*, 404–405.
- [7] A. Drozdetskiy, C. Cole, J. Procter, G. J. Barton, *Nucleic Acids Res.* **2015**, *43*, W389–W394.
- [8] B. Zhang, L. Li, Q. Lü, *Biomol. Eng.* **2008**, *8*, 33.
- [9] D. T. H. Chang, H. Y. Huang, Y. T. Syu, C. P. Wu, *BMC Bioinf.* **2008**, *9*, 1–12.
- [10] L. Esposito, A. Simone, A. Zagari, L. Vitagliano, *J. Mol. Biol.* **2005**, *347*, 483–487.
- [11] M. Kumar, M. Bhasin, N. K. Natt, G. P. Raghava, *Nucleic Acids Res.* **2005**, *33*, 154–159.
- [12] J. F. Xia, M. Wu, Z. H. You, X. M. Zhao, X. L. Li, *Protein Pept. Lett.* **2010**, *17*, 1123–1128.
- [13] X. Z. Hu, Z. L. Qian, *Protein J.* **2008**, *27*, 115–122.

- [14] J. Jumper, R. Evans, A. Pritzel, T. Green, M. Figurnov, O. Ronneberger, K. Tunyasuvunakool, R. Bates, A. Zidek, A. Potapenko, A. Bridgland, *Nature* **2021**, *596*, 583–589.
- [15] Y. Yang, J. Gao, J. Wang, R. Heffernan, J. Hanson, K. Paliwal, Y. Zhou, *Briefings Bioinf.* **2018**, *19*, 482–494.
- [16] M. Torrisi, G. Pollastri, Q. Le, *Comput. Struct. Biotechnol. J.* **2020**, *18*, 1301–1310.
- [17] P. Kountouris, J. D. Hirst, *BMC Bioinf.* **2009**, *10*, 1–14.
- [18] J. Lyons, A. Dehzangi, R. Heffernan, A. Sharma, K. Paliwal, A. Sattar, Y. Zhou, Y. Yang, *J. Comput. Chem.* **2014**, *35*, 2040–2046.
- [19] M. J. Wood, J. D. Hirst, *Proteins* **2005**, *59*, 476–481.
- [20] X. Miao, P. J. Waddell, H. Valafar, *J. Bioinform. Comput. Biol.* **2008**, *6*, 163–181.
- [21] Y. M. Huang, C. Bystroff, *Bioinformatics* **2006**, *22*, 413–422.
- [22] E. Faraggi, Y. Yang, S. Zhang, Y. Zhou, *Structure* **2009**, *17*, 1515–1527.
- [23] C. Zhang, J. Hou, S. H. Kim, *Proc. Natl. Acad. Sci. USA* **2002**, *99*, 3581–3585.
- [24] W. Zhang, S. Liu, Y. Zhou, *PLoS One* **2008**, *3*, 2325.
- [25] R. Karchin, M. Cline, Y. Mandel-Gutfreund, K. Karplus, *Proteins* **2003**, *51*, 504–514.
- [26] M. R. Betancourt, J. Skolnick, *J. Mol. Biol.* **2004**, *342*, 635–649.
- [27] C. Zhang, J. Hou, S. H. Kim, *PNAS* **2002**, *99*, 3581–3585.
- [28] R. Karchin, M. Cline, Y. Mandel-Gutfreund, K. Karplus, *Proteins* **2003**, *51*, 504–514.
- [29] C. Mooney, A. Vullo, G. Pollastri, *J. Comput. Biol.* **2006**, *13*, 1489–1502.
- [30] G. N. Ramachandran, C. Ramakrishnan, V. Sasisekharan, *J. Mol. Biol.* **1963**, *7*, 95–99.
- [31] O. Zimmermann, U. H. Hansmann, *Bioinformatics* **2006**, *22*, 3009–3015.
- [32] C. Bystroff, V. Thorsson, D. Baker, *J. Mol. Biol.* **2000**, *301*, 173–190.
- [33] A. G. deBrevin, C. Etchebest, S. Hazout, *Proteins* **2000**, *41*, 271–287.
- [34] D. L. Dowe, L. Allison, T. I. Dix, L. Hunter, C. S. Wallace, T. Edgoose, In *Pacific symposium on biocomputing*, Vol. 96 (Eds: L. Hunter, T. E. Klein), World Scientific, Singapore, **1996**.
- [35] C. Mooney, A. Vullo, G. Pollastri, *J. Comput. Biol.* **2006**, *13*, 1489–1502.
- [36] S. Neal, M. Berjanskii, H. Zhang, D. S. Wishart, *Magn. Reson. Chem.* **2006**, *44*, S158–S167.
- [37] M. V. Berjanskii, S. Neal, D. S. Wishart, *Nucleic Acids Res.* **2006**, *34*, W63–W69.
- [38] R. Kuang, C. S. Leslie, A. S. Yang, *Bioinformatics* **2004**, *20*, 1612–1621.
- [39] S. Zhang, S. Jin, B. Xue, *Front. Biol.* **2013**, *8*, 353–361.
- [40] H. Gong, P. J. Fleming, G. D. Rose, *PNAS* **2005**, *102*, 16227–16232.
- [41] O. Dor, Y. Zhou, *Proteins* **2007**, *68*, 76–81.
- [42] S. Wu, Y. Zhang, *PLoS One* **2008**, *3*, 3400.
- [43] J. Song, H. Tan, M. Wang, G. L. Webb, T. Akutsu, *PLoS One* **2012**, *7*, 30361.
- [44] B. Xue, O. Dor, E. Faraggi, Y. Zhou, *Proteins* **2008**, *72*, 427–433.
- [45] E. Faraggi, T. Zhang, Y. Yang, L. Kurgan, Y. Zhou, *J. Comput. Chem.* **2012**, *33*, 259–267.
- [46] E. Faraggi, B. Xue, Y. Zhou, *Protein* **2009**, *74*, 847–856.
- [47] S. Wu, Y. Zhang, *PLoS One* **2008**, *3*, 3400.
- [48] R. Heffernan, K. Paliwal, J. Lyons, A. Dehzangi, A. Sharma, J. Wang, A. Sattar, Y. Yang, Y. Zhou, *Sci. Rep.* **2015**, *5*, 1–11.
- [49] S. Gao, Y. Zhang, K. Jia, J. Lu, Y. Zhang, *IEEE Trans. Inf. Forensics Secur.* **2015**, *10*, 2108–2118.
- [50] S. Hochreiter, J. Schmidhuber, *Neural Comput.* **1997**, *9*, 1735–1780.
- [51] M. Schuster, K. Paliwal, *IEEE Trans. Signal Process.* **1997**, *45*, 2673–2681.
- [52] K. He, S. Zhang, S. Ren, J. Sun, In: *Proceedings of the IEEE Conference on Computer Vision and Pattern Recognition* **2016**, 770–778.
- [53] L. Alzubaidi, J. Zhang, A. J. Humaidi, A. Al-Dujaili, Y. Duan, O. Al-Shamma, J. Santamaria, M. A. Fadhel, M. Al-Amidie, L. Farhan, *J. Big Data* **2021**, *8*, 1–74.
- [54] Y. Yu, X. Si, C. Hu, J. Zhang, *Neural Comput.* **2019**, *31*, 1235–1270.
- [55] A. Sherstinsky, *Physica* **2020**, *404*, 132306.
- [56] A. D. Dongare, R. R. Kharde, A. D. Kachare, *Int. J. Eng. Innov. Technol.* **2012**, *2*, 189–194.
- [57] S. C. B. Lo, H. P. Chan, J. S. Lin, H. Li, M. T. Freedman, S. K. Mun, *Neural Netw.* **1995**, *8*, 1201–1214.
- [58] Y. Gao, S. Wang, M. Deng, J. Xu, *BMC Bioinf.* **2018**, *19*, 73–84.
- [59] Q. Wu, K. Ding, B. Huang, *J. Intell. Manuf.* **2020**, *31*, 1621–1633.
- [60] S. Min, B. Lee, S. Yoon, *Briefings Bioinf.* **2017**, *18*, 851–869.
- [61] S. Singh, A. Mahmood, *IEEE Access* **2021**, *9*, 68675–68702.
- [62] G. Xu, Q. Wang, J. Ma, *Bioinformatics* **2020**, *36*, 5021–5026.
- [63] V. Vapnik, In *Nonlinear modelling*, (Eds: J. A. K. Suykens, J. Vandewalle), Springer, Boston, **1998**, 55–85.
- [64] Y. D. Cai, P. W. Ricardo, C. H. Jen, K. C. Chou, *J. Theor. Biol.* **2004**, *226*, 373–376.
- [65] R. Heffernan, Y. Yang, K. Paliwal, Y. Zhou, *Bioinformatics* **2017**, *33*, 2842–2849.
- [66] J. Hanson, K. Paliwal, T. Litfin, Y. Yang, Y. Zhou, *Bioinformatics* **2019**, *35*, 2403–2410.
- [67] M. Remmert, A. Biegert, A. Hauser, J. Soding, *Nat. Methods* **2012**, *9*, 173–175.
- [68] Q. Jiang, X. Jin, S. J. Lee, S. Yao, *J. Mol. Graphics Modell.* **2017**, *76*, 379–402.
- [69] W. Kabsch, C. Sander, *Biopolymers* **1983**, *22*, 2577–2637.
- [70] O. Dor, Y. Zhou, *Proteins* **2007**, *66*, 838–845.
- [71] J. Schonbrun, W. J. Wedemeyer, D. Baker, *Curr. Opin. Struct. Biol.* **2002**, *12*, 348–354.
- [72] M. Remmert, A. Biegert, A. Hauser, J. Soding, *Nat. Methods* **2012**, *9*, 173–175.
- [73] S. Fahlman, C. Lebiere, *Adv Neural Inf Process Syst* **1989**, *2*.
- [74] J. A. Cuff, G. J. Barton, *Proteins* **1999**, *34*, 508–519.
- [75] Nissen S, Nemerson E. Fast artificial neural network. Available at <http://fann.sourceforge.net>.
- [76] Chang C.-C., Lin C.-J. LIBSVM: a library for support vector machines. Available at <http://www.csie.ntu.edu.tw/~cjlin/libsvm>.
- [77] R. Heffernan, Y. Yang, K. Paliwal, Y. Zhou, *Bioinformatics* **2017**, *33*, 2842–2849.
- [78] R. Heffernan, K. Paliwal, J. Lyons, J. Singh, Y. Yang, Y. Zhou, *J. Comput. Chem.* **2018**, *39*, 2210–2216.
- [79] H. Li, J. Hou, B. Adhikari, Q. Lyu, J. Cheng, *BMC Bioinf.* **2017**, *18*, 1–13.
- [80] C. Fang, Y. Shang, D. Xu, *IEEE/ACM Trans Comput Biol Bioinform.* **2018**, *16*, 1020–1028.
- [81] C. Fang, Z. Li, D. Xu, Y. Shang, *Bioinformatics* **2020**, *36*, 1293–1295.
- [82] M. S. Klausen, M. C. Jespersen, H. Nielsen, K. K. Jensen, V. I. Jurtz, C. K. Soenderby, M. O. A. Sommer, O. Winther, M. Nielsen, B. Petersen, P. Marcatili, *Proteins* **2019**, *87*, 520–527.
- [83] B. Petersen, T. N. Petersen, P. Andersen, M. Nielsen, C. Lundegaard, *BMC Struct.* **2009**, *9*, 1–10.
- [84] M. A. Newton, F. Mataeimoghadam, P. Zaman, A. Sattar, *BMC Bioinf.* **2022**, *23*, 1–14.
- [85] C. N. Magnan, P. Baldi, *Bioinformatics* **2014**, *30*, 2592–2597.
- [86] F. Mataeimoghadam, M. A. Newton, A. Dehzangi, A. Karim, B. Jayaram, S. Ranganathan, A. Sattar, *Sci. Rep.* **2020**, *10*, 1–12.
- [87] G. E. Sims, S. H. Kim, *PNAS* **2006**, *103*, 4428–4432.
- [88] C. Cao, S. Xu, *Sci. Rep.* **2016**, *6*, 1–12.

Submitted: August 31, 2022

Accepted: January 13, 2023



Advances in the understanding of protein misfolding and aggregation through molecular dynamics simulation

Aziza Rahman, Bondeepa Saikia, Chimi Rekha Gogoi, Anupaul Baruah*

Department of Chemistry, Dibrugarh University, Dibrugarh, 786004, Assam, India

ARTICLE INFO

Keywords:

Neurodegenerative diseases
Molecular dynamics
Aggregation mechanism
Therapeutic strategy

ABSTRACT

Aberrant protein folding known as protein misfolding is counted as one of the striking factors of neurodegenerative diseases. The extensive range of pathologies caused by protein misfolding, aggregation and subsequent accumulation are mainly classified into either gain of function diseases or loss of function diseases. In order to seek for novel strategies for treatment and diagnosis of neurodegenerative diseases, insights into the mechanism of misfolding and aggregation is essential. A comprehensive knowledge on the factors influencing misfolding and aggregation is required as well. An extensive experimental study on protein aggregation is somewhat challenging due to the insoluble and noncrystalline nature of amyloid fibrils. Thus there has been a growing use of computational approaches including Monte Carlo simulation, docking simulation, molecular dynamics simulation in the study of protein misfolding and aggregation. The review presents a discussion on molecular dynamics simulation alone as to how it has emerged as a promising tool in the understanding of protein misfolding and aggregation in general, detailing upon three different aspects considering four misfold prone proteins in particular. It is noticeable that all four proteins considered in this review i.e prion, superoxide dismutase1, huntingtin and amyloid β are linked to chronic neurodegenerative diseases with debilitating effects. Initially the review elaborates on the factors influencing the misfolding and aggregation. Next, it addresses our current understanding of the amyloid structures and the associated aggregation mechanisms, finally, summarizing the contribution of this computational tool in the search for therapeutic strategies against the respective protein-deposition diseases.

1. Introduction

A protein manifests biological functionality only after the translationally produced polypeptide undergoes folding from its random coil state into a native three dimensional state (Dobson, 2001; Hartl, 2017). This folding should follow a correct pathway, failing which, the folding results in the production of a misfolded protein. The protein quality control (PQC) machinery in the body confirms correct folding of proteins and presence of no unfolded proteins. This cellular machinery is equipped with specialized proteins called chaperones that initially try repairing, refolding and in extreme cases of irreparable damage, degradation of misfolded proteins. Despite the numerous check processes guided by PQC, there still remain some proteins which escape these processes and eventually become toxic. These misfolded proteins which are resultant of inappropriate folding are likely to form toxic aggregates comprising of soluble oligomers and insoluble fibrillar amyloid deposits (Hartl, 2017). Amyloid fibrils formed from different

proteins have the common characteristic of being dominantly composed of β -sheets. It is observed that increase in life expectancy is strongly correlated to protein misfolding and neurodegenerative diseases. A deterioration in the efficiency of molecular chaperones occur with age which in turn contributes to a decrease in responses to unfolded proteins, thereby confirming that when function of PQC is compromised by age, the likelihood of protein misfolding and aggregation increases (Dobson, 2003). Numerous other phenomena that pose as controlling factors in the process of protein misfolding include genetic and somatic mutations, translational errors, thermal or oxidative stress, pH (Gavrin et al., 2012), local and non-local interactions (Kumar et al., 2017), conformational heterogeneity (Baruah et al., 2012; Saikia et al., 2021), incomplete complex formation, metal ions and abnormal protein modifications (Gavrin et al., 2012). Interestingly, aberrant protein folding has been linked to an extensive range of pathologies that may be classified into two categories: loss-of-function diseases and gain-of-function diseases (Gavrin et al., 2012; Hartl, 2017). On one hand, loss of function

* Corresponding author.

E-mail address: anupaulbaruah@dibru.ac.in (A. Baruah).

<https://doi.org/10.1016/j.pbiomolbio.2022.08.007>

Received 11 April 2022; Received in revised form 19 August 2022; Accepted 23 August 2022

Available online 28 August 2022

0079-6107/© 2022 Elsevier Ltd. All rights reserved.

(LOF) diseases occur when a protein is deprived of its functional three-dimensional conformation due to inappropriate folding or when it fails to reach the destined site of action within the cell. On the other hand, gain of function (GOF) diseases occur due to accumulation of proteins leading to protein aggregation or toxic oligomer formation which harmfully affect cell function. The LOF diseases are strongly associated with inherited or somatic mutations. These include lysosomal storage diseases such as Gaucher disease, neurodegenerative Huntington disease (HD), cystic fibrosis, α 1-antitrypsin deficiency, and certain cancers. Neurodegenerative diseases such as Parkinson's disease (PD), Alzheimer's disease (AD), Amyotrophic lateral sclerosis, Transmissible spongiform encephalopathies and a wide range of amyloidoses fall under GOF diseases. This process of protein misfolding followed by aggregation and then accumulation is considered a hallmark event in neurodegenerative diseases. Though distinct misfold prone proteins are associated with different neurodegenerative diseases, their process of misfolding and aggregation including the intermediates and the end products formed is quite similar. In neurodegenerative diseases, protein misfolding and oligomerization subsequently leads to progressive accumulation of misfolded protein aggregates in the brain in the form of highly ordered fibers called amyloid. Until recently, it was thought that these protein deposits found in brain were neurotoxic and pathogenic but later studies suggested that soluble misfolded oligomers are the real cause of neurodegeneration (Hoffmann et al., 2013). These oligomers which act as precursors of fibrillar aggregates are heterogeneous group of species and are highly dynamic.

The primary risk factor for most neurodegenerative diseases is ageing. One in ten elderly individuals with age >65 years suffer from age-related neurodegenerative diseases including Alzheimer's disease and Parkinson's disease (Hou et al., 2019). Sadly, very few effective treatments are available against these diseases at present. The development of novel approach for the treatment and diagnosis of neurodegenerative diseases demand the understanding of the various factors

influencing misfolding and aggregation stability of the associated protein along with the mechanism involved in the misfolding process. For such studies of protein biomolecular systems computational approaches are being increasingly employed. Computational approaches cover many strategies like Monte Carlo simulation, docking simulation, molecular dynamics (MD) simulation and so on. In some *in silico* studies on protein misfolding and their associated neurodegenerative diseases, the use of an array of computational approaches including MD simulation is seen while in some studies MD simulation alone has been used to gain insights on protein misfolding and aggregation. Literature is not much enriched with reviews covering MD simulation aided study of protein misfolding and related protein deposition diseases. Nevertheless there are a handful of them that includes description of various atomistic and coarse-grained models used in the study of protein aggregation (Morris-Andrews and Shea, 2015), insights into pathogenic mechanisms of amyloidosis diseases (Liu et al., 2018) along with novel drug discovery against neurodegenerative diseases (Liu et al., 2018; Makhouri and Ghaseem, 2018), insights into protein misfolding and the associated diseases by combining MD simulations with experimental analyses (Wille et al., 2019) and study of structural and dynamical transitions of the huntingtin protein (Moldoveanu and Chis, 2019). This review addresses the methods of MD simulation and its various impacts in gaining a comprehensive knowledge on protein misfolding and aggregation in general detailing upon three different aspects (one discussing factors regulating misfolding and aggregation stability, one discussing aggregation mechanism and yet another discussing therapeutic strategies) considering four misfold prone proteins in particular. These misfold prone proteins are: prion protein, superoxide dismutase1 (SOD1), huntingtin (Htt) and amyloid β (A β). Fig. 1 depicts the correctly folded and aggregated fibril structure of both amyloid β and SOD1 proteins. The figure clearly captures the change in secondary structure content in the aggregated form.

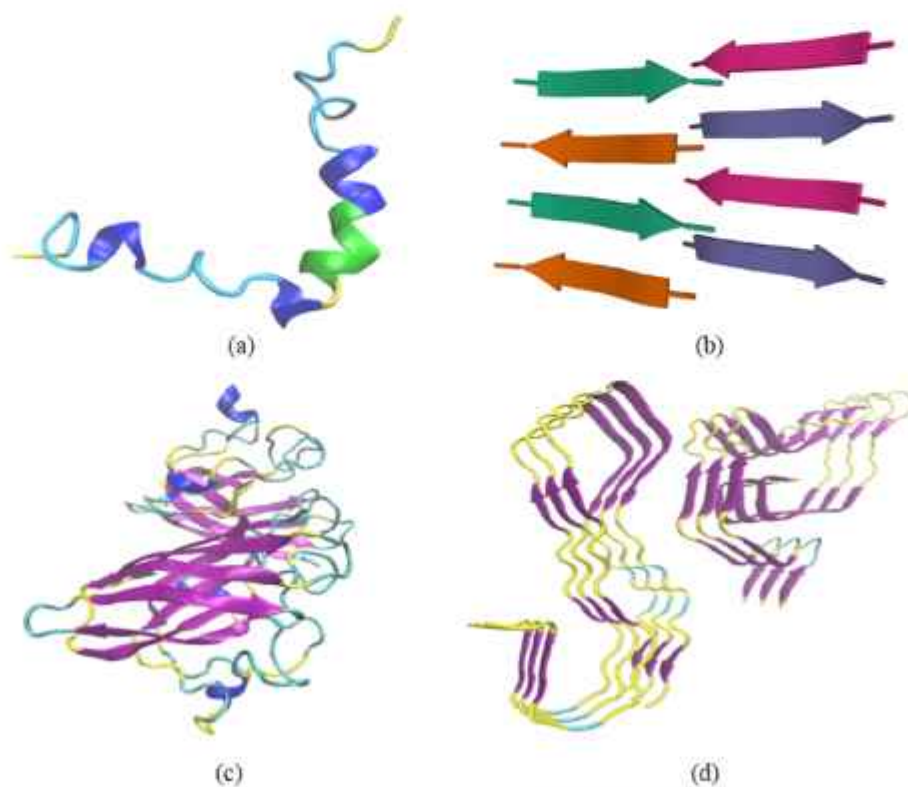


Fig. 1. 3-D structures of proteins (a) NMR structure of A β peptide (1–42), PDB ID 120Q (Tomaselli et al., 2006); (b) Fibrillar structure of A β (35–40), PDB ID 2ONA (Sawaya et al., 2007); (c) X-ray crystal structure of human SOD1, PDB ID 2V0A (Strange et al., 2007); (d) Cryo-EM structure of amyloid fibril formed by full-length human SOD1, PDB ID 7VZF (Wang et al., 2022).

2. Study of factors influencing misfolding and aggregation stability of proteins using molecular dynamics simulations

2.1. Prion protein

In prion diseases, the normal form of prion protein (PrP^C) undergoes misfolding into its pathogenic scrapie form (PrP^{Sc}) involving an ambiguous mechanism. The heterogeneous nature of prion aggregates enable pathogenic PrP^{Sc} to self propagate particular strains resulting in diseases with different characteristics. Transmissible spongiform encephalopathies (TSEs) form a fatal class of neurodegenerative disorder related to prion protein lacking any effective cure till date. Though a detailed mechanism of conversion of a normal to a pathogenic prion is obscure, a number of factors are seen to be involved, some of which contribute to the reinforcement of the conversion while some to its resistance. A few environmental factors that might enhance the conversion are low pH (Vila-Vigosa et al., 2012), high temperature (Ding et al., 2005), oxidative stress (Pushie et al., 2009), etc. Similarly presence of a PrP^{Sc} sample may act as a template and hence increase the conversion to the pathogenic form (Vila-Vigosa et al., 2012). Another trigger that significantly enhances the formation of PrP^{Sc} is the presence of pathogenic mutations (Chen et al., 2010; Borgohain et al., 2016; Ning et al., 2015) in the prion sequence. Regions having high concentration of solvent exposed backbone H bonds are also reported to induce formation of PrP^{Sc} (De Simone et al., 2005). On the other hand membrane environment, *in vivo* post-translational modifications (Cheng et al., 2017) and protective prion mutations (Ning et al., 2015; Zhou et al., 2016) may disfavour the conversion. There exist huge differences in structure between PrP^C and PrP^{Sc}, mainly in terms of secondary structure. The normal prion protein has a high content of α -helix and low β -sheet content. Contrastingly, the α -helix content in PrP^{Sc} decreases to ~30% while acquiring a high content of β -sheet. Experimental study on a 17-residue engineered peptide by Kammerer et al. (2004), features a temperature driven transition from α -helix to β -sheet conformation. MD simulation study on the same peptide reveals the presence of a critical temperature supporting the experimental finding. At temperatures lower than this critical temperature, the peptide folds into an α -helix coiled-coil state whereas at temperatures above it, the peptide adopts an amyloid-like structure which is rich in coiled anti-parallel β -sheets with the cross- β signature of amyloid fibrils (Ding et al., 2005). When computational methods were used to study the pH effects on the structure of normal prion proteins it was observed that with decrease in pH too, there is a clear trend of loss of helical structures and a gain of β -structures (Campos et al., 2010) which suggest that a low pH can induce prion misfolding. Many computational (Alonso et al., 2001; Gu et al., 2003) and experimental (Bjorn Dahl et al., 2011) studies were performed and it was observed that the pH 7 has a stabilizing effect on the structure of the prion protein. The reversibility of misfolding of prion protein induced by low pH was observed too both experimentally (Jackson et al., 1999) and computationally (Campos et al., 2010). Constant-pH molecular dynamics approach proved helpful in understanding the molecular details of this prion misfolding reversibility process (Vila-Vigosa et al., 2012).

According to the protein-only hypothesis, in the misfolding process of PrP^C, pathogenic PrP^{Sc} can behave as a template and it is the only infectious agent responsible for propagation and transmission of prion misfolding diseases. This misfolded form (PrP^{Sc}) easily aggregates and precipitates, causing a hindrance in the study of its molecular structure using X-ray diffraction and NMR. In addition, there is no knowledge on the molecular details of the conformational transition of PrP^C to PrP^{Sc}. Considering these limitations, computational approaches act as a powerful tool in explaining the details of the structural transition and accordingly, the structural details of prion misfolding and aggregation has been studied by MD simulations (El-Bastawisy et al., 2001; Gu et al., 2003; Shamsir and Dalby, 2005).

The normal prion protein is a GPI anchor membrane-bound protein, usually diglycosylated at Asn181 and Asn197. Recombinant PrP, the

primary construct employed in experimental studies, however lacks the glycans and the GPI anchor. Studies show that expression of PrP, its distribution, and *in vivo* deposition of PrP^{Sc} has been influenced by N-linked glycans (Dearmond et al., 1999). Thus non-protein moieties also affect the process of misfolding and aggregation of prion. Most MD simulation studies of prion protein avoided the post-translational modifications along with the membrane environment, thus focused on the protein-only portion. Only few MD studies (Cheng et al., 2017; DeMareo and Daggett, 2009) on membrane have focused on the GPI-anchored diglycosylated PrP^C. These studies helped in observing interactions between the protein and non-protein moieties which exert a controlling influence on the conversion of PrP^C to PrP^{Sc}. In the simulation study of the glycosylated, membrane bound PrP^C, initially the protein is kept perpendicular to the lipid membrane which subsequently tilts towards the membrane surface such that the supposed PrP^{Sc} oligomerization sites on the protein becomes inaccessible. Thus the simulation study observed that membrane-bound normal prion protein has a tilted conformation and can avoid PrP^{Sc}-induced misfolding (Baron et al., 2002; Baron and Caughey, 2003; Cheng et al., 2017). Possible mechanisms have also been put forward on how the membrane environment together with the post-translational modifications contribute to the resistance of prion misfolding (Cheng et al., 2017). Prion diseases are caused due to a change in conformation of the soluble form (normal prion protein) to its insoluble isoform (pathogenic prion). Interactions with water molecules play a remarkable role in defining the factors that decide whether the protein will adopt the soluble form or the insoluble one. Studies reveal that there usually exist a great number of insufficiently dehydrated H bonds referred to as under-dehydrated hydrogen bonds (UDHBs) in proteins (including PrP^Cs) which have high tendency to form amyloid (Fernández, 2002; Fernández and Scheraga, 2003). These very regions have a high chance of influencing protein aggregation. Also, there are regions in the prion protein where there is presence of tightly bound water molecules. High resolution X-ray studies on the structures of human C-terminal prion protein and the sheep prion protein have established helpful description of the surface of the protein and the partially buried water molecules present in them. Acquiring knowledge on the role of these conserved water molecules and the influence of the surrounding solvent around the poorly protected regions in the stability of the normal prion protein will help in understanding the relation between the aggregation of the PrP with its solvation behaviour. Experimentally it is very difficult to obtain information on the solvent behaviour at a protein surface though some characterization on protein hydration dynamics has been made. A powerful tool in this regard is MD simulation through which mobility of water molecules and its arrangement around proteins can be studied. The structural importance of the highly conserved water molecules has been studied through MD simulation (De Simone et al., 2005). These conserved water molecules play a role in keeping a residue intact in its place which otherwise is involved in a disease causing mutation related to Gerstmann-Straussler-Scheinker disease (Liemann and Glockshuber, 1999). The regions having high probability to form amyloids are the structurally unstable regions. In normal prion protein, there are a large number of unprotected hydrogen bonds with flanking hydrophobic residue. Such regions of the protein having high concentration of UDHBs encourage protein aggregation. Increased oxidative stress can also be considered as a hallmark of prion disease besides PrP^{Sc} containing fibrils (Pushie et al., 2009). PrP has two structural domains including a folded alpha-helical C-terminal region and a flexible disordered N-terminal domain. There are a total of six histidine residues in the flexible N-domain, four in the octapeptide (OR) region and two (His96 and His111) outside the OR region. In prion diseases, conformational change is observed in the folded C-terminal domain of PrP. Also, the N-terminal domain of PrP selectively binds Cu²⁺ over other biologically relevant divalent cations like Mn²⁺, Zn²⁺, Ni²⁺, etc. The low occupancy (1:1) of Cu²⁺ being redox-active reduces Cu²⁺ to Cu⁺ which in turn forms reactive oxygen species (ROS). The exposure to ROS results in the occurrence of

β -cleavage at the OR region as opposed to the normal α -cleavage mediated by proteases. After β -cleavage and loss of OR region, Cu²⁺ binds to His96 and His111 present outside the OR region and induces formation of localized β -sheet structure adjacent to the pathogenic region of PrP. Subsequent propagation of β -sheet structure into the C-domain after its nucleation in the conserve hydrophobic stretch of residues is believed to be a significant conformational transition in the pathogenesis of prion disease (Pushie et al., 2009; Pushie and Vogel, 2008; Requena et al., 2001).

Pathogenic mutations occurring at different positions of the prion protein are a major cause of prion diseases. Investigation on six mutants (S170N, S170N, R220K, M166V, E200K and D178N) located in conserved sequences of human prion proteins showed instability of all six mutants with respect to the wild type model with D178N showing a greater loss in stability as inferred from RMSD, RMSF and SASA. Further with support from MD simulation study, this investigation concluded that there is participation of cation- π interaction in the stability of prion proteins (George Priya Doss et al., 2013). In the classical MD simulation study on the native prion protein along with two pathogenic mutations, T193I and R148H, located at helix H2 and H1 of the prion protein respectively, it was indicated that both the mutants lead to a decrease in native β -sheet content. In case of R148H mutation, there is appearance of two new turn regions and conversion of a 3_{10} region to coil form while in case of the T193I mutation there is appearance of a new 3_{10} region (Borghain et al., 2016). When the wild type PrP106-126 along with its two mutated forms viz. A117V and the H111S were studied, it was found that both the mutations showed contrasting effects on the aggregation of PrP106-126. The pathogenic A117V mutant displayed higher propensity

to form β -hairpin structures and an increase in the hydrophobic solvent accessible surface areas than the WT. On the contrary, the protective H111S mutant showed higher contents of helical structures and reduced exposure of hydrophobic residues (Ning et al., 2015). When mutations in the hydrophobic core of the protein including V180I, F198S, V203I, V210I and a related mutation T183A were studied, it was found that these pathogenic mutations significantly affect the dynamics and stability of the protein thereby promoting its misfolding (van der Kamp and Daggett, 2010). Certain mutations positioned at the first strand of the native β -sheet are seen to affect the same in different ways. Three such mutants, namely, G131V, A133V and S132I are related to the misfolding of the native β -sheet. Mutation G131V elongates while A133V disrupts the native β -sheet and S132I converts it to an α -sheet. Reorientation of side chain-side chain interactions occurring due to introduction of mutation is the cause for these β -sheet related changes (Chen et al., 2010). Despite having minute effects on the protein structure, the mutations D202N, E211Q, and Q217 greatly change the overall electrostatic potential distributions. These mutations positioned in helix 3 of the human prion protein also affect the thermodynamic stability of the protein (Guo et al., 2012a). Simulation study of three mutations T188K, T188R and T188A located in helix 2 of the human prion protein indicated that they have multiple effects on the dynamic properties of the protein. Though the native structure of the protein is almost not altered but its stability is perturbed. The multiple effects include the shift of H1, lengthening of the native β -sheet, and the change of S2-H2 loop to a 3_{10} helix (Guo et al., 2012b). Further, studies reveal that V127 is a protective variant of prion protein which is resistant to prion conversion and propagation (Asante et al., 2015; Mead et al., 2009). MD simulation was conducted to

Table 1
Details of simulation setup and mutations studied for prion protein.

Ref	Protein, mutation studied	Mutation type	Structure/PDB files used for simulation	Simulation package and technique	Specifications (T = temperature, ST = simulation time)	Remark
George Priya Doss et al., 2013	Prion, S170N, R220K, M166V, E200K, D178N	Pathogenic	Native (1QM2), mutants: 1E1S, 1E1P, 1E1U, 1E1G, 1PKC, 2KID	GROMACS	GROMOS96 43a1 force field; SPC water model; T = 300 K; ST = 6 ns	Loss of stability in all mutants was observed with D178N showing a greater loss. Mutations might have some local influences on protein interactions
Borghain et al. (2016)	Prion, T193I, R148H	Pathogenic	WT-prion (1HJN), modeled T193I and R148H mutant structures	AMBER12, NPT ensemble	AMBERff12SB force field; TIP3P water model; T = 310 K; ST = 3 structures \times 50 ns	Mutations cause no major structural transitions, however affect the local environment diversely
Chen et al. (2010)	Prion, G131V, A133V, S132I	Pathogenic	Modeled WT-SOD1 with residue 90-230, 3 modeled mutant structures	in <i>vacuo</i> molecular mechanics (Iimm), NVE ensemble	Levitt et al., force field; F9C water model; T = 310 K; ST = 50 ns	G131V causes elongation, A133V disruption and S132I conversion of the native β -sheet
Ning et al. (2015)	Prion, A117V, H111S	A117V: pathogenic, H111S: protective	PrP106-126 WT, PrP106-126 A117V, PrP106-126 H111S	AMBER10, replica exchange MD	AMBER ff99SB force field; T = 270-600 K; ST = 200 ns/replica	A117V show higher propensity to form β -hairpin structures and increases hydrophobic solvent accessible surface area, H111S show higher contents of helical structures and reduces exposure of hydrophobic residues
van der Kamp and Daggett (2010)	Prion, V180I, V203I, F198S, V210I, T183A	Pathogenic	5 modeled mutant structures	in <i>vacuo</i> molecular mechanics (Iimm)	Levitt et al., force field; F9C water model; ST = 3 runs \times 50 ns \times 5 mutants	F198S and T183A increases flexibility in parts of the protein structure that are otherwise stable. V180I, V210I, V203I cause changes similar to those seen in low-pH related misfolding events
Guo et al., 2012a	Prion, D202N, E211Q, Q217R	Pathogenic	WT-prion (1HJN), 3 modeled mutant structures	AMBER10, NPT ensemble	AMBER ff03 force field; TIP3P water model; T = 310 K; ST = 3 runs \times 50 ns \times 4 structures	Mutants have little effects on protein structure, considerable effects on thermodynamic stabilities and show large changes of electrostatic surface of PrP
Guo et al., 2012b	Prion, T188K, T188R, T188A	Pathogenic	WT-prion (1HJN), 3 modeled mutant structures	AMBER10, NPT ensemble	AMBER ff03 force field; TIP3P water model; T = 310 K; ST = 3 runs \times 50 ns \times 4 structures	Mutations diversely affect the dynamic properties of PrP, though the globular domain is rather conserved
Zhou et al. (2016)	Prion, G127V, M129V	Protective	5 constructed dimer systems, 4 constructed oligomer systems	AMBER14, NPT ensemble	AMBER ff99SB force field; TIP3P water model; T = 300 K; ST = 100 ns	V127 variant can weaken both the inter and intralayer interactions of fibrils. It can also reduce H-bond interactions between monomers of prion dimer

gain insights into the structural basis of this protective effect shown by V127 (Zhou et al., 2016). It was found that V127 reduces the interaction of the main-chain H-bonds between monomers and thus becomes unfavourable to form dimer, a key process of prion propagation. Also, the V127 variant is unfavourable to form a stable core and fibril, which is another key process of prion propagation. Table 1 summarizes the studied mutations and the findings together with details of simulation setup for prion protein.

2.2. Superoxide dismutase 1

Amnoretrophic lateral sclerosis (ALS) is a devastating neurodegenerative disorder eventually leading to paralysis and death of the patient. Nearly 90% of the ALS cases occur without any family history or known cause and the remaining 10% cases are inherited (Banerjee et al., 2016). The first class of ALS is termed "sporadic" (sALS) while the other class is termed "familial" (fALS). Approximately 20% of fALS cases result from mutations in the gene encoding the enzyme copper-zinc superoxide dismutase 1 (SOD1). Studies reveal that SOD1 mutants are highly prone to misfolding and aggregation. It is suggested that pathogenic mutations could affect SOD1 stability, flexibility, compactness, solvent-accessible surface and also the secondary structure. Computational methods are useful in the identification of variants and analysis of their impact at a structural level.

Some point mutations have a dramatic effect on the stability of a protein. Since all sites of a protein are not equivalent, mutations at some sites may exert stabilizing effect while at others may exert destabilizing effect (Baruah and Biswas, 2014). Here we provide a report on how MD simulation has helped in learning about the role of various point mutations on the misfolding and aggregation of SOD1. Information gained from MD simulations on the role of various point mutations would definitely help in understanding the molecular basis of the ALS, in gaining new insights in the area of rational drug design and also in identifying sites where satisfactory changes might help in stabilizing the mutant structure. Mutation A4V is positioned in a highly conserved region of SOD1 (Da Silva et al., 2019). MD simulation studies on A4V mutant and WT SOD1 revealed that the overall stability of the A4V mutant is less than that of WT SOD1 protein. There is presence of a completely solvent accessible free cysteine residue in the A4V mutant. Also, there is a decrease in the zinc-binding affinity owing to disruption in the zinc-binding site (Schmidlin et al., 2009). Simulation studies of A4V in aqueous trifluoroethanol reported that due to increase in local dynamics in the active site loops of A4V SOD1, there is destabilization of the β -barrel along with loss of hydrophobic contacts (Kumar et al., 2018). Moreover, the pathway involved in the A4V induced unfolding at biological temperature is found similar to that of high temperature induced unfolding of SOD1 at early stages (Schmidlin et al., 2013). Discrete molecular dynamics (DMD) simulation study on the native SOD1 and the metal binding mutant D83G (Srinivasan and Rajasekaran, 2018 a) highlighted the same results as that of general MD simulation study carried on the WT SOD1 and C146A mutant. Both the respective mutants exhibited loss of structural stability upon mutation in SOD1 together with reduced intramolecular protein interactions. In addition to this, Steered molecular dynamics (SMD) simulation helped provide authentication to the analysis that there is loss of Zn ion coordination in the mutant D83G compared to that of native SOD1 due to the impact of mutation on Zn binding residues (Srinivasan and Rajasekaran, 2018 a). Simulation studies have also suggested that the A4F mutation which is located in a highly conserved region of SOD1 decreases the SOD1 stability along with increasing the aggregation tendency of the protein (Da Silva et al., 2019). In a similar simulation study, the metal binding mutant H80R was seen to have lower stability than the native SOD1 protein while SMD simulation helped provide authentication to the analysis that there occurs early unbinding of Zn ion in H80R mutant as compared to the native SOD1 protein (Srinivasan and Rajasekaran, 2017 a). DMD simulation on the G85R mutant suggested that the mutation

completely alters the overall backbone of the protein compared to the wild type, thus causing a change in structural deviation and residual flexibility of the SOD1 protein (Srinivasan and Rajasekaran, 2017 b). 19 mutations (E121G, D124G, D124V, D125H, L126S, G127R, E132K, E133V, S134N, S134T, T137A, T137R, G138E, N139D, N139H, N139K, A140G, G141A, G141E) reported in the electrostatic loop were studied through DMD simulation. Among these 19 mutants, L126S, N139H and G141A were found to be the most destabilizing and disease-causing ones (Srinivasan and Rajasekaran, 2019). The V14M, E100G and E100K mutants are positioned far away from the metal binding sites as well as the dimer interface. But irrespective of their location, V14M (Tompa and Kadhirvel, 2018) is found to alter the conformation of the Arg143 residue which is known for its catalytic importance while mutants E100G and E100K are found to cause a loss of protein electrostatic interactions on the outer surface along with increasing the flexibility in the IV loop, i. e. the Zn binding loop of SOD1 (Tompa et al., 2020). MD simulation studies on mutants H46R, H48Q, H80R and H80G found that there is decrease in the conformational stability and flexibility in mutated structures (Keerthana and Kolandaivel, 2015). Effects of mutation on the occupancy of hydrogen bonds within the protein, hydrogen bonds between the protein and water molecules and water bridges was also studied with the help of MD simulation for 38 SOD1 mutants viz. A4V, C6A, C6G, V7E, L8Q, G10V, G12R, F20C, G37R, L38V, G41D, G41S, H43R, H46R, H48Q, D76V, L84V, G85R, N86K, D90A, G93R, V94A, E100G, D101N, S105L, L106V, C111S, I112M, I112T, G114A, V118L, D125H, N139H, L144S, and V148I (Alemasov et al., 2017) and it was found that there is an increase in the propensity for local destabilization of SOD1 owing to the hydrogen bonds and the water bridges. Different simulation strategies have been applied to gain insights into the role of G37R mutant of SOD1 and it found that upon mutation in SOD1, there occurs a reduction in the affinity for Cu (II) ion and creation of a novel H-bond network originating around Arg37. It was further suggested that the dimer dissociation process remains unaffected by this G37R mutation (Milardi et al., 2010). Another MD simulation study considering mutations A4V, G37R, and H46R, all positioned at different regions of SOD1 pointed out a common effect of diverse point mutations on the SOD1 dimer and suggested it to be loss of coupled motions between monomers upon mutation of the mutant dimer. There occurs disruption of the β -plug which is considered as a key stabilizing structural element. This in turn leads to de-protection of edge strands (Khare and Dokholyan, 2006). Both T2D and C111S mutations stabilize SOD1 even in the presence of A4V, a mutation which is considered as a major SOD1-destabilizing mutation. The stabilization effect of the T2D mutation was explained through DMD simulations (Fay et al., 2016). It was suggested that T2-Phosphorylated SOD1 share common characteristics with the phosphomimetic T2D mutated SOD1. This phosphomimetic T2D mutation has the ability of increasing the stability of the native conformation of the SOD1 protein. On comparing the simulation studies on WT SOD1, A4V mutant and the A4V_C111S mutant, it was found that when substitution of S at C111 position in the A4V mutant occurred, the lost structural stability and protein compactness along with secondary structural propensity was found to be regained (Srinivasan and Rajasekaran, 2018 b). Table 2 summarizes the studied mutations and the findings together with details of simulation setup for SOD1.

2.3. Huntingtin protein

The productive folding of multidomain proteins, which form 75% of the eukaryotic proteome, suffer from competition with protein misfolding where misfolding leads to a range of debilitating medical conditions (Borgia et al., 2011). Evolutionary pressure reduces the sequence similarity existing between neighbouring repeat domains of multidomain proteins to avoid interdomain misfolding (Dave et al., 2019). However, multiple identical domains are found to be present in many natural proteins (Dave et al., 2019). These repeat proteins are fast folders (Gruebele et al., 2016) but due to possibility of inter-domain

Table 2
Details of simulation setup and mutations studied for SOD1.

Ref	Protein, mutation studied	Mutation type	Structure/PDB files used	Simulation package and technique	Specifications (T = temperature, ST = simulation time)	Remark
Da Silva et al. (2019)	SOD1, A4V, A4F	Pathogenic	WT-SOD1 (2C9V), modeled A4V and A4F mutants	GROMACS	AMBER99SB-ILDN force field; TIP3P water model; T = 300 K; ST = 150 ns	A4V and A4F mutations could affect protein stability, flexibility, protein's compactness and solvent-accessible surface area
Schmidlin et al. (2013)	SOD1, A4V	Pathogenic	1HLS (Chain A)	in vacuo molecular mechanics (ilmm), NVE ensemble	Levitt et al., force field; P3C water model; 6 independent simulations: 2 simulations for 33 ns at 498 K; 3 simulations for 5 ns at 498 K; 1 simulation for 21 ns at 298 K	There is similarity between high temperature induced unfolding of SOD1 at early stages with conformation changes associated with A4V mutation at physiological temperature
Schmidlin et al. (2009)	SOD1, A4V	Pathogenic	WT-SOD1 (1HLS, chain A), A4V (1UXM, chain A, apo demetalled)	in vacuo molecular mechanics (ilmm), NVE ensemble	Levitt et al., force field; P3C water model; T = 310 K; ST = 2 structures × 3 runs × 60 ns	Possible explanation for reduced dimerization, reduced metal binding affinity and oligomerization cited
Kumar et al. (2018)	SOD1, A4V	Pathogenic	WT-SOD1 (1N16), A4V pWT-SOD1 (1N19)	GROMACS, NPT ensemble	CHARMM27 force field; SPC216 water model; T = 300 K; ST = 250ns	At lower TFE concentrations, TFE induced aggregation of A4V SOD1 is due to TFE inducing structural fluctuations leading to unfolding of β -barrel along with exposure of hydrophobic core
Srinivasan and Rajasekaran (2018)a	SOD1, D83G	Pathogenic	Native SOD1 (2V0A, chain A), modeled D83G mutant	Discrete MD	Medusa force field; T = 300K; ST = 1×10^5 TU (≈ 5 ns)	Mutation leads to structural instability, reduced intramolecular interactions and early unfolding of SOD1
				YASARA, Steered MD	AMBER03 force field; T = 298K	Mutation leads to early dissociation of Zn ion in the mutant from its binding site as compared to that in the native
Srinivasan and Rajasekaran (2017)a	SOD1, H80R	Pathogenic	Native SOD1 (2V0A, chain A), modeled H80R mutant	Discrete MD	Medusa force field	Mutation leads to loss of protein stability, loss of Zn-binding of the mutant compared to the native
				YASARA, Steered MD	AMBER03 force field; T = 298 K	There occurs early unbinding of Zn ion in the H80R mutant as compared to native SOD1
Srinivasan and Rajasekaran (2017)b	SOD1, G85R	Pathogenic	WT-SOD1 (2V0A, chain A), mutant G85R (2VR7, chain A)	Discrete MD	Medusa force field	Absence of Zn ion triggers loss of conformational stability and residual flexibility
				YASARA, Steered MD	AMBER03 force field; T = 298 K	Mutation leads to reduced Zn-binding in SOD1 protein
Srinivasan and Rajasekaran (2019)	SOD1, E121G, D124G, D124V, D125H etc (Total 19 mutations are studied)	Pathogenic	WT-SOD1 (2V0A, chain A), 19 modeled mutant structures	Discrete MD	Medusa force field; T = 298 K; ST = 5ns	L126S, N199H and G141A are found to be the most destabilizing and disease-causing ones
Toppa and Kadhirvel (2018)	SOD1, V14M	Pathogenic	Dimeric WT-SOD1 (1HLS, chain A and H), V14M mutant construct	GROMACS	OPLS force field; SPC water model; T = 298 K; ST = 80 ns	Alters the conformation of the catalytically important Arg143 residue
Toppa et al. (2020)	SOD1, E100G, E100K	Pathogenic	Dimeric WT-SOD1 (1HLS, chain A and H), model of E100G and E100K mutant	GROMACS	GROMOS96 54a7 force field; SPC water model; T = 298 K; ST = 50 ns	Both mutations could increase flexibility in the Zn-binding loop thereby triggering destabilization of SOD1
Keerthana and Kolanidavel, 2015	SOD1, H46R, H48Q, H80R, H80G	Pathogenic		GROMACS	OPLS-AA force field; SPC water model; T = 300 K; ST = 20 ns	The number of intramolecular hydrogen bonds decrease which in turn affects the SOD1 catalytic mechanism
Alemasov et al. (2017)	SOD1, A4V, C6A, C6G, V7E, L8Q etc (Total 38 mutations are studied)	Pathogenic	WT-SOD1 (2V0A), 38 mutant SOD1 dimers	AMBER12	AMBERff99SB force field; TIP3P water model; T = 300 K; ST = 50 ns	Hydrogen bonds and water bridges increase the probability for local destabilization of SOD1
Milardi et al. (2010)	SOD1, G37R	Pathogenic	WT-SOD1 (1SPD), G37R mutant (1AEV), Apo SOD1, apo G37R mutant	Thermodynamic Integration MD, NVT ensemble CHARMM33, Implicit solvent constant temperature MD	CFF force field with harmonic restraint; T = 300 K; ST = 200 steps × 20 ps CHARMM19 force field; EEF1 solvent model; T = 300 K; ST = 52.10 ns	G37R mutant, situated far from both the metal sites and the monomer-monomer interface, has a decreased affinity for Cu(II) ion. Mutation leads to the formation of a new and stable Lys36, Arg37, Leu38 and Lys91 involved H-bond network
			Monomeric apo proteins	Steered MD	CHARMM19 force field; T = 300 K	
	SOD1, A4V, G37R, H46R	Pathogenic	WT-SOD1 (1SPD), A4V (1N19), G37R	AMBER	TIP3P water model; T = 300 or 400 K; ST = 5 ns	

(continued on next page)

Table 2 (continued)

Ref	Protein, mutation studied	Mutation type	Structure/PDB files used	Simulation package and technique	Specifications (T = temperature, ST = simulation time)	Remark
Khare and Dokholyan (2006)			(1AZV), H46R (1OZT)			Mutation induces disruption of dynamic coupling between monomers of mutant dimer
Fay et al. (2016)	SOD1, T2D	Protective	Modeled T2D-SOD1	Replica exchange discrete MD	ST (for monomer species) = 12 replicas × 100 ns; ST (for dimer species) = 16 replicas × 50 ns	T2D mutation being phosphomimetic stabilizes the SOD1 dimer interface thereby inhibiting dimer dissociation
Srinivasan and Rajasekaran (2015)b	SOD1, C111S	Protective	WT-SOD1 (2V0A, chain A), A4V mutant (1UXM, chain A), modeled A4V_C111S mutant	GROMACS, discrete MD	GROMOS 43a5 force field; SPC water model; T = 300 K	The C111S mutation helps in recovering the loss of structural stability, protein compactness and secondary structure propensity seen in pathogenic A4V mutant

aggregation some of these proteins are also prone to misfolding (Dave et al., 2019; Saunders and Bottomley, 2009). For example WW domain is a well studied short domain which is seemingly a two state folder (Dave et al., 2016) and commonly found in repeat proteins becomes prone to aggregation as the number of repeat increases (Dave et al., 2019). Huntingtin protein which is a large, multidomain, HEAT repeat protein (Li et al., 2006) is also prone to aggregation. The exon 1 of the huntingtin protein consists of an N-terminal domain with 17 amino acids and at the 18th amino acid position there begins the polyQ domain which is immediately followed by a polyP region. Several neurodegenerative diseases are found to be associated with the misfolding and aggregation of proteins containing mutant polyQ sequence in the form of expanded polyQ sequence. One such neurodegenerative disease is the Huntington Disease (HD) caused by the polyQ expansion at the N-terminal of exon1 of the huntingtin protein. All polyQ proteins linked to polyglutamine diseases are very dissimilar but share the common region of expanded poly Q tract. All polyQ diseases with the exception of SCA6 occur when the threshold length of the polyQ segment is approximately 35–40 residues. In HD, the Htt protein misfolds and aggregates while experimentally it has been found that the polyglutamine segment alone aggregates into pathogenic conformations like amyloid fibrils. Thus, intensive studies on polyQ segments have been performed to gain insight into the structure (Laghaei and Mousseau, 2010), structural stability (Stork et al., 2005; Merlino et al., 2006; Ogawa et al., 2008; Esposito et al., 2008) and aggregation propensity (Wen et al., 2017) of polyglutamine segments. During aggregation of huntingtin exon1 protein, there occurs conformational transition of the polyQ to a β rich structure. Studies have suggested that before the polyQ tract contributes to the aggregation mechanism, the early role is played by flanking sequences of the polyQ region (Saunders and Bottomley, 2009). However, the polyP tract present at the C-terminal region can suppress this polyQ aggregation (Priya and Gromiha, 2019).

Perutz et al. were the first to propose a β -helix structure of polyglutamines based on their β -helix model (Perutz et al., 2002). The stability of this Perutz nanotube β -helix model has been studied by many using Molecular Dynamics. Stork et al. suggested that circular polyQ β -helices with 18 residues per turn are unstable while those with 20 residues per turn along with being unstable go to a triangular structure after 10 ns (Stork et al., 2005). Two-coiled triangular polyQ β -helices are unstable but get stabilized on dimerization. This study shows that the number of glutamine residues present affects the aggregation of polyQ segment. Another MD simulation study (Wen et al., 2017) on polyQ monomers show that as the lengths of polyQ tract increases solvent-polyQ interaction propensity decreases which in turn encourage polyQ aggregation. Merlino et al. simulated β -helices having 36, 41, 61 and 161 residues polyQ with 20 residues in one turn. The β -helices having residues 41 and less are found to be unstable in this study (Merlino et al., 2006). Ogawa et al. showed that Perutz nanotube β -helices having 30, 37 and 40 residues polyQ with 18.5 and 20 residues per turn are stable in 1 ns simulation when the hydrogen bond

parameters between main chain units are appropriate. Thus, backbone hydrogen bonds are crucial to the stability of the polyQ β -helical structure (Ogawa et al., 2008). Esposito et al. studied the stability of the cross β -spine steric zipper by employing MD simulation (Esposito et al., 2008). The 17 N-terminal residue headpiece of this Htt protein is N17^{Htt}. Experimental studies have shown that N17^{Htt} promotes rapid polyGln aggregation and the hydrophobic residues present in N17^{Htt} are essential for polyGln aggregation while the polar residues control the rate of aggregation. Simulated tempering molecular dynamics simulations have been performed to gain insights into the thermodynamics of the head-piece of the Htt protein (Kelley et al., 2009). N17^{Htt} is involved in the rate determining step associated with the critical transition from random coil to β -sheet structure in Htt aggregation. It has been proposed that this N17^{Htt} initiates the dimerization and pulls the polyQ chains close enough for the nucleation event to begin.

2.4. Amyloid β

Alzheimer's disease (AD) is associated with the aggregation of amyloid β (A β) peptide (Nazica-Labouze et al., 2015). This peptide has variable length, consisting of 39–40 amino acids while the most distinguished forms have residues 40 to 42. Studies suggest that soluble oligomers of A β are the principal toxic species in AD. However, the insoluble fibrillar amyloid aggregates of A β also contribute to neurotoxicity. Thus, various MD simulation studies have been performed on A β fragments, oligomers and fibrils. A fragment of the full length A β peptide is the A β 10–35 peptide possessing most of the amyloidogenic properties related to its full-length counterpart. Replica Exchange Molecular Dynamics (REMD) simulation of the 26 amino acid long A β 10–35 peptide suggests that the monomeric conformations of this peptide possess a pre-folded structural motif extending across residues D23 to K28 that encourages fast aggregation (Baumketner and Shea, 2007). Additionally, the REMD study reveals that under ambient physiological conditions the A β 10–35 peptide instead of folding to a unique native state remains as an ensemble of inter-converting conformations. Further, experimental work suggested that the peptide possessed a structured core around which the carboxy and amino terminal parts formed a mobile halo. This finding however contrasts with the result of simulation which indicates that the ensemble of conformations populated by A β 10–35 is not as narrowly centred on the central structural motif (Baumketner and Shea, 2007). Replica-exchange algorithm employed here helped in improving conformational sampling issues faced by prior simulation studies. This method is pertinent for studying conformation space of peptides whose energy landscapes are dominated by deep basins isolated by high barriers. REMD studies on the A β 21–30 peptide concluded that this fragment while being resistant to protease degradation and aggregation, nucleates the folding of the full-length A β peptide (Baumketner et al., 2006). Resistance to protease degradation may be due to preservation of peptide structure in the denatured state even at high temperatures. Experimental studies have been made on the

various aspects of cellular function such as pH (Kirkpatrick et al., 2001), salt concentration (Klement et al., 2007) and interactions of A β with metal ions (Smith et al., 2007) that may play an important role in the early steps of A β aggregation. Another such aspect is the interactions of A β peptide with anionic cellular membranes. Unconstrained and umbrella sampling MD simulation has been conducted to study the interactions between the 42 amino acid A β peptide and model bilayers of lipids (Davis and Berkowitz, 2009). It has been found that the interactions occurring between A β peptide and lipid bilayer encourages a peptide distribution on the surface of the lipid bilayer that is susceptible to peptide-peptide interactions. Thus interactions of the A β peptide with anionic cellular membranes can act as a potential mediator in the conversion of the A β monomer to oligomer. Previous Molecular Dynamics simulation (Buchete et al., 2005) on A β ₉₋₄₀ protofilament demonstrated that the intermolecular Asp23-Lys28 salt bridges along with the inter and intramolecular hydrophobic packing between the β -strands contribute to the stability of the mature A β fibril. Between the non-polar residues of the β -strand regions, there exist strong hydrophobic interactions which lead to the formation of a well-packed core. This core acts as a crucial element in the stability of β -amyloid fibrils. Also, charges inside the core are compensated by the staggered intermolecular arrangement of the Asp23-Lys28 contacts and by the interior hydration of the core. These factors too may contribute to the stability of amyloid fibrils. Similarly, another simulation study (Tarus et al., 2008) suggests that inside the core of the fibril, there is a region of internal hydration which in turn promotes the stability of the salt bridge. Later, standard MD along with center-of-mass pulling and umbrella sampling has been employed to study the effects of various mutations on the stability of A β protofibrils (Lemkul and Bevan, 2010). This study further found that the packing of the β 2 region against β 1, particularly in the vicinity of the Asp23-Lys28 salt bridge, is crucial to the stability of protofibril. Also it was proposed that the packing between the residues Ile32 and Leu34 in

the core of the protofibril helps regulate the level of hydration in the core thereby rigidifying the Asp23-Lys28 salt bridge.

Various mutations in the A β precursor protein sequence pose as another major factor towards familial AD. Different familial AD mutations show strikingly different effects on the misfolding and aggregation process of A β protein. MD simulation is widely used to study the impact of various mutations on aggregation of A β protein. The summary of the studied mutations and the findings together with details of simulation setup for amyloid β are provided in Table 3. MD simulation studies reveal that the E22Q (Baumketter et al., 2008), D7H, D7N and H6R mutations have the ability to increase A β aggregation propensity (Xu et al., 2014) while the A21G mutation plays a role in slowing down aggregation of A β ₁₋₄₀ but not A β ₁₋₄₂ (Huet and Derreumaux, 2006). The A2T mutation has a protective effect while the A2V mutation has a harmful effect against AD (Das et al., 2015). Since different familial AD mutations show different effects on the A β misfolding and aggregation, so as to gain information on the mechanism of the disease, simulation studies were performed to find out how these different mutations modify the process of A β aggregation. It is known that aggregation propensity is linked to α -helix propensity. This propensity to form α -helix is significantly influenced by pathogenic mutations E22K, E22Q, E2G and D23N whereby the mutations E22K and E22Q favour helix formation around residue 20–24 (Lin et al., 2012; Lin and Pande, 2012) and D23N disfavours helix formation around residue 23 (Lin and Pande, 2012). The mutations E22K and E22Q encourage rapid peptide aggregation than D23N.

Table 4 provides the details of simulation set up used in various studies that addresses the impact of factors affecting misfolding/aggregation other than mutation. In all the tables (Tables 1–4) it is evident that short simulations with multiple runs are commonly used to efficiently sample conformational space. In this regard different techniques like REMD, DMD, etc. are also frequently used.

Table 3
Details of simulation setup and mutations studied for A β

Ref	Protein, mutation studied	Mutation type	Structure used	Simulation package and technique	Specifications (T = temperature, ST = simulation time)	Remark
Baumketter et al. (2008)	Amyloid β , E22Q	Pathogenic	A β ₁₅₋₂₈ WT and A β ₁₅₋₂₈ E22Q (1st set); A β ₂₁₋₃₀ E22Q (2nd set); A β ₉₋₄₀ (3rd set)	GROMACS, replica exchange MD	OPLS-AA force field; TIP3P water model; 3 sets of simulations: 1st: T = 277–600 K, ST = 60 replicas \times 28 ns; 2nd: T = 277–600 K, ST = 2 runs \times 25 ns \times 40 replicas; 3rd: T = 300, 500 K, ST = 10 runs \times 5 ns	Mutation weakens the interactions between the central hydrophobic cluster and the E22-K28 bend of the A β peptide
Xu et al. (2014)	Amyloid β , D7H, D7N, H6R	Pathogenic	A β ₁₋₄₂ (120Q) and modeled mutant structure	AMBER, replica exchange MD	AMBER ff99SB force field; T = 280–400 K; ST for A42: 100 ns/replica extended to 200ns/replica; ST for D7H: 7.52 μ s (940 ns/replica); ST for D7N: 4.21 μ s (526 ns/replica); ST for H6R: 4.21 μ s (526 ns/replica)	Studied A β N terminus mutations increase the β -sheet propensity of both N and C termini. Mutations lead to an increase in solvation free energy and thereby enhance aggregation of A β monomers
Huet and Derreumaux (2006)	Amyloid β , A21G	Length-dependent; protective in A β ₁₋₄₀ but not in A β ₁₋₄₂	2002 NMR A β ₄₀ fibril model, modeled A β ₄₂ -A21G, modeled A β ₄₀ -A21G	GROMACS, NPT ensemble	GROMOS96 force field; SPC water model; T = 400 K; ST = 10 ns	All four species studied have no common structural features. Influence of mutation on the structure and dynamics of A β depends on the length of A β , whether occurring in A β ₄₀ or A β ₄₂ . A2V mutant displays an increased double-hairpin topology, A2T mutant displays a population consisting only of C-terminal hairpin
Das et al. (2015)	Amyloid β , A2T, A2V	A2T: Protective, A2V: Protective in heterozygous form and pathogenic in homozygous form	WT A β ₁₋₄₂ , A2V A β ₁₋₄₂ , A2T A β ₁₋₄₂	GROMACS, replica exchange MD	OPLS-AA force field; TIP3P water model; T = 276–592 K; ST = 64 replicas \times 175 ns	Formation of helix occurs in the region of residues 20–24 due to the E22K mutation
Lin et al. (2012)	Amyloid β , E22K	Pathogenic	A β ₁₋₄₀ , A β ₁₋₄₂ , A β ₁₋₄₂ -E22K mutant	NPT ensemble	AMBER ff99SB force field; TIP3P water model; T = 300 K; ST = 10 ps	Increase in helix propensity in the region of residues 20–23 occurs due to E22K and E22Q mutations. Decrease in helix propensity in the region of residues 33–36 occurs in all four mutations
Lin and Pande (2012)	Amyloid β , E22K, E22Q, E22G, D23N	Pathogenic	A β ₁₋₄₂ -E22K, A β ₁₋₄₂ -E22Q, A β ₁₋₄₂ -E22G, A β ₁₋₄₂ -D23N	NPT ensemble	AMBER ff99SB force field; TIP3P water model; T = 300 K; ST = 10 ps	

Table 4
Details of simulation setup of various studies on factors affecting protein misfolding and aggregation.

Ref	Protein involved	Structure/PDB used for simulation	Simulation package and technique	Specifications (T = temperature, ST = simulation time)	Remark
De Simone et al., 2005	Prion	5 prion C-terminus structures viz. 1UWS, 1TQC, 1TPX, 1TQB, model1 of 1HJN	GROMACS, NPT ensemble	GROMOS96 force field; T = 300 K; SPC/E water model; pH = 7; ST = 10 ns	Tightly bound water molecules play an important role in holding the local elements of the fold at their place
Vila-Viquez et al. (2012)	Prion	1HJM, segment 125–226 combined with segment 90–123 from 2PRP	GROMACS, constant-pH MD	GROMOS96 53A6 force field; T = 310 K; SPC water model; pH = 7; ST = 10 ns, 39 short pH jump simulations and 40 ns, 12 long pH jump simulations	Insights obtained at a molecular level on the reversibility of PrP misfolding induced by pH
Cheng et al. (2017)	Prion	PrP ^{Sc} system: 1QLX with added missing residues 90–127, PrP ^{Sc} system: constructed	in lucon molecular mechanics (llmm)	Levitt et al., force field; T = 310 K; pH = neutral, mid, low; ST for PrP ^{Sc} system: 3 runs × 3 different pH × 50 ns; ST for PrP ^{Sc} system: 3 runs × 3 different pH × 80 ns	Membrane-bound PrP ^{Sc} is resistant to PrP ^{Sc} -induced misfolding owing to its tilted conformation
Campos et al. (2016)	Prion	4 different constructs of human PrP 90–231	GROMACS, constant-pH MD	GROMOS96 53A6 force field; T = 310 K; SPC water model; ST = 40 ns simulation at pH 2 and 4, 30 ns simulation at pH 5, 6, 7	A pH-dependent conformational change is observed whereby a decrease in helix content and an increase in β content is seen towards acidic pH. Protonation of His 167 may play a significant role in PrP misfolding
Gu et al. (2003)	Prion	HuPrP 125–226 based on NMR structure of HuPrP 23–230	GROMACS	GROMOS96, SPC water model; at neutral pH environment: T = 298 K, 350 K; at strongly acidic environment: T = 300 K; at weakly acidic environment: T = 300 K; ST = 4 runs × 10 ns and 2 additional 10 ns runs	Simulations both at low pH and high temperature reveal unfolding of helices and extension of β -sheets but tertiary structure changes are observed only in low pH simulation
Alonso et al. (2001)	Prion	1B10 Model 4 with residues 109–219	ENCAD	Levitt et al., force field; T = 300 K; P3C water model; pH = neutral and low; ST = 10 ns	At acidic pH, there occurs lengthening of the native β -sheet and formation of new β -structure in the N terminus of the protein
Shamair and Dalby (2005)	Prion	4 variants based on 1QLX: native methionine and native valine polymorphism of PrP; methionine and valine polymorphism of PrP D178N mutant	GROMACS	GROMOS96 force field, T = 300, 500 K; SPC water model; pH = 7; ST = 4 variants × 3 runs × 1 ns	In the globular region of D178N mutants, there occurs formation of new β -sheets at 500 K. This D178N mutation has no influence of either Met or Val at residue 129
El-Bastawisy et al. (2001)	Prion	WT-homology model, WT-NMR structure, D178N mutant model	AMBERS, NVT ensemble	AMBER 94 force field; TIP3P water model; T = 300 K, 500 K	The β -sheet content of the D178N mutant increases owing to the movement of loop regions
DeMarco and Daggett (2009)	Prion	2 human prion protein constructs: PrP ^{Sc} ₂₃₀₋₂₃₁ , PrP ^{Sc} ₁₂₁	in lucon molecular mechanics (llmm), NVE ensemble	Levitt et al., force field; T = 298 K; pH = 6–4.3 (low), 7.9–6.1 (neutral); ST = 15 ns	There is no significant alterations in the structure or dynamics of PrP ^{Sc} due to glycosylation and membrane anchoring but there is modifications in the surface accessibility of the PrP ^{Sc} polypeptide
Ding et al. (2005)	Prion	Modeled cc β peptides	Discrete MD	ST = 10 ⁶ TU	Presence of a critical temperature, above which the peptide misfolds
Pushie and Vogel (2003)	Prion	Cu ²⁺ -bound OR ₄ model	GROMACS	OPLS-AA force field; SPC water model; T = 300 K; ST = 200 ns	Close association of particular Trp and Gly residues with the bound Cu ²⁺ ion under low Cu ²⁺ occupancy condition can lead to generation of ROS
Pushie et al. (2009)	Prion	DFJ model	GROMACS	OPLS-AA force field; SPC water model; T = 300 K	Binding of Cu ²⁺ to His96 and His111 residues can induce formation of localized β -sheet structure
Baumlechner and Shea (2007)	Amyloid β	A β 10–35 peptide	GROMACS, replica exchange MD	OPLS force field; TIP3P water model; T = 280–580 K; ST = 72 replicas × 95 ns	Presence of a pre-folded structural motif in monomeric conformations of A β 10–35 encourage fast aggregation of A β 10–35 peptide
Baumlechner et al. (2006)	Amyloid β	A β 21–30	GROMACS, replica exchange MD	OPLS/AA empirical force field; TIP3P water model; T = 300 K–600 K; ST = 24ns/replica	Resistance of A β 21–30 to protease degradation and aggregation may be due to preservation of peptide structure in the denatured state even at higher temperatures
Davis and Berkowitz (2009)	Amyloid β	Random coil structures	GROMACS, Umbrella sampling MD	GROMACS force field; T = 323 K; SPC/E water model; pH = 3, 5, 7; ST = 80 ns/window	Provides quantitative aspect of A β binding to dipalmitoylphosphatidylcholine and anionic dioleoylphosphatidylserine bilayer
Buchete et al. (2005)	Amyloid β	Models of both finite and infinite A β _{1–42} fibrils	NAMD2, NPT ensemble	CHARMM 27 force field, AMBER94 force field, AMBER 94 force field modified by Garcia & Sanbonmatsu; T = 298 K; TIP3P water model; ST = 10 ns	Structural characterization of simulated amyloid fibrils done to gain insights into their molecular surface, backbone dihedral angles, left-handed twisted configuration, interior hydration and internal salt-bridges
Tarus et al. (2008)	Amyloid β	A β _{11–30} peptide	CHARMM	PARAM22 all-atom force field; T = 300 K; TIP3P water model	Region of internal hydration inside the core of the fibril promotes stability of the salt bridge
Lemkul and Bevan (2010)	Amyloid β	A β protofibril	GROMACS, steered MD	GROMOS96 53A6 force field; SPC water model; ST = 31 windows × 10 ns	Stability of the Asp29-Lys28 salt bridge is maintained by the packing of residues Ile32 and Leu34 in the core of the fibril
	Huntingtin				

(continued on next page)

Table 4 (continued)

Ref	Protein involved	Structure/PDB used for simulation	Simulation package and technique	Specifications (T = temperature, ST = simulation time)	Remark
Laghajei and Mousseau (2010)		30, 40 and 50 residue random structures of polyQ monomers; 30 and 40 residue random structures of polyQ dimers; 30, 35, 37 and 40 residue nanotube units of dimers	Replica exchange MD	OPEP implicit solvent force field; T = 250–700 K; ST for monomers = 200 ns; ST for dimers = 150, 300 ns	Monomers do not spontaneously form β -sheet structure but adopt random coil structures from α -helical structures. Dimers with 40 residues spontaneously form antiparallel β -sheets along with triangular and circular β -helical structures
Stork et al. (2005)	Huntingtin	Modeled polyQ β -helices	EGO-MMII, NPT ensemble	CHARMM22 force field; TIP3P water model (CHARMM variant); T = 300 K; ST = 2–10 ns	Initial aggregation seed of Huntingtin require dimers of atleast 36 Q repeats
Merlino et al. (2006)	Huntingtin	4 β -helix models of different sizes (36, 41, 61 and 161 Gln)	GROMACS	SPC water model; T = 300 K; ST = 4 models \times 5 ns	Shorter β -helix models are unstable and give irregular structures. Longer helix models with residues more than 40 give a dynamic regular structure
Ogawa et al. (2008)	Huntingtin	Models with 20Q, 25Q, 30Q, 37Q and 40Q having 18.5 and 20 residues per coil	AMBER7	AMBER99 force field; TIP3P water model; T = 310 K; ST = 1 ns	An increase in the number of Q repeats provide stability to the structure. Presence of a critical Q number is observed around 30Q, above which the structure is kept stable
Esposito et al. (2008)	Huntingtin	PolyQ polymeric and monomeric forms assembled by cross- β -spine steric zipper motifs	GROMACS; NVT ensemble for 300 K simulations; NPT ensemble for 500 K simulations	GROMOS43a1 force field; SPC water model; T = 300, 500 K; ST = 10, 15, 20 and 50 ns	The overall stability of the models is greatly influenced by the glutamine side chains.
Wen et al. (2017)	Huntingtin	PolyQ monomers with 18, 32 and 46 repeats	AMBER14	AMBER ff99SB force field; TIP3P water model; T = 310 K; ST = 3 structures \times 6 runs \times 150 ns	A decrease in solvent-polyQ interaction propensity is observed with an increase in the length of polyQ monomer.
Kelley et al. (2009)	Huntingtin	A helix structure with 78.3% helical content, a random-coil structure having no helical content	GROMACS; simulated tempering MD	AMBER2008 force field; TIP3P water model; T = 285–592 K; ST = 100 ps	A two-helix bundle is predicted to be the most populated state for N17 ^{RH} , though a considerable percentage of the structures still adopted a single linear helix.
Priya and Gromiha (2019)	Huntingtin	6 models of protein having different Q lengths: Q ₁₇ , Q ₂₇ P ₁₁ , Q ₃₄ , Q ₃₈ , Q ₄₂ , Q ₄₀ , Q ₃₀ , Q ₃₀ P ₁₁	GROMACS	AMBER99SB-ILDN force field; SPC water model; T = 300 K; ST = 500 ns	The presence of flanking domains in the huntingtin exon-1 makes it prone to aggregation while the presence of a proline rich C-terminal inhibits aggregation.

3. Insights into the protein aggregation mechanisms and the amyloid structures by molecular dynamics simulation

In ALS, prion and AD, soluble proteins aggregate into insoluble amyloid fibrils rich in β -sheets following major conformational transition of their respective natively alpha-helical proteins to a predominantly β -sheet structure (Ding et al., 2005). The development of final cure of such amyloidogenic diseases demand the understanding of the molecular mechanism of this transition which is laborious to study owing to the complicated interaction network among amino acids and the large sizes of involved proteins in some cases. The time scales of these conformational rearrangements are usually experimentally inaccessible and as such computational approaches are required in studying the conformational dynamics accompanying the conformational changes. Thus, computational methods are emerging as an encouraging analytical tool in understanding the mechanism of protein aggregation. Moreover, gaining insights into the structure of amyloid, the principles underlying amyloid formation and the molecular mechanism and pathways would possibly be the first step or a major step (if not first) in fighting against diseases associated with protein aggregation and amyloid formation. There are certain factors that make the experimental study of protein aggregation quite difficult. These are participation of cell membrane in protein aggregation, their insolubility in water and heterogeneous nature (Ma and Nussinov, 2006). These difficulties fascinated computational methods as a complement to experimental analysis. MD simulation studies are increasingly being utilized to study protein misfolding and aggregation. *In vitro* studies on the general features of protein fibrillization can provide a helping hand in understanding the origins of numerous protein misfolding diseases. The systems studied range from the initial single misfold-prone peptide to the usual final product of misfolding i.e. highly ordered mature amyloid fibrils. On fulfilment of appropriate conditions, fibril formation can be said to be an intrinsic property of all polypeptides (Nguyen and Hall,

2006). This suggests that the forces that lead to stabilization of fibrils are the forces common to all polypeptides and not those that are linked to specific interactions occurring between side chains.

High resolution MD simulations of fibril-forming isolated peptides have been carried out to study the formation of fibrils from random coils (Grponer et al., 2003; Mager, 1998). Considerable information regarding the properties of fibrils and the mechanism involved in their formation were gained. However, one drawback of this system is that it does not contain enough peptides. MD simulation of multipolypeptide system having already-formed fibrillar aggregates have also been performed (George and Howlett, 1999; Li et al., 1999). Low resolution MD simulation studies on protein aggregation have been conducted too (Harrison et al., 1999; Leonhard et al., 2004). These studies provide significant insights into the basic physics involved in the aggregation of proteins. This system nevertheless meets the drawback of not sufficiently considering forces that play significant role in fibril formation, like the hydrogen bonding. After that came the study of fibril formation by MD simulations using intermediate-resolution models of protein (Sikorski et al., 1998, 2000). Due to the built-in bias of Go potential towards native conformation, PRIME (Protein Intermediate-Resolution Model) was designed to be used with discontinuous MD (Alder and Wainwright, 1959; Rapaport, 1978), which works more suitably in the study of fibril formation from random coil conformation. At present the study of fibril formation from systems possessing between 12 and 96 polyaniline peptides in random state, where the polyaniline peptides are of 16 residues is also possible (Nguyen and Hall, 2006).

3.1. Prion protein

Aggregation of proteins in prion diseases is preceded by protein conformational transition from alpha-helices to β -sheets. Prusiner proposed a template-mediated aggregation mechanism for prion (Prusiner, 1998) wherein it is proposed that the refolding of PrP^C (an alpha-helix

rich form) into PrP^{Sc} (a β -sheet rich state) is directed by existing PrP^{Sc}. This transition is difficult to study through experimental characterization because of the complicated interaction network existing among amino acids. Many computational studies were carried out in support of this template model of generating conformational changes. A number of simulation studies among them employ artificial constrain (Lipfert et al., 2005; Matolepsza et al., 2005). Using a simple 17-residue peptide (cc β) designed by Kammerer et al. (2004), Ding et al. studied this conformational transition employing unconstrained DMD as constrained studies are likely to be influenced by the artificial biases present in the simulation. In the course of simulations, it is observed that several peptides form a β -sheet. Stable β -sheets having exposed hydrophobic surfaces and unsaturated H bonds and located close to an alpha helix promotes the conversion of the alpha helix to a β -strand. These simulations provided computational evidence in support of the Prusiner's template-mediated aggregation mechanism (Ding et al., 2005) and suggested a general mechanism for prion-like infectivity associated with protein misfolding.

It has been speculated that the toxic PrP^{Sc} form is generated via oligomerization of PrP^{C*} (where PrP^{C*} is an intermediate conformational state (Thirumalai et al., 2003)) state which may be preceded by substantial unfolding of the native PrP^C form to the more stable PrP^{C*} state (Thirumalai et al., 2003). When this unfolding mechanism of human prion protein was studied through well-tempered metadynamics (WTMD) simulation, it was found that there are several possible unfolding pathways (Singh et al., 2017). The simulation study computationally proved that PrP^{C*} corresponds to the global minimum and PrP^C is metastable on the conformational free energy landscape. Strikingly, the global minima states are seen to not possess increased beta sheet content contrasting to the findings of prior simulation studies according to which development of beta rich isoforms encourage PrP^{Sc} formation. These prior simulations were carried out using REMD, high temperature, low pH (Langella et al., 2004; Chakroun et al., 2013), etc. When the conformational change of the prion protein was monitored, experimentally it was observed that H₂ and H₃ helices of the prion protein are stable while H₁ has a high beta sheet propensity (Eghiaian et al., 2004). On the contrary, some MD simulation studies indicated that not only H₁ is unusually stable, the helical propensity of H₂ and H₃ is highly reduced (Dima and Thirumalai, 2004; Chakroun et al., 2013). The helices H₂ and H₃ are the initiation sites of prion misfolding. Later, WTMD simulation study by Singh et al. (2017), showed that neither the individual helices nor the protein as a whole is stable, rather an intermediate unfolded state possess metastability. This study concluded that tertiary contacts and solvation forces stabilize only feebly the secondary structural elements of the prion protein. As such substantial unfolding of the prion protein may occur under the influence of pressure, temperature, pH, etc.

Experimental investigation coupled with metadynamics simulation was used to gain insights into the T183A huPrP^C aggregation under physiological conditions (Sanz-Hernández et al., 2021). The study indicated that T183A variant of PrP is capable of inducing amyloid formation under natural conditions solely by the C-terminal domain of the prion protein, though a prior simulation study has suggested the presence of a high unfolding barrier which restrict spontaneous prion misfolding under physiological conditions (Chen and Thirumalai, 2013). However, this amyloid conversion under physiological conditions is expected to be unique to this T183A mutation.

3.2. Superoxide dismutase]

The SOD1 misfolding in ALS appears to involve a gain-of-interaction mechanism (Brujin et al., 1998; Gurney et al., 1994) in which the misfolded SOD1 protein forms aberrant interactions with proteins (these include various cellular proteins and other SOD1 molecules), called protein-protein-interactions (PPI) and thus interfere with their normal functioning. The phenomenon of SOD1 misfolding in SOD1-related ALS has been studied by SMD. Characterization of the backbone dynamics

landscape of the pathogenic misfolded SOD1 locates surface areas inclined to abnormal PPIs. This analysis helped in framing a working hypothesis for the obscure gain-of-function mechanism of SOD1 misfolding (Banerjee et al., 2016). According to this hypothesis, an abnormal potential to participate in PPI results from the increased surface backbone mobility of the SOD1. Based on the results obtained from computational and experimental studies on the apo SOD1 monomer, it was hypothesized that the various mutations causing destabilization of the apo SOD1 monomer is due to mutations causing distinct local unfolding dynamics. The partially unfolded structure is prone to aggregate while the residual folded structure containing the peptide segments form the "building block" for aggregation. This hypothesis was tested by studying the aggregation of wild type, G37R and I149T variants of SOD1 by employing simulation technique and was found consistent with experiments. They suggested the local unfolding caused by apo-monomer leading to formation of aggregation "building blocks" as the mechanism of SOD1 aggregation (Ding et al., 2012).

3.3. Huntingtin protein

Experimentally it has been found that polyglutamine aggregation follows nucleated growth polymerization (Chen et al., 2002). A monomer functioning as the critical nucleus initiates this polymerization. The conformation of the polyQ stretch in the nucleus that initiates fibrillization is later accessed through atomistic MD simulation. This study showed that in the initiation of polyQ fibrillization, β -hairpin-based or α -helical conformations can act as a template. However, steric zipper or nanotube-like structures being kinetically not stable enough, cannot initiate polyQ fibrillization (Miettinen et al., 2012). MD simulation study on polyQ template made from natural proteins suggested that in polyQ aggregation, left-handed triangular and right-handed rectangular conformations having atleast 3 rungs can act as possible nucleation seeds in the very early stage of aggregation (Zhou et al., 2011).

Using coarse grained REMD simulations (Leghæi and Mousseu, 2010), determination of structure of polyQ aggregates has been performed. Simulation of monomers with varying lengths having random structures revealed that all monomers showed transition from α -helices structure to random coil. They spontaneously do not adopt β -rich structure. The 40-residue dimer organizes into a final antiparallel double-stranded nanotube. These nanotubes are later simulated explicitly by Mosseau et al. (Côte et al., 2012) to study the hexamers and octamers of Q_N and N17^{Htt}Q_N where N17^{Htt} is the N-terminal residues of Huntingtin. According to this study dimeric nanotubes can act as building blocks in the formation of longer nanotubes like hexamers and octamers. Also, N17^{Htt} increases the stability of the dimmers.

3.4. Amyloid β

In Alzheimer's disease (AD), there occurs accumulation of 40- or 42-residue A β proteins. Studies (Jarrett and Lansbury Jr, 1993) manifest that the extracellular aggregation propensity and neurological toxicity of A β 42 compared to A β 40 is more. There is evidence that the proximate effectors of synaptic change in AD are the small oligomers of A β 42 and not the extracellular amyloid fibrils (Walsh and Selkoe, 2007). Thus, to design therapeutics against AD, understanding of the structure of all species involved in the early A β aggregation and the mechanism behind this aggregation process of A β 42 is required. However, this study faces some experimental limitations because on one hand the monomer has a quick aggregation propensity in water and on the other the fibrils are extremely insoluble. Theoretical and computational approaches proved beneficial in this regard. Multiple all-atom MD simulations have been used to characterize most plausible aggregation prone structure (APS) of A β 42 (Lee and Ham, 2011). Based on this characterization, a plausible mechanism of A β fibril formation from APS has been proposed. According to this mechanism, when the starting seed conformation for A β monomer is the proposed APS, A β fibril formation from APS would

accompany breakage of intramolecular backbone H-bonds followed by the side chain flip and subsequent formation of intermolecular H-bonds between each A β monomer unit. This study also includes characterization of the early transitions of the misfolding in a lag phase.

4. Molecular dynamics simulation as a beneficial tool in the search for therapeutic strategies relating to protein aggregation diseases

The development of effective therapies against neurodegenerative diseases has seen only little success despite the tremendous advances in our understanding of these diseases. Investigations in this direction make use of both experimental and computational approaches. Among them, MD simulation is of particular importance in the field of drug discovery. It proves valuable both qualitatively and quantitatively in the process of lead optimization where a ligand is modified as required in order to improve some properties like efficacy, etc. At a qualitative level, simulation can be used to predict rearrangements induced by a ligand on the binding site on protein targets. At a quantitative level, simulation-based computational methods give estimates of ligand binding affinities more precisely than others like docking (Hollingsworth and Drox, 2018). Such information is crucial in guiding the process of novel drug discovery. The following gives an account of how MD simulation helps in the study of interaction mechanism between a ligand and a protein and thereby helps in establishing or in further designing of potent inhibitors that may act as effective therapeutic agent against neurodegenerative diseases.

There are small molecule inhibitors that help aberrant proteins attain a native or a near-native conformation by restricting the conformational changes necessary for protein aggregation. Small molecules thus offer innovative opportunities in the area of drug discovery relating to protein misfolding diseases. Structural diversity along with low cytotoxicity and druggability makes compounds from natural products (including resveratrol, caffeine, curcumin, etc) an attractive area of study (Li et al., 2017).

Nanomaterials such as graphene, carbon nanotubes, and fullerenes which fall under the category of carbon nanomaterials are drawing considerable attention in the field of biomedicine against neurodegenerative diseases. These carbon nanomaterials having remarkable adsorption capacity possess ultrasmall size due to which they can easily access cells and interact with amyloid proteins (Zhou et al., 2018). Thus potential therapeutic effect along with biological toxicity of carbon nanoparticles (NP) have been intensively explored in regard to protein misfolding diseases.

4.1. Prion protein

Experimentally it was revealed that resveratrol could impede prion fibrillation but capturing structural details of this fibrillation process through conventional experiments is quite challenging. Thus, to study the dynamic process of prion misfolding, MD simulation was used. The PrP₁₂₇₋₁₄₇ fragment of the prion protein is a widely used model which exhibits typical characteristics of full length PrP^{Sc} and shows aggregation ability in *in vitro* conditions. In the MD simulation study of inhibition mechanism of resveratrol on prion aggregation, it was suggested that the PrP₁₂₇₋₁₄₇ peptide is stabilized by resveratrol mostly through π - π stacking interactions while the hydrogen bonds interactions between them further reduces the propensity of PrP₁₂₇₋₁₄₇ to aggregate. Furthermore, the presence of resveratrol interrupts in-chains salt bridge formation and encourages inter-chains salt bridge formation. This stabilization of the PrP₁₂₇₋₁₄₇ peptides together with the inter-chains salt bridge formation could contribute to the stabilization of the overall structure of the prion protein and thereby inhibit aggregation of prion protein (Li et al., 2017). This result supported the experimental results thereby proving the inhibitory effect of resveratrol on prion aggregation (Li et al., 2017). The effect of carbon NPs on the prion protein

aggregation along with the associated inhibition mechanism is studied through experiments and atomistic simulations. Simulation study suggested that due to decrease in interpeptide interactions, there is a reduction in the aggregation propensity of PrP₁₂₇₋₁₄₇. Moreover, π - π stacking interactions between aromatic residues are seen to contribute to the inhibitory effects of Carbon NPs (Zhou et al., 2018).

4.2. Superoxide dismutase I

Docking simulation together with SMD simulation and MM/PBSA were used to study the mechanism of mutant A4V and L84F SOD1 aggregation in the presence of curcumin (Srinivasan and Rajasekaran, 2016) and epigallocatechin-3-gallate (EGCG) (Srinivasan and Rajasekaran, 2017c) respectively and both studies obtained similar results. It was suggested that binding of curcumin to the A4V mutant SOD1 reduces the mutationally induced destabilizing effect on SOD1 i.e. binding of curcumin aids in retention of stability of the mutant SOD1. DMD simulation study of another polyphenol, resveratrol reveals that upon binding of resveratrol to the G93A mutant of SOD1, a reduction in the β -sheet propensity helps inhibition of aggregates formed in the mutant SOD1 indicating the potential of this polyphenol as an inhibitor of fibrillar aggregation in G93A mutant (Srinivasan and Rajasekaran, 2018c). Thus corroborating well with the experimental findings, these computational approaches extended promising treatment against mutant SOD1, using curcumin, EGCG and resveratrol, all of which are natural polyphenols (Bhatia et al., 2015; Koh et al., 2006; Mancuso et al., 2014). This approach seems beneficial in designing therapeutics against the neurodegenerative disorder ALS.

A study on non-covalent interactions between SOD1 and a number of flavanoids indicated that naringin amongst all has the strongest binding affinity. MD simulation results suggested that naringin upon binding to the interface of SOD1 dimer could reduce the dissociation of the dimers through hydrogen bond interactions. This study further concluded that stabilization of the SOD1 dimer depends very much on the number of hydrogen bond donor or acceptor of the small molecule bound to the dimer interface (Zhuang et al., 2016).

4.3. Amyloid β

Experimental studies observed that NPs either promote or inhibit the formation of amyloid aggregation but could not cite the underlying molecular mechanism. Coarse-grained DMD simulation later provided a molecular mechanism describing how NP-protein attraction affects amyloid aggregation (Radic et al., 2015). Increase of NP-protein attraction initially promoted protein aggregation on the surface of the NP till the optimum value is reached but further increase of NP-protein attraction inhibited amyloid aggregation. DMD simulation (Radic et al., 2015) highlighted the fact that nanomedicine may act as potential drug candidate against amyloid diseases including AD. A β -peptide deposition is a neuropathological characteristic of AD. NP may play an eminent role in decreasing the severity of this disease. MD simulation study (Baweja et al., 2015) has shown that adsorption of A β on graphene based nanomaterials, graphene oxide (GO) and reduced graphene oxide (rGO) could inhibit the toxic conformational transition of α -helix to β -sheet in A β . The rGO is seen to be a more effective inhibitor, possibly due to increase in hydrophobic π regions on its surface.

It is believed that the development of AD can be impeded through caffeine and experimental analyses together with MD simulation helped in investigating the effect of caffeine on the aggregation of amyloid- β derived switch-peptide with varied stoichiometric ratio of caffeine to peptide. MD simulation established that only when caffeine to peptide ratio is 10:1 or greater, the formation of β -sheet conformation which was observed from a much early stage during simulation is inhibited to a great extent. Also, one significant contributing factor to the formation and stabilization of β -sheet rich protein is the inter-protein hydrogen bonding which is seen to get weakened due to formation of hydrogen

bonds between caffeine molecules and peptides. Thus caffeine prevents formation of an ordered β -sheet and aggregation of switch peptide (Sharma et al., 2016). Absence and presence of the therapeutic molecule curcumin showed contrasting effects on two A β 42 mutants viz. A2T and A2V. The protective mutant A2T which exhibited least stability in the absence of curcumin, exhibits highest stability in its presence while the harmful mutant A2V becomes least stable in the presence of curcumin which otherwise was stable in the absence of curcumin. MD simulation study suggested curcumin to be a more efficient inhibitor for the protective A2T mutant as compared to the harmful A2V mutant (Awasthi et al., 2018). Curcumin is structurally similar to salvianolic acid which is a polyphenolic derivative and both have caffeic acid as a common scaffold. When MD simulation combined with experimental analyses was performed to study the inhibitory effects of salvianolic acid A on the formation of A β fibrils, it was found that salvianolic acid stabilizes the β -helical conformations via binding to the C-terminus of A β and thereby inhibits A β aggregation (Cao et al., 2013). In a comparative study on curcumin and ferulic acid where ferulic acid is a weaker A β inhibitor, it was found that curcumin affects the primary nucleation process of A β 1–42 peptides to a larger extent than ferulic acid. Curcumin in fact has been reported to inhibit the primary nucleation process of protein amyloid aggregation. The primary nucleus formed in the presence of curcumin is of bigger size and the peptide chains present in it are less flexible and more disordered. Also, there is a decrease in the number of non-native contacts and H bonds between the chains (Doytchinova et al., 2020). All atom MD simulation on EGCG constituting the major bioactive compound of green tea shows that EGCG acts as an inhibitor of A β protofibril in membrane environment (Dong et al., 2021). The A β 42 protofibril disruption caused by EGCG is greatly influenced by the presence of membrane environment. There occurs enhancement in the structural stability of the protofibril in the presence of lipid bilayers and as such A β 42 protofibril disruption occurs to a lesser extent in its presence than that in the membrane-free environment.

4.4. Huntingtin protein

Many experimental studies focused on the search for therapeutic strategies against polyglutamine aggregation causing Huntington's disease. The studied compounds range from NPs like TiO₂ (titanium oxide) (Ceccon et al., 2018) and MnFe₂O₄ NPs (Zhang et al., 2019) to nano form of natural flavonoid quercetin (Debnath et al., 2019) to resveratrol derivatives with silyl modifications and their corresponding prodrugs with acyl, glucosyl and carbamoyl modifications (Belmonte-Reche et al., 2021). Experimental studies indicated that among the *O*-silyl resveratrol derivatives, di-triethylsilyl and di-triisopropylsilyl derivatives have better anti-inflammatory activity and neuroprotective capacity than the parent compound resveratrol. Among the disilyl resveratrol prodrugs with acyl, glucosyl and carbamoyl modifications, 3, 5-triethylsilyl-4'-(6''-OO octanoylglucopyranosyl) resveratrol was capable of reducing the severity of 3-nitropropionic acid-induced Huntington disease-like symptoms (Belmonte-Reche et al., 2021). When the anti-amyloidogenic action of nanoquercetin at low quercetin concentration was studied experimentally, it was found that nanoquercetin inhibits mutant huntingtin aggregation in the cell model of Huntington's disease (Debnath et al., 2019). TiO₂ NPs are seen to decrease aggregation of huntingtin peptides possessing both the N-terminal domain and a C-terminal polyglutamine tract of ten residues (htt^{NT}Q₁₀). This decrease is due to surface-catalysed oxidation of Met⁷ to a sulfoxide by TiO₂ NPs (Ceccon et al., 2018). Another study suggested that synthesized MnFe₂O₄ NPs displaying 74 glutamine repeats [Htt(Q74)] could accelerate the selective clearing of mutant huntingtin through ubiquitin-proteasome system of the PQC machinery (Zhang et al., 2019). This study therefore concluded that bioactive nanomaterials could be a potential therapeutic strategy for Huntington and other neurodegenerative diseases. Thus, intensive experimental studies (including those cited above) on exploration of promising therapeutic strategies for HD

have been carried out from time to time. However, not many MD simulation studies for drug discovery against HD are there to the best of our knowledge. This may be an important and interesting area of research in the near future. Table 5 summarizes the details of simulation setup, therapeutic agents, binding location and inhibition mode.

5. Overview on force fields and simulation methods

The modeling of large systems such as proteins and protein fragments can be accomplished through MD simulations since these employ only an implicit representation of electrons in atoms and molecules. MD simulations, since their invention are seen to successfully complement experimental methods. The success of the employed force fields and algorithms used to carry out a simulation is judged by the degree to which they are capable of accurately reproducing experimental observables. However, MD simulations face challenges in terms of system size and simulation time and experience limitations in terms of the quality of force field used for proteins. Moreover, frequently used algorithmic constrains such as LINC, SHAKE employed for performing a simulation (Childers and Daggett, 2018; Wille et al., 2019) can also impact the outcome of the simulation. In addition, the choice of water models is also crucial to reproduce experimental observations; mostly due to two reasons: first, different water models have their own limitations and abilities (Somavarsapu and Kepp, 2015), second, their additive use with specific force fields (Robustelli et al., 2018) can also affect the accuracy of the simulations. Most force fields at the initial stage were co-optimized with specific water models, for example, the AMBER force field with the TIP3P model, the CHARMM force field with the modified TIP3P model, the GROMOS force field with the SPC and SPC/E model and the OPLS-AA force field with the TIP4P model. However, from the literature and also from the current review, it is seen that different combination of force fields and water models are being frequently employed to carry out simulation studies (Baumketner et al., 2006; Kumar et al., 2018; Keerthans and Kolandaivel, 2015). The purpose of application of some particular force fields in some particular work mentioned in this review demands special emphasis. For example, both Lin et al. (2012) and Lin and Pande (2012) used AMBER ff99SB and TIP3P water since the force field could satisfactorily reproduce the experimental *J*-coupling values, as well as the residual dipolar coupling data for A β 42. Pushie et al. (2009) used the OPLS-AA force field since it is built on structures and properties calculated using DFT. The DFT models used in the DFT calculations performed in their work are directly portable to MD simulations because of the use of the OPLS force field. Laghaci and Mouzeau (2010) used the coarse-grained OPEP force field since the prediction of the native and equilibrium structures of many peptides along with their thermodynamic properties could be accurately made by this force field. Also, this force field provides accuracy with a reasonable computational cost. Both Ning et al., 2015 and Zhou et al. (2018) used the AMBER ff99SB force field. Avoiding any biased tendency towards α -helix structure unlike AMBER ff99 force field, the AMBER ff99SB force field can attain a better balance of secondary structures including extended/ β -strand and α -helix. Also, the AMBER ff99SB force field could reproduce the secondary structure of graphene sheet-adsorbed peptides and that structure was found to be comparable to experimental measurements. AMBER ff12SB force field parameters were used by Borgohain et al. (2016) in order to obtain accurate secondary structure propensities. In the study of protein misfolding and aggregation it is important for the force field to be unbiased to any of the secondary structure since misfolding transitions mostly are associated with significant change in secondary structure content. Cheng et al. (2017) used the Levitt et al., force field since the lipid parameters were derived to be consistent with this force field. However, the used DMD force field by Ding et al. (2005), being a simplified one was seen to be incapable of distinguishing between β -hairpins and coiled-strands. Thus, a mixture of both the types of β -structures was observed in their work.

In an effort to overcome the challenges faced during MD simulation

Table 5
Details of simulation setup, therapeutic agents, binding location and inhibition mode.

Ref	Protein involved and structures used	Therapeutic agent	Location of binding	Mode of inhibition of aggregation	Simulation package, technique and force field
Li et al. (2017)	Prion; tetrameric construct of PrP ₁₂₇₋₁₄₇ peptide	Resveratrol	Resveratrol molecules randomly placed around PrP ₁₂₇₋₁₄₇ tetramer	Stabilization of the PrP ₁₂₇₋₁₄₇ peptide through π - π stacking and hydrogen bond interactions interaction and formation of in-chains and inter-chains salt bridge respectively	AMBER10; GAFF force field for resveratrol and AMBER ff99SB force field for peptides
Zhou et al. (2018)	Prion; tetramer of PrP ₁₂₇₋₁₄₇ peptide, tetramer in the presence of carbon nanotube, tetramer in the presence of graphene	Carbon Nps: graphene and carbon nanotubes	PrP ₁₂₇₋₁₄₇ peptides randomly placed	Decrease in the interpeptide interactions which in turn inhibits β -sheet formation	AMBER16; AMBER ff99SB force field
Srinivasan and Rajasekaran (2016)	SOD1; curcumin bound native and A4V mutant SOD1 complex	Curcumin	Active site predicted theoretically	Retention of stability of the mutant A4V SOD1 upon binding to curcumin	YASARA; steered MD; AMBER03 force field
Srinivasan and Rajasekaran (2018)c	SOD1; resveratrol bound native and G93A mutant SOD1 complex	Resveratrol	A large sized cavity identified by CastP	Reduction of β -sheet propensity	Discrete MD; medusa force field
Srinivasan and Rajasekaran (2017)c	SOD1; EGCG bound native and LS4F mutant SOD1 complex	EGCG	Predicted through blind molecular docking using AutoDock	Reduction of β -sheet propensity	YASAR; Steered MD; AMBER03 force field
Zhuang et al. (2016)	SOD1; naringin and naringenin bound SOD1 complex	Naringin and Naringenin	Interface of SOD1 dimer	Reduction of SOD1 dimer dissociation by naringin through interaction with the dimer interface	NAMD
Baweja et al. (2015)	Amyloid β ; models of graphene oxide and reduced graphene oxide on A β	Carbon Nps: graphene oxide and reduced graphene oxide	Adsorption of A β on graphene oxide and reduced graphene oxide	Restriction of α -helix to β -sheet conformational transition	GROMACS; NPT ensemble; GROMOS53a6 force field
Sharma et al. (2016)	Amyloid β ; amyloid β derived switch peptide	Caffeine	Caffeine molecules randomly placed	Weakening of the interstrand hydrogen bonds by forming hydrogen bonds with peptide	AMBER12; NPT ensemble; AMBER ff99SB force field
Awasthi et al. (2018)	Amyloid β ; A2V and A2T mutant structures of A β 42	Curcumin	Curcumin molecules randomly placed around A β	Alteration in the equilibrium of the A β aggregation pathway	GROMACS; GROMOS96 43a1 force field
Cao et al. (2015)	Amyloid β ; salivianolic acid A bound A β 42 complex	Salivianolic acid A	Predicted through molecular docking using AutoDock	Stabilization of the α -helical conformations via binding to the C-terminus of A β	GROMACS; GAFF force field for salivianolic acid A and AMBER ff03 force field for peptides
Doytchinova et al. (2020)	Amyloid β ; 5 models of A β ₁₋₄₂	Curcumin	Curcumin molecules randomly placed around A β	Inhibition of primary nucleation process of protein amyloid aggregation	AMBER18; GAFF force field for curcumin and AMBER ff14SB force field for peptides
Dong et al. (2021)	Amyloid β ; LS-shaped tetrameric A β ₄₂ protofibril in presence of lipid bilayers, tetrameric A β ₄₂ protofibril in presence of both lipid bilayer and EGCG	EGCG	EGCG molecules randomly added	Disruption of A β protofibril	GROMACS; NPT ensemble; Jämbeck force field for lipids, AMBER99SB-ILDN force field for EGCG and protein

regarding the computational time and sampling of conformational space, various methods are seen to be applied. The current review too delineates the use of a variety of such approaches since both these challenges are significant in case of study of misfolding/aggregation. Generation of multiple independent (short) MD trajectories against a single (long) one is a simple yet widely used approach. When multiple short simulations instead of a single long one are performed, the sampling of protein conformational space turns out to be better provided the total sampling time remains same in both cases (Guo et al., 2012a; Guo et al., 2012b; van der Kamp and Daggett, 2010). Another alternative is to use generalized-ensemble algorithms. MD simulations of complex protein systems with many degrees of freedom are likely to be trapped in local minima in free energy landscape. Methods like simulated tempering (Kelley et al., 2009) and parallel tempering (or replica exchange method) (Ning et al., 2015; Baumketner and Shea, 2007) perform a random walk in temperature space and can facilitate the system to escape from being trapped in local minima. DMD is also seen to be frequently used in misfolding/aggregation studies as it decreases the computational time while increasing sampling with reasonable accuracy if all atom description of the protein is used (Ding et al., 2005; Fay et al., 2016; Srinivasan and Rajasekaran, 2018 a). Another possibility is to use coarse-grained molecular dynamics simulations with implicit solvent models (Milardi et al., 2010). In the coarse-grained

method, groups of atoms, or sometimes residue or even the entire peptide chain, is treated as one particle. This method though appears to be a suitable alternative; it compromises with the atomistic description of the studied systems. Similarly use of implicit solvent models significantly decreases the computational time however at the cost of loss in accuracy. In case of misfolding/aggregation water mediated interactions, salt bridge formation etc. are important and implicit solvent models cannot accurately capture such interactions. Center-of-mass pulling simulations or steered molecular dynamics simulations can be used when the behaviour of the studied system has to be deliberately made biased toward a particular phenomenon that might otherwise not be accessible on the conventional MD time scale. In the present review, the use of steered molecular dynamics simulations is seen particularly in the study of potential drug candidates against ALS (Srinivasan and Rajasekaran, 2016; Srinivasan and Rajasekaran, 2017c). This tool proves beneficial in the study of relative binding energies between potential drugs and the targeted misfold prone proteins along with the associated binding mechanisms by considering the mechanical components such as flexibility of both the drug and the target. The use of thermodynamic integration (Milardi et al., 2010) and umbrella sampling (Davis and Berkowitz, 2009) is also seen in the review, both of which are commonly applied methods used to calculate free energy differences.

6. Conclusion

The study of large biomolecular systems including proteins are now increasingly employing MD simulations since these can provide an atomistic detail including time evolution of many biochemical processes. Moreover, MD simulation immensely assists in the study of various responses produced by biomolecules to perturbations like mutation, addition or removal of a ligand, etc. This *in silico* method has proved to be a highly complementary tool in researching debilitating diseases related to four misfold prone proteins viz. prion, superoxide dismutase1 (SOD1), amyloid β (A β) and huntingtin, all linked to chronic neurodegenerative diseases. Various point mutations occurring in misfold prone proteins either favour the process of aggregation or disfavor amyloid formation. For prions, SOD1 and amyloid protein study of both protective and harmful mutations have been addressed. On one hand there is discussion of factors acting as potential mediators in protein aggregation and on the other discussion of those that contribute to its resistance. The current understanding of the mechanisms associated to aggregation of the pathological proteins has been mentioned. MD simulation has come up as a beneficial tool in improving the efficiency of lead optimization by helping to obtain accurate binding modes and binding abilities of potential lead compounds. The contribution of this computational tool in the search for therapeutic strategies against three neurodegenerative diseases viz. ALS, TSE and AD have been mentioned. However, there is very scanty or barely any study on drug discovery for HD using MD simulation technique.

The current review provides adequate information to reinforce the fact that MD simulation has immensely assisted in the study of misfold prone proteins, although in terms of degree of accuracy and quantitative description regarding protein motions, molecular simulations are seen to have certain limitations (Childers and Daggett, 2018). The two factors that hinder the predictive capability of molecular simulations are the sampling problem and the accuracy problem. The problem of sampling occurs since the correct description of properties of certain dynamical processes require lengthy simulations while the problem of accuracy arises due to the various approximations associated with the mathematical forms of force fields and their related parametrizations. Some additional factors including the water model, motion restraining algorithms, employed simulation ensemble also influence the results of MD simulations. In order to overcome the sampling problem, various methods including simulated tempering, parallel tempering, coarse-grain modeling, etc are being applied. With the current computational power (even in high performance computing facilities), simulations up to microseconds regimes are reported to be feasible for systems having up to 10^5 atoms (Wille et al., 2019). Though the early events of misfolding could be sufficiently captured under such time-scales, however, some of the events of misfolding are missed out. However, in future with increase in computational efficiency, improved force fields and algorithms, when longer timescale simulations with higher accuracy would become feasible, this tool would prove to be even more helpful in understanding events like misfolding/aggregation and in developing therapeutics against neurodegenerative diseases.

Declaration of competing interest

The authors declare that they have no known competing financial interests or personal relationships that could have appeared to influence the work reported in this paper.

Acknowledgements

The authors gratefully acknowledge DST, India [Project No. ECR/2017/000494], and UGC, India [Project No 30-406/2017 (BSR)] for financial assistance. The financial assistance of the DST-FIST and UGC-SAP program to the Department of Chemistry, Dibrugarh University, is also gratefully acknowledged.

References

- Alder, B.J., Wainwright, T.E., 1959. Studies in molecular dynamics. I. General method. *J. Chem. Phys.* 31, 459–466. <https://doi.org/10.1063/1.1730376>.
- Alemasov, N.A., Ivanisenko, N.V., Medvedev, S.P., Zakian, S.M., Kolchanov, N.A., Ivanisenko, V.A., 2017. Dynamic properties of SOD1 mutants can predict survival time of patients carrying familial amyotrophic lateral sclerosis. *J. Biomol. Struct. Dyn.* 35, 645–656. <https://doi.org/10.1080/07391102.2016.1158666>.
- Alonso, D.O.V., DeArmond, S.J., Cohen, F.E., Daggett, V., 2001. Mapping the early steps in the pH-induced conformational conversion of the prion protein. *Proc. Natl. Acad. Sci. USA* 98, 2985–2989. <https://doi.org/10.1073/pnas.061555898>.
- Azante, E.A., Smidak, M., Grimshaw, A., Houghton, R., Tomlinson, A., Jeelani, A., Jakubcova, T., Hamdan, S., Richard-Londt, A., Linehan, J.M., Brandner, S., Alpers, M., Whitfield, J., Mead, S., Wadsworth, Jonathan D.F., Collinge, J., 2015. A naturally occurring variant of the human prion protein completely prevents prion disease. *Nature* 522, 478–481. <https://doi.org/10.1038/nature14510>.
- Awasthi, M., Singh, S., Pandey, V.P., Dwivedi, U.N., 2018. Modulation in the conformational and stability attributes of the Alzheimer's disease associated amyloid-beta mutants and their favorable stabilization by curcumin: molecular dynamics simulation analysis. *J. Biomol. Struct. Dyn.* 36, 407–422. <https://doi.org/10.1080/07391102.2017.1279078>.
- Banerjee, V., Shani, I., Katzman, B., Vyzamensky, M., Papo, N., Israelson, A., Engel, S., 2016. Superoxide dismutase 1 (SOD1)-Derived peptide inhibits amyloid aggregation of familial amyotrophic lateral sclerosis SOD1 mutants. *ACS Chem. Neurosci.* 7, 1595–1606. <https://doi.org/10.1021/acscchemneuro.6b00227>.
- Baron, G.S., Caughey, B., 2003. Effect of glycerylphosphatidylinositol anchor-dependent and-independent prion protein association with model raft membranes on conversion to the protease-resistant isoform. *J. Biol. Chem.* 278, 14883–14892. <https://doi.org/10.1074/jbc.M210840200>.
- Baron, G.S., Wehrly, K., Dorward, D.W., Chesebro, B., Caughey, B., 2002. Conversion of raft associated prion protein to the protease-resistant state requires insertion of PrP^{Sc} into contiguous membranes. *EMBO J.* 21, 1031–1040. <https://doi.org/10.1093/emboj/21.5.1031>.
- Baruah, A., Biswas, P., 2014. The role of site-directed point mutations in protein misfolding. *Phys. Chem. Chem. Phys.* 16, 13964–13973. <https://doi.org/10.1039/C3CP55367A>.
- Baruah, A., Bhattacharjee, A., Biswas, P., 2012. Role of conformational heterogeneity on protein misfolding. *Soft Matter* 8, 4432–4440. <https://doi.org/10.1039/C2SM06608D>.
- Baumkemer, A., Shea, J.E., 2007. The structure of the Alzheimer amyloid β 10–35 peptide probed through replica-exchange molecular dynamics simulations in explicit solvent. *J. Mol. Biol.* 366, 275–288. <https://doi.org/10.1016/j.jmb.2006.11.015>.
- Baumkemer, A., Bernstein, S.L., Wyttenbach, T., Lazo, N.D., Teplov, D.B., Bowers, M.T., Shea, J.E., 2006. Structure of the 21–30 fragment of amyloid β -protein. *Protein Sci.* 15, 1239–1247. <https://doi.org/10.1110/ps.062076806>.
- Baumkemer, A., Krone, M.G., Shea, J.E., 2008. Role of the familial Dutch mutation E22Q in the folding and aggregation of the 15–28 fragment of the Alzheimer amyloid- β protein. *Proc. Natl. Acad. Sci. USA* 105, 6027–6032. <https://doi.org/10.1073/pnas.0708193105>.
- Baweja, L., Balaramurugan, K., Subramanian, V., Dhawan, A., 2015. Effect of graphene oxide on the conformational transitions of amyloid beta peptide: a molecular dynamics simulation study. *J. Mol. Graph. Model.* 61, 173–185. <https://doi.org/10.1016/j.jmgm.2015.07.007>.
- Belmonte-Reche, E., Penálver, P., Caro-Moreno, M., Mateos-Martín, M.L., Adán, N., Delgado, M., González-Rey, E., Morales, J.C., 2021. Silyl reversion derivatives as potential therapeutic agents for neurodegenerative and neurological diseases. *Eur. J. Med. Chem.* 223, 113655. <https://doi.org/10.1016/j.ejmech.2021.113655>.
- Bhatia, N.K., Srivastava, A., Katyal, N., Jain, N., Khan, M.A.I., Kundu, B., Deep, S., 2015. Curcumin binds to the pre-fibrillar aggregates of Cu/Zn superoxide dismutase (SOD1) and alters its amyloidogenic pathway resulting in reduced cytotoxicity. *Biochim. Biophys. Acta, Proteins Proteomics* 1854, 426–436. <https://doi.org/10.1016/j.bbapap.2015.01.014>.
- Bjorndahl, T.C., Zhou, G.P., Liu, X., Perez-Pineiro, R., Semenchenko, V., Saleem, P., Acharya, S., Bujold, A., Sobsey, C.A., Wishart, D.S., 2011. Detailed biophysical characterization of the acid-induced PrP^{Sc} to PrP^D conversion process. *Biochemistry* 50, 1162–1173. <https://doi.org/10.1021/bi101435c>.
- Borgia, M.B., Borgia, A., Bear, R.B., Steward, A., Nettels, D., Wunderlich, B., Schuler, B., Clarke, J., 2011. Single-molecule fluorescence reveals sequence-specific misfolding in multidomain proteins. *Nature* 474, 662–665. <https://doi.org/10.1038/nature10099>.
- Borghain, G., Dan, N., Paul, S., 2016. Use of molecular dynamics simulation to explore structural facets of human prion protein with pathogenic mutations. *Biophys. Chem.* 213, 32–39. <https://doi.org/10.1016/j.bpc.2016.03.004>.
- Bruijn, L.I., Houseweart, M.K., Kato, S., Anderson, K.L., Anderson, S.D., Ohama, E., Reaume, A.G., Scott, R.W., Cleveland, D.W., 1998. Aggregation and motor neuron toxicity of an ALS-linked SOD1 mutant independent from wild-type SOD1. *Science* 281, 1851–1854. <https://doi.org/10.1126/science.281.5394.1851>.
- Buchete, N.V., Tycko, R., Hummer, G., 2005. Molecular dynamics simulations of Alzheimer's β -amyloid protofibrillaments. *J. Mol. Biol.* 353, 804–821. <https://doi.org/10.1016/j.jmb.2005.08.066>.
- Campoio, S.R.R., Machuqueiro, M., Baptista, A.M., 2010. Constant-pH molecular dynamics simulations reveal a β -rich form of the human prion protein. *J. Phys. Chem. B* 114, 12692–12700. <https://doi.org/10.1021/jp104733a>.
- Cao, Y.Y., Wang, L., Ge, H., Lu, X.L., Pei, Z., Gu, Q., Xu, J., 2013. Salvianolic acid A, a polyphenolic derivative from *Salvia miltiorrhiza* bunge, as a multifunctional agent for

- the treatment of Alzheimer's disease. *Mol. Divers.* 17, 515–524. <https://doi.org/10.1007/s11030-013-9452-z>
- Ceccon, A., Tugarinov, V., Clore, G.M., 2018. TiO₂ nanoparticles catalyze oxidation of huntingtin exon 1-derived peptides impeding aggregation: a quantitative NMR study of binding and kinetics. *J. Am. Chem. Soc.* 141, 94–97. <https://doi.org/10.1021/jacs.8b11441>
- Chakroun, N., Fornili, A., Prigent, S., Kleinjung, J., Dreiss, C.A., Rezaei, H., Fraternali, F., 2013. Deciphering prion protein conversion into a β-rich conformer by molecular dynamics. *J. Chem. Theor. Comput.* 9, 2455–2465. <https://doi.org/10.1021/ct301118j>
- Chen, J., Thirumalai, D., 2013. Helices 2 and 3 are the initiation sites in the PrP^C → PrP^{Sc} transition. *Biochemistry* 52, 310–319. <https://doi.org/10.1021/bi3005472>
- Chen, S., Ferrone, F.A., Wetzel, R., 2002. Huntington's disease age-of-onset linked to polyglutamine aggregation nucleation. *Proc. Natl. Acad. Sci. USA* 99, 11884–11889. <https://doi.org/10.1073/pnas.182276099>
- Chen, W., van der Kamp, M.W., Daggert, V., 2010. Diverse effects on the native β-sheet of the human prion protein due to disease-associated mutations. *Biochemistry* 49, 9874–9881. <https://doi.org/10.1021/bi101449f>
- Cheng, C.J., Koldes, H., Van der Kamp, M.W., Schiuff, B., Daggert, V., 2017. Simulations of membrane-bound diglycosylated human prion protein reveal potential protective mechanisms against misfolding. *J. Neurochem.* 142, 171–182. <https://doi.org/10.1111/jnc.14044>
- Childers, M.C., Daggert, V., 2018. Validating molecular dynamics simulations against experimental observables in light of underlying conformational ensembles. *J. Phys. Chem. B* 122, 6673–6689. <https://doi.org/10.1021/acs.jpcc.8b02144>
- Coñate, S., Wei, G., Mousseau, N., 2012. All-atom stability and oligomerization simulations of polyglutamine nanotubes with and without the 17-amino-acid N-terminal fragment of the huntingtin protein. *J. Phys. Chem. B* 116, 12168–12179. <https://doi.org/10.1021/jp306661c>
- Da Silva, A.N.R., Pereira, G.R.C., Moreira, L.G.A., Rocha, C.F., De Mesquita, J., 2019. SOD1 in amyotrophic lateral sclerosis development in silico analysis and molecular dynamics of A4F and A4V variants. *J. Cell. Biochem.* 120, 17822–17830. <https://doi.org/10.1002/jcb.29048>
- Dar, P., Murray, B., Belfort, G., 2015. Alzheimer's protective A2T mutation changes the conformational landscape of the Aβ_{1–42} monomer differently than does the A2V mutation. *Biophys. J.* 108, 738–747. <https://doi.org/10.1016/j.bpj.2014.12.015>
- Dave, K., Jager, M., Nguyen, H., Kelly, J.W., Gruebele, M., 2016. High-resolution mapping of the folding transition state of a WW domain. *J. Mol. Biol.* 426, 1617–1636. <https://doi.org/10.1016/j.jmb.2016.02.008>
- Dave, K., Gasic, A.G., Cheung, M.S., Gruebele, M., 2019. Competition of individual domain folding with inter-domain interaction in WW domain engineered repeat proteins. *Phys. Chem. Chem. Phys.* 21, 24393–24405. <https://doi.org/10.1039/C8CP07775D>
- Davis, C.H., Berkowitz, M.L., 2009. Interaction between amyloid-β (1–42) peptide and phospholipid bilayers: a molecular dynamics study. *Biophys. J.* 96, 785–797. <https://doi.org/10.1016/j.bpj.2008.09.053>
- De Simone, A., Dodson, G.G., Verma, C.S., Zagari, A., Fraternali, F., 2005. Prion and water: tight and dynamical hydration sites have a key role in structural stability. *Proc. Natl. Acad. Sci. USA* 102, 7535–7540. <https://doi.org/10.1073/pnas.0501748102>
- Dearmond, S.J., Qui, Y., Sanchez, H., Spilman, P.R., Nünchak-Casey, A., Alonso, D., Daggert, V., 1999. PrP^C glycoform heterogeneity as a function of brain region: implications for selective targeting of neurons by prion strains. *J. Neurochem. Exp. Neurol.* 58, 1000–1009. <https://doi.org/10.1097/00005072-199909000-00010>
- Debnath, K., Jana, N.R., Jana, N.R., 2019. Quercetin encapsulated polymer nanoparticle for inhibiting intracellular polyglutamine aggregation. *ACS Appl. Bio Mater.* 2, 5295–5305. <https://doi.org/10.1021/acsaahm.9b00518>
- DeMarco, M.L., Daggert, V., 2009. Characterization of cell-surface prion protein relative to its recombinant analogue: insights from molecular dynamics simulations of diglycosylated, membrane-bound human prion protein. *J. Neurochem.* 109, 60–73. <https://doi.org/10.1111/j.1471-4159.2009.05892.x>
- Dima, R.I., Thirumalai, D., 2004. Probing the instabilities in the dynamics of helical fragments from mouse PrP^C. *Proc. Natl. Acad. Sci. U.S.A.* 101, 15355–15360. <https://doi.org/10.1073/pnas.0404235101>
- Ding, F., LaRocque, J.J., Dokholyan, N.V., 2005. Direct observation of protein folding, aggregation, and a prion-like conformational conversion. *J. Biol. Chem.* 280, 40235–40240. <https://doi.org/10.1074/jbc.M506872000>
- Ding, F., Furukawa, Y., Nukina, N., Dokholyan, N.V., 2012. Local unfolding of Cu, Zn, superoxide dismutase monomer determines the morphology of fibrillar aggregates. *J. Mol. Biol.* 421, 548–560. <https://doi.org/10.1016/j.jmb.2011.12.029>
- Dobson, C.M., 2001. The structural basis of protein folding and its links with human disease. *Philos. Trans. R. Soc. B356*, 133–145. <https://doi.org/10.1098/rstb.2000.0758>
- Dobson, C.M., 2003. Protein folding and misfolding. *Nature* 426, 884–890. <https://doi.org/10.1038/nature02261>
- Dong, X., Tang, Y., Zhan, C., Wei, G., 2021. Green tea extract EGCG plays a dual role in Aβ_{1–42} protofibril disruption and membrane protection: a molecular dynamic study. *Chem. Phys. Lipids* 234, 105024. <https://doi.org/10.1016/j.chemphyslip.2020.105024>
- Doytchinova, I., Atanasova, M., Salamanova, E., Ivanov, S., Dimitrov, I., 2020. Curcumin inhibits the primary nucleation of amyloid-beta peptide: a molecular dynamics study. *Biomolecules* 10, 1323. <https://doi.org/10.3390/biom10091323>
- Eghiazian, F., Grosclaude, J., Lescau, S., Debey, P., Doublier, B., Tréguer, E., Rezaei, H., Kozlov, M., 2004. Insight into the PrP^C → PrP^{Sc} conversion from the structures of antibody-bound ovine prion scrapie-susceptibility variants. *Proc. Natl. Acad. Sci. U.S.A.* 101, 10254–10259. <https://doi.org/10.1073/pnas.0400014101>
- El-Bastawisy, E., Knaggs, M.H., Gilbert, I.H., 2001. Molecular dynamics simulations of wild-type and point mutation human prion protein at normal and elevated temperature. *J. Mol. Graph. Model.* 20, 145–154. [https://doi.org/10.1016/S1093-3263\(01\)00113-9](https://doi.org/10.1016/S1093-3263(01)00113-9)
- Esposito, L., Paladino, A., Pedone, C., Vitagliano, L., 2008. Insights into structure, stability, and toxicity of monomeric and aggregated polyglutamine models from molecular dynamics simulations. *Biophys. J.* 94, 4031–4040. <https://doi.org/10.1529/biophysj.107.118935>
- Fay, J.M., Zhu, C., Proctor, E.A., Tao, Y., Cui, W., Ke, H., Dokholyan, N.V., 2016. A phosphomimetic mutation stabilizes SOD1 and rescues cell viability in the context of an ALS-associated mutation. *Structure* 24, 1898–1906. <https://doi.org/10.1016/j.str.2016.08.011>
- Fernández, A., 2002. Insufficient hydrogen-bond desolvation and prion-related disease. *Eur. J. Biochem.* 269, 4165–4169. <https://doi.org/10.1046/j.1432-1033.2002.03116.x>
- Fernández, A., Scheraga, H.A., 2003. Insufficiently dehydrated hydrogen bonds as determinants of protein interactions. *Proc. Natl. Acad. Sci. USA* 100, 113–118. <https://doi.org/10.1073/pnas.0136885100>
- Gavin, L.K., Denny, R.A., Saiah, E., 2012. Small molecules that target protein misfolding. *J. Med. Chem.* 55, 10823–10843. <https://doi.org/10.1021/jm301152j>
- George, A.R., Howlett, D.R., 1999. Computationally derived structural models of the β-amyloid found in Alzheimer's disease plaques and the interaction with possible aggregation inhibitors. *Biopolymers* 50, 733–741. [https://doi.org/10.1002/\(SICI\)1097-0282\(199912\)50:7<733::AID-BIOP6>3.0.CO;2-7](https://doi.org/10.1002/(SICI)1097-0282(199912)50:7<733::AID-BIOP6>3.0.CO;2-7)
- George Priya Dosa, C., Rajith, B., Rajasekaran, R., Srajan, J., Nagasundaram, N., Debajyoti, C., 2013. In silico analysis of prion protein mutants: a comparative study by molecular dynamics approach. *Cell Biochem. Biophys.* 67, 1307–1318. <https://doi.org/10.1007/s12013-013-9663-z>
- Gruebele, M., Dave, K., Sukenik, S., 2016. Globular protein folding in vitro and in vivo. *Annu. Rev. Biophys.* 45, 233–251. <https://doi.org/10.1146/annurev-biophys-062215-011236>
- Geponer, J., Habertur, U., Caffisch, A., 2003. The role of side-chain interactions in the early steps of aggregation: molecular dynamics simulations of an amyloid-forming peptide from the yeast prion Sup35. *Proc. Natl. Acad. Sci. USA* 100, 5154–5159. <https://doi.org/10.1073/pnas.0835307100>
- Gu, W., Wang, T., Zhu, J., Shi, Y., Liu, H., 2003. Molecular dynamics simulation of the unfolding of the human prion protein domain under low pH and high temperature conditions. *Biophys. Chem.* 104, 79–94. [https://doi.org/10.1016/S0301-4622\(02\)00340-X](https://doi.org/10.1016/S0301-4622(02)00340-X)
- Guo, J., Ren, H., Ning, L., Liu, H., Yao, X., 2012a. Exploring structural and thermodynamic stabilities of human prion protein pathogenic mutants D202N, E211Q and Q217R. *J. Struct. Biol.* 178, 225–232. <https://doi.org/10.1016/j.jsb.2012.03.009>
- Guo, J., Ning, L., Ren, H., Liu, H., Yao, X., 2012b. Influence of the pathogenic mutations T188K/R/A on the structural stability and misfolding of human prion protein: insight from molecular dynamics simulations. *BBA* 1820, 116–123. <https://doi.org/10.1016/j.bbagen.2011.11.013>
- Gurney, M.E., Pu, H., Chiu, A.Y., Dal Canto, M.C., Polchow, C.Y., Alexander, D.D., Caliendo, J., Hentati, A., Ronn, Y.W., Deng, H.-X., Chen, W., Zhai, P., Sufit, R.L., Siddique, T., 1994. Motor neuron degeneration in mice that express a human Cu,Zn superoxide dismutase mutation. *Science* 264, 1772–1775. <https://doi.org/10.1126/science.8209258>
- Harrison, P.M., Chan, H.S., Prusiner, S.B., Cohen, P.E., 1999. Thermodynamics of model prions and its implications for the problem of protein folding. *J. Mol. Biol.* 286, 593–606. <https://doi.org/10.1006/jmbi.1998.2497>
- Hard, P.U., 2017. Protein misfolding diseases. *Annu. Rev. Biochem.* 86, 21–26. <https://doi.org/10.1146/annurev-biochem-061516-044518>
- Hoffmann, A., Neupane, K., Woodside, M.T., 2013. Single-molecule assays for investigating protein misfolding and aggregation. *Phys. Chem. Chem. Phys.* 15, 7934–7948. <https://doi.org/10.1039/C3CP44564J>
- Hollingsworth, S.A., Dror, R.O., 2018. Molecular dynamics simulation for all. *Neuron* 99, 1129–1143. <https://doi.org/10.1016/j.neuron.2018.08.011>
- Hou, Y., Dan, X., Babbar, M., Wei, Y., Hasselbalch, S.G., Croteau, D.L., Bohr, V.A., 2019. Ageing as a risk factor for neurodegenerative disease. *Nat. Rev. Neurol.* 15, 565–581. <https://doi.org/10.1038/s41582-019-0244-7>
- Huet, A., Derreumaux, P., 2006. Impact of the mutation A21G (Flemish variant) on Alzheimer's β-amyloid dimers by molecular dynamics simulations. *Biophys. J.* 91, 3829–3840. <https://doi.org/10.1529/biophysj.106.090993>
- Jackson, G.S., Hosszu, L.L.P., Power, A., Hill, A.F., Kenney, J., Saibil, H., Craven, C.J., Walko, J.P., Clarke, A.R., Collinge, J., 1999. Reversible conversion of monomeric human prion protein between native and fibrillogenic conformations. *Science* 283, 1935–1937. <https://doi.org/10.1126/science.283.5409.1935>
- Jarrett, J.T., Lansbury Jr., P.T., 1993. Seeding "one-dimensional crystallization" of amyloid: a pathogenic mechanism in Alzheimer's disease and scrapie? *Cell* 79, 1055–1058. [https://doi.org/10.1016/0092-8674\(93\)90635-4](https://doi.org/10.1016/0092-8674(93)90635-4)
- Kammerer, R.A., Kostrewa, D., Zurdo, J., Denke, A., García-Echeverría, C., Green, J.D., Müller, S.A., Meier, B.H., Winkler, P.K., Dobson, C.M., Steinmetz, M.O., 2004. Exploring amyloid formation by a *de novo* design. *Proc. Natl. Acad. Sci. U.S.A.* 101, 4435–4440. <https://doi.org/10.1073/pnas.0306786101>
- Keerthana, S.P., Kolandaivel, P., 2015. Study of mutation and misfolding of Cu-Zn SOD1 protein. *J. Biomol. Struct. Dyn.* 33, 167–183. <https://doi.org/10.1080/07391102.2013.865104>
- Kelley, N.W., Huang, X., Yam, S., Spiess, C., Frydman, J., Pande, V.S., 2009. The predicted structure of the headpiece of the huntingtin protein and its implications on huntingtin aggregation. *J. Mol. Biol.* 388, 919–927. <https://doi.org/10.1016/j.jmb.2009.01.032>

- Khare, S.D., Dokholyan, N.V., 2006. Common dynamical signatures of familial amyotrophic lateral sclerosis-associated structurally diverse Cu, Zn superoxide dismutase mutants. *Proc. Natl. Acad. Sci. USA* 103, 3147–3152. <https://doi.org/10.1073/pnas.0511266103>.
- Kirkitadze, M.D., Condon, M.M., Teplow, D.B., 2001. Identification and characterization of key kinetic intermediates in amyloid β -protein fibrillogenesis. *J. Mol. Biol.* 312, 1103–1119. <https://doi.org/10.1006/jmbi.2001.4970>.
- Klement, K., Wieligmann, K., Meinhardt, J., Hortschansky, P., Richter, W., Fändrich, M., 2007. Effect of different salt ions on the propensity of aggregation and on the structure of Alzheimer's A β (1–40) amyloid fibrils. *J. Mol. Biol.* 373, 1321–1333. <https://doi.org/10.1016/j.jmb.2007.06.065>.
- Koh, S.-H., Lee, S.M., Kim, H.Y., Lee, K.-Y., Lee, Y.J., Kim, H.-T., Kim, J., Kim, M.-H., Hwang, M.S., Song, C., Yang, K.-W., Lee, K.W., Kim, S.H., Kim, O.H., 2006. The effect of epigallocatechin gallate on suppressing disease progression of ALS model mice. *Neurosci. Lett.* 395, 103–107. <https://doi.org/10.1016/j.neulet.2005.10.056>.
- Kumar, A., Baruah, A., Biswas, P., 2017. Role of local and nonlocal interactions in folding and misfolding of globular proteins. *J. Chem. Phys.* 146, 065102. <https://doi.org/10.1063/1.4975325>.
- Kumar, V., Prakash, A., Lynn, A.M., 2018. Alterations in local stability and dynamics of A4V SOD1 in the presence of trifluoroethanol. *Biopolymers* 109, e23102. <https://doi.org/10.1002/bip.23102>.
- Laghaei, R., Mousseau, N., 2010. Spontaneous formation of nanotubes with molecular dynamics simulations. *J. Chem. Phys.* 132, 165102. <https://doi.org/10.1063/1.3383244>.
- Langella, E., Improta, R., Barone, V., 2004. Checking the pH-induced conformational transition of prion protein by molecular dynamics simulations: effect of protonation of histidine residues. *Biophys. J.* 87, 3623–3632. <https://doi.org/10.1529/biophysj.104.043443>.
- Lee, C., Ham, S., 2011. Characterizing amyloid-beta protein misfolding from molecular dynamics simulations with explicit water. *J. Comput. Chem.* 32, 349–355. <https://doi.org/10.1002/jcc.21628>.
- Lemkul, J.A., Bevan, D.R., 2010. Assessing the stability of Alzheimer's amyloid protofibrils using molecular dynamics. *J. Phys. Chem. B* 114, 1652–1660. <https://doi.org/10.1021/jp9110794>.
- Leonhard, K., Prausnitz, J.M., Radke, C.J., 2004. Solvent-amino acid interaction energies in three-dimensional-lattice Monte Carlo simulations of a model 27-mer protein: folding thermodynamics and kinetics. *Protein Sci.* 13, 358–369. <https://doi.org/10.1110/ps.03198204>.
- Li, L., Darden, T.A., Bartolotti, L., Kominos, D., Pedersen, L.G., 1999. An atomic model for the pleated β -sheet structure of A β amyloid protofibrils. *Biophys. J.* 76, 2871–2878. [https://doi.org/10.1016/S0006-3495\(99\)77442-4](https://doi.org/10.1016/S0006-3495(99)77442-4).
- Li, W., Serpell, L.C., Carter, W.J., Rubinstein, D.C., Huntington, J.A., 2006. Expression and characterization of full-length human huntingtin, an elongated HEAT repeat protein. *J. Biol. Chem.* 281, 15916–15922. <https://doi.org/10.1074/jbc.M511007200>.
- Li, L., Zhu, Y., Zhou, S., An, X., Zhang, Y., Bai, Q., He, Y.-X., Liu, H., Yao, X., 2017. Experimental and theoretical insights into the inhibition mechanism of prion fibrillation by reveratrol and its derivatives. *ACS Chem. Neurosci.* 8, 2698–2707. <https://doi.org/10.1021/acscchemneuro.7b00240>.
- Liemann, S., Glockshuber, R., 1999. Influence of amino acid substitutions related to inherited human prion diseases on the thermodynamic stability of the cellular prion protein. *Biochemistry* 38, 3258–3267. <https://doi.org/10.1021/b9982714g>.
- Lin, Y.S., Pande, V.S., 2012. Effects of familial mutations on the monomer structure of A β . *Biophys. J.* 103, L47–L49. <https://doi.org/10.1016/j.bpj.2012.11.009>.
- Lin, Y.S., Bowman, G.R., Beauchamp, K.A., Pande, V.S., 2012. Investigating how peptide length and a pathogenic mutation modify the structural ensemble of amyloid beta monomer. *Biophys. J.* 102, 315–324. <https://doi.org/10.1016/j.bpj.2011.12.002>.
- Lipfert, J., Franklin, J., Wu, P., Doniach, S., 2005. Protein misfolding and amyloid formation for the peptide GNNQQNY from yeast prion protein Sup35: simulation by reaction path Annealing. *J. Mol. Biol.* 349, 648–658. <https://doi.org/10.1016/j.jmb.2005.03.083>.
- Liu, X., Shi, D., Zhou, S., Liu, H., Liu, H., Yao, X., 2018. Molecular dynamics simulations and novel drug discovery. *Expert Opin. Drug Discov.* 13, 23–37. <https://doi.org/10.1080/17460441.2018.1463419>.
- Ma, B., Nussinov, R., 2006. Simulations as analytical tools to understand protein aggregation and predict amyloid conformation. *Curr. Opin. Chem. Biol.* 10, 445–452. <https://doi.org/10.1016/j.copcb.2006.08.018>.
- Mager, P.P., 1998. Molecular simulation of the amyloid β -peptide A β (1–40) of Alzheimer's disease. *Mol. Simulat.* 20, 201–222. <https://doi.org/10.1080/08927029808024178>.
- Malkhousi, F.R., Ghasemi, J.B., 2018. In silico studies in drug research against neurodegenerative diseases. *Curr. Neuropharmacol.* 16, 664–725. <https://doi.org/10.2174/1570159X15666170823095628>.
- Malolepsza, E., Boniacki, M., Kolinski, A., Piela, L., 2005. Theoretical model of prion propagation: a misfolded protein induces misfolding. *Proc. Natl. Acad. Sci. U.S.A.* 102, 7835–7840. <https://doi.org/10.1073/pnas.0409389102>.
- Mancuso, R., del Valle, J., Modol, L., Martinez, A., Granada-Serrano, A.B., Ramirez-Núñez, O., Pallás, M., Portero-Otin, M., Osta, R., Navarro, X., 2014. Resveratrol improves motoneuron function and extends survival in SOD1^{G20A} ALS mice. *Neurotherapeutics* 11, 419–432. <https://doi.org/10.1007/s13311-013-0253-y>.
- Mead, S., Whitfield, J., Poulter, M., Shah, P., Uphill, J., Campbell, T., Al-Dujaily, H., Hummerich, H., Beck, J., Mein, C.A., Verzilli, C., Whitaker, J., Alpers, M.P., Collinge, J., 2009. A novel protective prion protein variant that colocalizes with kuru exposure. *N. Engl. J. Med.* 361, 2056–2065. <https://doi.org/10.1056/NEJMoa0809716>.
- Merlino, A., Esposito, L., Vitagliano, L., 2006. Polyglutamine repeats and β -helix structure: molecular dynamics study. *Proteins* 63, 918–927. <https://doi.org/10.1002/prot.20941>.
- Miettinen, M.S., Knecht, V., Monticelli, L., Ignatova, Z., 2012. Assessing polyglutamine conformation in the nucleating event by molecular dynamics simulations. *J. Phys. Chem. B* 116, 10259–10265. <https://doi.org/10.1021/jp305065c>.
- Milardi, D., Pappalardo, M., Grasso, D.M., La Rosa, C., 2010. Unveiling the unfolding pathway of FALS associated G37R SOD1 mutant: a computational study. *Mol. Biosci.* 6, 1032–1039. <https://doi.org/10.1039/b918662j>.
- Moldovean, S.N., Chig, V., 2019. Molecular dynamics simulations applied to structural and dynamical transitions of the huntingtin protein: a review. *ACS Chem. Neurosci.* 11, 105–120. <https://doi.org/10.1021/acscchemneuro.9b00561>.
- Morris-Andrews, A., Shea, J.E., 2015. Computational studies of protein aggregation: methods and applications. *Annu. Rev. Phys. Chem.* 66, 643–666. <https://doi.org/10.1146/annurev-physchem-040513-103738>.
- Nasica-Labouze, J., Nguyen, P.H., Sterpone, F., Berthoumieu, O., Buchete, N.V., Cote, S., Simone, A.D., Doig, A.J., Faller, P., Garcia, A., Laio, A., Li, M.S., Melchioni, S., Mousseau, N., Mu, Y., Paravara, A., Pasquali, S., Rosenman, D.J., Strodel, B., Tarus, B., Viles, J.H., Zhang, T., Wang, C., Derreumaux, P., 2015. Amyloid β protein and Alzheimer's disease: when computer simulations complement experimental studies. *Chem. Rev.* 115, 3518–3563. <https://doi.org/10.1021/cr500683n>.
- Nguyen, H.D., Hall, C.K., 2006. Spontaneous fibril formation by polyalanines; discontinuous molecular dynamics simulations. *J. Am. Chem. Soc.* 128, 1890–1901. <https://doi.org/10.1021/ja053914o>.
- Ning, L., Pan, D., Zhang, Y., Wang, S., Liu, H., Yao, X., 2015. Effects of the pathogenic mutation A117V and the protective mutation H111S on the folding and aggregation of PrP106-126: insights from replica exchange molecular dynamics simulations. *PLoS One* 10, e0125899. <https://doi.org/10.1371/journal.pone.0125899>.
- Ogawa, H., Nakano, M., Watanabe, H., Starikov, E.B., Rothstein, S.M., Tanaka, S., 2008. Molecular dynamics simulation study on the structural stabilities of polyglutamine peptides. *Comput. Biol. Chem.* 32, 102–110. <https://doi.org/10.1016/j.compbiolchem.2007.11.001>.
- Perutz, M.F., Finch, J.T., Berriman, J., Lesk, A., 2002. Amyloid fibres are water-filled nanotubes. *Proc. Natl. Acad. Sci. USA* 99, 5591–5595. <https://doi.org/10.1073/pnas.042681399>.
- Priya, S.B., Gromiha, M.M., 2019. Structural insights into the aggregation mechanism of huntingtin exon 1 protein fragment with different polyQ-lengths. *J. Cell. Biochem.* 120, 10519–10529. <https://doi.org/10.1002/jcb.38338>.
- Prusiner, S.B., 1998. Prions. *Proc. Natl. Acad. Sci. USA* 95, 13363–13363. <https://doi.org/10.1073/pnas.95.23.13363>.
- Pushie, M.J., Vogel, H.J., 2008. Modeling by Assembly and molecular dynamics simulations of the low Cu2+ occupancy form of the mammalian prion protein octarepeat region: gaining insight into Cu2+-mediated β -cleavage. *Biophys. J.* 95, 5084–5091. <https://doi.org/10.1529/biophysj.108.139568>.
- Pushie, M.J., Raul, A., Jurik, F.R., Vogel, H.J., 2009. Can copper binding to the prion protein generate a misfolded form of the protein? *Biometals* 22, 159–175. <https://doi.org/10.1007/s10534-009-9196-x>.
- Radic, S., Davis, T.P., Keb, P.C., Ding, F., 2015. Contrasting effects of nanoparticle-protein attraction on amyloid aggregation. *RSC Adv.* 5, 105489–105498. <https://doi.org/10.1039/C5RA20182A>.
- Rapaport, D.C., 1978. Molecular dynamics simulation of polymer chains with excluded volume. *J. Phys. A Math.* 11, L213–L217. <https://doi.org/10.1088/0305-4470/11/8/008>.
- Requena, J.R., Groth, D., Legname, G., Stadtman, E.R., Prusiner, S.B., Levine, R.L., 2001. Copper-catalyzed oxidation of the recombinant SHa (29–231) prion protein. *Proc. Natl. Acad. Sci. U.S.A.* 98, 7170–7175. <https://doi.org/10.1073/pnas.121190898>.
- Robustelli, P., Fiama, S., Shaw, D.E., 2018. Developing a molecular dynamics force field for both folded and disordered protein states. *Proc. Natl. Acad. Sci. U.S.A.* 115, E4758–E4766. <https://doi.org/10.1073/pnas.1800690115>.
- Saikia, B., Gogoi, C.R., Rahman, A., Baruah, A., 2021. Identification of an optimal foldability criterion to design misfolding resistant protein. *J. Chem. Phys.* 155, 144102. <https://doi.org/10.1063/5.0057833>.
- Sanz-Hernández, M., Barritt, J.D., Sobek, J., Hornemann, S., Aguzzi, A., De Simone, A., 2021. Mechanism of misfolding of the human prion protein revealed by a pathological mutation. *Proc. Natl. Acad. Sci. U.S.A.* 118, e2019631118. <https://doi.org/10.1073/pnas.2019631118>.
- Saunders, H.M., Bonomley, S.P., 2009. Multi-domain misfolding: understanding the aggregation pathway of polyglutamine proteins. *Protein Eng. Des. Sel.* 22, 447–451. <https://doi.org/10.1093/protein/gfp035>.
- Sawaya, M.R., Sambashivan, S., Nelson, R., Ivanova, M.I., Sievers, S.A., Apostol, M.I., Thompson, M.J., Balbirnie, M., Wiltzius, J.J.W., McFarlane, H.T., Madsen, A.O., Riekel, C., Eisenberg, D., 2007. Atomic structures of amyloid cross- β spines reveal varied steric zippers. *Nature* 447, 453–457. <https://doi.org/10.1038/nature06695>.
- Schmidlin, T., Kennedy, B.K., Daggett, V., 2009. Structural changes to monomeric CuZn superoxide dismutase caused by the familial amyotrophic lateral sclerosis-associated mutation A4V. *Biophys. J.* 97, 1709–1718. <https://doi.org/10.1016/j.bpj.2009.06.043>.
- Schmidlin, T., Ploeger, K., Jonsson, A.L., Daggett, V., 2013. Early steps in thermal unfolding of superoxide dismutase 1 are similar to the conformational changes associated with the ALS-associated A4V mutation. *Protein Eng. Des. Sel.* 26, 503–513. <https://doi.org/10.1093/protein/gzr030>.
- Shamsir, M.S., Dalby, A.R., 2005. One gene, two diseases and three conformations: molecular dynamics simulations of mutants of human prion protein at room temperature and elevated temperatures. *Proteins* 59, 275–290. <https://doi.org/10.1002/prot.20401>.

- Sharma, B., Kalita, S., Paul, A., Mandal, B., Paul, S., 2016. The role of caffeine as an inhibitor in the aggregation of amyloid forming peptides: a unified molecular dynamics simulation and experimental study. *RSC Adv.* 6, 78548–78556. <https://doi.org/10.1039/C6RA17602J>.
- Sikorski, A., Kolinski, A., Skolnick, J., 1998. Computer simulations of de novo designed helical proteins. *Biophys. J.* 75, 92–105. [https://doi.org/10.1016/S0006-3495\(98\)77497-1](https://doi.org/10.1016/S0006-3495(98)77497-1).
- Sikorski, A., Kolinski, A., Skolnick, J., 2000. Computer simulations of the properties of the α_1 , α_2 C, and α_2 D de novo designed helical proteins. *Proteins* 39, 17–28. [https://doi.org/10.1002/\(SICI\)1097-0134\(20000101\)39:1<17::AID-PROT3>3.0.CO;2-V](https://doi.org/10.1002/(SICI)1097-0134(20000101)39:1<17::AID-PROT3>3.0.CO;2-V).
- Singh, R.K., Chamachi, N.G., Chakrabarty, S., Mukherjee, A., 2017. Mechanism of unfolding of human prion protein. *J. Phys. Chem. B* 121, 550–564. <https://doi.org/10.1021/acs.jpcc.6b11416>.
- Smith, D.G., Cappai, R., Barnham, K.J., 2007. The redox chemistry of the Alzheimer's disease amyloid β peptide. *Biochim. Biophys. Acta Biomembr.* 1769, 1976–1990. <https://doi.org/10.1016/j.bbmem.2007.02.002>.
- Somavazaru, A.K., Kepp, K.P., 2015. The dependence of amyloid- β dynamics on protein force fields and water models. *ChemPhysChem* 16, 3278–3289. <https://doi.org/10.1002/cphc.201500415>.
- Srinivasan, E., Rajasekaran, R., 2016. Computational investigation of curcumin, a natural polyphenol that inhibits the destabilization and the aggregation of human SOD1 mutant (Ala4Val). *RSC Adv.* 6, 102744–102753. <https://doi.org/10.1039/C6RA21927F>.
- Srinivasan, E., Rajasekaran, R., 2017. Probing the inhibitory activity of epigallocatechin-gallate on toxic aggregates of mutant (L84F) SOD1 protein through geometry based sampling and steered molecular dynamics. *J. Mol. Graph. Model.* 74, 288–295. <https://doi.org/10.1016/j.jmgm.2017.04.019>.
- Srinivasan, E., Rajasekaran, R., 2017a. Computational simulation analysis on human SOD1 mutant (H60R) exposes the structural destabilization and the deviation of Zn binding that directs familial amyotrophic lateral sclerosis. *J. Biomol. Struct. Dyn.* 35, 2645–2653. <https://doi.org/10.1080/07391102.2016.1227723>.
- Srinivasan, E., Rajasekaran, R., 2017b. Exploring the cause of aggregation and reduced Zn binding affinity by G88R mutation in SOD1 rendering amyotrophic lateral sclerosis. *Proteins Struct. Funct. Genet.* 55, 1276–1286. <https://doi.org/10.1002/prot.25288>.
- Srinivasan, E., Rajasekaran, R., 2018. Cysteine to serine conversion at I111th position renders the disaggregation and retains the stabilization of detrimental SOD1 A4V mutant against amyotrophic lateral sclerosis in human — a discrete molecular dynamics study. *Cell Biochem. Biophys.* 76, 231–241. <https://doi.org/10.1007/s12013-017-0830-5>.
- Srinivasan, E., Rajasekaran, R., 2018a. Deciphering the loss of metal binding due to mutation D63G of human SOD1 protein causing FALS disease. *Int. J. Biol. Macromol.* 107, 521–529. <https://doi.org/10.1016/j.jbiomac.2017.09.019>.
- Srinivasan, E., Rajasekaran, R., 2018b. Quantum chemical and molecular mechanics studies on the assessment of interactions between resveratrol and mutant SOD1 (G93A) protein. *J. Comput. Aided Mol. Des.* 32, 1347–1361. <https://doi.org/10.1007/s10822-018-0175-1>.
- Srinivasan, E., Rajasekaran, R., 2019. Computational investigation on electrostatic loop mutants instigating destabilization and aggregation on human SOD1 protein causing amyotrophic lateral sclerosis. *Protein J.* 38, 37–49. <https://doi.org/10.1007/s10930-018-09809-0>.
- Stork, M., Giese, A., Kretschmar, H.A., Javan, P.S., 2005. Molecular dynamics simulations indicate a possible role of parallel β -helices in seeded aggregation of poly-gln. *Biophys. J.* 88, 2442–2451. <https://doi.org/10.1529/biophysj.104.052415>.
- Strange, R.W., Yong, C.W., Smith, W., Hainan, S.S., 2007. Molecular dynamics using atomic-resolution structure reveal structural fluctuations that may lead to polymerization of human Cu-Zn superoxide dismutase. *Proc. Natl. Acad. Sci. U.S.A.* 104, 10040–10044. <https://doi.org/10.1073/pnas.0703857104>.
- Tarus, B., Straub, J.E., Thirumalai, D., 2008. Structures and free-energy landscapes of the wild type and mutants of the A β _{1–21} peptide are determined by an interplay between intrapeptide electrostatic and hydrophobic interactions. *J. Mol. Biol.* 379, 815–829. <https://doi.org/10.1016/j.jmb.2008.04.028>.
- Thirumalai, D., Klimov, D.K., Dima, R.I., 2003. Emerging ideas on the molecular basis of protein and peptide aggregation. *Curr. Opin. Struct. Biol.* 13, 146–159. [https://doi.org/10.1016/S0959-440X\(03\)00032-0](https://doi.org/10.1016/S0959-440X(03)00032-0).
- Tomaselli, S., Esposito, V., Vangone, P., van Nuland, N.A., Bonvin, A.M., Guerrini, R., Tancredi, T., Temussi, P.A., Picone, D., 2006. The α -to- β conformational transition of Alzheimer's A β (1–42) peptide in aqueous media is reversible: a step by step conformational analysis suggests the location of β conformation seeding. *ChemBiochem* 7, 257–267. <https://doi.org/10.1002/cbic.200500223>.
- Tompa, D.R., Kadhirvel, S., 2018. Molecular dynamics of a far positioned SOD1 mutant V14M reveals pathogenic misfolding behavior. *J. Biomol. Struct. Dyn.* 36, 4085–4098. <https://doi.org/10.1080/07391102.2017.1407675>.
- Tompa, D.R., Muthusamy, S., Srikanth, S., Kadhirvel, S., 2020. Molecular dynamics of far positioned surface mutations of Cu/Zn SOD1 promotes altered structural stability and metal-binding site: structural clues to the pathogenesis of amyotrophic lateral sclerosis. *J. Mol. Graph. Model.* 100, 107678. <https://doi.org/10.1016/j.jmgm.2020.107678>.
- van der Kamp, M.W., Daggert, V., 2010. Pathogenic mutations in the hydrophobic core of the human prion protein can promote structural instability and misfolding. *J. Mol. Biol.* 404, 732–748. <https://doi.org/10.1016/j.jmb.2010.09.060>.
- Vila-Vieira, D., Campos, S.R., Baptista, A.M., Machado, M., 2012. Reversibility of prion misfolding: insights from constant-pH molecular dynamics simulations. *J. Phys. Chem. B* 116, 8812–8821. <https://doi.org/10.1021/jp3034837>.
- Walsh, D.M., Selkoe, D.J., 2007. A β Oligomers — a decade of discovery. *J. Neurochem.* 101, 1172–1184. <https://doi.org/10.1111/j.1471-4159.2006.04426.x>.
- Wang, L.Q., Ma, Y., Yuan, H.Y., Zhao, K., Zhang, M.Y., Wang, Q., Huang, X., Xu, W.C., Dai, B., Chen, J., Li, D., Zhang, D., Wang, Z., Zou, L., Yin, P., Liu, C., Liang, Y., 2022. Cryo-EM structure of an amyloid fibril formed by full-length human SOD1 reveals its conformational conversion. *Nat. Commun.* 13, 1–10. <https://doi.org/10.1038/s41467-022-31240-4>.
- Wen, J., Scoles, D.R., Facelli, J.C., 2017. Molecular dynamics analysis of the aggregation propensity of polyglutamine segments. *PLoS One* 12, e0176333. <https://doi.org/10.1371/journal.pone.0176333>.
- Wille, H., Dorosh, L., Amidan, S., Schmitt-Ulms, G., Stepanova, M., 2019. Combining molecular dynamics simulations and experimental analyses in protein misfolding. *Adv. Protein Chem. Struct. Biol.* 116, 93–110. <https://doi.org/10.1016/b9.acpb.2019.10.001>.
- Xu, L., Chen, Y., Wang, X., 2014. Dual effects of familial Alzheimer's disease mutations (D7H, D7N, and H6R) on amyloid β peptide: correlation dynamics and zinc binding. *Proteins* 82, 3286–3297. <https://doi.org/10.1002/prot.24669>.
- Zhang, L., Wei, P.F., Song, Y.H., Dong, L., Wu, Y.D., Hao, Z.Y., Fan, S., Tai, S., Meng, J.L., Lu, Y., Xue, J., Liang, C.Z., Wen, L.P., 2019. MnFe₂O₄ nanoparticles accelerate the clearance of mutant huntingtin selectively through ubiquitin-proteasome system. *Biomaterials* 216, 119248. <https://doi.org/10.1016/j.biomaterials.2019.119248>.
- Zhou, Z.-L., Zhao, J.-H., Liu, H.-L., Wu, J.W., Liu, K.-T., Chuang, C.-K., Tsai, W.-B., Ho, Y., 2011. The possible structural models for polyglutamine aggregation: a molecular dynamics simulation study. *J. Biomol. Struct. Dyn.* 28, 743–758. <https://doi.org/10.1080/07391102.2011.10506503>.
- Zhou, S., Shi, D., Liu, X., Liu, H., Yao, X., 2016. Protective V127 prion variant prevents prion disease by interrupting the formation of dimer and fibril from molecular dynamics simulations. *Sci. Rep.* 6, 1–12. <https://doi.org/10.1038/srep21804>.
- Zhou, S., Zhu, Y., Yao, X., Liu, H., 2018. Carbon nanoparticles inhibit the aggregation of prion protein as revealed by experiments and atomistic simulations. *J. Chem. Inf. Model.* 59, 1909–1918. <https://doi.org/10.1021/acs.jcim.8b00725>.
- Zhuang, X., Zhao, B., Liu, S., Song, F., Cui, P., Liu, Z., Li, Y., 2016. Noncovalent interactions between superoxide dismutase and flavonoids studied by native mass spectrometry combined with molecular simulations. *Anal. Chem.* 88, 11720–11726. <https://doi.org/10.1021/acs.analchem.6b03359>.



Ionospheric variations during geomagnetic storms of 7-8 September, 2017

Barsha Dutta¹, Rumajyoti Hazarika², Bitap Raj Kalita³, Kalyan Bhuyan³,
Pradip Kumar Bhuyan³, Aditi Pandey¹ and Adrika kakoty⁴

¹Dibrugarh University Institute of Engineering and Technology,
Dibrugarh University, Dibrugarh 786004, Assam, India

²Jengraimukh College, Majuli, Assam, India

³Centre for Atmospheric Studies, Dibrugarh University, Dibrugarh 786004, Assam, India

⁴SRM Institute of Science and Technology, Kattankulathur, Tamil Nadu 603203, Assam

E-mail: barshaduttakakoty@gmail.com; hrumajyoti@gmail.com; bitapkalita@gmail.com; kalyanbhuyan@gmail.com;
aditipa0@gmail.com; pkbhuyan@gmail.com; adrikakakoty2002@gmail.com

Abstract

Two very intense solar flares of magnitudes X2.2 and X9.3 erupted on September 6, 2017 at 09:10 UT and 12:02 UT triggering large space weather modulations on earth. We analyze the ionospheric response to the geomagnetic storm event that occurred post the flares on 7-8 September 2017 on five selected stations in the northern (Lhasa, Lucknow, Dibrugarh, Quezon City) and southern hemisphere (Cocos). This storm occurred just after the X9.3 solar flare on 6th September. The following figure represents the effect of the storm on Vertical Total Electron Content. It is seen that the VTEC increased significantly on 6-7 September in the northern hemisphere while TEC remained nearly uniform in the southern hemisphere. The TEC decreased on 8-10 September in the NH while in the SH, TEC decreased on 9th and then increased on 10th onwards. There is a sudden rise in the average VTEC on 11th September more than pre flare levels in all stations. Ionograms obtained over Cocos showed that for the solar flare day E layer disappears whereas, for geomagnetic storm days sporadic E is observed. The inter hemispheric asymmetric variation in TEC and E layer activities over Cocos are further examined using electron density profiles, maximum electron concentration (N_mF_2) and data from COSMIC, GRACE and SWARM satellites. The results from this comprehensive analysis will be presented.

1. Introduction

Three processes may determine the storm time energy deposition in high latitudes viz. heating of particles in higher latitudes due to the precipitation of auroral electrons and protons; Joule's heating effect

because of relative motion of plasma and neutrals and drifts of ions. Joule's heating effect is the major source of atmospheric energy during geomagnetic storms (Fuller-Rowell et al., 1996; Sharbar et al., 1998, Lu et al., 1998). Electric current produced due to the friction between neutrals and ions is the main source of Joule's heating. The enhancement of Joule's heating in high latitudes during storm changes globally the thermospheric wind circulation and neutral composition (Fuller-Rowell et al., 1996).

Apart from the effect of global neutral dynamical changes on the distribution of electron density at low latitudes the ionospheric electrodynamics is also affected from mid to low latitude due to the prompt penetration of storm time high latitude interplanetary electric field (Sastri et al., 1997). The storm induced ionospheric electric field perturbation redistributes can create the irregularities in plasma density in low latitudinal regions (Sastri et al., 2000; Bagiya et al., 2011). The response of ionosphere to the geomagnetic storm or the influence of storm on space weather has created an extensive attraction from the scientific research point of view.

2. Data and Methodology

The storm indices data are taken from <https://wdc.kugi.kyoto-u.ac.jp/wdc/Sec3.html> from 4th September, 2017 to 11th September, 2017. The vertical TEC data is obtained from IGS stations <https://cddis.nasa.gov/archive/gnss/data/daily/> as well as from GNSS receiver. Australian ionogram viewer is used to get ionograms over Cocos. Topside view of ionosphere is done by using Cosmic Radio Occultation, GRACE satellites and Swarm satellites.

3. Results

Figure 1 shows plots of geomagnetic storm indices viz AE index, AL index, AU index, Dst index, Kp index and SYM-H from 4th September, 2017 to 11th September, 2017. The Inhibition of VTEC in mid-latitude stations in both hemispheres whereas enhancement in VTEC in low latitude station is noticed during Storm period (Figure 2). Topside Electron Density profile is viewed by using COSMIC Radio Occultation on the day of Geomagnetic Storm i.e. 8th September, 2017 (Figure 3). Enhancement of the electron density is observed in E layer which is not visible in solar quiet days. There is a sudden fluctuation in the vertical TEC as observed from

the ground based receiver (GNSS and IGS) during the main phase of the storm (Figure 4). Figure 5 shows simultaneous L band scintillations only in southern hemisphere. No scintillation is noted in northern hemisphere during the fluctuation of TEC which implies the occurrence of scintillations is not due to the formation of plasma bubbles. Plasma bubbles formed due to Rayleigh Taylor instability drift with the magnetic lines symmetrically towards both hemispheres. Similar fluctuations are detected when it is viewed from topside.

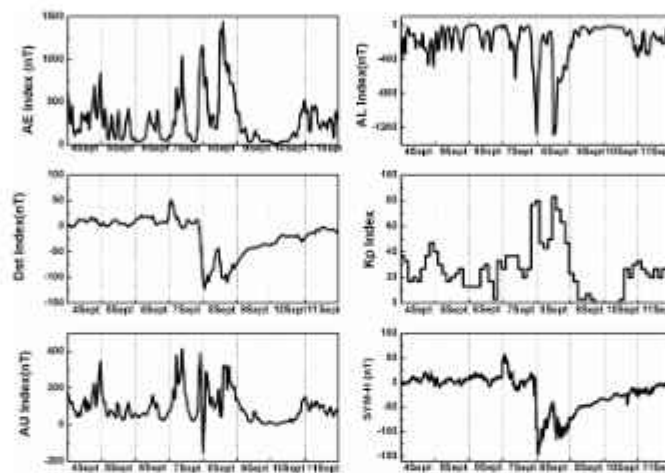


Figure. 1 Plots of AE index, AL index, Dst index, Kp index, AU index and SYM-H from 4th September to 11th September, 2017

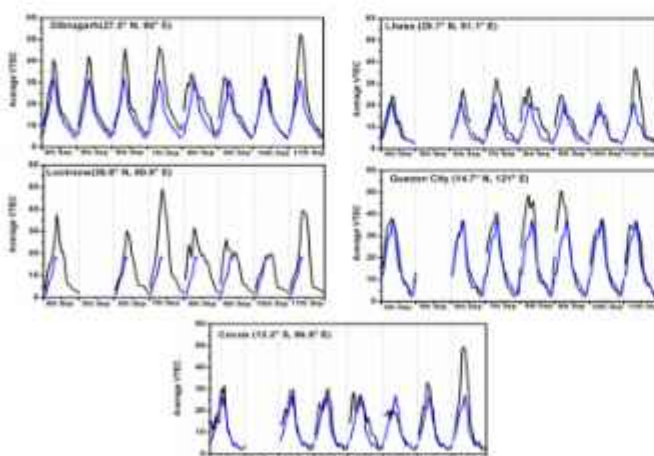


Figure.2 Plots of average vertical TEC from 4th September to 11th September, 2017. Blue line represents the average VTEC for a solar quiet day 21st September, 2017.

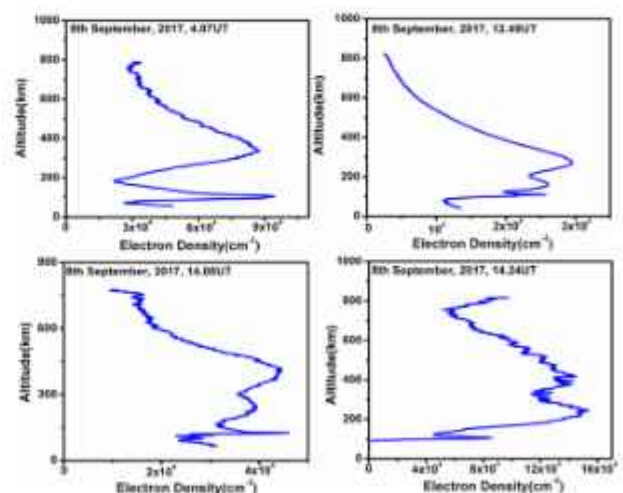


Figure. 3 Variation of electron density with altitude during geomagnetic storm

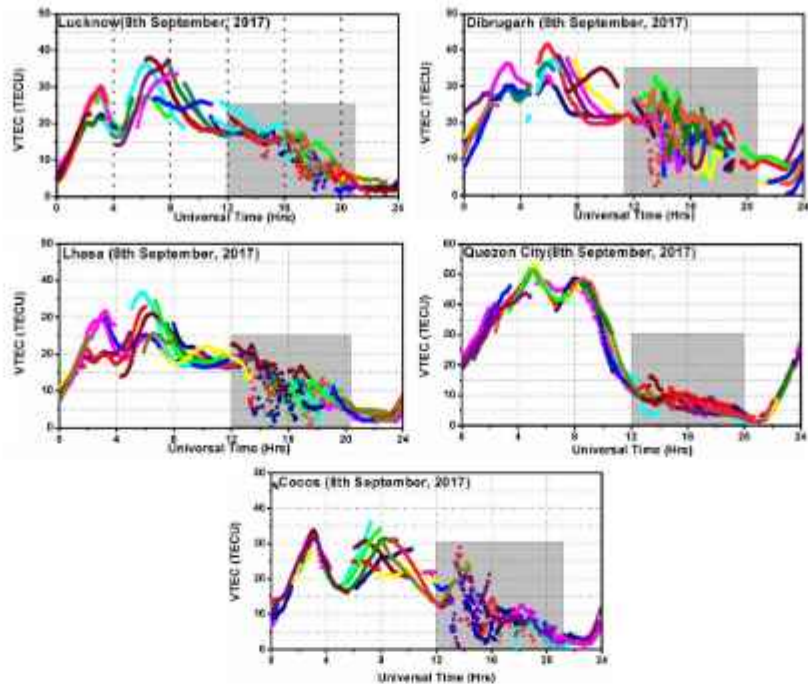


Figure. 4 Plots of vertical TEC for all PRNs with universal time over five stations viz. Cocos, Quezon City, Lucknow, Dibrugarh and Lhasa

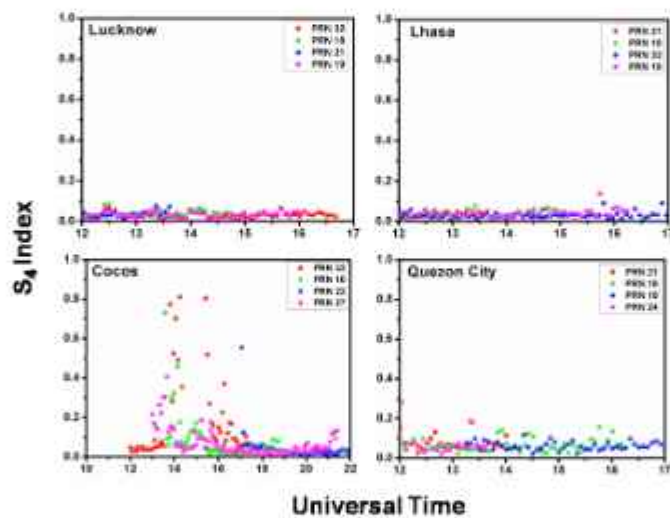


Figure. 4 Plots of vertical TEC for four PRNs with universal time over five stations viz. Cocos, Quezon City, Lucknow, and Lhasa

4. Conclusion

- The VTEC increased significantly on 6-7 September, 2017 in the northern hemisphere while TEC remained nearly uniform in the southern hemisphere. The TEC decreased on 8-10 September, 2017 in the NH while in the SH, TEC decreased on 9th and then increased on 10th onwards. There is a sudden rise in the average VTEC on 11th September more than pre flare levels in all stations.
- The Electron density shows two peaks at altitudes (100-200) km and (300-400) km during Storm period which implies irregularities in ionosphere.
- Ionograms obtained over Cocos showed that for the solar flare day E layer disappears whereas, for geomagnetic storm days sporadic E is observed.
- Sudden fluctuation of VTEC is noticed during main phase of Storm as observed from ground based receivers (GPS and GNSS).

- Almost similar pattern of fluctuation in VTEC is observed from topside view by using GRACE and SWARM satellites.
- Simultaneous amplitude scintillation is noticed in southern hemisphere whereas no scintillation occurs in northern hemisphere during storm.

5. References

1. Bagiya, M. S., K. N. Iyer, H. P. Joshi, S. V. Thampi, T. Tsugawa, S. Ravindran, R. Sridharan, and B. M. Pathan (2011), Low-latitude ionospheric/thermospheric response to storm time electrodynamical coupling between high and low latitudes, *J. Geophys. Res.*, 116, A01303, doi:10.1029/2010JA015845.
2. Fuller-Rowell, T. J., M. V. Codrescu, R. J. Moffett, and S. Quegan (1996), On the seasonal response of the thermosphere and ionosphere to geomagnetic storms, *J. Geophys. Res.*, 101, 2343–2353, doi:10.1029/95JA01614.
3. Lu, G., X. Pi, A. D. Richmond, and R. G. Roble (1998), Variations of total electron content during geomagnetic disturbances, *Geophys. Res. Lett.*, 25, 253–256, doi:10.1029/97GL03778.
4. Sastri, J. H., M. A. Abdu, and J. H. A. Sobral (1997), Response of equatorial ionosphere to episodes of asymmetric ring current activity, *Ann. Geophys.*, 15, 1316–1323, doi:10.1007/s00585-997-1316-3.
5. Sastri, J. H., N. Jyoti, V. V. Somayajulu, H. Chandra, and C. V. Devasia (2000), Ionospheric storm of early November 1993 in the Indian equatorial region, *J. Geophys. Res.*, 105, 18,443–18,455, doi:10.1029/1999JA000372.
6. Sharber, J. R., R. A. Frahm, R. Link, G. Crowley, J. D. Winningham, E. E. Gaines, R.W. Nightingale, D. L. Chenette, B. J. Anderson, and C. A. Gurgiolo (1998), UARS particle environment monitor observations during the November 1993 storm: Auroral morphology, spectral characterization, and energy deposition, *J. Geophys. Res.*, 103, 26,307–26,322, doi:10.1029/98JA01287.

Sampriti

Vol : Vol.-VIII, Issue-1, March 2022

ISSN: 2454-3837

pages : 513-524

Challenges Faced by Transwomen and Hijras In Assam With Special Reference To NRC And CAA Debate

Nandita Deka

*Research Scholar, Department of Political Science
Gauhati University*

Prof. Nani Gopal Mahanta

Department of Political Science, Gauhati University

Abstract

Transgender is a community that has always been discriminated against in almost all societies around the world. India is no exception to this. In developing societies, especially those that are travelling through the path of conservatism to modernization the term "transgender" often creates confusion. Transgender community were exploited since the time of British rule in India and these discriminations still exists in Indian as well as in Assamese society. This paper will try to highlight the challenges faced by the Transwomen and Hijras from the transgender community at the time of crisis situation in Assam. It mainly highlights the challenges that they faced during the time of NRC & CAA debate in Assam. To bring the contemporary issues into limelight, this paper will try to highlight the historical existence of them in India.

Key words: Transgender, Transwomen, Hijras, Nrc, Caa, Historical Existence

Sampriti, Vol. VIII, Issue-1 † 515

Introduction:

Transgender community in India as well as in Assam has always been excluded from the mainstream Indian society. India is a country where multiculturalism and heterogeneity have always been an important part but the transgender community have been discriminated, excluded and isolated since the time of British rule. The paper will try to highlight the recent challenges that the community faced on the prevailing situation of Assam.

According to WHO, "Transgender is an umbrella term for people whose gender identity and expression does not conform to the norms and expectations traditionally associated with the sex assigned to them at birth" (WHO). Transgender used to incorporate people of various gender identification including Transsexual (a person who has to undergo surgical intervention to live full time as a member of opposite sex), Transman (A female to male transsexual), Transwomen (A male to Female Transsexual), Intersex (Whose sexual organ is in between penises and vagina), cross dresser (A person who occasionally cross-dresses in Private), and most popularly in India the hijras etc. It is a part of the broad community called as "LGBTQA+" (Lesbian, Gay, Bisexual, Transgender, Queer, Asexual and other identities). The study mainly focusses on transwomen and hijras because in case of Assam, we can mostly see the transwomen and hijras from the community of transgender. Though there are other transgender that exist in Assam but these two communities are most visible and open about their gender identity. So, the study mainly focusses on these two groups from transgender community. At the beginning we have to go through the definition of Transwoman and Hijras.

A transgender person who has transitioned from male to female. We can classify transwomen in two form - firstly, who has gone through hormone replacement therapy, sex reassignment surgery and transitioned to female from male body and secondly the other who does not feel the necessity of sex reassignment but consider themselves as the opposite gender that is female.

"Hijra is a biological male or intersex people who rejects the masculine identity and choose to identify themselves as women, or not men, in-between man and women or neither man nor women" (Nanda 1999:65). It has two types- one is intersex people (who do not fit in the typical definition of male and female body) or a male who wanted to become and behave like female gender. Regarding the case

of male there is a process call "castration" through which they can become hijra. There are various regional variation of hijras. For example, Kinnars (Delhi, Assam) and Aravanis (Tamil Nadu), Eunuch - a person who is born male but is castrated or emasculated. The paper will try to highlight the existence of transgender from history to present day, their organizational structure, their issues and government responses and finally the role of state and non-state actors for their rights.

Area of Research:

The main area of the research is Gender studies. Most of the time gender identity and gender discrimination studies are limited with male and female studies. Very often the issues of third gender domination are taken as secondary issues. Therefore, the study attempts to cover the issues of transgender community in Assam with special reference to the recent debates and situations. Transgender is a very broader concept which covers different gender variant identities. The present research paper will try to highlight the issues of Transwomen and hijras in Assam which are the larger community among transgender in Assam.

Objectives:

- To study the concept of transgender and how it is related to transwomen and hijras?
- To study the historical reasons behind the deprivation and alienation of the third gender in society
- To study the status and problems of the transgender
- To study the status of Transgender in the NRC/CAA debate in Assam

Methodology:

For the purpose of the present study, data has been collected from both primary and secondary sources. The primary sources have been collected through interview method by preparing questionnaires relevant to the study about the hijra and transwomen of the transgender community in Assam. Government papers and policies for implementing transgender as a category of gender in India have also been studied upon. Secondary sources of data has been collected from various newspapers, books, articles written by different writers and also by people from the transgender community with special reference to Assam.

Discussion:

Historical existence of Transgender, Present Status and response of the Government:

Historically Transgender in India were stereotyped to doing certain derogatory tasks in several region of the country. This stereotyped continued in British era that was further perpetuated with the implementation of section 377 of the Indian Penal Code. However, in the present context Transgender has started speaking against all discrimination subjected towards them. They have started and participated in movement emphasizing on their rights and empowerment especially targeting section 377 of IPC. In Assam as well, we see the existence of active social movement concentrating on Transgender rights. As a result of these movement on 2018 the Supreme Court of India has decriminalized those section of 377 which criminalize homosexuality.

Existence of transgender is seen since the time of Vedic literature in Indian history. Ancient India's literatures like Sanskrit writings, art and architectures proves acceptance of the Transgender community. They were mostly regarded as the "TRITIYO PRAKRITI" at that time. Transgender persons had been part of Indian society for centuries. The concept of "tritiyaprakriti" or "napumsaka" had been an integral part of the Hindu mythology, folklore, epic and early Vedic and Puranic literatures. Indian Mythology is also enshrined with tales of hijras. In Ramayana and Mahabharata also, we can see different glorified dimensions of hijras. We can refer about the transgender character that exhibit in Indian Mythology like, Shikhandi, Brihannata Ardhanarishivara, Mohini etc.

Transgenders played a very prestigious role in the royal courts of the Islamic world, particularly in the Mughal empire in Medieval India. During the time of the Mughal empire, transgenders were popularly known as "khwasaras" or eunuchs and they played a very respectable role in public as well as private life of the Mughal emperor. They rose to well-known positions as political advisors, administrators, generals as well as guardians of the harems. Transgenders were considered clever, trustworthy and fiercely loyal and had free access to all spaces and sections of population, thereby playing a crucial role in the politics of empire building in the Mughal era. But their status and position has declined with the emergence of colonialism.

The situation of Transgenders started deteriorating when British colonial rulers came with their ideologies of sex/ gender binary bodies and heteronormative sexuality perspectives. The hijra body was problematic because of its ambiguity and its difference with the abled procreative/heterosexual body, i.e., the British notion of an ideal human

being- "able-bodied white heterosexual male" (Blackswan, 2004:25). Gradually various laws against hijras were introduced due to which the hijra community were deprived of their earlier privileges. Some of such deprivations are as follows-

The Criminal Tribes Act (Act 27) of 1871, and most importantly the Section 377 of the Indian Penal Code (IPC)- it was introduced during the colonial period since 1860. The Section banned same sex sexual relationship and is often referred to as 'Anti sodomy Law'. This Section states "Whoever voluntarily has carnal intercourse against the order of nature with any man, woman or animal shall be punished with imprisonment for life, or with imprisonment of either description for a term which may extend to ten years, and shall also be liable to fine". The ambit of section 377, extends to any sexual union involving penile insertion. Thus, even consensual sexual acts such as fellatio and anal penetration may be punishable under this law.

Transgender community has a great history of movement for uplifting their position in society which is continuing till date. Mention may be made of the journey of the community like-

Table 1: Chronological History of Section 377 in India

Year	Event
1860	Implementation Section 377 of the IPC by the British administration
1947	Independence of India, Section 377 continued to be a law in the country
2009	Decriminalization of Section 377 in India by Delhi High Court (if people participating in the sexual act were adults and had consent)
2013	Overturing of the decision of the High Court by the Supreme Court
2014	Supreme Court's path-breaking National Legal Services Authority (NALSA) vs. Union of India and others judgements concerning the identity of transgenders in India
2014	Proposed for the rights of Transgender Persons Bill
2015	Passed by Rajya Sabha
2016	Petition submitted by the Naz Foundation to the Supreme Court against the 2013 decision
2016	Introduction of Transgender Person Bill in the Lok Sabha
2018	On 6th September 2018 legalized the section 377 of IPC

Though India achieved independence on 1947 from British rule but transgender communities are still under such draconian laws. However, in 2018 the Supreme Court of India has decriminalized those section of 377 which criminalize homosexuality. But the implementation of different laws of the last 100 years still has its impact in the minds of people. People do not consider transgender as part of the society till now whole heartedly.

Theoretically India follows the policy of "live and let live". But in practical field it is vague for the transgender community. This community have to struggle in every aspect starting from identity issue to their day-to-day life. Transgender has faced discrimination at home, socializing agencies like school, colleges, religion, peer group, culture etc. are also discriminatory towards transgender community. Health issues, problems in employment are other challenges that transgender face more than the ordinary citizen.

Transgender Identity, NRC and CAA debate in Assam:

In Assam the community is facing lots of identity issues. Though reference about transgenders exist in Assam since ancient time but their open presence in the state is a new concept for its citizen. In 2019 NRC issue was in the limelight in Assam. The NRC issue also affected the transgender community.

So, the identity crisis of transgender community in the prevailing situation of Assam can be discussed as below-

- ❖ **NRC and transgender community:** The National Register of Citizen (NRC) is a registry maintained by the Government of India containing names and certain relevant information for the identification of genuine Indian citizen in the state of Assam. The problems of transgender population have started with the updating of document regarding NRC. The final document that was published on 31st August, 2019 had excluded most of the transgender community in Assam. In an interview with "Wire" Bidhan Baruah said in detail about all the reasons and issues of transgender community. According to her the main reason behind exclusion of transgender community are-
 - Unable to procure proper documentation
 - Most of the transgenders are disowned by their family
 - Most of them are included in the gender list that they no longer identify themselves with.
 - It is extremely difficult to establish link with the families of

transgender and provide proof that they belong to families that have been living in Assam before 25th March 1971.

- They use another name after inclusion in the hijra community or after transformation as transwomen/transman. And this transition is not documented or even if documented it was not reflected in the legacy data.

According to the chief of All Assam Transgender Association the state's transgender population is near to 200,000, where around 2000 transgender excluded from the states' 33 districts and the included people are mostly mentioned as male. Swati Bidhan Baruah has filed an Intervention Application (IA) in 2018 at the Apex Court to highlight the issues affecting the transgender community in the State in the context of NRC. She had also filed a petition in the Supreme Court of India seeking its direction over the issue of excluded transgender member from NRC. The 2014 NALSA judgement declared transgender people to be the third gender. After that many transgender people changed their name and gender suited to their identity. But the legacy document under NRC do not reflect their changed identity. And this created problem in their identity status in Assam. So, their only hope is the Supreme Court decision for them, which is still pending.

CAA movement in Assam and the identity crisis of the transgender community:

Constitutional Amendment Bill of 2019 in India had created lot of disruptive situations in the country. The Act led to lots of protest in the country and with much higher intensity in Assam. It is an Act that was passed in the parliament on 11th December 2019. It amended the 1955 Citizenship Act thereby allowing Indian citizenship for Hindu, Sikh, Buddhist, Jain, Parsi and Christian religious minorities who fled from the neighboring Muslim majority countries of Pakistan, Bangladesh and Afghanistan before December 2014 due to "religious persecution". However, the Act excludes Muslims. The Act also relaxed residence requirement for the naturalization of these migrants from eleven years to five. The Act was criticized on various ground like it was discriminatory against the Muslim and violate the fundamental features of Indian constitution like sovereignty, equality etc. The protest has taken a very violent turn in the Northeastern state specifically in Assam. Assam is already fighting for its illegal migrant issue since the time of Assam Movement. According to protesters, this Act will threaten the indigenous culture, language and tradition of the original inhabitant of

Assam. It will also put pressure on the economic and employment sector. The transgender population of Assam also felt unsafe under this Act and took part in the protest nationwide. While taking part in the protests various transgender activists expressed their grievances against the government. Bittu, a professor at Asoka university who took part in the protest said that "almost 2000 transgenders were excluded from the National Register of Citizen during the exercise in Assam. We understand what discrimination is. The CAA, NRC are discriminatory in nature and we oppose them." Samiran Kabir, a fashion designer said that "the NRC-CAA-Trans act combination is suicidal for the trans community. We already know that trans law that has been passed, one has to prove one's trans-ness by undergoing a medical check. With the NRC now it will be a double thing. You have to fight for your background, your documents where are you coming from. One is already fighting with one's gender and identity and upon which you are fighting to prove that you are a citizen of this country." Here the transgender community claim that CAA is not sympathetic towards sexual minority, gender minority. In Assam most of the hijras are from Muslim background. Since the Act exclude Muslims as a result, they are all the more afraid of being thrown out from the country. Raficul, a muslim queer worker in Assam while stating his personal experience said that "through CAA, we will be filtered out being a Muslim trans person and through NRC we would be shunned for being a member of the LGBTQ community who is actually unable to produce the legal documents".

Transgender identity crisis starts from family to government. And the new citizenship rules implemented by the government doubled their burden.

Problems of Transgenders in Assam:

❖ There are lot of differences of opinion and status among the whole community i.e LGBTQA+. In Assam we have mostly seen the hijras and transwomen from this community. But they have lots of differences starting from their physical appearance to their status, acceptance, opinion in society. There are two main organization from Assam who fought for the rights of transgender in Assam viz "Xukia" and "All Assam Transgender Association". But we have never seen these two organizations work unitedly in a single movement. There are lots of differences of opinion amongst them. So, it is very necessary for them to organize unitedly in order to

strengthen their movement in Assam.

- ❖ Lack of education is the main problem for most of the hijra community. The hijra community is not aware of their rights. In the present time, Government of India introduced a number of welfare policies and schemes such ascensus, documentation, issuing of the citizenship ID Cards, issuing passports, socio-economic development and constitutional safeguards for the transgender people. But many people of hijra community is not aware of these rights. In case of Assam, we have seen most of the hijras are uneducated and most of them are school dropout. But there are some transwomen who are well educated and fight for their right now. Education is the main tool through which an individual can develop themselves properly.
- ❖ The economic condition of hijra community is not so strong in Assam. Main source of livelihood for them are badhai, begging and prostitution. But in Assam they don't get so much option for badhai and prostitution. Thus, begging becomes the only option of livelihood for the hijra in Assam. However, the picture is quite different for the transwomen in Assam.
- ❖ Transgender community specially the hijras in Assam are afraid of the police as most of the time police play a very negative role for the community. In Assam the hijras are harassed by police in their day-to-day life. In an interview with the hijras of maligaon gharana one hijra named Bina informs that police have made some false cases against hijras and demand them money in every week. If they refuse to pay the money then they are harassed by the police without any reason(interview with a Hijra called Bina from Maligaon on 22nd July, 2017) According to a study by the National Institute of Epidemiology conducted with 60,000 transgenders across 17 states of India, it has been found that the greatest perpetrators of violence against transgender people are the Police and law-enforcement officials.
- ❖ Media plays a very important role in the changing mindset of people. But question arises as to how the media portray transgender community in front of the public. It is seen that in many cases role of media is not so positive and favourable towards the transgender community. Newspapers and other print media rarely focus the issues of transgender. Visual media is the strong force through which people can experience and can connect with transgender.

Here role of television, movies, news channels are very important. Now a days media is becoming sensitive towards transgender community comparing to the earlier times. But positive representation of transgender is very rare and limited. There are lots of T.V shows where we can find that some categories of transgender community are represented as center of jokes. Man dressed up as woman, woman depicted as man are often portrayed for public amusement. There are some comedy shows where men dress up as women and change their voices to make the audience laugh. The same thing happens in cinemas also. Transgender are often portrayed as either villain or comic character in Indian cinema. But recently in Assam a film titled, "Fireflies-Junaki porua" (2019) directed by Prakash Deka highlighted the struggle of a village-based transwomen and her journey of a transwomen to hijra. This film has got lots of positive feedback from the society and lead actor Benjamin Daimary who portray the role of transwomen has won the jury special mention for best actor in 67th National Film Award. Moreover, even in Bollywood recent films like Chandigarh Kare Ashique, Badhaai Do have shown serious struggles of these people in the society and also with a strong message that society should accept them as normal since they are not different from other two sex- male and female in any way.

Conclusion :

Transgender people have a long history of movement for their rights in India. But as a consequence, they are not getting much achievement in Indian perspective as well in Assam. The major achievement that they have got are like the recognition as third gender in 2014, the Supreme Court decision of decriminalizing homosexuality in 2018 and the Transgender Person Protection of Rights Bill, 2019. Practically in India they got these 3 achievements after years of struggle. But they are not satisfied with these achievements because they think that these achievements do not give them proper identification nor allow them to live with full freedom. "Transgender Person Protection of Rights Bill 2019" is supposed to be the greatest achievement for transgender community in India as well as in Assam. But this Act is highly criticized by the member of transgender community due to its unequal treatment to the community in the eyes of law. Bidhan Baruah from Assam has taken very active step against this Act and filed a petition to challenge the constitutionality of this Act.

In 2020 the Assam government has set up a Transgender Welfare Board which is very great achievement for the transgender community in Assam. All the members of transgender community is very much hopeful that the present government would take some positive step for the upliftment of their status in society and would give them all the rights as equal human being.

"Tritiya Nivas-A ray of hope" is another great achievement for the transgender community. It is a Shelter Home cum Skill Development Centre located at Hatigaon area of Guwahati city. It is a joint initiative of "North East Voluntary Association of Rural Development" and the "All Assam Transgender Association" under the supervision of "Social Welfare Department". It provides free food and shelter with skill training.

In Assam, the concept of transgender has become more popular now a days in comparison to last few years. It is due to the organizational strength of some educated personalities from the community and the Supreme Court decision about section 377 have also created awareness about transgender population among the masses. But it will take time to accept them as part of the society as normal as other two gender.

Bibliography:

Books:

- Currah, R., Juang, R., & Minter, S. *Transgender Rights*. Minneapolis: University of Minnesota Press, 2006. Print
- Gayle, G. *Assuming A Body: Transgender and Rhetorics of Materiality*. New York: Columbia University Press, 2010. Print
- Geney, B. & Susan, R. *The lives of Transgender people*. New York: Columbia University Press, 2011. Print
- Michel, F. *History of Sexuality, an Introduction-Vol-1*. Translated by Robert Hurley. New York: Pantheon Books, 1976. Print
- Philomena, E., David, G.T., Audrey, K. *A Comparison to Gender Studies*. New Jersey: Blackwell Publishing, 2005. Print
- Rajesh, T. *The Third Sex and Human rights*. New Delhi: Gyan Publishing House, 2016. Print
- Scrona, N. *Neither Man nor Women The hijras of India*. Canada: Wadsworth Publishing Company, 1999. Print
- Sharma, S.K. *Hijras: The labelled deviant*. New Delhi: Gyan Publication House, 2009. Print
- Suzanne, K.J. & Kenna, M.C. *Gender an Ethnomethodological Approach*. Itarcience publication, 1978. Print
- Wilhelm, A.D. *Tritiya-Prakriti: People of the Third Sex*. Philadelphia: Xlibris Corporation, 2003. Print

Articles:

- Arrials, R. Elvia. "Gender Inequality: Lesbians, Gays and Feminist Legal Theory". *Berkeley journal of gender, law & justice*. Vol 9. issue 1. September 2013.
- Chettiar, A. "Problem faced by hijras (male to female transgender) in Mumbai with reference to their health and harassment by police". *International Journal of Social Science and Humanities*. VOL. 5. No 9. September 2015.
- Corbin, J. & Morse, J.M. "The unstructured interactive interview: issues of reciprocity and risk when dealing with sensitive topics". *Qualitative Inquiry*, 9. 2003.
- Elmir, R., Schmied, V., Jackson, D. & Wilkes, L. "Interviewing people about potentially sensitive topics". *Nurse Researcher*, 19(1), 2011. PP.12-16.
- Dasgupta, R.K. "Articulating dissident citizenship, belonging and queerness on cyberspaces". *South Asian Review*. Vol 35. No 3. 2014.
- Kakati, P.B. "Negotiating with the State: Public-Private and Assimilationism in India's LGBT Movement". *Journal of Political Science*. Gauhati University. October, 2012. Print.
- Lal, Vinay. Not This, Not That: The Hijras of India and the Cultural Politics of Sexuality, *Social Text*, No. 61, *Out Front: Lesbians, Gays, and the Struggle for Workplace Rights*. Winter, 1999.
- Narrain, S. "Being a Eunuch", New Delhi: *Frontline*. 14 October 2003 Issue. 2003.
- Parker, R. & Aggleton, P. "Culture, Society and Sexuality: A reader", *Routledge*, 1999. Print.
- Raymer, J. "The Third Sex, When a baby boy is not a boy, nor a girl". *Life Magazine*, 1998. Print.
- Rohi, A. "Decriminalizing homosexuality: Looking through the eyes of Indian society", article from *JSTORS*
- S. Ashton. "Researcher or Nurse? Difficulties on undertaking semi structured interviews on sensitive topics". *Nurse Researcher*, 22 (1), 2014. PP.27-31.

Newspaper and Internet Sources:

- *New Statesman*, Various Issues.
- *The Guardian*, Various Issues.
- *The Hindu*, Various Issues.
- *The Times of India*, Various Issues.
- *The wire*, October 8, 2019, Gaurav Das
- *The Swadle*, 26th December, 2019, by Rajiv Desai
- *Times of India* online, January 9, 2020, 13:39 IST
- The quint.com, by Garvita Khybri, 10 January 2020, 8:31 AM IST
- The citizen is hopeful.com, by Jyoti Thakur, 3 January, 2020
- Timesofindia.com, April 18, 2016
- Sentinellassam.com, 22nd March 2021, 11.21 pm

Winter Issue 2021, Vol 13

ISSN 2349-3410



PIERIAN SPRING

Fountain of Learning

A Bi-Annual Peer-Reviewed Multi-Disciplinary International Journal

Editor in Chief
Dr. Jai Ram Jha

Associate Editor
Dr. Md. Ejaz Alam
Dr. Swapan Kumar Chutia



CREATIVE WRITERS' CIRCLE
PUBLICATIONS



www.qr.net/QRPU

ARTICLES

- ❖ অনুবাধা শৰ্মা পূজাবীৰ উপন্যাসৰ ভাষা-শৈলী : এক অধ্যয়ন Page 01 – 19
শ্ৰ অপু বৰা
- ❖ মহখেদা উৎসৱ মহো-হো আৰু ভঠেলি উৎসৱঃ এক সমীক্ষাত্মক অধ্যয়ন Page 20 – 35
শ্ৰ ড° দীপক পাঠক
- ❖ সত্ৰীয়া নৃত্যত তাণ্ডবধৰ্মীতাৰ প্ৰয়োগ —এক অধ্যয়ন Page 36 – 47
শ্ৰ বিজুমনি গগৈ
- ❖ অসমত লোকসংস্কৃতি চৰ্চাৰ প্ৰাৰম্ভিক স্তৰ : ড° বিৰিঞ্চি কুমাৰ বৰুৱাৰ লোকসংস্কৃতিচৰ্চা Page 48 – 57
শ্ৰ ড° দীপশিখা গগৈ
- ❖ মিচিং জনগোষ্ঠীৰ জন্ম, মৃত্যু আৰু বিবাহ-সম্পৰ্কীয় লোকবিশ্বাস Page 58 – 63
শ্ৰ ড° পংকজ শইকীয়া
- ❖ অসমীয়া বাতৰিকাকতৰ বাতৰি লেখনত জতুৱা-ঠাঁচৰ প্ৰয়োগ Page 64 – 71
শ্ৰ বিজু বেখা বৰি

মিচিং জনগোষ্ঠীৰ জন্ম, মৃত্যু আৰু বিবাহ-সম্পৰ্কীয় লোকবিশ্বাস

ড° পংকজ শইকীয়া

সহকাৰী অধ্যাপক, অসমীয়া বিভাগ

জেংৰাইমুখ মহাবিদ্যালয়

ডাক-জেংৰাইমুখ, জিলা-মাজুলী

পিন-৭৮৫১০৫

মোৱাইল নং-৭০০২০৬৮৯০৪

০.০০ প্ৰস্তাৱনা :

জনসংখ্যাৰ দিশৰপৰা মিচিংসকলেই হ'ল উত্তৰ-পূৰ্বাঞ্চলৰ দ্বিতীয় বৃহৎ জনজাতি। অতীজতে এওঁলোকক 'মিৰি' বুলি জনা গৈছিল। মিচিংসকল অসমৰ ধেমাজি, লখিমপুৰ, শোণিতপুৰ, তিনিচুকীয়া, ডিব্ৰুগড়, শিৱসাগৰ, যোৰহাট আৰু গোলাঘাট জিলাত প্ৰধানভাৱে বসবাস কৰে। অৰুণাচলৰ পাহাৰৰপৰা ভৈয়ামলৈ প্ৰব্ৰজন কৰি এওঁলোকে উজনি অসমৰ জিলাসমূহত নিগাজীকৈ থাকিবলৈ লয়।

ভাষাগতভাৱে মিচিংসকল বৃহৎ তিব্বত-বৰ্মী ভাষাগোষ্ঠীৰ অন্তৰ্ভুক্ত। অসমৰ যিবোৰ জনগোষ্ঠী লোক-সংস্কৃতিৰ ক্ষেত্ৰত চহকী, সেইবোৰৰ ভিতৰত এই জনগোষ্ঠীৰ স্থান আগশাৰীত। প্ৰজাতিগতভাৱে এওঁলোকৰ মাজত মংগোলীয় সংস্কৃতিৰ লক্ষণবোৰ বিদ্যমান। লোকগীত, লোকনৃত্য, লোক-উৎসৱ, বিভিন্ন ভৌতিক সংস্কৃতি যেনে— খাদ্য বন্ধন আৰু সংৰক্ষণ, বোৱা-কটা আৰু পিন্ধা-উৰা, গৃহ-নিৰ্মাণ আদিৰ ক্ষেত্ৰত মিচিংসকল বৰ্ণাঢ়া লোক-সাংস্কৃতিক পৰম্পৰাৰ অধিকাৰী। আনহাতে, এই জনগোষ্ঠীৰ মানুহৰ মাজত অতীজৰেপৰা কেতবোৰ লোকবিশ্বাস প্ৰচলিত হৈ আহিছে। এই লোকবিশ্বাসসমূহ বৃক্ষ, চৰাই, পশু, জন্ম-মৃত্যু-বিবাহ, উৎসৱ-পাৰ্বণ, দৈহিক লক্ষণ আদিৰ লগত সম্পৰ্কিত।

কোনো জনগোষ্ঠীয়ে যুগ যুগ ধৰি আহৰণ কৰা অভিজ্ঞতাসমূহৰ সামূহিক প্ৰকাশেই হ'ল লোকবিশ্বাস। এইবোৰৰ বিশ্লেষণৰদ্বাৰা সংশ্লিষ্ট জনগোষ্ঠীটোৰ মানসিক স্তৰ, চিন্তা-চেতনা, ঐতিহ্য-ভাবনা, ঐতিহাসিক ক্ৰমবিকাশৰ আভাস পাব পাৰি। লগতে সামিধ্যলৈ অহা আন আন জনগোষ্ঠীৰ সাংস্কৃতিক উপাদান কেনেধৰণে আৰু কি ৰূপত সানমিহলি হৈ আছে তাকো নিৰ্ণয় কৰিব পাৰি। সেইদৰে জনগোষ্ঠীটোৱে যুগ যুগ ধৰি বহন কৰি অহা ক্ষোভ, মনোবেদনা আদিও লোকবিশ্বাসসমূহৰ মাজত প্ৰতিফলিত হয়।

১.০০ মিচিংসকলৰ জন্ম, মৃত্যু আৰু বিবাহ-সম্পৰ্কীয় লোকবিশ্বাস :

জন্ম আৰু মৃত্যু মানৱৰ লগতে সমগ্ৰ জীৱকুলৰে এবাৰ নোৱাৰা বিষয়। বিবাহো মানৱ-জীৱনৰ এটা গুৰুত্বপূৰ্ণ সংস্কাৰ। এই তিনি উপলক্ষ্যত পৃথিৱীৰ বিভিন্ন জনগোষ্ঠীয়ে কিছুমান পৰম্পৰাগত নিয়ম-নীতি পালন কৰে। বাৰেবহীয়া লোক-সংস্কৃতিৰ অধিকাৰী অসমৰ মিচিংসকলেও জন্ম-মৃত্যু-বিবাহক কেন্দ্ৰ কৰি কিছুমান বৈচিত্ৰ্যময় আচাৰ আৰু ৰীতি পালন কৰি আহিছে। এনে পৰম্পৰাৰ সবহভাগেই তেওঁলোকৰ মাজত পূৰ্বাপৰ প্ৰচলিত লোকবিশ্বাসৰ আধাৰত প্ৰতিষ্ঠিত।

সন্তান-জন্ম কাৰ্যটো কেতিয়াবা অতি কষ্টকৰ হয় আৰু কেতিয়াবা প্ৰসৱ-বেদনাও অতি জটিল আৰু দীঘলীয়া হয়। এনে অৱস্থাক কেন্দ্ৰ কৰি মিচিংসকলৰ মাজত কিছুমান লোকবিশ্বাস প্ৰচলিত আছে।

তেনেদৰে মৃত্যু আৰু বিবাহৰ ক্ষেত্ৰতো বিশেষত্বপূৰ্ণ লোকবিশ্বাস লক্ষ্য কৰা যায়।

১.০১ জন্ম-সম্পৰ্কীয় লোকবিশ্বাস :

সন্তান জন্ম হোৱাটো যিদৰে আনন্দ আৰু সুখৰ মুহূৰ্ত, সেইদৰে ই অতি বিপদ-আপদেৰে ভৰা। সেয়েহে গৰ্ভাৱস্থা, সন্তান-প্ৰাপ্তি আৰু তাৰ পৰৱৰ্তী সময়খিনিত মিচিংসকলে সাৱধানতা অৱলম্বন কৰে। স্বামী-স্ত্ৰীৰ বাবে পৰিয়াল তথা সমাজে কিছুমান বাধা-নিষেধ আৰোপ কৰি থৈছে। ইয়াৰে বেছিভাগেই কু-সংস্কাৰ। গৰ্ভধাৰণ-কালত স্বামী-স্ত্ৰীয়ে কোনো জীৱ-জন্তু বধ কৰাটো নিষেধ বুলি গণ্য কৰে। সচৰাচৰ আহাৰ হিচাপে গ্ৰহণ কৰা হাঁহ-পাৰ বধ কৰাটোৱো নিষেধ। সেইদৰে কুকুৰাৰ কণী খালে প্ৰসৱৰ সময়ত জটিলতা আহিব পাৰে বুলি বিশ্বাস কৰে। পঘা ডেই যোৱাতো বাধা আছে। ইয়াৰ অন্যথা হ'লে সন্তানৰ নাড়ী পাক খাই বুলি বিশ্বাস কৰে। অজ্ঞাতে স্বামীৰ গাত ভৰি লাগিলে সেই দোষ খণ্ডন কৰিবলৈ কোনো কোনো খেলত স্বামীৰ ভৰি ধুওৱা পানী গৰ্ভৱতী তিৰোতাগৰাকীক খুওৱাৰ নিয়ম প্ৰচলিত আছে। কেতিয়াবা সগৰ্ভা তিৰোতাই কোনো অপৰাধ (মিচিং ভাষাত— 'ইমুৰ-গুমুৰ') কৰিলে তাক খণ্ডন কৰিবলৈ স্বীকাৰোক্তিৰ ব্যৱস্থা আছে। ইয়াৰ বিপৰীতে যদি অপৰাধ স্বীকাৰ নকৰে, তেনে ক্ষেত্ৰত সন্তানৰ জন্ম কঠিন হয় বুলি লোকবিশ্বাসৰ প্ৰচলন আছে। গৰ্ভৱতী তিৰোতাৰ স্বামীয়ে সাপ হত্যা কৰিব নাপায় বুলি বিশেষভাৱে মনা হয়। সেইদৰে স্বামীয়ে কঠীয়াৰ টোম বন্ধাত বাধা আছে।

মিচিংসকলৰ অধিকাংশ লোকেই ভূত-প্ৰেত আদি অপদেৱতাৰ স্থিতিক বিশ্বাস কৰে। এনে অপদেৱতাই প্ৰসূতি আৰু গৰ্ভস্থিত সন্তানৰ ক্ষতি কৰিব পাৰে বুলি বিশ্বাস কৰি পৰিগ্ৰাণৰ বাবে দুৱাৰ-খিৰিকীৰ ওপৰত মাছ ধৰা জাল আঁৰি থয়। কিছুমানে জুইত সৰিয়হ, শুকান জলকীয়া আদি দিয়ে।

সন্তান জন্মৰ পাছতো বহু অন্ধ-সংস্কাৰ মানি চলা হয়। কেঁচুৱাৰ বেমাৰ-আজাৰ হ'লে সেয়া ভূত-পিশাচৰ কাৰণেই হৈছে বুলি ভাবে। সন্তানক অপদেৱতাৰ কোপৰপৰা ৰক্ষা কৰিবৰ বাবে জুই ধৰি থোৱা হয়। জুইত সৰিয়হ, শুকান জলকীয়া দিয়াৰ ব্যৱস্থা আছে। কিছুমান লোকে কেঁচা নহৰু এৰা সূতাত সী সদ্যজাত সন্তানৰ ডিঙিত আঁৰি দিয়ে। কেঁচুৱাৰ শিতানত সৰিয়হ আৰু কটাৰী এখন গুঁজি থোৱা হয়। কেতিয়াবা কেঁচুৱাই শুবৰ বাবে কোনো লোকে সৰিয়হেৰে প্ৰস্তুত কৰা গাৰুৰ ব্যৱস্থা কৰে। কোনো অমংগলীয়া লোকৰ 'মুখ' লাগিব পাৰে বুলি ভাবি সন্তানৰ হাত

আৰু ভৰিত বঙীন সূতা বান্ধি দিয়া হয়।

প্ৰসূতিয়ে অন্যহি অহা-যোৱা কৰা দুৱাৰ আৰু জখলাৰে আহ-যাহ কৰিব নাপায় বুলি বিশ্বাস কৰে। সেয়েহে বেৰ কাটি বেলেগ দুৱাৰ আৰু উঠা-নমাৰ বাবে পৃথক জখলাৰ ব্যৱস্থা কৰি দিয়ে।

সাধাৰণতে পাঁচ দিনৰ দিনা চূড়াকৰণ পাতি সন্তানক বাহিৰলৈ উলিওৱা হয়। এইদিনাই শাস্তিপানী খুৱাই প্ৰসূতি আদিক 'শুদ্ধি' কৰাৰ নিয়ম আছে। ঠাই-বিশেষে সন্তানৰ চুলিবোৰ বোকাত পুতি ৰখা হয়। ঠাইভেদে আকৌ জন্মৰপৰা শুদ্ধি কিম্বা এমাহ পৰ্যন্ত পিতৃয়ে চিকাৰ, খৰি সংগ্ৰহ আদি কাৰ্য কৰাত বাধা আছে।

১.০২ মৃত্যু-সম্পৰ্কীয় লোকবিশ্বাস :

মৃত্যু অৱধাৰিত বুলি জানিও প্ৰায় সকলো লোকেই মৰিবলৈ নিবিচাৰে অথবা মৃত্যুলৈ ভয় কৰে। ভয়-শংকা জড়িত থকাৰ বাবেই মৃত্যুক কেন্দ্ৰ কৰি অনেক লোকবিশ্বাস বা অন্ধসংস্কাৰ জনসমাজত বৰ্তি থাকে। মিচিং সমাজে এনে লোকবিশ্বাসৰপৰা মুক্ত নহয়।

মিচিংসকলে কোনো ব্যক্তিৰ মৃত্যুৰ কিছু সময় পাছতে মৃতকৰ ঘৰত ঢোল বজাই আত্মীয়-কুটুম্বক জাননী দিয়ে। মৃতকক গা ধুৱাই মিঠাতেল ঘঁহি দিয়ে আৰু নতুন বস্ত্ৰ পিন্ধায়। এইবোৰ কাম সদায় ওলোটাকৈ কৰা হয়। কাৰণ মৃতকক ইতৰ প্ৰাণী বুলি ভবা হয়। চিতালৈ নিয়াৰ আগতে সকলোৱে শৰক উদ্দেশ্যি সেৱা কৰে। শৰ ঘৰৰপৰা শ্মশানলৈ নিয়াৰ আগে আগে এটা কুকুৰা পোৱালিৰ ডিঙি মুচৰি দিয়াৰ লোকবিশ্বাস আছে। ইয়াৰ অন্যথা হ'লে মৃতকৰ প্ৰেতাআই ঘৰখনলৈ অমংগল আনিব পাৰে বুলি বিশ্বাস কৰে।

মিচিং জনজাতীয় লোকে সাধাৰণতে মৃতদেহ কবৰ দিয়ে অৰ্থাৎ গাত খান্দি পোতে। অৱশ্যে হিন্দুধৰ্মীয় আচাৰৰ প্ৰভাৱত বহুতে আজিকালি শৰ দাহ কৰিবলৈ লৈছে। কবৰস্থ কৰাৰ আগে আগে জীয়াই থকা কালত ব্যৱহাৰ কৰা কেতবোৰ বস্ত্ৰ মৃতদেহৰ ওচৰত স্থাপন কৰা হয়।

মৰিশালিৰপৰা ঘূৰি অহা মানুহবোৰৰ গালৈ গৃহস্থই সৰিয়হ ছটিয়ায়। এনে কৰাৰ কাৰণ হ'ল— তেওঁলোকৰ গাত অপদেৱতা লাগি অহা বুলি কৰা বিশ্বাস। আনহাতে, শৰ সংকাৰ কৰি উলটি আহোঁতে পিছলৈ ঘূৰি চোৱা নহয়। কিয়নো এনে কৰিলে গাত অপদেৱতা লস্কি আহে বুলি মিচিং জনগোষ্ঠীৰ লোকে বিশ্বাস কৰে।

মৃত্যুৰ তিনি দিনৰ দিনা মৃতকৰ গৃহস্থই 'তিলনি'ৰ আয়োজন কৰে। ইয়াৰ পৰৱৰ্তী কালত 'উৰম আপিন' (পিণ্ড) আৰু সাধাৰণতে দহ দিনত 'দদগাং' (আদ্যাশ্ৰদ্ধ) পতা হয়। অৱশ্যে তিলনিক বাদ দি বাকী দুটা পতাৰ ক্ষেত্ৰত সময়ৰ কোনো বাধ্যবাধকতা নাই; বহুতে অৰ্থগত দিশৰপৰা টনকিয়াল হ'লেহে পতাৰ ব্যৱস্থা কৰে।

মৃত্যুক কেন্দ্ৰ কৰি আন আন বহুতো বাধা-নিষেধ তথা লোকবিশ্বাসৰ প্ৰচলন মিচিং সমাজত আছে। গাঁৱৰ কোনো সন্মানীয় লোকৰ মৃত্যু হ'লে সাধাৰণতে তাঁতশালৰ কামৰপৰা আঁতৰি থকা হয়। ঘৰৰ মুখত কপৌ চৰায়ে ৰণ দিলে মৃতকৰ আত্মাই ভোক-পিয়াহত আতুৰ হৈ মাতিছেহি বুলি ভাবে। কুকুৰে নিশা বিশেষ শব্দৰে ভুকিলে মৃতকৰ আত্মাই আহ-যাহ দেখি ভুকিছে বুলি বিশ্বাস কৰে। গাঁৱৰ কোনোবা লোকৰ অস্বাভাৱিক ধৰণে মৃত্যু মুখত পৰিলে চাংঘৰৰ বানীৰ (গোটা বাঁহৰ পথালিকৈ খুঁটাত দিয়া বিশেষ)ফুটাবোৰ ধানখেৰ, জাৰৰ আদিৰে বন্ধ কৰে, কিয়নো সেইবোৰত

ভূত-প্ৰেত (উমাল) সোমাই লুকাই থাকিব পাৰে বুলি ভাবে। পিতৃ-মাতৃৰ মৃত্যু হোৱাৰ বাৰত শুভ কাম সম্পাদন কৰাত বাধা-নিষেধ আছে। শোৱাৰ ক্ষেত্ৰতো মৃত্যু-সম্পৰ্কীয় লোকবিশ্বাসে মিচিংসকলৰ জীৱন নিয়ন্ত্ৰণ কৰে। তেওঁলোকে পশ্চিমমূৱাকৈ শোৱাটো অযুগুত বুলি গণ্য কৰে। কিয়নো পশ্চিমমূৱাকৈ শুলে মৃত্যু সোনকালে ওচৰ চাপে বুলি লোকবিশ্বাসৰ প্ৰচলন আছে। কোনো ব্যক্তিৰ হঠাতে পেটৰ বিষ হ'লে তেওঁৰ গাত অপদেৱতা লগা বুলি ভাবে আৰু তাৰপৰা পৰিত্ৰাণৰ বাবে 'উৰম বিনাম' (পূজা-পাতল) কৰাৰ ব্যৱস্থা আছে। অপদেৱতাই জলকীয়া বেয়া পোৱাৰ কাৰণেই মৃতকৰ সকামত এই দ্ৰব্য ব্যৱহাৰ কৰা নহয়। আত্মালৈ খাদ্যদ্ৰব্য অৰ্পণ কৰোঁতে তেওঁলোকে বাঁওহাতখন ব্যৱহাৰ কৰে। কিয়নো প্ৰেতাআই ওলোটাকৈহে দেখে বুলি বিশ্বাস প্ৰচলিত আছে।

১.০৩ বিবাহ-সম্পৰ্কীয় লোকবিশ্বাস :

বিশেষকৈ মিচিং সমাজত বিয়া-বাৰু দুই ধৰণে সম্পাদন কৰা হয়। তাৰে ভিতৰত 'দুগলা যামনে লানাম' (পলুৱাই নি পতা সাধাৰণ বিয়া) আৰু 'মিদাং' (শুভবিবাহ)। বিবাহ এক মাংগলিক কাৰ্য। সেয়েহে মিচিংসকলে কেতবোৰ বিশ্বাস মানি চলে, যাতে অপায়-অমংগল সাধন নহয়। কইনাক বিয়া কৰাই আনি চাংঘৰলৈ উঠোৱাৰ আগে আগে জখলাত দুটা ঘট পানীৰে পৰিপূৰ্ণ কৰি ৰখা হয়। কাৰণ পানীৰে পৰিপূৰ্ণ পাত্ৰ দেখিলে যাত্ৰা শুভ হয় বুলি বিশ্বাস প্ৰচলিত আছে। আনহাতে, ঠাই-বিশেষে ন-কইনাক পানী আনিবৰ বাবে এযোৰ কলহ লগত দিয়ে। পানী লৈ সুকলমে ঘৰত আহি উপস্থিত হ'লে বৈবাহিক জীৱন সুখৰ হ'ব বুলি ধাৰণা কৰা হয়। কিন্তু কলহ হাতৰপৰা পৰি ভাগিলে অমংগলৰ আগজাননী বুলি গণ্য কৰে।

জীয়ৰীৰ নামত গা-ধন লোৱা আচাৰটোৱো লোকবিশ্বাসৰ আধাৰত প্ৰতিষ্ঠিত। তেওঁলোকে বিশ্বাস কৰে যে সামান্য পৰিমাণৰ হ'লেও গা-ধন লোৱা উচিত। ইয়াৰ বিপৰীতে বিয়া দিয়াৰ পাছত ছোৱালীজনীৰ ভৱিষ্যতৰ সংসাৰ কল্যাণকৰ নহ'বও পাৰে। আনুষ্ঠানিক বিয়াত কইনা খুজিবলৈ যাওঁতে লগত কুটি মাছ নিয়াৰ এটা নিয়ম মিচিং সমাজত আছে। ইয়াৰ অবিহনে কথা নৰজে বুলি বিশ্বাস কৰা হয়।

১.০৪ লোকবিশ্বাসসমূহৰ বিশ্লেষণ :

মিচিং জনগোষ্ঠীৰ লোকবিশ্বাসসমূহৰ বেছিভাগেই অন্ধবিশ্বাস বা অন্ধসংস্কাৰ। এনে কেতবোৰ লোকবিশ্বাসৰ সাম্প্ৰতিক কালত কোনো প্ৰাসংগিকতা নাই। বৰং এইবোৰৰ ক্ষতিকাৰক প্ৰভাৱহে পৰিদৃষ্ট হয়। সদ্যজাত সন্তানৰ বেমাৰ-আজাৰৰ প্ৰসংগতে কথাটো খাটে। ৰোগগ্ৰস্ত সন্তানক আধুনিক চিকিৎসা প্ৰদান নকৰি, কোটিকলীয়া বেজ-কবিৰাজৰ আশ্ৰয় লৈ মহাবিপদৰ মুখলৈ ঠেলি দিয়াটো বৰ্তমানো লক্ষ্য কৰা যায়। আকৌ বয়সস্থ লোকৰ হঠাৎ হোৱা পেটৰ বিষৰ কাৰণ উপৰিপুৰুষৰ কু-দৃষ্টি বুলি ভাবি বিপদত পৰাটোৱো সচৰাচৰ ঘটি থকা ঘটনা।

ভূত-প্ৰেতৰ ওপৰত থকা বিশ্বাসৰ বাবেই মিচিংসকল এতিয়াও অন্ধবিশ্বাস কবলত আছে। ইয়াৰ ফলত সুবিধাবাদী লোকে তেওঁলোকৰ অজ্ঞতা আৰু ভয়ক হাতিয়াৰ হিচাপে ব্যৱহাৰ কৰিছে। ভণ্ড বেজ-কবিৰাজৰ হাতত নিজৰ সা-সম্পত্তিৰ লগতে জীৱনো হেৰুৱাব লগা হৈছে।

আচাৰ-বিশ্বাসৰ দোহাই দি মিচিং নাৰীক পুৰুষতন্ত্ৰিক সমাজখনে কেতিয়াবা যে অতি নিম্ন পৰ্যায়ৰ ব্যৱহাৰ

কৰে তাৰ প্ৰমাণ লোকবিশ্বাসৰ মাজতে বিদ্যমান। দেখা যায়, গৰ্ভৱতী তিবোতাক স্বামীৰ ভৰি ধুওৱা পানী খুওৱাটো এক গৰ্হিত কাৰ্য। সেইদৰে ন-কইনাৰ ক্ষেত্ৰত মংগল-অমংগলৰ বিচাৰ কৰি তেওঁলোকক কাৰ্যতঃ অপমানহে কৰা হয়। এনে ক্ষেত্ৰত অমংগলীয়া বুলি গণ্য হোৱা নাৰী পাৰিবাৰিক আৰু সামাজিক লাঞ্ছনা-গঞ্জনাৰ সন্মুখীন হোৱাৰ পূৰ্ণ আশংকা আছে। গা-ধন লোৱা ব্যৱস্থাটোৱেও নাৰীক এক পণ্যদ্রব্যৰ শাৰীলৈহে পৰ্যবসিত কৰে।

মৃতকৰ পৰিয়ালক কিছুমান লোকবিশ্বাসে হাৰাশাস্তিহে কৰে। প্ৰেতাছা ৰুষ্ট হোৱাৰ ভয়ত আৰু আদ্যাশ্ৰাদ্ধৰ নামত তেওঁলোকে ধন খৰচ কৰি ভোজ-ভাত দিয়ে। ইয়াৰ ফলত দুখীয়া পৰিয়ালবোৰ অৰ্থনৈতিকভাৱে ভাগি পৰা পৰিলক্ষিত হয়।

অৱশ্যে কিছুমান লোকবিশ্বাসৰ সদৰ্থক দিশো আছে। সন্তান জন্মৰ আগৰ আৰু পাছৰ সময়ছোৱাত মাক অৰু সন্তানৰ প্ৰতি বিশেষ চকু দিয়াটো অতি প্ৰয়োজনীয়। 'অশৌচ খেদা'ৰ দৰে কিছু সংস্কাৰ মানি চলাটোও উপযোগী। চাফ-চিকুণতাই মাতৃ আৰু সন্তানক নিৰোগী কৰি ৰখাত সহায় কৰে।

আজিকালি হিন্দুধৰ্মীয় আচাৰৰ লগতে আধুনিকতাৰ প্ৰৱেশে মিচিংসকলৰ লোকবিশ্বাসত প্ৰভাৱ পেলাইছে। 'চূড়াকৰণ', 'তিলনি' আদি সংস্কাৰ হিন্দুধৰ্মীয় আচাৰ। আধুনিক চিন্তা-চেতনাৰ ফলত বহুতে কিছু লোকবিশ্বাস বৰ্জন কৰিছে; বৈজ্ঞানিক যুক্তিৰে বিচাৰ কৰি ভূত-পিশাচৰ ভিত্তি নস্যাত্ কৰিবলৈ লৈছে।

২.০০ উপসংহাৰ :

১. বেমাৰ-আজাৰ আদিৰ কাৰণ বহুতে অপদেৱতা বুলি ভবাৰ কাৰণে কেতিয়াবা ভয়াৱহ বিপদৰ সন্মুখীন হ'বলগীয়া হয়।
২. ভূত-প্ৰেতৰ ওপৰত থকা বিশ্বাসে এটা কথা প্ৰতিপন্ন কৰে, তেওঁলোক একবিংশ শতিকাৰ দ্ৰুত প্ৰযুক্তিগত উন্নতিৰ যুগতো পিছপৰি ৰৈছে।
৩. মিচিং সমাজত নাৰীসকলক কিছু পৰিমাণে হ'লেও অৱদমন কৰা হৈছে।
৪. আধুনিক সংস্কাৰকামী মনোভাবৰ প্ৰৱেশে লাহে লাহে মিচিং সমাজৰপৰা বহু অন্ধসংস্কাৰৰ অৱসান ঘটাব বুলি আশা কৰিব পাৰি।

প্ৰসংগ-সূত্ৰ আৰু টোকা :

১. "নৃজাতি বিজ্ঞানবিদৰ বাবে লোক-সংস্কৃতিৰ অধ্যয়ন অতিকৈ প্ৰয়োজনীয়, যিহেতু ই সমসাময়িক জীৱনধাৰা, পৰম্পৰাগত আচৰণ, বিশ্বাসপদ্ধতি আৰু পুঞ্জীভূত মনোবেদনা আদিৰ স্বৰূপ উদ্ঘাটনত প্ৰচুৰভাৱে সহায় কৰিব পাৰে।"

অসমীয়া লোক-সংস্কৃতিৰ আভাস, নবীন চন্দ্ৰ শৰ্মা, ২০০৫, পৃ.৬২

২. মিচিং সংস্কৃতি, জৱাহৰ জ্যোতি কুলি, ২০০৯, পৃ.১১০

৩. 'মিচিং বিবাহ পদ্ধতি', দুৰ্গা বেগন, মিচিং সংস্কৃতিৰ আলোচ্য, ভৃগুমণি কাগয়ুং, ১৯৭০, পৃ.১৯৯

প্ৰসংগ-গ্ৰন্থ :

- কাগয়ুং, ভৃগুমণি (সম্পা.) : মিচিং সংস্কৃতিৰ আলেখ্য
গুৱাহাটী-৫, ১৯৭০
- কুলি, জৱাহৰ জ্যোতি : মিচিং সংস্কৃতি
কৌস্তভ প্ৰকাশন, ডিব্ৰুগড়-৩, ছেপ্টেম্বৰ, ২০০৯
- গগৈ, চাও লোকেশ্বৰ : অসমৰ লোক-সংস্কৃতি
চাও দেৱজিৎ বৰুৱা আৰু নাং বন্দনা বৰুৱা (গগৈ),
মধ্যপ্ৰদেশ
দ্বিতীয় প্ৰকাশ, আগষ্ট, ২০০৯
- দলে, বসন্ত কুমাৰ (সম্পা.) : অসমৰ জনগোষ্ঠী
কিবণ প্ৰকাশন, ধেমাজি, প্ৰথম প্ৰকাশ, ফেব্ৰুৱাৰী, ২০০৯
- দলে, দীপক কুমাৰ (সম্পা.) : গামিগ
শব্দ প্ৰকাশ, যোৰহাট-১, ফেব্ৰুৱাৰী, ২০১০
- পাতিৰ, সুৰবালা : এক মিচিং কৃষক কন্যাৰ জীৱনৰ অভিজ্ঞতা
আৰু মিচিং সংস্কৃতিৰ বেঙণি
পাতিৰ প্ৰকাশন, গুৱাহাটী-৩, প্ৰথম প্ৰকাশ, জানুৱাৰী,
২০০৩
- মহন্ত বেজবৰা, নীৰাজনা : লোকতত্ত্ব জিজ্ঞাসা
বনলতা, ডিব্ৰুগড়-১, প্ৰথম সংস্কৰণ, এপ্ৰিল, ২০০৪
- ৰাজবংশী, পৰমানন্দ (সম্পা.) : অসমীয়া জাতি আৰু সংস্কৃতি
অসমীয়া বিভাগ, প্ৰাগজ্যোতিষ কলেজ, গুৱাহাটী-৯,
প্ৰথম সংস্কৰণ, অক্টোবৰ, ২০০৩
- শৰ্মা, নবীন চন্দ্ৰ : অসমীয়া লোক-সংস্কৃতিৰ আভাস
বাণী প্ৰকাশ প্ৰাইভেট লিমিটেড, গুৱাহাটী-১, তৃতীয়
প্ৰকাশ ২০০৫

□□□



Removal of organic solvents and oils from wastewater by absorption with crosslinked poly (ethylene-co-vinyl acetate) modified by cetyl alcohol

Riku Dutta^a, Sibani Dhar^b, Kankana Baruah^b, Nipu Dutta^b, Simanta Doley^c, Pitambar Sedai^d, S.K. Dolui^{b,*}, B.C. Ray^a, Bholanath Karmakar^a

^a Jadavpur University, Jadavpur, Kolkata, West Bengal 700032, India

^b Tezpur University, Napaam, Tezpur, Assam 784028, India

^c Jengraimukh College, Jengraimukh, Majuli, Assam 785105, India

^d Lokanayak Omro Kumar Das College, Dhakiajuli, Assam 784110, India

ARTICLE INFO

Keywords:

EVA
Oil absorbent
Melt mixing
Oil spill cleanup

ABSTRACT

In this first investigation on the oil absorption capacity of poly (ethylene-co-vinyl acetate), a novel crosslinked poly (ethylene-co-vinyl acetate) (EVA) based absorbent was prepared by the grafting of maleic anhydride (MA) and cetyl alcohol (CA) in the presence of benzoyl peroxide (BP). Although EVA has been widely used in various applications like drug delivery, encapsulation, and footwear industry, however, its application in environmental remediation has not been studied in detail. In this study, melt mixing was carried out in the Brabender mixture at 120 °C. The grafted polymer was post-cured in the hot air oven at 100 °C for 24 h. The post-cured sorbent showed excellent absorption capacity in toluene (2200 %), gasoline (1720 %), crude oil (1105 %), and kerosene (390 %). The contact angle measurement reveals its hydrophobic nature (123°). The absorption properties of this hydrophobic composite remain stable even after 10 absorption/desorption cycles with absorption capacity remaining constant. The crosslinked polymer was characterized by FTIR, XRD, TGA, and SEM.

1. Introduction

During the last decade, environmental pollution has got an increasing public concern and the government has come up with stringent rules to address this issue. One such pollutant produced at an alarming rate is the water contaminated during drilling operations for hydrocarbon extraction. The huge amount of produced water must be safely disposed of in accordance with the numerous regulatory requirements. Thousands of new oil and gas wells are drilled each year all over the world, resulting in millions of barrels of generated water. As oil fields produced water containing a significant amount of oil and grease and numerous organic and inorganic elements and other suspended particles, it cannot be directly disposed of immediately or pumped into the subsurface for secondary recovery according to environmental regulations [1]. To utilize this water for various industrial applications, these pollutants must be eliminated. During the last few decades, many researchers have investigated several methods of separating these organic pollutants from the water. Naturally occurring absorbents such as kapok fiber, cotton fiber, bagasse, and other agricultural wastes have

been investigated to determine their absorption efficiency but these absorbents have shown low hydrophobic character and poor oil/water selectivity [1–5].

Various natural materials have been studied to determine their oil absorption capacity. These include activated carbon [6,7] wool fibers [8], zeolites [9,10], straw [11], etc. However, these materials were not abundantly used as oil absorbents because of their low absorption properties, and poor reusability. Polymeric absorbents and organogels have proven to be the most effective strategies to eliminate oil and other organic pollutants from contaminated water. Nam et al. [12] studied the absorption of polymer absorbent based on polyolefin and reported that the absorbent had an excellent absorption capacity of 40 g/g in crude oil. Yan et al. [13] used biomorphic MgO fiber with hollow structure as inorganic components to make acrylate composites. The composites had high absorbency for chloroform (28.22 g/g), carbon tetrachloride (25.23 g/g), toluene (15.13 g/g), and gasoline (10.44 g/g) however its reusability was less. Kizil et al. [14] investigated the absorption capacity of poly(alkoxysilane)s on oils and several other organic solvents. The organogel was synthesized by the bulk polymerization method using

* Corresponding author at: Dept. of Chemical Sciences, Tezpur University, Napaam, Tezpur 784028, Assam, India.

E-mail address: dolui@tezu.ernet.in (S.K. Dolui).

Table 1
Composition of different absorbent samples and their codes.

Sample	EVA (g)	MA (wt% of EVA)	BP (wt% of EVA)	CA (wt% of EVA)
EVAP	40	0	5	–
EVAM1	40	3	5	6
EVAM2	40	5	5	10
EVAM3	40	10	5	15

1,3-benzenedimethanol and alkoxy silanes at 160 °C without adding any catalyst. The poly(alkoxy silane)s were reported to absorb about 7.25 g/g of their weight in various organic solvents like dichloromethane (DCM) but its absorption capacity reduces to about 0.5 g/g in oils like gasoline and diesel. Polyurethane (PU) absorbents are also predominantly used in the field of oil absorption due to their promising qualities which include corrosion and wear resistance, microstructure, and lower density. Zhang et al. [15] synthesized an excellent oil absorbent from MnO₂ nanowires/PU foams, with PU sponge being porous was used as the substrate whereas nanowires from MnO₂ were the modifiers. The material was found to be having excellent absorbing capacity of 36.42 g/g in chloroform, 14.66 g/g in toluene, and 4.54 g/g in edible oils. Wang et al. [16] adopted a feasible method to fabricate a PU sponge reinforced with carbon nanotubes (CNTs) that shows superhydrophobic and superoleophobic properties. It was found from the study that the prepared sorbent absorbed various organic solvents and swelled up to 34.9 times its initial weight. Sykam et al. reported a simple low-cost absorbent with exfoliated graphite that can absorb organic solvents up to 40–120 g of its own weight [17]. Son T. Nguyen et al. [18] prepared a novel absorbent using cellulose fiber from waste paper. Methyltrimethoxysilane (MTMS) functionalized absorbent was then prepared to increase its hydrophobic nature. The MTMS-coated recycled aerogel from cellulose had a high contact angle of 143° and 145° in water. The aerogel had high swelling abilities of 18.4, 18.5, and 20.5 g/g for different crude oils measured at 25 °C, respectively however from the second cycle of application, the absorption capacity of this absorbent reduces drastically thus indicating its poor recycle efficiency. Chatterjee et al. [19] reported a novel adsorbent from graphene oxide nanocomposite which showed an absorption capacity of more than ten times the adsorption capacity of commercial activated carbon. Zheng et al. [20] investigated the compatibility of cellulose-based polymer for oil absorption. An environment-friendly freeze-drying process was used to fabricate cross-linked hybrid aerogels from a synthetic polymer (polyvinyl alcohol) and cellulose nanofibril (CNF), which were subsequently modified with

methyl trichlorosilane by thermal chemical vapor deposition method [20]. A magnetic cellulose/TiO₂ aerogel with high porosity and exhibiting good swelling properties was prepared by Chin et al. [21] where TiO₂ was used as a surface coating.

In a recent study, a sorbent was prepared by the process of grafting methacrylic acid onto polypropylene fibers with divinylbenzene used as a cross-linking agent. The sorbent evinced a good absorbing efficiency of 20.8 g/g in various organic solvents [22]. A novel sorbent from natural sponge was synthesized by Heidari et al. [23] showing excellent hydrophobicity and oil/water absorption capacity of 11.92 g/g. In another study, a magnetic poly(styrene-divinylbenzene) foam with an oil-absorbing capacity of roughly 23 times its own weight was also reported [24]. Oil absorbency for crude oil was found to be around 9 g/g in a porous copolymer made with monomers of styrene and butyl methacrylate [25]. In another novel study using polyethylene terephthalate (PET), [26] although the absorption capacity of the sorbent was found to be about 1.5–2.5 g/g, however, this study opened new avenues for the research on waste plastic as a potential oil absorbent. Magnetic sponges were fabricated from composite polydimethylsiloxane PDMS/MWNT which could absorb 6–12 g/g of its own weight [27]. In another recent study, Wang et al. [28] reported a polyacrylonitrile/reduced graphene oxide porous composite capable of absorbing oil from 42.8 to 177.2 times its own weight. Cross-linked poly(tetrahydrofuran) was found to be having promising swelling abilities in one of the studies where the polymer demonstrated an absorbing capacity of 18 g/g in dichloromethane and 10 g/g in toluene [29]. In another recent study, Prakash et al. studied the oil recovery efficiency in degummed silk fibers. The fibers showed performance efficiency of 559 % in engine oil, 517 % in diesel, and 389 % in petrol and could be reused for 10 separation cycles with more than 50 % efficiency [30]. Krishnan et al. studied the absorption capacity of 3D-poly(styrene-methyl methacrylate)/divinylbenzene-2D-nanosheet composite polymeric networks in various oils and organic solvents. The prepared absorbent could absorb 12 g/g of chloroform and about 6 g/g of oils [31].

The present study delineates the grafting of poly(ethylene-co-vinyl acetate) (EVA) by maleic anhydride (MA) and cetyl alcohol (CA) in the Brabender mixture using benzoyl peroxide (BP) as the reaction initiator. Since the last decade, the use of EVA in the wire and cable industry [32], and the encapsulation of PV modules [33] have been widely studied. More recently modified vinyl acetate copolymers have been found to be a good pour point depressant to enhance the properties of crude oil [34]. However, as far as we are aware there is no record of the use of EVA copolymers as an oil absorbent and therefore in this study we have

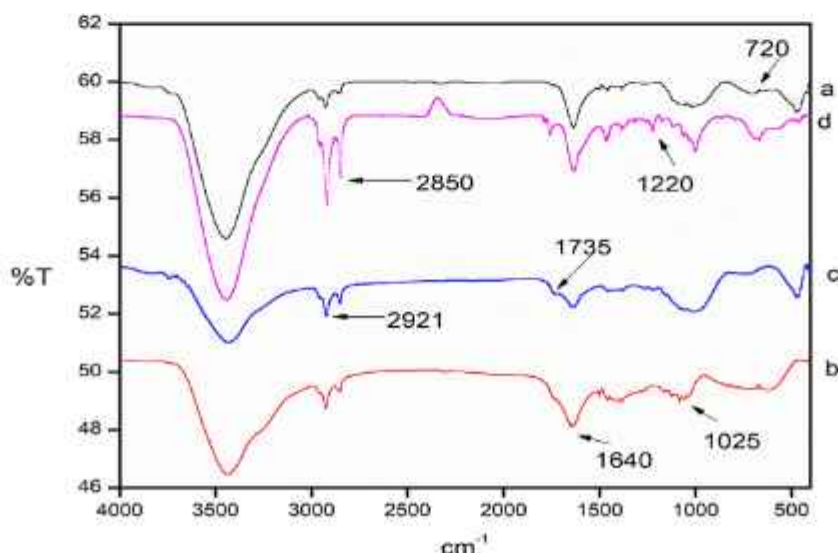
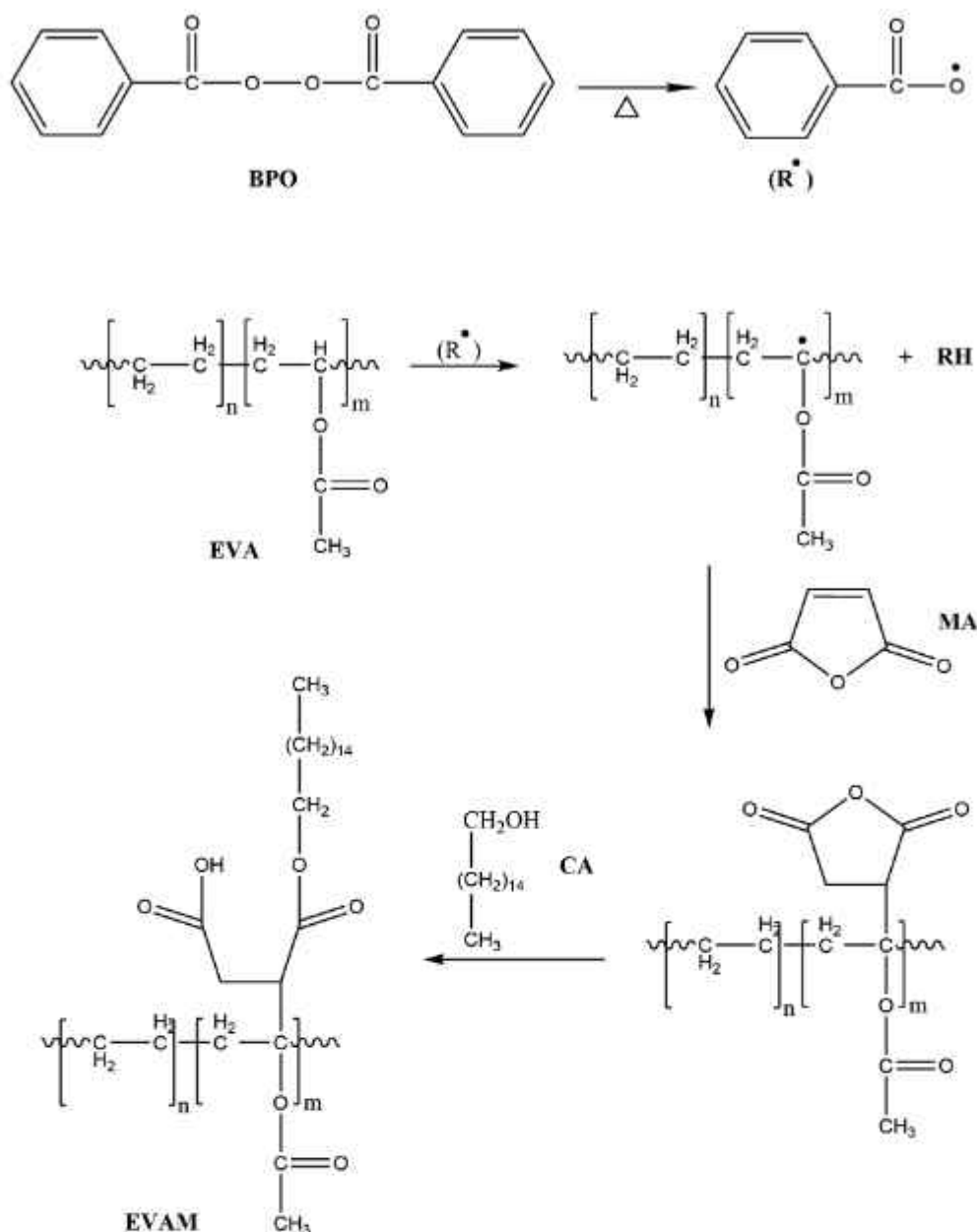


Fig. 1. FT-IR spectra of a) EVAM1 b) EVAM2 c) EVAM3 d) EVAP.



Scheme 1. Plausible mechanism for grafting of MA and cetyl alcohol on EVA.

attempted to investigate its oil absorption capacity in detail. In the present study, the absorption capacity of the synthesized EVA sorbent was investigated in various oils and organic solvents. It was found that unmodified EVA absorbs and swells in various solvents and disintegrates. However, when we have modified it using CA and MA, due to increase in crosslinking density it absorbs oils and organic solvents and remains stable. The swelling capacity of this sorbent was also explored in oil-water mixtures to demonstrate its efficiency even in practical oil spills. The re-usability of the sorbent was studied for up to 10 cycles and hence this EVA-based sorbent could be used as a novel and promising oil absorbent for water treatment and oil spill cleanup.

2. Experimental

2.1. Materials

The chemicals used in this study include poly (ethylene-co-vinyl acetate) (EVA) (with 18 % vinyl acetate content, melt index 15.08 g/10

min, and molecular weight 142,849 Da) (Max Speciality Films limited), maleic anhydride (MA) (Merck), cetyl alcohol (CA) (Loba Chemie Pvt. Ltd.), and benzoyl peroxide (BP) (G.S Chemical Testing Lab and Allied Industries). Solvents include toluene (Merck), dimethyl formamide (DMF) (Merck), dimethyl sulphoxide (DMSO) (Merck), and various oils like kerosene (locally collected), gasoline (locally collected), and crude oil (ONGC).

2.2. Methods

2.2.1. Absorption studies

The absorption studies of the prepared sorbents were performed by immersing sorbents in various oils and solvents viz. toluene, gasoline, crude oil, kerosene, DMF, and DMSO. A known weight of the sample (S_1) was taken and then immersed in 60 ml of oil or organic solvent taken in a beaker. The weight of the swelled samples (S_2) in the oil or solvent was measured at an interval of 2, 4, 8, 12, and 24 h. The absorption percentage in oil/organic solvent was determined by Eq. (1)

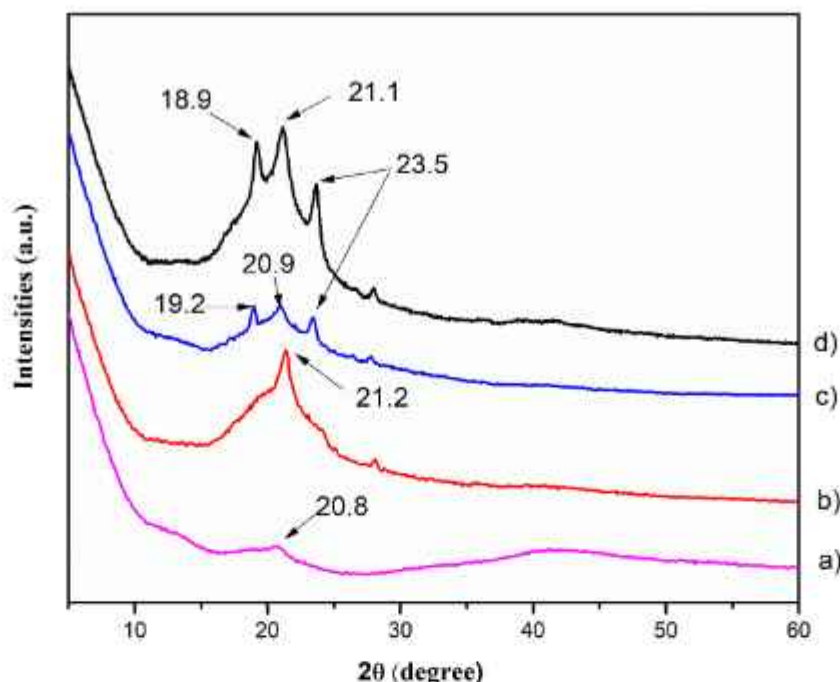


Fig. 2. XRD spectra of a) EVAM3 b) EVAM2 c) EVAP d) EVAM1.

Table 2
Thermal analysis of EVAM1, EVAM2, EVAM3, and EVAP.

Sample	T_i^a	T_m^b	T_n^c	T_d^d (°C) at different weight loss (%)				RW ^e % at 600 °C
				20 %	40 %	60 %	80 %	
EVAM1	316	345	462	316	428	457	470	6.19
EVAM2	326	344	460	339	441	464	476	3.92
EVAM3	328	347	466	364	454	465	477	3.92
EVAP	312	332	456	320	427	456	470	4.88

^a Initial decomposition temperature.

^b Maximum pyrolysis 1st step.

^c Maximum pyrolysis 2nd step.

^d Decomposition temperature at different weight loss.

^e Residual weight.

$$S\%(w/w) = \frac{S_t}{S_i} \times 100 \quad (1)$$

where S_t is the weight (g) of the swelled sample at the measured time interval (t) and S_i (g) is the initial dry weight of the sample. This process was repeated for all the prepared adsorbents in the various oils and organic solvents under study.

2.2.2. Reusability

The reusability of sorbent was also evaluated by the absorption and desorption process. The sorbent was immersed in toluene and allowed to swell for 24 h to reach near its maximum swelling capacity. After 24 h, the swollen sample was subjected to thermal heating at 50 °C for 1 h for the desorption process. The desorption was verified by a comparison between the initial weight of the adsorbent and its dry weight after desorption. This process was repeated for 10 absorption-desorption cycles.

2.2.3. Separation of oils from oil-water mixture

For demonstrating the direct removal of oils from the mixture of oil and water, 20 ml of gasoline and 20 ml of water were mixed to form an oil-water suspension. 0.3 g of the sorbent was dropped on the oil-water

mixture and the absorption capacity was monitored as a function of time.

2.2.4. Kinetic study

The kinetic study was performed by plotting the absorption capacities as a function of time [29,35]. The adsorbents were immersed in various oils and organic solvents and their weight was noted at regular intervals (20, 40, 60, 80, ... min). The first order absorption kinetics is expressed by the equation:

$$\frac{dW_t}{dt} = K(W_{\infty} - W_t) \quad (2)$$

where W_t is the sample weight after absorption at time t, and W_{∞} is the sample weight after absorption at equilibrium.

Integrating Eq. (2), we get,

$$\ln W_{\infty}/(W_{\infty} - W_t) = Kt. \quad (3)$$

If the graph obtained by plotting $\ln W_{\infty}/(W_{\infty} - W_t)$ vs t represents a straight line we can conclude that the absorption follows first-order kinetics.

The second-order absorption kinetics is expressed by the equation:

$$\frac{dW_t}{dt} = K(W_{\infty} - W_t)^2 \quad (4)$$

Integrating Eq. (4), we get,

$$\frac{t}{W_t} = \frac{1}{KW_{\infty}^2} + \frac{1}{W_{\infty}} \quad (5)$$

If the graph obtained by plotting t/W_t vs t gives a straight line we can conclude that the absorption follows second-order kinetics.

3. Characterization studies on synthesized adsorbents

EVAM1, EVAM2, EVAM3 and EVAP samples were characterized using Fourier transform infrared spectroscopy (FTIR) instrument (PerkinElmer, Frontier MIR-FIR) with a scanning range between 400 and 4000 cm^{-1} . X-ray diffraction (XRD) studies were conducted with an X-ray diffractometer (Bruker Axis, Germany, Scanning rate-10 min^{-1}) with

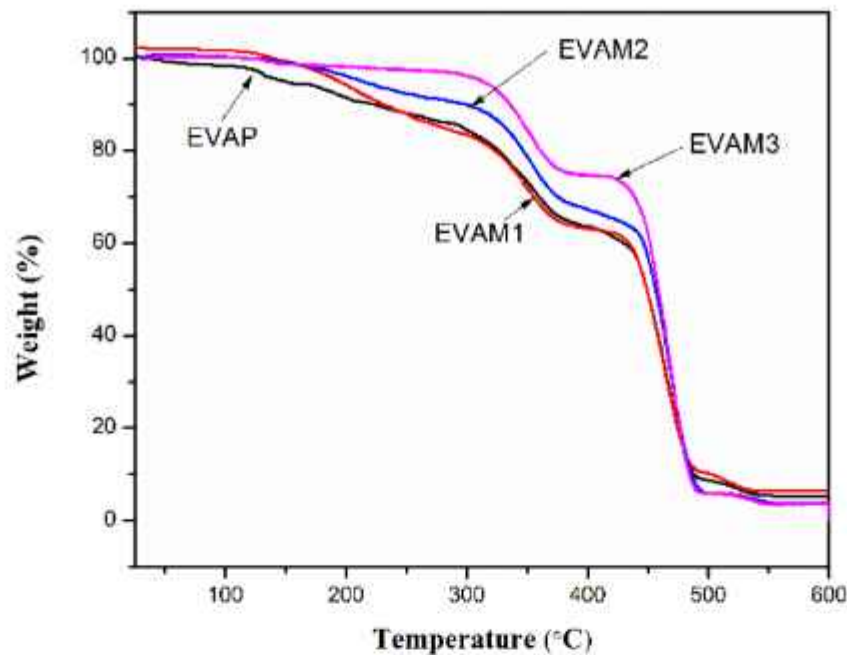


Fig. 3. TGA thermogram of EVAP, EVAM1, EVAM2 and EVAM3.

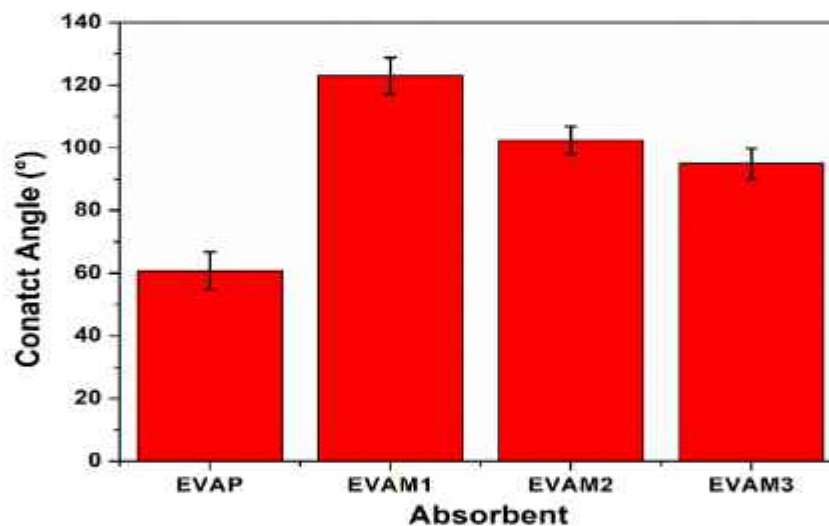


Fig. 4. Contact angle measurement of EVAP, EVAM1, EVAM2 and EVAM3.

the angle varying from 70 to 500. The study on thermal behavior of the prepared composites was performed using Thermogravimetric Analysis (TGA) instrument (TGA-50, Shimadzu, Japan). Contact angle goniometer (Kyowa, DMS401) setup was used to evaluate the wettability parameter. The morphology of the prepared absorbent was investigated using a scanning electron microscopy (SEM) (JEOL, JSM Model 6390 LV) with a 15 kV accelerating voltage. For this work, the fractured surface of the composites was set on a brass holder and platinum sputtering was conducted.

4. Results and discussion

4.1. Synthesis of EVA-based absorbent

40 g of EVA was mixed with 2 g of benzoyl peroxide and different weight percentages of MA and CA (Table 1) and transferred into the chamber of the Brabender Plasticiser for melt mixing and grafting. This

process of blending was carried out at a temperature of 120 °C for 10 min at 50 rpm. The resultant mixture was then shifted to the desiccator to preserve the samples from moisture.

4.2. FTIR spectroscopy

FTIR spectra of crosslinked EVA are shown in Fig. 1. The characteristic peak of EVA at 2916–2919 cm^{-1} and 2849–2852 cm^{-1} [36] are observed which represents the C–H bond deformation (symmetric and asymmetric) of methane, methylene, and methyl groups in ethylene-vinyl acetate copolymer. The typical absorption peak of the carbonyl group (C=O) of maleic anhydride is observed at 1735 cm^{-1} [36]. A band at 1220–1238 cm^{-1} represents the asymmetric C–O–C deformation of the acetate group, while the band at 1016–1022 cm^{-1} represents the symmetric C–O–C group of acetate. The absorption band representing 720 cm^{-1} and 610 cm^{-1} are the typical vibration groups CH_2 and C=O [36]. The characteristic peak at 1456–1466 cm^{-1} corresponds to the

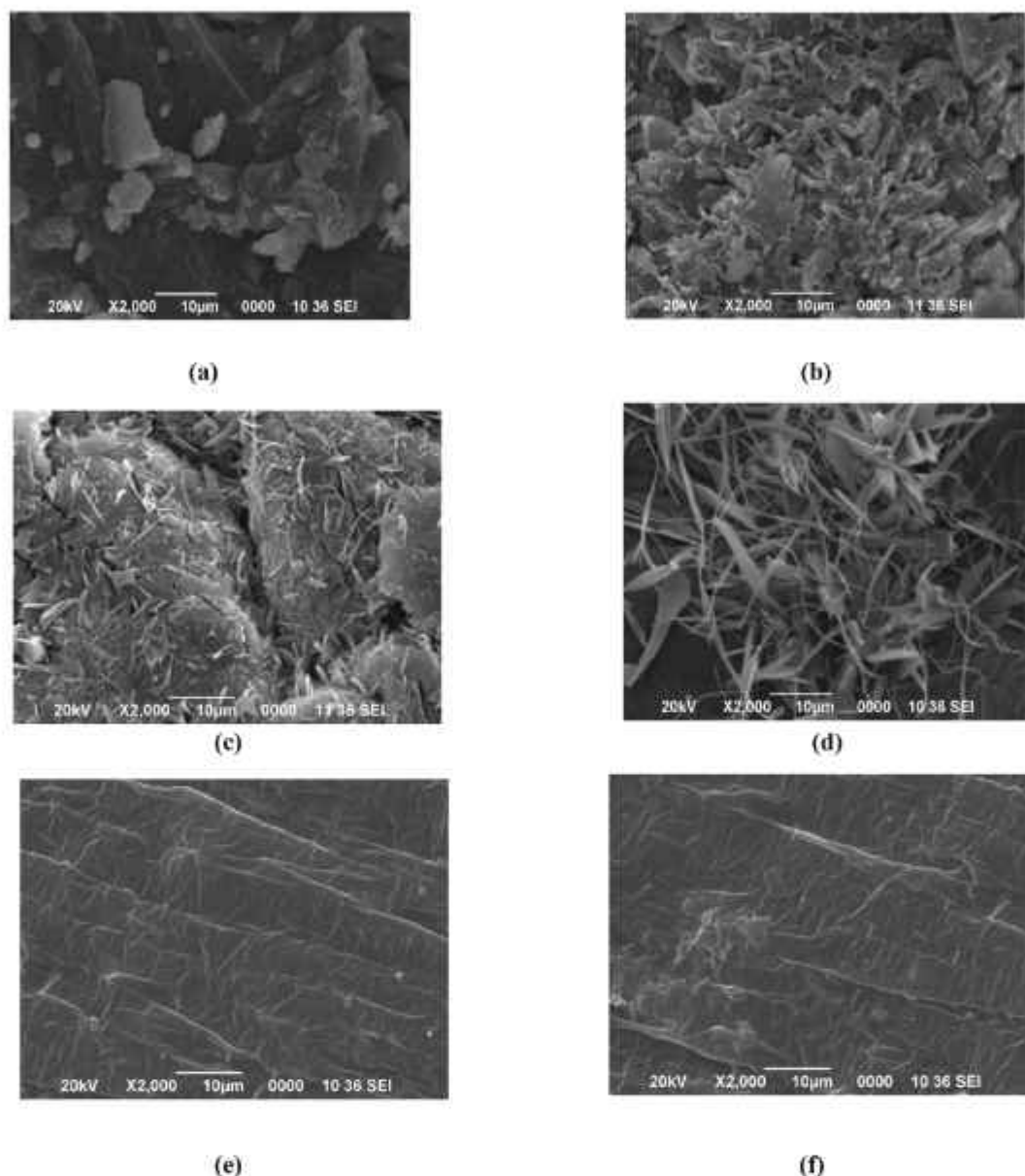


Fig. 5. SEM micrographs of (a) EVAP (b) EVAM1 (c) EVAM2 before reflux (d) EVAM3 before reflux (e) EVAM2 after reflux (f) EVAM3 after reflux.

deforming CH_2 group in the main chain. The absorption peak at 1371 cm^{-1} represents the methylene groups (deformation vibration in the plane of C—H in CH_3). It can be clearly visible from the IR curves that the intensities of the MA characteristic stretching peak of C=O at 1857 cm^{-1} and 1778 cm^{-1} disappeared which confirms the ring-opening reaction of maleic anhydride with the -OH group of cetyl alcohol which is also evident from the mechanism in Scheme 1.

4.3. X-ray diffraction

Fig. 2 indicates the XRD pattern of EVAP, EVAM1, EVAM2, and EVAM3. XRD peaks at $21.1^\circ 2\theta$ (110 plane) and $23.5^\circ 2\theta$ (200 plane) are observed in EVAM1 and EVAP which corresponds to the crystalline and amorphous regions of EVA respectively. This indicates that the crystalline behavior of EVA remains unaltered on varying the composition of the components. In addition to this, with an increase in MA and CA in EVAM2 and EVAM3, the intensity of diffraction peaks decreases as the restricted alkyl side groups have low crystallization ability onto the backbone of the synthesized copolymer.

4.4. Thermogravimetry (TG)

The initial decomposition temperature (T_i), maximum decomposition temperature (T_m), decomposition temperature at different weight loss (T_D %), and residual weight (RW %) for the prepared absorbents are given in Table 2. TGA curves showed two-stage weight loss events. The initial weight loss occurring between 340°C and 375°C can be attributed to the autocatalytic deacetylation of vinyl acetate [37]. The second weight-loss event is associated with the chain scission of the polyethylene chains of EVA in the interval of 460°C – 485°C . The cross-linked copolymers EVAM2 and EVAM3 have a slight increase in degradation temperature because of their crosslinked network which plays a crucial role in elevating the thermal resistance of the cross-linked absorbents which is also evident in Scheme 1 (Fig. 3).

4.5. Wettability measurements

The wettability study in terms of contact angle is reported in Fig. 4. EVAM1 and EVAM2 show good hydrophobic character. EVA contains

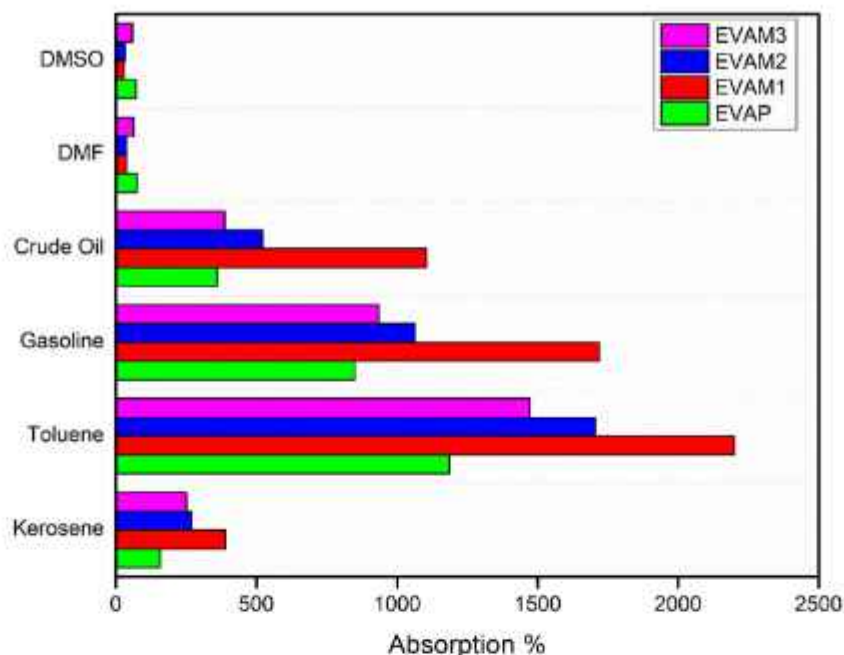


Fig. 6. Absorption capacities of the synthesized EVA based absorbents.

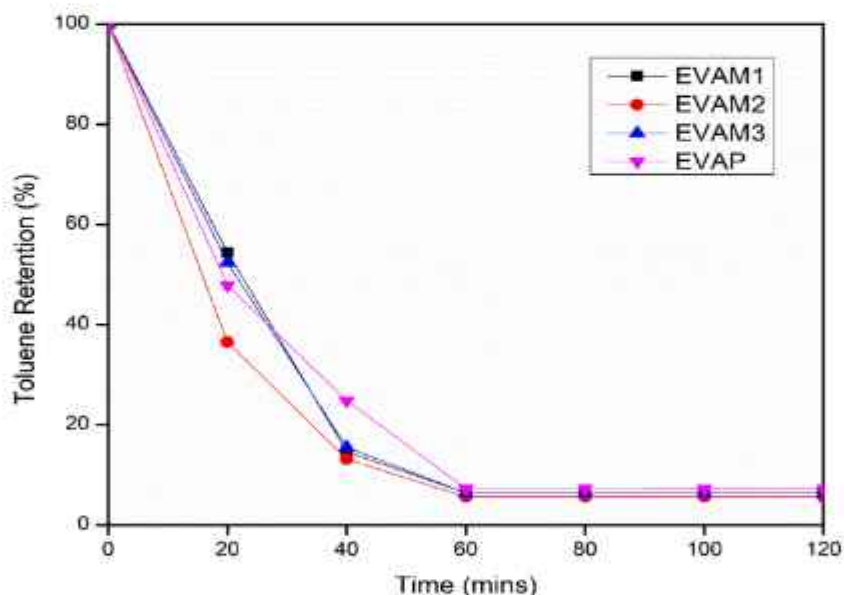


Fig. 7. Toluene retention of the synthesized absorbents.

both hydrophobic ethylene groups as well as hydrophilic vinyl acetate groups. Due to the presence of hydrophobic ethylene groups, weaker adhesion interaction occurs between the ethylene groups and the water surface, and hence the hydrophobicity increases. With the incorporation of CA in the absorbents, the contact angle increases from 60.8° to 123° indicating an increase in hydrophobic nature. However, with a higher CA content (EVAM2 and EVAM3), contact angle decreases due to the presence of a higher amount of unreacted CA groups on the absorbent surface. Similar findings are also reported by J. Gu et al. [39]. But as the unreacted portions in EVAM2 and EVAM3 were removed using chloroform in a reflux reaction at 40°C for 30 min, more uniform morphology could be observed with contact angles of 125° and 126° respectively (Fig. 5).

4.6. Scanning electron microscopy (SEM) study

SEM micrographs of the synthesized sorbents with varying percentages of MA and CA are given in Fig. 5. The micrographs of EVAP depict a rough surface with lumps which signify poor interactions among the various components. A better interaction could be observed in the morphology of EVAM1 (Fig. 5b) along with pore spaces. The micrographs of EVAM2 and EVAM3 (Fig. 5c and d) depict a rough surface with needle-like structures which may be attributed to the unreacted portions as the MA% content and CA% content increase. These unreacted portions were removed using chloroform in a reflux reaction at 40°C for 30 min. The SEM images thus obtained show a more uniform morphology (Fig. 5e and f) with no significant pore spaces as compared to EVAM1. This is mainly due to the increase in crosslinking density with the

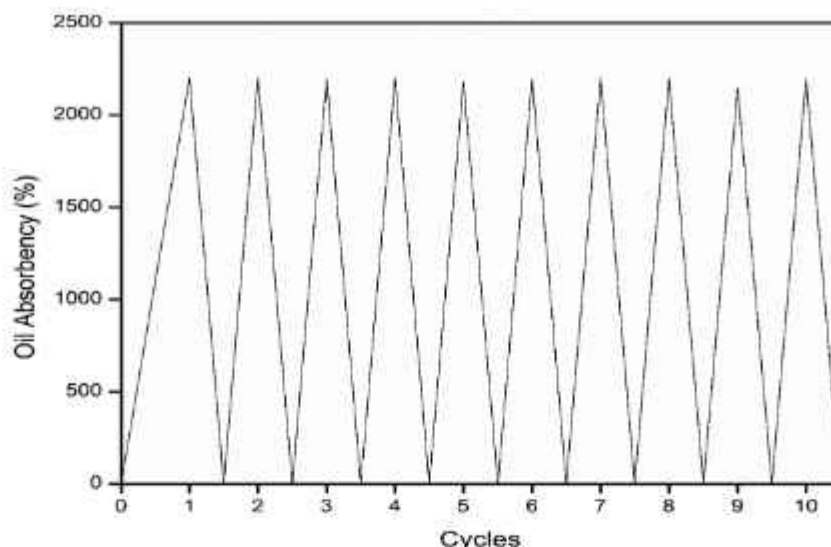


Fig. 8. Reusability of the synthesized absorbent for various absorption-desorption cycles.

increase in MA and CA content. This results in a decrease in absorption capacity in EVAM2 and EVAM3 as evident from the absorption study.

4.7. Oil absorption capacity

The equilibrium or maximum swelling capacity reaches within 24 h for all these sorbents. The maximum absorption capacity of these sorbents in various oils and organic solvents is shown in Fig. 6.

The sorbents show excellent absorption characteristics in oils and organic solvents. Scheme 1 lucidly explains the mechanism of the grafting reaction. All the sorbents have high swelling capacity in toluene at room temperature. This is mainly due to the small molecule which can readily penetrate into the pores present in the polymer. On the other hand, the long-chain oils like gasoline, crude oil, and kerosene also showed good absorption into the polymer network due to the hydrophobic nature of the polymeric network. But absorption is low compared to toluene as longer molecular chains containing molecules are mostly adsorbed on the surface of the polymer and therefore blocked the adsorption of other molecules. On the other hand, since the prepared polymer consists of a long aliphatic chain (mainly from cetyl alcohol) as evident from Scheme 1, they are mainly non-polar in nature, and hence polar nature molecules like DMF, and DMSO exhibit lower absorption on the polymer (Scheme 1). Dutta et al. [35] in their work also found similar results where the prepared sorbent showed excellent absorption in non-polar organic solvents like chloroform (690–750 %) and poor absorption in case of polar solvents. The acrylic ester resin composites prepared by Yan et al. [13] had also demonstrated high absorbency for chloroform (28.22 g/g), carbon tetrachloride (25.23 g/g), toluene (15.13 g/g), and gasoline (10.44 g/g) and poor absorbency in polar solvents. The content of MA and CA in the prepared polymer has a potential effect on the absorption of both the organic solvents and crude oil. From Fig. 5, it is found that maximum absorption is achieved for EVAM1 as compared to EVAM2, EVAM3 and EVAP. EVAM1 showed the highest absorption percentage in toluene (2200 %). Similar cross-linked poly(tetrahydrofuran) sorbents [29] also showed an absorption capacity of 18 g/g in dichloromethane and 10 g/g in toluene. Cross-linked 3D-poly(styrene-methyl methacrylate)/divinylbenzene-2D-nanosheet composite polymeric networks have also reported to absorb 12 g/g of chloroform and about 6 g/g of oils [31]. Although, the only EVA-based polymer (EVAP) also gives good absorption but due to the lower cross-linking density of the polymer it is unstable in organic solvents and some small weight loss of the polymer is observed in the given solvent. In the case of absorbents with higher weight % of MA and CA (EVAM2 and

EVAM3), the prepared polymer displays higher cross-linked polymer networks resulting in a decrease in the effective pore volume of the polymer and thus giving lower absorption capacities (evident from SEM image). From the SEM image, it is also observed that the concentration of MA and CA in EVAM1 results in an expandable polymer network which is appropriate for better absorption of organic solvents and oils and therefore it has shown the best absorption performance in contrast to those which are prepared with higher amounts of CA and MA (EVAM2 and EVAM3) (Fig. 6).

4.8. Reusability of the synthesized absorbents

The retention time for the various swollen sorbents was examined in toluene by evaluating the weight loss at 50 °C. The sorbents recovered their original dry weight within 1 h after releasing the absorbed solvent from its matrix (Fig. 7). The sorbent was again immersed in toluene to study its absorbing efficiency. This absorption-desorption process was continued for 10 cycles. The absorption capacity of the sorbents remained almost unaltered even after 10 cycles (Fig. 8). Thus, the sorbent can be regenerated and reused after eliminating oils and organic solvents from the environment. Zhang et al. [15] also observed that their foam composite had excellent reusability characteristics of more than 5 absorption-desorption cycles. Son T. Nguyen et al. [18] observed that the absorbent prepared from cellulose showed a high absorption capacity of 18.4 g/g in cycle 1. However, the absorption efficiency reduced to 0.96, 0.68, 0.59, and 0.63 g/g in cycles 2, 3, 4, and 5, respectively. Some other absorbents with carbon nanotubes (CNT) [16] showed excellent reusability and can be applied for 150 cycles while maintaining similar absorption capacity.

4.9. Swelling kinetics

For practical applications, the swelling rate of the absorbent is another important parameter in addition to higher swelling capacity. To obtain the kinetic curves the absorption percentage was plotted as a function of time for oils and various organic solvents. The absorption initially increased at a rapid rate until it reached equilibrium in about 12 h. The swelling kinetics for EVAM1, EVAM2, EVAM3, and EVAP resemble each other.

The rate constant of the absorption process was determined by plots of $\ln W_{\infty} / (W_{\infty} - W_t)$ vs t (from Eq. (3)) and t / W_t vs t (from Eq. (5)). It was observed that the experimental kinetic data gave linearized curves as per the pseudo-second-order rate equations (Fig. 9) with correlation

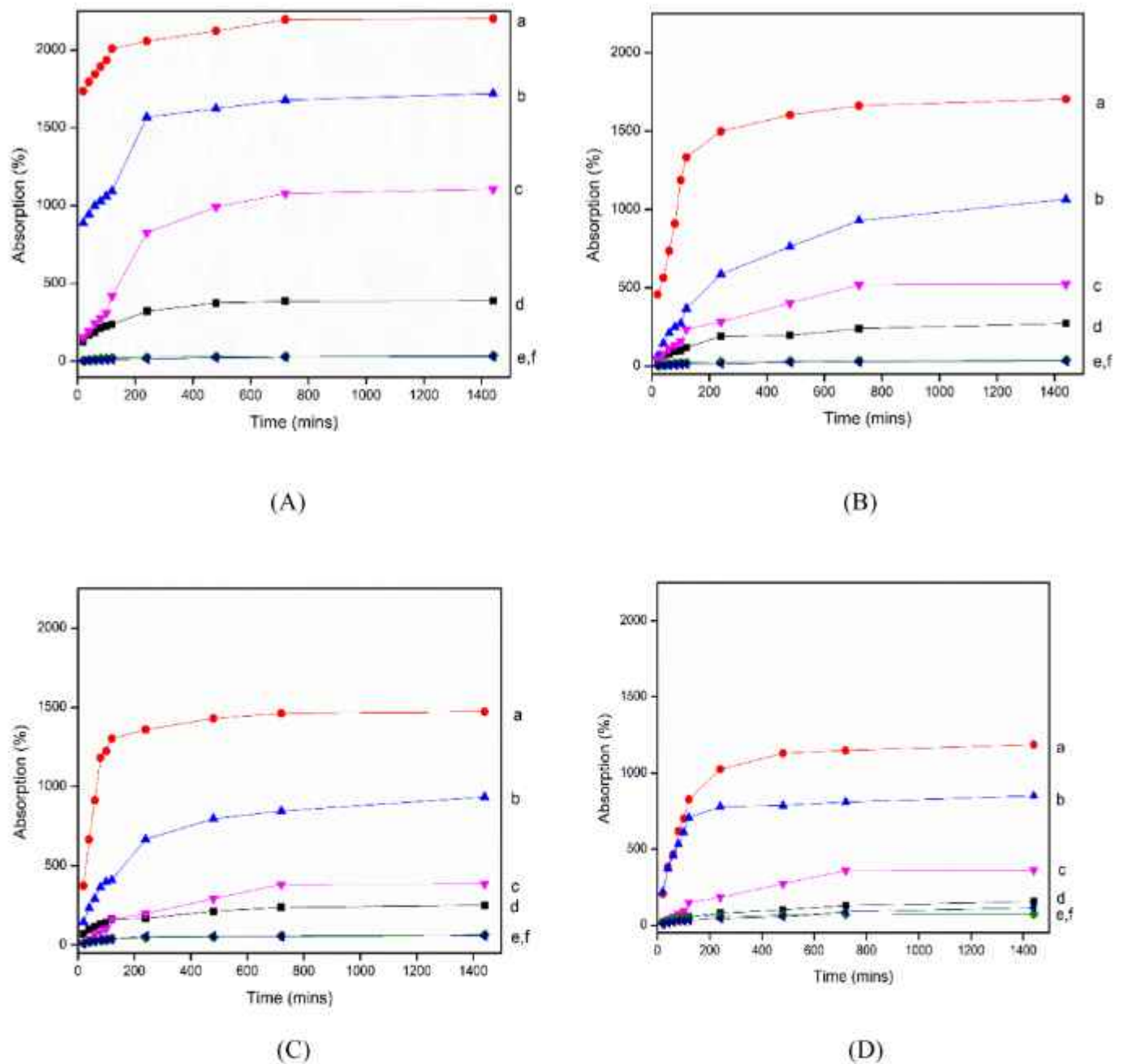


Fig. 9. Absorption kinetics in a) toluene b) gasoline c) crude oil d) kerosene e) DMF f) DMSO for (A) EVAM1 (B) EVAM2 (C) EVAM3 (D) EVAP.

Table 3
Pseudo-second-order parameters for EVAP, EVAM1, EVAM2 and EVAM3.

Oil/organic solvent	Rate constant (K_2)				Correlation coefficients (R^2)			
	EVAP	EVAM1	EVAM2	EVAM3	EVAP	EVAM1	EVAM2	EVAM3
Toluene	3.15×10^{-4}	9.62×10^{-4}	1.4×10^{-4}	14.1×10^{-4}	0.99166	0.99876	0.99955	0.99939
Gasoline	29.6×10^{-4}	34.7×10^{-4}	2×10^{-4}	3.92×10^{-4}	0.99924	0.99988	0.997	0.99805
Crude oil	11×10^{-4}	2.67×10^{-4}	3.2×10^{-4}	3.15×10^{-4}	0.99959	0.99074	0.99628	0.99166
Kerosene	8.23×10^{-4}	9.74×10^{-4}	5.5×10^{-4}	9.16×10^{-4}	0.99714	0.99926	0.99764	0.99825
DMF	23.7×10^{-4}	22.7×10^{-4}	22.7×10^{-4}	25.5×10^{-4}	0.99984	0.99958	0.99981	0.99977
DMSO	11.3×10^{-4}	26.8×10^{-4}	26.8×10^{-4}	18.7×10^{-4}	0.99805	0.99975	0.99989	0.99937

coefficients R^2 of 0.99. The pseudo-second-order parameters for all the absorbents with different oils and solvents are summarized in Table 3.

4.10. Separation of oil-water mixture

The rate at which absorption of oils occurs from the water surface and stability in water is another significant parameter that determines

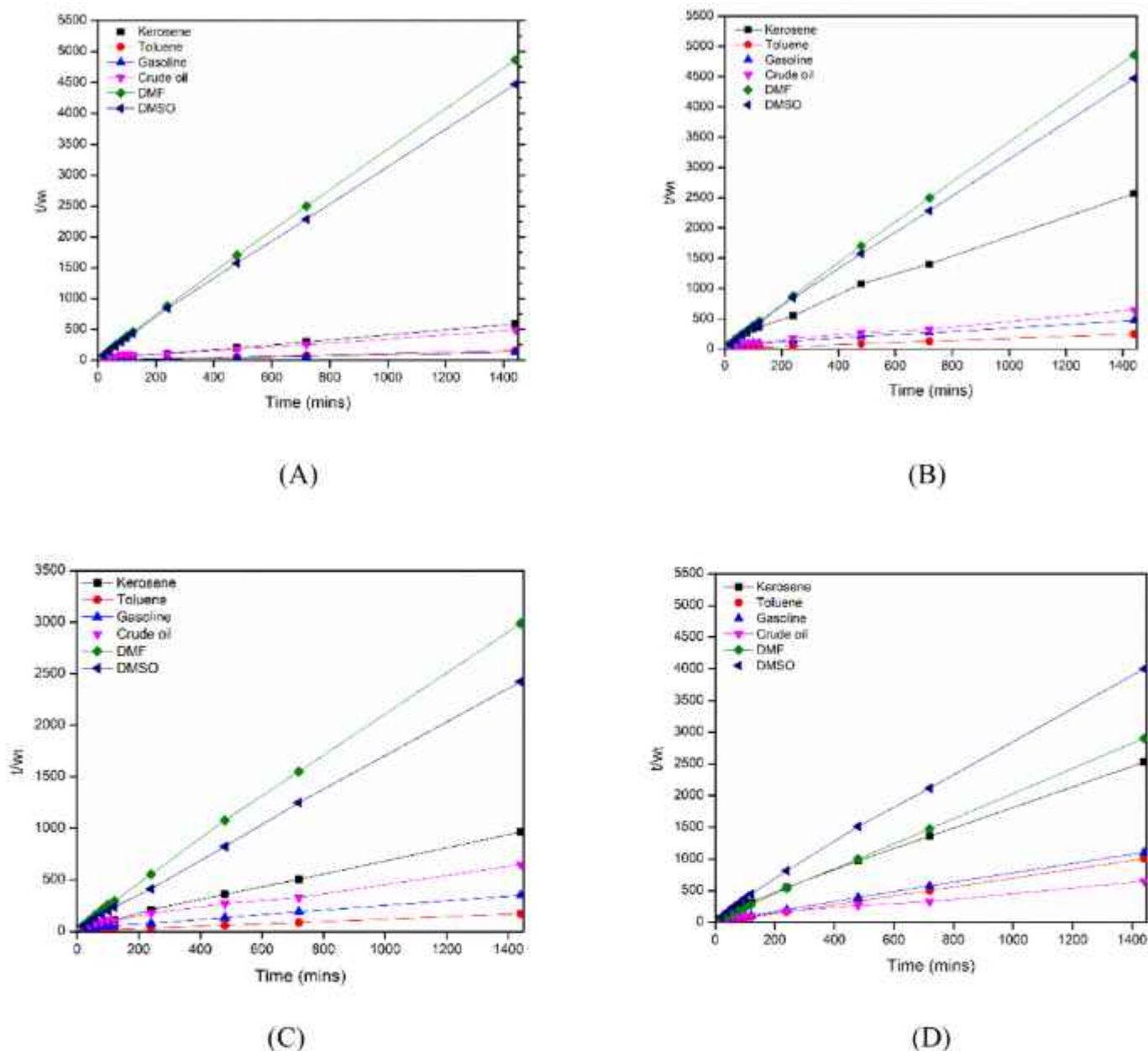


Fig. 10. Pseudo-second-order absorption kinetics for (A) EVAM1 (B) EVAM2 (C) EVAM3 (D) EVAP.

the efficiency of sorbents in a real-time oil spill environment. The study on the separation of oil from the oil-water mixture by the synthesized absorbent is represented in Fig. 10. The pictures depict the absorption of gasoline from the surface of the oil-water mixture with the use of EVAM1 absorbent which showed the best absorption in this study. The sorbent absorbed most of the gasoline within 30 min leaving behind water in the beaker. This study demonstrates its effectiveness in practical oil spills and its stable oil absorption efficiency even in the presence of water (Fig. 11).

5. Conclusion

In this study, elastic and hydrophobic reusable crosslinked poly (ethylene-co-vinyl acetate) (EVA) copolymer modified with cetyl alcohol-based sorbent has been successfully prepared. The modified EVA sorbents are excellent absorbents of oil and organic solvents. Maximum efficiency was found in toluene with an absorption capacity of 22 g per 1 g of the sorbent. High absorption capacity was also seen in

various oils and organic solvents. The absorbent shows good hydrophobic nature with contact angle of 123° . The reusability of the absorbent was studied and it was found that the absorbent could be recycled for more than 10 absorption-desorption cycles. Since EVA is an important widely used commercial synthetic material, the synthesis of high swelling capacity and reusable absorbent proposes its application in a new field of oil absorption. In addition to its high absorption capacity, its reusable nature makes it a potential candidate for use in various practical industrial fields such as water treatment and environmental cleanups.

Funding

This research did not receive any specific grant from funding agencies in the public, commercial, or not-for-profit sectors.

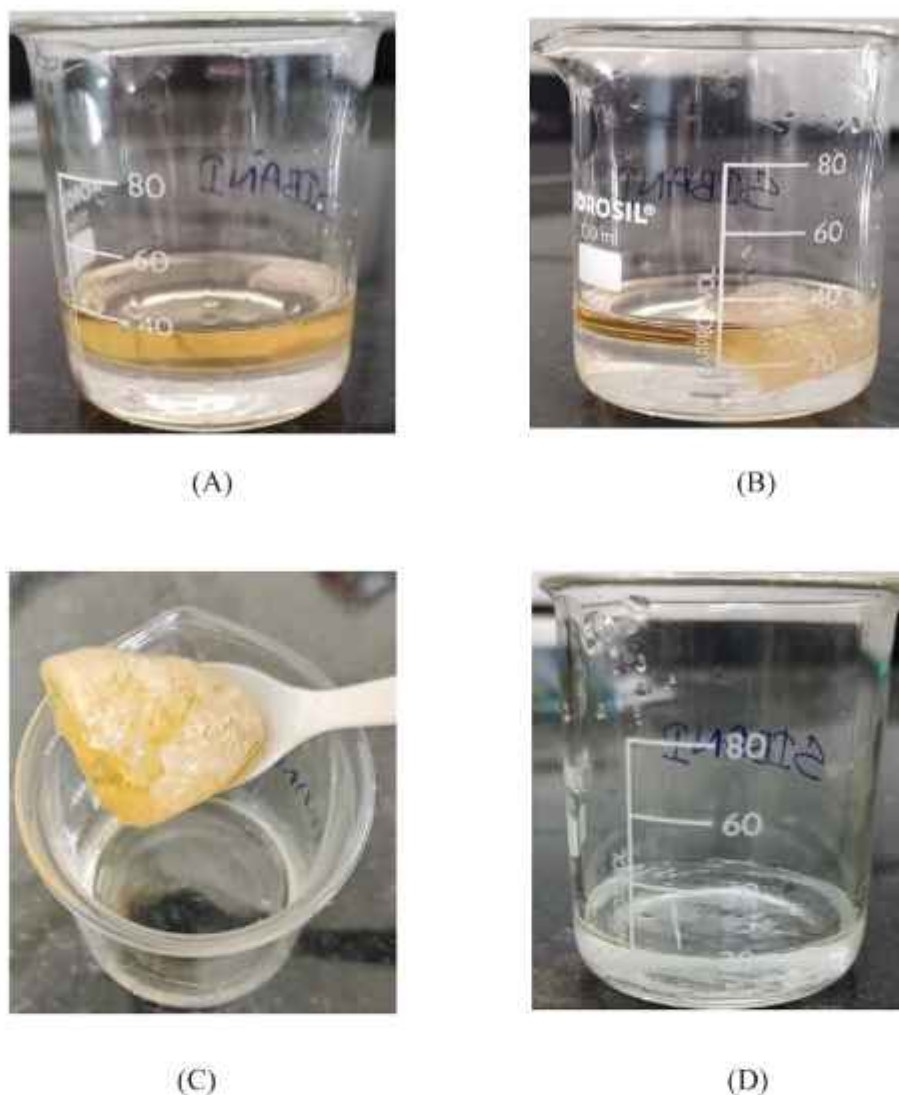


Fig. 11. Gasoline absorption from water surface by EVAMI; (A) EVAMI sample immersed in the oil-water mixture (B) gasoline absorption by EVAMI sample after 15 min (C) EVAMI sample after absorption of gasoline (D) separated water from the oil-water mixture.

Declaration of competing interest

The authors declare that they have no known competing financial interests or personal relationships that could have appeared to influence the work reported in this paper.

Data availability

Data will be made available on request.

References

- [1] M.A. Al-Ghouti, M.A. Al-Kaabi, M.Y. Ashfaq, D.A. Da'na, Produced water characteristics, treatment and reuse: a review, *J. Water Process Eng.* 28 (2019) 222–239, <https://doi.org/10.1016/J.JWPE.2019.02.001>.
- [2] A. Egypt, Heavy oil spill cleanup using low grade raw cotton fibers: trial for practical application, <http://www.academicjournals.org/IPTAF>, 2011.
- [3] G. Lugito, A. Kustiana, R. Martuani, I.G. Werten, Kapok fibre as potential oil-absorbing material: modification mechanism and performance evaluation, in: *IOP Conference Series: Materials Science and Engineering*, Institute of Physics Publishing, 2020, <https://doi.org/10.1088/1757-699X/823/1/012033>.
- [4] A.E.A.A. Said, A.G. Ludwick, H.A. Aglan, Usefulness of raw bagasse for oil absorption: a comparison of raw and acylated bagasse and their components, *Bioresour. Technol.* 100 (2009) 2219–2222, <https://doi.org/10.1016/J.BIORTECH.2008.09.060>.
- [5] A. Shahi, Kraft lignin: a novel alternative to oil spill cleanup recycling industrial waste, *Can. Young Sci. J.* 2014 (2014) 42–46, <https://doi.org/10.13034/cyjs-2014-021>.
- [6] P.K. Malik, Dye removal from wastewater using activated carbon developed from sawdust: adsorption equilibrium and kinetics, *J. Hazard. Mater.* 113 (2004) 81–88, <https://doi.org/10.1016/J.JHAZMAT.2004.05.022>.
- [7] K.G. Raj, P.A. Joy, Coconut shell based activated carbon-iron oxide magnetic nanocomposite for fast and efficient removal of oil spills, *J. Environ. Chem. Eng.* 3 (2015) 2068–2075, <https://doi.org/10.1016/J.JECE.2015.04.028>.
- [8] E. Cao, W. Xiao, W. Duan, N. Wang, A. Wang, Y. Zheng, Metallic nanoparticles roughened *Calotropis gigantea* fiber enables efficient absorption of oils and organic solvents, *Ind. Crop. Prod.* 115 (2018) 272–279, <https://doi.org/10.1016/J.INDCROP.2018.02.052>.
- [9] S.L. Hailu, B.U. Nair, M. Redi-Abshiro, I. Diaz, M. Tessema, Preparation and characterization of cationic surfactant modified zeolite adsorbent material for adsorption of organic and inorganic industrial pollutants, *J. Environ. Chem. Eng.* 5 (2017) 3319–3329, <https://doi.org/10.1016/j.jece.2017.06.039>.
- [10] S. Samadi, S.S. Yand, H. Abdoli, P. Jafari, M. Aliabadi, Fabrication of novel chitosan/PAN/magnetic ZSM-5 zeolite coated sponges for adsorption of oil from water surfaces, *Int. J. Biol. Macromol.* 105 (2017) 370–376, <https://doi.org/10.1016/J.IJBIOMAC.2017.07.050>.
- [11] F. Beshkar, H. Khojasteh, M. Salavati-Niasari, Recyclable magnetic superhydrophobic straw soot sponge for highly efficient oil/water separation, *J. Colloid Interface Sci.* 497 (2017) 57–65, <https://doi.org/10.1016/J.JCS.2017.02.016>.
- [12] C. Nam, G. Zhang, T.C.M. Chung, Polyolefin-based interpenetrating polymer network absorbent for crude oil entrapment and recovery in aqueous system, *J. Hazard. Mater.* 351 (2018) 285–292, <https://doi.org/10.1016/J.JHAZMAT.2018.03.004>.

- [13] L. Yan, Q. Li, X. Wang, H. Song, H. Chi, Y. Qiao, Y. Zhai, D. Liu, Synthesis and absorption performance of acrylic Ester and Hollow fiber MgO nanoparticle resin composite, *Polym. Plast. Technol. Eng.* 56 (2017) 1857–1865, <https://doi.org/10.1080/03602559.2017.1295310>.
- [14] S. Kizil, K. Karadag, G. Ozan Aydin, H. Bulbul Sommez, Poly(alkoxysilane) reusable organogels for removal of oil/organic solvents from water surface, *J. Environ. Manag.* 149 (2015) 57–64, <https://doi.org/10.1016/j.jenvman.2014.09.030>.
- [15] T. Zhang, L. Kong, Y. Dai, X. Yue, J. Rong, F. Qiu, J. Pan, Enhanced oils and organic solvents absorption by polyurethane foams composites modified with MnO₂ nanowires, *Chem. Eng. J.* 309 (2017) 7–14, <https://doi.org/10.1016/j.cej.2016.08.085>.
- [16] H. Wang, E. Wang, Z. Liu, D. Gao, R. Yuan, L. Sun, Y. Zhu, A novel carbon nanotubes reinforced superhydrophobic and superoleophilic polyurethane sponge for selective oil-water separation through a chemical fabrication, *J. Mater. Chem. A* 3 (2015) 266–273, <https://doi.org/10.1039/c4ta03945a>.
- [17] N. Sykam, N.D. Jayram, G.M. Rao, Highly efficient removal of toxic organic dyes, chemical solvents and oils by mesoporous exfoliated graphite: synthesis and mechanism, *J. Water Process Eng.* 25 (2018) 128–137, <https://doi.org/10.1016/j.jwpe.2018.05.013>.
- [18] S.T. Nguyen, J. Feng, N.T. Le, A.T.T. Le, N. Hoang, V.B.C. Tan, H.M. Duong, Cellulose aerogel from paper waste for crude oil spill cleaning, *Ind. Eng. Chem. Res.* 52 (2013) 16386–16391, <https://doi.org/10.1021/ie4032567>.
- [19] R. Chatterjee, C. Majumder, Uptake of azarabic 2-methylpyridine by pre-cooled carboxyl functionalized graphene nanocomposite: detection, sorption and optimization, *J. Water Process Eng.* 39 (2021), <https://doi.org/10.1016/j.jwpe.2020.101686>.
- [20] Q. Zheng, Z. Cai, S. Gong, Green synthesis of poly(vinyl alcohol (PVA)-cellulose nanofibril (CNF) hybrid aerogels and their use as superabsorbents, *J. Mater. Chem. A* 2 (2014) 3110–3116, <https://doi.org/10.1039/c3ta14642a>.
- [21] S.F. Chin, A.N. Binti Romainor, S.C. Pang, Fabrication of hydrophobic and magnetic cellulose aerogel with high oil absorption capacity, *Mater. Lett.* 115 (2014) 241–243, <https://doi.org/10.1016/j.matlet.2013.10.061>.
- [22] H. Thu Ha, L.T. Son, Oil sorbents based on methacrylic acid-grafted polypropylene fibers: synthesis and characterization, *J. Chem. Eng. Process Technol.* 07 (2016), <https://doi.org/10.4172/2157-7048.1000290>.
- [23] M.K. Heidari, M. Fouladi, H.A. Sooreh, O. Tavakoli, Superhydrophobic and superoleophilic natural sponge sorbent for crude oil/water separation, *J. Water Process Eng.* 48 (2022), 102783, <https://doi.org/10.1016/j.jwpe.2022.102783>.
- [24] N. Zhang, W. Jiang, T. Wang, J. Gu, S. Zhong, S. Zhou, T. Xie, J. Fu, Facile preparation of magnetic poly(styrene-divinylbenzene) foam and its application as an oil absorbent, *Ind. Eng. Chem. Res.* 54 (2015) 11033–11039, <https://doi.org/10.1021/acs.iecr.5b01647>.
- [25] Y. Du, P. Fang, J. Chen, X. Hou, Synthesis of reusable macroporous St/BMA copolymer resin and its absorbency to organic solvent and oil, *Polym. Adv. Technol.* 27 (2016) 393–403, <https://doi.org/10.1002/pat.3679>.
- [26] E.A. Bukharova, E.A. Yatarintseva, L.N. Ol'Shanskaya, Production of polyethylene terephthalate based sorbent and its use for waste and surface water cleaning from oil products, *Chem. Pet. Eng.* 50 (2015) 595–599, <https://doi.org/10.1007/s10556-014-9947-1>.
- [27] A. Turco, C. Malitesta, G. Barillaro, A. Greco, A. Maffezzoli, E. Mazzotta, A magnetic and highly reusable macroporous superhydrophobic/superoleophilic PDMS/MWNT nanocomposite for oil sorption from water, *J. Mater. Chem. A* 3 (2015) 17685–17696, <https://doi.org/10.1039/c5ta04353k>.
- [28] S. Wang, Z. Wen, S. Shi, W. Hou, Preparation and oil absorption performance of polyacrylonitrile/reduced graphene oxide composite porous material, *J. Water Process Eng.* 41 (2021), 102092, <https://doi.org/10.1016/j.jwpe.2021.102092>.
- [29] I. Yan, G. Ozan Aydin, H. Bulbul Sommez, Cross-linked poly(tetrahydrofuran) as promising sorbent for organic solvent/oil spill, *J. Hazard. Mater.* 309 (2016) 210–218, <https://doi.org/10.1016/j.jhazmat.2016.02.014>.
- [30] P.M. Gore, M. Naebe, X. Wang, B. Kandasubramanian, Silk fibres exhibiting biodegradability & superhydrophobicity for recovery of petroleum oils from oily wastewater, *J. Hazard. Mater.* 389 (2020), <https://doi.org/10.1016/j.jhazmat.2019.121823>.
- [31] M.R. Krishnan, Y.F. Aldavvazi, E.H. Alkharash, 3D-poly(styrene-methyl methacrylate)/divinyl benzene-2D-nanosheet composite networks for organic solvents and crude oil spill cleanup, *Polym. Bull.* (2021), <https://doi.org/10.1007/s00289-021-03565-5>.
- [32] I.L. Hozier, A.S. Vaughan, S.G. Swingle, An investigation of the potential of ethylene vinyl acetate/polyethylene blends for use in recyclable high voltage cable insulation systems, *J. Mater. Sci.* 45 (2010) 2747–2759, <https://doi.org/10.1007/s10553-010-4262-5>.
- [33] S. Jiang, K. Wang, H. Zhang, Y. Ding, Q. Yu, Encapsulation of PV modules using ethylene vinyl acetate copolymer as the encapsulant, *Macromol. React. Eng.* 9 (2015) 522–529, <https://doi.org/10.1002/mren.201400065>.
- [34] T.T.H. Tran, T.T.M. Phan, V.B. Luu, N.L. Pham, Synthesis and modification of maleic anhydride-vinyl acetate copolymer by a long alkyl chain alcohol for cold flow improvers of biodiesel, *Viet. J. Sci. Technol. Eng.* 60 (2018) 3–8, [https://doi.org/10.31276/VJSTE.60\(3\).03](https://doi.org/10.31276/VJSTE.60(3).03).
- [35] P. Dutta, B. Gogoi, N.N. Dass, N. Sen Sarma, Efficient organic solvent and oil sorbent co-polyesters: poly-9-octadecylacrylate/methacrylate with 1-hexene, *React. Funct. Polym.* 73 (2013) 457–464, <https://doi.org/10.1016/j.reactfuncpolym.2012.11.017>.
- [36] C.B.B. Luna, E. da Silva Barbosa Pereira, D.D. Siqueira, E.A. dos Santos Filho, E. M. Araújo, Addition of the ethylene-vinyl acetate copolymer (EVA) with maleic anhydride (MA) and dicumyl peroxide (DCP): the impact of styrene monomer on cross-linking and functionalization, *Polym. Bull.* (2021), <https://doi.org/10.1007/s00289-021-03856-x>.
- [37] T. Hoang, N.T. Chinh, N.T.T. Trang, T.T.X. Hang, D.T.M. Thanh, D.V. Hung, C. S. Ha, M. Aufray, Effects of maleic anhydride grafted ethylene/vinyl acetate copolymer (EVA) on the properties of EVA/silica nanocomposites, *Macromol. Res.* 21 (2013) 1210–1217, <https://doi.org/10.1007/s13233-013-1157-8>.
- [38] J. Gu, Y. Bai, L. Zhang, L. Deng, C. Zhang, Y. Sun, H. Chen, VTOS cross-linked PDMS membranes for recovery of ethanol from aqueous solution by pervaporation, *Int. J. Polym. Sci.* 2013 (2013), <https://doi.org/10.1155/2013/529474>.



Removal of oils and organic solvents from wastewater through swelling of porous crosslinked poly(ethylene-co-vinyl acetate): Preparation of adsorbent and their oil removal efficiency

Riku Dutta^a, Kankana Baruah^b, Sibani Dhar^b, Asfi Ahmed^b, Nipu Dutta^b, Simanta Doley^c, Pitambar Sedai^d, S.K. Dolui^{b,*}, B.C. Ray^a, Bholanath Karmakar^a

^a Jadavpur University, Jadavpur, Kolkata, West Bengal 700032, India

^b Tezpur University, Napaam, Tezpur, Assam 784028, India

^c Jengraimukh College, Jengraimukh, Majuli, Assam 785105, India

^d Lokanayak Omro Kumar Das College, Dhekiajuli, Assam 784110, India

ARTICLE INFO

Keywords:

Poly (ethylene-co-vinyl acetate)

Crosslinked

Leaching

Porosity

Absorption

Recycle

ABSTRACT

In this novel study, an attempt has been made to prepare porous crosslinked poly(ethylene-co-vinyl acetate) polymer (C-EVA). The porous C-EVA was prepared by grafting of maleic anhydride and cetyl alcohol onto the polymer backbone with addition of NaCl as porogen in the brabender mixture at 120 °C and 80 rpm. This was followed by leaching of NaCl with water extraction to generate a highly porous polymer structure which was evident from its SEM micrographs. The polymer was found to have excellent swelling capacity in various oils and organic solvents and showed good selective absorption capacity. The reusability of the synthesized polymer was studied and it was found that it could be reused for more than 30 absorption-desorption cycles without undergoing much change in its absorption capacity. The cross-linked polymeric composite was further characterized by FTIR, TGA, XRD, and SEM.

1. Introduction

Poly(ethylene-co-vinyl acetate) or EVA is a thermoplastic copolymer of ethylene and vinyl acetate. Depending on the ethylene and vinyl acetate (VA) content this polymer exhibits different properties like melting point, crystallinity, stiffness and polarity. A wide number of literatures is available on the use of EVA as a drug delivery substance. These include drug delivery in cervical cancer (Kalachandra et al., 2006) oral delivery of antifungal and anti-microbial (Lin et al., 2003), controlled release of dopamine (Bibbiani et al., 2005), delivery of levodopa for a continuous extended period (Sabel et al., 1990) among various other chemicals used in pharmaceutical Science. The most common industrial processing technique which is used for the synthesis of various EVA-based products is the hot-melt extrusion process which is a combination of melting, blending, and shaping and also a solvent free process that is compatible with various polymeric applications (Almeida et al., 2011, 2012).

EVA has been widely used as an encapsulating material because of its superior properties like high transmission value, good toughness at low temperature, UV resistance, and high volume resistivity (Jiang et al.,

2015). Kdampafitis and Richards (2011) have reported that luminescent material added to the EVA layer as encapsulating material resulted in improving the efficiency of silicon solar cell. Yuwawech et al. (2015) modified EVA encapsulating film using esterified bacterial cellulose nanofibers and observed the increase of mechanical, as well as barrier properties of EVA encapsulating film. Even various studies have also been conducted to investigate the causes and effects of EVA encapsulation degrading behavior in U-V radiations (Oliveira et al., 2018).

EVA has also been used to develop microcellular foams blended with polybutadiene rubber (BR) for footwear applications having higher tensile strength, wear and tear properties with low hardness (Maiti et al., 2012). Bahattab et al. (2010) have also reported the synthesis of cross-linked EVA/LDPE/metal hydroxide composites for wire and cable application because of higher mechanical and other physical properties with easier processing. Bidsorkhi et al. (2015) prepared EVA nanocomposites where halloysite nanotubes (HNT) are dispersed in the EVA matrix and found that as the HNT concentration increases the tensile strength of the EVA nanocomposites also gets increased.

Here in this work, we have investigated the potential of EVA

* Corresponding author at: Dept. of Chemical Sciences, Tezpur University, Napaam, Tezpur, 784028, Assam, India.

E-mail address: dolui@tezu.ernet.in (S.K. Dolui).

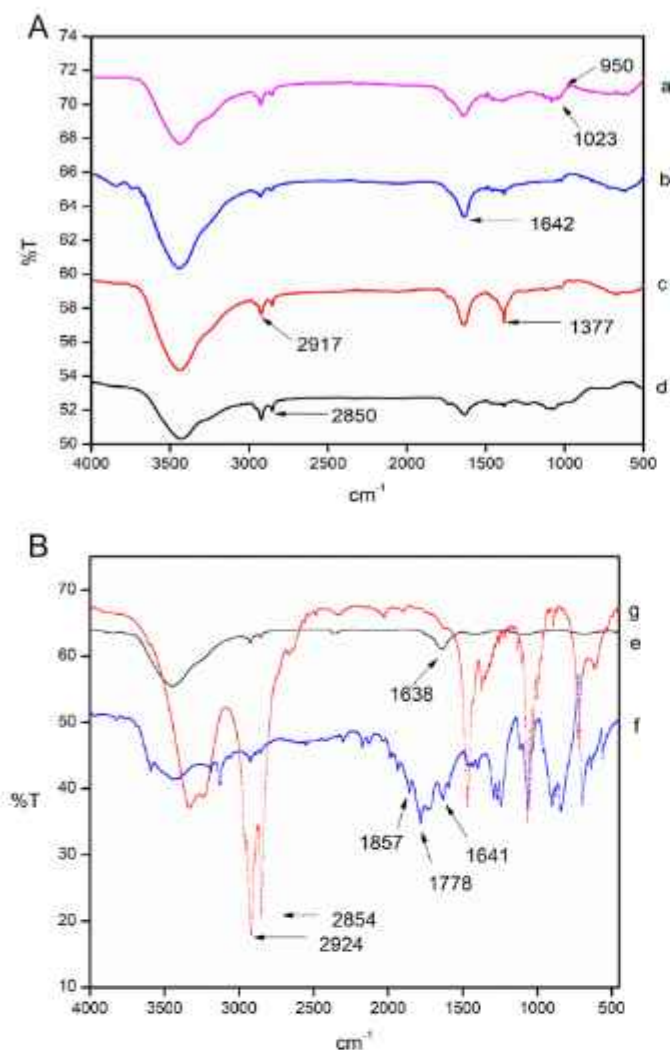


Fig. 1. (A): FT-IR spectra of a) EVAM, b) EVAMN5, c) EVAMN10 and d) EVAMN15. (B): FT-IR spectra of e) EVA, f) maleic anhydride (MA) and g) cetyl alcohol (CA).

composites in environmental applications like water treatment and oil spill removal and studied its absorbing capacity in various oils and organic solvents in detail. In our previous studies, we have noticed considerable oil/organic solvent absorption efficiency of EVA (Dutta et al., 2022).

Removal of oil and organic solvents from wastewater has gained immense attention in the recent times owing to its non-biodegradable properties and detrimental effect on human health, as well as aquatic flora and fauna (Mishra et al., 2022). The source of this wastewater is basically from hydrocarbon drilling, textile, paper, and pulp industries, etc. where water is produced as an effluent. Although three approaches namely physical, chemical and biological have been widely used in the removal of these contaminants from wastewater, owing to certain technical as well as economic drawbacks these approaches have become stagnant, and the use of polymeric composites as oil absorbents has gained wide popularity during recent times. Some of the most promising polymeric composites which are being widely used all over the world as oil absorbents are based on polyurethane (Li et al., 2012), poly(alkoxysilane)s (Ozan Aydin and Bulbul Sonmez, 2015), polypropylene (Li and Wei, 2012), polymethacrylate (Tang et al., 2020), and polystyrene (Lin et al., 2012).

In this work, we have attempted to increase the porosity of C-EVA by adding sodium chloride (NaCl) into the polymer network as porogen and

followed by leaching out of NaCl from the polymer matrix by water extraction. This will influence the porosity of polymer matrix. Although the use of NaCl as porogens to increase the porosity of scaffolds in tissue engineering has been widely studied but to the best of our knowledge, there is no report on studies relating to the use of NaCl porogens in oil absorbing polymers to increase its oil-absorbing efficiencies in various oils and organic solvents. Tran et al. (2011) developed an effective facile method to improve the control on the NaCl size distribution ($13.78 \pm 1.18 \mu\text{m}$) from the traditional method having size ($13.89 \pm 12.49 \mu\text{m}$) and fabricated scaffolds with improved interconnectivity and micro-channels. Kang et al. (2021) studied the effect of NaCl particles in AZ91 alloy foams and found that the addition of NaCl resulted in an increase in pore structure providing excellent compressive strength to A91 foams. Yu et al. (2008) studied the effect of variant pore sizes and porosity created by the different particle sizes of NaCl porogens on the mechanical properties and microstructure of poly- ϵ -caprolactone-hydroxyapatite composites and concluded that the use of varied particle size of porogens in HA-PCL scaffolds results in altered porous features and mechanical properties. Xia et al. (Xia et al., 2011) had studied the effect of NaCl porogens on the pore structure of silk fibroin (SF)/hydroapatite (HA) composites and results from this study indicated that the increase in NaCl content, particle size distribution, and particle size of NaCl porogens have significant improvement in pore connectivity and mechanical properties of the synthesized composite.

2. Materials and methods

Poly(ethylene-co-vinyl acetate) (18 % vinyl acetate content, melt index 15.06 g/10 min, and molecular weight 142,849 Da) used in this work was supplied by Max Speciality Films Limited. For cross-linking of poly(ethylene-co-vinyl acetate), benzoyl peroxide (BP) obtained from G. S. chemical testing lab and allied industries, Maleic Anhydride (MA) obtained from Merck and cetyl alcohol (CA) supplied by Loba Chemie Pvt. Ltd. was used. Sodium chloride (NaCl) 99 % pure was obtained from Merck. Various solvents (toluene, dichloromethane, chloroform, dimethyl formamide, dimethyl sulphoxide) used in the absorption study were supplied by Merck. Kerosene and gasoline were locally collected whereas crude oil was collected from GGS, ONGC.

2.1. Preparation of crosslinked EVA polymers

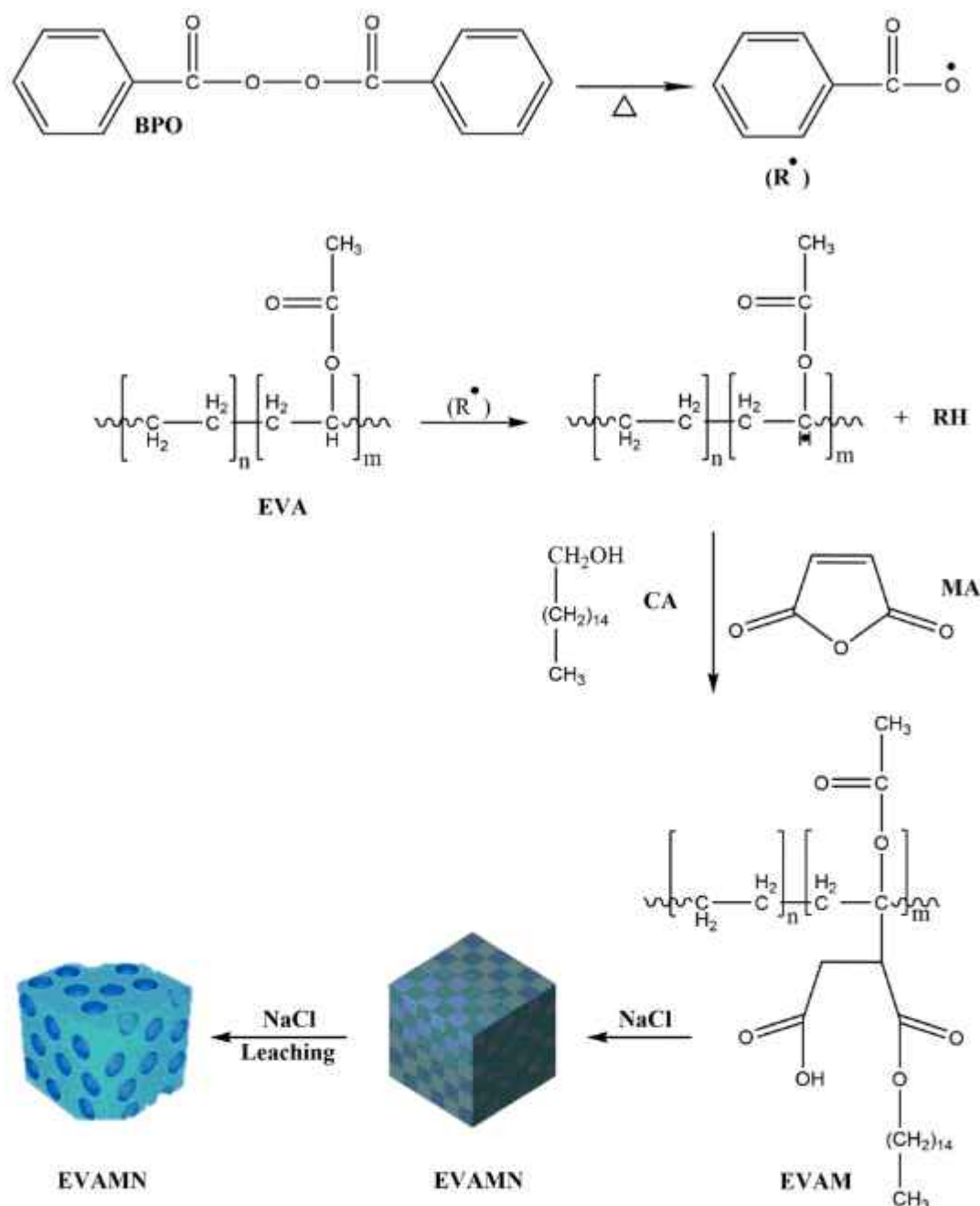
40 g of EVA, 1.2 g of MA, 2 g of BP, 2.4 g of CA and different content of NaCl (2.5–3 μm) (5, 10, 15 %) were measured in an electronic balance. Sodium chloride (99 % pure) was finely grounded in a mortar and pestle. Four different samples (EVAM, EVAMN5, EVAMN10, and EVAMN15) were then prepared using 0, 5, 10, and 15 % NaCl respectively by melt mixing in a Brabender plasticorder. This blending process was carried out at 50 rpm for 10 min at a temperature of 120 °C. The as prepared samples were then cured for 24 h at 100 °C in a hot air oven. Finally, the samples were stored in a desiccator to protect them from moisture.

2.2. Leaching of NaCl from the prepared polymer

The process of leaching NaCl from the polymers was carried out at a temperature of 50 °C. About 80 ml of distilled water was taken in a beaker and the samples were then stirred in the beaker using a magnetic stirrer at 250 rpm for 4 h. The samples were then dried in a hot air oven at a temperature of 70 °C for about an hour to eliminate all the moisture from their surface and again transferred to the desiccator until further experimental procedures.

2.3. Porosity measurement

To measure the porosity of the leached polymer samples, the liquid displacement technique was used. In this process a known volume of



Scheme 1. Plausible mechanism for grafting of MA and CA on EVA and pore formation after NaCl leaching

water (V_1) was taken in a measuring cylinder and the sample was immersed in water for 24 h. The volume rise of water was observed and the total volume of the water along with the sample in the cylinder was measured (V_2). The volume of the liquid in the cylinder after withdrawing the sample from the cylinder was taken as V_3 . Three test results were obtained for each sample and average porosity was evaluated from them. The porosity of the samples can be evaluated from the equation,

$$\text{Porosity} = \frac{V_1 - V_3}{V_2 - V_3} \times 100\%$$

2.4. Absorption studies in oils/organic solvents

ASTMF726-99-Standard Test Method was used to study the absorption behavior of the polymer samples. In this method the prepared polymeric samples were immersed in various organic solvents viz.

toluene, dichloromethane (DCM), chloroform, dimethyl formamide (DMF), dimethylsulphoxide (DMSO) and oils like kerosene, gasoline and crude oil taken in different beakers. The dry weight of the samples (W_i) were measured prior to immersing the samples in the beakers. After an interval of 2 h, the swelled samples were taken out from the beaker, held undisturbed for 10 s to drain off any liquid which had adhered on its surface and then weighed (W_t) in a precision electronic balance. This process was repeated after 4, 8, 12 and 24 h. The absorption capacity of the samples was measured using Eq. (1)

$$\text{Oil absorption (g/g)} = \frac{W_t - W_i}{W_i} \quad (1)$$

where W_t is the weight in grams of the immersed samples at a measured time interval (t).

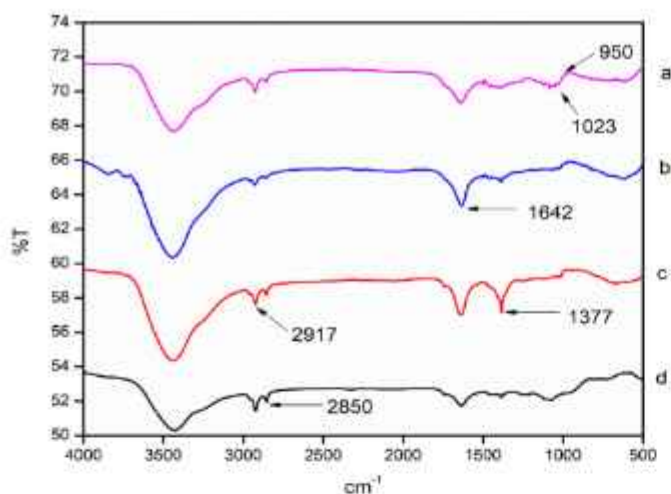
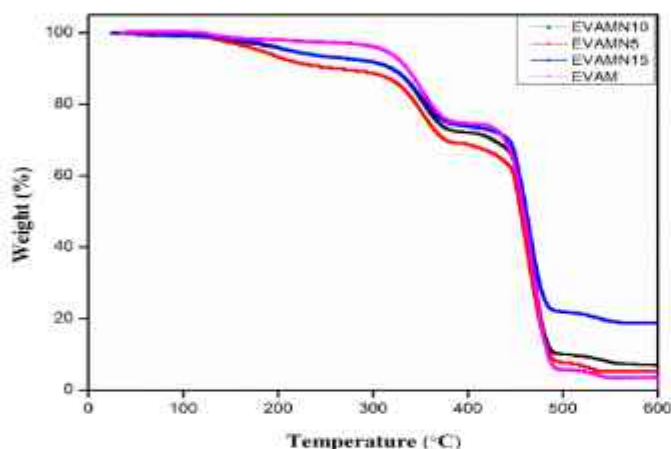
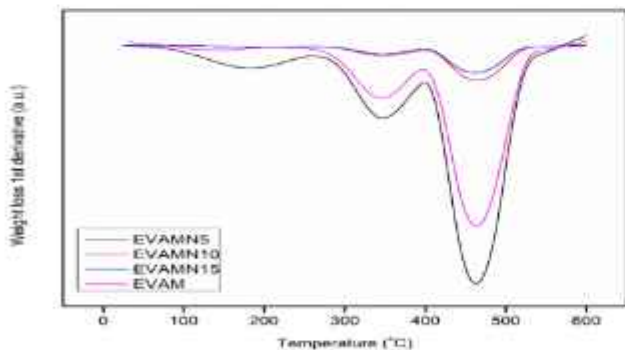


Fig. 2. XRD spectra of a) EVAM, b) EVAMN5, c) EVAMN10 and d) EVAMN15.



(a)



(b)

Fig. 3. (a) TGA thermogram of EVAM, EVAMN5, EVAMN10 and EVAMN15, (b) DTG curves of EVAM, EVAMN5, EVAMN10 and EVAMN15.

2.5. Study on recyclability

Recyclability of the polymer was tested by the absorption-desorption process. The sample with the best absorption performance from the previous absorption study was evaluated for its recyclability. EVA polymer was immersed in Toluene and the weight of the swelled sample

was taken after 24 h as it reaches its maximum absorption. The sample was then heated at 50 °C for 1 h to allow the absorbed toluene to escape the polymer lattice. This absorption-desorption process was repeated more than 30 times.

2.6. Kinetic study

For the kinetic study, the absorption capacities of the polymer samples were plotted as a function of time (Dutta et al., 2013; Yati et al., 2016). The samples were immersed in different oils and organic solvents and allowed to swell. The swelled samples were then weighed (W_t) at regular intervals i.e. 20, 40, 60, 80, ... min. Eq. (2) represents the first order absorption kinetics:

$$\frac{dW_t}{dt} = K(W_\infty - W_t) \quad (2)$$

where W_t is the weight of the sample after absorption at time t , and W_∞ is the weight of the sample after absorption reaches equilibrium.

Integrating Eq. (2), we get,

$$\ln W_\infty / (W_\infty - W_t) = Kt \quad (3)$$

If the graph obtained by plotting $\ln W_\infty / (W_\infty - W_t)$ vs t represents a straight line the absorption follows first-order kinetics.

Eq. (4) represents the second order absorption kinetics:

$$\frac{dW_t}{dt} = K(W_\infty - W_t)^2 \quad (4)$$

Integrating Eq. (4), we get,

$$\frac{t}{W_t} = \frac{1}{KW_\infty^2} + \frac{1}{W_\infty}t \quad (5)$$

If the graph obtained by plotting t/W_t vs t is a straight line, the absorption follows second-order kinetics.

2.7. Characterization

Fourier transform infrared spectroscopy (FTIR) instrument (PerkinElmer, Frontier MIR-FIR) with a scanning range of 400–4000 cm^{-1} was used for the IR study of EVAM, EVAMN5, EVAMN10, and EVAMN15 samples. X-ray diffractometer (Bruker Axis, Germany, Scanning rate-10 min^{-1}) with angle varying from 70 to 500 was used to investigate the X-ray diffraction (XRD) pattern of the polymer samples. Thermogravimetric Analysis (TGA) instrument (TGA-50, Shimadzu, Japan) was used to conduct the thermal study of the prepared polymers. The hydrophobicity of the samples was determined in a Contact angle goniometer (Kyowa, DMs401) setup. A scanning electron microscope (SEM) (JEOL, JSM Model 6390 LV) elucidated the surface morphology of the porous polymer framework. The hardness of the prepared polymers were measured using ASTM-D-2240 by means of a durometer of RR12 model measured in units of shore D hardness. The pore size was evaluated from the SEM micrographs using g ImageJ (NIH) software. The results obtained are expressed as the average of three trials with standard deviation.

3. Results and discussion

3.1. FTIR study

From the FTIR study (Fig. 1) it is clearly visible that the stretched deformation of C–H bond in CH_3 and CH_2 appears clearly at a wavelength of 2917 cm^{-1} and 2850 cm^{-1} (Luna et al., 2021). The absorption peak at 1642 cm^{-1} represents the C=C characteristic peak. A typical absorption peak of methylene group due to CH_2 deformation is observed at 1377 cm^{-1} (Tran et al., 2018). A band at 1023 cm^{-1} represents the C–O–C symmetric group of acetate (Luna et al., 2021). The presence of

Table 1
Thermal analysis of EVAM, EVAMN5, EVAMN10, and EVAMN15.

Sample	T _i	T _m ^a	T _m ^b	T _{0.05}	T _{0.5}	T _D (°C) at different weight loss (%)				RW % at 600 °C
						20 %	40 %	60 %	80 %	
EVAM	332	347	466	309	458	364	456	465	473	3.35
EVAMN5	330	348	464	180	456	344	450	464	477	5.07
EVAMN10	328	348	464	210	458	354	456	465	473	6.79
EVAMN15	312	392	458	210	456	320	456	465	473	19

^a Maximum pyrolysis 1st step.

^b Maximum pyrolysis 2nd step.

Table 2
Contact angles of the synthesized polymers.

Absorbent	Contact angle (°)
EVAM	123°
EVAMN5	97.66°
EVAMN10	90.50°
EVAMN15 (before soxhlet extraction)	101.25°
EVAMN15 (after soxhlet extraction)	90.38°

vinyl acetate is also confirmed by the presence of characteristic band of C–H at 950 cm⁻¹ (Tran et al., 2016). The characteristic C=O bands of MA at 1857 cm⁻¹ and 1778 cm⁻¹ disappeared in the FTIR curves due to the ring-opening reaction of maleic anhydride with the –OH group of cetyl alcohol which clearly confirms the formation of the polymer (Scheme 1).

3.2. X-ray diffraction

The XRD pattern of EVAM, EVAMN5, EVAMN10, and EVAMN15 are depicted in the Fig. 2. XRD peaks at 21.06° 2θ (110 plane) and 23.56° 2θ (200 plane) are visible for EVAM which corresponds to the crystalline and amorphous regions of EVA respectively. This indicates that the crystalline behavior of EVA remains unaltered during the crosslinking process. However, with an increase in NaCl porogens, the diffraction peaks gradually disappear. This is mainly due to the occurrence of pores after the leaching out of NaCl.

3.3. Thermogravimetry (TG)

The thermal behavior of the polymer was studied by the TGA measurement and the results from the study are shown in Fig. 3. It is evident from this study that the synthesized polymer undergoes two-step degradation. The initial weight loss which is completed at about 400 °C is mainly due to the autocatalytic deacetylation in the vinyl acetate fraction (Hoang et al., 2013). The second weight loss which is observed between 404 °C and 491 °C corresponds to the completion of the chain scission of the residual polyethylene main chain. The thermal stability of all the crosslinked EVA is similar. The value for T_{0.05} for all the composites was found to be above 200 °C, however, T_{0.05} in the case of EVAMN5 was observed at around 180 °C (Fig. 3b) which may be due to the elimination of moisture from the composite. Temperature exhibiting 50 % mass loss (T_{0.5}) for all the polymers remains almost similar as evident from the TGA curves. It is observed that considerable residual weight is left out after 600 °C. EVAMN15 having a higher percentage of NaCl shows the highest residual weight (19 %). This is due to incomplete leaching of NaCl from the crosslinked polymer (Chen et al., 2015).

The initial degradation temperature (T_i), maximum degradation temperature (T_m), different weight loss temperature (T_D), and residual weight at 600 °C for the polymers are tabulated in Table 1.

3.4. Contact angle measurement

The effect of NaCl concentration on the wetting characteristics of the polymers was determined by measuring the contact angles which are presented in Table 2. Although the synthesized polymers show hydrophobic nature, however it was observed from the contact angle measurement that as the NaCl porogen concentration was increased there was a decline in the contact angle. This could be attributed to the fact that with the addition of NaCl, larger pores are formed on the polymer surface which allows liquid drops to diffuse through them, thus elevating the wetting characteristics of the polymer (Vazirnejad et al., 2016). EVAMN15 shows a higher contact angle which may be due to agglomerations at a higher NaCl concentration. But however, after Soxhlet extraction from the sample, the contact angle of EVAMN15 was found to be 90.38° (Fig. 4).

3.5. Scanning electron microscopy (SEM) study

The fractured surface of the polymer blends was studied under SEM to evaluate its pore size, shape, and pore distribution. The surface morphology of EVAM, EVAMN5, EVAMN10, and EVAMN15 is shown in Fig. 5. In the SEM images, significant pores are visible which are formed as the NaCl particles are pulled out from the polymer matrix by leaching. This indicates a weak interfacial affinity between NaCl and the polymer network. The pore size increases from 107 μm in EVAMN5 to 136 μm in EVAMN10 as the porogen concentration increases. However, it has been evident from the SEM image (c) that with the increase in NaCl content (EVAMN15) porosity of the polymer decreases as the NaCl particles remain entrapped in the polymer matrix even after leaching (Chen et al., 2014).

3.6. Porosity measurement

The porosity of the synthesized samples was obtained by the liquid displacement method and tabulated in Table 3. The results clearly show that as the porogen concentration increases from 5 % to 10 % there is a simultaneous increase in the porosity of the polymer samples. But, with further increase in concentration (EVAMN15), the porosity decreases due to similar reasons already stated in the SEM morphology study. However, after soxhlet extraction from the sample, the porosity of EVAMN15 further increases as shown in Table 3.

3.7. Absorption studies in oils/organic solvents

The polymers show excellent oil absorption capacity and equilibrium is obtained after 24 h of exposure in various oils and organic solvents. Molecules of toluene, chloroform, and DCM being smaller get penetrated in the pores readily and thus show excellent affinity towards the polymers. On the other hand, due to the presence of long aliphatic chain (from cetyl alcohol), these polymers also allow long chain oils like gasoline, kerosene and crude oil to be adsorbed on its surface thus showing good oil absorption capacity. However, solvents like DMF and DMSO show very weak affinity towards the polymers because of their polar nature. The absorption capacity of the polymers in various oils and

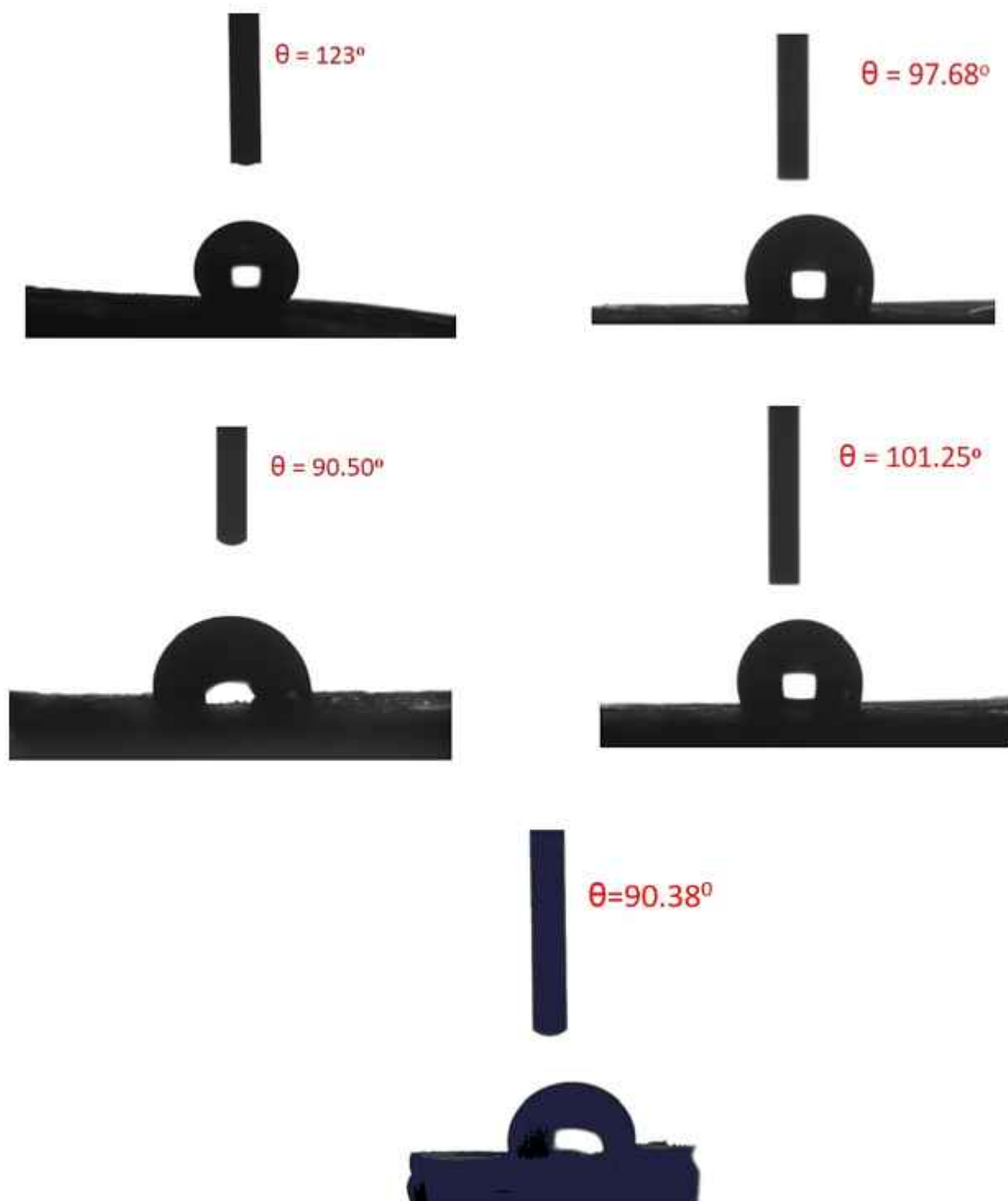


Fig. 4. Contact angle measurements of a) EVAM, b) EVAMN5, c) EVAMN10, d) EVAMN15 before Soxhlet extraction and e) EVAMN15 after Soxhlet extraction.

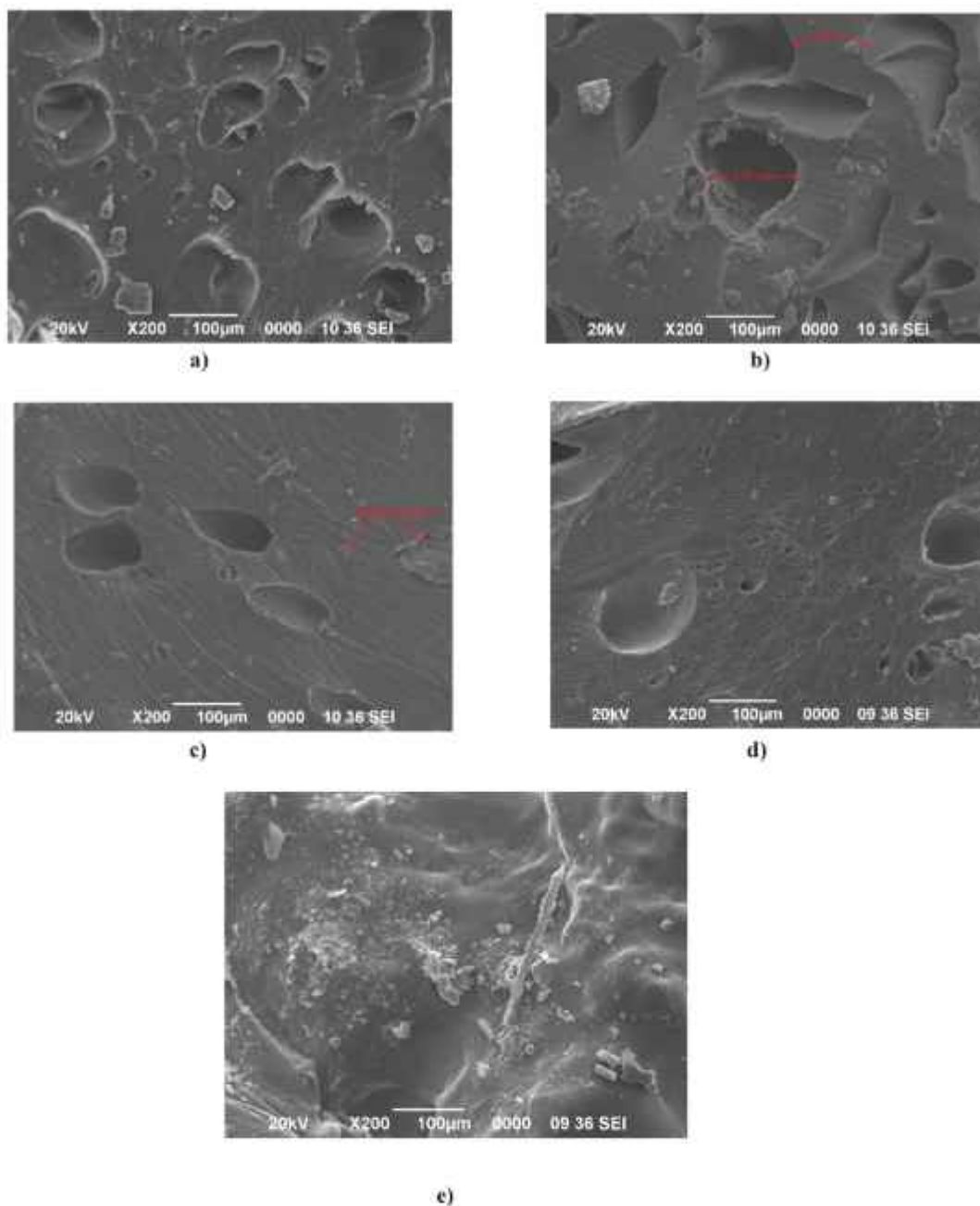


Fig. 5. SEM micrographs of a) EVAMN5, b) EVAMN10, c) EVAMN15, d) EVAM and e) EVAMN10 after reusability study.

Table 3
Pore diameter and measured porosity of the polymer samples.

Sample code	Pore diameter	Porosity (%)
EVAM	89 ± 16 μm	27.27 ± 1.6
EVAMN5	107 ± 10 μm	33.33 ± 1.4
EVAMN10	136 ± 12 μm	42.85 ± 1.2
EVAMN15 (before Soxhlet extraction)	82 ± 10 μm	11.11 ± 1.3
EVAMN15 (after Soxhlet extraction)	82 ± 10 μm	32.47 ± 1.6

organic solvents is shown in Fig. 6. It is evident from the absorption study that EVAMN10 shows the maximum absorption in toluene (27.39 g/g) followed by gasoline (20.26 g/g) and chloroform (16.15 g/g). It could also be observed that EVAMN10 shows excellent absorption capacity in various oils and organic solvents in comparison to the other synthesized polymers. This is mainly because as the NaCl content

increases larger pores and porosity is obtained after leaching which is evident from the SEM micrographs. However, EVAMN15 with 15 % NaCl content rather shows decreased absorption capacity. This may be attributed to the fact that as the porogen (NaCl) content increases, during the adsorption process the ions get closely packed onto the inner wall of the pores which results in reducing the total pore volume (Liu et al., 2016). Also because of the high content of NaCl, the NaCl particles gets agglomerated and gets entrapped in the pore spaces which results in a decrease in the porosity of the polymers (Chen et al., 2014).

3.6. Effect of curing time on absorption

To evaluate the effect of curing time on the absorption capacity, the polymers were post cured for 1 h, 4 h, 6 h, 12 h and 24 h after synthesis. Fig. 7 shows the relationship between time of curing and absorption capacity of EVAM in toluene and gasoline. It was found that as the curing

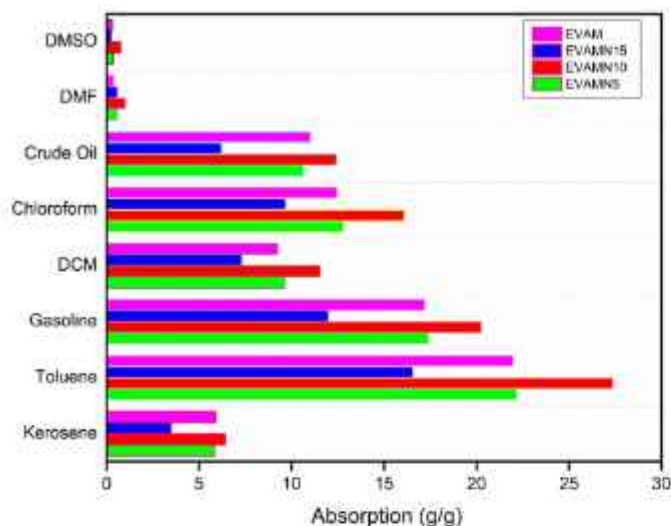


Fig. 6. Absorption capacities of the synthesized polymers.

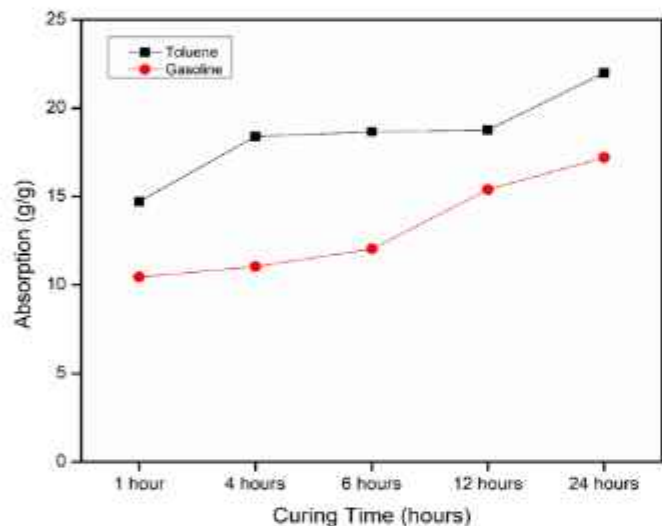


Fig. 7. Curing time vs absorption curves of EVAM in toluene and gasoline.

time is increased the absorption capacity also increases. EVAM showed the best absorption at 24 h curing. Allowing higher time for curing results in more amount of crosslinking in the polymeric chain which increases its stability. On the other hand with shorter time for curing, the polymers do not crosslink sufficiently and remains stable for about 6 h when submerged in various oils and organic solvents. But eventually loss in weight occurs and thus decreasing its absorption capacity (Fig. 8). Similar findings were also observed in case of EVAMN5, EVAMN10 and EVAMN15.

3.9. Hardness test

The hardness characteristics of the crosslinked polymers were measured using a durameter. It was observed that hardness was maximum in EVAM (16 shore D) due to their cross-linked structure. However, it decreases in EVAMN5 (13 shore D) and EVAMN10 (12 shore D) as porosity increases after porogen (NaCl) leaching. Hardness in case of EVAMN15 (14 shore D) has increased slightly due to agglomeration of NaCl particles and decrease in pore volume.

3.10. Recyclability

Fig. 9 represents the reusability nature of the polymers. It was observed that the absorption capacity of the polymer remains unchanged even after 15 absorption-desorption cycles. However, the absorption efficiency gradually declines from the 15th cycle and it reduces

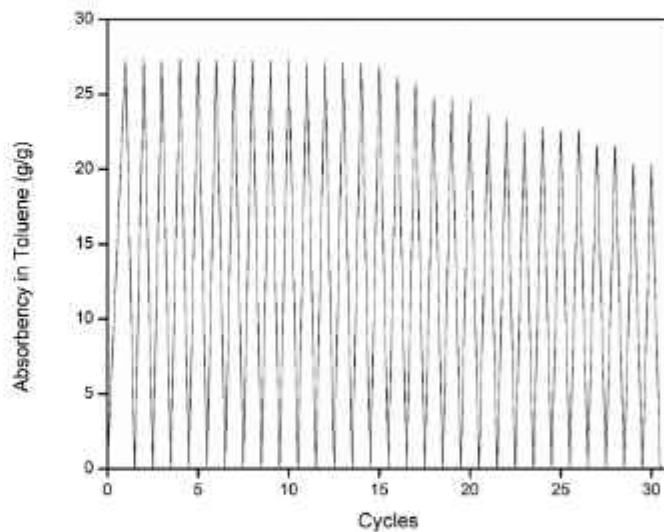
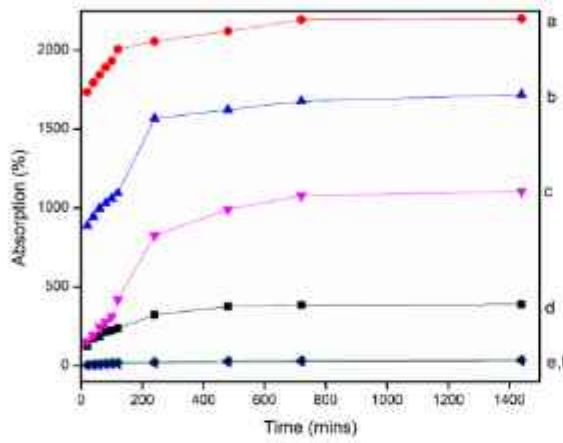


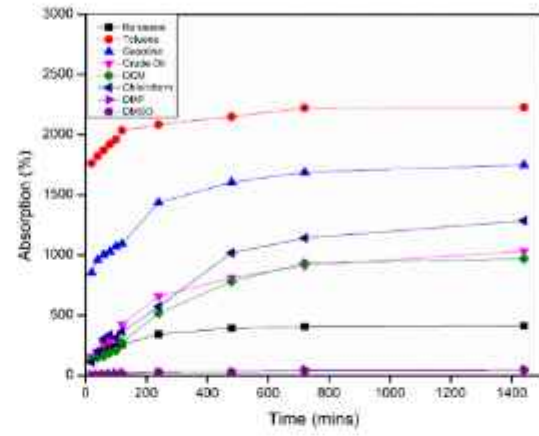
Fig. 9. Reusability of EVAMN10 for various absorption-desorption cycles.



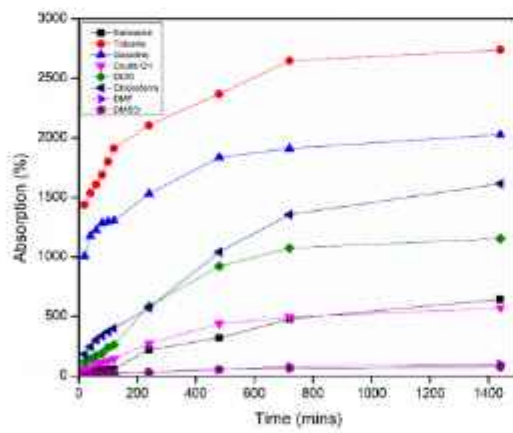
Fig. 8. Images of EVAM samples after 24 h absorption a) curing 1 h, b) curing 4 h and c) curing 24 h.



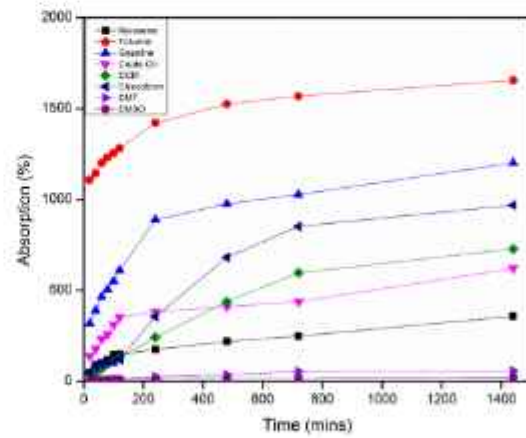
a)



b)



c)



d)

Fig. 10. Absorption kinetics for a) EVAM, b) EVAMN5, c) EVAMN10 and d) EVAMN15.

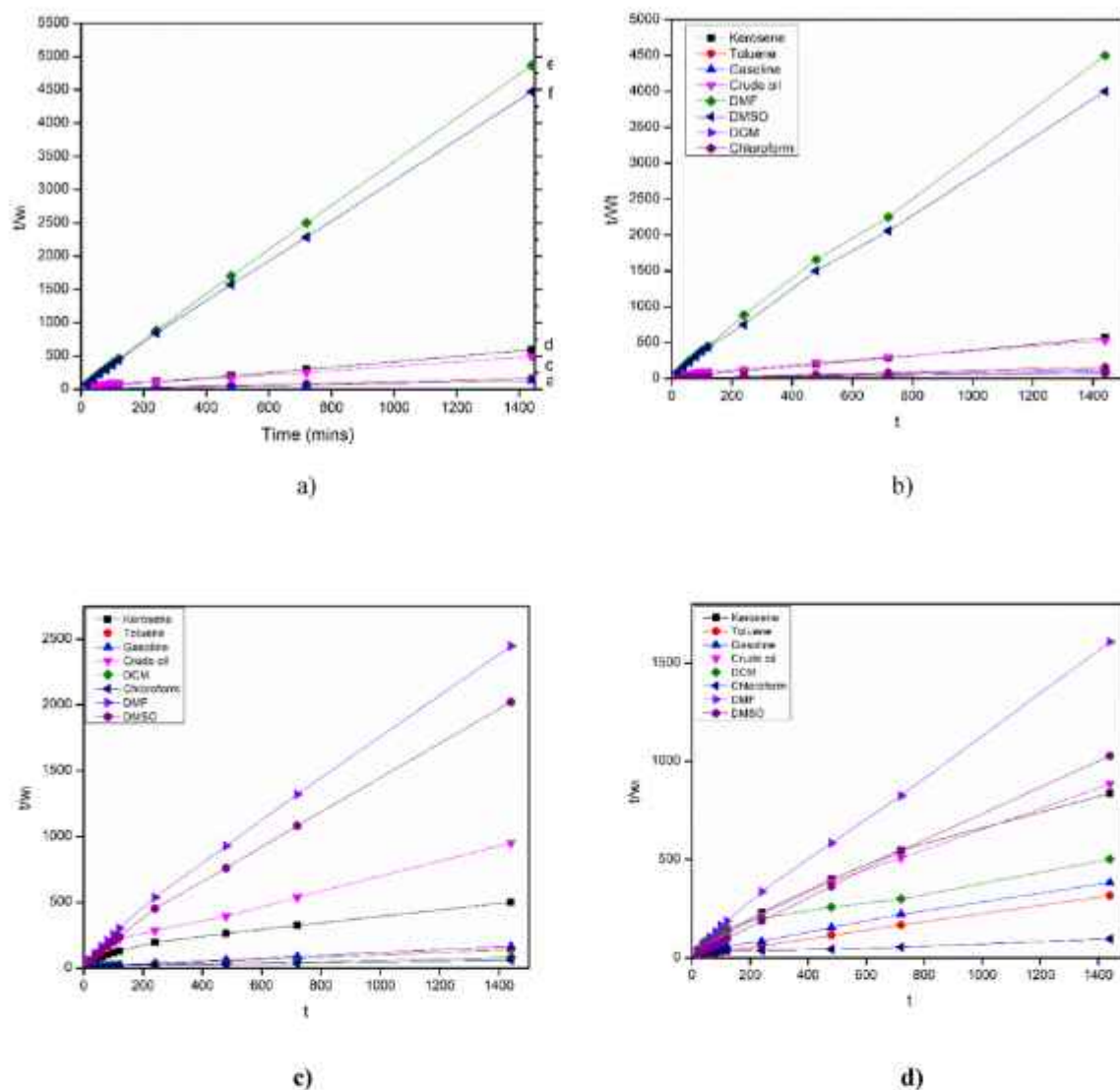


Fig. 11. Pseudo-second-order absorption kinetics for a) EVAM, b) EVAMN5, c) EVAMN10 and d) EVAMN15.

by 24 % at the end of the 30th cycle which may be the result of a decrease in porosity due to continuous absorption and thermal desorption process as revealed from the SEM image (Fig. 5c). Thus, it can be very well concluded that polymer have excellent reusability and can be recycled for more than 30 absorption-desorption cycles.

3.11. Absorption kinetics

To elucidate the reaction routes and mechanism the adsorption kinetics was studied on the absorption of oils and organic solvents by the prepared crosslinked polymers. The study was conducted by plotting the absorption percentage in various oils and organic solvents as a function of time. It was observed from the kinetic curves (Fig. 10) that there is a steep rise in the absorption initially but the rate gradually decreases and reaches equilibrium after 12 h. This absorption rate remains almost constant till 24 h. The absorption rate constant was determined by

plotting the experimental data in to the pseudo first order and second order equations. The experimental data fits almost perfectly in the first order kinetic equation with correlation factor (R^2) ~ 0.99 (Fig. 11) whereas it does not fit in the second order kinetics. These findings clearly suggests that the rate of reaction and the absorption process is governed by the pseudo second order kinetic equation.

3.12. Crude oil/water separation experiment

The selective removal of oil from oil-water mixture as well as stability in oils and organic solvents determines another parameter of efficiency of the polymers used in absorption application. Fig. 12 demonstrates the experiment conducted to determine such selective removal ability of our polymer EVAMN10 showing best absorption results in our study (Table 4). The polymer absorbed most of the crude oil from the water surface within 24 h. This experiment very well

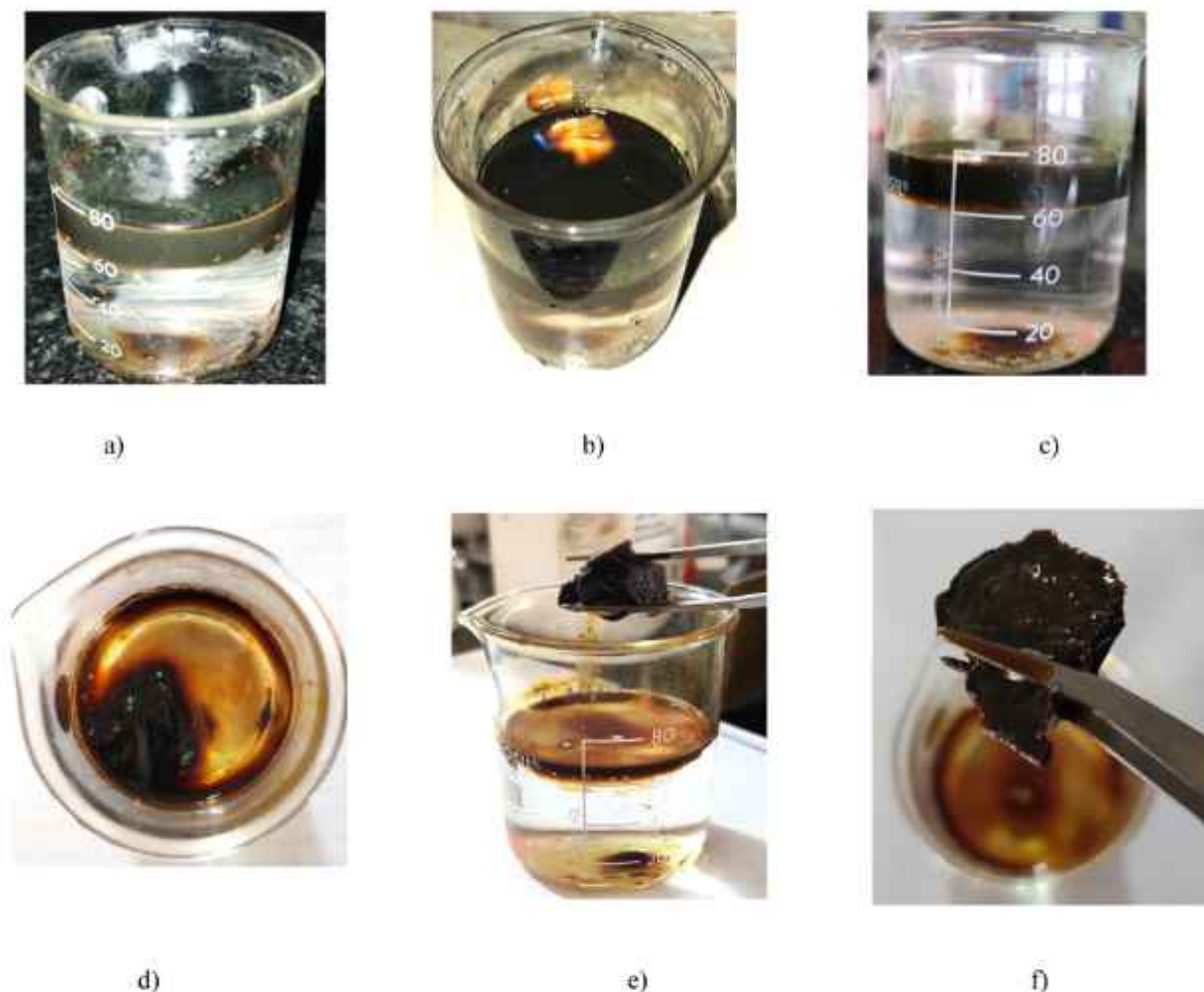


Fig. 12. Sequence of events during selective removal of crude oil from oil-water mixture.

Table 4
Pseudo-second-order parameters for EVAMN10.

Oil/organic solvent	Rate constant (K_2)	Correlation coefficients (R^2)
Toluene	0.00196	0.99773
Gasoline	0.00231	0.99805
Crude oil	0.00310	0.99774
Kerosene	0.00130	0.99046
DCM	0.00017	0.96150
Chloroform	0.00013	0.96817
DMF	0.03411	0.99707
DMSO	0.03411	0.99707

demonstrates the efficiency of the grafted polymer in cleaning natural oil spills and water treatment operations.

4. Conclusion

Poly(ethylene-co-vinyl acetate) (EVA) was successfully crosslinked using maleic anhydride and cetyl alcohol to prepare a polymer composite with increased strength and stability. The NaCl leaching technique was successfully utilized to increase the pore content and porosity of the polymer. SEM images confirmed the formation of large pores on the polymer morphology. It was observed that with the increase of NaCl content from 5 % to 10 % although a porous framework was obtained however the thermal properties, wetting characteristics and hardness of the polymer declines. But, with further increase in the porogen content

these properties shows an increasing trend but the porosity of the polymer decreases. The oil absorption test reveals that the polymer has excellent absorption capacity in various oils and organic solvents with absorption capacity in toluene as high as 27.39 g/g. Thus it can be concluded that this EVA polymer has immense potential to be used in advanced fields of environmental operations like natural oil spill clean up and waste water treatment.

This research did not receive any specific grant from funding agencies in the public, commercial, or not-for-profit sectors.

CRediT authorship contribution statement

Riku Dutta: Conceptualization, Methodology, Formal analysis, Investigation, Writing- original draft preparation, Visualization. Kanakana Baruah: Formal analysis, Data curation, Writing- reviewing and editing. Sibani Dhar: Writing- reviewing and editing. Asfi Ahmed: Writing- reviewing and editing. Nipu Dutta: Resources, Project administration. Simanta Doley: Writing- reviewing and editing. Pitambar Sedai: Resources. S.K Dolui: Formal analysis, Data curation, Resources, Writing- reviewing and editing. B.C Ray: Validation, Supervision. Bholanath Karmakar: Resources, Writing- reviewing and editing.

Declaration of competing interest

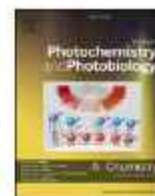
The authors declare that they have no known competing financial interests or personal relationships that could have appeared to influence the work reported in this paper.

Data availability

Data will be made available on request.

References

- Almeida, A., Claeys, B., Remon, J.P., Vervaet, C., 2012. 3 Hot-melt Extrusion Developments in the Pharmaceutical Industry.
- Almeida, A., Possemiers, S., Boone, M.N., de Beer, T., Quinten, T., van Hoorebeke, L., Remon, J.P., Vervaet, C., 2011. Ethylene vinyl acetate as matrix for oral sustained release dosage forms produced via hot-melt extrusion. *Eur. J. Pharm. Biopharm.* 77, 297–305. <https://doi.org/10.1016/j.ejpb.2010.12.004>.
- Bahatab, M.A., Moznicek, J., Basfar, A.A., Shukri, T.M., 2010. Cross-linked poly (ethylene vinyl acetate) (EVA)/lowdensity polyethylene (LDPE)/metal hydroxides composites for wire and cable applications. *Polym. Bull.* 64, 569–580. <https://doi.org/10.1007/s00289-009-0194-0>.
- Bibbiani, F., Costantini, L.C., Patel, R., Chase, T.N., 2005. Continuous dopaminergic stimulation reduces risk of motor complications in parkinsonian primates. *Exp. Neurol.* 192, 73–78. <https://doi.org/10.1016/j.expneurol.2004.11.013>.
- Bidsovki, H.C., Adelinia, H., Heidar Pour, R., Soheilimoghaddam, M., 2015. Preparation and characterization of ethylene-vinyl acetate/halloysite nanotube nanocomposites. *J. Mater. Sci.* 50, 3237–3245. <https://doi.org/10.1007/s10853-015-8891-6>.
- Chen, B.Y., Jing, X., Mi, H.Y., Zhao, H., Zhang, W.H., Peng, X.P., Turng, L.S., 2015. Fabrication of polylactic acid/polyethylene glycol (PLA/PEG) porous scaffold by supercritical CO₂ foaming and particle leaching. *Polym. Eng. Sci.* 55, 1339–1348. <https://doi.org/10.1002/polb.24073>.
- Chen, B.-Y., Wang, Y.-S., Mi, H.-Y., Yu, P., Kuang, T.-R., Peng, X.-P., Wen, J.-S., 2014. Effect of poly(ethylene glycol) on the properties and foaming behavior of macroporous poly(lactic acid)/sodium chloride scaffold. *J. Appl. Polym. Sci.* 131. <https://doi.org/10.1002/app.41181> n/a-n/a.
- Dutta, P., Gogoi, B., Dass, N.N., Sen Sarma, N., 2013. Efficient organic solvent and oil sorbent co-polyesters: poly-9-octadecenyloctylacrylate/methacrylate with 1-hexene. *React. Funct. Polym.* 73, 457–464. <https://doi.org/10.1016/j.reactfunctpolym.2012.11.017>.
- Dutta, R., Dhar, S., Baruah, K., Dutta, N., Doley, S., Sedai, P., Dohi, S.K., Ray, B.C., Karmakar, B., 2022. Removal of organic solvents and oils from wastewater by absorption with crosslinked poly(ethylene-co-vinyl acetate) modified by cetyl alcohol. *J. Water Process Eng.* 49. <https://doi.org/10.1016/j.jwpe.2022.103073>.
- Hoang, T., Chinh, N.T., Trang, N.T.T., Hang, T.T.X., Thanh, D.T.M., Hung, D.V., Ha, C.S., Aufray, M., 2013. Effects of maleic anhydride grafted ethylene/vinyl acetate copolymer (EVA) on the properties of EVA/silica nanocomposites. *Macromol. Res.* 21, 1210–1217. <https://doi.org/10.1007/s13233-013-1157-8>.
- Jiang, S., Wang, K., Zhang, H., Ding, Y., Yu, Q., 2015. Encapsulation of PV modules using ethylene vinyl acetate copolymer as the encapsulant. *Macromol. React. Eng.* 9, 522–529. <https://doi.org/10.1002/mren.201400065>.
- Kalachandra, S., Takamata, T., Lin, D.M., et al., 2006. Stability and release of antiviral drugs from ethylene vinyl acetate (EVA) copolymer. *J. Mater. Sci.: Mater. Med.* 17, 1227–1236. <https://doi.org/10.1007/s10856-006-0596-6>.
- Kang, L., Shi, Y., Luo, X., 2021. Effects of sodium chloride on structure and compressive properties of foamed AZ91. *AIP Adv.* 11. <https://doi.org/10.1063/5.0033314>.
- Klampfuis, E., Richards, B.S., 2011. Improvement in multi-crystalline silicon solar cell efficiency via addition of luminescent material to EVA encapsulation layer. *Prog. Photovolt. Res. Appl.* 19, 345–351. <https://doi.org/10.1002/pip.1019>.
- Li, H., Liu, L., Yang, P., 2012. Hydrophobic modification of polyurethane foam for oil spill cleanup. *Mar. Pollut. Bull.* 64, 1648–1653. <https://doi.org/10.1016/j.marpolbul.2012.05.039>.
- Li, S., Wei, J., 2012. Evaluation of the influence of homopolymerization on the removal of water-insoluble organics by grafted polypropylene fibers. *Mar. Pollut. Bull.* 64, 1172–1176. <https://doi.org/10.1016/j.marpolbul.2012.03.021>.
- Lin, D.M., Kalachandra, S., Valiyaparambil, J., Offenbacher, S., 2003. A polymeric device for delivery of anti-microbial and anti-fungal drugs in the oral environment: effect of temperature and medium on the rate of drug release. *Dent. Mater.* 19, 589–596. [https://doi.org/10.1016/S0109-5641\(02\)00109-4](https://doi.org/10.1016/S0109-5641(02)00109-4).
- Lin, J., Shang, Y., Ding, B., Yang, J., Yu, J., Al-Deyab, S.S., 2012. Nanoporous polystyrene fibers for oil spill cleanup. *Mar. Pollut. Bull.* 64, 347–352. <https://doi.org/10.1016/j.marpolbul.2011.11.002>.
- Lu, H., Zhang, Q., Dong, Y., Li, J., Zhang, X., 2016. The adsorption capacity, pore structure, and thermal behavior of the modified clay containing SSA. *Adv. Mater. Sci. Eng.* 2016. <https://doi.org/10.1155/2016/9894657>.
- Luna, C.B.B., da Silva Barbosa Ferreira, E., Siqueira, D.D., dos Santos Filho, E.A., Araújo, E.M., 2021. Addition of the ethylene-vinyl acetate copolymer (EVA) with maleic anhydride (MA) and dicumyl peroxide (DCP): the impact of styrene monomer on cross-linking and functionalization. *Polym. Bull.* <https://doi.org/10.1007/s00289-021-03856-x>.
- Maiti, M., Jaisra, R.V., Rustom, S.K., Chaki, T.K., 2012. Microcellular foam from ethylene vinyl acetate/polybutadiene rubber (EVA/BR) based thermoplastic elastomers for footwear applications. *Ind. Eng. Chem. Res.* 51, 10607–10612. <https://doi.org/10.1021/ie300396m>.
- Mishra, S., Chauhan, G., Verma, S., Singh, U., 2022. The emergence of nanotechnology in mitigating petroleum oil spills. *Mar. Pollut. Bull.* 176, 113609. <https://doi.org/10.1016/j.marpolbul.2022.113609>.
- Oliveira, M.C.C.de, Diniz Cardoso, A.S.A., Viana, M.M., Lima, V.de P.C., 2018. The causes and effects of degradation of encapsulant ethylene vinyl acetate copolymer (EVA) in crystalline silicon photovoltaic modules: a review. *Renew. Sustain. Energy Rev.* <https://doi.org/10.1016/j.rser.2017.06.039>.
- Ozan Aydin, G., Bulbul Sommez, H., 2015. Hydrophobic poly(alkoxysilane) organogels as sorbent material for oil spill cleanup. *Mar. Pollut. Bull.* 96, 155–164. <https://doi.org/10.1016/j.marpolbul.2015.05.033>.
- Sabel, B.A., Dominiak, P., Häuser, W., Düring, M.J., Freese, A., 1990. Extended levodopa release from a subcutaneously implanted polymer matrix in rats. *Ann. Neurol.* 28, 714–717.
- Tang, H., Gou, Y., Yan, L., Hu, Q., Zhang, P., Xiao, Q., Zhong, Y., Zhu, W., 2020. Copolymerization of 2-(perfluorohexyl)ethyl methacrylate with divinylbenzene to fluorosorbent porous polymeric materials as fluorophilic absorbents. *Microporous Mesoporous Mater.* 305. <https://doi.org/10.1016/j.micromeso.2020.110398>.
- Iran, R.T., Nazeri, E., Kolasnikov, A., Bai, X., Yang, J., 2011. A new generation of sodium chloride porogen for tissue engineering. *Biotechnol. Appl. Biochem.* 58, 335–344. <https://doi.org/10.1002/bab.44>.
- Iran, T.T.H., Phan, T.T.M., Luu, V.B., Pham, N.L., 2016. Synthesis and modification of maleic anhydride-vinyl acetate copolymer by a long allyl chain alcohol for cold flow improvers of biodiesel. *Vietnam J. Sci. Technol. Eng.* 60, 3–8. [https://doi.org/10.31276/VJSTE.60\(3\).03](https://doi.org/10.31276/VJSTE.60(3).03).
- Vazirnejad, T., Karimi-Sabet, J., Dastbar, A., Moosavian, M.A., Ghorbanian, S.A., 2016. Application of salt additives and response surface methodology for optimization of PVDF hollow fiber membrane in DDM and AGMD processes. *J. Membr. Sci. Res.* 2, 169–178.
- Xia, Z., Luo, M., Zhang, Q., Qu, J., Li, M., 2011. Effects of addition amount, particle size distribution and average particle size of NaCl porogen on the pore connectivity of silk fibroin (SF)/hydroxyapatite (HA) porous composites. *Adv. Mater. Res.* 1904–1909. <https://doi.org/10.4028/www.scientific.net/AMR.1904.1904>.
- Yari, I., Ozan Aydin, G., Bulbul Sommez, H., 2016. Cross-linked poly(tetrahydrofuran) as promising sorbent for organic solvent/oil spill. *J. Hazard. Mater.* 309, 210–216. <https://doi.org/10.1016/j.jhazmat.2016.02.014>.
- Yu, H., Matthew, H.W., Wooley, P.H., Yang, S.Y., 2006. Effect of porosity and pore size on microstructures and mechanical properties of poly-ε-caprolactone-hydroxyapatite composites. *J. Biomed. Mater. Res. B Appl. Biomater.* 66, 541–547. <https://doi.org/10.1002/jbm.b.31054>.
- Yuwawech, K., Wootthikanokkhan, J., Tanpichai, S., 2015. Enhancement of thermal, mechanical and barrier properties of EVA solar cell encapsulating films by reinforcing with esterified cellulose nanofibres. *Polym. Test.* 46, 12–22. <https://doi.org/10.1016/j.polymtest.2015.09.007>.



A hierarchically porous MOF confined CsPbBr₃ quantum dots: Fluorescence switching probe for detecting Cu (II) and melamine in food samples

Shahnaz Ahmed^a, Suman Lahkar^a, Simanta Doley^b, Dambarudhar Mohanta^c, Swapan Kumar Dolui^{a,*}

^a Department of Chemical Sciences, Tezpur University, Napaam, Tezpur, Assam 784028, India

^b Jangraimukh College, Majuli, Assam 784028, India

^c Department of Physics, Tezpur University, Napaam, Tezpur, Assam 784028, India

ARTICLE INFO

Keywords:
CsPbBr₃/HZIF-8
Metal organic framework
Stability
Cu (II)
Melamine
Fluorescence sensor

ABSTRACT

The hypersensitivity of Perovskite quantum dots (PQDs) towards external environmental conditions and the water quenching of their fluorescence have limited their practical analytical applications. In this work highly luminescent CsPbBr₃ was confined into a hierarchically porous ZIF-8 metal organic framework (HZIF-8) through a simple two step in situ growth method. XRD, FTIR, SEM, TEM, and XPS investigations confirmed the successful synthesis of the CsPbBr₃/HZIF-8 nanocomposite. CsPbBr₃ PQDs are uniformly distributed within the HZIF-8 MOF matrix and exhibited intense green emission at 510 nm with a FWHM value of 25 nm in ambient conditions. The nanocomposite showed enhanced stability against moisture and UV light. The intense PL emission of the nanocomposite was well maintained in an aqueous solution also, with no noticeable change in fluorescence characteristics for 15 days of storage in aqueous solution. The CsPbBr₃/HZIF-8 composite was then utilized as an on-off-on luminescent probe for the detection of Cu²⁺ metal ions and melamine in real samples. Because of the porous nature of the MOF, the target analytes can be quickly located and this nanosensor is found to be very sensitive toward Cu²⁺ and melamine detection. A linear relationship from 3 to 500 nM and 30–1500 nM was found for melamine and Cu²⁺ under an optimal experimental condition, with a limit of detection value of around 4.66 nM and 2.64 nM for Cu²⁺ and melamine respectively.

1. Introduction

With the continued growth of the world population, the demand for food safety and environmental pollution is expected to rise, and it is quickly becoming a global concern that earns widespread attention. Simultaneously, heavy metal ion pollutants can easily accumulate in the human body. They are not only a dangerous hazard to the environment but also constitute a serious health risk to humans. Particularly, the Cu²⁺ ion, which is involved in many enzyme activities, has a considerable impact on both human health and plants. Excessive consumption of Cu²⁺ will disrupt homeostasis, leading to a number of risks including Wilson's and Alzheimer's disease, among others. Also, industrial wastewater contains Cu as heavy metal ion waste. Therefore, it is important to quantify the Cu²⁺ ions in environmental and biological systems using simple and sensitive methods [1–3].

2,4,6-triamino-1,3,5-triazine (Melamine) is a nitrogen rich organic base and an industrial raw material, generally used in the production of

melamine-formaldehyde resins for plastic and paint industries, adhesives, coatings, and fire-retardant materials, etc. However, melamine has received major attention in the aspects of food safety following a crisis concerning melamine-contaminated milk in 2008 [4]. Owing to its high nitrogen content, melamine is illegally added to dairy products, and feedstuffs to enhance the protein content and thus misguided the consumers. Cyanuric acid, the hydrolysis product of melamine, has generated a less soluble melamine cyanurate complex and eventually precipitates in the renal tubules, causing further tissue injury and urinary calculus [5]. Consuming melamine-containing food over an extended period of time at levels above the safety limit (20 μM in the USA and EU, 8 μM for infant formula in China) can possibly be fatal, especially in infants and children [6]. Therefore, it is crucial to develop an efficient detection technique for traces of melamine in the food and feed industries to prevent adulteration and protect food safety. Advanced analytical techniques such as high-performance liquid chromatography (HPLC) [7], liquid chromatography-mass spectrometry (LC-

* Corresponding author.

E-mail address: dolui@tezu.ernet.in (S. Kumar Dolui).

MS) [8], electrochemical methods [9], colorimetry [10], surface-enhanced Raman spectroscopy [11], enzyme-linked immunosorbent assays [12], Fourier transform infrared spectroscopy (FT-IR), and fluorescence spectroscopy have been used to develop potential assays for melamine detection [4]. Amongst them, the fluorimetric method provides a simple, low-cost, highly selective, and sensitive method for the successful detection of melamine. Smart fluorescent materials that can alter their physical parameters when exposed to an external stimulus have caught the attention of researchers due to their potential applications in a variety of disciplines such as sensing, anti-counterfeiting, bioimaging, etc. [13–17]. Most of the luminescent sensing applications are based on organic fluorophores and dyes, polymer nanocomposite, metal oxide nanoparticles, metal chalcogenide quantum dots, etc. [18–21]. However, these materials possess limitations including weak PL intensity, low photoluminescence quantum yield (PLQY) value, low color purity, photo bleaching, and wide emission line limiting sensitivity of detection. Thus, the introduction of a new fluorescent nanomaterial with enhanced luminescent performance remains essential.

With the emergence of nanotechnology, metal halide perovskite nano crystals (PeNCs) with very high PLQY, narrow and intense emission, tunable emission and absorption over the entire visible spectrum, long carrier lifetime have attracted massive attention, making them a promising material in lighting and display technology, photovoltaic solar cells, photodetectors, sensors along with many others [22–24]. Inorganic CsPbX₃ (X = Br, Cl, I) PeNCs with the conventional perovskite architecture have recently demonstrated great potential as chemical sensor materials [25–28] owing to their high fluorescence characteristics. But the most of the analytical applications of CsPbX₃ PeNCs are limited to non-aqueous medium, thereby hindering practical applications. The relatively low lattice formation energy and the ionic nature of perovskite crystals result in poor stability leading to a loss of PL intensity under extreme environmental conditions (light, humidity, water, and high temperature). This concern has sparked a lot of research interest in CsPbX₃ PeNC stabilization. Numerous efforts have been made to stabilize perovskite quantum dots (PeQDs) either through surface passivation or encapsulation in an inorganic matrix (SiO₂, zeolite, Al₂O₃, TiO₂) [29–32]. Among these conventional inorganic materials, metal organic frameworks (MOFs) have earned a significant attention due to their high porosity, functional diversity, tunable pore size, structural adjustability, and very high specific surface area [33]. It has been shown that encapsulating CsPbX₃ PeNCs in the MOF matrices to create host-guest composites is an easy and effective approach [34–38]. Additionally, the strong host-guest interactions and the MOFs' substantial surface area, stabilize the nano confined guest species without the need for additional stabilizing agents. The pore diameters of frequently employed MOF hosts are in the microporous region, which is unfavorable for reactant access due to the substantial diffusion resistance and resulted into a limited loading of PeNCs [34,38]. In recent years, MOFs have been increasingly utilized as chemical sensors [39,40], but their low PLQY originating from either poor intrinsic luminescence of inorganic or organic components, or luminescence resulting from the weak metal to ligand charge transfer, limit the applications of these MOFs as sensor [41]. Furthermore, to improve the luminescence properties in MOFs lanthanide metal ions are introduced along with complex organic linkers, which are difficult to produce via synthesis. Therefore, utilizing the ultrahigh porosity of MOF as host matrices for various luminescent guest molecules with high PLQY has been alternatively designed to produce functionalized luminescent MOF based nanocomposite [42,43].

Zeolitic imidazolate framework (ZIF-8) with superior chemical stability having zinc as the metal source and 2-methyl imidazole as the organic linker is a subclass of microporous MOF. ZIF-8 MOF thus exhibits pore size lies in microporous region i.e. < 2 nm. As mentioned earlier, the microporous system has limited diffusion of guest molecules, thereby hierarchically porous ZIF-8 (HZIF-8) has great interest. In HZIF-8, mesopores are introduced in the ZIF-8 that results in a mixture type of both micropores and mesopores in ZIF-8 that increase the diffusion rate

of reactants. To increase the material's stability, CsPbX₃ QDs can be enclosed in HZIF-8.

In an effort to widen the analytical applications of PeNCs, our present work introduces a confined synthesis of CsPbBr₃ PeNCs within the hierarchically porous MOF (HZIF-8) via an in situ growth method. The method uses HZIF-8 as support to grow PeQDs directly within the MOF system with uniform crystal size and highly luminescent properties. HZIF-8 was synthesized following a triethylamine-assisted method. The stability of PeNCs within the MOF is highly improved and maintains the bright PL in harsh environmental conditions (moisture, water, temperature, light, etc.). Functionalization of CsPbBr₃ quantum dots (QDs) with the HZIF-8 MOF host combines the advantages of both the unique and outstanding luminescence properties of perovskite nanocrystals and the ability of efficient accumulation and adsorption of target analytes by the MOF matrix enabling them to be effective sensing probe and thereby demonstrating great selectivity and sensitivity. Therefore, CsPbBr₃/HZIF-8 composites were utilized as fluorescence turn-off-on sensors for the quantitative detection of copper metal ions and melamine in food samples with a very low limit of detection (LOD) value of 4.66 nM and 13.84 nM respectively. Here, the metal ion (Cu²⁺) acts as a quenching agent for the green PL signal of CsPbBr₃/H-ZIF8 composite. Melamine as a multifunctional system can competitively adsorb Cu²⁺ from the surface of the sensing probe due to the strong interaction between melamine nitrogen and Cu and the quenched PL signal is restored and thus develops an on-off-on fluorescence sensor.

2. Experimental section

2.1. Chemicals

Lead bromide (PbBr₂, 99.9%, alfa aesar), Cesium bromide (CsBr, 99.9%, alfa aesar), oleic acid (OA, 90%, alfa aesar), oleylamine (OAm, 99%, alfa aesar), zinc nitrate hexahydrate (Zn(NO₃)₂·6H₂O, 99%, alfa aesar), 2-methyl imidazole (HmIM), (99%, SRL chemicals), methanol (MeOH, 99.5%, SRL chemicals) N,N-dimethylformamide (DMF, 99%, Merck), toluene (C₇H₈, Merck), triethyl amine (TEA), melamine (C₃H₆N₆, 99%, alfa aesar). Ultrapure water was used for all purposes. The chemicals in this work were purchased from commercial sources and used exactly as received.

2.2. Synthesis procedure

2.2.1. Synthesis of HZIF-8:

HZIF-8 was synthesized according to a previously used method with minor modifications [44]. In this process, 0.8 ml of Zn(NO₃)₂·6H₂O solution (0.8 mmol) in deionized water was first mixed with 0.10 ml (0.70 mmol) of TEA, and then 2.3 ml of the HmIM solution was added (6.4 mmol). The final molar ratio of metal to linker was 1:8. Using deionized water, the reaction volume was filled to a total of 28 ml. After a continuous stirring of 30 min at room temperature, the white precipitates were formed which were collected using centrifugation. The obtained products were washed several times with water/ethanol mixture and dried overnight at 70 °C in a vacuum oven.

2.2.2. CsPbBr₃/HZIF-8 composite:

In a typical synthesis procedure of CsPbBr₃/HZIF-8 composite, the HZIF-8 MOF (150 mg) was first dispersed in 10 ml DMF. Then 2 mmol of PbBr₂ was added into the dispersion with continuous stirring for 5 h. The PbBr₂@MOF powder was collected by filtering the solution. In the second step, the resulting powder was dispersed in toluene (10 ml) with stirring. Then, the CsBr/methanol solution (1.0 mmol) was quickly injected into the toluene dispersion that induces the crystallization of perovskite quantum dots and finally produced perovskite@MOF composite. The whole experiment was performed at room temperature in an ambient atmosphere. The yellowish colored precipitates were collected by filtration and washed thoroughly with methanol.

2.2.3. Sample preparations and fluorescence measurements

This part is included in the [supporting information file](#).

2.3. Instrumentations

X-ray powder diffraction (PXRD) patterns were recorded on D8 Focus and MINIFIEX (Bruker AXS, Germany) instrument operated at 40 kV and 40 mA using Cu K α radiation ($\lambda = 1.5406 \text{ \AA}$). Fourier transform infra-red (FTIR) spectra of the sample were carried out using a Nicolet Impact-410 IR spectrometer instrument. UV-Vis absorption spectra and photoluminescence spectra of the samples were performed at room temperature using a Shimadzu UV-2450 and a Hitachi F-2700 fluorescence spectrophotometer. The relative PLQY of the composite was measured using fluorescein as the reference standard (Quantum Yield = 0.95 in 0.1 M NaOH). Time resolved PL decay (TRPL) measurement was performed on a Lifespec II pico second time resolved fluorimeter instrument. The surface morphologies of the samples were investigated using scanning electron microscopy (SEM, Jeol JSM 6390LV) images provided with the energy dispersive X-ray spectroscopy (EDX). X-ray photoelectron spectroscopy (XPS) was conducted on ESCALAB 220 XL spectrometer. A TECNAI G2 20 S-TWIN (200KV) was used to capture the transmission electron microscopy (TEM) and high resolution transmission electron microscopy (HRTEM) images of CsPbBr₃/HZIF-8 hybrid composite. Quantachrome instrument (version 5.21) was used to obtain N₂ adsorption-desorption isotherm and pore size distribution graph at 77 K.

3. Results and discussion

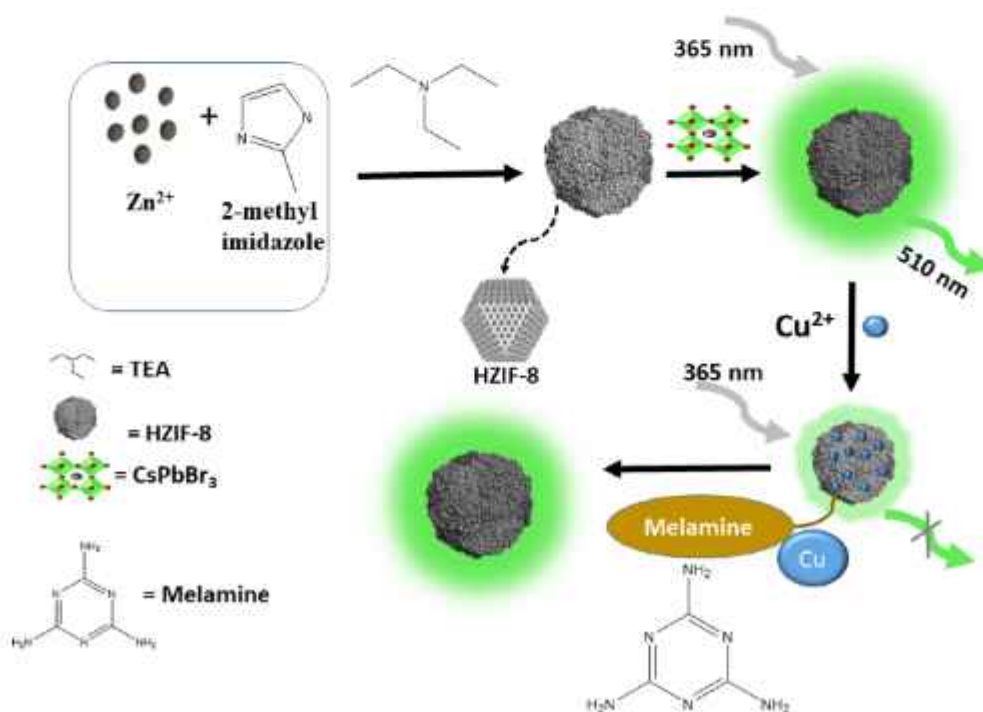
The hierarchically porous MOF, HZIF-8 was synthesized by a template free simple triethylamine assisted method, in which free mesopores are generated in ZIF-8 without removing the template. The as synthesized HZIF-8 was utilized to embed the CsPbBr₃ (CPB) PeNCs by a surfactant free two-step approach. The CsPbBr₃/HZIF-8 nanohybrids were developed, as illustrated in [Scheme 1](#), to create a high-performance sensing probe. All the synthesized materials were characterized with various analytical tools.

3.1. Structural and morphological description of MOF and the composite material

The highly crystalline structure of the synthesized ZIF-8 and HZIF-8 MOF powder was identified using powder X-ray diffraction (XRD), which is shown in [Fig. 1d](#). The diffraction peaks were located at around $2\theta = 7.60, 10.57, 12.85, 14.8, 16.6, 18.12, 19.70, 24.6, 25.75, 26.78, 29.74, 30.66$ and 32.36 , corresponding to the (011), (002), (112), (022), (013), (222), (114), (233), (224), (134), (044), (244) and (235) planes of the ZIF-8 MOF [45]. The distinctive peaks of the PXRD pattern of HZIF-8 are in good agreement with those of the ZIF-8 pattern.

FTIR spectra presented in [Fig. S1b](#) for HZIF-8 and CPB@HZIF-8 display bands at around 3190 cm^{-1} and 2933 cm^{-1} , assigning to the stretching vibrations of C–H from the methyl group of the ZIF-8. All the peaks in the region of $500\text{--}1600 \text{ cm}^{-1}$ are resulting from the stretching and bending vibration of the imidazole ring in ZIF-8 [44]. The C–N absorption band of HZIF-8 shows strong peaks in the region $1100\text{--}1400 \text{ cm}^{-1}$. The characteristic Zn–N vibration bonding was assigned a peak at 421 cm^{-1} , observed for both HZIF-8 and CPB@HZIF-8, indicating the coordination of Zn²⁺ with the 2-methylimidazole ligand. MOF integrated with PeQDs was synthesized without a surfactant, the organic components in ZIF-8 were primarily responsible for the vibrational peaks of the CPB@HZIF-8. The FTIR spectrum of CPB@HZIF-8 preserves the specific vibrations of MOF, indicating that the MOF matrix successfully passivated the PeQDs.

The occupancy of CsPbBr₃ in the MOF matrix can further be confirmed by the XPS and EDX analysis. EDX spectra of the composite show the presence of Cs, Pb, and the signal of Br along with Zn and N demonstrating the successful formation of CsPbBr₃ in the HZIF-8 MOF matrix ([Fig. S2](#)). XPS analysis was carried out to determine the surface characteristics and chemical state of the CsPbBr₃/H-ZIF8 MOF composite. As illustrated in the survey XPS spectrum ([Fig. 2a](#)), the presence of desired signals of Cs, Pb, and Br on the surface of the PeQD@MOF composite coupled with the C, N, and Zn²⁺ signal from the HZIF-8 matrix, clearly validate the formation of CsPbBr₃ nanocrystal in the MOF matrix. The XPS fine spectra displays feature peaks of Cs 3d_{5/2} (724.2 eV) and Cs 3d_{3/2} (738.2 eV), Pb 4f_{7/2} (138.1 eV), Pb 4f_{5/2} (143 eV) and Br 3d_{5/2} (67.9 eV), Br 3d_{3/2} (69.1 eV). These values are closely



Scheme 1. Schematic illustration of the development of CsPbBr₃/HZIF-8 MOF nano composite and its sensing mechanism.

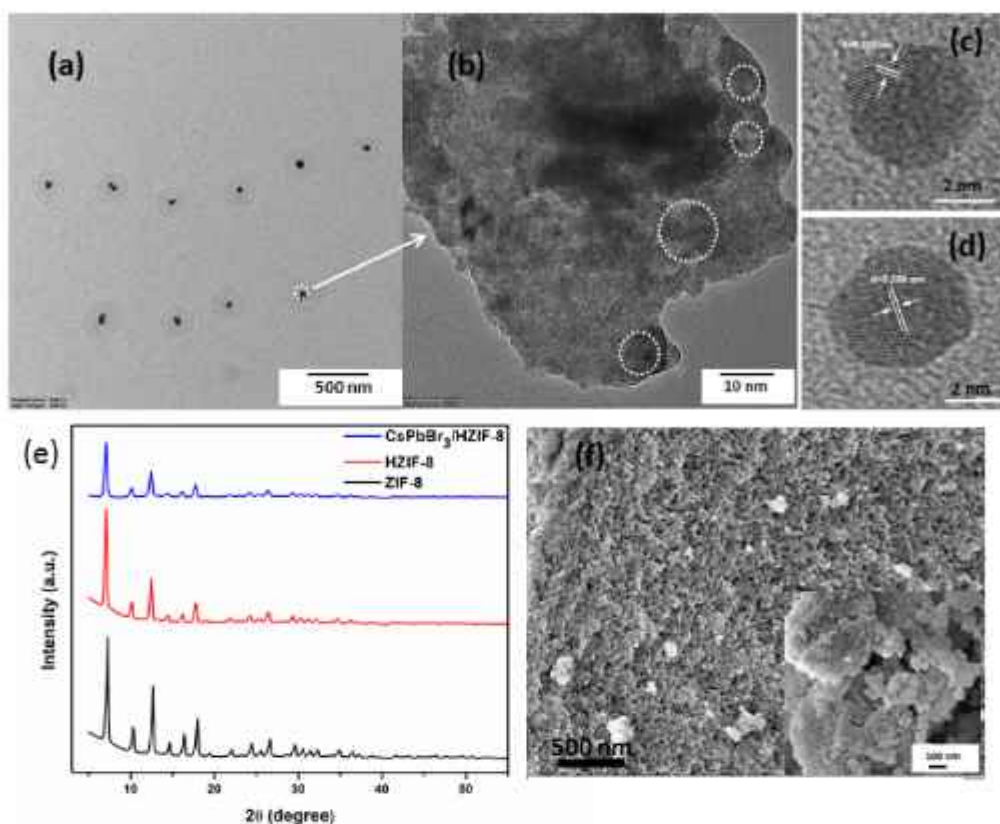


Fig. 1. TEM images of CsPbBr₃/HZIF-8 MOF composite (a, b), HRTEM images of enlarged view of the core of the composite/selected zone (c, d), XRD pattern of MOF and PeQD/MOF composite (e) and SEM image of HZIF-8, inset: close up view of the MOF (f).

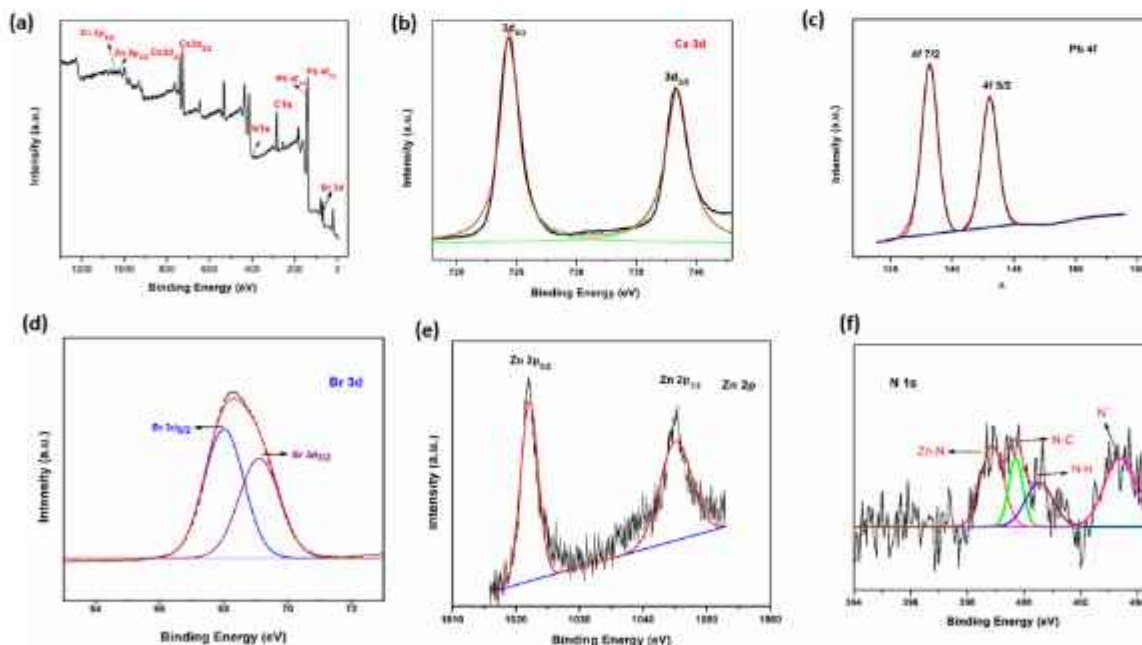


Fig. 2. XPS survey spectra of CsPbBr₃/HZIF-8 composite (a), XPS fine spectrum of Cs 3d (b), Pb 4f (c), Br 3d (d), Zn 2p (e), N 1s (f).

matched with the previous literature reported for CsPbBr₃ PeQD [46]. It should be noted that the binding energies of Cs, Pb, and Br are not significantly affected by the insertion of CsPbBr₃ PeQD in the MOF. Aside from the PeQDs, Zn 2p peaks appeared at binding energies of 1022 eV and 1045.1 eV (Fig. 2e) and were derived from Zn 2P_{3/2} and Zn 2P_{1/2} states respectively from the HZIF-8. Fig. S1a shows the high-

resolution XPS spectrum of C1s, which further can be deconvoluted into two peaks at 284.6 eV (C-H/ C = C) and 285.2 eV (C-N), both of which are from imidazole ring. Similarly, the N1s spectrum could be fitted into four peaks centered at 398.6 eV, 399.6 eV, 400.3 eV, and 403 eV. The peak at 398.6 eV corresponding to N-Zn coordinate bond and the peaks at 399.6 eV, 400.3 eV mainly contributed to the N-C and N-H

moieties (Fig. 2f). Higher energy N1s peak at 403 eV assigned to the quaternary nitrogen ion which indicates the existence of N-Pb interaction through non coordinated nitrogen from 2-methyl imidazole linker, thereby signifying a close interaction between PeQDs and the MOF matrix. The XPS analysis results strongly support the formation of the CsPbBr₃/HZIF-8 MOF composite.

To better understand the micro-morphology and structural evolution of CsPbBr₃/HZIF-8 composite throughout the formation of nano-composite material, SEM and TEM micrograph pictures were taken. The SEM images of pristine HZIF-8 show monodisperse bouquet-like morphology with a densely packed surface with an average size of about 70 nm (Fig. 1f). The CsPbBr₃/HZIF-8 MOF composite maintains MOF's morphology that has been revealed from TEM images (Fig. 1a-d). The hierarchical porous characteristics of HZIF-8 encompassing both meso and microporosity are confirmed by the N₂ adsorption-desorption isotherm with a prominent hysteresis loop. The pore size distribution of HZIF-8 in Fig. 3d and Table S1 illustrates the mixture of type I and type IV adsorption-desorption isotherms in HZIF-8. BET (Brunauer-Emmett-Teller) surface area of the HZIF-8 is calculated to be 2065.237 m²g⁻¹. When the nonporous PeQDs further grow in situ into the pore channels of HZIF-8, pore volume and the BET surface area of the perovskite confined MOF are significantly decreased, attributed to the successful incorporation of the PeQDs in the MOF matrix. Further, TEM images of the CsPbBr₃/HZIF-8 show the well-defined CsPbBr₃ PeNCs, are embedded by the porous MOF matrix forming a core shell type structure. A large number of CsPbBr₃ quantum dots (QDs) can be seen as dark circular areas without any visible particles outside the HZIF-8 MOF matrix. The high-resolution transmission electron microscopy (HR-

TEM) image of the constrained CsPbBr₃ PeNCs in HZIF-8 MOF with clearly defined lattice spacing is shown in Fig. 1c and 1d, demonstrating their great crystallinity. The interplanar spacing (*d*-spacing) calculated from the lattice fringes are 0.288 nm and 0.238 nm corresponding to the (200) and (211) planes of the cubic CsPbBr₃ respectively [35]. Based on the aforementioned results, the CsPbX₃ QDs are safeguarded by the protective MOF shell that would lead to improved stability of the perovskite MOF binary composite.

Additionally, the identical diffraction peaks of CsPbBr₃/HZIF-8 imply that the growth of CsPbBr₃ PeQDs into HZIF-8 does not compromise its crystalline integrity. Because of the small size of CsPbBr₃ and very high crystallinity of HZIF-8 MOF in comparison to CsPbBr₃, the peak intensities associated with it could be screened by the diffraction peaks of the MOF matrix and hence the XRD pattern does not exhibit any prominent peaks of CsPbBr₃. From the TEM images of the CsPbBr₃/HZIF-8 composite the average grain size of the PeQDs was found to be about 4 nm (<5 nm), much smaller than that of the MOF host. The relative intensities of the diffraction peak diminished and broadened which is likely due to the changes in electron density within the matrix with the loading of the CsPbBr₃ into pores of the MOF matrix. Therefore the framework structure of MOF is preserved in all the prepared samples. Similar results were found in other literature also [34,35].

3.2. Photophysical properties:

Furthermore, we have explored the optical properties of all the synthesized materials. Fig. 3b displays the UV-Vis spectra of HZIF-8 and CPB/HZIF-8 where the MOF exhibits a weak absorption. In the presence

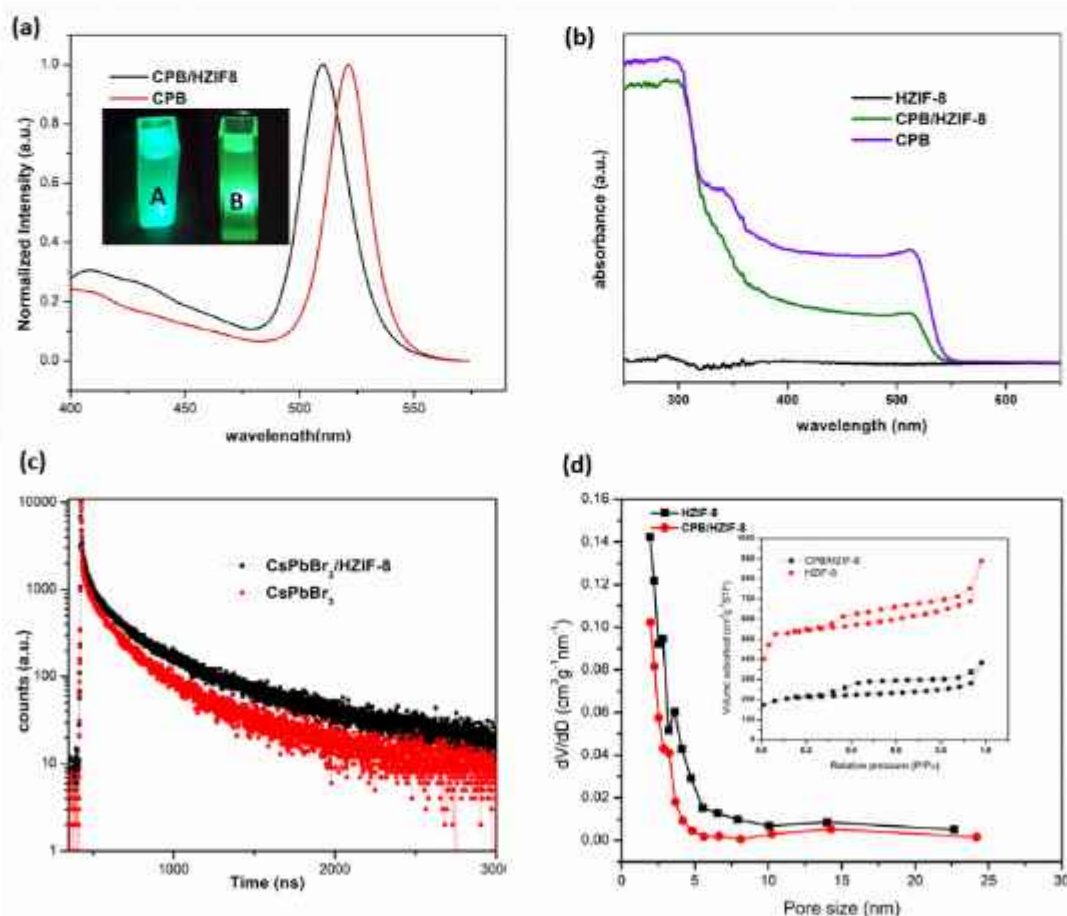


Fig. 3. Emission spectra of CsPbBr₃ (No MOF- Red) and CsPbBr₃/HZIF-8 (Black), inset: corresponding photographs of CsPbBr₃ (B) and CsPbBr₃/HZIF-8 (A) under 365 nm UV lamp (a); Absorption spectra of HZIF-8 (black), CsPbBr₃/HZIF-8 (green) and CsPbBr₃ (purple) (b); TRPL decay graphs of CsPbBr₃ (red) and CsPbBr₃/HZIF-8 (black) (c); Pore size distributions and N₂ adsorption-desorption isotherms (inset) of HZIF-8 and CsPbBr₃/HZIF-8 (d).

of PeQDs, the absorption of HZIF-8 increases with an absorption peak at 509 nm. The PeQDs without the MOF matrix shows similar absorption behavior with the CPB/HZIF-8 composite with the maxima starts at 512 nm. The composite shows an intense green emission with a peak centered at 510 nm with FWHM value of 25 nm on excitation with a light of 365 nm wavelength. The narrow FWHM value demonstrates both the color purity and the uniformity of the composite in terms of size and defects. A small blue shift of 12 nm with a slight wider FWHM from the CsPbBr₃ without the HZIF-8 matrix indicates the confinement effect of the PeQD due to size restriction of the PeQDs by the MOF matrix. The PLQY of CPB/HZIF-8 composite in toluene solution was calculated to be 45.5 % using fluorescein as the reference standard.

The time resolved PL decay dynamics of bare CsPbBr₃ and CPB/HZIF-8 composite were further studied in which the MOF embedded CsPbBr₃ shows slower decay kinetics than the bare CsPbBr₃. The decay curves were fitted using a tri-exponential fitting model and the decay parameters are summarized in Table 1. The average life times for bare CsPbBr₃ and CPB/HZIF-8 were calculated to be 25.23 ns and 40.13 ns respectively. The increase in the life time of CsPbBr₃ is associated with the surface defect passivation of PeQDs by the MOF matrix. The formula used to calculate average life time is-

$$\tau_{avg} = \left(\sum A_i \tau_i^2 \right) / \sum A_i \tau_i, \quad i = 1, 2, 3 \quad (1)$$

where τ_i signifies parameters of lifetime decay and A_i is a constant termed as pre-exponential factors, τ_{avg} denotes the average lifetime [47].

3.3. Stability test of HZIF-8/CsPbBr₃ composite:

In general, due to the extra sensitive nature of CsPbBr₃ PeNCs, their applications in analytical field are limited. The HZIF-8 MOF matrix provides extra stability to the PeNCs, making it highly stable in ambient conditions. Fig. 4 shows the stability of the composite powder against long term storage in open air conditions at room temperature (~70% humidity). The resulting powder retains its 95 % of luminescence intensity for about two months whereas the PL intensity of CPB PeNCs is practically quenched. It's encouraging to find that our composite has great moisture resistance, ascribed to the MOF protective shell which effectively prevents CsPbBr₃ from oxygen and moisture leakage. Furthermore, the UV photo-stability of the CsPbBr₃/HZIF-8 composite was tested by being exposed to 365 nm UV light in an ambient atmosphere, with the PL intensity being checked at various intervals of exposure time. On exposure of 80 h, the composite maintains 80 % of its initial PL intensity. The use of PeQDs is limited exclusively to non-polar solvents. However, when the PeQDs are absorbed inside the pores of MOF, the aforementioned restriction is eliminated. The aqueous stability of the prepared CsPbBr₃/HZIF-8 composite was investigated by recording its PL after soaking the composite powder in an aqueous solution. The composite formed a well dispersed solution in water while

Table 1
Summary of TRPL decay lifetimes result.

	τ_1 (ns)	τ_2 (ns)	τ_3 (ns)	τ_{avg} (ns)
CsPbBr ₃ /HZIF-8	13.37	26.75	53.51	40.13
CsPbBr ₃	8.329	16.66	33.33	25.23
CsPbBr ₃ /HZIF-8 Melamine	13.18	26.36	52.73	39.54
CsPbBr ₃ /HZIF-8 Cu(100 nM)	7.20	14.40	28.82	21.60
CsPbBr ₃ /HZIF-8 Cu(160 nM)	6.42	12.84	25.72	19.29
CsPbBr ₃ /HZIF-8 Cu Melamine (50 nM)	7.38	14.77	29.54	22.15
CsPbBr ₃ /HZIF-8 Cu Melamine (250 nM)	12.49	24.88	49.77	37.32
CsPbBr ₃ /HZIF-8 Cu Melamine (400 nM)	13.13	26.50	52.50	39.45

maintaining its intense green emission. We checked the emission spectra of the water dispersed solution for a time period of 15 days (Fig. 4c). Also, the composite maintains its intense green emission in other polar protic solvents.

3.4. CsPbBr₃/HZIF-8 composite in chemical sensing application:

As discussed above, the highly improved fluorescence properties of CsPbBr₃/HZIF-8 composite material enable them to utilize in optical sensing applications. Therefore, the potential use of the suggested material in the field of fluorescence chemo sensing was examined.

3.4.1. Detection of Cu²⁺ ions:

When exposed to various metal ions, the PeQD-encapsulated HZIF-8 exhibits a PL quenching response. Here, we looked at the feasibility of employing the CsPbBr₃/HZIF-8 composite for copper ion detection in aqueous solutions. Fig. 5a displays the PL response of CsPbBr₃/HZIF-8 with increasing concentration of Cu²⁺. The intense green emission of CsPbBr₃/HZIF-8, centered at 510 nm was quenched with the addition of Cu²⁺ from 30 to 1500 nM concentration. The dilution had a very small impact on quenching and there was no solvent interference in the quenching of the green signal. Therefore, we can say that the Cu²⁺ ion in the probe solution is responsible for the observed quenching. Stern-Volmer equation (2) was used to analyze the quenching behavior of the CsPbBr₃/HZIF-8 where the quenched ratio F_0/F and copper concentration are shown to be linearly correlated (Fig. 5b) in the range of 30–1500 nM.

$$F_0/F = 1 + K_{SV}[C] \quad (2)$$

where F_0 and F denote the PL intensities of PeQD before and after the addition of the analyte respectively, $[C]$ is the concentration of Cu²⁺ in solution (nM) and K_{SV} represents the Stern-Volmer quenching constant. The calibration curve was successfully fitted to the equation, $Y = 0.0045 X - 0.305$, with a correlation coefficient (R^2) of 0.9957. The quenching constant (K_{SV}) value was found to be $4.5 \times 10^6 \text{ M}^{-1}$. The limit of detection (LOD) of Cu²⁺ was determined to be 4.66 nM using the relation $3\sigma/S$, where S is slope of the linear calibration graph and σ represents standard deviation [48]. LOD for Cu²⁺ is significantly below the World Health Organization (WHO) recommendation value of Cu²⁺ in drinking water, that is 1 g L^{-1} [49]. When compared to previous literatures for Cu²⁺ detection, our sensing method reflects a competitive sensitivity value for luminescence based Cu²⁺ detection in aqueous media (Table S2).

Response time and stability, important parameters which indicate the performance of a sensing system were recorded for Cu²⁺ detection. The quenching proceeded so quickly that the emission intensity reduced in less than two min, and no effective change in intensity was detected after that, showing the system's remarkable stability. The curve of PL intensity of CsPbBr₃/HZIF-8 in the presence of a particular quantity of Cu²⁺ during a 2 h incubation time is shown in Fig. 5c. This result verifies the system's capacity to detect Cu²⁺ regardless of reaction time.

The effects of PL quenching of CsPbBr₃/HZIF-8 with different metal ions solution including Zn²⁺, Bi²⁺, Sr²⁺, Fe²⁺, Mg²⁺, Ni²⁺, Al³⁺, Ca²⁺, K⁺, Na⁺, Cd²⁺, Mn²⁺, Pb²⁺, Pt²⁺, Ag⁺, Pd²⁺, Fe³⁺, Co²⁺, Sn⁴⁺ and Ti⁴⁺, etc. (1 μM) were investigated to assess the selectivity of CsPbBr₃/HZIF-8 towards Cu²⁺ detection. When compared to other metal ions, Cu²⁺ displayed the highest quenching of the PL signal, indicating the obvious selectivity of the sensing probe towards Cu²⁺. Fig. 5d shows the interference of different metal ions in the relative fluorescence intensity of the composite with or without the presence of Cu²⁺. No noticeable change in the PL quenching of Cu²⁺ was observed with other metal ions confirming the practical applicability of this method for the determination of Cu²⁺. Variations in various parameters, such as steric interactions, redox potential differences, and metal-surface interactions, are expected to complicate this selectivity [3], while the precise causes

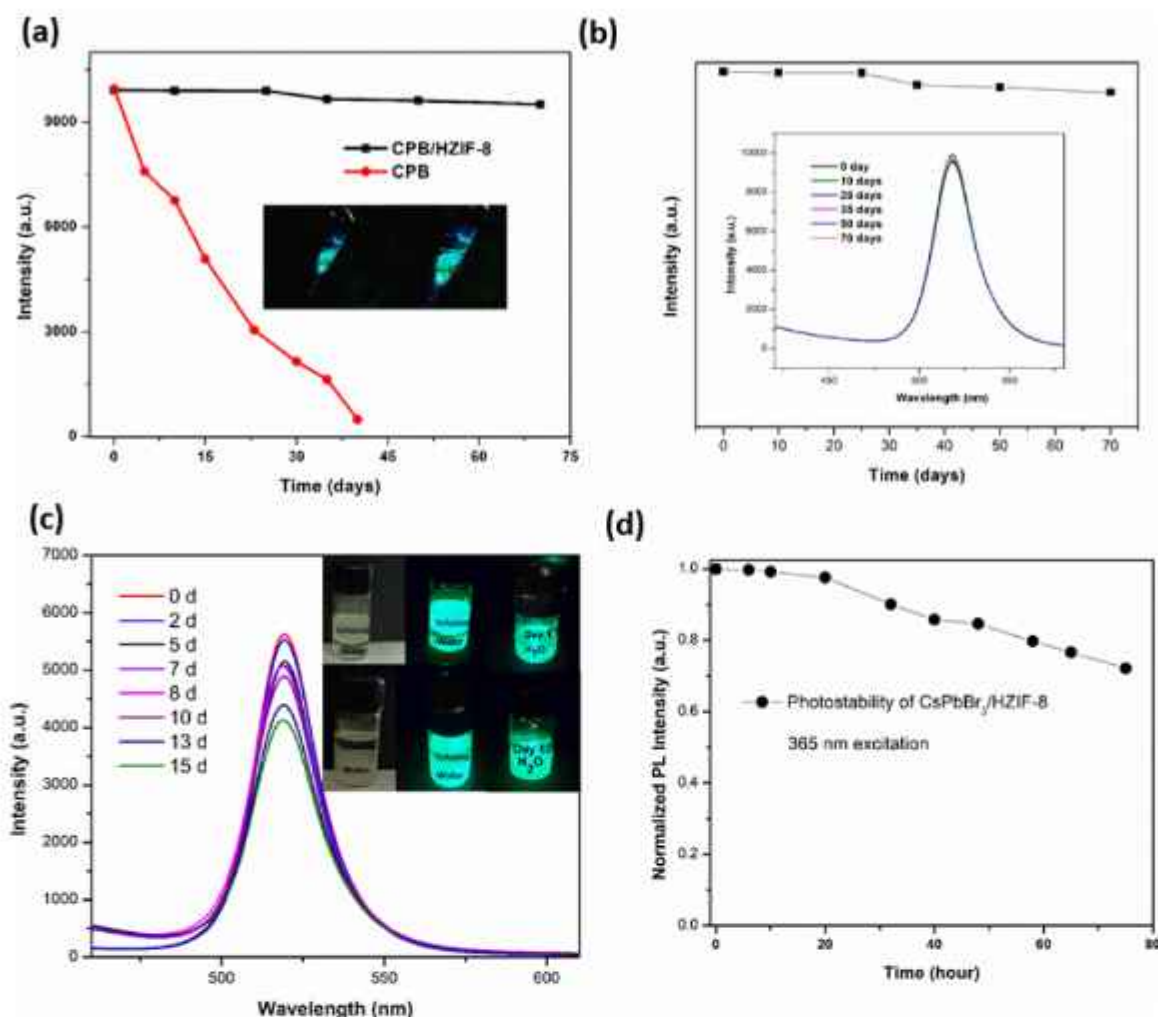


Fig. 4. Storage test of CsPbBr₃/HZIF-8 (a, b) Intensity vs. time plot of bare CsPbBr₃ (red) and CsPbBr₃/HZIF-8 (black), inset: Photographs of CsPbBr₃/HZIF-8 powder in day 1 and day 60 under 365 nm UV light, (c) Emission spectra evolution of aqueous CsPbBr₃/HZIF-8 dispersion for 15 days and (d) UV Photo-stability test of the composite.

of these discrepancies are beyond the purview of this investigation. We can conclude that of the studied metal ions, the designed CsPbBr₃/HZIF-8 composite reveals a high selectivity for Cu²⁺ ion detection. This approach was further employed to detect Cu traces in tap water samples. As a result, the suggested approach has high accuracy and reliability for identifying low concentrations of Cu in natural samples (Table 2).

3.4.2. Analytical performance for melamine sensing

When melamine is added to CsPbBr₃/HZIF-8-Cu²⁺ system under optimum experimental conditions, it could release the adsorbed copper ion from the surface of CsPbBr₃/HZIF-8, and eventually restore the quenched signal. The addition of only melamine to the CsPbBr₃/HZIF-8 has negligible impact on the emission spectrum of the composite (Fig. 6a). In order to achieve the optimal and sensitive "off-on" response of CsPbBr₃/HZIF-8 probe for melamine detection, the influence of reaction time and pH value was studied (Fig. S3b and c). The recovery of the PL signal begins within a minute and rises with time from 0 to 5 min, and reaches a maximum at 10 min. The system becomes steady after 10 min and has been tested for up to 30 min. Similarly, with the increasing pH from 4.5 to 6.5, the recovery increases and then decreases at higher pH. An incubation time of 10 min and a solution pH of 6.5 was used for further sensing experiments. The PL response of CsPbBr₃/HZIF-8-Cu²⁺ system with the increasing concentration of melamine from 0 to 500 nM is presented in Fig. 6b. Fig. 6c shows the correlation between the

concentration of melamine and the PL recovery efficiency $(F_0 - F)/F_0$, F_0 and F represent the PL intensity of the composite in presence and absence of melamine, respectively. It is possible to express the calibration curve as a linearly fitted equation $(F - F_0)/F_0 = 0.0051C + 0.0866$ ($R^2 = 0.9906$). The LOD (3 σ /s) for melamine detection was estimated to be 2.64 nM, which is equivalent to and even better than those described in the literature (Table S3).

3.5. A plausible mechanism of sensing:

3.5.1. Quenching mechanism:

To discuss the quenching phenomenon by Cu²⁺ ion, we first studied the UV-Vis absorption spectra of the fluorophore and the analyte. Fig. 7a shows that the absorption spectrum of Cu²⁺ has no significant overlap with the excitation and emission spectra of the CsPbBr₃/HZIF-8, which eliminates the possibility of the FRET (Forster resonant energy transfer) and IFE (Inner filter effect) mechanism of quenching. Additionally, no shift or alteration of the absorption and emission spectra has been seen following the introduction of Cu²⁺ into the probe solution (Fig. S4a). It indicates that the crystal structure or conformation of the MOF protected QDs has not changed, excluding the static quenching mechanism that leads to the production of a ground state complex. XPS analysis was done prior to and after the interaction with Cu²⁺ to establish the adsorption of Cu ion on the surface of the CsPbBr₃/HZIF-8

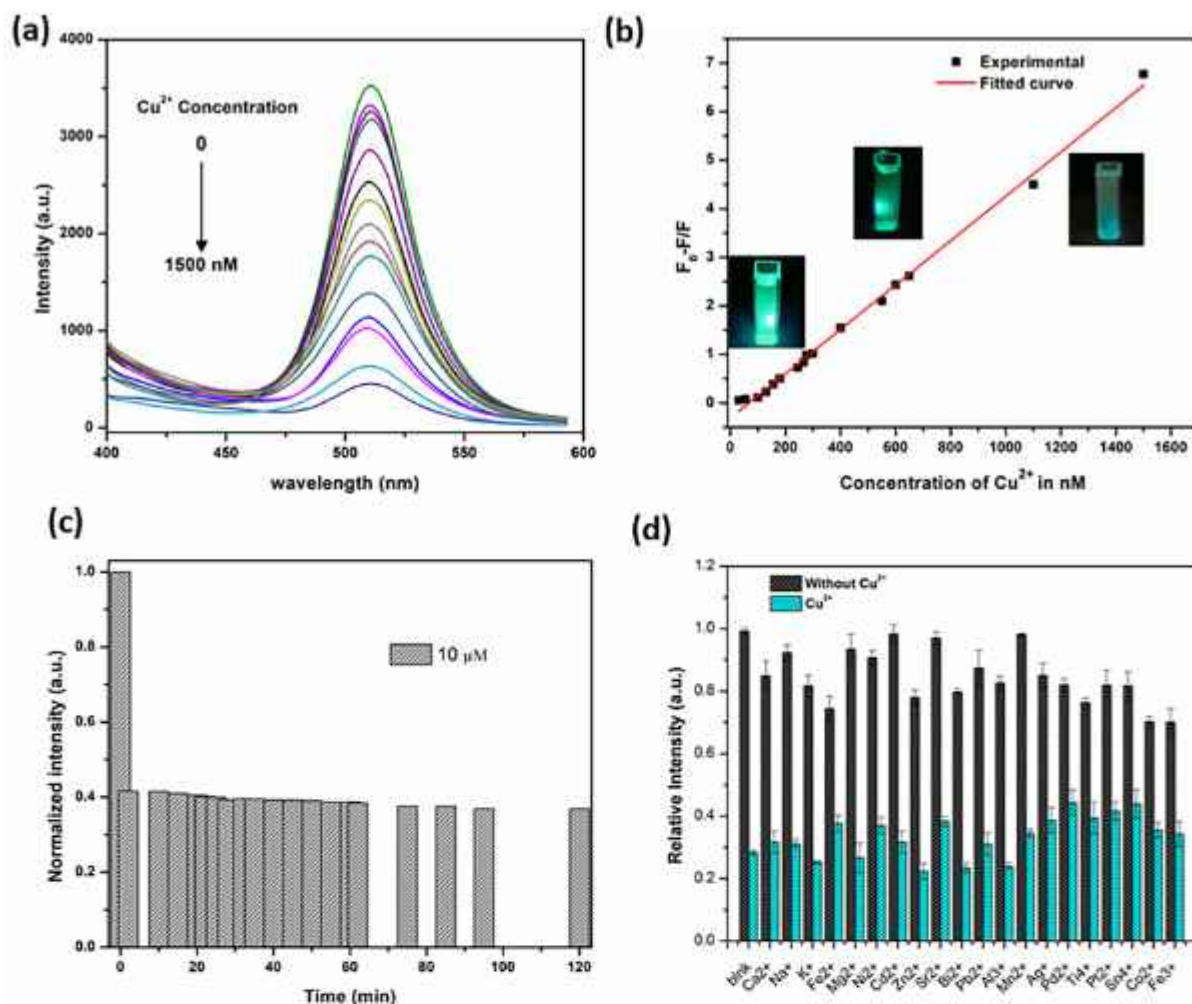


Fig. 5. Cu^{2+} sensing-PL spectra of $\text{CsPbBr}_3/\text{HZIF-8}$ with various concentration of Cu^{2+} (a), Calibration graph versus concentration of Cu^{2+} (b), graph showing the change in PL intensity of the sensor throughout the incubation period of 120 min (c), relative PL intensity of the composite with various other metal ion before (black) and after the addition of Cu^{2+} (cyan) (d).

Table 2
 Cu^{2+} detection in real aqueous solution.

Sample	Spiked (nM)	Detected (nM)	Recovery %	RSD% (n = 5)
Tap water	0	Not detected	—	—
	85	84.4	99.29	3.36
	140	135	96.4	2.81
	150	162	108	3.75

composite (Fig. 8a). High resolution XPS spectra of Cu 2p showed a strong signal at 932.5 eV, which was assigned to Cu $2p_{3/2}$ hybrid orbitals, (Fig. S5) on $\text{CsPbBr}_3/\text{HZIF-8}$ MOF surface.

TRPL decay dynamics were explored to analyze the sensor's quenching kinetics. The fluorescence lifetime of $\text{CsPbBr}_3/\text{HZIF-8}$ composite decreases as Cu^{2+} concentration increases. As shown in Fig. 7b when 160 nM and 100 nM Cu^{2+} is present, the average lifetime drastically drops to 19.29 ns and 21.61 ns from 40.13 ns (Table 1). Faster decay dynamics of the fluorophore in presence of the target analyte offer a clear illustration of the nonradiative recombination pathways. It indicates a dynamic quenching process. The redox potential of $\text{Cu}^{2+}/\text{Cu}^+$ located in between the VB and CB of the $\text{CsPbBr}_3/\text{HZIF-8}$ composite (VB & CB = 1.03 eV and 1.39 eV vs NHE). Electron transfer might occur to the Cu^{2+} (Scheme 2) [50]. Cyclic voltammetry (CV) analysis of $\text{CsPbBr}_3/\text{HZIF-8}$ composite was performed to determine the highest occupied molecular orbital (HOMO) and lowest unoccupied molecular orbital

(LUMO) energy levels (details mentioned in the supporting file). Since the HZIF-8 MOF provide binding sites for Cu^{2+} ion and then it diffuses rapidly to the CsPbBr_3 perovskite. In perovskite lattices, ion migration occurs very easily due to its ionic nature. A coordination complex (-Br-Cu-N-MOF) can be formed due to the interaction between Br⁻ ion of CsPbBr_3 and Cu metal ion. In the FTIR spectra (Fig. S6b) of the composite after Cu^{2+} addition, we have observed a distinct peak shifting of N-H stretching vibration indicating the formation of coordination complex. Also, the XPS spectra of Br was positively shifted after interaction with Cu^{2+} ion (Fig. 9a), indicating the coordination between bromine of the perovskite and Cu metal ion. Thus, the interaction with Cu^{2+} might produce some new surface states or defect levels in the perovskite nanocrystals facilitating nonradiative pathways for electron/hole recombination and finally quench the FL signal of CsPbBr_3 perovskite composite. After the formation of an exciton, the hole created in the HOMO of the perovskite is favoured to be filled by these new states [3,27,50–52].

3.5.2. Fluorescence recovery by melamine:

As mentioned in the above section, the PL quenching process can be explained by both electron transfer and defect level mediated dynamic process due to their coordinative interaction with Cu^{2+} ion. When melamine is added, there is a competitive binding interaction between perovskite and the melamine. Due to strong binding interaction of melamine with Cu, it removes the Cu ion from the surface of the

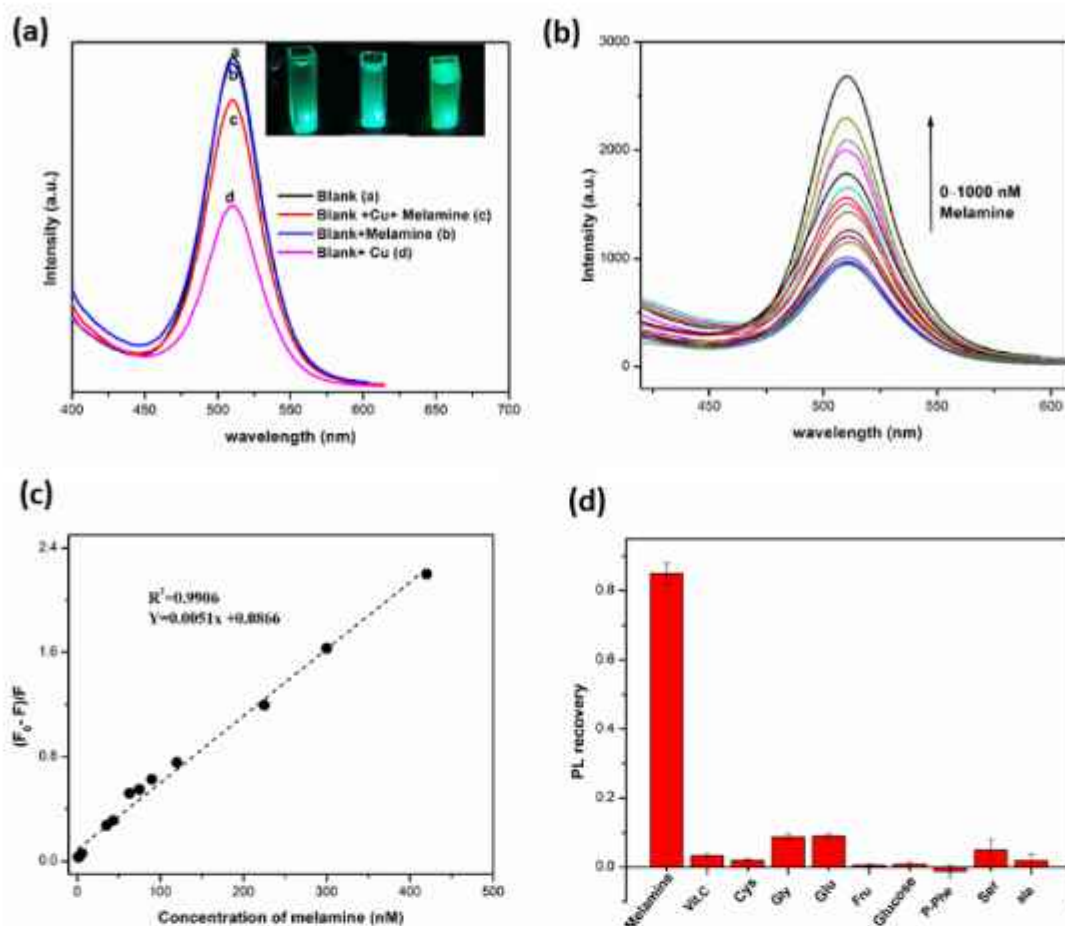


Fig. 6. $\text{CsPbBr}_3/\text{HZIF-8}$ for melamine sensing- (a) inset: Photographs showing the recovery of green emission of $\text{CsPbBr}_3/\text{HZIF-8-Cu}$ with melamine addition (left to right); (b) PL response of ($\text{CsPbBr}_3/\text{HZIF-8} + \text{Cu}$) with the addition of different concentration of melamine; (c) Calibration curve of fluorescence recovery vs. concentration of melamine; (d) PL recovery efficiency of the sensing probe system with other biological molecules.

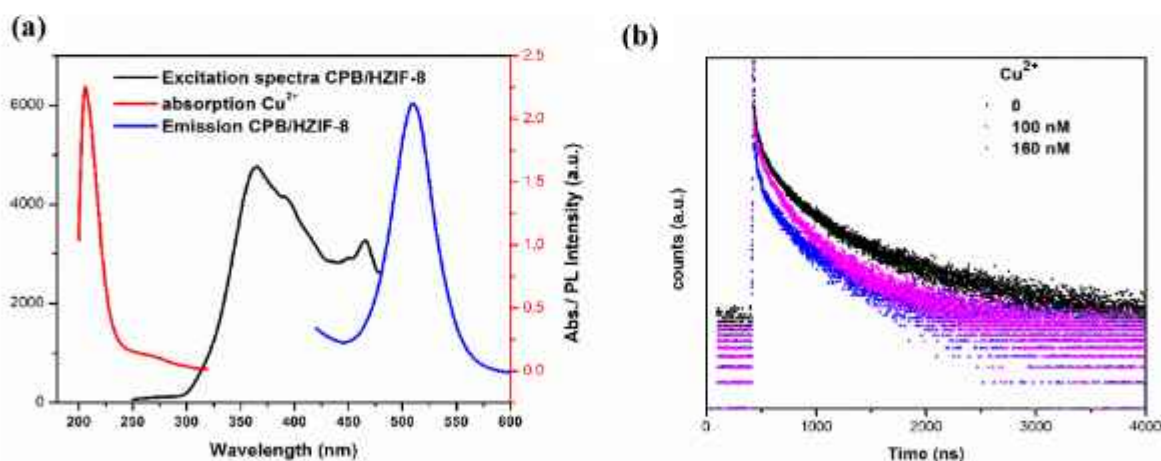


Fig. 7. (a) UV-vis absorption spectra of Cu^{2+} (Red), excitation (black) and emission spectra (blue) of $\text{CsPbBr}_3/\text{HZIF-8}$, (b) TRPL decay dynamics of $\text{CsPbBr}_3/\text{HZIF-8}$ in presence of different concentration of Cu^{2+} .

composite, thereby eliminating the nonradiative pathways of recombination of electron/hole and finally recovers the PL. TRPL decay dynamics of $\text{CsPbBr}_3/\text{HZIF-8-Cu}$ in presence of melamine is presented in Fig. 8b. The melamine itself showed no significant change in the FL lifetime of the $\text{CsPbBr}_3/\text{HZIF-8}$. The reduced average lifetime of $\text{CsPbBr}_3/\text{HZIF-8-Cu}$ was restored from 19.28 ns to 37.32 ns after the

introduction of 250 nM melamine (Table 1) signifying the removal of non-radiative recombination pathways. The interaction of melamine with Cu can be verified by the UV-Vis absorption spectra presented in Fig. 8c, where the presence of Cu significantly changes the absorption spectrum of melamine. The absorption peak of melamine at 202 nm shifts towards the right and the peak at about 234 nm disappears with

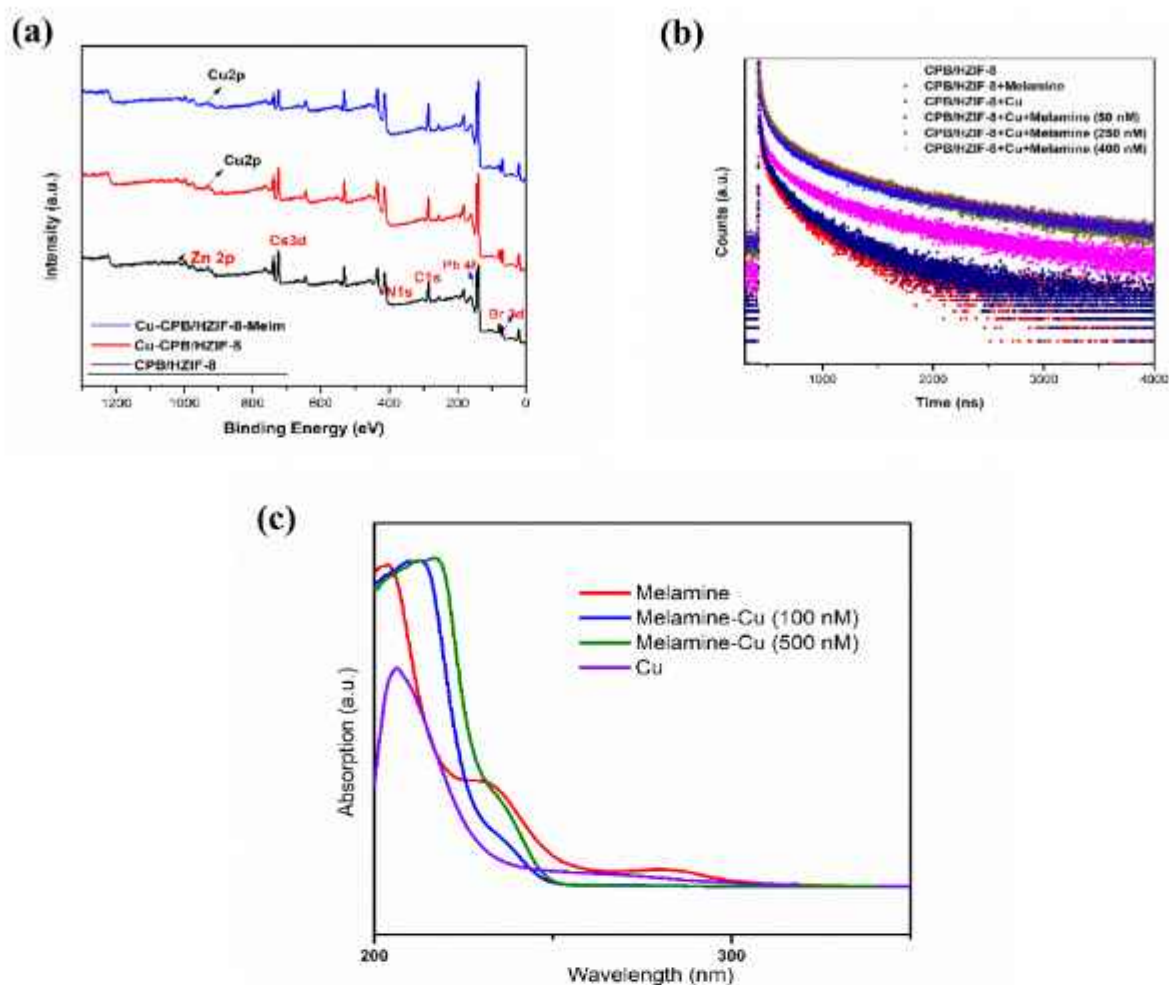
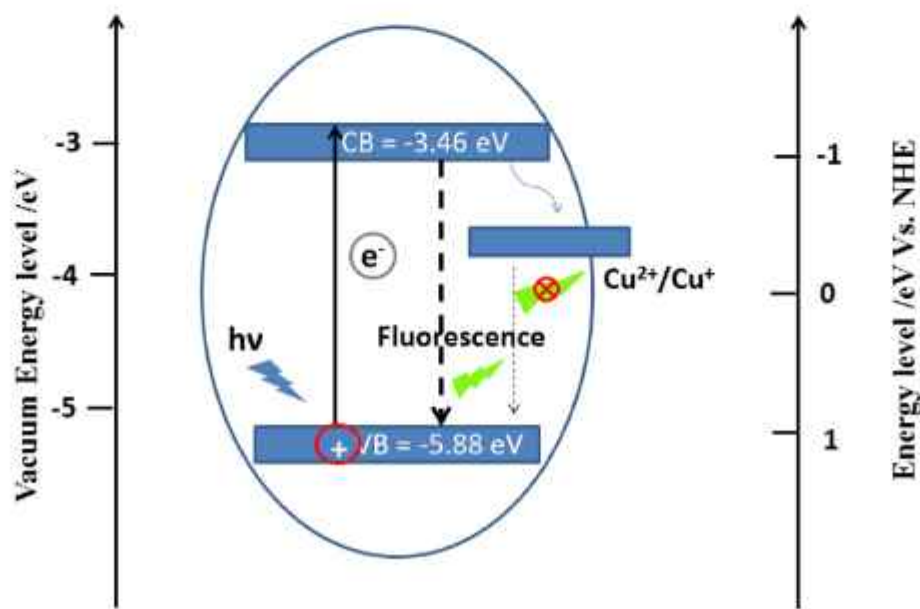


Fig. 8. (a) XPS spectra of the CsPbBr₃/HZIF-8 in presence of Cu (red) and melamine (blue), (b) Fluorescence decay graph of CsPbBr₃/HZIF-8-Cu with various concentration of melamine, (c) UV-vis absorption spectra of melamine (red), Cu²⁺ (purple), Cu-melamine (blue, green).



Scheme 2. Band energy alignment of CsPbBr₃/HZIF-8 composite with Cu metal ion.

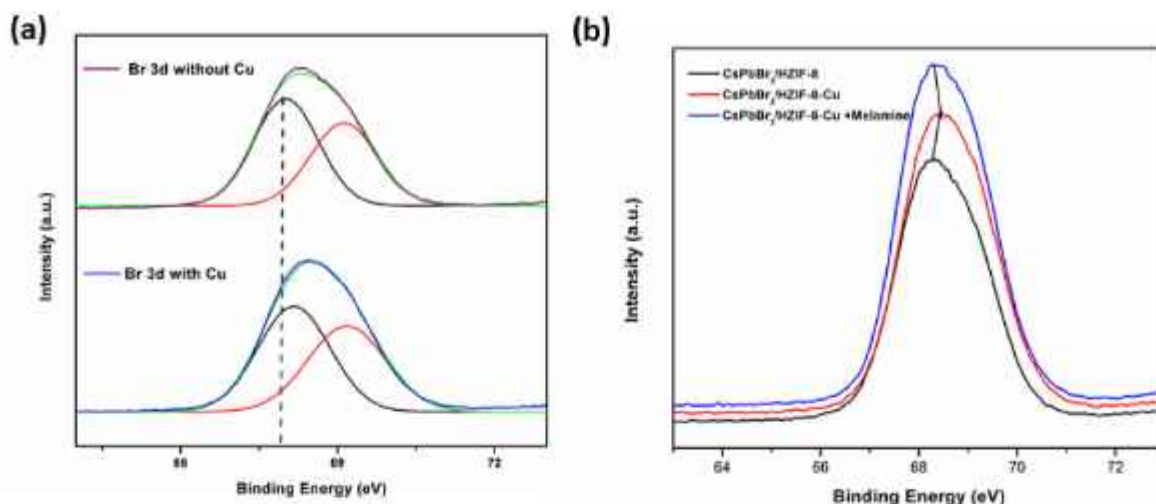


Fig. 9. (a) High resolution XPS spectra of Br with and without the addition of Cu^{2+} metal ion, (b) Comparison with the XPS spectra of Br after melamine addition to the $\text{CsPbBr}_3/\text{HZIF-8-Cu}$.

the addition of Cu^{2+} . The FTIR spectra also show a minor change in peak with the addition of Cu^{2+} (Fig. S4b). All these findings prove the strong affinity of melamine towards Cu metal ion that is partially competitively captured by melamine. This statement is also supported by the XPS spectra, where the intensity of the Cu signal from the sensing probe decreased after melamine was added to the $\text{CsPbBr}_3/\text{HZIF-8-Cu}$ system (Fig. S5). Moreover the shift noticed in the XPS spectrum of Br after Cu metal ion addition was disappeared after melamine was added to the sensing probe confirms the aforesaid findings (Fig. 9b).

Furthermore, to investigate the framework stability of the composite after the sensing experiment, P-XRD of the sample was analyzed (Fig. S7). No change in the characteristic diffraction peaks in XRD from the pristine MOF indicates that the framework is not damaged.

Selectivity: To determine the selectivity of the sensing system for the detection of melamine, the effect of some possible interfering substances including glycine (Gly), Cysteine (Cys), Glutamic acid (Glu), P-phenylenediamine (P-Phe), Serine (Ser), alanine (ala), Fructose, Glucose, vit. C were examined. Fig. 6d shows the luminescence of the $\text{CsPbBr}_3/\text{HZIF-8-Cu}$ composite is not significantly impacted by other substances except melamine with multifunctional heterocyclic system. The foregoing data imply that our sensor has an adequate selectivity.

3.6. Practical application of PeQD embedded HZIF-8 for melamine detection in milk samples

To know the practicability of the sensor, we further employ this switchable fluorescent nano sensor to detect melamine in milk samples (liquid raw milk and infant formula). Due to the absence of melamine in the aforementioned milk samples, the standard spiked recovery studies were utilized to assess the precision of our established probe. The melamine was spiked at various quantities in each sample, and the fluorescence signal was then assessed. The data presented in Table 3 showed

Table 3
Summary of melamine detection in real samples.

Sample	Spiked (nM)	Detected (nM)	Recovery %	RSD % (n = 3)
Raw Milk	0	Not detected	–	–
	45	45.4	100.8	2.73
	85	80.5	94.7	6.37
	145	141.5	97.58	2.27
Infant formula	0	Not detected	–	–
	45	44.5	98.8	5.68
	85	85.2	100.2	5.37
	145	140.5	96.8	4.88

the melamine recoveries in the spiked samples at three different concentration from 94.7 % to 100.8 % with RSD (relative standard deviation) not exceeding 6.37 %, signifying that the proposed fluorescent sensing platform is a reliable method for the detection of melamine in dairy products and has a good applicability.

4. Conclusion

In this approach, we designed a stable and effective sensing platform by loading CsPbBr_3 PeQDs into the porous HZIF-8, using an easy two step in-situ growth method. Hierarchically porous HZIF-8 MOF diffuses PeQD better than microporous MOF hosts, enabling uniform PeQD distribution and provide better stability to the PeQD than bare PeQDs. All the relevant properties of $\text{CsPbBr}_3/\text{HZIF-8}$ composite were thoroughly analyzed. Good fluorescence intensity and great stability were maintained after the transition of the produced $\text{CsPbBr}_3/\text{HZIF-8}$ composites to the aqueous phase. Further, this nano sensor has been utilized for the on-off-on detection of Cu^{2+} and melamine. The Cu^{2+} analyte can act as an effective quencher that quenches the green emission of CsPbBr_3 through a dynamic quenching and electron transfer process. The quenched emission of $\text{CsPbBr}_3/\text{HZIF-8}$ can be restored by the competitive adsorption of Cu^{2+} from the surface of the sensor by the functional amine group of melamine. This sensor is found to be very sensitive towards the detection of Cu^{2+} and melamine and a good linear relationship was found. Because copper has a strong attraction to melamine, this FL assay is more sensitive and selective and is used to find melamine in real samples with satisfactory recoveries. Notably, the approach of embedding CsPbBr_3 nanoparticles with hierarchically porous matrix to generate some custom tailored properties would enhance experimental design process of stable PeQDs and broaden its application window in sensing field.

CRedit authorship contribution statement

Shahnaz Ahmed: Writing – original draft, Validation, Methodology, Formal analysis, Conceptualization. Suman Lahkar: Visualization. Simanta Doley: Visualization. Dambarudhar Mohanta: Investigation, Resources. Swapan Kumar Dolui: Supervision, Investigation, Writing – review & editing.

Declaration of Competing Interest

The authors declare that they have no known competing financial interests or personal relationships that could have appeared to influence

the work reported in this paper.

Data availability

Data will be made available on request.

Acknowledgements

The author would like to acknowledge SAIF, CSIR-NEIST, Jorhat, Assam, India for XPS analysis, Material Analysis & Research Centre, Bengaluru for BET analysis, UGC-SAP-DRS-II, Tezpur University for TRPL analysis and Sophisticated Analytical Instrumentation Centre (SAIC), Tezpur University, India for providing remaining analytical support. The author is grateful to DST-INSPIRE Fellowship, DST, Govt. of India for funding.

Appendix A. Supplementary data

Supplementary data to this article can be found online at <https://doi.org/10.1016/j.jphotochem.2023.114821>.

References

- M. Jaishankar, T. Teeten, N. Ambalagan, B. B. Mathew, K. N. Beeregowda, *Interdisciplinary toxicology*, 7 (2014) 60. <https://doi.org/10.2478/s21202-2014-0009>.
- X. Guo, J. Huang, M. Wang, L. Wang, *Sens. Actuators B* 309 (2020), 127766, <https://doi.org/10.1016/j.smb.2020.127766>.
- H. Li, W. Yin, C.K. Ng, R. Huang, S. Du, M. Sharma, J.J. Jasieniak, *Nanoscale* 14 (2022) 11952–11953, <https://doi.org/10.1039/D2NR02737B>.
- L. Li, G. Wu, T. Hong, Z. Yin, D. Sun, E.S. Abdel-Halim, J.J. Zhu, *ACS Appl. Mater. Interfaces* 6 (2014) 2858–2864, <https://doi.org/10.1021/am405305r>.
- L. Zhu, G. Ganes, H. Chen, K. Chingia, R. Zenobi, *Chem. Commun.* 5 (2009) 559–561, <https://doi.org/10.1039/B816541G>.
- Q. Lu, J. Zhao, S. Xue, P. Yin, Y. Zhang, S. Yao, *Analyst* 140 (2015) 1155–1160, <https://doi.org/10.1039/C4AN01647H>.
- G. Venkatasami, J.R. Sowa Jr., *Anal. Chim. Acta* 665 (2010) 227–230, <https://doi.org/10.1016/j.aca.2010.03.037>.
- S. Goscinny, V. Hanot, J.F. Halbardier, J.Y. Michelet, J. Van Looc, *Food Control* 22 (2011) 226–230, <https://doi.org/10.1016/j.foodcont.2010.04.032>.
- C.W. Liao, Y.R. Chen, J.L. Chang, J.M. Zen, *J. Agric. Food Chem.* 59 (2011) 9762–9767, <https://doi.org/10.1021/jf201999f>.
- W. Chen, H.H. Deng, L. Hong, Z.Q. Wu, S. Wang, A.L. Liu, X.H. Xia, *Analyst* 137 (2012) 5382–5386, <https://doi.org/10.1039/C2AN55962F>.
- J. Liu, Y. Zhong, J. Liu, H. Zhang, J. Xi, J. Wang, *Food Control* 21 (2010) 1482–1487, <https://doi.org/10.1016/j.foodcont.2010.04.018>.
- L.M. Chen, Y.N. Liu, *ACS Appl. Mater. Interfaces* 3 (2011) 3091–3096, <https://doi.org/10.1021/am200603y>.
- J. Guan, Y.Z. Shen, Y. Shu, D. Jin, Q. Xu, X.Y. Hu, *Adv. Mater. Interfaces* 5 (2021) 2100598, <https://doi.org/10.1021/acami.1c04948>.
- L. Yang, Y.L. Liu, X.X. Ji, C.G. Liu, Y. Fu, F. Ye, J. Taiwan Inst. Chem. Eng. 126 (2021) 173–181, <https://doi.org/10.1016/j.jtice.2021.07.028>.
- Y. Liu, L. Yang, Q. Bai, W. Li, Y. Zhang, Y. Fu, F. Ye, *Chem. Eng. J.* 420 (2021), 129939, <https://doi.org/10.1016/j.cej.2021.129939>.
- Y. Liu, L. Li, M. Yue, L. Yang, F. Sun, G. Xu, F. Ye, *Chem. Eng. J.* 430 (2022), 132756, <https://doi.org/10.1016/j.cej.2021.132756>.
- L. Li, S. Gao, L. Yang, Y.L. Liu, P. Li, P. Ye, Y. Fu, *J. Hazard. Mater.* 404 (2021), 124015, <https://doi.org/10.1016/j.jhazmat.2020.124015>.
- C.H. Lei, X.E. Zhao, S.L. Jiao, L. He, Y. Li, S.Y. Zhu, J.M. You, *Anal. Methods* 8 (2016) 4438–4444, <https://doi.org/10.1039/C6AY01063P>.
- V.V. Halali, C.G. Sanjayan, V. Su. ina, M. Sakar, R.G. Balakrishna, *Inorg. Chem. Front.* 7 (2020) 2702–2725, <https://doi.org/10.1039/D0QI00306A>.
- D.C. Wang, Y. Lei, W. Jiao, Y.F. Liu, C.H. Mu, X. Jian, *Rare Met.* 40 (2021) 3–19, <https://doi.org/10.1007/s12598-020-01623-y>.
- F. Sun, L. Yang, S. Li, Y. Wang, L. Wang, P. Li, Y. Fu, *J. Agric. Food Chem.* 69 (2021) 12661–12673, <https://doi.org/10.1021/acs.jafc.1c05246>.
- F. Zhang, H. Zhong, C. Chen, X.G. Wu, X. Hu, H. Huang, Y. Dong, *ACS Nano* 9 (2015) 4533–4542, <https://doi.org/10.1021/acsnano.5b01154>.
- Y. Wang, M.I. Dar, L.K. Orio, T. Zhang, M. Kan, Y. Li, Y. Zhao, *Science* 365 (2019) 591–595, <https://doi.org/10.1126/science.aaa8680>.
- L.Q. Lu, T. Tan, X.K. Tian, Y. Li, P. Deng, *Anal. Chim. Acta* 966 (2017) 109–114, <https://doi.org/10.1016/j.aca.2017.07.014>.
- X. Chen, C. Sun, Y. Liu, L. Yu, K. Zhang, A.M. Asiri, S. Wang, *Chem. Eng. J.* 379 (2020), 122360, <https://doi.org/10.1016/j.cej.2019.122360>.
- X. Xiang, H. Ouyang, J. Li, L. Fu, *Sens. Actuators B* 346 (2021), 130547, <https://doi.org/10.1016/j.smb.2021.130547>.
- X. Sheng, Y. Liu, Y. Wang, Y. Li, X. Wang, X. Wang, X. Xu, *Adv. Mater.* 29 (2017) 1700150, <https://doi.org/10.1002/adma.201700150>.
- C. Huangfu, L. Feng, *Sens. Actuators B* 344 (2021), 130193, <https://doi.org/10.1016/j.smb.2021.130193>.
- H. Yang, W. Yin, W. Dong, L. Gao, C.H. Tan, W. Li, J. Zhang, *J. Mater. Chem. C* 6 (2020) 14439–14445, <https://doi.org/10.1039/D0CC03510F>.
- J.Y. Sun, P.T. Rabouw, X.P. Yang, X.Y. Huang, X.P. Jing, S. Ye, Q.Y. Zhang, *Adv. Funct. Mater.* 27 (2017) 1704371, <https://onlinelibrary.wiley.com/doi/10.1002/adfm.201704371>.
- Q. Zhong, M. Cao, H. Hu, D. Yang, M. Chen, P. Li, Q. Zhang, *ACS Nano* 12 (2018) 8379–8387, <https://doi.org/10.1021/acsnano.8b04209>.
- Δ.J. Li, E. Hofman, J. Li, A.H. Davis, C.H. Tung, L.Z. Wu, W. Zheng, *Adv. Funct. Mater.* 28 (2018) 1704288, <https://doi.org/10.1002/adfm.201704288>.
- T. Xia, Y. Lin, W. Li, M. Ju, *Chin. Chem. Lett.* 32 (2021) 2975–2984, <https://doi.org/10.1016/j.ccl.2021.02.058>.
- J. Cuan, D. Zhang, W. Xing, J. Han, H. Zhou, Y. Zhou, *Chem. Eng. J.* 425 (2021), 131596, <https://doi.org/10.1016/j.cej.2021.131596>.
- J. Ren, T. Li, X. Zhou, X. Dong, A.V. Shorokhov, M.B. Semenov, Y. Wang, *Chem. Eng. J.* 358 (2019) 30–39, <https://doi.org/10.1016/j.cej.2018.09.149>.
- S. Mollick, T.N. Mandal, A. Jana, S. Pajal, A.V. Desai, S.K. Ghosh, *ACS Applied Nano Materials* 2 (2019) 1333–1340, <https://doi.org/10.1021/acsnm.5b02214>.
- J.H. Cha, K. Noh, W. Yin, Y. Lee, Y. Park, T.K. Ahn, O. Terasaki, *The J. Phys. Chem. Lett.* 10 (2019) 2270–2277, <https://doi.org/10.1021/acs.jpclett.9b00510>.
- Y. Cao, Y. Zhou, Y. Lin, J.J. Zhu, *Anal. Chem.* 93 (2020) 1818–1825, <https://doi.org/10.1021/acs.analchem.0c04717>.
- L. Yang, Y.L. Liu, C.G. Liu, F. Ye, Y. Fu, *J. Hazard. Mater.* 381 (2020), 120966, <https://doi.org/10.1016/j.jhazmat.2019.120966>.
- X.L. Yang, C. Ding, R.F. Guan, W.H. Zhang, Y. Feng, M.H. Xie, *J. Hazard. Mater.* 403 (2021), 123698, <https://doi.org/10.1016/j.jhazmat.2020.123698>.
- J.M. Yang, X.W. Hu, Y.X. Liu, W. Zhang, *Microporous Mesoporous Mater.* 274 (2019) 149–154, <https://doi.org/10.1016/j.micromeso.2018.07.042>.
- L. Guo, Y. Liu, R. Kong, G. Chen, H. Wang, X. Wang, F. Qu, *Sens. Actuators B* 295 (2019) 1–6, <https://doi.org/10.1016/j.smb.2019.05.064>.
- R. Jalili, A. Khataee, M.R. Rashidi, R. Luque, *Sens. Actuators B* 297 (2019), 126775, <https://doi.org/10.1016/j.smb.2019.126775>.
- H.N. Abdelhamid, Δ. Huang, A.M. El-Zohry, H. Zheng, X. Dou, *Inorg. Chem.* 56 (2017) 9139–9146, <https://doi.org/10.1021/acs.inorgchem.7b01191>.
- Z. Zhang, X. Luo, B. Wang, J. Zhang, *ACS Applied Energy Materials* 2 (2019) 2760–2768, <https://doi.org/10.1021/acsaem.9b00098>.
- Δ.C. Kong, J.P. Liao, Y.J. Dong, Y.F. Xu, H.Y. Chen, D.B. Kuang, C.Y. Su, *ACS Energy Lett.* 3 (2018) 2656–2662, <https://doi.org/10.1021/acscenergylett.8b01658>.
- M. Worku, Y. Tian, C. Zhou, H. Lin, M. Chaaban, L.J. Xu, B. Ma, *Sci. Adv.* 6 (2020) eaaz5961, <https://doi.org/10.1126/sciadv.aaz5961>.
- N. Ding, D. Zhou, G. Pan, W. Xu, X. Chen, D. Li, H. Song, *A.C.S. Sustain. Chem. Eng.* 7 (2019) 8397–8404, <https://doi.org/10.1021/acssuschemeng.9b00030>.
- X. Jin, H. Chen, W. Zhang, B. Wang, W. Shen, H. Lu, *Appl. Organomet. Chem.* 32 (2015) e4577.
- J. Tian, Q. Liu, A.M. Asiri, A.O. Al-Youbi, X. Sun, *Anal. Chem.* 85 (2013) 5595–5599, <https://doi.org/10.1021/ac400924r>.
- S. Huang, M. Guo, J. Tan, Y. Geng, J. Wu, Y. Tang, Y. Liang, *ACS Appl. Mater. Interfaces* 10 (2018) 39056–39063, <https://doi.org/10.1021/acami.8b14472>.
- L.H. Jin, C.S. Han, *Anal. Chem.* 86 (2014) 7209–7213, <https://doi.org/10.1021/ac501515f>.



Grafted polymeric organogel using low molecular weight gelator as an effective medium for expulsion and purification of cationic dyes and organic pollutants from contaminated surface water

Kankana Baruah ^a, Riku Dutta ^b, Simanta Doley ^c, Swapan Kumar Dolui ^{a,*}

^a Department of Chemical Sciences, Tezpur University, Napaam, Assam 784028, India

^b Department of Chemical Engineering, Jadavpur University, Kolkata, West Bengal 700032, India

^c Department of Chemistry, Jengraimukh College, Majuli, Assam 785105, India

ARTICLE INFO

Keywords:

Organogel

Absorption capacity

Removal efficiency

Solvent selectivity

Cationic dye adsorption

ABSTRACT

An increase in water pollution is a major concern for the safety of living organisms. The present work revolves around synthesizing an organogel capable of absorbing contaminated pollutants like solvents and removing cationic dyes from water surfaces. The organogel prepared using a LMWG (low molecular weight gelator) was characterized using FT-IR, SEM, NMR, TGA, and XRD spectra. Water contact angle determination was also carried out to observe the hydrophobicity. Swelling kinetics, adsorption isotherm, and intra-particle diffusion model are reported after the respective absorption and adsorption study by the gel. The highest swelling was observed in Acetic acid with swelling of 10 times its original weight. Adsorption of dyes exhibited the highest removal efficiency of 99.35% within 60 min. The organogel holds the capability to reuse dye solutions for up to 10 cycles while also holding the capacity to remove from a binary mixture of dyes. The prepared organogel serves as a potential adsorbent for environmental remediation with the potential of maximum swelling and selectivity for cationic dyes.

1. Introduction

With the advancement in technologies and building up of industries, tainting of aqueous resources has rapidly outgrown in nearby related areas, due to the spillage of pollutants and toxic chemicals onto water bodies as residual entities. The untreated wastewater discharged mostly consisting of organic and inorganic materials among the primary sources is causing threats to the entire ecosystem [1,2]. Although the textile and paper industry [3] has been heavily dependent on dyes imparting colors while emanating more than 80% of effluents [4] as they are vastly depleted onto water surfaces polluting the environment unmitigatedly with toxic extricates causing carcinogenic issues since they are highly water soluble and arduously inseparable [5,6]. Owing to the presence of multiple aromatic rings in the structure of the dyes makes them vulnerable to biodegradability content. Apart from dyes [7,8], industrial dissipation also includes spillage of organic contaminants as solvents

[9–11] while inorganic defilement includes lethal heavy metals [12,13], and hydrocarbons [14,15] creating strenuous activity for eradication of such toxic pollutants [16] as they sustain for a prolonged period affecting aquatic terrestrials polluting the environment [17,18].

Although there appear several approaches for removal including membrane filtration, coagulation and flocculation, exchange method, advanced oxidation process, electrochemical oxidation, and microbial technologies [19–23] however, each of the methods lacks productivity in some or another way as the filtration method requires very high differential pressure along with high-cost repairing. Coagulation in chemical and electrochemical forms requires the addition of chemicals leading to sludge formation whose disposal act as a concern for the environment, while in the ion exchange method, the reducibility of the capacity of exchange and the fluid regenerated contains harmful ions.

Among the above-mentioned process, the physical method of adsorption [24,25], as well as photocatalytic degradation [26,27]

* Corresponding author at: Department of Chemical Sciences, Tezpur University, Napaam, Assam 784028, India.

E-mail address: dolui@tezu.ernet.in (S.K. Dolui).

Table 1
Composition chart of the prepared PACSG gels.

SAMPLE	PVA (mM)	AMPS (mM)	Stearic Acid (mM)	Nature of material	WCA (°)
PACSG-26	0.214	0.34	26.01	Gel	85.2
PACSG-39	0.214	0.34	39.02	Gel	103.2
PACSG-52	0.214	0.34	52.03	Gel	104.6

evidenced to be promising sources for the removal of toxic dye. However, for the photocatalytic process, there persist scavenging materials in the treated water which may trigger threats to the subaquatic species while leading to serious health issues in humans [28,29]. To avoid and mitigate the consequences of this challenge and to provide effective treatment of the generated unproductive scrap products, adsorbent-based systems contribute as a safer initiative in environmental terms since they are widely used for their adequate selectivity [30], highly efficient, effective adaptability [31], easy producibility [32], and eco-friendly with cost-effectiveness [33] materials used. Herein, an organogel has been employed for the selective absorption of organic solvents [34] engendered and the adsorption of discharged dyes (specifically cationic) from contaminated water sources caused by industrial wastes.

Polymers in the form of composites [35–38], activated carbon [39,40], and polymer hybrids [41,42] are widely used for the removal of dye molecules. A soft form of polymer, hydrogel has also been used for removal purpose, however cases with organogel has been rarely reported [43,44]. A solvent-based gel, when dipped in water will infuse less amount of water and bind with the dye molecules through electrostatic attraction and surface adsorption thereby will adsorb more of the toxic pollutants mixed with water rather than hydrogel which might infuse a heavy amount of water, chances of leaving behind toxic molecules. Hence an organogel has been preferred for use in wastewater treatment. With this content, a modification of our previous work, the synthesis of organogel used for the removal of organic solvents from contaminated water sources [45] has further been modified to adsorb dye molecules for the remedial treatment of water resources.

The current work intended on the usage of adsorbent as propitious material for the removal of effluents from untreated wastes by modifying the previous work with the addition of acrylamide-methylpropane sulfonic acid as a co-monomer with methylene-bis-acrylamide as a crosslinker for selective adsorption of cationic species due to the presence of the negatively charged sulfonic group. On experimentation, it was found that apart from favorable absorption of solvents, the organogel was also able to selectively adsorb cationic dyes (crystal violet, gentian violet, ethyl purple) from aqueous solution due to the interaction between the sulfonic group and positively charged species providing a suitable sorbent for water purification. However, this work primarily focuses on the absorption of both solvent and adsorption of cationic dyes from the contaminated water surface. Apart from kinetic equations, isothermic and diffusion models were studied to depict the mechanism of the adsorption procedure.

The significance/novelty of this manuscript lies in the usage of LMWGs. Although its usage has been applied in broad fields for various sectors of industry apart from its usage in environmental remediation [46]. Hence an attempt has been made to make conventional use of LMWG for purification purposes of contaminated sources using octadecanoic acid (commonly known as Stearic Acid) to be used as a LMWG, further grafted and modified for removal of contaminated water bodies such as toxic dyes or harmful organic pollutants using simple and cost-

effective materials, fatty acid and PVA material grafted with AMPS-based organogel as adsorbent with simple condensation method beneficial for sustainable development following its biodegradable and recyclable nature.

2. Experimental section

2.1. Materials

Acrylamidomethylpropanesulfonic acid (AMPS), Methylene bisacrylamide (MBA), and Crystal violet were purchased from Sigma Aldrich. Rankem chemicals provided Methyl violet (Gentian violet B), chloroform, and tetrahydrofuran. Dimethyl sulfoxide (DMSO), methanol, benzene, ethylene glycol, acetic acid, dichloromethane, toluene, and carbon tetrachloride were procured from Merck. Ammonium persulfate (APS) and dimethylformamide (DMF) were brought from SRL while stearic acid (SA) from Loba Chemie Pvt. Ltd. Polyvinyl Alcohol (PVA) (MW:14000) was obtained from Otto (Chemika-biochemika reagents) while p-toluenesulfonic acid (98%) from BDH laboratory supplies and Ethyl violet (ethyl purple) from Himedia. Absolute alcohol was purchased from Helix India. All the chemicals received were of analytical grade and were used as received.

2.2. Preparation of the adsorbent (organogel)

The organogel was prepared by a reaction between PVA, Stearic acid, AMPS along with MBA and oxidant APS. Herein, 0.214 mmol of PVA was stirred with 15 mL of DMSO in a round bottom flask equipped with a thermometer placed over a magnetic stirrer at a temperature of about (80–85) °C. p-TSA was added to the RB along with stearic acid (Table 1) of different concentrations and the mixture was allowed for continuous stirring for 1 h. To the dissolved mixture, subsequently, AMPS (0.34 mM) in correspond to PVA was added. It was proceeded by further addition of a solution of initiator APS (2.6 μM) and cross-linker MBA (0.202 mM) while the reaction was stirred for another 6 h until the formation of a 'gel-like substance appears. The product was washed several times with sodium bicarbonate solution followed by ethanol for neutralization and removal of unreacted components. The obtained gel was dried in a vacuum oven for 72 h at 25 °C (Fig. 1).

2.3. Characterization

The surface morphology of the adsorbent was investigated using a scanning electron microscope modeled JSM-6390 LV, JEOL equipped with an energy-dispersive X-ray detector. FT-IR spectra of the adsorbent were recorded using Nicolet Impact-410 IR (Matsen, UK) spectrophotometer within frequency ranging from 4000 to 400 cm^{-1} with samples on KBr pellets. ^{13}C NMR spectra for chemical structure determination were confirmed using a JOEL FT-NMR spectrometer. XRD analysis for layered spacings of the adsorbent was analyzed using D8 FOCUS, Bruker AXS powder XRD diffractometer with Cu K α radiation ($\lambda = 0.154 \text{ nm}$) at an incidence angle of 2θ ranging between 10° to 80° . Thermal stability of the adsorbent was monitored by TGA analysis using NETZSCH TG209 F1 Libra® with purge gas as nitrogen flowing at a rate of 20 mL/min. The heat flow associated with transitions of the adsorbent was determined using NETZSCH DSC 214Polyma. Water Contact angle (WCA) determination was done using KYOWA Interface Measurement and Analysis System (FAMAS). Quantitative determination of the analytes was performed using UV-Vis spectrophotometer SHIMADZU UV-2600L.

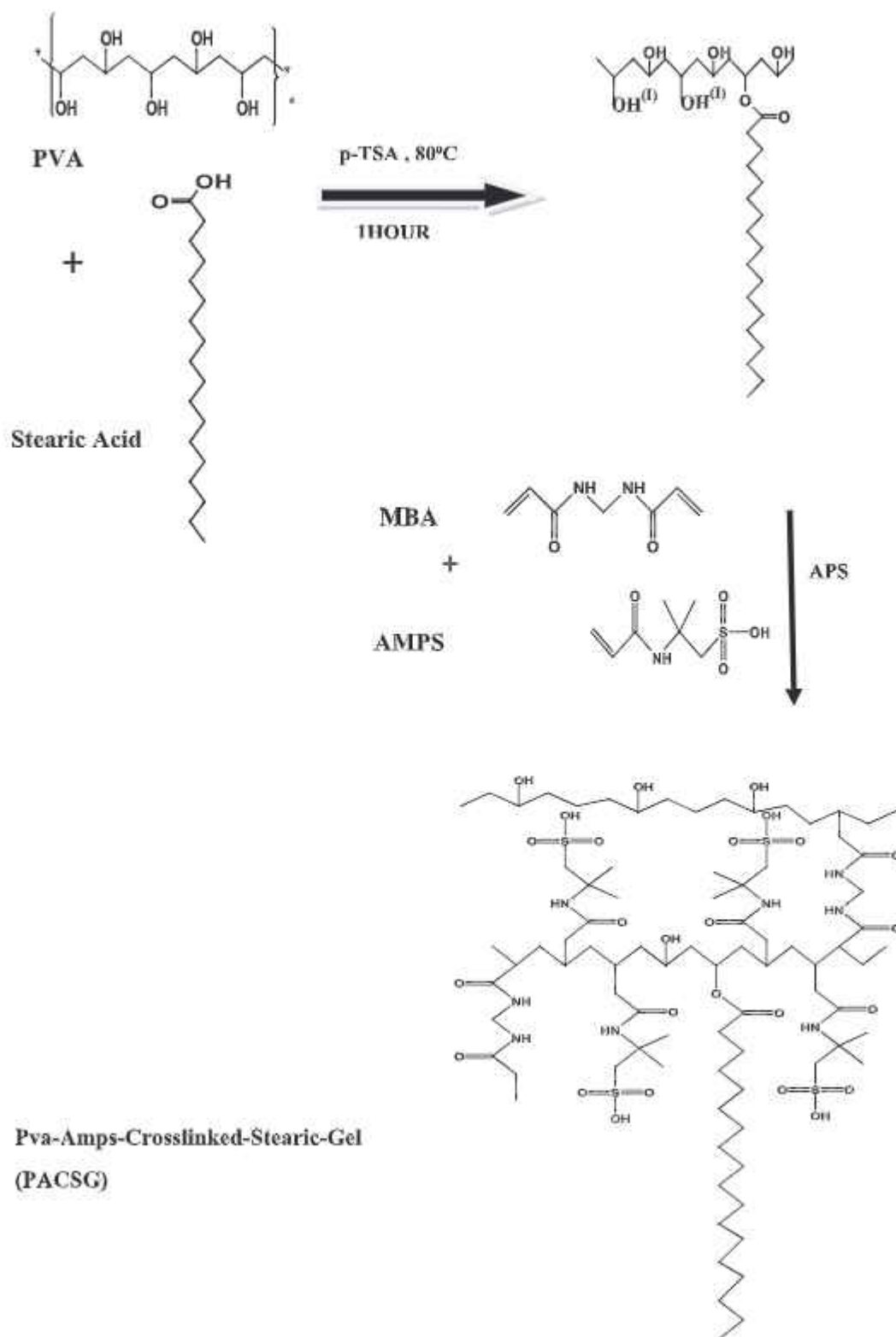


Fig. 1. Plausible structure of the cross-linked organogel PACSG.

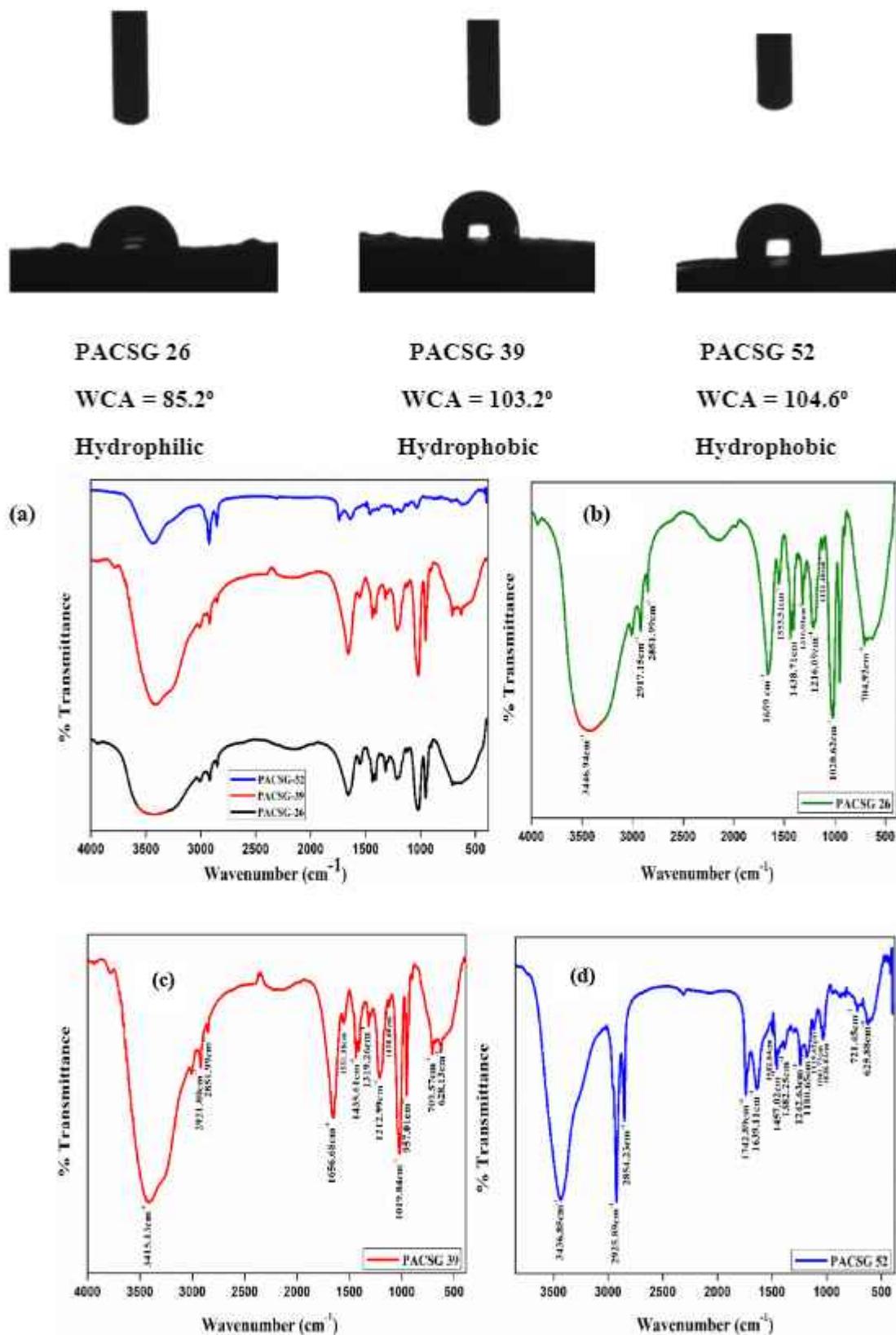


Fig. 2. FT-IR spectra of (a) the prepared PACSGs, (b) PACSG-26, (c) PACSG-39, (d) PACSG-52.

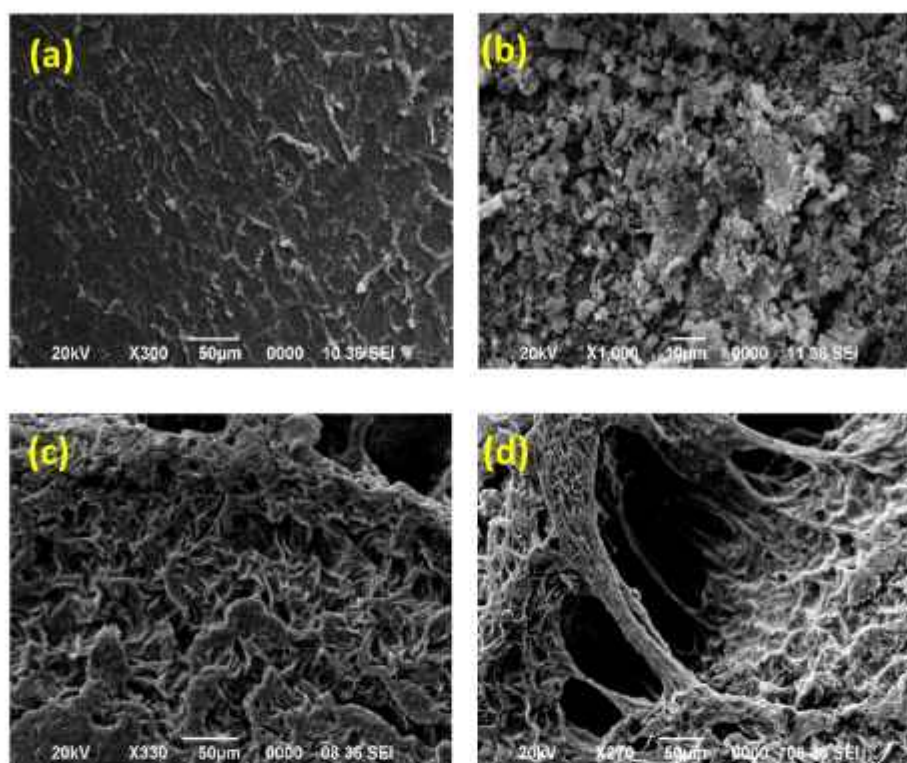


Fig. 3. SEM micrographs of (a) PVA, (b) AMPS, (c) PACSG, (d) cross-linked pores of PACSG.

3. Results and discussions

3.1. Preparation and characterization of the adsorbent

PVA reacts with stearic acid through an esterification reaction. With the addition of AMPS and MBA, it forms a cross-linked structure. The nature of part of the gel is hydrophobic due to stearic acid however, the other part is hydrophilic with the addition of ionizable AMPS, along with MBA as a crosslinker. This cross-linked inter-penetrating network of the gel gets enlarged, opening pores inside the gel matrix and making space available for entrapping solvents. The interweaving of the sulphonic groups also creates hydrophilic centers inside the matrix of the gel along with anionic sites capable of adsorbing cationic species resulting in the increase of swelling as well as adsorption ability. The gel thus consists of balanced nature of both hydrophobic as well as hydrophilic character. The presence of the sulphonic group greatly enhances the adsorption ability of the adsorbent. It was also observed that while increasing the stearic acid content in the organogel, the water contact angle (WCA) seemed to increase drastically from a hydrophilic PVA chain to a hydrophobic state of gel formation (Images can be viewed below).

The synthesis of the prepared organogel was verified by FT-IR spectra determination as shown in Fig. 2. The characteristic peak assigned at 1639.11 cm^{-1} is due to the C=O vibrational stretching of MBA and AMPS grafting onto the PVA backbone while 1502.84 cm^{-1} refers to the N-H bending of the amine. The absorption peak at 1242.63 cm^{-1} refers to the C-N group while frequencies at 1180.65 cm^{-1} and 1041.73 cm^{-1} are due to the asymmetric and symmetric group of the SO_3H group. 1382.25 cm^{-1} and 1026.84 cm^{-1} refers to the S=O and S-O stretching of the sulfonic group [47]. Peaks at 1742.89 cm^{-1} and 1119.42 cm^{-1} contributed to the C=O stretching and C-O stretching of

the formed ester group. The broad peaks at 3436.85 cm^{-1} are due to the overlapping of the O-H and N-H groups with strong hydrogen bonding. Obtained peaks at 225.89 cm^{-1} , 2854.23 cm^{-1} , and 1457.02 cm^{-1} prefers the stretching of CH_3 and CH_2 groups along with bending vibration of C-H thus confirming the structural formation. Fingerprint region peaks at 721.45 cm^{-1} and 625.88 cm^{-1} are attributed to the cis and trans bending of C-H.

Corresponding images for the morphological structure were investigated using SEM. As shown in Fig. 3a, the pristine PVA indicated an unvarying structural feature while that of AMPS (Fig. 3b) consisted of some bristle-like arrangement which however on reaction with MBA transformed into a rough framework with further deposition of stearic acid. Grafting of AMPS led to an accumulation of sulfonic groups on the surface which was not observed in our previous work. However, the opening of porous surface and cross-linking sites were observed on the insertion of MBA as a cross-linker conferring an insight onto the morphological study of organogel. EDX spectra of the organogel with elemental percentage are described in Fig. S1 (Supplemental file).

The ^{13}C NMR spectra of the organogel PACSG-52 were analyzed and the results are described in Fig. S2 (Supplemental file). The values of chemical shift at $\delta = 14.1\text{ ppm}$ (a) and 29.6 ppm (d) correspond to the carbon related to CH_3 and CH_2 groups of the PVA chain as well as the aliphatic chain, while values at $\delta = 26.4\text{ ppm}$ (b) and 27.3 ppm (c) refer to the methyl groups of AMPS and the carbon through which AMPS is linked to the PVA chain. δ value at 27.4 ppm (e) attributes to $\text{C}(\text{C}=\text{O})\text{CH}_2$ of the crosslinking MBA group. The values at $\delta = 32.7\text{ ppm}$ (f) and 34.2 ppm (g) are due to the carbon through which MBA is linked to the PVA chain and of the methylene group related to the carbonyl group of stearic acid in $\text{C}(\text{C}=\text{O})\text{H}_2$. The shift at $\delta = 40.8\text{ ppm}$ (h) refers to the methylene group of the PVA chain, $\delta = 43.1\text{ ppm}$ (i) refers to carbon C $(\text{CH}_2)_2(\text{C})\text{NH}$ in the AMPS chain, and $\delta = 43.2\text{ ppm}$ (j) refers to the

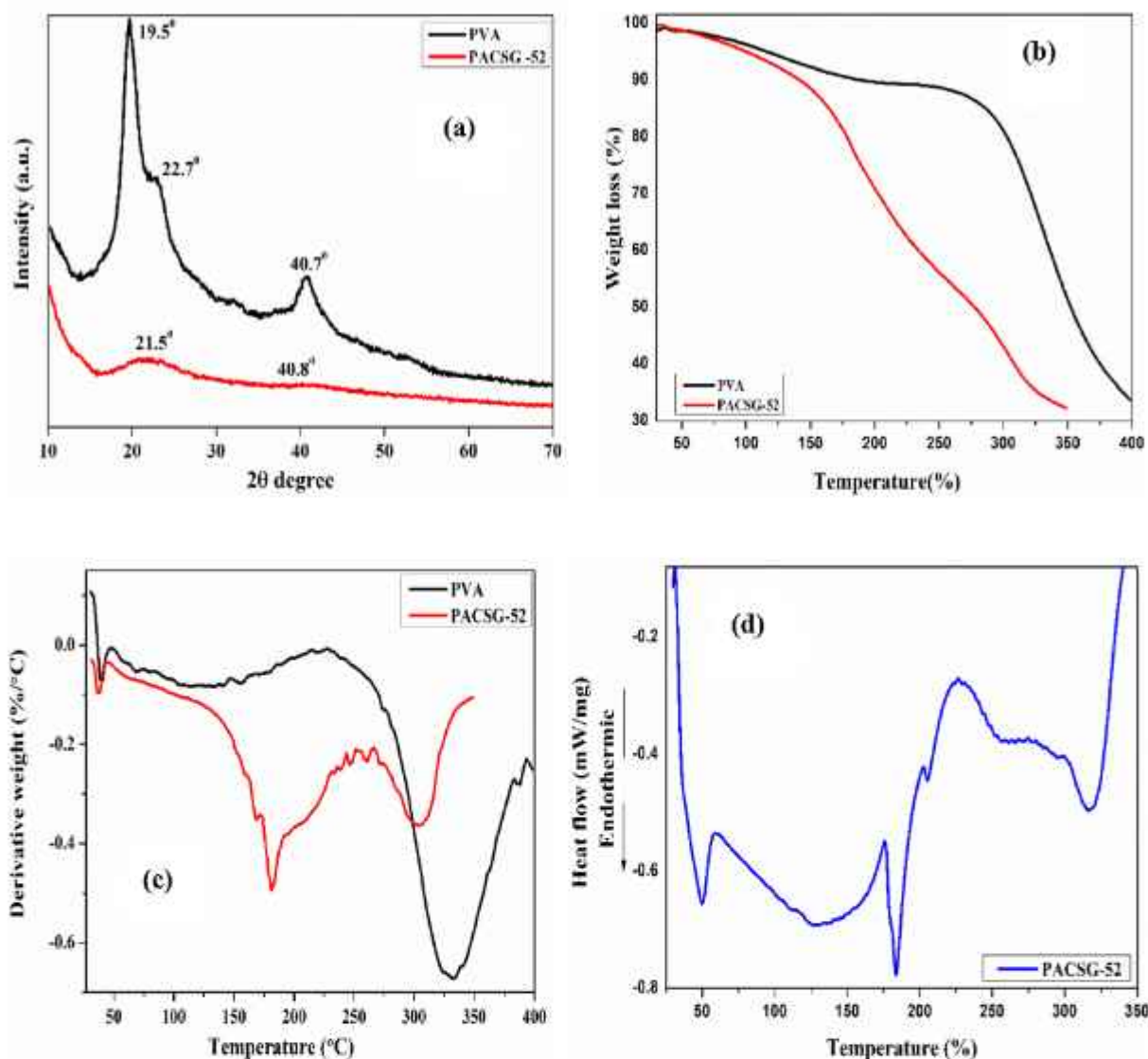


Fig. 4. (a) XRD spectra, (b) TGA thermogram, (c) DTG curve, (d) DSC plot of PACSG-52.

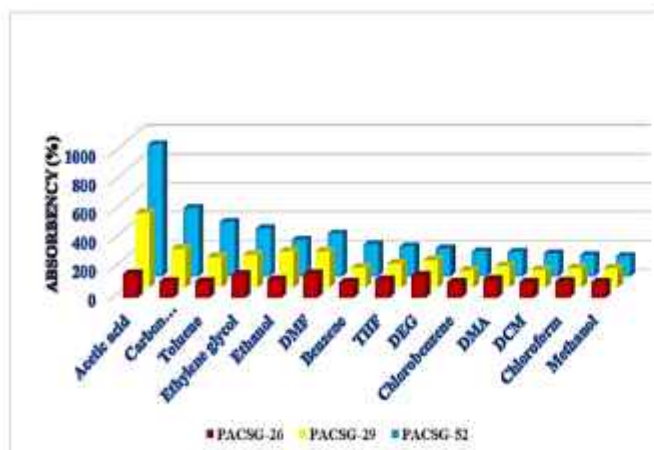


Fig. 5. Swelling analysis of the prepared PACSG-26,39,52 gels.

carbon linked to PVA chain and C = O of the AMPS group. δ value at 53.4 ppm (k) and 66.6 ppm (l) corresponds to carbon linked to the sulphonic group in AMPS. The chemical shift at $\delta = 170$ ppm (m) corresponds to the carbonyl group in the AMPS group and MBA chain as both the carbonyl group are attached to methylene and NH group while the shift at $\delta = 178$ ppm (n) refers to the carbonyl ester group formed in the aliphatic stearic acid group. While the chemical shift values ranging from $\delta = (125-140)$ ppm (o) are attributed to the presence of the catalyst, *para*-toluene sulfonic acid was left behind during the formation of the organogel.

XRD data (Fig. 4a) of PVA shows the peak of 2θ degrees at 19.5° , 22.7° , and 40.7° with planes corresponding to (101), (200), and (102) [48]. On further insertion of AMPS, the crystalline nature of PVA diminished to a greater extent. The peaks associated with PVA can be attained from the modified composite based on PVA and magnetite prepared by Modrojan et al. [48]. The broad peak with the plane (102) observed around 40.7° in PVA-SA interaction was seen to diminish indicating an extreme amorphous nature of the gel.

The thermal stability was characterized using TGA (Fig. 4b). Pristine PVA observed degradation around 320°C which can be perceived from a PVA-based organogel [45] however PVA-SA was seen around 220°C . Although on further addition of AMPS to the PVA chain, the degradation

Table 2
Absorption capacities for prepared PACSG organogels.

SOLVENTS	DIELECTRICCONSTANT (ϵ')	POLARITY	PACSG-26	PACSG-39	PACSG-52
Acetic acid	6.2	Polar protic	165.66	514.37	914.49
Carbon tetrachloride	2.6	Non-polar	112.70	266.12	474.5
Ethylene glycol	37.0	Polar aprotic	160.63	327.56	393.20
Toluene	2.38	Non-polar	111.39	209.41	377.73
DMF	36.7	Polar aprotic	168.62	247.63	297.28
Methanol	32.6	Polar protic	130.76	140.5	282.71
Ethanol	24.5	Polar protic	128.40	134.50	248.38
DEG	31.70	Polar aprotic	186.36	192.38	228.66
Benzene	2.27	Non-polar	108.74	135.49	222.49
THF	7.58	Non-polar	126.54	164.3	207.4
DCM	8.93	Non-polar	118.42	158.13	200.84
Chloroform	4.61	Non-polar	132.52	148.88	199.58
Chlorobenzene	5.62	Non-polar	108.75	115	171.62
DMA	4.40	Non-polar	128.3	147.43	167.64

*<https://cem.com/cn/microwave-chemistry/solvent-choice>.

*http://dept.washington.edu/eooptic/linkfiles/dielectric_chart%5B1%5D.pdf.

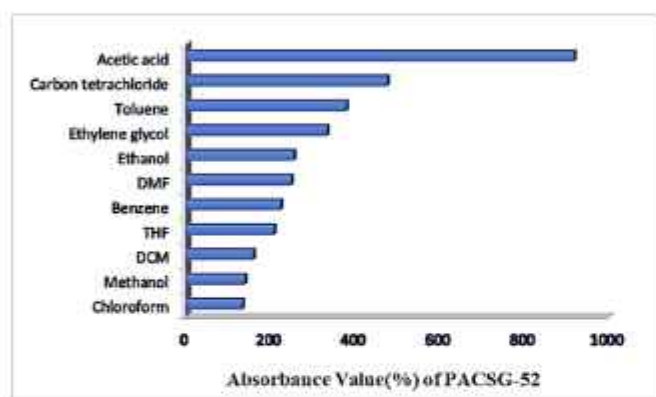


Fig. 6. Swelling behavior observed in PACSG-52.

rate increased due to lower blending stability between PVA and bulky AMPS group. However, the first degradation was seen around 167.63 °C which further decreased down to 273.27 °C due to evaporation or decomposition of SO₂ and SO₃ groups [49]. The next degradation around 328.36 °C was due to the breaking of the PVA chain.

From the DTG curve (Fig. 4c), it can be perceived that dual-step weight loss was attained. The first melting temperature was observed

around 182.32 °C which however observed an early degradation due to the decomposition of functional groups present. A slight decrease around 254.05 °C was due to the breakage of cross-linking bonds. Nonetheless, the second weight loss of around 304.74 °C was due to the splitting of PVA bonds.

Fig. 4d demonstrates the DSC curves which indicated the T_{max} temperature at 184.49 °C due to the onset of thermal degradation of PVA-AMPS while a lower drop around 127.30 °C was observed due to loss of water molecules. Deterioration of cross-linking bonds was observed around 258.79 °C which further correlates with TG and DTG curves.

Table 3
Parameters for first and second-order kinetic models.

SAMPLE	pseudo-first-order kinetics model			pseudo-second-order kinetics model		
	k ₁ (min ⁻¹)	Q _{max} (gg ⁻¹)	R ²	k ₂ (gg ⁻¹ min ⁻¹)	Q _{max} (gg ⁻¹)	R ²
PACSG-26	4.479 × 10 ⁻⁴	0.275	0.88	0.238 × 10 ⁻⁴	2.796	0.96
PACSG-39	2.833 × 10 ⁻⁴	0.823	0.85	2.99 × 10 ⁻⁴	0.767	0.98
PACSG-52	3.819 × 10 ⁻⁴	0.631	0.92	1.96 × 10 ⁻⁴	0.832	0.97

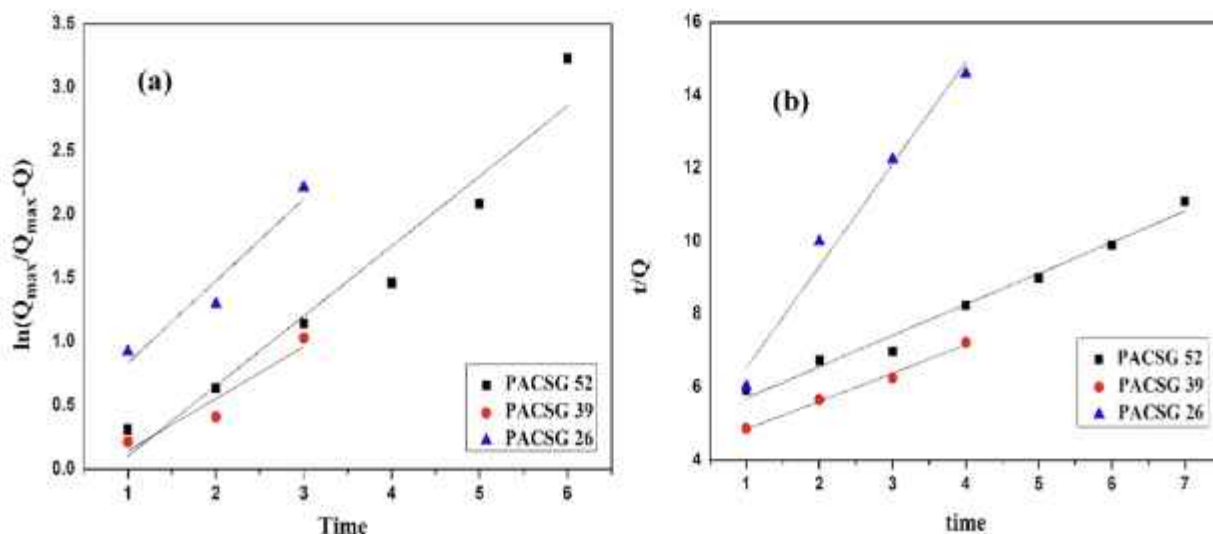


Fig. 7. Plot for (a) first order, (b) second order kinetics graph of PACSG-52 gel.

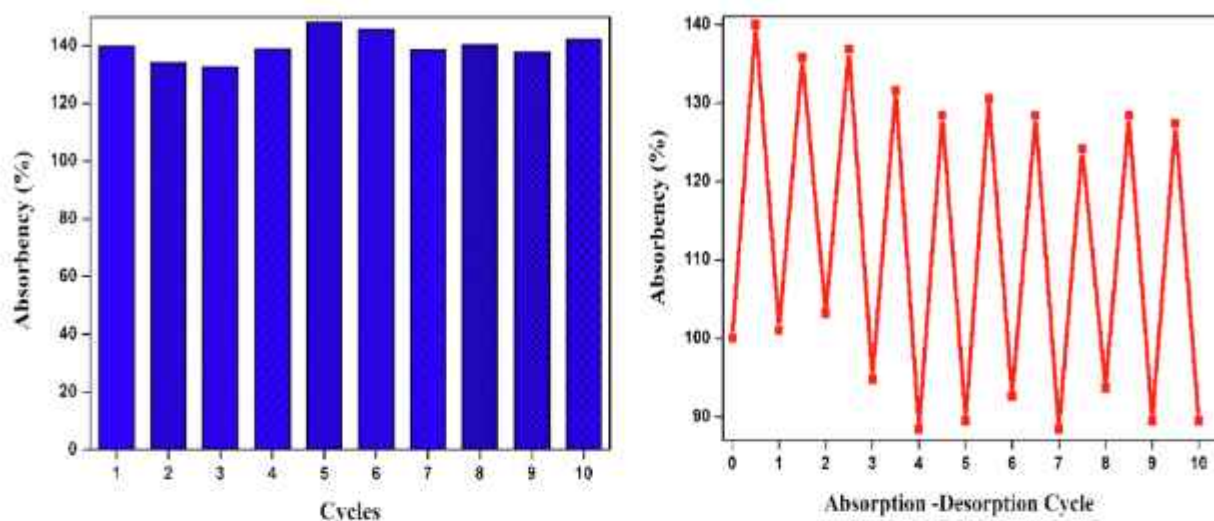


Fig. 8. Recyclability data: (a) Solvent absorbance percentage with each cycle, (b) Absorption-desorption cycle of the solvent.

Table 4
Removal efficiency of dyes with concentration before and after removal.

Adsorbate	Concentration before adsorption (M)	Concentration after adsorption (M)	Removal Efficiency (%)
Crystal Violet	3.24×10^{-5}	0.16×10^{-5}	95.06
Ethyl Violet	3.10×10^{-5}	0.02×10^{-5}	99.35
Methyl Violet	3.32×10^{-5}	0.24×10^{-5}	92.71

3.2. Swelling analysis

The structure demonstrated in Fig. 3d obtained from SEM images alluded to the entrapment of organic solvents inside the gel matrix. The uptake of different organic solvents with varying polarities such as acetic acid, carbon tetrachloride, toluene, ethylene glycol, ethanol, dimethylformamide, benzene, tetrahydrofuran, diethylene glycol, chlorobenzene, dimethylaniline, chloroform along with methanol was investigated by the prepared cross-linked gels PACSG (26,39,52) as shown in Fig. 5.

However, among the three, PACSG-52 displayed excellent swelling behavior of organic solvents. The results of which are displayed in Table 2 and Fig. 6.

The gels can absorb both polar and non-polar solvents as the gel possess dual functional groups of being hydrophobic for the stearic group and hydrophilic for the sulfonated group. It was ascertained from the swelling studies that the organogel swelled maximal in acetic acid for all the sets. The highest absorbance was exhibited by set PACSG-52 with swelling of more than 900% for acetic acid while carbon tetrachloride, toluene, ethylene glycol, and dimethyl formamide exhibited swelling in the range of 500–300% whereas ethanol, benzene, tetrahydrofuran, diethylene glycol, chlorobenzene, dimethyl aniline, dichloromethane, chloroform, and methanol lies in the range 250–150%.

However, the absorption values of solvents can be correlated with both the dielectric constant values as well as the polarity of the organic solvents as they can simultaneously absorb both polar as well as non-polar solvents. Lower dielectric values denote a lesser ability to

stabilize the charges present resulting in the probability of dipole-dipole interaction between sorbent and acetic acid being observed to be higher than those of dipole-induced dipole interaction in non-polar solvents or the involvement of hydrogen bonding in polar protic solvents.

3.3. Swelling kinetics of solvent

The solvent absorption efficiency of organic solvents onto the sorbent was investigated by a kinetic study using equations (v) and (vi) (Supplementary file). The swelling kinetics of the prepared set of gels were evaluated considering the solvent of high absorbance, Acetic acid. Fig. 7 displays the linear fitted curves for pseudo-first order and pseudo-second order kinetics models. However, the curves obtained a suitable linear correlation regression value (R^2) from a pseudo-second-order kinetics graph 7b in which the plot of t/Q against time confirmed the absorption of solvents to the sorbent following the second-order model. The correlation coefficient value of 0.98 suggested a similar concordance between actual and experimented values. Values of k_1 , and k_2 along with Q_{max} and R^2 for both models can be procured from Table 3.

3.4. Reusability of solvent

The reusability (absorption and desorption) of the sorbent for solvent was examined using chloroform as the solvent. A certain weight of the sorbent was immersed in the solvent for a period of 24 h. After the completion of 24 h, the swollen gel was allowed to release the solvent from the gel-matrix structure by letting it dry at room temperature. The process was continued for 10 repetitive cycles to study the absorbance efficiency. Fig. 8a depicts the percentage of solvent absorbance with each cycle. The study of recyclability was reported under the absorption and desorption cycle (Fig. 8b) and with each cycle, the absorbed solvent was completely able to desorb and thus regain back its original shape to absorb solvent. Thus, it can be concluded that the sorbent can be regenerated multiple times after the desorption of solvent absorbed by the sorbent which suggests the use of sorbent for further removal of solvent from polluted water sources.

3.5. Dye adsorption

Of the prepared organogels, the one with excessive swelling PACSG-

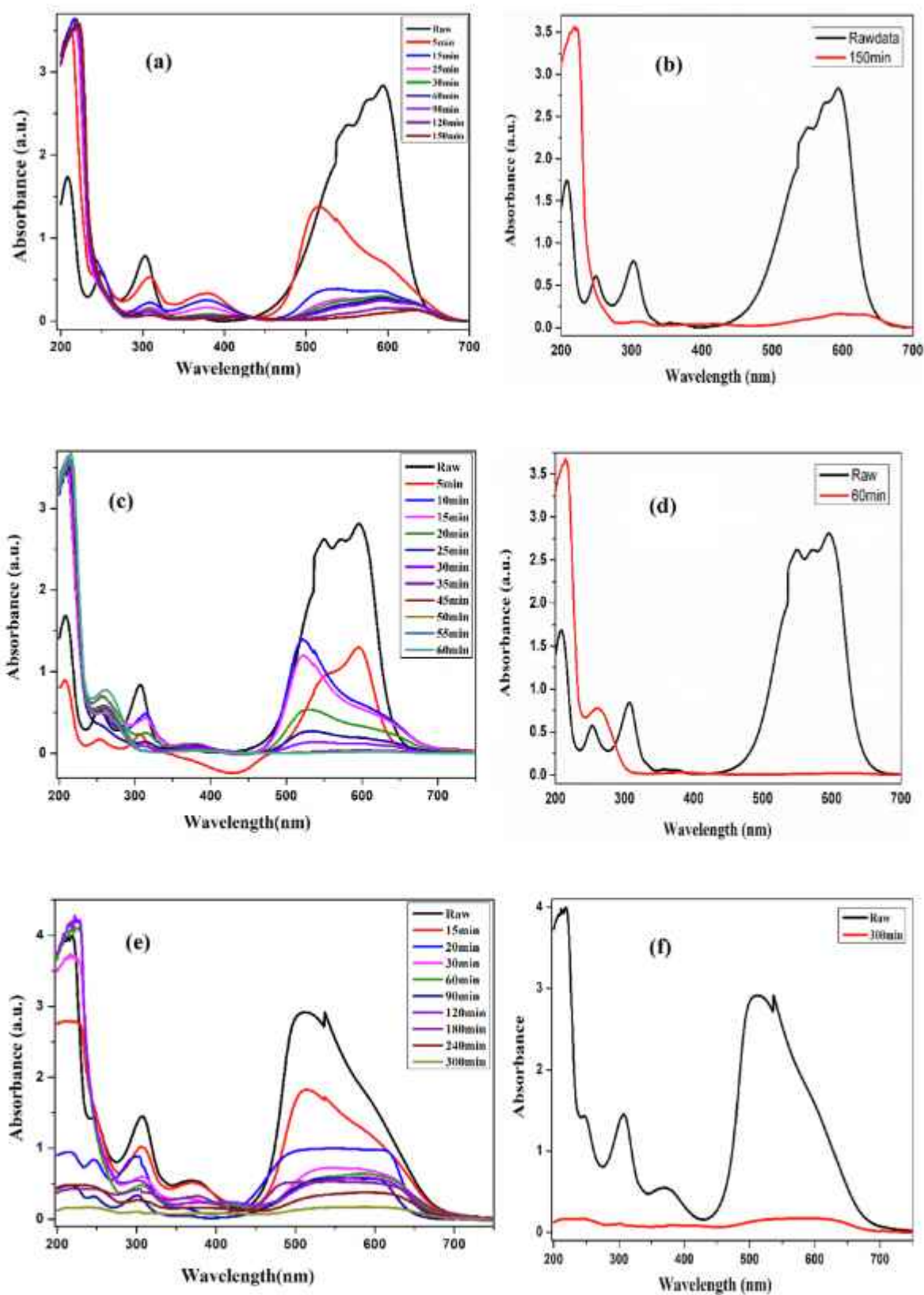


Fig. 9. UV-Vis spectra of the adsorbent with time for (a,b) CV dye, (c,d) EV dye, and (e,f) MV dye.

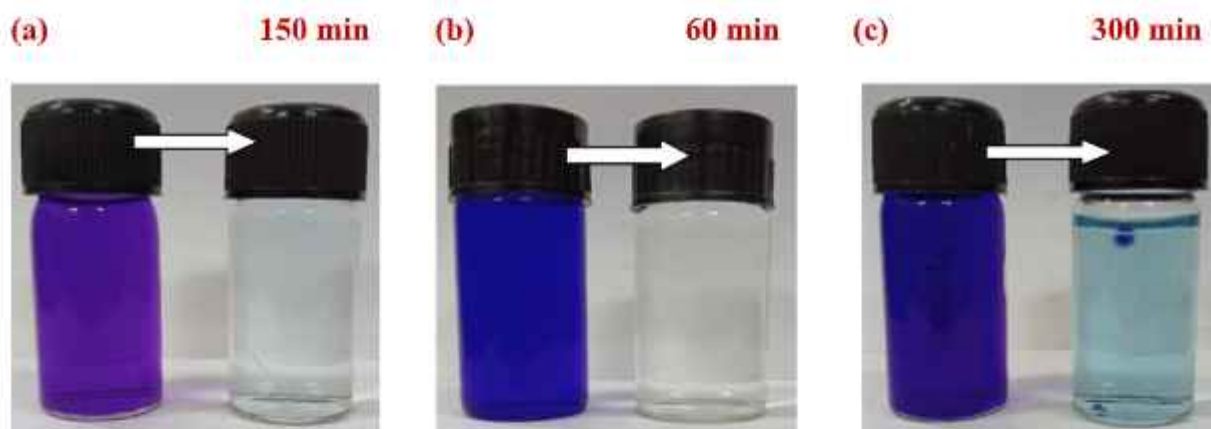


Fig. 10. Digital images of (a) CV, (b) EV, and (c) MV dyes before and after removal by the adsorbent.

52 was chosen as sorbent for adsorption of cationic dyes CV, EV, and MV. The adsorption of dyes concerning time was recorded via UV-Vis spectroscopy, where it was seen that after the insertion of sorbent into the dye solution, the concentration of dyes gradually decreases with an increase in time.

It can be concluded from Table 4 that the uptake of Ethyl violet was the maximum out of the three selected cationic dyes. The presence of negatively charged sulfonic groups present in the gel-matrix acts as an active site for interaction with cationic polluted dyes speeding up the adsorption rate. It can be perceived from the UV plot (Fig. 9) that the sorbent can adsorb EV dye and the change of color can be noticed within 60 min while that of CV in 150 min and MV in 300 min respectively. Images of dye, before and after removal by the adsorbent can be obtained from Fig. 10.

The removal efficiency includes 99.35% for EV dye, 95.06% for CV, and 92.71% for MV dye (Table 4). The quicker removal can be explained due to the involvement of the easily ionizable sulfonic group in abundance as active sites reacting with imine groups present in the dyes interacting electrostatically along with the involvement of hydrogen bonding.

The presence of porous sites acts as an addendum for the entrapment of dye molecules within the sorbent matrix. As can be perceived from the morphological data that the initial structure of the organogel varied from the dye-adsorbed SEM images (Fig. 11a-c). It can be vividly seen that a thick layer has been deposited over the initial surface which is due to the accumulation of dye molecules on the surface of the sorbent. Significant changes were also observed from the dye-adsorbed FT-IR spectrum (Fig. 11d-f). Due to the formation of the N-O bond as a result of the interaction between the SO_3^- and N^+ (R_2) group of the dye molecules, stretching vibrations occurs around $1550\text{--}1540\text{ cm}^{-1}$. The stretching frequency of the S=O and S-O bond also shifts to a lower wavenumber around $1050\text{--}850\text{ cm}^{-1}$ (based on the three dyes) due to the reaction between the dye and the sorbent.

A comparative study of different dye adsorbed gels compared to the current work has been shown in Table 8.

3.6. Kinetics of adsorption

The adsorption efficiencies and time dependence of the adsorption process of the respective dyes obtained from the experimental data were evaluated using kinetics models (v) and (vi) (Supplementary file) to study the interaction between sorbent and the dye molecules. Rate

constants were studied using plots $\ln(q_e - q_t)$ vs time and t/Q_t vs time, where it was observed that the adsorption of the dyes (CV, EV, MV) in plot t/Q_t vs time provided a linear fitted relation. Thus, it can be conferred that the kinetic and correlation coefficient (R^2) is best suited to the pseudo-second-order model for the adsorption of the dyes onto the sorbent, acting as a rate-limiting step between the sorbent and the dye molecules. The value for regression coefficient (R^2) was seen to be the highest (0.99) for all the three experimented dyes. Hence, kinetic adsorption of cationic dyes was better presaged using second order kinetics model. Attainment of equilibrium sites however proved that all of the active sites had been fully employed for adsorption by cationic dyes.

Fitted kinetics plots for the dyes were displayed in Fig. 12 while the respective kinetic parameters can be obtained from Table 5.

3.7. Adsorption isotherm

The interaction action between equilibrium adsorption capacity and equilibrium concentration was evaluated using Langmuir Isotherm(vii), Freundlich Isotherm(viii), and Temkin Isotherm(ix) models in their non-linear forms as it furnishes a complicated procedure for determination of kinetic parameters circumventing the complications of linearization (Fig. 13). The correlation coefficients (R^2) along with their respective parameters of the proposed isothermic models were obtained from Table 6 which, however, suggested that the regression coefficient for the Langmuir model was founded to be close to 1 in comparison to Freundlich and Temkin models in addition to the remarkable fitting of the curve with the experimental data. The results of R^2 and the lower separation factor (R_L) values from Langmuir isotherm suggest that the process of adsorption between sorbent and dye molecule involves a chemisorption process since the value of $R_L \leq 1$ which effectively describes the better affinity between adsorbate and the sorbent leading to deposition of a monolayer on the surface of the sorbent revealing the presence of strong electrostatic attraction between adsorbent and adsorbate.

3.8. Mass transfer model

The adsorbate can be transported from the aqueous phase to the sorbent through the intra-particle diffusion model(x) of Weber and Morris. The intake of dyes on the surface of the sorbent was executed using the model as shown in Fig. 14. It can be interpreted from the diffusion plot of q_t vs $t^{1/2}$ that it exhibited a multi-stage sorption process.

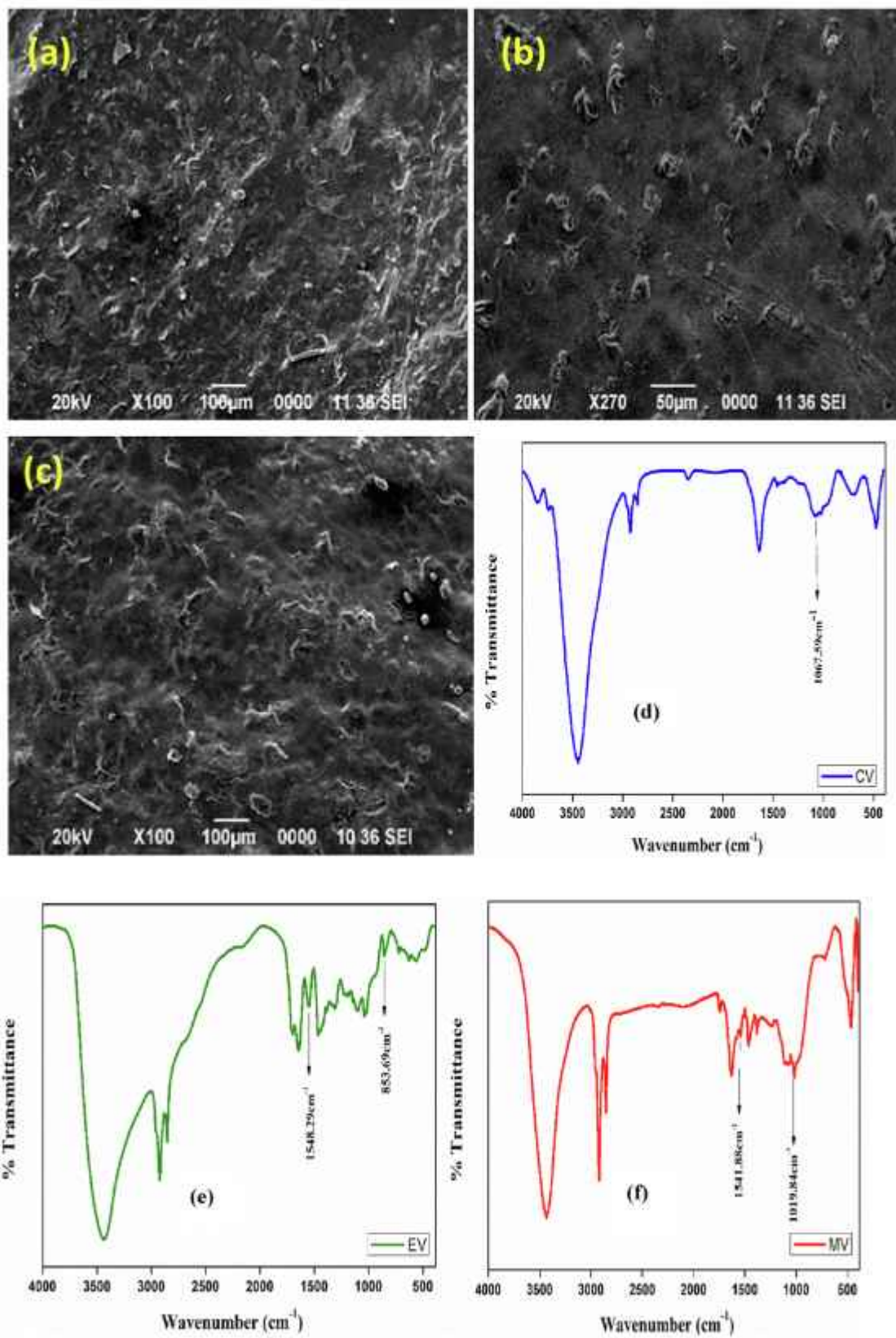


Fig. 11. SEM images of the adsorbent after removal of (a)CV, (b)EV, (c) MV dye, FT-IR spectra of the adsorbent after dye removal for (d)CV, (e) EV, and (f) MV dye.

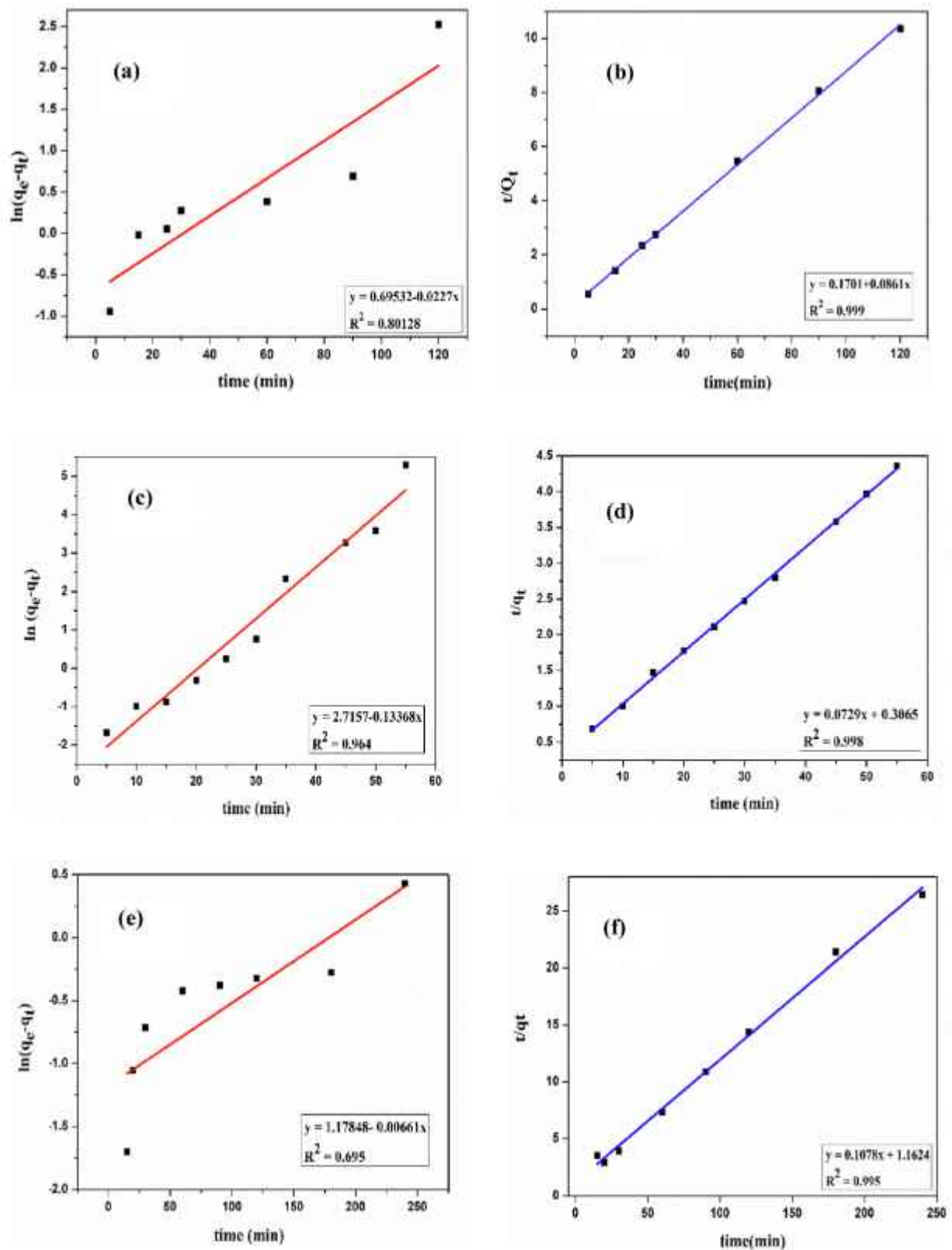


Fig. 12. First-order kinetics graph (a,c,e) and second-order kinetics graph (b,d,f) for CV, EV, and MV dyes.

Table 5
Kinetic parameters for first and second-order kinetics plot for adsorbed dye.

SAMPLE	pseudo-first order-kinetics model		pseudo-second-order-kinetics model		
	k_1 (min^{-1})	R^2	k_2 ($\text{gg}^{-1}\text{min}^{-1}$)	q_e (gg^{-1})	R^2
CV	4.63×10^{-2}	0.801	8.51×10^{-2}	11.67	0.999
EV	2.22×10^{-2}	0.964	8.61×10^{-2}	12.38	0.998
MV	3.92×10^{-2}	0.695	9.79×10^{-2}	9.68	0.995

In the very first step, a rapid increase has been detected due to the diffusion of the cationic dye molecules from the solution to the external boundary of the sorbent and then to the interior surface through boundary thickness. Meanwhile, the second step denotes the incremental stage of adsorption followed by the third step where with the increase in time, accumulation of molecules occurs at sites lowering the diffusion process until it attains an equilibrium position.

As obtained from the three graphs (Fig. 14), the value for EV was seen to be highest at equilibrium with 12.64 mg/g, while 10.71 mg/g for CV and 9.1 mg/g for that of MV (which correlates with the value obtained from Table 5 for q_e). Parameter C relates to the thickness of the boundary layer; as with the increase in intercept, the boundary layer increases (Table 7). The diffusion rate follows the order K_{1d} ($EV > CV > MV$) accordingly with the fast absorbance of the dye onto the sorbent.

Since cationic dyes are conventionally basic dyes, consequently after adsorption of the respective dyes, the adsorbent will be able to emancipate the adsorbed dye on treatment with an acidic solution. Ensuring the drying of the sorbent, it can be again re-used for further adsorption of dyes demonstrating its reusable properties.

3.9. Mechanism of adsorption

The mechanism for dye adsorption, observed in the experiment is greatly carried out through the chemisorption process as the deposition of monolayer surface can be observed. As observed from Fig. 15, along with the chemical interactions, there prevails hydrogen bonding between Nitrogen and Hydrogen, Oxygen and Hydrogen, between the aromatic ring of the dye and methyl groups present in the adsorbent which further helps in the swelling/adsorption process.

While the most important antecedent for the occurrence of adsorption is the electrostatic interaction between the negatively charged groups of the sorbent with the cationic dye molecule. The mechanism has been discussed in detail for further analysis.

The adsorption process of the sorbent includes three stages for the dyes.

- (i) At first, there occurs the movement of dyes in the aqueous phase toward the sorbent surface.
- (ii) Secondly, the diffusion of dyes from the outer surface through the pores to the inner surface
- (iii) Thirdly, the adsorption of dye ensues at the active sites of the sorbent via electrostatic interaction until the attainment of the equilibrium position.

3.10. Study of mixed dyes

Dye industrial effluents contain both cationic as well as anionic dyes as their discharge components. Since the prepared sorbent has responded to the adsorption of cationic dyes as per experimental results, an attempt has been made to explore its efficacy in the presence of mixed dyes. Three anionic dyes Congo Red, Eriochrome Black T, and Methyl Orange were used to prepare a binary solution with the most efficient

Ethyl Violet dye with a concentration of 40 mg/L each mixed in a 1:1 ratio. Fig. 16(a-c) shows the UV-Vis spectrum of the three different mixed dyes. From the spectra, it can be interpreted that in each of the three cases, the sorbent was completely able to remove cationic dye with partial removal of the anionic species. This can be predicted from the Ethyl Violet – Methyl Orange solution (Fig. 16c) where the EV was adsorbed up to 97.29% while MO received a removal percentage of 48.64%. While in the case of EV-CR and EV-EBT solutions (Fig. 16a-b), the removal was not distinguished due to the shifting and merging of the peaks of the mixed dyes. Thus, the sorbent can be termed as a compelling one for the removal of dye effluents from wastewater with an advanced affinity towards cationic dyes.

3.11. Reusability

For reasonable claims to be used for industrial purposes, the recyclability and stability of the adsorbent are observed as a substantial factor. Here, a dye solution of 40 ppm was prepared and 0.5gm of the sorbent was added to 100 mL of the prepared dye solution of Ethyl Violet. After the adsorption of the dye, the clear solution was analyzed using UV-Vis spectroscopy. The clear solution obtained was decanted while the same sorbent was again used in another 100 mL of the dye solution. The cycle was repeated with the same adsorbent about 10 times. From the results obtained in Fig. 17, it can be observed that the same sorbent was able to clear dye solutions besides the removal percentage was almost the same for around 4 cycles after which a slight decrease was detected which was obvious since the sorbent was used repeatedly for 10 cycles without desorption. However, after the 4th cycle, the duration of adsorption slightly increased between 2 and 5 h due to the presence of pre-existed dye molecules. From the attained results, it can be proven that the solvent can act as a prudent and effectual material for the removal of accumulated cationic dyes and is exceedingly beneficial for its use in industrial sectors.

4. Conclusion

Current work revolves around the preparation of an organogel with high absorption and adsorption capacity. The presence of AMPS introduced active sites onto the gel which further cross-linking opened up pores as well as improved adsorption capacity. The gel was able to absorb solvent up to nearly 10 times its original weight while it successfully performed reusability of the solvent up to 10 times. In terms of adsorption, the gel was able to selectively adsorb cationic dyes from polluted water sources with maximum adsorption of 12.68 mg/g, 11.67 mg/g, 12.38 mg/g, and removal efficiency of 99.35% for ethyl violet dye, 95.06% for crystal violet, 2.71% for methyl violet dyes within a timespan of 60 min, 150 min, and 300 min respectively.

The sorbent followed the kinetic mechanism of the pseudo-second-order model while following the Langmuir adsorption isotherm of monolayer deposition of particles using the chemisorption process. It also went through a time-dependent intra-particle diffusion model which prove to be one of the rate-determining steps in the process.

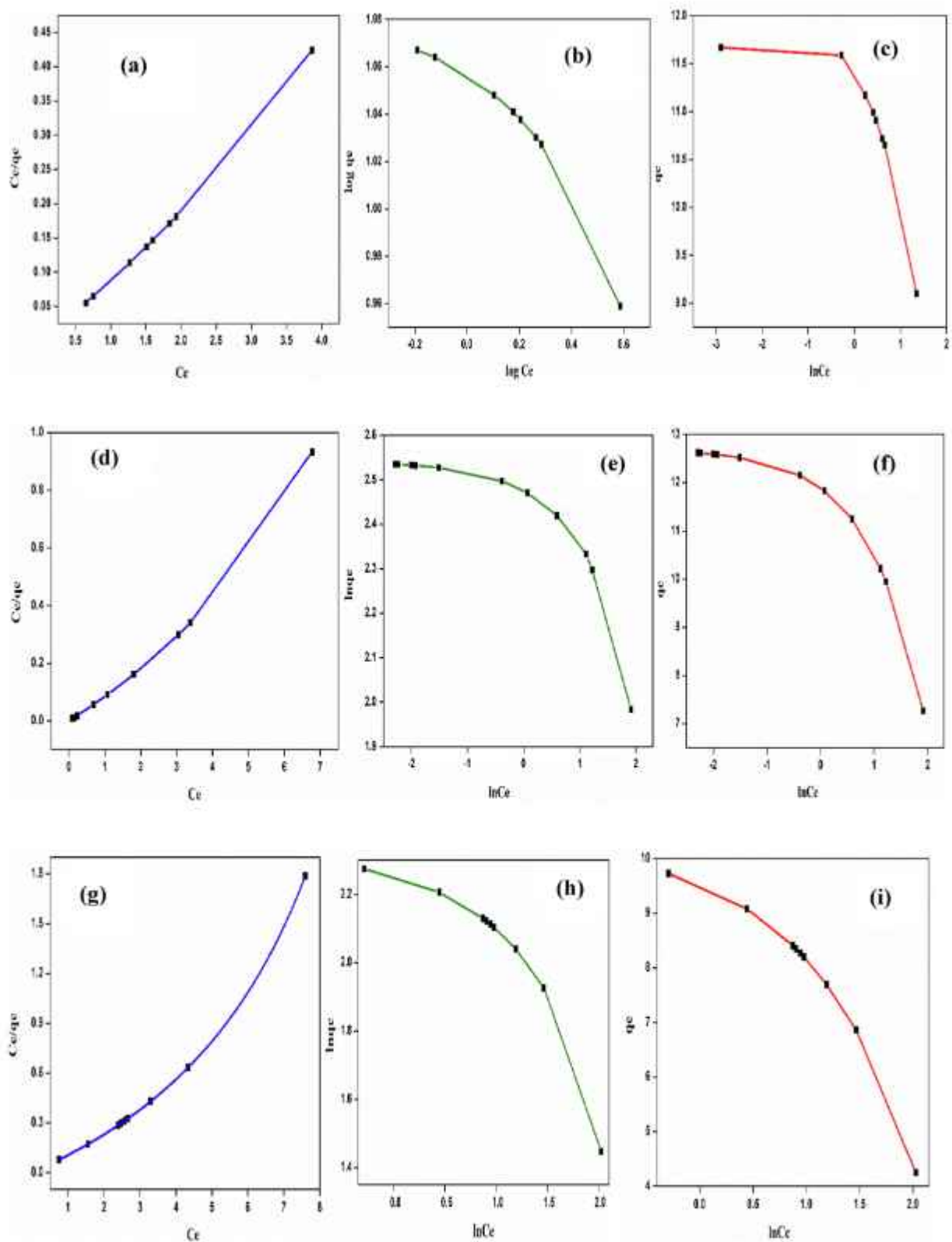


Fig. 13. The plot of C_e/q_e vs C_e (Langmuir) for CV, EV, and MV dyes (a,d,g), the plot of $\ln q_e$ vs $\ln C_e$ (Freundlich) for CV, EV, and MV dyes (b,e,h), the plot of q_e vs $\ln C_e$ (Temkin) for CV, EV, and MV dyes (c,f, i).

Table 6
Parameters for adsorption isotherms of the respective dyes.

ISOTHERMS	PARAMETERS	ADSORBATE		
		CV	EV	MV
LANGMUIR	$q_s(\text{mg}\cdot\text{g}^{-1})$	11.67	12.36	9.68
	$K_L \times 10^2 (\text{L}\cdot\text{mg}^{-1})$	3.59	4.05	7.74
	R^2	0.992	0.969	1
	R_L	0.5	0.15	0.56
FREUNDLICH	$1/n$	0.05	0.04	0.24
	$K_F(\text{mg}^{1-1/n}\cdot\text{L}^{1/n}\cdot\text{g}^{-1})$	226.3	224.7	200.36
	R^2	0.85	0.66	0.72
TEMPIN	$A(\text{L}\cdot\text{g}^{-1})$	1.727	6.46E43	2.25E43
	B	0.127	0.10	0.07
	$b_T(\text{J}\cdot\text{mol}^{-1})$	17.75	22.63	29.66
	R^2	0.40	0.74	0.62

However, the mechanism primarily involved electrostatic interaction between adsorbent and adsorbate molecules and dipole-induced dipole interaction for the absorption process. From the mixed solution of dyes, the sorbent successfully removed 97.29% of Ethyl Violet and 48.64% of

Table 7
Parameters for diffusion model of the dyes.

INTRA-PARTICLE DIFFUSION	PARAMETERS	
	k_{id}	C
CV	0.157	10.05
EV	1.067	8.84
MV	0.119	6.47

Methyl Orange. The adsorbent can be recycled up to 10 times without going through a desorption procedure. Thus, making it a potential competitor for solvent removal as well as the removal of harmful dyes through adsorption from contaminated water sources.

CRedit authorship contribution statement

Kankana Baruah: Methodology, Investigation, Writing – original draft. Riku Dutta: Data curation. Simanta Doley: Resources, Visualization. Swapam Kumar Dolui: Writing – review & editing, Supervision.

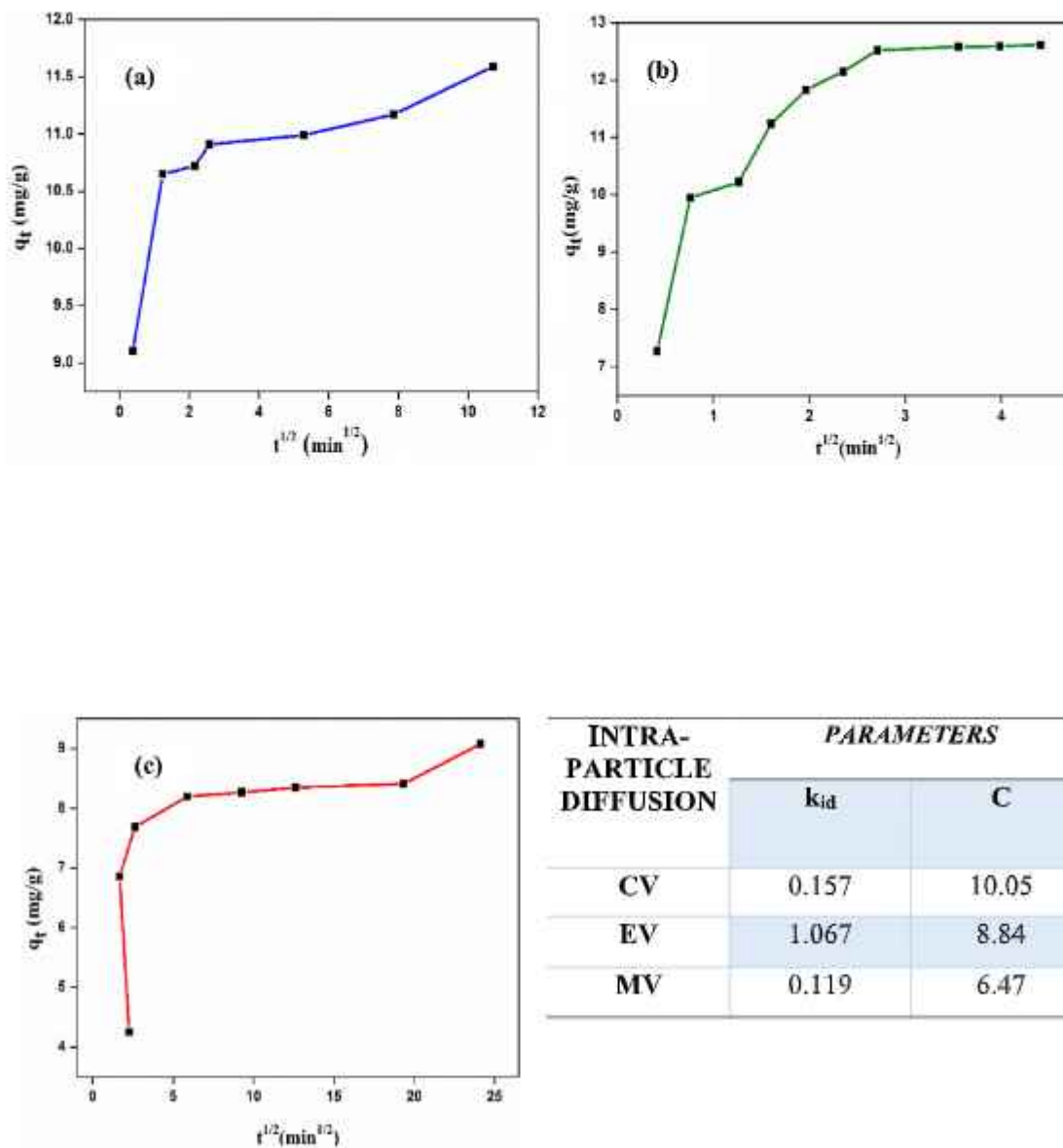


Fig. 14. The plot of q_t vs $t^{1/2}$ for intra-particle diffusion of (a)CV, (b)EV, and (c)MV dyes.

Table 8
A comparative study of the dyes using different gel-based adsorbents.

Gel adsorbents	Dye used	Contact time	Removal %	Reference
Glutamic acid-derived organogel	CV	24hr	99	[50]
Low Molecular Weight amphiphilic dipeptides	CV	24hr	97%	[51]
Acrylic acid-hydroxyethyl acrylate polymer	MV	30hr	67	[52]
Sodium acrylate-hydroxyethyl methacrylate polymer			80	
Acrylic acid-hydroxyethyl methacrylate-Na alginate			90	
Sodium acrylate-hydroxyethyl methacrylate-Na alginate			95	
Terpyridine-based smart hybrid gel	CV	30hr	94.2	[53]
Catechol-based metal-organic gels	MV	3hr	93.99	[54]
Bidirectionally zwitterionic polymer hydrogel	MV	24hr	10	[55]
Pectin-based ZnO-g-copolymer hybrid nanocomposite	CV	2hr	95.7	[36]
Low molecular weight gelator grafted polymeric organogel	EV	1hr	99.35	This work
	CV	2.5hr	95.06	
	MV	5hr	92.71	

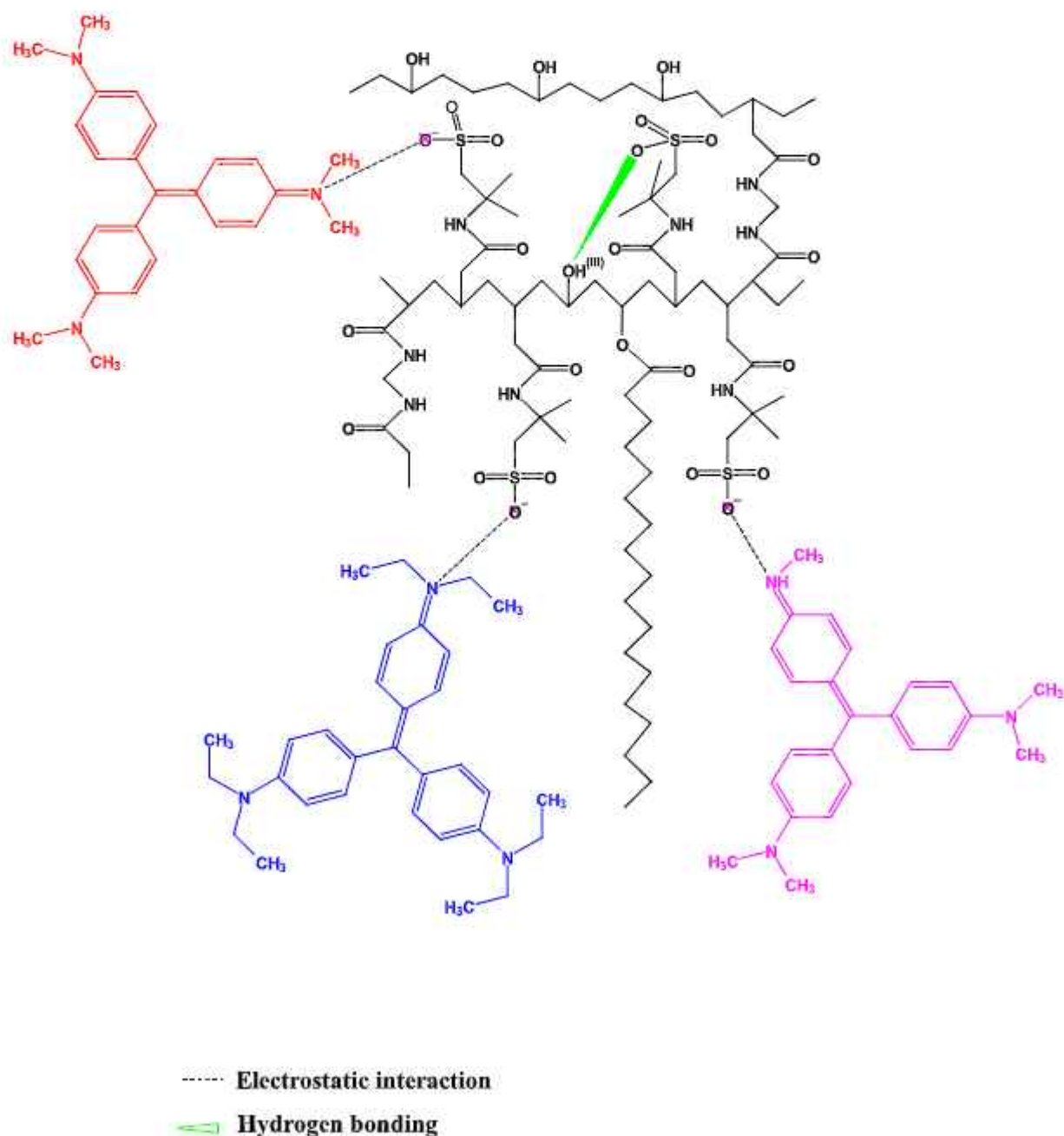


Fig. 15. Schematic representation for the mechanism of adsorption of dyes CV, EV, MV by the organogel.

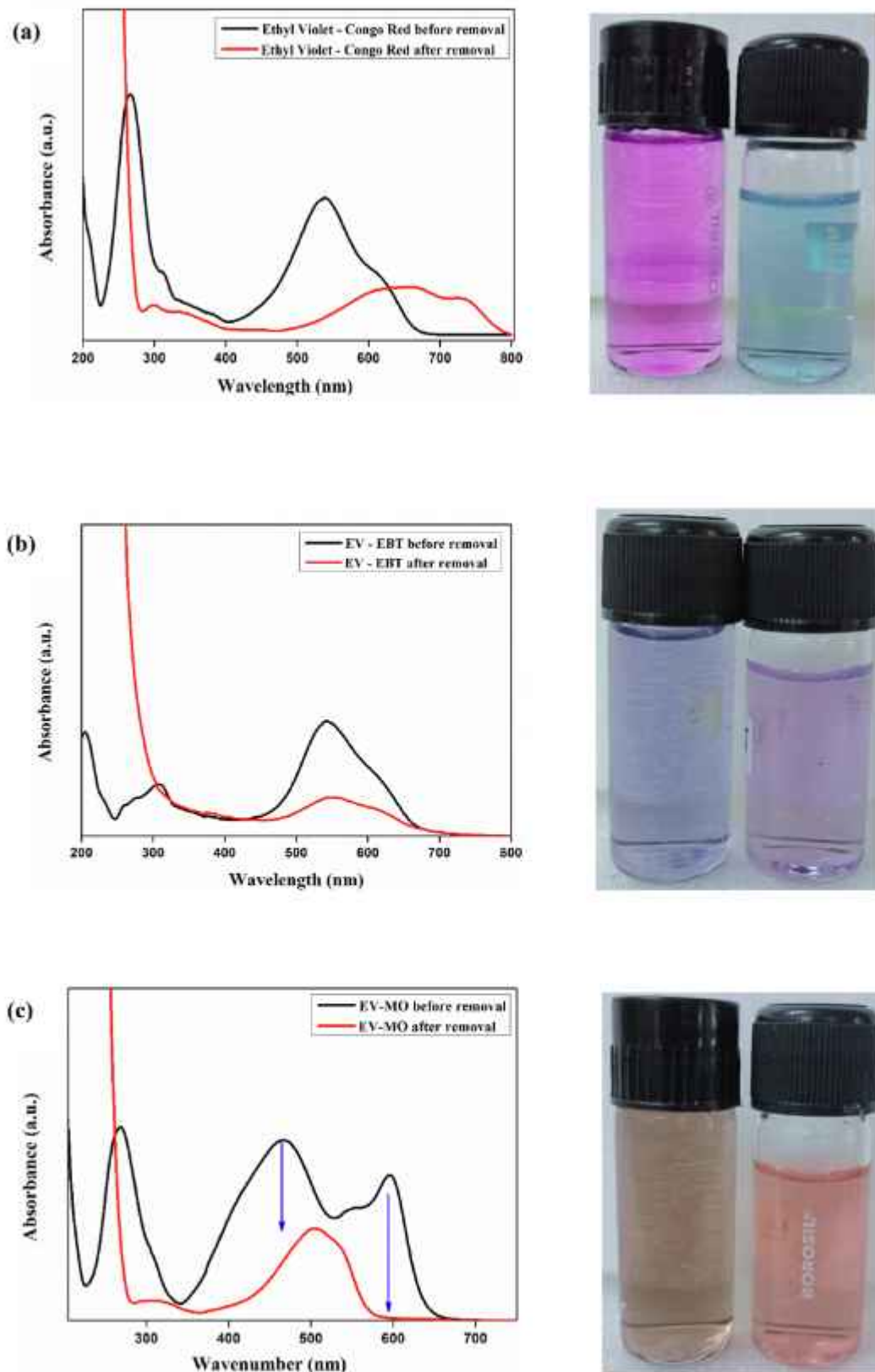


Fig. 16. UV-Vis spectrum and optical images of the mixed dyes (a) Ethyl Violet-Congo Red, (b) Ethyl Violet-Eriochrome Black T, (c) Ethyl Violet-Methyl Orange before and after adsorption.

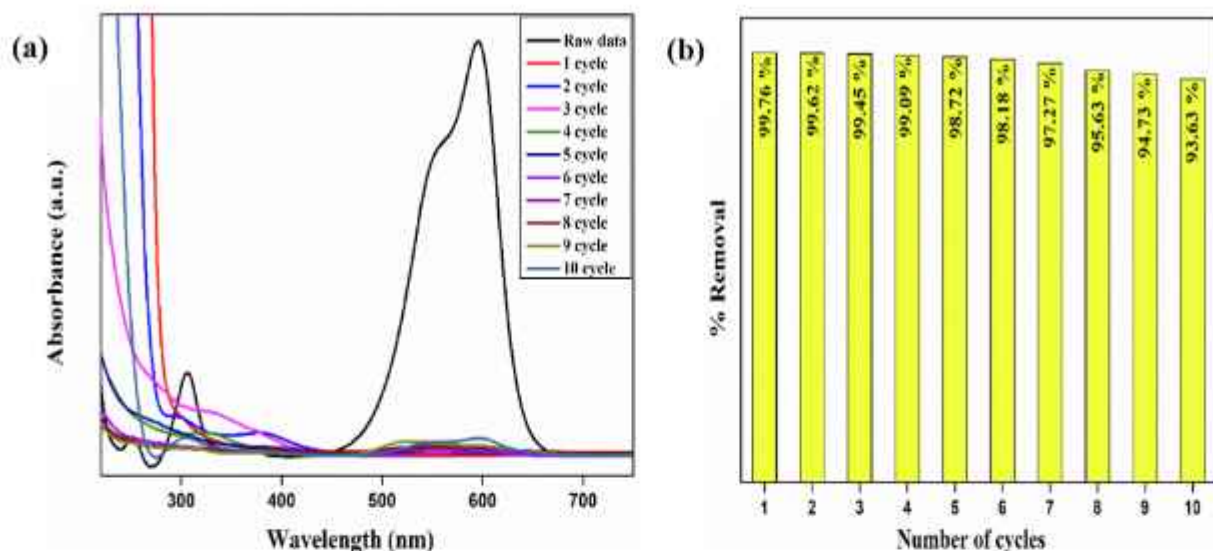


Fig. 17. (a) UV-Vis spectra and (b) bar plot for the recyclability study of the Ethyl Violet dye.

Declaration of Competing Interest

The authors declare that they have no known competing financial interests or personal relationships that could have appeared to influence the work reported in this paper.

Data availability

Data will be made available on request.

Acknowledgements

We would like to express our gratitude of thanks to the Sophisticated Analytical Instrumentation Centre (SAIC), Tezpur University for providing analytical support and also acknowledge Tezpur University for the financial assistance received.

Appendix A. Supplementary material

Supplementary data to this article can be found online at <https://doi.org/10.1016/j.eurpolymj.2023.112213>.

References

- [1] K. Singh, P. Kumar, R. Srivastava, An overview of textile dyes and their removal techniques: Indian perspective, *Poll Res.* 36 (2017) 790–797.
- [2] S. Dutta, B. Gupta, S.K. Srivastava, A.K. Gupta, Recent advances on the removal of dyes from wastewater using various adsorbents: a critical review, *Mater. Adv.* 2 (2021) 4497–4531, <https://doi.org/10.1039/d1ma00354h>.
- [3] A. Desore, S.A. Narula, An overview on corporate response towards sustainability issues in textile industry, *Environ. Dev. Sustain.* 20 (2018) 1439–1459, <https://doi.org/10.1007/s10668-017-9949-1>.
- [4] V. Hegde, U.T. Uthappa, O.R. Arvind swami, S.S. Han, H.Y. Jung, T. Alkalhi, M. D. Kurkuri, Sustainable green functional nano aluminum fumarate-MOF decorated on 3D low-cost natural diatoms for the removal of Congo red dye and fabric whitening agent from wastewater: batch & continuous adsorption process, *Mater. Today Commun.* 32 (2022), <https://doi.org/10.1016/j.mtcomm.2022.103887>.
- [5] F.M. Drummond Chequer, G.A.R. de Oliveira, E.R. Anastacio Ferraz, J. Carvalho, M. V. Boldrin Zanoni, D.P. de Oliveira, Textile dyes: dyeing process and environmental impact, *Eco-Friend. Text. Dye. Finish.* (2015), <https://doi.org/10.5772/53659>.
- [6] A. Bafana, S.S. Devi, T. Chakrabarti, Azo dyes: past, present and the future, *Environ. Rev.* 19 (2011) 350–370, <https://doi.org/10.1139/er11-018>.
- [7] E. Forgacs, T. Cségháti, G. Oroz, Removal of synthetic dyes from wastewaters: a review, *Environ. Int.* 30 (2004) 953–971, <https://doi.org/10.1016/j.envint.2004.02.001>.
- [8] W. Przytyca, E. Zablocka-Godlewska, E. Grabinska-Sota, Biological removal of azo and triphenylmethane dyes and toxicity of process by-products, *Water Air Soil Pollut.* 223 (2012) 1581–1592, <https://doi.org/10.1007/s11270-011-0966-7>.
- [9] J. Karpińska, U. Kotowska, Removal of organic pollution in the water environment, *Water (Switzerland)*. 11 (2019), <https://doi.org/10.3390/w11102017>.
- [10] R. Huang, K.N. McPhedran, N. Sun, P. Chelme-Ayala, M. Gamal El-Din, Investigation of the impact of organic solvent type and solution pH on the extraction efficiency of naphthenic acids from oil sands process-affected water, *Chemosphere* 146 (2016) 472–477, <https://doi.org/10.1016/j.chemosphere.2015.12.054>.
- [11] D.R. Joshi, N. Adhikari, An overview on common organic solvents and their toxicity, *J. Pharm. Res. Int.* (2019) 1–18, <https://doi.org/10.9794/jpri/2019/v2i1330203>.
- [12] M. Tian, L. Fang, X. Yan, W. Xiao, K.H. Row, Determination of heavy metal ions and organic pollutants in water samples using ionic liquids and ionic liquid-modified sorbents, *J. Anal. Methods Chem.* 2019 (2019), <https://doi.org/10.1155/2019/1946965>.
- [13] R.A. Fallahzadeh, R. Khosravi, B. Dehdashti, E. Ghahramani, F. Omidi, A. Adli, M. Miri, Spatial distribution variation and probabilistic risk assessment of exposure to chromium in ground water supplies; a case study in the east of Iran, *Food Chem. Toxicol.* 115 (2018) 260–266, <https://doi.org/10.1016/j.fct.2018.03.019>.
- [14] L.C. Ozaei, A. Ahmed, A. Hassan, F.S. Hamid, Remediation of soil and water contaminated with petroleum hydrocarbon: a review, *Environ. Technol. Innov.* 17 (2020), <https://doi.org/10.1016/j.eti.2019.100526>.
- [15] A. Truszkiewicz, T.D. Gundry, L.S. Khudur, A. Kolobaric, M. Taha, A. Aburto-Medina, A.S. Ball, E. Shahevari, Petroleum hydrocarbon contamination in terrestrial ecosystems – fate and microbial responses, *Molecules* 24 (2019), <https://doi.org/10.3390/molecules24183400>.
- [16] P. Ortiz, A.I. del Río, J. Molina, J. Bonastre, P. Cases, Electrochemical treatment of real textile wastewater: trichrome Procion HEXLE®, *J. Electroanal. Chem.* 808 (2018) 387–394, <https://doi.org/10.1016/j.jelechem.2017.06.051>.
- [17] B. Lellis, C.Z. Favaro-Polonio, J.A. Pamphile, J.C. Polonio, Effects of textile dyes on health and the environment and bioremediation potential of living organisms, *Biotechnol. Res. Innov.* 3 (2019) 275–290, <https://doi.org/10.1016/j.biori.2019.09.001>.
- [18] M.M. Hassan, C.M. Carr, A critical review on recent advancements of the removal of reactive dyes from dyehouse effluent by ion-exchange adsorbents, *Chemosphere* 209 (2018) 201–219, <https://doi.org/10.1016/j.chemosphere.2018.06.043>.
- [19] P. Marchetti, M.F. Jimenez Solomon, G. Szekely, A.G. Livingston, Molecular separation with organic solvent nanofiltration: a critical review, *Chem. Rev.* 114 (2014) 10735–10806, <https://doi.org/10.1021/cr500006j>.
- [20] Y. Wei, X. Cheng, A. Ding, J. Xu, Magnesium silicate polymer as a coagulant for reactive dye removal from wastewater: considering the intrinsic pH in magnesium silicate polymer and coagulation behavior, *ACS Omega* 5 (2020) 26094–26100, <https://doi.org/10.1021/acsomega.0c03625>.
- [21] G.K.G. Carvalho Barroo, L.J.N. Duarte, R.P.F. Melo, F.W.B. Lopes, E.L. Barros Neto, Ionic dye removal using solvent-assisted ionic micellar flocculation, *J. Polym. Environ.* 30 (2022) 2534–2546, <https://doi.org/10.1007/s10924-021-02360-7>.
- [22] W. Li, Y. Zhang, T. Liu, J. Huang, Y. Wang, Comparison of ion exchange and solvent extraction in recovering vanadium from sulfuric acid leach solutions of stone coal, *Hydrometall.* 131–132 (2013) 1–7, <https://doi.org/10.1016/j.hydromet.2012.09.009>.
- [23] I.M. Saaidharan Pillai, A.R. Gupta, Effect of inorganic anions and oxidizing agents on electrochemical oxidation of methyl orange, malachite green and 2,4-dinitrophenol, *J. Electroanal. Chem.* 762 (2016) 66–72, <https://doi.org/10.1016/j.jelechem.2015.12.027>.
- [24] G. Sriram, U.T. Uthappa, M. Kigga, H.Y. Jung, T. Alkalhi, V. Brahmakhatri, M. D. Kurkuri, Xerogel activated diatoms as an effective hybrid adsorbent for the

- efficient removal of malachite green, *New J. Chem.* 43 (2019) 3810–3820, <https://doi.org/10.1039/c9nj00015a>.
- [25] U.T. Uthappa, S. Bhat, S. Soo Han, H.H. Jeong, T. Altalhi, H.Y. Jung, M.D. Kurkuri, Tailoring of 2D MoS₂ microspheres on 3D low-cost DE for the efficient removal of hazardous cationic dyes, *Adv. Powder Technol.* 33 (2022), <https://doi.org/10.1016/j.apt.2022.103800>.
- [26] C. Sahoo, A.K. Gupta, Photocatalytic degradation of methyl blue by silver ion-doped titania: identification of degradation products by GC-MS and IC analysis, *J. Environ. Sci. Health A Tox. Hazard. Subst. Environ. Eng.* 50 (2015) 1333–1341, <https://doi.org/10.1080/10934529.2015.1059107>.
- [27] A.K. Gupta, A. Pal, C. Sahoo, Photocatalytic degradation of a mixture of Crystal Violet (Basic Violet 3) and Methyl Red dye in aqueous suspensions using Ag⁺ doped TiO₂, *Dyes Pigm.* 69 (2006) 224–232, <https://doi.org/10.1016/j.dyepig.2005.04.001>.
- [28] R. Saravanan, P. Gracia, A. Stephen, Basic Principles, Mechanism, and Challenges of Photocatalysis, 2017, pp. 19–40. doi: 10.1007/978-3-319-62446-4_2.
- [29] G. Iervolino, I. Zammit, V. Vaiano, L. Rizzo, Limitations and prospects for wastewater treatment by UV and visible-light-active heterogeneous photocatalysis: a critical review, *Top. Curr. Chem.* 378 (2020), <https://doi.org/10.1007/s41061-019-0272-1>.
- [30] J.Y.C. Lim, S.S. Goh, S.S. Liow, K. Xue, X.J. Loh, Molecular gel sorbent materials for environmental remediation and wastewater treatment, *J. Mater. Chem. A Mater.* 7 (2019) 18759–18791, <https://doi.org/10.1039/c9ta05782j>.
- [31] I. Yan, G. Ocan Aydin, H. Bulbul Sommez, Cross-linked poly(tetrahydrofuran) as promising sorbent for organic solvent/oil spill, *J. Hazard. Mater.* 309 (2016) 210–218, <https://doi.org/10.1016/j.jhazmat.2016.02.014>.
- [32] I. Yan, K. Karadag, H.B. Sommez, Amphiphilic poly(ethylene glycol) gels and their swelling features, *Polym. Adv. Technol.* 26 (2015) 635–644, <https://doi.org/10.1002/pat.3498>.
- [33] S. de Gisi, G. Lofrano, M. Grassi, M. Notarnicola, Characteristics and adsorption capacities of low-cost sorbents for wastewater treatment: a review, *Sust. Mater. Technol.* 9 (2016) 10–40, <https://doi.org/10.1016/j.susmat.2016.06.002>.
- [34] B. Zhao, K. Rohm, P. Wang, X. Gong, I. Manas-Zloczower, D.L. Feke, A compact volume-expandable sorbent for oil and solvent capture, *ACS Appl. Polym. Mater.* 3 (2021) 494–503, <https://doi.org/10.1021/acscpm.0c01324>.
- [35] V. Hegde, U.T. Uthappa, M. Suneeha, T. Altalhi, S. Soo Han, M.D. Kurkuri, Functional porous Ce-UO₂-66 MOP@Keratin composites for the efficient adsorption of trypan blue dye from wastewater: a step towards practical implementations, *Chem. Eng. J.* 461 (2023), <https://doi.org/10.1016/j.cej.2023.142103>.
- [36] X.S. Hu, R. Liang, G. Sun, Super-adsorbent hydrogel for removal of methylene blue dye from aqueous solution, *J. Mater. Chem. A Mater.* 6 (2018) 17612–17624, <https://doi.org/10.1039/c8sm04722g>.
- [37] G.R. Mahdavinia, H. Aghaie, H. Sheykhlou, M.T. Vardini, H. Etemadi, Synthesis of CarAlg/MDA nanocomposite hydrogels and adsorption of cationic crystal violet, *Carbohydr. Polym.* 98 (2013) 358–365, <https://doi.org/10.1016/j.carbpol.2013.05.096>.
- [38] A.K. Kodoth, V. Badalamoole, Pectin based graft copolymer ZnO hybrid nanocomposite for the adsorptive removal of crystal violet, *J. Polym. Environ.* 27 (2019) 2040–2053, <https://doi.org/10.1007/s10924-019-01488-x>.
- [39] S. Bhat, U.T. Uthappa, T. Sadhasivam, T. Altalhi, S. Soo Han, M.D. Kurkuri, Abundant cilantro derived high surface area activated carbon (AC) for superior adsorption performances of cationic/anionic dyes and supercapacitor application, *Chem. Eng. J.* 459 (2023), <https://doi.org/10.1016/j.cej.2023.141577>.
- [40] A. Srivastava, B. Gupta, A. Majumder, A.K. Gupta, S.K. Nimbhorkar, A comprehensive review on the synthesis, performance, modifications, and regeneration of activated carbon for the adsorptive removal of various water pollutants, *J. Environ. Chem. Eng.* 9 (2021), <https://doi.org/10.1016/j.jece.2021.106177>.
- [41] S. Das, P. Chakraborty, R. Ghosh, S. Paul, S. Mondal, A. Panja, A.K. Nandi, Folic acid-polyaniline hybrid hydrogel for adsorption/reduction of chromium(VI) and selective adsorption of anionic dye from water, *ACS Sustain. Chem. Eng.* 5 (2017) 9325–9337, <https://doi.org/10.1021/acscu.chemeng.7b02342>.
- [42] L. Wang, X. Wu, W. Xu, X. Huang, J. Liu, A. Xu, Stable organic–inorganic hybrid of Polyaniline@Zirconium.pdf, *Appl. Mater. Interfaces* (2012) 2658–2692.
- [43] A. Pan, S.G. Roy, U. Haldar, R.D. Mahapatra, G.R. Harper, W.L. Lov, P. De, J. G. Hardy, Uptake and release of species from carbohydrate containing organogels and hydrogels, *Gels* 5 (2019), <https://doi.org/10.3390/gels5040043>.
- [44] S. Ren, P. Sun, A. Wu, N. Sun, L. Sun, B. Dong, L. Zheng, Ultra-fast self-healing PVA organogels based on dynamic covalent chemistry for dye selective adsorption, *New J. Chem.* 43 (2019) 7701–7707, <https://doi.org/10.1039/c9nj00891h>.
- [45] K. Baruah, A. Ahmed, R. Dutta, S. Ahmed, S. Lakkar, S.K. Dolui, Removal of organic solvents from contaminated water surface through a fatty acid grafted polyvinyl alcohol based organogel, *J. Appl. Polym. Sci.* (2022) 1–13, <https://doi.org/10.1002/app.53123>.
- [46] B.O. Okesola, D.K. Smith, Applying low-molecular weight supramolecular gelators in an environmental setting-self-assembled gels as smart materials for pollutant removal, *Chem. Soc. Rev.* 45 (2016) 4226–4251, <https://doi.org/10.1039/c6cs00124f>.
- [47] X. Zheng, H. Zheng, R. Zhao, Z. Xiong, Y. Wang, Y. Sun, W. Ding, Sulfonic acid-modified polyacrylamide magnetic composite with wide pH applicability for efficient removal of cationic dyes, *J. Mol. Liq.* 319 (2020), 114161, <https://doi.org/10.1016/j.molliq.2020.114161>.
- [48] C. Modroga, S. Căprărescu, A.M. Dănciul, O.D. Orbule, A.M. Grumesciu, V. Purcar, V. Radiciu, R.C. Pterascu, Modified composite based on magnetite and polyvinyl alcohol: synthesis, characterization, and degradation studies of the methyl orange dye from synthetic wastewater, *Polymers (Basel)* 13 (2021), <https://doi.org/10.3390/polym13223911>.
- [49] A.K. Kodoth, V. Badalamoole, Silver nanoparticle-embedded pectin-based hydrogel for adsorptive removal of dyes and metal ions, *Polym. Bull.* 77 (2020) 541–564, <https://doi.org/10.1007/s00289-019-02757-4>.
- [50] P. Sar, S.G. Roy, P. De, S. Ghosh, Synthesis of glutamic acid derived organogels and their applications in dye removal from aqueous medium, *Macromol. Mater. Eng.* 305 (2020), <https://doi.org/10.1002/mame.201900809>.
- [51] T. Kar, S. Debnath, D. Das, A. Shome, P.K. Das, Organogelation and hydrogelation of low-molecular-weight amphiphilic dipeptides: pH responsiveness in phase-selective gelation and dye removal, *Langmuir* 25 (2009) 8639–8648, <https://doi.org/10.1021/la904235e>.
- [52] B. Mandal, S.K. Ray, Synthesis of interpenetrating network hydrogel from poly(acrylic acid-co-hydroxyethyl methacrylate) and sodium alginate: Modeling and kinetics study for removal of synthetic dyes from water, *Carbohydr. Polym.* 98 (2013) 267–269, <https://doi.org/10.1016/j.carbpol.2013.05.093>.
- [53] E.J. Cho, I.Y. Jeong, S.J. Lee, W.S. Han, J.K. Kang, J.H. Jung, Terpyridine-based smart organic-inorganic hybrid gel as potential dye-adsorbing agent for water purification, *Tetrahedron Lett.* 49 (2008) 1076–1079, <https://doi.org/10.1016/j.tetlet.2007.11.212>.
- [54] Y. Hong, Z. Gao, M. Chen, J. Hao, S. Dong, Metal-organic gels of catechol-based ligands with Ni(II) acetate for dye adsorption, *Langmuir* 34 (2018) 9435–9441, <https://doi.org/10.1021/acs.langmuir.8b01065>.
- [55] R. Wei, W. Song, F. Yang, J. Zhou, M. Zhang, X. Zhang, W. Zhao, C. Zhao, Bidirectionally pH-responsive zwitterionic polymer hydrogels with switchable selective adsorption capacities for anionic and cationic dyes, *Ind. Eng. Chem. Res.* 57 (2018) 8209–8219, <https://doi.org/10.1021/acs.iecr.8b01027>.



Solvability of Bigeometric Differential Equations by Numerical Methods *

Khirod Boruah, Bipan Hazarika* and A. E. Bashirov

ABSTRACT: The objective of this paper is to derive and analyze Bigeometric-Euler, Taylor's Bigeometric-series and Bigeometric-Runge-Kutta methods of different orders for the approximation of initial value problems of Bigeometric-differential equations.

Key Words: Bigeometric-calculus, geometric real numbers, geometric arithmetic.

Contents

1 Introduction	204
2 α-generator and geometric real field	204
3 Basic definitions and results	207
3.1 Geometric Binomial Formula	207
3.2 Geometric Factorial	207
3.3 Generalized Geometric Forward Difference Operator	207
3.4 Generalized Geometric Backward Difference Operator	208
3.5 Geometric Newton-Gregory formula for forward interpolation	208
3.6 Geometric Newton-Gregory formula for backward interpolation	208
3.7 G-Derivative	208
3.8 Geometric Taylor's Series	209
4 Numerical Methods and Solution of G-differential Equations	209
4.1 G-Euler's Method	210
4.2 Taylor's G-Series Method	212
4.3 G-Runge-Kutta Method:	217
4.3.1 G-Runge-Kutta Method of order four:	218
5 Conclusion	221

* The corresponding author.
 2010 *Mathematics Subject Classification:* 26A06, 11U10, 08A05, 65L99.
 Submitted September 12, 2017. Published March 11, 2018

1. Introduction

Differential and integral calculi were created independently by Isaac Newton and Gottfried Wilhelm Leibniz in the second half of the 17th century. After that Leonhard Euler redirected calculus by giving a central place to the concept of function, and thus founded analysis. Differentiation and integration are the basic operations in calculus and analysis. Actually, they are the infinitesimal versions of the subtraction and addition on numbers, respectively. Often this calculus is referred as Newtonian calculus. The underlying feature of Newtonian calculus is that it studies functions by comparing them with linear functions.

In the period between 1967 to 1970 Michael Grossman and Robert Katz [12] indicated that Newtonian calculus can be realised in the forms of comparison of functions with nonlinear functions calling them non-Newtonian calculi. Multiplicative and bigeometric calculi are the two most popular non-Newtonian calculi. In fact, they are modification of each other. In these calculi the role of addition and subtraction are changed to multiplication and division.

Bigeometric calculus was prompted by Grossman [11]. We refer to Stanley [20], Jane Grossman [13], Grossman et al. [14], Grossman et al. [15], Grossman [16], Campbell [9], Michael Coco [10], Córdova-Lepe [18], Bashirov et al. [3,4], Spivey [19], Bashirov and Rıza [2], Çakmak and Başar [8], Kadak and Özliik [17], Tekin and Başar [21], Türkmen and Başar [22] for different types of non-Newtonian calculi and applications. For numerical analysis we refer the book of Burden and Faires [7].

Bigeometric-calculus is an alternative to the usual calculus of Newton and Leibniz. It provides differentiation and integration tools based on multiplication instead of addition. Every property in Newtonian calculus has an analog in bigeometric-calculus. Generally, in growth related problems, price elasticity, numerical approximation problems bigeometric-calculus can be advocated instead of a traditional Newtonian one. Below in Section 2, a quick outlook on generators of arithmetic and geometric arithmetic is given. Then we establish relations between geometric arithmetic and classical arithmetic. In Section 3, we mention some previously established results which are essential to deduce new results in the present paper. In Section 4, we introduce numerical new methods, namely, bigeometric Euler method, Taylor's bigeometric series method and bigeometric Runge Kutta method for approximation of bigeometric initial value problems together with examples.

Throughout the article, instead of the phrase "bigeometric calculus" term "G-calculus" will be used because, depending on the pioneering works of Grossman [11] and Grossman and Katz's [12], we are trying to develop their work with the help of geometric arithmetic system.

2. α -generator and geometric real field

A generator is a one-to-one function whose domain is the set \mathbb{R} of real numbers and range is a subset $B \subset \mathbb{R}$. Each generator generates exactly one arithmetic and each arithmetic is generated by exactly one generator. For example, the identity function generates classical arithmetic and exponential function generates geomet-

ric arithmetic. As a generator, we choose the function α such that whose basic algebraic operations are defined as follows:

$$\begin{array}{ll} \alpha - \text{addition} & x \dot{+} y = \alpha[\alpha^{-1}(x) + \alpha^{-1}(y)], \\ \alpha - \text{subtraction} & x \dot{-} y = \alpha[\alpha^{-1}(x) - \alpha^{-1}(y)], \\ \alpha - \text{multiplication} & x \dot{\times} y = \alpha[\alpha^{-1}(x) \times \alpha^{-1}(y)], \\ \alpha - \text{division} & x \dot{/} y = \alpha[\alpha^{-1}(x)/\alpha^{-1}(y)], \\ \alpha - \text{order} & x \dot{<} y \Leftrightarrow \alpha^{-1}(x) < \alpha^{-1}(y) \end{array}$$

for x and y from the range of the function α .

If we choose the exponential function $\alpha(x) = e^x$ for $x \in \mathbb{R}$ as an α -generator then $\alpha^{-1}(z) = \ln z$ and α -arithmetic turns out to be geometric arithmetic.

$$\begin{array}{ll} \text{geometric addition} & x \oplus y = e^{(\ln x + \ln y)} = x \cdot y, \\ \text{geometric subtraction} & x \ominus y = e^{(\ln x - \ln y)} = x/y, \\ \text{geometric multiplication} & x \odot y = e^{(\ln x \ln y)} = x^{\ln y} = y^{\ln x}, \\ \text{geometric division} & x \oslash y = e^{(\ln x \div \ln y)} = x^{\frac{1}{\ln y}}, y \neq 1. \end{array}$$

Since the logarithmic function is strictly increasing, that is $\ln(x) < \ln(y)$ for $0 < x < y$, without loss of generality, we use $x < y$ instead of the geometric order.

Türkmen and Başar [22] defined the sets of geometric integers, geometric real numbers and geometric complex numbers $\mathbb{Z}(G), \mathbb{R}(G)$ and $\mathbb{C}(G)$, respectively, as follows:

$$\begin{aligned} \mathbb{Z}(G) &= \{e^x : x \in \mathbb{Z}\} \\ \mathbb{R}(G) &= \{e^x : x \in \mathbb{R}\} = (0, \infty) \\ \mathbb{C}(G) &= \{e^z : z \in \mathbb{C}\} = \mathbb{C} \setminus \{0\}. \end{aligned}$$

If $\bar{\mathbb{R}} = \mathbb{R} \cup \{\pm\infty\}$ is the extended real number line, then $\bar{\mathbb{R}}(G) = [0, \infty)$.

Remark 2.1. $(\mathbb{R}(G), \oplus, \odot)$ is a field with the neutral elements of addition and multiplication to be 1 and e , respectively, since

1. $(\mathbb{R}(G), \oplus)$ is a geometric additive Abelian group with geometric zero 1,
2. $(\mathbb{R}(G) \setminus 1, \odot)$ is a geometric multiplicative Abelian group with geometric identity e ,
3. \odot is distributive over \oplus .

But $(\mathbb{C}(G), \oplus, \odot)$ is not a field. This is a consequence of a multivalued nature of complex logarithm. Let us show that the geometric binary operation \odot is not associative in $\mathbb{C}(G)$. Take $x = e^{1/4}$, $y = e^4$, and $z = e^{(1+i\pi/2)} = ie$. Then $(x \odot y) \odot z = e \odot z = z = ie$ while $x \odot (y \odot z) = x \odot e^4 = e$.

Let us define geometric positive real numbers and geometric negative real numbers as follows:

$$\mathbb{R}^+(G) = \{x \in \mathbb{R}(G) : x > 1\}$$

$$\mathbb{R}^-(G) = \{x \in \mathbb{R}(G) : x < 1\}.$$

For $x \in \mathbb{R}(G)$, define its geometric absolute value by

$$|x|^\alpha = \begin{cases} x, & \text{if } x > 1 \\ 1, & \text{if } x = 1 \\ \frac{1}{x}, & \text{if } 0 < x < 1 \end{cases}$$

Then for all $x, y \in \mathbb{R}(G)$, the following relations hold:

- $x \oplus y = xy$.
- $x \ominus y = x/y$.
- $x \odot y = x^{\ln y} = y^{\ln x}$.
- $x \oslash y$ or $\frac{x}{y} \alpha = x^{\frac{1}{\ln y}}, y \neq 1$.
- $x^{2\alpha} = x \odot x = x^{\ln x}$.
- $x^{p\alpha} = x^{\ln^{p-1} x}$.
- $\sqrt{x}^\alpha = e^{(\ln x)^{\frac{1}{2}}}$.
- $x^{-1\alpha} = e^{\frac{1}{\ln x}}$.
- $x \odot e = x$ and $x \oplus 1 = x$.
- $e^n \odot x = x^n$.
- $|x|^\alpha \geq 1$.
- $\sqrt{x^{2\alpha}^\alpha} = |x|^\alpha$
- $|e^y|^\alpha = e|y|$.
- $|x \odot y|^\alpha = |x|^\alpha \odot |y|^\alpha$.
- $|x \oplus y|^\alpha \leq |x|^\alpha \oplus |y|^\alpha$.
- $|x \oslash y|^\alpha = |x|^\alpha \oslash |y|^\alpha$.
- $|x \ominus y|^\alpha \geq |x|^\alpha \ominus |y|^\alpha$.
- $(0_\alpha \ominus 1_\alpha) \odot (x \ominus y) = y \ominus x$.

Briefly, the last relation can be written as $\ominus(x \ominus y) = y \ominus x$. Further, $e^{-x} = \ominus e^x$ holds for all $x \in \mathbb{Z}^+$. Thus the set of all geometric integers turns out to the following:

$$\mathbb{Z}(G) = \{\dots, e^{-3}, e^{-2}, e^{-1}, e^0, e^1, e^2, e^3, \dots\} = \{\dots, \ominus e^3, \ominus e^2, \ominus e, 1, e, e^2, e^3, \dots\}.$$

3. Basic definitions and results

The following definitions and results were introduced and studied by Boruah and Hazarika [5,6].

3.1. Geometric Binomial Formula

$$\begin{aligned} \text{(i)} \quad (a \oplus b)^{2c} &= a^{2c} \oplus e^2 \odot a \odot b \oplus b^{2c}. \\ \text{(ii)} \quad (a \oplus b)^{3c} &= a^{3c} \oplus e^3 \odot a^{2c} \odot b \oplus e^3 \odot a \odot b^{2c} \oplus b^{3c}. \end{aligned}$$

In general

$$\begin{aligned} \text{(iii)} \quad (a \oplus b)^{nc} &= a^{nc} \oplus e^{\binom{n}{1}} \odot a^{(n-1)c} \odot b \\ &\oplus e^{\binom{n}{2}} \odot a^{(n-2)c} \odot b^{2c} \oplus \dots \oplus b^{nc} \\ &= \sum_{r=0}^n e^{\binom{n}{r}} \odot a^{(n-r)c} \odot b^{rc}. \end{aligned}$$

Similarly

$$(a \ominus b)^{nc} = \sum_{r=0}^n (\ominus e)^{rc} \odot e^{\binom{n}{r}} \odot a^{(n-r)c} \odot b^{rc}.$$

Note: $x \oplus x = x^2$. Also $e^2 \odot x = x^{\ln(e^2)} = x^2$. So, $e^2 \odot x = x^2 = x \oplus x$.

3.2. Geometric Factorial

In [5], we defined geometric factorial notation $!_G$ as

$$n!_G = e^n \odot e^{n-1} \odot e^{n-2} \odot \dots \odot e^2 \odot e = e^{n!}.$$

3.3. Generalized Geometric Forward Difference Operator

Let

$$\begin{aligned} \Delta_G f(a) &= f(a \oplus h) \ominus f(a). \\ \Delta_G^2 f(a) &= \Delta_G f(a \oplus h) \ominus \Delta_G f(a) \\ &= f(a \oplus e^2 \odot h) \ominus e^2 \odot f(a \oplus h) \oplus f(a). \\ \Delta_G^3 f(a) &= \Delta_G^2 f(a \oplus h) \ominus \Delta_G^2 f(a) \\ &= f(a \oplus e^3 \odot h) \ominus e^3 \odot f(a \oplus e^2 \odot h) \oplus e^3 \odot f(a \oplus h) \ominus f(a). \end{aligned}$$

Thus n^{th} forward difference is

$$\Delta_G^n f(a) = \sum_{k=0}^n (\ominus e)^{kc} \odot e^{\binom{n}{k}} \odot f(a \oplus e^{n-k} \odot h), \text{ with } (\ominus e)^{0c} = e.$$

3.4. Generalized Geometric Backward Difference Operator

Let

$$\begin{aligned}\nabla_G f(a) &= f(a) \ominus f(a \ominus h). \\ \nabla_G^2 f(a) &= \nabla_G f(a) \ominus \nabla_G f(a \ominus h) \\ &= f(a) \ominus e^2 \odot f(a \ominus h) \oplus f(a \ominus e^2 \odot h). \\ \nabla_G^3 f(a) &= \nabla_G^2 f(a) \ominus \nabla_G^2 f(a \ominus h) \\ &= f(a) \ominus e^3 \odot f(a \ominus h) \oplus e^3 \odot f(a \ominus e^2 \odot h) \ominus f(a \ominus e^3 \odot h).\end{aligned}$$

Thus, n^{th} geometric backward difference is

$$\nabla_G^n f(a) = \sum_{k=0}^n (\ominus e)^{k\sigma} \odot e^{\binom{n}{k}} \odot f(a \ominus e^k \odot h).$$

3.5. Geometric Newton-Gregory formula for forward interpolation

In [5], we introduced the Geometric Newton-Gregory formula for forward interpolation as follows:

$$\begin{aligned}f(a \oplus h \odot x) &= f(a) \oplus x \odot \Delta_G f(a) \oplus \frac{x \odot (x \ominus e)}{2!_G} \odot \Delta_G^2 f(a) \\ &\oplus \frac{x \odot (x \ominus e) \odot (x \ominus e^2)}{3!_G} \odot \Delta_G^3 f(a) \oplus \dots \\ &\oplus \frac{x \odot (x \ominus e) \odot (x \ominus e^2) \odot \dots \odot (x \ominus e^{n-1})}{n!_G} \odot \Delta_G^n f(a).\end{aligned}\tag{3.1}$$

3.6. Geometric Newton-Gregory formula for backward interpolation

In [5] we introduced the Geometric Newton-Gregory formula for backward interpolation as follows:

$$\begin{aligned}f(a \oplus e^n \odot h \oplus x \odot h) &= f(a \oplus e^n \odot h) \oplus x \odot \nabla_G f(a \oplus e^n \odot h) \\ &\oplus \frac{x \odot (x \oplus e)}{2!_G} \odot \nabla_G^2 f(a \oplus e^n \odot h) \\ &\oplus \frac{x \odot (x \oplus e) \odot (x \oplus e^2)}{3!_G} \odot \nabla_G^3 f(a \oplus e^n \odot h) \oplus \dots \\ &\oplus \frac{x \odot (x \oplus e) \odot (x \oplus e^2) \odot \dots \odot (x \oplus e^{n-1})}{n!_G} \\ &\odot \nabla_G^n f(a \oplus e^n \odot h).\end{aligned}\tag{3.2}$$

3.7. G-Derivative

[6] G-differentiation of a bi-positive function f is defined as

$$\frac{d^\sigma f}{dx^\sigma} = f^\sigma(x) = {}_c \lim_{h \rightarrow 1} \frac{f(x \oplus h) \ominus f(x)}{h} \odot \text{ for } h \in \mathbb{R}(\mathbb{G}).\tag{3.3}$$

Equivalently

$$\begin{aligned} \frac{d^G f}{dx} &= {}_c \lim_{h \rightarrow 1} \frac{f(x \oplus h) \ominus f(x)}{h} {}_c \\ &= \lim_{h \rightarrow 1} \left[\frac{f(hx)}{f(x)} \right]^{\frac{1}{\ln h}}. \end{aligned}$$

The n^{th} G-derivative of $f(x)$ is denoted by $f^{[n]}(x)$. The relation between G-derivative and classical derivative is

$$f^G(x) \text{ or } f^{[1]}(x) = e^x \frac{f'(x)}{f(x)}. \tag{3.4}$$

3.8. Geometric Taylor's Series

If f possesses G-derivative of every order in $[x, xh]$ then its Taylor's expansion is

$$f(xh) = f(x) \cdot [f^{[1]}(x)]^{\ln h} \cdot [f^{[2]}(x)]^{\frac{\ln^2 h}{2!}} \dots [f^{[n]}(x)]^{\frac{\ln^n h}{n!}} \dots = \prod_{n=0}^{\infty} [f^{[n]}(x)]^{\frac{\ln^n h}{n!}}. \tag{3.5}$$

which can be written in geometric form as follows:

$$\begin{aligned} f(x \oplus h) &= f(x) \oplus h \odot f^{[1]}(x) \oplus \frac{h^2 {}_c}{2!_G} \odot f^{[2]}(x) \oplus \dots \oplus \frac{h^n {}_c}{n!_G} \odot f^{[n]}(x) \oplus \dots \\ &= {}_c \sum_{n=0}^{\infty} \frac{h^n {}_c}{n!_G} \odot f^{[n]}(x), \end{aligned} \tag{3.6}$$

where $n!_G = e^{n^2}$ and $h^n {}_c = h^{\ln(n-1)h}$. The equivalent expressions (3.5) and (3.6) are called Taylor's product and Geometric Taylor's series, respectively.

4. Numerical Methods and Solution of G-differential Equations

An equation involving G-differential coefficient is called a G-differential equation. If the exact solution of a given G-differential equation can not be determined, numerical approximation methods can be adopted to determine the solution of the equation at different mesh points. Of course, to compare the exact value and the approximated value, we will take examples of initial value problems whose exact solutions are known. Here we deduce the Euler's, Taylor's and Runge-Kutta methods to compute numerical solutions of initial value problems of G-calculus. In [1] Aniszewska has been developing such methods for multiplicative calculi taking arguments as $a, a + h, a + 2h, \dots$ which form an arithmetic progression. But, all the methods going to be discussed here are based on geometric arithmetic and G-calculus [5]. So, values of the argument will be taken as $a, a \oplus h, a \oplus e^2 \odot h, a \oplus e^2 \odot h, \dots$ i.e. in ordinary sense, values of the argument form a geometric progression a, ah, ah^2, ah^3, \dots .

4.1. G-Euler's Method

In classical calculus, Euler's method is the most elementary approximation technique for solving initial value problems. Here we deduce Euler's method for G-derivatives which we'll call as G-Euler's method. Though it gives weak approximation in practice, the simplicity of its derivation can be used to illustrate the techniques involved in the construction of more advanced techniques.

The objective of G-Euler's method is to obtain approximations to initial value problems having unique solution at given value of the argument. Let us consider the initial value problem

$$\frac{d^{\alpha}y}{dx^{\alpha}} = f(x, y), y(a) = y_0, \quad a \leq x \leq b \text{ and } a \geq 1. \quad (4.1)$$

We first make the stipulation that the mesh points form a geometric progression throughout the interval $[a, b]$. For, we choose a positive integer N and selecting the mesh points

$$x_i = ah^i, \text{ for each } i = 0, 1, 2, \dots, N.$$

The common geometric ratio $h = \left(\frac{b}{a}\right)^{\frac{1}{N}} = \frac{x_{i+1}}{x_i}$ will be called step size.

We will use Geometric Taylor's Theorem stated in [6] to derive G-Euler's method. Let $y(x)$ be the unique solution to (4.1) having two consecutive G-derivatives on $[a, b]$, so that for each $i = 0, 1, 2, \dots, N - 1$,

$$y(x_{i+1}) = y(x_i) \cdot [y^{[1]}(x_i)]^{\ln\left(\frac{x_{i+1}}{x_i}\right)} \cdot [y^{[2]}(\xi_i)]^{\frac{\ln^2\left(\frac{x_{i+1}}{x_i}\right)}{2}}$$

for some $\xi \in (x_i, x_{i+1})$. Putting $h = \frac{x_{i+1}}{x_i}$, we get

$$y(x_{i+1}) = y(x_i) \cdot [y^{[1]}(x_i)]^{\ln h} \cdot [y^{[2]}(\xi_i)]^{\frac{\ln^2 h}{2}}.$$

As $y(x)$ satisfies the differential equation (4.1),

$$y(x_{i+1}) = y(x_i) \cdot [f(x_i, y(x_i))]^{\ln h} \cdot [y^{[2]}(\xi_i)]^{\frac{\ln^2 h}{2}}. \quad (4.2)$$

Neglecting second and higher order G-derivatives, let ω_i be the approximation to $y(x_i)$, i.e. $\omega_i \approx y(x_i)$, for $i = 0, 1, 2, 3, \dots, N - 1$. Thus the G-Euler's method is

$$\begin{aligned} \omega_0 &= y_0, \\ \omega_{i+1} &= \omega_i \cdot [f(x_i, \omega_i)]^{\ln h}, \text{ for } i = 0, 1, 2, 3, \dots, N - 1. \end{aligned} \quad (4.3)$$

In terms of geometric arithmetic, G-Euler's method can written as

$$\begin{aligned} \omega_0 &= y_0, \\ \omega_{i+1} &= \omega_i \oplus h \odot f(x_i, \omega_i), \text{ for } i = 0, 1, 2, 3, \dots, N - 1. \end{aligned} \quad (4.4)$$

Equation (4.4) will be called G-difference equation associated to G-Euler's Method.

Example 4.1. We consider an G-initial value problem as

$$\frac{d^G y}{dx^G} = e^{\left(\frac{x-1}{x}\right)}, 1 \leq x \leq 4, y(1) = 1 \tag{4.5}$$

whose exact solution is

$$y(x) = x - \ln x \tag{4.6}$$

and corresponding ordinary initial value problem is

$$\frac{dy}{dx} = 1 - \frac{1}{x}, 1 \leq x \leq 4, y(1) = 1. \tag{4.7}$$

To approximate (4.5) with the help of G-Euler’s method, we consider $N = 6$. Then

$$\begin{aligned} h &= \left[\frac{b}{a}\right]^{1/N} = \left[\frac{4}{1}\right]^{1/6} = 1.25992105 \\ x_i &= a.h^i = (1.25992105)^i, \quad \omega_0 = 1, \text{ and} \\ \omega_{i+1} &= \omega_i \cdot [f(x_i, \omega_i)]^{\ln h} = \omega_i \cdot \left[e^{\left(\frac{x_i-1}{\omega_i}\right)} \right]^{\frac{\ln 4}{6}}, \text{ for } i = 0, 1, 2, \dots, 6. \end{aligned}$$

Therefore

$$\begin{aligned} \omega_1 &= \omega_0 \cdot \left[e^{\left(\frac{x_0-1}{\omega_0}\right)} \right]^{\frac{\ln 4}{6}} = 1 \cdot \left[e^{\left(\frac{1-1}{1}\right)} \right]^{\frac{\ln 4}{6}} = 1, \\ \omega_2 &= \omega_1 \cdot \left[e^{\left(\frac{x_1-1}{\omega_1}\right)} \right]^{\frac{\ln 4}{6}} = 1 \cdot \left[e^{\left(\frac{1.25992105-1}{1}\right)} \right]^{\frac{\ln 4}{6}} \\ &= e^{(0.25992105 \times 0.23104906)} = 1.061894433, \end{aligned}$$

and so on.

On the other hand, corresponding actual values $y_0, y_1, y_2, \dots, y_6$ are given by

$$y_i = y(x_i) = x_i - \ln(x_i), \text{ for } i = 0, 1, 2, \dots, 6.$$

TABLE 1 shows the comparison between approximated values ω_i and corresponding actual values y_i at x_i . Also we have shown the error $y_i - x_i$.

Table 1: G-Euler’s Approximation at $x = 4$

i	x_i	ω_i	Exact value = $y_i = y(x_i)$	Error = $ y_i - \omega_i $
0	1.000000000	1.000000000	1.000000000	0.000000000
1	1.259921050	1.000000000	1.028871990	0.028871990
2	1.587401052	1.061894433	1.125302932	0.063408498
3	2.000000000	1.206667442	1.306852819	0.100185377
4	2.519842100	1.461318892	1.595645859	0.134326967
5	3.174802104	1.858261811	2.019556803	0.161294992
6	4.000000000	2.435246520	2.613705639	0.178459118

From the TABLE 1, it is seen that error grows rapidly as the value x_i increases. Though errors can be minimized by increasing the number of steps, i.e. N , still they are not negligible errors. That is why G-Euler's method will be less admissible for better approximation. Of course G-Euler method gives better accuracy than the ordinary Euler's method with same number of steps. For, we consider the corresponding ordinary initial value problem given in the above example by equation (4.7). In this case

$$h = \frac{b-a}{N} = \frac{4-1}{6} = 0.5$$

$$x_i = a + ih = 1 + 0.5i, \quad \omega_0 = 1, \text{ and difference equations are given by}$$

$$\omega_{i+1} = \omega_i + h.f(x_i, \omega_i) = \omega_i + 0.5\left(1 - \frac{1}{x_i}\right), \text{ for } i = 0, 1, 2, \dots, 6.$$

TABLE 2 gives the approximate value of the function at $x = 4$ with respect to the ordinary initial value problem.

Table 2: Ordinary Euler's Approximation at $x = 4$

i	x_i	ω_i	Exact value = $y_i = y(x_i)$	Error = $ y_i - \omega_i $
0	1.0	1.000000000	1.000000000	0.000000000
1	1.5	1.000000000	1.094534892	0.094534892
2	2.0	1.166666667	1.306852819	0.140186153
3	2.5	1.416666667	1.583709268	0.167042601
4	3.0	1.716666667	1.901387711	0.184721045
5	3.5	2.050000000	2.247237032	0.197237032
6	4.0	2.407142857	2.613705639	0.206562782

From TABLE 1, $\omega_4 = 2.435246520$ and from Table 2, $\omega_4 = 2.407142857$ whereas the exact value of the function at $x = 4$ is $y(4) = 2.613705639$. Thus, it is clear that G-Euler's method gives better approximation.

4.2. Taylor's G-Series Method

We consider an initial value problem having first order G-derivative as

$$\frac{d^a y}{dx^a} = f(x, y), y(a) = y_0, \quad a \leq x \leq b \text{ and } a \geq 1. \quad (4.8)$$

We take

$$h = \left(\frac{b}{a}\right)^{\frac{1}{N}},$$

where $N \in \mathbb{N}$ will be called number of steps and h , the step-size. We denote, $x_0 = a, x_1 = ah, x_2 = ah^2, \dots, x_N = ah^N = b$. For fixed a and b , values of h decreases as N increases. But N should be so chosen that $h > 1$ and hence x_0, x_1, x_2, \dots will be in increasing order.

Let $y(x) = F(x)$ be the solution of (4.8) such that $F(a) \neq 1$ and $y(x)$ has $(n+1)$ continuous G-derivatives. Then from [6], if we expand the solution, $y(x)$, in terms of n^{th} Taylor product about a point $x_i = ah^i$ and evaluate at $x_{i+1} = ah^{i+1}$, we obtain

$$y(x_{i+1}) = y(x_i) \cdot [y^{[1]}(x_i)]^{\ln h} \cdot [y^{[2]}(x_i)]^{\frac{\ln^2 h}{2!}} \dots [y^{[n]}(x_i)]^{\frac{\ln^n h}{n!}} \cdot [y^{[n+1]}(\xi_i)]^{\frac{\ln^{(n+1)} h}{(n+1)!}} \quad (4.9)$$

for some $\xi_i \in (x_i, x_{i+1})$.

But from (4.8), we have

$$y^{[1]} = f(x, y) = F_1(x, y) \text{ (say)}. \quad (4.10)$$

Then its successive G-differentiation gives

$$\begin{aligned} y^{[2]} &= f^{[1]}(x, y) = \frac{\partial^c F_1}{\partial x^c} \oplus \frac{\partial^c F_1}{\partial y^c} \odot y^{[1]} = F_2(x, y, y^{[1]}), \text{ (say)}, \\ y^{[3]} &= f^{[2]}(x, y) = \frac{\partial^c F_2}{\partial x^c} \oplus \frac{\partial^c F_2}{\partial y^c} \odot y^{[1]} \oplus \frac{\partial^c F_2}{\partial y^{[1]c}} \odot y^{[2]} = F_3(x, y, y^{[1]}, y^{[2]}), \text{ (say)}, \\ y^{[4]} &= f^{[3]}(x, y) = \frac{\partial^c F_3}{\partial x^c} \oplus \frac{\partial^c F_3}{\partial y^c} \odot y^{[1]} \oplus \frac{\partial^c F_3}{\partial y^{[1]c}} \odot y^{[2]} \oplus \frac{\partial^c F_3}{\partial y^{[2]c}} \odot y^{[3]} \\ &= F_4(x, y, y^{[1]}, y^{[2]}, y^{[3]}), \text{ (say)}. \end{aligned}$$

Proceeding in this way, we have

$$\begin{aligned} y^{[n]} &= f^{[n-1]}(x, y) = \frac{\partial^c F_{n-1}}{\partial x^c} \oplus \frac{\partial^c F_{n-1}}{\partial y^c} \odot y^{[1]c} \\ &\oplus \frac{\partial^c F_{n-1}}{\partial y^{[1]c}} \odot y^{[2]} \oplus \dots \oplus \frac{\partial^c F_{n-1}}{\partial y^{[n-2]c}} \odot y^{[n-1]} \\ &= F_n(x, y, y^{[1]}, y^{[2]}, \dots, y^{[n-1]}), \text{ (say)}. \end{aligned}$$

Putting $x = x_i, y_i = y(x_i)$ in above equations, and substituting these values into (4.9) we get

$$\begin{aligned} y(x_{i+1}) &= y(x_i) \cdot [f(x_i, y_i)]^{\ln h} \cdot [f^{[1]}(x_i, y_i)]^{\frac{\ln^2 h}{2!}} \cdot [f^{[2]}(x_i, y_i)]^{\frac{\ln^3 h}{3!}} \dots \\ &\dots [f^{[n-1]}(x_i, y_i)]^{\frac{\ln^n h}{n!}} \cdot [f^{[n]}(\xi_i, y_i)]^{\frac{\ln^{(n+1)} h}{(n+1)!}}. \quad (4.11) \end{aligned}$$

Neglecting the remainder term involving ξ_i , we get the approximation equations (or difference equations) for **Taylor G-series method of order n** as

$$\begin{aligned} \omega_0 &= y_0, \\ \omega_{i+1} &= y(x_i) \cdot [T^{[n]}(x_i, \omega_i)]^{\ln h}, \end{aligned} \quad (4.12)$$

where

$$T^{[n]}(x_i, \omega_i) = f(x_i, y_i) \cdot \left[f^{[1]}(x_i, y_i) \right]^{\frac{\ln h}{h}} \dots \left[f^{[n-1]}(x_i, y_i) \right]^{\frac{\ln^{n-1} h}{h}}, \quad i = 1, 2, 3, \dots, N. \quad (4.13)$$

It is observed that G-Euler method is Taylor G-series method of order one.

Definition 4.2. *If the difference method*

$$\begin{aligned} \omega_0 &= y_0, \\ \omega_{i+1} &= \omega_i \cdot [\phi(x_i, \omega_i)]^{\ln h}, \quad \text{for } i = 0, 1, 2, \dots, N-1 \end{aligned}$$

approximates an initial value problem, we define its local truncation error as

$$\begin{aligned} \tau_{i+1}(h) &= \left[\frac{y_{i+1}}{y_i \cdot \{\phi(x_i, y_i)\}^{\ln h}} \right]^{\frac{1}{\ln h}}, \\ &= \left[\frac{y_{i+1}}{y_i} \right]^{\frac{1}{\ln h}} \cdot \frac{1}{\phi(x_i, y_i)}. \end{aligned}$$

for each $i = 0, 1, 2, \dots, N-1$, where y_i and y_{i+1} denote the solution at x_i and x_{i+1} , respectively.

Theorem 4.3. *Local truncation error in G-Euler's method is $O(\ln h)$.*

Proof: From (4.3), difference equations for G-Euler's method are

$$\begin{aligned} \omega_0 &= y_0, \\ \omega_{i+1} &= \omega_i \cdot [f(x_i, \omega_i)]^{\ln h}, \quad \text{for } i = 0, 1, 2, 3, \dots, N-1. \end{aligned}$$

Therefore local truncation error is

$$\tau_{i+1}(h) = \left[\frac{y_{i+1}}{y_i} \right]^{\frac{1}{\ln h}} \cdot \frac{1}{f(x_i, y_i)}.$$

But, from equation (4.2),

$$\tau_{i+1}(h) = \left[y^{[2]}(\xi_i) \right]^{\frac{\ln h}{2}}$$

If $y^{[2]}(x_i)$ is bounded by a constant, say M on $[a, b]$, then

$$|\tau_{i+1}(h)| \leq M^{\frac{\ln h}{2}}.$$

So, the local truncation error in G-Euler's method is $O(\ln h)$. □

Example 4.4. Apply Taylor's G-series method of order two with $N = 6$ to approximate the solution of the G-initial value problem

$$\frac{d^G y}{dx^G} = x^2, \quad 1 < x < 4, \quad y(1) = 1. \quad (4.14)$$

Solution: To compare the solutions, it is to be noted that exact solution of the equation (4.14) is

$$y = x^{\ln x},$$

and its corresponding ordinary initial value problem is

$$\frac{dy}{dx} = \frac{2y \ln x}{x}, \quad 1 < x < 4, \quad y(1) = 1. \quad (4.15)$$

Since, $N = 6$, we have

$$\begin{aligned} h &= \left[\frac{b}{a} \right]^{1/N} = \left[\frac{4}{1} \right]^{1/6} = 1.25992105 \\ x_i &= a.h^i = h^i, \\ \omega_0 &= 1, \quad \text{and} \\ \omega_{i+1} &= \omega_i \cdot \left[T^{[2]}(x_i, \omega_i) \right]^{\ln h} \quad \text{for } i = 0, 1, 2, \dots, 6. \end{aligned}$$

For the method of order two, we need the first G-derivative of $f(x, y) = x^2$ with respect to the variable x .

$$f^{[1]}(x, y) = e^2,$$

so

$$\begin{aligned} T^{[2]}(x_i, \omega_i) &= f(x_i, \omega_i) \cdot \left[f^{[1]}(x_i, \omega_i) \right]^{\frac{\ln h}{2}} \\ &= x_i^2 \cdot (e^2)^{\frac{\ln h}{2}} \\ &= (h^i)^2 \cdot h = h^{2i+1}. \end{aligned}$$

Now

$$\begin{aligned} \omega_{i+1} &= \omega_i \cdot \left[T^{[2]}(x_i, \omega_i) \right]^{\ln h} \\ &= \omega_i \cdot h^{(2i+1) \ln h} \\ &= \omega_i \cdot \left(4^{1/6} \right)^{\frac{(2i+1) \ln 4}{6}} \\ &= \omega_i \cdot \left(2^{\frac{\ln 2}{3}} \right)^{(2i+1)} \\ &= \omega_i \cdot (1.054834274)^{2i+1}. \end{aligned}$$

Therefore the first step gives the approximation

$$y(1.2599210499) \approx \omega_1 = 1 \times (1.054834274)^1 = 1.054834274.$$

Second approximation is given by

$$y(1.5874010520) \approx \omega_2 = 1.054834274 \times (1.054834274)^2 = 1.238046424.$$

and so on. From the table, it is seen that in the first four steps, approximated values are same as the exact value of the function at corresponding mesh points. In the table, though it seems that in fifth and sixth steps, approximated values and exact values are equal too. But, if we extend the decimal places, actually they are differed by a very very small value after 14th places of decimal. Here, we are using just the Taylor's G-series method of order two. If we use fourth order method, definitely it will give more accurate values. Therefore Taylor G-series approximation gives extremely reliable approximation.

Table 3: Taylor's G-series approximation of order 2 at $x = 4$

i	x_i	ω_i	Exact value $y(x_i)$	Error $ y(x_i) - \omega_i $
0	1.0000000000	1	1	0
1	1.2599210499	1.054834274	1.054834274	0
2	1.5874010520	1.238046424	1.238046424	0
3	2.0000000000	1.616806672	1.616806672	0
4	2.5198420998	2.349349994	2.349349994	0
5	3.1748021039	3.798444745	3.798444745	4.44089×10^{-15}
6	4.0000000000	6.833329631	6.833329631	9.76996×10^{-15}

To compare the values with approximation of ordinary initial value problem, we consider the corresponding initial value problem (4.15) with same number of steps, i.e. $N = 6$. In this case,

$$y' = f(x, y) = \frac{2y \ln x}{x},$$

Differentiating with respect to x , we get

$$\begin{aligned}
 f'(x, y) &= \frac{2y}{x^2}(2\ln^2 x - \ln x + 1). \\
 h &= \frac{4-1}{6} = 0.5 \\
 T^{(2)}(x_i, \omega_i) &= f(x_i, \omega_i) + \frac{h}{2}f'(x_i, \omega_i) \\
 &= \frac{2\omega_i \ln(x_i)}{x_i} + \frac{h}{2}(2\ln^2(x_i) - \ln(x_i) + 1) \\
 &= \frac{\omega_i}{x_i^2} [2x_i \ln(x_i) + h(2\ln^2(x_i) - \ln(x_i) + 1)] \cdot \omega_{i+1} \\
 &= \omega_i + hT^{(2)}(x_i, \omega_i) \\
 &= \omega_i + \frac{h\omega_i}{x_i^2} [2x_i \ln(x_i) + h(2\ln^2(x_i) - \ln(x_i) + 1)].
 \end{aligned}$$

TABLE 4 shows the approximation with the help of ordinary Taylor’s series method. From the table, it is clear that ordinary Taylor’s series method of order two gives poor approximation than Taylor’s G-series method of order two.

Table 4: Ordinary Taylor series approximation of order 2 at $x = 4$

i	x_i	ω_i	Exact value $y(x_i)$	Error $ y(x_i) - \omega_i $
0	1.0	1	1	0
1	1.5	1.250000000	1.054834274	0.195165726
2	2.0	1.716129090	1.238046424	0.478082666
3	2.5	2.446871475	1.616806672	0.830064803
4	3.0	3.516232022	2.349349994	1.166882028
5	3.5	5.030031744	3.798444745	1.231586999
6	4.0	7.126707955	6.833329631	0.293378324

4.3. G-Runge-Kutta Method:

Objective of a numerical techniques is to determine accurate approximations with minimal effort. Since, local truncation error in G-Euler’s method is $O(\ln h)$. So, G-Euler’s method is not applicable in practice. Higher order Taylor’s G-series methods discussed above have higher order truncation error, but disadvantage of higher order Taylor’s G-series methods is that they require the computation and evaluation of higher order G-derivatives of $f(x, y)$, which is complicated in practice. So, Taylor’s methods are rarely used. Here we discuss about G-Runge-Kutta method, which has higher-order local truncation error as like Taylor’s G-series methods but no need to compute higher order G-derivatives of $f(x, y)$.

4.3.1. *G-Runge-Kutta Method of order four:* To approximate the solution of the initial value problem

$$\frac{d^{\alpha}y}{dx^{\alpha}} = f(x, y), y(a) = y_0, a \leq x \leq b \text{ and } \alpha \geq 1 \quad (4.16)$$

in the interval $[a, b]$, we take

$$\begin{aligned} h &= \left(\frac{b-a}{N}\right)^{\frac{1}{\alpha}}; \\ x_0 &= a, x_i = ah^i, \text{ for } i = 1, 2, \dots, N; \\ \omega_0 &= y_0. \end{aligned}$$

Then for $x_1 = ah$, the first increment in y is computed from the formulae

$$\begin{aligned} k_1 &= [f(x_0, y_0)]^{\ln h}, \\ k_2 &= [f(x_0 + \sqrt{h}, y_0 + \sqrt{k_1})]^{\ln h}, \\ k_3 &= [f(x_0 + \sqrt{h}, y_0 + \sqrt{k_2})]^{\ln h}, \\ k_4 &= [f(x_0 + h, y_0 + k_3)]^{\ln h}, \\ \omega_1 &= \omega_0 \cdot (k_1 \cdot k_2^2 \cdot k_3^2 \cdot k_4)^{\frac{1}{6}}, \end{aligned}$$

taken in the given order. In similar manner, the second and successive approximation ω_i to y_i are computed by means of the formulae

$$\begin{aligned} k_1 &= [f(x_i, y_i)]^{\ln h}, \\ k_2 &= [f(x_i + \sqrt{h}, y_i + \sqrt{k_1})]^{\ln h}, \\ k_3 &= [f(x_i + \sqrt{h}, y_i + \sqrt{k_2})]^{\ln h}, \\ k_4 &= [f(x_i + h, y_i + k_3)]^{\ln h}, \\ \omega_{i+1} &= \omega_i \cdot (k_1 \cdot k_2^2 \cdot k_3^2 \cdot k_4)^{\frac{1}{6}} \end{aligned}$$

which can be written in terms of of geometric arithmetic as follows:

$$\begin{aligned} k_1 &= h \odot f(x_i, y_i), \\ k_2 &= h \odot f\left(x_i \oplus \frac{h}{2}, y_i \oplus \frac{k_1}{2}\right), \\ k_3 &= h \odot f\left(x_i \oplus \frac{h}{2}, y_i \oplus \frac{k_2}{2}\right), \\ k_4 &= h \odot f(x_i \oplus h, y_i \oplus k_3), \\ \omega_{i+1} &= \omega_i \oplus \left(\frac{k_1 \oplus e^2 \odot k_2 \oplus e^2 \odot k_3 \oplus k_4}{e^6} \odot c\right). \end{aligned}$$

Example 4.5. We take the same initial value problem mentioned in Example 4.1 with $N = 6$.

Then, $\omega_0 = 1, x_0 = a = 1, h = 1.25992105, x_i = (1.25992105)^i$. Now

$$k_1 = |f(x_0, y_0)|^{\ln h} = \left[e^{\left(\frac{x_0-1}{\omega_0}\right)} \right]^{\frac{\ln h}{h}} = \left[e^{\left(\frac{1-1}{1}\right)} \right]^{\frac{\ln h}{h}} = 1,$$

$$\begin{aligned} k_2 &= \left[f(x_0\sqrt{h}, y_0\sqrt{k_1}) \right]^{\ln h} = \left[e^{\left(\frac{x_0\sqrt{h}-1}{\omega_0\sqrt{k_1}}\right)} \right]^{\frac{\ln h}{h}} \\ &= \left[e^{\left(\frac{1\cdot\sqrt{1.25992105}-1}{1\sqrt{1}}\right)} \right]^{\frac{\ln h}{h}} = e^{(0.122462048 \times 0.23104906)} = 1.02869884, \end{aligned}$$

$$\begin{aligned} k_3 &= \left[f(x_0\sqrt{h}, y_0\sqrt{k_2}) \right]^{\ln h} = \left[e^{\left(\frac{x_0\sqrt{h}-1}{\omega_0\sqrt{k_2}}\right)} \right]^{\frac{\ln h}{h}} \\ &= \left[e^{\left(\frac{1\cdot\sqrt{1.25992105}-1}{1\sqrt{1.02869884}}\right)} \right]^{\frac{\ln h}{h}} = e^{\left(\frac{0.122462048 \times 0.23104906}{1.01424918}\right)} = 1.028290036, \end{aligned}$$

$$\begin{aligned} k_4 &= |f(x_0h, y_0k_3)|^{\ln h} = \left[e^{\left(\frac{x_0h-1}{\omega_0k_3}\right)} \right]^{\frac{\ln h}{h}} \\ &= \left[e^{\left(\frac{1\cdot 2.28290036-1}{1.028290036}\right)} \right]^{\frac{\ln h}{h}} = e^{\left(\frac{0.26992105 \times 0.23104906}{1.028290036}\right)} = 1.060141416, \end{aligned}$$

$$\begin{aligned} \therefore \omega_1 &= \omega_0 \cdot (k_1 \cdot k_2^2 \cdot k_3^2 \cdot k_4)^{\frac{1}{4}} \\ &= 1 \cdot [1 \times (1.02869884)^2 \times (1.028290036)^2 \times 1.060141416]^{\frac{1}{4}} = 1.028873369. \end{aligned}$$

Similarly we can compute successive approximations. Results and their errors computed with the help of Excel are shown in the TABLE 5. In the table, some decimal places are reduced to limit the size of the table for convenience.

Table 5: Approximation by G-Runge-Kutta Method at $x = 4$

i	x_i	ω_i	Exact Value $y_i - y(x_i)$	Error $ y_i - \omega_i $	k_1	k_2	k_3	k_4
1	1.0000	1.0000000	1.0000000	0.000000	1.0000000	1.0286988	1.0282900	1.0601414
2	1.2599	1.0288734	1.0288720	0.000001	1.0601063	1.0945491	1.0929819	1.1282728
3	1.5874	1.1253093	1.1253029	0.000006	1.1281797	1.1631425	1.1604835	1.1935436
4	2.0000	1.3068688	1.3068528	0.000016	1.1933875	1.2232075	1.2201887	1.2463427
5	2.5198	1.5956740	1.5956459	0.000028	1.2461625	1.2676501	1.2650937	1.2826374
6	3.1748	2.0195966	2.0195568	0.000040	1.2824921	1.2956043	1.2939032	1.3037598
7	4.0000	2.6137542	2.6137056	0.000049	1.3036815	1.3102060	1.3093238	1.3135512

From the table it is seen that though error grows as values of x increases, still errors in respective steps are not huge enough. We can compare the approximation given by ordinary Runge-Kutta Method of order 4. For, we consider the

corresponding ordinary initial value problem as stated in equation (4.7) as

$$\frac{dy}{dx} = 1 - \frac{1}{x}, 1 \leq x \leq 4, y(1) = 1.$$

If we consider $N = 6$, then $h = \frac{b-a}{N} = \frac{4-1}{6} = 0.5$ and the ordinary Runge-Kutta method gives the approximation equations as follows:

$$\begin{aligned} k_1 &= hf(x_i, y_i), \\ k_2 &= hf\left(x_i + \frac{h}{2}, y_i + \frac{k_1}{2}\right), \\ k_3 &= hf\left(x_i + \frac{h}{2}, y_i + \frac{k_2}{2}\right), \\ k_4 &= hf(x_i + h, y_i + k_3), \\ \omega_{i+1} &= \omega_i + \left(\frac{k_1 + 2k_2 + 2k_3 + k_4}{6}\right). \end{aligned}$$

Table 6: Approximation by Ordinary Runge-Kutta Method at $x = 4$

i	x_i	ω_i	Exact Value $y_i = y(x_i)$	Error $ y_i - \omega_i $	k_1	k_2	k_3	k_4
1	1.0	1.0000000	1.0000000	0.0000000	0.0000000	0.1000000	0.1000000	0.1666667
2	1.5	1.0944444	1.0945349	0.0000905	0.0431472	0.2142857	0.2142857	0.2500000
3	2.0	1.2861595	1.3068528	0.0206933	0.1112457	0.2777778	0.2777778	0.3000000
4	2.5	1.5398856	1.5837093	0.0438237	0.1753006	0.3181818	0.3181818	0.3333333
5	3.0	1.8367791	1.9013877	0.0646086	0.2277844	0.3461538	0.3461538	0.3571429
6	3.5	2.1650362	2.2472370	0.0822008	0.2690570	0.3666667	0.3666667	0.3750000
7	4.0	2.5168235	2.6137056	0.0968821	0.3013369	0.3823529	0.3823529	0.3888889

From the both tables, if we observe the approximation at $x = 4$, it is obvious that G-Runge-Kutta method gives much better approximation than ordinary Runge-Kutta method. Of course, here, in the ordinary initial value problem, $f(x, y) = 1 - \frac{1}{x} = f(x)$, i.e. it is free from y . So, k_1, k_2, k_3, k_4 have less effect on the approximations in this particular example. That is also a reason for giving worse approximation.

In the G-Runge-Kutta method, if value of N is increased, error will be decreased. If we take $N = 10$, following table shows the approximation at $x = 4$ giving lesser error than for $N = 6$.

Table 7: Approximation by G-Runge-Kutta Method at $x = 4$ with $N = 10$

i	x_i	ω_i	Exact Value	Error	k_1	k_2	k_3	k_4
			$y_i = y(x_i)$	$ y_i - \omega_i $				
1	1.00000	1.000000	1.000000	0.0000000	1.000000	1.010000	1.009950	1.020621
2	1.14870	1.010069	1.010069	0.0000001	1.020618	1.031900	1.031723	1.043420
3	1.31951	1.042249	1.042249	0.0000003	1.043414	1.055417	1.055093	1.067174
4	1.51572	1.099829	1.099828	0.0000006	1.067164	1.079178	1.078719	1.090456
5	1.74110	1.186585	1.186583	0.0000012	1.090442	1.101746	1.101197	1.111927
6	2.00000	1.306855	1.306853	0.0000020	1.111909	1.121918	1.121341	1.130583
7	2.29740	1.465623	1.465620	0.0000028	1.130565	1.138922	1.138378	1.145894
8	2.63902	1.668613	1.668610	0.0000037	1.145877	1.152471	1.152003	1.157779
9	3.03143	1.922402	1.922398	0.0000045	1.157766	1.162680	1.162309	1.166493
10	3.48220	2.234542	2.234537	0.0000051	1.166484	1.169924	1.169653	1.172481
11	4.00000	2.613711	2.613706	0.0000057	1.172476	1.174699	1.174520	1.176254

Also from TABLE 1 and TABLE 5, it is clear that fourth order G-Runge-Kutta method gives much better approximation than G-Euler’s method.

5. Conclusion

From the whole discussion, it has come to light that numerical methods deduced for G-initial value problems are much reliable than ordinary numerical approximation methods. It is observed that if local truncation error in an ordinary method is $O(h^p)$, then local truncation error in the corresponding G-initial value problem is $O(\ln^p h)$. So, converting the ordinary initial value problems to G-initial value problem, we can get better approximated value. Of course, there are some demerits in the methods for G-initial value problems too. G-initial value problems with $x_0 \leq 0$ can not be approximated with the help of above methods. We hope, these barriers will be removed in near future with suitable approximation methods.

Acknowledgments

It is pleasure to thank Prof. M. Grossman for his constructive suggestions and inspiring comments regarding the improvement of the Bigeometric-calculus.

References

1. D. Aniszewska, *Multiplicative Runge-Kutta methods*, Nonlinear Dyn. 50, 265-272, (2007).
2. A. E. Bashirov, M. Riza, *On Complex multiplicative differentiation*, TWMS J. Appl. Eng. Math. 1(1), 75-85, (2011).
3. A. E. Bashirov, E. Mısırlı, Y. Tandođdu and A. Özyapıcı, *On modeling with multiplicative differential equations*, Appl. Math. J. Chinese Univ. 26(4), 425-438, (2011).
4. A. E. Bashirov, E. M. Kurpınar and A. Özyapıcı, *Multiplicative Calculus and its applications*, J. Math. Anal. Appl. 337, 36-48, (2008).
5. K. Boruah, B. Hazarika, *Application of Geometric Calculus in Numerical Analysis and Difference Sequence Spaces*, J. Math. Anal. Appl. 449(2), 1265-1285, (2017).
6. K. Boruah, B. Hazarika, *G-Calculus*, TWMS J. Appl. Eng. 8(1), pp. 94-105, 2018.
7. R. L. Burden, J. D. Faires, *Numerical Analysis*, Ninth Edition, Youngstown State University.
8. A. F. Çakmak, F. Başar, *On Classical sequence spaces and non-Newtonian calculus*, J. Inequal. Appl. 2012, Art. ID 932734, 12pp, (2012).
9. D. Campbell, *Multiplicative Calculus and Student Projects*, Department of Mathematical Sciences, United States Military Academy, West Point, NY,10996, USA.

10. M. Cocco, *Multiplicative Calculus*, Lynchburg College.
11. M. Grossman, *Bigesimal Calculus: A System with a scale-Free Derivative*, Archimedes Foundation, Massachusetts, 1983.
12. M. Grossman, R. Katz, *Non-Newtonian Calculus*, Lee Press, Pigeon Cove, Massachusetts, 1972.
13. J. Grossman, M. Grossman, R. Katz, *The First Systems of Weighted Differential and Integral Calculus*, University of Michigan, 1980.
14. J. Grossman, *Meta-Calculus: Differential and Integral*, University of Michigan, 1981.
15. J. Grossman, R. Katz, *Averages: A new Approach*, University of Michigan, 1983.
16. M. Grossman, *The First Nonlinear System of Differential and Integral Calculus* University of California, 1979.
17. U. Kadak, M. Özlük, *Generalized Runge-Kutta method with respect to non-Newtonian calculus*, Abst. Appl. Anal., Vol. 2015 , Article ID 594685, 10 pages, (2015).
18. F. Córdova-Lepe, *The multiplicative derivative as a measure of elasticity in economics*, TMAE Revista Latinoamericana de Ciencias e Ingeniería, 2(3), 8 pages, (2006).
19. M. Z. Spivey, *A Product Calculus*, University of Puget Sound, Tacoma, Washington 98416-1043.
20. D. Stanley, *A multiplicative calculus*, Primus IX 4 (1999) 310-326.
21. S. Tekin, F. Başar, *Certain Sequence spaces over the non-Newtonian complex field*, Abst. Appl. Anal. 2013. Article ID 739319, 11 pages, (2013).
22. C. Türkmen, F. Başar, *Some Basic Results on the sets of Sequences with Geometric Calculus*, Commun. Fac. Sci. Univ. Ank. Series A1. Vol G1. No 2, 17-34, (2012).

Khirod Boruah,
Department of Mathematics,
Rajiv Gandhi University,
Rono Hills, Doimukh-791112, Arunachal Pradesh,
India.
E-mail address: khirodb10@gmail.com

and

Bipan Hazarika,
Department of Mathematics,
Rajiv Gandhi University,
Rono Hills, Doimukh-791112, Arunachal Pradesh,
India.
Department of Mathematics,
Gauhati University, Guwahati-781014,
India
E-mail address: bh_rgu@yahoo.co.in

and

A.E. Bashirov
Department of Mathematics,
Eastern Mediterranean University,
Gazimagusa - North Cyprus, via Mersin 10,
Turkey.
E-mail address: agamirza.bashirov@emu.edu.tr

Some basic properties of bigeometric calculus and its applications in numerical analysis

Khirod Boruah & Bipan Hazarika

Afrika Matematika

ISSN 1012-9405

Volume 32

Combined 1-2

Afr. Mat. (2021) 32:211-227

DOI 10.1007/s13370-020-00821-1

Your article is protected by copyright and all rights are held exclusively by African Mathematical Union and Springer-Verlag GmbH Deutschland, ein Teil von Springer Nature. This e-offprint is for personal use only and shall not be self-archived in electronic repositories. If you wish to self-archive your article, please use the accepted manuscript version for posting on your own website. You may further deposit the accepted manuscript version in any repository, provided it is only made publicly available 12 months after official publication or later and provided acknowledgement is given to the original source of publication and a link is inserted to the published article on Springer's website. The link must be accompanied by the following text: "The final publication is available at link.springer.com".



Some basic properties of bigeometric calculus and its applications in numerical analysis

Khirod Boruah¹ · Bipan Hazarika¹

Received: 3 June 2020 / Accepted: 1 August 2020 / Published online: 8 August 2020

© African Mathematical Union and Springer-Verlag GmbH Deutschland, ein Teil von Springer Nature 2020

Abstract

Objective of this paper is to visualize a new type of number line which will be called geometric number line based on geometric arithmetic introduced by Grossman and Katz in the book Non-Newtonian calculus (Grossman and Katz, Lee Press, Massachusetts, 1972). Then, we introduce different types of interpolation formulae for geometrically equal and geometrically unequal values of the argument. In our whole discussion, we'll use geometric increment to the arguments instead of linear increments. We will apply the new formulae to different problems of numerical analysis.

Keywords Geometric calculus · Geometric integers · Geometric real numbers

Mathematics Subject Classification 26A06 · 11U10 · 08A05 · 46A45

1 Introduction

In the area of non-Newtonian calculus, pioneering work carried out by Grossman and Katz [15] which we call as multiplicative calculus. We refer to Grossman and Katz [15], Stanley [19], Bashirov et al. [3,4], Grossman [14] for elements of multiplicative calculus and its applications. An extension of multiplicative calculus to functions of complex variables is handled in Bashirov and Rıza [2], Uzer [23], Çakmak and Başar [10], Çakir [6], Kadak et al. [17,18], Tekin and Başar [20], Türkmen and Başar [21,22], Kadak and Özlük [16] studied the generalized Runge–Kutta method with respect to non-Newtonian calculus. Çakmak and Başar [11] constructed the field \mathbb{C}^* of $*$ -complex numbers. Çakmak and Başar [12], the line and double integrals in the sense of $*$ -calculus are given. Moreover, in the sense of $*$ -calculus, the fundamental theorems of calculus for line integrals and double integrals are stated with some applications. Çakmak and Başar [13], characterized matrix transformations

✉ Bipan Hazarika
bh_rgu@yahoo.co.in; bh_gu@gauhati.ac.in

Khirod Boruah
khirodb10@gmail.com

¹ Department of Mathematics, Gauhati University, Guwahati 781014, Assam, India

in sequence spaces based on multiplicative calculus. In [8,9], Boruah and Hazarika discussed basic properties of Bigeometric differential calculus and integral calculus.

2 α -generator and geometric complex field

A generator is a one-to-one function whose domain is \mathbb{R} (the set of real numbers) and whose range is a subset $B \subset \mathbb{R}$. Each generator generates exactly one arithmetic and each arithmetic is generated by exactly one generator. For example, the identity function generates classical arithmetic, and exponential function generates geometric arithmetic. As a generator, we choose the function α such that its basic algebraic operations are defined, as follows:

$$\begin{aligned} \alpha - \text{addition } x \dot{+} y &= \alpha[\alpha^{-1}(x) + \alpha^{-1}(y)], \\ \alpha - \text{subtraction } x \dot{-} y &= \alpha[\alpha^{-1}(x) - \alpha^{-1}(y)], \\ \alpha - \text{multiplication } x \dot{\times} y &= \alpha[\alpha^{-1}(x) \times \alpha^{-1}(y)], \\ \alpha - \text{division } x \dot{/} y &= \alpha[\alpha^{-1}(x) / \alpha^{-1}(y)], \\ \alpha - \text{order } x \dot{<} y &\Leftrightarrow \alpha^{-1}(x) < \alpha^{-1}(y). \end{aligned}$$

for $x, y \in A$, where A is a domain of the function α .

If we choose \exp as an α -generator defined by $\alpha(z) = e^z$ for $z \in \mathbb{C}$ then $\alpha^{-1}(z) = \ln z$ and α -arithmetic turns out to geometric arithmetic.

$$\begin{aligned} \alpha - \text{addition } x \oplus y &= \alpha[\alpha^{-1}(x) + \alpha^{-1}(y)] = e^{(\ln x + \ln y)} = x \cdot y \text{ geometric addition,} \\ \alpha - \text{subtraction } x \ominus y &= \alpha[\alpha^{-1}(x) - \alpha^{-1}(y)] = e^{(\ln x - \ln y)} = x \div y, \quad y \neq 0 \text{ geometric subtraction,} \\ \alpha - \text{multiplication } x \odot y &= \alpha[\alpha^{-1}(x) \times \alpha^{-1}(y)] = e^{(\ln x \times \ln y)} = x^{\ln y} \text{ geometric multiplication,} \\ \alpha - \text{division } x \oslash y &= \alpha[\alpha^{-1}(x) / \alpha^{-1}(y)] = e^{(\ln x \div \ln y)} = x^{\frac{1}{\ln y}}, \quad y \neq 1 \text{ geometric division.} \end{aligned}$$

It is obvious that $\ln(x) < \ln(y)$ if $x < y$ for $x, y \in \mathbb{R}^+$. That is, $x < y \Leftrightarrow \alpha^{-1}(x) < \alpha^{-1}(y)$. So, without loss of generality, we use $x < y$ instead of the geometric order $x \dot{<} y$.

Depending on the different arithmetics, various calculi can be introduced. For example, using geometric arithmetic Grossman and Katz created three calculi, namely, geometric calculus, bigeometric calculus and anageometric calculus. It is to be noted that

- (i) In geometric calculus, changes in functional values are measured by ratios but arguments are measured by linear differences.
- (ii) In bigeometric calculus, changes in both functional values and arguments are measured by ratios.
- (iii) In anageometric calculus, changes in functional values are measured by linear differences but arguments are measured by ratios.

In existing literature, geometric calculus is also known as multiplicative calculus as geometric addition is ordinary product.

Accordingly, different arithmetics give rise to different calculi. Bashirov [1] developed two calculi based on hyperbolic tangent.

Türkmen and Başar [21] defined the sets of geometric integers $\mathbb{Z}(G)$, geometric real numbers $\mathbb{R}(G)$ and geometric complex numbers $\mathbb{C}(G)$, respectively, as follows:

$$\begin{aligned}\mathbb{Z}(G) &= \{e^x : x \in \mathbb{Z}\} = \mathbb{Z} \setminus \{0\}, \\ \mathbb{R}(G) &= \{e^x : x \in \mathbb{R}\} = \mathbb{R}^+ \setminus \{0\}, \\ \mathbb{C}(G) &= \{e^z : z \in \mathbb{C}\} = \mathbb{C} \setminus \{0\}.\end{aligned}$$

Remark 2.1 $(\mathbb{R}(G), \oplus, \odot)$ is a field with geometric zero 1 and geometric identity e , since the following statements hold:

- $(\mathbb{R}(G), \oplus)$ is a geometric additive Abelian group with geometric zero 1.
- $(\mathbb{R}(G) \setminus \{1\}, \odot)$ is a geometric multiplicative Abelian group with geometric identity e .
- \odot is distributive over \oplus .

However, the geometric binary operation \odot is not associative in $\mathbb{C}(G)$; $(\mathbb{C}(G), \oplus, \odot)$ is not a field. In fact, if we take $x = e^{1/4}$, $y = e^4$ and $z = e^{(1+ix/2)} = ie$, then $(x \odot y) \odot z = e \odot z = z = ie$ but $x \odot (y \odot z) = x \odot e^4 = e$.

To remove this deficiency, Bashirov and Norozpour [5] have replaced \mathbb{C} by the Riemann surface \mathbb{B} of complex logarithm so that it becomes a field.

Let us define the sets of geometric positive real numbers $\mathbb{R}^+(G)$ and geometric negative real numbers $\mathbb{R}^-(G)$, as follows:

$$\begin{aligned}\mathbb{R}^+(G) &= \{x \in \mathbb{R}(G) : x > 1\}, \\ \mathbb{R}^-(G) &= \{x \in \mathbb{R}(G) : x < 1\}.\end{aligned}$$

2.1 Some useful relations between geometric operations and ordinary arithmetic operations

For all $x, y \in \mathbb{R}(G)$, the following statements hold:

- $x \oplus y = xy$
- $x \ominus y = x/y$
- $x \odot y = x^{\ln y} = y^{\ln x}$
- $x \oslash y$ or $\frac{x}{y}^G = x^{1/\ln y}$, $y \neq 1$
- $x^{2G} = x \odot x = x^{\ln x}$
- $x^{pG} = x^{\ln^{p-1} x}$
- $\sqrt{x}^G = e^{(\ln x)^{1/2}}$
- $x^{-1G} = e^{1/\log x}$
- $x \odot e = x$ and $x \oplus 1 = x$
- $e^n \odot x = \underbrace{x \oplus x \oplus \dots \oplus x}_{n \text{ terms}}$
- $|x|^G = \begin{cases} x, & \text{if } x > 1, \\ 1, & \text{if } x = 1, \\ 0, & \text{if } x < 1 \end{cases}$ That is to say that $|x|^G \geq 1$.
- $\sqrt{x^{2G}} = |x|^G$
- $|e^y|^G = e^{|y|}$
- $|x \odot y|^G = |x|^G \odot |y|^G$
- $|x \oplus y|^G \leq |x|^G \oplus |y|^G$

- $|x \otimes y|^G = |x|^G \otimes |y|^G$
- $|x \oplus y|^G \geq |x|^G \oplus |y|^G$
- $0_G \oplus 1_G \oplus (x \oplus y) = y \oplus x$, i.e. in short $\oplus (x \oplus y) = y \oplus x$.

Further $e^{-x} = \ominus e^x$ holds for all $x \in \mathbb{Z}^+$. Thus, the set of all geometric integers turns out to be the following:

$$\mathbb{Z}(G) = \{\dots, e^{-3}, e^{-2}, e^{-1}, e^0, e^1, e^2, e^3, \dots\} = \{\dots, \ominus e^3, \ominus e^2, \ominus e, 1, e, e^2, e^3, \dots\}.$$

3 Basic definitions

In this section, we define the basic notions and introduce geometric co-ordinate system.

3.1 Geometric binomial formula

For $a, b \in \mathbb{R}(G)$ and $n \in \mathbb{Z}^+(G)$, we have the following identities:

- (i) $(a \oplus b)^{2G} = (a \oplus b) \otimes (a \oplus b) = a \otimes a \oplus a \otimes b \oplus b \otimes a \oplus b \otimes b = a^{2G} \oplus e^2 \otimes a \otimes b \oplus b^{2G}$.
- (ii) $(a \oplus b)^{3G} = a^{3G} \oplus e^3 \otimes a^{2G} \otimes b \oplus e^3 \otimes a \otimes b^{2G} \oplus b^{3G}$.
- (iii) In general,

$$\begin{aligned} (a \oplus b)^{nG} &= a^{nG} \oplus e^{\binom{n}{1}} \otimes a^{(n-1)G} \otimes b \oplus e^{\binom{n}{2}} \otimes a^{(n-2)G} \otimes b^{2G} \oplus \dots \oplus b^{nG} \\ &= {}_G \sum_{r=0}^n e^{\binom{n}{r}} \otimes a^{(n-r)G} \otimes b^r. \end{aligned}$$

Similarly,

$$(a \ominus b)^{nG} = {}_G \sum_{r=0}^n (\ominus e)^r \otimes e^{\binom{n}{r}} \otimes a^{(n-r)G} \otimes b^r.$$

Note: $x \oplus x = x^2$. Also, $e^2 \otimes x = x^{\ln(e^2)} = x^2$. So, $e^2 \otimes x = x^2 = x \oplus x$.

3.2 Geometric real number line

For $x, y \in \mathbb{R}(G)$, there exist $u, v \in \mathbb{R}$ such that $x = e^u$ and $y = e^v$. Also consecutive natural numbers are equally spaced by one unit in real number line, but the geometric integers e, e^2, e^3, \dots are not equally spaced in ordinary sense, e.g. $e^2 - e \cong 4.6708, e^3 - e^2 \cong 12.6965$. But they are geometrically equidistant as $e^2 \oplus e = e^{2-1} = e, e^3 \oplus e^2 = e^{3-2} = e$ etc. Furthermore, it can be easily verified that $(\mathbb{R}(G), \oplus, \otimes)$ is a complete field with geometric identity e and geometric zero 1 . So we can consider a new type of geometric real number line as shown in Figure 1.



Fig. 1 Geometric number line

3.3 Geometric co-ordinate system

We consider two mutually perpendicular geometric real number lines which intersect each other at (1, 1) as shown in Figure 2.

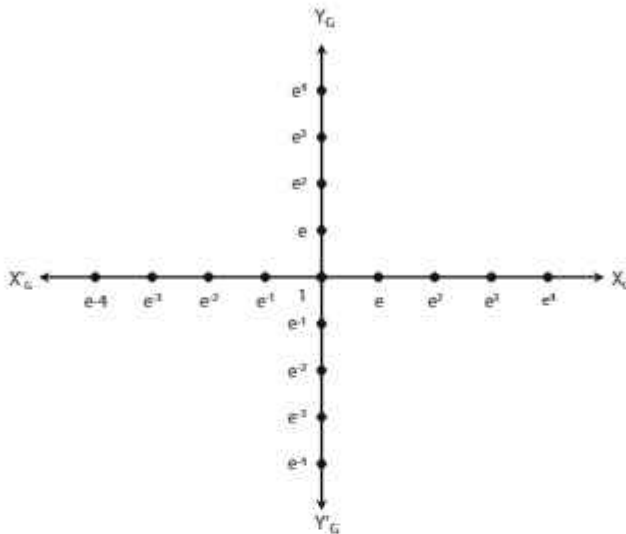


Fig. 2 Geometric co-ordinate system

If we compare the geometric axes with respect the ordinary cartesian coordinate system (Figure 3), the points e, e^2 etc. will not be equidistant.

Since, consecutive geometric integers are equidistant in geometric sense and $(\mathbb{R}(G), \oplus, \odot)$ is a complete field, so, almost all the properties of ordinary cartesian coordinate system will be valid for geometric coordinate system under geometric arithmetic.

4 Bigeometric derivative in terms of geometric arithmetic

Bashirov et al. [4] defined the multiplicative differentiation f^* of a function $f : \mathbb{R} \rightarrow \mathbb{R}$ by

$$\frac{d^* f}{dx} = f^*(x) = \lim_{h \rightarrow 0} \left[\frac{f(x+h)}{f(x)} \right]^{1/h}.$$

We define the bigeometric differentiation f^G of f , in terms of geometric arithmetic as follows:

$$\frac{d^G f}{dx} = f^G(x) = {}_G \lim_{h \rightarrow 1} \frac{f(x \oplus h) \ominus f(x)}{h} G \text{ for } h \in \mathbb{R}(G).$$

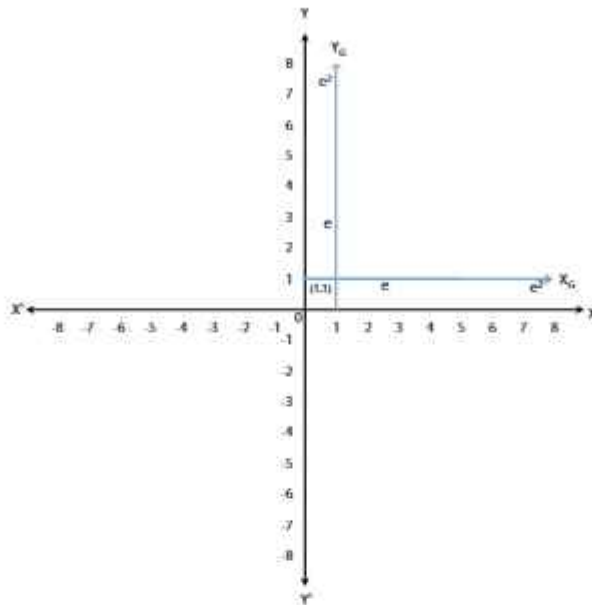


Fig. 3 Comparison of geometric axes w.r.t. ordinary axes

Equivalently

$$\begin{aligned} \frac{d^G f}{dx} &= {}_G \lim_{h \rightarrow 1} \frac{f(x \oplus h) \ominus f(x)}{h} G \\ &= {}_G \lim_{h \rightarrow 1} \left[\frac{f(hx)}{f(x)} \right]^{1/\ln h} \\ &= {}_G \lim_{u \rightarrow 0} \left[\frac{f(e^u \cdot x)}{f(x)} \right]^{1/u}, \text{ where } h = e^u \in \mathbb{R}(G). \end{aligned}$$

It is to be noted that some authors use the notation $f^{\mathbb{N}}$ to denote bigeometric differentiation. The second derivative $f^{(2G)}(x)$ of $f(x)$ is defined as

$$\frac{d^{2G} f}{dx^{2G}} = f^{(2G)}(x) = {}_G \lim_{h \rightarrow 1} \frac{f^{(G)}(x \oplus h) \ominus f^{(G)}(x)}{h} G.$$

Similarly, the n^{th} derivative $f^{(nG)}(x)$ of $f(x)$ is

$$\frac{d^{nG} f}{dx^{nG}} = f^{(nG)}(x) = {}_G \lim_{h \rightarrow 1} \frac{f^{((n-1)G)}(x \oplus h) \ominus f^{((n-1)G)}(x)}{h} G.$$

Example 4.1 If $f(x) = x^{nG}$, then $f^G(x) = e^n \ominus x^{(n-1)G}$ and $f^{(nG)} = e^{n!}$. Indeed, a straightforward calculation shows that

$$\begin{aligned}
 f^G(x) &= {}_G \lim_{h \rightarrow 1} \frac{(x \oplus h)^{n_G} \ominus x^{n_G}}{h} G \\
 &= {}_G \lim_{h \rightarrow 1} \frac{x^{n_G} \oplus e^{\binom{n}{1}} \odot x^{(n-1)G} \odot h \oplus e^{\binom{n}{2}} \odot x^{(n-2)G} \odot h^2 \oplus \dots \oplus h^{n_G} \ominus x^{n_G}}{h} G \\
 &= {}_G \lim_{h \rightarrow 1} \frac{e^{\binom{n}{1}} \odot x^{(n-1)G} \odot h \oplus e^{\binom{n}{2}} \odot x^{(n-2)G} \odot h^2 \oplus \dots \oplus h^{n_G}}{h} G \\
 &= {}_G \lim_{h \rightarrow 1} \left[e^{\binom{n}{1}} \odot x^{(n-1)G} \oplus e^{\binom{n}{2}} \odot x^{(n-2)G} \odot h \oplus \dots \oplus h^{(n-1)G} \right] \\
 &= e^n \odot x^{(n-1)G}.
 \end{aligned}$$

Similarly, we get

$$\begin{aligned}
 f^{(2G)}(x) &= e^n \odot e^{n-1} \odot x^{(n-2)G} \\
 &= e^{n(n-1)} \odot x^{(n-2)G}.
 \end{aligned}$$

Continuing this process, we get $f^{(nG)}(x) = e^{n!}$, as desired.

Example 4.2 Let $f(x) = x$. Then, since $h^{\frac{1}{\ln h}} = e$ one can easily see that

$$\begin{aligned}
 \frac{d^G f}{dx^G} &= {}_G \lim_{h \rightarrow 1} \frac{(x \oplus h) \ominus x}{h} G \\
 &= {}_G \lim_{h \rightarrow 1} \frac{h}{h} G \\
 &= {}_G \lim_{h \rightarrow 1} h^{\frac{1}{\ln h}} \\
 &= e.
 \end{aligned}$$

5 Application of bigeometric calculus in numerical analysis

5.1 Geometric factorial

The geometric factorial notation $n!_G$ has been recently defined by Boruah and Hazarika [7] as follows:

$$n!_G = e^n \odot e^{n-1} \odot e^{n-2} \odot \dots \odot e^2 \odot e = e^{n!}.$$

For example,

$$\begin{aligned}
 0!_G &= e^{0!} = e^0 = 1 \\
 1!_G &= e^{1!} = e = 2.71828 \\
 2!_G &= e^{2!} = e^2 = 7.38906 \\
 3!_G &= e^{3!} = e^6 = 4.03429 \times 10^2 \\
 4!_G &= e^{4!} = e^{24} = 2.64891 \times 10^{10} \\
 5!_G &= e^{5!} = e^{120} = 1.30418 \times 10^{52} \text{ etc.}
 \end{aligned}$$

5.2 Generalized bigeometric forward difference operator

Let

$$\begin{aligned} \Delta_G f(a) &= f(a \oplus h) \ominus f(a), \\ \Delta_G^2 f(a) &= \Delta_G f(a \oplus h) \ominus \Delta_G f(a) \\ &= \{f(a \oplus e^2 \odot h) \ominus f(a \oplus h)\} \ominus \{f(a \oplus h) \ominus f(a)\} \\ &= f(a \oplus e^2 \odot h) \ominus e^2 \odot f(a \oplus h) \oplus f(a), \\ \Delta_G^3 f(a) &= \Delta_G^2 f(a \oplus h) \ominus \Delta_G^2 f(a) \\ &= \{f(a \oplus e^3 \odot h) \ominus e^2 \odot f(a \oplus e^2 \odot h) \oplus f(a \oplus h)\} \\ &\quad \ominus \{f(a \oplus e^2 \odot h) \ominus e^2 \odot f(a \oplus h) \oplus f(a)\} \\ &= f(a \oplus e^3 \odot h) \ominus e^3 \odot f(a \oplus e^2 \odot h) \oplus e^3 \odot f(a \oplus h) \ominus f(a). \end{aligned}$$

Thus, n^{th} forward difference is

$$\Delta_G^n f(a) = {}_G \sum_{k=0}^n (\ominus e)^{kG} \odot e^{\binom{n}{k}} \odot f(a \oplus e^{n-k} \odot h), \text{ with } (\ominus e)^{0G} = e.$$

5.3 Generalized bigeometric backward difference operator

Let

$$\begin{aligned} \nabla_G f(a) &= f(a) \ominus f(a \ominus h), \\ \nabla_G^2 f(a) &= \nabla_G f(a) \ominus \nabla_G f(a \ominus h) \\ &= \{f(a) \ominus f(a \ominus h)\} \ominus \{f(a \ominus h) \ominus f(a \ominus e^2 \odot h)\} \\ &= f(a) \ominus e^2 \odot f(a \ominus h) \oplus f(a \ominus e^2 \odot h), \\ \nabla_G^3 f(a) &= \nabla_G^2 f(a) \ominus \nabla_G^2 f(a - h) \\ &= \{f(a) \ominus e^2 \odot f(a \ominus h) \oplus f(a \ominus e^2 \odot h)\} \\ &\quad \ominus \{f(a \ominus h) \ominus e^2 \odot f(a \ominus e^2 \odot h) \oplus f(a \ominus e^3 \odot h)\} \\ &= f(a) \ominus e^3 \odot f(a \ominus h) \oplus e^3 \odot f(a \ominus e^2 \odot h) \ominus f(a \ominus e^3 \odot h). \end{aligned}$$

Thus, n^{th} bigeometric backward difference is

$$\nabla_G^n f(a) = {}_G \sum_{k=0}^n (\ominus e)^{kG} \odot e^{\binom{n}{k}} \odot f(a \ominus e^k \odot h).$$

5.4 Divided difference

Let $f(x_0), f(x_1), \dots, f(x_n)$ be the entries corresponding to the arguments x_0, x_1, \dots, x_n ; where the intervals $x_1 \ominus x_0, x_2 \ominus x_1, \dots, x_n \ominus x_{n-1}$ not necessarily equal, i.e. values of the argument are not geometrically equispaced. Then the first divided difference of $f(x)$ for the arguments x_0, x_1 is defined as $\frac{f(x_1) \ominus f(x_0)}{x_1 \ominus x_0} G$ or $\frac{f(x_0) \ominus f(x_1)}{x_0 \ominus x_1} G$ and is denoted by $\blacktriangle_{x_1} f(x_0)$ or $f(x_0, x_1)$. i.e.

$$f(x_0, x_1) = \frac{f(x_1) \ominus f(x_0)}{x_1 \ominus x_0} G = \left[\frac{f(x_1)}{f(x_0)} \right]_{\ln(\frac{x_1}{x_0})} = \blacktriangle_{x_1} f(x_0). \text{ Similarly}$$

$$\begin{aligned}
 f(x_1, x_2) &= \frac{f(x_2) \ominus f(x_1)}{x_2 \ominus x_1} G = \left[\frac{f(x_2)}{f(x_1)} \right]^{\frac{1}{\ln(\frac{x_2}{x_1})}} = \blacktriangle_{x_2}^G f(x_1) \\
 f(x_2, x_3) &= \frac{f(x_3) \ominus f(x_2)}{x_3 \ominus x_2} G = \left[\frac{f(x_3)}{f(x_2)} \right]^{\frac{1}{\ln(\frac{x_3}{x_2})}} = \blacktriangle_{x_3}^G f(x_2) \\
 &\vdots \\
 f(x_{n-1}, x_n) &= \frac{f(x_n) \ominus f(x_{n-1})}{x_n \ominus x_{n-1}} G = \left[\frac{f(x_n)}{f(x_{n-1})} \right]^{\frac{1}{\ln(\frac{x_n}{x_{n-1}})}} = \blacktriangle_{x_n}^G f(x_{n-1}).
 \end{aligned}$$

The second geometric divided difference of $f(x)$ for the three arguments x_0, x_1 and x_2 is defined as

$$f(x_0, x_1, x_2) = \frac{f(x_1, x_2) \ominus f(x_0, x_1)}{x_2 \ominus x_0} G = \left[\frac{f(x_1, x_2)}{f(x_0, x_1)} \right]^{\frac{1}{\ln(\frac{x_2}{x_0})}} = \blacktriangle_{x_1, x_2}^2 f(x_0).$$

The n^{th} divided difference is given by

$$\begin{aligned}
 f(x_0, x_1, \dots, x_n) &= \frac{f(x_1, x_2, \dots, x_n) \ominus f(x_0, x_1, \dots, x_{n-1})}{x_n \ominus x_0} G \\
 &= \left[\frac{f(x_1, x_2, \dots, x_n)}{f(x_0, x_1, \dots, x_{n-1})} \right]^{\frac{1}{\ln(\frac{x_n}{x_0})}} \\
 &= \blacktriangle_{x_1, x_2, \dots, x_n}^n f(x_0).
 \end{aligned}$$

For convenience, we'll write $\blacktriangle_{x_1, x_2, \dots, x_n}^n f(x_0)$ instead of $\blacktriangle_{x_1, x_2, \dots, x_n}^n f(x_0)$.

Remark 5.1 If two of the arguments coincide, the divided difference can be given by taking limit as:

$$\begin{aligned}
 f(x_0, x_0) &= \lim_{\epsilon \rightarrow 1} f(x_0, x_0 \oplus \epsilon) = \lim_{\epsilon \rightarrow 1} \frac{f(x_0 \oplus \epsilon) \ominus f(x_0)}{\epsilon} G \\
 &= f^G(x_0), \text{ which is the bigeometric derivative of } f(x) \text{ at } x_0.
 \end{aligned}$$

Similarly, $f(\underbrace{x_0, x_0, x_0, \dots, x_0}_{(m+1) \text{ arguments}}) = \frac{f}{f^m} G \odot f^{(mG)}(x_0)$.

Remark 5.2 The n^{th} divided differences of a bigeometric polynomial of degree n are constant.

Proof First, we consider a function $f(x) = x^{nG}$, i.e. in ordinary sense $f(x) = x^{\ln^{n-1} x}$. Then, the first divided differences of this function are given by

$$\begin{aligned}
 f(x_r, x_{r+1}) &= \frac{f(x_{r+1}) \ominus f(x_r)}{x_{r+1} \ominus x_r} G = \frac{x_{r+1}^{nG} \ominus x_r^{nG}}{x_{r+1} \ominus x_r} \\
 &= x_{r+1}^{(n-1)G} \oplus x_{r+1}^{(n-2)G} \odot x_r \oplus x_{r+1}^{(n-3)G} \odot x_r^2 \oplus \dots \oplus x_{r+1} \odot x_r^{(n-2)G} \oplus x_r^{(n-1)G},
 \end{aligned}$$

which is a homogeneous expression of degree $(n - 1)$ in x_r and x_{r+1} . The second divided differences are given by

$$f(x_r, x_{r+1}, x_{r+2}) = \frac{f(x_{r+1}, x_{r+2}) \ominus f(x_r, x_{r+1})}{x_{r+2} \ominus x_r} G$$

$$\begin{aligned}
 &= \frac{x_{r+2}^{(n-1)G} \oplus x_{r+2}^{(n-2)G} \odot x_{r+1} \oplus x_{r+2}^{(n-3)G} \odot x_{r+1}^2 \oplus \dots \oplus x_{r+1}^{(n-1)G}}{x_{r+2} \oplus x_r} G \\
 &\ominus \frac{x_{r+1}^{(n-1)G} \oplus x_{r+1}^{(n-2)G} \odot x_r \oplus x_{r+1}^{(n-3)G} \odot x_r^2 \oplus \dots \oplus x_r^{(n-1)G}}{x_{r+2} \oplus x_r} G \\
 &= \frac{x_{r+2}^{(n-1)G} \ominus x_r^{(n-1)G}}{x_{r+2} \oplus x_r} G \oplus x_{r+1} \odot \frac{x_{r+2}^{(n-2)G} \ominus x_r^{(n-2)G}}{x_{r+2} \oplus x_r} G \oplus \\
 &\quad \dots \oplus x_{r+1}^{(n-2)G} \odot \frac{x_{r+2} \oplus x_r}{x_{r+2} \oplus x_r} G \\
 &= \left(x_{r+2}^{(n-2)G} \oplus \dots \oplus x_r^{(n-2)G} \right) \oplus x_{r+1} \odot \left(x_{r+2}^{(n-3)G} \oplus \dots \oplus x_r^{(n-3)G} \right) \oplus \\
 &\quad \dots \oplus x_{r+1}^{(n-2)G} \tag{5.1}
 \end{aligned}$$

which is a homogeneous expression of degree $n - 2$ in x_r, x_{r+1} and x_{r+2} .

By induction it can be shown that the n^{th} divided difference of $f(x) = x^{nG}$ is an expression of degree zero, i.e. a constant, and therefore independent of the values $x_r, x_{r+1}, \dots, x_{r+n}$. Since the n^{th} bigeometric divided difference of x^{nG} are constant, therefore, the bigeometric divided differences of x^{nG} of order less than n will all be zero.

If $f(x) = a \odot x^{nG}$, where $a \in \mathbb{R}(G)$ is a constant, then the n^{th} bigeometric divided difference of $f(x) = a \odot (n^{\text{th}}$ bigeometric divided difference of $x^{nG})$, which is a constant.

Therefore, if $f(x) = a_0 \odot x^{nG} \oplus a_1 \odot x^{(n-1)G} \oplus \dots \oplus a_{n-1} \odot x \oplus a_n$ be a bigeometric polynomial of degree n , so that $a_0, a_1, \dots, a_n \in \mathbb{R}(G)$, then the n^{th} bigeometric divided difference of all terms will be vanished except that $a_0 \odot x^n$ turns to constant. Hence n^{th} bigeometric divided difference of the whole polynomial is constant. \square

In the paper [7], we derive Bigeometric Newton-Gregory forward interpolation and backward interpolation formulae for geometrically equidistant values of the argument. Here, we derive divided difference interpolation formula for unequal values of the argument.

5.5 Divided difference Interpolation formula

Let $f(x_0), f(x_1), \dots, f(x_n)$ be the values of $f(x)$ corresponding to the arguments x_0, x_1, \dots, x_n not necessarily geometrically equally spaced. Then, we have by the definition of divided differences

$$\begin{aligned}
 f(x, x_0) &= \frac{f(x) \ominus f(x_0)}{x \ominus x_0} G \\
 (x \ominus x_0) \odot f(x) &= f(x) \ominus f(x_0) \\
 \implies f(x) &= f(x_0) \oplus (x \ominus x_0) \odot f(x).
 \end{aligned}$$

Also,

$$\begin{aligned}
 f(x, x_0, x_1) &= \frac{f(x, x_0) \ominus f(x_0, x_1)}{x \ominus x_1} G \\
 \implies f(x, x_0) &= f(x_0, x_1) \oplus (x \ominus x_1) \odot f(x, x_0, x_1) \\
 \therefore f(x) &= f(x_0) \oplus (x \ominus x_0) \odot \{ f(x_0, x_1) \oplus (x - x_1) \odot f(x, x_0, x_1) \} \\
 &= f(x_0) \oplus (x \ominus x_0) \odot f(x_0, x_1) \oplus (x \ominus x_0)(x - x_1) \odot f(x, x_0, x_1).
 \end{aligned}$$

Again,

$$f(x, x_0, x_1) = f(x_0, x_1, x_2) \oplus (x - x_2) \odot f(x, x_0, x_1, x_2).$$

Similarly,

$$f(x, x_0, x_1, x_2) = f(x_0, x_1, x_2) \oplus (x - x_3) \odot f(x, x_0, x_1, x_2, x_3)$$

$$\vdots$$

$$f(x, x_0, x_1, \dots, x_{n-1}) = f(x_0, x_1, \dots, x_n) \oplus \dots \oplus (x - x_n) \odot f(x, x_0, x_1, \dots, x_n).$$

Therefore, we get by substituting successively that

$$\begin{aligned} f(x) &= f(x_0) \oplus (x \ominus x_0) \odot f(x_0, x_1) \oplus (x \ominus x_0) \odot (x \ominus x_1) \odot f(x_0, x_1, x_2) \oplus \\ &\quad \dots \oplus (x \ominus x_0) \odot (x \ominus x_1) \odot \dots \odot (x \ominus x_{n-1}) \odot f(x_0, x_1, \dots, x_n) \oplus R_n. \end{aligned} \quad (5.2)$$

where the the remainder R_n is given by

$$R_n = (x \ominus x_0) \odot (x \ominus x_1) \odot \dots \odot (x \ominus x_n) \odot f(x, x_0, x_1, \dots, x_n).$$

If $f(x)$ is a bigeometric polynomial of degree n , then $f(x, x_0, x_1, \dots, x_n) = 1$. So, the equality (5.2) becomes

$$\begin{aligned} f(x) &= f(x_0) \oplus (x \ominus x_0) \odot f(x_0, x_1) \oplus (x \ominus x_0) \odot (x \ominus x_1) \odot f(x_0, x_1, x_2) \oplus \\ &\quad \dots \oplus (x \ominus x_0) \odot (x \ominus x_1) \odot \dots \odot (x \ominus x_{n-1}) \odot f(x_0, x_1, \dots, x_n). \end{aligned} \quad (5.3)$$

This is the divided difference interpolation formula for geometrically unequal intervals.

5.6 Relation between divided differences and bigeometric forward interpolation

Let the values of the argument x_0, x_1, \dots, x_n be equally spaced, i.e., $x_1 = x_0 \oplus e \odot h$, $x_2 = x_0 \oplus e^2 \odot h$, $x_3 = x_0 \oplus e^3 \odot h$, \dots , $x_n = x_0 \oplus e^{n-1} \odot h$ and let $\frac{x \ominus x_0}{h} G = u$. Then,

$$\begin{aligned} f(x_0, x_1) &= \frac{f(x_1) \ominus f(x_0)}{x_1 \ominus x_0} G \\ &= \frac{f(x_0 \oplus h) \ominus f(x_0)}{x_0 \oplus h \ominus x_0} G \\ &= \frac{\Delta_G f(x_0)}{h} G \\ f(x_0, x_1, x_2) &= \frac{f(x_1, x_2) \ominus f(x_1, x_0)}{x_2 \ominus x_0} G \\ &= \frac{\frac{\Delta_G f(x_1)}{h} G \ominus \frac{\Delta_G f(x_0)}{h} G}{e^2 \odot h} G \\ &= \frac{\Delta_G^2 f(x_0)}{e^2 \odot h \odot h} G \\ &= \frac{\Delta_G^2 f(x_0)}{2!_G \odot h^2_G} G. \end{aligned}$$

Similarly,

$$\begin{aligned} f(x_0, x_1, x_2, x_3) &= \frac{\Delta_G^3 f(x_0)}{3!_G \odot h^{3G}} G, \\ &\vdots \\ f(x_0, x_1, \dots, x_n) &= \frac{\Delta_G^n f(x_0)}{n!_G \odot h^{nG}} G. \end{aligned}$$

Substituting these values of divided differences in (5.3) we get

$$\begin{aligned} f(x) &= f(x_0) \oplus u \odot \Delta_G f(x_0) \oplus \frac{u \odot (u \ominus e)}{2!_G} G \odot \Delta_G^2 f(x_0) \\ &\oplus \frac{u \odot (u \ominus e) \odot (u \ominus e^2)}{3!_G} G \odot \Delta_G^3 f(x_0) \oplus \dots \\ &\oplus \frac{u \odot (u \ominus e) \odot (u \ominus e^2) \odot \dots \odot (u \ominus e^{n-1})}{n!_G} G \odot \Delta_G^n f(x_0). \end{aligned} \quad (5.4)$$

This is the Newton–Gregory formula for bigeometric forward interpolation about which has been discussed in [7].

Remark 5.3 The bigeometric divided differences are symmetrical in all their arguments, i.e. the value of any difference is independent of the order of the arguments.

Proof Let $f(x_0), f(x_1), \dots, f(x_n)$ be the values of $f(x)$ corresponding to the arguments x_0, x_1, \dots, x_n . We have the first bigeometric divided difference (BGDD) is

$$\begin{aligned} f(x_0, x_1) &= \frac{f(x_1) \ominus f(x_0)}{x_1 \ominus x_0} G = \frac{f(x_0) \ominus f(x_1)}{x_0 \ominus x_1} G = f(x_1, x_0) \\ &= \frac{f(x_0)}{x_0 \ominus x_1} G \oplus \frac{f(x_1)}{x_1 \ominus x_0} G = G \sum \frac{f(x_0)}{x_0 \ominus x_1} G, \end{aligned}$$

showing that $f(x_0, x_1)$ is symmetrical in x_0, x_1 . Again, the second BGDD is

$$\begin{aligned} f(x_0, x_1, x_2) &= \frac{f(x_1, x_2) \ominus f(x_0, x_1)}{x_2 \ominus x_0} G \\ &= \frac{e}{x_2 \ominus x_0} G \odot \left[\left\{ \frac{f(x_1)}{x_1 \ominus x_2} G \oplus \frac{f(x_2)}{x_2 \ominus x_1} G \right\} \ominus \left\{ \frac{f(x_0)}{x_0 \ominus x_1} G \oplus \frac{f(x_1)}{x_1 \ominus x_0} G \right\} \right] \\ &= \frac{f(x_0)}{(x_0 \ominus x_1) \odot (x_0 \ominus x_2)} G \oplus \frac{f(x_1)}{(x_1 \ominus x_0) \odot (x_1 \ominus x_2)} G \\ &\quad \oplus \frac{f(x_2)}{(x_2 \ominus x_0) \odot (x_2 \ominus x_1)} G \\ &= G \sum \frac{f(x_0)}{(x_0 \ominus x_1) \odot (x_0 \ominus x_2)} G, \text{ showing that second BGDD is symmetrical.} \end{aligned}$$

Let us assume that $(n - 1)^{\text{th}}$ BGDD is symmetrical, i.e.

$$\begin{aligned}
 f(x_0, x_1, \dots, x_{n-1}) &= \frac{f(x_0)}{(x_0 \ominus x_1) \odot \dots \odot (x_0 \ominus x_{n-1})} G \\
 &\oplus \frac{f(x_1)}{(x_1 \ominus x_0) \odot (x_1 \ominus x_2) \odot \dots \odot (x_1 \ominus x_{n-1})} G \oplus \dots \\
 &\oplus \frac{f(x_{n-1})}{(x_{n-1} \ominus x_0) \odot (x_{n-1} \ominus x_1) \odot \dots \odot (x_{n-1} \ominus x_{n-2})} G \\
 &= G \sum \frac{f(x_0)}{(x_0 \ominus x_1) \odot \dots \odot (x_0 \ominus x_{n-1})} G.
 \end{aligned}$$

Then,

$$\begin{aligned}
 f(x_0, x_1, \dots, x_n) &= \frac{f(x_0, \dots, x_{n-1}) \ominus f(x_1, \dots, x_n)}{x_0 \ominus x_n} G \\
 &= \frac{e}{x_0 \ominus x_n} G \odot \left\{ G \sum \frac{f(x_0)}{(x_0 \ominus x_1) \odot \dots \odot (x_0 \ominus x_{n-1})} G \right\} \\
 &\ominus \frac{e}{x_0 \ominus x_n} G \odot \left\{ G \sum \frac{f(x_1)}{(x_1 \ominus x_0) \odot (x_1 \ominus x_2) \odot \dots \odot (x_1 \ominus x_n)} G \right\} \\
 &= \frac{f(x_0)}{(x_0 \ominus x_1) \odot \dots \odot (x_0 \ominus x_n)} G \tag{5.5} \\
 &\oplus \frac{f(x_1)}{(x_1 \ominus x_0) \odot (x_1 \ominus x_2) \odot \dots \odot (x_1 \ominus x_n)} G \oplus \dots \\
 &\oplus \frac{f(x_n)}{(x_n \ominus x_0) \odot (x_n \ominus x_1) \odot \dots \odot (x_n \ominus x_{n-1})} G \\
 &= G \sum \frac{f(x_0)}{(x_0 \ominus x_1) \odot \dots \odot (x_0 \ominus x_n)} G.
 \end{aligned}$$

□

5.7 Lagrange's bigeometric Interpolation formula for unequal intervals

Let $y = f(x)$ be a bigeometric polynomial of degree n which takes the values $y_0 = f(x_0), y_1 = f(x_1), \dots, y_n = f(x_n)$ as x takes the values x_0, x_1, \dots, x_n , respectively. Then the $(n + 1)^{\text{th}}$ BGDD of this polynomial are zero. Hence,

$$f(x, x_0, x_1, \dots, x_n) = 0. \tag{5.6}$$

Again from equality (5.5)

$$\begin{aligned}
 f(x, x_0, x_1, \dots, x_n) &= \frac{y}{(x \ominus x_0) \odot (x \ominus x_1) \odot \dots \odot (x \ominus x_n)} G \\
 &\oplus \frac{y_0}{(x_0 \ominus x) \odot (x_0 \ominus x_1) \odot \dots \odot (x_0 \ominus x_n)} G \\
 &\oplus \frac{y_1}{(x_1 \ominus x) \odot (x_1 \ominus x_0) \odot \dots \odot (x_1 \ominus x_n)} G \oplus \dots \\
 &\oplus \frac{y_n}{(x_n \ominus x) \odot (x_n \ominus x_0) \odot \dots \odot (x_n \ominus x_{n-1})} G.
 \end{aligned} \tag{5.7}$$

Using (5.6), we get

$$\begin{aligned} & \frac{y}{(x \ominus x_0) \odot (x \ominus x_1) \odot \dots \odot (x \ominus x_n)} G \\ & \oplus \frac{y_0}{(x_0 \ominus x) \odot (x_0 \ominus x_1) \odot \dots \odot (x_0 \ominus x_n)} G \\ & \oplus \frac{y_1}{(x_1 \ominus x) \odot (x_1 \ominus x_0) \odot \dots \odot (x_1 \ominus x_n)} G \oplus \dots \\ & \oplus \frac{y_n}{(x_n \ominus x) \odot (x_n \ominus x_0) \odot \dots \odot (x_n \ominus x_{n-1})} G = 0. \end{aligned} \tag{5.8}$$

Transposing all terms except the first term, to the right hand side, we get

$$\begin{aligned} & \frac{y}{(x \ominus x_0) \odot (x \ominus x_1) \odot \dots \odot (x \ominus x_n)} G \\ & = \frac{y_0}{(x \ominus x_0) \odot (x_0 \ominus x_1) \odot \dots \odot (x_0 \ominus x_n)} G \\ & \oplus \frac{y_1}{(x \ominus x_1) \odot (x_1 \ominus x_0) \odot \dots \odot (x_1 \ominus x_n)} G \oplus \dots \\ & \oplus \frac{y_n}{(x \ominus x_n) \odot (x_n \ominus x_0) \odot \dots \odot (x_n \ominus x_{n-1})} G. \end{aligned} \tag{5.9}$$

Multiplying both sides by $(x \ominus x_0) \odot (x \ominus x_1) \odot \dots \odot (x \ominus x_n)$, we get

$$\begin{aligned} y &= \frac{(x \ominus x_1) \odot \dots \odot (x \ominus x_n)}{(x_0 \ominus x_1) \odot (x_0 \ominus x_2) \odot \dots \odot (x_0 \ominus x_n)} G \odot y_0 \\ & \oplus \frac{(x \ominus x_0) \odot \dots \odot (x \ominus x_n)}{(x_1 \ominus x_0) \odot (x_1 \ominus x_2) \odot \dots \odot (x_1 \ominus x_n)} G \odot y_1 \\ & \oplus \frac{(x \ominus x_0) \odot (x \ominus x_1) \odot (x \ominus x_3) \odot \dots \odot (x \ominus x_n)}{(x_2 \ominus x_0) \odot (x_2 \ominus x_1) \odot (x_2 \ominus x_3) \odot \dots \odot (x_1 \ominus x_n)} G \odot y_2 \oplus \dots \\ & \oplus \frac{(x \ominus x_0) \odot (x \ominus x_1) \odot \dots \odot (x \ominus x_{n-1})}{(x_n \ominus x_0) \odot (x_n \ominus x_1) \odot \dots \odot (x_n \ominus x_{n-1})} G \odot y_n. \end{aligned} \tag{5.10}$$

Example 5.1 Given, $f(x) = f(e^t) = \sin(e^t)$. From the following table, find $\sin(e^{0.14})$ using geometric divided difference formula.

x	$e^{0.12}$	$e^{0.15}$	$e^{0.19}$	$e^{0.21}$
$f(x)$	0.903341	0.917534	0.935351	0.943712

Solution. The geometric divided difference table for given geometrically unequal data is, as follows:

It is to be noted that here in the table,

$$\begin{aligned} \blacktriangle_G f(x_0) &= \left[\frac{0.917534}{0.903341} \right]^{\ln\left(\frac{e^{0.15}}{e^{0.12}}\right)} = (1.0157116748)^{\frac{1}{0.03}} = 1.681421 \\ \blacktriangle_G f(x_1) &= \left[\frac{0.935351}{0.917534} \right]^{\ln\left(\frac{e^{0.19}}{e^{0.15}}\right)} = 1.617367 \text{ and so on. Similarly,} \end{aligned}$$

x (in radian)	$f(x)$	$\blacktriangle_G f(x)$	$\blacktriangle_G^2 f(x)$	$\blacktriangle_G^3 f(x)$
$e^{0.12}$	0.903341	1.681421		
$e^{0.15}$	0.917534	1.617367	0.574158	
$e^{0.19}$	0.935351	1.560421	0.55024	0.623266
$e^{0.21}$	0.943712			

$$\blacktriangle_G^2 f(x_0) = \left[\frac{1.617367}{1.681421} \right]^{\ln\left(\frac{e^{0.19}}{e^{0.12}}\right)} = 0.574158 \text{ etc.}$$

Now, using the geometric divided difference formula, we get

$$\begin{aligned} f(x) &= f(x_0) \oplus (x \ominus x_0) \odot \blacktriangle_G f(x_0) \oplus (x \ominus x_0) \odot (x \ominus x_1) \odot \blacktriangle_G^2 f(x_0) \\ &\quad \oplus (x \ominus x_0) \odot (x \ominus x_1) \odot (x \ominus x_2) \odot \blacktriangle_G^3 f(x_0) \oplus \dots \\ f(e^{0.14}) &= 0.903341 \oplus (e^{0.14} \ominus e^{0.12}) \odot 1.681421 \\ &\quad \oplus (e^{0.14} \ominus e^{0.12}) \odot (e^{0.14} \ominus e^{0.15}) \odot 0.574158 \\ &\quad \oplus (e^{0.14} \ominus e^{0.12}) \odot (e^{0.14} \ominus e^{0.12}) \odot (e^{0.15} \ominus e^{0.19}) \odot 0.623266 \\ &= 0.903341 \oplus e^{0.14-0.12} \odot 1.681421 \oplus (e^{0.14-0.12} \odot e^{0.14-0.15}) \odot 0.574158 \\ &\quad \oplus (e^{0.14-0.12} \odot e^{0.14-0.12} \odot e^{0.15-0.19}) \odot 0.623266 \\ &= 0.903341 \oplus e^{0.02} \odot 1.681421 \oplus (e^{0.02} \odot e^{-0.01}) \odot 0.574158 \\ &\quad \oplus (e^{0.02} \odot e^{-0.01} \odot e^{-0.05}) \odot 0.623266 \\ &= 0.903341 \oplus e^{0.02} \odot 1.681421 \oplus e^{0.02(-0.01)} \odot 0.574158 \oplus e^{0.02(-0.01)(-0.05)} \odot 0.623266 \\ &= 0.903341 \oplus e^{0.02} \odot 1.681421 \oplus e^{-0.0002} \odot 0.574158 \oplus e^{0.00001} \odot 0.623266 \\ &= 0.903341 \oplus (1.681421)^{0.02} \oplus (0.574158)^{\frac{1}{1000}} \oplus (0.623266)^{0.00001} \\ &= 0.903341 \oplus 1.010447 \oplus 1.000111 \oplus 0.999995 \\ &= 0.903341 \times 1.010447 \times 1.000111 \times 0.999995 \\ &= 0.912875 \end{aligned}$$

Hence $\sin(e^{0.14}) = 0.912875$ which is accurate upto the last place of decimal (i.e. sixth place). Thus, geometric divided difference interpolation formula gives values of transcendental functions at given points upto desired degree of accuracy.

Example 5.2 Solve the problem explained in Example 5.1 by Lagrange's geometric interpolation formula.

Solution. Given

x	$e^{0.12}$	$e^{0.15}$	$e^{0.19}$	$e^{0.21}$
$f(x)$	0.903341	0.917534	0.935351	0.943712

Here $x = e^{0.14}$, $x_0 = e^{0.12}$, $x_1 = e^{0.15}$, $x_2 = e^{0.19}$ and $x_3 = e^{0.21}$. Now, Lagrange's interpolation formula gives

$$\begin{aligned} f(x) &= \frac{(x \ominus x_1) \odot (x \ominus x_2) \odot (x \ominus x_3)}{(x_0 \ominus x_1) \odot (x_0 \ominus x_2) \odot (x_0 \ominus x_3)} G \odot f(x_0) \\ &\oplus \frac{(x \ominus x_0) \odot (x \ominus x_2) \odot (x \ominus x_3)}{(x_1 \ominus x_0) \odot (x_1 \ominus x_2) \odot (x_1 \ominus x_3)} G \odot f(x_1) \\ &\oplus \frac{(x \ominus x_0) \odot (x \ominus x_1) \odot (x \ominus x_3)}{(x_2 \ominus x_0) \odot (x_2 \ominus x_1) \odot (x_2 \ominus x_3)} G \odot f(x_2) \\ &\oplus \frac{(x \ominus x_0) \odot (x \ominus x_1) \odot (x \ominus x_2)}{(x_3 \ominus x_0) \odot (x_3 \ominus x_1) \odot (x_3 \ominus x_2)} G \odot f(x_3). \end{aligned}$$

Putting the values we get

$$\begin{aligned} f(e^{0.14}) &= \frac{(e^{0.14} \ominus e^{0.15}) \odot (e^{0.14} \ominus e^{0.19}) \odot (e^{0.14} \ominus e^{0.21})}{(e^{0.12} \ominus e^{0.15}) \odot (e^{0.12} \ominus e^{0.19}) \odot (e^{0.12} \ominus e^{0.21})} G \odot f(e^{0.12}) \\ &\oplus \frac{(e^{0.14} \ominus e^{0.12}) \odot (e^{0.14} \ominus e^{0.19}) \odot (e^{0.14} \ominus e^{0.21})}{(e^{0.15} \ominus e^{0.12}) \odot (e^{0.15} \ominus e^{0.19}) \odot (e^{0.15} \ominus e^{0.21})} G \odot f(e^{0.15}) \\ &\oplus \frac{(e^{0.14} \ominus e^{0.12}) \odot (e^{0.14} \ominus e^{0.15}) \odot (e^{0.14} \ominus e^{0.21})}{(e^{0.19} \ominus e^{0.12}) \odot (e^{0.19} \ominus e^{0.15}) \odot (e^{0.19} \ominus e^{0.21})} G \odot f(e^{0.19}) \\ &\oplus \frac{(e^{0.14} \ominus e^{0.12}) \odot (e^{0.14} \ominus e^{0.15}) \odot (e^{0.14} \ominus e^{0.19})}{(e^{0.21} \ominus e^{0.12}) \odot (e^{0.21} \ominus e^{0.15}) \odot (e^{0.21} \ominus e^{0.19})} G \odot f(e^{0.21}) \\ &= e^{\frac{(-0.01)(-0.05)(-0.07)}{(-0.03)(-0.07)(-0.09)}} \odot 0.903341 \oplus e^{\frac{(0.02)(-0.05)(-0.07)}{(0.03)(-0.04)(-0.06)}} \odot 0.917534 \\ &\oplus e^{\frac{(0.02)(-0.01)(-0.07)}{(0.07)(0.04)(-0.02)}} \odot 0.935351 \oplus e^{\frac{(0.02)(-0.01)(-0.05)}{(0.09)(0.06)(0.02)}} \odot 0.943712 \\ &= e^{\frac{5}{27}} \odot 0.903341 \oplus e^{\frac{35}{36}} \odot 0.917534 \oplus e^{\frac{1}{4}} \odot 0.935351 \oplus e^{\frac{5}{24}} \odot 0.943712 \\ &= (0.903341)^{\frac{5}{27}} \oplus (0.917534)^{\frac{35}{36}} \oplus (0.935351)^{\frac{1}{4}} \oplus (0.943712)^{\frac{5}{24}} \\ &= 0.981351 \oplus 0.91973 \oplus 1.016849 \oplus 0.99465 \\ &= 0.981351 \times 0.91973 \times 1.016849 \times 0.99465 \\ &= 0.912875 \end{aligned}$$

Therefore, $\sin(e^{0.14}) = 0.912875$ which is correct upto the sixth place of decimal. \square

6 conclusion

Here, we have visualized geometric number line. Also we have discussed the different bigeometric interpolation formulae together with their applications. In multiplicative calculus, ordinary sum(+) is used to produce increment to the independent variable x such as $x_0, x_0 + h, x_0 + 2h, \dots$. In that case some problems arise to discuss independently about the arithmetic system ($\oplus, \ominus, \odot, \oslash$). That is why, in our whole discussion, we have taken geometric sum (\oplus) to produce increment to the independent variable x such as $x_0, x_0 \oplus h, x_0 \oplus e^2 \odot h, \dots$. Instead of mixing the ordinary arithmetic system ($+, -, \times, \div$) and geometric arithmetic system ($\oplus, \ominus, \odot, \oslash$), we are trying to formulate basic identities independently. We discussed in [7] that the ordinary interpolation formulae are based upon the fundamental assumption that the data are expressible or can be expressed as a polynomial function with fair degree of accuracy. But geometric interpolation formulae have no such

restriction. Because geometric interpolation formulae are based on geometric polynomials which are transcendental expressions in ordinary sense. So geometric interpolation formulae can be used to generate transcendental functions, mainly to compute exponential and logarithmic functions.

References

1. Bashirov, A.E.: Relativistic velocity addition and calculi based on hyperbolic tangent. In: Focus on Calculus, Nova Science Publisher, New York. ISBN: 978-1-53617-337-6, pp. 111–123 (2020)
2. Bashirov, A.E., Rıza, M.: On complex multiplicative differentiation. TWMS J. Appl. Eng. Math. **1**(1), 75–85 (2011)
3. Bashirov, A.E., Mısırlı, E., Tandoğdu, Y., Özyapıcı, A.: On modeling with multiplicative differential equations. Appl. Math. J. Chin. Univ. Ser. A **26**(4), 425–438 (2011)
4. Bashirov, A.E., Kurpınar, E.M., Özyapıcı, A.: Multiplicative calculus and its applications. J. Math. Anal. Appl. **337**, 36–48 (2008)
5. Boshpov, A.E., Norozpour, S.: On an alternative view to complex calculus. Math. Methods Appl. Sci. **41**, 7313–7324 (2018)
6. Çakır, Z.: Spaces of continuous and bounded functions over the field of geometric complex numbers. J. Inequal. Appl. **363**, 5 (2013)
7. Boruah, K., Hazarika, B.: Application of geometric calculus in numerical analysis and difference sequence spaces. J. Math. Anal. Appl. **449**(2), 1265–1285 (2017)
8. Boruah, K., Hazarika, B.: G -Calculus. TWMS J. Appl. Eng. Math. **8**(1), 94–105 (2018)
9. Boruah, K., Hazarika, B.: Bigeometric integral calculus. TWMS J. Appl. Eng. Math. **8**(2), 374–385 (2018)
10. Çakmak, A.F., Başar, F.: On the classical sequence spaces and non-Newtonian calculus. J. Inequal. Appl. **12**, Art. ID 932734 (2012)
11. Çakmak, A.F., Başar, F.: Certain spaces of functions over the field of non-Newtonian complex numbers. Abstr. Appl. Anal. **12**, Article ID 236124 (2014)
12. Çakmak, A.F., Başar, F.: On line and double integrals in the non-Newtonian sense. AIP Conf. Proc. **1611**, 415–423 (2014)
13. Çakmak, A.F., Başar, F.: Some sequence spaces and matrix transformations in multiplicative sense. TWMS J. Pure Appl. Math. **6**(1), 27–37 (2015)
14. Grossman, M.: Bigeometric Calculus: A System with a Scale-Free Derivative. Archimedes Foundation, Massachusetts (1983)
15. Grossman, M., Katz, R.: Non-Newtonian Calculus. Lee Press, Pigeon Cove, Massachusetts (1972)
16. Kadak, U., Özlük, M.: Generalized Runge-Kutta method with respect to non-Newtonian calculus. Abstr. Appl. Anal. **10**, Article ID 594685 (2015)
17. Kadak, U., Efe, H.: Matrix transformation between certain sequence spaces over the non-newtonian complex field. Sci. World J. **12**, Article ID 705818 (2014)
18. Kadak, U., Kirişçi, M., Çakmak, A.F.: On the classical paranormed sequence spaces and related duals over the non-Newtonian complex field. J. Funct. Spaces Appl. **11**, Article ID 416906 (2015)
19. Stanley, D.: A multiplicative calculus. Primus IX **4**, 310–326 (1999)
20. Tekin, S., Başar, F.: Certain sequence spaces over the non-Newtonian complex field. Abstr. Appl. Anal. **11**, Article ID 739319 (2013)
21. Türkmen, C., Başar, F.: Some basic results on the geometric calculus. Commun. Fac. Sci. Univ. Ankara, Ser. A **1** 61(2) 17–34 (2012)
22. Türkmen, C., Başar, F.: Some basic results on the sets of sequences with geometric calculus. AIP Conf. Proc. **1470**, 95–98 (2012)
23. Uzer, A.: Multiplicative type complex calculus as an alternative to the classical calculus. Comput. Math. Appl. **60**, 2725–2737 (2010)



Tunable Phosphorescence Hot Paper

Arylene Diimide Phosphors: Aggregation Modulated Twin Room Temperature Phosphorescence from Pyromellitic Diimides

Swadhin Garain, Suman Kuila, Bidhan Chandra Garain, Meenal Kataria, Aditya Borah, Swapan K. Pati, and Subi J. George*

Abstract: Arylene diimide derived ambient organic phosphors are seldom reported despite their potential structural characteristics to facilitate the triplet harvesting. In this context, highly efficient room temperature phosphorescence (RTP) from simple, heavy-atom substituted pyromellitic diimide derivatives in amorphous matrix and crystalline state is reported here. Multiple intermolecular halogen bonding interactions among these phosphors, such as halogen-carbonyl and halogen- π resulted in the modulation of phosphorescence, cyan emission from monomeric state and orange-red emission from its aggregated state, to yield twin RTP emission. Remarkably, the air-stable phosphorescence presented here own one of the highest quantum yield ($\approx 48\%$) among various organics in orange-red emissive region.

Design of ambient organic phosphors is one of the most actively pursued research in recent times as promising alternative to the toxic, metal-based organometallic phosphors for various applications.^[1] One of the important challenges in realizing the RTP from organic molecules is to stabilize the triplet states by minimizing the vibrational and oxygen mediated triplet quenching.^[2a] Recently, very elegant design strategies in this direction have been reported to achieve ambient RTP from organic phosphors both in their crystalline states^[2] and by embedding them in polymeric matrix^[3] or in various supramolecular scaffolds.^[4] However, new molecular designs with high quantum yield phosphors are required for the further advancement in this field. Since phosphorescence is a spin-forbidden process, a strong spin-orbit coupling (SOC) is considered as a basic design to promote the intersystem crossing process (ISC) between a singlet (S_0) and triplet state (T_1).^[1a-5] In this respect, we envisage that arylene diimides present an important class of

molecules to be explored, with its multiple carbonyl groups in the backbone and with the diverse synthetic strategies available for their core-substitution with heavy atoms to increase the SOC and thus the resultant ISC efficiency.^[6] Although arylene diimides have been extensively investigated for various optoelectronic applications as electron-deficient semiconductors, their ambient triplet harvesting properties are rarely explored.^[7] While arylene monoimides such as naphthalene monoimides and phthalimide derivatives are recently shown to exhibit ambient RTP, corresponding diimide derivatives are seldom exploited for triplet harvesting.^[8] In this context, we have recently reported the ambient triplet harvesting of core-substituted naphthalene diimides via RTP^[8a] and thermally activated delayed fluorescence (TADF).^[9]

Further we envision that, well-studied supramolecular chemistry of arylene diimides would give an opportunity to realize multimode phosphorescence via tunable intermolecular interactions. Recently, (supramolecular) aggregation of organic phosphors has been elegantly used by the groups of Huang^[2c,10] and Yang^[11] for realizing dual-mode phosphorescence, which is of great importance for various applications such as white-light phosphorescence.^[10,12] Herein we report novel heavy-atom core-substituted pyromellitic diimide (**PmDI**) derivatives, as efficient orange-red ambient RTP emitters stable in air (Figure 1). Such intense RTP emission

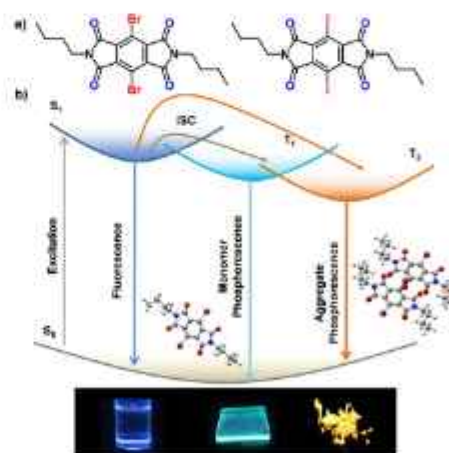


Figure 1. a) Molecular structures of **BrPmDI** and **IPmDI**. b) Simplified Jablonski diagram to explain the monomer and aggregated phosphorescence and other photophysical process. Inset: Monomeric and dimeric optimized geometry of **BrPmDI** at the first triplet excited state. Photographs of the monomer fluorescence in solution, phosphorescence in the polymer matrix and phosphorescence in crystal of **BrPmDI** under 365 nm light is also shown.

[*] S. Garain, S. Kuila, B. C. Garain, M. Kataria, Prof. Dr. S. K. Pati, Prof. Dr. S. J. George
New Chemistry Unit and School of Advanced Material (SAMat),
Jawaharlal Nehru Centre for Advanced Scientific Research (JNCASR)
Jakkur, Bangalore 560064 (India)
E-mail: george@jncasr.ac.in
subijg@gmail.com

B. C. Garain, Prof. Dr. S. K. Pati
Theoretical Science Unit, Jawaharlal Nehru Centre for Advanced
Scientific Research (JNCASR) (India)

A. Borah
Department of Chemistry, Indian Institute of Technology Bombay
Mumbai 400076 (India)

Supporting information and the ORCID identification number(s) for the author(s) of this article can be found under:
<https://doi.org/10.1002/anie.202101538>.

with one of the highest quantum yield ($\approx 48\%$) in the long-wavelength region of the visible spectrum is unprecedented. Further, we show that the phosphorescence emission could be modulated from cyan of the monomeric state to orange-red of aggregated state of the phosphors, by exploiting various intermolecular halogen bonding interactions such as halogen- π and halogen-carbonyl interactions, which facilitates the stacking of the phosphors and increases the SOC significantly. Although triplet harvesting of **PmDI** has recently been explored as polymer phosphors, small molecule-based phosphors are not yet reported.^[13]

First, we have synthesized **BrPmDI** and **IPmDI**, from a durene derivative and were fully characterized by NMR, mass spectrometry, single crystal X-ray diffraction and HPLC (See Supporting Information, Scheme S1). Spectroscopic characterization of these molecules in solution and solid states was subsequently performed using steady-state and time-resolved emission experiments. In solution state (THF, 0.05 mM), absorption spectra of **BrPmDI** and **IPmDI** showed characteristic S_0-S_2 ($\pi-\pi^*$) transition with a maximum at 360 nm and 380 nm, respectively (Figure S1).^[13] In solution, both molecules exhibited only weak fluorescence emission in the 400–550 nm regions with a short average lifetime of ≈ 0.8 ns (Figure S1, Table S1). On the other hand, when the experiments were performed at 77 K (THF) in the glassy matrix to reduce the vibrational dissipation, red-shifted emission in the 425 to 700 nm region with an emission maximum at 504 and 507 nm for **BrPmDI** ($\tau_{\text{avg}} = 7.7$ ms) and **IPmDI**, ($\tau_{\text{avg}} = 1.9$ ms), respectively was observed (Figure 2b,e, S1 and Table S2). The high lifetime of this red-

shifted emission suggests its phosphorescence origin. In order to harvest the triplets by minimizing the vibrational dissipation under ambient conditions, we first dispersed the molecules in poly(methylmethacrylate) (PMMA) matrix, an amorphous polymeric host known to stabilize RTP, at very low concentrations (1 wt. % with respect to PMMA).^[34] Remarkably, a strong cyan emission was observed for both PMMA films with maximum at 480 and 487 nm along with very weak fluorescence emission for **BrPmDI** and **IPmDI**, respectively under ambient conditions (Figure 2b,e, Figure S2, Table S3). High lifetime of these red-shifted emissions (1.4 ms and 6.3 μ s for **BrPmDI** and **IPmDI**, respectively) and its similarity with that of the emission of the pure molecules in frozen THF at 77 K clearly suggests the phosphorescence origin from monomeric states (Figures 2c,f, S1 and Tables S2, S4). The absolute phosphorescence quantum efficiencies of **BrPmDI** and **IPmDI** in 1 wt. % PMMA matrix were 18% and 2%, respectively under air (Table S5). Therefore, it is evident that a strong internal heavy-atom effect is operative in these derivatives to facilitate substantial ISC and subsequent efficient RTP in amorphous matrix (Table S6). We hypothesized that higher phosphorescence efficiency of the **BrPmDI** compared to the **IPmDI** in 1 wt. % PMMA matrix is due to higher ISC rate (k_{ISC}), lower non-radiative decay rate (k_{nr}) and the more number of ISC channels present in monomeric state (Figure S3, Table S6). It is worth mentioning that 1 wt. % amorphous films of **BrPmDI** when under vacuum displayed an impressive phosphorescence quantum yield of 54% (Table S5). Interestingly, on increasing the concentration of these phosphors in the PMMA matrix (5 to 50 wt. %

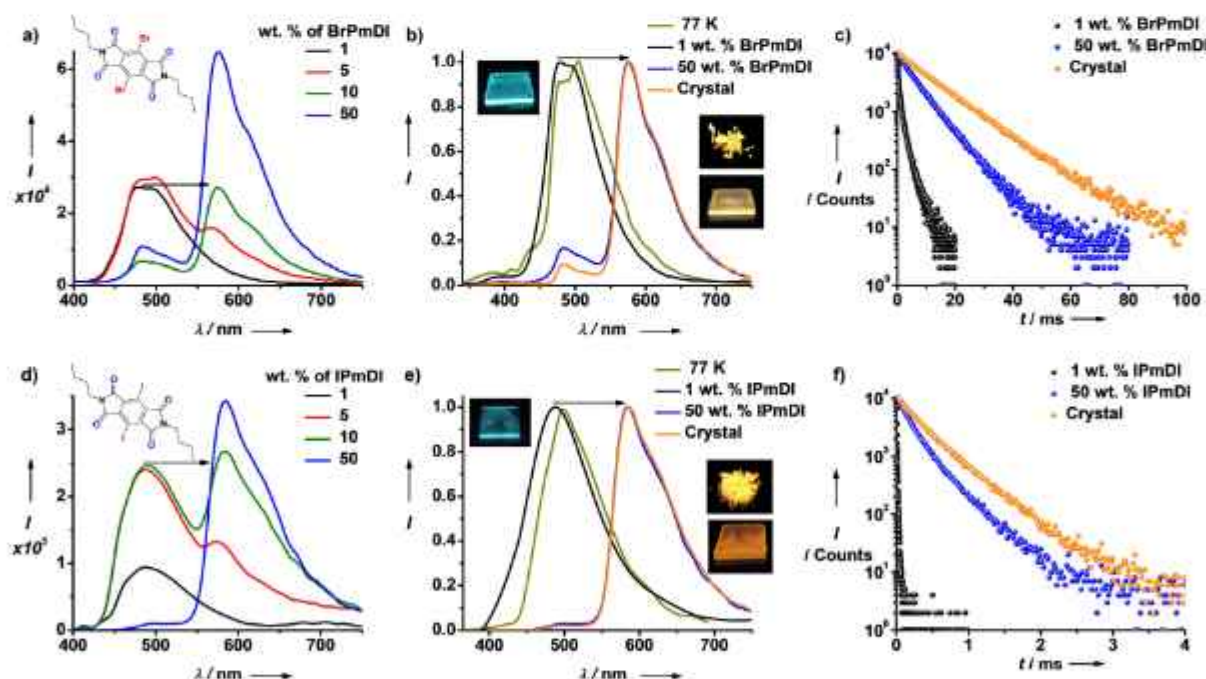


Figure 2. Steady-state emission spectra of PMMA films with different wt. % of a) **BrPmDI** and d) **IPmDI**. Normalized emission spectra of b) **BrPmDI** and e) **IPmDI** in frozen THF at 77 K, in PMMA films with 1 wt. % and 50 wt. % of phosphors and in crystalline state (Inset: photographs of **BrPmDI** and **IPmDI** in PMMA films with 1 wt. % and 50 wt. % of phosphors and in crystalline state under 365 nm UV-lamp excitation, $\lambda_{\text{exc}} = 330$ and 350 nm for **BrPmDI** and **IPmDI**, respectively). Phosphorescence lifetime decay profiles of c) **BrPmDI** and f) **IPmDI** in PMMA films with 1 wt. % and 50 wt. % of phosphors and in crystalline state ($\lambda_{\text{exc}} = 330$ and 350 nm for **BrPmDI**, **IPmDI** respectively, $\lambda_{\text{collected}} = 500$ nm for monomer and 650 nm for aggregate/crystal, all experiments were performed in air).

with respect to PMMA) gradual appearance of a red-shifted emission (orange-red region) with maximum at 576 and 585 nm for **BrPmDI** and **IPmDI** respectively with the concomitant disappearance of monomeric cyan phosphorescence, was observed (Figures 2a and d). The lifetime in the millisecond time scale for these films suggests the phosphorescence modulation of these phosphors via intermolecular interactions ($\tau_{avg} = 5.2, 0.32$ ms and $\Phi_p = 17.5\%, 30\%$ for **BrPmDI** and **IPmDI** respectively in 50 wt. % with respect to PMMA under air) (Figures 2c,f, S4 and Tables S5, S7). Drop-casted films of **BrPmDI** and **IPmDI** showed similar emission features with lower quantum yield, which confirms the emission from aggregated phosphors (Figure S5 and Table S8). Aggregation of phosphors in the polymer matrix at higher wt. % is further evident from the increased scattering and red-shift in the absorption spectra as well as red-shifted excitation spectra monitored at 650 nm (Figure S6, S7). We envisage that the presence of multiple non-covalent interactions in the aggregated state stabilizes the triplet energy level.^[10,11]

In an attempt to characterize the various intermolecular interactions in the stacked state of these phosphors, single crystals of **BrPmDI** and **IPmDI** were further investigated. Interestingly, single crystals of **BrPmDI** and **IPmDI** showed intense orange-red phosphorescence emission with a maximum at 576 and 585 nm for **BrPmDI** and **IPmDI**, respectively similar to that of the PMMA films with aggregated phosphors (Figure 2b,e). The high lifetimes of 11.4 ms and 0.61 ms for **BrPmDI** and **IPmDI** crystals, respectively and gated emission spectra (delay time = 0.5 ms) confirms the phosphorescent nature of the emission (Figures 2c,f, S8 and Table S9). Selective excitation of the aggregated absorption also resulted in similar red-shifted phosphorescence emission suggesting the assembled state of the phosphors in crystals (Figure S9 and Table S10). Remarkably, both **BrPmDI** and **IPmDI** crystals showed high absolute phosphorescence quantum efficiencies of 26% and 48% (statistical data presented in Table S11), respectively under air, which is the highest phosphorescence quantum yield in the arylene diimide family and also one of

the highest phosphorescence quantum yield reported in the orange-red region among various ambient organic phosphors (Tables S5, S12 and Scheme S2). Remarkably, the phosphorescence quantum yield of **IPmDI** crystals has increased to 68% under vacuum (Tables S5). Higher phosphorescence quantum efficiency of **IPmDI** crystals compared to the **BrPmDI** could be attributed to a stronger SOC and high ISC rate (k_{ISC}) in the former, which is also supported by its faster phosphorescence lifetime (Figures 2c,f and Table S6, S9), as expected in heavy-atom organic phosphors.

X-ray diffraction analysis of the crystals further provided insights into the molecular organization of the phosphors in the aggregated state. Single crystals of **BrPmDI** exhibited a layered slip-stacked molecular organization with an inter-layer distance of 3.8 Å (Figures 3a,b and Table S13) which justifies the stabilization of orange-red emissive, red-shifted phosphorescence of the aggregated state in the crystalline phase. Further stacked arrangement of phosphors is stabilized by the halogen- π ($C \cdots Br$, 3.5 Å) and the interdigitated alkyl chains between molecules of adjacent layers. In addition, within each layer, these molecules are connected by $C=O \cdots Br$ intermolecular non-covalent interactions (3.1 Å) (Figure 3c). It has been well-established that halogen bonding can enhance the SOC by external heavy-atom effect.^[24] We envisage that, rigid 3D network due to the various non-covalent interactions specially halogen bonding help the triplet stabilization via minimizing the vibrational dissipation and by enhancing the SOC. In addition, strong intramolecular $C=O \cdots Br$ (3.2 Å) (Figure 3b) interactions can also contribute to high SOC even in the molecular dispersed and glassy matrix. Similar organization was also observed in the crystals of **IPmDI** (Figure S10, Table S13). Since the crystal packing is similar in both molecules with closely matching short-contact distances, we envision that the extent of external/internal heavy-atom effect determines the differences in their RTP intensity. To validate the stabilization of triplets in the crystal state we have performed time-dependent density functional theory (TDDFT) calculations. The calculated energy levels of the optimized geometry of the first

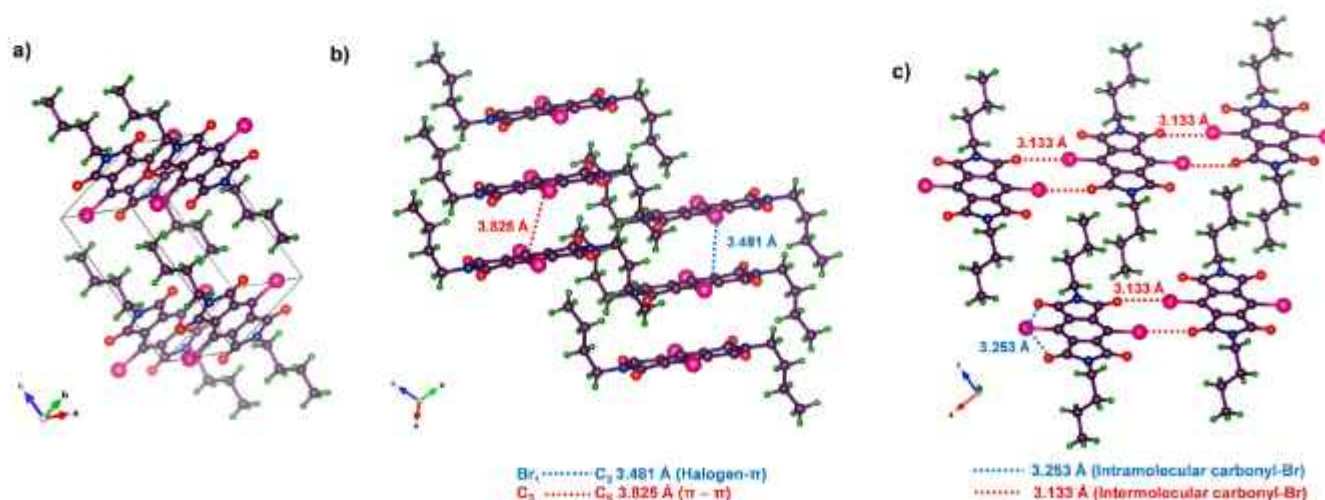


Figure 3. a) Unit cell, b) slipped stacked arrangement showing various intermolecular interactions, c) intramolecular and intermolecular halogen-carbonyl interaction of **BrPmDI** single crystal.

excited triplet state of monomeric and dimeric **BrPmDI**s supports the observed red shift in phosphorescence in the aggregated state (Figure S11, Table S14). Further, reduced density gradient (RDG) plot of the dimeric triplet state also clearly shows the intra- and intermolecular non-covalent interactions observed in the crystalline state, which can enhance the ISC/SOC efficiency (Figure S12).

The fundamental prerequisite for the triplet emission in arylene diimide based systems is to access the triplet excited state. Therefore, in order to have a qualitative understanding of ISC efficiency in **PmDI** derivatives reported here, we investigated their excited state characteristics by detailed TDDFT calculations using CAM-B3LYP exchange-correlation functional (Figure S13–S18, Table S15). The rate of ISC is dependent on the SOC strength and this is estimated quantitatively by calculating the SOC matrix element (SOCME) between S_1 and its closely lying triplet states (T_n) (Table S16). In both these cases, multiple triplet states are present below the S_1 excited state and thus provide a thermodynamically favorable ISC route (Figure S3). In **BrPmDI**, there are two main contributing pathways for ISC according to corresponding SOC matrix element (Figure 4, S3, S13 and S15). These are S_1 ($n-\pi^*$) to T_6 ($\pi-\pi^*$) and S_1 to T_2 , where corresponding calculated SOCME are 16 and 523 cm^{-1} , respectively (Figures 4, S13 and Table S16). It is important to note that the closely-lying T_3 and T_4 possess the similar molecular orbital (MO) configuration as that of S_1 and this does not follow El-Sayed rule; therefore, the magnitude is much lower than that between S_1 and T_2 having different electron-hole configurations (Figure S15). In addition, both these transitions are also facilitated by the presence of heavy Br atoms. For **IPmDI** monomers, the ISC pathway is facilitated by close-lying S_1 - T_2 which follow El-Sayed rule and since Iodine is expected to show a stronger heavy-atom effect as compared to Br, the magnitude of SOCME is three

times higher than **BrPmDI** (Figure S3, S16 and Table S16). Upon aggregation, number of intersystem crossing channels increases significantly as evident from the ground state optimized geometries of **BrPmDI** dimers (Figure 4, S13 and S17) which could be one of the reasons for the high phosphorescence efficiency in the crystalline state compared to the monomeric state. As a control, we also investigated the un-substituted **HPmDI**, and the only possible ISC pathway in this case is between S_1 and T_1 state with substantially low SOCME (Figure S18 and Table S16).

In conclusion, we have introduced a new class of small organic molecule based efficient, ambient organic phosphors from the smallest member of arylene diimide family, that is, pyromellitic diimides, by a rational “heavy-atom” substitution strategy. The **PmDI** derivatives reported here showed high phosphorescence quantum yield ($\approx 48\%$ and $\approx 68\%$, in air and vacuum, respectively) with exceptional air stability. Further the tunable phosphorescence emission could also be achieved by the stacking of phosphors using multiple intermolecular halogen bonding interactions. Although many organic room temperature phosphors are reported recently, the present system is unique with respect to its new molecular design, high quantum yield and halogen bonding induced tunable phosphorescence.^[1] We envisage that arylene diimide phosphors, with its rich chemistry of core-substitution and appropriate molecular structure conducive for efficient SOC and ISC, offers plethora of opportunities in the frontier research area of organic phosphors.

Acknowledgements

Funding from SwarnaJayanti Fellowship (DST/SJF/CSA01/2016–2017) is acknowledged. S.K.P. thanks SERB, DST and J. C. Bose Fellowship for financial support. S.G. and B.C.G. thanks CSIR, S.K. and A.B. thanks UGC, Government of India for fellowship. We thank Prof. R. Murugavel for single crystal X-ray diffraction studies.

Conflict of interest

The authors declare no conflict of interest.

Keywords: aggregation · dual phosphorescence · noncovalent interactions · photochemistry · pyromellitic diimide

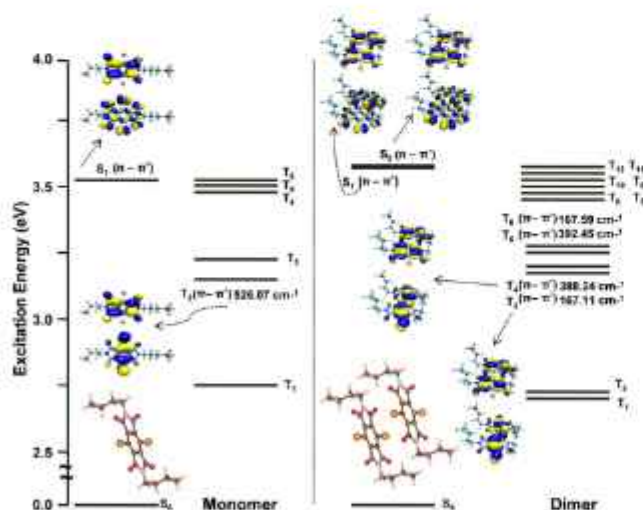


Figure 4. Ground state geometries, relative excitation energies and their corresponding hole, electron wavefunctions and SOC matrix elements for both monomeric and dimeric **BrPmDI**s (Hole and electron wavefunctions are shown below and above in the schematic, respectively. Inset: monomeric and dimeric structure of **BrPmDI**s obtained from crystal structure).

- [1] a) S. Hirata, *Adv. Opt. Mater.* **2017**, *5*, 1700116; b) Kenry, C. Chen, B. Liu, *Nat. Commun.* **2019**, *10*, 2111; c) W. Zhao, Z. He, J. W. Y. Lam, Q. Peng, H. Ma, Z. Shuai, G. Bai, J. Hao, B. Z. Tang, *Chem* **2016**, *1*, 592–602; d) T. Zhang, X. Ma, H. Wu, L. Zhu, Y. Zhao, H. Tian, *Angew. Chem. Int. Ed.* **2020**, *59*, 11206–11216; *Angew. Chem.* **2020**, *132*, 11302–11312; e) S. Xu, R. Chen, C. Zheng, W. Huang, *Adv. Mater.* **2016**, *28*, 9920–9940; f) X. Ma, J. Wang, H. Tian, *Acc. Chem. Res.* **2019**, *52*, 738–748.
[2] a) O. Bolton, K. Lee, H.-J. Kim, K. Y. Lin, J. Kim, *Nat. Chem.* **2011**, *3*, 205–210; b) W. Z. Yuan, X. Y. Shen, H. Zhao, J. W. Y. Lam, L. Tang, P. Lu, C. Wang, Y. Liu, Z. Wang, Q. Zheng, J. Z. Sun, Y. Ma, B. Z. Tang, *J. Phys. Chem. C* **2010**, *114*, 6090–6099; c) Z. An, C. Zheng, Y. Tao, R. Chen, H. Shi, T. Chen, Z. Wang,

- H. Li, R. Deng, X. Liu, W. Huang, *Nat. Mater.* **2015**, *14*, 685–690; d) A. D. Nidhankar, Goudappagouda, D. S. Mohana Kumari, S. K. Chaubey, R. Nayak, R. G. Gonnade, G. V. P. Kumar, R. Krishnan, S. S. Babu, *Angew. Chem. Int. Ed.* **2020**, *59*, 13079–13085; *Angew. Chem.* **2020**, *132*, 13179–13185; e) L. Gu, H. Shi, L. Bian, M. Gu, K. Ling, X. Wang, H. Ma, S. Cai, W. Ning, L. Fu, H. Wang, S. Wang, Y. Gao, W. Yao, F. Huo, Y. Tao, Z. An, X. Liu, W. Huang, *Nat. Photonics* **2019**, *13*, 406–411; f) J. Yang, X. Zhen, B. Wang, X. Gao, Z. Ren, J. Wang, Y. Xie, J. Li, Q. Peng, K. Pu, Z. Li, *Nat. Commun.* **2018**, *9*, 840; g) Y. Wang, J. Yang, Y. Tian, M. Fang, Q. Liao, L. Wang, W. Hu, B. Z. Tang, Z. Li, *Chem. Sci.* **2020**, *11*, 833–838; h) E. Hamzehpoor, D. F. Perepichka, *Angew. Chem. Int. Ed.* **2020**, *59*, 9977–9981; *Angew. Chem.* **2020**, *132*, 10063–10067.
- [3] a) D. Lee, O. Bolton, B. C. Kim, J. H. Youk, S. Takayama, J. Kim, *J. Am. Chem. Soc.* **2013**, *135*, 6325–6329; b) Y. Su, Y. Zhang, Z. Wang, W. Gao, P. Jia, D. Zhang, C. Yang, Y. Li, Y. Zhao, *Angew. Chem. Int. Ed.* **2020**, *59*, 9967–9971; *Angew. Chem.* **2020**, *132*, 10053–10057; c) H. Wu, W. Chi, Z. Chen, G. Liu, L. Gu, A. K. Bindra, G. Yang, X. Liu, Y. Zhao, *Adv. Funct. Mater.* **2019**, *29*, 1807243; d) Y. Su, S. Z. F. Phua, Y. Li, X. Zhou, D. Jana, G. Liu, W. Q. Lim, W. K. Ong, C. Yang, Y. Zhao, *Sci. Adv.* **2018**, *4*, eaas9732; e) M. Louis, H. Thomas, M. Gmelch, A. Haft, F. Fries, S. Reineke, *Adv. Mater.* **2019**, *31*, 1807887; f) H. Thomas, D. L. Pastoetter, M. Gmelch, T. Achenbach, A. Schlögl, M. Louis, X. Feng, S. Reineke, *Adv. Mater.* **2020**, *32*, 2000880; g) M. Gmelch, H. Thomas, F. Fries, S. Reineke, *Sci. Adv.* **2019**, *5*, eaau7310; h) A. Kirch, M. Gmelch, S. Reineke, *J. Phys. Chem. Lett.* **2019**, *10*, 310–315; i) S. Kuila, S. J. George, *Angew. Chem. Int. Ed.* **2020**, *59*, 9393–9397; *Angew. Chem.* **2020**, *132*, 9479–9483.
- [4] a) X. Yao, J. Wang, D. Jiao, Z. Huang, O. Mhirsí, F. Lossada, L. Chen, B. Haehnle, A. J. C. Kuehne, X. Ma, H. Tian, A. Walther, *Adv. Mater.* **2021**, *33*, 2005973; b) Z. Li, Y. Han, F. Wang, *Nat. Commun.* **2019**, *10*, 3735; c) Z. Li, Y. Han, F. Nie, M. Liu, H. Zhong, F. Wang, *Angew. Chem. Int. Ed.* **2021**, <https://doi.org/10.1002/anie.202015846>; *Angew. Chem.* **2021**, <https://doi.org/10.1002/ange.202015846>; d) J. Wang, Z. Huang, X. Ma, H. Tian, *Angew. Chem. Int. Ed.* **2020**, *59*, 9928–9933; *Angew. Chem.* **2020**, *132*, 10014–10019; e) D. Li, F. Lu, J. Wang, W. Hu, X.-M. Cao, X. Ma, H. Tian, *J. Am. Chem. Soc.* **2018**, *140*, 1916–1923; f) Z.-Y. Zhang, Y. Chen, Y. Liu, *Angew. Chem. Int. Ed.* **2019**, *58*, 6028–6032; *Angew. Chem.* **2019**, *131*, 6089–6093; g) H. Chen, X. Ma, S. Wu, H. Tian, *Angew. Chem. Int. Ed.* **2014**, *53*, 14149–14152; *Angew. Chem.* **2014**, *126*, 14373–14376; h) S. Kuila, K. V. Rao, S. Garain, P. K. Samanta, S. Das, S. K. Pati, M. Eswaramoorthy, S. J. George, *Angew. Chem. Int. Ed.* **2018**, *57*, 17115–17119; *Angew. Chem.* **2018**, *130*, 17361–17365; i) F.-F. Shen, Y. Chen, X. Dai, H.-Y. Zhang, B. Zhang, Y. Liu, Y. Liu, *Chem. Sci.* **2021**, <https://doi.org/10.1039/d0sc05343k>.
- [5] J. Xu, A. Takai, Y. Kobayashi, M. Takeuchi, *Chem. Commun.* **2013**, *49*, 8447–8449.
- [6] a) N. Sakai, J. Mareda, E. Vauthey, S. Matile, *Chem. Commun.* **2010**, *46*, 4225–4237; b) F. Würthner, S. Ahmed, C. Thalacker, T. Debaerdmacker, *Chem. Eur. J.* **2002**, *8*, 4742–4750.
- [7] a) J. H. Oh, S. L. Suraru, W.-Y. Lee, M. Könenmann, H. W. Höffken, C. Röger, R. Schmidt, Y. Chung, W.-C. Chen, F. Würthner, Z. Bao, *Adv. Funct. Mater.* **2010**, *20*, 2148–2156; b) A. Nowak-Król, K. Shoyama, M. Stolte, F. Würthner, *Chem. Commun.* **2018**, *54*, 13763–13772; c) Q. Zheng, J. Huang, A. Sarjeant, H. E. Katz, *J. Am. Chem. Soc.* **2008**, *130*, 14410–14411.
- [8] a) X. Chen, C. Xu, T. Wang, C. Zhou, J. Du, Z. Wang, H. Xu, T. Xie, G. Bi, J. Jiang, X. Zhang, J. N. Demas, C. O. Trindle, Y. Luo, G. Zhang, *Angew. Chem. Int. Ed.* **2016**, *55*, 9872–9876; *Angew. Chem.* **2016**, *128*, 10026–10030; b) B. Chen, W. Huang, H. Su, H. Miao, X. Zhang, G. Zhang, *Angew. Chem. Int. Ed.* **2020**, *59*, 10023–10026; *Angew. Chem.* **2020**, *132*, 10109–10112; c) X. Lin, J. Wang, B. Ding, X. Ma, H. Tian, *Angew. Chem. Int. Ed.* **2021**, *60*, 3459–3463; *Angew. Chem.* **2021**, *133*, 3501–3505.
- [9] S. Kuila, A. Ghorai, P. K. Samanta, R. B. K. Siram, S. K. Pati, K. S. Narayan, S. J. George, *Chem. Eur. J.* **2019**, *25*, 16007–16011.
- [10] F. Li, S. Guo, Y. Qin, Y. Shi, M. Han, Z. An, S. Liu, Q. Zhao, W. Huang, *Adv. Opt. Mater.* **2019**, *7*, 1900511.
- [11] Y. Wen, H. Liu, S. Zhang, Y. Gao, Y. Yan, B. Yang, *J. Mater. Chem. C* **2019**, *7*, 12502–12508.
- [12] a) Z. He, W. Zhao, J. W. Y. Lam, Q. Peng, H. Ma, G. Liang, Z. Shuai, B. Z. Tang, *Nat. Commun.* **2017**, *8*, 416; b) S. Hirata, M. Vacha, *Adv. Opt. Mater.* **2017**, *5*, 1600996; c) S. Kuila, S. Garain, S. Bandi, S. J. George, *Adv. Funct. Mater.* **2020**, *30*, 2003693.
- [13] K. Kanosue, S. Ando, *ACS Macro Lett.* **2016**, *5*, 1301–1305.
- [14] Deposition Number(s) 2014119 (**BrPmDI**) and 2014124 (**IPmDI**) contain(s) the supplementary crystallographic data for this paper. These data are provided free of charge by the joint Cambridge Crystallographic Data Centre and Fachinformationszentrum Karlsruhe Access Structures service www.ccdc.cam.ac.uk/structures.

Manuscript received: February 1, 2021

Revised manuscript received: February 24, 2021

Accepted manuscript online: March 4, 2021

Version of record online: ■■■■■■■■■■

Communications

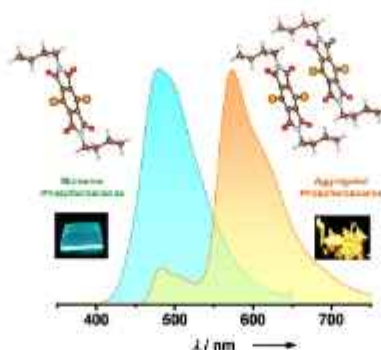


Tunable Phosphorescence

S. Garain, S. Kuila, B. C. Garain,
M. Kataria, A. Borah, S. K. Pati,
S. J. George*



Arylene Diimide Phosphors: Aggregation
Modulated Twin Room Temperature
Phosphorescence from Pyromellitic
Diimides



Highly efficient room-temperature phosphorescence, stable in air, from the simplest class of arylene diimides, i.e., pyromellitic diimides, is achieved. Aggregation modulated, colour tuneable phosphorescence emission from cyan to orange-red in amorphous film and crystalline state is observed. The role of molecular design and weak intermolecular interactions in the observed properties is explained.

Electron Paramagnetic Resonance Spectra of Pentagonal Bipyramidal Gadolinium Complexes

Jonatan B. Petersen, You-Song Ding, Sandeep Gupta, Aditya Borah, Eric J. L. McInnes, Yan-Zhen Zheng, Ramaswamy Murugavel, and Richard E. P. Winpenny*



Cite This: *Inorg. Chem.* 2023, 62, 8435–8441



Read Online

ACCESS |



Metrics & More

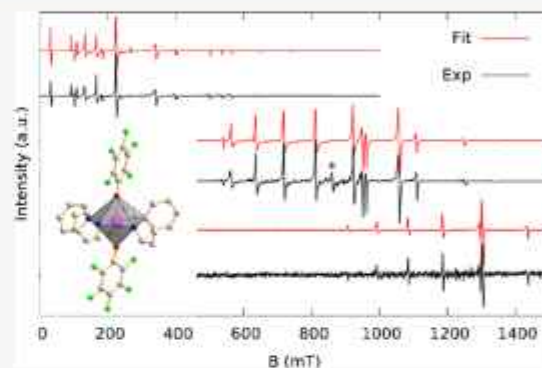


Article Recommendations



Supporting Information

ABSTRACT: Gadolinium is a special case in spectroscopy because of the near isotropic nature of the $4f^7$ configuration of the +3 oxidation state. Gd^{3+} complexes have been studied in several symmetries to understand the underlying mechanisms of the ground state splitting. The abundance of information in Gd^{3+} spectra can be used as a probe for properties of the other rare earth ions in the same complexes. In this work, the zero-field splitting (ZFS) of a series of Gd^{3+} pentagonal bipyramidal complexes of the form $[GdX_2(L_{eq})_5]^{n+}$ [$n = 1$, X = axial ligands: Cl^- , $^-O^tBu$, $^-OArF_5$ or $n = 3$, X = $^tBuPO(NH^iPr)_2$, L_{eq} = equatorial ligand: Py, THF or H_2O] with near fivefold symmetry axes along X^1-Gd-X^2 was investigated. The ZFS parameters were determined by fitting of room-temperature continuous wave electron paramagnetic resonance (EPR) spectra (at X-, K-, and Q-band) to a spin Hamiltonian incorporating extended Stevens operators compatible with C_5 symmetry. Examination of the acquired parameters led to the conclusion that the ZFS is dominated by the B_2^0 term and that the magnitude of B_2^0 is almost entirely dependent on, and inversely proportional to, the donor strength of the axial ligands. Surveying the continuous shape measure and the X^1-Gd-X^2 angle of the complexes showed that there is some correlation between the proximity of each complex to D_{5h} symmetry and the magnitude of the B_2^0 parameter, but that the deformation of the X^1-Gd-X^2 angle is more significant than other distortions. Finally, the magnitude of B_2^0 was found to be inversely proportional to the thermal barrier for the reversal of the magnetic moment (U_{eff}) of the corresponding isostructural Dy^{3+} complexes.



INTRODUCTION

For many years gadolinium(III) has intrigued spectroscopists, with its combination of shielded $4f$ orbitals and a half-filled shell in the +3 oxidation state and the resulting $L = 0$ ground state with no orbital angular momentum and therefore no first-order spin–orbit coupling.¹ This results in ground state splitting of typically less than 1 cm^{-1} which is the perfect magnitude for rich EPR spectra as well as relaxation times that are still relatively long.² Gd^{3+} doped into yttrium(III) complexes are presently being studied as potential qubits.^{3–5}

Crystal fields determine many of the properties of lanthanide ions and completely dominate their magnetic behavior. For example, the crystal field determines the barrier for reversal of the magnetic moment via the Orbach mechanism in lanthanide single-molecule magnets (SMMs),⁶ and the symmetry of the crystal field is thought to influence the rate of quantum tunneling of the magnetization circumventing this barrier.⁷ We therefore thought it would be worth using the EPR spectroscopy of Gd^{3+} to investigate the crystal field in complexes isostructural with Dy^{3+} SMMs.

Even though it has no formal orbital angular momentum, the splitting of the gadolinium(III) $^8S_{7/2}$ ground state still happens through spin–orbit coupling to excited states with $L \neq 0$ and

this splitting adheres to the same symmetry restrictions as crystal field splitting.⁸ It has therefore been suggested that the ZFS parameters obtained for gadolinium can help elucidate how close a family of lanthanide complexes comply with their approximate symmetry.⁹

Most investigations of the lanthanide crystal field and zero-field splitting have been performed in high symmetry environments to ensure the number of parameters needed is low enough to determine a unique best set of parameters from experimental data. In low symmetry, the elucidation of the crystal field parameters often requires ab initio calculations. Methods used such as density functional theory and complete active space self-consistent field (CASSCF) employ approximations that introduce significant errors and for $4f^7$ configurations like Gd^{3+} these errors are on the order of magnitude of the total splitting, rendering theoretical

Received: April 17, 2023

Published: May 12, 2023



calculations useless for obtaining accurate parameters for the ground state splitting in these systems.^{10,11}

Five-fold symmetry does not exist in regular crystals, and it follows that strict fivefold point symmetry is not crystallographically possible. However, molecules with near fivefold symmetry occur. Within the lanthanide series, dysprosium(III) compounds with pentagonal bipyramidal coordination geometries are important as many compounds with this geometry are SMMs with high thermal barriers for loss of magnetization.^{12–16}

In this work, we set out to investigate five gadolinium complexes with pentagonal bipyramidal coordination geometries (e.g., Figure 1); this geometry has not previously been

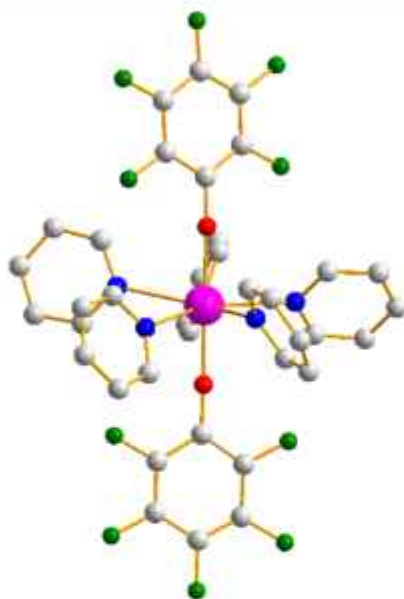


Figure 1. Solid-state structure of $[Y(OArF_5)_2(Py)_5]^+$ (**4**) showing the pentagonal bipyramidal coordination geometry. Color code: Y (magenta), F (green), O (red), N (blue), and C (gray). H atoms omitted.

investigated by EPR spectroscopy. The dysprosium analogues (and in one case even neodymium analogue) are SMMs, which is explained either by the strong axially of the crystal field or possibly the symmetry.^{12–16} This geometry is ideal for

stabilizing the highest M_J doublet in Dy^{3+} complexes, giving large barriers for reversal of the magnetic moment.¹⁷ For the current investigation, we measured the room temperature EPR spectra of Gd^{3+} doped into isostructural Y^{3+} complexes at multiple frequencies and examined how well they could be reproduced using a spin Hamiltonian consistent with the approximate symmetry.

EXPERIMENTAL SECTION

Six samples were produced for EPR measurements: $Gd@[YCl_2(Py)_5]BPh_4 \cdot THF$ **1**; $Gd@[YCl_2(THF)_5]BPh_4$ **2**; $Gd@[Y(O^tBu)Cl(THF)_4]BPh_4 \cdot 2THF$ **3**; $Gd@[Y(OArF_5)_2(Py)_5]B(ArF_5)_4 \cdot 0.5C_6H_{14}$ **4**; and $Gd@[YL_2(H_2O)_5][I]_3 \cdot H_2O \cdot 2L$ **5a** and $[GdL_2(H_2O)_5][I]_3 \cdot H_2O \cdot 2L$ **5b** [Py = pyridine, THF = tetrahydrofuran, ArF_5 = pentafluorophenyl, and $L = ^tBuPO(NH^tPr)_2$].

The samples were synthesized by modified versions of the published procedures for the analogous dysprosium complexes with DyX_3 substituted for YX_3 and GdX_3 ($X = Cl$ or I).^{13–15,18} Doping was done by using a mixture of $GdCl_3$ and YCl_3 (1–5% Gd) in the initial synthetic step.

All samples were studied as crystalline powders of yttrium compounds doped with their gadolinium analogue, with the exception of **5b** where the neat gadolinium compound was also measured. Crystallographic parameters are given in Table S1 and relevant geometrical parameters in Table S2.

X-band and Q-band EPR spectra were recorded on a Bruker EMXplus spectrometer equipped with ER 4122 SHQ or ER 5106 QT resonators. K-band EPR spectra were recorded on a Bruker E500 spectrometer equipped with an ER 6706 KT resonator. All spectra were recorded at room temperature with modulation frequencies of 100 kHz and modulation amplitudes of 5–10 G. The recorded spectra were baseline corrected with a first- or second-order polynomial and field corrected against a strong pitch standard sample supplied by Bruker. The samples were measured in sealed quartz tubes as samples **1–4** are moisture sensitive.

The spectra were modeled with a spin Hamiltonian of the form

$$\hat{H} = \mu_B (B_x B_x + B_y B_y + B_z B_z) \begin{pmatrix} g_x & 0 & 0 \\ 0 & g_y & 0 \\ 0 & 0 & g_z \end{pmatrix} \begin{pmatrix} \hat{s}_x \\ \hat{s}_y \\ \hat{s}_z \end{pmatrix} + \sum_{k,q} B_k^q \hat{O}_k^q \quad (1)$$

where μ_B is the Bohr magneton. The first term describes the Zeeman interaction between the magnetic moment of the spin (with spin operators \hat{s}_x , \hat{s}_y , and \hat{s}_z) and the external magnetic field (with components B_x , B_y , and B_z) through an axial g -tensor with principal values parallel ($g_{||}$) and perpendicular (g_{\perp}) to the unique axis (z). The

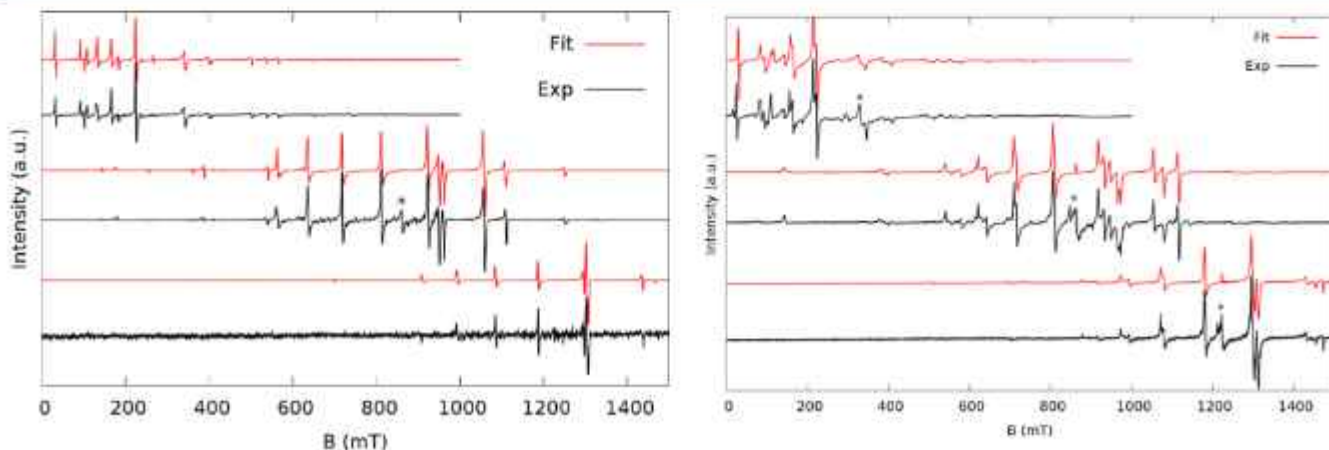


Figure 2. Spectra (black) and simulations (red) at X (top), K (middle), and Q-band (bottom) of **1** (left) and **2** (right). Simulation parameters are based on the parameters in Table 1 and exact frequencies of measurements are given in the Supporting Information. The stars indicate an impurity.

second term describes the ZFS of the ground state with Stevens operator equivalents \hat{O}_k^q , which are polynomials of spin operators of order $q < k$, parameterized with Stevens parameters B_k^q .¹⁹ To adhere to the approximate C_3 symmetry of the complexes, only B_2^0 , B_4^0 , B_6^0 , and B_6^6 were allowed non-zero values as these are the only allowed operators in the C_3 point group. Line widths were modeled assuming unresolved hyperfine interactions and strain in the g -factors and the dominant ZFS parameter by using axially anisotropic linewidths lw_{\perp} and lw_{\parallel} and a Gaussian distribution (strain) around the value of the B_2^0 parameter.

Spin Hamiltonian parameters were obtained by Levenberg–Marquardt least squares fitting using the multi-purpose EPR software written by Weihe after initial fitting by eye.^{20,21} The parameters were fitted against the spectra of all three frequencies simultaneously, except **5a** and **5b** where each frequency was fit separately to the spectra of both samples simultaneously.

Single crystals of **1**, **2**, and **4** (Y analogues) for crystal structure determination were obtained by recrystallization of the neat compounds from hexane. Single crystals of **5a** and **5b** were obtained directly from the reaction mixture using benzene and dichloromethane as reaction solvents following a similar procedure reported in the literature.^{16,18} X-ray diffraction was measured on Bruker Apex CCD II diffractometer using Mo $K\alpha$ radiation. Single-crystal X-ray diffraction study for **5b** was performed on a Rigaku Saturn 724+ CCD diffractometer.

RESULTS AND DISCUSSION

The experimental spectra of **1–5b** are shown along with the best fit simulations in Figures 2–5. All the samples gave

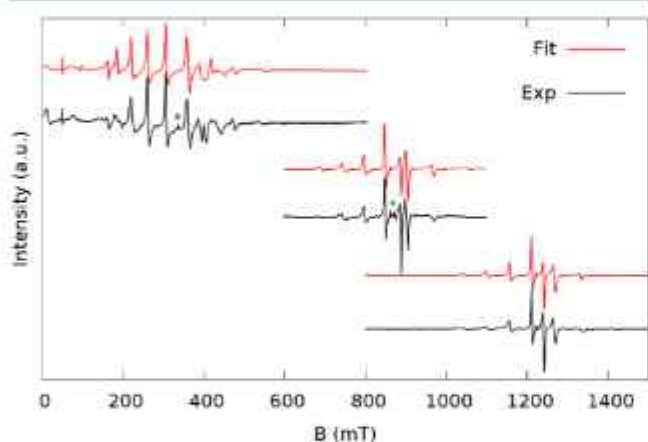


Figure 3. Spectra (black) and simulations (red) of **3** at X (top), K (middle), and Q-band (bottom). The stars indicate an impurity.

intense EPR signals and spectra with many observable transitions. In the K-band spectra, both $\Delta m_s = \pm 1$ and $\Delta m_s = \pm 2$ (<500 mT) transitions are observed for all samples with the exception of **3** where the smaller sample size meant that the field range was cut short to focus on the main part of the spectrum. The $\Delta m_s = \pm 2$ transitions are also accurately reproduced in the simulations, substantiating the validity of the model.

The spectra of **1** and **2** contain several intense narrow peaks and are presented in Figure 2. The simulation parameters used are given in Table 1. Both have the $\Delta m_s = \pm 1$ transitions spread over a wide range of as much as 800 mT, indicating large ZFS.

The multitude of very weak peaks, between the intense peaks, are caused by polycrystallinity effects, meaning that larger crystallites give more weight to certain orientations rather than a true average of the orientations. To prove this,

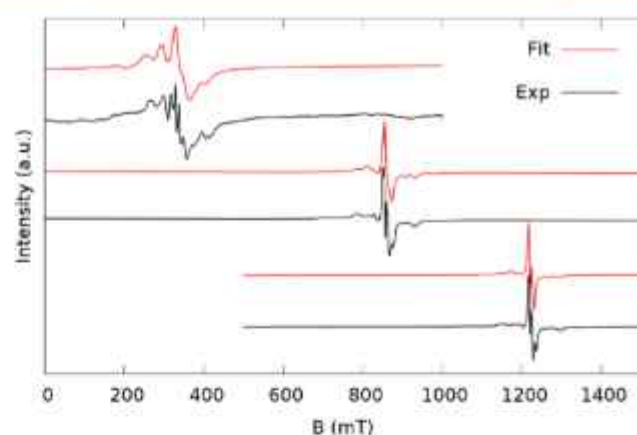


Figure 4. Spectra (black) and simulations (red) of **4** at X (top), K (middle), and Q-band (bottom).

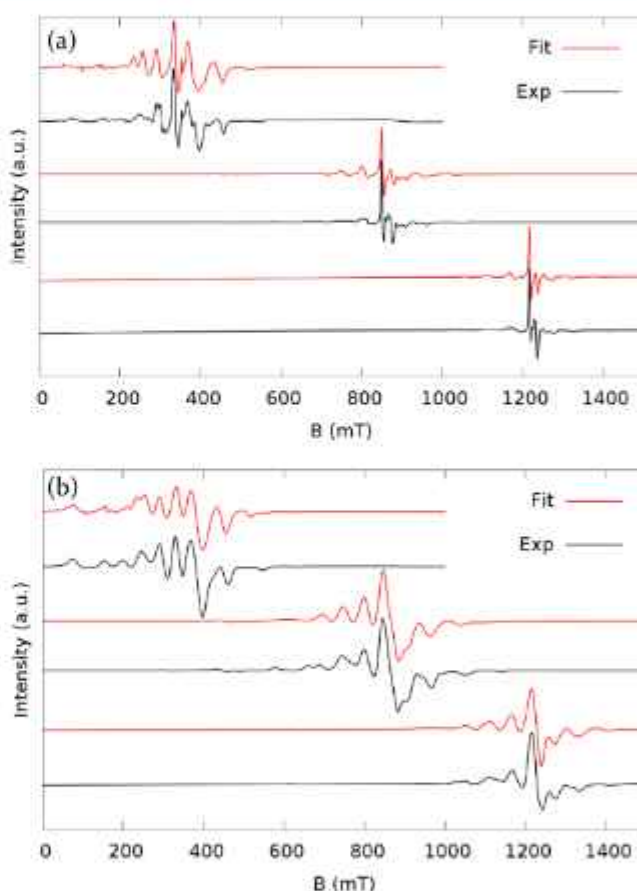


Figure 5. Spectra (black) and simulations (red) at X (top), K (middle), and Q-band (bottom) of **5a** (a) and **5b** (b).

the sample was turned 10° and a new spectrum measured where the position and shape of these minor peaks changed. This effect was seen even though the sample was thoroughly ground, which is due to the extraordinarily narrow linewidths and wide spectral range of **2**.

The spectra of **1** can be fit with the axial Hamiltonian (1) (Figure 2, left). The spectra of **2** are of similar spread, but have more transitions (Figure 2, right) than can be accounted for with axial symmetry. This could be because the asymmetric unit of the crystal structure contains two gadolinium complexes with slightly different geometries. The main peaks

Table 1. Best Fit Spin Hamiltonian Parameters for 1–5 from EPR Spectra and Structural Data from Gadolinium Crystal Structures^a

	g_{\perp}	g_{\parallel}	B_2^0 (10^{-3}cm^{-1})	B_4^0 (10^{-3}cm^{-1})	B_6^0 (10^{-3}cm^{-1})	B_2^2 (10^{-3}cm^{-1})	B_4^2 (10^{-3}cm^{-1})	$X_1\text{-Gd-X}_2$ (deg)	CShM D_{5h}	$B_6^5/\Delta E^f$ (10^{-5})	U_{eff} (K)
1	1.994(1)		3.63(1)	-1.3(1)	0	0.6(5)	0	176.8	0.093	0.46	^h
2 ^h	1.993(1)		3.705(2)	-0.92(4)	0	0	1.83(5)	179.3	0.244	3.7 ^e	78
								176.2	0.224		
3	1.992(1)		1.86(2)	-1.6(2)	0	-1.7(4)	0	178.7 ^c	0.274 ^c	-2.5	950
4	1.997(1)	1.991(2)	1.01(8)	-2(1)	-10(7)	-8(2)	0	178.4 ^c	0.979 ^c	-22	700
5 ^d	1.994(3)	1.999(5)	1.58(8)	-3(1)	-6(5)	-7(2)	0	174.5 ^c	0.173 ^c	-12	735.4

^aNumbers in parentheses are estimated standard deviations of the last digit. ^bCrystal structure contains two Gd sites in the asymmetric unit. ^cData from Y analogue crystal structure. ^dSpin-Hamiltonian parameters from simultaneous fit of 5a and 5b K-band spectra. ^eSee Table S3 for the fit of 2 with B_6^5 . ^f ΔE is the total splitting of the $^8S_{7/2}$ multiplet (separation of top and bottom Kramers doublet) in zero-field for the parameters in the table. ^g U_{eff} is the thermal barrier for the reversal of magnetization in the analogous Dy³⁺ complex. ^hNot measured.

are at positions similar to those in the spectra of 1 and the best fit parameters of 1 were used as the starting point for fitting of 2. The resulting simulated spectra resemble the experimental data, but the fitted parameters are less reliable (Figure S2). An attempt at fitting the spectra with two independent sets of axial parameters failed, as the spectra are too convoluted. We found that on exchanging B_6^5 for B_2^2 in the spin Hamiltonian, i.e., decreasing the symmetry, the spectra can be simulated almost to perfection (see Figure 2) and yields very similar values of B_2^0 and B_4^0 (Table 1). Deciding which parameter to include from B_6^5 and B_2^2 is not immediately obvious but the fit is noticeably better with rhombic symmetry for 2, i.e., lower than C_5 symmetry. A full single-crystal study EPR would be required for an unambiguous assignment.

In contrast to 1 and 2, the signals of 3 are found in a much narrower field range, indicating smaller ZFS, though still large enough that all features are resolved. The spectra could be modeled with the same set of axial ZFS terms, but different values, as used for 1. An attempt was made to fit 3 with the B_6^5 parameter exchanged with B_2^2 , as was necessary for 2, but this made no significant improvement. Hence, the ZFS of 3 conforms to the approximate C_5 symmetry.

In some of the spectra of 1, 2, and 3 a peak corresponding to a g -value of 1.993–1.995 is seen. This peak does not fit with the simulations, and we attribute it to a small impurity of an amorphous Gd species giving rise to an isotropic signal.

The spectra of 4 are less well resolved than for the other compounds. The spectra only extend over roughly 200 mT and, apart from one transition in the middle, the transitions have broader linewidths than the other spectra. The narrow spectral range is a result of a small ZFS of the ground state. The spectra can be simulated with a relatively large B_6^5 parameter, though to reproduce the linewidths a significant strain of the B_2^0 parameter with a standard deviation of 7.3% was needed. This is a great deal more than necessary for the other samples (>1%).

5 was measured both as a doped (5a) and neat (5b) compound. Both samples give rich spectra (Figure 5) which is surprising as neat gadolinium complexes often have line widths so broad that few transitions are observable. For comparison, Figure S3 shows the spectrum of neat $\text{GdCl}_2(\text{THF})_5$, which has linewidths so large that the spectrum resembles a single transition.

The narrow line widths of 5b, could be the result of the crystal structure containing both water and two additional uncoordinated ligand molecules and their iodide counterions increasing the distance between neighboring molecules and

hence a lower density of paramagnetic species. Like 4 and to some degree 3 the transitions of 5a are narrower toward the middle of the spectrum than at the edges, which again suggests an influential B_6^5 parameter or strain on B_2^0 . This effect is not seen in the spectrum of 5b. The spectra of 5a and 5b complement each other well, with 5a having narrow line width on the central transitions, giving a good measure of the g -values and 5b relatively even linewidths and thus giving a better fit of the splitting. The two samples contain the same complex and approximately the same ZFS would be expected, since the ionic radius of Y³⁺ is similar to that of Gd³⁺ (102 and 105 pm, respectively, in eight coordinate complexes).²² They were therefore fitted together to give a single set of spin-Hamiltonian parameters.

As fitting six data sets at a time was too cumbersome, the spectra were fitted in pairs of 5a and 5b at each frequency, starting with the K-band and then using the resulting parameters as a starting point for X- and Q-bands. The best fit parameters are presented in Table S4. The ZFS parameters obtained this way are mostly consistent, apart from B_4^0 which is an order of magnitude lower at X-band. The Zeeman parameters give conflicting values. X- and Q-band g -values (see Table S4) are lower than those from the K-band spectrum but within experimental error. The three parameter sets have the same trend with $g_{\perp} < g_{\parallel}$ by 0.005–0.009.

Overall, the fits match the experimental data well and give the well-defined parameters in Table 1. Since the spectra were recorded at room temperature, simulations are not sensitive to the sign of the ZFS parameters, though they are to their magnitude and relative signs. The parameters in Table 1 are arbitrarily written with positive values of B_2^0 .

Due to the high energy of the excited states of Gd³⁺, its g -factors are usually very close to the free electron g -value, with typical values in the range 1.99–2. The values of g_{\perp} and g_{\parallel} in Table 1 and fall in the normal range for Gd³⁺. In the case of 1, 2, and 3, the g was modeled as isotropic because, when allowed to refine as axial, the values of g_{\parallel} and g_{\perp} were close and the standard deviations were significantly larger than the difference. 4 and 5 were modeled with anisotropic g -values. The direction of the g -anisotropy is opposite in these two compounds: 4 has $g_{\perp} > g_{\parallel}$ and 5 the reverse. No explanation for this behavior presents itself.

B_2^0 is a measure of the axial crystal field. Here, we find the magnitude of B_2^0 follows the order opposite to the crystal field strength expected of the axial ligands. This observation is in line with already established results in the literature.²³ The

uncharged ligands in the plane of the bipyramid play only a minor role in defining the crystal field.

The thermal energy barrier (U_{eff}) of Dy^{3+} SMMs is always considered to be proportional to the axial crystal field. However, the axial crystal field has not been measured in most Dy^{3+} SMMs but rather calculated by CASSCF. There are significant exceptions.²⁶ Here, we have measured B_2^0 directly in a series of Gd^{3+} compounds. 2, 3, and 5 all have Dy^{3+} analogues with published values of U_{eff} .¹⁴ No Dy^{3+} analogues of 1 or 4 have been published, but a version of 4 with non-fluorinated phenoxide ligands is known with U_{eff} reported, though fluorinating the ligand could change the U_{eff} somewhat.^{14,24} Taking this series of compounds, we find that B_2^0 in the Gd^{3+} complexes has an inverse and linear correlation to the measured U_{eff} of the corresponding Dy^{3+} compounds (Figure 6). We propose that the inverse relationship is because ZFS in Gd^{3+} compounds arise from mixing of excited states.

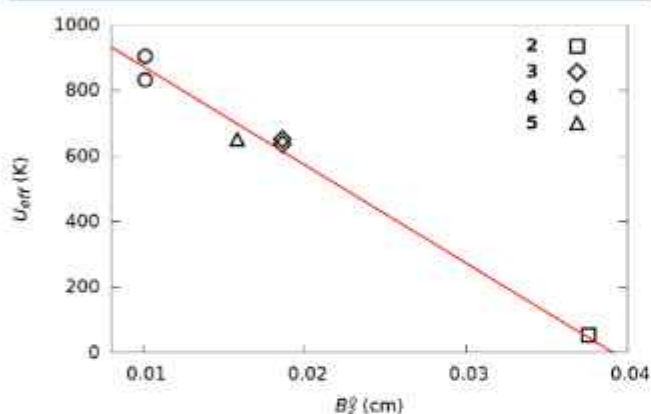


Figure 6. Comparison of the magnitude of B_2^0 and U_{eff} determined for the corresponding Dy^{3+} complex. $[\text{Dy}(\text{OPh})_2\text{Py}_3]$ is used as corresponding to $[\text{Gd}(\text{OArF}_5)_2\text{Py}_3]$ (4). The red line is a trendline to guide the eye. Two data points for U_{eff} are given where measurements of pure and doped Dy SMMs were reported.

The remaining axial ZFS parameters B_4^0 and B_6^0 have less influence on the spectra and are poorly defined. In particular, B_6^0 is of little importance and was so inadequately determined in the fits of 1, 2, and 3 that it was removed from the model.

The role of the \hat{O}_6^5 operator is to mix m_s states differ by $\Delta m_s = \pm 5$: in the case of gadolinium that is mixing of the $|\pm 7/2\rangle$ state with the $|\mp 3/2\rangle$ state and the intermixing of the $|\pm 5/2\rangle$ states. B_6^5 is the only off-diagonal parameter allowed to be non-zero under C_5 symmetry, so these states are therefore the only ones interacting at zero field. The compositions of the zero-field eigenstates derived from the ZFS parameters are given in Tables S6–S11.

Since B_6^5 is not allowed in D_{5h} symmetry, which is the idealized symmetry of the complexes other than 3, we explored the correlation between the magnitude of B_6^5 and the deviation from this symmetry. In order to test this hypothesis, continuous shape measures (CShMs)²⁵ were used as a parameter to describe the deviation of the first coordination sphere from pentagonal bipyramidal. To compare the B_6^5 parameters between the complexes, they were normalized by the overall splitting of the $^8S_{7/2}$ state in zero-field, ΔE (final column in Table 1). At first glance there is no obvious connection between CShM and B_6^5 [we neglect compound 2 here because B_6^5 is ill-defined due to the B_2^2 term and two

crystallographic sites]. The order is $1 < 5 < 3 < 4$ for CShM, while it is $1 < 3 < 5 < 4$ for B_6^5 . Thus, the ordering fails with regards to 3 and 5. Looking closer at 5, it is found that despite it having a low CShM value, the $X_1\text{-Gd-X}_2$ angle for the axial ligands is the furthest from 180° of the five complexes. The deformation of the axiality seems therefore to influence the off-diagonal ZFS more than distortions to the equatorial ligands, possibly due to the higher charge.

We also considered the use of the B_2^2 parameter to fit the spectra. In one case (2), this was more effective to simulate the spectra than B_6^5 . B_2^2 is not allowed if there is a fivefold rotation symmetry; it is a rhombic term. While we cannot draw strong conclusions from which of these two terms is used in which case, it is clear that the site symmetry in these SMMs as determined by EPR spectroscopy is never D_{5h} . This matches the ChSM, based on the X-ray structures, which also shows a symmetry below D_{5h} .

CONCLUSIONS

Six crystalline powder samples of pentagonal bipyramidal complexes of pure Gd^{3+} and Gd^{3+} doped into Y^{3+} have been prepared and investigated with EPR at variable frequency. They were found to give well-resolved spectra.

The EPR spectra could be simulated by splitting of the ground state with a spin-Hamiltonian based on the restrictions of D_{5h} symmetry but some off-axis terms were needed in all cases. Some correlation between the CShM of the complex toward D_{5h} point group symmetry and the relative magnitude of the off-diagonal parameter of the ZFS was found. However, it was also found that distortions in the positions of the axial ligands have more impact than distortions of the ligands in the plane, possibly due to the larger influence of the axial ligands on the crystal field. Furthermore, the nature of the axial ligands is the determining factor for the magnitude of the B_6^5 parameter.

The magnitude of B_2^0 is inversely proportional to the crystal field strength expected for the axial ligands. We therefore investigated whether this correlates with the thermal energy barrier (U_{eff}) for the Dy^{3+} analogues of these compounds which are SMMs. There is a good inverse correlation (Figure 6). The correlation is inverse because while the crystal field splitting in the Dy^{3+} SMMs is directly proportional to the U_{eff} in the Gd^{3+} complexes, the ZFS is due to mixing in of excited states into the ground state.

The energy barrier in lanthanide SMMs is often related to the crystal field splitting, and this has been regularly confirmed by high-level calculations.^{14–16,18,26–29} We have also reported a linear correlation between U_{eff} and $R \cos(\pi/(180 - \theta))$, where R = the Dy-axial ligand distance and θ is the angle at Dy between the axial ligands.³⁰ The EPR data reported here are rare experimental confirmation that this is correct. In the future, we will investigate whether this correlation of B_2^0 for Gd^{3+} correlates with U_{eff} in other Dy^{3+} SMMs.

ASSOCIATED CONTENT

Supporting Information

The Supporting Information is available free of charge at <https://pubs.acs.org/doi/10.1021/acs.inorgchem.3c01227>.

Crystallographic information, additional EPR spectra, and ground state compositions (PDF)

Accession Codes

CCDC 1451544, 2250360, and 2250394–2250395 contain the supplementary crystallographic data for this paper. These data can be obtained free of charge via www.ccdc.cam.ac.uk/data_request/cif, or by emailing data_request@ccdc.cam.ac.uk, or by contacting The Cambridge Crystallographic Data Centre, 12 Union Road, Cambridge CB2 1EZ, UK; fax: +44 1223 336033.

AUTHOR INFORMATION

Corresponding Author

Richard E. P. Winpenny – Department of Chemistry, School of Natural Science, The University of Manchester, Manchester M13 9PL, U.K.; orcid.org/0000-0002-7101-3963; Email: richard.winpenny@manchester.ac.uk

Authors

Jonatan B. Petersen – Department of Chemistry, School of Natural Science, The University of Manchester, Manchester M13 9PL, U.K.

You-Song Ding – Department of Chemistry, School of Natural Science, The University of Manchester, Manchester M13 9PL, U.K.; Frontier Institute of Science and Technology (FIST), Xi'an Jiaotong University, Xi'an 710049, China

Sandeep Gupta – Department of Chemistry, Indian Institute of Technology Bombay, Mumbai 400076, India; orcid.org/0000-0003-2432-933X

Aditya Borah – Department of Chemistry, Indian Institute of Technology Bombay, Mumbai 400076, India

Eric J. L. McInnes – Department of Chemistry, School of Natural Science, The University of Manchester, Manchester M13 9PL, U.K.; orcid.org/0000-0002-4090-7040

Yan-Zhen Zheng – Frontier Institute of Science and Technology (FIST), Xi'an Jiaotong University, Xi'an 710049, China; orcid.org/0000-0003-4056-097X

Ramaswamy Murugavel – Department of Chemistry, Indian Institute of Technology Bombay, Mumbai 400076, India; orcid.org/0000-0002-1816-3225

Complete contact information is available at:

<https://pubs.acs.org/10.1021/acs.inorgchem.3c01227>

Notes

The authors declare no competing financial interest.

ACKNOWLEDGMENTS

J.B.P. was supported by a European Research Council Advanced Grant to R.E.P.W. (ERC-2017-ADG-786734). We also thank the EPSRC(UK) EPR National Research Facility (EP/W014521/1, EP/V035231/1, EP/X034623/1) for access to EPR spectrometers. R.M. thanks the SERB, New Delhi for a J. C. Bose Fellowship grant (SB/S2/JCB- 85/2014).

REFERENCES

- (1) Abragam, A.; Bleaney, B. *Electron Paramagnetic Resonance of Transition Ions*, 1st ed.; Oxford: Clarendon press, 1970.
- (2) Buckmaster, H. A.; Shing, Y. H. A Survey of the EPR Spectra of Gd³⁺ in Single Crystals. *Phys. Status Solidi A* **1972**, *12*, 325–361.
- (3) Buch, C. D.; Kundu, K.; Marbey, J. J.; van Tol, J.; Weihe, H.; Hill, S.; Piligkos, S. Spin–Lattice Relaxation Decoherence Suppression in Vanishing Orbital Angular Momentum Qubits. *J. Am. Chem. Soc.* **2022**, *144*, 17597–17603.
- (4) López-Cabrelles, J.; Escalera-Moreno, L.; Hu, Z.; Prima-García, H.; Espallargas, G. M.; Gaita-Ariño, A.; Coronado, E. Near Isotropic

D_{4d} Spin Qubits as Nodes of a Gd(III)-Based Metal–Organic Framework. *Inorg. Chem.* **2021**, *60*, 8575–8580.

(5) Luis, F.; Alonso, P. J.; Roubeau, O.; Velasco, V.; Zueco, D.; Aguilà, D.; Martínez, J. I.; Barrios, L. A.; Aromí, G. A dissymmetric [Gd₂] coordination molecular dimer hosting six addressable spin qubits. *Commun. Chem.* **2020**, *3*, 176.

(6) Blagg, R. J.; Ungur, L.; Tuna, F.; Speak, J.; Comar, P.; Collison, D.; Wernsdorfer, W.; McInnes, E. J. L.; Chibotaru, L. F.; Winpenny, R. E. P. Magnetic Relaxation Pathways in Lanthanide Single-Molecule Magnets. *Nat. Chem.* **2013**, *5*, 673.

(7) Gatteschi, D.; Sessoli, R. Quantum Tunneling of Magnetization and Related Phenomena in Molecular Materials. *Angew. Chem., Int. Ed.* **2003**, *42*, 268–297.

(8) Newman, D. J. Origin of the Ground State Splitting of Gd³⁺ in Crystals. *Chem. Phys. Lett.* **1970**, *6*, 288–290.

(9) Sørensen, M. A.; Weihe, H.; Vinum, M. G.; Mortensen, J. S.; Doerren, L. H.; Bendix, J. Imposing High-Symmetry and Tuneable Geometry on Lanthanide Centres with Chelating Pt and Pd Metalloligands. *Chem. Sci.* **2017**, *8*, 3566–3575.

(10) Senn, F.; Helm, L.; Borel, A.; Daul, C. A. Electronic Fine Structure Calculation of [Gd(DOTA)(H₂O)][−] Using LF-DFT: The Zero Field Splitting. *C. R. Chim.* **2012**, *15*, 250–254.

(11) Lasoroski, A.; Vuilleumier, R.; Pollet, R. Vibrational Dynamics of Zero-Field-Splitting Hamiltonian in Gadolinium-Based MRI Contrast Agents from Ab Initio Molecular Dynamics. *J. Chem. Phys.* **2014**, *141*, 014201.

(12) Ding, Y.-S.; Chilton, N. F.; Winpenny, R. E. P.; Zheng, Y.-Z. On Approaching the Limit of Molecular Magnetic Anisotropy: A Near-Perfect Pentagonal Bipyramidal Dysprosium(III) Single-Molecule Magnet. *Angew. Chem., Int. Ed.* **2016**, *55*, 16071–16074.

(13) Ding, Y.-S.; Yu, K.-X.; Reta, D.; Ortu, F.; Winpenny, R. E. P.; Zheng, Y.-Z.; Chilton, N. F. Field- and Temperature-Dependent Quantum Tunneling of the Magnetisation in a Large Barrier Single-Molecule Magnet. *Nat. Commun.* **2018**, *9*, 3134.

(14) Ding, Y.-S.; Han, T.; Zhai, Y.-Q.; Reta, D.; Chilton, N. F.; Winpenny, R. E. P.; Zheng, Y.-Z. A Study of Magnetic Relaxation in Dysprosium(III) Single-Molecule Magnets. *Chem.—Eur. J.* **2020**, *26*, 5893–5902.

(15) Gupta, S. K.; Rajeshkumar, T.; Rajaraman, G.; Murugavel, R. An Air-Stable Dy(III) Single-Ion Magnet with High Anisotropy Barrier and Blocking Temperature. *Chem. Sci.* **2016**, *7*, 5181–5191.

(16) Gupta, S. K.; Rajeshkumar, T.; Rajaraman, G.; Murugavel, R. An Unprecedented Zero Field Neodymium(III) Single-Ion Magnet Based on a Phosphonic Diamide. *Chem. Commun.* **2016**, *52*, 7168–7171.

(17) Gupta, S. K.; Murugavel, R. Enriching Lanthanide Single-Ion Magnetism Through Symmetry and Axiality. *Chem. Commun.* **2018**, *54*, 3685–3696.

(18) Gupta, S. K.; Rajeshkumar, T.; Rajaraman, G.; Murugavel, R. Is a Strong Axial Crystal-Field the Only Essential Condition for a Large Magnetic Anisotropy Barrier? The Case of Non-Kramers Ho(III) versus Tb(III). *Dalton Trans.* **2018**, *47*, 357–366.

(19) Stevens, K. W. H. Matrix Elements and Operator Equivalents Connected with the Magnetic Properties of Rare Earth Ions. *Proc. Phys. Soc., London, Sect. A* **1952**, *65*, 209.

(20) Jacobsen, C. J. H.; Pedersen, E.; Villadsen, J.; Weihe, H. ESR Characterization of Trans-Diacidatotetrakis(Pyridine)Vanadium and -Manganese Trans-VII(Py)₄X₂ and Trans-MnII(Py)₄X₂ (X = NCS, Cl, Br, I; Py = Pyridine). *Inorg. Chem.* **1993**, *32*, 1216–1221.

(21) Husein Mor, H.; Weihe, H.; Bendix, J. Fitting of EPR Spectra: The Importance of a Flexible Bandwidth. *J. Magn. Reson.* **2010**, *207*, 283–286.

(22) Shannon, R. D. Revised Effective Ionic Radii and Systematic Studies of Interatomic Distances in Halides and Chalcogenides. *Acta Crystallogr., Sect. A: Cryst. Phys., Diffr., Theor. Gen. Crystallogr.* **1976**, *32*, 751–767.

(23) Levin, L. I.; Gorlov, A. D. Gd³⁺ Crystal-Field Effects in Low-Symmetric Centres. *J. Phys.: Condens. Matter* **1992**, *4*, 1981–1992.

(24) Ma, Y.; Zhai, Y.-Q.; Luo, Q.-C.; Ding, Y.-S.; Zheng, Y.-Z. Ligand Fluorination to Mitigate the Raman Relaxation of DyIII Single-Molecule Magnets: A Combined Terahertz, Far-IR and Vibronic Barrier Model Study. *Angew. Chem., Int. Ed.* **2022**, *61*, No. e202206022.

(25) Alvarez, S.; Alemany, P.; Casanova, D.; Cirera, J.; Llunell, M.; Avnir, D. Shape Maps and Polyhedral Interconversion Paths in Transition Metal Chemistry. *Coord. Chem. Rev.* **2005**, *249*, 1693–1708.

(26) Norel, I.; Darago, L. E.; Le Guennic, B.; Chakarawet, K.; Gonzalez, M. I.; Olshansky, J. H.; Rigaut, S.; Long, J. R. A Terminal Fluoride Ligand Generates Axial Magnetic Anisotropy in Dysprosium Complexes. *Angew. Chem., Int. Ed.* **2018**, *57*, 1933–1938.

(27) Goodwin, C. A. P.; Ortu, F.; Reta, D.; Chilton, N. F.; Mills, D. P. Molecular Magnetic Hysteresis at 60 Kelvin in Dysprosocenium. *Nature* **2017**, *548*, 439–442.

(28) Randall McClain, K.; Gould, C. A.; Chakarawet, K.; Teat, S.; Groshens, T. J.; Long, J. R.; Harvey, B. G. High-Temperature Magnetic Blocking and Magneto-Structural Correlations in a Series of Dysprosium(III) Metallocenium Single-Molecule Magnets. *Chem. Sci.* **2018**, *9*, 8492–8503.

(29) Guo, F.-S.; Day, B. M.; Chen, Y.-C.; Tong, M.-L.; Mansikkamäki, A.; Layfield, R. A. Magnetic Hysteresis up to 80 Kelvin in a Dysprosium Metallocene Single-Molecule Magnet. *Science* **2018**, *362*, 1400–1403.

(30) Ding, Y.-S.; Winpenny, R. E. P.; Zheng, Y.-Z. 3d and 4f-based single molecule magnets. In *Comprehensive Coordination Chemistry III*; Constable, E. C., Parkin, G., Que, L., Jr., Eds., 2021; Vol. 9, pp 595–619.



Review

Magnetic relaxation in single-ion magnets formed by less-studied lanthanide ions Ce(III), Nd(III), Gd(III), Ho(III), Tm(II/III) and Yb(III)

Aditya Borah, Ramaswamy Murugavel*^{*}

Department of Chemistry, IIT Bombay, Powai, Mumbai 400075, India

ARTICLE INFO

Article history:

Received 15 August 2021

Accepted 20 October 2021

Available online 27 November 2021

Keywords:

Single-ion magnets

Lanthanide magnets

Mononuclear complexes

Relaxation dynamics

Molecular symmetry

ABSTRACT

Recent growth in the area of single-molecule magnets (SMMs) in general, and single-ion magnets (SIMs) in particular, is due to the potential applications of this class of compounds in high density data storage devices, molecular spintronics and quantum computing devices. Among all the reported SIMs, Dy(III) based symmetry constrained molecules have been achieving the highest barrier of magnetisation reversal (U_{eff}) and blocking temperature (T_B). Apart from Dy(III), SIMs based on two other Ln(III) ions, viz. Er(III) and Tb(III) have also been explored to a considerable extent. However, SIMs formed by other lanthanide ions have remained unexplored to a great extent for various reasons. During the last few years, many successful attempts have however been made to realize SIMs of these less-explored Ln(III) ions, mainly those of Ce(III), Nd(III), Ho(III) and Yb(III) along with Gd(III) and Tm(II/III), with the objective of attaining significant U_{eff} and T_B values through suitably designed ligand field (LF) around the respective prolate or oblate Ln(III) ion. These recent investigations have paved way to a deeper understanding of the relaxation dynamics of these molecules. This review article attempts to summarize the important advances in this area.

© 2021 Elsevier B.V. All rights reserved.

Contents

1. Introduction	1
1.1. General remarks on molecular magnetism	1
1.2. Development of Ln(III) based SIMs	2
2. Single-ion magnets of less investigated Ln(III) ions	3
2.1. Cerium(III) based mononuclear SMMs	3
2.2. Neodymium(III) based mononuclear SIMs	6
2.3. Gadolinium(III) based mononuclear SMMs	12
2.4. Holmium(III) based mononuclear SMMs	12
2.5. Thulium(II/III) based mononuclear SMMs	17
2.6. Ytterbium (III) based mononuclear SMMs	19
3. Conclusions and future outlook	31
Declaration of Competing Interest	31
Acknowledgements	31
References	31

* Corresponding author.

E-mail address: rmw@chem.iitb.ac.in (R. Murugavel).

1. Introduction

1.1. General remarks on molecular magnetism

Magnetically bistable molecules exhibiting slow relaxation of magnetisation below a critical temperature (T_B) are named as single-molecule magnets (SMMs). The research area of molecular magnetism has received momentous attention in recent times due to the applications of SMMs (a) in designing high density data storage devices [1-3], (b) molecular spintronics [4-6] and (c) quantum computing devices [7-10] owing to the ability of the SMMs to block the magnetisation reversal for longer durations [11-14]. Gatteschi and coworkers first observed the existence of slow relaxation of magnetisation at very low temperature in a mixed-valent dodecanuclear Mn_{12} cluster which was synthesized by Lis and co-workers in 1980. They have employed a combination of high field electronic paramagnetic resonance (HF-EPR) and magnetic measurements to find the origin of such slow relaxation of magnetisation and found that the magnetization hysteresis observed for this cluster is of molecular origin, which is totally different from traditional bulk magnets [15,16]. This discovery led to design of a large number of polynuclear clusters based on transition metal ions, specially Mn^{3+} ion as the axially Jahn-Teller distorted Mn^{3+} ions usually possess considerable magnetic anisotropy [17-20]. In case of transition metal based SMMs, the magnetic property arises from large spin ground state (S) and uniaxial magnetic anisotropy or zero field splitting parameters (D), where the energy barrier (U_{eff}) separating the two spin states is described as $U_{eff} = |D| \cdot S^2$ (for integer spin) or $U_{eff} = |D| \cdot (S^2 - 0.25)$ (for half integer spin) [21-24]. Initial attempts to achieve larger anisotropy barrier were primarily focussed on increasing S by gathering paramagnetic centres with suitable magnetic interactions in the form of polynuclear complexes, whose formation was aided by the use of suitable bridging ligands [18,19,25,26]. The magnetic anisotropy of the polynuclear cluster is highly sensitive to the alignment of the individual local anisotropy axes and is drastically reduced with increasing nuclearity if the local anisotropy axes become misaligned [27]. Moreover, the ferromagnetic coupling among the spins is favourable as it increases S , while antiferromagnetic interactions cancel the spins and hence it is undesirable. Unfortunately, antiferromagnetic interactions are in general more common in polynuclear clusters as compared to ferromagnetic interactions [28-30]. Most importantly, increasing S in this straightforward approach also results in very small values of D , since these two quantities are inversely related [18,31]. Consequently this polynuclear complexes based strategy results in lower U_{eff} values. A proof for this behaviour is the example of an Mn_{19} cluster, made up of twelve $Mn(III)$ and seven $Mn(II)$ ions. This cluster with $S = 83/2$ ground state is found to exhibit no slow relaxation of magnetisation with a very small magnetic anisotropy (D is negligibly small). In contrary, another $Mn(III)$ cluster with just six $Mn(III)$ ions shows significant magnetic anisotropy with a D value of -0.43 cm^{-1} although its S value of 12 is far smaller than that of the Mn_{19} cluster [18,32]. These observations suggest that the idea of designing polynuclear clusters having high S is not necessarily productive enough. It led to the shift of attention towards mononuclear complexes where the ion has significant inherent magnetic anisotropy that is dictated by modulating the local symmetry around the ion [27]. The discovery of slow relaxation of magnetisation phenomenon in double-decker mononuclear $Tb(III)$ and $Dy(III)$ complexes, $[Pc_2Ln][TBA][33]$ (where Pc is the dianion of phthalocyanine and $TBA^+ = N(C_4H_9)_4^+$) by Ishikawa and co-workers in 2003 provided a novel strategy to design high performance SMMs. Subsequent to this observation, the field of molecular magnetism has gradually shifted its attention from polynuclear clusters to the mononuclear discrete molecules

recording very high barrier of spin reversal and blocking temperature [34,35]. The recent investigations prove that trivalent lanthanide ions ($Ln(III)$) are better candidates over transition metal ions in the context of achieving larger U_{eff} and hence high T_B .

1.2. Development of $Ln(III)$ based SMMs

For the last few decades, $Ln(III)$ based SMMs are being vigorously investigated as compared to their transition metal counterparts. The remarkable attention on $Ln(III)$ ions during this time is due to (a) their intrinsic single-ion anisotropy arising from the high anisotropic electronic charge distribution of 4f orbitals and (b) considerable unquenched orbital angular momentum along with large spin-orbit coupling in the ground state [36,37]. Although, the crystal field splitting in $Ln(III)$ ions is much smaller compared to the transition metal (TM) ions, due to weak interaction of the ligand field (LF) with highly shielded 4f orbitals, the local symmetry around the $Ln(III)$ centre plays a vital role in enhancing its SIM behaviour. The work of Long and co-workers set the initial tone towards designing an appropriate ligand field in order to enhance the intrinsic anisotropy of $Ln(III)$ ions based on the shape of the 4f electron density. [38] For example, oblate shaped $Ln(III)$ ions (e.g: $Ce(III)$, $Nd(III)$, $Tb(III)$, $Dy(III)$, $Ho(III)$ etc.) require strong axial ligands along with weaker or absence of equatorial ligand, while the prolate shaped ions (eg: $Er(III)$, $Yb(III)$ etc.) require strong equatorial ligands and weak (or ideally no) axial ligands. Such strategy has been found to be highly productive in designing SIMs with larger U_{eff} and T_B based on both oblate and prolate shaped $Ln(III)$ ions.

The slow relaxation of magnetisation in SMMs can occur via different pathways, viz., Orbach, Raman, direct and quantum tunnelling of magnetisation (QTM). Except QTM, all other molecular level relaxation processes are dependent on the temperature to different extents which can be demonstrated by the following equation:

$$\tau^{-1} = \tau_{QTM}^{-1} + AT + CT^n + \tau_0^{-1} \exp(-U_{eff}/k_B T) \quad (1)$$

The first term of equation (1) represents the relaxation via QTM, while second and third terms model the relaxation via direct and Raman processes, respectively, and the fourth term accounts for the Orbach relaxation pathway. These relaxation pathways are demonstrated in Fig. 1. It is not necessary that all the relaxation processes should be present in the relaxation dynamics of a

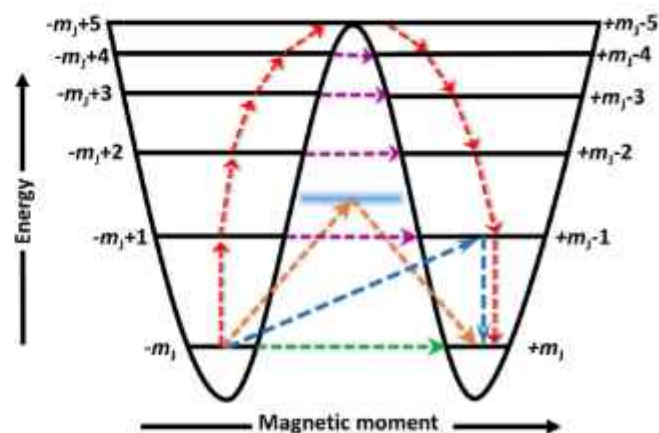


Fig. 1. Possible pathways for relaxation of magnetisation. The green and purple arrows represent quantum tunnelling of magnetisation (QTM) occurring at ground state and the thermally assisted quantum tunnelling of magnetisation (TA-QTM) which occur at higher m_j levels, respectively. The orange arrows represent the Raman pathway which occurs via a virtual excited state shown in light blue. The red and blue lines demonstrate Orbach pathways.

single-molecule magnet. The extent of dominance of a relaxation process over other processes strongly depends on factors such as the Ln(III) ion under consideration, the ligand field and any external stimuli such as light, pressure, temperature etc. The relaxation processes occur at different temperature region, QTM occurs at very low temperature, Raman process operates at moderate temperature and Orbach process operates at higher temperature region. It has been predicted that the U_{eff} can be maximized with one- or two-coordinated perfectly linear Ln(III) complexes, where the inclination for ground-state QTM is insignificant due to the existence of negligible transverse anisotropies [23,39–43]. Synthesis and stabilisation of such low coordinated lanthanide complexes are highly challenging due to their larger ionic radii which allow the ions to form complexes with larger coordination numbers. This problem has been overcome to some extent by placing the ion in suitable ligand field maintaining higher order local symmetry. Recent attempts of sandwiching a Dy(III) ion in between two substituted cyclopentadienyl rings can be mentioned here, achieving the barrier heights of even higher than 2000 K and opening of magnetic hysteresis loop above liquid-nitrogen temperature ($T_{\text{H}} = 80$ K) [44–50]. These findings unlock new hope towards development of nanomagnets based devices functionable at practical temperatures. Ln(III) complexes with higher order rotational symmetry, e.g. square antiprismatic (D_{4d}) [51,52], pentagonal bipyramidal (D_{3h}) [53–60], hexagonal bipyramidal (D_{6h}) [61,62] and sandwich type (D_{∞}) [63–66] have also been found to exhibit significant SMM behaviour.[67–73] Hence, constructing a compatible ligand field around the metal ion is the most important step. Among the lanthanide ions, Dy(III) and to some extent Tb(III) and Er(III) receive much attention for synthesizing new SMMs due to the existence of large m_j values and also comparatively less difficulty in enhancing the magnetic anisotropy by designing an appropriate ligand field. However, successful attempts have also been made to some extent in designing molecules with slow magnetisation of relaxation based on other Ln(III) ions (except diamagnetic La(III) and Lu(III), radioactive Pm(III) apart from Eu(III) which has a non-magnetic ground state 7F_0). In general, attempts to design SMMs with these uncommon lanthanides are mostly based on accumulation of sole Ln(III) ions or combination of Ln(III) ions with either main group metal ions or transition metal ions. However, the lack of synthetic control over the symmetry of coordination sphere as well as on the interactions among the paramagnetic centres result in smaller or even no barrier for spin reversal. Unlike polynuclear SMMs, mononuclear complexes based on these Ln(III) ions are less explored. Different strategies, such as selection of suitable ligand field, modification of secondary coordination sphere etc., can result in the enhancement of magnetic anisotropy of these unexplored Ln(III) based SIMs to reasonable extent. Thus, a detailed study on the behaviours of these SIMs is really needed. Herein, we critically review the recent developments of these less explored mononuclear Ln(III) (Ln = Ce, Nd, Gd, Ho, Tm and Yb) SIMs and their relaxation behaviour.

In the context of this review, it should be noted that Pointillart *et al.* have published a review in 2017 on the magnetic properties of less-common lanthanides based single-molecule magnets known at that time [74]. Since then, there has been a lot of interest in mononuclear SMMs (more commonly known as single-ion magnets, SIMs) of lanthanides, especially those derived from dysprosium. The phenomenal success with Dy(III) based SIMs during the last few years with reports describing large barriers and blocking temperatures have propelled intense research activity on SIMs derived from earlier less investigated lanthanides ions such as Ce, Nd, Gd, Ho, Tm and Yb. This review is hence aimed to comprehensively summarize such activities, focussing the coverage on all known SIMs of these metal ions.

2. Single-ion magnets of less investigated Ln(III) ions

2.1. Cerium(III) based mononuclear SMMs

Ce is the most abundant and low-cost rare-earth element. It has been reported that the magnetic properties of $\text{Nd}_2\text{Fe}_{14}\text{B}$, one of the strongest permanent magnets exists, can be improved to some extent by using Ce(III) as dopant instead of Dy(III) [75]. Among all Ln(III) ions, Ce(III) has the simplest electronic configuration, i.e. f^1 , with $^2F_{5/2}$ ground electronic state and hence it has smaller magnetic moment ($J = L - S$) as well as smaller spin-orbit (SO) coupling as compared to heavier lanthanides. Moreover, manipulation of the electronic levels of Ce(III) are easier compared to other ions as its natural isotopes do not possess any nuclear spin. On placing Ce(III) ion in a suitable ligand field, the six-fold degenerate ground state is split into three sets of Kramers pairs, i.e. $|m_j| = 5/2, 3/2, \text{ and } 1/2$. To enhance the magnetic anisotropy around Ce(III) having oblate electronic density for the ground electronic state, the appropriate ligand field should be axially stressed and equatorially relaxed [38]. A theoretical study on some Ce(III) based models by Rajaraman and co-workers suggests that use of very strong ligand, OH^- , in axial position and no ligand in equatorial position, resulting in a $[\text{Ce}(\text{OH})_2]^{2+}$ model, can yield the largest theoretical barrier for Ce(III) based SIMs [48]. However, due to its large ionic radius, it becomes impossible practically to stabilise a complex with such a small ligand. So, the choice of ligands should be in such a way that they can provide enough steric protection to the metal centre to form a complex with low coordination number. Though a number of Ce(III) based polymeric chains and polynuclear complexes showing SMM behaviour are already known, examples of mononuclear Ce(III) SMMs are limited in number [76–80].

Using a bulkier ligand such as bis(trimethylsilyl)-cyclooctatetraenyl dianion, $[\text{COT}]^{2-}$, Murugesu and co-workers have reported the first mononuclear Ce(III) based Cerocene complex, $\text{Li}(\text{DME})_3[\text{Ce}^{\text{III}}(\text{COT})_2]$ (**1**) (Fig. 2) [81]. Ce(III) ion in this complex is sandwiched between two COT^{2-} ligands (COT^{2-} : bis(trimethylsilyl) cyclooctatetraenyl dianion) in a η^8 fashion with a $\text{Li}(\text{DME})_3$ counter cation. The $\text{C}_{\text{COT}^{2-}}$ atoms of one ring are staggered with respect to the $\text{C}_{\text{COT}^{2-}}$ atoms of the other, due to the presence of the bulky TMS (trimethylsilyl) groups[82] and hence the $(\text{COT}^{\text{centroid}})_{\text{Ce}^{\text{III}}}-\text{COT}^{\text{centroid}}$ angle deviates from perfect linearity by 3.75° . The ac susceptibility measurements revealed that **1** does not show any ac signal in the absence of applied dc field. However, under optimised dc field of 400 Oe, a strong temperature and frequency dependent out-of-phase (χ'') signal was observed up to 7.5 K. The gradual broadening of the peaks at lower temperature (below 3.5 K) and appearance of a second maxima at higher frequency region clearly suggests that multiple magnetic relaxation processes are involved in the relaxation dynamics of **1**. The linear fitting of $\ln\tau$ vs $1/T$ at higher temperature region yields an effective energy barrier of 30 K, which is comparable with its Dy analogue ($U_{\text{eff}} = 25$ –K at 0 Oe; 28 K at 100 Oe) [83] (Table 1).

Two air stable mononuclear Ce(III) based SMMs were reported by Kajiwarra and co-workers using 18-crown-6 or its 1,10-diaza derivative as the equatorial ligand and three NO_2 anions occupying the vacant axial positions, yielding $[\text{Ce}(\text{NO}_2)_3(18\text{-crown-6})]$ (**2**) and $[\text{Ce}(\text{NO}_2)_3(1,10\text{-diaza-18-crown-6})]$ (**3**) (Fig. 3) [84]. Both 18-crown-6 and 1,10-diaza-18-crown-6 bind to the metal centre in a wavy fashion due to the presence of sp^3 carbon atoms. So, all the equatorially coordinated O/N atoms do not strictly lie in a plane. A coordination number of 12 is observed around Ce(III) ion in both **2** and **3**. Both these complexes do not show any out-of-phase signal of the magnetic susceptibility in absence of any magnetic field due to the presence of strong QTM, which can however be suppressed to highest possible extent by applying the optimised dc field (1000

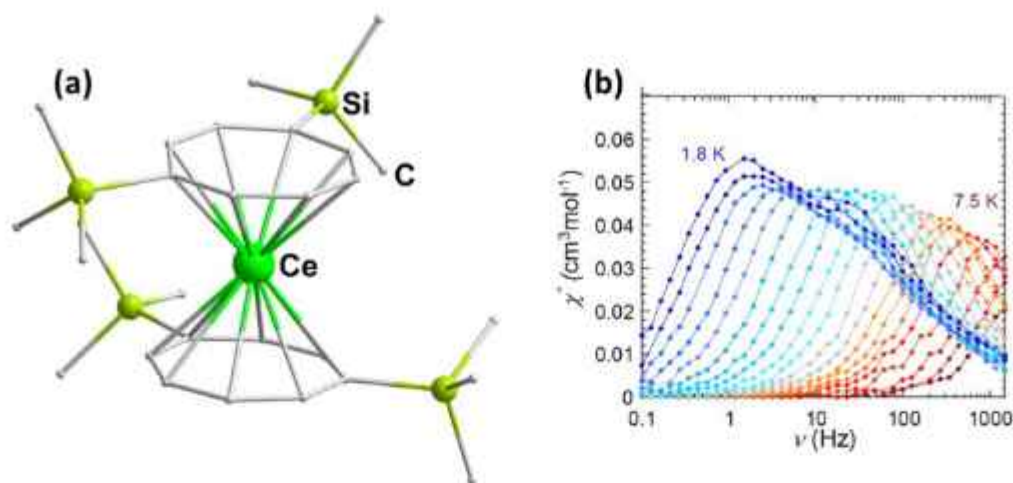


Fig. 2. (a) Structure of the anionic part of $[\text{Li}(\text{DME})_2][\text{Ce}^{\text{III}}(\text{CO1}^*)_2]$ (**1**). The cationic part, $\text{Li}(\text{DME})_2$, is omitted for clarity. (b) Frequency dependence of out-of-phase (χ'') magnetic susceptibility of **1** between 1.8 and 7.5 K in presence of 400 Oe dc field. Adopted from [81]. Copyright 2014 Royal Society of Chemistry.

Table 1

Mononuclear Ce(III) based single-ion magnets ($U_{\text{eff},ac}$ represents the barrier obtained from ac susceptibility measurements; $U_{\text{eff},cal}$ represents the barrier obtained from computational studies, C and n are the parameters obtained from the fitting of temperature dependence of relaxation time plot using Raman process):

Sl no.	Ce(III) SIMs	$U_{\text{eff},ac} / \text{K}$	$U_{\text{eff},cal} / \text{K}$	τ_0 / s	$\tau_{\text{QTM}} / \text{s}$	$C / \text{s}^{-1} \text{K}^{-n}$	n	H / Oe	Reference
1	$[\text{Li}(\text{DME})_2][\text{Ce}^{\text{III}}(\text{CO1}^*)_2]$, (1)	30	–	1.2×10^{-6}	–	–	–	400	[81]
2	$[\text{Ce}(\text{NO}_3)_2(18\text{-crown-6})]$, (2)	31.4	–	1.8×10^{-7}	–	–	–	1000	[84]
		30.3	–	2.3×10^{-7}	–	0.108	5	–	
3	$[\text{Ce}(\text{NO}_3)_2(1,10\text{-diazza-18-crown-6})]$, (3)	44	–	2.3×10^{-8}	–	–	–	1000	[84]
		44	–	2.6×10^{-7}	–	0.52	5	–	
4	$[\text{Ce}(\text{NO}_3)_2(\text{HL})_2]$, (4)	37.5	501	2.76×10^{-8}	0.076	0.154	7.36	3000	[91]
5	$[\text{Ce}(\text{fdh})_2(\text{bpy})]$, (5)	33.3	–	1.8×10^{-7}	–	0.40	6	2000	[92]
6	$[\text{Ce}(\text{NO}_3)_2\text{L}_2]$, (6)	21.5	317	2.7×10^{-7}	–	–	–	200	[94]
		–	–	–	–	1.44	6.8	200	

Table 2

Mononuclear Nd(III) based single-ion magnets ($U_{\text{eff},ac}$ represents the barrier obtained from ac susceptibility measurements; $U_{\text{eff},cal}$ represents the barrier obtained from computational study, C and n are the parameters obtained from the fitting of temperature dependence of relaxation time plot using Raman process):

Sl no.	Nd(III) SIMs	$U_{\text{eff},ac} / \text{K}$	$U_{\text{eff},cal} / \text{K}$	τ_0 / s	$\tau_{\text{QTM}} / \text{s}$	$C / \text{s}^{-1} \text{K}^{-n}$	n	H/Oe	Ref
1	$[\text{NdTf}_2]$ (7)	4	165	2.6×10^{-4}	–	–	–	100	[100]
2	$[\text{Li}(\text{DME})_2][\text{Nd}^{\text{III}}(\text{CO1}^*)_2]$ (8)	21	–	5.5×10^{-5}	–	–	–	1000	[101]
3	$[\text{Nd}(\text{NO}_3)_2(18\text{-crown-6})]$ (9)	29.9	–	2.9×10^{-9}	–	–	–	1000	[84]
		30.9	–	2.2×10^{-9}	–	4.1	5	1000	
4	$[\text{Nd}(\text{NO}_3)_2(1,10\text{-diazza-18-crown-6})]$ (10)	69	–	2.1×10^{-10}	–	–	–	1000	[84]
		73	–	1.4×10^{-10}	–	0.00107	9	1000	
5	$[\text{Nd}(\text{NO}_3)_2\text{L}]\text{PF}_6 \cdot \text{MeCN}$ (11)	36	–	4.4×10^{-9}	–	2.8(2)	5	1000	[16]
6	$[\text{L}_2\text{Nd}(\text{H}_2\text{O})_2][\text{I}]\text{I}_2 \cdot \text{L}_2 \cdot (\text{H}_2\text{O})$ (12)	16.08	302	2.6×10^{-4}	1×10^{-3}	4.2×10^{-18}	5	0	[55]
		24.69	–	5.0×10^{-6}	–	–	–	0	
		39.21	–	8.9×10^{-7}	–	0.0292	5	2000	
7	$[\text{Nd}(\text{CyPh}_2\text{PO})_2(\text{H}_2\text{O})_2]_2 \cdot 2(\text{CyPh}_2\text{PO}) \cdot 3\text{EtOH}$ (13)	–	–	–	5.1×10^{-3}	–	–	5.12	0
		–	–	–	–	–	–	6.54	2000
8	$[\text{Cp}^*_2\text{Nd}(\text{BPh}_4)]$ (14)	41.7	–	1.4×10^{-6}	–	0.0286	5.2	1000	[109]
9	$[\text{Nd}^{\text{III}}(\text{TfA})(\text{MeOH})_2] \cdot (0.5\text{Azo-py})$ (15)	19.7	–	3.8×10^{-7}	8.3×10^{-3}	–	–	1000	[111]
10	15 after Heating	27.3	–	8.5×10^{-8}	–	–	–	1000	[111]
10	C_1 symmetric $[\text{C}(\text{NH}_2)_2]_2[\text{Nd}(\text{CO}_3)_4(\text{H}_2\text{O})] \cdot 2\text{H}_2\text{O}$ (16)	30.7	–	1.1×10^{-7}	–	0.89	6.08	1500	[112]
		–	–	–	–	–	–	1500	
11	C_4 symmetric $[\text{C}(\text{NH}_2)_2]_4[\text{H}_2\text{O}][\text{Nd}(\text{CO}_3)_4(\text{H}_2\text{O})] \cdot 9 \cdot 5\text{H}_2\text{O}$ (17)	9.25	–	2.1×10^{-6}	–	413.85	3.63	1500	[112]

Oe). Under this optimised field, strong temperature and frequency dependent out-of-phase (χ'') signal was observed up to 7 K for **2** and 6.5 K for **3** within a frequency range of 0–10000 Hz (Fig. 3). The fitting to plot of $\ln \tau$ vs $1/T$ at high temperature region yields an energy barrier of 31.4 K and $\tau_0 = 1.8 \times 10^{-7}$ s for **2** and $U_{\text{eff}} = 44$ K and $\tau_0 = 2.3 \times 10^{-8}$ s for **3**. The plots for both the single-ion magnets can be best fitted by considering Orbach and Raman relaxation processes with $U_{\text{eff}} = 30.3$ K, $\tau_0 = 2.3 \times 10^{-7}$ s, $C = 0.108 \text{ s}^{-1} \text{K}^{-n}$ and $n = 5$ for **2** and $U_{\text{eff}} = 44$ K, $\tau_0 = 2.6 \times 10^{-7}$ s, $C = 0.52 \text{ s}^{-1} \text{K}^{-n}$

and $n = 5$ for **3**. Though both these complexes have a similar coordination geometry, **3** has higher barrier and shorter relaxation time compared to **2** due to the presence of different donor atom sets surrounding Ce(III) ion. Being oblate, the electronic distributions of the highest $|J_z|$ sublevels in Ce(III) is expanding in the equatorial plane. Thus, the nitrate anions effectively destabilise the electronic distribution of sublevels having components along the z-axis through electronic repulsion. However, the extent of destabilization of the ground $|J_z|$ sublevels by neutral ether ligands is

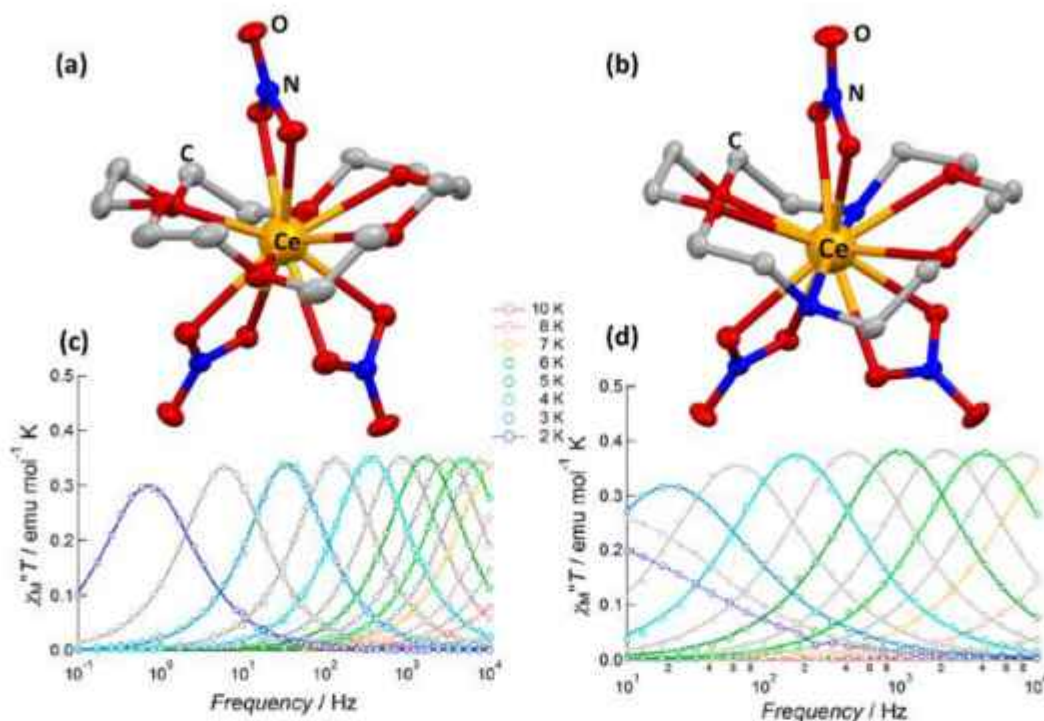


Fig. 3. Molecular X-ray structure of (a) $[\text{Ce}(\text{NO}_3)_3(18\text{-crown-6})]$ (**2**) and (b) $[\text{Ce}(\text{NO}_3)_3(1,10\text{-diaz-18-crown-6})]$ (**3**). Their frequency dependence of out-of-phase (χ'') magnetic susceptibility in presence of 1000 Oe dc field are shown in (c) and (d), respectively. Adopted from [84]. Copyright 2017 American chemical society.

relatively weak. This is reflected in the difference between the energy of ground and excited sublevels. The bending angle to the ideal equatorial plane with respect to the Ce(III) centre is larger in **3** as compared to **2**, demonstrating that the deviation of donor atoms from equatorial plane is larger in **3**. This reduces the repulsion between the ether ligands and the electronic distribution of the ground sublevels, resulting in a larger separation between the ground and first excited sublevels in **3** and hence higher energy barrier of magnetisation reversal.

The chemistry of lanthanide Schiff base complexes is rich because of their large variety of applications, such as in catalysis, redox reactions, cancer diagnosis and therapy, antibacterial activity, molecular magnetism etc [85–90]. A Ce(III) based mononuclear Schiff base complex, $[\text{Ce}(\text{NO}_3)_3(\text{HL})_3]$ (**4**), where HL = 2-methoxy-6-[(E)-phenylimino-methyl]phenol, was reported by Shanmugam and co-workers where Ce(III) ion is coordinated by twelve oxygen atoms (six oxygens from three Schiff base ligands and rest are from three nitrates), resulting in a distorted icosahedron environment around the metal ion (Fig. 4) [91]. Complex **4** does not show any out-of-phase ac susceptibility signals in the absence of an external magnetic field due to the dominance of QTM over a thermally activated relaxation mechanism. On application of an optimized dc field of 3000 Oe, complex **4** shows well-resolved frequency-dependent out-of-phase susceptibility signals with clear maxima up to 7 K. This complex relaxes via single relaxation pathway with $0.03 < \alpha < 0.29$. The relaxation occurs in this case via Orbach, Raman along with QTM. By fitting the higher temperature linear portion of the plot $\ln \tau$ vs $1/T$, U_{eff} is estimated to be 37.5 K with $\tau_0 = 2.76 \times 10^{-8}$ s. Computational studies on **4** suggest that the energy of the first excited state is higher by 501 K as compared to the ground state. The mismatch of the experimental and computational results indicates the presence of other relaxation processes along with Orbach process. The plot $\ln \tau$ vs $1/T$ over the whole temperature range is best fitted by using Orbach, Raman and QTM with the parameters: $C = 0.154 \text{ s}^{-1} \text{ K}^{-n}$, $n = 7.36$ and $\tau_{\text{QTM}} = 0.076$ s.

Another air stable mononuclear Ce(III) based complex was reported by Gao and co-workers in 2018 [92]. The complex was synthesized from 1,1,1-fluoro-5,5-dimethyl-hexa-2,4-dione (fdh) and bipyridine (bpy) giving $[\text{Ce}(\text{fdh})_3(\text{bpy})]$ (**5**) (Fig. 5), where Ce(III) is in typical "paddle-wheel" shaped coordination environment resulting from six oxygen atoms from three fdh ligands and two nitrogen atoms from bpy. There is no out-of-phase signal in absence of any dc field. However, strong frequency-dependent and temperature-dependent out-of-phase peaks were observed ranging from 4 K to 6 K in the frequency range of 100–10000 Hz under an optimized dc field of 2000 Oe, clearly indicating slow relaxation of magnetization. The Arrhenius fitting to the plot of $\ln \tau$ vs $1/T$ at higher temperature region yields an energy barrier of 33.3 K and $\tau_0 = 1.8 \times 10^{-7}$ s. The overall relaxation is dominated not only by Orbach, but also by Raman process as well; the $\ln \tau$ vs $1/T$ plot can be best fitted with the mentioned U_{eff} and τ_0 and the Raman parameters, $C = 0.40 \text{ s}^{-1} \text{ K}^{-n}$ and $n = 6$.

The oxophilicity of Lanthanide (III) ions provides different approaches to modify the ligand field. It has been found that P = O donor ligands can coordinate to the lanthanides very strongly [93]. Recently, Gupta et al. have reported an air-stable nine coordinate Ce(III) complex, $[\text{Ce}(\text{NO}_3)_3\text{L}_3]$ (**6**), $\text{L} = {}^t\text{BuP}(\text{O})(\text{NHPr})_2$, where three P = O donor ligands and three nitrate anions coordinate to Ce(III) centre resulting in a muffin-like coordination environment around the metal ion [94]. Although **6** does not show any frequency dependent χ'' signals in absence of any external magnetic field, application of a very small dc field of ~ 20 Oe is sufficient to observe appearance of maxima in the frequency dependent χ'' signals. Under the presence of optimised dc field, i.e. 200 Oe, **6** shows frequency dependent χ'' signals up to 3.5 K, estimating an energy barrier of reversal of magnetisation, $U_{\text{eff}} = 21.5$ K and $\tau_0 = 2.7 \times 10^{-7}$ s. To reduce the intermolecular magnetic interaction, the sample of **6** is diluted to 29% with isomorphous La(III) matrix. However, no significant change has been observed in the relaxation dynamics as compared to the pure sample. This clearly

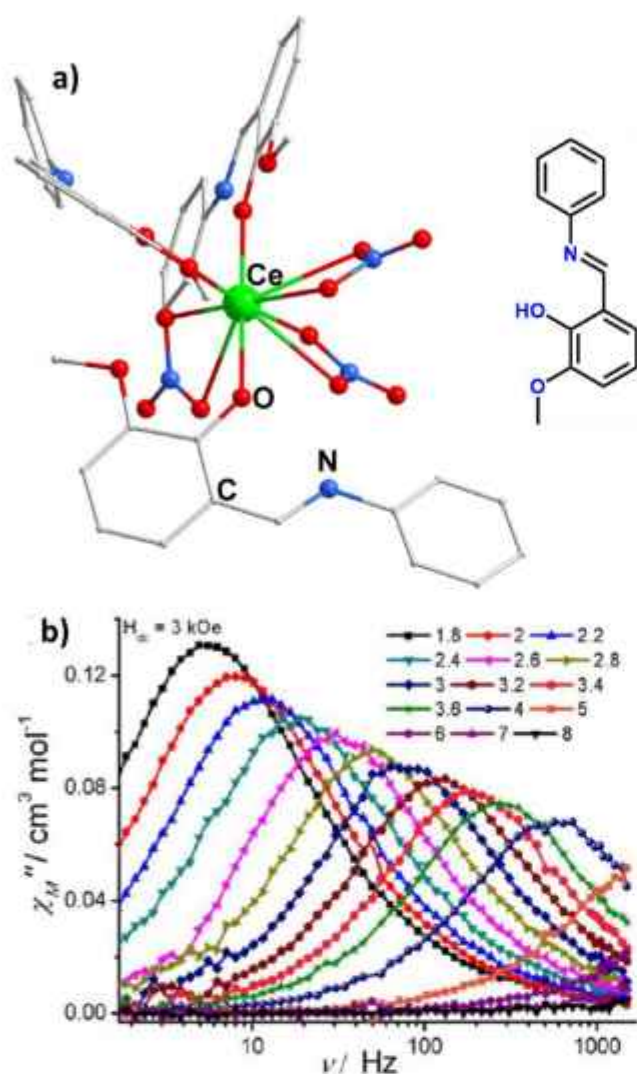


Fig. 4. (a) Crystal structure of $[\text{Ce}(\text{NO}_3)_2(\text{HL})_2]$ (**4**) (along with the Schiff base ligand used in complexation). (b) The frequency-dependent out-of-phase (χ'') ac susceptibility signals of **4** in the presence of 3000 Oe external magnetic field. Adopted from [91]. Copyright 2017 American chemical society.

indicates that the intermolecular interaction has negligible contribution in the slow relaxation of **6**. Ab initio calculations reveal that there exists large negative charge on the oxygen atoms of phosphonic diamide ligand in **6** as compared to the nitrate oxygens. Analysis of g -tensors of ground state Kramers doublet (KD) shows the existence of transverse anisotropy (g_{xx} and g_{yy} are greater than g_{zz}). The first excited state is found to lie at 317 K, which is far higher than the experimental results, suggesting that along with Orbach process, there exists other relaxation mechanisms such as direct, Raman process and/or non-negligible intermolecular magnetic interactions. A number of attempts have been carried out to fit the non-linear plot of $\ln\tau$ vs $1/T$ can be obtained by considering only direct and Raman process ($\tau^{-1} = AT + CT^n$) with parameters $A = 99.5 \text{ s}^{-1} \text{ K}^{-1}$, $C = 1.44 \text{ s}^{-1} \text{ K}^{-n}$ and $n = 6.8$. To achieve higher energy barrier with this phosphonic diamide ligand, two models have been proposed with three-coordinate ($[\text{L}_2\text{Ce}]^{3+}$ and two coordinate ($[\text{L}_2\text{Ce}]^{3+}$, estimating $U_{\text{eff,cal}} = 902 \text{ K}$ and 3450 K , respectively (Fig. 6c and 6d). The decrease in coordination number results in the quenching of quantum tunnelling and eventually the stabilization of higher m_l levels in the ground state. This results in the molecules relaxing via higher excited states.

It is interesting to note that there is no single example of zero field mononuclear Ce(III)-SIM reported in the literature till date. The only zero-field SMM based on Ce(III) ion is the linear trinuclear complex, $[\text{Ce}(\text{Zn}(\text{L}))_2(\text{MeOH})]\text{BPh}_4$ (where L is *o*-vanillin based Schiff-base ligand), reported by Kajiwara and co-workers [76]. The *o*-vanillin based Schiff base ligand coordinates to diamagnetic Zn(II) ions provide two different types of oxygen atoms for ligation to Ce(III) ion. The phenoxo oxygen atoms have larger negative Mulliken charge than the other oxygen atoms. Being placed in a highly anisotropic ligand field, Ce(III) ion shows slow relaxation of magnetisation even in absence of any bias dc magnetic field [95–97].

2.2. Neodymium(III) based mononuclear SIMs

Neodymium is the third most abundant lanthanide after cerium and lanthanum [98]. The use of Neodymium to synthesize the strongest magnet, $\text{Nd}_2\text{Fe}_{14}\text{B}$, which is widely employed in the industry, gives the confidence towards the application of Nd(III) based SMMs in designing magnetic materials for industrial use [99]. Nd(III) displays weaker spin-orbit coupling than the heavier Ln(III) ions, originating from electronic configuration f^3 with electronic ground state of $^4I_{3/2}$. Like Ce(III), Nd(III) is also an oblate ion, and hence a ligand field with stronger axial ligands and weaker

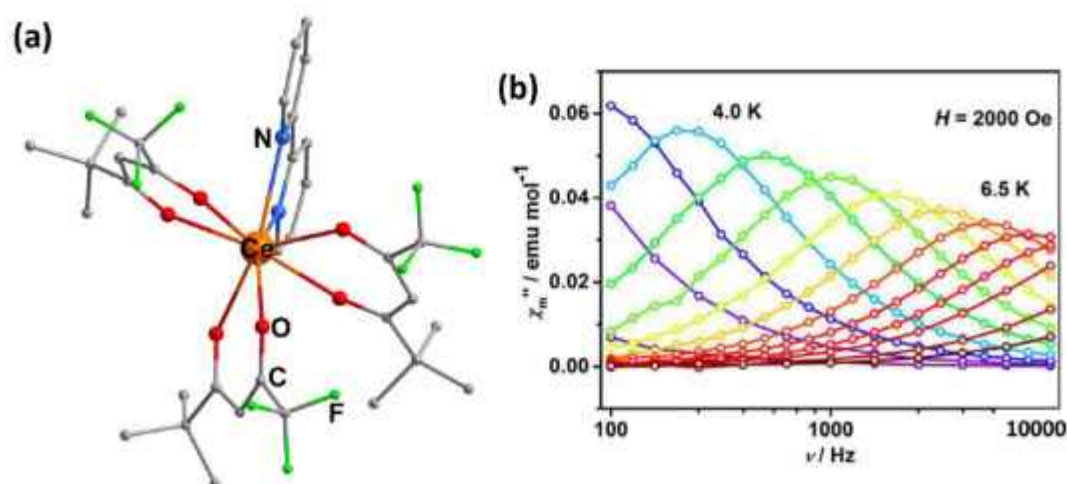


Fig. 5. (a) Crystal structure of $[\text{Ce}(\text{fdh})_1(\text{bpy})]$ (**5**). (b) Frequency dependence of out-of-phase (χ'') magnetic susceptibility signals in presence of 2000 Oe bias field. Adopted from [92]. Copyright 2018 Royal Society of Chemistry.

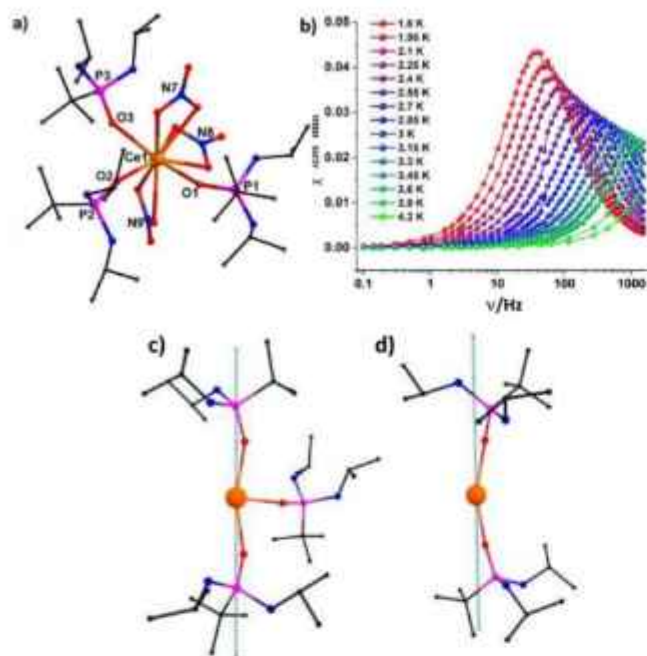


Fig. 6. (a) Molecular structure of $[\text{Ce}(\text{NO}_3)_3\text{L}_2]$ (**6**). (b) Frequency dependence of out-of-phase (χ'') ac susceptibility signals under the presence of 200 Oe dc field in the temperature range of 1.8–4.2 K. (c) Three coordinated and (d) two coordinated model compounds derived from **6** to achieve very high U_{eff} values. Dotted lines represent their CASSCF computed g_{eff} orientation of the ground state KD. Reprinted from [94]. Copyright 2019 Royal Society of Chemistry.

or no equatorial ligands is expected to be effective towards designing Nd(III) based SIMs with larger U_{eff} values.

Long and co-workers have reported the first mononuclear SIM based on Nd(III) ion, $[\text{NdTp}_3]$ (**7**) (Fig. 7) where Tp = trispyrazolylborate. Complex **7** displays a crystallographic three-fold symmetry with a tri-capped trigonal prismatic first coordination sphere to the Nd(III) [100]. Low temperature absorption spectroscopic studies suggest that the first-excited m_j level is higher in energy by 165 K as compared to the ground state m_j level. Though complex **7** displays slow relaxation of magnetisation under 100 Oe applied dc field, the anisotropy barrier is very small as compared to the barrier obtained from spectroscopic analysis ($U_{\text{eff}} = 4$ K, comparable to that observed for Uranium(III) analogue with $U_{\text{eff}} = 5.5$ K). This mismatch between the low-lying electronic structure and the observed relaxation behaviour originates from factors such as existence of dipolar interactions among the molecules, nuclear coupling as well as possibility of mixing of low-lying excited states. The interelectronic interactions are reduced by increasing the average distance between nearest Nd(III) centres through dilution of $[\text{NdTp}_3]$ in a $[\text{LaTp}_3]$ matrix to different extents, viz. 59, 15 and 3.8 mol% $[\text{NdTp}_3]$. Each successive dilution results in an increase of U_{eff} by ~ 1.3 K, affording 5.3 K for 3.8 mol% of $[\text{NdTp}_3]$.

The Nd(III) analogue of **1**, i.e. $[\text{Li}(\text{DME})_3][\text{Nd}^{\text{III}}(\text{COT}^{\text{tr}})_2]$ (**8**) was reported by Murugesu and co-workers in 2015 [101]. The (COT^{tr}centroid)–Nd^{III}–(COT^{tr}centroid) angle deviates from linearity by 3.8°, which is almost by same extent as in **1**. The ac susceptibility measurements revealed that in the absence of an external dc field, **8** does not show any AC signal. On application of an optimised 1000 Oe dc field, **8** exhibits a strong frequency-dependent in-phase (χ') and out-of-phase magnetic susceptibility (χ'') in a temperature range of 1.8–8 K. Arrhenius fit in the higher temperature range yields U_{eff} for **8** is 21 K, which is close to Ce(III) ($U_{\text{eff}} = 30$ K), [81] U(III) ($U_{\text{eff}} = 27$ K), [101] and Dy(III) ($U_{\text{eff}} = 25$ K at 0 Oe; 28 K at 100 Oe) analogues [83]. Remarkably, prolate shaped Er(III) analogue shows opening up of hysteresis loop up to 8 K with an energy

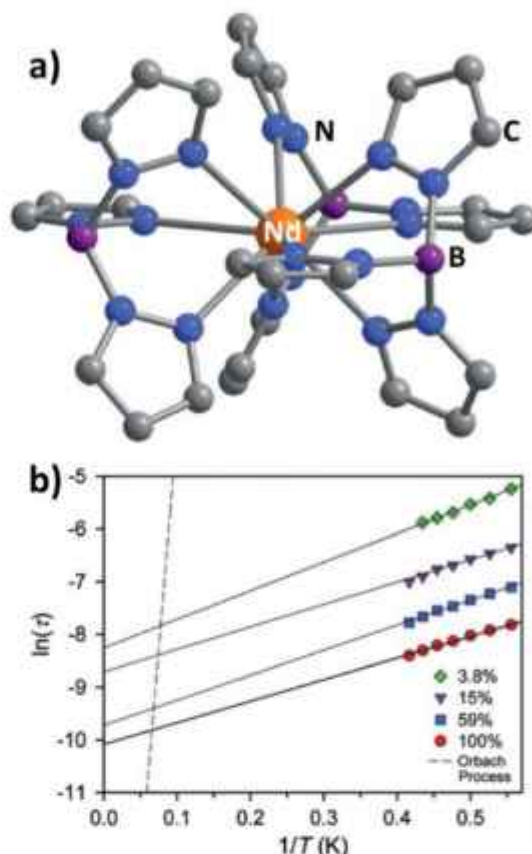


Fig. 7. (a) Molecular structure of $[\text{NdTp}_3]$ (**7**). (b) Plot of $\ln(\tau)$ vs. $1/T$ at various molar percentages of **7** in a $[\text{LaTp}_3]$ matrix. Reprinted from [100]. Copyright 2012 Royal Society of Chemistry.

barrier of 187 K, which is by far higher than that observed for all the known oblate shaped Ln(III) analogues [102]. This observation contradicts the assumption that a sandwich-type ligand field is favourable in oblate Ln(III) ions to afford improved SIM behaviour. The small value of U_{eff} in oblate shaped ions can be attributed to misalignment of the magnetic anisotropy axis. Ab-initio calculations suggest that the presence of trimethylsilyl (TMS) groups on the COT ring has large effect on the direction of the main magnetic anisotropy axis. The calculation also suggests that on removal of TMS groups from COT rings can result in enhancement of SIM behavior [83].

Crown ether based Nd(III) SMMs $[\text{Nd}(\text{NO}_3)_3(18\text{-crown-6})]$ (**9**) and $[\text{Nd}(\text{NO}_3)_3(1,10\text{-diaz-18-crown-6})]$ (**10**), structural analogues to **2** and **3**, behave as field induced single-molecule magnets [84]. In the presence of 1000 Oe field, they exhibit out-of-phase ac signals up to 3.8 K (for **9**) and 6 K (for **10**), respectively. The estimated U_{eff} values, from the fitting of the $\ln\tau$ vs T^{-1} are 29.9 K and 69 K for **9** and **10**, along with $\tau_0 = 2.9 \times 10^{-9}$ s and 2.1×10^{-10} s, respectively. The plot of $\ln\tau$ vs T^{-1} is non-linear due to the presence of relaxation processes other than Orbach process. The plot can be best fitted by considering Raman and TA-QTM with the parameters: $U_{\text{eff}} = 30.9$ K, $\tau_0 = 2.2 \times 10^{-9}$ s, $C = 4.1 \text{ s}^{-1}\text{K}^{-5}$, and $n = 5$ for **9**; $U_{\text{eff}} = 73$ K, $\tau_0 = 1.4 \times 10^{-10}$ s, $C = 0.00107 \text{ s}^{-1}\text{K}^{-9}$, and $n = 9$ for **10**. The higher U_{eff} value for **10**, as compared to **9**, has been explained using similar arguments put forth for the Ce(III) complexes **2** and **3**.

The magnetisation relaxation of Schiff-base based mononuclear Nd(III) SMM, $[\text{Nd}(\text{NO}_3)_2\text{L}]\text{PF}_6 \cdot \text{MeCN}$ (**11**) (where L is a single helical hexadentate Schiff base ligand, see Fig. 8 inset) has been

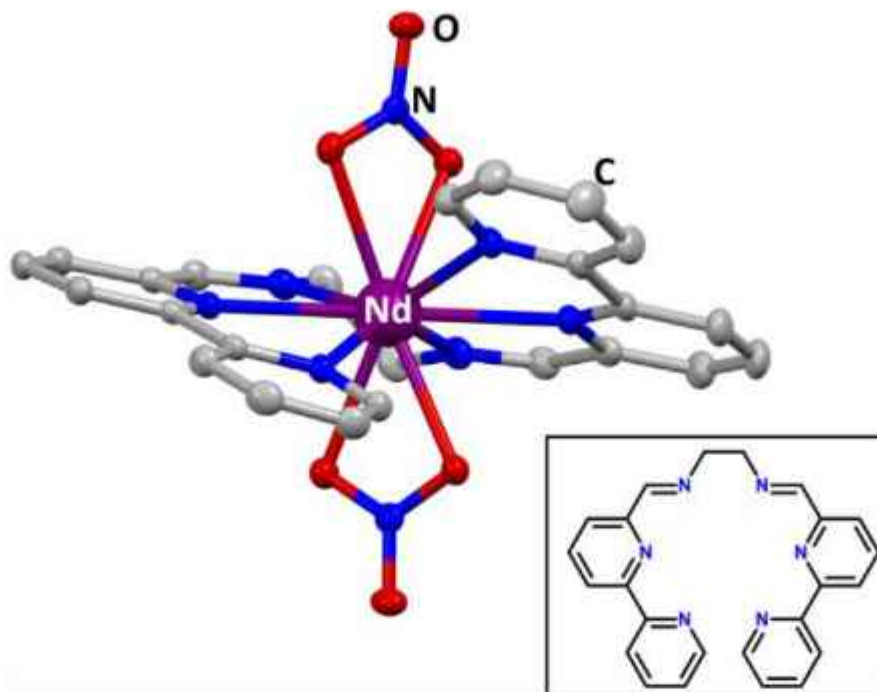


Fig. 8. Molecular structure of the cationic part of $[(\text{Nd}(\text{NO}_3)_2\text{L})\text{PF}_6\cdot\text{MeCN}]$ (**11**). Inset: The helical hexadentate Schiff base ligand present in **11**.

investigated by Kajiwara and co-workers. In this complex, the metal ion is coordinated to the hexadentate ligand through its six N-donor sites which occupy the equatorial sites and two nitrate ions in the axial positions [103,104]. The PF_6^- counter anion and solvent acetonitrile molecule are also present in the lattice. In absence of any dc magnetic field, there is no frequency dependent χ' and χ'' signals for **11**. However, in the presence of an optimized DC field of 1000 Oe, **11** exhibits frequency dependent χ' and χ'' signals up to 5.0 K in the AC frequency range 10–10,000 Hz. The non-linearity of the plot of $\ln\tau$ vs $1/T$ indicates that more than one relaxation process exists in the magnetisation relaxation dynamics. The linear fit of $\ln\tau$ vs $1/T$ plot at higher temperature using Arrhenius law affords $U_{\text{eff}} = 36$ K and $\tau_0^{-1} = 4.3(9) \times 10^{-9}$ s. The full plot can be fitted by considering both Orbach and Raman process with the parameters: $U_{\text{eff}} = 34$ K, $\tau_0^{-1} = 1.1(4) \times 10^{-8}$ s, $C = 2.8(2) \text{ s}^{-1} \text{ K}^{-5}$ for $n = 5$. The Tb(III) analogue of **11** does not possess significant SIM behaviour, while the Dy(III) analogue does with barrier height of 81(5) K.

Due to the presence of strong QTM in the ground state, almost all the Nd(III) based SMMs reported until 2016 were field induced [100,101,104–107]. Thus, designing of a suitable ligand field which would slow down QTM in the ground state is a crucial step towards realizing zero field Nd(III) SMMs. Towards this objective, an air stable mononuclear Nd(III) complex, $[(\text{L}_2\text{Nd}(\text{H}_2\text{O})_5)\text{I}_3 \cdot 2\text{L} \cdot (\text{H}_2\text{O})]$ (**12**), $\text{L} = {}^i\text{BuP}(\text{O})(\text{NH}^i\text{Pr})_2$, was reported by Gupta *et al.* This complex behaves as a SMM in absence of external magnetic field, the first example of a Nd(III)-based zero field SMM [55]. The seven coordinate Nd(III) ion is in a pseudo- D_{3h} symmetry; the five equatorial coordination sites are occupied by water molecules while the axial positions are occupied by phosphonic diamide ligands which coordinate to metal through the phosphoryl oxygen ($\text{P} = \text{O}$). The axial Nd–O(P) bonds are significantly shorter than the equatorial Nd–O (aqua) distances indicating tighter binding of phosphonamide ligands compared to water molecules. AC susceptibility measurements at zero field clearly show two maxima for the out-of-phase susceptibility component χ'' , one at the higher and other at lower frequency range. Fitting the relaxation time to the Arrhenius equation results in an anisotropic energy barrier U_{eff} of

16.08 K and 24.69 K for the fast and slow relaxation processes, respectively. The temperature-independent nature of the slow relaxation process below 4 K confirms the dominance of QTM at low temperature in the ground state Kramers doublet. The SMM behaviour of **12** is improved by quenching the QTM by applying a dc field of 2000 Oe. This elevates U_{eff} to 39.21 K. The relaxation takes place through a single relaxation process with Orbach and Raman as the dominant pathways. The non-linear fitting of $\ln\tau$ vs $1/T$ plot indicates that the relaxation dynamics of **12** is dominated by Orbach process and QTM with negligibly small Raman process in absence of any external magnetic field. On application of an external magnetic field, the dynamics is dominated strongly by Orbach and Raman process, as QTM is almost quenched. *Ab initio* calculations on **12** reveal that the g tensors of ground state KDs are strongly axial ($g_{xx} = 0.02$, $g_{yy} = 0.02$ and $g_{zz} = 6.30$) with very small transverse components. The g_{zz} axis of the ground state is found to lie close to the oxygen atom of the phosphonic amide. The g -tensors of the first excited state KDs possess large transverse terms ($g_{xx} = 0.10$, $g_{yy} = 0.42$ and $g_{zz} = 5.10$), revealing the possibility of relaxation via the first excited state which is estimated as an admixture of $m_j = |\pm 5/2\rangle$ and $m_j = |\pm 1/2\rangle$ states. The analysis of CASSCF charges on the oxygen atoms coordinated to the Nd(III) reveals that axial oxygens possess pronounced negative charge compared to the non-axial oxygen atoms leading to the stabilization of the $m_j = |\pm 9/2\rangle$ state as ground state, yielding the first instance of stabilization of the maximum m_j as ground state (Fig. 9). The calculated barrier $U_{\text{eff,cal}}$ of 302 K is far higher than the $U_{\text{eff,exp}}$ due to the presence of factors such as negligible ground state QTM, intermolecular interactions and possibility of non-Orbach relaxation pathways in the relaxation mechanism.

A similar pseudo- D_{3h} symmetric Nd(III) based SMM $[(\text{Nd}(\text{CyPh}_2\text{PO})_2(\text{H}_2\text{O})_5)\text{I}_3 \cdot 2(\text{CyPh}_2\text{PO})_3\text{EtOH}]$ (**13**) was reported by Tong and co-workers [58]. This complex also shows zero field SMM behaviour, and exhibits frequency dependent χ' and χ'' signals up to 11 K under zero field as well as 2000 Oe applied dc field. Unlike **12**, complex **13** shows single relaxation process at zero field with the Cole–Cole parameter, $\alpha = 0.13$ –0.29. However, in presence of 2000 Oe, the magnetic dynamic behaviour of **13** is remarkably

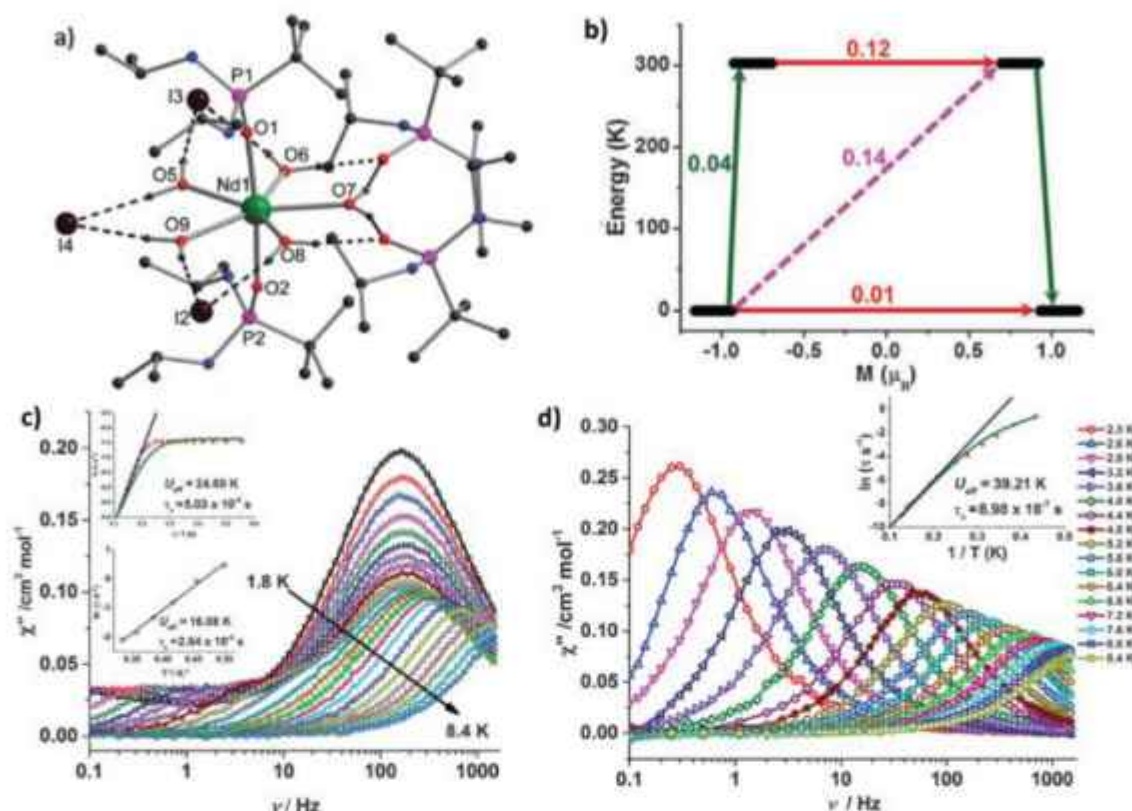


Fig. 9. (a) Molecular structure of $[(LnNd(H_2O)_9)_2] \cdot 2L \cdot (H_2O)$ (**12**) and (b) its CASSCF computed possible relaxation pathways. The frequency dependent χ'' component (c) in absence of a dc field and (d) in presence of 2000 Oe dc field. Inset of (c) and (d): corresponding plot of the relaxation time, τ in logarithmic scale versus T^{-1} . Reprinted from [55]. Copyright 2016 Royal Society of Chemistry.

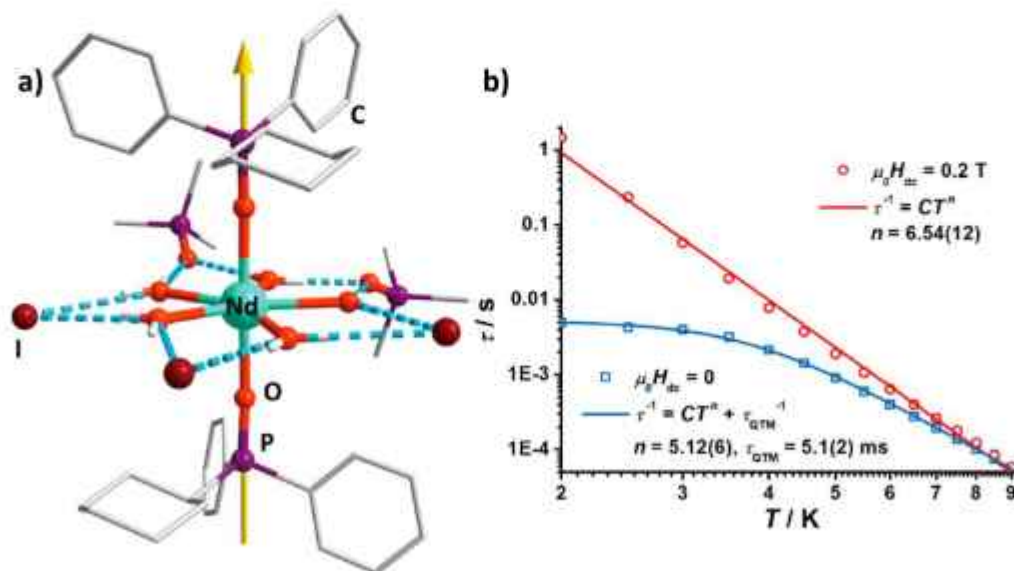


Fig. 10. (a) Molecular structure of $[(Nd(CyPh_2PO)_2(H_2O)_9)]_2 \cdot 2(CyPh_2PO) \cdot 3EtOH$ (**13**). The arrow represents the CASSCF computed g_{xx} orientation of the ground state KD. (b) Temperature dependence of the relaxation time τ in a zero dc field (blue) and 2000 Oe dc field (red) for **13**. Reprinted from [58]. Copyright 2018 American chemical society. (For interpretation of the references to colour in this figure legend, the reader is referred to the web version of this article.)

close that of **12**, which is expected as both complexes have quite similar core structure. The plot of τ vs T shows that at zero dc field, τ rises slowly with the decrease of T , and tends to become temperature-independent below ~ 3 K due to QTM and finally reaches 5.0 ms at 2 K. However, in the applied field of 2000 Oe,

the rise of τ with lowering T is linear to reach 1.46 s at 2 K. The data do not fit well with common Arrhenius law, but shows an improved fit by using the combination of a Raman and a QTM term, i.e., $\tau^{-1} = CT^n + \tau_{QTM}^{-1}$, with $n = 5.12$ and $\tau_{QTM} = 5.1$ ms in zero dc field (Fig. 10). The data for magnetic dynamics in a 2000 Oe dc field

shows almost perfect linear dependency in a log–log scale, which can be fitted solely by one Raman term with $n = 6.54$. The opening up of hysteresis loop near zero field is consistent with the long relaxation time at low T . Ab initio calculations shows that the calculated g -tensors are strongly axial, comparable to **12**, as expected from a strong axial ligand field. Reinvestigation of the magnetic dynamics of **12** in the presence 2000 Oe dc field reveals linear rising of τ with lowering T , as in case of **13**; the τ vs T plot can be fitted by considering solely Raman term with $n = 6.29$. It has also been suggested that if a system can relax through several relaxation pathways whose relaxation rates differ by several orders of magnitude, the fastest process dominates the whole relaxation dynamics resulting in the observation of that process only.

Organometallic Ln(III) SIMs based on cyclopentadienyl (Cp) derivatives, mainly those of Dy(III) SIMs, have gained large interest due to high U_{eff} and T_B values exhibited by such low-coordinate Ln SIMs. In 1998, Ziller and co-workers have synthesized a series of trivalent organo-lanthanide complexes with pentamethylcyclopentadienyl (C_5Me_5) ligand [108]. The Ln(III) centre is sandwiched between two Cp^* rings ($Cp^* = \text{pentamethylcyclopentadienyl anion}$) in a bent fashion and the tetraphenylborate anion interacts weakly with Nd(III) via two of its phenyl rings forming $Cp^*_2Ln(BPh_4)$ complex. Long and co-workers have investigated the slow relaxation behaviour in Nd(III) analogue, i.e. $Cp^*_2Nd(BPh_4)$ (**14**), and found that the complex shows slow relaxation of magnetisation in presence of an external magnetic field (Fig. 11) [109]. On application of a dc field of 1000 Oe, obvious peaks for frequency dependent χ' and χ'' were observed in the temperature range of 2–9 K. The linear nature of the plot of the $\ln\tau$ versus $1/T$ at high T estimates the $U_{\text{eff}} = 41.7$ K and $\tau_0 = 1.4 \times 10^{-6}$ s. The non-linearity behaviour of the plot confirms the presence of multiple relaxation processes. The plot is fully well fitted by considering a combination of relaxation processes, viz., Orbach, direct and Raman relaxation processes with the parameters of $AH = 1.1 \text{ s}^{-1}\text{K}^{-1}$, $C = 0.0286 \text{ s}^{-1}\text{K}^{-n}$ and $n = 5.2$. The Dy(III), Tb(III) and Er(III) analogues of **14** also possess slow relaxation of magnetisation behaviour, but the Ho(III) analogue does not. The U_{eff} value of **14** is comparable with the prolate shaped Er(III) analogue ($U_{\text{eff}} = 22.6$ K) but far more lower than oblate shaped Tb(III) ($U_{\text{eff}} = 318$ K) and Dy(III) ($U_{\text{eff}} = 452$ K) analogues [110].

Ohkoshi and co-workers have reported neodymium β -diketonate mononuclear complex, $[Nd^{III}(\text{TTA})_3(\text{MeOH})_2] \cdot 0.5$ (Azo-py) (**15**) where TTA = thenoyl(trifluoro)acetate and Azo-py = 4,4'-azopyridine. In the complex **15**, three TTA ligands and two methanol molecules coordinate to Nd(III) centre to result in a distorted square antiprism geometry around the metal ion

(Fig. 12a) [111]. Each monomer is supported by hydrogen bonding between lattice Azo-py moiety and coordinated methanol. This complex is not only emissive in the NIR region, but also behaves as a field induced SMM. Under an optimised 1000 Oe dc field, **15** shows out-of-phase (χ'') components of the ac magnetic susceptibility up to 7 K with $U_{\text{eff}} = 19.7(7)$ K and $\tau_0 = 3.7(8) \times 10^{-7}$ s. The non-linear Arrhenius plot can be fitted by considering QTM along with the Orbach processes. The two co-ordinating methanol molecules can be removed by heating **15** at 370 K. This enhances the U_{eff} value to 27.3 K with $\tau_0 = 8.5 \times 10^{-8}$ s and $\tau_{\text{QTM}} = 0.0008$ s. The enrichment in barrier height is due to the improvement of the magnetic anisotropy of the Nd^{3+} ion on the removal of two MeOH molecules. This also increases the luminescence intensity almost by fivefold, assigned to the thermally stimulated emission, due to the suppression of all non-radiative relaxation pathways.

Recently Wang and co-workers have reported two nine-coordinated capped square antiprism neodymium moieties $[C(\text{NH}_2)_3]_3[Nd(\text{CO}_3)_4(\text{H}_2\text{O})] \cdot 2\text{H}_2\text{O}$ (**16**) and $[C(\text{NH}_2)_3]_4[\text{H}_3\text{O}][Nd(\text{CO}_3)_4(\text{H}_2\text{O})] \cdot 9.5\text{H}_2\text{O}$ (**17**). Both the complexes are with slightly different local symmetries, viz. C_1 for **16** and C_4 for **17** (Fig. 13a and b) [112]. Both the complexes do not show any out-of-phase ac susceptibility (χ'') signal in absence of an external dc field. However, frequency dependence of χ'' signals were clearly observed under small external dc field, due to the magnetic field-suppressed QTM or the strong phonon bottleneck effect [113]. However, on application of 1500 Oe, both complexes slow magnetic relaxation up to 4.4 K for **16** and 3.0 K for **17**, respectively. The non-linear nature of $\ln\tau$ vs T^{-1} demonstrates the presence of multiple relaxation mechanisms. By fitting the linear part in high temperature range, the U_{eff} was estimated to be 30.7 K with $\tau_0 = 1.053 \times 10^{-7}$ s for **16** and 9.25 K with $\tau_0 = 2.093 \times 10^{-6}$ s for **17**, respectively. These energy barriers are far smaller than the calculated energy gap between ground and first excited state. This again suggests the possibility of dominance of Raman process over other processes in the overall relaxation dynamics. The plot $\ln\tau$ vs T^{-1} over the whole temperature range can be fitted by considering Raman and direct process with the parameters, $A = 125.89 \text{ K}^{-1} \text{ s}^{-1}$, $C = 0.89 \text{ s}^{-1} \text{ K}^{-n}$ and $n = 6.08$ for **16** and $A = 0$, $C = 413.85 \text{ s}^{-1} \text{ K}^{-n}$ and $n = 3.63$ for **17**. The value of exponent n is 6.08 (close to 9) for **16** indicates that the acoustic vibration is dominated in the relaxation process. On the other hand, for **17**, $n = 3.63$ (close to 3) predicts that both acoustic and optical vibrations are dominant in the relaxation dynamics. In order to confirm the “easy-plane” anisotropy, HF-EPR measurements were carried out at 4.2 K (Fig. 13e and f). HF-EPR spectra reveals that the relevant g -factors are $g_x = 3.00(2)$ and $g_y = 2.56(2)$ for **16** and $g_x = g_y = 2.79(2)$ for **17**, respectively, signifying the existence of “easy-plane” magnetic anisotropy.

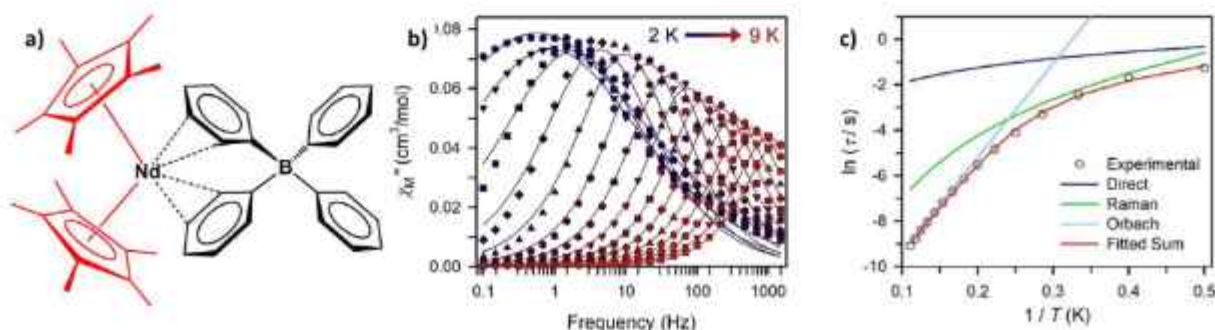


Fig. 11. (a) Structure of $[Cp^*_2Nd(BPh_4)]$ (**14**). (b) out-of-phase (χ'') components of the ac magnetic susceptibility of **14** under 1000 dc field from 2 K (blue circles) to 9 K (red circles). (c) The plot of $\ln\tau$ vs $1/T$ and fitting of the plot (red line) over the whole temperature range, obtained by considering direct, Raman and Orbach processes. The individual contributions of the multiple magnetic relaxation pathways are also indicated in the figure. Reprinted from [109]. Copyright 2018 Elsevier. (For interpretation of the references to colour in this figure legend, the reader is referred to the web version of this article.)

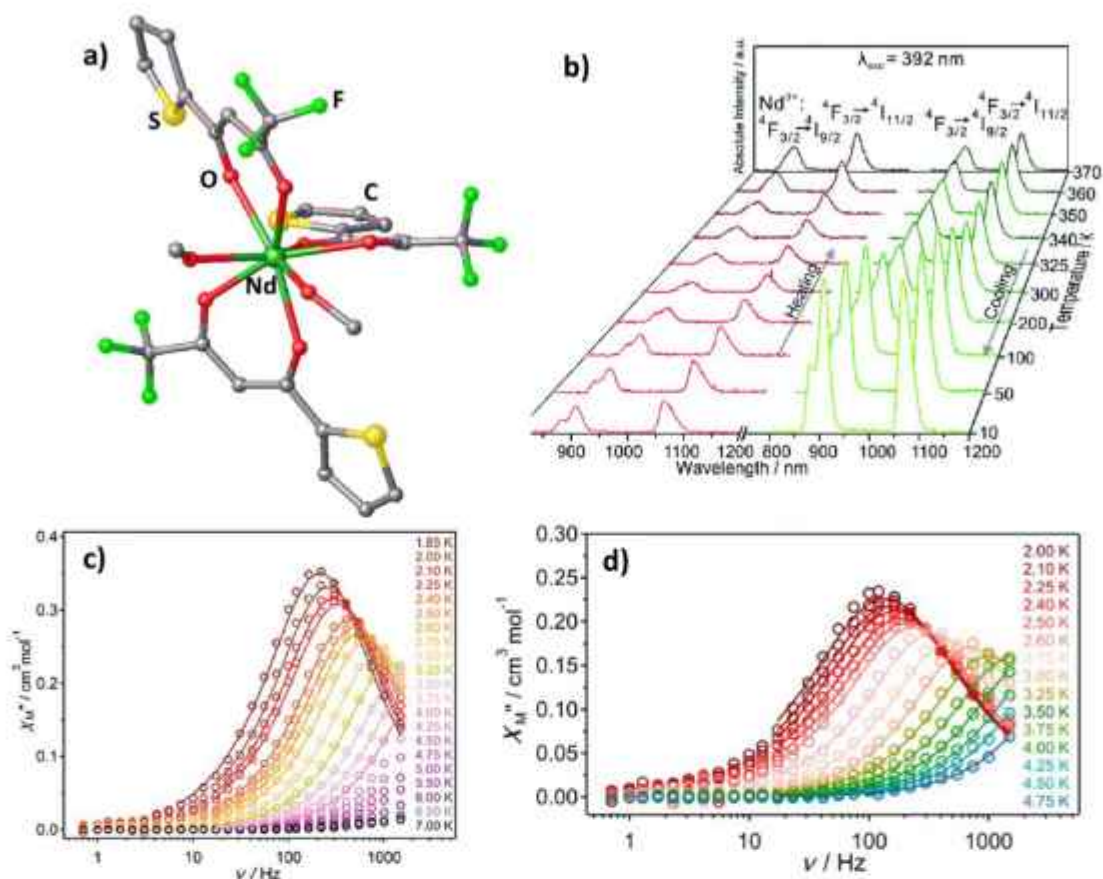


Fig. 12. (a) Molecular structure of $[\text{Nd}^{\text{III}}(\text{TTA})_2(\text{MeOH})_2]$ (**15**). (b) Solid-state temperature dependent (10 \rightarrow 370 \rightarrow 10 K) NIR emission spectra of **15** under excitation wavelength, λ_{exc} , of 392 nm. Frequency dependence χ_M'' components of magnetic susceptibility for **15** (c) and heated **15** (d) under optimised dc field at indicated temperatures. Reprinted from [111]. Copyright 2019 Royal Society of Chemistry.

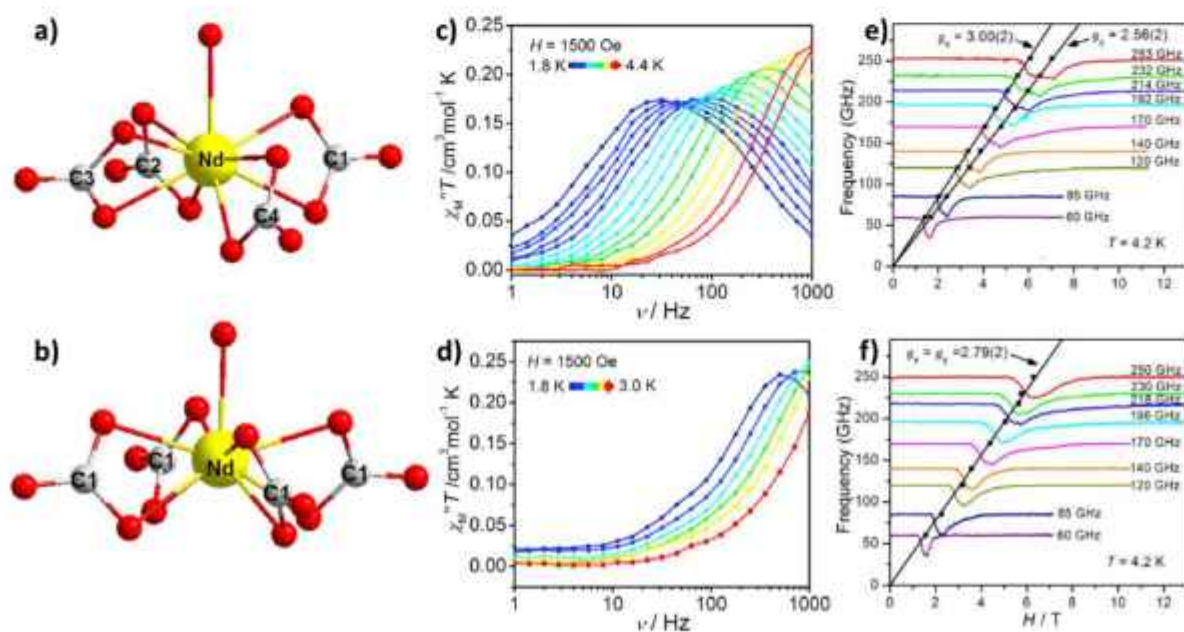


Fig. 13. Molecular structure of the anionic parts ($[\text{Nd}(\text{CO}_3)_3(\text{H}_2\text{O})]^{3-}$) of **16** (a) and **17** (b). Frequency dependent ac magnetic susceptibilities of **16** (c) and **17** (d) in presence of 1500 Oe external magnetic field. Variable-frequency HF-EPR spectra of **16** (e) and **17** (f) at 4.2 K. Reprinted from [112]. Copyright 2020 Elsevier.

2.3. Gadolinium(III) based mononuclear SMMs

Gadolinium is widely popular for its applications in fields such as neutron capture cancer therapy [114,115], radiography [116], solid oxide fuel cells [117], phosphors [118] etc. With half-filled f-orbital electronic configuration, $4f^7$, Gd(III) ions are commonly used in MRI contrast agents [119–121]. As Gd(III) is magnetically isotopic, due to the lack of spin–orbit coupling ($S = 7/2$, $L = 0$), the energy levels are almost degenerate. Due to the presence of strong quantum tunnelling, the magnetic relaxation rates in Gd(III) complexes are usually very fast. A number of Gd(III) based complexes reported can act as magnetic refrigerators due to their high Curie Temperature and significant magnetocaloric effect (MCE) [122–136]. However, very few complexes based on Gd(III) pursuing slow magnetic relaxation has been reported and all of them are either polymers or multinuclear clusters [105,137–144]. The non-negligible magnetic interactions between the Gd(III) ions in such polymers and multinuclear complexes result in mixed mechanisms of spin–lattice, spin–phonon and spin–spin relaxations.

Till date, there are only two reports in the literature on mononuclear Gd(III) based field induced magnets. In 2013, Gao and co-workers have reported two THD (THD = 2,2,6,6-tetramethyl heptane-3,5-dione) based Gd(III) complexes, $\text{Gd}(\text{THD})_2\text{L}$ (where L = phenanthroline (phen) (**18**) and bipyridine (bpy) (**19**)) [145]. Gd(III) ion in both these complexes is eight-coordinated with D_{4d} local symmetry. These complexes exhibit field induced magnetic relaxation and magnetocaloric effect. The mode of dependency of relaxation time (τ) on temperature and applied magnetic field suggests that there is a competition between the direct process and the phonon bottleneck effect. The later mechanism is predominant when the applied field is lower than 1 T and the former one plays a significant role when the field is larger than 2 T.

Recently, Tong and co-workers have reported another mononuclear Gd(III) complex, $[\text{Gd}(\text{bbpen})\text{Cl}]$ (**20**), (H_2bbpen = N,N' bis (2 hydroxybenzyl) N,N' bis(2 picolyl)ethylenediamine), where the ion is in pentagonal-bipyramidal local symmetry (Fig. 14) [146]. Both **20** and 5% diluted **20@Y** do not show any slow relaxation of magnetisation in the absence of external dc field due to the presence of fast relaxation processes and/or strong QTM, which can be suppressed by the application of external magnetic field. Under the application of an appropriate field (4000 Oe for **20** and 3000 Oe for **20@Y**), both exhibit typical patterns for SMMs. At a given temperature, the relaxation time for **20@Y** is always longer than **20**, due to the weakening of intermolecular magnetic interactions in the former. The magnetic relaxation dynamics associated with **20** and **20@Y** do not obey the Arrhenius law, but fit well with power law. But the n values (1.27 for **20** and 1.89 for **20@Y**) are close to direct process ($n = 1$) along with non-negligible contribution from phonon bottleneck effect ($n = 2$) instead of Raman process ($n = 7$ or 9). This observation provides an indication for dominance of direct

process resulting from stronger dipole–dipole interactions in **20** as compared to the diluted sample.

2.4. Holmium(III) based mononuclear SMMs

As stated earlier, SMMs made of heavier lanthanides, mainly Dy(III) and Er(III), have been in the limelight for a while and hence have been experiencing profound development. Unfortunately, their neighbour in the periodic table, the non-Kramers Ho(III) ion, has been rarely explored. Though Ho(III) is oblate shaped like Dy(III), the reason why Ho(III) is off the main track of SIMs resides mainly in the fact that non-Kramers ions cannot guarantee doubly degenerate ground states. A strong QTM probably occurs between the lowest two m_j states. It is possible for the ground states to have double degeneracy when the ligand fields around the Ho(III) centre have strict symmetry [68]. Ho(III), with ground term symbol 3I_6 , has not even gathered comparable explorations in SMMs to another non-Kramers ion Tb(III). Thus choosing a suitable ligand field is the key task to perceive relaxation behaviour in oblate shaped Ho(III) complexes. Nevertheless, recent developments on Ho based systems are promising towards storage of data in atomic level [2]. Brune and co-workers have reported the existence of magnetic remanence originating from individual Ho atoms when deposited on MgO (100) layer grown over a Ag(100) layer, showing opening up of hysteresis loop up to 30 K [147]. This indicates the potential of Ho(III) ion towards the storage of data even in atomic level. Thus, development of SIMs based on this ion warrant detailed investigations.

In 2003, Ishikawa and co-workers reported first ever mononuclear Ho(III) based SIM, $[(\text{Pc})_2\text{Ho}]$ (**21**) (Pc = phthalocyaninato), which is analogue of the first Ln(III) based SMM, $[(\text{Pc})_2\text{Tb}]^-$ [33,148–150]. The energy difference between the ground state ($m_j = 1 \pm 5 >$) and first excited state ($m_j = 1 \pm 4 >$) for **21** is predicted theoretically to be 21.6 K with the help of parameters extracted from NMR and the magnetic susceptibility data. Two years later, they reported that when **21** is placed in a diamagnetic matrix formed from its Y(III) analogue, it shows opening of hysteresis loop below 0.5 K. The clear staircase-like structure of hysteresis loops at 0.04 K, which are located equidistantly along the magnetic field axis at $\mu_0 H_n = n \times 23.5$ mT ($n = 0, 1, 2, 3, \dots$) (Fig. 15b and c), indicates the existence of QTM.

In 2012, a series of Ln(III) organometallic mixed sandwich mononuclear complexes, $(\text{Cp}^*)\text{Ln}(\text{COT})$, (Ln = Tb, Dy, Ho, Er and Tm) were reported by Gao and co-workers, where the Ln(III) ion is sandwiched between Cp^* and COT rings (Fig. 16a) [151]. The molecular structure reveals that the COT rings in the complexes are having disorder arising from the fact that they crystallize in two static conformations: staggered and eclipse with a ratio 40:60. The asymmetric interactions between adjacent molecules result in tilting of the rings (from linearity), which destroys high uniaxial local symmetry around Ln(III), resulting in point group

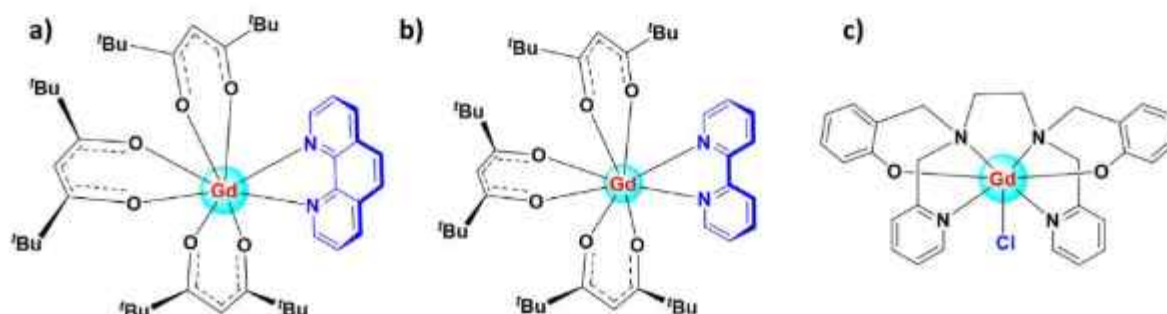


Fig. 14. Structure of (a) $[\text{Gd}(\text{THD})_2(\text{phen})]$ (**18**), (b) $[\text{Gd}(\text{THD})_2(\text{bpy})]$ (**19**) and (c) $[\text{Gd}(\text{bbpen})\text{Cl}]$ (**20**).

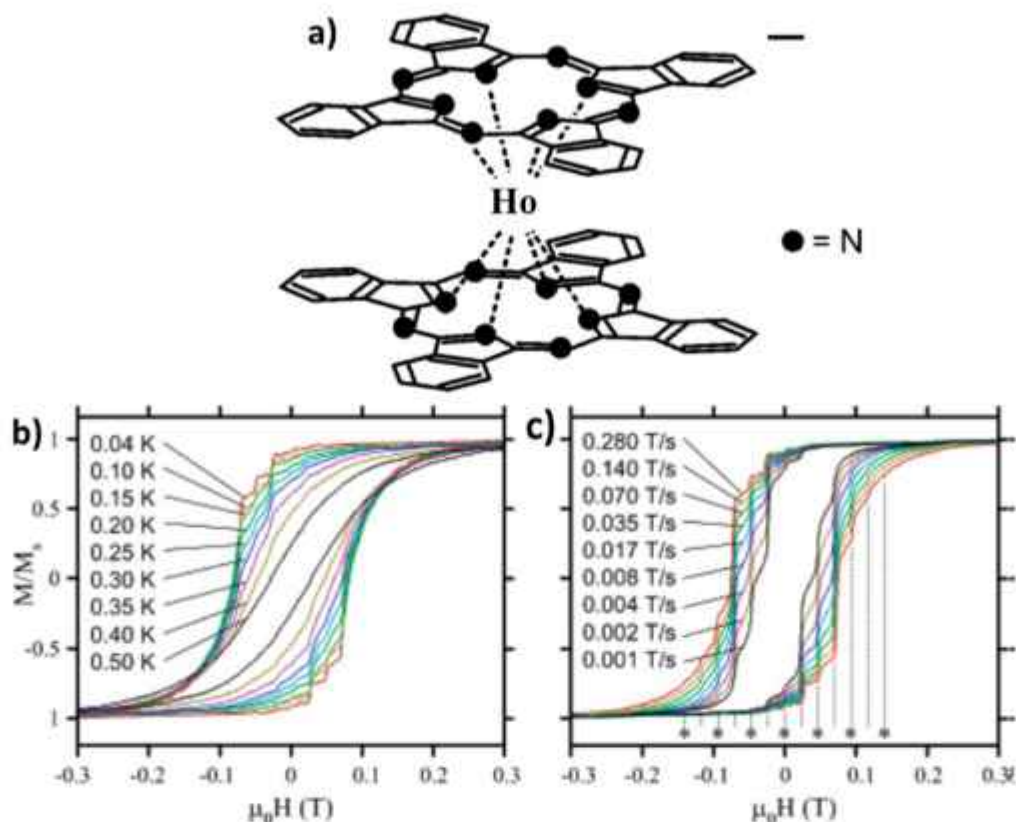


Fig. 15. (a) Molecular structure of $[(PCp)_2Ho]^-$ anion (**21**). (b) Hysteresis loops of a single crystal of $2x$ **21@Y**, measured with field scan rate of 0.28 T/s at indicated temperatures. (c) Hysteresis loops at 0.04 K measured at mentioned field scan rates. Reprinted from [150]. Copyright 2005 American chemical society.

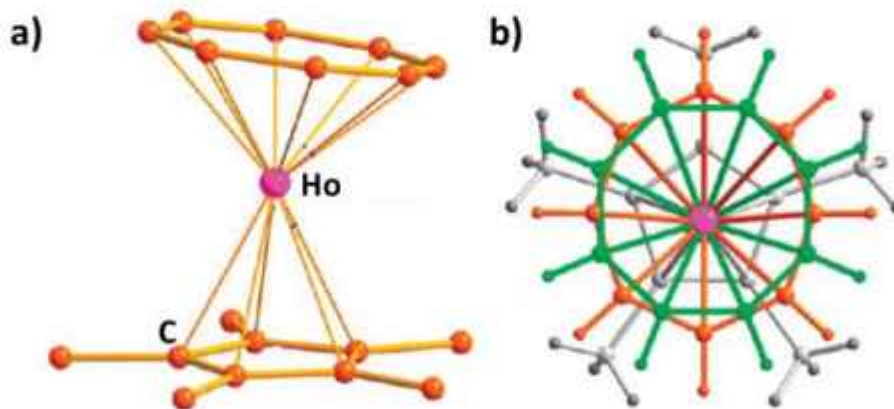


Fig. 16. (a) Molecular structure of $[(Cp^*)Ho(COT)]$ (**22**). (b) Representation of the COT ring disorder with staggered form shown in green and eclipsed form in golden yellow in the ratio 40:60. Reprinted from [151] copyright 2012 American chemical society.

C_5 (Fig. 16b). The Ho(III) analogue, $(Cp^*)Ho(COT)$ (**22**) shows slow relaxation of magnetization in the absence of magnetic field; frequency dependence of χ'' signals can be observed below 20 K. There are two distinct relaxation processes present for **22** with $U_{eff} = 3.6$ K and 7.4 K, respectively. The small U_{eff} value suggests the existence of strong QTM. QTM is partially suppressed by the application of an external field of 6000 Oe as well as by 5% dilution of **22** in a diamagnetic matrix, resulting in improvement of U_{eff} to 24.4 K and 33.8 K. An important result obtained from the fitting of Cole-Cole plot, by considering two relaxation processes, is that the ratio of weights of the relaxation processes is consistent with the ratio of the two conformers. Thus, the two relaxation processes

associated with **22** seem to originate from the static disorder in the molecule. This result also thus suggests that the static disorder can play a key role in the relaxation dynamics of a given system.

A series of mononuclear heavy lanthanide complexes (Tb, Ho, Er and Lu) were reported by Shanmugam and co-workers by using the same Schiff base ligand that has been employed to synthesize **4** [91]. The metal centre in the Ho(III) analogue, $[Ho(HL)_2(NO_3)_4]$ (where HL = 2-methoxy-6-[(E)-phenyliminomethyl]phenol) (**23**), is coordinated by three nitrate and two Schiff base ligands resulting in a coordination number of ten around the metal. Complex **23** does not show any out-of-phase ac susceptibility (χ'') signal, in the absence of an external dc field. However, clear dependence

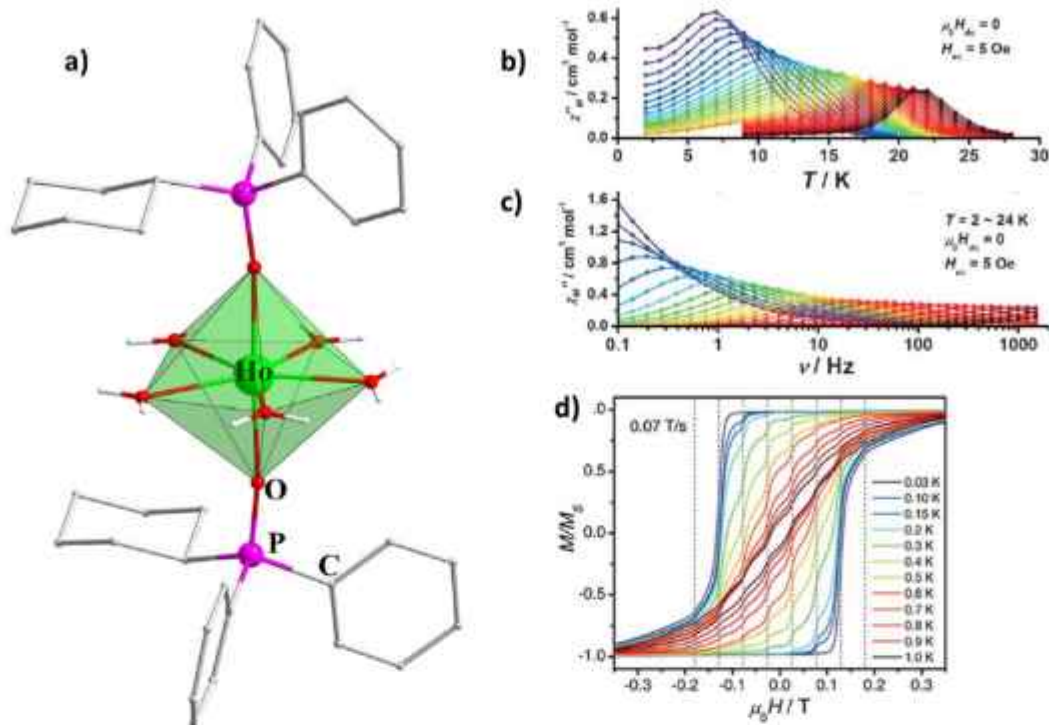


Fig. 17. (a) Molecular structure of $[\text{Ho}(\text{CyPh}_2\text{PO})_2(\text{H}_2\text{O})_5]^{4+}$ (**24**). The iodides, ligands present in the lattice and hydrogen atoms of Ph- and Cy- groups are omitted for clarity. (b) Temperature and (c) frequency dependence of χ'' signal in a zero dc field for **24** (d) Normalized magnetic hysteresis loops for a single crystal of **24** at different temperatures with field sweep rate of 0.07 T. Adopted from [153]. Copyright 2017 Wiley-VCH.

of χ'' on frequency can be observed up to 8 K, under an external magnetic field of 3000 Oe. The fitting of high temperature linear region of $\ln\tau$ vs T^{-1} with Arrhenius Law yields $U_{\text{eff}} = 63.5$ K and $\tau_0 = 2.35 \times 10^{-9}$ s. The non-linearity of $\ln\tau$ vs T^{-1} plot clearly confirms the presence of different relaxation processes, and the plot yields a good fit by considering Raman and QTM along with Orbach process with $C = 0.056 \text{ s}^{-1}\text{K}^{-n}$, $n = 4.08$ and $\tau_{\text{QTM}} = 0.0691$ s.

The P=O donor ligands are found to be popular in synthesizing air stable SIMs whether it is Kramers Dy(III) or non-Kramers Ho(III) ions, especially in the case of D_{5h} symmetric SIMs. In the last few years, it is found that the ligand field with two axial P=O donor ligands and five weak equatorial ligands (mainly H_2O) are perfect for Ho(III) ions to enhance its anisotropy to a significant level.

The first example of D_{5h} symmetric Ho(III) based SIM was reported by Tong and co-workers in 2017. They reported that the Ho(III) analogue of **13**, i.e. $[\text{Ho}(\text{CyPh}_2\text{PO})_2(\text{H}_2\text{O})_5]^{4+} \cdot 2(\text{CyPh}_2\text{PO}) \cdot 3\text{EtOH}$ (**24**), where Ho(III) ion is in a D_{5h} symmetric environment, behaves as single-ion magnet [152,153]. The frequency dependence of the ac magnetic susceptibility measurements show that **24** exhibits out-of-phase signals up to 24 K in absence of any external field (Fig. 17b and c). The temperature dependence of relaxation time can be fitted using different relaxation processes, i.e. Orbach, Raman and QTM. At higher temperatures, relaxation time perfectly follows Arrhenius law, with $U_{\text{eff}} = 341$ K and $\tau_0 = 1.7 \times 10^{-11}$ s. At moderate temperatures, Raman process is dominant over other processes with $n = 4.22$ while QTM is the most effective at low temperature region with $\tau_{\text{QTM}} = 11.6$ s. Ab initio calculations predict that the first and second excited doublets are separated from the ground state by 287 K and 327 K higher in energy, respectively, which clearly suggests that the Orbach relaxation occurs through the second excited doublet. The diluted sample of **24** shows an almost similar behaviour with a small change in U_{eff} ($=353$ K), τ_0 ($=9.9 \times 10^{-12}$ s) and n ($=4.40$) indicating that the slow relaxation of magnetisation is the property of the discrete mole-

cules of **24**. The nature of dc field dependence of relaxation times for both **24** and **24@Y** are similar indicating that the slow relaxation of magnetisation is purely molecular property. However, the effect of QTM is significantly weakened by dilution proving that intermolecular magnetic interactions are the prime cause of QTM in **24**. As the natural abundance for ^{165}Ho ($I = 7/2$) is 100%, there exists hyperfine interactions through the coupling between the electronic spin energy states and the nuclear spin. For **24**, thus hyperfine interactions are observed with calculated hyperfine-interaction parameter, $A_{\text{hf}} = 0.03 \text{ cm}^{-1}$. Though this behaviour is somewhat comparable to that observed in **21**, the observable QTM originating from transverse magnetic field is absent in **24**. The hyperfine interactions are confirmed by performing the magnetization measurements on a single crystal of **24**. Typical hysteresis loops are observed with regular steps up to 3 K, due to resonant tunnelling at the field of avoided level crossings (Fig. 17d).

Using a P=O donor phosphonamide ligand, a mononuclear D_{5h} symmetric Ho(III) SMM, $[\text{L}_2\text{Ho}(\text{H}_2\text{O})_5]^{3+} \cdot \text{L}_2 \cdot (\text{H}_2\text{O})$ (**25**), $\text{L} = ^t\text{BuP}(\text{O})(\text{NH}^t\text{Pr})_2$, analogous to **12**, was reported by Gupta *et al.* in 2018 [57]. Complex **25** shows clear maxima in frequency dependent out-of-phase signals up to 27 K in absence of external dc field. In the high temperature region, linear part of $\ln\tau$ vs $1/T$ plot can be fitted with $U_{\text{eff}} = 355$ K and $\tau_0 = 1.54 \times 10^{-10}$ s. The non-linearity of the plot $\ln\tau$ vs $1/T$ over the whole temperature region can be fitted by considering a combination of QTM ($\tau_{\text{QTM}} = 1.65$ s), Raman ($C = 0.03 \text{ s}^{-1}\text{K}^{-n}$, $n = 3.5$) and Orbach processes. As in **24**, dilution of **25** also reveals similar relaxation dynamics but the QTM arising from intermolecular interactions is almost quenched. The field dependent magnetisation of **25** reveals opening up of the magnetic hysteresis loop up to 4.0 K with coercivity as large as ~ 500 Oe at 2.0 K with sweep rate, 0.027 T s^{-1} . Interestingly, the isomorphous Tb(III) complex does not show any zero field SMM behaviour due to the strong QTM that exists between the ground states. Ab initio calculations confirm that the ground state in **25** is purely $m_J = \pm 8$

and that the relaxation proceeds via first excited state, which lies 374.7 K above the ground state. Three molecules were modelled to enhance the slow magnetic relaxation (Fig. 18c–e). Enhancement of U_{eff} to 477.5 K is estimated on removal of secondary coordination sphere entities, i.e. iodides and free ligands. It suggests that the moieties present in secondary coordination sphere play important role in stabilising lower m_j levels ($m_j = |\pm 3|$ is dominated) and hence enhances U_{eff} . On removal of the equatorial water molecules, U_{eff} is further improved to 760 K by stabilising $m_j = |\pm 7|$ as first excited state. The U_{eff} can be further enhanced for $[\text{Ho}(\text{OH})_2]^+$ model complex ion as the relaxation associated with this can happen through higher excited states as a result of higher symmetry (D_{3h}) and stronger donor interaction from the two axial OH ligands.

In 2020, Wang and co-workers have used another P = O ligand hexamethylphosphoric triamide (HMPA) and synthesized another two D_{3h} symmetric Ho(III) based SIMs, $[\text{Ho}(\text{HMPA})_2(\text{H}_2\text{O})_5]_2\text{Cl}_6 \cdot 2\text{HMPA} \cdot 2\text{H}_2\text{O}$ (**26**) and $[\text{Ho}(\text{HMPA})_2(\text{H}_2\text{O})_5]_2\text{Br}_4 \cdot 2\text{HMPA}$ (**27**) (Fig. 19a). [154] **27** is a discrete molecule while in case of **26**, there are two crystallographically different $[\text{Ho}(\text{HMPA})_2(\text{H}_2\text{O})_5]^{3+}$ moieties interacted each other via weak intermolecular H-bonding. Both the complexes show slow relaxation of magnetisation in absence of magnetic field up to 25 K. The $\ln\tau$ vs $1/T$ plot suggests

that Raman process (dominate at lower than 17 K) and the Orbach process (dominate above 17 K) are present in the relaxation of magnetisation process over the whole temperature range for both the complexes. The fitting of the plot yields $U_{\text{eff}} = 290$ K, $\tau_0 = 7.55 \times 10^{-11}$ s, $C = 0.00591$ s $^{-1}$ K $^{-n}$, and $n = 4.18$ for **26** and $U_{\text{eff}} = 320$ K, $\tau_0 = 1.42 \times 10^{-11}$ s, $C = 0.00237$ s $^{-1}$ K $^{-n}$, and $n = 4.47$ for **27**. As there is no significant divergence between variable temperature zero field-cooled (ZFC) susceptibilities and field-cooled (FC) susceptibilities as well as no opening up of hysteresis loop observed for both **26** and **27** confirming that both the molecules are having negligibly small T_B .

Very recently in 2021, Cheng and co-workers have two D_{3h} symmetric Ho(III) based SIMs were reported using another P=O ligand, i.e. trispyrrolidinophosphineoxide (tprpo) [155]. The two complexes, $[\text{Ho}(\text{tprpo})_2(\text{H}_2\text{O})_5]_2\text{X}_4 \cdot 2\text{H}_2\text{O}$ ($X = \text{Cl}$ for **28** and Br for **29**) contain two tprpo ligands in the axial positions and equatorial positions are occupied by five water molecules (Fig. 19b). Both complexes show typical SIM behaviour up to 30 K in absence of any external magnetic field. The Orbach process dominates at higher temperature while Raman process is significant in the low temperature region. The non-linear $\ln\tau$ vs $1/T$ plot can be best fitted over the whole temperature range by considering both Orbach and Raman process, with $U_{\text{eff}} = 351$ K, $\tau_0 = 7.19 \times 10^{-11}$ s,

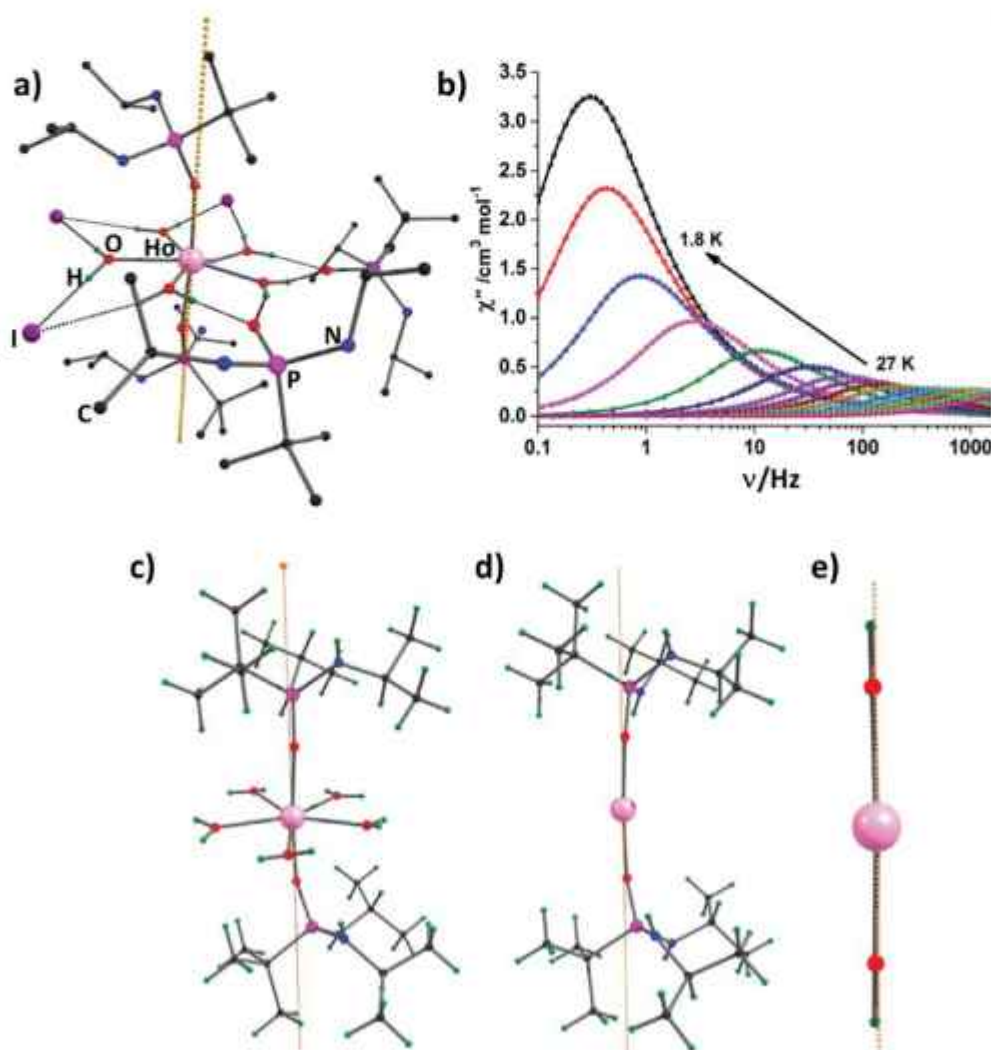


Fig. 18. (a) Molecular structure of $[\text{Ho}(\text{H}_2\text{O})_5]_2\text{I}_2 \cdot 2\text{H}_2\text{O}$ (**25**) (b) Frequency dependence of χ'' measured in the temperature range of 1.8–27 K in zero applied dc field for **25**. (c–e) Model compounds derived from **25** to improve the U_{eff} values. The yellow dotted lines in the structures represent the CASSCF computed g_{zz} orientation of the ground state pseudo doublets. Reprinted from [57]. Copyright 2018 Royal Society of Chemistry.

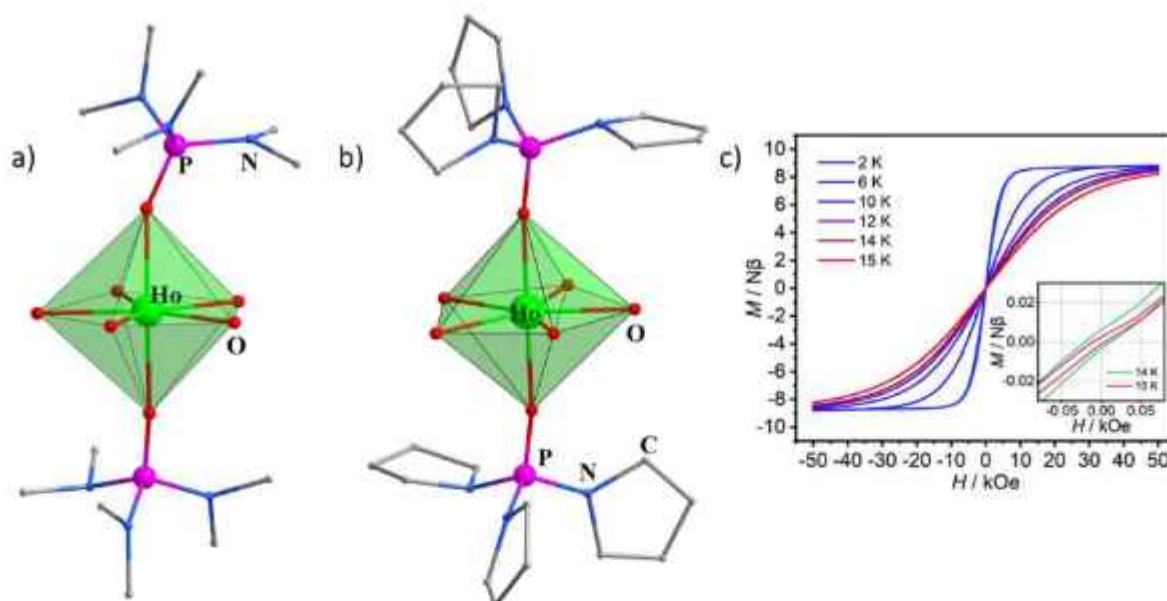


Fig. 19. Molecular structure of (a) $[\text{Ho}(\text{HMPA})_2(\text{H}_2\text{O})_5]\text{Br}_3 \cdot 2\text{HMPA}$ (**27**) and (b) $[\text{Ho}(\text{tpmpo})_2(\text{H}_2\text{O})_5]\text{Br}_3 \cdot \text{H}_2\text{O}$ (**29**). (c) Hysteresis loop of **29** clearly shows that the opening up to the loop occurs up to 15 K, which is highest among any Ho(III) SIMs. Reprinted from [154] and [155]. Copyright 2020 Royal Society of Chemistry.

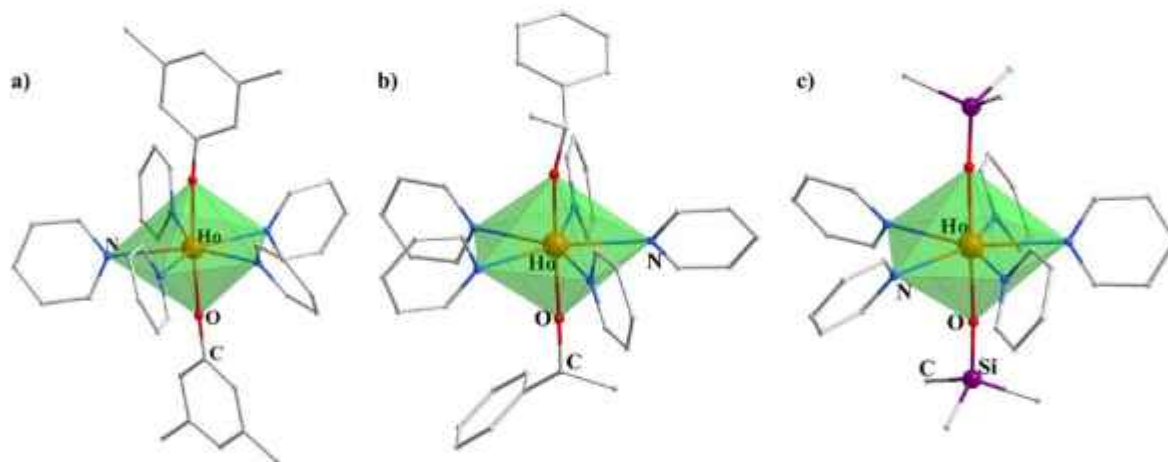


Fig. 20. Molecular structures of (a) $[\text{Ho}(\text{OC}_6\text{H}_3(\text{CH}_3)_2)(\text{py})_5][\text{BPh}_4]$ (**30**) (b) $[\text{Ho}(\text{OC}_6\text{H}_3(\text{CH}_3)_2)(\text{py})_5][\text{BPh}_4]$ (**31**) and (c) $[\text{Ho}(\text{OSi}(\text{CH}_3)_3)(\text{py})_5][\text{BPh}_4]$ (**32**). The counteranion $[\text{B}(\text{C}_6\text{H}_5)_4]^-$ present in the lattice and H-atoms are omitted for clarity. Adopted from [156].

$C = 0.00179 \text{ s}^{-1} \text{ K}^{-n}$ and $n = 3.95$ for **28** and $U_{\text{eff}} = 418 \text{ K}$, $\tau_0 = 1.76 \times 10^{-11} \text{ s}$, $C = 0.0111 \text{ s}^{-1} \text{ K}^{-n}$ and $n = 3.31$ for **29**. The hysteresis loops open up to 8 K for **28** while **29** holds the record blocking temperature of 15 K among all Ho(III) SIMs at the sweep rate of 20 Oe/s. (Fig. 19c and Table 4). The deviation of variable temperature zero field-cooled (ZFC) susceptibilities from field-cooled (FC) susceptibilities appear at 6 K for **28** and 7 K for **29**.

In the context of D_{5h} symmetric Ho(III) SIMs, three Ho(III) complexes, with compressed pentagonal bipyramidal geometry, were reported by Zheng and co-workers in 2020 [156]. In these mononuclear complexes, $[\text{Ho}(\text{L})_2(\text{py})_5][\text{BPh}_4]$ ($\text{L} = 3, 5\text{-OC}_6\text{H}_3(\text{CH}_3)_2$ (**30**), $-\text{OCH}(\text{CH}_3)\text{C}_6\text{H}_5$ (**31**), $-\text{OSi}(\text{CH}_3)_3$ (**32**), the equatorial positions around Ho(III) centre are fixed with five weakly coordinating pyridine ligands and the two axial positions are fine-tuned by alkoxide/siloxide ligands with near linear O–Ho–O angle ($\sim 176^\circ$) (Fig. 20). AC susceptibility measurements show clear maxima in frequency dependent χ'' signals up to 26 K for **30**, 34 K for **31** and 43 K for **32**. All three complexes exhibit very high U_{eff} values,

viz. 397 K for **30**, 499 K for **31** and 715 K for **32**; **32** exhibits the highest U_{eff} value among all the Ho(III) based SIMs (Table 3). The relaxation dynamics is highly dominated by Orbach and Raman process in case of **30** and **32**, while QTM is also present along with Orbach and Raman process in case of **31**. Unlike other D_{5h} SMMs mentioned above, none of these complexes **30–32** show any opening up of hysteresis loop even at 2 K, although they have higher U_{eff} values. Ab initio calculations predict that the Orbach relaxation in **32** occurs via the second excited states and higher bunched states. Moreover, the LoProp approach [157] confirms that charge on the O atoms follow the trends $\mathbf{32} > \mathbf{31} > \mathbf{30}$, which reflects the coordination strength to Ho(III) ion, highest in **32**. Higher negative charge on the O atoms stabilizes of largest m_l values as the ground state, hence **32** achieves highest U_{eff} among these three complexes Table 4.

Although, the core structure, $[\text{Ho}(\text{R}_3\text{PO})_2(\text{H}_2\text{O})_5]^{3+}$, is almost similar those found in **24–29**, the U_{eff} values are found to differ to a large extent. The LF with shorter Ho–O_{axial} bonds, longer

Table 3

The variation of the barrier height for spin reversal (U_{eff}) with Ho-O_{axial} and Ho-O_{equatorial} bond lengths, O_{axial}-Ho-O_{axial} bond angles and the deviation of coordination geometry from the ideal D_{3h} symmetry as calculated from SHAPE [161] in case of D_{3h} symmetric Ho(III) SIMs.

Molecule	Ho-O _{axial}	Ho-O _{equatorial}	O _{axial} -Ho-O _{axial}	U_{eff} /K	Deviation(SHAPE analysis)	Ref
[Ho(CyPh ₂ P ₂ O) ₂ (H ₂ O) ₂] ₂ (24)	2.198	2.364	177.94	341	0.160	[146]
[Ho ⁺ Bu ⁺ (O)(Nt ⁺ Pr) ₂] ₂ (H ₂ O) ₂ (25)	2.194	2.343	175.07	355	0.20	[57]
[Ho(HMPA) ₂ (H ₂ O) ₂][Br ₃] (27)	2.213	2.348	179.2	320	0.105	[154]
[Ho(tp ⁺ po) ₂ (H ₂ O) ₂][Cl ₃] (28)	2.210	2.353	177.94	351	0.112	[155]
[Ho(tp ⁺ po) ₂ (H ₂ O) ₂][Br ₃] (29)	2.196	2.353	178.80	418	0.132	[155]
[Ho(OC ₆ H ₄ (CH ₂) ₂ (py) ₂)] ₂ [BPh ₄] (30)	2.141	2.554	175.68	397	0.991	[156]
[Ho(OCH(CH ₃)C ₆ H ₅) ₂ (py) ₂]] ₂ [BPh ₄] (31)	2.115	2.544	174.51	499	0.778	[156]
[Ho(OSi(CH ₃) ₂ (py) ₂)] ₂ [BPh ₄] (32)	2.140	2.539	176.12	712	0.754	[156]

Table 4

Mononuclear Ho(III) based single-ion magnets (U_{eff} represents the barrier obtained from ac susceptibility measurements; $U_{\text{eff,cal}}$ represents the barrier obtained from computational study. C and n are the parameters obtained from the fitting of temperature dependence of relaxation time plot using Raman process)

Sl no.	Ho(III) SIMs	$U_{\text{eff, ac}}$ /K	$U_{\text{eff, cal}}$ /K	τ_0 /s	τ_{QTM} /s	$C/S^{-2}K^{-n}$	n	H/Oe	Hyst (K)	Sweep rate (Oe/s)	Ref
1	[(Pc) ₂ Ho] ⁻ (21)	21.6	—	—	—	—	—	—	—	—	[150]
2	21@Y	—	—	—	—	—	—	—	0.5	2800	[150]
3	(Cp ⁺)Ho(COT) (22)	7.4	—	4.0×10^{-5}	—	—	—	0	—	—	[151]
		3.6*	—	1.3×10^{-4}	—	—	—	—	—	—	
4	22@Y	33.8	—	2.4×10^{-5}	—	—	—	0	—	—	[151]
		24.4	—	7×10^{-6}	—	—	—	—	—	—	
5	[Ho(HL) ₂ (NO ₃) ₂] (23)	63.5	—	2.4×10^{-9}	0.0691	0.056	4.08	3000	—	—	[91]
6	[Ho ₂ (H ₂ O) ₂] ₂ ·2L·3EtOH (24)	341	237	1.7×10^{-11}	11.60	—	4.22	0	3	1400	[152,153]
7	[L ₂ Ho(H ₂ O) ₂][1 ₁ ·1 ₂ ·(H ₂ O) (25)	355	374.7	1.5×10^{-10}	1.65	0.03	3.5	0	4	270	[57]
8	[Ho(HMPA) ₂ (H ₂ O) ₂][Cl ₃ ·2HMPA·2H ₂ O] (26)	290	—	7.6×10^{-11}	—	0.0059	4.18	0	—	—	[154]
9	[Ho(HMPA) ₂ (H ₂ O) ₂][Br ₃ ·2HMPA] (27)	320	—	1.4×10^{-11}	—	0.00237	4.47	0	—	—	[154]
10	[Ho(tp ⁺ po) ₂ (H ₂ O) ₂][Cl ₃ ·H ₂ O] (28)	351	—	7.2×10^{-11}	—	0.00129	3.95	0	8	—	[155]
11	[Ho(tp ⁺ po) ₂ (H ₂ O) ₂][Br ₃ ·H ₂ O] (29)	418	—	1.8×10^{-11}	—	0.0111	3.31	0	15	—	[155]
12	[Ho(OC ₆ H ₄ (CH ₂) ₂ (py) ₂)] ₂ [BPh ₄] (30)	397	299	1.1×10^{-11}	—	7.9	2.18	0	—	—	[156]
13	[Ho(OCH(CH ₃)C ₆ H ₅) ₂ (py) ₂]] ₂ [BPh ₄] (31)	499	354	6.8×10^{-12}	0.01	0.048	3.59	0	—	—	[156]
14	[Ho(OSi(CH ₃) ₂ (py) ₂)] ₂ [BPh ₄] (32)	715	682	1.3×10^{-12}	—	0.081	3.38	0	—	—	[156]
15	Ho(CH ₂ SiMe ₂) ₂ (THF) ₂ (33)	76	<100	1.7×10^{-10}	0.0003	170.86	2.27	0	—	—	[162]

* Both 22 and 22@Y exhibit two different U_{eff} due to the static disorders in the complex. The static disorder arises from the existence of two different conformers, i.e. eclipsed isomer (major) and staggered conformers (minor).

Ho-O_{equatorial} bonds and near to linear O_{axial}-Ho-O_{axial} angles around Ho(III) ion is expected to be ideal to achieve better SIM behaviour. In case of D_{3h} symmetric Dy(III) SIMs, the trend of an increase in the U_{eff} values with decreasing axial Dy-L distance is well known. This is due to the fact that for an oblate shaped ion stronger axial ligand field which is represented by a shorter Dy-L distances exerts large energy splitting among different KDs in the ground multiplet leading to a high blocking barrier [158]. However such straight magneto-structural correlation cannot be established for Ho(III) SIMs. The variation of U_{eff} with Ho-O_{axial} bond lengths, Ho-O_{equatorial} bond lengths and O_{axial}-Ho-O_{axial} angles are shown in Table 3 and Fig. 21. Another factor which can effect on U_{eff} value is the second coordination sphere. [57] This effect is prominent in D_{3h} symmetric Dy(III) SIMs. For example, the barrier heights are found to be inversely proportional to the average Dy-X (X = Cl⁻/Br⁻/I⁻) distances in case of [Dy(HMPA)₂(H₂O)₂][Cl₃·HMPA·H₂O] (U_{eff} = 460 K), [Dy(HMPA)₂(H₂O)₂][Br₃·HMPA·H₂O] (U_{eff} = 556 K) and [Dy(HMPA)₂(H₂O)₂][I₃·2HMPA] (U_{eff} = 600 K). [159,160] In case of 24–29, it can be suggested that the moieties present in the second coordination sphere play an important rule in the observed SIM behaviour. [57] The same trend can be expected for D_{3h} symmetric Ho(III) SIMs when the first coordination sphere is identical. Hence, the U_{eff} of 27 is higher than that of 26 while that of 29 is higher than 28. The U_{eff} is found to be inversely proportional to Ho-X average bond distances. Thus, it can be concluded that all the factors e.g. Ln-O_{axial} bond lengths, Ln-O_{equatorial} bond lengths, O_{axial}-Ln-O_{axial} bond angle, the second coordination sphere and intermolecular

magnetic interactions etc. play decisive in determining the SIM behaviour of a molecule.

Gao and co-workers reported a series of adducts of tris(alkyl) Ho(III) complexes. The ligand field in these mononuclear complexes, Ho(CH₂SiMe₂)₂L_x, consist of three -CH₂SiMe₂ groups, along with THF (x = 2, 33) / quinuclidine (x = 2, 34) / OPCy₃ (x = 2, 35) or lutidine (x = 3, 36) [162]. AC susceptibility measurements show that only 33 exhibits frequency dependent χ'' signals in the absence of any external magnetic field for the temperature range 2–7 K with U_{eff} = 76 K, which is higher than that observed for the Dy(III) congener (U_{eff} = 40 K). Application of 5000 Oe dc field suppresses the QTM, but there is negligible improvement in U_{eff} (81 K). Moreover, the negligible improvement is observed for the diluted samples of 33. The other three complexes 34–36 do not show slow relaxation even after the application of dc field owing to the presence of strong QTM.

2.5. Thulium(II)/(III) based mononuclear SMMs

Thulium based SIMs are exceedingly rare in the literature. Gao and co-workers have reported two half-sandwich-type thulium complexes, [(Tp)Tm(COT)] (37) [163] and [(Tp⁺)Tm(COT)] (38), where the ligand field is made up of one hydrotris(1-pyrazolyl) borate (Tp) along with a COT in 37 and one hydrotris(3,5-dimethyl-1-pyrazolyl)borate (Tp⁺) and one COT ligand in 38 [164]. AC susceptibility measurements show that both 37 and 38 exhibit frequency-dependent out-of-phase signals, albeit very weak.

Table 5

Mononuclear Yb(III) based single-ion magnets ($U_{\text{eff,ac}}$ represents the barrier obtained from ac susceptibility measurements; $U_{\text{eff,optic}}$ represents the barrier calculated from spectroscopic techniques; $U_{\text{eff,cal}}$ represents the barrier obtained from computational study; C and n are the parameters obtained from the fitting of temperature dependence of relaxation time plot using Raman process):

Sl no.	Yb(III) SIMs	$U_{\text{eff,ac}}$ K	$U_{\text{eff,optic}}$ K	$U_{\text{eff,cal}}$ K	τ_0 /s	τ_{QTM} /s	$C/\text{s}^{-1}\text{K}^{-n}$	n	H/Oe	Ref
1	[N(C ₂ H ₅) ₄] ₂ [Ln(dipic) ₂] (41)	–	187	–	–	–	–	–	1000	[187]
2	[Yb(H ₂ L) ₂][Cl ₂ ·5CH ₃ OH·2H ₂ O] (42)	7	226–270.5	–	2.0×10^{-5}	–	–	–	400	[188]
3	[Yb(Tpaz) ₂ Bpz] ₂ ·CH ₂ Cl ₂ (43)	29	–	–	2×10^{-11}	–	–	–	1500	[190]
4	[Yb(Tpaz) ₂ NO ₃] (44)	–	119	158	–	–	0.00636	9	2000	[192]
5	[Cp*Yb(DAD)(THF)]·C ₂ H ₆ (45)	20	–	–	1.74×10^{-6}	–	0.00208	9	1500	[195]
6	Yb(trensai) (46)	54.7	668	–	1.5×10^{-8}	–	–	–	2000	[197]
	46 as single crystal	–	–	–	–	–	0.044	6.9	2000	
	46 as powdered form	–	–	–	–	–	0.15	6.2	2000	
7	[Yb(tra) ₂ (L)]·2CH ₂ Cl ₂ (47)	6	337	337	1.9×10^{-5}	–	–	–	1000	[205]
8	[Yb(QR ₁) ₂ (tra) ₂ ·CH ₃ OH] (49)	16.1	–	–	1.78×10^{-7}	–	–	–	1000	[207]
9	[Yb(QR ₁) ₂][NO ₃](CH ₃ OH)(H ₂ O) _{0.5} (50)	5.37	–	–	1.0×10^{-5}	–	–	–	1000	[207]
10	[Yb(L) ₂] (51)	11.7	–	–	4.6×10^{-6}	–	82.1	3.6	1000	[208]
11	[Yb(L) ₂ (TMH)(CH ₃ OH)] (52)	29.7	–	–	3.5×10^{-7}	–	0.2	6.5	1000	[208]
12	[Yb(L) ₂ (tra)(CH ₃ OH)] (53)	30.3	–	–	2.0×10^{-7}	–	0.3	6.5	1000	[208]
13	(Et ₃ NH)[Yb(3-NO ₂ -salen) ₂] (54)	7.5	–	–	4.1×10^{-8}	–	–	–	1500	[209]
14	[Yb(H ₂ Bmsbp)(DMF) ₂ Cl ₂ ·DMF·1.5H ₂ O] (55)	14.5	–	–	2.4×10^{-5}	–	12.2	3.6	1500	[210]
15	[Yb(H ₂ Bmsbp)(DMF) ₂ Cl ₂ ·H ₄ Bmsbp] (56)	38.3	–	288	7.16×10^{-7}	–	0.38	5.6	600	[210]
16	[Yb(PyCOO)(acac) ₂ (H ₂ O) ₂] (57)	54	–	–	7.4×10^{-8}	–	0.013	7	2000	[211]
17	[Yb(L ₂ (OTf) ₂)(OTf)] (58)	11.7	–	–	4.6×10^{-6}	–	6	0.3	1000	[212]
18	[Yb(L ₂ (NO ₃) ₂ (MeOH)]·MeCN (59)	17.8	–	–	8.7×10^{-7}	–	4	0.6	1000	[212]
19	[Yb(H ₂ O) ₂ (18-crown-6)](ClO ₄) ₂ (60)	5.9	–	91	2.61×10^{-5}	0.00075	0.3289	5.8	500	[213]
20	Yb(NO ₃) ₃ (ⁿ Bu ₃ PO) ₂ (61)	23	–	335.5	6.8×10^{-7}	–	–	–	1000	[214]
		–	–	–	–	–	0.29	7.01	–	
21	[Ln(NAS) ₂ (H ₂ O) ₆](NAS)·3H ₂ O (62)	45	–	–	5.1×10^{-8}	0.385	6.8×10^{-4}	9.3	1000	[215]
22	[Yb(depma) ₂ (H ₂ O) ₆][Cl ₂ ·3H ₂ O·CH ₂ O] (63)	28.9	–	–	4.6×10^{-8}	–	483.4	2.1	750	[217]
23	[Yb(H ₂ O) ₂ (NCS) ₃ ·H ₂ O] (64)	50	–	–	2.3×10^{-8}	–	440	8.55	2500	[218]
24	[Yb(H ₂ O)(bpy) ₂ (NCS) ₃ ·0.5(bpy)·H ₂ O] (65)	47	–	–	1.7×10^{-8}	–	72.6	7.99	1000	[218]
25	[Yb(H ₂ O)(phen) ₂ (NCS) ₃ ·phen·0.5H ₂ O] (66)	22	–	–	4.5×10^{-7}	–	0.061	4.53	1000	[218]
26	[Hbpy][Yb(bpy) ₂ (NCS) ₄ ·H ₂ O] (67)	44	–	–	2.9×10^{-8}	–	72.8	7.98	1000	[218]
27	[Hphen][Yb(phen) ₂ (NCS) ₄] (68)	37	–	–	8.4×10^{-8}	–	0.59	5.16	1000	[218]
28	[Yb(Ph ₃ PO) ₄ (NO ₃) ₂][NO ₃] (69)	9.2	–	130	1.8×10^{-8}	–	–	–	2500	[219]
29	[Yb(Ph ₃ PO) ₄ (OTf) ₂][OTf] (70)	28.2 (SK)	–	474	2.88×10^{-8}	–	0.445	5.53	2000	[219]
		27.0 (FR)	–	–	3×10^{-7}	0.276	4.02	3.58	2000	
30	[Yb(Ph ₃ PO) ₄ (t ₁ -t ₃ -B ₁₀ C ₇ (U ₁₂ Cl ₁₀))][t ₁] (71)	21.3	–	556.6	8.34×10^{-7}	–	11.4	4.49	1000	[219]

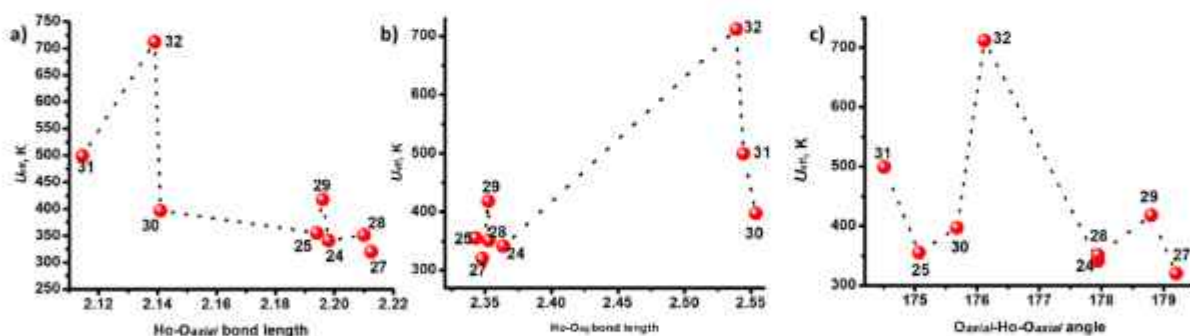


Fig. 21. The variation of U_{eff} with (a) Ho–O_{axial} bond length, (b) Ho–O_{equatorial} bond length and (c) O_{axial}–Ho–O_{axial} bond angles in case of D_{3h} symmetric Ho(III) SIMs (24–32). The trend roughly suggests that on increasing the Ho–O_{axial} bond lengths U_{eff} decreases while the reverse is true for Ho–O_{equatorial} bond lengths.

However, on application of optimized dc field of 2000 Oe, strong frequency-dependent and temperature-dependent out-of-phase ac susceptibility signals were observed in the temperature range of 2–30 K for **37** and 2–20 K for **38**. The non-linear behaviour of the plot of $\ln \tau$ vs $1/T$ indicates that multiple processes are involved in the relaxation dynamics for both the complexes. The data of high-temperature ac measurements were fitted with Arrhenius law to yield U_{eff} values of 111(2) K for **37** and 46(1) K for **38**. The plot of $\ln \tau$ vs T^{-1} can be fitted well over the whole temperature range by considering Orbach and Raman with $n = 4.21$ for **37** and Orbach, Raman and QTM with $n = 3.92$ and $\tau_{\text{QTM}} = 1.033$ s for **38**. Interestingly, on dilution both these complexes show clear frequency-dependent χ'' , even in zero dc field up to 25 K and 22 K for **37@Y** and **38@Y**, respectively, indicating enhancement

of SIM behaviour by reducing dipolar interactions. Complexes **37** and **38** are the first examples of thulium based zero field SIMs. The U_{eff} value for **37@Y** is 44 K in zero dc field and 108 K in the presence of 1000 Oe applied dc field. The local magnetic anisotropies of Tm(III) in both the complexes have been determined by using the angular-resolved magnetometry method [165]. Rotation along y and z axes, in case of **38**, results in strong magnetic anisotropy even at ambient temperature. However, the magnetisation is ten times smaller for rotation along x (x is parallel to the crystallographic b axis) indicating that the Tm(III) ion exhibits strong easy axis anisotropy close to the crystallographic b axis. The susceptibility tensor for **38** is obtained from the fitting of sine curves at 2 K, suggesting that the direction of the easy axis is divergent by approximately 23° from the Tm–COT(centroid) (Fig. 22e). The

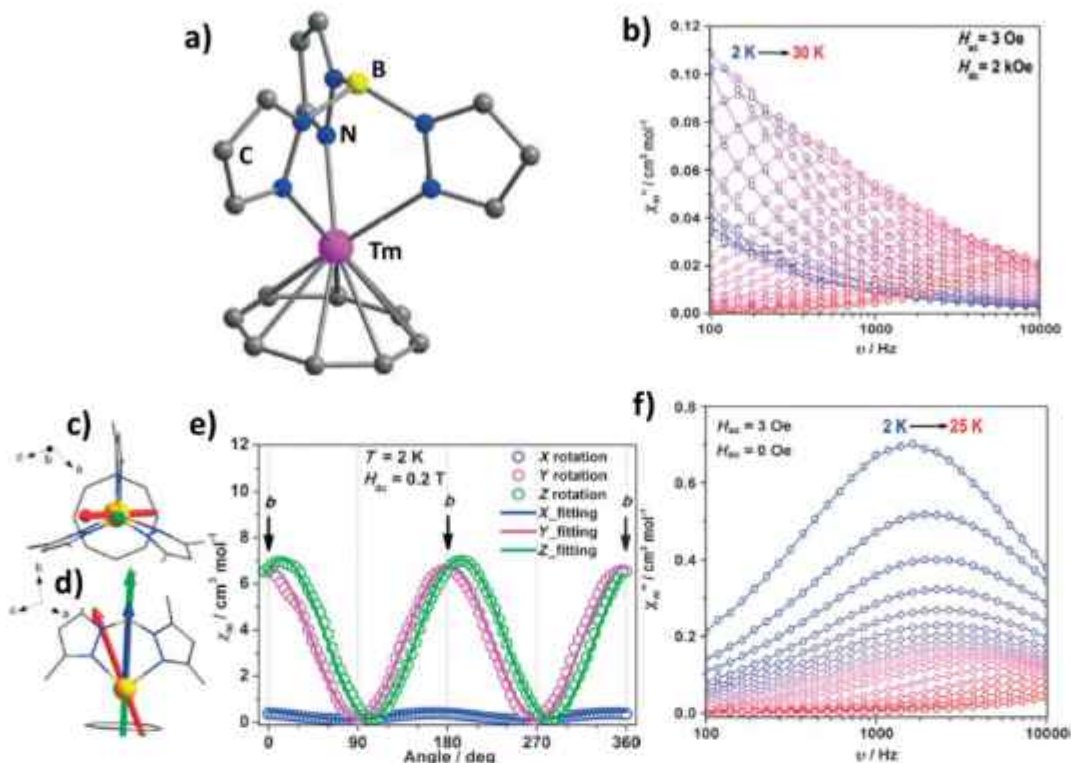


Fig. 22. (a) Molecular structure of $[(\text{Tp}^*)\text{Tm}(\text{CDT})]$ (**37**). Frequency dependence of χ'' signal for **37**, (b) at 2000 Oe field and (f) zero dc field. (c) Top and (d) side view of $[(\text{Tp}^*)\text{Tm}(\text{CDT})]$ (**38**) along with the magnetic easy axis orientations obtained from experiment (red arrow), CACSCF calculations (green arrow) and the electrostatic model (blue arrow). e) The angular-dependent susceptibility plots and the corresponding fitting at 0.2 T external magnetic field. In Y and Z rotation, the initial position is defined as a b axis parallel to magnetic field. Reprinted from [164]. Copyright 2016 Wiley-VCH.

χ_{mT} measurements in the range 1.9–20 K show that χ_{zz} is much larger than χ_{xx} and χ_{yy} , confirming that **38** possesses strong Ising-type anisotropy. Similar way, **37** also exhibits Ising-type anisotropy.

Unlike Uranium, whose compounds are known to exist in several oxidation states (e.g. U(III) and U(V)) and exhibit SMM behaviour, lanthanide elements exhibit SMM behaviour exclusively in their +3 oxidation state. None of the commonly existing divalent lanthanides, Eu(II) (isotopic, half-filled f orbitals), Yb(II) (diamagnetic with closed-shell f^{14}) and Sm(II) (have $J = 0$ ground state) can fulfil the primary requirement to behave as single-ion magnet [166]. Moreover, stabilisation of +2 oxidation state requires complicated syntheses like complexation with bulky-crown ligands [167].

Though some examples are known where +2 oxidation state is stabilized for thulium by employing bulky ligands such as substituted trispyrazolylborates [168,169], cyclopentadienyl ligands [170] and bulky silylamide ligands [171,172], their SIM behaviour has not been investigated so far. Nocton and co-workers have reported that two Tm(II) based complexes, $[\text{Tm}]_2(18\text{-crown-6})$ (**39**) and $[\text{Tm}(\text{BH}_4)(18\text{-crown-6})]$ (**40**) which are exception to the above generalization (Fig. 23a and b) [173]. 18-crown-6 ligand wraps the metal ion in the equatorial position in both these complexes. In compound **39**, both the axial positions are taken by two iodide anions while one iodide and one BH_4^- anion occupy the two axial positions in **40**. Interestingly, both these complexes show slow magnetic relaxation on varying ac frequency in the presence of an external magnetic field. In presence of optimum dc field of 600 Oe for **39** and 800 Oe for **40**, both show frequency dependent χ'' signals up to 5.5 K. The fitting of the high-temperature portion of the plot for $\log \tau$ vs T^{-1} with Arrhenius law yields the barrier 35 K for **39** and 16 K for **40**. The non-linear nature of $\log \tau$ vs T^{-1} plot can

be perfectly fitted by considering both direct and Raman process, $\tau^{-1} = C\text{T}^n + A\text{H}^m$, for both the complexes with the parameters $C = 0.13 \text{ s}^{-1}\text{K}^{-n}$, $n = 6.73$ and $A = 3.55 \times 10^{-10} \text{ Oe}^{-4}\text{s}\text{K}^{-1}$ for **39** and $C = 0.13 \text{ s}^{-1}\text{K}^{-n}$, $n = 5.69$ and $A = 4.44 \times 10^{-10} \text{ Oe}^{-4}\text{s}\text{K}^{-1}$ for **40**.

2.6. Ytterbium (III) based mononuclear SMMs

Yb(III) is the heaviest paramagnetic trivalent lanthanide ion with f^{13} electronic configuration. Being prolate, the magnetic anisotropy of Yb(III) ion can be enhanced by a ligand field having either very weak or no axial ligands and sufficiently strong equatorial ligands. Attempts to place ligands only in equatorial position with no axial ligands have been successful to some extent, e.g. for prolate Er(III) ion by using bulkier ligands such as bis(trimethylsilyl)amine [174], 2,6-di-tert-butyl-p-cresolate and bis(trimethylsilyl)methyl [175]. Construction of this type of ligand field is not so easy as Ln(III) ions tend to display high coordination numbers due to their large ionic radii. The complexity in designing a compatible, if not ideal, ligand field around Yb(III) has hugely hampered investigations of Yb(III) SIMs as compared to other heavier Ln(III) SIMs (e.g. Tb(III), Dy(III) and Er(III)).

Ligation to Ln(III) with an appropriate ligand can be advantageous as its complexation to an appropriate Ln(III) ion can allow the combination of luminescence behaviour with the magnetic properties. The parity and sometimes spin forbidden f-f transitions require a secondary excitation using a sensitizer which transfers the absorbed energy to the Ln(III) centre by antenna effect. So, the choice of ligand to achieve a bifunctional luminescent SMM is a tricky job, which allows deep insight to the origin of SMM behaviour in the molecule. The bifunctionality nature of Dy(III) based luminescent SMMs has been primarily explored among all

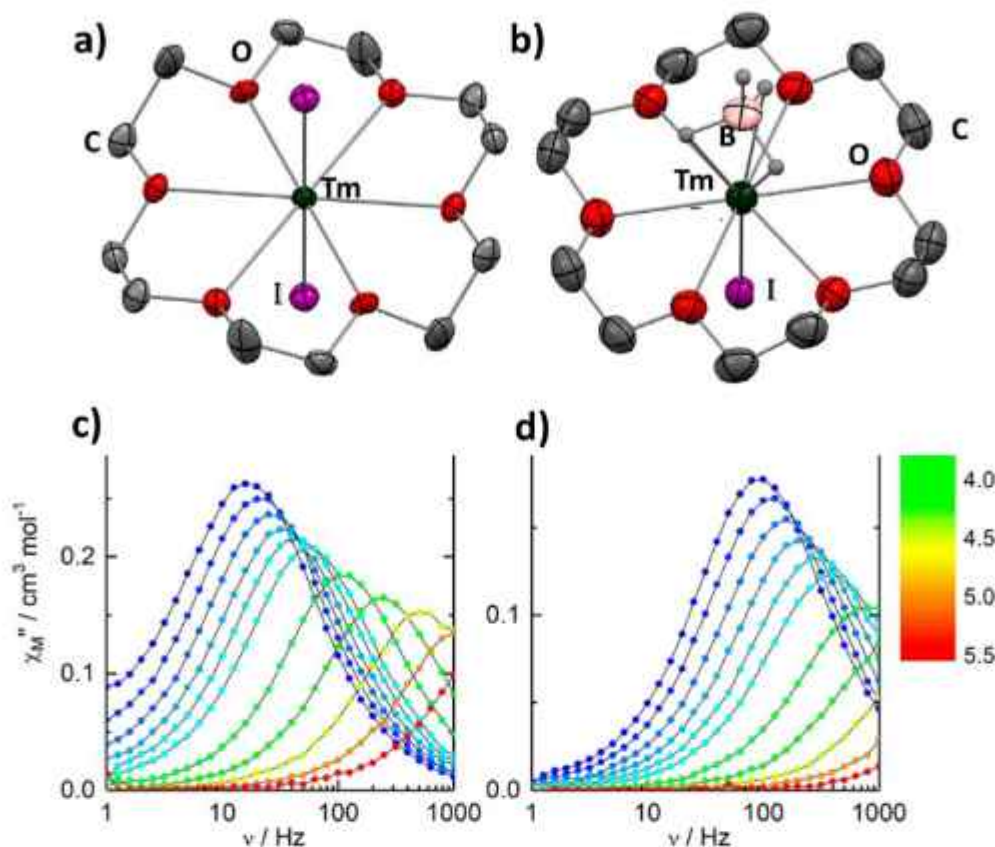


Fig. 23. Molecular structure of (a) $[Tm_2(18\text{-crown-6})]$ (**39**) and (b) $[Tm(BH_4)(18\text{-crown-6})]$ (**40**). Frequency dependent out-of-phase susceptibility of (c) **39** and (d) **40** in presence of external magnetic field of 600 Oe and 800 Oe, respectively. Reprinted from [173]. Copyright 2019 American chemical society.

the Ln(III) based SMMs [72,88,176–186], followed by Yb(III) SIMs. The Yb(III) SIMs exhibit luminescence in the NIR region due to the single $^2F_{5/2} \rightarrow ^2F_{7/2}$ transition. The slow magnetic relaxation in Yb(III) complexes is rare unlike Dy(III), due to smaller J values in the former than the later, and hence the examples of Yb(III) luminescent SMMs are very few as compared to Dy(III). So bifunctional luminescent SMM, with enhanced properties, can be designed by choosing appropriate ligand system around Yb(III) ion.

The first mononuclear Yb(III) SIM was reported by Kaizu and co-workers in 2006, along with a series of mononuclear heavy Ln(III) carboxylates, $[N(C_2H_5)_4]_3[Ln(dipic)_3] \cdot nH_2O$ (Ln = Tb, Dy, Ho, Er, Tm, or Yb (**41**); (dipic : pyridine-2,6-dicarboxylate), where the Ln(III) ions are in trigonal (D_3) symmetry [187]. Although **41** does not show any out-of-phase signals in absence of magnetic field, clear maxima can be observed at 2.4, 3.0, and 4.0 K corresponding to frequencies 10, 100, and 997 Hz, respectively, in the presence of an external magnetic field of 1000 Oe. The Er and Dy analogues of **41** also show out-of-phase signals in presence of 1000 Oe, but the Tb, Ho, and Tm analogues do not. The sublevel structures of the ground-state multiplet of **41** have been determined by finding the set of ligand field parameters with the help of 1H NMR paramagnetic shifts and the magnetic susceptibilities measured at various temperatures. Among all the Ln(III) complexes, **41** displays the highest energy gap of 187 K between ground and the first excited states (Table 5). However, the relaxation dynamics of **41** was not very clear at that time.

Another Yb(III) based mononuclear complex showing slow relaxation of magnetisation was reported by Tong and co-workers in 2012. In this *o*-vanillin derived Schiff base ligated complex, $[Yb(H_3L)_2]Cl_2 \cdot 5CH_3OH \cdot 2H_2O$ (**42**) (L = tris((2-hydroxy-3-methoxybenzyl)amino)ethyl)-amine) (Fig. 24b), the Yb(III) centre

is in a distorted octahedral coordination environment resulting in pseudo- S_6 geometry around the metal ion (Fig. 24a) [188]. Complex **42** does not show slow magnetic relaxation in the absence of external magnetic field due to strong QTM occurring in the ground states. Maximising the suppression of QTM by applying 400 Oe results in the observation of frequency dependent χ'' signals up to 5 K. Fitting of the high temperature region in τ vs T plot using Arrhenius Law yields $U_{eff} = 7$ K which is two orders smaller than the calculated U_{eff} (226 – 270.5 K), suggesting that slow relaxation of magnetisation occurs via processes other than the thermally activated type. The relaxation dynamics of **42** is dominated by direct process over Orbach process, which can be confirmed from the dependence of τ on applied field, i.e. the increase of τ on increasing the external dc field till 400 Oe is due to the suppression of QTM, which however decreases on further increasing the field due to the dominance of single-phonon direct process [189]. Thus, **42** relaxes via direct process rather than Orbach process. The observation of large contributions of the transversal g components, g_x and g_y , as compared to g_z suggests the existence of easy plane like anisotropy in **42**. This can be confirmed from the observation of a butterfly shaped hysteresis cycle on the application of magnetic field in the easy plane during low-temperature single-crystal magnetization measurements (Fig. 24d).

Using two scorpionate-type ligands, hydrotris(pyrazolyl)-borate (Tpz) and dihydrotris(pyrazolyl)-borate (Bpz), a series of 9-coordinated Ln(III) (Ln = Gd, Tb, Dy, Ho and Yb) based complexes have been reported by Luneau and co-workers in 2015 [190]. The Ln(III) ions are present in the tricapped trigonal regular prism geometry formed by eight nitrogen atoms from two Tpz and one Bpz ligand along with one B–H...Ln agostic interaction (Fig. 25).

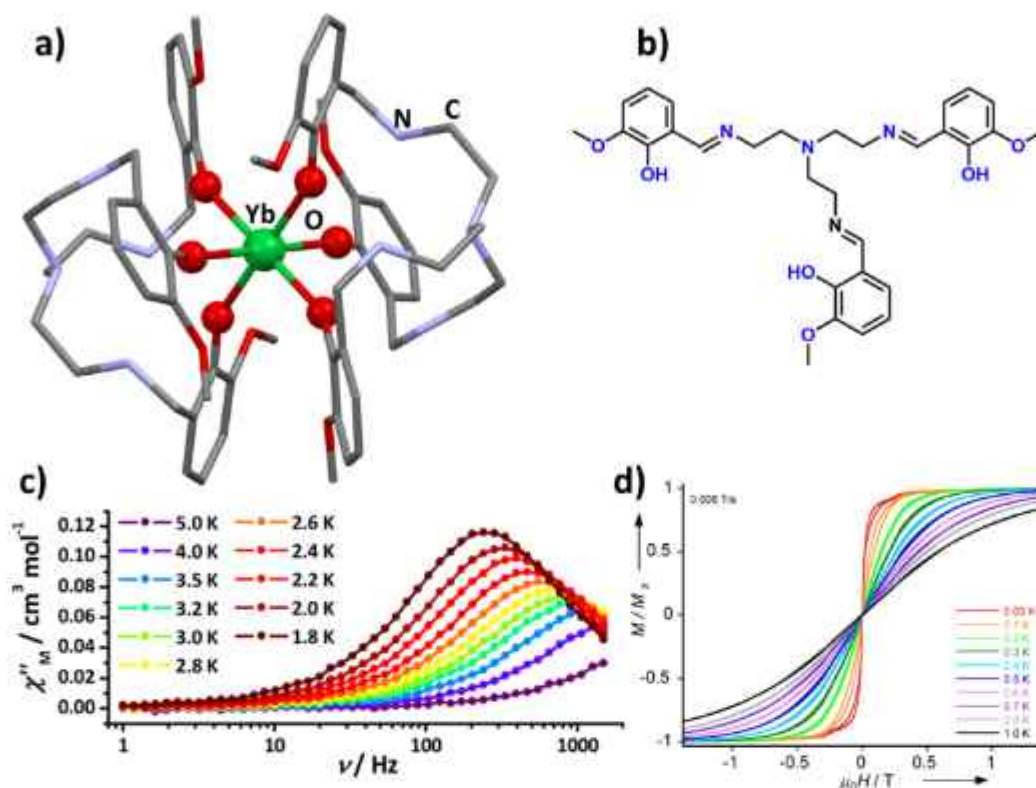


Fig. 24. (a) Molecular structure of the cationic part of $[[\text{Yb}(\text{H}_3\text{L})_2]\text{Cl}_2 \cdot 5\text{CH}_3\text{OH} \cdot 2\text{H}_2\text{O}]$ (**42**). (b) The structure of *o*-vanillin derived Schiff base ligand. (c) Frequency dependent out-of-phase susceptibility of **42** in the presence of 400 Oe external magnetic field. (d) field dependence of magnetisation at different temperatures with a sweep rate of 0.008 T/s. Reprinted from [188]. Copyright 2012 American chemical society.

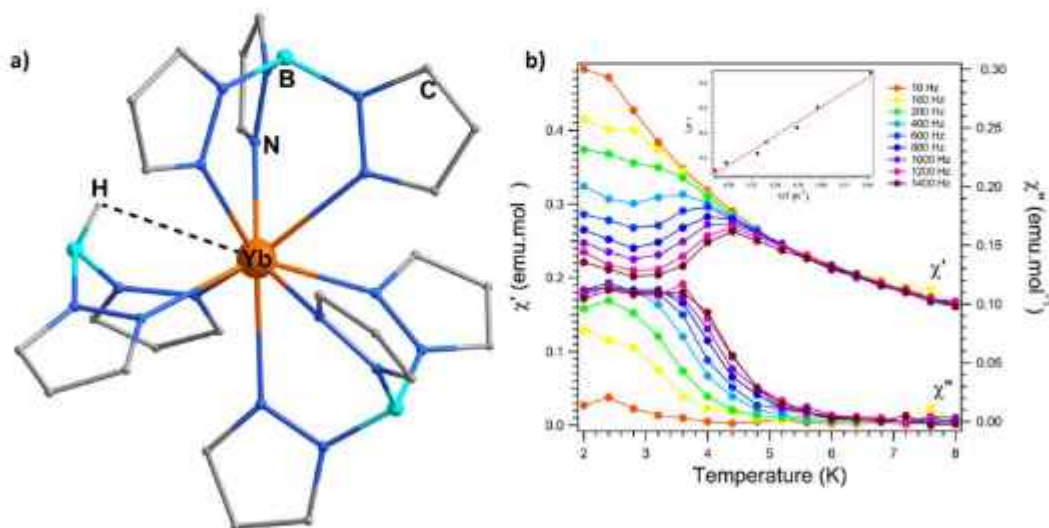


Fig. 25. (a) Molecular structure of $[[\text{Yb}(\text{Tpz})_2\text{Bpz}]\text{CH}_2\text{Cl}_2]$ (**43**). The hydrogen atoms (except one involved with B–H–Yb agostic interaction) and the lattice solvent molecules are omitted for clarity. (b) Temperature dependence of in-phase (top) and out-of-phase magnetic susceptibility (bottom) of **43** in presence of 1500 Oe field. The inset shows the variation of $\ln\tau$ with $1/T$ at 1500 Oe. Adopted from [190]. Copyright 2015 American chemical society.

The Yb(III) complex, $[[\text{Yb}(\text{Tpz})_2\text{Bpz}]\text{CH}_2\text{Cl}_2]$ (**43**), shows frequency dependent χ'' signals at 1500 Oe having $U_{\text{eff}} = 29$ K and $\tau_0 = 2 \times 10^{-8}$ s, considering that the relaxation occurs via Orbach process. However, fitting of magnetic susceptibility data by using PH1 [191] shows that the energy gap between ground and excited states is a mismatch with the experimentally obtained U_{eff} . This suggests that the magnetisation relaxation does not occur solely via Orbach but also other processes such as Raman are operative.

The Dy(III) analogue of **43** also shows slow relaxation of magnetisation with slightly smaller barrier height of 20 K as compared to **43**. However, Tb(III) and Ho(III) analogue don't possess any SIM behaviour although they are in same coordination environment.

Recently, using the Tpz ligand, the same group has reported an eight-coordinated Yb-complex $[\text{YbTpz}_2\text{NO}_3]$ (**44**) (Fig. 26a) and investigated its magnetic anisotropy through low temperature near-IR luminescence, polarised neutron diffraction (PND) and

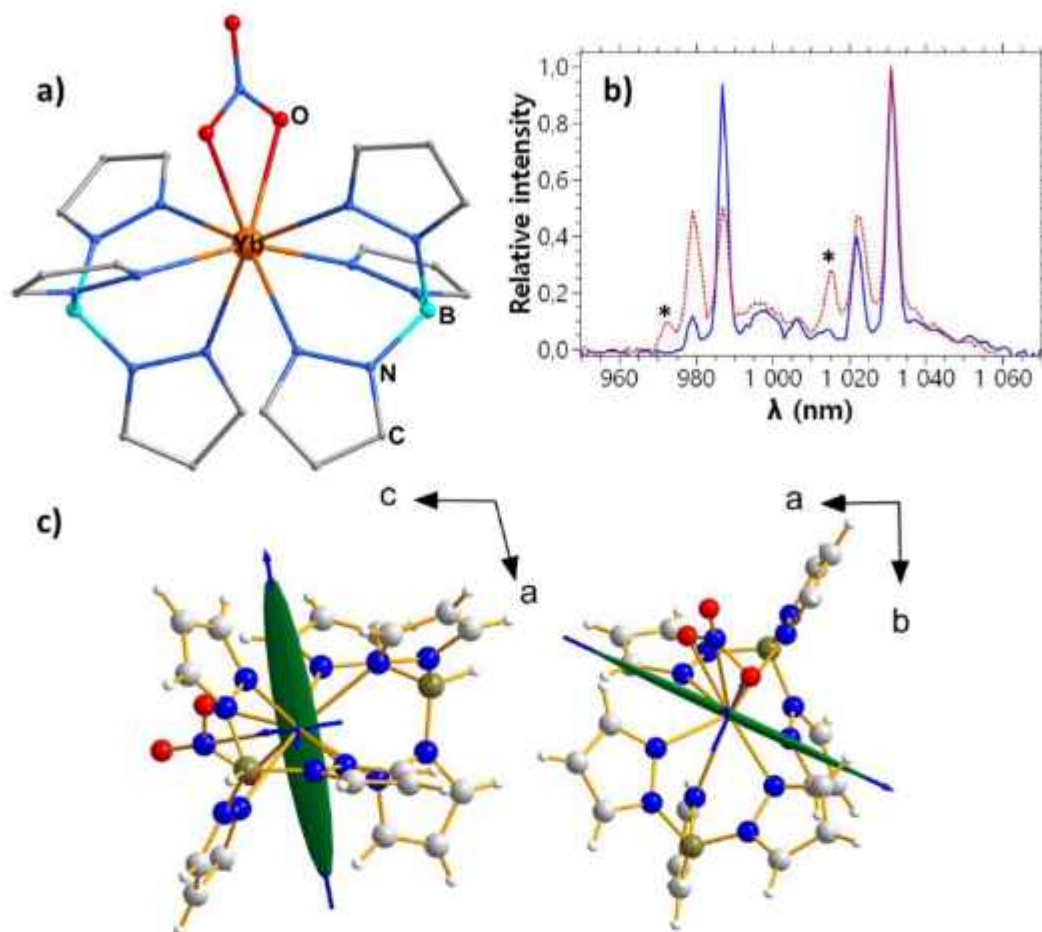


Fig. 26. (a) Molecular structure of $[\text{Yb}(\text{trensal})\text{NO}_3]$ (**44**). (b) Luminescence spectrum for **44** collected below 10 K (blue line) and at 77 K (red dashed line) and under excitation of light of wavelength 300 nm. Black asterisks represent the hot band transitions. (c) PND measurements deduced susceptibility tensor, blue arrows represent the magnetic axes present in the molecule. Reprinted from [192]. Copyright 2019 Royal Society of Chemistry.

single crystal SQUID measurements [192]. The ${}^2F_{5/2} \rightarrow {}^2F_{7/2}$ transition occurring in the NIR region (upon 300 nm excitation at 10 K and 77 K) estimates the relative energy of the first excited state to be 119.5 K with a total splitting value as 516 cm^{-1} . These values are well supported by ab initio calculations carried out on **44** (158 K and 759 K respectively), suggesting the existence of strong magnetic anisotropy. This was also confirmed by single crystal SQUID measurements and PND experiments. The PND measurement predicts the easy axis of magnetisation is close to the crystallographic a-axis (almost coplanar with the nitrate ligand), while the hard axes are found near b and c axes (Fig. 26c). Even though a large magnetic anisotropy is expected from these data, there is no out-of-phase magnetic susceptibility in the absence of any external magnetic field, suggesting rapid magnetisation relaxation due to non-negligible QTM. Under the application of 2000 Oe magnetic field, **44** shows frequency and temperature dependence of χ' and χ'' signals in the temperature range 2–6 K. The plot of τ vs T can be best fitted by considering Raman spin-phonon coupling along with either QTM or direct process with $C = 0.00636 \text{ s}^{-1} \text{ K}^{-n}$ and $n = 9$, this excludes the possibility of the presence of Orbach process in relaxation dynamics.

In 2015, Larionova and co-workers have explored magnetic properties of a mononuclear organoytterbium(III) complex, $[\text{Cp}^*\text{Yb}(\text{DAD})(\text{THF})]\cdot\text{C}_7\text{H}_8$ (**45**) (where, DAD = 2,6- $\text{Me}_2\text{C}_6\text{H}_3\text{N}=\text{CHCH}=\text{NC}_6\text{H}_3\text{Me}_2\cdot 2,6$) [193,194] where coordination environment of the Yb(III) ion consists of η^5 -coordinated Cp^* ligand, a $2\sigma:\eta^2$ -coordinated DAD^{2-} dianion, and one THF molecule

forming a heteroleptic half-sandwich structure (Fig. 27a) [195]. Complex **45** does not show any slow magnetic relaxation in the absence of an external magnetic field. However, frequency dependent out-of-phase ac susceptibility signals can be observed after applying dc fields, with clear maxima in the presence of dc fields larger than 300 Oe. The maxima can be observed up to 4.4 K in the presence of an optimum dc field of 1500 Oe. The nonlinear behaviour of $\ln \tau$ vs T^{-1} confirms the presence of multiple relaxation processes. The data were fitted by considering Orbach, two phonon Raman and direct relaxation processes with the equation, $\tau^{-1} = \tau_0^{-1} \exp(-U_{\text{eff}}/kT) + CT^m + AT$ (first term for an Orbach process, while the second and third ones stand for two phonon Raman and direct relaxation processes). The best fitted data over the whole temperature range yields $U_{\text{eff}} = 20 \text{ K}$, $\tau_0 = 1.74 \times 10^{-6} \text{ s}$, $C = 0.00208 \text{ s}^{-1} \text{ K}^{-n}$, $n = 9$ and $A = 518.33 \text{ s}^{-1} \text{ K}^{-1}$. The relaxation dynamics is dominated by both Orbach at higher temperature and direct processes at low temperature region.

Pilgkos and co-workers have reported a trensal ligand based mononuclear Yb(III) complex $[\text{Yb}(\text{trensal})]$ (**46**) ($\text{H}_3\text{trensal} = 2,2',2''\text{-tris}(\text{salicylideneimino})\text{triethylamine}$ (Fig. 28a and b) [196]) [197]. Single-crystal X-band EPR spectra of $\sim 5\%$ **46**, doped in isostructural $\text{Eu}(\text{trensal})$ matrix, clearly confirms the anisotropic nature of g tensor ($g_{\parallel} = 4.29$, and $g_{\perp} = 2.90$) (Fig. 28c). With the help of high resolution absorption and near infrared luminescence spectroscopies of pure **46** and $\sim 10\%$ **46** doped in isomorphous $\text{Y}(\text{trensal})$, the energy separation ($U_{\text{eff, spec}}$) between the ground and first excited Kramers doublets of ${}^2F_{7/2}$ has been estimated as

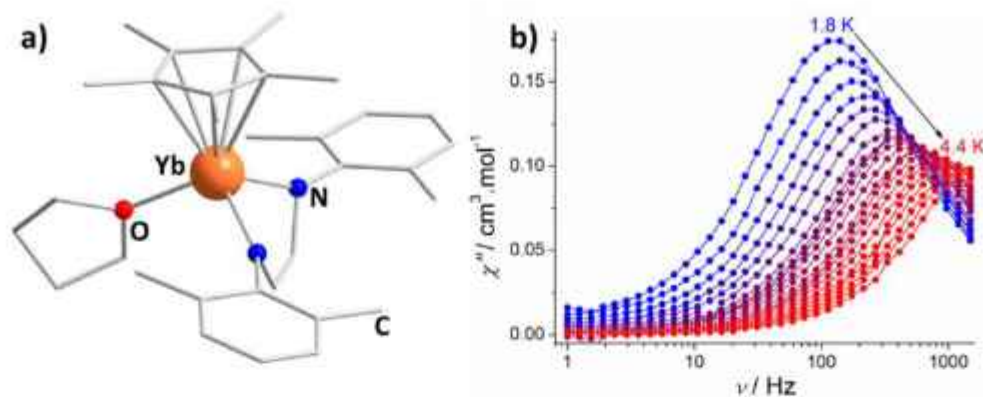


Fig. 27. (a) Molecular structure of complex $[[\text{Cp}^*\text{Yb}(\text{DAD})(\text{THF})] \text{C}_7\text{H}_{11}]$ (**45**). (b) Frequency dependence of the out-of-phase susceptibility in presence of optimum dc field of 1500 Oe. Reprinted from [195]. Copyright 2015 American chemical society.

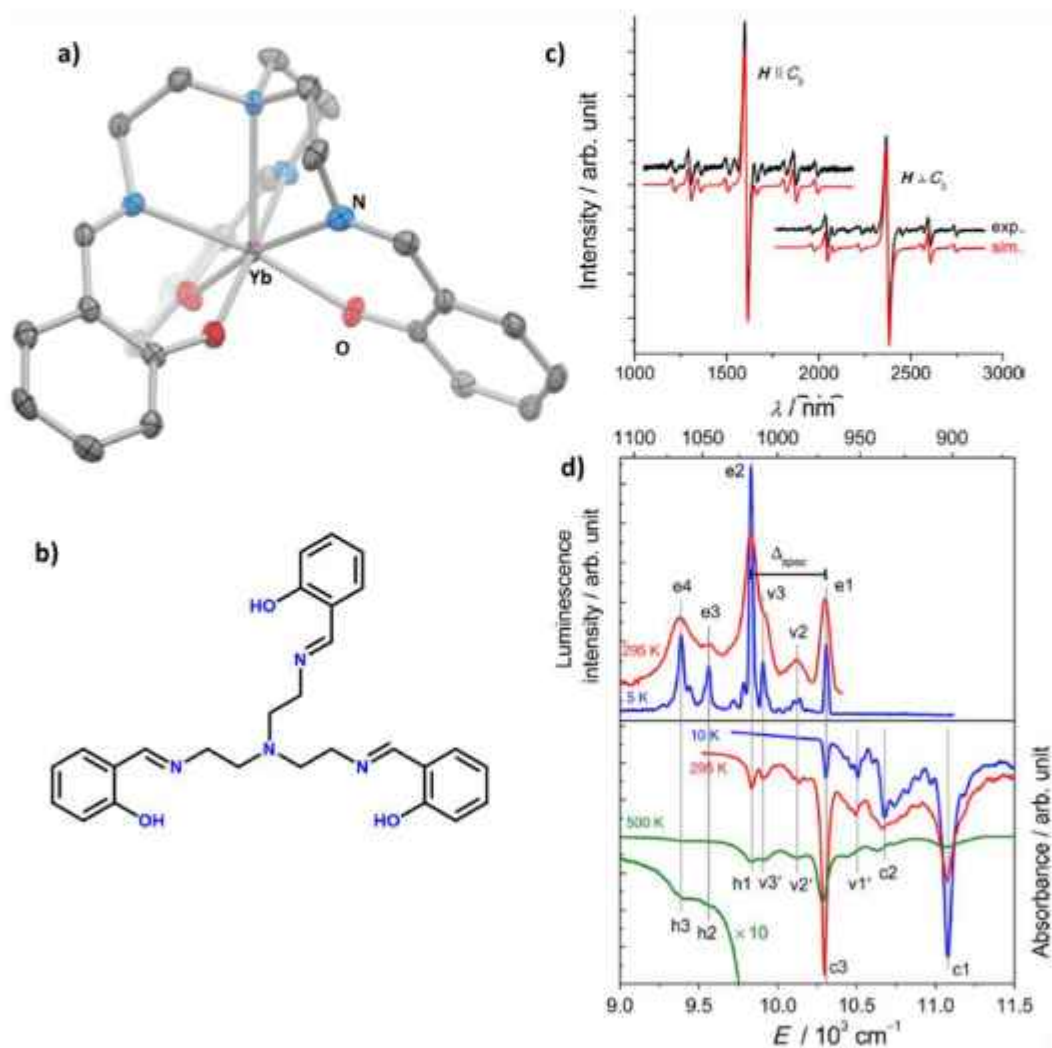


Fig. 28. (a) Molecular structure of complex $[\text{Yb}(\text{trensal})]$ (**46**). (b) The trensal ligand used in **46**. (c) Single-crystal X-band ($f = 9.62$ GHz) EPR spectra at $T = 10$ K of **46** ($\sim 5\%$) in $\text{Eu}(\text{trensal})$ lattice (black and red lines represent the experimental and simulated graph). (d) The luminescence (above) and NIR absorption (bottom) spectra for **46**; c, h, e, and v correspond to the cold absorption, hot absorption, emission, and vibrational transitions, respectively, associated with **46**. Reprinted from [197]. Copyright 2015 American chemical society.

668 K (Fig. 28d). The high separation obtained from energy spectrum led to inspection of the dynamic properties of the system. AC susceptibility measurements have been carried out on both

single-crystal and powder form of **46**. Though neither of them shows out-of-phase signal in the absence of a static dc field, on the application of a small dc field, clear χ'' maxima are observed

in both $H_{ac}||C_3$ and $H_{ac}\perp C_3$ orientations (where H_{ac} is the applied dc field and C_3 is the three-fold rotational axis present in **46**) of the crystal as well as the powdered sample of **46**. This reveals the anisotropic behaviour of relaxation times *w.r.t.* the alignment of the applied field. At optimised dc field of 2000 Oe, clear maxima can be observed up to 10 K for single crystal placed in $H_{ac}||C_3$ direction and for powdered sample and 5.9 K for single crystal placed in $H_{ac}\perp C_3$ direction. The U_{eff} (54.7 K) obtained by fitting of τ to an Orbach model for higher temperature region is far smaller than that predicted from absorption and luminescence spectra (668 K), implying the dominance of other relaxation processes, but not Orbach process. The plots were fitted by considering the equation, $\tau^{-1} = CT^n + DT^m$, where the first term is dominant at high T and second is dominant at low T. For $H_{ac}||C_3$, the data were fitted with the parameters: $C = 0.044 \text{ s}^{-1} \text{ K}^{-6.9}$, $n = 6.9$, $D = 19 \text{ s}^{-1} \text{ K}^{-2}$ and $m = 2$, expecting the presence of Raman as well as phonon-bottleneck-limited direct processes [198]. In case of the powdered sample of **46**, the parameters corresponding to the best fitted plot are: $C = 0.15 \text{ s}^{-1} \text{ K}^{-6.2}$, $n = 6.2$, $D = 258 \text{ s}^{-1} \text{ K}^{-1}$ and $m = 1$ indicating the presence of normal direct process along with the Raman process. They have further observed that quantum coherence is detected in isotope selective pulsed-EPR spectroscopy on an oriented single crystal of **46**. This complex is expected to be a good candidate as SIM qubit for quantum information processing [199].

The chemistry of tetrathiafulvalene (TTF)-based ligands has been well explored over the years due to their efficient electron donation ability and consequent electronic conductivity [200–203]. The lanthanide complexes based on TTF are popular due to their optical properties arising from their strong electronic delocalization [204]. Ouahab and co-workers have reported a complex with a modified TTF ligand, $[\text{Yb}(\text{tta})_3(\text{L})] \cdot 2\text{CH}_2\text{Cl}_2$ (**47**) (tta: 2-thenoyltrifluoroacetate and L: 4,5-ethylenedioxy-4',5'-bis(2-pyridyl)-N-oxidemethylthio)tetrathiafulvalene) and investigated its relaxation dynamics with the help of both luminescent and SQUID measurements [205]. Complex **47** does not show any frequency dependent χ'' signals in the absence of any external field. However, signals exist up to nearly 4 K on application of external field of 1000 Oe. The $\ln\tau$ vs T plot fits well with the help of only thermally activated process with $\tau_0 = 1.9 \times 10^{-5} \text{ s}$ and $U_{eff} = 6 \text{ K}$. The TTF

derived ligand highly enhances the sensitisation of the luminescent property of Yb(III) complex through antenna effect, that can be correlated to its magnetic data. Investigation of photophysical properties of **47** with the help of absorption and emission spectroscopy suggest that the energy splitting between the ground state ($m_j = \pm 5/2$) and first excited state ($m_j = \pm 7/2$) is 337 K, which is confirmed from the results of MS-CASPT2/RASSI-SO calculations.

Replacement of 4,5-ethylenedioxy-4',5'-bis(2-pyridyl)-N-oxide methylthio)tetrathiafulvalene (L) in **47** by 2-(1-methylpyridyl)-4,5-(4,5-bis(propylthio)tetrathiafulvalenyl)-1H-benzimidazol-2-yl)pyridine (L') ligand results in Yb(III) complex, $[\text{Yb}(\text{tta})_3(\text{L}')] \cdot \text{C}_6\text{H}_{14}$ (**48**), possessing a D_{4d} symmetric distorted-square-antiprism coordination environment around the metal ion. [206] (see Fig. 29a and b for L and L') Interestingly, **48** does not show any SIM behaviour even in presence of external magnetic field. Unlike its Dy(III) analogue, **48** does not behave as an Ising system (confirmed with angular-resolved magnetometry on single crystal) and hence no SIM behaviour.

Two Yb(III) complexes derived from a rhodamine-based ligand (HQR₁), $[\text{Yb}(\text{QR}_1)(\text{tta})_2] \cdot \text{CH}_3\text{OH}$ (**49**) and $[\text{Yb}(\text{QR}_1)_2][\text{NO}_3] \cdot (\text{CH}_3\text{OH})(\text{H}_2\text{O})_{0.5}$ (**50**) (HQR₁ = rhodamine-6G-2-(hydrozinomethyl)quinolin-8-ol; Fig. 30c) were reported by Jiang and co-workers. The two complexes were synthesised from the reaction of $\text{Ln}(\text{tta})_3 \cdot 2\text{H}_2\text{O}$ and HQR₁ ligand [207]. In both the complexes, Yb(III) is in eight coordinated environment having YbO_6N_2 (in **49**) and YbN_6O_4 (in **50**) coordination sphere. At zero external magnetic field, no χ'' signals were observed while in presence of an external field of 1000 Oe, these complexes show frequency dependence of χ'' signals up to 6 K. The magnetisation relaxation in both cases occur via a thermally activated mechanism with $U_{eff} = 16.1 \text{ K}$ and $\tau_0 = 1.78 \times 10^{-7} \text{ s}$ for **49** and $U_{eff} = 5.37 \text{ K}$ and $\tau_0 = 1.0 \times 10^{-5} \text{ s}$ for **50**, based on the Arrhenius law. These results suggest that even a small modification in coordination sphere can largely affect the magnetic relaxation dynamics in Yb(III) complexes. The electronic effective g-values for both the complexes were estimated with the help of X-band EPR spectra collected at 5 K as $g_{eff} = 5.35$ for **49** and $g_{eff} = 6.05$ for **50**.

Herrera and co-workers have reported a set of three mononuclear ytterbium complexes **51–53**, based on a tridentate ligand

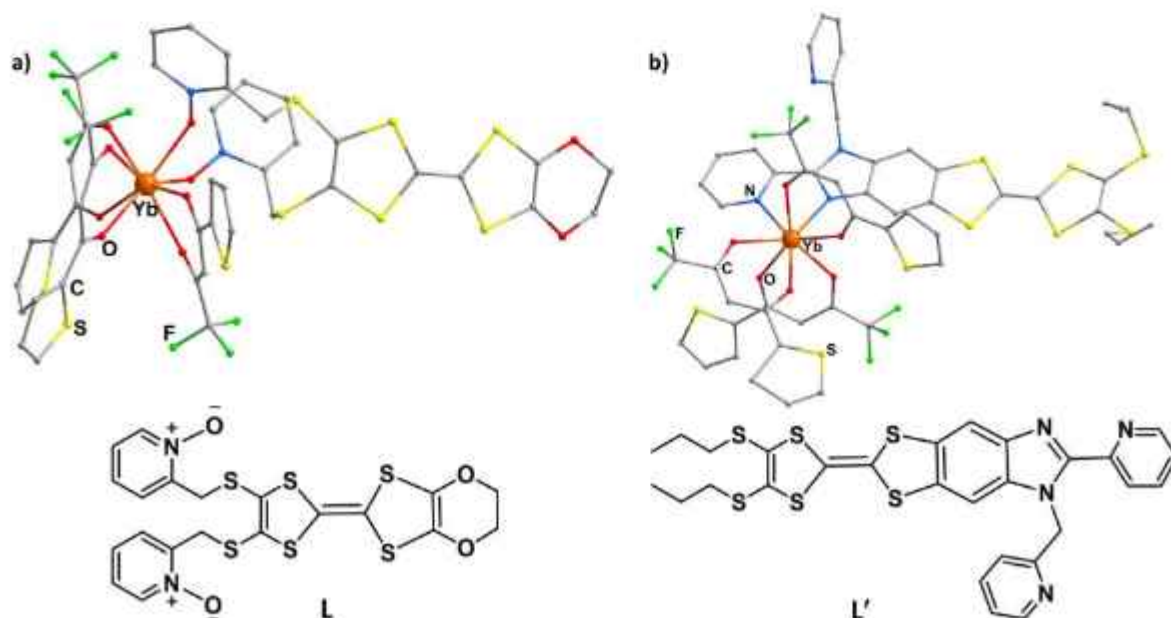


Fig. 29. The molecular structure of the complexes: (a) $[\text{Yb}(\text{tta})_3(\text{L})] \cdot 2\text{CH}_2\text{Cl}_2$ (**47**) and (b) $[\text{Yb}(\text{tta})_3(\text{L}')] \cdot \text{C}_6\text{H}_{14}$, (**48**). The lattice molecules and the hydrogen atoms are omitted for clarity. Regenerated and Reprinted from [205–206]. Copyright 2014 Wiley-VCH.

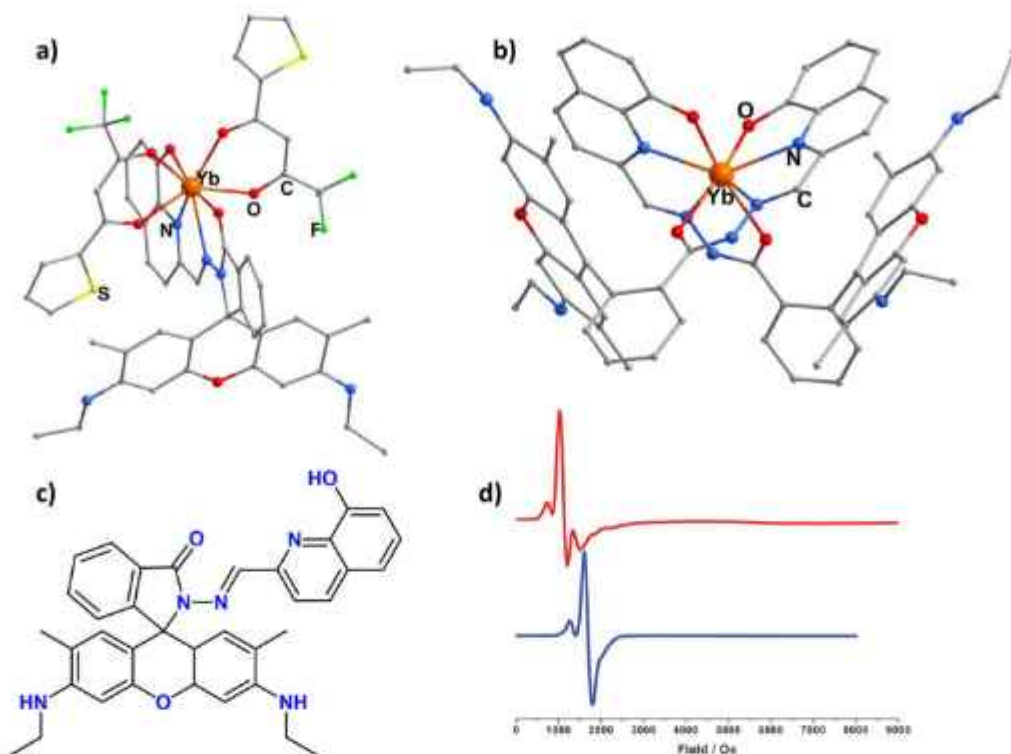


Fig. 30. Molecular structure of (a) $[\text{Yb}(\text{OR})_2(\text{tta})_2] \cdot \text{CH}_3\text{OH}$ (**49**) and (b) $[\text{Yb}(\text{OR})_2](\text{NO}_3)_2 \cdot (\text{CH}_3\text{OH})(\text{H}_2\text{O})_{0.5}$ (**50**), (c) the HQR ligand used and (d) X-band EPR spectra of powder samples of **49** (red) and **50** (blue) collected at 5 K. Reprinted from [207]. Copyright 2017 Royal Society of Chemistry.

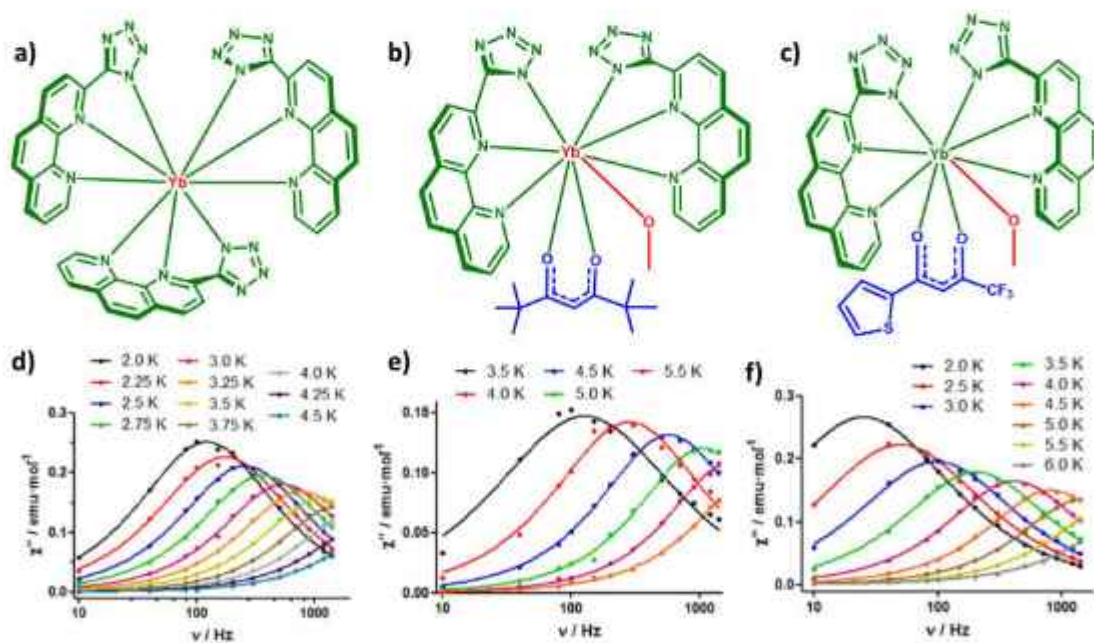


Fig. 31. Structures of Yb(III) complexes (a) $[\text{Yb}(\text{L})_3]$ (**51**), (b) $[\text{Yb}(\text{L})_2(\text{TMH})(\text{CH}_3\text{OH})]$ (**52**) and (c) $[\text{Yb}(\text{L})_2(\text{tta})(\text{CH}_3\text{OH})]$ (**53**). The frequency dependence of χ'' signals Oe for (d) **51**, (e) **52** and (f) **53** in presence of 1000 Oe external magnetic field. Reprinted from [208]. Copyright 2016 Wiley-VCH.

2-(tetrazole-5-yl)-1,10-phenanthroline (HL) (Fig. 31) [208]. Three of the ligands coordinate to the Ln(III) centre resulting an LnN_9 coordination sphere in case of the first complex. The second and third have been synthesized by replacement of one of the three ligands by a combination of one methanol molecule and a β -diketonate ligand (either by 2,2,6,6-tetramethylheptane-3,5-dione (TMH) or 2-thenoyltrifluoroacetone (tta)). These modifica-

tions result in creating LnN_6O_3 coordination sphere in **52** and **53**. In all the three complexes, Yb(III) ion is in spherical capped square antiprism shaped coordination environment. None of the three Yb(III) complexes, i.e. $[\text{Yb}(\text{L})_3]$ (**51**), $[\text{Yb}(\text{L})_2(\text{TMH})(\text{CH}_3\text{OH})]$ (**52**) and $[\text{Yb}(\text{L})_2(\text{tta})(\text{CH}_3\text{OH})]$ (**53**), display χ'' signals in the absence of an external dc field. But they exhibit frequency dependence of χ'' signals in the presence of 1000 Oe external field, indicating effective

suppression of QTM. The Arrhenius fitting of $\ln\tau$ vs $1/T$ yields U_{eff} values of 11.7 K, 29.7 K and 30.3 K for **51**, **52** and **53**, respectively. However, as Raman relaxation process usually dominates the other processes in Yb(III) SMMs, attempt to fit the data with sole contribution from Raman process ($1/\tau = BT^n$) was carried out. The Raman dominance of magnetisation relaxation dynamics yields good agreement with the experimental data with the parameters $C = 82.1 \text{ s}^{-1}\text{K}^{-n}$ and $n = 3.6$ for **51**, $C = 0.2 \text{ s}^{-1}\text{K}^{-n}$ and $n = 6.5$ for **52** and $C = 0.3 \text{ s}^{-1}\text{K}^{-n}$ and $n = 6.5$ for **53** suggesting that the relaxation proceeds via an optical-acoustic Raman-like process rather than Orbach process.

Carlos and co-workers have reported a series of mononuclear Ln(III) complexes (Ln = Eu, Tb, Dy, Ho, Er and Yb) based on N,N'-3-Nitrosalicylaldehydeethylenediamine ligand (Fig. 32b) where Ln(III) centre is encapsulated by two 3-NO₂-salen²⁻ ligands with meridional arrangement and one triethylammonium cation outside the coordination sphere [209]. The Yb(III) analogue, (Et₃NH)[Yb(3-NO₂-salen)₂] (**54**) does not show any non-zero χ'' signals in the absence of a bias field. On application of 1500 Oe dc field, it shows frequency dependent χ'' signals up to 2.8 K, without any maxima, affording $U_{\text{eff}} = 7.5 \text{ K}$ and $\tau_0 = 4.1 \times 10^{-6} \text{ s}$ (fitted with Arrhenius Law). The magnetisation barrier is much smaller than the corresponding Dy(III) analogue ($U_{\text{eff}} = 39.7 \text{ K}$), suggesting that the meridional configuration is more favourable for oblate shaped ion as compared to prolate ions to achieve higher barrier of magnetic reversal.

Although Dy(III) based SMMs with D_{5h} symmetry have been found to have higher U_{eff} and T_B , the same credentials for Yb(III) have not been explored until 2017. Though D_{5h} symmetric ligand field with strong axial ligands is more favourable for oblate shaped ions rather than for prolate ions, Wang and co-workers have examined two Yb(III) complexes where Yb(III) is in D_{5h} symmetric ligand field consisting of two axial chloride ions and the equatorial positions are occupied by the N and O atoms from the monodeprotonated ligand H₃Bmsp along with two dimethylformamide (DMF) ligands. Complexes [(Yb(H₃Bmsp)(DMF)₂Cl₂)]·DMF·1.5H₂O (**55**) and [(Yb(H₃Bmsp)(DMF)₂Cl₂)]·H₄Bmsp (**56**), (H₄Bmsp = 2,6-bis[(3-methoxysalicylidene)hydrazinecarbonyl]-pyridine) (Fig. 33b) [210] have been synthesized from the reaction of one equivalent of YbCl₂·6H₂O with one or two equivalents of H₃Bmsp ligand, respectively. Both the D_{5h} symmetric coordination environment around the Yb(III) ion as well as the molecules of **55** and **56** are almost similar except one extra non-coordinating ligand H₄Bmsp present in the lattice. Interestingly, this minor difference in structures of the two complexes result in significant change in their slow relaxation of magnetisation behaviour. Though there is no ac susceptibility signal in the absence of a dc field for both these complexes, they show frequency dependent χ'' signals with clear maxima up to 5 K on the application of optimised field (1500 Oe for **55** and 600 Oe for **56**). The U_{eff} values can be estimated by the fitting of high temperature data points of $\ln\tau$ vs T^{-1} plot yielding U_{eff} of 14.5 K and 38.3 K for **55** and **56**, respectively, which are

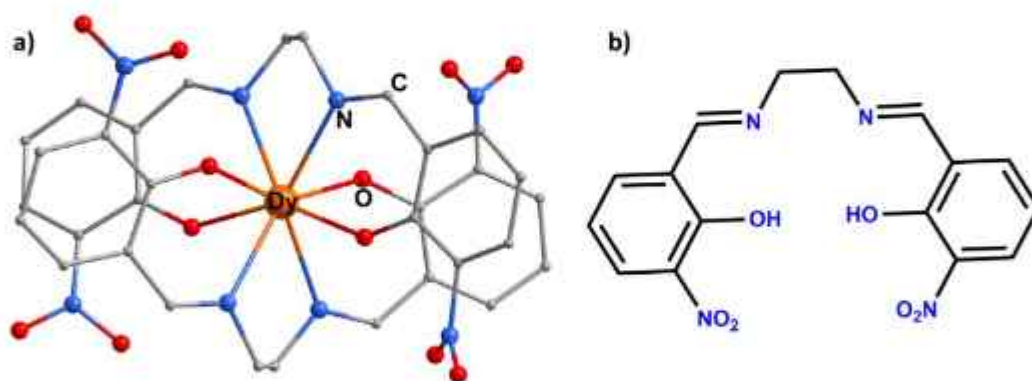


Fig. 32. Structure of (a) the anionic part of Dy analogue of **54** and (b) 3-NO₂-salenH₂.

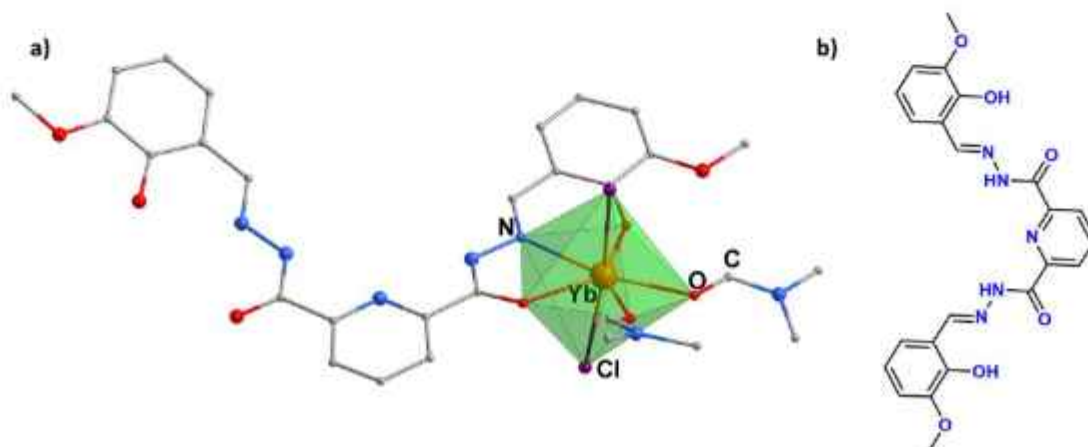


Fig. 33. Molecular structure of (a) [(Yb(H₃Bmsp)(DMF)₂Cl₂)]·DMF·1.5H₂O (**55**) along with the D_{5h} symmetric coordination polyhedra around Yb(III) ion. (b) The ligand H₄Bmsp, used in **55** and **56**. Reprinted from [210]. Copyright 2017 Royal Society of Chemistry.

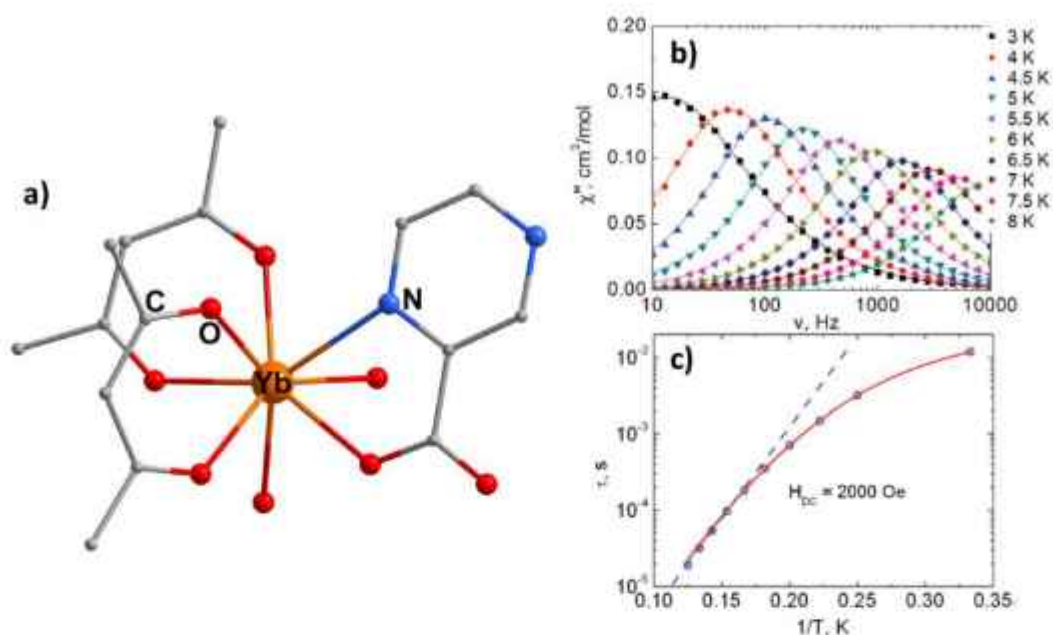


Fig. 34. (a) Crystal structure, (b) frequency dependence of out-of-phase (χ'') component in presence of 2000 Oe, and (c) plots of τ vs $1/T$ for $[\text{Yb}(\text{PyCOO})(\text{acac})_2(\text{H}_2\text{O})_{11}]$ (**57**). Blue dashed line : best fit to Arrhenius law for the temperature range 6.5–8 K, solid red line: best fit by considering direct, Raman and Orbach relaxation mechanisms. Reprinted from [211]. Copyright 2017 Royal Society of Chemistry.

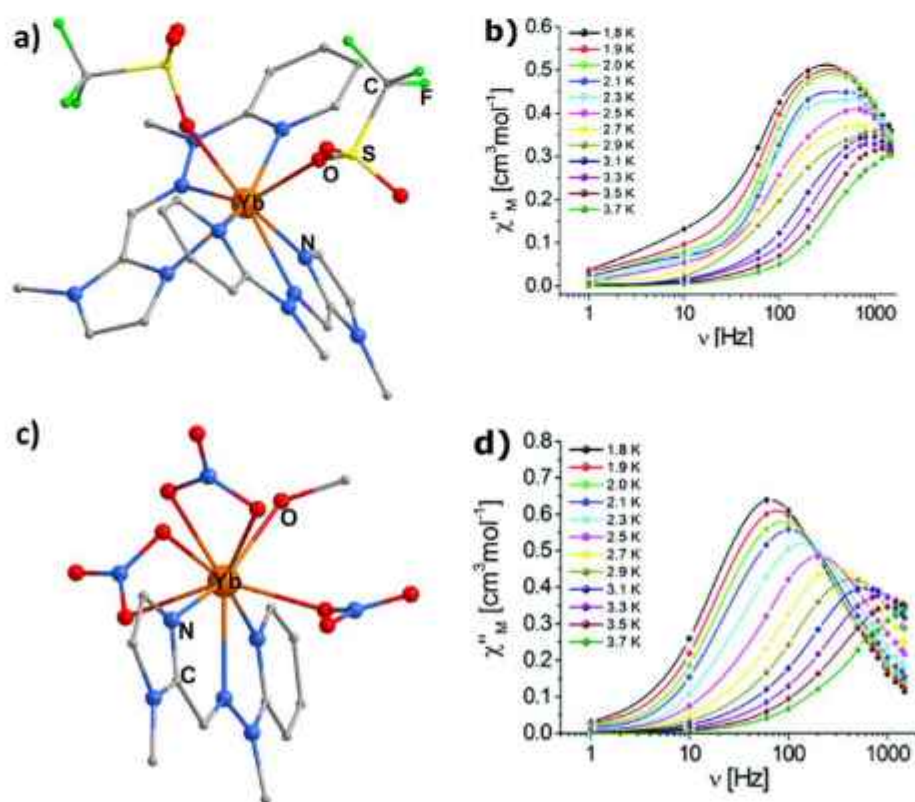


Fig. 35. Crystal structures of (a) $[\text{YbL}_2(\text{OTf})_2](\text{OTf})$ (**58**) and (c) $[\text{YbL}(\text{NO}_3)_3](\text{MeOH})\text{MeCN}$ (**59**). Lattice solvent molecules and anions are omitted for clarity. Their frequency-dependence of the out-of-phase ac susceptibility components for (b) **58** and (d) **59**. Adopted from [212].

far smaller than the energy calculated from ab-initio calculations (calculated U_{eff} values are close to 290 K). This suggests the dominance of different relaxation pathways like direct and Raman over Orbach in the relaxation dynamics. In case of **55**, incorporating Orbach relaxation does not give good fit, but can be better fitted by considering both direct and Raman process with $A = 368.1 \text{ s}^{-1} \text{ K}^{-1}$, $C = 12.2 \text{ s}^{-1} \text{ K}^{-n}$, and $n = 3.6$. The plot of $\ln \tau$ vs T^{-1} for **56** can be fitted by considering direct, Raman, and Orbach relaxation processes with $A = 10.2 \text{ s}^{-1} \text{ K}^{-1}$, $C = 0.38 \text{ s}^{-1} \text{ K}^{-n}$, $n = 5.6$, $\tau_0 = 5.77 \times 10^{-7} \text{ s}$ and $U_{\text{eff}} = 43.82 \text{ K}$. The U_{eff} value is still far smaller than calculated, suggesting that Raman and direct process have large dominance over the thermal process.

Novotortsev and co-workers have reported a series of isomorphous mononuclear eight coordinated Ln(III), Ln = Eu–Yb and Y, complexes. These molecules contain a pyrazine-2-carboxylate ligand (PyCOO^-) ligand along with two water molecules and two acetylacetonate (acac^-) co-ligands, resulting a LnO_7N_1 sphere (Fig. 34) [211]. Among these, Tb, Dy, Er and Yb derivatives exhibit SMM behaviour to different extent. The Yb derivative, $[\text{Yb}(\text{PyCOO})(\text{acac})_2(\text{H}_2\text{O})_2]$ (**57**), however does not show any χ'' signals when there is no external magnetic field. On application of 2000 Oe external field, **57** shows non zero χ'' signals with clear maxima in the temperature range of 3–8 K. The fitting of τ vs $1/T$ reveals that **57** relaxes via Orbach, direct and Raman processes, yielding $U_{\text{eff}} = 54 \text{ K}$ and $\tau_0 = 7.4 \times 10^{-8} \text{ s}$, $A_{\text{direct}} = 1.1 \times 10^{-12} \text{ s}^{-1} \text{ Oe}^{-4} \text{ K}^{-1}$, $m_{\text{direct}} = 4$ and $C_{\text{Raman}} = 0.013 \text{ K}^{-7} \text{ s}^{-1}$ and $n_{\text{Raman}} = 7$. Complex **57** has the highest barrier for magnetisation reversal among all the reported Yb(III) carboxylate based SIMs.

Patroniak and co-workers have reported Yb(III) complexes, $[\{\text{YbL}_2(\text{OTf})_2\}(\text{OTf})]$ (**58**) and $[\{\text{YbL}(\text{NO}_3)_3(\text{MeOH})\} \cdot \text{MeCN}]$ (**59**), (L = 2-(1-methyl-2-((1-methyl-1H-imidazol-2-yl)methylene)hydrazinyl)pyridine), having YbN_6O_2 (triangular dodecahedron, D_{2d} symmetric) (**58**) and LnN_3O_6 (Capped square antiprism, C_{4v} symmetric) (**59**) coordination spheres [212]. In **58**, two OTf^- ions and two L and in **59**, one L, three nitrate ions (two bidentate and one monodentate) with one MeOH molecules are coordinated to the Yb(III) centres. Though there is no SMM behaviour in absence of dc field, both show frequency and temperature dependent non zero χ'' signals with clear maxima up to 3.7 K. The U_{eff} values have been found to be 11.7 K and 17.8 K for **58** and **59**, respectively. Along with Orbach process, Raman process is also operative in the relaxation of magnetisation for both the complexes. The best fit of $\ln \tau$ vs T^{-1} plot yields $C = 6 \text{ s}^{-1} \text{ K}^{-n}$, $n = 0.3$ for **58** and $C = 4 \text{ s}^{-1} \text{ K}^{-n}$, $n = 0.6$ for **59**. In case of Er analogue of **58** and **59**, only Orbach process is operative with $U_{\text{eff}} < 10 \text{ K}$. A magneto-structural correlation

suggests that the use of N donor anions in place of O-donor anions (nitrate and triflate) can increase the barrier height further by stabilisation of the easy-axis of magnetisation.

Ruiz and co-workers have reported an Yb(III) based complex $[\{\text{Yb}(\text{H}_2\text{O})_3(18\text{-crown-6})\}(\text{ClO}_4)_3]$ (**60**) where Yb(III) centre is wrapped by 18-crown-6 in a zig-zag fashion through equatorial plane and three water molecules coordinated in an ‘Y’ fashion (Fig. 36a) [213]. The complex shows non-zero χ'' signals up to 6 K only in the presence of an external field of 500 Oe. The best fit to τ^{-1} vs T plot suggests that the molecule relaxes via Orbach, Raman processes along with QTM with the parameters: $C = 0.3289 \text{ s}^{-1} \text{ K}^{-n}$, $n = 5.80$, and $\tau_{\text{QTM}} = 0.00075 \text{ s}$ with U_{eff} is around 5.9 K and $\tau_0 = 2.61 \times 10^{-9} \text{ s}$, which is far smaller than the Dy(III) analogues (67 K). This observation suggests that the ligand consisting of equatorial 18-crown-6 and axial water molecules, is better for the oblate shaped Ln(III) ions rather than the prolates. Computational study reveals the anisotropic nature of the g-tensor in **60**, although small ($g_x = 0.23$, $g_y = 2.38$ and $g_z = 5.49$). The β electron density and electrostatic potentials indicate that the relatively smaller magnetic anisotropy obtained in such complexes is due to the small repulsions from the axial ligands, i.e. three water molecules (Fig. 36b).

Examples of lanthanide complexes with hexagonal bipyramidal geometry having SIM behaviour are fewer in number. Luo and co-workers have reported an air-stable P=O based Yb(III) complex, $[\text{Yb}(\text{NO}_3)_3(\text{Bu}_3\text{P}=\text{O})_2]$ (**61**), where three coplanar nitrate ions are in equatorial position and two $\text{Bu}_3\text{P}=\text{O}$ occupy the axial positions, resulting hexagonal bipyramidal LnO_8 geometry with ideal D_{3h} symmetry [214]. The axial Yb–O(P) bonds are shorter than the equatorial Yb–O(N) bonds. In absence of any external magnetic field, **61** does not show any frequency dependence χ'' signals. However, in presence of optimised dc field (1000 Oe), it shows non-zero χ'' signals up to 4 K. The fitting of the plot of $\ln \tau$ vs $1/T$ by using the Arrhenius law in the high temperature regime yields $U_{\text{eff}} = 23.0 \text{ K}$, which is far smaller than the calculated energies gap between ground and first excited state ($U_{\text{eff, cal}} = 335.5 \text{ K}$). This observation excludes the possibility of the presence of Orbach process in relaxation dynamics of **61**. The data can be best fitted by a combination of direct and Raman processes ($\tau^{-1} = AT + CT^n$) with $A = 23.5 \text{ s}^{-1} \text{ K}^{-1}$, $C = 0.29 \text{ s}^{-1} \text{ K}^{-n}$, and $n = 7.01$. Raman process dominates in the region of higher temperature (2.2–4.0 K), while in lower temperature region (1.8–2.0 K) direct process dominates over Raman process. The individual contribution of the relaxation processes are shown in Fig. 37b. The g tensors of the ground state ($g_x = 4.575$, $g_y = 4.553$ and $g_z = 1.171$) indicates the existence of

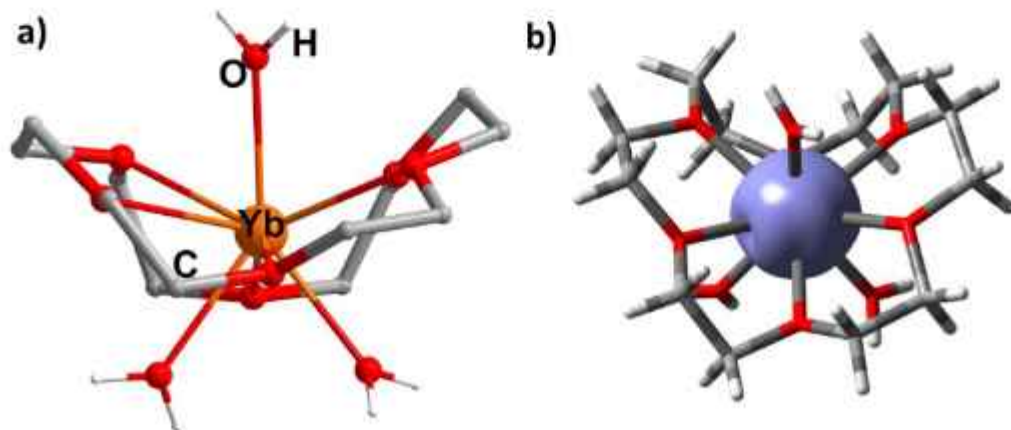


Fig. 36. (a) Molecular structure and (b) isosurface of the calculated β electron density of $[\{\text{Yb}(\text{H}_2\text{O})_3(18\text{-crown-6})\}(\text{ClO}_4)_3]$ (**60**). Reprinted from [213], Copyright 2018 American Chemical Society.

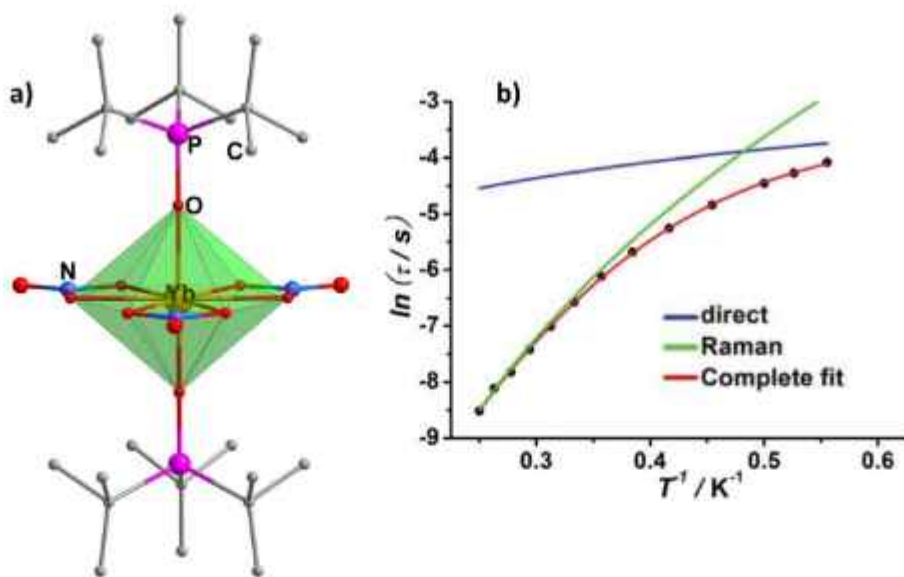


Fig. 37. (a) Crystal structure of $[\text{Yb}(\text{NO}_3)_4(\text{Bu}_3\text{P}-\text{O})]$ (**61**). b) The plot of temperature dependence of relaxation times. The non-linear fit can be fitted well by considering Raman and direct process. The individual contribution of direct and Raman processes are shown in green and blue line, respectively. Reprinted from [214]. Copyright 2019 Royal Society of Chemistry.

easy-plane magnetic anisotropy in **61**. Unlike **61**, the Tb(III) analogue does not show any χ'' signals even after application of an external magnetic field.

Kostakis and co-workers have reported a series isostructural sulfonate ligand based mononuclear Ln(III) complexes $[\{\text{Ln}(\text{NAS})_2(\text{H}_2\text{O})_6\}(\text{NAS})\cdot 3\text{H}_2\text{O}]$ (Ln = Tb, Dy, Er and Yb), where two 2-naphthalenesulfonate (NAS) ligands and six water molecules coordinate to the Ln(III) centre forming a square antiprismatic geometry (D_{4d}) [215,216]. All the complexes crystallise in chiral $P2_1$ space group, which has been confirmed from single crystal circular dichroism (CD) spectra having opposite Cotton effect. The Yb(III) analogue **62** behaves as a field induced SMM, showing non-zero χ'' signals with clear maxima up to 6 K in presence of an optimised bias field of 1000 Oe. The fit of the linear parts corresponding to high temperature range of plot $\ln\tau$ vs $1/T$ yields $U_{\text{eff}} = 45$ K and $\tau_0 = 5.1 \times 10^{-8}$ s. The non-linear nature of this plot indicates the presence of multiple relaxation processes in the relaxation dynamics of **62** (Fig. 38). The plot of $\ln\tau$ vs $1/T$ over the entire temperature range can be fitted by considering both Raman and QTM process with $C = 6.8 \times 10^{-4} \text{ K}^{-n}$, $n = 9.3$, $\tau_{\text{QTM}} = 0.385$ s. This observation suggests that the relaxation is dominated by Raman and QTM, but not Orbach process.

Zheng and co-workers have reported a series of Ln(III) (Ln = Gd, Dy, Er and Yb) complexes based on an anthracene based phosphonate ligand [217]. The ligand field around the Ln(III) centre is almost identical to that in **62**, except two depma ligands (depma = 9-diethylphosphonomethylanthracene) are present here in place of NAS. Two depma ligands bonded to the Yb(III) centre via P=O ligands and six water molecules forming a slightly distorted triangular dodecahedron (D_{2d} symmetry) coordination environment. The Yb(III) analogue, $[\{\text{Yb}(\text{depma})_2(\text{H}_2\text{O})_6\}(\text{Cl})\cdot 3\text{H}_2\text{O}(\text{CH}_3\text{O})]$ (**63**) does not show any non-zero χ'' signals in absence of an external magnetic field, but it exists clearly up to 6 K in the presence of an optimum dc field (750 Oe). The $\ln\tau$ vs $1/T$ curve is fitted by considering both Orbach and Raman process in the relaxation dynamics of **63** yielding $U_{\text{eff}} = 28.9$ K, $\tau_0 = 4.6 \times 10^{-8}$ s, $C = 483.4 \text{ K}^{-n} \text{ s}^{-1}$ and $n = 2.1$. Thus, **63** behaves as a field induced SMM, similar to Er(III) analogues, but Dy(III) performs as zero field SMM, suggesting that the LF is more suitable for oblate ions.

Efimov and co-workers have reported five Yb(III) heteroleptic thiocyanate complexes $[\text{Yb}(\text{H}_2\text{O})_5(\text{NCS})_3]\cdot\text{H}_2\text{O}$ (**64**), $[\text{Yb}(\text{H}_2\text{O})_4(\text{bpy})_2(\text{NCS})_3]\cdot 0.5(\text{bpy})\cdot\text{H}_2\text{O}$ (bpy = 2,2'-bipyridine) (**65**), $[\text{Yb}(\text{H}_2\text{O})_3(\text{phen})_2(\text{NCS})_3]\cdot\text{phen}\cdot 0.5\text{H}_2\text{O}$ (phen = 1,10-phenanthroline) (**66**), $[\text{Hbpy}][\text{Yb}(\text{bpy})_2(\text{NCS})_4]\cdot\text{H}_2\text{O}$ (**67**) and $[\text{Hphen}][\text{Yb}(\text{phen})_2(\text{NCS})_4]$ (**68**) and investigated the effect of the coordination environment on their magnetic relaxation dynamics (Fig. 39) [218]. The Yb(III) ion in all these complexes are octacoordinated with either bicapped trigonal prism (**64** and **66**) or square antiprism (**65**, **67** and **68**) coordination geometry. None of the complexes show any non-zero ac susceptibility signals in the absence of an external magnetic field due to the presence of strong QTM. However, on application of an optimised field (2500 Oe for **64** and 1000 Oe for **65–68**), these complexes show non-zero χ'' signals up to different temperatures. Fitting of the plot of relaxation time vs inverse of temperature using Arrhenius law at higher temperature range yields U_{eff} values of 50 K (**64**), 47 K (**65**), 22 K (**66**), 44 K (**67**) and 37 K (**68**). The overall $\ln\tau$ vs T^{-1} plot can be fitted by considering both Raman and Orbach process with the parameters: $C = 440 \text{ s}^{-1} \text{ K}^{-n}$ and $n = 8.55$ for **64**, $C = 72.6 \text{ s}^{-1} \text{ K}^{-n}$ and $n = 7.99$ for **65**, $C = 0.061 \text{ s}^{-1} \text{ K}^{-n}$ and $n = 4.53$ for **66**, $C = 72.8 \text{ s}^{-1} \text{ K}^{-n}$ and $n = 7.98$ for **67** and $C = 0.59 \text{ s}^{-1} \text{ K}^{-n}$ and $n = 5.16$ for **68**.

Recently, a study on the effect of axial ligand field on three Yb(III) SIMs has been reported by Borah *et al.* The equatorial ligand field in these complexes has been kept constant with four Ph_3PO ligands and the axial field is varied by changing the anionic ligands i.e. NO_3^- , OTf^- and $\text{I}^-/\text{Br}^-/\text{Cl}^-$ resulting in $[\text{Yb}(\text{Ph}_3\text{PO})_4(\text{NO}_3)_2][\text{NO}_3]$ (**69**), $[\text{Yb}(\text{Ph}_3\text{PO})_4(\text{OTf})_2][\text{OTf}]$ (**70**), and $[\text{Yb}(\text{Ph}_3\text{PO})_4(\text{I}_{0.38}\text{Br}_{0.62})][\text{I}_3]$ (**71**) (Fig. 40a-c) [219]. Metal ion in complex **69** is eight-coordinated with D_{2d} symmetry while in **70** and **71** it is six-coordinated with O_h and D_{4h} symmetry, respectively. None of these complexes exhibit χ'' signals in the absence of an external magnetic field due to strong QTM. However, in presence of an optimised dc field (2.5 KOe for **69**, 2 KOe for **70** and 1 KOe for **71**), **69** shows χ'' signals up to 3.4 K while **70** and **71** show signals up to 6.4 K and 6.95 K, respectively. The barrier of magnetic reversal was estimated as 9.2 K for **69**, 28.2 K (in slow relaxation) and 27.0 K (in fast relaxation) for **70** and 21.3 K for **71**, by fitting the linear part of higher temperature region of Arrhenius plot. Complexes

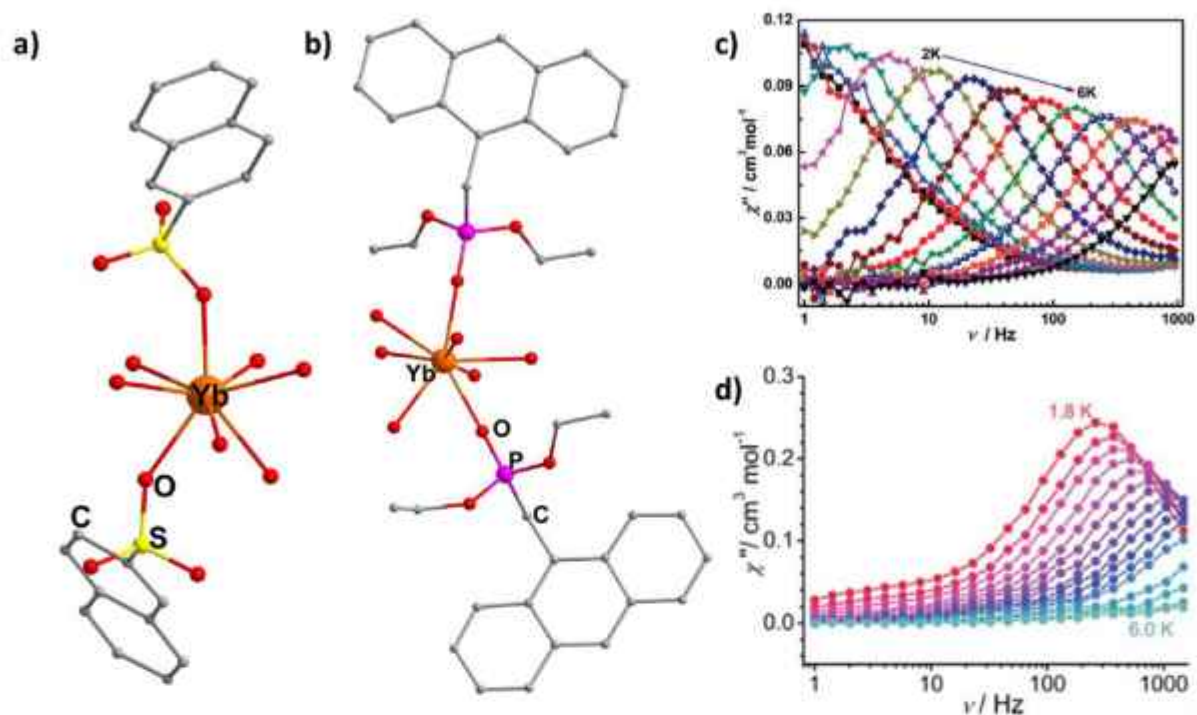


Fig. 38. Crystal structure of (a) $[\text{Yb}(\text{NAS})_2(\text{H}_2\text{O})_6](\text{NAS})\cdot 3\text{H}_2\text{O}$ (**62**) and (c) $[\text{Yb}(\text{depma})_2(\text{H}_2\text{O})_6]\text{Cl}\cdot 3\text{H}_2\text{O}$ (**63**). Frequency dependence of χ'' signals for (b) **62** and (d) **63** in presence of optimised dc fields at indicated temperatures. Reprinted from [215] and [217]. Copyright 2018 and 2019 Royal Society of Chemistry.

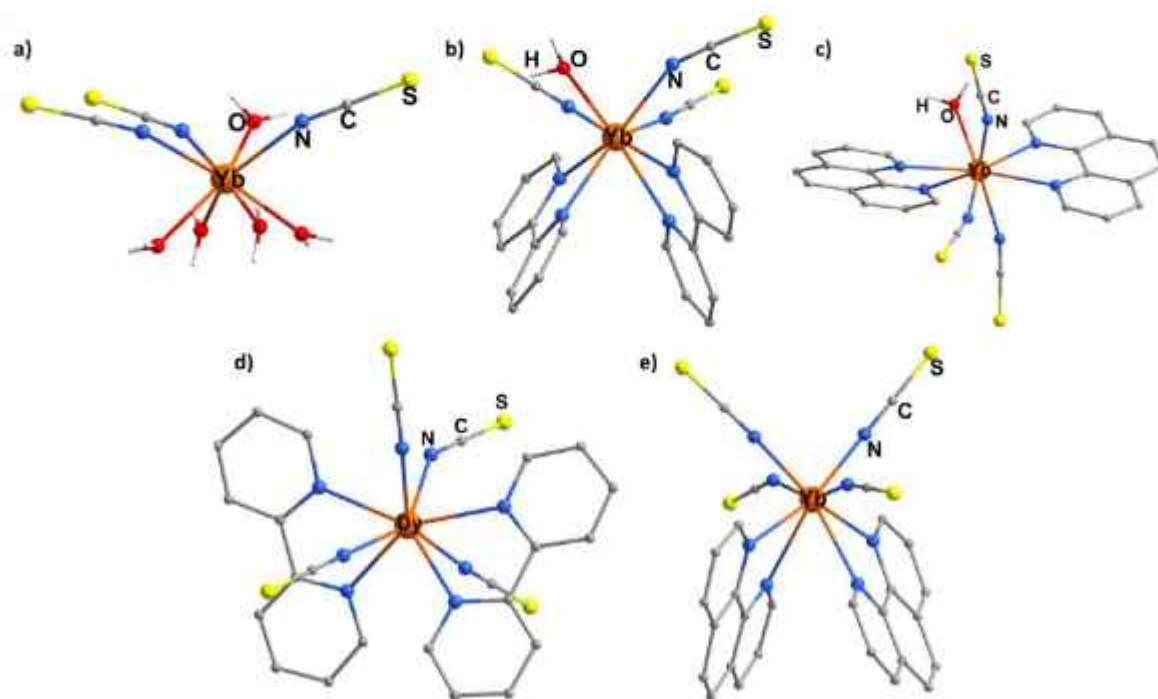


Fig. 39. Crystal structures of (a-c) **64–66**, (e) **68** and (d) Dy analogue of **67**. Reprinted from [218]. Copyright 2019 Royal Society of Chemistry.

70 and **71** possess the largest U_{eff} values among six coordinated Yb (III) based SIMs. The experimental energy barriers ($U_{\text{eff, exp}}$) are smaller than the calculated barriers ($U_{\text{eff, cal}} = 130 \text{ K}$ for **69**, 474 K for **70** and 556.6 K for **71**) due to the dominance of QTM even after the application an external magnetic field. The non-linearity of $\ln\tau$

vs $1/T$ plot in **70** and **71** suggests that different relaxation processes are operative in the relaxation dynamics along/without Orbach process. In case of **70**, The non-linear $\ln\tau$ vs $1/T$ plot can be best fitted by considering direct, Raman and Orbach process with $C = 0.445 \text{ s}^{-1} \text{ K}^{-n}$, $n = 5.53$, $A = 164.45 \text{ s}^{-1} \text{ K}^{-1}$ for slow relaxation

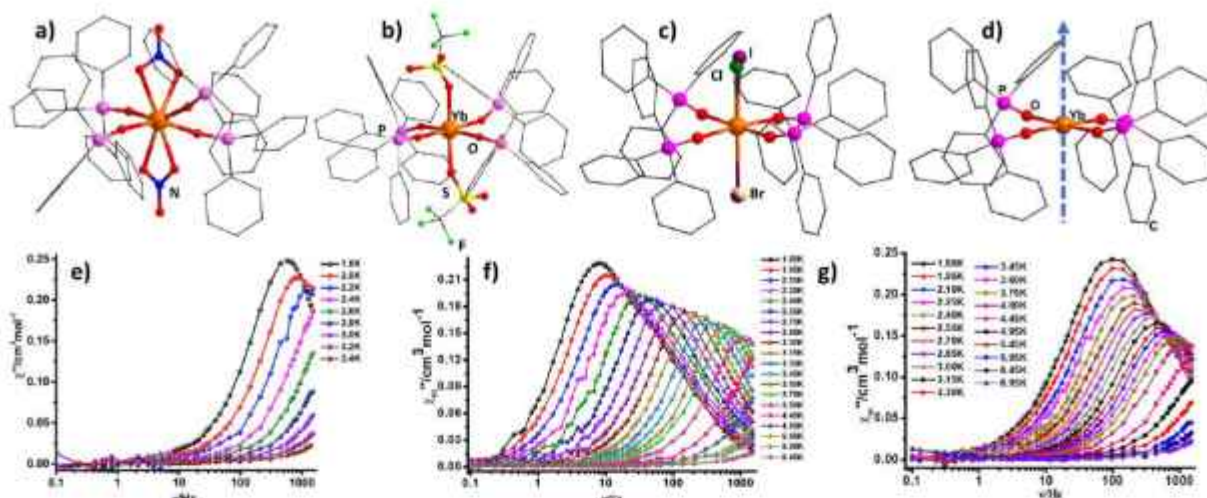


Fig. 40. Molecular structure of (a) $[\text{Yb}(\text{Ph}_3\text{PO})_4(\text{NO}_3)_2][\text{NO}_3]$ (**69**), (b) $[\text{Yb}(\text{Ph}_3\text{PO})_4(\text{OTf})_2][\text{OTf}]$ (**70**), and (c) $[\text{Yb}(\text{Ph}_3\text{PO})_4(\text{I}_{0.53}\text{Br}_{0.47})(\text{I}_{0.38}\text{Cl}_{0.62})][\text{I}_3]$ (**71**) and (d) the derived model to achieve higher barrier. Frequency dependence of χ^m signals for **69–71** (e–g) in presence of their optimised dc fields within the frequency range 0.1–1500 Hz. Reprinted from [219]. Copyright 2020 Royal Society of Chemistry.

and for fast relaxation, it can be fitted by Raman, QTM along with Orbach process with $C = 4.02 \text{ s}^{-1} \text{ K}^{-n}$, $n = 3.58$, $\tau_{\text{QTM}} = 0.276 \text{ s}$. The best fit for **71** can be obtained by direct, Raman and Orbach processes with the parameters: $A = 308.12 \text{ s}^{-1} \text{ K}^{-1}$, $C = 11.4 \text{ s}^{-1} \text{ K}^{-n}$ and $n = 4.49$. The plot of β -electron density of Yb(III) in **69–71** indicates that the shape of electron density is prolate suggesting the presence of strong equatorial ligand field. A model molecule is suggested with four Ph_3PO ligands in equatorial position and no axial ligands which can attain an energy separation between ground and 1st excited state as high as 1556.6 K with a negligible QTM probability ($0.01 \mu_B$) (Fig. 40d). This model sets an example to present how a suitable ligand field on Ln(III) ion can be helpful to achieve so higher U_{eff} .

3. Conclusions and future outlook

For the last two decades, the area of molecular magnetism has significantly expanded with trivalent lanthanides leading over transition metals by displaying higher barrier of magnetisation reversal as well as noteworthy blocking temperatures. Among the Ln(III) SIMs, the best performing SIMs to date are based on Dy(III) ion. To use SIMs for practical applications, this area still has to expand and achieve very high U_{eff} barriers which in turn can lead to hold the slow relaxation of magnetization at higher temperature (higher T_B). This is possible only when the relaxation happens via higher excited states, by nullifying the possibility of occurrence of QTM and other relaxation processes to the maximum possible extent. The current knowledge as showcased from the above described examples accentuate the importance of choice of proper paramagnetic centre and an appropriate ligand field for that ion. The recent development in this area further shows that the accurate ligand field can be designed and achieved by joint efforts of theoretical and synthetic chemists, achieving higher U_{eff} and blocking temperatures. Theoretically it has been already demonstrated that these less common lanthanide-based SIMs can be potential candidates if certain ligand fields can be provided to certain metal ions. Moreover, the magnetic relaxation dynamics in the SIMs discussed in this review are not yet very clear unlike in the case of some of the best performing Dy(III) based SMMs or SIMs. The dynamics can be understood better in light of other techniques like their photophysical properties in case of luminescent SIMs (mainly in case of Yb(III) SIMs) along with appropriate theoretical

modeling. The recent observations clearly show that further work needs to be done in the time to come in order to understand the mechanism of relaxation in these less common title Ln(III) ions, so that these SIMs can be the potential applicants in near future.

Declaration of Competing Interest

The authors declare that they have no known competing financial interests or personal relationships that could have appeared to influence the work reported in this paper.

Acknowledgements

R. M. thanks SERB for financially supporting our molecular magnetism work through a J.C. Bose National Fellowship (SB/S2/JCB-85/2014) and a SUPRA research grant (SPR/2019/001145). A. B. thanks UGC for a research fellowship.

References

- [1] M. Mannini, F. Pineider, P. Sainctavit, C. Danieli, E. Otero, C. Sciancalepore, A. M. Talarico, M.-A. Arrio, A. Cornia, D. Gatteschi, R. Sessoli, *Nat. Mater.* **8** (2009) 194–197.
- [2] F.D. Natterer, K. Yang, W. Paul, P. Wilke, T. Choi, T. Greber, A.J. Heinrich, C.P. Lutz, *Nature* **543** (2017) 226–228.
- [3] R.E. Winpenny, *Angew. Chem. Int. Ed.* **47** (2008) 7992–7994.
- [4] M. Urdampilleta, S. Klyatskaya, J.-P. Cleuziou, M. Ruben, W. Wernsdorfer, *Nat. Mater.* **10** (2011) 502–506.
- [5] A.R. Rocha, V.M. Garcia-Suarez, S.W. Bailey, C.J. Lambert, J. Ferrer, S. Sanvito, *Nat. Mater.* **4** (2005) 335–339.
- [6] R. Vincent, S. Klyatskaya, M. Ruben, W. Wernsdorfer, F. Balestro, *Nature* **488** (2012) 357–360.
- [7] P.C. Stamp, A. Gaita-Arino, *J. Mater. Chem.* **19** (2009) 1718–1730.
- [8] M.N. Lueningberger, D. Loss, *Nature* **410** (2001) 789–793.
- [9] G. Aromí, D. Aguilá, P. Gamez, F. Luis, O. Roubeau, *Chem. Soc. Rev.* **41** (2012) 537–546.
- [10] M. Alfronte, *J. Mater. Chem.* **19** (2009) 1731–1737.
- [11] S.G. McAdams, A.-M. Ariciu, A.K. Kostopoulos, J.P. Walsh, F. Tuna, *Coord. Chem. Rev.* **346** (2017) 216–239.
- [12] K.L. Harriman, D. Errulat, M. Murugesu, *Trends Chem.* **1** (2019) 425–439.
- [13] M. Dey, N. Gogoi, *Angew. Chem. Int. Ed.* **52** (2013) 12780–12782.
- [14] V. Rechkenner, F.D. Breitgoff, M. Van Der Meer, M. Atanasov, M. Hald, M. Orlita, P. Neugebauer, F. Neese, B. Sarkar, J. Van Slageren, *Nat. Commun.* **7** (2016) 10467.
- [15] A. Caneschi, D. Gatteschi, R. Sessoli, A.L. Barra, L.C. Brunel, M. Guillot, *J. Am. Chem. Soc.* **113** (1991) 5873–5874.
- [16] R. Sessoli, D. Gatteschi, A. Caneschi, M. Novak, *Nature* **365** (1993) 141–143.
- [17] R. Bagai, G. Christou, *Chem. Soc. Rev.* **38** (2009) 1011–1026.
- [18] C.J. Milios, A. Vinslava, W. Wernsdorfer, S. Moggach, S. Parsons, S.P. Perlepes, G. Christou, E.K. Brechin, *J. Am. Chem. Soc.* **129** (2007) 2754–2755.

- [19] M. Murugesu, M. Habrych, W. Wernsdorfer, K.A. Abboud, G. Christou, *J. Am. Chem. Soc.* 126 (2004) 4766–4767.
- [20] A.J. Tasiopoulos, A. Vinslava, W. Wernsdorfer, K.A. Abboud, G. Christou, *Angew. Chem.* 116 (2004) 2169–2173.
- [21] G. Christou, D. Gatteschi, D.N. Hendrickson, R. Sessoli, *MRS Bull.* 25 (2000) 66–71.
- [22] F. Neese, D.A. Pantazis, *Faraday Discuss.* 148 (2011) 229–238.
- [23] D. Gatteschi, R. Sessoli, *Angew. Chem. Int. Ed.* 42 (2003) 268–297.
- [24] G.A. Craig, M. Murrie, *Chem. Soc. Rev.* 44 (2015) 2135–2147.
- [25] R.J. Blagg, C.A. Muryn, E.J. McInnes, F. Tuna, R.E. Winpenny, *Angew. Chem. Int. Ed.* 50 (2011) 6530–6533.
- [26] A.M. Aho, I.J. Hewitt, V. Mereacre, R. Clérac, W. Wernsdorfer, C.E. Anson, A.K. Powell, *Angew. Chem. Int. Ed.* 118 (2006) 4926–4929.
- [27] J. Cířera, E. Ruiz, S. Alvarez, F. Neese, J. Kortus, *Chem. Eur. J.* 15 (2009) 4078–4087.
- [28] T. Glaser, *Chem. Commun.* 47 (2011) 116–130.
- [29] D. Gatteschi, A. Caneschi, L. Pardi, R. Sessoli, *Science* 265 (1994) 1054–1058.
- [30] M. Mannini, F. Pineider, C. Danieli, F. Totti, L. Sorace, P. Saintavrit, M.-A. Arrio, E. Otero, L. Joly, J.C. Ceazar, A. Cornia, R. Sessoli, *Nature* 468 (2010) 417–421.
- [31] E. Ruiz, J. Cířera, J. Cano, S. Alvarez, C. Loose, J. Kortus, *Chem. Commun.* (2008) 52–54.
- [32] A.M. Aho, I.J. Hewitt, V. Mereacre, R. Clérac, W. Wernsdorfer, C.E. Anson, A.K. Powell, *Angew. Chem. Int. Ed.* 45 (2006) 4926–4929.
- [33] N. Ishikawa, M. Sugita, T. Ishikawa, S.-Y. Koshihara, Y. Kaizu, *J. Am. Chem. Soc.* 125 (2003) 8694–8695.
- [34] R.A. Layfield, *Organometallics* 33 (2014) 1084–1099.
- [35] D.N. Woodruff, R.E. Winpenny, R.A. Layfield, *Chem. Rev.* 113 (2013) 5110–5148.
- [36] L. Sorace, C. Benelli, D. Gatteschi, *Chem. Soc. Rev.* 40 (2011) 3092–3104.
- [37] F. Habib, M. Murugesu, *Chem. Soc. Rev.* 42 (2013) 3278–3288.
- [38] J.D. Kinehart, J.R. Long, *Chem. Sci.* 2 (2011) 2078–2085.
- [39] N.F. Chilton, C.A. Goodwin, D.P. Mills, R.E. Winpenny, *Chem. Commun.* 51 (2015) 101–103.
- [40] L. Ungur, L.F. Chibotaru, *Phys. Chem. Chem. Phys.* 13 (2011) 20086–20090.
- [41] N.F. Chilton, *Inorg. Chem.* 54 (2015) 2097–2099.
- [42] J.M. Zadrozny, D.J. Xiao, M. Atanasov, G.J. Long, F. Grandjean, F. Neese, *J.R. Long, Nature Chem.* 5 (2013) 577–581.
- [43] R.J. Blagg, L. Ungur, F. Tuna, J. Speak, P. Comar, D. Collison, W. Wernsdorfer, E. J. McInnes, L.F. Chibotaru, R.E. Winpenny, *Nature Chem.* 5 (2013) 673–678.
- [44] F.-S. Guo, B.M. Day, Y.-C. Chen, M.-L. Tong, A. Mansikkamäki, R.A. Layfield, *Angew. Chem. Int. Ed.* 56 (2017) 11445–11449.
- [45] F.-S. Guo, B.M. Day, Y.-C. Chen, M.-L. Tong, A. Mansikkamäki, R.A. Layfield, *Science* 362 (2018) 1400–1403.
- [46] C.A. Goodwin, F. Ortu, D. Reta, N.F. Chilton, D.P. Mills, *Nature* 548 (2017) 439–442.
- [47] P. Evans, D. Reta, G.F. Whitehead, N.F. Chilton, D.P. Mills, *J. Am. Chem. Soc.* 141 (2019) 19935–19940.
- [48] S.K. Singh, T. Gupta, L. Ungur, G. Rajaraman, *Chem. Eur. J.* 21 (2015) 13812–13819.
- [49] C.A. Gould, K.R. McClain, J.M. Yu, T.J. Groshens, F. Fierche, B.G. Harvey, *J.R. Long, J. Am. Chem. Soc.* 141 (2019) 12967–12973.
- [50] K.R. McClain, C.A. Gould, K. Chakarawet, S.J. Teat, T.J. Groshens, J.R. Long, B.G. Harvey, *Chem. Sci.* 9 (2018) 8492–8503.
- [51] W. Cao, C. Gao, Y.-Q. Zhang, D. Qi, T. Liu, K. Wang, C. Duan, S. Gao, J. Jiang, *Chem. Sci.* 6 (2015) 5947–5954.
- [52] S.D. Jiang, B.W. Wang, G. Su, Z.M. Wang, S. Gao, *Angew. Chem. Int. Ed.* 49 (2010) 7448–7451.
- [53] Y.-C. Chen, J.-L. Liu, L. Ungur, J. Liu, Q.-W. Li, L.-F. Wang, Z.-P. Ni, L.F. Chibotaru, X.-M. Chen, M.-L. Tong, *J. Am. Chem. Soc.* 138 (2016) 2829–2837.
- [54] Y.S. Ding, N.F. Chilton, R.E. Winpenny, Y.Z. Zheng, *Angew. Chem. Int. Ed.* 55 (2016) 16071–16074.
- [55] S.K. Gupta, T. Rajeshkumar, G. Rajaraman, R. Murugavel, *Chem. Commun.* 52 (2016) 7168–7171.
- [56] S.K. Gupta, T. Rajeshkumar, G. Rajaraman, R. Murugavel, *Chem. Sci.* 7 (2016) 5181–5191.
- [57] S.K. Gupta, T. Rajeshkumar, G. Rajaraman, R. Murugavel, *Dalton Trans.* 47 (2018) 357–366.
- [58] Y.-C. Chen, X.-S. Huang, J.-L. Liu, M.-L. Tong, *Inorg. Chem.* 57 (2018) 11782–11787.
- [59] Y.-S. Ding, K.-X. Yu, D. Reta, F. Ortu, R.E. Winpenny, Y.-Z. Zheng, N.F. Chilton, *Nat. Commun.* 9 (2018) 3134.
- [60] M.S. Norre, C. Gao, S. Dey, S.K. Gupta, A. Borah, R. Murugavel, G. Rajaraman, *J. Overgaard, Inorg. Chem.* 59 (2020) 717–729.
- [61] Z.H. Li, Y.Q. Zhai, W.P. Chen, Y.S. Ding, Y.Z. Zheng, *Chem. Eur. J.* 25 (2019) 16219–16224.
- [62] A.B. Canaj, S. Dey, E.J. Martí, C. Wilson, G. Rajaraman, M. Murrie, *Angew. Chem. Int. Ed.* 58 (2019) 14146–14151.
- [63] K.R. Meilhaus, J.R. Long, *J. Am. Chem. Soc.* 135 (2013) 17952–17957.
- [64] L. Ungur, J.J. Le Roy, I. Korobkov, M. Murugesu, L.F. Chibotaru, *Angew. Chem. Int. Ed.* 53 (2014) 4413–4417.
- [65] M. Jeletic, P.-H. Lin, J.J. Le Roy, I. Korobkov, S.I. Gorelsky, M. Murugesu, *J. Am. Chem. Soc.* 133 (2011) 19286–19289.
- [66] S.-D. Jiang, B.-W. Wang, H.-L. Sun, Z.-M. Wang, S. Gao, *J. Am. Chem. Soc.* 133 (2011) 4730–4733.
- [67] A.K. Bar, P. Kalita, M.K. Singh, G. Rajaraman, V. Chandrasekhar, *Coord. Chem. Rev.* 367 (2018) 163–216.
- [68] J.-L. Liu, Y.-C. Chen, M.-L. Tong, *Chem. Soc. Rev.* 47 (2018) 2431–2453.
- [69] S.T. Liddle, J. van Slageren, *Chem. Soc. Rev.* 44 (2015) 6655–6669.
- [70] R. Sessoli, A.K. Powell, *Coord. Chem. Rev.* 253 (2009) 2328–2341.
- [71] S.K. Gupta, R. Murugavel, *Chem. Commun.* 54 (2018) 3685–3696.
- [72] G. Cucinotta, M. Perfetti, J. Luzon, M. Etienne, P.E. Car, A. Caneschi, G. Calvez, K. Bernot, R. Sessoli, *Angew. Chem. Int. Ed.* 51 (2012) 1606–1610.
- [73] P.-E. Car, M. Perfetti, M. Mannini, A. Favre, A. Caneschi, R. Sessoli, *Chem. Commun.* 47 (2011) 3751–3753.
- [74] F. Pointillart, O. Gador, B. Le Guennic, L. Ouahab, *Coord. Chem. Rev.* 346 (2017) 150–175.
- [75] A.K. Pathak, M. Khan, K.A. Gschneidner Jr, R.W. McCallum, L. Zhou, K. Sun, K. W. Dennis, C. Zhou, F.E. Pinkerton, M.J. Kramer, *Adv. Mater.* 27 (2015) 2663–2667.
- [76] S. Hino, M. Maeda, K. Yamashita, Y. Kataoka, M. Nakano, T. Yamamura, H. Nojiri, M. Kofu, O. Yamamuro, T. Kajiwara, *Dalton Trans.* 42 (2013) 2683–2686.
- [77] A.B. Khélifa, M.S. Belkhiria, G. Huang, S. Fresslon, O. Guillou, K. Bernot, *Dalton Trans.* 44 (2015) 16458–16464.
- [78] C. Takehara, P.L. Then, Y. Kataoka, M. Nakano, T. Yamamura, T. Kajiwara, *Dalton Trans.* 44 (2015) 18276–18283.
- [79] P.L. Then, C. Takehara, Y. Kataoka, M. Nakano, T. Yamamura, T. Kajiwara, *Dalton Trans.* 44 (2015) 18038–18048.
- [80] H. Tsurugi, Y. Ikeda, K. Shinohara, S. Shirase, N. Toya, S. Tanaka, K. Mashima, *Inorg. Chem.* 58 (2019) 12565–12572.
- [81] J.J. Le Roy, I. Korobkov, J.E. Kim, E.J. Schelter, M. Murugesu, *Dalton Trans.* 43 (2014) 2737–2740.
- [82] V. Lorenz, B.M. Schmiede, C.G. Hrib, J.W. Ziller, A. Edelmann, S. Blaurock, W.J. Evans, F.T. Edelmann, *J. Am. Chem. Soc.* 133 (2011) 1257–1259.
- [83] J.J. Le Roy, M. Jeletic, S.I. Gorelsky, I. Korobkov, L. Ungur, L.F. Chibotaru, M. Murugesu, *J. Am. Chem. Soc.* 135 (2013) 3502–3510.
- [84] H. Wada, S. Ooka, T. Yamamura, T. Kajiwara, *Inorg. Chem.* 56 (2017) 147–155.
- [85] M.T. Kaczmarek, M. Zabizszak, M. Nowak, R. Jastrzab, *Coord. Chem. Rev.* 370 (2018) 42–54.
- [86] D. Fenton, P. Vigato, *Chem. Soc. Rev.* 17 (1988) 69–90.
- [87] C. Camp, V. Guidal, B. Biswas, J. Pécaut, L. Dubois, M. Mazzanti, *Chem. Sci.* 3 (2012) 2433–2448.
- [88] J. Long, *Front. Chem.* 7 (2019) 63.
- [89] D. Sinha, A.K. Tiwari, S. Singh, G. Shukla, P. Mishra, H. Chandra, A.K. Mishra, *Eur. J. Med. Chem.* 43 (2008) 160–165.
- [90] Y. Jia, J. Li, *Chem. Rev.* 115 (2015) 1597–1621.
- [91] A. Upadhyay, K.R. Vignesh, C. Das, S.K. Singh, G. Rajaraman, M. Shanmugam, *Inorg. Chem.* 56 (2017) 14260–14276.
- [92] M.-X. Xu, Y.-S. Meng, J. Xiong, B.-W. Wang, S.-D. Jiang, S. Gao, *Dalton Trans.* 47 (2018) 1966–1971.
- [93] A.W. Platt, *Coord. Chem. Rev.* 340 (2017) 62–78.
- [94] S.K. Gupta, S. Shanmugam, T. Rajeshkumar, A. Borah, M. Damjanović, M. Schulze, W. Wernsdorfer, G. Rajaraman, R. Murugavel, *Dalton Trans.* 48 (2019) 15928–15935.
- [95] M. Maeda, S. Hino, K. Yamashita, Y. Kataoka, M. Nakano, T. Yamamura, T. Kajiwara, *Dalton Trans.* 41 (2012) 13640–13648.
- [96] A. Watanabe, A. Yamashita, M. Nakano, T. Yamamura, T. Kajiwara, *Chem. Eur. J.* 17 (2011) 7428–7432.
- [97] T. Kajiwara, M. Nakano, K. Takahashi, S. Takaishi, M. Yamashita, *Chem. Eur. J.* 17 (2011) 196–205.
- [98] S.B. Castor, J.B. Hedrick, *Society for Mining, Metallurgy, and Exploration, Inc.* (2006) 769–792.
- [99] P.K. Deheri, V. Swaminathan, S.D. Bhame, Z. Liu, R.V. Ramanujan, *Chem. Mater.* 22 (2010) 6509–6517.
- [100] J.D. Kinehart, J.R. Long, *Dalton Trans.* 41 (2012) 13572–13574.
- [101] J.J. Le Roy, S.I. Gorelsky, I. Korobkov, M. Murugesu, *Organometallics* 34 (2015) 1415–1418.
- [102] J.J. Le Roy, I. Korobkov, M. Murugesu, *Chem. Commun.* 50 (2014) 1602–1604.
- [103] M. Hasegawa, H. Ohtsu, D. Kodama, T. Kasai, S. Sakurai, A. Ishii, K. Suzuki, *New J. Chem.* 38 (2014) 1225–1234.
- [104] H. Wada, S. Ooka, D. Iwasawa, M. Hasegawa, T. Kajiwara, *Magnetochemistry* 2 (2016) 43.
- [105] A. Arauzo, A. Lazarescu, S. Shova, E. Bartolomé, R. Cases, J. Luzón, J. Bartolomé, C. Turta, *Dalton Trans.* 43 (2014) 12342–12356.
- [106] J.J. Baldoví, J.M. Clemente-Juan, E. Coronado, Y. Duan, A. Gaita-Ariño, C. Giménez-Saiz, *Inorg. Chem.* 53 (2014) 9976–9980.
- [107] A.K. Jassal, N. Aliaga-Alcalde, M. Corbella, D. Aravena, E. Ruiz, G. Hundal, *Dalton Trans.* 44 (2015) 15774–15778.
- [108] W.J. Evans, C.A. Seibel, J.W. Ziller, *J. Am. Chem. Soc.* 120 (1998) 6745–6752.
- [109] S. Demir, K.R. Meilhaus, J.R. Long, *J. Organomet. Chem.* 857 (2018) 164–169.
- [110] S. Demir, J.M. Zadrozny, *J.R. Long, Chem. Eur. J.* 20 (2014) 9524–9529.
- [111] K. Kumar, D. Abe, K. Komori-Orisaku, O. Stefanczyk, K. Nakabayashi, J.R. Shukirova, S.P. Tunik, S.-I. Ohkoshi, *RSC Adv.* 9 (2019) 23444–23449.
- [112] J. Li, L. Yi, S.-J. Xiong, X.-L. Wu, F. Yu, Z.-W. Ouyang, Z.-C. Xia, Y.-Q. Zhang, J. van Tol, Y. Song, Z. Wang, *Science* 23 (2020) 100926.
- [113] J.M. Zadrozny, J. Liu, N.A. Piro, C.J. Chang, S. Hill, J.R. Long, *Chem. Commun.* 48 (2012) 3927–3929.
- [114] G. De Stasio, P. Casalbore, R. Paffini, B. Gilbert, F. Sanita, M.T. Ciotti, G. Rosi, A. Festinesi, L.M. Larocca, A. Rinelli, D. Perret, D.W. Mogk, P. Perfetti, M.P. Mehta, D. Mercanti, *Cancer Res.* 61 (2001) 4272–4277.
- [115] G. Leinweber, D.P. Barry, M. Trbovich, J. Burke, N. Drindak, H. Knox, R. Ballard, R. Block, Y. Danon, L. Severnyak, *Nucl. Sci. Eng.* 154 (2006) 261–279.

- [116] H.S. Thomsen, P. Leander, Radiography with gadolinium-based contrast media, in: *Contrast Media*, Springer, 2014, pp. 193–200.
- [117] A.J. Jacobson, *Chem. Mater.* 22 (2010) 660–674.
- [118] Y. Lee, J. Shin, K. Oh, S. Noh, D. Kim, J. Kim, J. Hong, S. Park, S. Nam, *J. Instrum.* 8 (2013) P03018.
- [119] P. Caravan, J.J. Ellison, T.J. McMurty, R.B. Lauffer, *Chem. Rev.* 99 (1999) 2293–2352.
- [120] K.N. Raymond, V.C. Pierre, *Bioconjugate Chem.* 16 (2005) 3–8.
- [121] D.V. Hingorani, A.S. Bernstein, M.D. Pagel, *Contrast Media Mol. Imaging* 10 (2015) 245–265.
- [122] V.K. Pecharsky, K.A. Coehneider Jr., *J. Magn. Magn. Mater.* 200 (1999) 44–56.
- [123] B. Yu, Q. Gao, B. Zhang, X. Meng, Z. Chen, *J. Int. Acad. Refrig.* 26 (2003) 622–636.
- [124] R. Bjørk, C.J.H. Bahl, A. Smith, N. Pryds, *J. Int. Acad. Refrig.* 33 (2010) 437–448.
- [125] M. Evangelisti, D. Koubou, E. Palacios, A. Camón, T.N. Hooper, E.K. Brechin, J.J. Alonso, *Angew. Chem. Int. Ed.* 50 (2011) 6606–6609.
- [126] F.-S. Guo, Y.-C. Chen, J.-L. Liu, J.-D. Leng, Z.-S. Meng, P. Vrābel, M. Orendáč, M.-L. Tong, *Chem. Commun.* 48 (2012) 12219–12221.
- [127] T.N. Hooper, J. Schnack, S. Piligkos, M. Evangelisti, E.K. Brechin, *Angew. Chem. Int. Ed.* 51 (2012) 4633–4636.
- [128] G. Lorusso, M.A. Palacios, G.S. Nichol, E.K. Brechin, D. Koubou, M. Evangelisti, *Chem. Commun.* 48 (2012) 7592–7594.
- [129] L.-X. Chang, C. Xiong, L. Wang, P. Cheng, B. Zhao, *Chem. Commun.* 49 (2013) 1055–1057.
- [130] G. Lorusso, J.W. Sharples, E. Palacios, O. Koubou, E.K. Brechin, K. Sessoli, A. Rossin, F. Tuna, E.J. McInnes, D. Collison, M. Evangelisti, *Adv. Mater.* 25 (2013) 4653–4656.
- [131] J.-L. Liu, Y.-C. Chen, F.-S. Guo, M.-L. Tong, *Coord. Chem. Rev.* 281 (2014) 26–49.
- [132] J.W. Sharples, D. Collison, E.J. McInnes, J. Schnack, E. Palacios, M. Evangelisti, *Nat. Commun.* 5 (2014) 5321.
- [133] Y.-Z. Zheng, G.-J. Zhou, Z. Zheng, R.E. Winpenny, *Chem. Soc. Rev.* 43 (2014) 1462–1475.
- [134] C. Das, A. Upadhyay, K.U. Ansari, N. Ogiwara, T. Kitao, S. Horike, M. Shanmugam, *Inorg. Chem.* 57 (2018) 6584–6598.
- [135] S.-J. Liu, S.-D. Han, J.-P. Zhao, J. Xu, X.-H. Bu, *Coord. Chem. Rev.* 394 (2019) 39–52.
- [136] S.K. Gupta, A.A. Dar, T. Rajeshkumar, S. Kuppaswamy, S.K. Langley, K.S. Murray, G. Rajaraman, R. Murugavel, *Dalton Trans.* 44 (2015) 5961–5965.
- [137] M. Orendáč, L. Sedláčková, E. Čizmar, A. Orendáčová, A. Feher, S. Zvyagin, J. Wosnitzer, W. Zhu, Z. Wang, S. Gao, *Phys. Rev. B* 81 (2010) 214410.
- [138] M. Martínez-Pérez, S. Cardona-Serra, C. Schlegel, F. Moro, P. Alonso, H. Prima-García, J. Clemente-Juan, M. Evangelisti, A. Gaita-Ariño, J. Sesé, J.v. Slagereen, E. Coronado, L. F., *Physical review letters*, 108 (2012) 247213.
- [139] R.J. Holmberg, L. Ungur, I. Korobkov, L.F. Chibotaru, M. Murugesu, *Dalton Trans.* 44 (2015) 20321–20325.
- [140] A.J. Calahorra, I. Oyarzabal, B. Fernández, J.M. Seco, T. Tian, D. Fairen-Jimenez, E. Colacio, A. Rodríguez-Diéguez, *Dalton Trans.* 45 (2016) 591–598.
- [141] O. Khalifaoui, A. Beghidja, J. Long, A. Boussadia, C. Beghidja, Y. Guari, *J. Lariionova, Dalton Trans.* 46 (2017) 3943–3952.
- [142] T. Yoshida, G. Cosquer, D.C. Izuogu, H. Ohtsu, M. Kawano, Y. Lan, W. Wernsdorfer, H. Nojiri, B.K. Breedlove, M. Yamashita, *Chem. Eur. J.* 23 (2017) 4551–4556.
- [143] D.C. Izuogu, T. Yoshida, H. Zhang, G. Cosquer, K. Katoh, S. Ogata, M. Hasegawa, H. Nojiri, M. Damjanović, W. Wernsdorfer, T. Uruga, T. Ina, B.K. Breedlove, M. Yamashita, *Chem. Eur. J.* 24 (2018) 9285–9294.
- [144] A. Vrāblová, M. Tomáš, L.R. Falvello, E. Dlháň, J. Titiš, J. Černák, R. Boča, *Dalton Trans.* 48 (2019) 13943–13952.
- [145] Q. Kang, W. Hingwu, W. Zhemin, S. Gang, G. Song, *Acta Chim. Sin.* 71 (2013) 1022–1028.
- [146] Y.-C. Chen, Y.-Y. Peng, J.-L. Liu, M.-L. Tong, *Inorg. Chem. Commun.* 107 (2019) 107449.
- [147] F. Donati, S. Rusponi, S. Stepanow, C. Wäckerlin, A. Singha, L. Persichetti, R. Baltic, K. Diller, F. Patthey, E. Fernandes, J. Dreiser, Ž. Šljivančanin, K. Kummer, C. Nistor, P. Gambardella, H. Bruene, *Science* 352 (2016) 318–321.
- [148] N. Ishikawa, M. Sugita, T. Okubo, N. Tanaka, T. Iino, Y. Kaizu, *Inorg. Chem.* 42 (2003) 2440–2446.
- [149] N. Ishikawa, M. Sugita, T. Ishikawa, S.-Y. Koshihara, Y. Kaizu, *J. Phys. Chem. B* 108 (2004) 11265–11271.
- [150] N. Ishikawa, M. Sugita, W. Wernsdorfer, *J. Am. Chem. Soc.* 127 (2005) 3650–3651.
- [151] S.-D. Jiang, S.-S. Liu, L.-N. Zhou, B.-W. Wang, Z.-M. Wang, S. Gao, *Inorg. Chem.* 51 (2012) 3079–3087.
- [152] Y.C. Chen, J.L. Liu, W. Wernsdorfer, D. Liu, L.F. Chibotaru, X.M. Chen, M.L. Tong, *Angew. Chem. Int. Ed.* 56 (2017) 4996–5000.
- [153] T. Kajiwar, *Angew. Chem. Int. Ed.* 56 (2017) 11306–11308.
- [154] L.-L. Li, H.-D. Su, S. Liu, W.-Z. Wang, *Dalton Trans.* 49 (2020) 6703–6709.
- [155] K. Jia, X. Meng, M. Wang, X. Gou, Y.-X. Wang, N. Xu, W. Shi, P. Cheng, *Chem. Commun.* 57 (2021) 3607–3610.
- [156] Y. Ma, Y.-Q. Zhai, Y.-S. Ding, T. Han, Y.-Z. Zheng, *Chem. Commun.* 56 (2020) 3979–3982.
- [157] I. Gagliardi, R. Lindh, G. Karlström, *J. Chem. Phys.* 121 (2004) 4494–4500.
- [158] P. Kalita, J. Acharya, V. Chandrasekar, *J. Magn. Magn. Mater.* 498 (2020) 166098.
- [159] A.B. Canaj, M.K. Singh, C. Wilson, G. Rajaraman, M. Murrie, *Chem. Commun.* 54 (2018) 8273–8276.
- [160] L.-L. Li, H.-D. Su, S. Liu, Y.-C. Xu, W.-Z. Wang, *Dalton Trans.* 48 (2019) 2213–2219.
- [161] M. Llunell, D. Casanova, J. Cirera, P. Alemany, S. Alvarez, *Universitat de Barcelona, Barcelona, Spain*, 2103 (2013).
- [162] S.-M. Chen, Y.-Q. Zhang, J. Xiong, B.-W. Wang, S. Gao, *Inorg. Chem.* 59 (2020) 5835–5844.
- [163] H.-D. Amberg, F.T. Edelmann, J. Gottfriedsen, K. Herbst-Irmer, S. Jank, U. Kilmann, M. Noltemeyer, H. Reddmann, M. Schäfer, *Inorg. Chem.* 48 (2009) 760–772.
- [164] Y.S. Meng, Y.S. Qiao, Y.Q. Zhang, S.D. Jiang, Z.S. Meng, B.W. Wang, Z.M. Wang, S. Gao, *Chem. Eur. J.* 22 (2016) 4704–4708.
- [165] K. Bernot, J. Luzon, L. Bogani, M. Etienne, C. Sangregorio, M. Shanmugam, A. Caneschi, R. Sessoli, D. Gatteschi, *J. Am. Chem. Soc.* 131 (2009) 5573–5579.
- [166] J.H. Van Vleck, *The Theory of Electric and Magnetic Susceptibilities*, Clarendon Press, 1932.
- [167] F. Nief, *Dalton Trans.* 39 (2010) 6589–6598.
- [168] M. Kühling, R. McDonald, P. Liebing, L. Hilfert, M.J. Ferguson, J. Takats, F.T. Edelmann, *Dalton Trans.* 45 (2016) 10118–10121.
- [169] J. Cheng, J. Takats, M.J. Ferguson, R. McDonald, *J. Am. Chem. Soc.* 130 (2008) 1544–1545.
- [170] M.E. Fieser, M.R. MacDonald, B.T. Krull, J.E. Bates, J.W. Ziller, F. Furche, W.J. Evans, *J. Am. Chem. Soc.* 137 (2015) 369–382.
- [171] C.A. Goodwin, N.F. Chilton, L.S. Natrajan, M.-E. Boulon, J.W. Ziller, W.J. Evans, D.P. Mills, *Inorg. Chem.* 56 (2017) 5959–5970.
- [172] C.A. Goodwin, N.F. Chilton, G.F. Vettese, E. Moreno Pineda, L.F. Crowe, J.W. Ziller, R.E. Winpenny, W.J. Evans, D.P. Mills, *Inorg. Chem.* 55 (2016) 10057–10067.
- [173] M. Xernard, M. Cordier, F. Molton, C. Duboc, B. Le Guennic, O. Maury, O. Cadot, C. Nocton, *Inorg. Chem.* 58 (2019) 2872–2880.
- [174] P. Zhang, L. Zhang, C. Wang, S. Xue, S.-Y. Lin, J. Tang, *J. Am. Chem. Soc.* 136 (2014) 4484–4487.
- [175] H. Zhang, R. Nakanishi, K. Katoh, B.K. Breedlove, Y. Kitagawa, M. Yamashita, *Dalton Trans.* 47 (2018) 302–305.
- [176] Y. Bi, X.-T. Wang, W. Liao, X. Wang, R. Deng, H. Zhang, S. Gao, *Inorg. Chem.* 48 (2009) 11743–11747.
- [177] C.-S. Liu, M. Du, E.C. Sañudo, J. Echeverria, M. Hu, Q. Zhang, L.-M. Zhou, S.-M. Fang, *Dalton Trans.* 40 (2011) 9366–9369.
- [178] X. Yi, K. Bernot, F. Pointillart, G. Poneti, G. Calvez, C. Daiguebonne, O. Guillou, R. Sessoli, *Chem. Eur. J.* 18 (2012) 11379–11387.
- [179] Y. Bi, X.-T. Wang, Y. Ma, X. Yang, J. Tang, P. Cheng, Q.-L. Wang, L.-C. Li, D.-Z. Liao, *Inorg. Chem.* 52 (2013) 7380–7386.
- [180] M. Gregson, N.F. Chilton, A.-M. Ariciu, F. Tuna, L.F. Crowe, W. Lewis, A.J. Blake, D. Collison, E.J. McInnes, R.E. Winpenny, S.T. Liddle, *Chem. Sci.* 7 (2016) 155–165.
- [181] J.P. Costes, S. Tinos-Padilla, I. Oyarzabal, T. Gupta, C. Duhayon, G. Rajaraman, E. Colacio, *Chem. Eur. J.* 21 (2015) 15785–15796.
- [182] J. Long, R. Vallat, R.A. Ferreira, L.D. Carlos, F.A.A. Paz, Y. Guari, J. Lariionova, *Chem. Commun.* 48 (2012) 9974–9976.
- [183] J. Long, J. Rouquette, J.M. Thibaud, R.A. Ferreira, L.D. Carlos, B. Donnadieu, V. Vieru, L.F. Chibotaru, L. Konczewicz, J. Haines, Y. Guari, J. Lariionova, *Angew. Chem. Int. Ed.* 54 (2015) 2236–2240.
- [184] E.L. Gavey, M. Al Hareri, J. Regier, L.D. Carlos, R.A. Ferreira, F.S. Razavi, J.M. Rawson, M. Pilkington, *J. Mater. Chem. C* 3 (2015) 7738–7747.
- [185] M. Al Hareri, E. Gavey, J. Regier, Z.R. Ali, L. Carlos, R. Ferreira, M. Pilkington, *Chem. Commun.* 52 (2016) 11335–11338.
- [186] J. Long, Y. Guari, R.A. Ferreira, L.D. Carlos, J. Lariionova, *Coord. Chem. Rev.* 363 (2018) 57–70.
- [187] M. Sugita, N. Ishikawa, T. Ishikawa, S.-Y. Koshihara, Y. Kaizu, *Inorg. Chem.* 45 (2006) 1299–1304.
- [188] J.-L. Liu, K. Yuan, J.-D. Leng, L. Ungur, W. Wernsdorfer, F.-S. Guo, L.F. Chibotaru, M.-L. Tong, *Inorg. Chem.* 51 (2012) 8538–8544.
- [189] A. Abragam, B. Bleaney, *Electron paramagnetic resonance of transition ions*, OUP Oxford, 2012.
- [190] A. Lannes, D. Luneau, *Inorg. Chem.* 54 (2015) 6736–6743.
- [191] N.F. Chilton, R.P. Anderson, L.D. Turner, A. Soncini, K.S. Murray, *J. Comput. Chem.* 34 (2013) 1164–1175.
- [192] F. Guégan, J. Jung, B. Le Guennic, F. Riobé, O. Maury, B. Gillon, J.-F. Jacquot, Y. Guyot, C. Morell, D. Luneau, *Inorg. Chem. Front.* 6 (2019) 3152–3157.
- [193] A.A. Trifonov, L.A. Borovkov, E.A. Fedarova, G.K. Fukin, J. Lariionova, N.O. Druzhkov, V.K. Cherkasov, *Chem. Eur. J.* 13 (2007) 4981–4987.
- [194] B.G. Shestakov, T.V. Mahrova, J. Lariionova, J. Long, A.V. Cherkasov, G.K. Fukin, K.A. Lyssenko, W. Scherer, C. Hauf, T.V. Magdesieva, O.A. Levitskiy, I. A. Organometallics, 34 (2015) 1177–1185.
- [195] A.A. Trifonov, B. Shestakov, J. Long, K. Lyssenko, Y. Guari, J. Lariionova, *Inorg. Chem.* 54 (2015) 7667–7669.
- [196] P.V. Bernhardt, B.M. Hanagan, M.J. Röley, *Aust. J. Chem.* 53 (2000) 229–231.
- [197] K.S. Pedersen, J. Dreiser, H. Weihe, K. Sible, H.V. Johannesen, M.A. Sørensen, B.E. Nielsen, M. Sigrist, H. Mutka, S. Rols, J. Bendix, S. Piligkos, *Inorg. Chem.* 54 (2015) 7600–7606.
- [198] P. Scott, C. Jeffries, *Phys. Rev.* 127 (1962) 32.
- [199] K.S. Pedersen, A.-M. Ariciu, S. McAdams, H. Weihe, J. Bendix, F. Tuna, S. Piligkos, *J. Am. Chem. Soc.* 138 (2016) 5801–5804.
- [200] A. Kobayashi, E. Fujiwara, H. Kobayashi, *Chem. Rev.* 104 (2004) 5243–5264.
- [201] T. Enoki, A. Miyazaki, *Chem. Rev.* 104 (2004) 5449–5478.
- [202] D. Lorc, N. Bellec, M. Fourmigué, N. Avarvari, *Coord. Chem. Rev.* 253 (2009) 1398–1438.

- [203] E. Coronado, P. Day, *Chem. Rev.* 104 (2004) 5419–5448.
- [204] A. D'Aléo, F. Pointillart, L. Ouahab, C. Andraud, O. Maury, *Coord. Chem. Rev.* 256 (2012) 1604–1620.
- [205] K. Soussi, J. Jung, F. Pointillart, B. Le Guennic, B. Lefevre, S. Golhen, O. Cador, Y. Cuyot, O. Maury, L. Ouahab, *Inorg. Chem. Front.* 2 (2015) 1105–1117.
- [206] J. Jung, T.T. da Cunha, B. Le Guennic, F. Pointillart, C.L.M. Pereira, J. Luzon, S. Golhen, O. Cador, O. Maury, L. Ouahab, *Eur. J. Inorg. Chem.* 2014 (2014) 3888–3894.
- [207] W. Huang, J. Xu, D. Wu, X. Huang, J. Jiang, *New J. Chem.* 39 (2015) 8650–8657.
- [208] J.-R. Jimenez, I.F. Diaz-Ortega, E. Ruiz, D. Aravena, S.J. Pope, E. Colacio, J.M. Herrera, *Chem. Eur. J.* 22 (2016) 14548–14559.
- [209] M. Ren, Z.-L. Xu, S.-S. Bao, T.-T. Wang, Z.-H. Zheng, R.A. Ferreira, L.-M. Zheng, I.D. Carlos, *Dalton Trans.* 45 (2016) 2974–2982.
- [210] D.-Q. Wu, D. Shao, X.-Q. Wei, F.-X. Shen, L. Shi, Y.-Q. Zhang, X.-Y. Wang, *Dalton Trans.* 46 (2017) 12884–12892.
- [211] A.V. Gavrikov, N.N. Efimov, Z.V. Dobrokhotova, A.B. Ilyukhin, P.N. Vasilyev, V. M. Novotortsev, *Dalton Trans.* 46 (2017) (1816) 11806–11811.
- [212] A. Górczyński, D. Marcinkowski, M. Kubicki, M. Löffler, M. Korabik, M. Karbowski, P. Wiśniewski, C. Rudowicz, V. Patroniak, *Inorg. Chem. Front.* 5 (2018) 605–618.
- [213] L. Maxwell, M. Amoa, E. Ruiz, *Inorg. Chem.* 57 (2018) 13225–13234.
- [214] W. Zhao, H. Cai, X.-Y. Chen, G. Yi, L. Chen, A. Yuan, C.-L. Luo, *Dalton Trans.* 48 (2019) 5621–5626.
- [215] G. Peng, Y.-Y. Zhang, B. Li, X.-F. Sun, H.-L. Cai, D.-J. Li, Z.-G. Gu, G.E. Kostakis, *Dalton Trans.* 47 (2018) 17349–17356.
- [216] Y. Ohki, Y. Suzuki, M. Nakamura, M. Shimoi, A. Ouchi, *Bull. Chem. Soc. Japan* 58 (1985) 2968–2974.
- [217] Q. Zou, X.-D. Huang, J.-C. Liu, S.-S. Bao, L.-M. Zheng, *Dalton Trans.* 48 (2019) 2735–2740.
- [218] S.P. Petrosyants, K.A. Babeshkin, A.V. Gavrikov, A.B. Ilyukhin, E.V. Belova, N.N. Efimov, *Dalton Trans.* 48 (2019) 12644–12655.
- [219] A. Borah, S. Dey, S.K. Gupta, M.G. Walawalkar, G. Rajaraman, R. Murugavel, *Chem. Commun.* 56 (2020) (1882) 11879–11881.

Ligand-Field Directed Electronic Effects in Heterogenized Bifunctional Co(II) Molecular Clusters Accomplish Efficient Overall Water Splitting

Aditya Borah, Jayeeta Saha,[†] Sunita Sharma,[†] Savi Chaudhary, Sandeep K. Gupta, Gopalan Rajaraman,^{*} Chandramouli Subramaniam,^{*} and Ramaswamy Murugavel^{*}



Cite This: *ACS Catal.* 2023, 13, 8535–8550



Read Online

ACCESS |

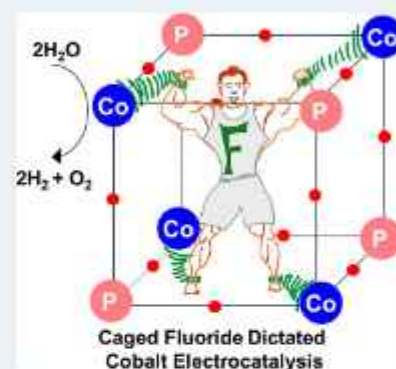
Metrics & More

Article Recommendations

Supporting Information

ABSTRACT: We demonstrate a hitherto unknown approach of employing cobalt organophosphate D4R cage-clusters, $[(RO)PO_3Co(L)]_4$ (1–4) and $[nBu_4N][F@((RO)PO_3Co(L))_4]$ (1F–4F), where L = DMSO (1 or 1F), pyridine (2 or 2F), 4-formylpyridine (3 or 3F), and 4-cyanopyridine (4 or 4F), as bifunctional heterogeneous catalysts for electrochemical water splitting in near-neutral conditions. Electronic and steric modifications on the clusters are achieved through a synergistic combination of endohedral trapping of fluoride ion and exohedral functionalization of pyridines. This two-pronged approach significantly reduces the charge density at the metal leading to energetically favorable water coordination with a perceptible enhancement in the kinetics of overall water splitting, with 4F exhibiting the lowest cell overpotential of 0.949 V (overall cell potential 2.179 V), observed among molecular catalysts. Density functional calculations highlight the importance of cooperativity between the cobalt centers. The unique D4R geometry stabilizes the high-valent metal-oxo/hydroperoxo species, emphasizing the need for polynuclear clusters to catalyze such challenging reactions, as has been well-established in the evolutionary PS-II.

KEYWORDS: bifunctional catalysts, molecular catalysis, overall water-splitting, geometry-driven cooperativity, ligand field design, DFT calculations, cobalt phosphates



INTRODUCTION

Earth-abundant, heterogeneous electrocatalysts for energy-efficient water splitting has been the holy grail for realizing a hydrogen-driven economy.^{1–19} Various design approaches such as doping, nanostructuring, and strain-engineering have been adopted for developing electrocatalysts that function close to the thermodynamic value.^{20–27} Interface-driven heterogeneous electrocatalysts for water splitting have been predominantly based on transition metal-based nanosystems and their variants for achieving energy-efficient kinetic enhancements.^{28–31} Among the systems that have been investigated, Co-based molecular systems and extended solid-state materials occupy a considerable space owing to the unique multivalent redox properties associated with the Co-center, as has been exemplified by the initial report on the Co(II)-phosphoric acid system in aqueous alkaline conditions.^{32–35} Since then, well-defined, atom-precise Co-based clusters (either as Co(II)/Co(III)) are being extensively explored to not only glean mechanistic aspects of water splitting but also to improve the overall energy-efficiency.^{36–38} In this direction, a cubane-like $[Co(III)_4O_4]$ cluster (a clone inspired by photosystem Mn_4Ca cluster) has been a promising candidate for unravelling the molecular pathways leading to

water splitting.^{39–44} The use of well-defined atom-precise molecular Co systems, stabilized by appropriate ligand fields, have been largely inaccessible due to the lack of design approaches and inability to prevent aggregation during catalysis. Interestingly, there have not been any significant attempts to investigate Co(II) based molecular systems for this purpose, especially those built from phosphate-based ligands, despite the fact that Co(II) state has been established as a key state through both theoretical and experimental mechanistic investigations.^{3,45}

Our interest in this area stems from our earlier observations that Co(II) centers can easily be stabilized by phosphoric acid diesters, leading to both discrete or polymeric organic-soluble and water insoluble materials.^{46–48} Subsequent investigations on these Co(II) based systems by us and Tilley et al. have indeed established that these thermo-labile systems can be

Received: December 2, 2022

Revised: May 15, 2023

Published: June 13, 2023



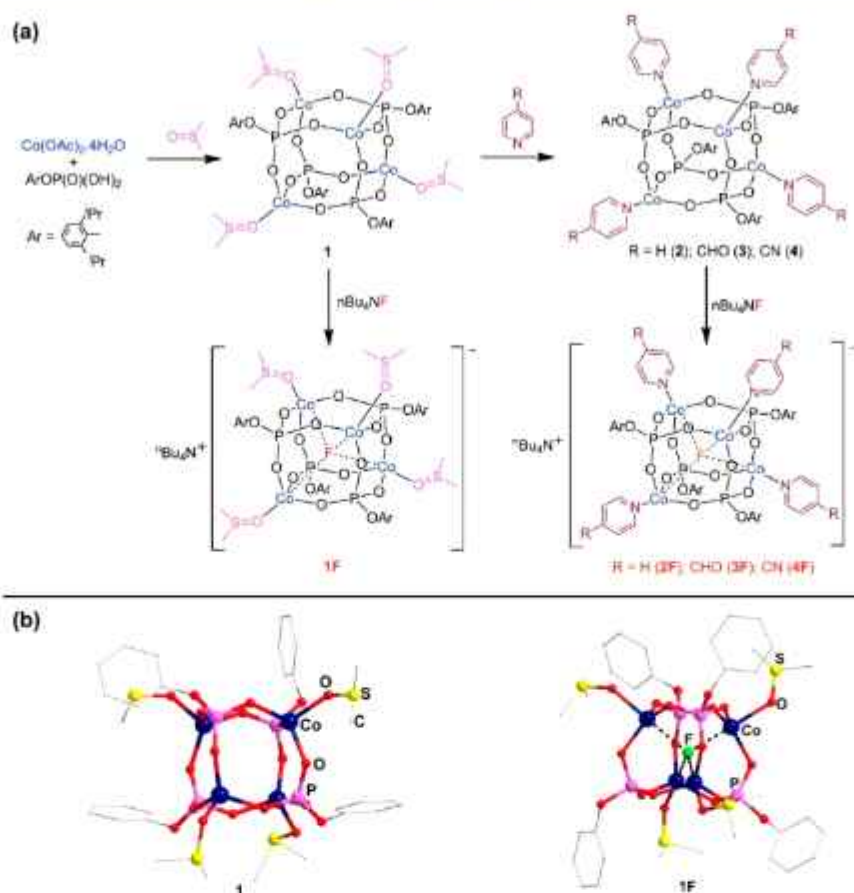


Figure 1. (a) Synthetic strategy employed for preparing cobalt phosphate clusters **1–4** and **1F–4F**. (b) Molecular structures of **I** and anionic part of **1F** as representative example. H atoms and isopropyl groups of phenyl rings are omitted for clarity.

transformed into useful electrocatalysts either in their pristine or immobilized states using suitable hosts.^{3,49} These dialkyl phosphates however are not amenable for their use in molecular/cluster catalysis owing to the fact that they are both thermally unstable and lack functional diversities which can be used to fine-tune the electronic effects that lead to superior catalytic efficiencies. Hence, it becomes important to design ligands that can embrace more metal ions leading to the preferential formation of clusters, rather than solid-state materials. Thus, in a renewed attempt to achieve this synergism in synthesis for driving the desired electronic effects, we have switched over to a phosphoric acid monoester whose metal harvesting pocket is PO_3^{2-} , rather than the earlier diesteric PO_2^- units. Indeed this strategy was extremely successful in assembling molecular clusters that resemble zeolitic D4R, D6R and D8R units incorporating a range of redox active metal centers.^{50–55} In this direction, we have recently shown that a cubane shaped D4R Co cluster can be assembled using a simple neutralization reaction between cobalt acetate and 2,6-diisopropylphenylphosphate under ambient conditions.⁵⁶ The structural resemblance of these Co(II) phosphate clusters to the Mn_4Ca photosystem⁵⁷ warranted a systematic investigation into their electrocatalytic water splitting behavior both in their pristine and electronically enhanced variations. In order to achieve the latter objective, we have relied on incorporation of fluoride anion inside the D4R cubane⁵⁸ with concurrent exocubane ligand-driven modulation of charge-density on the Co(II) center. The results of these investigations leading to exceptional kinetic enhancement to HER, OER and overall

water splitting, with activities rivalling traditional Pt/IrO₂ catalysts, are presented in this communication.

RESULTS AND DISCUSSION

Design Principles. Formation of cubane-like clusters essentially make use of corner sharing tetrahedral ions of the type EO_4^{n-} as has been established in zeolite science.⁵⁹ While SiO_4^{4-} ions, along with sporadically substituted with Al^{3+} ions, have been the essential building blocks for the Bronsted acidic zeolites, much of the more-recent hydrophobic neutral aluminophosphates (AIPOs) chemistry originates from PO_4^{3-} and Al^{3+} ions.⁶⁰ Pruning the dimensionality of the phosphate-based extended solids to discrete entities would warrant suitable modification of the phosphoric acid to its dianionic $(\text{RO})\text{PO}_3^{2-}$ form rather than the original trianionic form.^{45,61} This not only restricts the growth of the structures in the third dimension, but also paves the way for incorporation of divalent cationic centers such as Co(II), instead of Al(III). This strategy has been a mainstay in our design principles to introduce the entire first row transition metals in their divalent form into a cubane-like architecture that resembles the D4R building block. Importantly, the high propensity for Co(II) ions to adopt a tetrahedral geometry over other coordination polyhedra enables realization and isolation of a range of tetrahedral Co(II) tetranuclear clusters.⁵⁶ An added advantage of using such systems stems from the fact that the electronic state of Co(II) metal centers can be precisely engineered through a two-pronged approach consisting of: (a) incorporation of a highly electronegative F ion which acts as a charge

sink and (b) introduction of an exocubane ligand at each Co(II) center which can be substituted with either an electron-donating (e.g., $-\text{NH}_2$) or -withdrawing para-substituent (e.g., $-\text{CN}$) on the donor pyridinic ring. Figure 1a summarizes these design principles employed in the present study.

Synthesis and Structures of the Clusters. An equimolar reaction between the monoaryl phosphate, $(\text{RO})\text{PO}_3\text{H}_2$ ($\text{R} = 2,6$ -diisopropylphenyl) and cobalt(II) acetate in DMSO under ambient conditions yields $[(\text{RO})\text{PO}_3\text{Co}(\text{DMSO})]_4$ (**1**) as single crystals directly from the reaction mixture (Figure 1). Addition of more Lewis basic pyridines to the above reaction mixture results in replacement of DMSO by the corresponding pyridinic ligands to yield $[(\text{RO})\text{PO}_3\text{Co}(\text{L})]_4$ ($\text{L} =$ pyridine (**2**), 4-formylpyridine (**3**) and 4-cyanopyridine (**4**)). These D4R shaped clusters **1–4** further react with tetrabutylammonium fluoride, once again under ambient conditions, resulting in the formation of fluoride-incorporated cubane clusters $[\text{tBu}_4\text{N}][\text{F}@(\text{RO})\text{PO}_3\text{Co}(\text{L})]_4$ ($\text{L} =$ DMSO (**1F**), pyridine (**2F**), 4-formylpyridine (**3F**) and 4-cyanopyridine (**4F**)), respectively. The pristine and fluoride incorporated clusters **1–4** and **1F–4F** have been extensively characterized through analytical and spectroscopic techniques. Raman spectroscopy, in particular, provides clear evidence of the symmetry breaking in **1F–4F**, as compared to **1–4**. Characteristic peaks at 560 cm^{-1} (Co–O , F_{2g}) and 460 cm^{-1} (Co–O , E_g) and 699 cm^{-1} (P–O) and 1020 cm^{-1} (pyridine, **2–4** and **2F–4F**) are observed for all the cubanes (**1–4** and **1F–4F**). In addition, a prominent Co–F vibrational mode ($420\text{–}440\text{ cm}^{-1}$) is observed for **1F–4F**. Interestingly, the strength of this Co–F vibrational mode varies with the inductive effect of the distal, exocubane functional group, with a red-shift observed for **4F** compared to **1F**, indicating the more polarized Co–F bond (Figure S2).

The molecular structures of both pristine and fluoride incorporated clusters have been unambiguously established through single crystal X-ray structure determination of **1**, **2**, **3**, **1F**, **2F**, **3F**, and **4F**. The structures of **3** and **3F** have been established as the hemiacetal forms rather than the original aldehydic forms in view of the fact that the diffraction quality single crystals could be obtained only in methanol. While the molecular structures of **1** and **1F** are shown in Figure 1b, the details of other molecular structures and key bond parameters are elaborated in the ESI (Figure S3–S9). It can be seen that the pristine clusters (**1**, **2**, and **3**) have close structural resemblance to the zeolitic D4R SBU, whose central $\text{Co}_4\text{P}_4\text{O}_{12}$ core is a face-to-face dimer of two single-4-crowns. The bulky aryloxides on the phosphorus along with the pyridinic ligands on the cobalt offer an organic envelope for the inorganic core. This protective coating ensures stabilization of cobalt(II) centers. The way in which the eight heavy atoms and 12 oxygen centers are arranged in the cluster leaves sufficient void inside the cubane for incorporation of lighter anions. Such anion inclusion in the case of $(\text{PhSi})_8\text{O}_{12}$ silasesquioxane clusters have been previously observed when their synthesis was achieved through hydrolysis of silyl esters in the presence of an anionic source.⁶² The fact that the $\text{Co}_4\text{P}_4\text{O}_{12}$ is far less covalent than a Si_8O_{12} core offers opportunities to introduce an anion inside the core post assembly of the clusters. Thus, the compounds **1F–4F** derived by such postsynthetic anion inclusion of clusters **1–4** house fluoride anions at the center of the cubane as depicted in the molecular structure of **1F** in Figure 1b, as a representative example.

This inclusion of fluoride anion inside the cubane brings about significant structural distortions on the shape of the cluster as well as the coordination geometry of the metal ion. For example, the tendency of the fluoride ion to simultaneously interact with all the four Co(II) ions, results in their inward movement toward the central fluoride ion accompanied by an outward movement of the phosphorus centers. These movements of heavy atoms also have a bearing on the position of the oxygen centers. As a result, the local symmetry around the L–CoO_3 unit in **1–4** changes from an apparent C_{3v} symmetry to a pseudo- D_{3h} symmetry for the $\text{F}@(\text{LCoO}_3)$ units in **1F–4F**, a structural transformation pictorially represented in Figure 2 for the conversion of **1** to **1F** by the

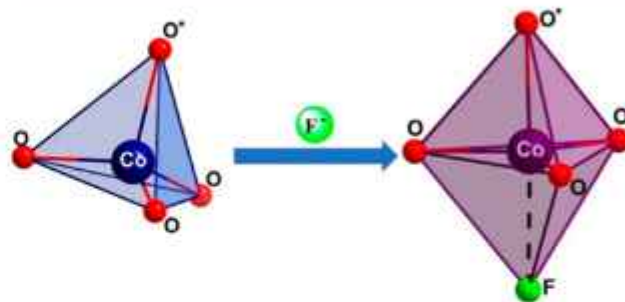


Figure 2. Effect of fluoride ion incorporation at the center of cubane **1** to produce **1F**. O^* is the O atom of DMSO and other three oxygens are from phosphate. Only one of the four Co-centers of the D4R cluster is depicted as a representative case.

endohehedral addition of fluoride ion. In **1**, the three $\text{Co–O}(\text{P})$ bonds around each cobalt exhibit an average bond length of 1.915 Å. On fluoride encapsulation, these bonds elongate to 1.951 Å, an effective average elongation of 36 pm for each bond. Interestingly, the fluoride incorporation also elongates the exocubane $\text{Co–O}(\text{DMSO})$ bond from 2.007 to 2.110 Å, with a net lengthening of 113 pm. Thus, the Co–O bond trans to fluoride is significantly elongated compared to those equatorial Co–O bonds (cis to fluoride). This lengthening is quite significant in spite of the fact that the fluoride ion is only weakly interacting and almost equidistant to the four cobalt ions (average $\text{Co–F} = 2.316$ Å). Similar elongations have also been observed for **2F–4F**. Concurrently, the tetrahedral O–Co–O angles in **1** are transformed to cis and trans trigonal bipyramidal (tbp) angles of 120° , 90° , and 180° in **1F**, respectively (see ESI, Table S11 and S12).

To investigate the type of magnetic interactions among the Co(II) centers in pristine and fluorinated clusters, the temperature dependence of magnetization ($\chi_M T$ vs T) has been explored on polycrystalline powder of **1** and **1F** under an applied magnetic field of 1000 Oe in the temperature range of 2–300 K. The temperature dependence of $\chi_M T$ for complex **1** and **1F** is depicted in Figure S51. The room temperature $\chi_M T$ values are found to be $10.78\text{ cm}^3\text{ K mol}^{-1}$ for **1** and $9.65\text{ cm}^3\text{ K mol}^{-1}$ for **1F**. These values are higher than that expected ($7.5\text{ cm}^3\text{ K mol}^{-1}$) for four noninteracting high-spin Co(II) ions ($S = 3/2$, $g = 2.0$). On decreasing the temperature, the $\chi_M T$ values gradually decrease and sharply fall to 0.97 and $0.34\text{ cm}^3\text{ K mol}^{-1}$ at 2.0 K for **1** and **1F**, respectively, indicating a singlet ground magnetic state ($S_T = 0$) with antiferromagnetic exchange coupling between the high spin Co(II) ions. The data was modeled using the following spin Hamiltonian:

$$\hat{H} = \sum_i \mu_B g_i \hat{S}_i \cdot H - 2J_{ij} \sum_{i,j;i \neq j} \hat{S}_i \cdot \hat{S}_j$$

with an isotropic g -value for each Co(II) center ($S = 3/2$), and isotropic magnetic exchange interaction J (six interactions between the four Co(II) ions lying on the vertices of a tetrahedron were considered). The best fit yields $g = 2.31$, $J = -1.16 \text{ cm}^{-1}$ for **1** and $g = 2.36$, $J = -2.46 \text{ cm}^{-1}$ for **1F**, respectively. The computational analysis of complex **1** and **1F** reveals similar exchange coupling values ($J = -2.34$ and -4.16 cm^{-1} for **1** and **1F**, respectively).

These computed values indicate a weak antiferromagnetic coupling, reinforcing the experimental observations. In case of **1**, the weak antiferromagnetic exchange can be attributed to the absence of any direct one-atom linker between the cobalt centers, while in **1F** the fluoride ion offers additional exchange pathway enabling marginally stronger antiferromagnetic exchange. Although single F^- bridge is expected to yield stronger antiferromagnetic coupling, trapping of the F^- ion inside the cubane restricts the Co–F–Co angle ($\approx 108\text{--}109^\circ$), leading to a weak exchange interactions.^{53,63}

Electrochemistry. The Co(II) clusters (**1–4**, **1F–4F**) provide the synergistic combination of precisely tuned electronic states and redox active metal centers to elicit significant interest for electrocatalytic water splitting. This is further aided by their chemical stability in ambient conditions while preserving their molecular discreteness and remaining insoluble in neutral aqueous media. This prompted the use of such precisely defined molecular systems as heterogeneous electrocatalysts for OER, HER and thereby overall water splitting (Figures 3a,b and S17). The chemical versatility

enabled by the incorporation of fluorides and tuning of the exocubane two-electron donors provide a vast arena for a systematic exploration of these systems, leading to deeper fundamental understanding of the electronic effects associated with the water-splitting catalysis. As opposed to conventional molecular clusters such as Mn_4Ca and $\text{Co(III)}_4\text{O}_4$, which exhibit excellent activity toward either HER or OER, the quest has always been toward development of a single bifunctional molecular catalyst for overall water splitting.^{40–42} The electrochemical studies elaborated herein unravel such hitherto unknown molecular bifunctional catalytic clusters that exhibit an unparalleled energy efficiency and kinetically facile catalytic activity for both HER and OER under near-neutral conditions.

The cubane clusters are directly immobilized on the surface of glassy-carbon electrode with loading ranging from 0.23 to 0.25 mg/cm^2 . Notably, all the eight clusters tested were found to act as bifunctional catalysts for both HER and OER in near-neutral conditions ($\text{pH} = 7.0$), albeit to varying extents; a direct manifestation of the ligand-field effects and the associated electronic modulations. The observation of a prominent Co(II)/Co(III) redox couple (0.91 V vs RHE, Figure S18) in the cyclic voltammograms for all the eight clusters provides a robust fundamental basis of the OER proceeding via an oxo-bridge formation (Co(III)-OOH).⁶⁴ Furthermore, the signature of Co(III)/Co(IV) redox activity appearing at 1.24 V vs RHE uniformly across all the eight clusters confirms the formation of Co(III)-O* as an intermediate in the HER.⁶⁵ Thus, all the eight clusters are capable of promoting both OER and HER and thus are, to our knowledge, the first set of molecularly assembled bifunctional catalysts for overall water splitting.

Catalysis by 1–4. The cluster **2** with pyridine as the exocubane ligand (Figure 1) exhibits an overpotential of 850 mV for HER and an onset potential of 630 mV for OER in near-neutral conditions. The corresponding values for cluster **1** that contains DMSO as the exocubane ligand (Figure 1) are 900 and 730 mV. While the electronic effects exerted by DMSO cannot be modified, attendant changes can be made on the pyridinic ligand by placing either electron-donating or electron-withdrawing substituents. Furthermore, electron-donating substituents may not have any positive effect on the catalysis, placing electron-withdrawing substituents such as $-\text{NO}_2$, $-\text{CHO}$, $-\text{CN}$ can lead to depletion of charge-density at the cobalt center and thus facilitate coordination of water molecules to metal and trigger the electrocatalysis. Accordingly, formyl and cyano-substituted pyridines with increasing electron-withdrawing capabilities (**3** and **4**; Figure 1) were designed and evaluated for electrocatalysis. Consistent with the expectations, the distal functionalization on the para position of the pyridinic ring produces pronounced effect of HER and OER overpotentials for **3** and **4**. Specifically, the presence of a stronger electron withdrawing 4-cyano substituent on the pyridyl ring renders **4** as a superior catalyst compared to **3**. Effectively, these distal substituents on the pyridine ligand modulates the positive charge on the metal. This is further substantiated by theoretical investigations which reveal that charge on cobalt center increases by 0.04 au for **4** vis-a-vis **1** (*vide infra*). The estimation of electrochemical onset overpotentials further confirms the above reasoning based on substituent effects, as can be seen through the order of kinetic facility for overall water splitting ($4 > 3 > 2 > 1$). This completely correlates to the anticipated inductive effects. Such ability to tune the catalytic activity through precise chemical function-

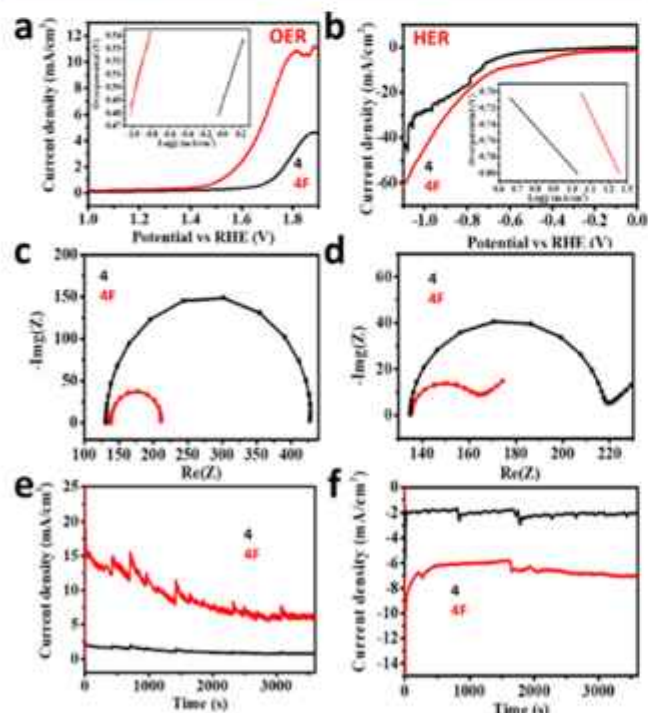


Figure 3. Linear sweep voltammograms (inset: Tafel slope) of **4** and **4F** for (a) OER and (b) HER in 1 M PBS electrolyte ($\text{pH} = 7$). Electrochemical impedance spectroscopy of **4** and **4F** for (c) HER and (d) OER. Chronoamperometry of **4** and **4F** for (e) HER and (f) OER. The spikes seen are due to evolution and delamination of gas bubbles.

alization is the first of its kind and opens up transformative pathways for rational chemical tailoring of heterogeneous catalysis.

The resulting order of onset overpotentials is in good agreement with the trends of interfacial charge-transfer resistance (R_{ct} of 300 Ω (HER) and 81.3 Ω (OER)) and the electrochemical double-layer capacitance (C_{dl} of 2.64 $\mu\text{F}/\text{cm}^2$ (HER) and 1.08 $\mu\text{F}/\text{cm}^2$ (OER)), values for 4 (Figure 3c, 3d, S21, Table S14). It can be discerned from Table S14 that 4 is the best catalyst among these four catalysts. The lower R_{ct} for 4 provides confirmatory evidence for facile charge-transfer through the active sites which in turn is driven by efficient and thermodynamically favored water coordination (*vide infra*). Similarly, the higher C_{dl} illustrates the crowding of water molecules around the electron-deficient Co(II) redox center, more so in case of electron-deficient 4, and thus reduces any mass-transfer polarization effects.

Catalysis by 1F–4F. In addition to the electronic modulations introduced by the distal functionalization, the presence of a central void in the cubane cage offers an attractive proposition for a more direct tuning of its electronic states. Accordingly, these clusters are rendered anionic through inclusion chemistry in an attempt to further improve the catalytic efficiency. Such an approach not only distorts the coordination symmetry of the cobalt from a pseudo- C_{3v} to an apparent- D_{3h} , but also further reduces the charge density on the metal thereby creating an ideal platform for facile water coordination (*vide infra*). Fluoride ion being the smallest of the anions (barring hydride) would be an ideal choice for the inclusion in the endocubane cavity.^{66,67} Additionally, being the most electronegative element, it can further deplete the electron density from the cobalt centers to which it is equidistantly placed at ~ 2.31 Å. Thus, it can be envisaged that oppositely directed electron drain by both fluoride and pyridine ligands would tend to serve the purpose of enhancing electrocatalytic efficiency. The change in the geometry around Co(II) also mimics a shuttle-relay mechanism, with a prominent effect on the kinetics of the electrocatalysis.

The synergistic effects of these processes result in 1F–4F exhibiting significantly lower potentials than their corresponding nonfluorinated counterparts 1–4. Such fluorinated cubanes also follow the same electronic order effected by the nature of L for overall water splitting ($4\text{F} > 3\text{F} > 2\text{F} > 1\text{F}$, Figure 3a, b, Table 1 and S18). Of particular importance is the overpotential

Table 1. Cell Overpotential of the Catalysts under Neutral pH

Catalyst	Cell overpotential (V)	Catalyst	Cell overpotential (V)
1	1.63	1F	1.28
2	1.48	2F	1.05
3	1.33	3F	0.985
4	1.26	4F	0.949

of HER and onset potential of OER processes in case of 4F, which reduces to 655 and 295 mV, respectively. Thus, the overall water splitting cell overpotential for 4F is estimated to be 0.949 V.^{68,69} This onset overpotential is also considerably lower than those reported for most solid-state materials, off-stoichiometric compounds and their combinations (Table S19). The redox peak assignments were carried out after evaluating the cyclic voltammograms at varying scan rates and ascribing them to Randles-Sevick analysis. The redox peak

positions were also in agreement with those observed in literature for Co-based systems.^{37,39,40,70,71} To the best of our knowledge, 4F is the best performing heterogenized molecular electrocatalyst on an electrode surface (Figure 4, S19–S20).

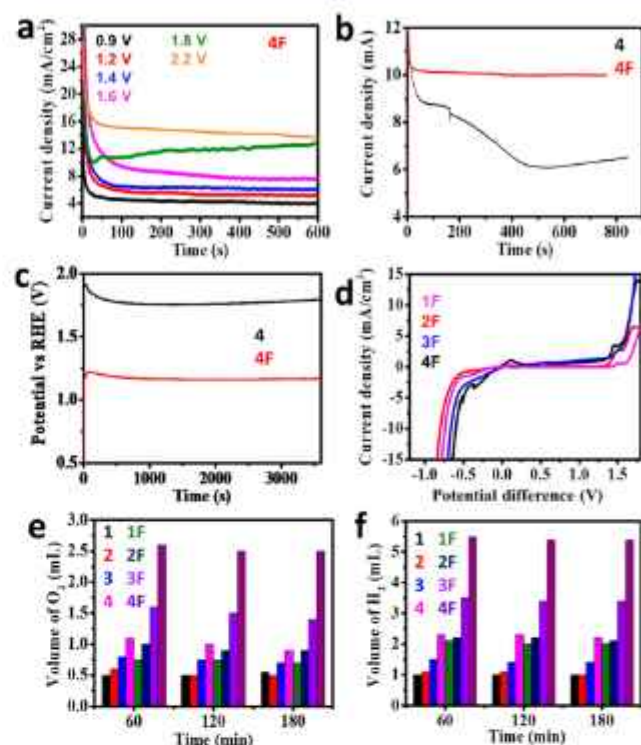


Figure 4. (a) Chronoamperometry of 4F at different applied potentials for overall water splitting in 1 M PBS electrolyte. (b) Chronoamperometry of 4 and 4F for overall water splitting in a two-electrode setup. The catalysts were drop-casted on carbon paper electrodes and ECSA estimated from Randles-Sevick plot. (c) Chronopotentiometry of 4 and 4F for overall water splitting in a two-electrode setup (carbon paper as electrodes). (d) Linear sweep voltammograms of 1F, 2F, 3F, and 4F for overall water splitting. Quantification of (e) O_2 and (f) H_2 for all catalysts in a three-electrode setup.

The stability of 4F catalyst was estimated by chronoamperometry at varying potentials (from 0.9 to 2.2 V) in a two-electrode setup (Figure 4). The catalyst 4F exhibits stable current density of 10 mA/cm^2 under an applied potential of 2.2 V for over 1 h, with no detectable change (Figure 4a). The electrochemical stability of 4F was evaluated by continued operation under chronopotentiometry (at 10 mA/cm^2 , Figure 4c) and chronoamperometry (Figure 4b). Furthermore, the current density is amenable for facile enhancement, without affecting the operational stability as established by driving the 4F system at 1.8 V to deliver a current density of 15 mA/cm^2 for over 1 h. In order to ascertain the electrochemical stability of 4F, the cyclic voltammetry has been carried out for 30 cycles in 1 M PBS buffer (pH = 7.4). The redox activity corresponding to the $\text{Co}^{3+} \leftrightarrow \text{Co}^{4+}$ is distinct and invariant during these 30 cycles (Figure S19), confirming the electrochemical stability of the molecular heterogeneous catalysts. Similarly, the chronoamperometry has been performed for 10 h, and it has been found that the catalytic activity is not changed over the entire period (Figure S30).

The bifunctionality of the catalyst is also demonstrated by overall linear sweep voltammograms (LSVs) and direct quantification of both H_2 and O_2 evolved during the process (Figure 4d–f). The overpotential and onset potential for both HER (655 mV) and OER (295 mV) is least for the cyano-substituent 4F catalyst, providing the minimal cell overpotential (0.949 V, Figure 4d). These trends are also reflected in the hydrogen and oxygen generation (Figure 4e,f).

Extensive XPS studies provide useful insights to the mechanistic aspects of the catalysis apart from providing evidence for the stability of the catalysts during prolonged usage. All the molecular clusters (1–4, 1F–4F) exhibit prominent peaks in X-ray photoelectron spectroscopy, arising due to the spin–orbit coupled Co(II) species (Figure S22–S25). The binding energy peaks at $2p_{3/2}$ and $2p_{1/2}$ observed at 781.2 and 797 eV for 1, remains invariant for 1F, in spite of change in coordination geometry. This is due to the balance of electron withdrawing endocubane substituent (fluoride) and the electron donating exocubane substituent (DMSO). In spite of this, both 1 and 1F exhibit shakeup satellite peaks at 785.6 and 802.2 eV, with an energy difference of 15.8 eV confirming the presence of Co(II) in the as synthesized clusters. Further, the stability of the catalysts can be established by chronoamperometry for 10 h (Figure S30).

In contrast, the remaining molecular clusters (2–4, 2F–4F) exhibit significant and systematic variations in the peak positions of Co(II). Distal substitution by an electron-withdrawing functionality results in the positive shift in binding energy to higher values. The magnitude of such shifts across 2 to 4 and 2F to 4F, are also in agreement with the electron-withdrawing ability of the -R group and thus follows the order $4 > 3 > 2$ and $4F > 3F > 2F$. Thereby, the molecular cluster 4F exhibits the highest binding energy of 781.7 and 804.5 eV, without compromising on the peak separation of 15.8 eV, reconfirming the Co(II) as the electroactive species.

The electron-deficiency on the Co(II), introduced by both endo- and exocubane functionalities are observed to produce a marked difference in their overall water splitting capabilities. The molecular cluster (4F) exhibiting the highest binding energy for Co(II) exhibits the lowest HER and OER onset overpotentials (655 and 295 mV, respectively). Although the cubanes investigated in this report exclusively contain Co(II), its atomic content is an important descriptor of the kinetic facility toward electrocatalysis (Figure 5a, Table S15). Importantly, the atomic content of Co(II) follows the exact order of their electrocatalytic performance and Tafel slope, with 4F having the highest Co(II) content (25.6%) and lowest onset overpotential and Tafel slope (Figure S17, Table S13, as current density cannot be reached up to 10 mA/cm^2 , the onset overpotential has been calculated by extrapolating the tangent in LSV).^{72,73} This provides critical information on the electron-deficient Co(II) as the active water coordination center for both HER and OER.

The electron-deficient Co(II) centers of cubane play an active role in water coordination. This is further reinforced through a quantitative estimation of the oxygen-deficiency in the molecular clusters. We would like to point out that the XPS spectra have been individually deconvoluted to estimate the proportion of oxygen that contributes to the water coordination. Therefore, while these numbers do not represent the molecular composition of the systems, it is a precise estimate of the role of oxygen and its availability for water coordination. Accordingly, cluster 4F exhibits the highest

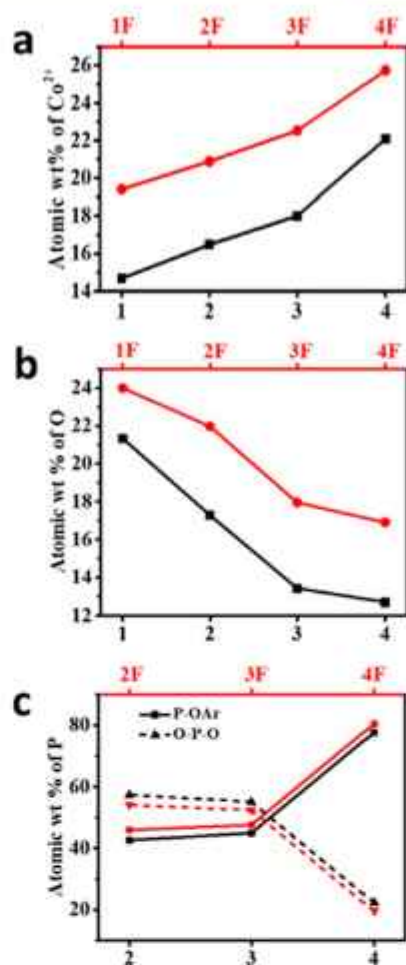


Figure 5. (a) Atomic% of Co(II), (b) atomic% of O, and (c) atomic% of P, calculated from XPS for the catalysts. Data collected from XPS spectra given in Figures S22–S25. The estimations provided here do not correspond to those obtained from survey spectrum, but to those derived from the deconvoluted high-resolution XPS spectra. Thus, the Co^{2+} from Co $2p_{3/2}$ (781 eV), P 2p (133 eV), originating from O–P–O and P–OAr (135 eV) and deconvoluted Co–O–P (532 eV) are taken into account to derive this plot.

oxygen deficiency (19.59%) among all the endocubane systems investigated (Figure 5b, S22–S25, Table S16), consistent with earlier observations. This enables the Co(II) center of 4F to have the largest propensity toward coordinating the water molecules. Another feature directing the ability of these clusters to act as bifunctional catalysts is the presence of the phosphate moiety. While the electron deficient Co(II) drives the coordination of water leading to HER, the O–P–O bridging unit is critical for the OER process. Thus, a higher content of P–O–Ar in 4F drives the subsequent OER process (Figures 5c, S22–S25, Table S17). This is in excellent agreement with the lowest bridging O–P–O content exhibited by 4F. Thus, the synergism between a highly electron deficient Co(II) center, the endocubane-influenced geometrical distortion and the facile exposure of the phosphate moiety drive the coordination of water for both HER and OER processes.

The strong thermodynamic and kinetic dependence on the distal substitutions affords an unambiguous associative pathway leading to overall water-splitting. This is also in line with the change in the coordination geometry as observed in X-ray structure and Raman spectra (*vide supra*). The Raman

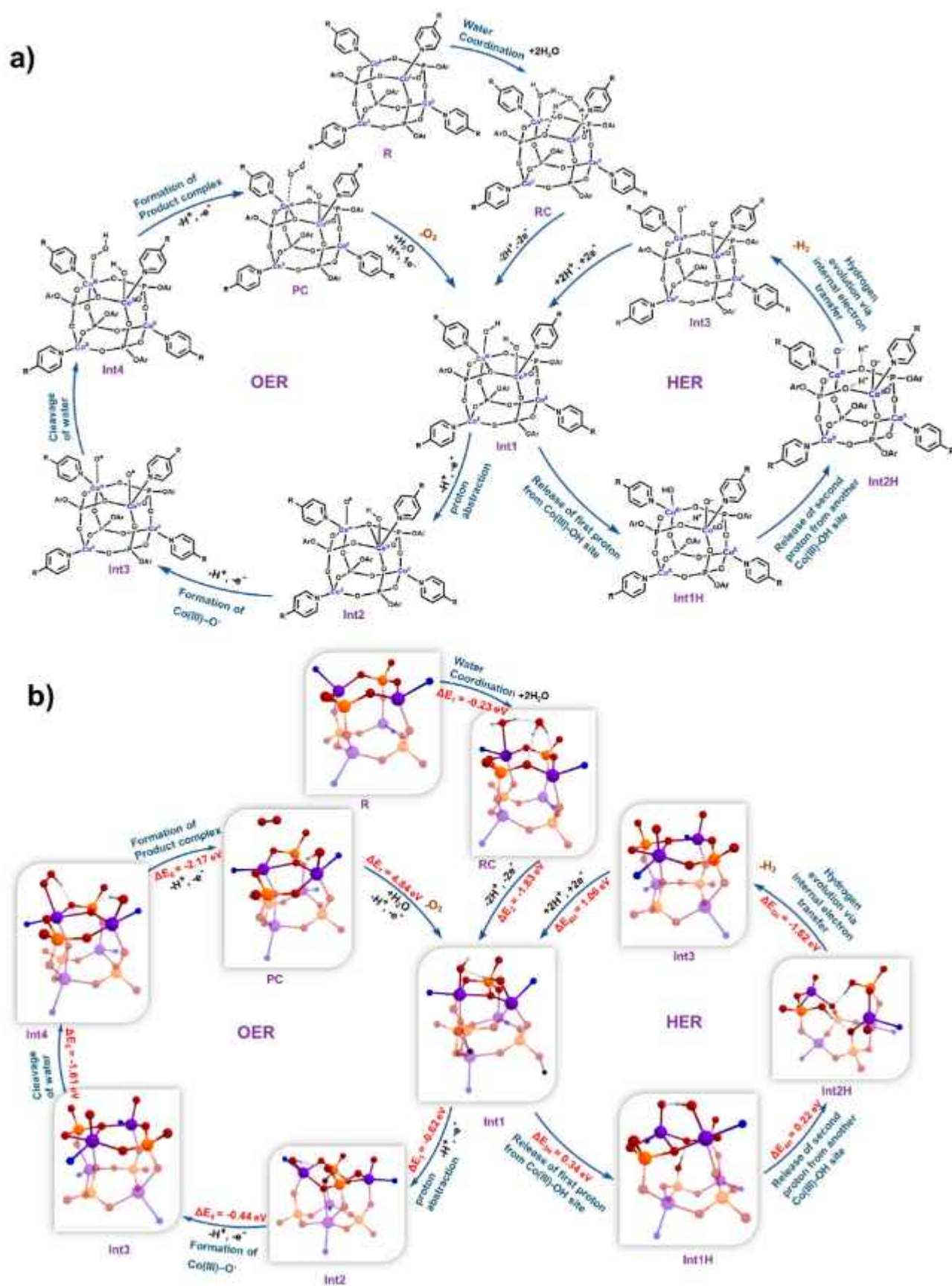


Figure 6. (a) Proposed mechanism for both OER and HER; (b) the catalytic cycles involved in both HER and OER in optimized 4 are shown as representative cases. Color code: violet-cobalt, red-oxygen, blue-nitrogen, orange-phosphorus, gray-carbon, and white-hydrogen.

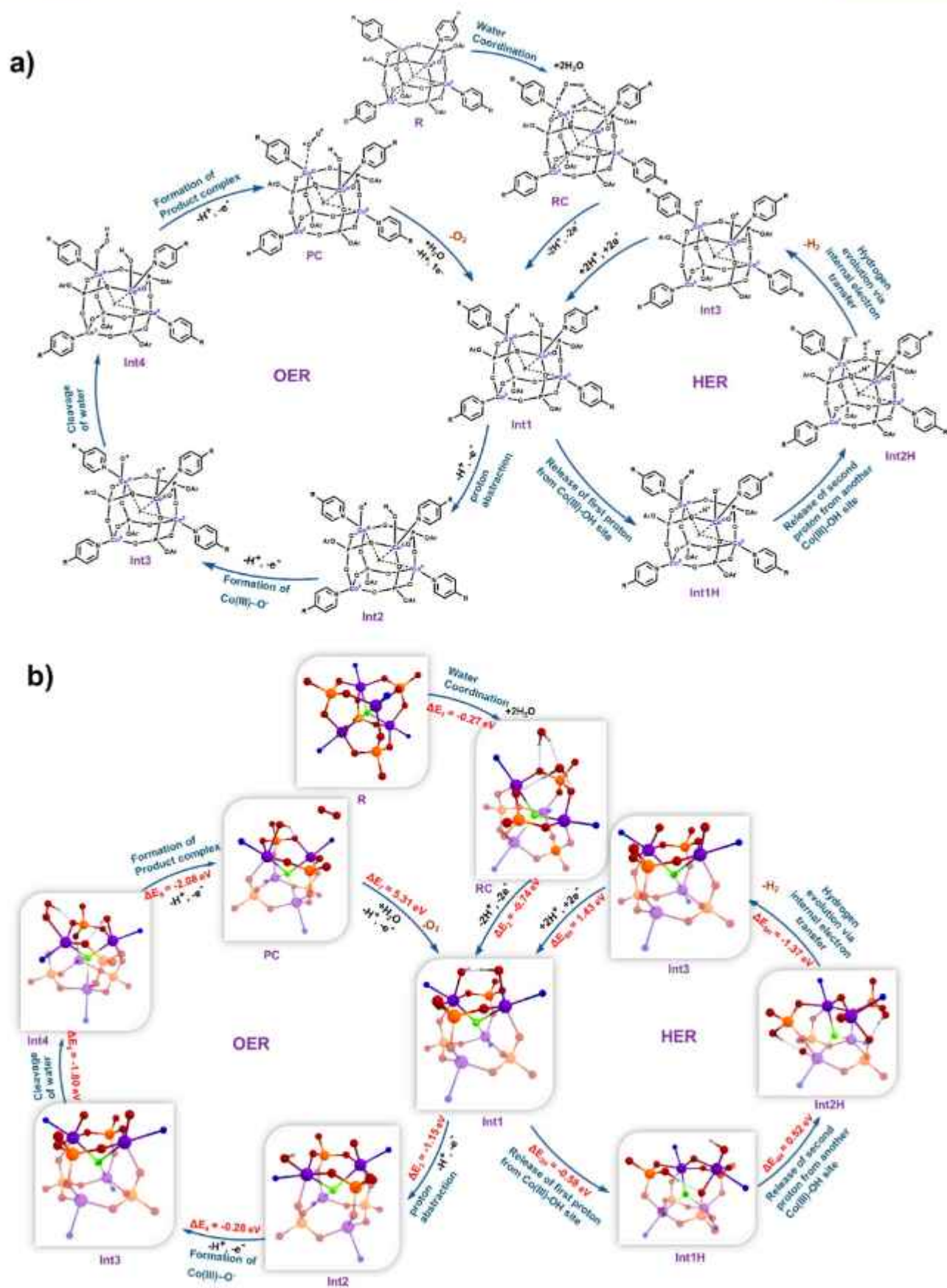


Figure 7. (a) Proposed catalytic mechanism for both OER and HER for 1F – 4F; (b) the catalytic cycles involved in both HER and OER in optimized 4F are shown as representative cases. Color code: violet-cobalt, red-oxygen, blue-nitrogen, orange-phosphorus, green-fluorine, gray-carbon, and white-hydrogen.

spectroscopy was performed before and after electrocatalysis to investigate the electronic changes occurs at the electrocatalytic centers (2F, 3F, and 4F). All the fluoride incorporated clusters 2F–4F have been characterized by Raman spectroscopy. The characteristic peaks at 560 cm^{-1} (Co–O, F_{2g}) and 460 cm^{-1} (Co–O, E_{1g}), and 699 cm^{-1} (P–O), 1750 cm^{-1} (CHO), 1020 cm^{-1} (pyridine, 2–4 and 2F–4F) and Co–F vibrational mode ($420\text{--}440\text{ cm}^{-1}$, 2F–4F) are observed for all catalysts (Figure S31). Interestingly, minor shifts in the pyridinic peaks (1020 cm^{-1}) were observed signifying the direct involvement of the ligand environment in the charge transfer processes accompanying water splitting. The Co–F vibrational peak was observed to have a red shift, confirming the participation toward the electrochemical reaction. The strength of this Co–F vibrational mode was modified due to the coordination formed with the electrocatalytic Co center. Moreover, the clear retention of all the peaks indicates both the stability of the catalyst during the electrochemical process and the preservation of its integrity during the catalysis. Such chemical stability of 4 and 4F is further confirmed by the means of powder X-ray diffraction studies. 4 and 4F are soaked in water for a prolonged time (72 h) and the PXRD patterns obtained prior and subsequent to the soaking are found to be identical which confirms the phase purity and stability of the catalysts (Figures S47 and S48). Further, the postelectrocatalytic stabilities of the fluorinated clusters are supported by X-ray photoelectron spectroscopy. No significant shifts in XPS observed for C 1s, Co 2p, and O 1s peaks reflects the integrity of the oxidation states of the metal centers in the clusters. The increase in binding energy for C 1s and Co 2p observed due to the partial oxidation of the catalyst indicating the decrease in current density in chronoamperometry (Figures S26–S29).

Additional conclusive evidence was obtained from operando Raman spectro-electrochemical measurements carried out on the best performing catalyst (4F, Figure S32). A custom-made electrochemical cell consisting of a 3 cm aperture for spectroscopic measurement equipped with a bottom Indium-doped tin-oxide conductive glass (ITO, sheet resistance = $10\ \Omega\ \text{sq}^{-1}$) acting as working electrode and Ag/AgCl, Pt wire serving as reference and counter electrode, respectively, was utilized for these measurements. Catalyst 4F was spray-coated on the ITO and served as the working electrode. Onset of HER is accompanied by the emergence of peaks at 1600 cm^{-1} (cyanopyridine group), 1350 cm^{-1} (C–C), and 600 cm^{-1} (peroxide). Similarly, the OER is accompanied by enhancement of the vibrational modes corresponding to 1600 cm^{-1} (cyanopyridine group), 1350 cm^{-1} (C–C), and 550 cm^{-1} (peroxide). These vibrational modes that are spectroscopically tracked are also validated from DFT studies that indicate the bond vibrations at 604 cm^{-1} (hydroxide), 556 cm^{-1} (peroxide), and $1601\text{--}1657\text{ cm}^{-1}$ (all cyanopyridine group) in the intermediate species ($^{15}\text{Int}_4$).

Computational Studies. To understand the mechanistic insights into the catalytic bifunctionality of 4 and 4F, DFT calculations were performed on 4 and 4F to bring out the salient feature of fluoride incorporation and simultaneously investigate the mechanistic information resulting in low overpotentials for OER and HER (see computational details for the methodology employed).⁷⁴ Both 4 and 4F consist of four Co(II) centers, albeit in tetrahedral or trigonal bipyramidal geometries, respectively. The phosphate bridges between the Co(II) centers enable exchange coupling between them. Besides, DFT optimization was carried out for 1–4 and

1F–4F in order to extract their charges, spin densities and structural parameters (details in Figure S33 and Table S20–23). However, single-point energy calculations were performed for 4F using its X-ray structure to ascertain the magnetic coupling using the established protocols.⁷⁵ The high symmetry around the Co(II) center in both 4 and 4F dictates the existence of a single exchange coupling constant (J), as is computed to be -2.24 and -3.15 cm^{-1} , respectively.^{76,77} Such low antiferromagnetic J values re-emphasize a diamagnetic ground state ($S = 0$) in these clusters (1–4, 1F–4F) and ensure close-lying exchange-coupled states that are easily accessible during overall water splitting.

Compared to the pristine clusters 1–4, the endocubane clusters 1F–4F exhibit longer Co–O, Co–N, and P–O bonds, consistent with the corresponding structural parameters obtained from X-ray diffraction, validating the computational methodology employed. In spite of the observed differences in the coordination geometry around Co(II) ion in complexes 4 and 4F, both these complexes exhibit similar electronic configuration of $(d_{yz})^2(d_{xz})^2(d_{x^2-y^2})^1(d_z^2)^1(d_{xy})^1$, albeit changes in orbital energy ordering (see Figure S34, S35). A weak overlap of SOMOs (Singly Occupied Molecular Orbitals) of Co(II) centers via d_{xy} and $d_{x^2-y^2}$ orbital leads to a weak antiferromagnetic coupling for both 4 and 4F. Furthermore, the presence of axial fluoride ion in 4F produces a significant lowering of the absolute charge on the individual Co(II) centers by ~ 0.1 au. This would, in turn, render the fluoride ion as the key player, both in generation and stabilization of higher oxidation states for cobalt during the catalysis, as has been elaborated *vide infra*.

To understand the possible pathways for enhanced water splitting efficiency of these complexes, the high-spin $S = 6$ state of both 4F and 4 were investigated in detail. The mechanistic outcome that emanates from these calculations is pictorially represented in Figures 6 and 7, in which there are two catalytic cycles representing HER and OER. Considerable variations in terms of both the geometry and the oxidation states of Co(II) centers have been envisaged in these catalytic cycles, the energies of various spin states associated with the Co centers have also been investigated in detail. Attempts have also been made to compare the reactivity of one versus two metal centers for both complexes, 4 and 4F.

The first catalytic step in both 4 and 4F involves the attachment of a water molecule to either two Co(II) centers or a Co(II) center, both of which were computed with the former found to be energetically favorable (-0.45 and -0.48 eV). The exothermicity of this step for both 4 and 4F (-0.23 and -0.27 eV , respectively) indicates an energetically favorable process. For 4 while one of the water molecules coordinate to the Co(II) center leading to a coordination expansion from trigonal bipyramidal, the second water molecule was found to have strong H-bonding interaction with the coordinated water molecule. For 4F, on the other hand, both the water molecules are in the vicinity of the Co(II) center without a concrete metal–ligand bond as the geometry around Co(II) is already trigonal bipyramidal, and expansion to octahedral is likely to generate greater distortion. For 4, the second water molecule is not only involved in H-bonding interaction with the coordinated H_2O (H...O distance of 1.764 \AA) but also with the phosphate group of $\{\text{Co}_4\text{O}_4\}$ cubane (H...O(P) distance of 1.862 and 1.912 \AA). For 4F, on the other hand, as both the waters are not coordinated, they were found to have strong H-bonding interaction with each other (1.938 \AA) and also with

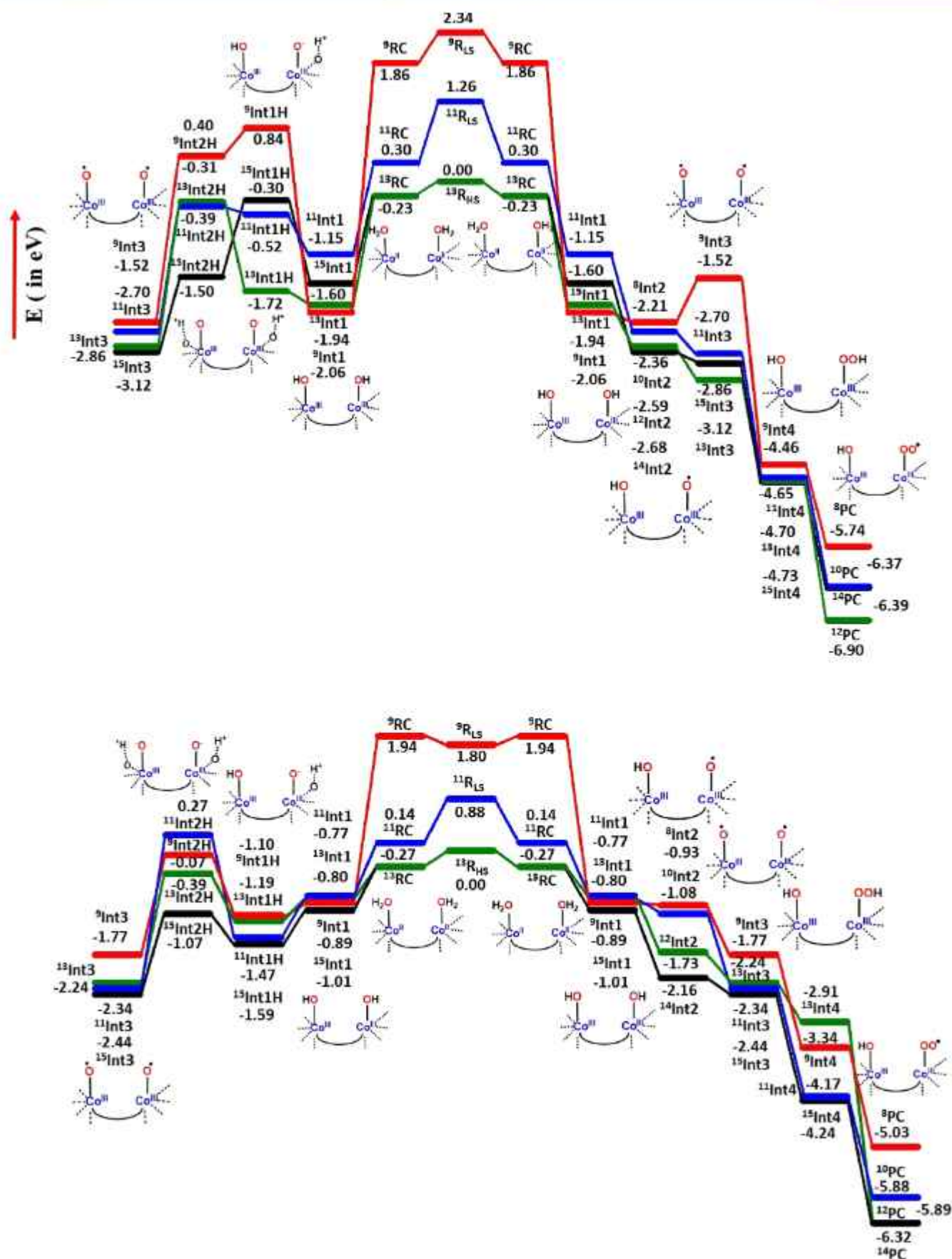


Figure 8. Potential energy profiles involved in catalysis by 4 and 4F with appropriate intermediates.

the phosphate group of the $\{Co_4O_4\}$ cubane (H \cdots O(P) distance of 1.835 and 1.906 Å). These H-bonding interactions indicate that the water molecules are already activated.

In the next step of the HER and OER cycle, the formation of the putative Co(III)–OH species ((Intermediate 1; **Int1**) in both metal centers is assumed. The Co(III) center, thus generated, was found to alter the nature of spin-state from high-spin to other spin states such as low-spin or intermediate spin state for **4** while for **4F** the entire reaction was found to occur on the high-spin surface. The associated energetics for all the possible spin-states ($S = 7, 6, 5$ and 4) indicates that complex **4** has $S = 4$ as its ground state, which arises from $S = 1$ state for the dimeric $\{(Co(III)–OH)_2\}$ unit and the other two Co(II) centers having $S = 3$ which is maintained through the reaction. In the reactive $\{(Co(III)–OH)_2\}$ site, one square pyramidal Co(III) center possesses $S = 1$ state, and the other octahedral Co(III) center has $S = 0$ state due to bidentate coordination of the phosphate. For the **4F**, on the other hand, $S = 7$ is found to be the ground state, with each of the two Co(III) units possessing $S = 2$. The high-spin ground state observed for the Co(III) is essentially due to weaker fluoride binding, which also switches its nature of binding from μ_4 to μ_3 at this intermediate. This reveals that the presence of F ion has the ability to manure different spin-state and hence the reactivity.

Nevertheless, the $S = 0$ state of the Co(III) centers are only 0.12 eV higher (see Figure 8). At the $S = 7$ state, the Co(III)–OH species shows a strong delocalization of the spin density on the oxygen of the Co(III)–OH species (~ 0.92), suggesting a strong radical character that is desired for the forthcoming steps. The formation of this intermediate is exothermic by -1.83 and -0.74 eV from the RC for **4** and **4F**, respectively (see computational details and Figures 6b and 7b). We have also performed the formation of Co(III)–OH species assuming the reactivity at a single Co(II) center, and this step is found to be less exothermic (-1.18 eV for **4F** and -1.32 eV for **4**, see the ESI). This emphasizes that a multinuclear cluster is important for water oxidation, and this is in line with other experiments where often multinuclear Co clusters were employed for the catalysts, with many examples reporting the absence of such reactivity for monomers.^{78–80}

In the next step, formation of (Intermediate 2; **Int2**) is assumed to take place via the release of one proton and an electron leading to the formation of the putative Co(III)–O \cdot species on one of the active centers with the other retaining the Co(III)–OH unit. Estimation of the energetics of all possible spin states on the Co(III)–O \cdot center ($S = 13/2, 11/2, 9/2$ and $7/2$) establishes that this step is exothermic for both **4** and **4F** by -0.62 and -1.15 eV from **Int1**, respectively (see Figures 6b and 7b). Oxidation of Co(III)–OH to Co(III)–O \cdot results in stabilization of $S = 3/2$ centers resulting in the ground state of $S = 13/2$ for both **4F** and **4**, respectively. As the generation of putative Co(III)–O \cdot centers is challenging, the presence of strongly electronegative F $^-$ ion help in such formation leading to greater exothermicity for **4F** compared to **4** in this step of the catalytic cycle. Careful analysis of the spin density plot of **Int2** reveals a significant oxyl radical character that suggests the formation of Co(III)–O \cdot species.⁸¹ Employing a correlation developed based on multireference calculations on such electromeric species yield 14% of Co(III)–O \cdot character for **4** and 15% of Co(III)–O \cdot for **4F**, suggesting greater oxyl radical character for **4F** compared to **4**.⁸² This is also reflected in the computed spin densities (0.96 vs 1.00). The role of Co(III)–O \cdot

species oxidation of water in a homogeneous catalytic environment is highlighted recently also support our proposal.⁸¹ The Co–O distance is estimated to be 1.627 and 1.611 Å in the case of complexes **4** and **4F**, respectively. Again, formation of such species computed at the single metal center was found to be exceedingly endothermic (2.12 eV for **4F** and 1.88 eV for **4**, see in ESI), while when both metals are involved, this was found to facilitate such oxidation by offering electronic cooperation.

Further in the OER cycle, **Int2** species loses one more proton as well as one electron to generate the aggressive dicobalt(IV)=O species (Intermediate 3; **Int3**) for the oxygen evolution process. The formation of this species is also found to be exothermic by -0.44 and -0.28 eV for complexes **4** and **4F**, respectively. The ground state for these two were observed to be $S = 6$ and $S = 7$, for **4** and **4F**, respectively. While all the putative Co(III)–O \cdot species exhibit a strong oxyl radical character, for **4F** one of the Co(III)–O \cdot species has high-spin $S = 5/2$ ground state suggesting a pure Co(III)–O \cdot character (Co–O bond length is 1.815 Å vs 1.609 Å). Strongly oxyl radical character has been attributed to greater reactivity in several high-valent oxo species earlier^{37,71,83,84} and might be attributed to greater reactivity of **4F** observed in the experiments. In the successive step, the generation of aggressive Co(III)–O \cdot is therefore expected to activate the next water molecule via O \cdots O bond formation, leading to the generation of Co(III)–OOH species (Intermediate 4; **Int4**). The formation of this Co(III)–OOH species is further confirmed through in situ spectroelectrochemical Raman measurements with **4F**, further validating the computed mechanism (vide supra). Herein, the emergence of peak corresponding to Co(III)–OOH intermediate is clearly observed in the temporal evolution of the spectra, collected during the catalysis (Figure S32).

Formation of Co(III)–OOH species has also been found to be exothermic by -1.61 and -1.80 eV for **4** and **4F**, respectively,⁸⁵ (see Figure 6b and 7b) for $S = 7$ ground state with both Co(III) species possessing $S = 2$ ground state. As the O \cdots O formation is the key step in the evolution of OER, we have also computed this step for a single Co center catalyst which is found to be exceedingly endothermic ($+2.05$ eV for **4** and $+2.65$ eV for **4F**, see in ESI). Addition of H \cdot and OH \cdot across dimeric Co(III)–O \cdot leading to the formation of Co(III)–OH and Co(III)–OOH species is found to be very favorable, suggesting strong cooperativity between two cobalt centers in the OER evolution again.

In the next step, hydrogen atom transfer from the Co(III)–OOH is assumed to take place and this results in the formation of O $_2$ and Co(II) species at the ground state and Co(III)–OO \cdot species at some excited spin states for both **4** and **4F** (see Figure 6b and 7b). This step is also found to be exothermic with respect to **Int4** by -2.08 eV for complex **4F** and -2.17 eV for complex **4**. It is important to note here that for **4F**, due to the presence of fluoride ion, the reactive metal centers maintain a high-spin state throughout the reaction and therefore, spin-crossover from one spin-state to the other is not necessary. For **4**, on the other hand, there are multiple spin-state crossovers detected during the course of the reaction. This spin-crossover with a lower oxidation state and weaker spin–orbit coupling results in larger energy penalties.^{86–88} Despite favorable energetics in some of the steps involved, this spin state crossing is likely to hinder reactivity of

4 compared to 4F, and this is in agreement with experimental observations.

For the HER cycle, the Co(III)–OH species is the starting point of the catalytic cycle. Various pathways based on experimental reports were attempted and this includes the formation of metal-hydride species and found that such mechanistic paths are energetically unfavorable for this reaction (See Table S24 in ESI). The mechanism for which favorable energetics are obtained is shown in Figures 6a and 7a. The first intermediate (Int1H) forms after the abstraction of a proton from the Co(III)–OH species by one of the phosphate oxygen atoms leading to the formation of Co(III)–O[−] species with $S = 6$ and $S = 7$ ground state for 4 and 4F, respectively. The deprotonation of the Co(III)–OH species to Co(III)–Oxo species was achieved earlier in a tetrahedral ligand framework supporting this hypothesis.⁸⁹ These spin state differences arise due to the stabilization of high-spin Co(III) $S = 2$ on both metal centers in the case of 4F, thanks to the presence of weak fluoride ion and formation of Co(III)–O–Co(III) species instead of a terminal Co(III)–O[−] expected. For 4, the Co(III)–O[−] found to have $S = 2$ ground state with the Co(III)–OH having $S = 1$ as its ground state. The formation of this intermediate is found to be endothermic for 4 (0.34 eV) and exothermic for 4F (−0.58 eV). A significant energy difference in this step suggests that the release of the proton is to be facilitated to a greater extent in the case of 4F, compared to 4, directly supporting the experimental observations. The next step is the formation of Int2H, which is formed upon the loss of another proton from the Co(III)–OH center. The formation of this species is found to be endothermic for both 4 (0.22 eV) and 4F (0.52 eV) for the $S = 7$ state.

In the next step, the H₂ release is expected from two abstracted protons, which are in the phosphate arms along with 2e[−] assumed to be released by the oxidation of metal ion from Co(III)–O[−] to Co(III)–O[•] (Int3).^{90,91} The formation of this species is exothermic by −1.62 and −1.37 eV for complex 4 and 4F, respectively. This is essentially due to the fact that these putative dicobalt(IV)=O species are in Co(III)–O[•] species and, therefore, one-electron oxidation from Co(III)–O[−] to Co(III)–O[•] is favorable. In the HER cycle as well, several spin-state crossings were noted for 4, while the entire reaction was found to occur in a high-spin surface for 4F. This is again expected to facilitate faster H₂ release in 4F compared to 4.

If we compare the potential energy surface developed between OER and HER cycles, it is clear that in OER, all the intermediates formation are facile and exothermic, while in HER cycle, many steps are endothermic, and therefore, releasing H₂ is an energy-demanding slow process compared to OER. This observation is consistent with the experiments (See Figures 6, 7 and 8). Earlier observations that mononuclear complex do not split water (neither HER nor OER) and the recent report of two Co sites involvement in water splitting by Co₃O₄ augment our proposal, strongly supporting cooperativity in HER/OER reactivity.^{78,92} Various potential intermediates for the HER mechanism, such as metal-hydride, Co(III)–O[−] have been explored, but the energetic cost associated with the formation of such species are unfavorable (see Table S24, S61). Although the proposed species is a high-valent oxo species, the Mulliken charges computed reveal that the charges are decreasing on the metal center as we move along the species computed along the HER pathway, suggesting a favorable reaction under cathodic potential as

observed in the experiments. Further, the internal hydrogen atom transfer that has been proposed here with organo-phosphate ligand is also supported by earlier studies on Cu(II) mediated HER reaction where phosphate ligands were found to be the proton acceptor and also another example of Zn(II) complex where N–H bonds in the ligands were found to facilitate the reaction,⁹³ offering confidence on the proposed mechanistic cycles from various perspective presented.⁹⁴

CONCLUSIONS

We have demonstrated, in this contribution, a simple and straightforward strategy of ligand-field tuning on discrete tetranuclear Co(II) clusters to electronically manipulate the charge density on the redox-active metal center. This transforms the atom-precise cubane cage cluster to a bifunctional, heterogeneous catalyst for overall water splitting at an extremely competitive cell overpotential of 0.949 V. This study highlights the importance of systematic regulation of the charge density on the redox-active Co(II) center, for achieving kinetically enhanced water splitting activity, through two synergistic and tangential approaches: (a) introduction of an appropriate electron-withdrawing para-substituted pyridinic ligand, constituting exohedral ligand-field effect, and (b) endohedral encapsulation of fluoride anion that produces concomitant geometric and electronics effects. Cluster 4F, representing the best combination of both these approaches, exhibits the lowest cell overpotential of 0.949 V among all known heterogeneous, molecular catalysts. Further, the DFT studies have unravelled the importance of cluster catalysis, where two phosphates and two Co(II) centers forming each face of the cubane clusters acts in tandem to provide the perfect environment for water coordination and subsequent HER and OER, respectively. A study of this sort, where suitably engineered molecular clusters can be rendered as heterogeneous catalysts opens up new avenues for overall electrochemical water splitting reactions. It is expected that these results will stimulate further interest in molecular cluster based heterogeneous catalysis, where the catalytically active metal ions such as cobalt and other transition metals will be placed in suitably chosen coordination environments for even better catalysis.

Although it has been possible to elucidate simultaneous OER and HER mechanisms of the parent (1–4) and fluorinated cubanes (1F–4F) through extensive computational studies described above, only a few of these proposed intermediates/key steps could be experimentally validated. This arises due to the complexity of the cluster systems and the presence of multiple reaction sites that cooperatively drive the overall water splitting. Given these limitations, currently it has not been possible to trap or characterize any further intermediates through in situ spectroscopic techniques. Thus, it would be prudent to further examine these complex systems through sized-down binuclear and mononuclear cobalt phosphate models. Work in this direction is currently underway in our laboratories.

ASSOCIATED CONTENT

Supporting Information

The Supporting Information is available free of charge at <https://pubs.acs.org/doi/10.1021/acscatal.2c05942>.

Additional figures and tables, crystallographic details, spectral characterization and computational details.

Crystallographic information on the clusters. CCDC numbers 1983455, 1983456, 2008048, 2008049, 2008222, and 2008223 contain the supplementary crystallographic data for this paper. These data can be obtained free of charge from The Cambridge Crystallographic Data Centre. Optimized geometries of complexes 1–4, and 1F–4F, selected structural parameters, Mulliken charges and spin densities of reactant, intermediates and product complexes. Energy profile diagram and proposed schemes for both OER and HER cycle (PDF)

X-ray data for 1, 1F, 3F, and 4F (CIF)

X-ray data for 2 and 2F (CIF)

Video of overall water splitting (MP4)

Water splitting video shot over 48 h (MOV)

AUTHOR INFORMATION

Corresponding Authors

Gopalan Rajaraman – Department of Chemistry, Indian Institute of Technology Bombay, Mumbai 400076, India; orcid.org/0000-0001-6133-3026; Email: rajaraman@chem.iitb.ac.in

Chandramouli Subramaniam – Department of Chemistry, Indian Institute of Technology Bombay, Mumbai 400076, India; orcid.org/0000-0001-8335-7395; Email: csubbu@chem.iitb.ac.in

Ramaswamy Murugavel – Department of Chemistry, Indian Institute of Technology Bombay, Mumbai 400076, India; orcid.org/0000-0002-1816-3225; Email: rmv@chem.iitb.ac.in

Authors

Aditya Borah – Department of Chemistry, Indian Institute of Technology Bombay, Mumbai 400076, India

Jayeeta Saha – Department of Chemistry, Indian Institute of Technology Bombay, Mumbai 400076, India

Sunita Sharma – Department of Chemistry, Indian Institute of Technology Bombay, Mumbai 400076, India

Savi Chaudhary – Department of Chemistry, Indian Institute of Technology Bombay, Mumbai 400076, India

Sandeep K. Gupta – Department of Chemistry, Indian Institute of Technology Bombay, Mumbai 400076, India; orcid.org/0000-0003-2432-933X

Complete contact information is available at: <https://pubs.acs.org/10.1021/acscatal.2c05942>

Author Contributions

[†](J.S., S.S.) These authors contributed equally to this work.

Notes

The authors declare no competing financial interest.

ACKNOWLEDGMENTS

We thank SERB, New Delhi and Department of Science and Technology, Government of India for financial support (grants EMR/2017/002767 and SB/S2/JCB-85/2014 to R.M.; grants DST/TMD/MES/2k17/41 and SERB/F/9022/2019-2020 to C.S.; grants CRG/2018/000430; DST/SJF/CSA-03/2018-10; SB/SJF/2019-20/12 to G.R.). A.B. and S.S. would like to thank UGC, and J.S. would like to thank CSIR for research fellowships. The authors thank the central facilities at IIT Bombay for providing various characterization data.

DEDICATION

Dedicated to Professor Vadapalli Chandrasekhar on the occasion of his 65th Birthday

REFERENCES

- (1) Yeo, B. S.; Bell, A. T. Enhanced activity of gold-supported cobalt oxide for the electrochemical evolution of oxygen. *J. Am. Chem. Soc.* **2011**, *133* (14), 5587–5593.
- (2) Surendranath, Y.; Lutterman, D. A.; Liu, Y.; Nocera, D. G. Nucleation, growth, and repair of a cobalt-based oxygen evolving catalyst. *J. Am. Chem. Soc.* **2012**, *134* (14), 6326–6336.
- (3) Ahn, H. S.; Tilley, T. D. Electrocatalytic water oxidation at neutral pH by a nanostructured Co(PO₃)₂ anode. *Adv. Funct. Mater.* **2013**, *23* (2), 227–233.
- (4) Cabán-Acevedo, M.; Stone, M. L.; Schmidt, J.; Thomas, J. G.; Ding, Q.; Chang, H.-C.; Tsai, M.-L.; He, J.-H.; Jin, S. Efficient hydrogen evolution catalysis using ternary pyrite-type cobalt phosphosulphide. *Nat. Mater.* **2015**, *14* (12), 1245–1251.
- (5) Wang, H.; Lee, H.-W.; Deng, Y.; Lu, Z.; Hsu, P.-C.; Liu, Y.; Lin, D.; Cui, Y. Bifunctional non-noble metal oxide nanoparticle electrocatalysts through lithium-induced conversion for overall water splitting. *Nat. Commun.* **2015**, *6* (1), 7261.
- (6) Wang, J.; Cui, W.; Liu, Q.; Xing, Z.; Asiri, A. M.; Sun, X. Recent progress in cobalt-based heterogeneous catalysts for electrochemical water splitting. *Adv. Mater.* **2016**, *28* (2), 215–230.
- (7) Zhou, H.; Yu, F.; Huang, Y.; Sun, J.; Zhu, Z.; Nielsen, R. J.; He, R.; Bao, J.; Goddard, W. A., III; Chen, S.; et al. Efficient hydrogen evolution by ternary molybdenum sulfoselenide particles on self-standing porous nickel diselenide foam. *Nat. Commun.* **2016**, *7* (1), 12765.
- (8) Xue, Z. H.; Su, H.; Yu, Q. Y.; Zhang, B.; Wang, H. H.; Li, X. H.; Chen, J. S. Janus Co/CoP nanoparticles as efficient Mott-Schottky electrocatalysts for overall water splitting in wide pH range. *Adv. Energy Mater.* **2017**, *7* (12), 1602355.
- (9) Hui, L.; Xue, Y.; Huang, B.; Yu, H.; Zhang, C.; Zhang, D.; Jia, D.; Zhao, Y.; Li, Y.; Liu, H.; et al. Overall water splitting by graphdiyne-exfoliated and-sandwiched layered double-hydroxide nanosheet arrays. *Nat. Commun.* **2018**, *9* (1), 5309.
- (10) Park, J.; Kwon, T.; Kim, J.; Jin, H.; Kim, H. Y.; Kim, B.; Joo, S. H.; Lee, K. Hollow nanoparticles as emerging electrocatalysts for renewable energy conversion reactions. *Chem. Soc. Rev.* **2018**, *47* (22), 8173–8202.
- (11) Wang, X.; Ma, W.; Ding, C.; Xu, Z.; Wang, H.; Zong, X.; Li, C. Amorphous multi-elements electrocatalysts with tunable bifunctionality toward overall water splitting. *ACS Catal.* **2018**, *8* (11), 9926–9935.
- (12) Xu, H.; Cheng, D.; Cao, D.; Zeng, X. C. A universal principle for a rational design of single-atom electrocatalysts. *Nat. Catal.* **2018**, *1* (5), 339–348.
- (13) Liu, Z.; Tan, H.; Liu, D.; Liu, X.; Xin, J.; Xie, J.; Zhao, M.; Song, L.; Dai, L.; Liu, H. Promotion of Overall Water Splitting Activity Over a Wide pH Range by Interfacial Electrical Effects of Metallic NiCo-nitrides Nanoparticle/NiCo₂O₄ Nanoflake/graphite Fibers. *Adv. Sci.* **2019**, *6* (5), 1801829.
- (14) Sultan, S.; Ha, M.; Kim, D. Y.; Tiwari, J. N.; Myung, C. W.; Meena, A.; Shin, T. J.; Chae, K. H.; Kim, K. S. Superb water splitting activity of the electrocatalyst Fe₃Co(PO₄)₄ designed with computation aid. *Nat. Commun.* **2019**, *10* (1), 5195.
- (15) Service, R. F. New electrolyzer splits water on the cheap. *Science* **2020**, *367* (6483), 1181–1181.
- (16) Yan, Z.; Hitt, J. L.; Turner, J. A.; Mallouk, T. E. Renewable electricity storage using electrolysis. *Proc. Natl. Acad. Sci. U. S. A.* **2020**, *117* (23), 12558–12563.
- (17) Oshima, T.; Nishioka, S.; Kikuchi, Y.; Hirai, S.; Yanagisawa, K.-i.; Eguchi, M.; Miseki, Y.; Yokoi, T.; Yui, T.; Kimoto, K.; et al. An Artificial Z-Scheme Constructed from Dye-Sensitized Metal Oxide Nanosheets for Visible Light-Driven Overall Water Splitting. *J. Am. Chem. Soc.* **2020**, *142* (18), 8412–8420.

- (18) Anantharaj, S.; Noda, S. Amorphous catalysts and electrochemical water splitting: an untold story of harmony. *Small* **2020**, *16* (2), 1905779.
- (19) Anantharaj, S.; Kundu, S.; Noda, S. The Fe Effect[®]: A review unveiling the critical roles of Fe in enhancing OER activity of Ni and Co based catalysts. *Nano Energy* **2021**, *80*, 105514.
- (20) Kanan, M. W.; Nocera, D. G. In situ formation of an oxygen-evolving catalyst in neutral water containing phosphate and Co²⁺. *Science* **2008**, *321* (5892), 1072–1075.
- (21) Smith, R. D.; Prévot, M. S.; Fagan, R. D.; Zhang, Z.; Sedach, P. A.; Siu, M. K. J.; Trudel, S.; Berlinguette, C. P. Photochemical route for accessing amorphous metal oxide materials for water oxidation catalysis. *Science* **2013**, *340* (6128), 60–63.
- (22) Ullman, A. M.; Liu, Y.; Huynh, M.; Bediako, D. K.; Wang, H.; Anderson, B. L.; Powers, D. C.; Breen, J. J.; Abruña, H. C. D.; Nocera, D. G. Water oxidation catalysis by Co(II) impurities in Co(III)₄O₄ cubanes. *J. Am. Chem. Soc.* **2014**, *136* (50), 17681–17688.
- (23) Yu, F.; Zhou, H.; Huang, Y.; Sun, J.; Qin, F.; Bao, J.; Goddard, W. A.; Chen, S.; Ren, Z. High-performance bifunctional porous non-noble metal phosphide catalyst for overall water splitting. *Nat. Commun.* **2018**, *9* (1), 2551.
- (24) Han, X.; Ling, X.; Wang, Y.; Ma, T.; Zhong, C.; Hu, W.; Deng, Y. Spatial Isolation of Zeolitic Imidazole Frameworks-Derived Cobalt Catalysts: From Nanoparticle, Atomic Cluster to Single Atom. *Angew. Chem., Int. Ed.* **2019**, *58*, 5359.
- (25) Yan, Z.; Zhu, L.; Li, Y. C.; Wycisk, R. J.; Pintauro, P. N.; Hickner, M. A.; Mallouk, T. E. The balance of electric field and interfacial catalysis in promoting water dissociation in bipolar membranes. *Energy Environ. Sci.* **2018**, *11* (8), 2235–2245.
- (26) Lazouski, N.; Chung, M.; Williams, K.; Gala, M. L.; Manthiram, K. Non-aqueous gas diffusion electrodes for rapid ammonia synthesis from nitrogen and water-splitting-derived hydrogen. *Nat. Catal.* **2020**, *3* (5), 463–469.
- (27) Yu, J.; Dai, Y.; He, Q.; Zhao, D.; Shao, Z.; Ni, M. A mini-review of noble-metal-free electrocatalysts for overall water splitting in non-alkaline electrolytes. *Mater. Today Energy* **2021**, *1* (2), 100024.
- (28) Wang, M.; Zhang, L.; He, Y.; Zhu, H. Recent advances in transition-metal-sulfide-based bifunctional electrocatalysts for overall water splitting. *J. Mater. Chem. A* **2021**, *9* (9), 5320–5363.
- (29) Tao, B. X.; Li, X. L.; Ye, C.; Zhang, Q.; Deng, Y. H.; Han, L.; Li, L. J.; Luo, H. Q.; Li, N. B. One-step hydrothermal synthesis of cobalt-vanadium based nanocomposites as bifunctional catalysts for overall water splitting. *Nanoscale* **2019**, *11* (39), 18238–18245.
- (30) Wang, J.; Yue, X.; Yang, Y.; Sirisomboonchai, S.; Wang, P.; Ma, X.; Abudula, A.; Guan, G. Earth-abundant transition-metal-based bifunctional catalysts for overall electrochemical water splitting: A review. *J. Alloys Compd.* **2020**, *819*, 153346.
- (31) Peng, J.; Dong, W.; Wang, Z.; Meng, Y.; Liu, W.; Song, P.; Liu, Z. Recent advances in 2D transition metal compounds for electrocatalytic full water splitting in neutral media. *Mater. Today Adv.* **2020**, *8*, 100081.
- (32) Peng, X.; Jin, X.; Gao, B.; Liu, Z.; Chu, P. K. Strategies to improve cobalt-based electrocatalysts for electrochemical water splitting. *J. Catal.* **2021**, *398*, 54–66.
- (33) Xu, Y.; Wang, C.; Huang, Y.; Fu, J. Recent advances in electrocatalysts for neutral and large-current-density water electrolysis. *Nano Energy* **2021**, *80*, 105545.
- (34) Huang, C.; Qin, P.; Luo, Y.; Ruan, Q.; Liu, L.; Wu, Y.; Li, Q.; Xu, Y.; Liu, R.; Chu, P. K. Recent progress and perspective of cobalt-based catalysts for water splitting: design and nanoarchitectonics. *Mater. Today Energy* **2022**, *23*, 100911.
- (35) Doan, T. L.; Nguyen, D. C.; Prabhakaran, S.; Kim, D. H.; Tran, D. T.; Kim, N. H.; Lee, J. H. Single-Atom Co-Decorated MoS₂ Nanosheets Assembled on Metal Nitride Nanorod Arrays as an Efficient Bifunctional Electrocatalyst for pH-Universal Water Splitting. *Adv. Funct. Mater.* **2021**, *31* (26), 2100233.
- (36) Surendranath, Y.; Kanan, M. W.; Nocera, D. G. Mechanistic studies of the oxygen evolution reaction by a cobalt-phosphate catalyst at neutral pH. *J. Am. Chem. Soc.* **2010**, *132* (46), 16501–16509.
- (37) Nguyen, A. I.; Ziegler, M. S.; Oña-Burgos, P.; Sturzbecher-Hohne, M.; Kim, W.; Bellone, D. E.; Tilley, T. D. Mechanistic investigations of water oxidation by a molecular cobalt oxide analogue: Evidence for a highly oxidized intermediate and exclusive terminal oxo participation. *J. Am. Chem. Soc.* **2015**, *137* (40), 12865–12872.
- (38) Nguyen, A. I.; Wang, J.; Levine, D. S.; Ziegler, M. S.; Tilley, T. D. Synthetic control and empirical prediction of redox potentials for Co₄O₄ cubanes over a 1.4 V range: Implications for catalyst design and evaluation of high-valent intermediates in water oxidation. *Chem. Sci.* **2017**, *8* (6), 4274–4284.
- (39) Das, B. K.; Chakrabarty, R. Cobalt (III)-oxo cubane clusters as catalysts for oxidation of organic substrates. *J. Chem. Sci.* **2011**, *123* (2), 163–173.
- (40) McCool, N. S.; Robinson, D. M.; Sheats, J. E.; Dismukes, G. C. A Co₄O₄ "cubane" water oxidation catalyst inspired by photosynthesis. *J. Am. Chem. Soc.* **2011**, *133* (30), 11446–11449.
- (41) Brodsky, C. N.; Hadt, R. G.; Hayes, D.; Reinhart, B. J.; Li, N.; Chen, L. X.; Nocera, D. G. In situ characterization of cofacial Co(IV) centers in Co₄O₄ cubane: Modeling the high-valent active site in oxygen-evolving catalysts. *Proc. Natl. Acad. Sci. U. S. A.* **2017**, *114* (15), 3855–3860.
- (42) Song, F.; Moré, R.; Schilling, M.; Smolentsev, G.; Azzaroli, N.; Fox, T.; Luber, S.; Patzke, G. R. {Co₄O₄} and {Co₂Ni₄O₄} Cubane Water Oxidation Catalysts as Surface Cut-Outs of Cobalt Oxides. *J. Am. Chem. Soc.* **2017**, *139* (40), 14198–14208.
- (43) Nguyen, A. I.; Van Allsburg, K. M.; Terban, M. W.; Bajdich, M.; Oktawiec, J.; Amtawong, J.; Ziegler, M. S.; Dombrowski, J. P.; Lakshmi, K.; Drisdell, W. S.; et al. Stabilization of reactive Co₄O₄ cubane oxygen-evolution catalysts within porous frameworks. *Proc. Natl. Acad. Sci. U. S. A.* **2019**, *116* (24), 11630–11639.
- (44) Menezes, P. W.; Panda, C.; Walter, C.; Schwarze, M.; Driess, M. A cobalt-based amorphous bifunctional electrocatalysts for water-splitting evolved from a single-source lazulite cobalt phosphate. *Adv. Funct. Mater.* **2019**, *29* (32), 1808632.
- (45) Murugavel, R.; Choudhury, A.; Walawalkar, M. G.; Pothiraja, R.; Rao, C. N. R. Metal complexes of organophosphate esters and open-framework metal phosphates: synthesis, structure, transformations, and applications. *Chem. Rev.* **2008**, *108* (9), 3549–3655.
- (46) Murugavel, R.; Sathiyendiran, M.; Walawalkar, M. G. Di-tert-butyl Phosphate Complexes of Cobalt(II) and Zinc(II) as Precursors for Ceramic M(PO₃)₂ and M₂P₂O₇ Materials: Synthesis, Spectral Characterization, Structural Studies, and Role of Auxiliary Ligands. *Inorg. Chem.* **2001**, *40* (3), 427–434.
- (47) Pothiraja, R.; Sathiyendiran, M.; Butcher, R. J.; Murugavel, R. Cobalt and Manganese Nets via Their Wires: Facile Transformation in Metal-Diorganophosphates. *Inorg. Chem.* **2004**, *43* (24), 7585–7587.
- (48) Pothiraja, R.; Sathiyendiran, M.; Butcher, R. J.; Murugavel, R. Non-Interpenetrating Transition Metal Diorganophosphate 2-Dimensional Rectangular Grids from Their 1-Dimensional Wires: Structural Transformations under Mild Conditions. *Inorg. Chem.* **2005**, *44* (18), 6314–6323.
- (49) Saha, J.; Verma, S.; Ball, R.; Subramaniam, C.; Murugavel, R. Compositional Control as the Key for Achieving Highly Efficient OER Electrocatalysis with Cobalt Phosphates Decorated Nanocarbon Florets. *Small* **2020**, *16*, 1903334.
- (50) Murugavel, R.; Kuppaswamy, S. Octameric and Decameric Aluminophosphates. *Angew. Chem., Int. Ed.* **2006**, *45* (42), 7022–7026.
- (51) Murugavel, R.; Kuppaswamy, S.; Boomishankar, R.; Steiner, A. Hierarchical Structures Built from a Molecular Zinc Phosphate Core. *Angew. Chem., Int. Ed.* **2006**, *45* (33), 5536–5540.
- (52) Dar, A. A.; Sen, S.; Gupta, S. K.; Patwari, G. N.; Murugavel, R. Octanuclear zinc phosphates with hitherto unknown cluster architectures: ancillary ligand and solvent assisted structural transformations thereof. *Inorg. Chem.* **2015**, *54* (19), 9458–9469.

- (53) Gupta, S. K.; Dar, A. A.; Rajeshkumar, T.; Kuppuswamy, S.; Langley, S. K.; Murray, K. S.; Rajaraman, G.; Murugavel, R. Discrete $(\text{Gd}^{\text{III}}\text{M})(\text{M}=\text{Gd}^{\text{III}}\text{ or Co}^{\text{II}})$ pentanuclear complexes: a new class of metal-organophosphate molecular coolers. *Dalton Trans.* **2015**, *44* (13), 5961–5965.
- (54) Gupta, S. K.; Kalita, A. C.; Dar, A. A.; Sen, S.; Patwari, G. N.; Murugavel, R. Elusive double-eight-ring zeolitic secondary building unit. *J. Am. Chem. Soc.* **2017**, *139* (1), 59–62.
- (55) Sharma, K.; Gupta, S. K.; Borah, A.; Murugavel, R. Hitherto unknown eight-connected frameworks formed from $\text{A}_4\text{B}_4\text{O}_{12}$ metal organophosphate heterocubanes. *Chem. Commun.* **2019**, *55* (55), 7994–7997.
- (56) Gupta, S. K.; Kuppuswamy, S.; Walsh, J. P.; McInnes, E. J.; Murugavel, R. Discrete and polymeric cobalt organophosphates: isolation of a 3-D cobalt phosphate framework exhibiting selective CO_2 capture. *Dalton Trans.* **2015**, *44* (12), 5587–5601.
- (57) Mishra, A.; Wernsdorfer, W.; Abboud, K. A.; Christou, G. The first high oxidation state manganese-calcium cluster: relevance to the water oxidizing complex of photosynthesis. *Chem. Commun.* **2005**, No. 1, 54–56.
- (58) Kalita, A. C.; Murugavel, R. Fluoride Ion Sensing and Caging by a Preformed Molecular D4R Zinc Phosphate Heterocubane. *Inorg. Chem.* **2014**, *53* (7), 3345–3353.
- (59) Baerlocher, C.; McCusker, L. B.; Olson, D. H. *Atlas of zeolite framework types*; Elsevier, 2007.
- (60) Wilson, S. T.; Lok, B. M.; Messina, C. A.; Cannan, T. R.; Flanigen, E. M. Aluminophosphate molecular sieves: a new class of microporous crystalline inorganic solids. *J. Am. Chem. Soc.* **1982**, *104* (4), 1146–1147.
- (61) Murugavel, R. Ceramic and porous framework metal silicates and phosphates from molecular precursors: an ever-evolving ambient synthesis approach. *Emergent Mater.* **2019**, *2*, 273.
- (62) Bassindale, A. R.; Pourny, M.; Taylor, P. G.; Hursthouse, M. B.; Light, M. E. Fluoride-Ion Encapsulation within a Silsesquioxane Cage. *Angew. Chem., Int. Ed.* **2003**, *42* (30), 3488–3490.
- (63) Langley, S. K.; Helliwell, M.; Teat, S. J.; Winpenny, R. E. P. Synthesis and characterisation of cobalt(II) phosphonate cage complexes utilizing carboxylates and pyridonates as co-ligands. *Dalton Trans.* **2012**, *41* (41), 12807–12817.
- (64) Wang, H.-Y.; Hung, S.-F.; Hsu, Y.-Y.; Zhang, L.; Miao, J.; Chan, T.-S.; Xiong, Q.; Liu, B. In situ spectroscopic identification of $\mu\text{-OO}$ bridging on spinel Co_3O_4 water oxidation electrocatalyst. *J. Phys. Chem. Lett.* **2016**, *7* (23), 4847–4853.
- (65) Saha, J.; Ball, R.; Sah, A.; Kalyani, V.; Subramaniam, C. The mechanistic role of a support-catalyst interface in electrocatalytic water reduction by Co_3O_4 supported nanocarbon florets. *Nanoscale* **2019**, *11* (28), 13532–13540.
- (66) Xue, Y.; Wang, Y.; Liu, H.; Yu, X.; Xue, H.; Feng, L. Electrochemical oxygen evolution reaction catalyzed by a novel nickel-cobalt-fluoride catalyst. *Chem. Commun.* **2018**, *54* (48), 6204–6207.
- (67) Kent, C. A.; Concepcion, J. J.; Dares, C. J.; Torelli, D. A.; Rieth, A. J.; Miller, A. S.; Hoertz, P. G.; Meyer, T. J. Water oxidation and oxygen monitoring by cobalt-modified fluorine-doped tin oxide electrodes. *J. Am. Chem. Soc.* **2013**, *135* (23), 8432–8435.
- (68) Ng, J. W. D.; Garcia-Melchor, M.; Bajdich, M.; Chakhranont, P.; Kirk, C.; Vojvodic, A.; Jaramillo, T. F. Gold-supported cerium-doped NiO_x catalysts for water oxidation. *Nat. Energy* **2016**, *1* (5), 16053.
- (69) Cheng, N.; Stambula, S.; Wang, D.; Banis, M. N.; Liu, J.; Riese, A.; Xiao, B.; Li, R.; Sham, T.-K.; Liu, L.-M.; et al. Platinum single-atom and cluster catalysis of the hydrogen evolution reaction. *Nat. Commun.* **2016**, *7* (1), 13638.
- (70) Sultan, S.; Ha, M.; Kim, D. Y.; Tiwari, J. N.; Myung, C. W.; Meena, A.; Shin, T. J.; Chae, K. H.; Kim, K. S. Superb water splitting activity of the electrocatalyst $\text{Fe}_3\text{Co}(\text{PO}_4)_4$ designed with computation aid. *Nat. Commun.* **2019**, *10* (1), 5195.
- (71) Nguyen, A. L.; Wang, J.; Levine, D. S.; Ziegler, M. S.; Tilley, T. D. Synthetic control and empirical prediction of redox potentials for Co_4O_4 cubanes over a 1.4 V range: Implications for catalyst design and evaluation of high-valent intermediates in water oxidation. *Chem. Sci.* **2017**, *8* (6), 4274–4284.
- (72) Ahn, H. S.; Tilley, T. D. Electrocatalytic water oxidation at neutral pH by a nanostructured $\text{Co}(\text{PO}_3)_2$ anode. *Adv. Funct. Mater.* **2013**, *23* (2), 227–233.
- (73) Saha, J.; Verma, S.; Ball, R.; Subramaniam, C.; Murugavel, R. Compositional Control as the Key for Achieving Highly Efficient OER Electrocatalysis with Cobalt Phosphates Decorated Nanocarbon Florets. *Small* **2020**, *16* (12), 1903334.
- (74) Grimme, S.; Antony, J.; Ehrlich, S.; Krieg, H. A consistent and accurate ab initio parametrization of density functional dispersion correction (DFT-D) for the 94 elements H-Pu. *J. Chem. Phys.* **2010**, *132* (15), 154104.
- (75) Noodleman, L. Valence bond description of antiferromagnetic coupling in transition metal dimers. *J. Chem. Phys.* **1981**, *74* (10), 5737–5743.
- (76) Baskar, V.; Shanmugam, M.; Sañudo, E. C.; Shanmugam, M.; Collison, D.; McInnes, E. J.; Wei, Q.; Winpenny, R. E. Metal cages using a bulky phosphonate as a ligand. *Chem. Commun.* **2007**, No. 1, 37–39.
- (77) Murugavel, R.; Shanmugam, S. Seeking tetrameric transition metal phosphonate with a D4R core and organising it into a 3-D supramolecular assembly. *Chem. Commun.* **2007**, No. 12, 1257–1259.
- (78) Dey, A.; Kumar, V.; Pal, S.; Guha, A.; Bawari, S.; Narayanan, T. N.; Chandrasekhar, V. A tetranuclear cobalt (II) phosphate possessing a D4R core: an efficient water oxidation catalyst. *Dalton Trans.* **2020**, *49* (15), 4878–4886.
- (79) Okamura, M.; Kondo, M.; Kuga, R.; Kurashige, Y.; Yanai, T.; Hayami, S.; Praneeth, V. K.; Yoshida, M.; Yoneda, K.; Kawata, S.; et al. A pentanuclear iron catalyst designed for water oxidation. *Nature* **2016**, *530* (7591), 465–468.
- (80) Ansari, A.; Ansari, M.; Singha, A.; Rajaraman, G. Interplay of Electronic Cooperativity and Exchange Coupling in Regulating the Reactivity of Diiron (IV)-oxo Complexes towards C-H and O-H Bond Activation. *Chem.—Eur. J.* **2017**, *23* (42), 10110–10125.
- (81) Mondal, B.; Chattopadhyay, S.; Dey, S.; Mahammed, A.; Mitra, K.; Rana, A.; Gross, Z.; Dey, A. Elucidation of Factors That Govern the $2e^-/2\text{H}^+$ vs $4e^-/4\text{H}^+$ Selectivity of Water Oxidation by a Cobalt Corrole. *J. Am. Chem. Soc.* **2020**, *142* (50), 21040–21049.
- (82) Sen, A.; Rajaraman, G. Can you break the oxo-wall? A multiconfigurational perspective. *Faraday Discuss.* **2022**, *234*, 175–194.
- (83) Amtawong, J.; Nguyen, A. L.; Tilley, T. D. Mechanistic Aspects of Cobalt-Oxo Cubane Clusters in Oxidation Chemistry. *J. Am. Chem. Soc.* **2022**, *144* (4), 1475–1492.
- (84) Ullman, A. M.; Brodsky, C. N.; Li, N.; Zheng, S.-L.; Nocera, D. G. Probing edge site reactivity of oxidic cobalt water oxidation catalysts. *J. Am. Chem. Soc.* **2016**, *138* (12), 4229–4236.
- (85) McAlpin, J. G.; Surendranath, Y.; Dinca, M.; Stich, T. A.; Stoian, S. A.; Casey, W. H.; Nocera, D. G.; Britt, R. D. EPR evidence for Co (IV) species produced during water oxidation at neutral pH. *J. Am. Chem. Soc.* **2010**, *132* (20), 6882–6883.
- (86) Yang, T.; Quesne, M. G.; Neu, H. M.; Cantú Reinhard, F. G.; Goldberg, D. P.; de Visser, S. P. Singlet versus triplet reactivity in an $\text{mn}(\text{v})\text{-oxo}$ species: testing theoretical predictions against experimental evidence. *J. Am. Chem. Soc.* **2016**, *138* (38), 12375–12386.
- (87) Harvey, J. N.; Aschi, M.; Schwarz, H.; Koch, W. The singlet and triplet states of phenyl cation. A hybrid approach for locating minimum energy crossing points between non-interacting potential energy surfaces. *Theor. Chem. Acc.* **1998**, *99* (2), 95–99.
- (88) Carreón-Macedo, J.-L.; Harvey, J. N. Do spin state changes matter in organometallic chemistry? A computational study. *J. Am. Chem. Soc.* **2004**, *126* (18), 5789–5797.
- (89) Goetz, M. K.; Hill, E. A.; Filatov, A. S.; Anderson, J. S. Isolation of a terminal Co (III)-oxo complex. *J. Am. Chem. Soc.* **2018**, *140* (41), 13176–13180.

(90) Karunadasa, H. L.; Chang, C. J.; Long, J. R. A molecular molybdenum-oxo catalyst for generating hydrogen from water. *Nature* **2010**, *464* (7293), 1329–1333.

(91) Yadav, P.; Nigel-Etinger, L.; Kumar, A.; Mizrahi, A.; Mohammed, A.; Fridman, N.; Lipstman, S.; Goldberg, I.; Gross, Z. Hydrogen evolution catalysis by terminal molybdenum-oxo complexes. *Science* **2021**, *24* (8), 102924.

(92) Curutchet, A.; Colinet, P.; Michel, C.; Steinmann, S. N.; Le Bahers, T. Two-sites are better than one: revisiting the OER mechanism on CoOOH by DFT with electrode polarization. *Phys. Chem. Chem. Phys.* **2020**, *22* (13), 7031–7038.

(93) Haddad, A. Z.; Garabato, R. D.; Kozłowski, P. M.; Buchanan, R. M.; Grapperhaus, C. A. Beyond metal-hydrides: non-transition-metal and metal-free ligand-centered electrocatalytic hydrogen evolution and hydrogen oxidation. *J. Am. Chem. Soc.* **2016**, *138* (25), 7844–7847.

(94) Coggins, M. K.; Zhang, M. T.; Chen, Z.; Song, N.; Meyer, T. J. Single-Site Copper (II) Water Oxidation Electrocatalysis: Rate Enhancements with HPO₄²⁻ as a Proton Acceptor at pH 8. *Angew. Chem., Int. Ed.* **2014**, *53* (45), 12226–12230.

Cite this: *Dalton Trans.*, 2023, 52, 8943

Field-induced SIM behaviour in early lanthanide(III) organophosphates containing 18-crown-6†

Aditya Borah, Sourav Dey, Sandeep K. Gupta, Gopalan Rajaraman* and Ramaswamy Murugavel*

Single-ion magnets (SIMs) have attracted wide attention in recent years. Despite tremendous progress in late lanthanide SIMs, reports on early lanthanides exhibiting SIM characteristics are scarce. A series of five novel 18-crown-6 encapsulated mononuclear early lanthanide(III) organophosphates, $[(18\text{-crown-6})\text{Ln}(\text{dippH})_3\{(18\text{-crown-6})\text{Ln}(\text{dippH})_2(\text{dippH}_2)\}]_3$ [Ln = Ce (**1**), Pr (**2**), Nd (**3**)] and $[(\text{Ln}(18\text{-crown-6})(\text{dippH})_2(\text{H}_2\text{O}))_2]_2$ [Ln = Sm (**4**) and Eu (**5**)], have been synthesised in the present study. 18-crown-6 coordinates to Ln(III) ions in an equatorial position while the axial positions are occupied by either three phosphate moieties as in **1–3** or two phosphate moieties and one water molecule as in **4** and **5**, resulting in a muffin-shaped coordination geometry around the Ln(III) centres. Magnetic susceptibility measurements reveal that Ce and Nd complexes are field-induced single-ion magnets with significant barrier heights. Furthermore, the *ab initio* CASSCF/RASSI-SO/SINGLE_ANISO calculations on complexes **1** and **3** reveal significant QTM in the ground state rationalising the field-induced single-ion magnetism behaviour of these complexes.

Received 21st April 2023,
Accepted 23rd May 2023

DOI: 10.1039/d3dt01206a

rsc.li/dalton

Introduction

We live in an era where a large amount of information is stored in electronic form. These data are saved in conventional devices where the binary language (1 and 0; called the bit information unit) is employed. Unfortunately, the development of data storage devices cannot meet the rate of exponential production of data, due to different factors such as dimensions of the nanoparticles used, limited thermal activation barriers and smaller blocking temperatures. Single-molecule magnets (SMMs)¹ can be an alternative and better option in this context as they provide the opportunity to store data at the molecular level, which can reduce the size of the devices by at least ten times. SMMs are molecules with a bistable ground spin state exhibiting slow relaxation of magnetisation below the blocking temperature (T_B). The work of Donati *et al.*, on storing data in single holmium atoms adsorbed on a magnesium oxide film grown on a silver substrate, proved that it is possible to store data even at the atomic level.^{2,3} At the molecular level, the strategy of designing high-performing SMMs has shifted from clusters to mononuclear complexes, known as single-ion magnets (SIMs).^{4–6} A high-performance SMM is

characterised by two parameters namely the barrier height of spin reversal (U_{eff}) and blocking temperature (T_B). In the past two decades, trivalent lanthanide(III) ion based SIMs have gained unprecedented interest over transition metal ion SIMs, due to their strong spin-orbit coupling and large intrinsic magnetic anisotropy. Among Ln(III) ions, oblate-shaped Dy(III) based SIMs lead the race in achieving a higher T_B that surpasses liquid nitrogen temperature (80 K).^{3,7–24} In the context of designing single-ion magnets, late Ln(III) ions, such as Dy(III), Er(III) and Tb(III), have been heavily explored while early Ln(III) ions are scarcely studied due to smaller magnetic momentum ($J = L - S$) and weaker spin-orbit coupling.^{25–27} Interestingly, lighter lanthanides, especially samarium and neodymium, are used in classical hard magnets for industrial use (e.g. SmCo_5 and $\text{Nd}_2\text{Fe}_{14}\text{B}$).²⁸ Moreover, the magnetic properties of $\text{Nd}_2\text{Fe}_{14}\text{B}$ can be enhanced by doping ions such as dysprosium(III) and cerium(III) ions.²⁹ Thus, early Ln(III) ions also have the potential to exhibit SIM behaviour.

With the rapid progress in this field, it is conceivable that designing a suitable ligand field (LF) for a given metal ion is the most crucial task: an axially stressed LF is best for oblate-shaped Ln(III) ions while an equatorially stressed LF is for prolate-shaped Ln(III) ions.³⁰ On placing a Ln(III) ion in a suitable LF, the inherent magnetic anisotropy can be enhanced to a large extent. Being oblate, a Ce(III) ion (configuration: f^1 ; ground state: $^2F_{5/2}$) requires an axially stressed LF, where the six-fold degenerate ground state is split into three sets of Kramers pairs, $|J_z| = 5/2, 3/2, \text{ and } 1/2$, where J_z sublevels with

Department of Chemistry, Indian Institute of Technology, Powai, Mumbai, India.
E-mail: rmv@chem.iitb.ac.in† Electronic supplementary information (ESI) available. CCDC: 2257887–2257891. For ESI and crystallographic data in CIF or other electronic format see DOI: <https://doi.org/10.1039/d3dt01206a>

higher electron density along the z axis (e.g. $|J_z| = 1/2$) are destabilised more than $|J_z| = 5/2$ sublevels.³¹ To realise an easy axis anisotropy, other oblate shaped early Ln(III) ions, such as Pr(III), Nd(III) etc., also need the same strategy as that for the Ce(III) ion. On employing such a strategy, a number of Ce and Nd ion based single-ion magnets have been successfully designed (Tables 1 and 2).

The selective metal encapsulation chemistry of crown ethers (e.g.: Li⁺ in 12-crown-4, Na⁺ in 15-crown-5, K⁺ in 18-crown-6, etc.), due to their precise cavity size with the metal ions, offers an opportunity for axially stressed C_n ($n = 4, 5, 6$) symmetric LFs. Like K⁺, the Ln(III) ions are the best fit for the cavity of 18-crown-6, while in the case of smaller crown ethers, Ln(III) ions sit out of the cavity. As crown ether oxygen centers interact only weakly with the Ln(III) centres, using a ligand field comprising strong axial ligands and weak equatorial 18-crown-6^{32–34} would be expected as the ideal strategy for designing high-performance SIMs derived from oblate lanthanides.^{33–38}

Based on these earlier observations and building up on our recent results on phosphorus ligand based SIMs,^{39–42} we report here a series of early Ln(III) (Ln: Ce, Pr, Nd, Sm and Eu) organophosphate complexes $[\{(18\text{-crown-6})\text{Ln}(\text{dippH})_3\}(\{(18\text{-crown-6})\text{Ln}(\text{dippH})_2(\text{dippH}_2)\})\}_3]$ [Ln = Ce (1), Pr (2), Nd (3)] and $[\{\text{Ln}(18\text{-crown-6})(\text{dippH})_2(\text{H}_2\text{O})\}_3]$ [Ln = Sm (4) and Eu (5)], derived from 2,6-diisopropylphenylphosphate (dippH₂) as axial ligands, containing 18-crown-6 ligand in the equatorial positions. Hexadentate 18-crown-6 produces a pseudo hexagonal equatorial plane around the Ln(III) centre. A number of oblate-shaped Ln(III) ion (especially Dy(III) ion) based single-ion magnets with an hexagonal equatorial plane are found to have significantly high barrier heights of spin reversal.^{32,33,43–48} Such complexes with a local hexagonal bipy-

ramidal geometry fulfill the strong magnetic axiality and high coordination number providing air stability to the complexes.

Experimental section

Instruments and methods

All the reactions were performed under ambient reaction conditions. Fourier-transform infrared spectra were recorded on a PerkinElmer Spectrum One spectrometer using KBr diluted pellets. Microanalyses were performed on a Thermo Finnigan (FLASH EA 1112) microanalyser. Powder X-ray diffractions were recorded on a Philips X'pert Pro (PANalytical) diffractometer using Cu K α radiation ($\lambda = 1.54190 \text{ \AA}$). The magnetic properties of the polycrystalline samples were measured using a Quantum Design MPMS-XL SQUID magnetometer equipped with a 7 T magnet in the temperature range of 2–300 K. The data were corrected for background contribution and consequently Pascal's constants. Alternating current (ac) susceptibility measurements were performed with an oscillating ac field of 3.5 Oe at indicated frequencies between 0.1 and 1500 Hz.

Materials

Commercial grade solvents were purified by employing conventional procedures.⁶³ Lanthanide iodides were prepared from Ln(III) oxides and hydroiodic acid. 2,6-Diisopropylphenol and phosphorous oxychloride were procured from commercial sources and used as received. 2,6-Diisopropylphenyl phosphate was synthesised as described previously in the literature.⁶⁴

General procedure for the synthesis of compounds 1–5

To a solution of hydrated LnI₃·xH₂O (Ln = Ce(1), Pr(2), Nd(3), Sm(4) and Eu(5)) (0.1 mmol) in ethanol (5 mL), 18-crown-6

Table 1 Ce(III) based single-ion magnets ($U_{\text{eff,ac}}$ represents the barrier obtained from ac susceptibility measurements, $U_{\text{eff,cal}}$ represents the barrier obtained from computational studies, and C and n are the parameters obtained from the fitting of the temperature dependence of relaxation time corresponding to the Raman process)

Sl no.	Ce(III) SIMs	C.N. ^a	Orbach process			QTM t_{QTM}/s	Raman		H/Oe	Ref.	
			$U_{\text{eff,ac}}/K$	τ_0/s	$U_{\text{eff,cal}}/K$		$C s^{-1} K^{-n}$	n			
1	Compound 1	9	16.4 16.3	6.0×10^{-10} 2.2×10^{-6}	671 —	0.079 0.0025	—	—	350	This work	
2	Li(DME) ₃ [Ce(III)(COT ²⁻) ₂]	16 (η^6)	30	1.2×10^{-6}	—	—	—	—	400	49	
3	[Ce(NO ₃) ₃ (18-crown-6)]	12	31.4 30.3	1.8×10^{-7} 2.3×10^{-7}	—	—	—	0.108	5	1000 34	
4	[Ce(NO ₃) ₃ (1,10-diaza-18-crown-6)]	12	44 44	2.3×10^{-8} 2.6×10^{-7}	—	—	—	0.52	5	1000 34	
5	[Ce(NO ₃) ₃ (HL ¹) ₃]	12	37.5	2.76×10^{-8}	501	0.076	0.154	7.36	3000	50	
6	Ce(fdh) ₃ (bpy)	8	33.3	1.8×10^{-7}	—	—	0.40	6	2000	51	
7	[Ce(NO ₃) ₃ L ²] ₃	9	21.5	2.7×10^{-7}	317	—	—	—	200	52	
8	[Ce(ntfa) ₃ (MeOH) ₂]	8	46.4	8.13×10^{-10}	460	—	—	—	2.98	200	53
9	[Ce(ntfa) ₃ (5,5'-me ₂ bipy)]	8	13.6	3.53×10^{-6}	371	—	—	—	8.01	200	53
10	[Ce(ntfa) ₃ (bpy) ₂]	8	22.7	1.61×10^{-6}	468	—	—	—	1.28	200	53
11	[Ce(dppbO ₂) ₂ Cl ₂]	6	54	2×10^{-10}	420	—	—	—	31	100	54

COT²⁻: bis(trimethylsilyl)cyclooctatetraenyl dianion; HL¹ = 2-methoxy-6-[(*E*)-phenylimino-methyl]phenol; fdh: 1,1,1-fluoro-5,5-dimethyl-hexa-2,4-dione; bpy: 2,2'-bipyridine; L²: ^tBuP(O)(NH⁺Pr)₂; Ntfa: 4,4,4-trifluoro-1-(naphthalen-2-yl)butane-1,3-dionato, 5,5'-Me₂bipy: 5,5'-dimethyl-2,2'-dipyridyl; dppbO₂: 1,2-bis(diphenylphosphino)benzene dioxide. ^a C.N. = coordination number.

Table 2 Nd(III) based single-ion magnets ($U_{\text{eff,ac}}$ represents the barrier obtained from ac susceptibility measurements; $U_{\text{eff,cal}}$ represents the barrier obtained from computational studies, and C and n are the parameters obtained from the fitting of the temperature dependence of relaxation time corresponding to the Raman process)

Sl no.	Nd(III) SIMs	C.N. ^a	$U_{\text{eff,ac}}/\text{K}$	τ_0/s	$U_{\text{eff,cal}}/\text{K}$	$\tau_{\text{QTM}}/\text{s}$	$C/\text{s}^{-1}\text{K}^{-n}$	n	H/Oe	Ref.
1	Compound 3	9	6	1.0×10^{-5}	259	—	501	3	1500	This work
2	[NdTP ₃]	9	4	2.6×10^{-4}	165	—	—	—	100	55
3	[Li(DME) ₃][Nd ^{III} (COT ⁶⁻) ₂]	16 (η^6)	21	5.5×10^{-3}	—	—	—	—	1000	56
4	[Nd(NO ₃) ₃ (18-crown-6)]	12	29.9	2.9×10^{-9}	—	—	—	—	1000	34
			30.9	2.2×10^{-9}	—	—	4.1	5	1000	
5	[Nd(NO ₃) ₃ (1,10-diaza-18-crown-6)]	12	69	2.1×10^{-10}	—	—	—	—	1000	34
			73	1.4×10^{-10}	—	—	0.00107	9	1000	
6	[Nd(NO ₃) ₂ L ²][PF ₆ ·MeCN]	10	36	4.4×10^{-9}	—	—	2.8	5	1000	57
7	[L ² ₂ Nd(H ₂ O) ₃][Li ⁺ ·L ² ·(H ₂ O)]	7	16.1	2.6×10^{-4}	302	0.001	4.2×10^{-18}	5	0	58
			24.7	5.0×10^{-6}	—	—	—	—	0	
			39.2	8.9×10^{-7}	—	—	0.0292	5	2000	
8	[Nd(CyPh ₂ PO) ₂ (H ₂ O) ₃] ₂ ·2(CyPh ₂ PO)·3EtOH	7	—	—	—	0.005	—	5.12	0	59
			—	—	—	—	—	6.54	2000	
9	[Cp ⁺ ₂ Nd(BPh ₄)]	10	41.7	1.4×10^{-6}	—	—	0.0286	5.2	1000	60
10	[Nd ^{III} (TTA) ₃ (MeOH) ₂](0.5Azo-py)	8	—	—	—	—	—	—	1000	61
	Before heating		19.7	3.8×10^{-7}	—	0.008	—	—	1000	
	After heating		27.3	8.5×10^{-8}	—	—	—	—	—	
11	C ₃ symmetric [C(NH ₂) ₃] ₃ [Nd(CO ₃) ₄ (H ₂ O)]·2H ₂ O	9	30.7	1.1×10^{-7}	—	—	0.89	6.08	1500	62
12	C ₄ symmetric [C(NH ₂) ₃] ₄ [H ₃ O][Nd(CO ₃) ₄ (H ₂ O)]·9.5H ₂ O	9	9.25	2.1×10^{-6}	—	—	413.85	3.63	1500	62

Tp⁻: trispyrzolyborate; L²: a single helical hexadentate Schiff base ligand; TTA = thenoyl(trifluoro)acetate and Azo-py = 4,4'-azopyridine. ^a C.N. = coordination number.

(0.2 mmol, 53 mg) was added and stirred for an hour at room temperature, which produced a dark brown precipitate. To this reaction mixture, methanol (10 mL) was added and stirred until the solution became clear yellow. A solution of 2,6-diisopropylphenylphosphate (0.3 mmol, 77.5 mg) in methanol (5 mL) was added to it and stirred for 2 hours at 60 °C and then cooled to room temperature. The reaction mixture was filtered and the resultant clear yellow solution was left for crystallisation at ambient temperature through slow evaporation of the solvent to yield the respective metal phosphates as block shaped reddish-brown crystals after 1 week.

Characterisation of [((18-crown-6)Ce(dipph)₃){((18-crown-6)Ce(dipph)₂(dipph₂))}] [I₃] (1). M.p. > 250 °C; FTIR (KBr, cm⁻¹): 3061 (w), 2961 (s), 2868 (m), 2356 (br), 1667 (br), 1466 (s), 1439 (s), 1382 (m), 1352 (m), 1335 (s), 1255 (s), 1173 (s), 1091 (vs), 1046 (m), 964 (s), 944 (s), 912 (m), 880 (m), 840 (m), 799 (m), 769 (s), 746 (m), 660 (m), 592 (m), 548 (s), 513 (s); Anal. found (calculated) for C₉₆H₁₅₅I₃O₃₆P₆Ce₂: C, 41.97 (42.20); H, 5.57 (5.72).

Characterisation of [((18-crown-6)Pr(dipph)₃){((18-crown-6)Pr(dipph)₂(dipph₂))}] [I₃] (2). M.p. > 250 °C; FTIR (KBr, cm⁻¹): 3062 (w), 2964 (s), 2868 (m), 2358 (br), 1658 (br), 1466 (s), 1439 (s), 1383 (m), 1352 (m), 1335 (s), 1255 (s), 1175 (s), 1090 (vs), 1047 (m), 963 (s), 940 (s), 908 (m), 881 (m), 840 (m), 799 (m), 764 (s), 744 (m), 655 (m), 593 (m), 540 (s), 514 (s); Anal. found (calculated) for C₉₆H₁₅₅I₃O₃₆P₆Pr₂: C, 41.96 (42.11); H, 5.93 (5.71).

Characterisation of [((18-crown-6)Nd(dipph)₃){((18-crown-6)Nd(dipph)₂(dipph₂))}] [I₃] (3). M.p. > 250 °C; FTIR (KBr, cm⁻¹): 3065 (w), 2959 (s), 2868 (m), 2357 (br), 1626 (br), 1467 (s), 1445 (s), 1383 (m), 1349 (m), 1333 (s), 1252 (s), 1176 (s), 1103 (vs),

1084 (s), 960 (s), 883 (m), 835 (m), 803 (m), 770 (s), 749 (m), 661 (m), 594 (m), 542 (s), 514 (s); Anal. found (calculated) for C₉₆H₁₅₅I₃O₃₆P₆Nd₂: C, 42.09 (42.08); H, 5.54 (5.70).

Characterisation of [([Sm(18-crown-6)(dipph)₂(H₂O)]-[I₃]) (4). M.p. > 250 °C; FTIR (KBr, cm⁻¹): 3065 (w), 2964 (s), 2869 (m), 2355 (br), 1624 (br), 1466 (s), 1442 (s), 1384 (m), 1362 (m), 1350 (m), 1334 (s), 1256 (s), 1178 (vs), 1105 (vs), 1084 (s), 959 (vs), 835 (m), 799 (m), 770 (s), 749 (m), 662 (m), 593 (m), 538 (s), 513 (s); Anal. found (calculated) for C₄₈H₇₉I₃O₁₈P₃Sm₁: C, 32.78 (33.01); H, 4.69 (4.62).

Characterisation of [([Eu(18-crown-6)(dipph)₂(H₂O)]-[I₃]) (5). M.p. > 250 °C; FTIR (KBr, cm⁻¹): 3078 (w), 2952 (s), 2867 (m), 2348 (br), 1626 (br), 1466 (s), 1445 (s), 1383 (m), 1350 (m), 1332 (s), 1253 (s), 1176 (vs), 1105 (vs), 1083 (s), 961 (vs), 836 (m), 805 (m), 771 (s), 750 (m), 661 (m), 595 (m), 545 (s), 514 (s); Anal. found (calculated) for C₄₈H₇₉I₃O₁₈P₃Eu₁: C, 32.26 (32.52); H, 4.79 (4.70).

Single crystal X-ray crystallography

Single crystals of 1–5 suitable for diffraction studies were selected under an optical microscope and mounted on a Rigaku Saturn 724+ CCD diffractometer for unit cell determination and intensity data collection. Data integration and indexing were carried out using CrysAlisPro software. Using Olex software,⁶⁵ the structure was solved with the ShelXT⁶⁶ structure solution program using intrinsic phasing. The complete refinement of the structures was carried out with the ShelXL⁶⁷ refinement package using least squares minimisation. All non-hydrogen atoms were refined anisotropically. The hydrogen atoms were refined isotropically as rigid atoms.

Computational details

The *ab initio* calculations were performed using the MOLCAS 8.2 program package using the atomic position obtained from the X-ray structure. The anions were excluded from the calculations. The basis set for our calculations was taken from the ANO-RCC library as implemented in the MOLCAS program package. We used the following basis sets in our calculations: [Ce.ANO-RCC...8s7p5d3f2g1 h.] for Ce, [Nd.ANO-RCC...8s7p5d3f2g1 h.] for Nd, [P.ANO-RCC...4s3p1d.] for P, [O.ANO-RCC...3s2p1d.] for O, [C.ANO-RCC...3s2p.] for C and [H.ANO-RCC...2s.] for H. The Douglas-Kroll-Hess (DKH) Hamiltonian was employed to take into account the scalar relativistic effect. The disk space of our calculations was reduced by the Cholesky decomposition technique. The spin-free states of complexes **1** and **3** were generated by the CASSCF (complete active space self-consistent field) method with the CAS(1,7) and CAS(3,7) active space, respectively. Within this active space, we computed the energies of 7 doublets for **1** and 35 quartets and 112 doublets for **3**. The spin-orbit coupling between these spin-free states was considered perturbatively by the restricted active space state interaction (RASSI) method. We did not perform CASPT2 calculations due to the dominant ionic character of the Ln–ligand bond. Finally, the *g* tensor, magnetic moment, QTM/TA-QTM, blocking barrier *etc.*, were computed from the SINGLE_ANISO module of MOLCAS. The frequency dependent ac susceptibility plots, Cole–Cole plots and $1/\tau$ vs. *T* plots are fitted with CC-FIT2 software.⁶⁸

Results and discussion

Synthetic aspects

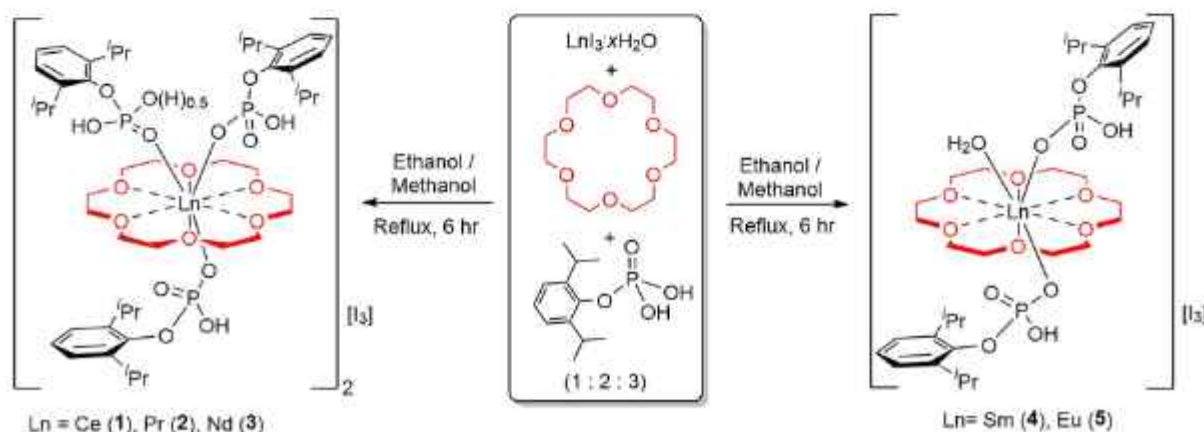
Considering the perfect fitting of Ln(III) ions in the void of 18-crown-6 and the oxophilic nature of Ln(III) ions, an organophosphate monoester (2,6-diisopropylphenylphosphate, dippH_2) and 18-crown-6 are used to design a suitable ligand field around the earlier mentioned Ln(III) ions. Fully deprotonated organophosphates (ArOPO_3^{2-}) generally act as polyden-

tate ligands which produce either polynuclear clusters or polymers.^{39,40} Such a polymerisation is controlled in this work by stopping full deprotonation of dippH_2 , by carrying out the reaction in the absence of any bases. This strategy successfully yields mononuclear 18-crown-6 ether encapsulated Ln(III) organophosphates. The reactions between $\text{LnI}_3 \cdot x\text{H}_2\text{O}$, 18-crown-6 and dippH_2 (1 : 2 : 3) were carried out at 60 °C in a solvent mixture of ethanol and methanol (Scheme 1). On evaporation of the reaction mixture, compounds **1–5** were obtained as air-stable block-shaped reddish-brown crystals within a period of 1–2 weeks. All five compounds were characterised by means of different analytical and spectroscopic techniques. Furthermore, the molecular structures of all the molecules were established by single crystal X-ray diffraction studies. The phase purity of all the complexes was confirmed with the help of powder X-ray diffraction studies on polycrystalline samples.

Molecular structures of 1–3

Slow evaporation of the respective reaction mixtures from the reaction between respective hydrated Ln(III) iodides, 18-crown-6 and dippH_2 in a solvent mixture of methanol and ethanol yields air-stable reddish-brown coloured good quality crystals under ambient conditions. Single crystal X-ray diffraction studies reveal that all five mononuclear complexes crystallise in the triclinic space group P1 (**1** and **2** are isostructural).

In all three cases, the Ln(III) centre fits perfectly in the void of 18-crown-6 and thus it wraps the Ln(III) ions through the equatorial plane in a non-planar fashion, as all the atoms of the crown are sp^3 hybridised (Fig. 1b and c). The three monocoordinated organophosphate ligands coordinate to the Ln(III) centre through axial positions in a “Y” fashion. The lattice triiodide ion is present at the centre of inversion, which is shared by two symmetrically equivalent Ln-moieties. Thus, the asymmetric unit has a half I_3^- ion along with one Ln complex. Thus, a full molecule of this class can be represented as $[\{(\text{18-crown-6})\text{Ln}(\text{dippH})_3\}\{(\text{18-crown-6})\text{Ln}(\text{dippH})_2(\text{dippH}_2)\}][\text{I}_3]$ (Ln: Ce(**1**), Pr(**2**) and Nd(**3**)). The asymmetric unit and molecular structure of **1** are shown as representative examples of **1–3**. The asymmetric units and mole-



Scheme 1 General synthetic scheme of **1–5**.

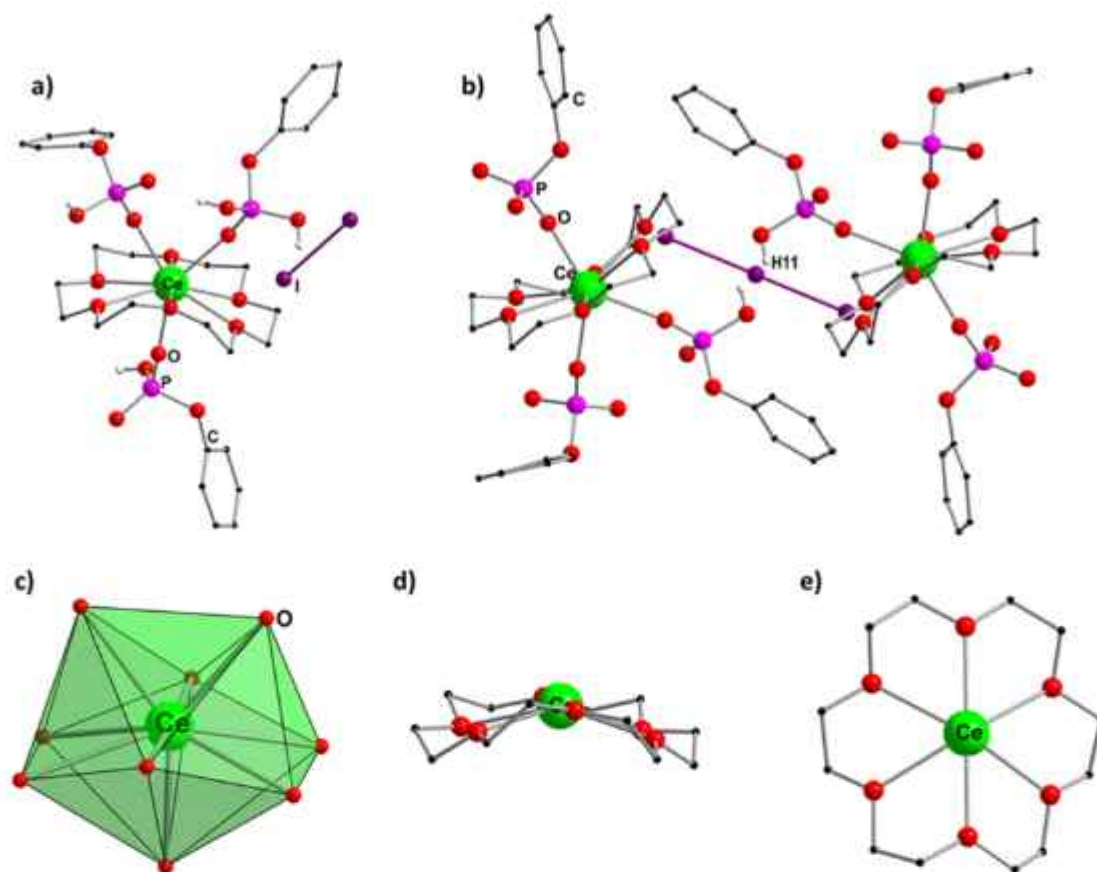


Fig. 1 Molecular structure of **1**. (a) The asymmetric unit and (b) full molecule of **1**. (c) Muffin shaped coordination polyhedra around the nine-coordinated Ce(III) ion. (d) The side view and (e) top view of the binding mode of 18-crown-6 to the Ce(III) centre, coordinating in a wavy fashion. The hydrogen atoms (except H11 present in the spatial position) and the solvent molecules are omitted for clarity. The coordination mode of 18-crown-6 and muffin shaped coordination polyhedra are the same for all three complexes, and hence those of **1** are shown as representative cases.

molecular structures of **2** and **3** are also shown in Fig. S3 and S5.† The average axial Ln–O(P) bond distances are shorter than the average equatorial Ln–O(crown) distances in **1–3** (Table 3), expecting an axially stressed ligand field around the metal centres. Such an axially stressed ligand field is suitable for all three Ln(III) ions (Ce(III), Pr(III) and Nd(III)), as they possess an oblate-shaped f-electron cloud. The selected bond lengths and bond angles of **1–3** are listed in Tables S1–S3† respectively.

Molecular structures of **4** and **5**

By employing the same reaction strategy of **1–3**, reddish brown coloured crystals of **4** and **5** were obtained by slow evaporation

Table 3 Ln–O bond comparison in **1–5**

Complex	Average Ln–O (axial)/Å	Average Ln–O (equatorial)/Å	Average Ln–O/Å	Ionic radii of Ln(III)/Å
1	2.383	2.654	2.564	10.10
2	2.362	2.622	2.535	9.90
3	2.351	2.608	2.522	9.83
4	2.324	2.559	2.481	9.58
5	2.292	2.560	2.471	9.47

of the solvent from the reaction mixture. The solid-state structures of both the complexes determined by single-crystal X-ray diffraction studies reveal that both **4** and **5** are mononuclear complexes, and crystallise in the triclinic $P\bar{1}$ space group. The asymmetric unit of **4** contains one complete molecule of **4** along with one I_3^- anion and one water molecule in the lattice. The asymmetric unit of **5** has two complete molecules along with two I_3^- anions and an ethanol molecule in the lattice. The molecular structure of **5** is shown in Fig. 2a. The core structures of **4** and **5** are slightly different from those of **1–3**. Instead of three axial aryldiphenylphosphates as in **1–3**, in the case of **4** and **5**, two aryldiphenylphosphates along with one water molecule occupy the three axial positions. Despite the fact that the same stoichiometry of metal and ligand was maintained (metal : ligand = 1 : 3) throughout the synthesis of all five complexes, the resultant products have significant differences in the coordination environment. This can be attributed to the smaller size of Sm(III) and Eu(III) than that of Ce(III), Pr(III) and Nd(III). The smaller size prevents the third aryldiphenylphosphate moiety from binding to the metal centres in **4** and **5**. Both the aryldiphenylphosphates are mono-deprotonated (dippH⁻) and the triiodide ion present in the lattice maintains the charge neutrality.

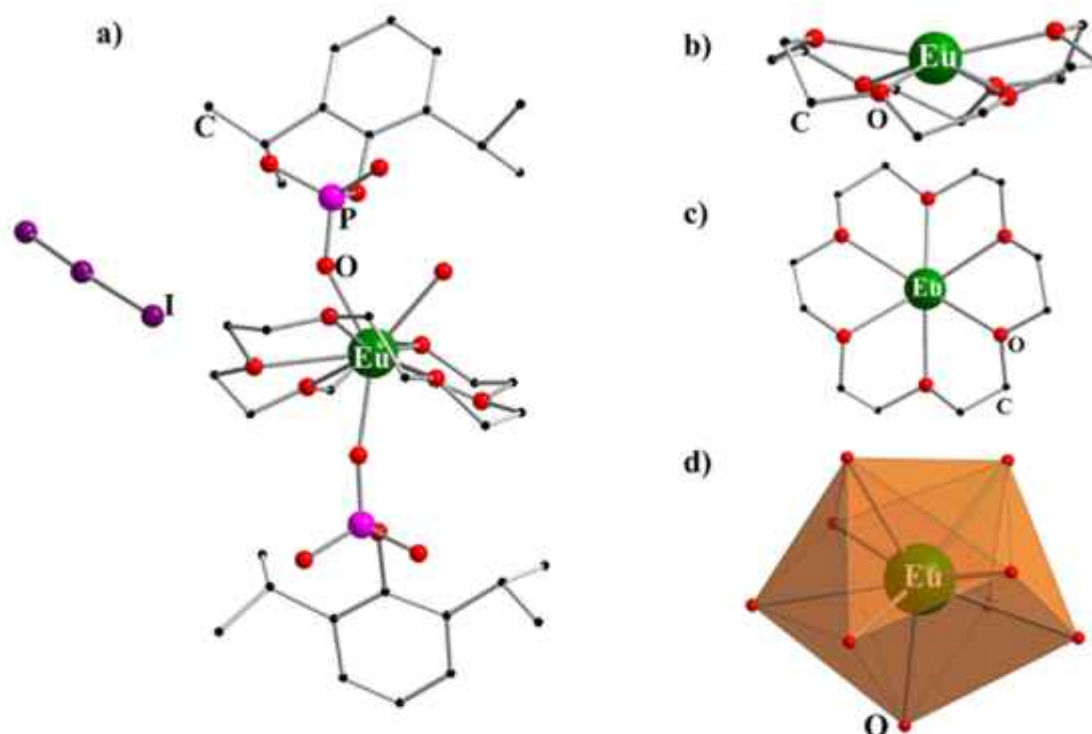


Fig. 2 (a) Molecular structure of **5**. The hydrogen atoms and the solvent molecules are omitted for clarity. (b) The side view and (c) the top view of the binding mode of 18-crown-6 to the Eu(III) centre, coordinating in a wavy fashion. (d) The coordination environment of the nine-coordinated Eu(III) ion. The molecular structure of **4** is added in the ESI.†

The presence of bulky organophosphate ligands, cyclic crown ethers, large triiodide ions and other lattice solvent molecules facilitate the long separation of the Ln(III) ions, ranging from 9.8 to 10.8 Å (Table S7†). The lattice arrangements in **2** and **5** are depicted in Fig. 3 (see the ESI† for **1**, **3** and **4**). The large distance between any two Ln(III) ions reduces the probability of any intermolecular magnetic interactions.

SHAPE analysis of 1–5

The coordination environments around the nine-coordinated Ln(III) ions have been analysed by continuous SHAPE measurements using SHAPE 2.1 software.⁶⁹ The continuous SHAPE measurements reveal that the {LnO₉} cores in **1–5** have minimal deviation from the ideal C_{3v} symmetry, indicating a muffin shaped geometry around the Ln(III) ions in all five com-

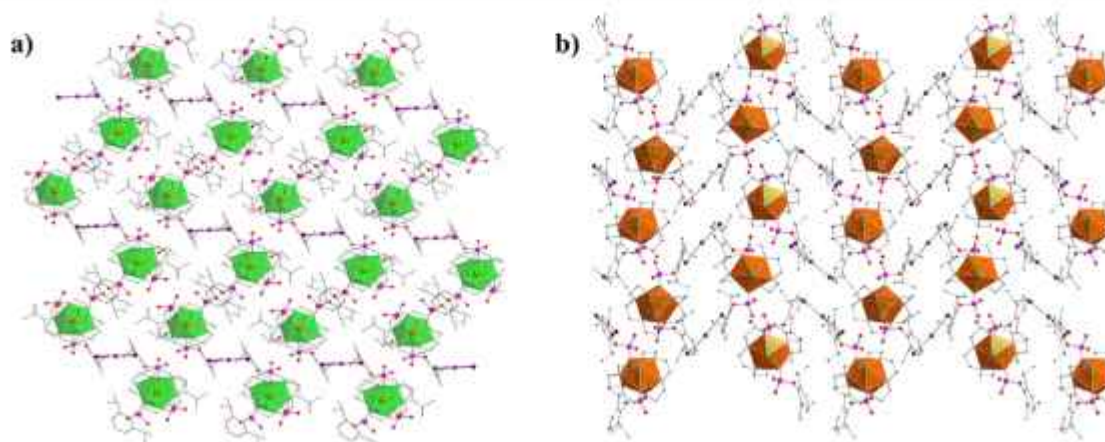


Fig. 3 Lattice arrangement of (a) **2** and (b) **5** viewed along the *b*-axis. H atoms are omitted for clarity; disordered I₃ ions with the largest occupancy are shown here. Colour code: Pr, orange; P, pink; O, red; C, black; I, violet. Due to the bulkiness in the phenyl rings and lattice triiodide anions and solvent molecules, Ln(III) centres are separated by at least 9.83 Å (in **2**) and 10.84 Å (in **5**).

plexes 1–5. The muffin shaped polyhedra of 1 and 5 are shown in Fig. 1c and 2d (also see the ESI†). The deviation from the perfect geometry in the $\{\text{LnO}_9\}$ core is listed in Table S8.†

Effect of lanthanide contraction

The difference in axial coordination in 1–3 (three phosphates) from 4 and 5 (two phosphates and one water molecule) is consistent with lanthanide contraction. Due to the gradually decreasing ionic radii from Ce(III) to Eu(III), three sterically hindered phosphates are not able to find enough room for coordination to Ln(III) centres in 4 and 5; instead, the third position is occupied by a sterically less-demanding water molecule. To understand the effect of the size of the Ln(III) ions, we have analysed the effect of lanthanide contraction on the average Ln–O bond lengths. It has been observed that the average Ln–O bond lengths decrease gradually from 1–5 with the same trend of decreasing ionic size. The decreasing Ln–O distance and ionic radii due to lanthanide contraction are shown in Fig. 4 and Table 3.

Powder X-ray diffraction studies of 1–5

In order to confirm the phase purity of the compounds in a bulk amount, powder X-ray diffraction (PXRD) analyses were carried out on the polycrystalline samples of 1–5. The agreement of the experimental PXRD pattern with the simulated PXRD pattern obtained from single crystal X-ray diffraction analysis confirms the purity of these compounds in the bulk phase (Fig. S11†).

Magnetic properties of 1–4

The static and dynamic properties of the crown-ether-based lanthanide organophosphates were investigated with the help of direct current (dc) and alternating current (ac) magnetic susceptibility measurements using an MPMS-XL SQUID mag-

netometer equipped with a 7.0 T magnet. All the magnetic measurements of 1–4 were carried out on phase pure powdered polycrystalline samples.

The temperature dependence of magnetisation was analyzed in the temperature range of 2–300 K under an applied field of 1000 Oe. The $\chi_{\text{M}}T$ values obtained experimentally for 1–4 are $0.94 \text{ cm}^3 \text{ K mol}^{-1}$, $1.45 \text{ cm}^3 \text{ K mol}^{-1}$, $1.48 \text{ cm}^3 \text{ K mol}^{-1}$ and $0.48 \text{ cm}^3 \text{ K mol}^{-1}$, respectively. These values are in good agreement with the calculated values for the respective isolated non-interacting lanthanide ions, except for Sm(III), at 300 K [Ce(III) ion: ground state term: $^2F_{5/2}$, calculated $\chi_{\text{M}}T$ value: $0.81 \text{ cm}^3 \text{ K mol}^{-1}$; Pr(III) ion: ground state term: 3H_4 , calculated $\chi_{\text{M}}T$ value: $1.60 \text{ cm}^3 \text{ K mol}^{-1}$; Nd(III) ion: ground state term: $^4I_{9/2}$, calculated $\chi_{\text{M}}T$ value: $1.64 \text{ cm}^3 \text{ K mol}^{-1}$; Sm(III) ion: ground state term: $^6H_{5/2}$ and calculated $\chi_{\text{M}}T$ value: $0.09 \text{ cm}^3 \text{ K mol}^{-1}$]. The temperature dependence of magnetisation is depicted in Fig. S12.† The room temperature $\chi_{\text{M}}T$ value for 4 is higher than the calculated $\chi_{\text{M}}T$ value for an isolated non-interacting Sm(III) ion ($S = 5/2$, $L = 5$, $J = 5/2$, $g_J = 2/7$). The ground-state multiplet ($J = 5/2$) of the free ion Sm(III) is separated from the first excited multiplet ($J = 7/2$) by only a small energy separation. In consequence, the susceptibilities observed are usually higher in the case of the samarium complex due to the admixture of states, as observed in some reported complexes of samarium(III).⁷¹

To investigate the existence of magnetic anisotropy, ac susceptibility measurements were carried out on the polycrystalline samples of 1–4 in the presence of an oscillating field of 3.5 Oe in the frequency range of 0.1–1500 Hz. None of the compounds shows frequency-dependent out-of-phase ac susceptibility signals (χ'') in the absence of any static magnetic field. This indicates that strong quantum tunnelling of magnetisation (QTM) is operative. As QTM can be quenched or partially suppressed by the application of an external magnetic field, the ac measurements were performed in the presence of an applied field. The field required to quench the QTM varies from molecule to molecule. In a specific external field, called an optimum field, QTM is suppressed to the greatest extent. The ac susceptibility measurements were carried out in the presence of various external fields in the range of 50–4000 Oe at 1.8 K to determine the optimum magnetic field. Non-zero frequency dependent out-of-phase ac susceptibility signals (χ'') were observed for 1 and 3, indicating that 1 and 3 behave as field-induced single-ion magnets. At the same time, 2 and 4 do not exhibit any such behaviour even upon the application of a high dc magnetic field.

In the case of 1, a small dc field of 350 Oe is enough to quench the undesired tunnelling to the greatest extent. Thus, all the ac susceptibility measurements have been carried out in the presence of this optimum dc magnetic field. Under the optimum magnetic field, there exists frequency dependence of out-of-phase magnetic susceptibility (χ'') signals in the temperature range of 1.8 K–3.6 K. The frequency dependent in-phase (χ') and out-of-phase susceptibility (χ'') components are shown in Fig. 5a. There are two distinct relaxation pathways observed corresponding to the high-frequency peaks (fast relaxation, FR) and low-frequency peaks (slow relaxation, SR).⁷²

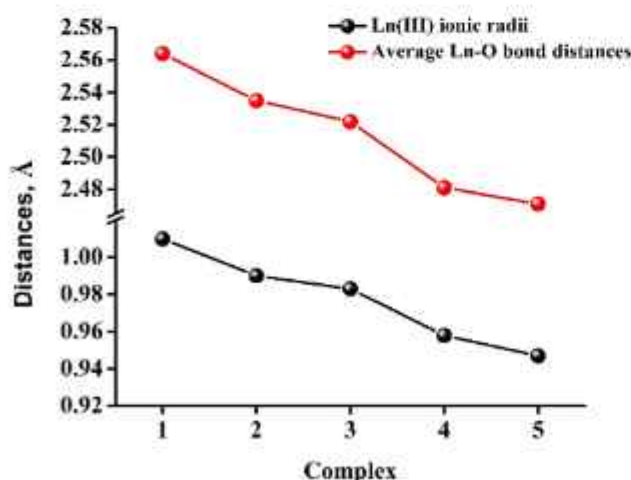


Fig. 4 The plot of average Ln–O bond lengths in 1–5 (red) and ionic radii of different Ln(III) ions in the octahedral symmetry (black). The variation in the average Ln–O bond lengths exactly follows the lanthanide contraction trend. The ionic radii of trivalent lanthanide ions are taken from Shannon–Prewitt ionic radii.⁷⁰

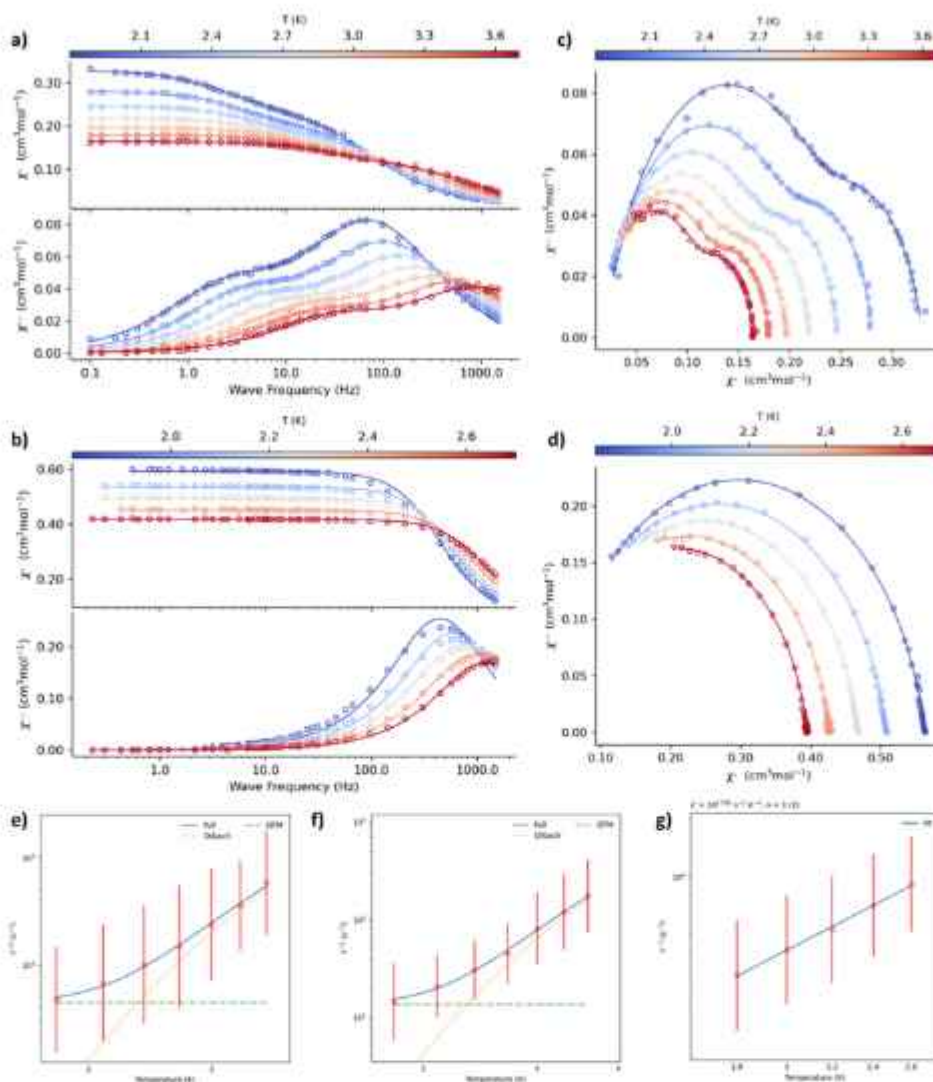


Fig. 5 Frequency-dependent in-phase and out-of-phase susceptibility signals of (a) **1** and (b) **3** in the indicated temperature range in the presence of an external magnetic field (350 Oe for **1** and 1500 Oe for **3**). The Cole–Cole plot of (c) **1** and (d) **3**. The plot of $1/\tau$ vs. T for (e and f) **1** and (g) **3**. The plots for **1** are well fitted by considering the Orbach (dotted red) and QTM (dotted green) processes (5e corresponds to SR and 5f corresponds to FR), while those of **3** are well fitted by considering the Raman process.

The two-semicircle shaped Cole–Cole plot (χ' vs. χ'') of **1** also confirms the existence of two relaxation processes (Fig. 5c). Thus the plot is well-fitted to a modified Debye model, by considering two relaxation pathways, indicating the presence of a narrow distribution of relaxation time ($0.11 < \alpha_1 < 0.17$ and $0.18 < \alpha_2 < 0.27$) (Table S9†). The temperature dependence of relaxation time (τ) associated with **1** has been estimated by plotting $1/\tau$ vs. T (Fig. 5e and f). The nonlinearity of the $1/\tau$ vs. T plot indicates the existence of more than one relaxation process in the relaxation dynamics of **1**. The dependency of relaxation time on temperature is different for different types of relaxation processes, except quantum tunnelling of magnetisation (QTM), which is not dependent on temperature. This can be summarised as follows:

$$1/\tau = 1/\tau_{\text{QTM}} + AT + CT^n + \tau_0^{-1} \exp(-U_{\text{eff}}/k_B T) \quad (1)$$

where the first term on the right-hand side of eqn (1) denotes the relaxation of magnetisation through QTM, the second and third terms represent the relaxation *via* direct and Raman processes, respectively, and the last term corresponds to the thermally-assisted Orbach relaxation pathway.

The high temperature region of the $1/\tau$ vs. T plot is linearly fitted well using the Arrhenius equation, $\tau^{-1} = \tau_0^{-1} \exp(-U_{\text{eff}}/k_B T)$, estimating $U_{\text{eff}} = 16.4(9)$ K, $\tau_0 = 6(1) \times 10^{-5}$ s for fast relaxation (FR) and $U_{\text{eff}} = 16.3(2)$ K, $\tau_0 = 2(1) \times 10^{-6}$ s for slow relaxation (SR). The overall $1/\tau$ vs. T plot can be best fitted by considering the Orbach and QTM pathways ($\tau_{\text{QTM}} = 0.079$ s in FR and 0.0025 s in SR). Even if the barrier heights for both the FR and SR are the same, there are two distinct relaxation processes (Fig. 5a and c). This is likely due to two structurally similar Ce(III) monomers possibly having different extents of dominance of QTM and Orbach processes in the overall relax-

ation dynamics of **1**. These barrier heights associated with **1** are comparable with those of the previously reported Ce(III) based single-ion magnets (Table 1).^{34,49–52,73–75} The fitting of the nonlinear plot of $1/\tau$ vs. T is depicted in Fig. 5e and f.

Similar to **1**, χ'' signals are absent in the case of **3** in the absence of any bias magnetic field. Thus, the optimum field is determined by collecting χ'' signals at 1.8 K in the frequency range of 0.1–1500 Hz from 0 to 4000 Oe (Fig. S14†). The QTM functioning on **3** is suppressed/quenched to the greatest extent in the presence of the optimum dc field, viz. 1500 Oe. Under this optimum field, frequency and temperature dependent χ'' signals were observed in the temperature range of 1.8–2.6 K. The frequency-dependent in-phase (χ') and out-of-phase susceptibility (χ'') components for **3** are depicted in Fig. 5b which clearly show a single maximum over the whole frequency range which shifts towards higher frequency on increasing temperature. The Cole–Cole plot of **3** confirms that the single relaxation process is operative throughout the relaxation, unlike **1**. The Cole–Cole plot is fitted with a generalised Debye equation (Fig. 5d). The fitting shows a very narrow distribution of the relaxation time with an α range of 0.08 to 0.11 (Table S10†). The temperature dependence of the relaxation time (τ) for **3** can be obtained by plotting $1/\tau$ vs. T . The linear plot of $1/\tau$ vs. T can be well fitted by the Orbach process, considering the Arrhenius equation, with $U_{\text{eff}} = 6.0$ K and $\tau_0 = 1.0 \times 10^{-5}$ s. However, at a low temperature range (up to 3 K), the Raman and the QTM processes are operative over the Orbach process. Attempts to fit the plot considering different combinations of relaxation processes other than the Orbach process were not successful. This plot can be best fitted by considering only the Raman process with the parameters $C = 10^{2.7(8)}$ s⁻¹ K⁻ⁿ and $n = 3(2)$. Thus, the slow relaxation of magnetisation dynamics in **3** is dominated by the Raman process.

The ac susceptibility measurements on **2** and **4** were also carried out to find whether these molecules can possess any slow relaxation of magnetisation behaviour. However, there are no significant frequency dependent in-phase and out-of-phase magnetic susceptibility signals observed even in the presence of an external magnetic field. This suggests that **2** and **4** do not behave as single-ion magnets.

Theoretical calculations

To get further insight into the magnetisation relaxation, *ab initio* CASSCF/RASSI-SO/SINGLE_ANISO calculations were performed on complexes **1** and **3** using the MOLCAS 8.2 program package. The Ce(III) and Nd(III) ions possess 4f¹ and 4f³ electron configurations, resulting in the ²F_{5/2} and ⁴I_{9/2} ground states, respectively. The *ab initio* calculations unveil axial anisotropy in both complexes with relatively large g_z values (Tables 4 and 5). We have estimated the crystal field parameters in both complexes using the Stevens Hamiltonian,

$$\hat{H}_{\text{CF}} = \sum_{k=2,4,6} \sum_{q=-k}^{q=k} B_k^q \hat{O}_k^q, \text{ where } B_k^q \text{ is the crystal field parameter}$$

(CFP) and \hat{O}_k^q is the Stevens operator. The probability of QTM becomes higher when non-axial terms ($k = 2, 4, 6$ and $q \neq 0$) are larger than or comparable to the axial terms ($k = 2, 4, 6$

Table 4 The CASSCF/RASSI-SO/SINGLE_ANISO calculated g tensor, m_j composition and g_{zz} angles of three ground state KDs of **1**

Energy (cm ⁻¹)	g_x	g_y	g_z	m_j composition	Angle between g_{zz} of higher KDs with KD1 (°)
0.0	0.553	0.784	3.670	0.96 +5/2>	
467.0	0.134	0.947	2.523	0.83 +3/2>+0.13 +1/2>	46.5
978.8	0.589	1.642	3.261	0.85 +1/2>+0.13 +3/2>	76.7

Table 5 CASSCF/RASSI-SO/SINGLE_ANISO calculated g tensor, m_j composition and g_{zz} angles of three ground state KDs of **3**

Energy (cm ⁻¹)	g_x	g_y	g_z	m_j composition	Angle between g_{zz} of higher KDs with KD1 (°)
0.0	0.590	1.041	5.390	0.85 +9/2>+0.06 +1/2>	
185.3	3.180	1.906	0.357	0.48 +7/2>+0.35 +5/2>+0.11 +3/2>	27.5
256.1	0.570	1.704	4.250	0.42 +3/2>+0.39 +5/2>+0.06 +7/2>	111.3
366.0	0.029	0.889	4.019	0.54 +1/2>+0.24 +3/2>+0.12 +7/2>	90.2
480.0	0.343	0.866	4.432	0.30 +7/2>+0.28 +1/2>+0.20 +5/2>+0.18 +3/2>	94.6

and $q = 0$). Here, the negative B_k^q values indicate the significant axiality in both complexes (Table 4). The computed g tensor ($g_x = 0.553$, $g_y = 0.784$ and $g_z = 3.670$ for **1** and $g_x = 0.590$, $g_y = 1.041$ and $g_z = 5.390$ for **3**, see Tables 4 and 5) reveals significant transverse anisotropy in the ground KD which is also reflected in the calculated non-negligible QTM values of ca. $0.20 \mu_B$ (see Fig. 6a–d). The ground states of complexes **1** and **3** are found to possess a dominant contribution from $m_j = |±5/2\rangle$ and $m_j = |±9/2\rangle$, respectively, where non-negligible mixing among other states explains the field-induced SIM behaviour of both complexes. The orientation of the computed g_{zz} axis is shown in Fig. 6. Basically, it is oriented in such a way that it avoids the oblate 4f electron density in the ground state and the 4f electron density lies along the longest metal–ligand bond. A very large QTM computed reveals that these molecules are unlikely to exhibit SIM behaviour in a zero field, as observed in the experiments. However, if a very large magnetic field is applied, this may partially quench the QTM at the ground state allowing relaxation *via* the first excited state. As demonstrated in the experiments, the optimum fields for **1** and **3** are 350 Oe and 1500 Oe, respectively. We have then extended the mechanism to the first excited state, assuming complete quenching of the ground state QTM, although this is expected to overestimate the theoretical barrier height.

The computed three KDs (belonging to ²F_{5/2}) for **1** are found to span up to 978.8 cm⁻¹, while the five KDs (belonging to ⁴I_{9/2}) for **3** span up to 480.0 cm⁻¹. The first excited KDs show significant mixing among m_j states ($m_j = |±3/2\rangle$ and $|±7/2\rangle$ are dominant for **1** and **3**, respectively) which leads to the very large transverse anisotropy ($g_x = 0.134$, $g_y = 0.947$ and $g_z =$

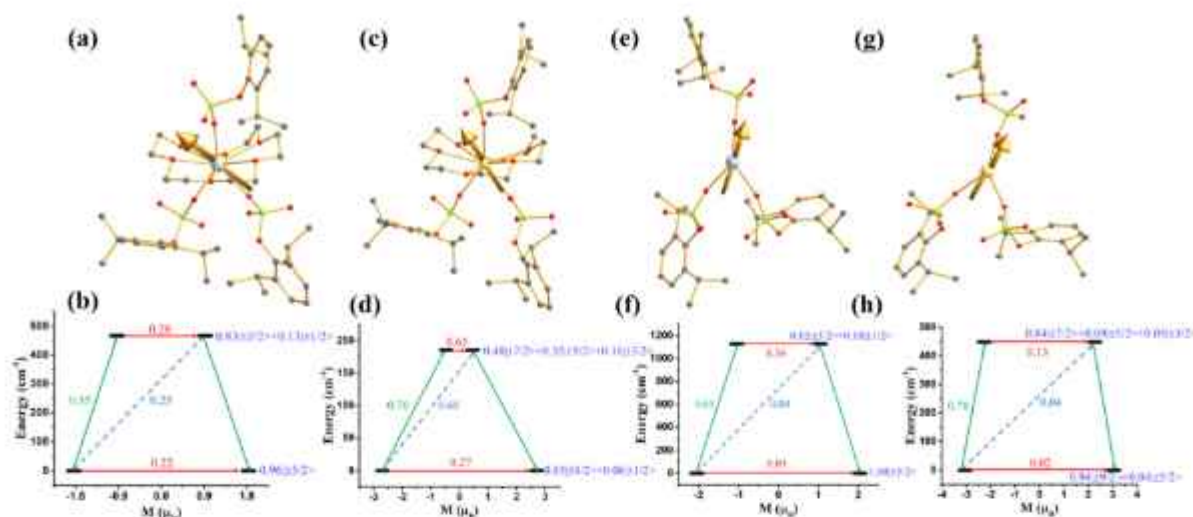


Fig. 6 The computed g_{zz} axis of the ground state of complexes (a) **1**, (c) **3**, (e) **1a**, and (g) **3a**. Colour code: Ce, blue white; Nd, yellow; P, green; O, red; C, grey. Hydrogen atoms are omitted for clarity. The mechanism of magnetisation relaxation of (b) **1** (d) **3** (f) **1a** and (h) **3a**. Here, the red arrows denote the QTM *via* the ground state and TA-QTM *via* the first excited state. The blue arrow denotes the Orbach process, and the green arrow signifies the most probable pathway of magnetisation relaxation. The blue characters represent the m_j composition of a KD.

2.523 for **1** and $g_x = 3.180$, $g_y = 1.906$ and $g_z = 0.357$ for **3**, see Tables 4 and 5). This promotes significant TA-QTM (thermally assisted QTM) for magnetisation relaxation. On the other hand, the g_{zz} axis of the first excited KDs strongly deviates from that of the ground KDs, reinforcing the magnetisation relaxation *via* the first excited KDs (Tables 4 and 5). This results in the U_{cal} values of 467.0 and 185.3 cm^{-1} for complexes **1** and **3**, respectively. The computed U_{cal} values are significantly overestimated compared to the experimental U_{eff} values, as expected. The larger U_{cal} value of **1** than that of **3** can be explained by the larger value of B_2^0 CFP in the former than that in the latter (Table S11†). This is also correlated with the computed L_{oprop} charges, where the charges in the crown ether are lower in **1** than in **3**, resulting in a stronger stabilisation of the oblate electron density in the former (see Table S12†).

To determine the role of equatorial crown ether in the magnetisation relaxation dynamics, we removed 18-crown-6 from complexes **1** and **3**, resulting in models **1a** and **3a**, respectively (Fig. 6e and h). The *ab initio* calculations on models **1a** and **3a** reveal quenching of QTM in the ground KDs, which is reflected in the smaller transverse anisotropies ($g_x = 0.063$, $g_y = 0.134$, and $g_z = 4.089$ for **1a** and $g_x = 0.049$, $g_y = 0.062$, and $g_z = 6.096$ for **3a**, see Fig. 6f, h and Tables S13, S14†). This is also reflected in the large B_2^0 CF parameter and an almost pure m_j ground state (Tables S11, S13 and S14). Furthermore, the computed KDs are found to span up to 2179.1 and 830.3 cm^{-1} in **1a** and **3a**, respectively, two times larger than those in **1** and **3** (Fig. 6f and h). The magnetisation relaxation occurs *via* the second excited KDs due to the significant TA-QTM and large deviation of the g_x axis with the ground state. This results in the U_{cal} values of 1128.2 and 449.6 cm^{-1} for **1a** and **3a**, respectively. A large increase in the U_{cal} value in the model complexes

can be ascribed to a large equatorial ligand field from six oxygen donor atoms of the crown ligand and also its non-planarity. Therefore, to increase the blocking barrier, the number of donor atoms in the crown ligand can be decreased. Removing one of the organophosphates at the axial position by employing a bulkier phosphate would also significantly strengthen the axiality and improve the SIM characteristics.

Conclusions

By placing an equatorial ligand field through hexadentate 18-crown-6 and facilitating further coordination using a bulky phosphate (dippH₂) or water ligand in the axial positions, five new mononuclear early Ln(III) organophosphates have been synthesised and characterised. Single-crystal X-ray diffraction studies reveal that the Ln(III) centres in all five complexes are in a muffin-shaped coordination sphere, where the equatorial plane is occupied by 18-crown-6 molecules while three phosphates are present in the axial positions in **1–3** or two phosphates along with one water are present in the axial positions in **4** and **5**. Such structural modifications are attributable to lanthanide contraction. Both dc and ac susceptibility measurements carried out on **1–4** reveal that **1** and **3** exhibit slow relaxation of magnetisation in the presence of an applied magnetic field. The relaxation dynamics associated with the slow relaxation of magnetisation of **1** and **3** have been investigated in detail, unveiling a rare pair of field-induced Ce and Nd SIMs with a performance similar to that of a handful of examples reported so far. The CASSCF calculations reveal that the ligand stabilises the highest m_j as the ground state for both the Ce and Nd complexes, but the transverse anisotropy is significant which facilitates strong ground state QTM effects. Efforts are

underway in our laboratory to improve the SIM characteristics further by designing bulkier organophosphate ligands.

Conflicts of interest

There are no conflicts to declare.

Acknowledgements

We thank the SERB (SB/SJF/2019-20/12; SPR/2019/001145; CRG/2022/001697) for funding. S. D. thanks the IITB for an IPDF fellowship.

References

- R. Sessoli, D. Gatteschi, A. Caneschi and M. Novak, Magnetic bistability in a metal-ion cluster, *Nature*, 1993, **365**(6442), 141–143.
- F. Donati, S. Rusponi, S. Stepanow, C. Wackerlin, A. Singha, L. Persichetti, R. Baltic, K. Diller, F. Patthey and E. Fernandes, Magnetic remanence in single atoms, *Science*, 2016, **352**(6283), 318–321.
- F. D. Natterer, K. Yang, W. Paul, P. Willke, T. Choi, T. Greber, A. J. Heinrich and C. P. Lutz, Reading and writing single-atom magnets, *Nature*, 2017, **543**(7644), 226–228.
- N. Ishikawa, M. Sugita, T. Ishikawa, S.-Y. Koshihara and Y. Kaizu, Lanthanide double-decker complexes functioning as magnets at the single-molecular level, *J. Am. Chem. Soc.*, 2003, **125**(29), 8694–8695.
- S. K. Gupta and R. Murugavel, Enriching lanthanide single-ion magnetism through symmetry and axiality, *ChemComm*, 2018, **54**(30), 3685–3696.
- D. N. Woodruff, R. E. Winpenny and R. A. Layfield, Lanthanide single-molecule magnets, *Chem. Rev.*, 2013, **113**(7), 5110–5148.
- F.-S. Guo, B. M. Day, Y.-C. Chen, M.-L. Tong, A. Mansikkamaki and R. A. Layfield, Magnetic hysteresis up to 80 kelvin in a dysprosium metallocene single-molecule magnet, *Science*, 2018, **362**(6421), 1400–1403.
- C. A. Goodwin, F. Ortu, D. Reta, N. F. Chilton and D. P. Mills, Molecular magnetic hysteresis at 60 kelvin in dysprosocenium, *Nature*, 2017, **548**(7668), 439–442.
- P. Evans, D. Reta, G. F. Whitehead, N. F. Chilton and D. P. Mills, Bis-monophospholyl dysprosium cation showing magnetic hysteresis at 48 K, *J. Am. Chem. Soc.*, 2019, **141**(50), 19935–19940.
- P. C. Stamp and A. Gaita-Arino, Spin-based quantum computers made by chemistry: hows and whys, *J. Mater. Chem.*, 2009, **19**(12), 1718–1730.
- M. N. Leuenberger and D. Loss, Quantum computing in molecular magnets, *Nature*, 2001, **410**(6830), 789–793.
- G. Arom, D. Aguila, P. Gamez, F. Luis and O. Roubeau, Design of magnetic coordination complexes for quantum computing, *Chem. Soc. Rev.*, 2012, **41**(2), 537–546.
- M. Affronte, Molecular nanomagnets for information technologies, *J. Mater. Chem.*, 2009, **19**(12), 1731–1737.
- M. Urdampilleta, S. Klyatskaya, J.-P. Cleuziou, M. Ruben and W. Wernsdorfer, Supramolecular spin valves, *Nat. Mater.*, 2011, **10**(7), 502–506.
- A. R. Rocha, V. M. Garcia-Suarez, S. W. Bailey, C. J. Lambert, J. Ferrer and S. Sanvito, Towards molecular spintronics, *Nat. Mater.*, 2005, **4**(4), 335–339.
- R. Vincent, S. Klyatskaya, M. Ruben, W. Wernsdorfer and F. Balestro, Electronic read-out of a single nuclear spin using a molecular spin transistor, *Nature*, 2012, **488**(7411), 357–360.
- M. Mannini, F. Pineider, P. Sainctavit, C. Danieli, E. Otero, C. Sciancalepore, A. M. Talarico, M.-A. Arrio, A. Cornia, D. Gatteschi and R. Sessoli, Magnetic memory of a single-molecule quantum magnet wired to a gold surface, *Nat. Mater.*, 2009, **8**(3), 194–197.
- R. E. Winpenny, Quantum information processing using molecular nanomagnets as qubits, *Angew. Chem., Int. Ed.*, 2008, **47**(42), 7992–7994.
- S. G. McAdams, A.-M. Ariciu, A. K. Kostopoulos, J. P. Walsh and F. Tuna, Molecular single-ion magnets based on lanthanides and actinides: Design considerations and new advances in the context of quantum technologies, *Coord. Chem. Rev.*, 2017, **346**, 216–239.
- K. L. Harriman, D. Errulat and M. Murugesu, Magnetic axiality: Design principles from molecules to materials, *Trends Chem.*, 2019, **1**(4), 425–439.
- M. Dey and N. Gogoi, Geometry-Mediated Enhancement of Single-Ion Anisotropy: A Route to Single-Molecule Magnets with a High Blocking Temperature, *Angew. Chem., Int. Ed.*, 2013, **52**(49), 12780–12782.
- Y. Rechkemmer, F. D. Breitgoff, M. Van Der Meer, M. Atanasov, M. Haki, M. Orlita, P. Neugebauer, F. Neese, B. Sarkar and J. Van Slageren, A four-coordinate cobalt(II) single-ion magnet with coercivity and a very high energy barrier, *Nat. Commun.*, 2016, **7**(10467), 10467.
- Z. Zhu, C. Zhao, T. Feng, X. Liu, X. Ying, X.-L. Li, Y.-Q. Zhang and J. Tang, Air-stable chiral single-molecule magnets with record anisotropy barrier exceeding 1800 K, *J. Am. Chem. Soc.*, 2021, **143**(27), 10077–10082.
- Z. Zhu and J. Tang, Metal-metal bond in lanthanide single-molecule magnets, *Chem. Soc. Rev.*, 2022, **51**, 9469–9481.
- A. Borah and R. Murugavel, Magnetic relaxation in single-ion magnets formed by less-studied lanthanide ions Ce(III), Nd(III), Gd(III), Ho(III), Tm(II/III) and Yb(III), *Coord. Chem. Rev.*, 2022, **453**, 214288.
- Z. Zhu and J. Tang, Lanthanide single-molecule magnets with high anisotropy barrier: where to from here?, *Natl. Sci. Rev.*, 2022, **9**(12), nwac194.
- A. Borah, S. Dey, S. K. Gupta, M. G. Walawalkar, G. Rajaraman and R. Murugavel, Enhancing the barrier

- height for Yb (iii) single-ion magnets by modulating axial ligand fields, *ChemComm*, 2020, **56**(79), 11879–11882.
- 28 P. K. Deheri, V. Swaminathan, S. D. Bhamé, Z. Liu and R. V. Ramanujan, Sol–gel based chemical synthesis of Nd₂Fe₁₄B hard magnetic nanoparticles, *Chem. Mater.*, 2010, **22**(24), 6509–6517.
- 29 A. K. Pathak, M. Khan, K. A. Gschneidner Jr., R. W. McCallum, L. Zhou, K. Sun, K. W. Dennis, C. Zhou, F. E. Pinkerton and M. J. Kramer, Cerium: an unlikely replacement of dysprosium in high performance Nd–Fe–B permanent magnets, *Adv. Mater.*, 2015, **27**(16), 2663–2667.
- 30 J. D. Rinehart and J. R. Long, Exploiting single-ion anisotropy in the design of f-element single-molecule magnets, *Chem. Sci.*, 2011, **2**(11), 2078–2085.
- 31 F. A. Mautner, F. Bierbaumer, R. C. Fischer, A. N. Tubau, S. Speed, E. Ruiz, S. S. Massoud, R. Vicente and S. Gómez-Coca, Insights into the Spin Dynamics of Mononuclear Cerium(III) Single-Molecule Magnets, *Inorg. Chem.*, 2022, **61**, 11124–11136.
- 32 A. B. Canaj, S. Dey, E. R. Martí, C. Wilson, G. Rajaraman and M. Murrie, Insight into D_{6h} Symmetry: Targeting Strong Axiality in Stable Dysprosium(III) Hexagonal Bipyramidal Single-Ion Magnets, *Angew. Chem., Int. Ed.*, 2019, **58**(40), 14146–14151.
- 33 Z. H. Li, Y. Q. Zhai, W. P. Chen, Y. S. Ding and Y. Z. Zheng, Air-Stable Hexagonal Bipyramidal Dysprosium(III) Single-Ion Magnets with Nearly Perfect D_{6h} Local Symmetry, *Chem. – Eur. J.*, 2019, **25**(71), 16219–16224.
- 34 H. Wada, S. Ooka, T. Yamamura and T. Kajiwara, Light lanthanide complexes with crown ether and its Aza derivative which show slow magnetic relaxation behaviors, *Inorg. Chem.*, 2017, **56**(1), 147–155.
- 35 Y.-S. Ding, T. Han, Y.-Q. Hu, M. Xu, S. Yang and Y.-Z. Zheng, Syntheses, structures and magnetic properties of a series of mono- and di-nuclear dysprosium(III)-crown-ether complexes: effects of a weak ligand-field and flexible cyclic coordination modes, *Inorg. Chem. Front.*, 2016, **3**(6), 798–807.
- 36 E. L. Gavey, M. Al Hareri, J. Regier, L. D. Carlos, R. A. Ferreira, F. S. Razavi, J. M. Rawson and M. Pilkington, Placing a crown on Dy III—a dual property Ln III crown ether complex displaying optical properties and SMM behaviour, *J. Mater. Chem. C*, 2015, **3**(29), 7738–7747.
- 37 F. Gao, F.-L. Yang, X. Feng, H. Xu, W. Sun, H. Liu and X.-L. Li, Half-sandwich lanthanide crown ether complexes with the slow relaxation of magnetization and photoluminescence behaviors, *Dalton Trans.*, 2017, **46**(4), 1317–1323.
- 38 A. K. Bar, P. Kalita, M. K. Singh, G. Rajaraman and V. Chandrasekhar, Low-coordinate mononuclear lanthanide complexes as molecular nanomagnets, *Coord. Chem. Rev.*, 2018, **367**, 163–216.
- 39 S. K. Gupta, S. K. Langley, K. Sharma, K. S. Murray and R. Murugavel, Pentanuclear lanthanide mono-organophosphates: synthesis, structure, and magnetism, *Inorg. Chem.*, 2017, **56**(7), 3946–3960.
- 40 S. K. Gupta, G. A. Bhat and R. Murugavel, Lanthanide organophosphate spiro polymers: synthesis, structure, and magnetocaloric effect in the gadolinium polymer, *Inorg. Chem.*, 2017, **56**(15), 9071–9083.
- 41 S. K. Gupta, A. A. Dar, T. Rajeshkumar, S. Kuppaswamy, S. K. Langley, K. S. Murray, G. Rajaraman and R. Murugavel, Discrete {Gd III₄ M}(M = Gd III or Co II) pentanuclear complexes: a new class of metal-organophosphate molecular coolers, *Dalton Trans.*, 2015, **44**(13), 5961–5965.
- 42 K. Sharma, S. K. Gupta, A. Borah and R. Murugavel, Hitherto unknown eight-connected frameworks formed from A₄B₄O₁₂ metal organophosphate heterocubanes, *ChemComm*, 2019, **55**(55), 7994–7997.
- 43 Q.-W. Li, R.-C. Wan, Y.-C. Chen, J.-L. Liu, L.-F. Wang, J.-H. Jia, N. F. Chilton and M.-L. Tong, Unprecedented hexagonal bipyramidal single-ion magnets based on metallacrowns, *ChemComm*, 2016, **52**(91), 13365–13368.
- 44 X. Cai, Z. Cheng, Y. Wu, R. Jing, S.-Q. Tian, L. Chen, Z.-Y. Li, Y.-Q. Zhang, H.-H. Cui and A. Yuan, Tuning the Equatorial Negative Charge in Hexagonal Bipyramidal Dysprosium(III) Single-Ion Magnets to Improve the Magnetic Behavior, *Inorg. Chem.*, 2022, **61**(8), 3664–3673.
- 45 W. Zhao, H. Cui, X.-Y. Chen, G. Yi, L. Chen, A. Yuan and C.-L. Luo, An eight-coordinate ytterbium complex with a hexagonal bipyramid geometry exhibiting field-induced single-ion magnet behaviour, *Dalton Trans.*, 2019, **48**(17), 5621–5626.
- 46 J. Li, S. Gómez-Coca, B. S. Dolinar, L. Yang, F. Yu, M. Kong, Y.-Q. Zhang, Y. Song and K. R. Dunbar, Hexagonal bipyramidal Dy(III) complexes as a structural archetype for single-molecule magnets, *Inorg. Chem.*, 2019, **58**(4), 2610–2617.
- 47 Y.-S. Ding, W. J. Blackmore, Y.-Q. Zhai, M. J. Giansiracusa, D. Reta, I. Vitorica-Yrezabal, R. E. Winpenny, N. F. Chilton and Y.-Z. Zheng, Studies of the Temperature Dependence of the Structure and Magnetism of a Hexagonal-Bipyramidal Dysprosium(III) Single-Molecule Magnet, *Inorg. Chem.*, 2021, **61**(1), 227–235.
- 48 C. Zhao, Z. Zhu, X.-L. Li and J. Tang, Air-stable chiral mono- and dinuclear dysprosium single-molecule magnets: steric hindrance of hexaazamacrocycles, *Inorg. Chem. Front.*, 2022, **9**(16), 4049–4055.
- 49 J. J. Le Roy, I. Korobkov, J. E. Kim, E. J. Schelter and M. Murugesu, Structural and magnetic conformation of a cerocene [Ce(CO)⁺]₂—exhibiting a uniconfigurational f¹ ground state and slow-magnetic relaxation, *Dalton Trans.*, 2014, **43**(7), 2737–2740.
- 50 A. Upadhyay, K. R. Vignesh, C. Das, S. K. Singh, G. Rajaraman and M. Shanmugam, Influence of the ligand field on the slow relaxation of magnetization of unsymmetrical monomeric lanthanide complexes: synthesis and theoretical studies, *Inorg. Chem.*, 2017, **56**(22), 14260–14276.
- 51 M.-X. Xu, Y.-S. Meng, J. Xiong, B.-W. Wang, S.-D. Jiang and S. Gao, Magnetic anisotropy investigation on light lanthanide complexes, *Dalton Trans.*, 2018, **47**(6), 1966–1971.

- 52 S. K. Gupta, S. Shanmugan, T. Rajeshkumar, A. Borah, M. Damjanović, M. Schulze, W. Wernsdorfer, G. Rajaraman and R. Murugavel, A single-ion single-electron cerrous magnet, *Dalton Trans.*, 2019, **48**(42), 15928–15935.
- 53 F. A. Mautner, F. Bierbaumer, R. C. Fischer, Å. Tubau, S. Speed, E. Ruiz, S. S. Massoud, R. Vicente and S. Gómez-Coca, Insights into the Spin Dynamics of Mononuclear Cerium(III) Single-Molecule Magnets, *Inorg. Chem.*, 2022, **61**(29), 11124–11136.
- 54 J.-D. Leng, Q.-Y. Hua, W.-T. Liu, Z.-X. Tao, N.-W. Tan, Y.-F. Wang and W.-Q. Lin, Slow magnetic relaxation of mononuclear complexes based on uncommon Kramers lanthanide ions Ce III, Sm III and Yb III, *Dalton Trans.*, 2022, **51**(33), 12661–12669.
- 55 J. D. Rinehart and J. R. Long, Slow magnetic relaxation in homoleptic trispyrazolylborate complexes of neodymium(III) and uranium(III), *Dalton Trans.*, 2012, **41**(44), 13572–13574.
- 56 J. J. Le Roy, S. I. Gorelsky, I. Korobkov and M. Murugesu, Slow magnetic relaxation in uranium(III) and neodymium(III) cyclooctatetraenyl complexes, *Organometallics*, 2015, **34**(8), 1415–1418.
- 57 H. Wada, S. Ooka, D. Iwasawa, M. Hasegawa and T. Kajiwara, Slow magnetic relaxation of lanthanide(III) complexes with a helical ligand, *Magnetochemistry*, 2016, **2**(4), 43.
- 58 S. K. Gupta, T. Rajeshkumar, G. Rajaraman and R. Murugavel, An unprecedented zero field neodymium(III) single-ion magnet based on a phosphonic diamide, *ChemComm*, 2016, **52**(44), 7168–7171.
- 59 Y.-C. Chen, X.-S. Huang, J.-L. Liu and M.-L. Tong, Magnetic Dynamics of a Neodymium(III) Single-Ion Magnet, *Inorg. Chem.*, 2018, **57**(18), 11782–11787.
- 60 S. Demir, K. R. Meihaus and J. R. Long, Slow magnetic relaxation in a neodymium metallocene tetraphenylborate complex, *J. Organomet. Chem.*, 2018, **857**, 164–169.
- 61 K. Kumar, D. Abe, K. Komori-Orisaku, O. Stefańczyk, K. Nakabayashi, J. R. ShkIROVA, S. P. Tunik and S.-I. Ohkoshi, Neodymium β -diketonate showing slow magnetic relaxation and acting as a ratiometric thermometer based on near-infrared emission, *RSC Adv.*, 2019, **9**(41), 23444–23449.
- 62 J. Li, L. Yin, S.-J. Xiong, X.-L. Wu, F. Yu, Z.-W. Ouyang, Z.-C. Xia, Y.-Q. Zhang, J. van Tol, Y. Song and Z. Wang, Controlling Electron Spin Decoherence in Nd-based Complexes via Symmetry Selection, *IScience*, 2020, **23**(3), 100926.
- 63 W. L. F. Armarego, *Purification of laboratory chemicals*, Butterworth-Heinemann, 2017, vol. 8.
- 64 G. M. Kosolapoff, C. K. Arpke, R. W. Lamb and H. Reich, Structural effects in reactions of organophosphorus compounds. I. Reactions of phosphorus oxychloride with hindered phenols, *J. Chem. Soc. C*, 1968, 815–818.
- 65 O. V. Dolomanov, L. J. Bourhis, R. J. Gildea, J. A. Howard and H. Puschmann, OLEX2: a complete structure solution, refinement and analysis program, *J. Appl. Crystallogr.*, 2009, **42**(2), 339–341.
- 66 G. M. Sheldrick, SHELXT: Integrating space group determination and structure solution, *Acta Crystallogr., Sect. A: Found. Adv.*, 2014, **70**, C1437.
- 67 G. M. Sheldrick, Crystal structure refinement with SHELXL, *Acta Crystallogr., Sect. C: Struct. Chem.*, 2015, **71**(1), 3–8.
- 68 D. Reta and N. F. Chilton, Uncertainty estimates for magnetic relaxation times and magnetic relaxation parameters, *Phys. Chem. Chem. Phys.*, 2019, **21**(42), 23567–23575.
- 69 M. Llunell, D. Casanova, J. Cirera, P. Alemany and S. Alvarez, *SHAPE, version 2.1*, Universitat de Barcelona, Barcelona, Spain, 2013, vol. 2103.
- 70 R. D. Shannon, Revised effective ionic radii and systematic studies of interatomic distances in halides and chalcogenides, *Acta Crystallogr., Sect. A: Found. Adv.*, 1976, **32**(5), 751–767.
- 71 J. Chakraborty, A. Ray, G. Pilet, G. Chastanet, D. Luneau, R. F. Ziessel, L. J. Charbonnière, L. Carrella, E. Rentschler and M. El Fallah, Syntheses, characterisation, magnetism and photoluminescence of a homodinuclear Ln(III)-Schiff base family, *Dalton Trans.*, 2009, (46), 10263–10272.
- 72 Y.-N. Guo, G.-F. Xu, P. Gamez, L. Zhao, S.-Y. Lin, R. Deng, J. Tang and H.-J. Zhang, Two-step relaxation in a linear tetranuclear dysprosium(III) aggregate showing single-molecule magnet behavior, *J. Am. Chem. Soc.*, 2010, **132**(25), 8538–8539.
- 73 T. Shi, Y. Xu, M.-X. Li, C.-M. Liu, E. N. Nfor and Z.-X. Wang, A 10-coordinate cerium(III) complex with a ferrocene-based terpyridine ligand exhibiting field-induced slow magnetic relaxation, *Polyhedron*, 2020, **188**, 114695.
- 74 F. A. Mautner, F. Bierbaumer, R. C. Fischer, Å. Tubau, S. Speed, E. Ruiz, S. S. Massoud, R. Vicente and S. Gómez-Coca, Insights into the Spin Dynamics of Mononuclear Cerium(III) Single-Molecule Magnets, *Inorg. Chem.*, 2022, **61**(29), 11124–11136.
- 75 J.-D. Leng, Q.-Y. Hua, W.-T. Liu, Z.-X. Tao, N.-W. Tan, Y.-F. Wang and W.-Q. Lin, Slow magnetic relaxation of mononuclear complexes based on uncommon Kramers lanthanide ions Ce III, Sm III and Yb III, *Dalton Trans.*, 2022, **51**, 12661–12669.